

**Crystal Engineering to Fabricate Au, Ag, and Au-Ag Alloy
Nanoparticles: Application in Technology, Pathology, and
Theranostics**

By

Sandip Kumar De

CHEM05201504003

Saha Institute of Nuclear Physics, Kolkata

A thesis submitted to the Board of Studies in Chemical Sciences

In partial fulfillment of requirements for the degree of

DOCTOR OF PHILOSOPHY

Of

HOMI BHABHA NATIONAL INSTITUTE



July, 2020



Homi Bhabha National Institute

Evaluation Report¹ of Ph.D. Viva-Voce

Board of Studies in Chemical Sciences

1. Name of the Constituent Institution: Saha Institute of Nuclear Physics, Kolkata

2. Name of the Student: Shri Sandip Kumar De

3. Enrolment Number: CHEM05201504003

4. Date of Enrolment in HBNI: 01 August 2015

5. Date of Submission of Thesis: 31 July 2020

Title of the Thesis: Crystal Engineering to Fabricate Au, Ag, and Au-Ag Alloy Nanoparticles: Application in Technology, Pathology and Theranostics

7. Number of Doctoral Committee Meetings held with respective dates:

Review Period	Date	Review Period	Date
1. 2016-17	22.09.2017	2. 2017-18	25.04.2018
3. 2018-19	26.05.2019	4.	
5.		6.	

8. Name and Affiliation of the Examiner 1: Prof. Rongchao Jin, Dept. of Chemistry, Carnegie Mellon University, Pittsburgh, USA

Recommendations of the Examiner 1 (Thesis Evaluation) (i) accepted, (ii) accepted after revisions, or (iii) rejected:

9. Name and Affiliation of the Examiner 2: Prof. Nikhil R Jana, School of Material Science, Indian Association for Cultivation of Sciences, Kolkata, India

Recommendations of the Examiner 2 (Thesis Evaluation) (i) accepted, (ii) accepted after revisions, or (iii) rejected:

¹ This is to be submitted by Dean-Academic to Central office and is not to be included in the thesis.

Recommendations of the Viva-Voce Board

1. Date of Viva Voce Examination: 22 September 2020

2. Recommendations for the award of the Ph.D. degree: Recommended / ~~Not Recommended~~

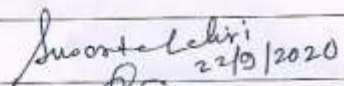



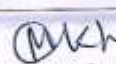
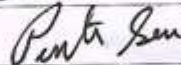
(If Recommended, give summary of main findings and overall quality of thesis)

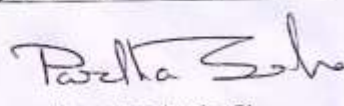
(If Not Recommended, give reasons for not recommending and guidelines to be communicated by Convener of the Doctoral committee to the student for further work)

Shri Sandip Kumar De has submitted a comprehensive thesis, entitled "Crystal Engineering to Fabricate Au, Ag, and Au-Ag Alloy Nanoparticles: Application in Technology, Pathology and Theranostics" where he has introduced the subject of Crystal Engineering followed by utilized these engineered materials for the application in technology, pathology, and theranostics. Based on the quality of the thesis work, knowledge acquired during Ph.D. tenure, good publication record in peer reviewed journals, and the ability to defend his thesis work in front of the External Examiner, Doctoral Committee members and other academic members, we strongly recommend that Shri Sandip Kumar De to be awarded the Ph.D. degree of the Homi Bhabha National Institute.

In case, Not Recommended, another date will be fixed by the Dean-Academic, CI, which shall not be earlier than a month after and not later than six months from the date of first viva.

3. Name and Signature of the Viva Voce Board (Doctoral Committee & External Examiner):

Sr No	Composition	Name	Signature with date
a.	Chairman	Prof. Susanta Lahiri	 22/9/2020
b.	Convener (Guide)	Prof. Dulal Senapati	 22.9.2020.
c.	Co-Guide/External Guide (if any)	None	
d.	External Examiner	Prof. Nikhil R. Jana, IACS-Kolkata	 22/9/2020
e.	Member	Prof. Padmaja Prasad Mishra	 22/09/2020
f.	Member	Prof. Montu K. Hazra	 22/09/2020
g.	Member	Prof. Pintu Sen, VECC	 22/09/2020

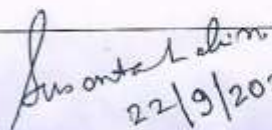

Dean-Academic, CI
28/9/2020

Homi Bhabha National Institute

Recommendations of the Viva Voce Committee

As members of the Viva Voce Committee, we certify that we have read the dissertation prepared by **Shri Sandip Kumar De** entitled "**Crystal Engineering to Fabricate Au, Ag, and Au-Ag Alloy Nanoparticles: Application in Technology, Pathology and Theranostics**" and recommend that it may be accepted as fulfilling the thesis requirement for the award of Degree of Doctor of Philosophy.

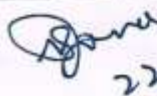
Chairman - Prof. Susanta Lahiri


22/9/2020

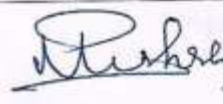
Guide / Convener - Prof. Dulal Senapati


22.9.2020

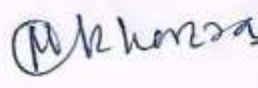
Examiner - Prof. Nikhil R. Jana, IACS-Kolkata


22/9/2020

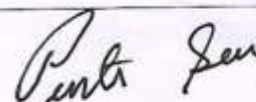
Member 1- Prof. Padmaja Prasad Mishra


22/09/2020

Member 2- Prof. Montu K. Hazra


22/09/2020

Member 3- Prof. Pintu Sen, VECC-Kolkata


22/09/2020

Final approval and acceptance of this thesis is contingent upon the candidate's submission of the final copies of the thesis to HBNI.

I hereby certify that I have read this thesis prepared under my direction and recommend that it may be accepted as fulfilling the thesis requirement.

Date: SINP, 22.09.2020

Place: KOLKATA

Signature

Guide


22.09.2020

STATEMENT BY AUTHOR

This dissertation has been submitted in partial fulfillment of requirements for an advanced degree at Homi Bhabha National Institute (HBNI) and is deposited in the Library to be made available to borrowers under rules of HBNI.

Brief quotations from this dissertation are allowable without special permission, provided that accurate acknowledgement of the source is made. Requests for permission for extended quotations from or reproduction of this manuscript in whole or in part may be granted by the Competent Authority of HBNI when in his or her judgment the proposed use of the material is in the interests of scholarship. In all other instances, however, permission must be obtained from the author.

Sandip Kumar De
Sandip Kumar De

DECLARATION

I, hereby declare that the investigation presented in the thesis has been carried out by me. The work is original and has not been submitted earlier as a whole or in part for a degree/diploma at this or any other Institution/University.

Sandip Kumar De
Sandip Kumar De

List of Publications arising from the thesis

Journal

- (1) Crystal-Defect-Induced Facet-Dependent Electrocatalytic Activity of 3D Gold Nanoflowers for the Selective Nanomolar Detection of Ascorbic Acid, De, S. K.; Mondal, S.; Sen, P.; Pal, U.; Pathak, B.; Rawat, K. S.; Bardhan, M.; Bhattacharya, M.; Satpati, B.; De, A.; Senapati, D. *Nanoscale* **2018**, *10* (23), 11091-11102.
<https://doi.org/10.1039/c8nr03087a>.
- (2) Zone-Specific Crystallization and a Porosity-Directed Scaling Marker for the Catalytic Efficacy of Au-Ag Alloy Nanoparticles, De, S. K.; Mondal, S.; Roy, A.; Kumar, S.; Mukherjee, M.; Das Chakraborty, S.; Sen, P.; Pathak, B.; Satpati, B.; Mukhopadhyay, M.; Senapati, D. *ACS Appl. Nano Mater.* **2019**, *2* (12), 7669-7685.
<https://doi.org/10.1021/acsanm.9b01748>.
- (3) Wide Range Morphological Transition of Silver Nanoprisms by Selective Interaction with As(III): Tuning-Detuning of Surface Plasmon Offers to Decode the Mechanism, Das Chakraborty, S.; Mondal, S.; Satpati, B.; Pal, U.; De, S. K.; Bhattacharya, M.; Ray, S.; Senapati, D. *J. Phys. Chem. C* **2019**, *123* (17), 11044-11054.
<https://doi.org/10.1021/acs.jpcc.8b10799>.
- (4) Au-Seeded Ag-Nanorod Networks for Electrocatalytic Sensing, De, S. K.; Kumar, S.; Ray, S.; Mondal, S.; Ray, A.; Bhattacharjee, G.; Nandy, A.; Roy, A.; Pathak, B.; Senapati, D. <https://doi.org/10.1021/acsanm.9c01976>

- (5) Unveiling the Excellent Electrocatalytic Activity of Grain-Boundary Enriched Anisotropic Gold Nanostructures towards Hydrogen Evolution Reaction: A Combined Approach of Experiment and Theory, Mondal, S.; De, S. K.; Jana, R.; Roy, A.; Mukherjee, M.; Datta, A.; Satpati, B.; Senapati, D. **(Under Revision)**
- (6) Fabrication of Highly Specific DNA Based Porous Au-Ag Nanobioconjugate as Electrode Coat for Impedimetric DENV-II Infected Direct Blood Sensing, De, S. K.; Roy, S.; Bhattacharyya, S.; Mondal, S.; Nandy, A.; Roy, A.; Sadhukhan, P.; Senapati, D. **(Communicated Work)**

Sandeep Kumar Pal.

ACKNOWLEDGEMENT

First of all, I would like to acknowledge my thesis supervisor Dr. Dulal Senapati for giving me academic freedom throughout my doctoral tenure. He has given me support with scientific discussion and proper guidance. I was a student from Organic Chemistry, and was introduced to a new field, Nanoscience and Nanotechnology in my PhD. My supervisor stands by me all the time by encouraging my motivation and by planning a perfect project with appropriate experimental and theoretical approaches. I would like to acknowledge my past and present HODs of our Chemical Sciences Division (CSD), Professor Samita Basu & Professor Susanta Lahiri, for sharing their scientific ideas with me and providing all academic help throughout my PhD tenure. A special thanks to Prof. Pintu Sen from Variable Energy Cyclotron Centre (VECC) for allowing me to use his instrumental facilities. I would like to express my sincere gratitude to Dr. Padmaja P. Mishra, Dr. Montu K. Hazra, Prof. Maitreyee Nandi, Prof. Munna Sarkar and all other CSD members along with Prof. Tapas Chini, Prof. Manabendra Mukherjee, Dr. Biswarup Satpati, Dr. Mrinmay Mukherjee, Prof. Sangam Banerjee, Mr. Goutam Sarkar, and Mr. Debraj Dey from Surface Physics and Material Science Division for all their help. I convey my sincere acknowledgement to Prof. Biswarup Pathak from IIT Indore for sharing his vast knowledge in theoretical simulation with our group. Throughout my PhD tenure, my lab members were part of my life. I express my thanks to my senior colleagues Dr. Subrata Mondal, Dr. Sarmistha Ray, Dr. Munmun Bardhan, Dr. Uttam Pal, Dr. Maitreyee Bhattacharya, Dr. Sudeshna Das Chakraborty and my junior colleagues Arpita, Anuradha, Sourav, and Manorama along with my Post-MSc friends. I feel lucky to get such parents who acted as supportive friends to assist me in all aspects of my life. I express my sincere thanks to our Guruji Sri Anukulchandra Chakravarty to appear as a philosopher in my life. My brother Subhadeep and sister Bunty are more than family member to me.

Contents:

Chapter-1: Introduction

1. Introduction.....	1
1.1 Zero-dimensional point defects.....	3
1.1a Vacancies.....	3
1.1b Interstitials.....	3
1.1c Impurities.....	5
1.1d Schottky defect and Frenkel defect.....	5
1.2 One dimensional line defects.....	6
1.2a Edge dislocation.....	6
1.2b Screw dislocation.....	6
1.3 Two-dimensional planer defects.....	8
1.3a Grain Boundary.....	8
1.3b Twin Boundary.....	9
1.3c Stacking Fault.....	10
1.4 3D Defects.....	11
1.5 Application of noble metal nanocatalyst in Pathological Industry.....	12
1.5a Sensing of Metabolites.....	12
1.5b Sensing of Trace Metal Ions.....	16
1.5c Sensing of Virus.....	18
1.6. Application in Fuel Cell Technology.....	21
1.6a Alcohol Fuel Cell.....	21
1.6b ORR activity.....	23
1.6c Reduction of CO ₂	24
1.6d HER and OER.....	26

1.7Theranostics Application of Plasmonic Noble Metal Nanoalloy.....	27
---	----

Chapter-2: Methodology and Experimental Set Up

2.1 Chemical Materials.....	30
2.2 Biochemical Materials.....	31
2.3 Biological materials.....	31
2.4 Methods.....	32
2.4.1 Ultraviolet-Visible-NearInfrared (UV-Vis-NIR) Absorption Spectroscopy.....	32
2.4.2 Dynamic Light Scattering and Zeta Potential Measurement.....	34
2.4.3 X-ray Photoelectron Spectroscopy.....	37
2.4.4 X-ray Diffraction Spectroscopy.....	39
2.4.5 Inductively Coupled Plasma Optical Emission Spectrometry.....	41
2.4.6 Surface-Enhanced Raman Spectroscopy.....	42
2.4.7 Atomic Force Microscopy.....	43
2.4.8 Scanning Electron Microscopy.....	45
2.4.9 Transmission Electron Microscopy.....	47
2.4.10 Electrochemical Measurements.....	49
2.4.10.1 Linear sweep voltammetry.....	50
2.4.10.2 Cyclic Voltammetry.....	51
2.4.10.3 Differential Pulse Voltammetry.....	53
2.4.10.4 Square Wave Voltammetry.....	54
2.4.10.5 Chronoamperometry.....	56
2.4.10.6 Electrochemical Impedance Spectroscopy.....	57

Chapter-3: Crystal Defect Induced Facet Dependent Electrocatalytic Activity of 3D Gold Nanoflower towards the Selective Nanomolar (*nM*) Detection of Ascorbic Acid

Outline.....	58
3.1 Introduction.....	59
3.2 Synthesis of AuNPs.....	62
3.3 Theoretical ab initio simulation.....	63
3.4 Density Functional Theory.....	64
3.5 Results & Discussion.....	64
3.6 Conclusion.....	89

Chapter-4: Zone-Specific Crystallization and a Porosity-Directed Scaling Marker for the Catalytic Efficacy of Au-Ag Alloy Nanoparticles

Outline.....	90
4.1 Introduction.....	91
4.2 Material Synthesis.....	95
4.3 Materials Purification.....	97
4.4 Theoretical Modeling of HNPr.....	97
4.5 Results and Discussion.....	98
4.6 Conclusion.....	136

Chapter-5: Wide Range Morphological Transition of Silver Nanoprism by Selective Interaction with As(III): Tuning-Detuning of Surface Plasmon Offers to Decode the Mechanism

Outline.....	137
5.1 Introduction.....	138
5.2 Synthesis of silver nanoprism.....	141
5.3 Results and Discussion.....	142
5.4 Conclusion.....	163

Chapter-6: Unveiling the Excellent Electrocatalytic Activity of Grain Boundary Enriched Anisotropic Pure Gold Nanostructures towards Hydrogen Evolution Reaction: A Combined Approach of Experiment and Theory

Outline.....	165
6.1 Introduction.....	166
6.2 Synthesis of AuNPs using HQ.....	170
6.3 Computational Details.....	171
6.4 Results and Discussion.....	173
6.4.1 Optical and Structural analysis of A ⁿ GNPs.....	173
6.4.2 Electrocatalytic Performance of A ⁿ GNPs for Hydrogen Evolution Reaction.....	182
6.4.3 Computational Studies.....	200
6.5 Conclusions.....	205

Chapter-7: Au-Seeded Ag-Nanorod-Based Thiol Mediated Strained 2D Network as Non-Enzymatic Universal Electrocatalytic Sensing Platform: A Mechanistic Exploration

Outline.....	206
7.1 Introduction.....	208
7.2 Material synthesis.....	212
7.2.1 Synthesis of Au Nanoseed.....	212
7.2.2 Synthesis of Au-seed induced Ag nanorod.....	213
7.2.3 Synthesis of Au-Ag Network.....	214
7.2.4 Collection and preparation of human serum samples.....	215
7.2.5 Theoretical modeling.....	215
7.3. Results and Discussion.....	216
7.4. Conclusion.....	271

Chapter-8: Fabrication of Highly Specific DNA Based Porous Au-Ag Nanobioconjugate as Electrode Coat for Rapid Impedimetric Direct Sensing of DENV-2 from Infected Whole Blood

Outline.....	272
Discussion.....	273

Chapter- 9A: Synthesis of Ag_{core}Au_{shell} nanostructures and the corresponding NP_{matrix} as a bifunctional catalyst for the fabrication of high throughput alcohol fuel cells

Outline.....	293
9A.1 Introduction.....	294
9A.2 Material Synthesis.....	296
9A.2.1 Synthesis of Au Nanoseed.....	296
9A.2.2 Synthesis of Au-Ag Nano-alloy.....	297
9A.2.3 Synthesis of Ag _{core} Au _{shell} structure by Template Method.....	298
9A.2.4 Synthesis of void Enriched Au-Ag Matrix (NP _{matrix}) by Galvanic Replacement Method.....	298
9A.3 Results and discussion.....	298
9A.4 Conclusion.....	302

Chapter- 9B Fabrication of Ag_{core}Au_{shell} nanostructure-based nanobioconjugate as an anti-dengue assay

Outline.....	303
Discussion.....	304
References.....	307

Thesis Abstract

The present thesis is an in-depth study of crystal growth and design of plasmonic Au, Ag, and Au-Ag alloy nanoparticles along with the observation and role of crystal irregularities like grain boundary, twin boundary, stacking faults, dislocation, etc, within the nanocrystal. The low coordinated crystal defects have been thoroughly studied through high-resolution Transmission Electron Microscopy (HRTEM) to find out the active centers of catalysis. The defect enriched nanostructures were then used for electrocatalytic sensing for different human metabolites and trace metal ions through the implication of Differential Pulse Voltammetry (DPV) and Electrochemical Impedance Spectroscopy (EIS). In **Chapter 1** we have discussed the origin of different crystal defects in various nanoparticles and their application in technology, pathology, theranostics, whereas **Chapter 2** comprises the detailed instrumentation techniques. In **Chapter 3**, we have highlighted the synthesis of different sized and shaped bud to blossom gold nanoflowers and their application in the sensing of Vitamin C. Experimental studies have been supported by theoretical *ab initio* simulation. In **Chapter 4**, we have provided the synthetic protocol of bimetallic Au-Ag nano prisms with the various extent of porosity at the center of gravity, and their tensile strain-dependent catalytic activity for uric acid oxidation. **Chapter 5** highlights the As^{3+} sensing through colorimetric and spectrometric approaches by studying the morphological transition of Ag nano prisms upon interaction with As^{3+} . **Chapter 6** provides grain boundary dependent hydrogen evolution reaction (HER) study through electrochemical linear sweep voltammetry (LSV) of different Au nanostructures. In **Chapter 7**, we describe the synthesis of porous 2D bimetallic Au-Ag nanoalloy and their application for electrocatalytic sensing of a series of human metabolites and trace metal ions. **Chapter 8** implements the idea of DNA-aptamer-based direct sensing of the DENV-2 virus in real samples through EIS approaches. In **Chapter 9**, we have given our future directions to use Au-Ag nano-alloy for alcohol fuel cell and antiviral assay.

List of Tables:

Table 3.1 Physical and electrostatic parameters of synthesized different flourishing stages of AuNFs.....	66
Table 3.2: Different structural parameters along with their total effective surface area calculated for our synthesized differently flourishing stages of AuNFs.....	68
Table 3.3: Experimental observations and system parameters deduced from DPV and EIS measurement towards the oxidation of AA on different flourishing AuNF coated GC electrode	72
Table 3.4: Density (nm^{-2}) of Different Crystal Defects (dislocation, steps, kinks, islands, and differently packed crystal boundaries) for Various Shaped AuNFs Synthesized at Tunable Concentration (M) of CTAB.....	74
Table 3.5: Calculated reaction free energy for the oxidation of AA on different crystal facets of gold	84
Table 4.1: Compositional Analysis and current responses of different HNPr and HNPr-modified GC electrode based on EDX, XPS, ICP-OES, DPV, SWV measurements.....	117
Table 4.2: Different kinetic parameters for cavity shuffled HNPrs obtained from the EIS measurements. Here R_{CT} indicates the charge transfer resistance, W as the Warburg Impedance, CPE_{as} constant phase element, i_0 as the exchange current, and k_0 as the heterogeneous rate constant.....	124
Table 4.3: Different crystal parameters along with induced strain along (111) basal plane and (220) vicinal plane	133
Table 5.1: Variation of zeta potential (ξ) and stacking length (L) as we vary the molar ratio (M) between NaBH_4 and AgNO_3	149
Table 5.2: Energies obtained at HF/3-21g* level of theory.....	154
Table 5.3: Optimized parameters of Ag_3AsO_3 and Ag_3AsO_4	155
Table 5.4: Variation of pH due to gradual the addition of NaAsO_2 and NaOH to 1mL AgNPr solution.....	159
Table 6.1: Comparison among different parameters related to HER activity of the electrocatalytic performance of different AuNPs in various electrolyte solutions.....	187

Table 6.2: Structural parameters of different A ⁿ GNPs.	200
Table 6.3: The position of DBCs for different AuNP grain boundary surfaces.....	203
Table 7.1: Estimation of developed strain within different Hy-Au@AgNRsand the targeted Hy-Au@AgNR ₈₄₀ -Ass from the measured FWHM (β) and θ values (in radian) in XRD spectra...239	
Table7.2: Theoretical strain calculation on different length rod.....	240
Table7.3: TheI-V responses in DPV for different system Au@AgNR ₈₄₀ -Ass/GC, Au@AgNR ₈₄₀ /GC, Au@AgNR ₄₅₀ /GC,	257
Table 7.4: Peak Potential of different metabolites and trace metal ions in I-V responses of DPV.....	269
Table 8.1: Parameters obtained from the Nyquist plot for DENV-2 as shown in Figure 3A by fitting into the Randles cell.....	289
Table 8.2: parameters obtained from the Nyquist plot for DENV-2 infected real blood samples drawn from 3 different patients.....	291

List of Figures:

Figure 1.1a: Point defect originating from vacancies	3
Figure 1.1b(i): Interstitial point defect created by foreign atom.....	4
Figure 1.1b(ii): Interstitial point defect created by moving an atom from a lattice point to an off-lattice site.....	4
Figure 1.1c: Point defect originating from impurity.....	5
Figure 1.2a: Schematic presentation of edge dislocation.....	6
Figure 1.2b: Schematic representation of edge dislocation and screw dislocation.....	7
Figure 1.2c: Presentation of burger vector.....	8
Figure 1.3a: Schematic Presentation of GB over a crystal lattice.....	9
Figure 1.3b: Schematic presentation of a twin boundary over a fcc lattice.....	10
Figure 1.3c: Schematic Presentation of intrinsic and extrinsic SF in fcc lattice.....	11
Figure 1.4: A fcc lattice with regular arrangement and void enriched arrangement.....	12
Figure 1.5a(i): A. DPV response for AuNP@MoS ₂ modified GCE for AA (1mM to 70mM), DA (0.01μM to 7μM), UA (.01mM to 12mM).	14
Figure 1.5a(ii): DPV responses of individual analytes in physiological concentration limit in presence of other analytes (Ref41).....	15
Figure 1.5b(i): (A) DPV response for AuNP/GC electrode for simultaneous detection of Cd ²⁺ , Pb ²⁺ , Cu ²⁺ , Hg ²⁺ at a time (Ref-43).....	17
Figure 1.5b(ii): Statistical distribution of AuNP used for the detection of different viruses in which HBV is the most reported one for using AuNP as a sensing probe.(Ref-44).....	18
Figure 1.5c: EIS response from the sensor with different concentrations of viral load by using an external pulse. (Ref-45).....	20
Figure 1.6a: Electrooxidation of methanol for different Au-Ag system(Ref-20).....	22

Figure 1.6b. Comparative ORR activity of Different AuNP system.(Ref-48).....	24
Figure 1.6c. Schematic Presentation of the Au-Cu system for selective conversion of CO ₂ to Formate (Ref-49).....	25
Figure 1.6d: OER Polarization curve (Ref-51).....	27
Figure 1.7: Antibacterial activity of Au-Ag NP(ref-55).....	29
Figure 2.1: (A) JASCO V-770 UV-Vis-NIR spectrophotometer with spectral range 190-3200 nm, (B) JASCO V-650 UV-Vis spectrometer fitted with Peltier for temperature dependent study with spectral range 190-900 nm.....	32
Figure 2.2: Optical configurations of the Malvern Zetasizer Nano series for dynamic light scattering measurements	36
Figure 2.3: Malvern Zetasizer ZS90 instrument.....	37
Figure 2.4: Experimental set up and lay out for XPS.....	39
Figure 2.5: Experimental set up and lay out for XRD.....	40
Figure 2.6: Experimental set up and lay out for ICP-OES.....	41
Figure 2.7: (A) Details of the SERS set up, (B) Layout of the instrument.....	42
Figure 2.8: Schematic presentation and picture of AFM.....	45
Figure 2.9: Schematic presentation and picture of SEM.....	47
Figure 2.10: Schematic presentation and picture of TEM.....	49
Figure 2.11: i-t-E curve for LSV (Ref-72).....	51
Figure 2.12: Representative curve for CV(Ref-72).....	52
Figure 2.13: (A) Representative DPV curve, (B) Working principle of DPV (Ref-72)....	54
Figure 2.14: Representative curve for SWV (Ref-72).....	56
Figure 3.1: TEM image of AuNFs.....	65

Figure 3.2: DPV for the oxidation of AA on AuNF modified GC electrode.....	70
Figure 3.3: Randomly selected crystal defects on bud structured AuNF.....	76
Figure 3.4: Different crystal defects on AuNF surfaces.....	77
Figure 3.5: HRTEM image of the bud shaped AuNF.....	78
Figure 3.6: Variation of defect density with different flourishing stages	81
Figure 3.7: Top and Side views of the optimized AA.	83
Figure 3.8: DPV response of AA at lower & higher concentration.....	85
Figure 3.9: optimized geometries of ascorbic acid in presence of gold clusters.....	87
Figure 3.10: Interference test of ascorbic acids.....	88
Figure 4.1: (A), (B) and (C) SEM images of HNPr ₂₅₀ with H ₂ AuCl ₄ .3H ₂ O addition rate (second step of seeded growth) of 1mL/min, 2mL/min and 3mL/min respectively. (D) Absorption spectra of different HNPrs.....	96
Figure 4.2: TEM image of individual HNPr synthesized by using a different amount of Ag seed.	99
Figure 4.3: Histogram of size distribution for each HNPr. 100 TEM frames have been considered for each HNPr to calculate their average edge length.....	100
Figure 4.4: TEM images of time-dependent (A: 10 min, B: 1 h and C: 6h) porosity generation at the center of gravity of HNPr ₂₅₀	102
Figure 4.5: SAED pattern and EDX profile of different HNPr.....	104
Figure 4.6: XRD pattern of HNPr ₅₀ , HNPr ₂₅₀ , and HNPr _{2K}	105
Figure 4.7: Fitted curve of XRD at {111} facet to calculate the strain.....	106
Figure 4.8a: EDX spectra and HAADF-STEM image of HNPr ₁₀₀ for the confirmation of bimetallic (Au-Ag) nature.....	107
Figure 4.8b: EDX spectra and HAADF-STEM image of HNPr ₅₀₀ for the confirmation of bimetallic (Au-Ag) nature.....	108
Figure 4.8c: EDX spectra and HAADF-STEM image of HNPr _{3K} for the confirmation of bimetallic (Au-Ag) nature.....	108

Figure 4.9: XPS study of HNPr ₁₀₀ , HNPr ₂₅₀ , and HNPr _{2K} nanostructures are shown in the top, middle and bottom panel respectively	110
Figure 4.10: XPS survey spectrum of Cl(2p), C(1s) and N(1s) in HNPr ₁₀₀ which confirms their presence in the sample.....	111
Figure 4.11: Porosity and Crystalline zone for different HNPr.....	113
Figure 4.12: Thickness Profile of HNPr ₂₅₀	114
Figure 4.13: Representative twin boundaries on the HNPr ₂₅₀ surface, spotted in three different zones outside the central cavity zone. The twin angle (with reference to the twin boundary) varies in the range of 55–57°	115
Figure 4.14: Appearance of different crystal defects on HNPr surfaces.	118
Figure 4.15: TEM images of the distribution of different grains over individual HNPr surface.....	119
Figure 4.16(a): Presentation of different HNPr ₂₅₀ frames for the calculation of Surface Grain Boundary Density (SGBD).....	120
Figure 4.16(b): Edge length and cavity radius determination in HNPr ₂₅₀ by using digital micrograph software.....	121
Figure 4.17: (A) and (B) represent DPV and SWV of 4×10 ⁻⁵ M UA at different HNPr/GC electrode. Inset in (A) represents the DPV of bare GC. (C) Nyquist plot for the electrooxidation of UA at an applied potential of 0.4V within a frequency range of 10 ⁵ to 10 ⁻² Hz. (D) Comparison of R _{CT} and k ₀ value of different HNPr/GC towards the oxidation of UA.....	123
Figure 4.18: Equivalent circuit for the Nyquist plot.....	126
Figure 4.19: SERS spectra of different HNPr with CV (crystal violet) as the Raman reporter in which HNPr ₂₅₀ shows maximum Raman intensity.....	127
Figure 4.20: Optimized structure for different HNPrs: (a) HNPr _{pureAu} , (b) HNPr _{pureAg} , (c) HNPr _A , (d) HNPr _B , and (e) HNPr _C . The leftmost figure of the top panel shows the model HNPr with different planes (basal and vicinal) along with different structural parameters.....	132
Figure 4.21: (A), (B) and (C) are chronoamperometry, SWV, and DPV responses respectively at variable concentrations of UA on the HNPr ₂₅₀ /GC electrode. (D) represents the linear fitting of DPV response with standard deviation. (E) Denotes the peak current shifting for electrooxidation	

process of 400 μ M UA in presence of different interfering agents	135
Figure 5.1: (A) Stacking length-dependent plasmon tuning through TEM study.....	143
Figure 5.2: Frontal and sideways bright-field and HRTEM of our synthesized nanoprisms with {111} lattice plane as the basal plane and 1/3{422} reflections indicate the presence of a single twinning boundary within the {111} planes.....	145
Figure 5.3: (A-H) Morphological change of AgNPr by destacking, followed by leaching of nanoprisms and emulsion induced controlled aggregation of silver seeds at increasing concentration of As(III).	146
Figure 5.4: EDX spectra obtained from two different areas (Area-1 and Area-2) of AgNPr stacking to analyze the relative abundance of different elements.....	150
Figure 5.5: Concentration dependent color codes sensing of As(III).....	152
Figure 5.6: Optimized structures of Ag ₃ AsO ₃ and Ag ₃ AsO ₄ . Ag is shown in blue, As in purple and O in red.....	154
Figure 5.7: Colorimetric change of AgNPr solution upon addition.....	156
Figure 5.8. SERS based assay to monitor the morphological modification of AgNPr on addition of different concentration NaAsO ₂	161
Figure 6.1: (A) Schematic representation for the synthesis and growth of A ⁿ GNPs inside the SDS micelle's core. Effects of HQ concentration (250-750 μ M) on (B) visual color appearance (pink to blue) and (C) plasmon spectra (540-660 nm) of colloidal A ⁿ GNPs.....	172
Figure 6.2: TEM, SAED of different AuNP.....	175
Figure 6.3: SEM image of flower or bloom shaped AuNPs i.e. AuNP ₇₅	176
Figure 6.4: EDAX spectra of flower or bloom shaped AuNPs i.e. AuNP ₇₅	177
Figure 6.5: XPS spectra of variable shaped A ⁿ GNPs.....	180
Figure 6.6: Wide range survey spectrum indicating the presence of different elements into (a) AuNP ₅₀ and (b) AuNP ₁₅₀	181
Figure 6.7 : Electrochemical performance of different A ⁿ GNPs modified electrode towards HER.....	183
Figure 6.8: Electrochemical Impedance Spectroscopy (EIS) study for HER.....	189

Figure 6.9: Linear sweep Voltammetric response of variable AuNPs modified GC electrode in 0.1M KOH solution. Scan rate 10 mV/s.....	190
Figure 6.10: The presence of different crystal plane into the synthesized variable shaped AuNPs (A) AuNP ₅₀ (B) AuNP ₇₅ (C) AuNP ₁₅₀ . The areas selected in (A), (B) and (C) show the FFT (Fast Fourier transformation) images. (D) and (E) show the HRTEM images of AuNP ₇₅ pertaining the appearance of high-density grain boundary.....	193
Figure 6.11: Different HRTEM images of AuNP ₇₅ in which the rectangular area in (A, B and C) is selected for determining the average grain sizes using Jeffries method.	196
Figure 6.12: Different TEM images of AuNP ₁₅₀ (A, B and C) and AuNP ₅₀ (D, E and F) in which the rectangular area is selected for determining the average grain sizes using Jeffries method.	197
Figure 6.13: Variations in defect density in various shaped AuNPs with 50 frames considered for each of the three different surface zones with surface areas of 400 (20×20) nm ² for each AuN.....	198
Figure 6.14: Optimized structure of (a) Au (111), (b) Au (200)and (c) Au (110) surfaces. Structures of H* adsorbed Au surfaces (d) H*-Au (111), (e) H*-Au (200), (f) H*-Au (110)...	201
Figure 6.15: Optimized structure of (a) GB _a , (b) GB _b and (c) GB _c Augrain boundary surfaces (dotted line shows grain boundary region). Structures of H* adsorbed Augrain boundary surfaces (d) H*-GB _a , (e) H*-GB _b , (f) H*-GB _c	201
Figure 6.16: Optimized structure of (a) GB _d , (c) GB _e Augrain boundary surfaces (dotted region shows smaller and larger grain diameter). Structures of H* adsorbed Au grain boundary surfaces (b) H*-GB _d , (d) H*-GB _e	202
Figure 6.17: (a) Free energy diagram for H* adsorption on various Au surfaces for HER, (b) DOS plots for GB _e and H*-GB _e Au surfaces, (c) PDOSs for Au-5d, Au-5p, Au-6s and H-1s of H*-GB _e Au surface, (d) DOSs on Au atoms for different grain boundary surfaces.	203
Figure 7.1: (A) True diameter from TEM image, (B) plasmon band from absorption spectra, (C) hydrodynamic size from DLS measurement, and (D) surface charge from the zeta-potential measurement of Au nanoseed.....	213
Figure 7.2: (A, B, C) and (D, E, F) are the SEM, TEM, and HRTEM images of Hy-Au@AgNR ₁₂₀ and Hy-Au@AgNR ₈₄₀ respectively.	218

Figure 7.3: Different colors of nanorods: From left to right Hy-Au@AgNR₈₄₀, Hy-Au@AgNR₄₅₀, Hy-Au@AgNR₁₂₀, Hy-Au@AgNR₈₄₀-Ass.....219

Figure 7.4: UV absorption spectra of different Hy-Au@AgNRs
and Hy-Au@AgNR₈₄₀-Ass.....220

Figure 7.5: A, B, C are the time-dependent 2D images of Hy-Au@AgNR₈₄₀-Ass formation. The images are taken after DTT addition to Hy-Au@AgNR₈₄₀ at 30 s, 60 s, and 120 s interval. The 3D images of A, B, C are D, E, F respectively.....221

Figure 7.6a: Unfiltered and Elastic TEM images of different Nanorod.....222

Figure 7.6b: Histogram of the nanorods (A) Hy-Au@AgNR₈₄₀, (B) Hy-Au@AgNR₄₅₀, and (C) Hy-Au@AgNR₁₂₀.....222

Figure 7.7a: A, B, C are Intensity (percent) vs size (nm) curve of Hy-Au@AgNR₈₄₀-Ass formation at 30 s, 60 s, and 120 s time interval in the reaction medium. D, E, F are the Correlation coefficient vs time (μ s) curves for the same time intervals.....227

Figure 7.7b: (A) Change in zeta potential during the formation of Hy-Au@AgNR₈₄₀-Ass at different time intervals, (B, C) Final ξ and d_{hyd} of all the Hy-Au@AgNRs and Hy-Au@AgNR₈₄₀-Ass respectively.....228

Figure 7.8: A, B, C are the frequency plot whereas D, E, F presents the phase shift and G, H, I are velocity distributions of Hy-Au@AgNR₈₄₀, Hy-Au@AgNR₄₅₀, and Hy-Au@AgNR₁₂₀ respectively.....231

Figure 7.9: A, B, C are frequency plot; D, E, F are phase plot; G, H, I are velocity distribution curve at 30 s, 60 s, and 120 s of reaction time. The negative phase shift in D and E implies zeta potential was negative at 30 s and 60 s but becomes positive at 120 s.....232

Figure 7.10: (A) SERS measurement of the time-dependent formation of Hy-Au@AgNR₈₄₀-Ass by adding Hy-Au@AgNR₈₄₀s into the DTT solution. (B) SERS spectra of different Hy-Au@AgNRs and Hy-Au@AgNR₈₄₀-Ass.....233

Figure 7.11: XPS spectra of nanorod and assembly structure.....234

Figure 7.12: A and B are the XPS of Ag3d5/2 and Ag3d3/2 lines for Hy-Au@AgNR₈₄₀ and Hy-Au@AgNR₈₄₀-Ass. In figure C the XRD of Hy-Au@AgNR₈₄₀ and Hy-Au@AgNR₈₄₀-Ass are shown whereas D shows the SAED pattern of Hy-Au@AgNR₈₄₀-Ass to confirm the {111} is the most intense plane.....235

Figure 7.13: The fitted curve of (A) Hy-Au@AgNR ₈₄₀ -Ass and (B) Hy-Au@AgNR ₈₄₀ at $2\theta \approx 38.25^\circ$ for $fcc\{111\}$ facet.....	237
Figure 7.14: (A) Modeled nanorod structure with $\langle 111 \rangle$ and $\langle 110 \rangle$ facets. (B) Possible Au seeding (spherical and rod-shaped) and spherical Au seeded Hy-Au@AgNRs. (C) The density of states (DOS) of pure Ag and Au-seeded AgNRs with 40 Å and 80 Å lengths.....	242
Figure 7.15: Creation of multiple low coordinated crystal sites like stepped surface, terrace, kinks, edges, etc., during the formation of Hy-Au@AgNR ₈₄₀ -Ass from the constituents Hy-Au@AgNR ₈₄₀ S.....	243
Figure 7.16a: Effect of temperature on Hy-Au@AgNR ₄₅₀ morphology, at (A) 60-70 °C, (B) 70-80 °C, and (C) 80-90 °C.	244
Figure 7.16b: Association of Au seed followed by Ag deposition at a higher temperature. Stacking up of Au seeds is verified by (A) TEM, (B) HAADF, (C) HRTEM, and (D) EDX.....	245
Figure 7.17a: Kinetics of Ag seed-based nanorod formation at (A) 30 min, (B) 60 min, and (C) 90 min and Au seed-based Hy-Au@AgNR ₁₂₀ formation at (A') 30 min, (B') 60 min, and (C') 90 min.	246
Figure 7.17b: The effect of the variation Au seed amount [(A) 1 mL, (B) 4 mL, and (C) 2 mL] on Hy-Au@AgNR ₁₂₀ synthesis.	247
Figure 7.18: Effect of AgNO ₃ concentration (in the reaction mixture) on the efficiency of Hy-Au@AgNR ₁₂₀ formation.....	248
Figure 7.19: Effect of CTAC concentration with (A) 0.025 gm CTAC in 45 mL water for the formation of Hy-Au@AgNR ₄₅₀ , (B) 0.05 gm CTAC in 45 mL water for the formation of Hy-Au@AgNR ₁₂₀ , and (C) 0.1 gm CTAC in 45 mL water for the formation of Hy-Au@AgNR ₅₀	249
Figure 7.20: The effect of the variation of AA concentration on Hy-Au@AgNR ₁₂₀ formation	250
Figure 7.21: The effect of the variation of DTT concentration on the efficiency of Hy-Au@AgNR-Ass formation	251
Figure 7.22: Formation of Hy-Au@AgNR with length ~1-1.2 μm by maintaining the molar ratio between AgNO ₃ and AA at 1:20 during synthesis.....	253
Figure 7.23: A is the DPV response for the reduction glucose (4×10^{-4} M) in 0.1 M HClO ₄ , B is DPV response for the oxidation of L-tryptophan (4×10^{-4} M) in 0.1 M HClO ₄ , C is the DPV response for the reduction of vitamin K3 (4×10^{-4} M) in 0.1 M LiClO ₄ + acetonitrile.....	256

Figure 7.24: A is the chronoamperometric response for the reduction glucose (4×10^{-4} M) in 0.1 M HClO ₄ , B is the chronoamperometric response for the oxidation of L-tryptophan (4×10^{-4} M) in 0.1 M HClO ₄ , C is the chronoamperometric response for the reduction of vitamin K3 (4×10^{-4} M) in 0.1 M LiClO ₄ + acetonitrile.....	258
Figure 7.25: A is the impedance response for the reduction glucose (4×10^{-4} M) in 0.1 M HClO ₄ , B is impedance response for the oxidation of L-tryptophan (4×10^{-4} M) in 0.1 M HClO ₄ , C is the impedance response for reduction of vitamin K3 (4×10^{-4} M) in 0.1M LiClO ₄ + acetonitrile.....	259
Figure 7.26: Electrochemical reduction of metal ions in 0.1 M HClO ₄ (A) Co ²⁺ , (B) Cr ³⁺ , (C) Cu ²⁺ (D) Hg ²⁺ , (E) Ni ²⁺ , (F) Fe ³⁺ , (G) Pb ²⁺ , (H) is for vitamin K3 oxidation in 0.1 (M) LiClO ₄ + acetonitrile.....	264
Figure 7.27a: Oxidation of metabolites in 0.1M NaOH medium: (A) AA , (B) Creatinine (C) Dopamine (DA), (D) thiamine, (E) riboflavin, (F) Pantothenic acid (PA) (G) urea (H) uric acid (UA), (I) inositol.....	265
Figure 7.27b: oxidation of metabolites in 0.1M NaOH; (A) Xanthine, (B) Cysteamine (Cyst) (C) glucose, (D) L-tryptophan, (E) folic acid (FA).....	266
Figure 7.28: I-C linear fitting for different water-soluble human metabolites as mentioned in the figure during their catalytic oxidation at their physiological concentration level.....	267.
Figure 7.29: Linear Calibration plot of metal ions. Just like human metabolites (Figure 7) where we did not find any linear relation with concentration we take logarithm as shown in (C) for Cu ²⁺ and in (G) for vitamin K3.....	268
Figure 7.30: Interference test through DPV assay for different metabolites.....	270
Figure 8.1: A and B are the bright field and fluorescence image of the control, respectively. C and D are the bright field and fluorescence image of the inactivated virus, respectively.....	281
Figure 8.2: SEM, TEM, HAADF, AFM of Au-Ag network.....	282
Figure 8.3: A panel of screen-printed electrode use for impedimetric assay.....	284
Figure 8.4: AFM and TEM images of activated and inactivated viruses.....	285
Figure 8.5: Nyquist plot and Impedance measurent for different DENV samples.....	286
Figure 8.6: Randles cell used for fitting Nyquist plot.....	288

Figure 8.7: Nyquist plot for real sample designated as Patient1, Patient 2, and Patient 3.....	290
Figure 9A.1: The synthesized $\text{Ag}_{\text{core}}\text{Au}_{\text{shell}}$ nanostructures as a function of the template volume. (A) 100 μL , (B) , (C) , and (D) 2 mL.....	299
Figure 9A.2: Fabrication of $\text{NP}_{\text{matrix}}$ from $\text{Ag}_{\text{core}}\text{Au}_{\text{shell}}$, and their elemental mapping.....	300
Figure 9A.3: Comparison of electrocatalytic activity of $\text{NP}_{\text{matrix}}$ structure with $\text{Ag}_{\text{core}}\text{Au}_{\text{shell}}$ and bare GC for the oxidation of methanol, ethylene glycol, and glycerol and reduction of oxygen.....	301
Figure 9B.1: Variation of cell viability as a function of available Ag concentration from the synthesized $\text{Ag}_{\text{core}}\text{Au}_{\text{shell}}$ nanostructure.....	306

Thesis Highlight

Name of the Student: Sandip Kumar De

Name of the CI/OCC: Saha Institute of Nuclear Physics **Enrolment No.:** CHEM05201504003

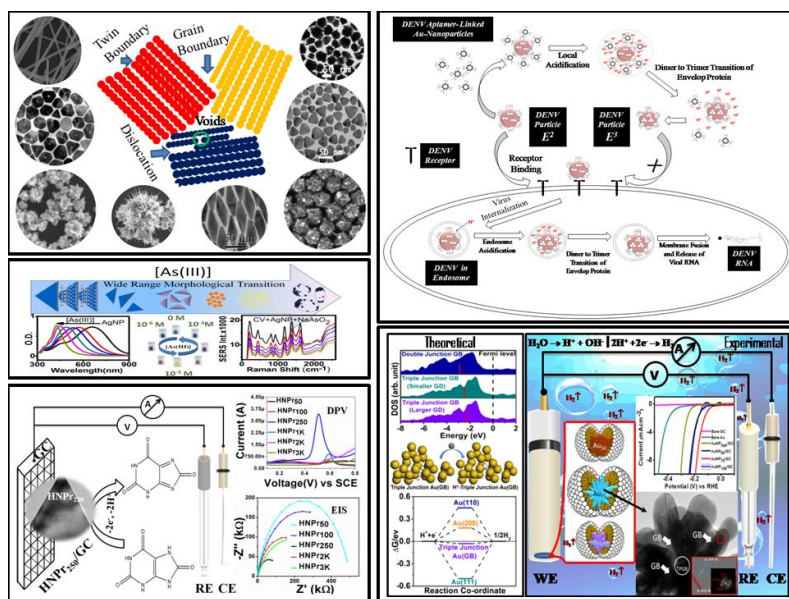
Thesis Title: Crystal Engineering to Fabricate Au, Ag, & Au-Ag Alloy Nanoparticles: Application in Technology, Pathology & Theranostics

Discipline: Chemical Sciences

Sub-Area of Discipline: Nanomaterials

Crystal designing of noble metal nanoparticles (Au, Ag, Au-Ag nanoalloy) is a striking field of research in present days due to their tremendous applications in technology, pathology, and theranostics. In this thesis, I have discussed in-depth about the fabrication of Au, Ag, and Au-Ag alloy nanoparticles with multiple reduced coordinated defects enriched active crystal sites like grain boundary, twin boundary, stacking fault, cracks, and voids which are responsible for internal tensile strain within the nanocrystal. We have performed different electrocatalytic redox reactions by using those strain-induced nanocrystals for sensing of metabolites like ascorbic acid, uric acid, L-tryptophan; etc via recording their characteristic I-V curves obtained from differential pulse voltammetry experiments. Besides various electrochemical techniques, we have also performed surface-enhanced Raman spectroscopy and ultraviolet-visible (UV-vis) spectroscopy for selective detection of metal ion like As^{3+} from real samples. Including their tremendous applications in the pathological field, we also found the parallel applications of Au-Ag alloy nanoparticles in fuel cell technology which include a methanol fuel cell, water oxidation, etc. We found that our developed nanomaterials are equally capable as a bifunctional catalyst for

oxidation of methanol, ethylene glycol, glycerol, and reduction of oxygen. Experimental observations have been verified by theoretical *ab initio* simulation by calculating the shift in the d-band center due to the appearance of crystal irregularities along with free energy calculation over different facets (like $\langle 111 \rangle$, $\langle 110 \rangle$, $\langle 200 \rangle$, etc) of Au nanocrystal, to find the energetically most favorable pathway. We have also performed theranostics applications of our synthesized highly porous nanomaterials and their assemblies for selective detection of dengue-II from clinical samples and its inhibition in the Vero cell line. Selective detection of dengue strain through highly sensitive impedimetric technique in the animal model along with inhibition of viral replication is an encouraging process to carry forward in the near future.



CHAPTER-1

Introduction

Nanoparticles are a collection of atoms or molecules (by considering a gold atom of radius 0.15 nm, at least 300, 3×10^5 , and 3×10^8 Au atoms are there in a spherical gold nanoparticle of radius 1, 10, and 100 nm respectively¹) within a regime of 1-100 nm if they are dispersed in gaseous, liquid or solid media. Nanoparticles having intermediate sizes between bulk and single atom shows different behavior in optical, electronic, magnetic, and catalytic properties from their counterparts.¹ This discrepancy in physiochemical properties is due to the (i) high surface to volume ratio (S/V),² (ii) ordered arrangement of electric and magnetic dipoles or multipoles,³ (iii) appearance of low coordinated crystal defects like grain boundary, twin boundary, stacking fault, dislocation,⁴ etc, to rearrange the bandgap, (iv) quantum size effect,⁵ and (iv) electrodynamic interactions.⁶ Out of several nanomaterials, noble metal nanoparticles have got catchy attention in the recent times and find enormous applications in various fields which include photo- and elctro-catalysis, pathological sensing, and theranostics^{4,7} This increased attention towards plasmonic noble metal nanoparticles and noble metal nano-alloy like gold-silver (Au-Ag) is due to their greater resistance to corrosion and oxidation in air, enhanced catalytic activity, larger stability, and our ability to make them tailored porous and layered structure.⁸ The plasmonic nanomaterials and nanoalloys can be prepared by various methodologies like electrochemical methods,⁹ hydrothermal methods,¹⁰ sonochemical methods,¹¹ etc. Out of the various methodologies, hydrothermal synthetic methodology has got the key attention in past decades due to its ease friendly approach e.g. (i) during a surfactant controlled

synthesis by CTAB, CTAC, and SDS, the size and shape of the nanomaterials can be altered simply by varying the surfactant concentration¹² whereas in a seed mediated synthesis the size and shape¹³ can be changed by varying the amount of seed, (ii) The standard reduction potential of Au^{3+} and Ag^+ are +1.5 V and +0.8 V, so they can easily be reduced to Au^0 or Ag^0 by using common mild reducing agents like AA, hydroquinone, hydrogen peroxide,⁷ etc, (iii) The plasmonic gold (Au), silver (Ag) or gold-silver (Au-Ag) nanomaterials prepared by chemical synthesis can easily be separated by fractional centrifugation,¹⁴ (iv) Due to the close lattice parameters of Au and Ag, the Au-Ag nano-alloy of different morphology can be prepared by co-precipitation method without applying any external mechanical force like pressure, temperature, magnetic field, etc⁷ and (v) The nanomaterials or nanoalloys with programmable defect enrichment can be prepared by wet chemical synthesis by monitoring their growth mechanism through direct imaging techniques like *in-situ* TEM.¹⁵ Without elaborating on all aspects, the present discussion will be highlighting mainly the origin of outstanding catalytic properties of homogeneous (Au or Ag) or heterogeneous (Au-Ag) nanoparticles. Based on their enhanced catalytic property, I will discuss their multidirectional applications as (a) biosensor for metabolites, virus, bacteria, etc, (b) electrocatalyst for fuel cell application in oxidation of methanol, ethanol, reduction of CO_2 , O_2 , etc, and (c) as an antiviral or antibacterial agent to prevent the infectious diseases caused by virus and bacteria in mammalian kingdom. In search of their outstanding catalytic activity, we have studied their crystal growth and resultant crystal patterns by high-resolution microscopy (TEM, SEM, and AFM) and atomic-scale spectroscopy (XRD, XPS, and ICP-OES) to correlate different crystal irregularities in nanocrystals with their catalytic activity for several redox reactions and are discussed in details in the following sections. Based on the dimensionality, crystal defects can be categorized into four different

groups and these are: (i) Zero-dimensional point defects (e.g. vacancy, doping, interstitial, substitutional, etc), (ii) One dimensional line defects (e.g. edge dislocation, screw dislocation, etc), (iii) two-dimensional planar defects (e.g. grain boundary, tilt boundary, twin boundary, microcracks, etc), and (iv) three-dimensional volume defects (e.g. void, pore, crack, inclusion, precipitation, etc). Throughout this thesis, these different crystals defects and their contributions will be elaborated.

1.1 Zero-dimensional point defects: Point defects are a type of defects where an atom is missing or extra plane (crystal) constituting atoms or impurity atoms are added to the normal crystal array. There are three major types of point defects: Vacancies, Interstitials, and Impurities¹⁶. They may be built-in with the original crystal growth or activated by heat. They may also be the result of radiation, electric current, etc.

1.1.a Vacancies: A Vacancy is the absence of an atom from a site normally occupied in the lattice.

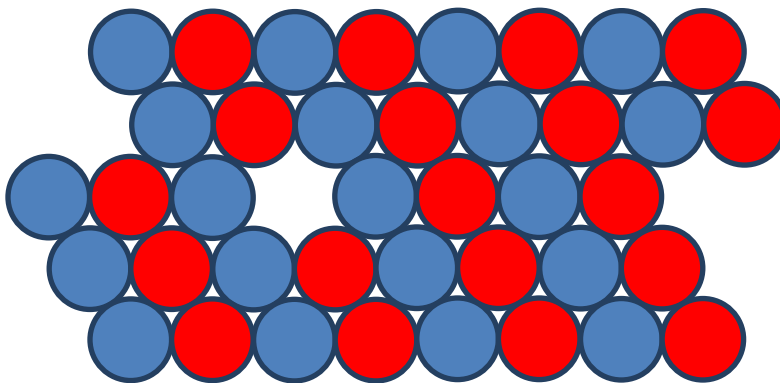


Figure 1.1a: Point defect originating from vacancies. Here the red and blue color circles show the normal lattice points and the empty space shows the position of the vacancy point defect.

1.1.b Interstitials: An Interstitial defect occurs when an atom takes the interstitial position (non-lattice site) of the lattice structure. There needs to be enough room to keep an atom in a non-

lattice site to create this type of defect. Hence, this type of defect occurs in open covalent structures or metallic structures with large atoms.

An interstitial may be a foreign atom or an off-lattice regular atom as shown below:

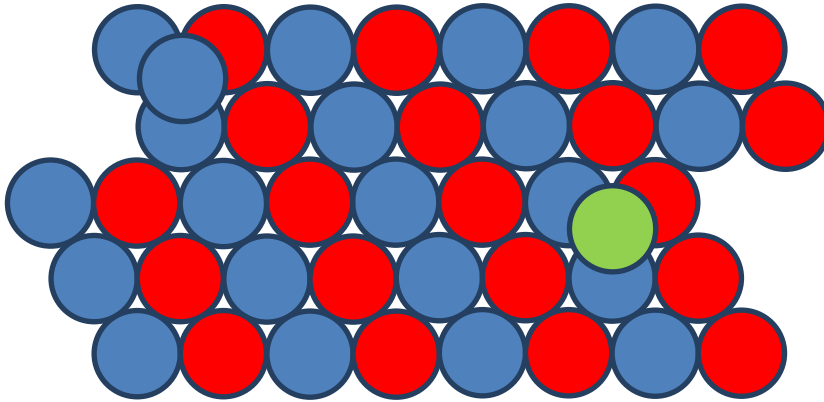


Figure 1.1b(i): Interstitial point defect created by foreign atom(s). Here the red and blue color (contain one off-lattice regular atom as an interstitial point) circles show the normal lattice points whereas the green circle indicates the foreign atom.

An interstitial defect may form by moving an atom from a lattice point to an off-lattice site and thereby creating a vacancy at the lattice point.

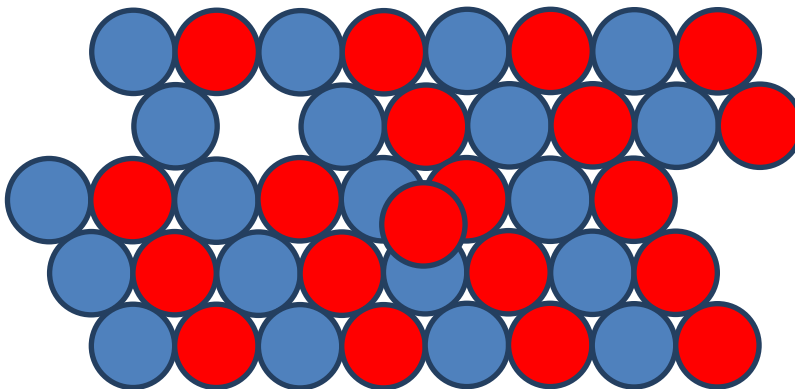


Figure 1.1b(ii): Interstitial point defect created by moving an atom from a lattice point to an off-lattice site. Here the red and blue color circles show the normal lattice points.

1.1.c Impurities: An Impurity is the substitution of a regular lattice atom with an atom that does not normally occupy that site. The atom may come from within the crystal (e.g. a Chlorine atom on a Sodium site in a NaCl crystal) or from the addition of impurities. This is also known as the **Substitutional Defect**. A foreign atom, or a regular atom out of place, is also defined as an **impurity**.

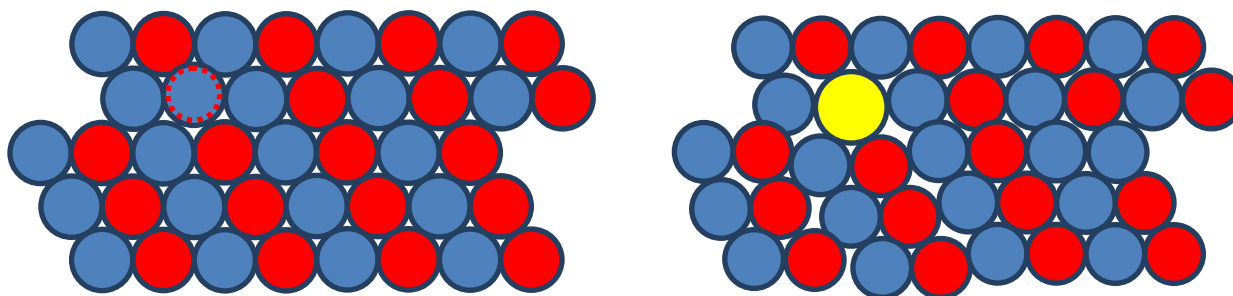


Figure 1.1c: (Left) Impurity atom comes from within the crystal (in a NaCl crystal, the impurity Cl atom is shown by the red dotted circle), and (Right) Impurity comes from an additional atom (shown by the yellow circle with a different radius) out of the crystal.

1.1d Schottky defect and Frenkel defect: Another two prominent defects are Schottky defect and Frenkel defect. The **Schottky defect** is a type of Point Defect that occurs in ionic crystals. The Schottky defect occurs when oppositely charged atoms (cation and anion) leave their corresponding lattice sites and create a pair of Vacancy Defects. **Frenkel defect** also occurs in ionic solids. It occurs when an ion jumps from a normal lattice point to an interstitial site, leaving behind a vacancy (vacancy + interstitial)¹⁷. Usually, this type of defect is observed in ionic solids, where the size of the anion is substantially larger than the size of the cation. Some of the examples of **Frenkel defect** are AgBr, ZnS, AgCl, and AgI.

The concentration of point defects in a crystal is typically between 0.1% and 1% of the atomic sites, however, extremely pure materials can now be grown. The concentrations and movement of point defects in a solid are very important in controlling their color and deformation.

1.2 One dimensional line defects: One-dimensional defects are also called as dislocations. They are abrupt changes in the regular ordering of atoms along a line, known as dislocation line, in a solid. They occur in high densities and strongly influence the mechanical properties of materials. There are two basic types of dislocation and they are:

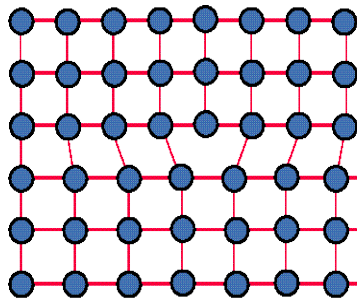


Figure 1.2a: Schematic representation of the edge dislocation

1.2.a Edge dislocation: An *Edge dislocation* in a Metal may be regarded as the insertion (or removal) of an extra half-plane of atoms in the crystal structure¹⁸.

The regions surrounding the dislocation line are made of essentially perfect crystal as shown in the above figure. The only severe disruption to the crystal structure occurs along the dislocation line (perpendicular to the crystal plane, here the page). Note that, perpendicular to the crystal plane, the line may step up or down. These steps are known as *jogs*.¹⁹

1.2.b Screw dislocation: Screw dislocation in the lattice structure of a crystal is a type of line dislocations in which the atoms are arranged in a helical pattern that is normal to the direction of the stress²⁰. Any type of dislocations either screw or edge is assigned by the burger vector (\vec{b}). In short, the burger vector is a measure of the lattice distortion due to dislocation line.

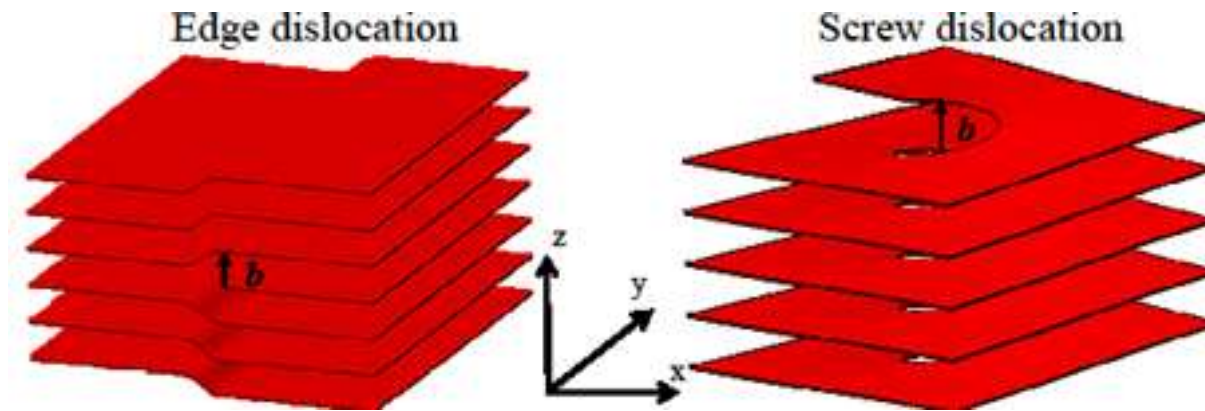


Figure 1.2b: Schematic representation of edge dislocation and screw dislocation

To quantify the burger vector one has to draw a circuit by connecting the lattice sites in a crystal e.g. A circuit is made around a dislocation line by clockwise direction such that each site of the lattice is connected to be fully coordinated, as shown in figure 1.2c, then it is transferred to a perfect lattice (figure 1.2c) where dislocation line is absent. The circuit will fail to close with its starting point in dislocation free lattice and the connecting line between endpoint & starting point of the circuit is called burger vector. The type of dislocations is assigned by burger vector i.e. in edge dislocation the burger vector lies in perpendicular to the dislocation line whereas in screw dislocation the burger vector lies parallel to the dislocation line. In fcc (Au, Ag, Au-Ag, Pt, Pd, etc) or bcc (Fe, Mo, W etc) crystal the burger vector is denoted by $b = a/2\langle hkl \rangle$ whereas in a cubic crystal it is denoted by $b = a\langle hkl \rangle$.

Besides, mentioning the direction of the dislocation line, the burger vector also signifies the direction of deformation or the slip plane in a lattice. In any type of crystal, there exist mainly two types of deformation named as, elastic deformation (in which a lattice get can back to its previous stage after feeling stress) and plastic deformation (where a lattice gets permanently distorted that is either tensed or compressed and can't get back to its previous stage). The plastic deformation in a lattice occurs through the slip plane, where the dislocation line can move very

easily e.g. in an fcc type of crystal 12 slip system exists whereas in bcc crystal 48 slip system can occur. Thereby, the elasticity and plasticity of a dislocation enriched crystal lattice are determined by the burger vectors which can be monitored through HRTEM, field ion microscopy, atom probe techniques, and chemical etching.

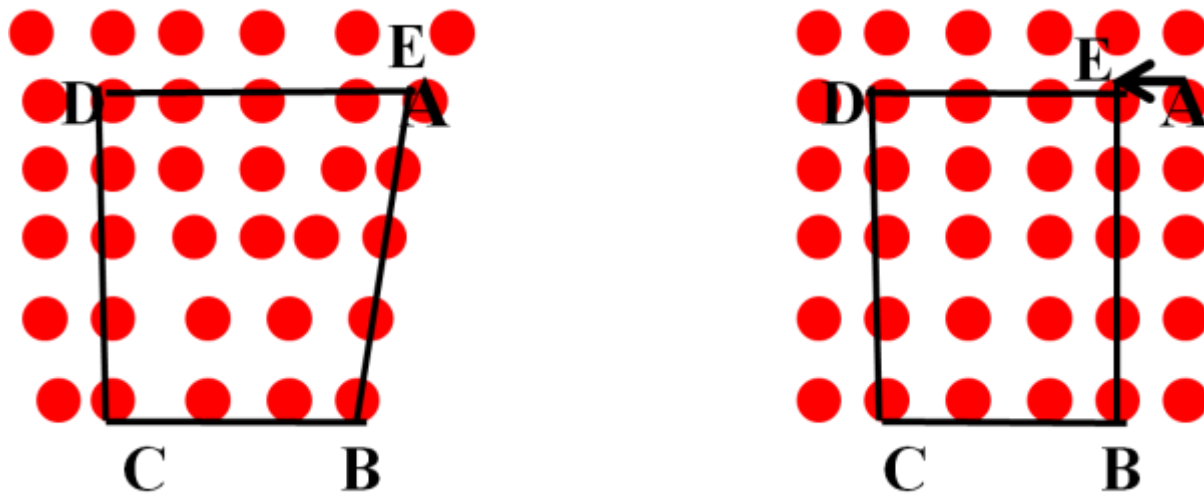


Figure: 1.2c: (Left) A dislocation enriched lattice where the starting point A and the endpoint E meets at a point to completes the circuit, (Right) A perfect lattice where A and E do not meet and the vector AE is defined as the burger vector.

1.3 Two-dimensional planer defects: A Planar Defect is a discontinuity of the perfect crystal structure across a plane. Planer defect can be of several different types which include (i) grain boundary, (ii) twin boundary, and (iii) stacking fault.

1.3a Grain Boundary:

A grain boundary (GB) is the interface between the two differently oriented crystals in a polycrystalline material.^{21,22} Depending upon the angle between the interfaces of two different crystals they are designated either low ($<5^\circ$) or high angle GB ($>5^\circ$). The smaller angle GB is

accounted for lower in energy than higher angle GB. Besides, angle-dependent difference GB can also be divided by the axis of rotation as a tilt boundary (where rotation axis is parallel to the boundary plane) and twist boundary (where the rotation axis is perpendicular to the boundary plane). Irrespective of the type, a GB on the lattice surface contains multiple reduced coordinated active sites and it retards the motion of a dislocation line, which accumulates near the GB. Thereby, a GB enriched crystal is considered to be highly strained than GB free crystal.

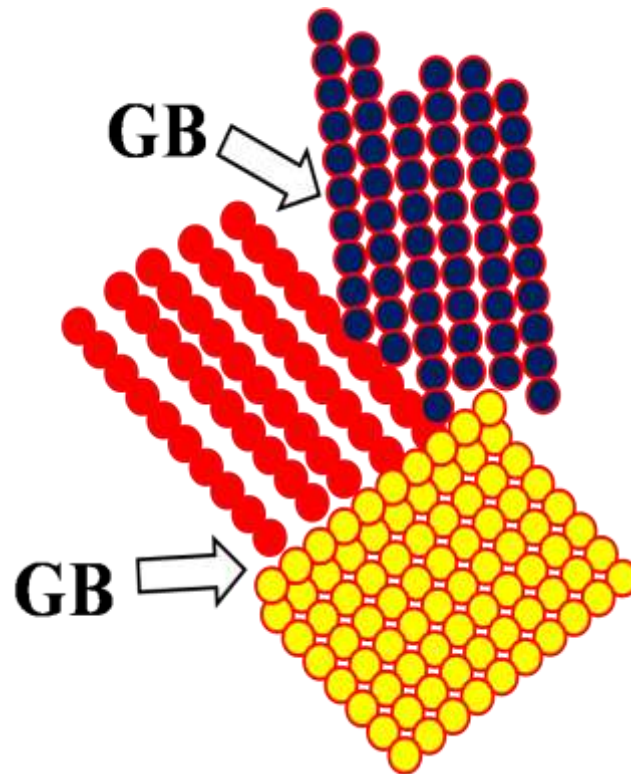


Figure1.3a: Schematic Presentation of GB over a crystal lattice.

1.3b Twin Boundary:

When two separate crystals share their plane in a symmetrical way i.e. one half of the plane becomes the mirror image of the other, they called a twin boundary (TB).^{23,24} There are mainly two types of twinning crystal named as transformation twins and deformation twins. Transformation twins sometimes designated as annealing twins and appear in fcc crystal during the cooling process. In short, when a metal is heated and leave for cooling suddenly, it can't get

back to its previous stage and twins are formed over the crystal to get a stable structure. Deformation twin is another type of twin that appears due to shear stress on it and is most prevalent in bcc and hcp type of crystal. A schematic presentation of the twin boundary that appears in an fcc lattice is shown below in **Figure 1.3b**. In an fcc lattice, the atomic rearrangement can be presented as ABCABCABC....twin boundary appears when one plane is shared symmetrically which can be represented as ABCABCBA. The plane C is the TB. Due to the non-planar nature, the atoms situated on the TB are unsaturated in coordination number and considered to be highly active than non-twinned atomic sites.

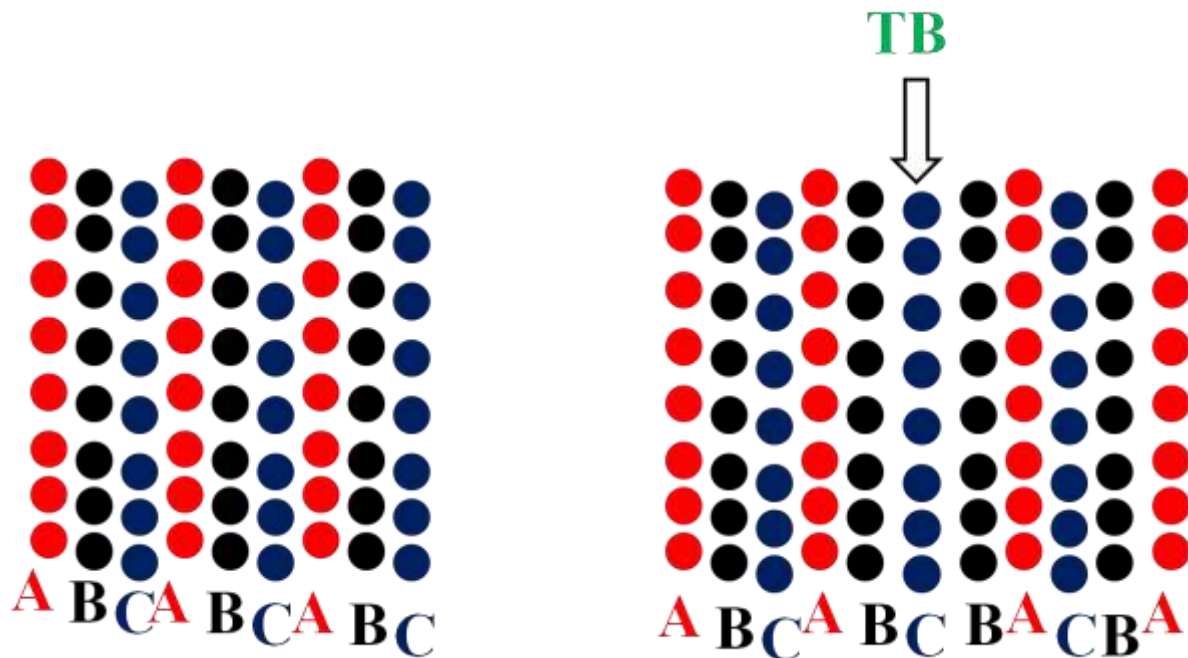


Figure 1.3b: Schematic presentation of a twin boundary over an fcc lattice.

1.3c Stacking Fault:

Stacking fault (SF) is a 2D effect that appears in fcc or hcp mainly.²⁵ SF can be of two types designated as intrinsic SF when a regular row of atoms is absent in a lattice or extrinsic SF when an extra row of atoms appear in a lattice e.g. in an fcc lattice, as we stated previously, the

stacking sequence is presented by ABCABCABC.... if one of the stacking is absent as shown in figure 1.3c, it will be an intrinsic stacking or if an extra stacking is present it will be termed as extrinsic stacking.

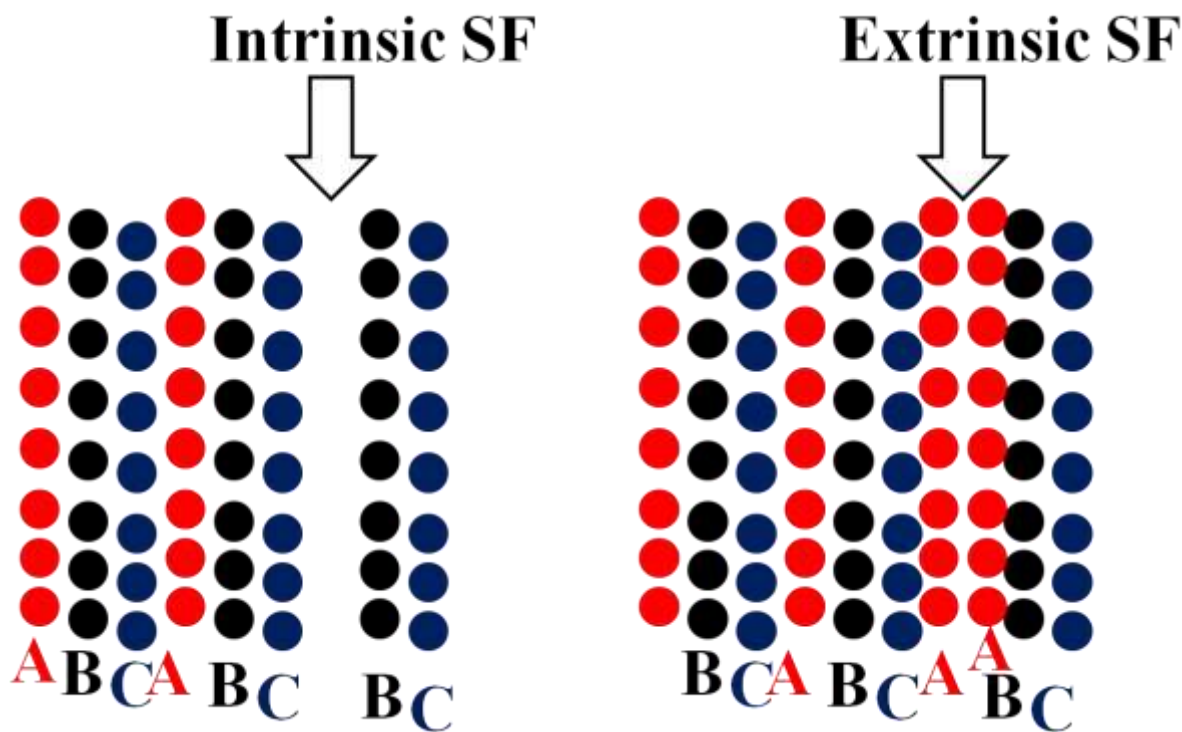


Figure 1.3c: Schematic Presentation of intrinsic and extrinsic SF in fcc lattice.

1.4 3D Defects:

3D defects are sometimes termed as volume defects²⁶ and cause overall changing in volume by creating voids (a small region within the crystal where a set of atoms are missing e.g. during the reaction of Ag nanoparticle with Au^{3+} , galvanic replacement occur and the Kirkendall voids¹⁵ are formed), inclusion²⁷ (a 3D defect when other phases trapped within the base material e.g. carbides in steels), cracks²⁸ (that appears due to the bond breaking or bond-forming within the crystal) etc.

A schematic presentation of the void defect is shown below in **Figure 1.4**.

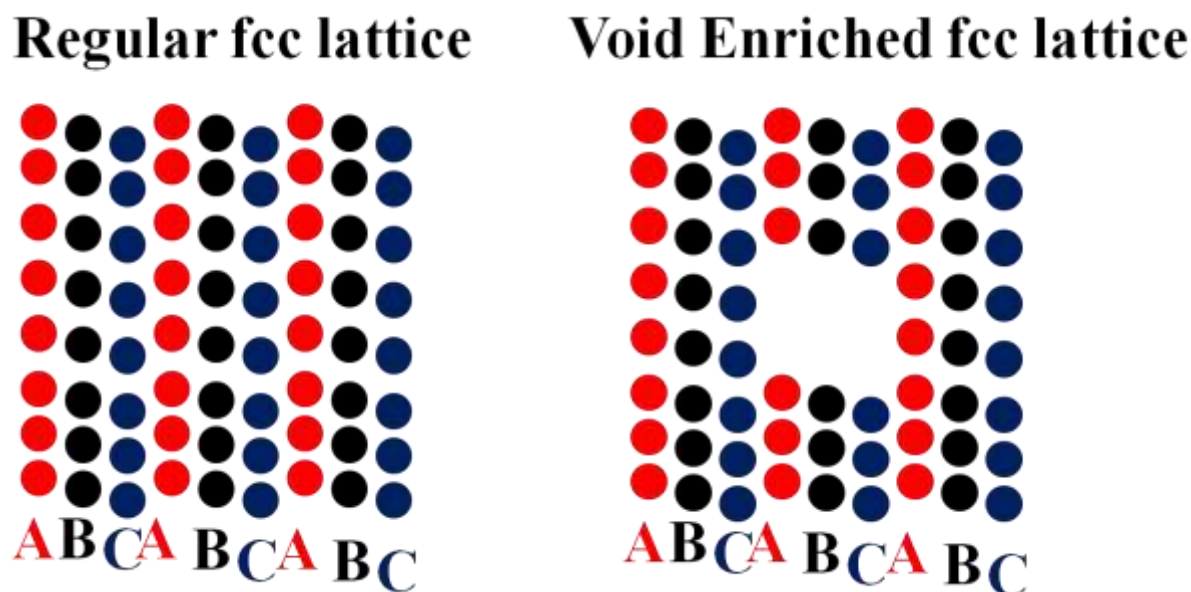


Figure1.4: An fcc lattice with the regular arrangement and void enriched arrangement.

1.5 Application of noble metal nanocatalyst in Pathological Industry

1.5a. Sensing of Metabolites

In the modern age of the clinical industry, we need rapid and accurate biochemical techniques to detect human metabolites like vitamin C, uric acid, vitamin K, Vitamin B, amino acids, glucose, etc. Most of the present methods to detect metabolites are based on the enzymatic assay. Application of enzyme as a catalytic biosensor is long known in the literature²⁹ but due to their possible denaturation and digestion in abnormal conditions (higher temperature, variable pH, non-aqueous environment, etc), high costs in preparation and purification, the requirement of expertise to handle enzyme-based assays, and lack of large scale production, the fabrication of enzymatic catalytic platform for daily use in industrial-scale is not become feasible till now.^{30,31} In comparison to catalytic enzyme biosensors³², electrochemical methods like DPV, EIS, Chronoamperometry can produce accurate results within the physiological concentration level

with an appropriate non-enzymatic electrode material. In this regard, noble metal nanoalloy is accounted for its well known catalytic property to oxidize or reduce metabolites by producing their characteristic I-V curve in physiological concentration limit. Hence for nonenzymatic, cost-effective, and time-saving techniques, electrochemical methods find promising applications in the pathological industry by using Au-Ag nanoalloy as an active electrode material. An additional benefit of electrochemical methods is its ability to detect more than one metabolite at a time. In a study by Su et al. the simultaneous detection of AA, DA, UA, and NO_2^- was done through DPV by modifying the working electrode with graphene nanoribbons.³³ In one of our studies, we have used our synthesized bud to blossom shaped gold nanoflowers with multifaceted orientations like {111}, {110}, etc as the electrode material for the oxidation of AA. We could not only easily achieve the detection limit of AA up to the nanomolar (nM) range but also were able to detect DA, UA, and glucose simultaneously.⁴ In our next study, we planned to explore the role of zone-specific crystallization and porosity directed crystal strain to control the catalytic oxidation of Uric Acid (UA) on Au-Ag nanoalloy material. In our last study in the direction of human metabolites sensing, we target to develop a universal nanoscale catalytic platform with enhanced catalytic activity governed by the inherent crystal defects and grain boundaries³⁴ within the nanomaterials, catalytic hotspots at the cross junctions,³⁵ durability due to efficient surface passivation,³⁶ excellent stability over a pH and solvent range,^{37,38} and low cost of fabrication. The catalytic activity of the designed material has been tested for a series of water-soluble metabolites, like AA, UA, DA, Pantothenic acid (PA), urea, uric acid (UA), etc in 0.1 (M) NaOH and water-insoluble metabolites, like vitamin E, vitamin K3, serotonin, etc. in 0.1 (M) LiClO_4 + acetonitrile medium. The utility of using the above electrolytes is that they are either acidic or basic in chemical nature. Whenever human serum is added to those electrolytes,

the plasma proteins are precipitated out but the other blood ingredients like salts (NaCl, KCl, CaCl_2 , etc) and metabolites (vitamins, amino acids, etc) will stay in the solution without any modification. Besides the protein precipitation, the other benefit of using a wide range of P_H is to record maximum current during the electrochemical study at an appropriate pH.

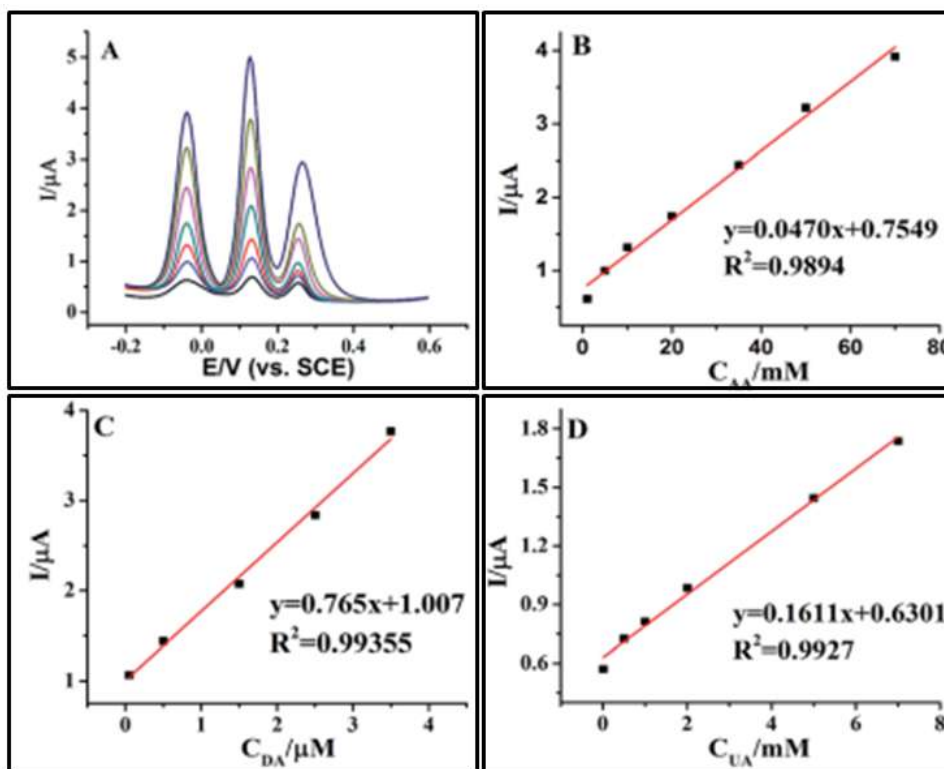


Figure 1.5a(i): (A) DPV response for AuNP@MoS₂ modified GCE for AA (1mM to 70mM), DA (0.01μM to 7μM), UA (.01mM to 12mM). (B-D) Corresponding linear calibration plots for AA, DA, UA with Peak current vs concentration in DPV response.³⁹

In a study by Farida et al.⁴⁰, it was found that the peak potential is shifted towards a more negative side with increasing pH for electrochemical oxidation of AA along with enhancement of peak current which signifies faster oxidation in a basic medium for AA than in acidic medium. Thereby Au-Ag nanocatalyst having the capacity to work in a wide range of pH and different solvents can be considered as an appropriate biosensor for human metabolites. Out of the several

electrochemical methods stated earlier like CV, DPV, EIS, Chronoamperometry, etc, the DPV method is used the most for simultaneous detection of more than one metabolite at a time because of producing sharp and characteristic peak potential and peak current for individual metabolites.

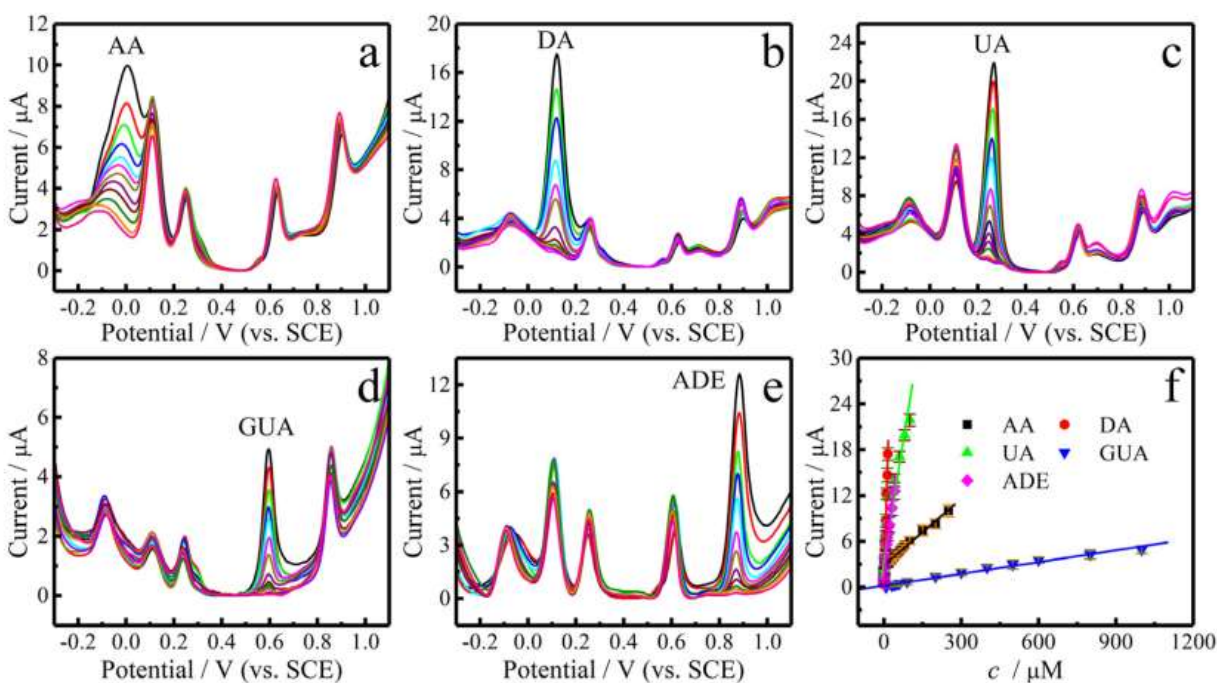


Figure 1.5a(ii): DPV responses of individual analytes in physiological concentration limit in presence of other analytes. (a) AA (5-250 μM), (b) DA (0.3-15 μM), (c) UA (0.5-100 μM), (d) GUA (7-1000 μM), (e) ADE (0.1-40 μM). In figure (f) linear calibration plot of each analyte has been shown.⁴¹

In a study by Sun et al.³⁹ has performed simultaneous detection of AA, UA, and DA by using AuNP@MoS₂ as the electrode material in DPV response with a significant peak potential separation between AA and DA as 151 mV, AA and UA as 288 mV, and UA and DA as 137 mV. They were able to perform the simultaneous detection of the above metabolites in physiological concentration limit and have got a linear calibration plot which was subsequently used for real sample analysis. In another study, Gao et al. have detected AA, DA, UA, guanine

(GUA), and adenine (ADE) simultaneously by electrochemical deposition of Au nanoparticle on horizontally graphene-modified tantalum wire.⁴¹ Thus Au and Ag nanoparticle or Au-Ag alloy nanoparticle modified electrodes can potentially be used as biosensors for human metabolite detection with high accuracy and cost-effectively.

1.5b. Sensing of Trace Metal Ions:

Besides molecular metabolites sensing, the detection of trace metal ion metabolites via electrochemical approaches can also be performed. Xu et al. has synthesized Au nanoparticle by a laser ablation method and deposited onto a glassy carbon (GC) electrode to make a AuNP/GC composite. The AuNP/GC is then used to detect Cd^{2+} , Pb^{2+} , Cu^{2+} , and Hg^{2+} simultaneously by using differential pulse anodic stripping voltammetric (DPASV) technique.⁴²

With the open-end ongoing pollution from industrial wastages, heavy metal contamination is growing up in daily foods (including vegetables, grains, fish, and meat) and drinking water at an alarming rate. Excess of metal ion concentration, compared to a normal physiological condition, in the human body may cause danger e.g. excess Cu^{2+} concentration in blood may damage the liver, high level of Pb^{2+} may cause neurological damage. etc. Thereby a rapid detection of these heavy metal ions is necessary from a pathological point of view. The ongoing noted methods of accurate metal ion detections include AAS, AFS, ICP-OES, ICP-MS, etc. But all the methods are time-consuming and complex due to their lengthy instrumentation analysis procedure and also expensive to find difficulty in common use.

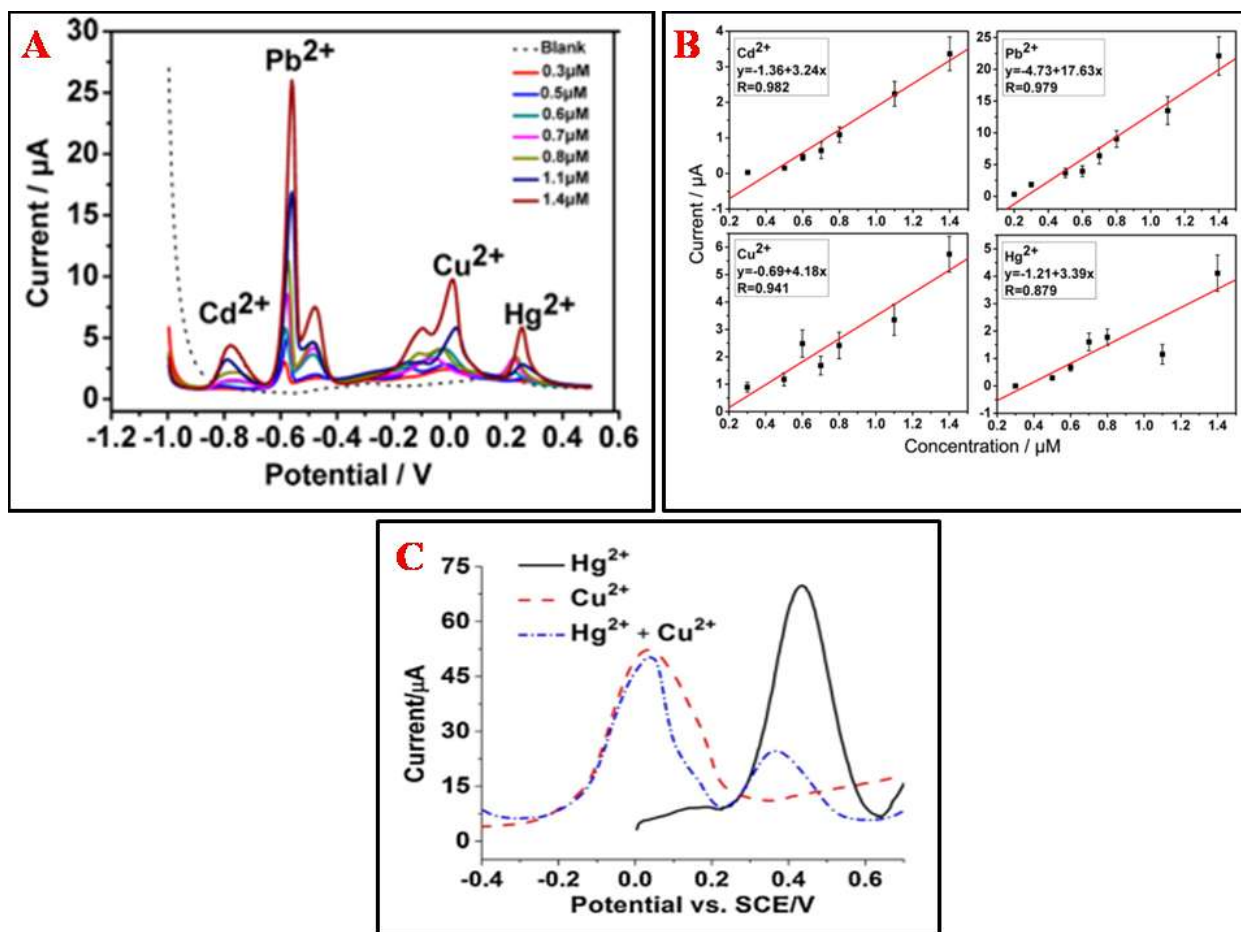


Figure 1.5b(i): (A) DPASV response for AuNP/GC electrode for simultaneous detection of Cd^{2+} , Pb^{2+} , Cu^{2+} , Hg^{2+} at a time over a concentration range of 0.1-1.4 μM , (B) Linear calibration plot for Cd^{2+} , Pb^{2+} , Cu^{2+} , Hg^{2+} from figure 1.5bi (A)⁴², (C) A comparison of anodic stripping voltammetry of 0.5 μM Hg^{2+} and 0.5 μM Cu^{2+} and a mixture of both.⁴³

In contrast, electrochemical techniques are less expensive and easy-to-handle but have advanced adequately to a level by which we can use them for rapid quantitative measurements too. In a recent report, Ting et al. have shown that graphene quantum dot (GQD) functionalized Au nanoparticle was used for low-level detection of Hg^{2+} (0.02 nM) and Cu^{2+} (0.05 nM).⁴³ They were also able to perform simultaneous detection of Hg^{2+} and Cu^{2+} by anodic stripping voltammetry as shown in **Figure 1.5(i)C**.

Therefore, noble metal nanocatalyst and nanocomposites are equally capable in both sensing and quantification of trace metal ion metabolites by producing characteristic peak potential and peak current in DPV response respectively. In our study, we have synthesized a highly porous Au-Ag network (Described in Chapter-7 in detail) and used it as an electrode material for reducing heavy metal ion metabolites like $\text{Hg}^{2+} \rightarrow \text{Hg}^0$, $\text{Cu}^{2+} \rightarrow \text{Cu}^0$, etc and were able to record sharp peaks for individual metal ions. We were also able to perform simultaneous electrochemical detection of multiple heavy metal ion metabolites by using our synthesized porous Au-Ag network as electrode material.

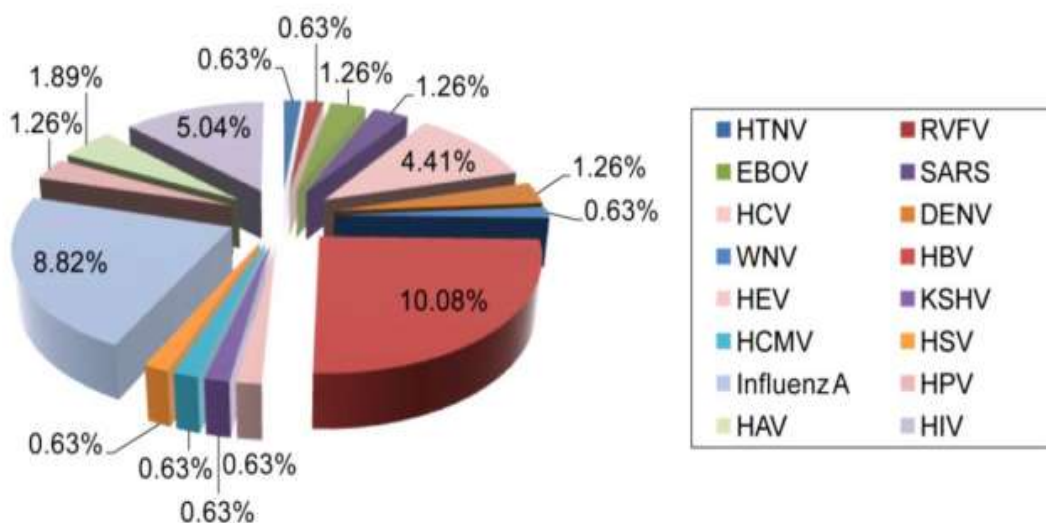


Figure 1.5b(ii): Statistical distribution of AuNP used for the detection of different viruses in which HBV is the most reported one for using AuNP as a sensing probe.⁴⁴

1.5c. Sensing of Virus:

AuNPs have widely been used before for the ultrasensitive detection of viruses. In a study by Draz et al.⁴⁴ have shown that AuNP-hybrid system composed of AuNP and a receptor (like DNA/RNA aptamer or antibody) has been widely used for the detection of different groups

of viruses like Bunyaviridae, Rift Valley Fever Virus, Coronaviridae, Filoviridae, Flaviviridae, etc.

Out of the several methodologies to detect viruses like zika, dengue, chikungunya, influenza, etc in the infected human serum, the most trusted one is the RT-qPCR for the specification of the serotype of a virus along with its quantification. But due to their cost-ineffectiveness, time-consuming nature, and complicated performance procedure, we do need to develop an ease-handling and low-cost approach to carry out sensing for viruses, bacteria, etc. Electrochemical techniques are much more accepted in this regard. In most of the reported electrochemical approaches, the EIS technique has been used for the detection of viral RNA both quantitatively and qualitatively. In a study by Dutta Chowdhury et al.⁴⁵, as shown in **Figure 1.5c**, the Hepatitis E virus has been detected by using gold nanoparticle embedded polyaniline nanowires and graphene quantum dot via EIS technique. The polyaniline chain was conjugated with the HEV-specific antibody and it was found that the sensor was very effective for each serotype of HEV and the result gives close agreement with the recorded RT-qPCR. It was shown that with the application of an external pulse between 0-1.2 V during viral loading, the sensitivity (in terms of impedance) was increasing accordingly. The Nyquist plot was then fitted to the equivalent Randles cell to obtain the charge transfer resistance (R_{ct}). The reason behind increasing the impedance with increasing viral load is that specific binding to the electrode surface with increasing virus concentration which results in less current passed across the electrode surface.

In recent times, DNA/RNA aptamers have been used instead of antibody and the applied aptamers can easily be modified by thiol group for specific binding to the Au-Ag nanoalloy due to the strong chemical affinity of the thiol group (-S-H) toward noble metals like Au, Ag, and

Cu. In our study also we have used a thiol modified aptamer for making a bioconjugate with the synthesized porous Au-Ag nanoalloy. The bioconjugate was then used as an electrode material for specific binding and the resultant detection of DENV-2 in presence of other related serotypes of DENV by impedimetric assay.

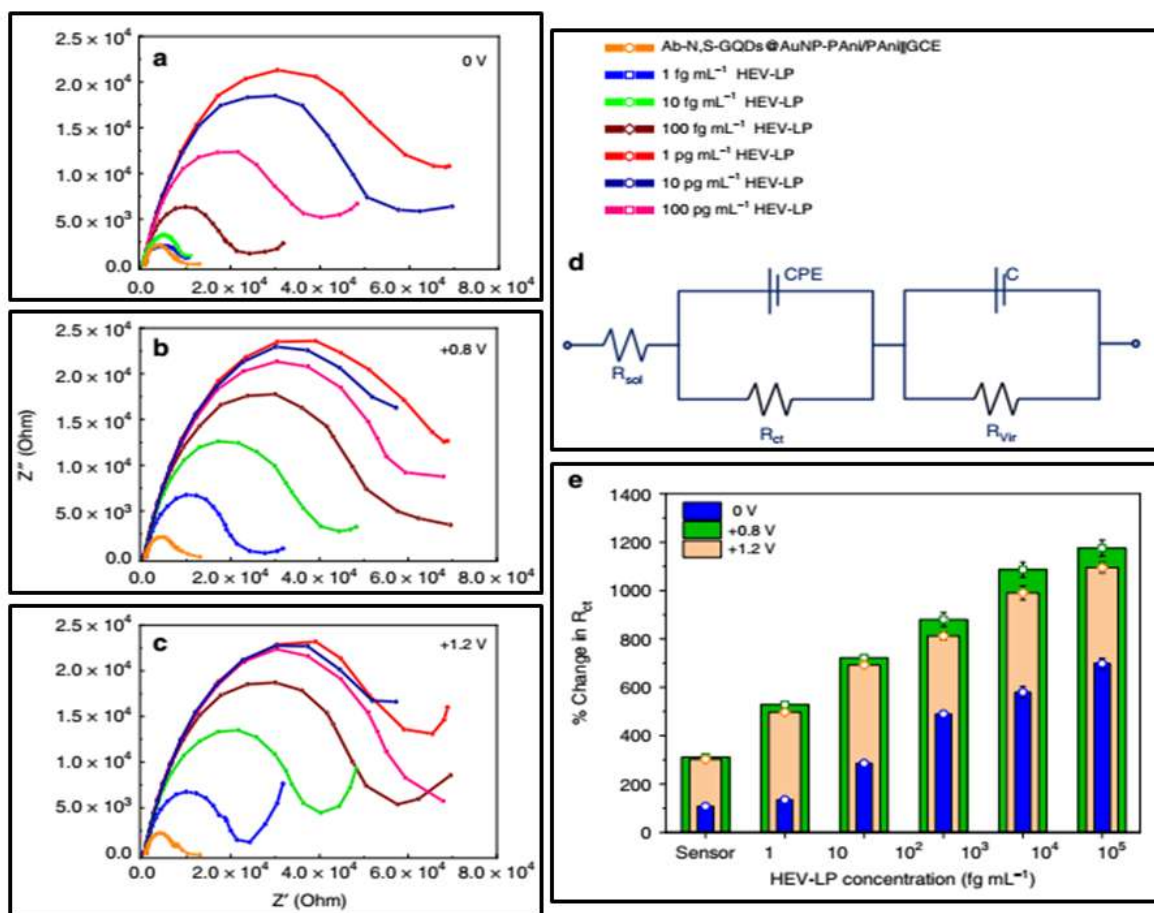


Figure 1.5c: EIS response from the sensor with different concentrations of viral load by using an external pulse of (a) 0 V, (b) + 0.8 V, and (c) + 1.2 V. In (d) an equivalent Randles cell has been shown to obtain the R_{ct} value. (e) A typical histogram is provided for sensitivity with a variable external pulse. It is clear at + 1.2V external pulse, maximum response with selectivity has been achieved.⁴⁵

The greater stability of AuNP or Au-Ag nanoalloy under an applied potential in electrochemical measurements allows us to detect the viruses accurately. Since a DNA- or RNA- aptamer cannot stabilize themselves on the electrode surface, here we have used the thiol-linked nanoalloy as a support material. Au-Ag nanoalloy being very easy to synthesize with high porosity and can bind the thiol modified aptamer by preparing a bioconjugate or nanohybrid system which is stable over the electrode surface.

1.6. Application in Fuel Cell Technology:

1.6a Alcohol Fuel Cell:

Direct-methanol fuel cells (DMFCs) are considered to be one of the most promising sustainable and cleaner energy alternatives compared to traditional fuels like petrol and diesel. Since in a direct methanol fuel cell we perform the oxidation of methanol, we pay more attention towards the anodic reaction to improve its faradic efficiency by applying suitable catalytic material on the anode surface. Out of the several electrocatalysts reported so far, Pt or Pt-based materials are considered to be the best. The presence of CO as a dissociative product of methanol plays a big role to reduce the catalytic efficiency (poisoning of catalyst) of Pt by blocking its active sites for the hydrogen oxidation reaction (HOR). In this regard Au-Ag electrocatalyst can be considered as an alternative for the electrooxidation of MeOH. In the past, Au is not considered to be suitable for any catalytic applications due to its high overpotential and low redox kinetics. Au is the only metal that has endothermic O₂ absorption energy and hence illustrating its inert behavior in an oxygen atmosphere ⁴⁶. On the contrary, tailored Au, Ag, or Au-Ag nanoparticles defect enriched active sites, acts as efficient as the Pt/C catalyst in alcohol oxidation. Xiong et al. ²⁰ in their study have observed that Au₃Ag nano-frame with multiple edges and screw dislocation defects act as active sites for efficient MeOH oxidation in 0.5M KOH

solution with greater faradic efficiency than the commercial Pt/C. Catalytic ability of Au₃Ag nano-frame by comparing with standard Pt/C and other nanoalloy has been detailed in **Figure 1.6a**. The onset potential for the Au₃Ag nano-frame appears at 0.3 V wherein for Pt/C the onset is 0.4 V. The peak current density is also lower for Pt/C than the corresponding Au₃Ag nano-frames. The CO stripping experiment indicates less CO poisoning for the Au₃Ag nano-frame than Pt/C. Besides MeOH, electrooxidation of other alcohols like EtOH (C₂H₅OH), ethylene glycol (C₂H₆O₂), and glycerol (C₃H₈O₃) has also been studied by using our synthesized Au-Ag nanoalloy and a detailed discussion has been included as a separate chapter in this thesis.

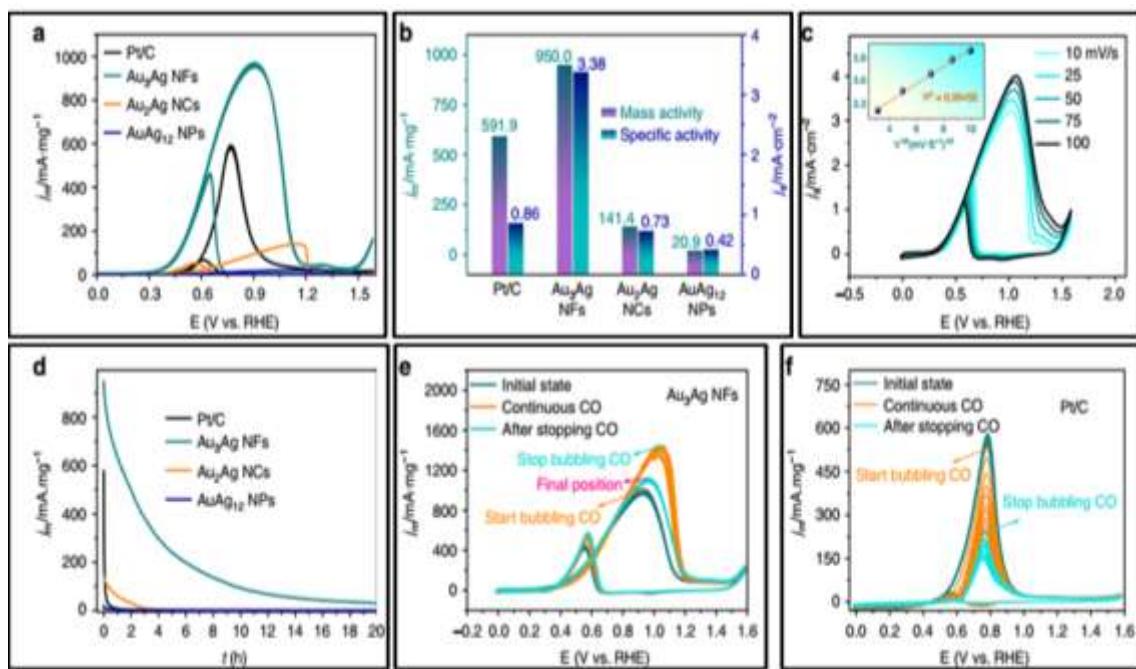


Figure 1.6a: (a) Comparison of CV for the electrooxidation of 2 M methanol in 0.5 M KOH at a scan rate of 20 mV/S with other related catalysts, (b) histogram for (a) with specific activity and mass activity, (c) CV of Au₃Ag nano-frame at different scan rate, (d) comparative chronoamperometric I-t curve for 20 h for different electrocatalysts, (e) CV curve for Au₃Ag nano-frame under CO supply with turn on and turn off mechanism, (f) CV curve for Pt/C under CO supply with turn on and turn off mechanism. ²⁰

1.6b ORR activity:

In an alcohol fuel cell, the overall reaction is represented as: $\text{ROH} + \text{O}_2 \rightarrow \text{CO}_2 + \text{H}_2\text{O}$, where ROH is the alcohol under study. This means that the efficiency of alcohol oxidation depends heavily on the effective simultaneous reduction of O_2 . In any kind of fuel cell, the reduction of O_2 is a key step to get an overall high faradic efficiency. In this regard, it is essential to develop a suitable catalyst that can support the faster reaction kinetics for both alcohol oxidation and O_2 reduction. Pt is always regarded as the best catalyst in this respect. But due to its high cost and scarcity in abundance, a substitute to Pt catalyst is absolutely necessary in the present scenario to find their profitable industrial applications. Literature is rich to find the potential application of noble metal electrocatalysts in oxygen reduction reaction (ORR). In a study by Shim et al.,⁴⁷ high faradic efficiencies were observed for AuNPs during ORR by electrochemical performances. In another study by Wang et al.⁴⁸ has shown that smaller gold nanoclusters supported on carbon (C) demonstrate high reactivity in comparison to that of commercial Pt/C. The smallest nanocluster Au_{25} shows the highest catalytic property with an onset potential of 0.92V to the reference hydrogen electrode (RHE) and a higher number of electron transfers within the potential range of + 0.5 to + 0.8 V as shown in **Figure 1.6b**.⁴⁸ Also, the number of electron transfer within the potential range + 0.5 to + 0.8 V was higher for Au_{25} and porous C composite (3.6-3.92) compared to other Au nanocluster (Au_{38} and Au_{144}) and porous carbon composites.

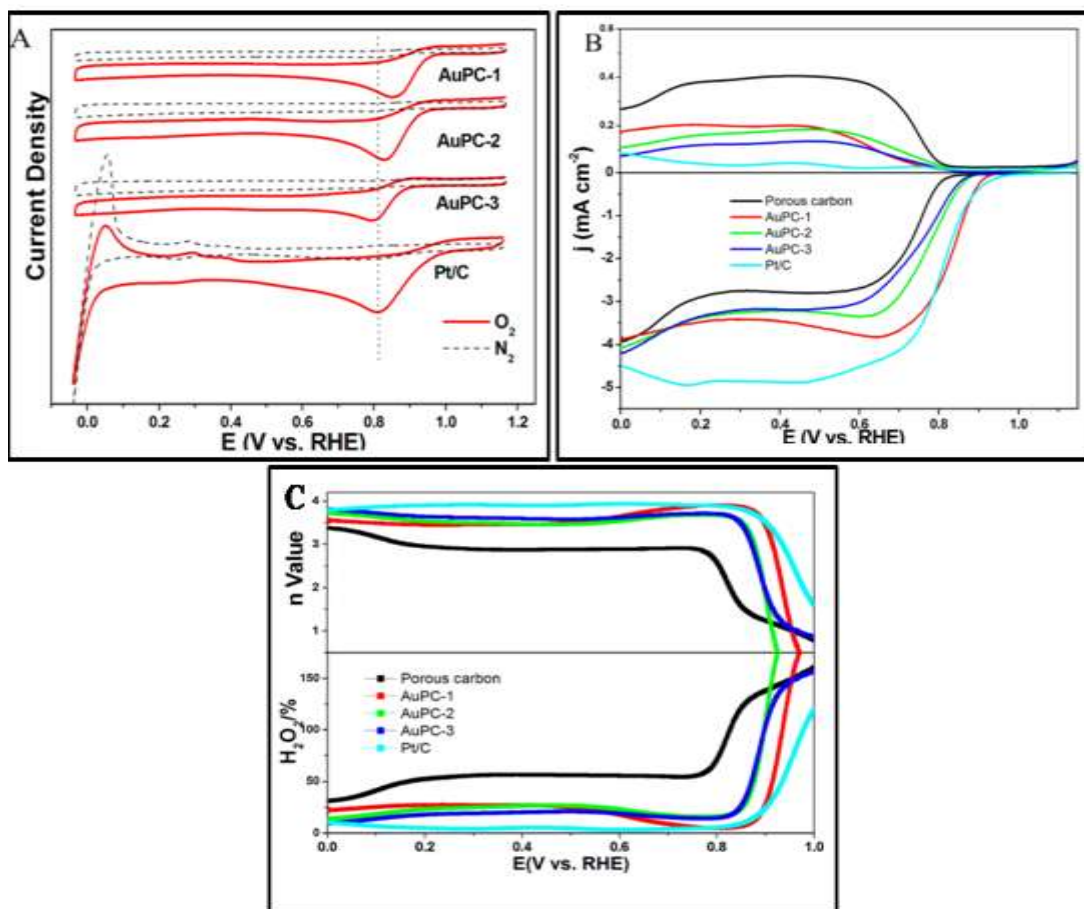


Figure 1.6b. (A) CV curves of AuPC-1, AuPC-2, AuPC-3 nanocomposites, and commercial Pt/C catalysts recorded in nitrogen-saturated and oxygen-saturated 0.1 M KOH. Here AuPC means Au nanocluster and porous C composite. (B) The ORR polarization curves of porous carbon, AuPC-1, AuPC-2, AuPC-3 nanocomposites, and commercial Pt/C catalysts in O₂-saturated 0.1 M KOH with a rotation speed of 2500 rpm. (C) Variation of H₂O₂ yield and electron transfer number at various potentials.⁴⁸

1.6c Reduction of CO₂:

During the combustion of fuel whether it is petrol, diesel, or alcohol, the resultant emitter is CO₂ which is one of the major greenhouse gases. To reduce this greenhouse burden from our

environment, conversion of CO_2 to fuel like methanol for close-end CO_2 recycling is very important and opens up a hot research topic in the present days. Recently it has been observed that Au-Cu bimetallic catalyst is very effective for CO_2 conversion to formate⁴⁹ though individually Au and Cu monometallic nanoparticles are not so attractive for the mentioned job. A schematic representation of the Au-Cu bimetallic system and its catalytic pathways is shown in **Figure 1.6c**. It was observed that Cu mesh when used as electrocatalyst converts CO_2 to CH_4 , CO , and C_2H_4 with a faradic efficiency $< 70\%$ at -0.96 V. Similarly, Au nanocatalyst tends to convert CO_2 to CO . Thus a high selectivity is always in demand for catalytic conversion of CO_2 to methanol. In a study by Tao et al. has shown that when Au nanoparticles are embedded in CuO , the resultant Au-Cu bimetallic system is highly efficient for CO_2 to formate conversion than CuO .

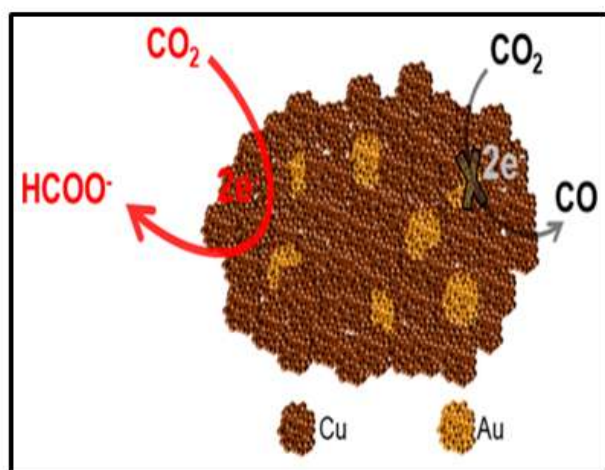


Figure 1.6c: A schematic presentation of the Au-Cu system where selectivity achieved for the conversion of CO_2 to formate and the reaction of CO_2 to CO has been hidden.⁴⁹

In the Au-Cu bimetallic system, Au acts as a promoter. Quasi in-situ XPS was performed to observe the oxidation state of Au and Cu and it was observed that Cu^+ exists in the Au-Cu system along with the existence of Au^0 and Cu^0 . Even after long term catalytic performances, the oxidation states of metals retained. The existence of Cu^+ is accounted for the selectivity for CO_2 to formate conversion which can be easily reduced to methanol.

1.6d HER and OER:

Photochemical or electrochemical water splitting to produce H_2 is a high-demanding research field to overcome the shortage of fuel. Hydrogen is regarded as a green fuel with high energy density and pollution-free (cost-effectiveness and environmentally friendly) which can be alternative and competitive to that of coal or oil. Thereby low-cost production and safe storage of H_2 are precious steps in the H_2 economy. Pt/C is regarded as the most efficient catalyst in this aspect. However, as discussed before, we need an alternative one for reducing the production price. In this regard tailored shaped Au nanoparticle with multiple active sites can be considered as an alternative. In a study by Tran et al.⁵⁰ have shown that Au nanoparticle with an average diameter of 13 nm acts as a good electrocatalyst for hydrogen evolution reaction (HER) with an overpotential around 200 mV and turnover frequency around 0.3 s^{-1} . In our study, we have designed sodium dodecyl sulfate (SDS) capped anisotropic gold nanoparticles (A^nGNPs) which exhibit outstanding catalytic activity (in terms of both overpotential and turnover frequency) towards hydrogen HER in different pH medium compared to that of normal spherical shaped gold nanoparticles (e.g. TSC-capped 25 nm S^pGNPs) in similar physical conditions (***Ref. ACS App. Ener. Mater., Communicated, chapter 6 in this thesis***)⁵¹ Besides, the designed nanomaterials require a mere 190 mV (vs RHE) of overpotential to achieve 10 mA cm^{-2} current density in 0.5 M H_2SO_4 medium.

Besides HER, plasmonic nanomaterials can also be used in oxygen evolution reaction (OER). In a study by Zhao et al. has shown that gold nanocluster Au_{25} , when embedded into CoSe_2 , the resultant $\text{Au}_{25}/\text{CoSe}_2$ composite exhibits high OER activity in alkaline medium with an overpotential of 0.43 V at 10 mA/cm^2 current density as shown in **Figure 1.6d**.⁵¹

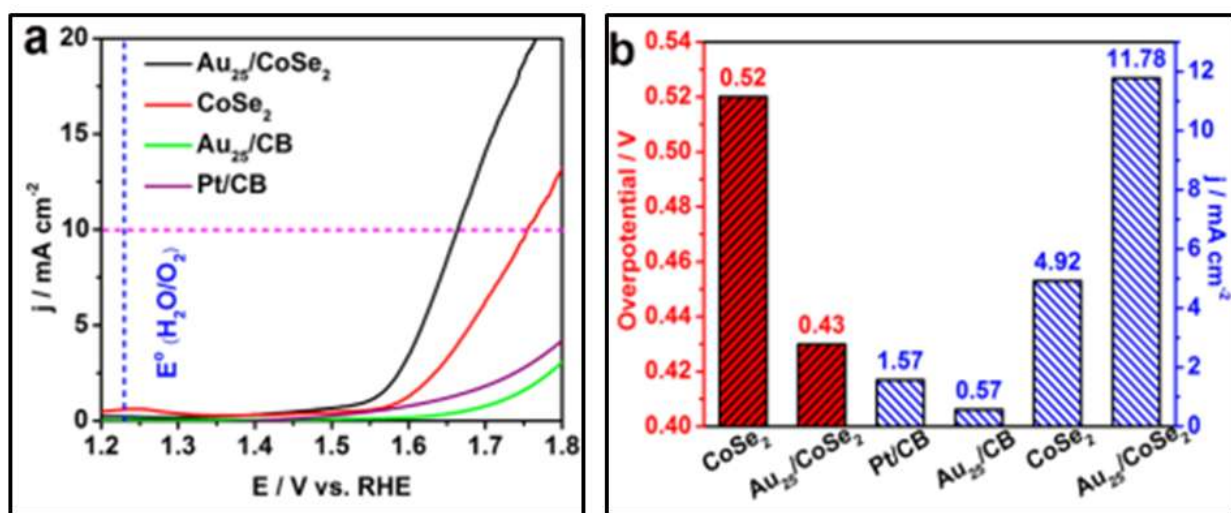


Figure 1.6d: (a) OER polarization curve for different systems in which $\text{Au}_{25}/\text{CoSe}_2$ shows the higher current, (b) a histogram for comparison of current density and overpotential for different systems.⁵¹

1.7. Theranostics Application of Plasmonic Noble Metal Nanoalloy:

Theranostics is a new field into which targeted therapy is carried out based on the specific diagnostic test rather than the traditional medicinal approach⁵². In modern days, DNA aptamer-based targeted therapy caught attention for reducing infections, pain, and wounds caused by viral or bacterial infections⁵³. There are enormous reports in the literature in which Au and Ag nanoparticles are used as antibacterial or antiviral agents in mammals. However, there is always a question that arises regarding their cyto- or geno-toxicity towards mammalian cells. In this regard, the synthesis of biocompatible tailored shaped plasmonic nano-alloy gets significant attention in the present days. Biocompatible Au, Ag, and Au-Ag nanoalloy can be prepared by

using several capping agents like chitosan, oligonucleotides, amino acids, etc.⁵⁴ However, the stability of those biocompatible nanomaterials is always under question. In physiological pH (in the blood) level, in presence of high-level salt concentration, nanomaterials get aggregated. To avoid these drawbacks and to improve their retention in physiological conditions for long term circulation in body fluid, surfactant capped Au, Ag, or Au-Ag nanoalloy can be used as a strategy. The use of surfactants should be at a minimal level, only to stabilize the nanoparticle and to get a monodisperse solution, without disturbing their inherent theranostics properties. The CTAB or CTAC (known to cytotoxic surfactants) capped plasmonic nanoalloys can be made biocompatible by coating with PVA. In our study, during targeted treatment against Dengue serotype-2 (DENV-2), we have used PVA capped tailored Au-Ag nanoalloy with diameter < 40nm. The toxicity was checked in HCT-116, RAW, and HEPG2 cell lines by MTT assay and it was observed that it was non-toxic in the concentration level which was used to inactivate the DENV-2.

Thus biocompatible Au, Ag or Au-Ag nanoalloy can be used as good substitutes for traditional antibacterial agents. In a study, by Jena et al.⁵⁵ have shown that Au-Ag nanoaggregates are effective for bacterial inhibitions compared to their non-aggregated monometallic or bimetallic counterparts, as shown in **Figure 1.7**. The result concludes that with multiple defects enrich surface sites, Au-Ag alloy nanoparticles are highly strained and efficient to prohibit bacterial growth at a low dose level where it is zero-toxic to mammals.

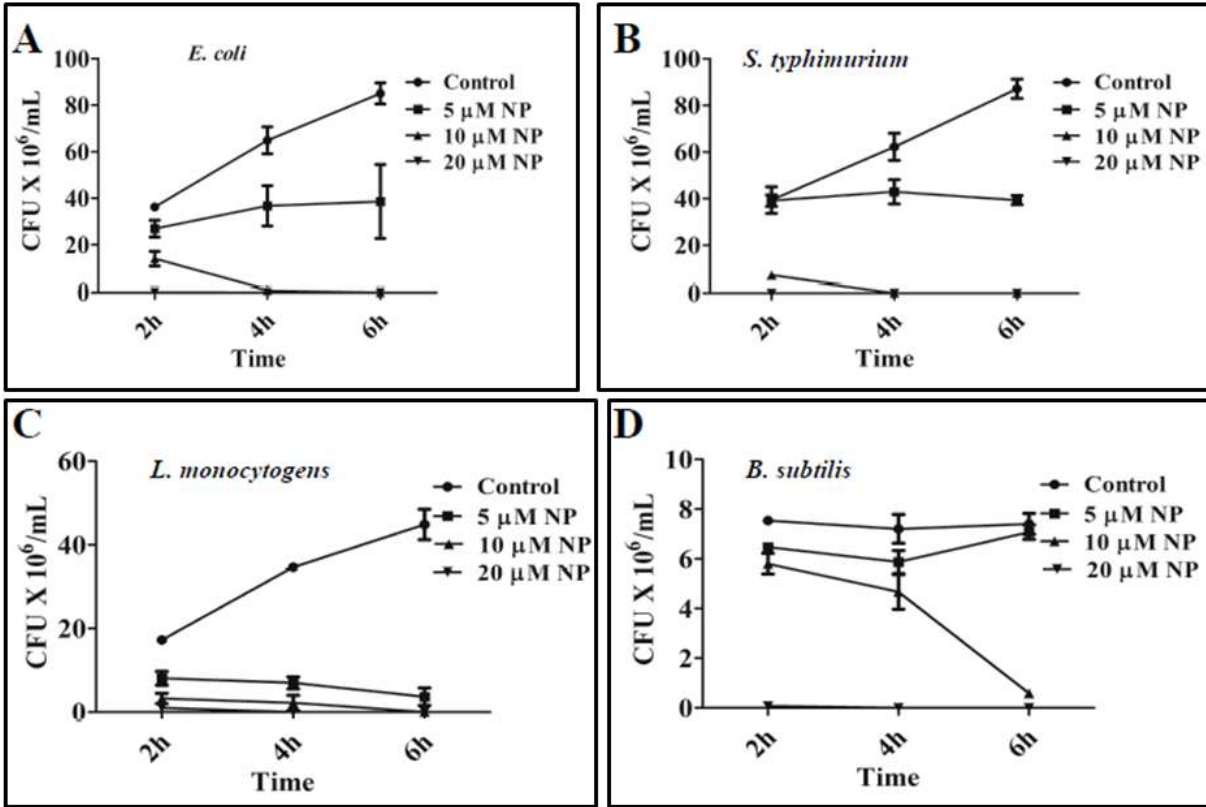


Figure 1.7: Antibacterial activity of Au-Ag NP. Viability determination of **A. *E. coli***, **B. *S. typhimurium***, **C. *L. monocytogenes***, **D. *B. subtilis*** in presence of different concentrations of Au-Ag NP for 2, 4 & 6 hours. Approximately $2-3 \times 10^7$ /mL number of bacteria were used at 0 hour time for *E. coli* and *S. typhimurium*, $1-2 \times 10^7$ /mL for *L. monocytogenes*, and 3×10^6 /mL for *B. subtilis*. The NP treated cultures were serially diluted after indicated time points and plated in LB agar to count the viable colonies. Results are shown with mean and SD. **E. Live-dead staining.** *E. coli* cells expressing MreB^{SW}-mVenus were incubated with Au-Ag NP, A22, and CCCP for 4 hours, stained with PI for 10 mins, washed and observed under the microscope to distinguish dead and live cells. Images shown for MreB are deconvolved.⁵⁵

CHAPTER-2

Methodology and Experimental Set-Up

2.1 Chemical Materials

Almost all the essential chemicals were purchased from Sigma Aldrich and used without any further purification. Milli-Q water with a resistivity of 18.2 MΩ.cm was used for all the preparation steps.

Reagent Name	Specification	Company
Ethylene glycol	EG, Anhydrous 99.8%	Sigma Aldrich
Gold(III) chloride trihydrate	HAuCl ₄ .3H ₂ O; ≥ 99.9%, trace metals basis	Sigma Aldrich
Silver Nitrate	Bioextra ≥ 99%, titration	Sigma Aldrich
Sodium borohydride	NaBH ₄ , 10-40mesh, 98%	Sigma Aldrich
L-ascorbic acid	C ₈ H ₈ O ₆ , ACS reagent, 99%	Sigma Aldrich
Hexadecyltrimethylammonium bromide, CTAB	C ₁₉ H ₄₂ BrN, assay, ≥ 99%, AT	Sigma Aldrich
Hexadecyltrimethylammonium Chloride, CTAC	C ₁₉ H ₄₂ BrN, ≥ 98%, NT	Sigma Aldrich
Sodium citrate tribasic dihydrate	C ₆ H ₅ Na ₃ O ₇ .2H ₂ O; Bioultra, for molecular biology, ≥ 99.5% (NT)	Sigma Aldrich
Spectrasol (EtOH)	Spectroscopic grade	Spectrochem
Water	Ultrapure, Milli-Q, resistivity 18.2 MΩ.cm at 25 °C	Merck Millipore
Polyvinyl alcohol, (PVA)	Powder, MW-30,000-70,000	Sigma Aldrich
Acetonitrile	Spectroscopic grade	Spectrochem
Sodium chloride	NaCl, AR, ≥ 99.9%	Sigma Aldrich

Phenol	BioUltra, for molecular biology, \geq 99.5% (GC)	Sigma Aldrich
Chloroform	EMPARTA ACS 99.4%	Merck
Phenol – chloroform – isoamyl alcohol mixture	BioUltra, for molecular biology, 25:24:1	Sigma Aldrich
Isopropanol	BioReagent, for molecular biology, \geq 99.5%	Sigma Aldrich
Sodium acetate	Anhydrous, for molecular biology, \geq 99%	Sigma Aldrich
Hydrochloric acid	HCl, ACS reagent, 37%	Sigma Aldrich
Trizma® base	T1503 Primary Standard and Buffer, \geq 99.9%	Sigma Aldrich
NH ₄ OH	ACS reagent 28-30% NH ₃ Basis	Sigma Aldrich
FeCl ₂	Reagent grade, 98%	Sigma Aldrich
FeCl ₃	Reagent grade, 97%	Sigma Aldrich

2.2 Biochemical Materials

The Dengue-2 specific aptamer was ordered from Ascension life science, India. The aptamer has a specific sequence ($MW=22680.0$) for DIII of DENV-2 and modified at 5' and 3' position by –SH group denoted as:

5'HS_ATACGGGAGCCAACACCATGGGGACCAACTGTCCGGAGAGAGTCCTGTCTGAG
GGAGAGCAGGTGTGACGGAT_SH3'

2.3 Biological materials

Different Dengue serotypes ((including Dengue-1, Dengue-2, Dengue-3, Dengue-4) infected serum was collected from Belegghata ID & BG Hospital with proper cautions and maintain ethical issues. The HCT-116 and Vero cell lines obtained from the National Centre of Cell Sciences (NCCS), Pune, India.

2.4 Methods

2.4.1 Ultraviolet-Visible-NearInfrared (UV-Vis-NIR) Absorption Spectroscopy

The UV-vis-NIR experiments are based on the principles of Beer-Lambert law: when a beam of monochromatic light falls on a solution and absorbed by the substances present within the solution, the rate at which the intensity of the beam decreases, is proportional to the concentration of the substance⁵⁶. Not like molecules, we need to know the exact extinction coefficient which varies with size and shape, to measure the exact concentration of nanoparticles in the solution by absorption spectroscopy. In most cases, we adopt a combination of TEM/SEM and Atomic Absorption Spectroscopy (AAS)/Inductively Coupled Plasma Mass Spectroscopy (ICPMS) to measure the concentration of a monodispersed geometric shaped nanoparticle. As a result, the absorption spectrum is always considered as an indirect technique to make an idea about the variation of concentration of a specific type of nanoparticle solution. In general, for plasmonic nanomaterials we measure their surface plasmon resonance (SPR) which is defined by the quantized oscillation of the surface charge produced by an external electromagnetic field and is characterized by a specific frequency associated with its absorbance.⁵⁷ Due to the different frequency of SPR, a similar size Au and Ag nanoparticles have different colors (red and yellow) in solution. The characteristics of Plasmon band depends on the following factors: (1) **Effect of Size:** Considering the surface free electrons in a one-dimensional potential box, red shifting of the Plasmon band is proportional to their size which means a nanoparticle with the same shape but with a bigger dimension shows a red-shifted Plasmon band and vice versa⁵⁷. (2) **Effect of shape:** Depending on the shape of the nanoparticle and hence the availability of different modes of free electron oscillations we may observe more than one Plasmon bands.⁵⁸ In general, for isotropic (uniformity in all orientations) nanoparticles we observe a single Plasmon band whereas

for anisotropic (property of being directionally dependent) nanoparticles we observe more than one Plasmon band and the number of observed bands increases with increasing the anisotropy.⁵⁹

For example, a spherical or isotropically surface-tip projected star-shaped nanoparticle shows a single Plasmon band⁶⁰ whereas a rod-shaped nanoparticle shows two Plasmon bands due to the presence of longitudinal and transverse surface electron oscillation modes. (3) ***Effect of***

refractive index: The refractive index (n) near the nanoparticle surface also influences the optical properties of the Au/Ag nanomaterials.⁶¹ As the refractive index near the nanoparticle surface increases, the extinction spectra of nanoparticles shift to longer wavelengths. Thus if we move from water ($n=1.33$) to air ($n=1$) media, Plasmon band of the nanoparticle will shift towards the shorter wavelength (blue-shifting) whereas if we move to oil ($n=1.5$) surface Plasmon will shift towards the higher wavelength (red-shifting) ; (4) ***Effect of particle association***: Followed by the

same principle of Molecular Orbital Theory (MOT), nanoparticle association induces the delocalization and hence sharing of conduction electron cloud among nearby nanoparticles to increase the path length of surface free electrons (in a one-dimensional potential box) which causes a lowering in Plasmon excitation energy and hence red shifting of Surface Plasmon Resonance band detectable primarily by UV-Vis-NIR absorption spectroscopy,⁶² and (5) ***Effect of mole fraction in an alloy***: Due to the modified electronic level structure, the absorption property of a plasmonic nanoalloy differs significantly from its monometallic counterpart. In a bimetallic Au-Ag nanoalloy, an increased mole fraction of Ag causes a blue-shifting whereas an increased mole fraction of Au causes a red-shifting of their Plasmon spectra.⁶³

All the UV-Vis-NIR spectral measurements are performed in JASCO V770 and JASCO V650 spectrophotometers, as shown in **Figure 2.1**. In general, before each measurement, we have

diluted the centrifuged solution to keep the overall absorbance below 1.0 following Beers law. For all absorbance measurements, we have used a quartz cuvette of 10 mm path length.



Figure 2.1: (A) JASCO V-770 UV-Vis-NIR spectrophotometer with spectral range 190-3200 nm, (B) JASCO V-650 UV-Vis spectrometer fitted with Peltier for temperature-dependent study with spectral range 190-900 nm.

2.4.2 Dynamic Light Scattering and Zeta Potential Measurement

The principle of dynamic light scattering (DLS) is based on the Brownian motion of particles in a liquid medium. Nanoparticles in a solution move randomly and collide with the fast-moving solvent molecules and thereby transfer their energy. This causes the prohibition of motion for smaller nanoparticles heavily than larger particles. If the other parameters (temperature, pressure, ionic strength, etc.) kept constant, one can determine the hydrodynamic size of the nanoparticle using Stokes-Einstein relation⁶⁴, $D = k_B T / 6\pi\eta R_H$, where D is the translational diffusion coefficient, k_B is the Boltzman constant, T is the temperature, η is the viscosity, and R_H is the hydrodynamic radius. A single-frequency laser (632.8 nm: He-Ne laser) is used as the light source in DLS measurements in our Malvern Zetasizer ZS90 instrument. The scattered light is detected at a certain angle (in our case 90°) and the signal is used to determine the diffusion coefficient using correlation function as programmed in the instrument. In our DLS

measurements, only the translational motion of the nanoparticles is considered during the execution of their Brownian motion and hence the obtained hydrodynamic diameter gets the contribution from the translational motion only. During all DLS measurements, we need to follow an important parameter called polydispersity index (PDI) which signifies the monodispersity of the nanomaterials. A value of $<10\%$ of PDI indicates a monodispersed sample. The optical set up for a DLS instrument is shown below (**Figure 2.2**) for the Malvern series where the detector is placed at different angles to identify the scattered light. An attenuator is used in the instrument for controlling the light intensity to the detector e.g. if the particles are very small then the intensity of scattered light will be less, hence the attenuator will allow more light to pass through whereas if the particles are large enough then the intensity of scattered light will be more and the attenuator will allow less light to pass through. In DLS measurements the concentration of the sample should be optimized during each measurement so that the scattering signal should not be oversaturated or too little to detect.

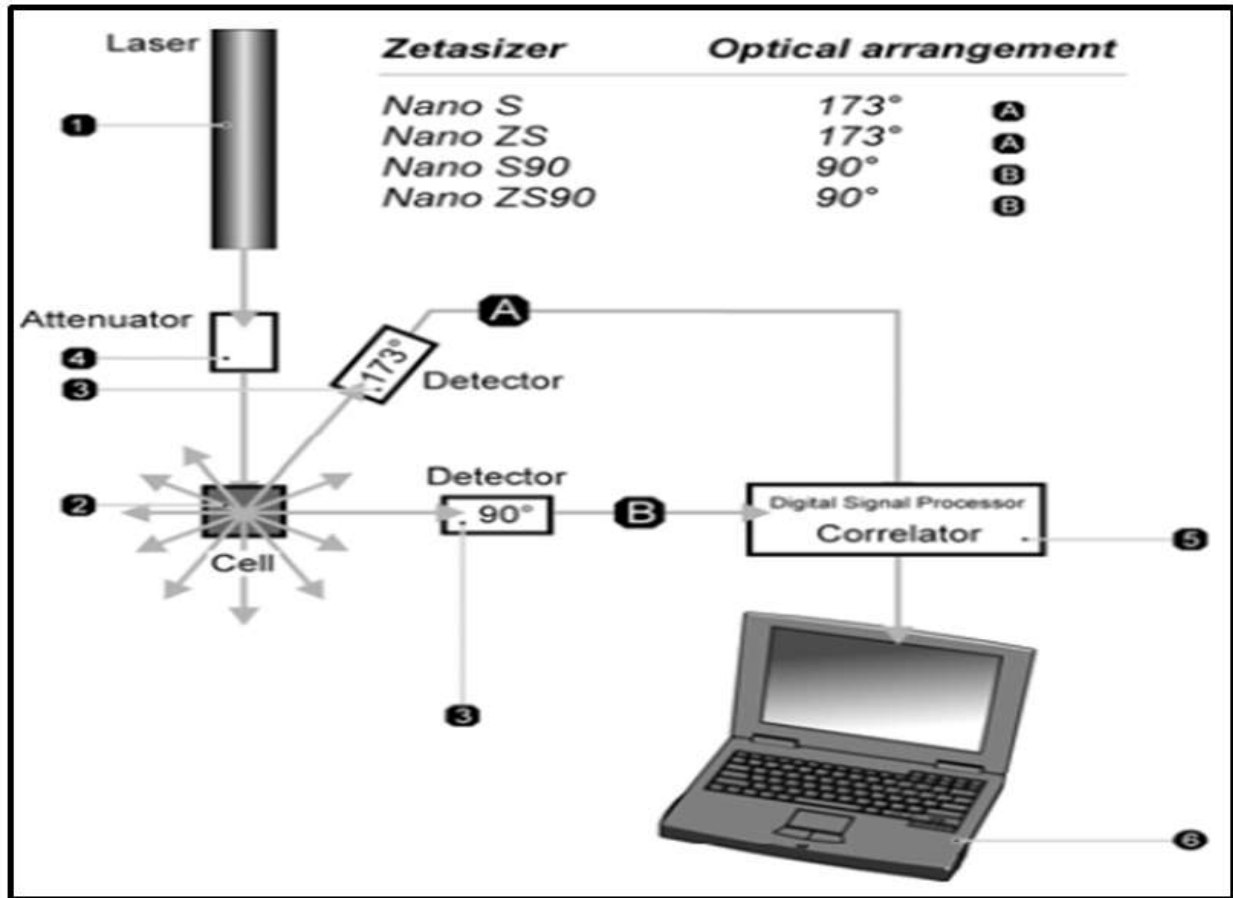


Figure 2.2: Optical configurations of the Malvern Zetasizer Nano series for dynamic light scattering measurements where ① is the laser source, ② is the sample cell, ③ is the detector, ④ is an attenuator, ⑤ is the digital processing board called a correlator, and ⑥ is the data processing computer. Here (A) represents the detector position at 173° and (B) at 90° with respect to the exciting light source. In all cases, the excitation wavelength is 632.8 nm.

The technique used in our Malvern Zetasizer ZS90 instrument (**Figure 2.3**) to measure the zeta potential is Electrophoretic Light Scattering (ELS) where a specific potential is applied between two electrodes (in our case Au electrode) and the ionic mobility is measured from the Doppler shift i.e. shift in the scattered and incident light. Depending upon the mobility (μ_e) of the nanoparticle, scattered light shifted from its original frequency. This shift is called Phase (or Doppler) shift⁶⁵ and measured by the difference between the frequency of the scattered (ν_{sca}) and incident (ν_{inc}) light ($|\nu_{sca}-\nu_{inc}|$). The nanoparticle velocity (V) is measured from the Doppler shift in $\mu\text{m/s}$ by applying the equation $\mu = V/E$, where E is the applied electric field. If nanoparticles are made up of any negative surfactants like SDS, trisodium citrate (TSC), etc, the particles possess an overall negative charge and hence move towards the positive electrode and show a negative zeta potential. The reverse case happens if we use any positive surfactants like CTAB, CTAC, etc where particles show positive ionic mobility and attracted towards the negative electrode to show a positive zeta potential.



Figure 2.3: Malvern Zetasizer ZS90 instrument

2.4.3 X-ray Photoelectron Spectroscopy:

X-ray photoelectron spectroscopy (XPS) is a surface-sensitive quantitative spectroscopic technique based on the principle of the photoelectric effect that can provide information about

the elemental composition of the material. Besides, XPS provides information regarding the oxidation states, overall electronic structure, and density of the electronic states of the material.⁶⁶

The oxidation states of constituent elements of the material can be determined from the shifting and splitting of the XPS peak for a particular element. In general, except hydrogen and helium, other elements can be detected from XPS survey spectra by scanning at a particular position where the element shows its ionization energy. From XPS spectra one can also predict the bonding nature of the element, e.g. if elements like N and S are detected in the survey spectra, then by analyzing their peak shifting one can identify whether there is any bonding between N and S and also the nature of the bond. All the XPS measurements are carried out in a vacuum ($\sim 10^6$ Pa) or an ultra-high vacuum ($< 10^7$ Pa). In a laboratory-based XPS instrument, we use either a 10-30 mm beam diameter non-monochromatic Al K α or Mg K α anode radiation or a focused 20-500 μ m beam diameter monochromatic Al K α radiation. Most of our XPS measurements have been carried out on the Omicron Multiprobe spectrometer (Omicron Nanotechnology GmbH, Germany) fitted with an EA125 hemispherical analyzer as shown in **Figure 2.4**. Monochromatic Al K α X-ray source operated at 150W was used for all of our XPS measurements. During our XPS measurements, we drop cast samples on a tilted (45° angle) Si wafers to prepare a monolayer of the sample on the wafer surface and dried it overnight in vacuum to remove any excess water present in samples.

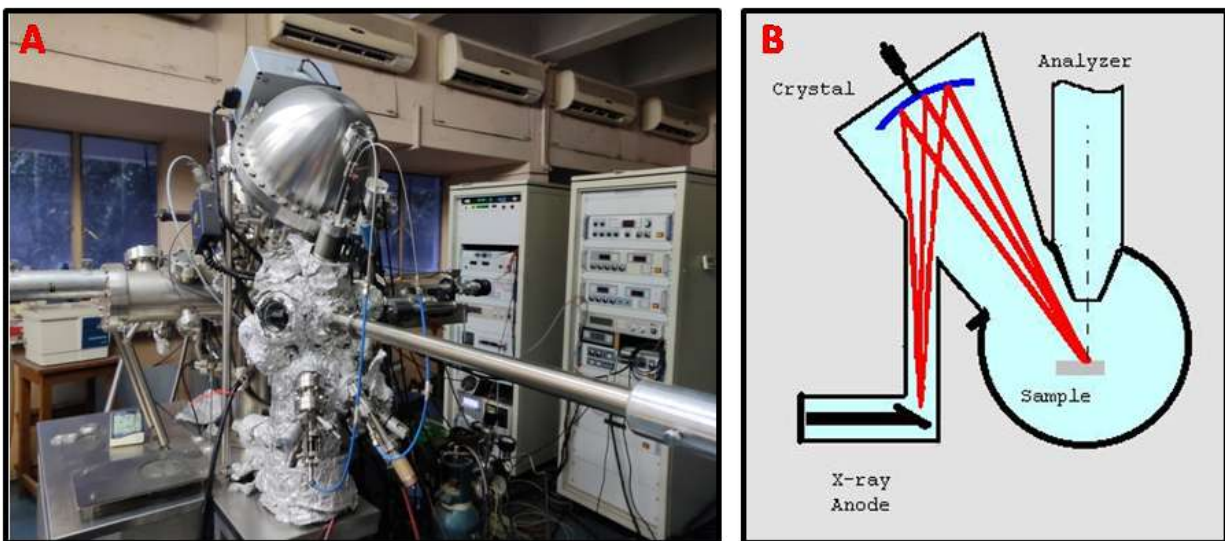


Figure 2.4: (A) Experimental set up for XPS measurement, (B) Layout of an XPS instrument.

2.4.4 X-ray Diffraction Spectroscopy:

X-rays are electromagnetic radiation of shorter wavelength produced by the electronic transition of inner orbital electrons of atoms. X-ray diffraction on nanostructures follows the Braggs law, ($n\lambda = 2d\sin\theta$) where λ is the wavelength of X-ray, θ is the angle of incident of X-ray on the nano surfaces and d is the interplanar distance.⁶⁷ From the XRD measurement, we can predict the number of facets present in a nanostructure like $\{111\}$, $\{110\}$, etc, along with their directions (towards the major axis, minor axis, etc) and relative densities of appearance. XRD gives us the information of a nanostructure on a macroscopic scale and hence the result might vary from TEM measurements which provide similar information on a microscopic scale. In this thesis, we have effectively used the obtained XRD results not only to know the crystal information but also to calculate the generated strain along a crystal plane within the nanocrystal by analyzing the broadening of XRD peaks for individual facets. An ideal crystal will show an appropriate sharp peak for a particular orientation like $\{111\}$ and if any irregularities or defects in crystal arise the XRD curve will be broadened due to the internal strain generated within it. By

fitting the curve and using the Williamson-Hall isotropic model we have calculated the strain generated within the nanocrystal and we observed that nanocrystals with more defect enriched sites show more broadening. The strain is defined as $\varepsilon = \beta/4\tan\theta_{hkl}$, where ε is the strain generated in the nanocrystal, β is the full-width at half maximum of the XRD curve (individual peak) at angle θ (2θ is the central peak position of the fitted XRD curve) in radian. Here, h, k, l denotes the miller indices. In general, to calculate the strain we select the most intense peak, i.e. if any XRD curve of nanocrystals shows multiple facets like $\{111\}$, $\{110\}$, $\{200\}$, etc, and $\{111\}$ is the most intense one among them, we select the $\{111\}$ plane as the reference for strain calculation. All our XRD measurements have been performed in a Rigaku Smartlab X-ray Diffractometer as shown in **Figure 2.5**. We have used a drop cast method for sample preparation. In short, we drop cast the sample on a tilted (45° angle) glass slide to prepare a monolayer over it and dried overnight under the vacuum. The strong adhesion property of our synthesized nanomaterials with glass slide doesn't require any binder to use.

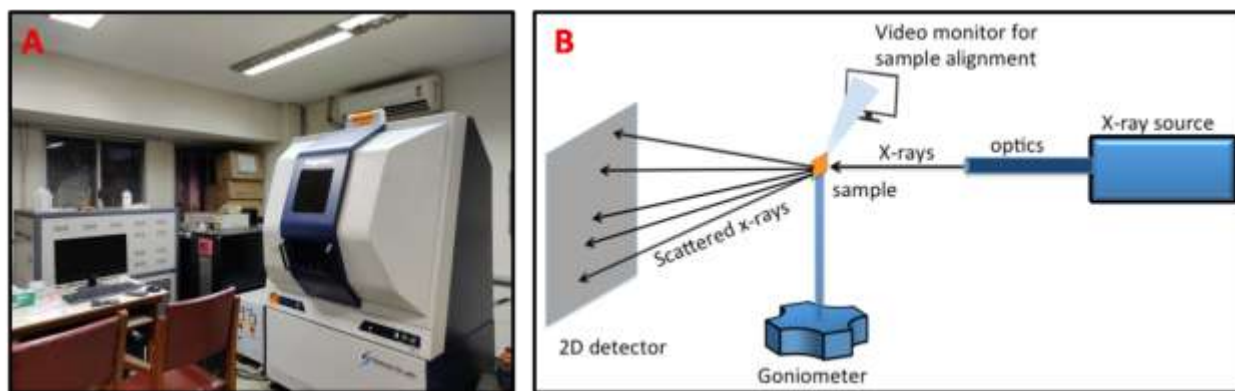


Figure 2.5: (A) Rigaku Smartlab X-ray Diffractometer, (B) Layout of an XRD instrument.

2.4.5 Inductively Coupled Plasma Optical Emission Spectrometry:

Inductively coupled Plasma Optical Emission Spectrometry (ICP-OES) is a technique where the plasma form of substances is used for the measurement of the qualitative and quantitative presence of elements. An energy source is used to atomize the test samples and high-resolution optics to analyze the optical emission spectra from different samples are used along with a detector to measure the intensity of the emitted light.⁶⁸ All our ICP-OES measurements have been carried out in a Thermo Scientific iCAP6000 spectrometer (Freemont CA, USA), as shown in **Figure 2.6**, with NIST standards of 50 ppb, 0.5 ppm, 1 ppm, 15 ppm, 25 ppm, 50 ppm, and 100 ppm. The wavelengths selected for Au are 242.7 nm, 267.5 nm, 283.5 nm and for Ag are 224.6 nm, 328.0 nm, 338.2 nm, and for S are 182.0 nm, 182.6 nm. Before each measurement the centrifuged samples are diluted (50 μ L to 5mL) in Milli-Q[®] ultrapure water and sonicated for 10 minutes.

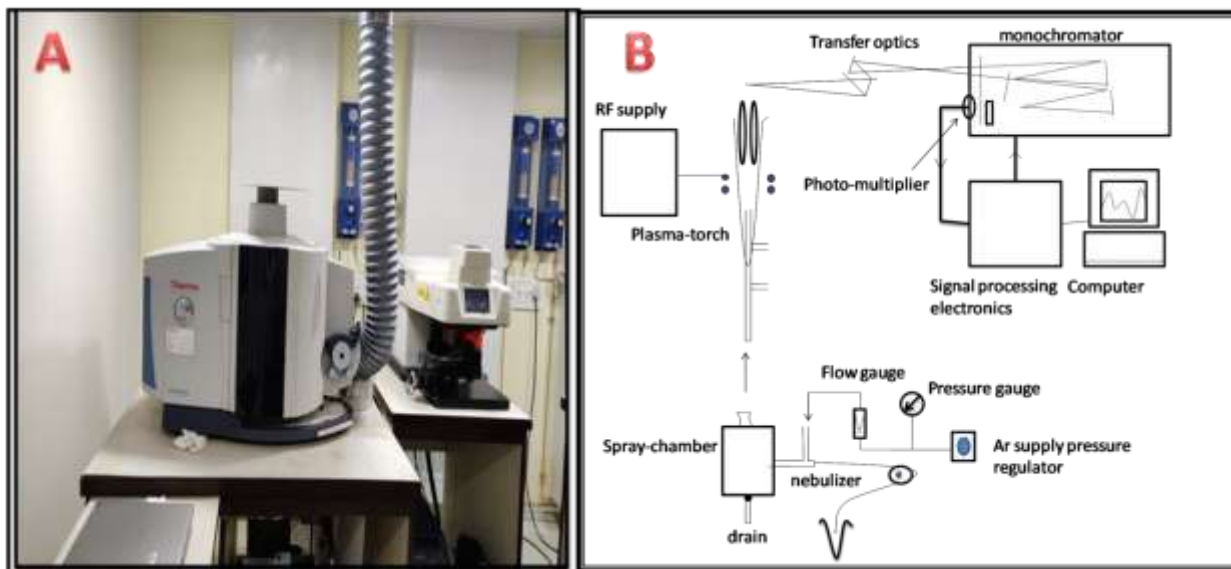


Figure 2.6: (A) Thermo Scientific iCAP6000 ICP-OES spectrometer (Freemont CA, USA), (B) Layout of an ICP-OES instrument.

2.4.6 Surface-Enhanced Raman Spectroscopy:

Surface-Enhanced Raman Spectroscopy (SERS) experiments were performed using a homemade Raman setup. We used a continuous-wavelength diode-pumped solid-state laser from Laserglow Technologies, Canada, operating at 671 (LRS0671-PFM-00300-03) or 532 nm (LRS0532-PFM-00300-03) as excitation light sources (at a fixed excitation energy of 3 mW, using neutral density filters throughout the experiment). For efficient focusing and filtering, we used In Photonicsmade 670 nm and 532 nm fiber optics Raman probe with a spectral range of 200–3900 cm^{-1} (Stokes) for sample excitation and data collection. The Raman probe consists of two single fibers (105 μm excitation fiber and 200 μm collection fiber) with filtering and steering micro-optics (numerical aperture 0.22). The excitation fiber was connected to a THORLABS made fiber port to align the laser, whereas the collection fiber was connected to a spectrometer. A miniaturized QE65000 scientific-grade spectrometer from Ocean Optics was used as the Raman detector with a spectral response range of 220–3600 cm^{-1} . The Raman spectrometer was equipped with a TE-cooled 2048 pixel charge-coupled device and was interfaced to a computer through a USB port. In the end, the Raman spectrum was collected using the Ocean Optics data acquisition Spectra Suite spectroscopy software. Details of the SERS set up and the layout of the instrument is shown in **Figure 2.7**.

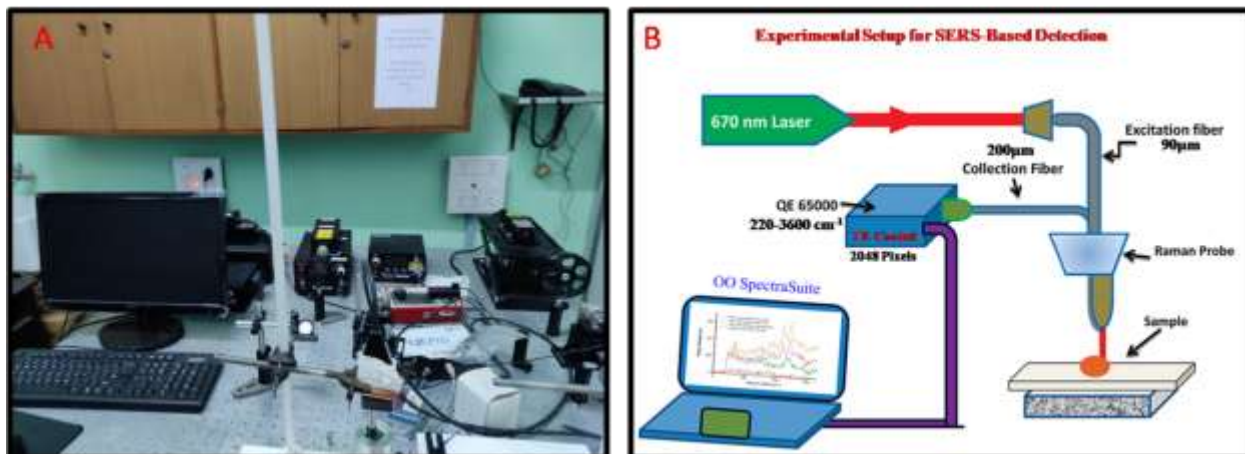


Figure 2.7: (A) Details of the SERS set up, (B) Layout of the instrument.

2.4.7 Atomic Force Microscopy:

Atomic Force Microscopy (AFM) or Scanning Force Microscopy (SFM) is a type of Scanning Probe Microscopy (SPM) with a very high resolution in the order of a fraction of nanometer which is 1000 times better than the optical diffraction limit. The principle of atomic force microscopy is based on the scanning of a specimen surface by a cantilever with a sharp tip, the probe, to construct the topography of that surface.⁶⁹ The cantilever is typically made of silicon or silicon nitride with a tip radius of curvature (κ) on the order of nanometers. When the tip is brought into the proximity of a sample surface, forces (mechanical force, chemical force, electrostatic force, thermal force, magnetic force, van der Waals force, capillary force, etc) between the tip and the sample lead to a deflection of the cantilever according to Hooke's law. The basic difference of AFM with other microscopies like SEM and TEM is that AFM directly measures the height of a surface by scanning it with a mechanical probe. Depending on the nature and extent of bending of the cantilever and thereby changing the amount of reflected laser light from the tip to the photodiode we can image the sample surface that corresponds to a constant probe-sample interaction. This mode of scanning thus allows us to achieve more accurate resolution and information on surface topography. Besides, for SEM and TEM techniques we need to create a vacuum environment for measurements, however, AFM need not, it can be done openly or in other words, AFM is an ambient imaging technique and the sample preparation is very easy and can be performed with very low concentrations too. The major components of an AFM instrument are (1) Microscope Stage: which combined a moving AFM tip, sample holder, and a force sensor; (2) Control Electronics: which have an optical microscope and a vibration controller; (3) Computer & Detector: Used for analysis of the force signal and

detecting it to construct the 3D topographic view. During the measurement in AFM, a piezoelectric transducer moves the tip over the surface and either the force transducer senses the force between the tip and the surface or the deflection of the laser light as it scans the surface depending on the surface topology. A schematic presentation of AFM measurement and the obtained force curve is shown in **Figure 2.8**. In general, for stiffness measurements, we record data during tip approaches and for adhesion experiments, we record data during tip retract.

Depending on the nature of tip motion, AFM operation is mainly divided into three different modes as contact mode (or static mode), tapping mode (or intermittent contact mode, AC mode, amplitude modulation mode), and non-contact mode (or frequency modulation mode). Most of our imaging of solid nanostructures is performed in tapping mode wherein to take any image in the liquid medium we have selected contact mode. All the AFM imaging was performed on mica plates by modifying their surfaces with 500 μM of 3-mercaptopropyltrimethoxysilane (MPTMS) solution which makes a monolayer of MPTMS (around ~ 2 nm in height from the blank mica plate). Diluted nanomaterial was then drop cast on the modified mica plate and kept undisturbed for 20 minutes for complete binding of nanomaterials sample with the mica surface through MPTMS. After complete binding, we wash the sample coated mica plate repetitively by Mili-Q[®] water to remove any excess unbounded nanostructures and finally dried it in a controlled ultrapure argon stream. All the AFM experiments were performed on a Bruker BioScope Catalyst AFM instrument using Nanoscope software as shown in **Figure 2.8C**.

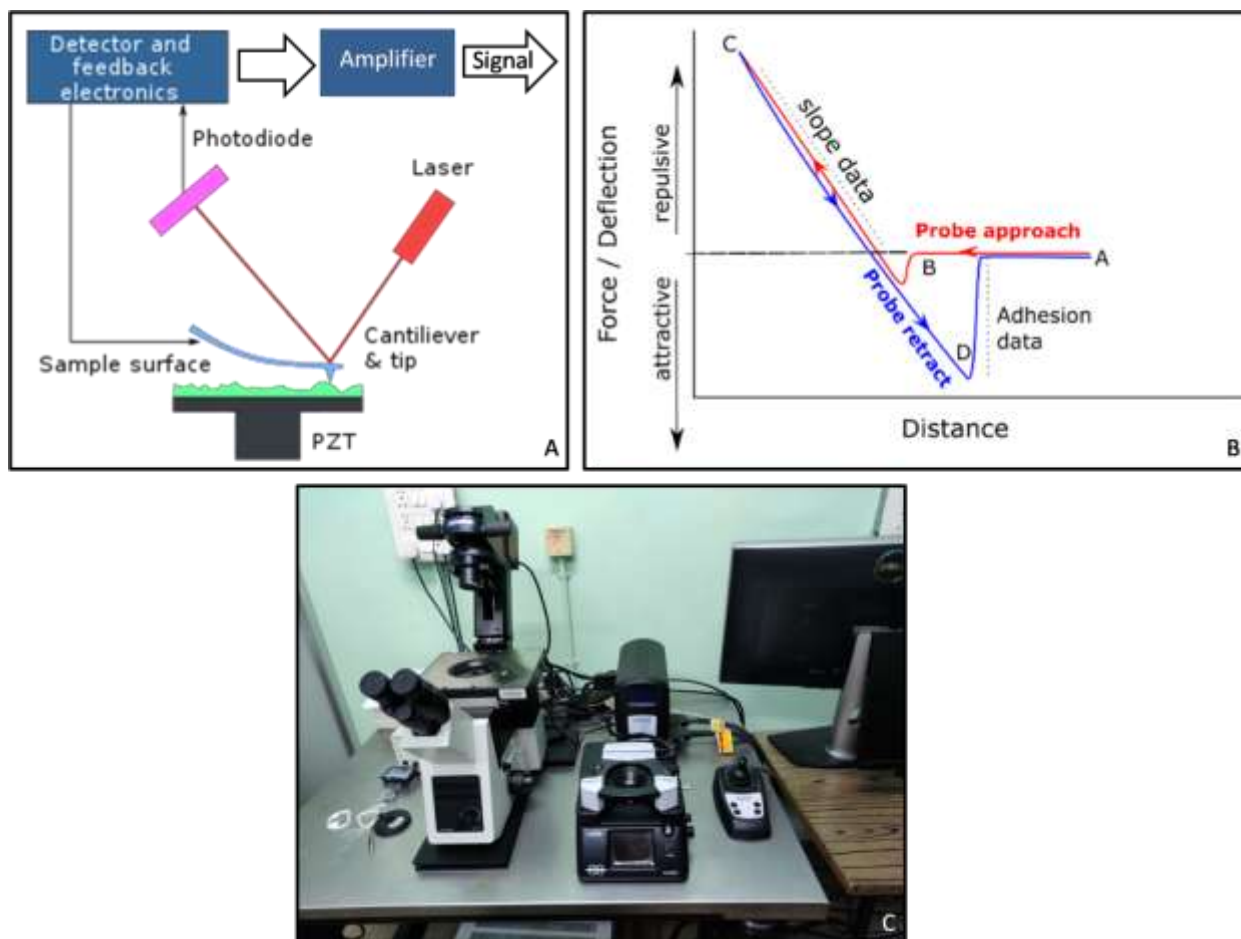


Figure 2.8: (A) schematic presentation of AFM measurement with essential components of the instrument, (B) Representative force curve as a function of distance, and (C) Bruker made BioScope Catalyst AFM instrument.

2.4.8 Scanning Electron Microscopy:

Scanning Electron Microscopy (SEM) is based on the principle of imaging of surface by scanning over it with a focused beam of electrons. Interactions of the electrons with surface atoms produce various signals that give preliminary information about the surface topography. In general, the nanostructures we have developed are observed under a high vacuum, whereas in environmental SEM, a low vacuum is used to study the biological sample.⁷⁰ Different reflected electrons by elastic scattering of the sample are emitted from different parts of the interaction

volume as a result of the interaction between the electron beam and the sample. Different signals include the Auger Electrons (AE) comes from the top layer of the sample which gives the information about the surface atomic composition, Secondary Electrons (SE) comes from the next layer of interaction volume which gives the information about the topographical information of the sample, and Backscattered Electrons (BSE) comes from a further dip of the sample layer which gives the information of atomic numbers. Followed by, photons of characteristic X-rays (EDX) and Cathodoluminescence (CL) from next dipper layers give information regarding thickness atomic composition and electronic state information respectively. Contrary to the reflected electrons, the transmitted electrons give the morphological information as we record from TEM measurements. Details about the zone-specific interaction of the focused electron beam and the thin sample are shown in **Figure 2.9A**. The resolution of SEM images obtained by secondary electrons is much higher than that of backscattered electrons. From SEM, we do not get any information about the atomic distribution of elements present in the sample. Throughout this thesis, we have used a Zeiss Supra 40 field emission electron microscope (**Figure 2.9B**) to record the SEM images of our synthesized nanomaterials. Before each measurement, we have thoroughly washed our sample to remove any excess surfactant over it because the interaction of the electrons beam with unused surfactant within the sample produces local heating that melts the sample under study which may also cause the damage to the detector. The surfactant-free samples then drop cast over a silicon wafer and dried overnight to remove any adsorbed water in the sample. During drop-casting, we have maintained a single layer of the nanostructures by injecting the sample on a tilted silicon wafer. The picture of the Zeiss Supra instrument is given below.

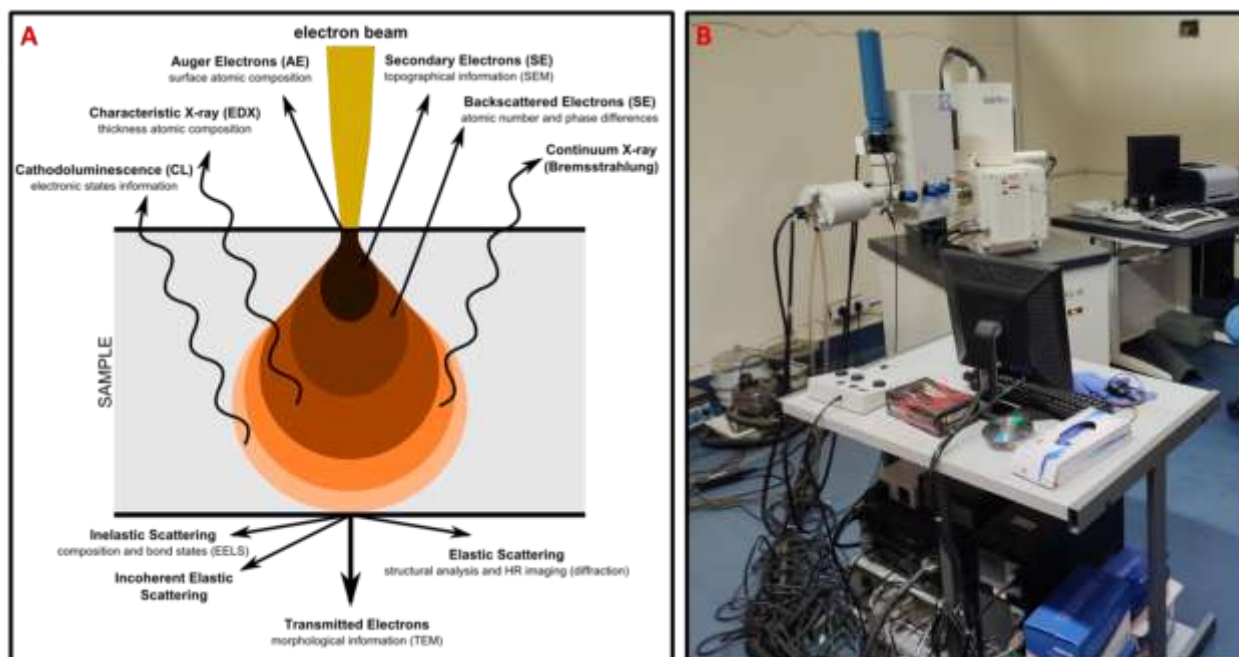


Figure 2.9: (A) Zone-specific interaction of focused electron beam and the thin sample, (B) Zeiss Supra 40 field emission electron microscope.

2.4.9 Transmission Electron Microscopy:

Transmission electron microscopy (TEM) is a technique where a beam of electrons is transmitted through a thin specimen with thickness $< 100\text{nm}$. In general, we use a carbon-coated Cu grid for preparing samples and in some special cases (especially for negatively charged particles) we use a formvar-coated Cu grid to avoid any grid induced aggregation. TEM generally provides more in-depth information including a column of atoms can be imaged from which we can determine the orientation of different crystal plane like $\{111\}$, $\{110\}$, $\{100\}$, etc. The technique called high-resolution TEM (HRTEM) to get atomic information of the imaged nanostructures. Besides the orientation of different crystal planes, we can determine crystal irregularities within the nanostructures from their respective HRTEM measurements.⁷¹ In general, the TEM instrument is coupled with other facilities that enable us to record the scanning TEM imaging (STEM) of samples, perform their energy-dispersive X-ray spectroscopy (EDX),

and obtain their diffraction spectra. The diffraction spectra help to analyze the crystal parameters like the presence of different facets, interplanar distances, etc. From EDX spectra we obtain an elemental mapping of the nanostructures from which atomic distribution of the nanostructures can be observed. In TEM, an electron gun (tungsten filament or lanthanum hexaboride) is used as the electron source. The electron gun is connected to a high voltage source (in our instrument the voltage source is 300 kV) and, given sufficient current, the gun begins to emit electrons either by thermionic or field electron emission into the vacuum. Often the combination of the cathode and a set of electrostatic lenses for effective electron beam shaping is called the “electron gun”. Upon the application of required voltage (here 300 kV), a beam of electrons ejected from the electron gun and transmitted through the sample, and finally, the obtained image is focused onto an imaging device, such a phosphor screen made by fine ZnS, a photographic film, or a dopped YAG screen attached to a Charge-coupled device (CCD). We use digital micrograph software for analysis of the TEM data. During sample preparation, a dip and dry method was followed in which we dipped a carbon-coated Cu grid in the surfactant-free concentrated colloidal solution; the hydrophobic carbon coating allowed us to make a monolayer of the sample to stick on the copper mesh which we dried in vacuum for overnight. The instrument used for the analysis is FEI Tecnai G2 F30 S-Twin microscope operating at 300 kV as shown in **Figure 2.10**.

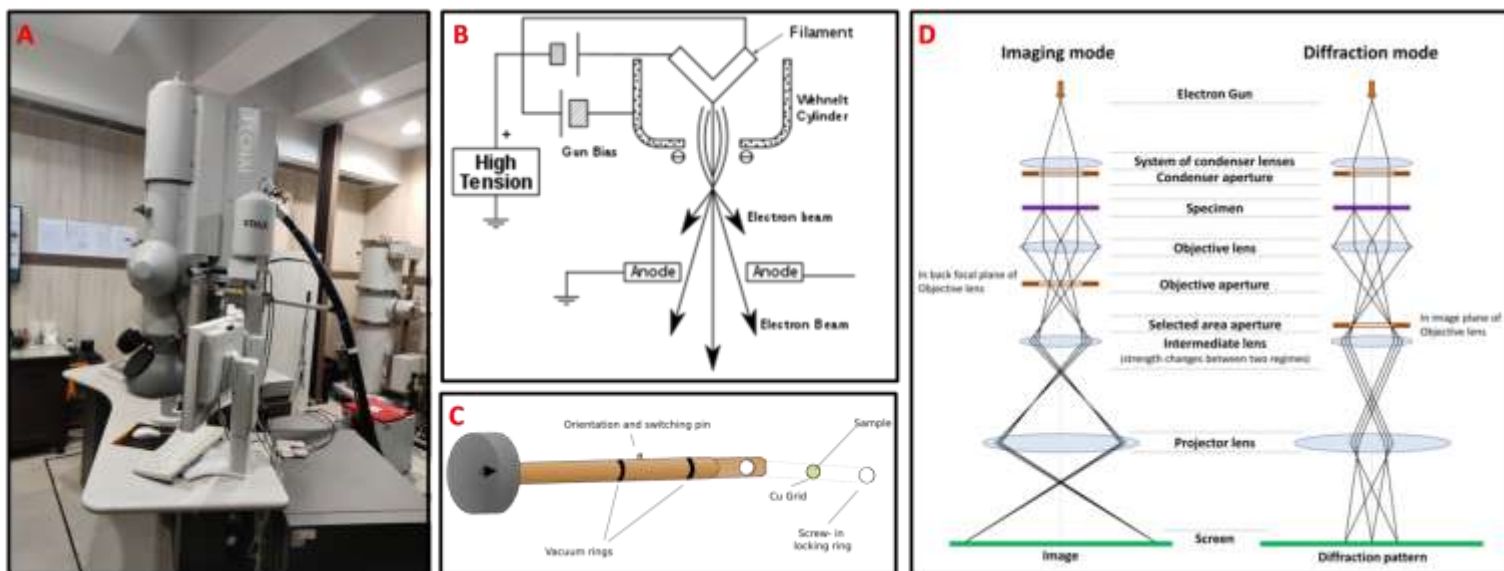


Figure 2.10: (A) FEI Tecnai G2 F30 S-Twin Transmission Electron Microscope (TEM) operating at 300 kV, (B) Electron gun assembly, (C) Single-axis tilt sample holder for insertion into a TEM goniometer, (D) Imaging and diffraction assembly.

2.4.10 Electrochemical Measurements:

All the electrochemical measurements have been performed in a CH6092E electrochemical work station (CH Instruments, USA) where we have used a Pt wire or graphite rod as a counter electrode and a Glassy Carbon (GC) electrode of 3 mm diameter as the working electrode. Saturated calomel electrode or Ag/AgCl was used as a reference. In most of the electrochemical measurements, we have used Cyclic Voltammetry (CV) for finding any redox peak in the system; Differential Pulse Voltammetry (DPV) for finding the most intense peak from I-V curve; Linear Sweep Voltammetry (LSV) for measuring the overpotential during HER; Electrochemical Impedance Spectroscopy (EIS) for measuring the resistance, the heterogeneous rate constant, exchange current density; etc. Besides, we have also used chronoamperometry to observe the long term catalytic stability of our developed nanomaterials. Prior to use, the Glassy carbon (GC) electrode was initially cleaned by polishing with alumina powder of different

grades (0.3 and 0.05 μm) followed by washing and sonication in Milli-Q water for five minutes. We performed traditional drop-casting methods for modifying the bare GC electrode, in which approximately 10 to 20 μL of concentrated nanomaterials (colloidal nanomaterials obtained after centrifugation) was dropped on the bare GC and dried for overnight. The strong adhesion property of our developed Au, Ag, Au-Ag alloy nanomaterials with GC electrodes allows us not to use any binder like nafion. Moreover, we did not use any other substances like Carbon powder or conducting polymers, e.g. polypyrrole, polyaniline, etc, to prepare a composite with our developed nanomaterials for enhancing current responses, due to the reason that the nanomaterials itself can produce sharp peaks in their I-V curves from DPV measurements. Thus it is encouraging to use our synthesized nanomaterials as an electrode material for sensing of biomolecules from their characteristic I-V curves obtained from DPV measurements or catalysis in alcohol/ H_2 fuel cells by checking their long term catalytic performances acquired from the corresponding Chronoamperometry measurements. The details of the electrochemical techniques are discussed below with an instrumental description.

2.4.10.1 Linear sweep voltammetry:

The electrochemical behavior of any redox system can be described by a three-dimensional i-t-E surface. To describe a stationary electrode with multisystem species, the i-t-E curve is complex to illustrate because in a multisystem species one could not identify each system systematically. Thus we can split the three-dimensional i-t-E curve into i-E and i-t curves for recognizing a particular redox system. In linear sweep voltammetry (LSV), the potential is swept with times and i-E curve is recorded directly from the instrument. In general, the potential is varied linearly with time and with sweep rates ranging from 10 mV/s to 1000 V/s in our

conventional electrodes like GC, Au, and Pt electrodes. Thus, the recording of ‘current (i)’ with ‘Potential (E)’ is equivalent to the record of ‘I’ with ‘time (t)’.

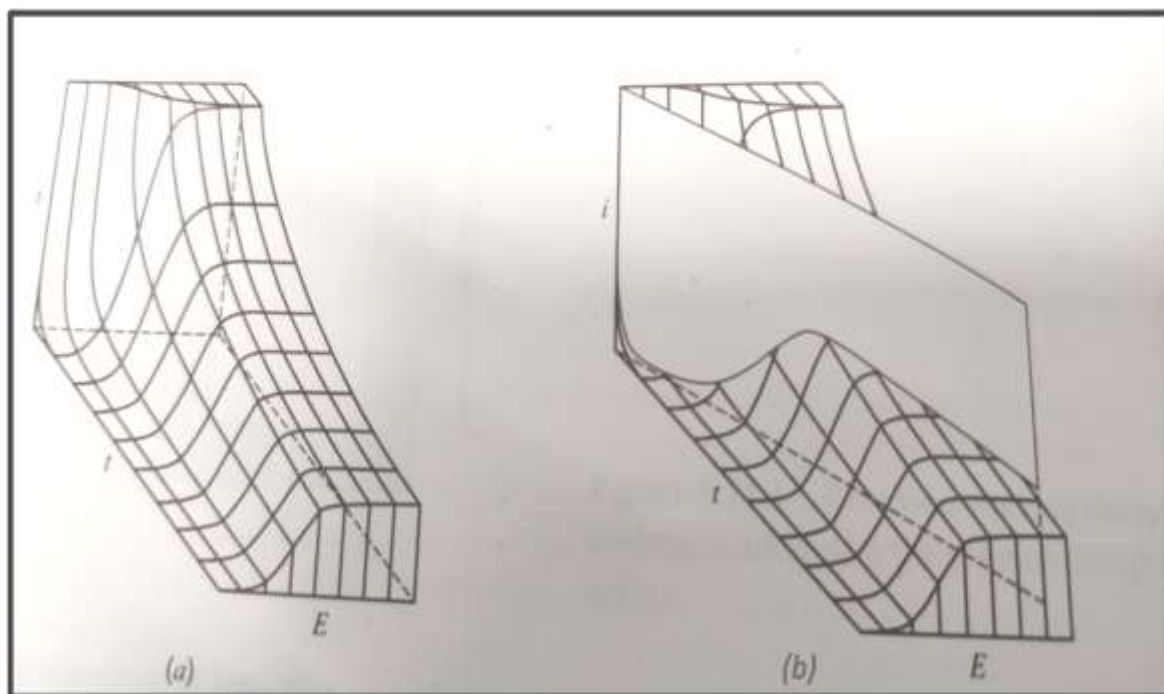


Figure 2.11: (a) A i-t-E surface in 3D for a Nernstian system, (b) linear potential sweep across the surface.⁷²

In an LSV experiment, the current responses are increased with increasing scan rate and different behaviors have been observed for reversible, quasi-reversible, and irreversible systems.

2.4.10.2 Cyclic Voltammetry:

Cyclic voltammetry (CV) is a technique where current is measured under a potential range. CV is performed by cycling the potential of a working electrode. In general, the reversal of LSV is performed by switching the potential at a certain time by the opposite scan. The potential at any time is given by

$$(0 < t < \lambda) E = E_i - vt$$

$$(t > \lambda) E = E_i - 2v\lambda + vt. \text{ Here 'v' is the scan rate.}$$

For a reversible Nernstian system, the two important parameters in i - E curve of cyclic voltammetry are i_{pc} (cathodic peak current) and i_{pa} (anodic peak current) and the separation in peak potential, i.e. $\Delta E_p = E_{pa} - E_{pc}$. For a reversible system, $i_{pa}/i_{pc} = 1$, regardless of scan rate and diffusion coefficients. ΔE_p is a function of switching potential E_λ , but should be very close to $2.3RT/nF$. If the cathodic sweep is stopped and the current is allowed to set zero then anodic sweep will be identical to cathodic sweep. CV for a reversible system at different E_λ values as a function of time is shown below in **Figure 2.12A**. A similar curve can also be plotted as a function of potential as shown below in **Figure 2.12B**.

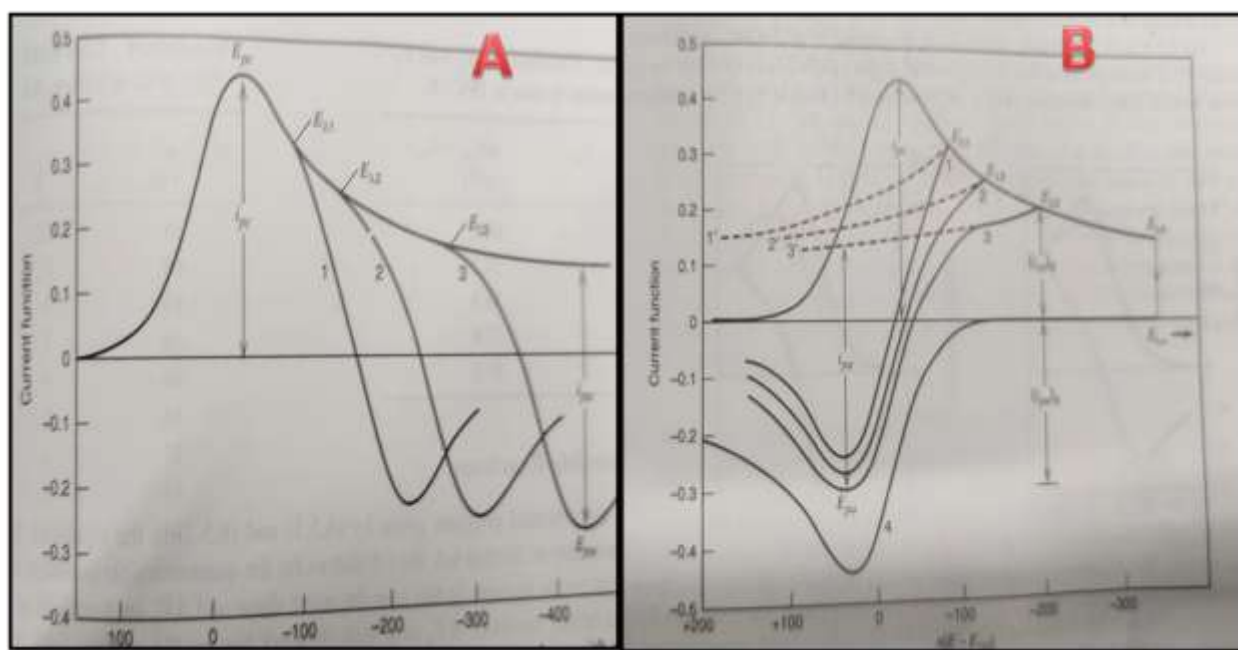


Figure 2.12: (A) CV for a reversible system at different E_λ values as a function of time, (B) CV for a reversible system at different E_λ values as a function of potential (E_λ).⁷²

The measurement of peak currents in CV is imprecise, as uncertainty arises during the correction of charging current. In the case of reversal processes uncertainty is more because the folded faradic response cannot be defined properly for the forward process as seen in 1', 2', and 3' in **Figure 2.12B**. Thus CV is not an ideal method for quantitative analysis, however, for qualitative

estimation, it can be used. The nature of a CV curve changes with moving from reversible to an irreversible or a quasi-reversible system where $i_{pa}/i_{pc} \neq 1$ and $\Delta E_p \neq 2.3RT/F$.

2.4.10.3 Differential Pulse Voltammetry:

In electrochemistry, Differential Pulse Voltammetry (DPV) is considered to be the most sensitive technique. The sensitivity can be achieved by applying a series of small amplitude regular voltage pulses, superimposed on the potential linear sweep or stairsteps as shown in **Figure 2.13**, and the current is measured immediately before each potential change. In DPV the measured current difference as a result of potential change is plotted as a function of potential. In the case of normal pulse voltammetry, the current from a series of ever large pulses is compared with the current at a constant 'baseline' voltage. Important characteristics of DPV are: (i) The base potential applied in DPV during drop fall is not constant rather it increases with time; (2) the pulse height lies between 10 to 100 mV and maintains a constant level with the base potential of the corresponding pulse; (3) two current samples are taken into consideration for the DPV measurement, one before the drop fall time, τ , and another after the drop fall time, τ' , (4) the experimental DPV curve is a result of plotting the current difference $\delta i = i(\tau) - i(\tau')$ versus the base potential.

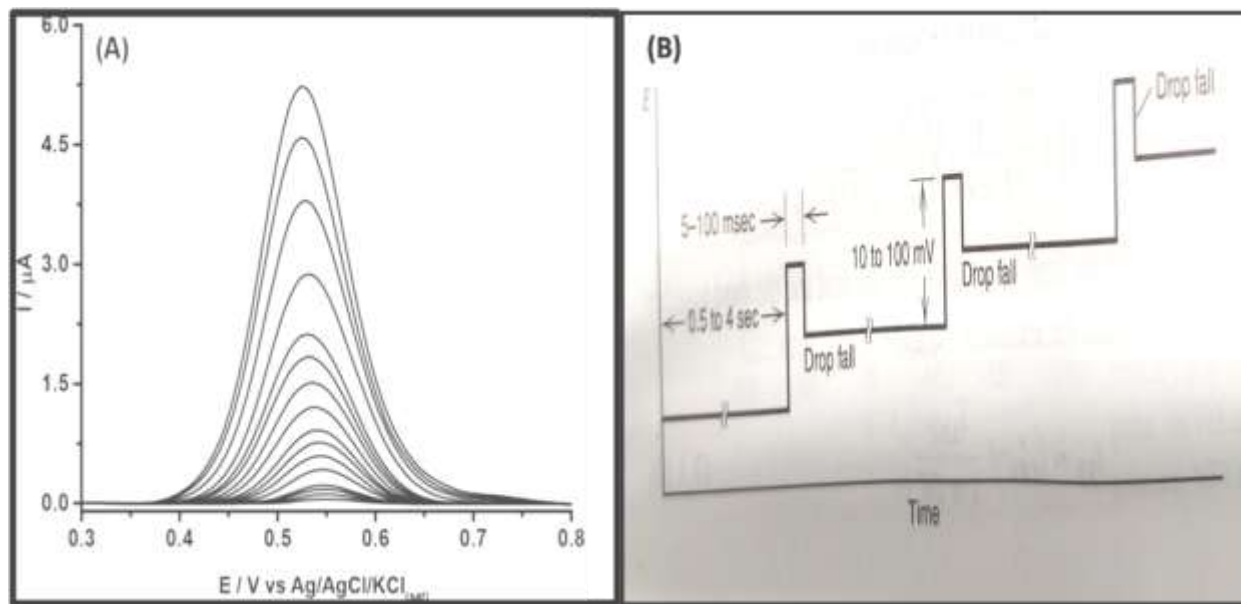


Figure 2.13: (A) Representative DPV curve, (B) Working principle of DPV.⁷²

Throughout the thesis, we have used DPV as a sensitive electrochemical detection tool for the selective determination of various analytes from their corresponding I-V curves. DPV is capable to produce specific peak potential with higher current densities than the corresponding CV measurements. As a result of this, DPV is considered to be a more appropriate electrochemical technique for the quantitative estimation of analytes than the CV.

2.4.10.4 Square Wave Voltammetry:

Square wave voltammetry (SWV) is a special technique that has been developed by combining the best aspects of several pulse voltammetric methods, including the background suppression and sensitivity of differential pulse voltammetry, the diagnostic value of normal pulse voltammetry, and the ability to interrogate products directly in much the manner of reverse pulse voltammetry. SWV also offers a wider time range compared to other pulse polarographic techniques.⁷² SWV is normally carried out at a stationary electrode. The basic difference between SWV and DPV is that SWV has no polarographic mode. The waveform used in SWV

can be viewed as a special case of that used for DPV (as shown in **Figure 2.13B**) where the preelectrolysis and pulse periods are of equal duration, and the pulse is in opposite from the scan direction as shown in **Figure 2.14**. The square waveform is characterized by various parameters as clearly shown in **Figure 2.14** and these are (i) Pulse height, ΔE_p : measured with respect to the corresponding tread of the staircase (shown as a thin horizontal line), (ii) Pulse width, t_p : time gap between the forward sample and reverse sample, (iii) Square wave frequency, f : pulse width and frequency in a square waveform is related by $f = 1/2 t_p$, (iv) Staircase shift, ΔE_s : the potential gap between two staircases at the beginning of each cycle, and it relates with the (v) Scan rate, v as: $v = \frac{\Delta E_s}{2t_p} = f\Delta E_s$.

In SWV, current samples are taken twice per, at the end of each pulse. The difference current, ΔI , is formulated as $\Delta i = i_f - i_r$, where i_f is the forward current sample arises from the first pulse in the direction of staircase and i_r is the reverse current sample is taken at the end of the second pulse. Thus the result of a single square wave run is the combination of three voltammograms showing forward, reverse, and difference currents vs. the potential on the corresponding staircase tread.

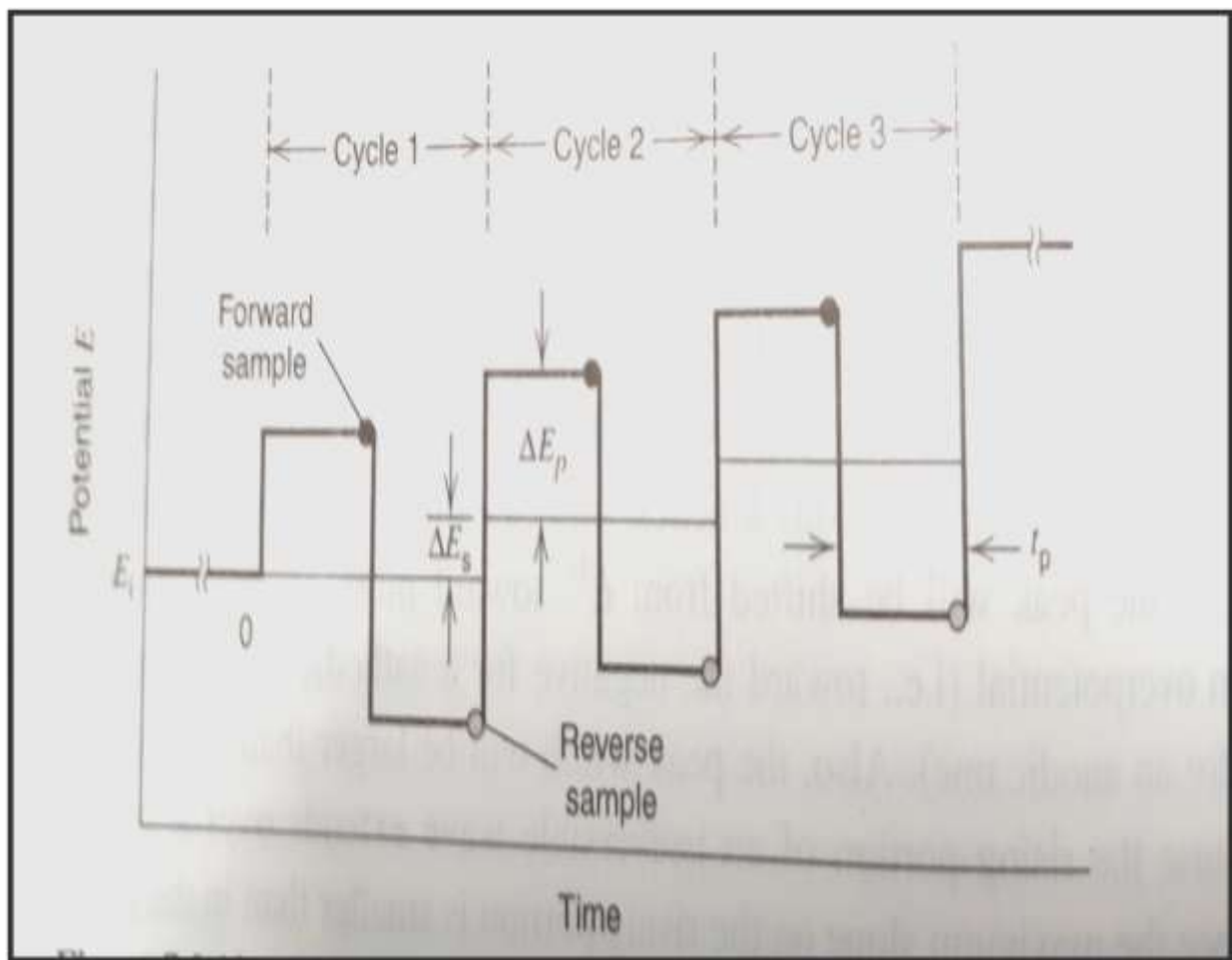


Figure 2.14: Waveform and measurement scheme along with different important parameters for SWV.⁷²

2.4.10.5 Chronoamperometry:

Chronoamperometry is a Current (i) vs time (t) plot for a faradic process where the potential of the working electrode is stepped and the resulting current is monitored as a function of time. In contrast to other stepped processes in electrochemistry, chronoamperometry generates a large current in any redox reaction and decays exponentially. Limited information can be achieved from the chronoamperometric i - t curve which includes (i) it gives the idea about the long term ability of a catalyst and its stability in the electrocatalytic environment, and (ii) the specific potential at which a redox reaction occurs.

2.4.10.6 Electrochemical Impedance Spectroscopy:

The term impedance refers to frequency-dependent resistance to current flow in a circuit.

Impedance Z_w is defined as $Z_w = E_w / I_w$.

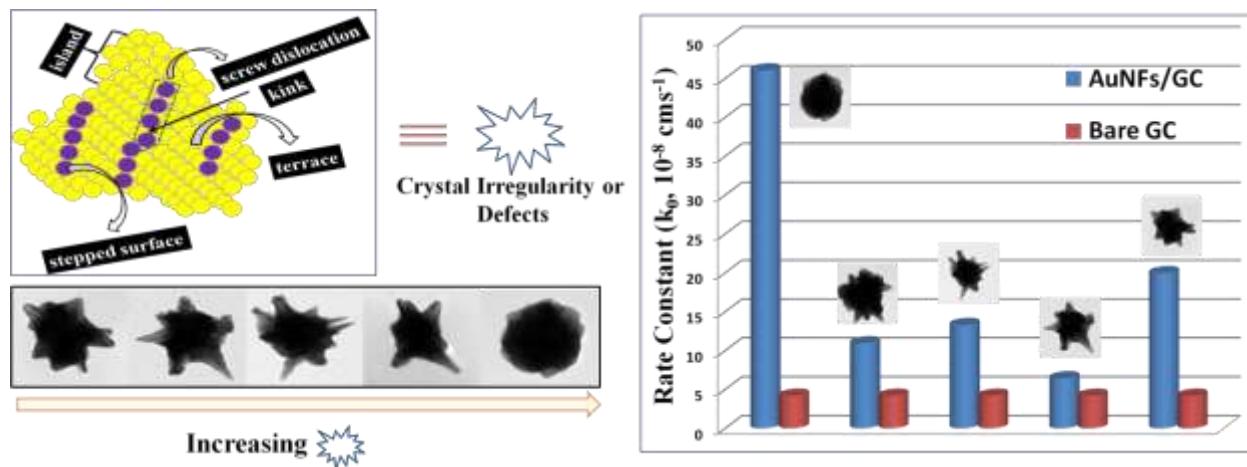
Though it is very complex to study frequency-dependent resistance, EIS is very helpful to carry out various electrochemical analyses as (i) EIS is an information-rich technique compared to any simple DC techniques. For example, by fitting the EIS (Nyquist plot) into Randles cell, one can gather information for various parameters like the heterogeneous rate constant, porosity, exchange current density, etc, (ii) EIS can identify diffusion-limited reactions, and (iii) EIS also gives information about the capacitive behavior of the system. The total impedance consists of two parts, one is the imaginary part and the other is the real part. The data extracted from EIS is fitted into the software with an equivalent circuit from which the parameters mentioned above can be determined. The most important parameter derived from EIS is the charge transfer resistance, R_{ct} . In Chapter 8, we have efficiently detected dengue serotype-2 (DENV-2) virus via impedimetric techniques where we have plotted R_{ct} as a function of known concentration of DENV-2 for calibration and unknown concentration of infected samples have been measured from the measured R_{ct} values. EIS is equally applicable in the sensing of other biological samples like cancer cells, bacteria, metabolites, etc.

CHAPTER-3

Crystal Defect Induced Facet Dependent Electrocatalytic Activity of 3D Gold Nanoflower towards the Selective Nanomolar (nM) Detection of Ascorbic Acid

OUTLINE: Specific Points of Discussion

- Role of crystal defects on the electrocatalytic activity of nanocrystals
- Role of surface energy (γ) of different facets in controlling the electrocatalytic activity of nanomaterials
- Bud shaped gold nanoflower (AuNF) shows the remarkable electrocatalytic efficiency towards the oxidation of ascorbic acid (AA) in the nanomolar (nM) concentration range.
- The ability of nano-bud in multi-component sensing [$i_p^{AuNF} (Bud)/i_p^{GC} \cong 100$] in a single potential sweep
- The role of different crystal facets and inter- & intra-molecular hydrogen bonding within AA molecules to control the resultant fingerprinted peak potentials at variable concentrations has been explored by ab initio and DFT calculation respectively



3.1 Introduction:

In this chapter, we have discussed the synthesis of bud to blossom gold nanoflower and their catalytic applications towards the electrochemical oxidation of Vitamin C. The specific peak potential for Vitamin C (Ascorbic acid, AA) helps us to find its signature in a pathological sample and thereby we can develop a potential biosensor for the pathological detection of AA. We have thoroughly analyzed the crystal structures of individual gold nanoflower to find out the presence of different active crystal sites within them and explored their role in controlling the unusually enhanced electrocatalytic oxidation of AA which is originally known to be a sluggish reaction. Instigation of unique catalytic activity of anisotropic gold nanoparticles (AuNP) encouraged modern science to shade lights on the concept of location and nature of active-site dependent catalysis.⁷³⁻⁷⁷ The unusual high catalytic activity of nanometer-sized gold particles (AuNPs) is primarily understood due to the generation of highly dense low coordination site atoms on edges, terraces, steps, ledges, kinks, etc.⁷⁸⁻⁸¹ Any crystal plane which remain at an angle $\theta \neq 0^\circ$ with a closely packed crystal plane, holds more number of broken bonds compared to the close-packed plane. In any general orientation of that additional crystal plane in a stereographic orientation with the close-packed crystal plane, generates ledges and kinks of certain density in an appropriate terrace orientation. These low coordinated site atoms then react more strongly because of their modified localized electronic structure.^{82,83} Most of the noble metal nanoparticles crystallizes according to the *fcc* pattern^{84,85} (However iron nanoparticles crystallize in *bcc* pattern,⁸⁶ gold and silver nanoparticles crystallizes as a superlattice in hexagonal close-packed structures⁸⁷ or simple cubic super crystals containing PbTe nanocubes⁸⁸) and the coordination number (C.N) of different facets in a unit cell of *fcc* are 7 for {110}, 8 for

{100} and 9 for {111} planes whereas the C.N of an atom in *fcc* unit cell is 12. Thus the highest number of bond breaking, i.e., $12-7 = 5$, takes place during the creation of {110} facets.⁸⁹ According to the broken bond model, the number of bond breaking is proportional to surface energy.⁸⁹ Hence the surface energy (γ) of different facets in an *fcc* crystal will follow the order as $\gamma(111) < \gamma(100) < \gamma(110)$,⁹⁰ reflecting that the {110} facet as the most reactive one among the lowest order crystal facets. Besides the broken bond model, microscopically the surface energy also directly depends on the atomic density of facets and geometry of the terraces, ledges, and kinks formed during anisotropic facet formation. The high reactivity of {110} facets can also be explained in terms of planar density (the number of atoms in a plane). Greater the number of atoms in a plane, greater will be the planar density and hence it will be described as the most closely packed facet. The planar density of different crystalline facets of an unit cell of *fcc* are $0.177/R^2$ for {110}, $0.25/R^2$ for {100} and $0.29/R^2$ for {111} where R is the radius of a gold atom.⁹¹ In other words, relative planar density of {110}, {100} and {111} crystalline planes follow the ratio of 1: 1.4: 1.6. Thus {111} plane is the most densely packed plane^{92,93} making it least reactive than the other two crystal planes, i.e., {100} and {110}. Besides broken bond generation and planar density modulation, a detailed microscopic study of gold nanostructure demonstrates that the catalytic activity increased effectively with the increment of surface energy as a result of increasing the density of dislocation planes.^{94,95,96} Generation of more number of dislocation planes increases the catalytic activity due to the crystal lattice irregularity.⁹⁷ The other dominant factors that control the catalytic activity are combined effective surface charge,⁹⁸ zeta potential,⁹⁹ charge density at the curvature,⁹⁸ and effective surface area.¹⁰⁰

In the present study, we have investigated the electrocatalytic behavior of different size and shaped [three dimensional (3D) bud to blossom¹², confirmed by electron tomography study]

gold nanoflowers (AuNFs) having a similar composition with variable curvature of the tips with different degree of crystal defects and crystalline orientations towards the electrochemical oxidation of ‘Vitamin C’ by considering the aforementioned possible catalytic factors. The anisotropic AuNFs with the increasing number of concave petals oriented towards energetically unfavorable crystal plane possesses efficient catalytic activity due to the increased number of crystal defects such as steps, kinks, and dislocation sites.^{78,82} The high over-potential and poor reproducibility (fouling effects) of bare electrodes usually limit the usage of them¹⁰¹ as efficient electrode materials. Driven by the needs, the cutting edge modification of bare electrodes is done in this study by drop-casting of AuNFs (on bare glassy carbon electrode) via covalent binding or electrostatic interaction¹⁰² to study the catalytic function on the oxidation of biologically active molecules like Vitamin C, uric acid, glucose, dopamine, etc. Dynamics of crystal facet dependent reaction for different size and shaped AuNP modified electrode has recently been reported where {100} and {110} facets of AuNPs show higher catalytic activity for oxygen reduction reaction (ORR).^{103–105} However, the modification of AuNPs with Cu and Ag layers leads to {111} facet the most reactive one for ORR.¹⁰⁶ Our experimental work reports here the study of the electrochemical activity of different tailored shaped bud to blossom AuNFs with single {110} to twin plane orientation of their tips (one-half of the tips oriented along the {111} and the other half along {100}). The residual Ag used during the synthesis plays the key factor by suppressing the dynamics of {111} facet and preserving the high density of crystal defects on {110} facet for greater chemical reactivity.⁷⁵ The experimental result of facet and crystal defect dependent catalytic activity is further supported by using a projected augmented wave (PAW)¹⁰⁷ method. We have also used Density Functional Theory based computational calculation to understand the molecular basis of the dynamics of peak potential as a function of AA concentration. **Scheme-**

3.1 shows the schematic presentation of facile electrostatic interaction between bare glassy carbon (GC) electrode and different AuNFs followed by crystal irregularity dependent AA oxidation.

The key driving force behind this electrochemical study of AA is due to its crucial role as a powerful antioxidant as well as an efficient scavenger for free radicals.¹⁰⁸ The ratio of Ascorbic Acid (AA) to dehydroascorbic acid (DHAA) acts as a biomarker of oxidative stress.

Various methods have been proposed for the quantitative estimation of AA like fluorimetric methods,¹⁰⁹ titration methods,¹⁰⁹ electrochemical detections,^{110,111} etc. However, most of these techniques suffer from interference due to the common basic molecular backbone of closely related pathological components like dopamine (DA), uric acid (UA), etc.^{112–114} which hinders their highly specific sensing applicability. Out of several other electrochemical methods, Differential Pulse Voltammetry (DPV) and Electrochemical Impedance Spectroscopy (EIS) are the two most powerful and error-free techniques used in the literature to measure the concentration of specific electro-active species in a fingerprinting voltammetric way and to get the insight on the kinetics of multiple electrochemical processes respectively. Thus the combination of DPV and EIS as active electrochemical techniques and facet originated crystal defect modulated nanomaterials as dynamic electrode coating offers the designing of most suitable transducer both to understand a surface-enhanced redox reaction as well as to use as a signal amplifier for ultrasensitive error-free fingerprinting detection in a multi-component physiological environment.

3.2 Synthesis of AuNPs:

The synthesis of different flourishing stages of AuNFs was carried out by using a nano-templated seeded growth technique (three-step synthesis protocol) as reported earlier by Bardhan

et al.¹² In brief, trisodium citrate capped ~5nm gold nanoparticles (GNPs) were synthesized in the first step by NaBH₄ reduction method which we used as the seed to prepare CTAB based gold nanopopcorn (GNPop) in the second step. In the third and final step, we used GNPpop as nanotemplates to prepare different flourishing stages of AuNF simply by employing different concentrations of CTAB as the surfactant. The different nano-templated growth solution was then kept overnight for completing the growth process. The generation of AuNFs was confirmed by recording their UV-vis-NIR absorption spectra or examining their SEM and TEM images.

3.3 Theoretical *ab initio* simulation:

Theoretical modeling to calculate the reaction free energy (ΔG) and the corresponding activation energy (ΔE) have been carried out by using a projected augmented wave (PAW)¹⁰⁷ method, as implemented in the Vienna *ab initio* Simulation Package (VASP).^{115–117} The exchange-correlation functional Perdew–Burke–Ernzerhof (PBE) described within the generalized gradient approximation¹¹⁸ implemented with the projector augmented wave function (PAW). The bulk Au{100}, Au{110}, Au{111}, and Au{211} surfaces are modeled with (4×4), (4×4), (5×5) and (2×5) supercell respectively to minimize the lateral interactions between the repeating images with four layers of gold atoms. A vacuum of more than 12Å is used along the z-direction to avoid periodic interactions. The Monkhorst–Pack generates a set of (5×5×1) K-points which is used to optimize the supercell of Au{100} and Au{211} facets, while (4×3×1) is used for the Au{110} facet. The Brillouin zone is sampled with a gamma point (5×5×1) for the Au{111} facet. All four layers are fully relaxed for the bulk surfaces, while two atomic layers from the bottom of the slab are fixed. Other layers are relaxed while performing the thermodynamic study. Plane-wave with a kinetic energy cut-off of 470 eV is used to expand the electronic wave functions. The convergence criteria for total energy and forces are set at 10⁻⁴ eV

and 0.02 eVÅ⁻¹ respectively while optimizing the geometry. The van der Waals interactions have been included using the Grimme's D3-type of semiempirical method while optimizing the structures for the thermodynamic calculations.¹¹⁹ Zero-point energy (ZPE) and entropy corrections have included for the reaction free energy calculations. Zero-point energy (ZPE) is calculated using the following equation:

$$\text{ZPE} = \sum_i \frac{1}{2} h \nu_i \quad (1)$$

Where 'h' is the Planck constant and 'ν_i' is the frequency of the ith vibrational mode.

3.4 Density Functional Theory:

Finer details of the interactions of vitamin C with different Au-clusters have been probed by density functional theory. The structure of L-ascorbic acid was obtained from PubChem (CID: 54670067). The structure of its dimer and the gold complexes with the monomer and dimer were modeled in GaussView 5.0. Two to four gold atom clusters were used in these models. Both the two possible orientations for the interaction of gold clusters with the monomer were explored. All the possible binding modes were geometry optimized with density functional theory at B3LYP level¹²⁰⁻¹²² using 6-31G (d) basis set for all H, C, and O atoms, whereas, Stuttgart/Dresden basis set, SDD/6-31G(d), for all the Au atoms.^{123,124} A scalar relativistic effective core potential was applied to all the Au atoms.¹²⁵ Frequency calculations were performed on the optimized structures using the same level of theory. Gaussian 09W Rev. C¹²⁶ was used for geometry optimization and frequency calculations. Molecular orbitals were generated in GaussView 5.

3.5 Results & Discussion:

This research work presents a comprehensive study on the role of different form of crystal defects along with other factors (crystal facet free energy, the curvature at sharp tips, total

surface area, surface charge, etc.) on an anisotropic gold nanoflower to control the electrocatalytic affinity of Vitamin C in a multi-component physiological/pathological sample. Obtained results will lead us to create a new field of research namely “potentiometric fingerprinting” for error-free Pathological sensing in the nanomolar (nM) concentration range which not only has academic importance to understand the mechanism of electro-catalysis on defective crystal lattice but also supports potential market value for the fabrication of prototype electrochemical sensors for rapid clinical assessment. The synthesized gold nanoparticles, as shown in **Figure 3.1**, were characterized by using SEM, TEM, and zeta potential measurements.

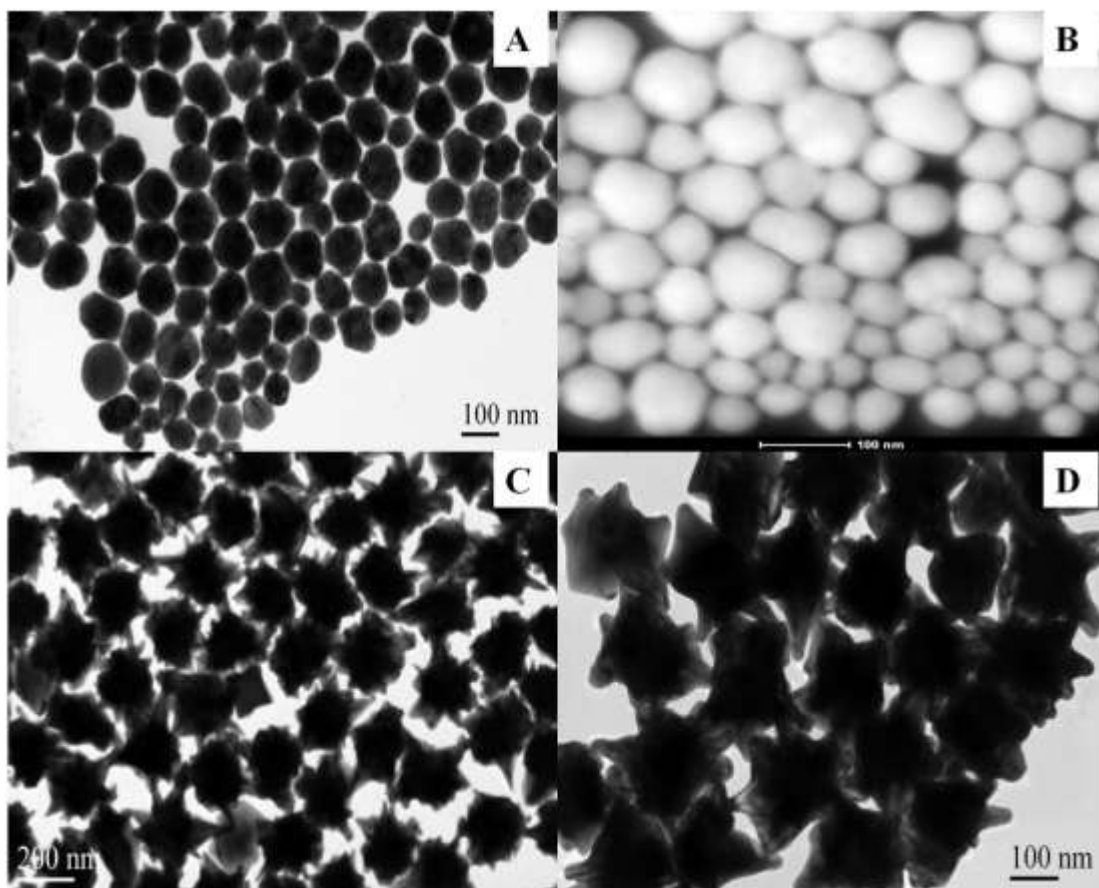


Figure 3.1: TEM image of AuNFs synthesized by using (A) 2.8×10^{-4} M CTAB, bud shape (B) HAADF of (A), (C) Fully blossomed AuNF at 2.8×10^{-2} M CTAB concentration and (D) over blossomed at 8.4×10^{-2} M CTAB.

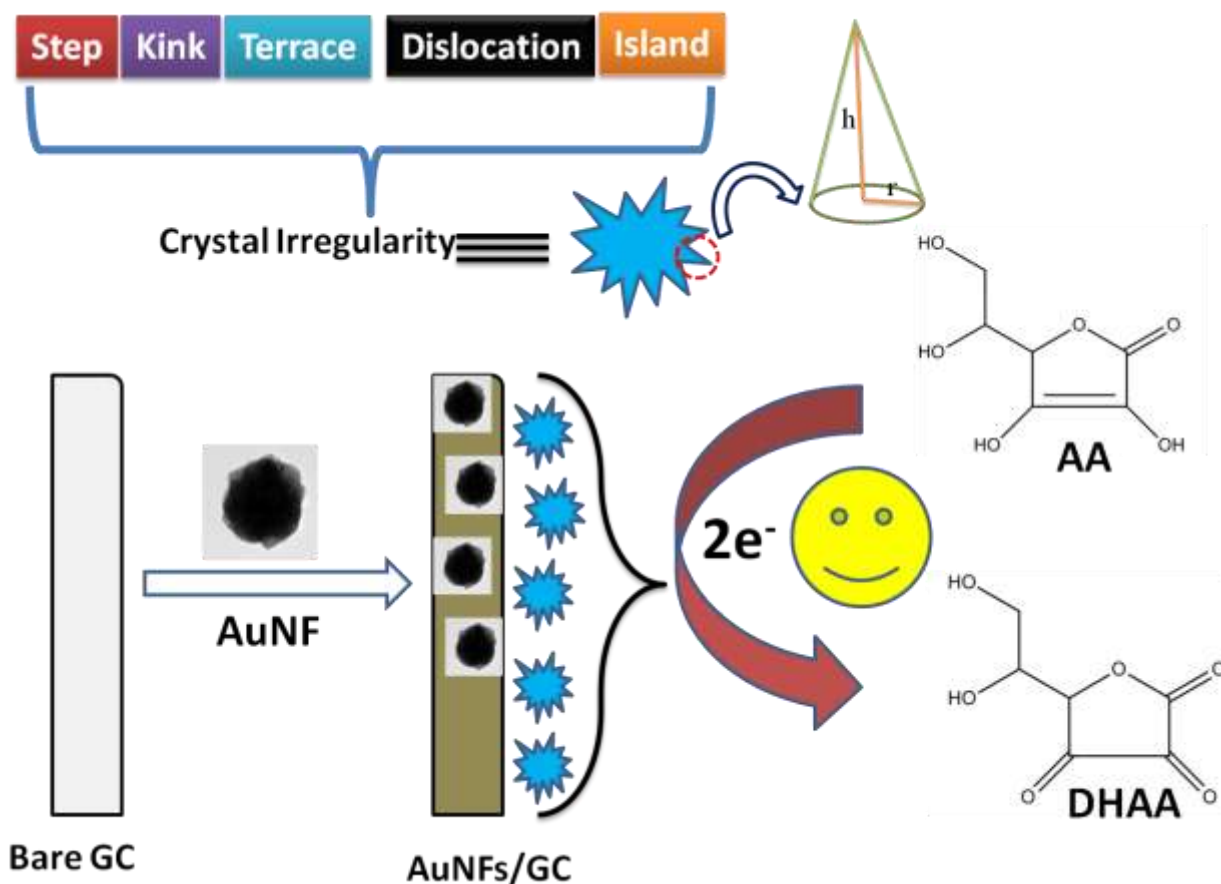
From our previously reported HRTEM measurements on AuNFs¹² it is clear that the lowest concentration of CTAB (2.8×10^{-4} M) generates bud structure with the crystal facets oriented in the $\{110\}$ plane. According to the literature survey, the surface free energy follows the order $\gamma(111) < \gamma(100) < \gamma(110)$.⁹⁰ Hence the bud structured AuNFs are energetically most unstable to provide maximum expected catalytic activity simply by receiving electrons (\equiv electrocatalytic oxidation) from the active molecular system (AA) to gain back the C.N. of an atom in *fcc* unit cell. As the CTAB concentration was increased to 2.8×10^{-2} M, crystal facet changes its direction towards energetically more stable planes to result in the formation of a half blossomed nanostructure where half of each petal directed along $\{111\}$ direction and another half towards the $\{100\}$ orientation. So, a mixed orientation of tipped petals has been obtained due to the synergistic effect of viscosity of the medium and crystal facet free energy as discussed in our previous report in details. The crystallographic direction of tips remain same in case of AuNFs synthesized at higher CTAB concentration (5.6×10^{-2} M) whereas they transform into blunted tipped structures along with energetically unfavorable $\{100\}$ crystalline packing at the CTAB concentration of 8.4×10^{-2} M. The TEM images of bud to blossom AuNFs as synthesized using variable concentration of CTAB exhibit highly homogeneity in shape and size as clearly visible from **Figure 3.1**. Obtained petal statistics from our TEM analysis along with the zeta potentials recorded for different nanoflower structures has been listed in **Table 3.1**.

Table 3.1 Physical and electrostatic parameters of synthesized different flourishing stages of AuNFs.

AuNFs at CTAB concentrations (M)	AuNF Core dia. (nm)	Individual average petal length (nm)	Average Number of petals	Zeta Potential (+ mV)
----------------------------------	---------------------	--------------------------------------	--------------------------	-----------------------

2.8×10^{-4}	110	0	0	11.9
2.8×10^{-3}	140	15	15	18.1
2.8×10^{-2}	155	85	54	27.3
5.6×10^{-2}	140	105	68	31.9
8.4×10^{-2}	135	70	45	34.8

By considering the above petal statistics, geometrical parameters of different AuNFs with different morphology were estimated by considering the core of different AuNFs as spherical and the tips as cone-shaped (**Scheme 3.1**). The surface area of the core is calculated by the formula $4\pi r^2$ and the surface to volume ratio (of the core) is defined as $\frac{4\pi r^2}{\frac{4}{3}\pi r^3} = \frac{3}{r}$ where r is the radius of the spherical core. On the other hand, the effective surface area of the core which is exposed to the environment is defined by $4\pi r^2 - N\pi r_c^2$ where r_c is the average radius of the base of each cone and N is the total number of cones. The mathematical term $N\pi r_c^2$ measures the extent of the surface area of the central core which is captured by N number of sharp tips. Similarly, the effective surface area (A) of the cone-shaped tips by disregarding the base area of cones can be expressed as $A = N\pi r_1 \left\{ \sqrt{r_c^2 + h_c^2} \right\}$ where h_c is the height of individual tips. The total effective surface area thus can be calculated by summing up the effective core area and effective petal areas for an individual AuNF. From the TEM images and by considering the above formulas, the detailed structural parameters are listed in **Table 3.2**.



Scheme 3.1: Schematic representation of the modification of the GC electrode (GCE) surface with positively charged AuNFs through electrostatic interaction followed by crystal defects dependent oxidation of ascorbic acid.

Table 3.2: Different structural parameters along with their total effective surface area calculated for our synthesized differently flourishing stages of AuNFs.

AuNF at CTAB Conc. (M)	Core radius (nm)	Effective surface area of core (mm ²)	S/V ratio of core (nm ⁻¹)	Cone-shaped tip base radius (nm)	Effective surface area of tips (nm ²)	Total effective surface area (nm ²)	Tip Diameter (nm)	Charge Density@ tip (cm ⁻¹)
------------------------	------------------	---	---------------------------------------	----------------------------------	---	---	-------------------	---

2.8×10^{-4}	55.0	38013.27	0.055	0	0	38013.3	No observed tip	-----
2.8×10^{-3}	70.0	61151.08	0.043	3	2162.57	63313.7	20	2.0×10^6
2.8×10^{-2}	77.5	26449.07	0.038	17	249993.17	276442.2	12	3.3×10^6
5.6×10^{-2}	70.0	~0	0.043	27	11486.38	611404.2	14	2.9×10^6
8.4×10^{-2}	67.5	25446.91	0.044	15	151810.42	177257.3	27	1.4×10^6

From the viewpoint of free energy, the catalytic activity of AuNFs should reduce with increase in the concentration of CTAB as at higher CTAB concentration the produced nanostructures are made up with petals having lower surface free energy by transforming from solely {110} to either a mixture of {111} and {100} or exclusively {100}. On the contrary, the extent of anisotropy (more number of petals) as well as the magnitude of surface charge (positive) increases with CTAB concentration should in turn enhance the catalytic oxidative power. Similarly, the effective surface area per AuNF increases monotonously and hence we can expect a gradual increment of catalytic power due to their ability to hold an increasing number of molecules on their surface. On the other hand, if we consider the charge (+Ve) density at the tip is the leading factor to control their catalytic oxidative power as we have shown in our previous result⁹⁸ then the reported AuNFs should show a fluctuating catalytic activity according to **Table 3.3**. To verify these expectations and assessments of the catalytic activity of different flourishing stages of AuNFs towards AA, we have measured their peak potential [E_p (V)] and peak current [i_p (μ A)] by using differential pulse voltammetry technique. **Figure 3.2A** depicts the differential pulse voltammogram of bare GC electrode in 0.4 mM AA wherein the anodic peak appears at 0.72 V due to the oxidation of AA. The modification of the GC electrode with different

geometries of AuNFs leads to a significant decrease in peak potential as well as enhancement in peak current for the electrooxidation of AA. This indicates that AuNFs exhibits electrocatalytic behavior for the oxidation of AA. However, the shift in peak potential and the magnitude of peak current alter with the different geometries of AuNFs for the electrooxidation of AA as can be inferred from **Figure 3.2A**. Among various AuNFs, the bud structure which was synthesized by using 2.8×10^{-4} M CTAB exhibits the highest catalytic activity in terms of $\Delta E_p(\text{V})$ and $i_p^{\text{AuNF}} / i_p^{\text{GC}}$ where ΔE_p is the shift in peak potential for the electrooxidation of AA at AuNFs/GC compared to the bare GC electrode and i_p^{AuNF} & i_p^{GC} represent the corresponding peak current for the oxidation of AA at AuNFs/GC and bare GC electrode respectively. A comparison analysis has provided in **Table 3.3** for the electrocatalytic activity of various-shaped AuNFs/GC electrodes towards the oxidation of AA.

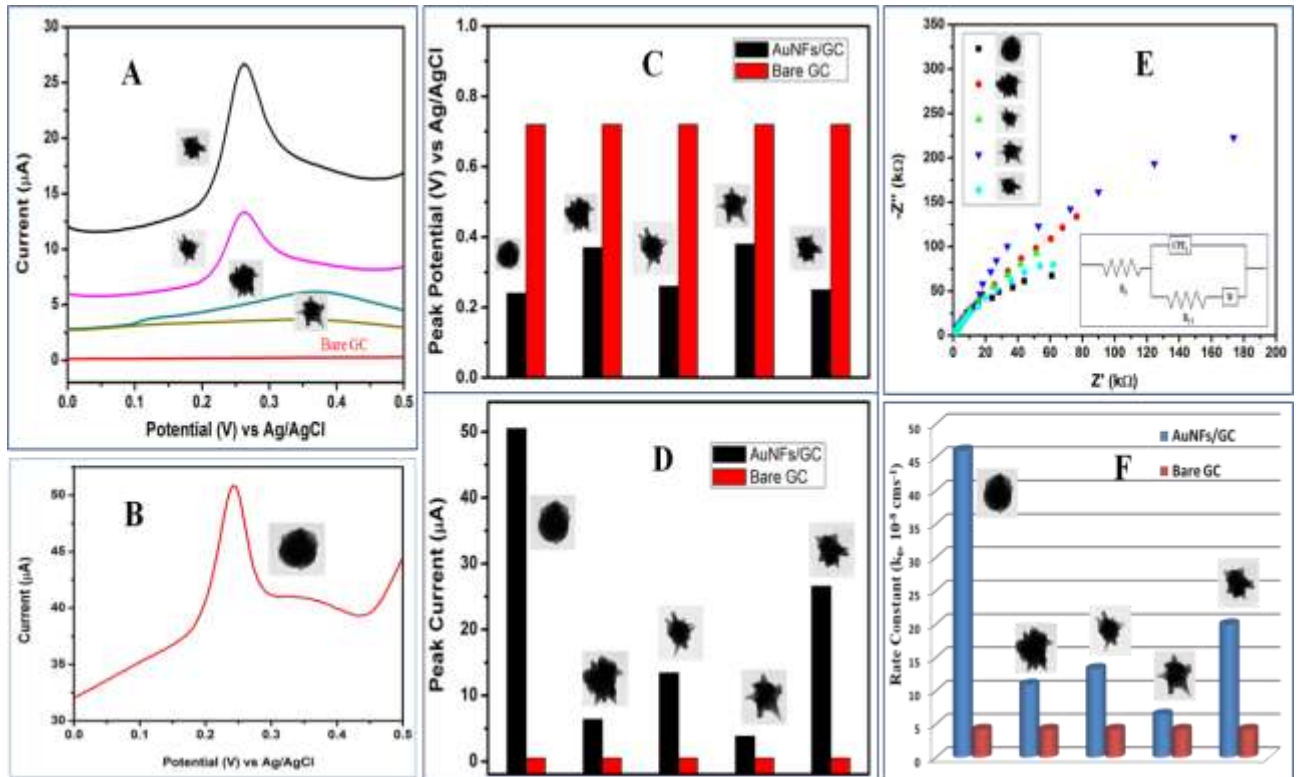


Figure 3.2: DPV for the oxidation of AA (4×10^{-4} M) on AuNF modified GC electrode synthesized using CTAB concentration as (A) 2.8×10^{-3} to 8.4×10^{-2} M, (B) 2.8×10^{-4} M, (C) and (D) show the comparison of modified GC and bare GC electrode in terms of peak potential and peak current respectively for the oxidation of AA, (E) Nyquist plot for different AuNFs modified electrode and the corresponding equivalent circuit for the Nyquist plot, (F) measured rate constant for the electro-catalytic oxidation of AA to DHAA on the surface of different AuNFs.

Interpretation of the DPV results confirms that the bud structure with crystal facet orientation towards $\{110\}$ is the most efficient one for the electrochemical catalytic conversion of AA to DHAA. The lowest peak potential (0.24 V) associated with the highest peak current (50.5 μ A) of the bud structure modified GC electrode is well supported by our previous argument of the dependence of electrocatalytic activity on facet energetic. Characteristic DPV for the oxidation of AA on bud shaped AuNF modified GC electrode is shown in **Figure 3.2B**, separately. Though the argument on facet energetic to explain the highest catalytic activity of bud structured AuNF shows the expected result, charge density at the tip does not support it due to the absence of any tip on the bud structure. Moreover, the trend of catalytic activity for different flowering stages of AuNFs does not follow a linear relation with the CTAB concentration as it is expected both from facet energetic and charge density consideration. In the same line of argument, other factors which include the extent of anisotropy (more number of petals), total surface charge, and effective surface charge, all increases monotonously with CTAB concentration and suppose to show a gradual increment of catalytic activity towards AA oxidation. Obtained catalytic activity (in terms of a shift in peak potential and relative peak current) shows a zig-zag pattern and cannot be explained by those above factors. These

observations forced us to consider other unexplored factors as major players to control their observed electrocatalytic activity.

Table 3.3: Experimental observations and system parameters deduced from DPV and EIS measurement towards the oxidation of AA on different flourishing AuNF coated GC electrode

AuNFs at CTAB concentrations (M)	Peak potentials, E_p (V)	Peak current (μA)	Relative peak current $\left[\frac{i_p^{\text{AuNF}}}{i_p^{\text{GC}}} \right]$	R_{CT} ($\text{k}\Omega$)	i_0 (10^{-8} A)	k_0 (10^{-6} cm s^{-1})
Bare GC	0.72	0.5	NA	2978.5	0.43	0.79
2.8×10^{-4}	0.24	50.5	101.0	51.4	25.08	46.03
2.8×10^{-3}	0.37	6.39	12.78	215.0	5.97	10.95
2.8×10^{-2}	0.26	13.44	26.88	177.4	7.25	13.30
5.6×10^{-2}	0.38	3.82	7.64	364.2	3.52	6.45
8.4×10^{-2}	0.25	26.58	53.16	117.1	10.9	19.97

Out of several other factors, the extent of crystal defect¹²⁷ could be a major aspect to control the observed catalytic activity. The HRTEM study clearly shows the presence of several different types of defects originating from crystal plane dislocations, stepped surface, kinks, islands, or from differently packed crystal boundaries. A pictorial representation of different types of crystal defects originates from bud structured and fully blossomed AuNFs are shown in **Figure 3.3** and **Figure 3.4**. In an *fcc* crystal, the normal stacking sequence of the planes generally represented as ABCABCABC..... pattern. Characteristic twin boundary (TB) generates when one plane acts as a mirror of the other two. In **Figure 3.3D** a twin defect appears via the unusual sequence

ABCBA patterning where the C presents a mirror plane to that of AB planes. The atoms situated on the twin boundary, C plane, have reduced coordination numbers and catalytically more active than the other closely packed planes. By comparing all five different flourishing stages of AuNF synthesized at different concentrations of CTAB, it has been observed that a greater defect density has been observed for the bud shaped structure compared to the other flourishing stages of AuNF.

A crystal plane at an angle θ to a close-packed plane can generate terraces (inclined surface with respect to the low indexed [low energy] atomically flat surface), ledges (structural defect which accommodate the terrace inclination) and kinks (defect in the ledge) to result in additional broken bonds in these inclined planes compared to the reference close-packed planes. Any general orientation within the stereographic triangle (Euler Triangle) can be constructed with ledges and kinks of a certain density in an appropriate terrace orientation.¹²⁸ These ledges and kinks are the sites where atoms of growing crystal or foreign atoms/molecules can preferentially attach compared to the flat terraces. By considering the angle between terraces and ledges as θ and between ledges (ledges are constructed as a combination of several kinks) and kinks as ϕ , mathematically we can define the surface energy offered by ledges and kinks are $\gamma(\theta) = (\gamma_T \cos\theta + \gamma_L \sin\theta)$ and $\gamma(\phi) = (\gamma_L \cos\phi + \gamma_K \sin\phi)$ respectively where 'T' stands for terrace, 'L' for ledges and 'K' for kinks.¹²⁸ Besides steps, kinks, and edges; dislocation planes^{94,96} (which is also a source of the active catalytic site) has also been observed in the growing tips of different AuNFs. In general, dislocation defects are formed when atoms in a regular crystal are out of position to form a distorted region. For a polycrystalline material, this disorientation of crystallites is known as boundary (grain or twin) defects. In general, these small misfits (angular: boundary defect and linear: same lattice defect) between crystals or crystal

planes can be accommodated by structural dislocations. Broadly this structural dislocation can be subdivided into three categories as tilt (rotation axis lies on the boundary plane), misfit (stretching of one particular plane), and twist (rotation axis lies perpendicular to the boundary plane) dislocation. Misfit and twist can also be defined as edge dislocation and screw dislocation as has been clearly shown in **Figure 3.3E & 3.3F** respectively on a bud structured AuNF. For a better understanding of crystal defects, we have also provided the HRTEM images for bud shaped AuNF in **Figure 3.5**, which shows the direction of the growing tip towards energetically unfavorable {110} facet.

A Crystal defect originated from the formation of islands is also a dominant feature to control their overall catalytic activity. In general, an island grows or shrinks to maintain equilibrium vacancy concentration via atom migration from the crystal to the surface.¹²⁹ A recent work by Ganesh et al.¹³⁰ has studied the intriguing catalytic activity of surface-active islands on nanostructures for efficient direct formic acid oxidation. The modulation of different crystal defects during their shapes evaluation to control the catalytic power^{80,81} of a nanoparticle is the main theme of this study to achieve the most suitable nanostructure with desired crystal orientation for the highest catalytic activity. A detail of this shape-dependent defect study is summarized in **Table 3.4** which includes different types of defects originated from structural dislocation, steps, kinks, islands, and differently packed crystal boundaries.

Table 3.4: Density (nm^{-2}) of Different Crystal Defects (dislocation, steps, kinks, islands, and differently packed crystal boundaries) for Various Shaped AuNFs Synthesized at Tunable Concentration (M) of CTAB.

Different Types of Crystal Defects	Density (nm^{-2}) of Different Crystal Defects for Different Shaped AuNFs Synthesized at Different Concentration (M) of CTAB
---------------------------------------	--

	2.8×10^{-4}	2.8×10^{-3}	2.8×10^{-2}	5.6×10^{-2}	8.4×10^{-2}
Edge dislocation	0.35	0.05	0.17	0.01	0.22
Screw dislocation	0.57	0.11	0.14	0.07	0.35
Stepped surface	0.18	0.06	0.08	0.02	0.13
kink	0.58	0.23	0.31	0.17	0.43
island	0.43	0.07	0.19	0.03	0.37
Twin boundary (TB)	1.11	0.05	0.85	0.01	0.93
Grain boundary (GB)	1.77	0.13	0.89	0.11	0.95

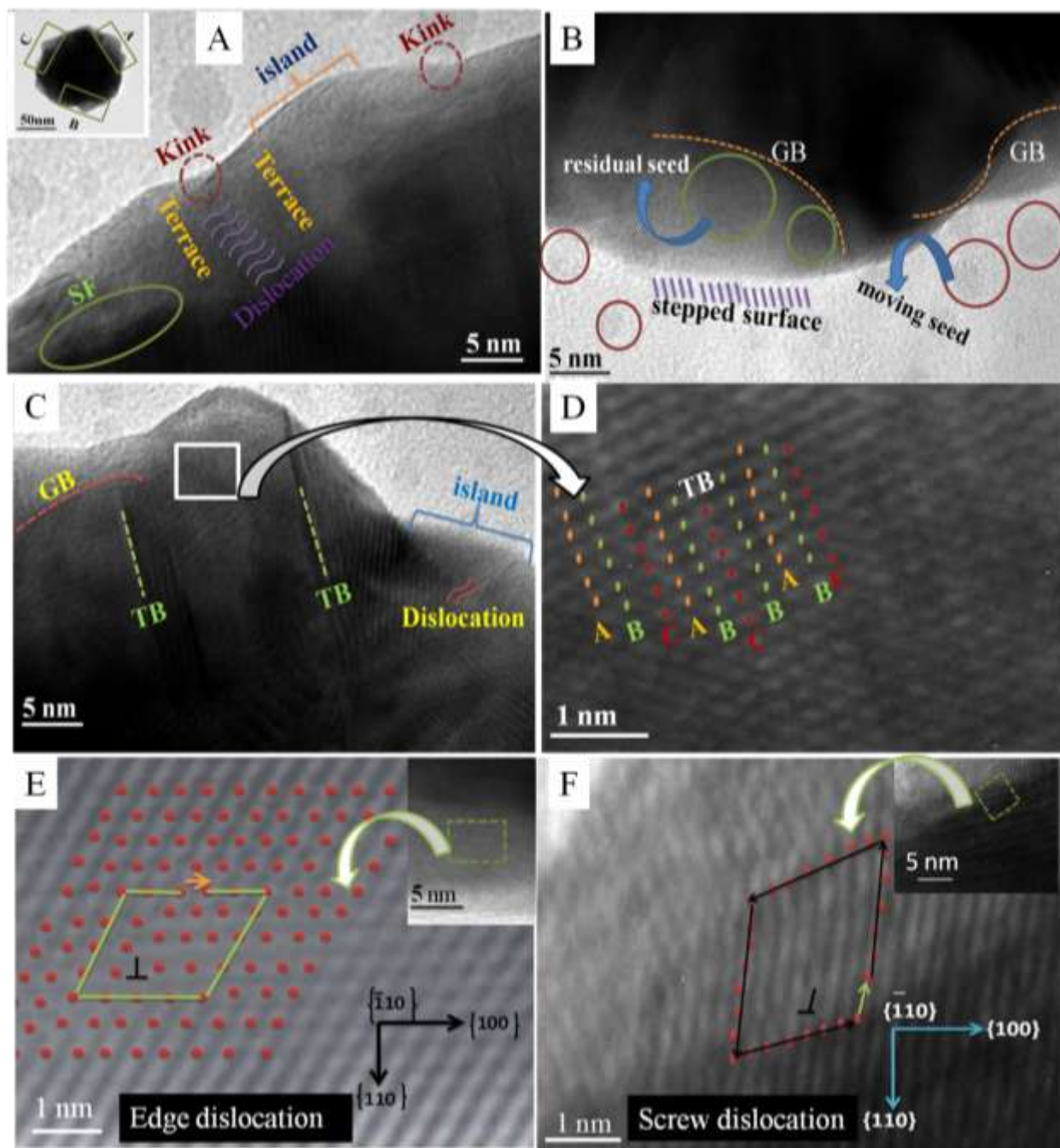


Figure 3.3: Randomly selected three different surface regions (A, B and C) of a bud structured AuNF to find out the existence of different crystal defects, (D) zoomed region on frame C to understand the crystal plane arrangement in twine boundary, detailed vectorial representation of (E) edge dislocation and (F) screw dislocation.

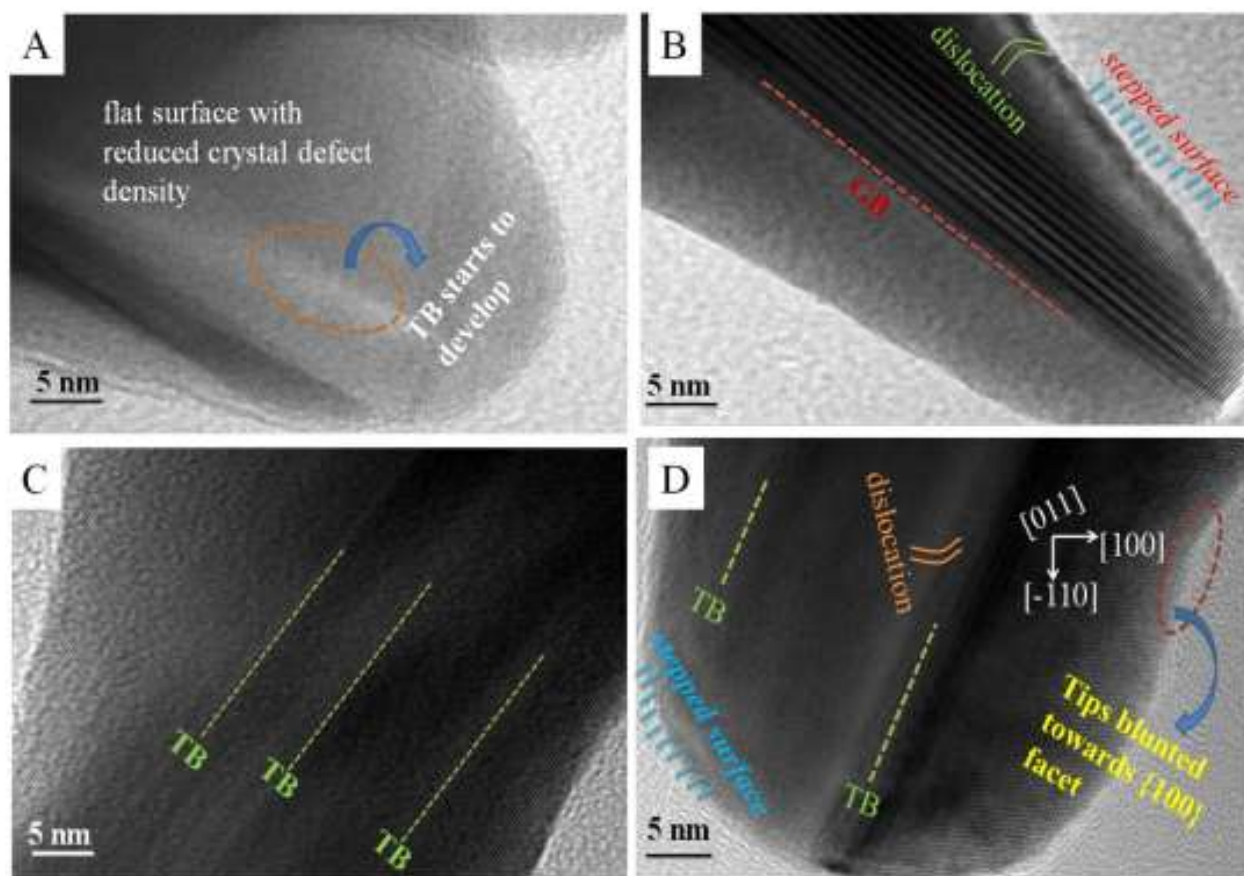


Figure 3.4: (A) AuNF synthesized at 2.8×10^{-3} M CTAB with reduced crystal defect density, (B) With increasing CTAB concentration at 2.8×10^{-3} M CTAB, the AuNF produced show enhanced crystal defect density, (C) Fully blossomed AuNF produced at 5.6×10^{-2} M CTAB Shows only twin boundary defect, (D) Overgrown AuNF synthesized at 8.4×10^{-2} M CTAB exhibit blunted tips towards energetically unfavorable $\{110\}$ facet.

HRTEM based density of different crystal defects (nm^{-2}) for different shaped AuNFs has been detailed in **Figure 3.6**. Our HRTEM study clearly shows that irrespective of the type of defects, the defect density is maximum for bud structure which reduces in a zigzag pattern as different flourishing stages of AuNF evolves at an increased concentration of CTAB. Incremental contribution of dislocation planes along with steps, kinks, islands, and differently

packed crystal boundaries supports the presence of a maximum number of catalytic active sites on leading highly energetic $\{110\}$ facets of bud shaped structure to offer highest AA oxidizing power.

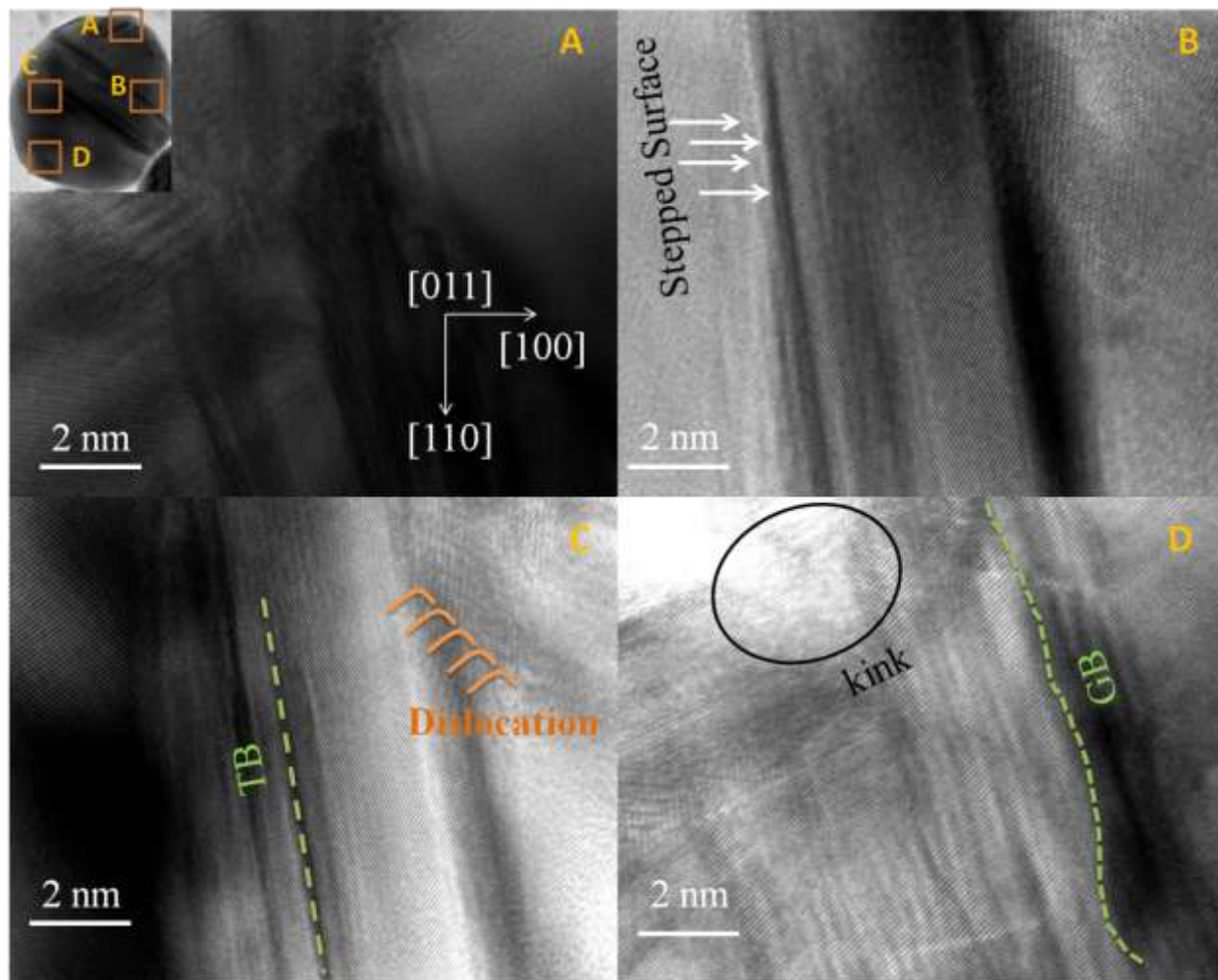


Figure 3.5: HRTEM image of the bud shaped AuNF. Different parts of the bud structure is focused where (A) indicates the direction of the growing tips towards $\{110\}$, and (B), (C), (D) indicates the presence of multiple crystal defects like stepped surface, GB, TB, Dislocation, etc.

Here CTAB concentration regulates the shape of the AuNFs and described in detail in our previous publication.¹² The oxidizing ability of AuNF at CTAB concentrations between $2.8 \times 10^{-3} \text{ M}$ and $8.4 \times 10^{-2} \text{ M}$ shows a zig-zag pattern. This observation can easily be described in terms of

the variation of defect density with different flourishing stages where for each shaped AuNFs we have considered three different surface zones with different surface areas (25, 100, and 225 nm²). For each surface zone of an individual structure, we have considered 100 frames and hence **Table 3.4** is bearing the statistics of 5×3×100 = 1500 frames. A detail of defect study is summarized in **Table 3.4** which includes different types of defects originated from structural dislocation, steps, kinks, islands, and differently packed crystal boundaries. Various type of crystal defects density was calculated by employing the expression as: Crystal defects density (CDD) = $\sum_{i=1}^{i=100} \frac{n_i}{A_i}$, where, n_i denotes the number of respective defects in the selected area A_i. Considering similar statistical analysis we have also presented the charge density at the apex in **Table 3.2** which gets maximum for the highest curvature tips.⁹⁸

Charge density is mathematically calculated as 2κ, where κ is the radius of curvature (κ=1/R) and R is the tip radius. Though the charge density at the tip is a formidable factor to achieve higher catalytic activity as we have reported previously.⁹⁸ The obtained result in this report does not explain their growing role over crystal defect density. Hence out of several factors which include (i) generation of crystal defects due to the presence of low coordination atoms on steps, kinks, islands, and edges, (ii) increment of internal surface area due to the dislocation, (iii) orientation of crystal facets on the projected tips of AuNFs, and (iv) charge density at the tip; the statistics of defect density leads the rally.

Though we used the DPV technique for fingerprinting the characteristic redox peak-current and peak-potentials of the electrocatalytic oxidation of AA; we have adopted here alternate EIS technique also to acquire the kinetics information as well as to measure the ability of a circuit to flow electrical current. Electrochemical impedance spectroscopy (EIS) is one of the most powerful and reliable techniques for getting various electrochemical parameters such as double-

layer capacitance (C_{dl}), charge transfer resistance (R_{CT}),¹³¹ solution resistance (R_s), the standard heterogeneous rate constant (k_0),¹³² etc. The typical Nyquist plot obtained from the EIS experiment indicates the variation of real and imaginary parts (of impedance) over a higher to lower frequency range (e.g. 10^5 to 10^{-2} Hz) at a fixed potential.⁷² The distorted semicircles are observed from the Nyquist plot (**Figure 3.2E**) for various shaped AuNFs modified GC electrode towards the electrooxidation of AA wherein diameter of the semicircle in the X-axis gives an estimation of R_{CT} value between the modified electrode and analyte (AA). However, a variation in the R_{CT} value is noticed for different morphology of AuNFs in which the fully flourished AuNF-modified GC electrodes exhibit the highest R_{CT} value while the bud shaped AuNF shows lowest R_{CT} values. R_{CT} values for other AuNFs lie in between the limits and their magnitude follows the trend as $R_{CT}^{2.8 \times 10^{-4}} < R_{CT}^{8.4 \times 10^{-2}} < R_{CT}^{2.8 \times 10^{-2}} < R_{CT}^{2.8 \times 10^{-3}} < R_{CT}^{5.6 \times 10^{-2}}$. From this R_{CT} value, we have estimated the exchange current densities (i_0) as well as the standard heterogeneous electron transfer rate constant (k_0) by adopting the following equations⁷²:

$$R_{CT} = \frac{RT}{nFi_0} \text{ and } i_0 = nFAC_{OX}^{(1-\alpha)} C_{Red}^{\alpha} k_0 \quad (2)$$

$$\text{by assuming } C_{OX}^{(1-\alpha)} = C_{Red}^{\alpha} = C, i_0 = nFACk_0$$

where ‘n’ denotes the number of electrons (here, $n = 2$), ‘A’ denotes the active surface area, C_{OX} and C_{Red} denote the bulk concentrations of ascorbic acid (AA) and dehydroascorbic acid

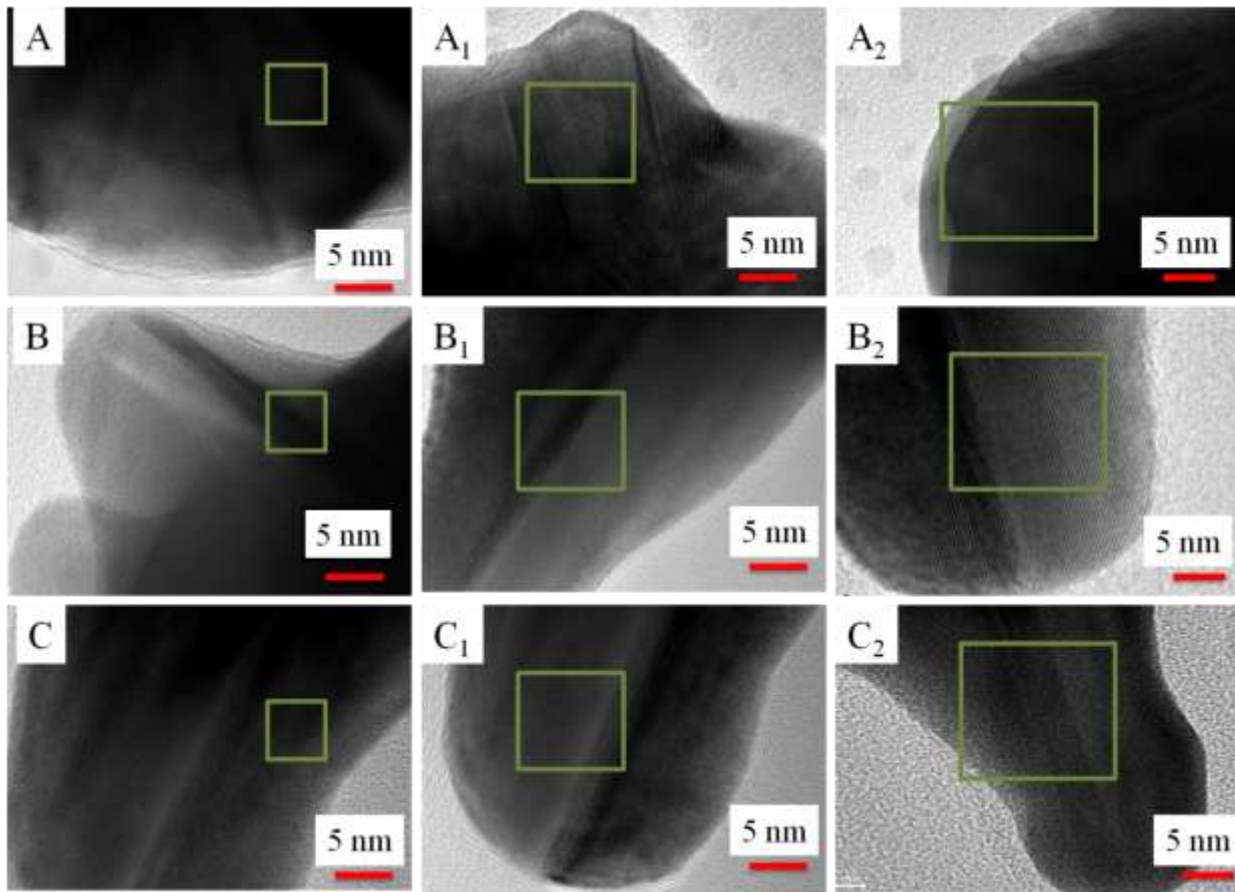


Figure 3.6: Variation of defect density with different flourishing stages (Top panel for bud structure with 2.8×10^{-4} M CTAB, Central panel for half blossomed AuNF with 2.8×10^{-2} M CTAB and bottom panel for the overgrown AuNF with 8.4×10^{-2} M CTAB) where for each shaped AuNFs we have considered 100 frames each for three different surface zones with different surface areas (25, 100 and 225 nm²).

(DHAA), respectively and α being the symmetry factor. For the quantitative evaluation of various system parameters, a modified Randles equivalent circuit (by blending the parameter constant phase element; CPE)¹³³ is constructed (**Figure 3.2E** inset) to fit the experimental Nyquist plot and the fitting parameters are tabulated in **Table 3.3**. As can be seen from **Table**

3.3, the bud shaped AuNFs (prepared using 2.8×10^{-4} M CTAB) shows the highest exchange current, as well as the utmost standard heterogeneous rate constant in comparison to other AuNF, modified electrodes. The heterogeneous rate constant follows the trend as: $k_0^{2.8 \times 10^{-4}} > k_0^{8.4 \times 10^{-2}} > k_0^{2.8 \times 10^{-2}} > k_0^{2.8 \times 10^{-3}} > k_0^{5.6 \times 10^{-2}}$. Indeed, this behavior is consistent with the DPV response of AuNFs/GC towards the electro-oxidation of AA. Thus, it can be concluded that the morphology which having higher crystal defects (steps, kinks, edges, dislocation) exhibits superior catalytic activity than that of others.

To get the idea about the feasibility of AA oxidation reaction on different crystal facets we have used here Vienna *Ab initio* Simulation Package (VASP) where the reaction free energy (ΔG) have been calculated by using the computational hydrogen electrode (CHE) model as proposed by Nørskov and co-workers.^{131,134}

For example, the reaction free energy for a general reaction is calculated at zero voltage as follow:



Reaction free energy: $\Delta G = G(A^*) + \left[\frac{1}{2} G(H_{2(g)}) \right] - G(AH^*)$ (4)

We have calculated the reaction free energy change for the reaction presented in **Scheme 3.1**. The optimized structures of AA on different crystalline gold facets have shown in **Figure 3.7**. Our calculated reaction free energy (**Table 3.5**) suggests that the oxidation of ascorbic acid shows different reactivity with different crystal facets of the gold surface. The Au{110} surface is more reactive with minimum activation energy (1.04 eV) and lowest reaction free energy (0.64 eV) compared to the {111} and {100} surfaces. On the other hand, the reaction is more favorable with the free energy change of 0.59 eV in the presence of stepped surface {211} which inclined towards {111} and {100} surfaces. Simulated results match exactly what we observed for

experimental electrocatalytic activity on different flourishing stages of AuNFs. Both experimental observation and simulated prediction show the highest catalytic activity for bud shaped AuNF with active crystal faces oriented towards $\{110\}$ direction.

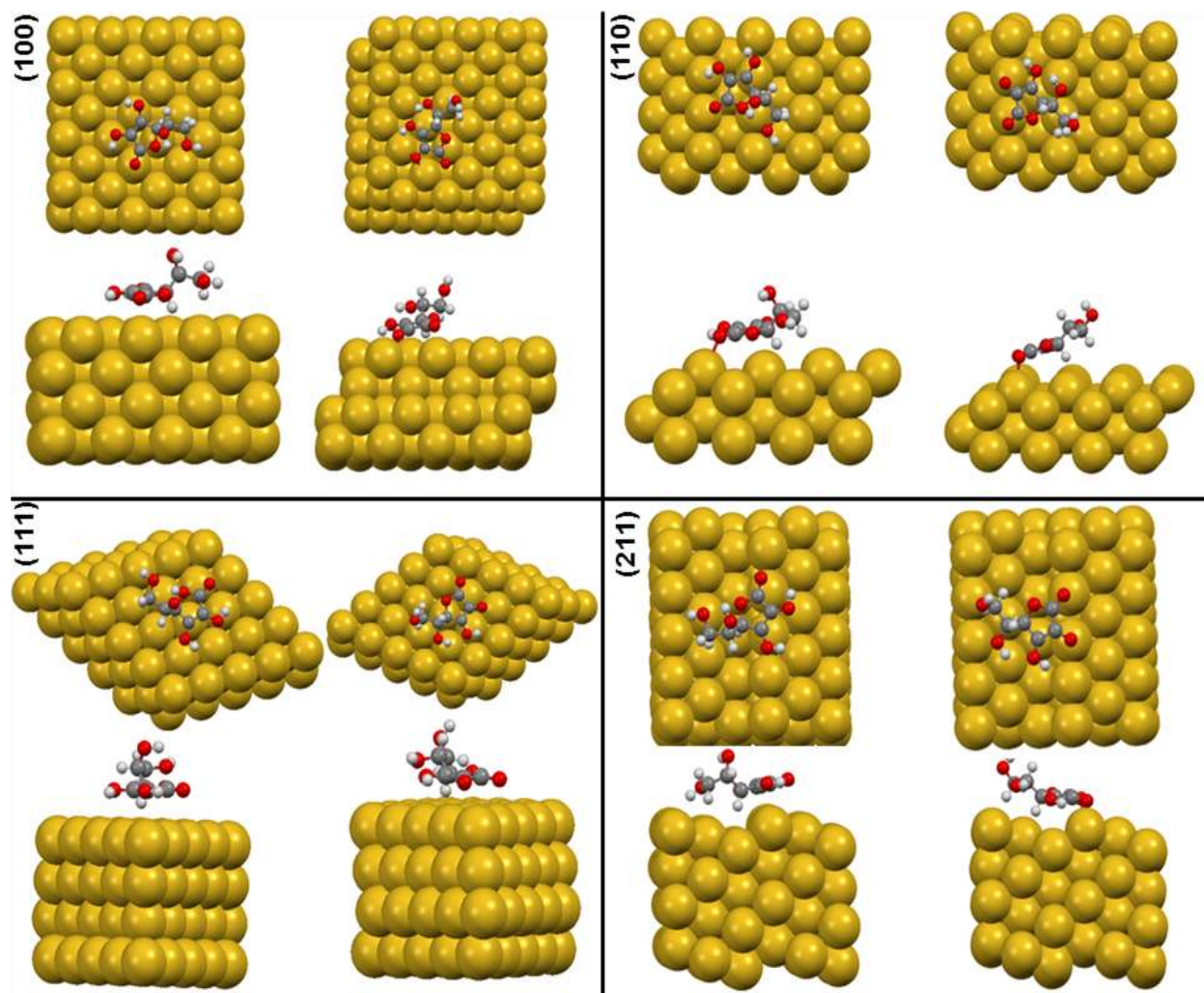


Figure 3.7: Top and Side views of the optimized AA on different crystalline lowest order $\{111\}$, $\{100\}$ and $\{110\}$ and stepped $\{211\}$ Au facets. Optimized molecules are shown in the ball-and-stick model where red balls indicate oxygen atoms, gray balls as carbon atoms and white balls as hydrogen atoms.

Table 3.5: Calculated reaction free energy for the oxidation of AA on different crystal facets of gold

Surface	$\Delta E(\text{eV})$	$\Delta G(\text{eV})$
100	1.14	0.70
110	1.04	0.64
111	1.51	1.05
211	0.97	0.59

The highest oxidizing power of the bud structured AuNF encouraged us to utilize this nanomaterial for AA sensing by utilizing electrochemical measurement techniques. The appearance of variable peak potentials at different concentrations and interpretation of the obtained result through the structural contribution of AA is quite interesting in terms of the intra- and inter-molecular hydrogen bonding¹³⁵ among themselves. At lower AA concentrations (**Figure 3.8A**) the peak potential appears at 0.345 V and the DPV curve at variable concentration is broad in nature. The current vs. concentration curve shows an exponential and linear growth type in the lower (4×10^{-5} to 4×10^{-8} M) and higher (10^{-3} to 10^{-4} M) range of AA concentrations respectively as shown in **Figure 3.8C** and **3.8D**. Single peak potential for AA oxidation can easily be explained by considering an intramolecular hydrogen bond to facilitate the oxidation of AA to DHAA. At intermediate concentration range (10^{-4} to 10^{-5} M), a dual humped curve has been observed indicating a two-electron oxidation of AA. As the concentration of AA increases and reaches above mM concentration, the distance between AA molecules reduces to allow both intramolecular and intermolecular hydrogen bonding to show an additional peak at 0.24 V origination from AA-dimers along with the original peak potential at 0.345 V due to the AA oxidation through intramolecular hydrogen bonding trajectory. The two-electron oxidation of AA is clearly shown in **Figure 3.8B** where one peak potential arises at 0.24 V and another one

at 0.345 V. At a very high concentration of AA ($>10^{-3}$ M), the peak potential shifts further to lower potential at 0.20 V indicates much faster oxidation. Thus, quantitative and qualitative fingerprinting of AA can easily be done from the prescribed electrochemical measurements.

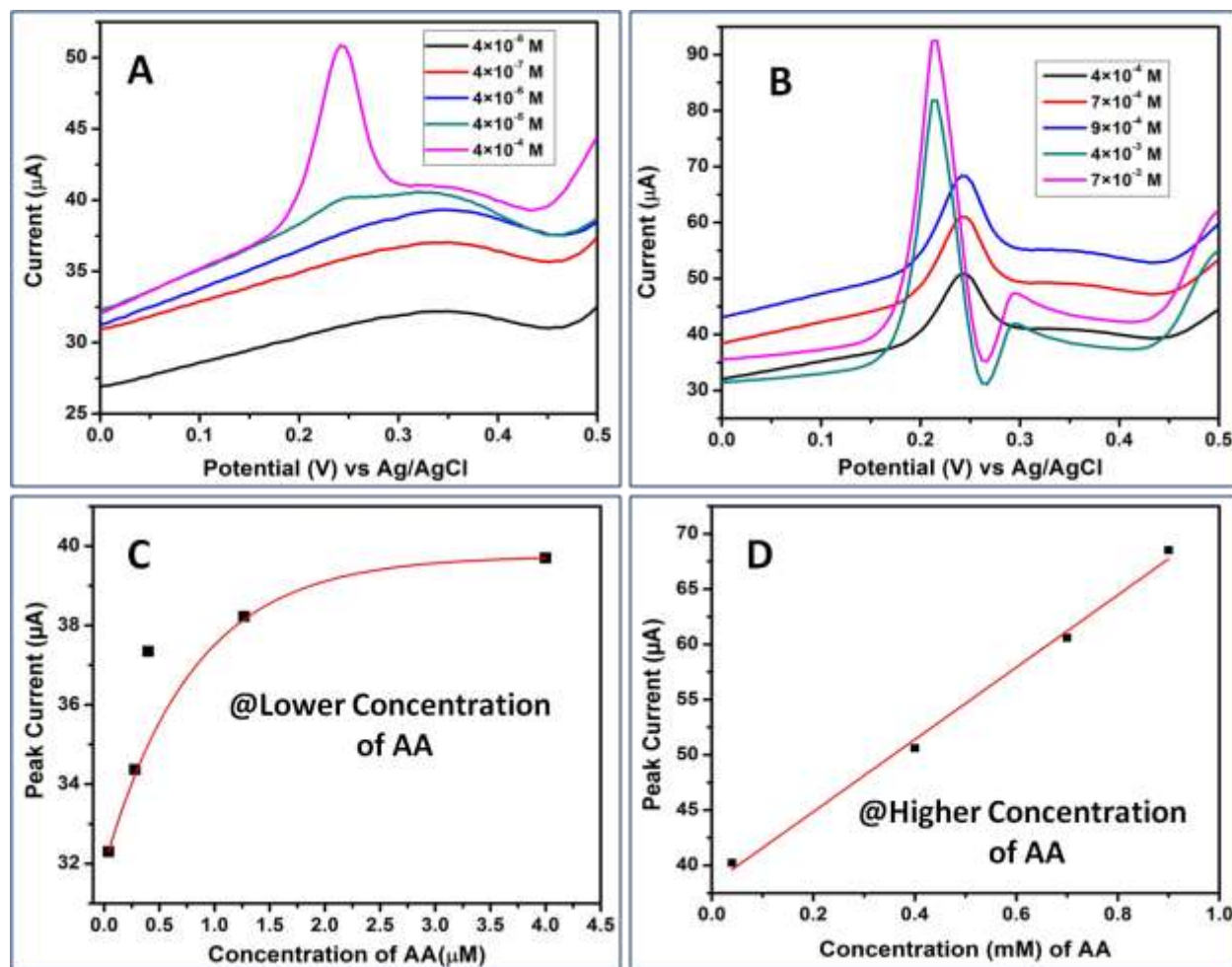


Figure 3.8: (A) DPV of AA at lower concentration level (4×10^{-5} to 4×10^{-8} M), (B) DPV of AA at higher concentration level (10^{-3} to 10^{-4} M), (C) The exponential growth of peak current at a lower concentration of AA, and (D) The linear variation of peak current at higher concentration of AA.

To understand the mechanism of AA oxidation in the molecular level, we have studied their redox reaction on a few atom gold clusters by using Density Functional Theory.^{120–122}

Using this quantum mechanical analysis we have obtained the optimized geometries of the

monomer, dimer, and the gold complexes of L-ascorbic acid (AA) as shown in **Figure 3.9a** and **3.9b**. Whereas the electron densities in the highest occupied molecular orbital (HOMO) and lowest unoccupied molecular orbital (LUMO) of the gold cluster complex with monomer and dimer of AA are shown in panel A and B of **Figure 3.9a** and **3.9b** respectively. The vibrational frequencies of the first O-H bond stretching in monomer as well as in the intermolecular hydrogen-bonded dimer were monitored in presence of increasing number of gold atoms and the changes are plotted in **Figure 3.9c** whereas the changes in the O-H bond lengths are shown in **Figure 3.9d**. O-H bond weakening was observed in monomer (bonded to Au through either H or O atom of AA) as well as in the dimer of ascorbic acid in presence of Au. In monomer, O-H stretching frequency was decreased by around 300 cm^{-1} , thus, facilitating the deprotonation process. Intermolecular hydrogen bonding also weakens this OH bond^{136,137} and the decrease in the stretching frequency was about 400 cm^{-1} . Au cluster was found to further decrease the stretching frequency by 300 cm^{-1} . Therefore at higher concentration AA, the presence of gold cluster reduces the OH stretching frequency up to 700 cm^{-1} effectively. Alternatively, at higher concentrations where ascorbic acid molecules remain hydrogen-bonded, oxidation occurs more easily in the presence of gold as we have observed experimentally. Experimentally we have observed that the peak potential for AA oxidation shifted from 0.345 V at very low concentration (4×10^{-5} to 4×10^{-8} M) to 0.24 V at an intermediate concentration (10^{-4} to 10^{-5} M) and finally shifted to 0.205 V at very high concentration ($>10^{-3}$ M) of AA. This directly provides the true mechanistic explanation behind the electrocatalytic oxidation of AA.

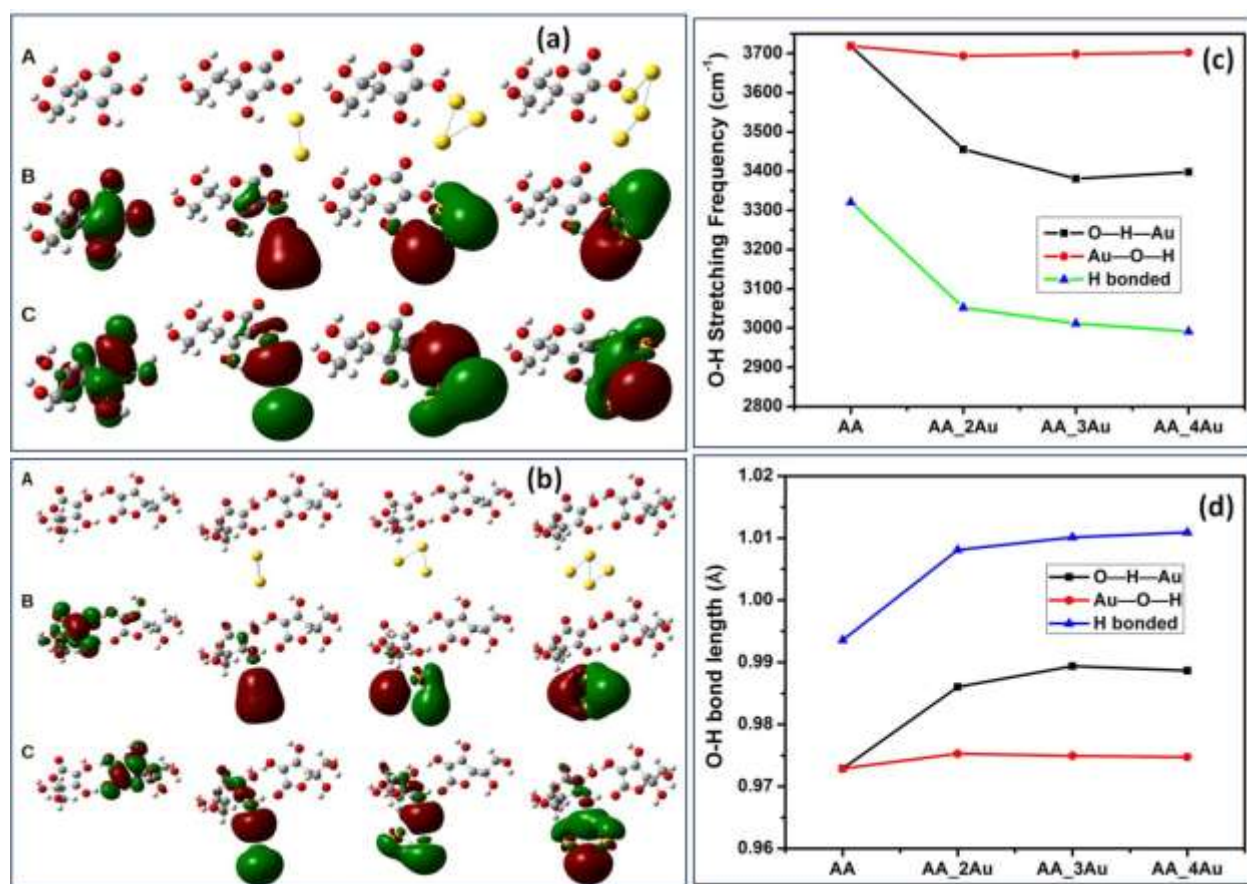


Figure 3.9: Optimized geometries and the electronic distributions of ascorbic acid monomer (a) and dimer (b) in the presence of gold. (A) Optimized geometries of ascorbic acid (monomer or dimer) and its gold complexes. (B) HOMO/SOMO of the respective complexes. (C) LUMO of the respective complexes. (c) Changes in the stretching frequency and (d) the bond length of the first OH group in L-ascorbic acid (AA) in presence of increasing number of Au atoms (two to four).

Based on the high catalytic activity of the bud structured AuNF and from the complete understanding about their mechanism of action along with molecular and crystal level driving forces for its enhanced activity, we encouraged to use this bud shaped AuNF structure for ultra-low sensing of AA in presence of other closely related biological components^{138,139} like DA, UA, and Glucose. The DPV response (**Figure 3.10A**) of bud shaped AuNF modified GC electrode at

the equimolar mixture of biological components show clear individual peaks for the respective components with unchanged peak position (0.245 V for AA, 0.41 V for DA, 0.535 V for UA and 0.63 V for glucose) for each element. As the peak potential for individual components is well separated from each other, in a single potential sweep we can identify all the available components in a multicomponent pathological sample. From the DPV response, we have constructed the calibration plot (**Figure 3.10B**) for all four components during the simultaneous detection of these species. This detection methodology holds true for those components which do not interact with each other to produce another component in the mixture of analytes.

The main criteria of a successful sensor is to show a linear variation of the identifiable and measurable quantity (here peak current) with concentration. It is clear from **Figure 3.10** that the peak current for individual components in a test sample shows a linear variation in a physiologically viable concentration range. Moreover, all the components can easily be identified in a single potential sweep from a multicomponent pathological sample. Hence, the bud structured AuNF has the unique potential to use it as an efficient electrocatalytic sensor for pathological sensing.

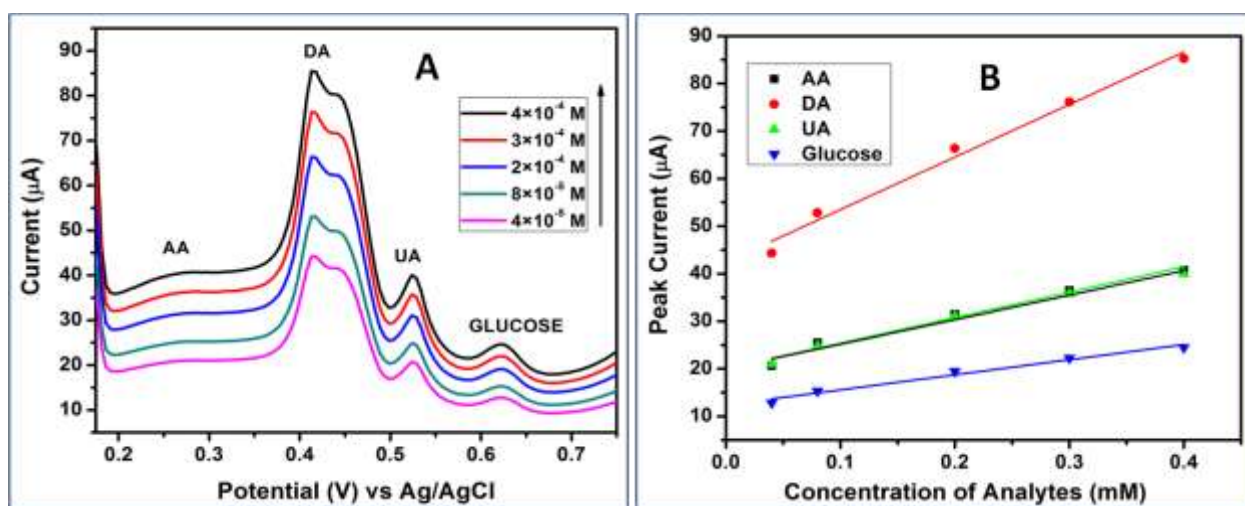


Figure 3.10: (A) DPV at a variable concentration of an equimolar mixture of AA, DA, UA, and Glucose. (B) A linear fit of peak current for individual components at a variable physiological concentration range.

3.6 Conclusion:

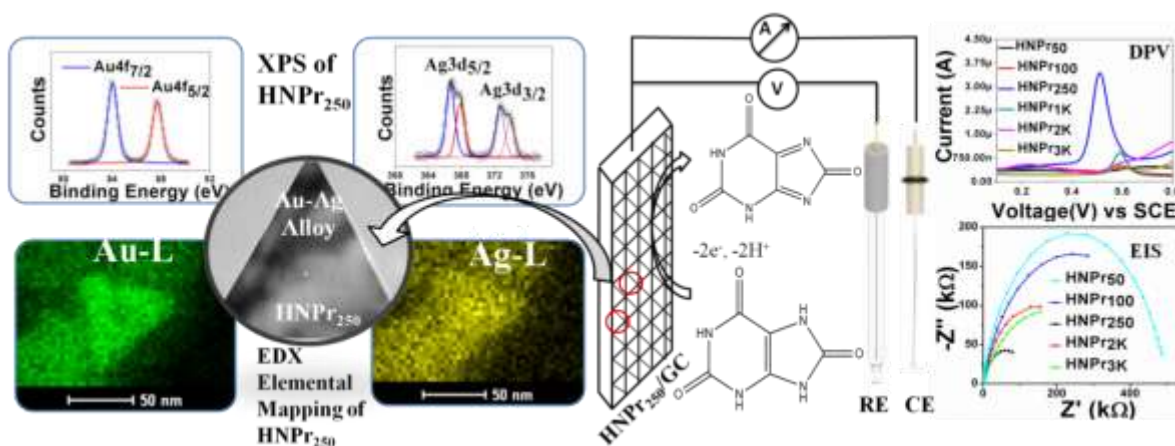
The DPV response and EIS data for the oxidation of AA clarify that there is a strong correlation between the electro-catalytic activity and the extent of crystal defect density (nm^{-2}) of different AuNFs. The defect density on nanocrystals has been calculated from the recorded HRTEM measurements by considering all possible defects originated during their growth. Among various controlling factors, the crystal defect density plays a crucial role in determining the superior catalytic ability. The bud shaped AuNF shows superior catalytic activity in comparison with other AuNFs due to the presence of the highest crystal irregularity on its surface. Moreover, bud shaped AuNF shows the effective fingerprinting ability of AA in the presence of other closely related compounds in a multi-component pathological sample. Besides, the role of different crystal facets [$\{111\}$, $\{100\}$, $\{110\}$, and $\{221\}$] on the catalytic performance of AuNFs has been explored by calculating the reaction free energy (ΔG) using computational hydrogen electrode (CHE) model on VASP platform which is consistent with our proposed mechanism. Variation of peak potential for AA oxidation at different concentration range has been demonstrated using DFT by considering their intramolecular (monomer) and intermolecular (dimer) interaction in the presence of different sized Au clusters. The fingerprinted peak potential and linear fit of peak current for individual components (AA, UA, DA, and glucose) at variable physiological concentration prove the ability of the bud shaped AuNF as an efficient electrocatalytic sensor for multicomponent pathological sensing.

CHAPTER-4

Zone-Specific Crystallization and a Porosity-Directed Scaling Marker for the Catalytic Efficacy of Au-Ag Alloy Nanoparticles

OUTLINE: Specific Points of Discussion

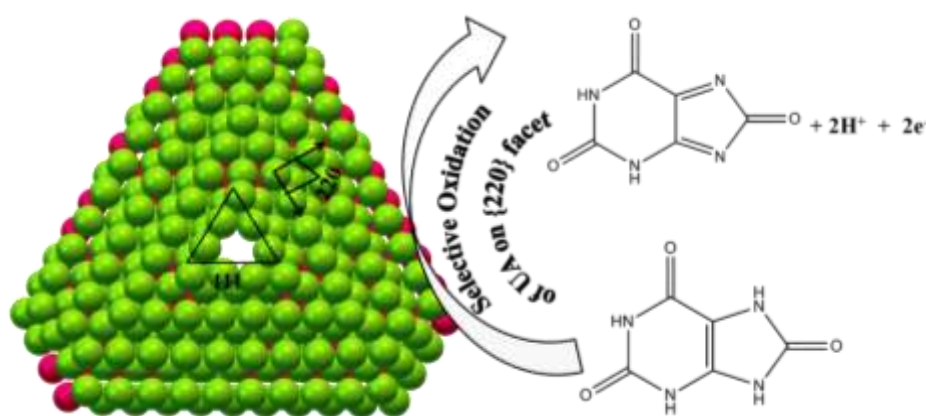
- Modified seed-mediated growth followed by the sacrificial galvanic replacement method has been adopted to synthesize Bimetallic Au-Ag hollow nano prisms (HNPr) with variable effective surface area, dynamic atomic composition (Au: Ag), and distinct stepped surface between the central porous region and crystalline periphery.
- The role of numerous low coordinated crystal defects along with extended d-orbital spacing in the central cavity region of HNPrs to control their adsorption efficiency for different redox reactions has been explored in detail.
- The presence of high-density grain boundary with preferable Au^0 : Ag^0 ratio in HNPr₂₅₀ helps to form an extensive porous ligamentous central cavity and accelerate the kinetics of the Uric Acid (UA) oxidation for their nM detection.
- Experimental observations have been supported by DFT calculation to approximate the effective Au-Au displacement in explaining their catalytic activity.



4.1 Introduction:

In this chapter, we have synthesized different bimetallic Au-Ag hollow nanoprisms and checked their catalytic activity through electrochemical oxidation of uric acid. Irregularities or defects of nano-crystalline materials differentiate them in novel properties from their bulk counterparts.¹⁴⁰ Alloying of noble metal induces a plethora of unknown and unexplored properties of nanomaterials which include superconductivity¹⁴¹, superparamagnetism¹⁴², highly stressed nanoscale materials to generate reactive oxygen,¹⁴³ etc. Besides these properties, the alloying of noble metal nanoparticles is believed to be one of the most crucial factors to generate defects like grain boundary, dislocations, etc. which drastically alters the catalytic property along with various Physico-chemical properties viz., mechanical strength (which include tensile strain, compressive strain, etc.) and toughness of the material.¹⁴⁴ It has been reported that nano-crystalline materials having grain boundary (GB) rich surface is effective for CO reduction¹⁴⁵ with high turnover frequency. Additionally, another controlling factor that enhances the catalytic property is the presence of multiple twin boundary (MTB) defects which are exposed to high energy facets.¹⁴⁶ The active site of a heterogeneous catalyst can be considered as a direct collection of atoms which can be introduced into the lattice by a high density of stacking faults and twin boundaries.¹⁴⁷ The multiple twinned gold nanoparticles supported on TiO₂ surface

exhibit superior catalytic performance for CO oxidation than twin-free gold nanocrystals.¹⁴⁸ Similarly, polycrystalline gold nanoparticles (most probably with an enormous number of grain boundaries but not analyzed extensively) show the enhanced catalytic activity of UA oxidation¹⁴⁹. In addition, the planner defects e.g., stacking fault, dislocations, etc. originate during the crystal growth of gold nanostructures that are found to be effective for electrocatalytic oxidation of methanol¹⁵⁰. Out of a large pool of available mixed metal nanomaterials, Au-Ag alloy nanomaterials draw special attention due to their similarity in lattice parameters (Au: 4.08 Å and Ag: 4.09 Å) to create most stable periodically folded atomic nanocrystals.¹⁵¹ Different strategies are reported and have been adopted to generate mixed metal nanomaterials either by adopting leaching methodology¹⁵² or selectively depositing on active sites.¹⁵³ Out of several different types of mixed metal nanostructures, designing specially engineered pseudo porous bimetallic nanomaterials is our target to generate novel materials that are expected to show the extraordinary catalytic property (along with several other exciting physical and chemical properties) contrary to their monometallic counterparts.¹⁵⁴ Schematic representation of two-electron oxidation of UA on Au-Ag alloy nanoprisms with the central porous cavity is shown in **Scheme 4.1**.



Scheme 4.1: Two electron electrochemical oxidation of uric acid on {220} facet of HNPr.

Origination of porosity during the growth of bimetallic Au-Ag nano-crystals constitutes various crystal imperfections¹⁵⁵ which are suitable for their enhanced catalytic activity. The low coordinated perimeter appears near the central cavity (or central porous moiety) of hollow nano prisms (HNPr) has been considered as the prime factor for generating active catalytic sites.^{156,157} It is believed that during the synthesis of nano-alloy (Au-Ag) Au-Ag alloy nanoparticles the residual Ag does not leach out (oxidation of Ag^0 seed by Au^{3+}) completely rather it segregate defect sites (steps, kinks, etc.) and void spaces near the two metal interfaces (i.e., the central porous region of HNPr) due to the differential diffusion rates between two inter-diffusing atomic species (here inward flux of Au^0 from surrounding and outward flux of Ag^0 from the core) which creates a net vacancy flux through Kirkendall Effect.¹⁵ The appearance of Kirkendall voids in Au-Ag alloy nanoparticle is linearly dependent on tensile strain or stress. Tensile stress again tends to exaggerate the grain boundaries and creates more vacancies whereas compressive stress cements the grain boundaries by reducing the extent of void formation. Therefore it is necessary to find the chemical marker of void formation in Au-Ag alloy nanoparticles.¹⁵⁸ The presence of different oxidation states of Au (Au^0 , Au^+ (aurous) and Au^{3+} (auric)) and Ag (Ag^+ and Ag^0) and their extent in the interfacial central porous region of HNPr plays a key role in alloy nanoparticle formation.¹⁵⁹ The percentage of metallic (Ag^0 and Au^0) and oxidized (Ag^+ , Au^+ , and Au^{3+}) form of silver and gold in the individual nanoporous HNPr can be monitored through XPS and EDX spectrum and the ratio Au^0/Ag^0 can be considered as a chemical marker for the atomic origin of high catalytic activity of different HNPrs. The building of atomic segregation in the bimetallic heterophase junction (Au-Ag) through Kirkendall Effect may generate dislocation and d-band shifting which in turn enhances the activity towards various electrochemical redox reactions.¹⁶⁰ In our previous study, we have estimated the concentration of ascorbic acid (AA) by performing

their electrochemical oxidation reaction on gold nanoflower (AuNF) surface and efficiently we could quantify different biologically active components like UA, dopamine (DA), AA and Glucose from a single pathological sample.⁴ Out of several components, UA shows the most prominent ion current peak in DPV response which encouraged us to consider it as the reference analyte to study the role of porosity induced tensile strain on a nanomaterial with minimal variation of crystal facets to influence their catalytic activity. Moreover, uric acid is a biologically important compound that plays a crucial role in metabolism. The purine metabolic product uric acid (UA), when present at higher concentrations (hyperuricemia) in the blood may cause several ailments like cardiovascular disease, gout (a form of arthritis), kidney disease, heart disease,^{161–163}, etc. Though not very common it is also possible to have too little UA in our body which points out the initiation of liver and kidney disease. In general, we define this symptom as Fanconi syndrome,¹⁶⁴ a disorder of the kidney tubules that prevent the absorption of uric acid and rapid removal by urine to reduce the UA level in the blood to create hypouricemia. Hence the quantification (high or low level) of UA is crucial from the pathological screening point of view too. The normal uric acid level for a healthy female is 142–356 μM (2.4–6.0 mg/dL) and for a healthy male is 202–416 μM (3.4–7.0 mg/dL).^{165,166} Various analytical approaches like chemiluminescence,¹⁶⁷ spectrofluorometric,¹⁶⁷ enzymatic processes,¹⁶⁸, etc. have been reported for the quantitative detection of UA to micromolar (μM) level. However, electrochemical techniques are more preferable in this context on account of their ease of handling, cost-effectiveness, and higher accuracy level to avoid any false positive signaling. Electrochemical techniques like differential pulse voltammetry (DPV), Chronoamperometry (CA), square wave voltammetry (SWV) are powerful tools among others to carry out sensing of UA at physiological concentration level by modifying the bare electrode with polymers¹⁶⁹

(ethylene glycol, methacrylate, dimethylaminoethyl methacrylate, etc.) and biomaterials^{170,171} (norepinephrine, propionylcholine, etc.). In the present study, we have examined the detailed structural analysis of seven different bimetallic Au-Ag HNPrs and their catalytic activity towards the electrochemical oxidation of UA (**Scheme 4.1**) to figure out their structure-catalytic activity relationship. The modification of the bare glassy carbon (GC) electrode by adsorbing different bimetallic Au-Ag HNPrs on their surface leads to efficient adsorption of UA and enhances the electron transfer kinetics. Further, HNPr modified GC electrodes encouraged us for fingerprinting of UA upto nano-molar (nM) level within a limited time interval. The prominent role of the chemical marker (Au^0/Ag^0) in the mixed metal HNPrs for the increment of tensile strain was explained through DFT calculations as implemented in Vienna *Ab initio* Simulation Package (VASP).

4.2 Material Synthesis:

The synthesis of different HNPrs was carried out in the two-step seeding method. In the first step, 500 μL of 10^{-2} M ice-cooled freshly prepared $AgNO_3$ was added at a constant rate of 1 mL/min into 19 mL of Milli-Q ($18\text{ M}\Omega\text{ cm}$) water kept under constant rate (150 rpm) of stirring. After that, we have added 500 μL of 10^{-2} M ice-cooled freshly prepared trisodiumcitrate (TSC) at the same rate of 1 mL/min to the diluted $AgNO_3$ solution. Immediately after the completion of TSC addition, we have added 60 μL of 10^{-1} M freshly prepared ice-cooled $NaBH_4$ at a time and left the mixture undisturbed for 30 s before we turn off the stirring. The solution turns immediately into a bright and transparent bumblebee yellow color. The solution was then kept undisturbed in the dark for 2 h under open mouth condition to release out evolved H_2 gas from the reaction mixture.

In the second step, 0.5 g of CTAB was dissolved in 45 mL of water by 10 min sonication at 30 °C. To this CTAB solution, maintained at 30 °C, 2 mL of 10^{-2} M AgNO_3 was added at a constant rate of 1 mL/min under steady stirring condition. Next, 300 μL of 10^{-2} M ice-cooled HAuCl_4 was added to the above mixture at a constant rate of 1 mL/min. The color of the solution turns transparent yellow-brown. This was followed by a dropwise addition (1 mL/min) of 320 μL of 10^{-1} M ice-cooled ascorbic acid (AA) that changes the color of the solution from yellow-brown to colorless due to Au(III) reduction. The stepwise addition of Au(III) and AA of the same respective volume are repeated for one more time with an additional rate of 2 mL/min. Quick or delayed addition of Au(III) than that of 2 mL/min in the second step may cause the loss of crystalline nature of our synthesized HNPrs and results in distorted structures with irregular shapes and sizes as shown in **Figure 4.1**. The porous ligaments in the central cavity region for different HNPrs were achieved through carefully maintaining the addition rate of gold solution

(2 mL/min) and the time gap (~3 to 4 s) between Au(III) and AA into the reaction mixture.

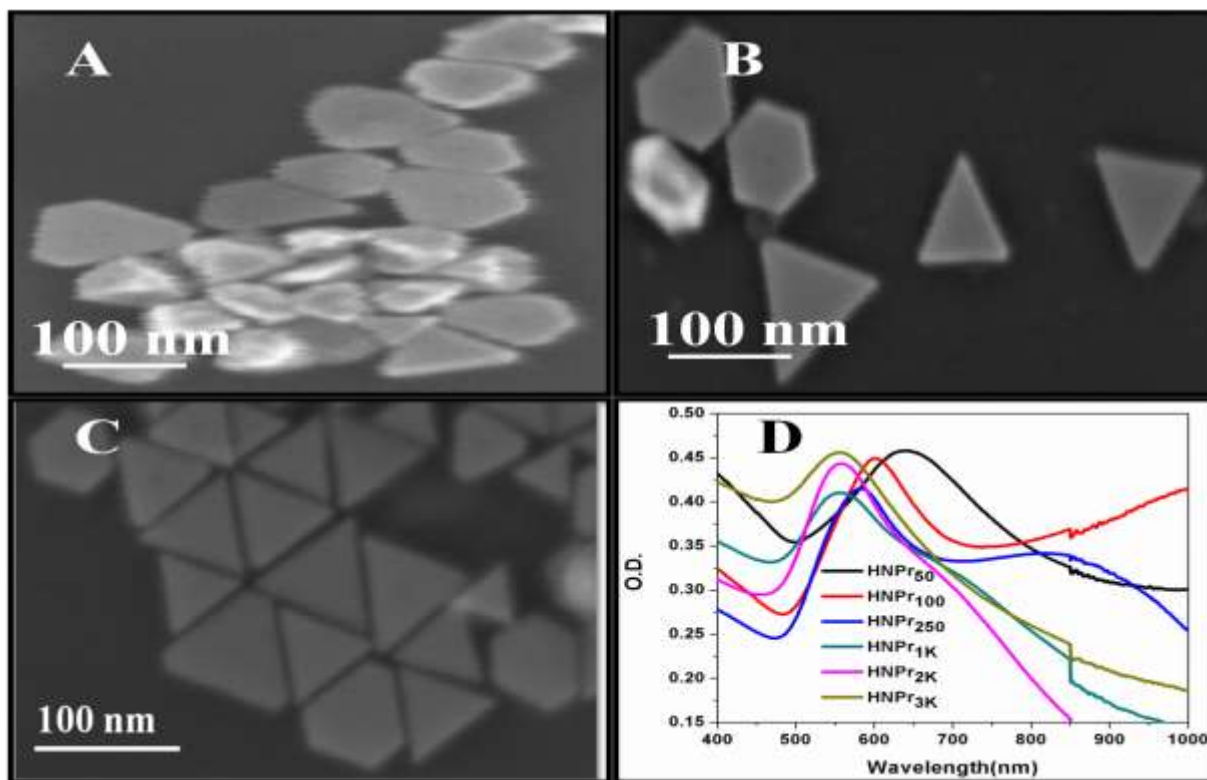


Figure 4.1: (A), (B) and (C) SEM images of HNPr₂₅₀ with HAuCl₄·3H₂O addition rate (second step of seeded growth) of 1 mL/min, 2 mL/min and 3 mL/min respectively. (D) Absorption spectra of different HNPrs.

Subsequently, a different amount (varying the amount between 50 μ L and 3 mL) of pre-synthesized seed solution was added into the reaction mixture. Variation in the amount of seed solution led to the formation of various HNPrs with different edge lengths and porous cavity diameters. Synthesized HNPrs by using 50, 100, 250, 500, 1000, 2000, and 3000 μ L of Ag seed are designated as HNPr₅₀, HNPr₁₀₀, HNPr₂₅₀, HNPr₅₀₀, HNPr_{1K}, HNPr_{2K}, and HNPr_{3K}, respectively. The plasmonic nature of individual HNPrs was confirmed from their UV-Vis-NIR spectra as shown in **Figure 4.1**. Throughout the synthesis, we have maintained the reaction

temperature at 30 °C. We have observed that in absence of seed by using the same protocol does not produce any nanoprisms (rather produces arbitrary shaped colloidal particles with no regular size) which directly proves the necessity of the seed to form the nano prisms structure or in other words, indeed this is a seed-mediated synthesis.

4.3 Materials Purification:

After synthesizing; the cavity diameter, shape, and size variable HNPrs; we kept them overnight to complete their growth and stabilization. Size of HNPr₅₀ and HNPr₁₀₀ are so big that they become settled down by leaving unreacted ligands and precursors in the top solution which we have decanted to separate the nanoparticles. Separated nanoparticles (~1 mL) then diluted by 5mL Milli-Q water and centrifuge at 1000 rpm for 1.5 h whereas for other HNPrs which didn't settle down with time have been centrifuged for two times at different rates. Firstly, they are centrifuged at 2000 rpm for 1.5 h and then at 3000 rpm for 30 minutes. Finally, we have collected the centrifuged nanoparticles each with a total volume of 500 μ L.

4.4 Theoretical Modeling of HNPr:

It is very difficult to construct a theoretical model for different HNPrs with variable Au:Ag composition because the introduction of Ag atom in the Au cluster will generate an infinite number of possible structures. Here, initially, we have constructed some structure based on TEM images and XPS data (**Table 4.1**). We have constructed flat surfaces of HNPrs parallel to {111} plane and faces having {220} planes according to the previously reported work.¹⁷² We have simulated a series of different HNPrs (each one made by a total of 363 atoms) with different Au:Ag composition. We have varied the Au⁰:Ag⁰ compositions among different HNPrs as: HNPr_A (3.03:1), HNPr_B (2.45:1), HNPr_C (2.02:1), HNPr_{pureAg} (0: ∞) and HNPr_{pureAu} (∞ :0). These compositions cover the entire HNPr series as reported in **Table 4.1**. The primary motive behind

the consideration of the above-mentioned compositions is to observe the effect of Ag impurity/doping on the pure Au clusters. For the geometrical optimization, we have used Generalized Gradient Approximation (GGA) and Perdew-Burke-Ernzerhof (PBE) functional as implemented in VASP for each Au:Ag composition. A gamma centered k-point was applied for the calculation and a force convergence criterion of -0.05 eV/\AA per atom was set to obtain the accurate bond-length between Au and Ag atoms. The PBE potential with the Methfessel-Paxton smearing method has been used to calculate the total energies.

4.5 Results and Discussion:

TEM analysis in **Figure 4.2** noticeably clarifies the formation of nano prism along with the appearance of hollowness at the center of the mass coordinate for each HNPr. It has been observed that the enrichment of Ag seed from 50 μL to 3 mL during synthesis leads to the linear increment of both the edge length between 150-25 nm and central porous cavity diameter between 1.5 - 11.5 nm. The TEM image of each HNPr (HNPr₅₀ to HNPr_{3K}) in **Figure 4.2** and the corresponding histogram in **Figure 4.3** proves that the synthesized HNPrs are highly monodispersed in nature. The HNPr₅₀ and HNPr₁₀₀ appear almost as two-dimensional triangles (thickness <10 nm) with sharp edges (edge lengths are 150 and 102 nm respectively) and a tiny cavity at the center. Compared to HNPr₅₀ and HNPr₁₀₀, edges of the HNPr₂₅₀ (edge length: 105 nm) are much more truncated in nature (**Figure 4.2**).

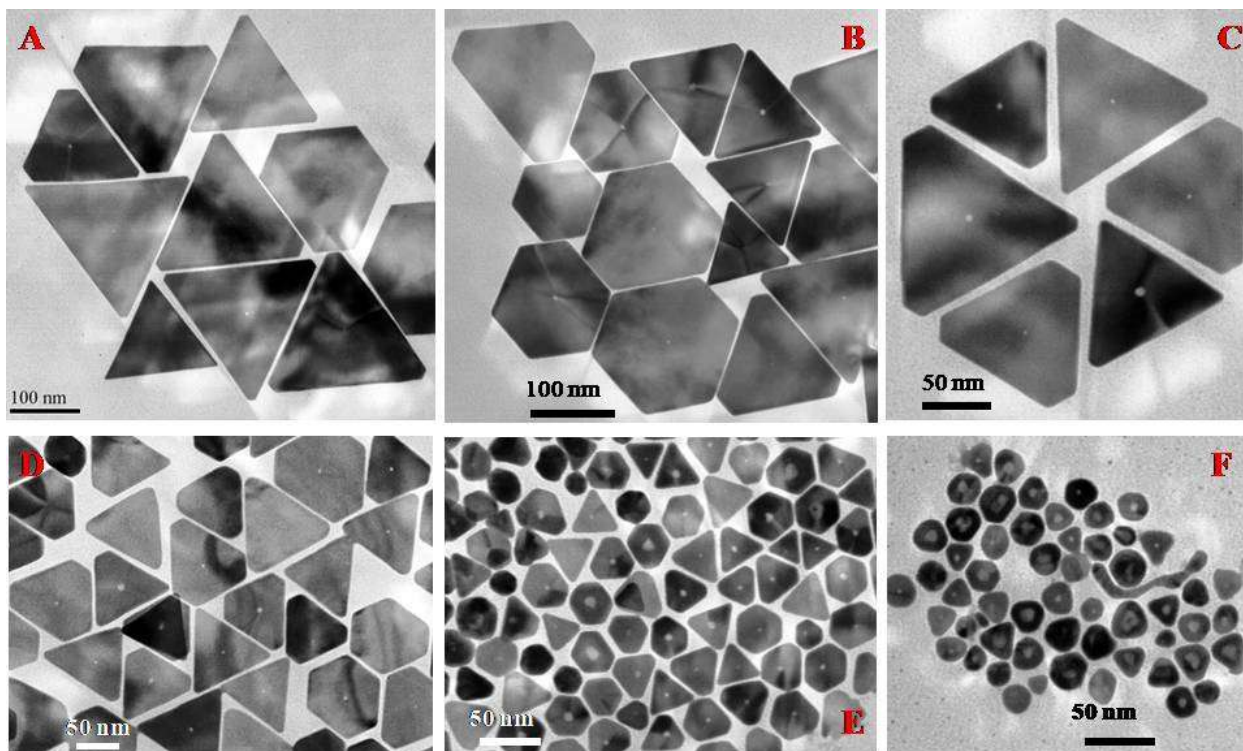


Figure 4.2: TEM image of individual HNPr synthesized by using a different amount of Ag seed. Here A-F represents the synthesized HNPrs by using 50 μL , 100 μL , 250 μL , 1 mL, 2 mL and 3 mL of Ag seed and abbreviated as HNPr₅₀, HNPr₁₀₀, HNPr₂₅₀, HNPr_{1K}, HNPr_{2K}, and HNPr_{3K} respectively. Due to the structural similarity with HNPr₂₅₀, we have not included the TEM image of HNPr₅₀₀ in this figure.

Further distortion from the prism structure was observed for HNPr₅₀₀, HNPr_{1K}, HNPr_{2K} (edge lengths are 102, 62 and 43 nm respectively) and a hollow sphere (diameter: 25 nm) appearance with a large cavity diameter around 11.5 nm for HNPr_{3K}. The role of Au(III) and the amount of seed in controlling the size and crystallinity of the central cavity can be explained by considering the reduction potentials of the component redox systems ($\text{Au}^{3+}/\text{Au}^0$, Ag^+/Ag^0 , AA^{2+}/AA) present in the reaction mixture.

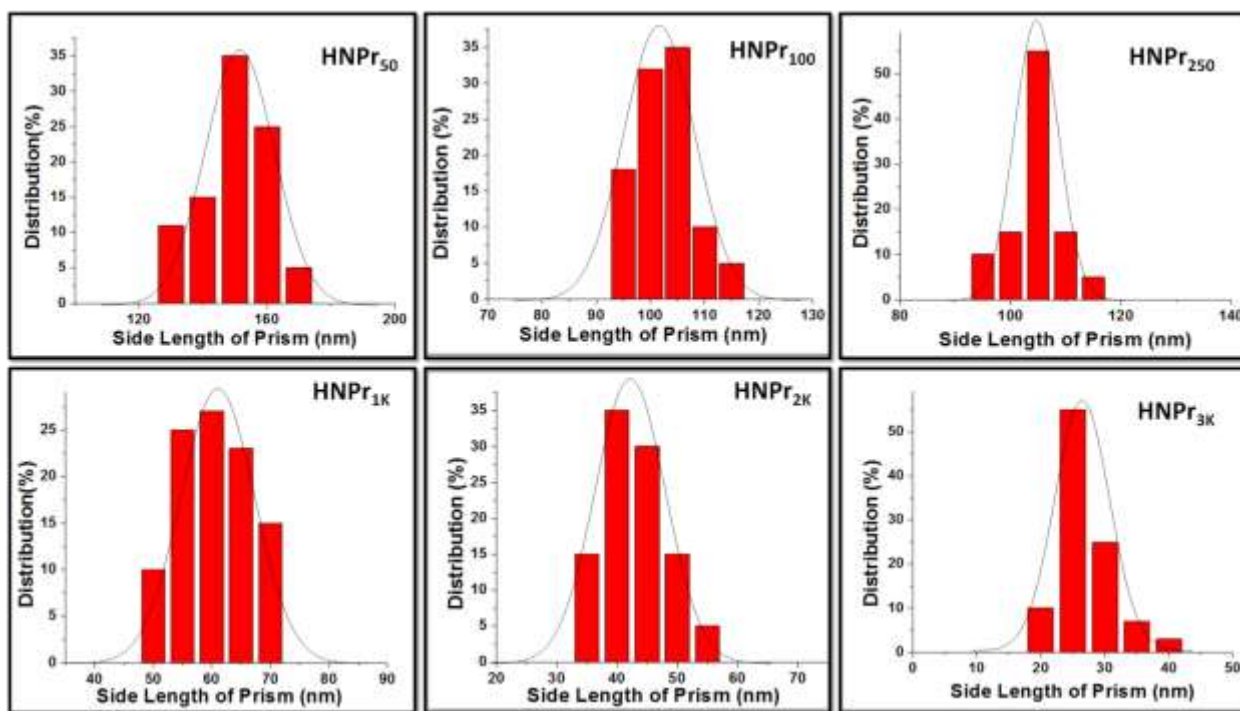


Figure 4.3: Histogram of size distribution for each HNPPr. 100 TEM frames have been considered for each HNPPr to calculate their average edge length.

Reported reduction potentials for $\text{Au}^{3+}/\text{Au}^0$, Ag^+/Ag^0 , AA^{2+}/AA are 1.5, 0.81, and -0.066 V (at pH:7) respectively.^{173,152} As explained before in our previous report¹⁷⁴ that the presence of Au(III) enhances the differential reduction potential of AA from 0.8 V (between Ag^+/Ag^0 and AA^{2+}/AA) to 1.5 V (between $\text{Au}^{3+}/\text{Au}^0$ and AA^{2+}/AA) which forces AA to acts as an efficient reducing agent and results in all the available AA being used in the reduction of Au(III) and Ag(I) to form seed-mediated alloy structure. When we add a little amount of seed then the volume to surface ratio i.e., $(\pi R^2 h)/(2\pi R^2)$ of the nucleation zone to accommodate all the Au^0 and Ag^0 into prismatic geometry should be very small compared to the total surface of the HNPPr and vice versa for a large amount of seed. Here we considered 'R' as the radius of the central cavity and 'h' is the approximate thickness (may vary due to stepped geometry) of the prism. Hence we should expect a gradual increment of cavity area with the amount of added seed

and matches well with our observed result. Moreover, when the nucleation zone is made by one or fewer nanoseeds the active crystal facets of seed can contribute more accurately in the crystallization to generate sharp edged HNPrs compared to a large collection of nanoseed as the nucleation centre. During seeded crystallization if there is any residual Au(III) leftover in the system then only it will try to contribute in the galvanic replacement reaction from the seed surface to result the amorphous nature of the central cavity. Depending on the relative ratios of Au^{3+} , Ag^+ and Ag^0 the extent of the resultant porous nature varies for different HNPrs. It is clear from our study that the crystalline central core (as nucleation centre) for individual HNPr gradually changes to amorphous porous cavity and the extent of porosity has been measured by recording their time dependent TEM image. TEM based growth kinetics and the associated porosity development in the central core for HNPr₂₅₀ is shown in **Figure 4.4**. Analysis of the HRTEM images through digital micrograph software along with XRD measurements and SAED pattern confirms the presence of high energy facets $1/3\{422\}$ and $\{220\}$ on each HNPr surface (**Figure 4.4, 4.5, and 4.6**). The thermal vibration of reduced coordination sites (steps, kinks, etc.) strengthens the average vibrational amplitude of vicinal surfaces ($1/3\{422\}$ and $\{220\}$). As a result, excess vibrational entropy of vicinal surfaces is much higher than that of low index $\{111\}$ surface.^{175,176} Thus, low coordinated atomic sites are considered to be chemically more active than that of close-packed Au-Ag surfaces (1st order *fcc* surfaces) and these defects stimulate the emergence of internal lattice strain.^{146,177}

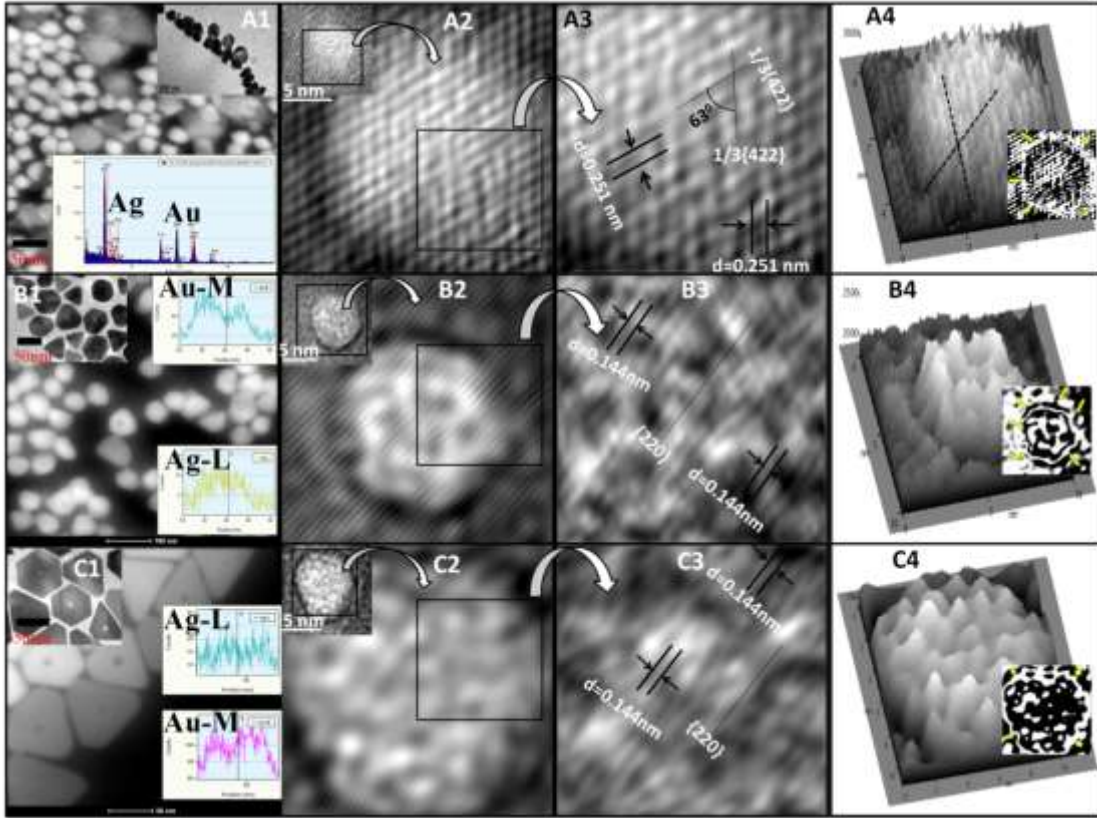


Figure 4.4: TEM images of time-dependent (A: 10 min, B: 1 h and C: 6 h) porosity generation at the center of gravity of HNPr₂₅₀. Porosity has started to develop after 1 hr and reaches a maximum after 6 hr. (A1), (B1) and (C1) are time variable HAADF-STEM images with their respective EDX line profiles; (A2), (B2), (C2) are IFFT images of HNPr₂₅₀ after 10 min, 1h and 6 h of synthesis; (A3), (B3) and (C3) are the zoomed version of the selected area on respective porous cavities; and (A4), (B4) and (C4) is the surface plot of (A2), (B2) and (C2) respectively to clarify the degree of porosity change with time whereas the contour plot is given as inset to identify the boundary between porous and crystalline surface of HNPr as marked by the yellow-colored arrow. Though at the beginning (10 min) of the HNPr growth there is only one active crystal plane i.e., $1/3\{422\}$ which has two different orientations with an internal angle of 63° , after 1 hr a new $\{220\}$ plane appears in the central cavity and the $1/3\{422\}$ plane disappears completely after 6 hr.

The lattice strain (compressive or tensile) in the nanocrystal leads to fluctuating different mechanical properties by modifying their energy band structures.¹⁷⁸ Although the $1/3\{422\}$ plane is forbidden, the appearance of this plane in the bimetallic Au-Ag plate-like structure has been reported earlier and this creates stacking faults laying parallel to the $\{111\}$ facets.¹⁷² In our synthesized HNPrs, we found that each HNPr contains the $1/3\{422\}$ plane both on the crystalline surface area as well as the central cavity area except for HNPr₂₅₀ where the $1/3\{422\}$ plane is missing in the central porous region. We have crosschecked the presence of $1/3\{422\}$ and $\{220\}$ planes along with $\{111\}$ plane in different HNPrs by performing their XRD measurements and verified it from JCPDS data as mentioned in **Figure 4.6**. Unfortunately, the S/N ratio for the recorder XRD plot is quite low and that could be due to high SAXS (small-angle X-ray scattering) background from the CTAB molecules and also the glass substrates at the low angle regime. To keep the nanostructures intact we could not wash the nanoparticles beyond two times as further washing could destroy the particles and results in very weak diffraction peaks. Here the important point is the peak position corresponding to $1/3\{422\}$ and this is also a supportive data to the strong evidence observed from HRTEM and SAED patterns. Collecting data over a quite long time may improve the SNR a little but this will not significantly improve the data quality. Moreover, as we know the errors in counts in scattering experiments follow the Poisson distribution and that results in little improvement in noise even if we collect data for a long time unless the peak is quite strong or data has been taken in much stronger x-ray source like x-ray synchrotron sources. The origin of the $1/3\{422\}$ peak is the stacking fault lying parallel to the $\{111\}$ surface and hence supposed to be very weak compared to the $\{111\}$ peak as observed in **Figure 4.6**.

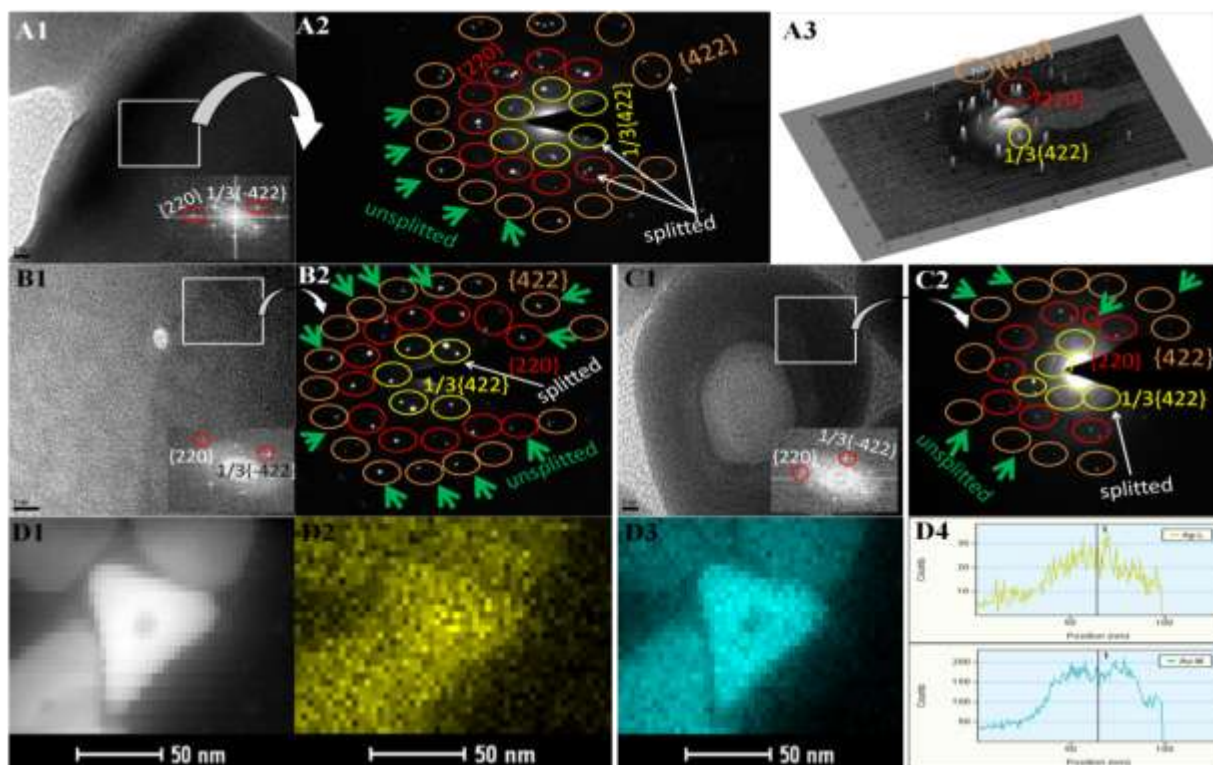


Figure 4.5: (A2) is the SAED pattern of HNPr₂₅₀ as marked by the white-colored square box in (A1) whereas corresponding FFT is given as inset to show the existence of $1/3\{422\}$ and $\{220\}$ and $\{422\}$ facets. All the diffraction spots in (A2) either along $1/3\{422\}$ or $\{220\}$ facets are completely splitted and some are unsplitted along $\{422\}$ as marked by the green color arrow. (A3) is the surface plot of (A2) which shows a better representation of splitted diffraction spots. (B2) and (C2) represents the SAED pattern from HNPr₁₀₀ and HNPr_{3K} whereas (B1) and (C1) is the corresponding TEM images of HNPr₁₀₀ and HNPr_{3K} respectively. Here diffraction spots are not completely splitted as we marked them unsplitted along $\{220\}$ and $\{422\}$ facets and indicates that these structures contain less number of twin boundaries compared to HNPr₂₅₀ along $\{220\}$ and $\{422\}$ planes. (D1) represents drift corrected STEM image for line profile; (D2) and (D3) is the EDX elemental mapping of Ag-L and Au-M respectively to clarify the distribution of Ag and Au over HNPr₂₅₀ surface; and (D4) confirms the Ag-L and Au-M line along the EDX line profile.

Though the spectra are bit noisy, still there is a clear sign of the peak for the $1/3\{422\}$ in the XRD pattern as the other two stronger peaks are clearly visible for all the three different HNPrs in **Figure 4.6**.

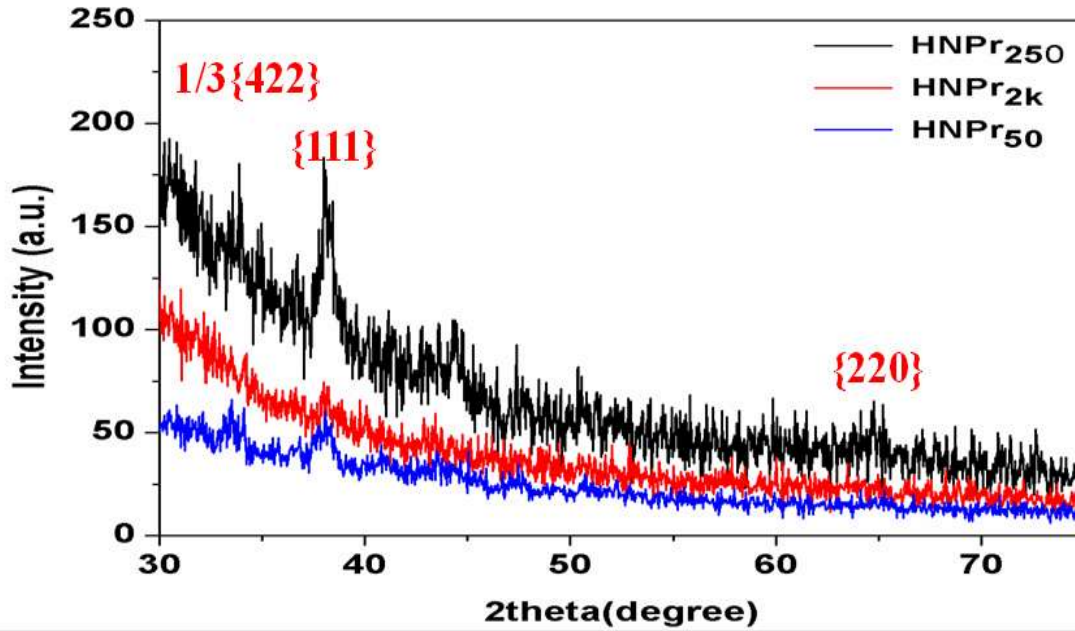


Figure 4.6: XRD pattern of HNPr₅₀, HNPr₂₅₀, and HNPr_{2K}.

So strong evidence in HRTEM and SAED pattern along with XRD (supportive) we think the existence of $1/3\{422\}$ is quite clear. Besides the signature of different planes from XRD data, we have calculated the generated strain along different planes from their respective line shapes (obtained 2θ) as shown in **Figure 4.7** specifically for $\{111\}$ facet. Recorded XRD pattern in **Figure 4.6** confirms the presence of $\{111\}$ at $2\theta \approx 38.25^\circ$, $1/3\{422\}$ at $2\theta \approx 34.00^\circ$, and $\{220\}$ at $2\theta \approx 65.00^\circ$ facets in HNPr₂₅₀, HNPr₅₀ and HNPr_{2K}. The broadening of the XRD curve in HNPr₂₅₀ at $\{111\}$ crystal facet ($2\theta \approx 38.25^\circ$) compared to that of HNPr₅₀ and HNPr_{3K} is owing to the lattice strain, which arises due to the (i) prevention of motion of dislocation from central porous region to the crystalline periphery by grain boundary (ii) appearance of Kirkendall voids during replacement of

Ag⁰ by Au³⁺ and (iii) various crystal irregularities. The strain (ϵ) within HNPr can be calculated through the Williamson–Hall isotropic strain model and represented by:

$$\epsilon = \beta_{\epsilon} / 4 \tan \theta_{hkl} \dots \dots \dots (1)$$

where $\{hkl\} = \{111\}$ in this case and β_{ϵ} is full-width half maxima⁴ for the diffraction peak. We have calculated the strain from XRD data by applying the above equation and it follows the same order as observed for catalytic activity: HNPr₂₅₀ \approx HNPr₅₀₀ > HNPr_{1K} > HNPr_{2K} > HNPr_{3K} > HNPr₁₀₀ > HNPr₅₀.

In the case of HNPr₂₅₀, the strain (dimensionless, as it is a ratio of two length unit) calculation is given here. We have fitted the curve at $2\theta \approx 38.25^\circ$ for HNPr₂₅₀ which is shown below:

where $\beta_{\epsilon} = 0.8^\circ$ (at $2\theta \approx 38.25^\circ$)

By converting β_{ϵ} in radian we can write $\beta_{\epsilon} = 0.0139$ radian

Hence, the calculated strain for HNPr₂₅₀ by equation (1) can be expressed as:

$\epsilon = 0.0139 / (4 \times \tan 0.33) = .01 = 1 \times 10^{-2}$. For this equation, we have converted the θ into radian too.

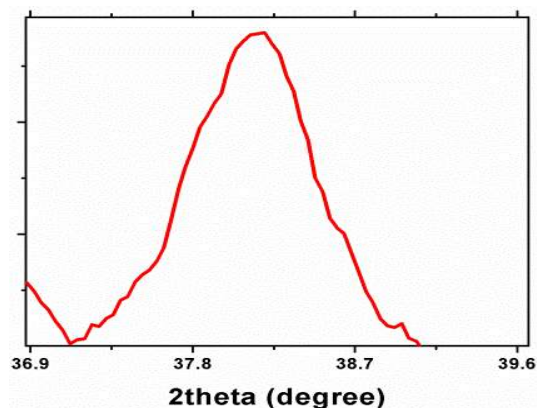


Figure 4.7: Fitted curve of XRD at $\{111\}$ facet to calculate the strain.

A similar curve fitting was carried out for other facets in the XRD curve like $1/3\{422\}$ and $\{220\}$. We then calculate the strain of each HNPr by taking the average of three fitted curves.

The EDX line profile of various HNPrs authenticates the bimetallic nature by confirming the existence of Ag-K, Ag-L, Au-L, and Au-M (**Figure 4.8a–4.8c**) lines. Besides that, we have

performed EDX elemental mapping (**Figure 4.5**) to show the presence of less amount of gold in the central porous region (a sudden dip of line profile in the central porous region) compared to the crystalline periphery in HNPr₂₅₀.

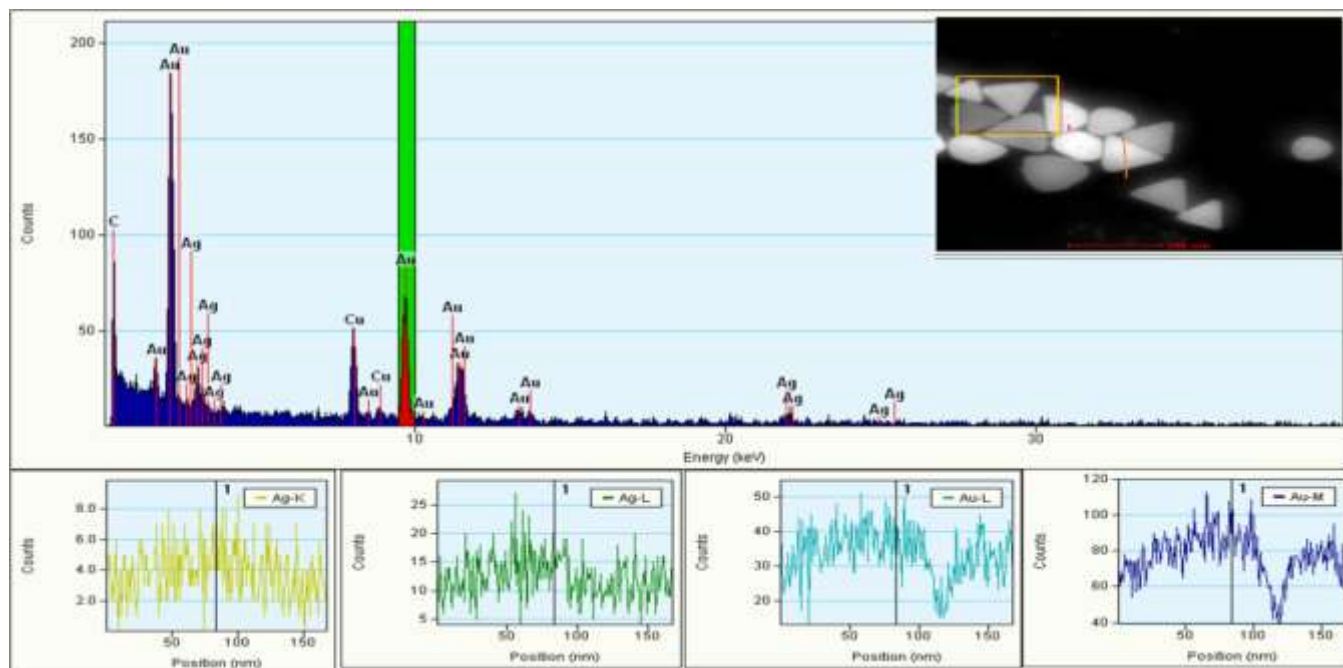


Figure 4.8a: EDX spectra and HAADF–STEM image of HNPr₁₀₀ for the confirmation of bimetallic (Au–Ag) nature.

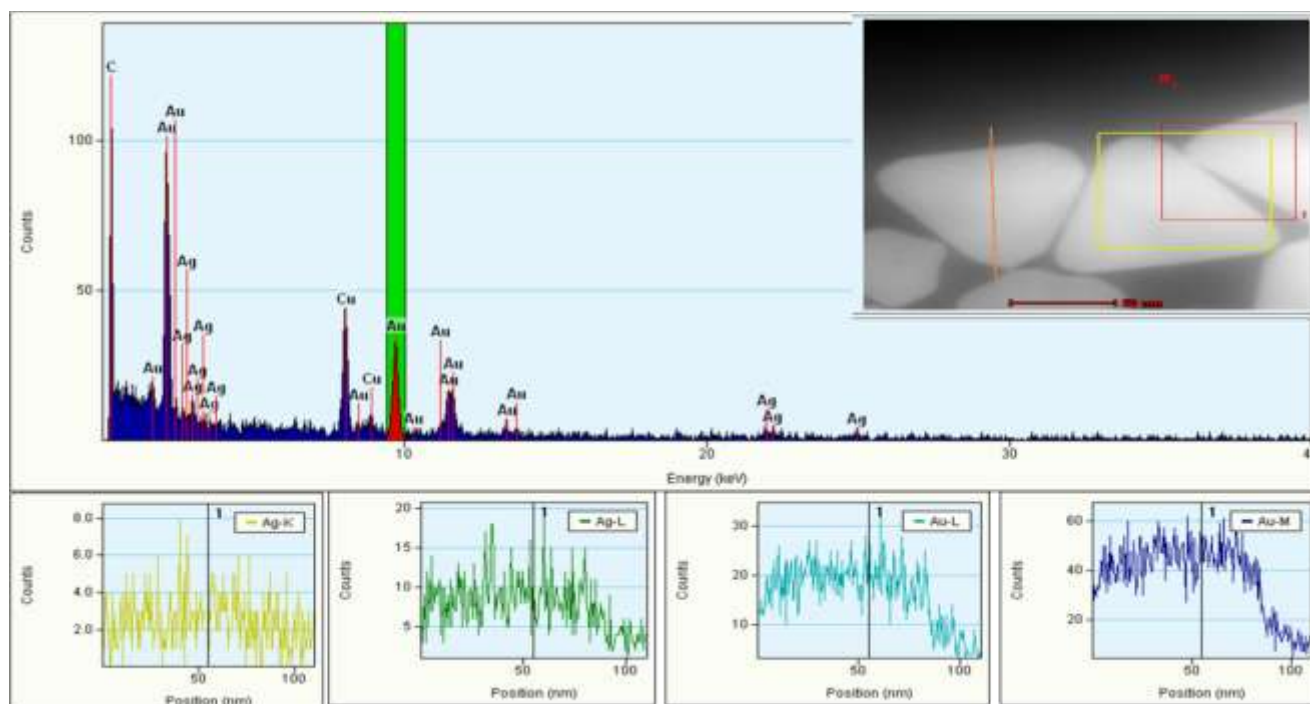


Figure 4.8b: EDX spectra and HAADF-STEM image of HNPr₅₀₀ for the confirmation of bimetallic (Au-Ag) nature.

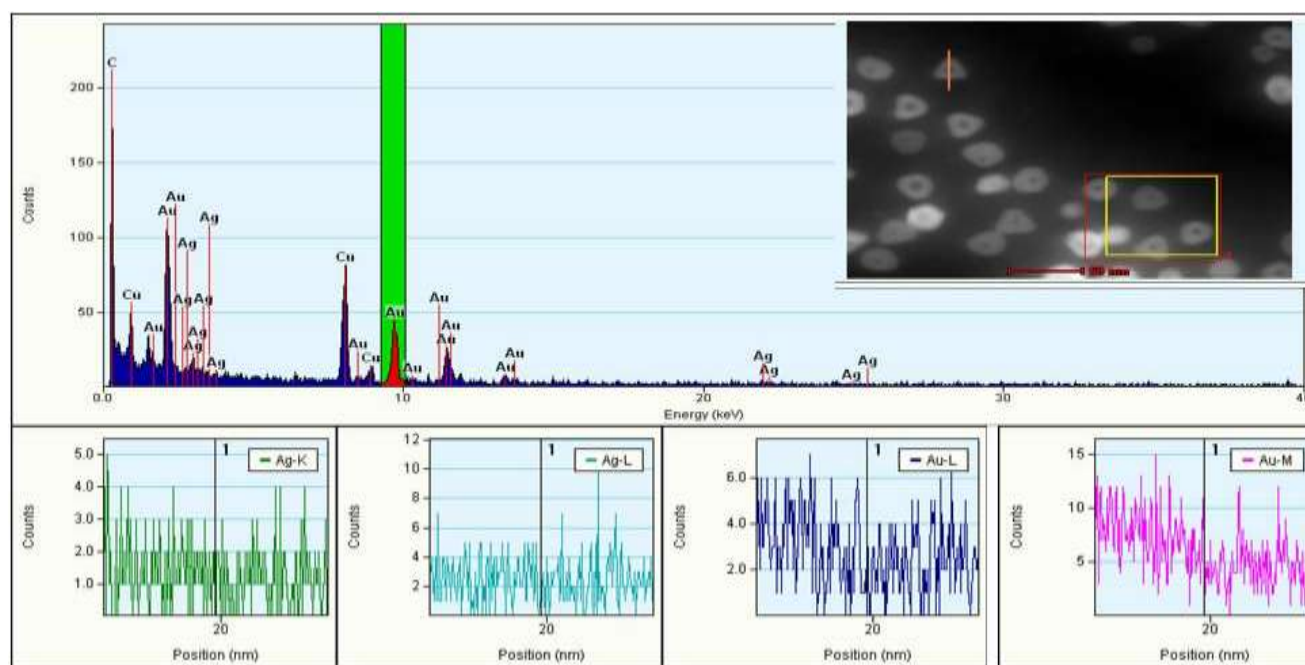


Figure 4.8c: EDX spectra and HAADF–STEM image of $\text{HNPr}_{3\text{K}}$ for the confirmation of bimetallic (Au–Ag) nature.

Elemental composition in different HNPrs was also verified through ICP-OES and XPS analysis. ICP-OES measures Au and Ag concentration in *ppm* (mg/L) level which is well-agreed with our predictions (**Table 4.1**). As the amount of Ag seed increases from 50 μL to 3 mL for synthesizing HNPr_{50} to $\text{HNPr}_{3\text{K}}$, the ICP-OES results show a gradual increment in Ag concentration while Au concentration remains almost the same. Since the ICP-OES measurements give the idea of total Ag ($\text{Ag}^0 + \text{Ag}^+$) concentration only, we have performed their XPS measurements to get precise knowledge about the ratio of oxidized silver (Ag^+) and metallic silver (Ag^0) in individual nanostructures. The fitted XPS curves of different HNPrs are given in **Figure 4.9** which clearly shows the presence of Au^0 , Ag^+ , and Ag^0 in HNPr_{50} , HNPr_{250} , $\text{HNPr}_{2\text{k}}$ with maximum splitting both for $\text{Ag}3\text{d}_{5/2}$ and $\text{Ag}3\text{d}_{3/2}$ peaks in HNPr_{250} . The absence of any splitting for $\text{Au}4\text{f}_{7/2}$ and $\text{Au}4\text{f}_{5/2}$ peaks indicates that the constituent gold atoms remain only in the metallic form (i.e., Au^0). Besides that, we have also noticed the presence of $\text{Br}^-(3\text{d})$, $\text{Cl}^-(2\text{p})$, $\text{N}(1\text{s})$ and $\text{C}(1\text{s})$ peaks in the XPS survey spectrum (**Figure 4.10**). The source of Br^- , N , and C is CTAB (during synthesis we use CTAB as a surfactant) whereas Cl^- comes from HAuCl_4 .

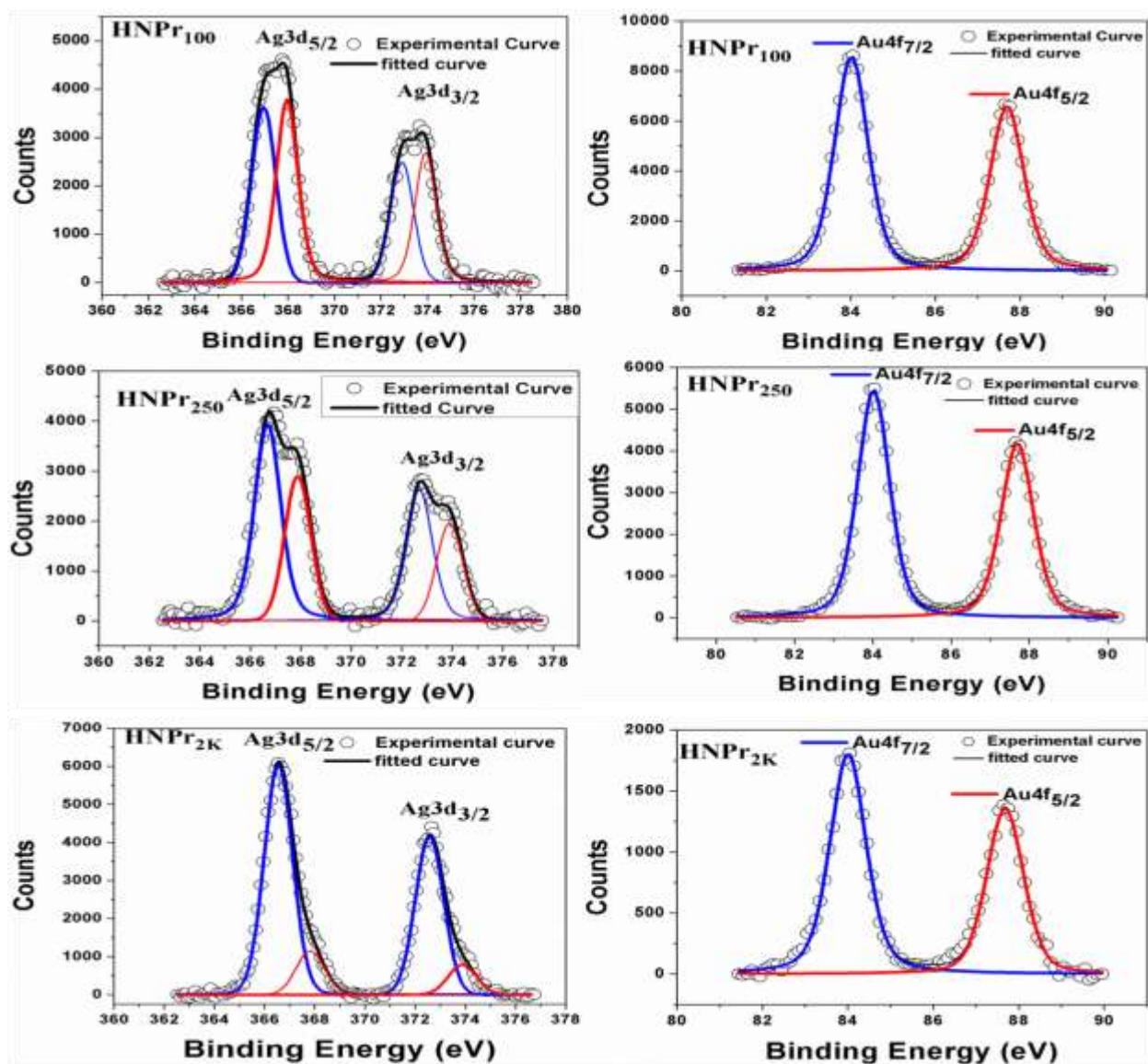


Figure 4.9: XPS study of HNPr₁₀₀, HNPr₂₅₀, and HNPr_{2K} nanostructures are shown in the top, middle and bottom panel respectively where the left and right figure in each panel corresponds to the XPS for Ag and Au separately. The Ag 3d_{5/2} and Ag 3d_{3/2} splitted in each HNPr and confirms the presence of ionic (Ag⁺) and metallic (Ag⁰) form, however Au present only in the metallic form i.e., Au⁰. The fitted blue curve in XPS for silver indicates the extent of Ag⁺ whereas the red curve indicates the % of Ag⁰. In the case of gold XPS, both the blue and red curves indicate the relative abundance of different spin-orbit states (Au 4f_{7/2} and Au 4f_{5/2}) of Au⁰ only.

Quantitative analysis of XPS (**Figure 4.9**) results for $\text{Ag}3d_{5/2}$ and $\text{Ag}3d_{3/2}$ peaks indicate that Ag^+ concentration is highest (80% Ag^+ and 20% Ag^0) for HNPr_{2K} which gradually falls to 61% and 48% for HNPr_{250} and HNPr_{100} respectively (**Table 4.1**). The observed core-level binding energies for most transition metals shift towards higher binding energies whereas silver is one such exception that shows lower binding energy in the oxidized state.¹⁷⁹ Though the Ag^+ in the central core region of HNPr is counterbalanced by Br^- from CTAB and stabilizes the low coordinated atomic sites, the relative abundance of Ag^0 over Ag^+ plays a crucial role to govern their differential porosity. According to Pauling's table, electronegativity for Au^0 is higher than that of Ag^0 .

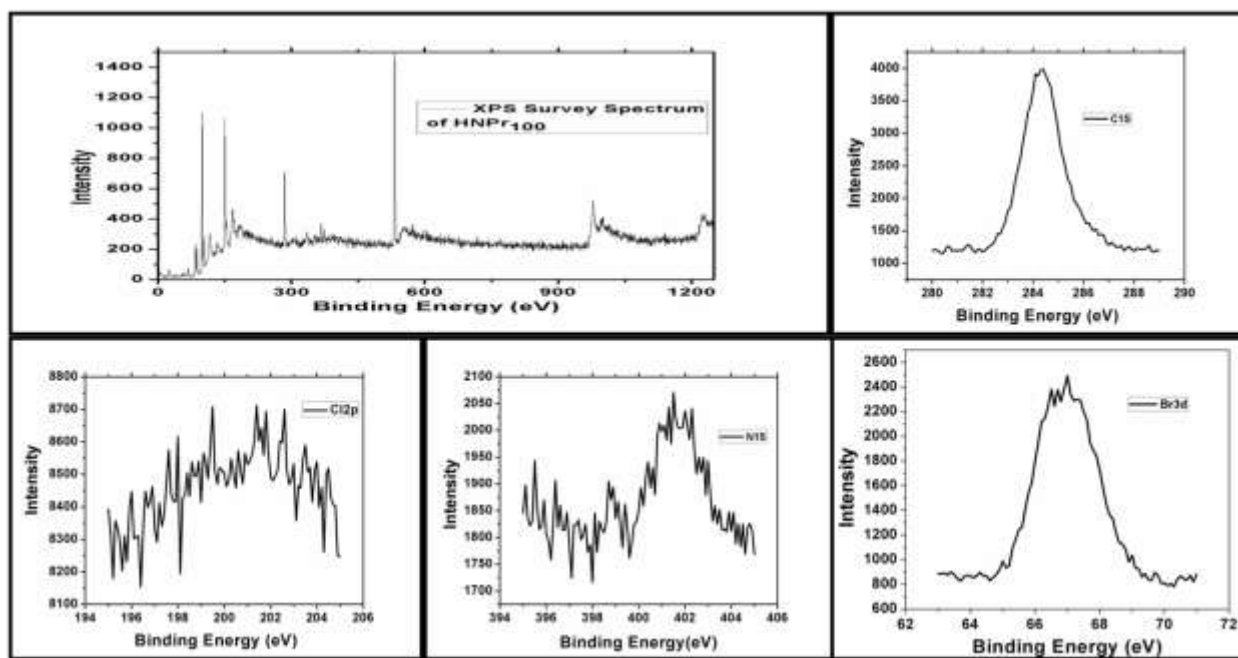


Figure 4.10: XPS survey spectrum of $\text{Cl}(2p)$, $\text{C}(1s)$, and $\text{N}(1s)$ in HNPr_{100} which confirms their presence in the sample.

By considering their minimal difference in lattice parameters, an intermediate ratio between Au^0 and Ag^0 (Au^0/Ag^0) can be defined as an ‘indicator’ to quantify their relative alloy

nature. The value of the ‘**indicator**’ ranges between ∞ and 0. A higher and lower value of the ‘indicator’ implies that HNPr contains more Au and Ag character respectively. Therefore the value of 2.42 for Au^0/Ag^0 in HNPr_{250} (**Table 4.1**) which appears as an intermediate value between 2.75 for HNPr_{50} and 1.83 for HNPr_{3K} can be considered as the suitable ‘**indicator**’ for alloy formation by transferring part of electron cloud from silver to the adjacent gold atom.¹⁸⁰ A shift towards the lower energy binding site for Au $4f_{5/2}$ in HNPr_{250} (Au $4f_{5/2}$ peak appears at 87.65 eV for HNPr_{250} whereas in case of pure gold it is 87.70 eV, however, due to the large distribution of Au^0 over Ag^0 on the crystalline HNPr surface, we are unable to get any signature of peak shifting in Au $4f_{7/2}$) proves the above fact of electron cloud transfer. Besides, the shifting of Ag $3d_{5/2}$ peak for Ag^0 in HNPr_{250} (367.85 eV) can be considered as a signature of alloy formation as Ag $3d_{5/2}$ appears at 368.3 eV for pure metallic silver (Ag^0). We have depicted earlier that silver is one such exception where lower binding energy is observed at higher oxidation state and hence we can get a crystal clear picture from the above fact that some electron cloud has been transferred from Ag^0 to Au^0 by forming a heterogeneous metallic network of the type $\text{Ag}^{\delta+}-\text{Au}^{\delta-}$. The $\text{Ag}^{\delta+}-\text{Au}^{\delta-}$ network creates zigzag porous ligaments in the central cavity of HNPr_{250} . In the case of HNPr_{100} and HNPr_{2K} the Ag $3d_{5/2}$ peak appears at 367.98 eV and 368.0 eV, which indicates less electron cloud transfer from metallic silver to metallic gold and thereby less probable for alloy formation.

It is evident from **Figure 4.11** that the porous ligaments are appearing gradually from HNPr_{50} and become prominent in HNPr_{100} which finally reaches a maximum for HNPr_{250} . The interconnected ligaments in the central cavity of HNPr_{250} developed in a zig-zag pattern which creates nanosized hollow space in between them. To understand the change in porous nature of the central cavity region of our synthesized HNPrs, we have performed the surface plot, HRTEM

and FFT (**Figure 4.11**) of the central porous region for four different cases (HNPr₅₀, HNPr₂₅₀, HNPr_{2K}, and HNPr_{3K}) which shows the transition in crystallinity in their corresponding HRTEM.

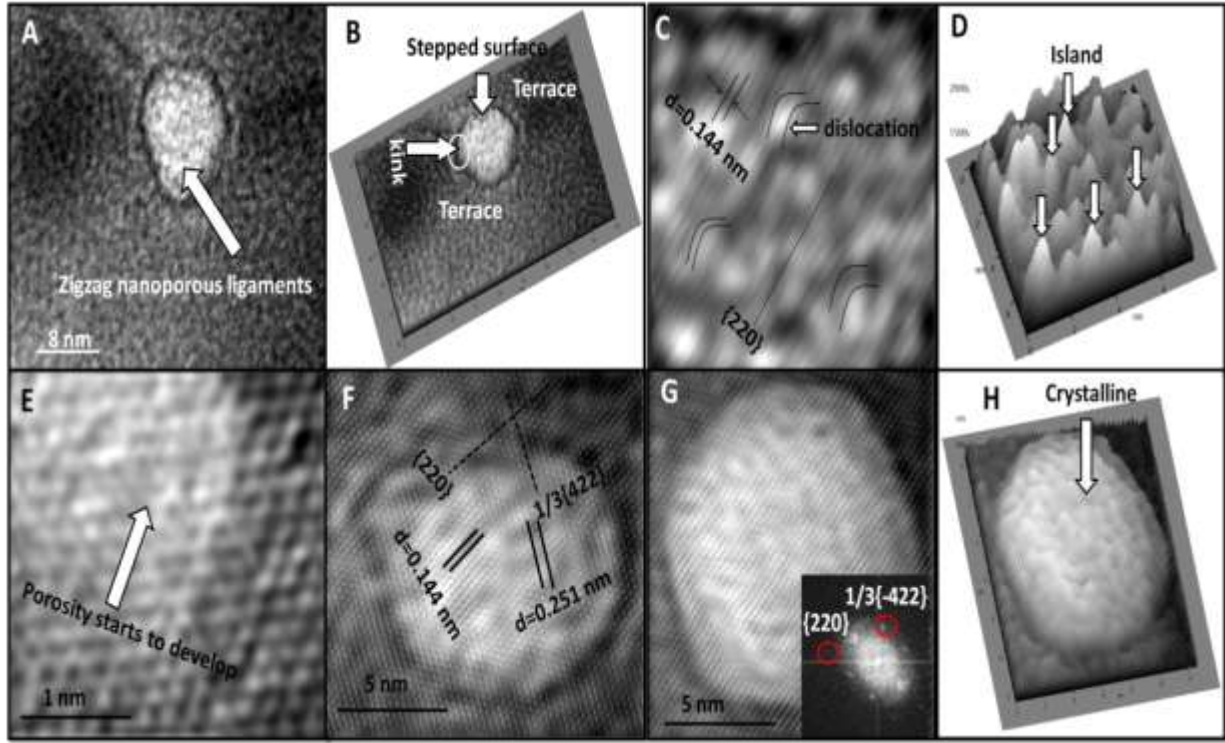


Figure 4.11: (A) is the TEM image of the central porous cavity of HNPr₂₅₀ where nanoporous ligaments have been observed. (B) is the surface plot to show the stepped surface along the cavity region whereas (C) is the corresponding HRTEM image to show the presence of {220} plane only (absence of 1/3{422} plane) in the central porous zone of HNPr₂₅₀ and (D) is the corresponding surface plot to highlight the existence of multiple islands in porous cavity region. (E) and (F) is the HRTEM images of the central cavity area of HNPr₅₀ and HNPr_{2K} respectively where we have shown how the porosity starts to develop in HNPr₅₀ and the coexistence of 1/3{422} and {220} planes in HNPr_{2K}. In (G) we have shown the FFT of HNPr_{3K} whereas (H) is the corresponding surface plot. Comparison of (D) and (H) show how the multiple low

coordinated islands are disappearing and crystalline structure appearing in the central cavity zone of HNPr_{3K}.

It is also clear from **Figure 4.11** that the atomic density in the porous cavity region is minimum for HNPr₂₅₀ which gives its plastic nature. The porous ligaments have a significant number of low coordinated atomic sites (kink, terrace, stepped surface, atomic islands, etc.). Interestingly, the porous nature is found to be reduced gradually from HNPr₂₅₀ to HNPr_{2K} and completely disappears for HNPr_{3K}.

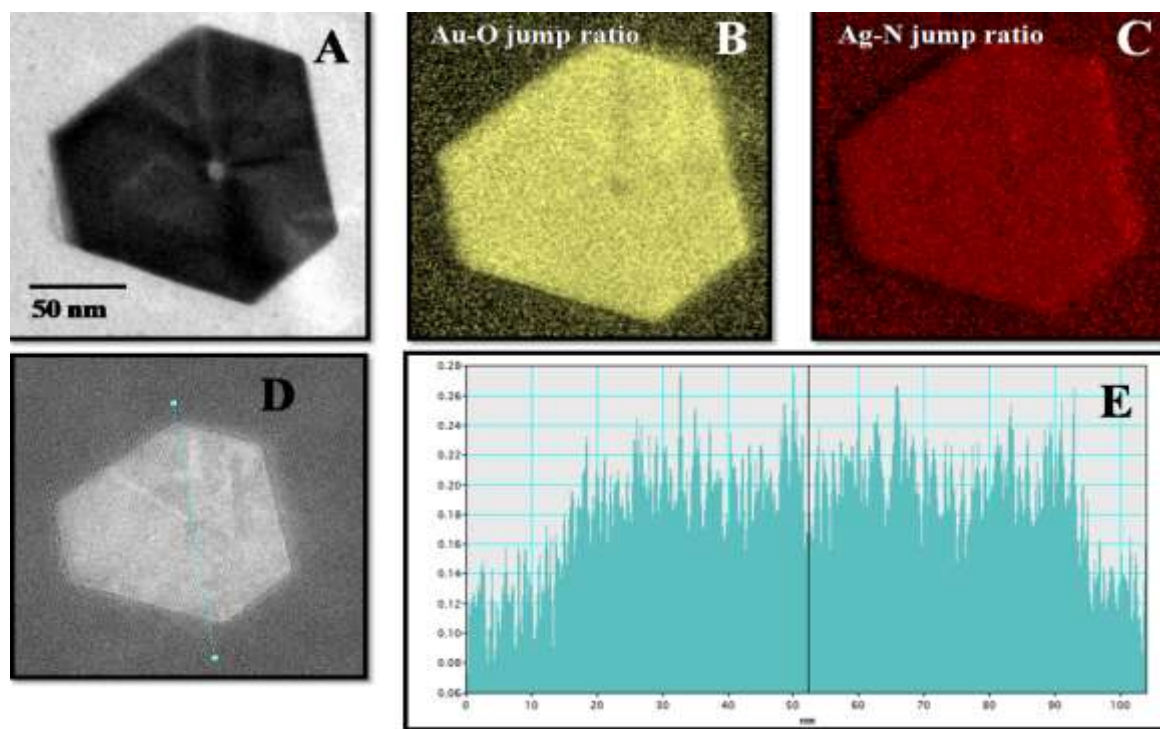


Figure 4.12: Thickness, as well as elemental mapping of HNPr₂₅₀ where (A) shows the TEM image of a single HNPr₂₅₀, (B) & (C), are the elemental mapping for Au and Ag respectively and the dark region in the central cavity region of Au mapping proves the presence of Ag in large extent compared to Au, (D) high annular dark field image of the single HNPr₂₅₀ with a scanning line through the central cavity in the green line, and (E) the corresponding thickness profile for opposite edge-to-edge 100 nm scanning.

Figure 4.11 clearly shows a pure crystalline nature of the central cavity region for HNPr_{3K}. The extent of porosity in different HNPrs can be explained through Kirkendall voids formation during galvanic replacement of Ag⁰ (nano seed) by Au³⁺. It is clear from **Figure 4.4** with time progression, a collection of voids has started to appear at the central cavity zone of HNPr₂₅₀. These voids accelerate the outward diffusion rate of Ag⁺ and grow spontaneously until a cage-like structure achieved¹⁸¹. As mentioned before, along with their porous nature, the thickness of the central cavity is different from their crystalline periphery to generate a stepped geometry. To show the stepped geometry at the central cavity we have performed the thickness profile for different HNPrs and specifically for HNPr₂₅₀ is shown in **Figure 4.12**.

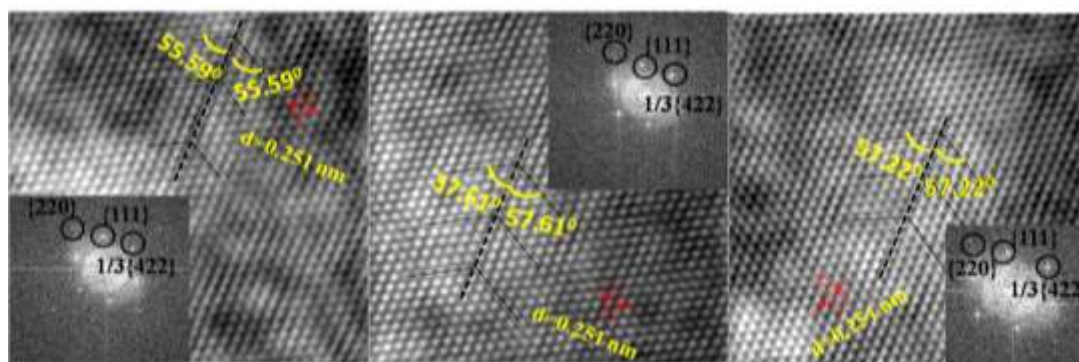


Figure 4.13: Representative twin boundaries on the HNPr₂₅₀ surface, spotted in three different zones outside the central cavity zone. The twin angle (concerning the twin boundary) varies in the range of 55–57°.

Our synthetic method is novel enough so that we can reach an optimized value of Au⁰/Ag⁰ to achieve maximum porosity at the center. During our synthesis, we have used a variable amount of Ag seed ranging from 50 µL to 3000 µL by keeping all other parameters constant and thereby we get different Au⁰/Ag⁰ for individual HNPr with different a rate of mass diffusion between Au and Ag for controlled voids formation. In HNPr₂₅₀, we can get a standard value of Au⁰/Ag⁰ to generate maximum voids which constitute porous ligaments and increases the lattice

mismatch.¹⁸² Besides, the lattice mismatch creates multiple reduced coordinated crystal irregularities on the crystalline HNPr surface (away from the central cavity regions). The splitted diffraction spots indicate the presence of multiple twin boundaries on different HNPr surfaces (**Figure 4.5**). Representative twin boundaries on the HNPr₂₅₀ surface are shown in **Figure 4.13**. Due to the nonplanar nature, the atoms situated on the twin boundary (TB) have less coordination number than the perfect crystal lattices and can be accounted for an active site for catalysis. According to the Fridel's theory¹⁸³ of four different twin types, the *fcc* crystal bears the signature with $\Sigma > 1$ and $\phi = 0$ where Σ is the inverse of the fraction of lattice sites common to the two components of the twin and ϕ (twin obliquity) is defined as disorientation of one crystal concerning the other. In the absence of axial chromatic aberration (Cc) or axial spherical aberration (Cs)-corrected HRTEM, the best characterization technique for identifying the presence of twin planes is the appearance of splitted diffraction spots. In the direct TEM images, the twin boundaries appear from translational interfaces because of the background intensity difference on the two sides of TB.¹⁸⁴ When the twin interface coincides with the mirror plane it is called coherent boundary. The mirror plane can be determined from the diffraction patterns and creates unsplit spots wherein the other reflections are splitted depending upon the distance from the common row. The HRTEM images and corresponding diffraction patterns in **Figure 4.5**, indicate that the diffraction spots are splitted for HNPr₂₅₀ however for HNPr₁₀₀ and HNPr_{3K} the diffraction, as well as XRD curve (**Figure 4.6**), does not show the desired splitting of diffraction spots to prove that HNPr₂₅₀ contains much more MTB compared to HNPr₁₀₀ and HNPr_{3K}. Besides TB, the low coordinated GB on HNPr₂₅₀ (**Figure 4.14** and **Figure 4.15**) surface plays a crucial role to create tensile stress within the alloy nanoparticle by retarding the motion of dislocation from central porous region to the crystalline periphery. HNPr₂₅₀ contains multiple

dislocations and is considered as one of the most active sites for heterogeneous catalyst. Recently it has been shown that twisted bismuth nanocrystals¹⁸⁵ containing lattice misfit and larger dislocation density is found to be much more active for CO₂ reduction than the corresponding dislocation deficit crystals.

Table 4.1: Compositional Analysis and current responses of different HNPr and HNPr modified GC electrode-based on EDX, XPS, ICP-OES, DPV, SWV measurements

System		HNPr ₅₀	HNPr ₁₀₀	HNPr ₂₅₀	HNPr ₅₀₀	HNPr _{1K}	HNPr _{2K}	HNPr _{3K}	Bare GC
Atomic composition	EDX	2.86	2.73	2.35	2.25	1.98	1.88	1.77	NA
	XPS	2.75	2.72	2.42	2.31	2.11	1.57	1.67	NA
Ag ⁺ /Ag ⁰	XPS	0.43	0.92	1.56	1.66	1.85	4	4.33	NA
Elemental composition	XPS	1.6	1.4	0.95	0.88	0.63	0.26	0.20	NA
	ICP-OES	1.49	1.29	1.01	0.93	0.58	0.33	0.25	NA
ξ (+mV)		55	61	74	71	69	69	68	NA
SGBD(nm ⁻²)		0.00035	0.0006	0.00287	0.0021	0.0018	0.0013	0.001	NA
Peak Current (μA)	DPV	.48	0.51	3.44	1.21	0.92	0.64	0.53	0.41
	SWV	0.42	0.46	3.8	1.55	0.95	0.77	0.49	0.41
Peak Potential(V)	DPV	0.69	0.61	0.51	0.55	0.59	0.60	0.60	0.72
	SWV	0.64	0.64	0.53	0.55	0.59	0.62	0.62	0.71
i _p ^{HNPr} /i _p ^{GC}	DPV	1.17	1.24	8.39	2.95	2.24	1.56	1.29	NA
	SWV	1.02	1.12	9.26	3.78	2.31	1.87	1.19	NA

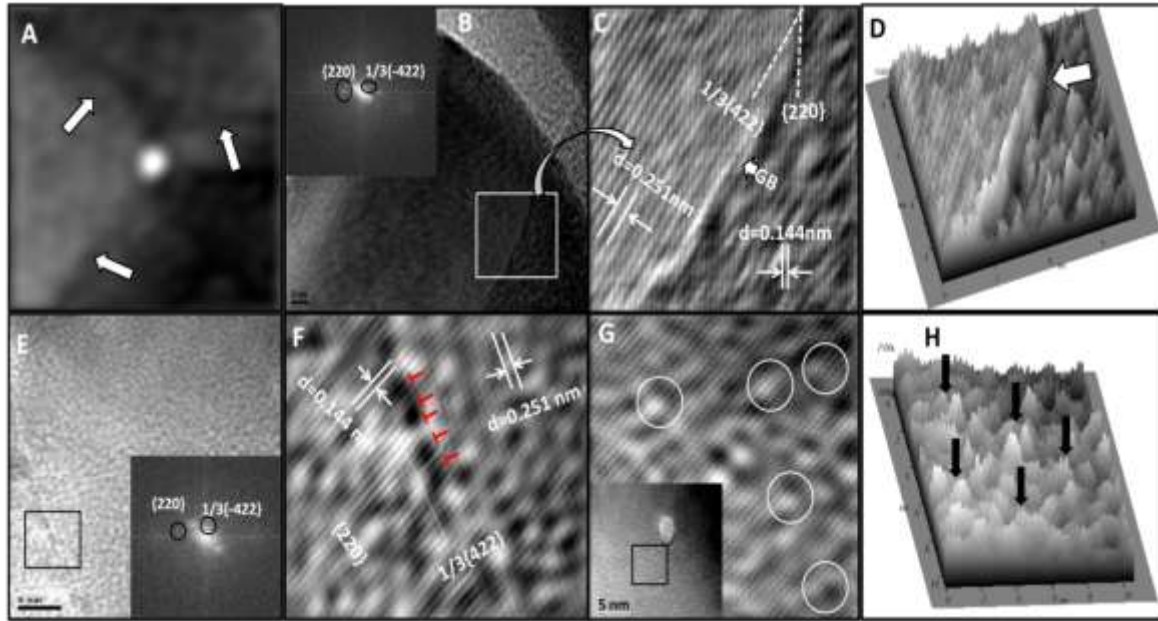


Figure 4.14: (A) IFFT of HNPr₂₅₀ to show the position of grain boundaries around the central cavity region of HNPr₂₅₀. (B) shows a specific GB over the HNPr₂₅₀ surface whereas (C) is the HRTEM of the marked square zone in (A). In (C) we have shown how a grain appears between two crystalline facets $1/3\{422\}$ and $\{220\}$ whereas the corresponding surface plot in (D) indicates the position of grain boundary as marked by the white-colored arrow. (E) is a dislocation enriched area over the HNPr₂₅₀ surface. The HRTEM of the marked square zone in (E) is shown in (F) where we have shown the position of dislocation(marked by reversed T) across the junction of $1/3\{422\}$ and $\{220\}$ planes. (G) is the HRTEM of HNPr₂₅₀ immediately outside the central cavity region in which we have detected multiple islands as marked by the white circles. (H) is the corresponding surface plot of (G) which signifies the islands are starting to create before entering into the porous regions. By comparing **Figure** (D) and (H), one can detect how the extent and pattern of crystallinity changing when we come across from the HNPr₂₅₀ crystalline surface to the central porous cavity.

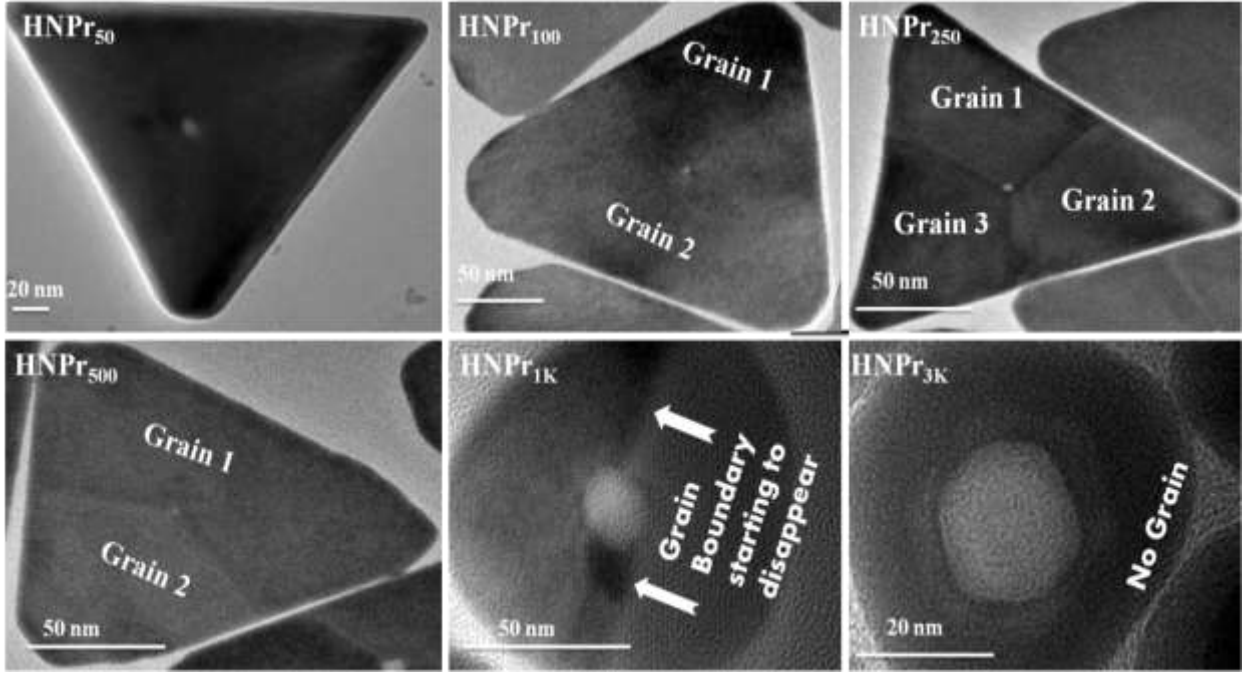


Figure 4.15. TEM images of the distribution of different grains over individual HNPr surface.

To accumulate a comprehensive study on surface GB density (SGBD) for the region surrounding the porous periphery, we have measured the SGBD for individual HNPrs (**Figure 4.16(a)**). For the statistical calculation of SGBD, we have selected different HNPr structures (**Table 4.1**) with at least 100 frames for each category as described details in **Figure 4.16(a)**. Characteristic SGBD (C_i) was measured by counting the number of GB (n_i) per unit area (nm^{-2}) in which the total area (A_i) is the surface area of the HNPr surface (calculated from the dimension off the HNPr as depicted in **Figure 4.16(b)**). SGBD of i 'th HNPr is formulated as

$$C_i = \sum_{i=1}^{i=100} n_i / A_i.$$

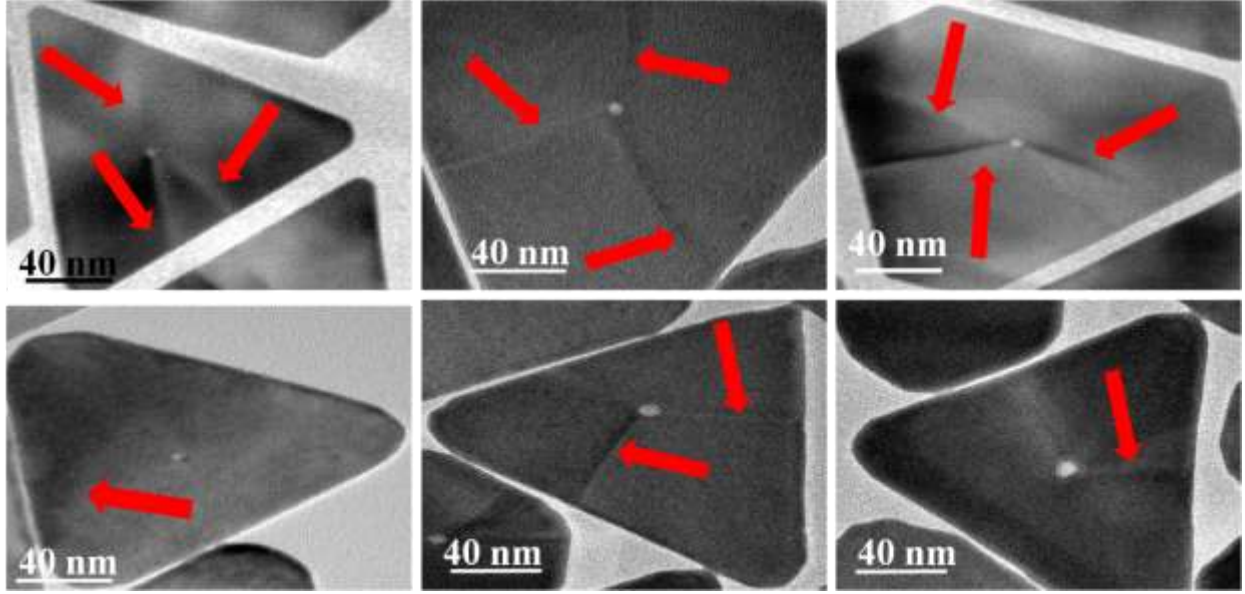


Figure 4.16(a): Presentation of different HNPr₂₅₀ frames for the calculation of Surface Grain Boundary Density (SGBD).

We have considered each HNPr as an equilateral triangle and central core as a sphere. Since there is no GB on the central cavity as we have discussed previously, the effective surface area is calculated by subtracting to the central spherical cavity area from the total HNPr area.

$$Ai = \frac{\sqrt{3}}{4} a^2 - \pi r^2$$

Where a is the side length of HNPr and r is the radius of the central cavity.

As an example,

For HNPr₂₅₀ (**Figure 4.16b**)

$$a \approx 105 \text{ nm and } r \approx 4.25 \text{ nm}$$

$$\begin{aligned} \text{So } Ai &= \left\{ \frac{\sqrt{3}}{4} (105)^2 - \pi * (4.25)^2 \right\} \text{ nm}^2 \\ &= 9491.18 \text{ nm}^2 \end{aligned}$$

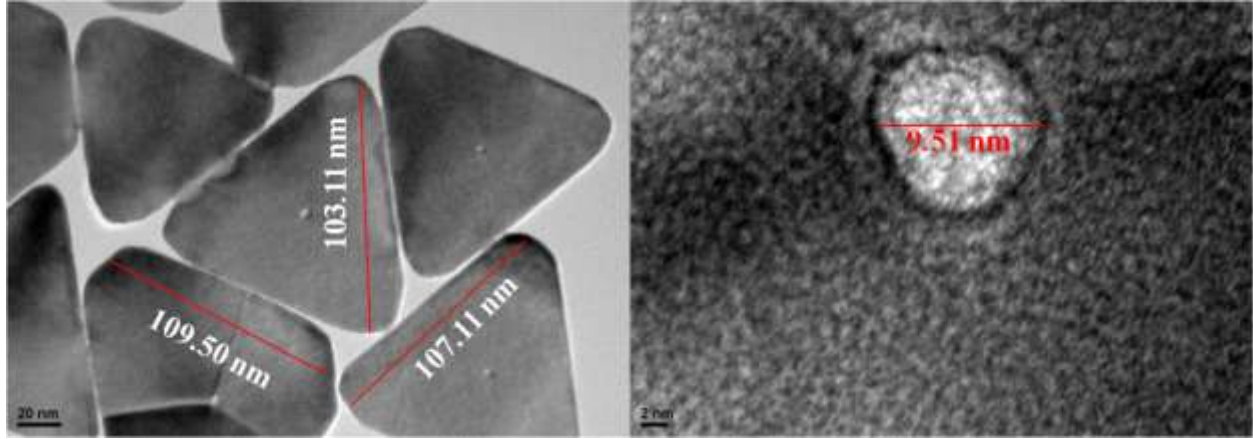


Figure 4.16(b): Edge length and cavity radius determination in HNPr₂₅₀ by using digital micrograph software.

So if we carry out the approximate calculation of SGBD according to **Figure 4.16a** by counting the number of GBs/ frame and carry out the calculation up to 100th frame,

It appears as:

$$C_i =$$

$$\frac{3}{9491.18} + \frac{3}{9491.18} + \frac{3}{9491.18} + \frac{1}{9491.18} + \frac{2}{9491.18} + \frac{1}{9491.18} + \dots \dots \dots +$$

$$\frac{3}{9491.18} \text{ (upto 100th term)}$$

$$= 0.00287 \text{ nm}^{-2}$$

Calculated C_i for individual HNPr perceptibly recognizes that the HNPr₂₅₀ has the maximum surface GB density with an estimated value of 0.00287 nm^{-2} as listed in **Table 4.1**.

The calculated C_i values (**Table 4.1**) have the following decreasing trend:

$$C_{\text{HNPr}_{250}} > C_{\text{HNPr}_{500}} > C_{\text{HNPr}_{1K}} > C_{\text{HNPr}_{2K}} > C_{\text{HNPr}_{3K}} > C_{\text{HNPr}_{100}} > C_{\text{HNPr}_{50}}$$

which is well-agreed with our observed catalytic power.

To investigate the catalytic activity of these HNPrs, the electrochemical oxidation of UA has been studied on the HNPr modified GC electrode (HNPr/GC). The DPV for the electro-oxidation of UA at bare GC electrode shows a poor voltammetric response in which the anodic peak potential appears at 0.72 V along with a lower peak current value of 0.41 μA (zoomed in the insets) as shown in **Figure 4.17A**. DPV and SWV response of the HNPr/GC electrode in $4 \times 10^{-5}\text{M}$ UA is depicted in **Figures 4.17A** and **4.17B** respectively where the peak potential (for the oxidation of UA) gets shifted towards the more negative region in comparison with bare GC electrode along with the enhancement in peak current. The decrease in peak potential and increase in peak current for various HNPr/GC demonstrates that different bimetallic HNPrs can act as efficient electrocatalysts for the oxidation

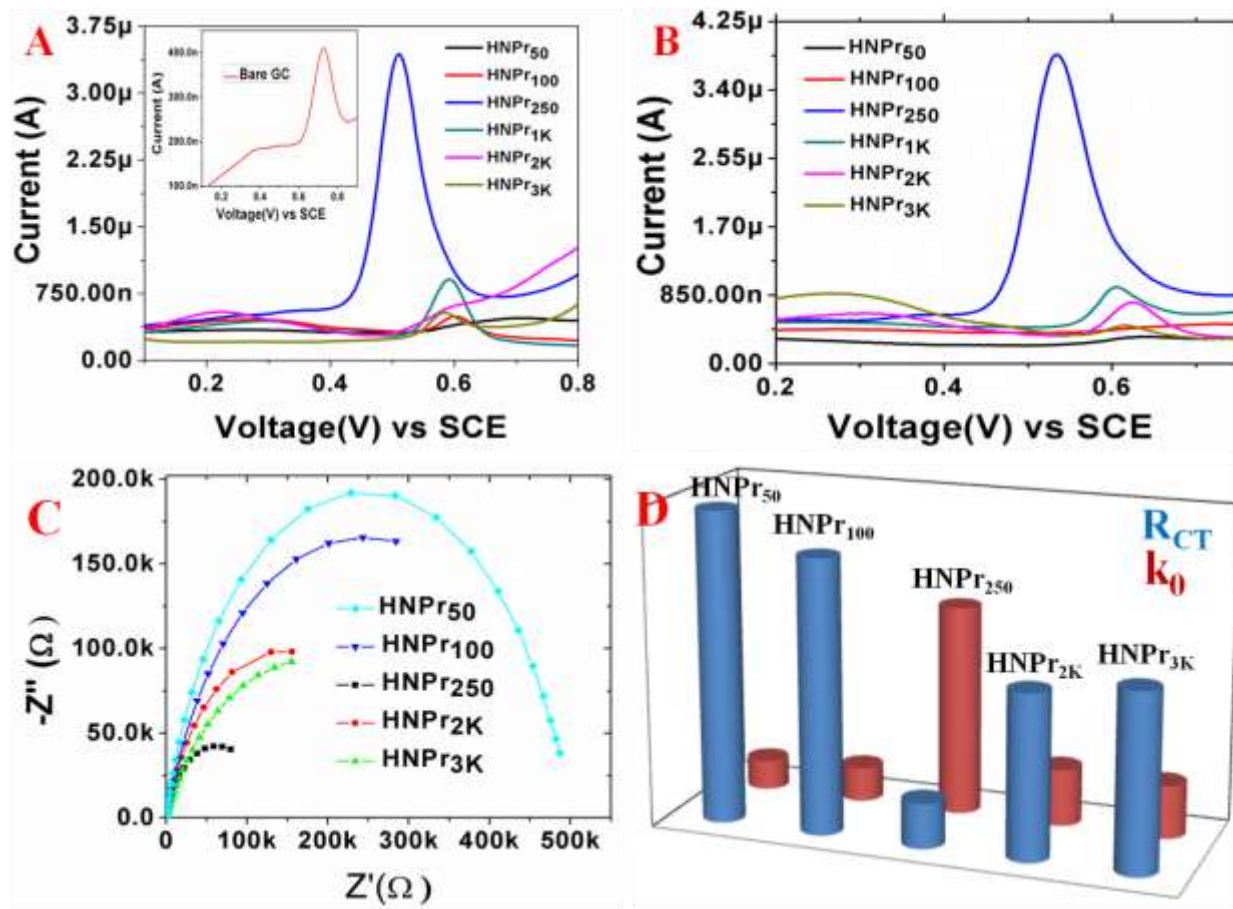


Figure 4.17: (A) and (B) represent DPV and SWV of 4×10^{-5} M UA at different HNPr/GC electrode. Inset in (A) represents the DPV of bare GC. (C) Nyquist plot for the electrooxidation of UA at an applied potential of 0.4V within a frequency range of 10^5 to 10^{-2} Hz (To avoid overcrowding we have not included impedance spectra of HNPr₅₀₀ and HNPr_{1K} in figure (C)), (D) Comparison of R_{CT} and k_0 value of different HNPr/GC towards the oxidation of UA.

However, the extent of catalytic activity differs from each other is worth to mention. The HNPr₂₅₀/GC composite exhibits superior catalytic activity in which the peak potential (0.51 V) gets shifted by ~ 210 mV towards the more negative region and the peak current also get boosted by ~ 8.39 times $\left(\frac{i_p^{HNPr_{250}}}{i_p^{GC}} = 8.39 \right)$ compared to that of the bare GC in DPV response.

Characteristic parameters obtained from DPV measurements for various HNPr/GC are tabulated in **Table 4.1**. The enhancement in peak current and decrease in peak potential in comparison with bare GC follows the trend as $\text{HNPr}_{50}/\text{GC} < \text{HNPr}_{100}/\text{GC} < \text{HNPr}_{250}/\text{GC} > \text{HNPr}_{500}/\text{GC} > \text{HNPr}_{1K}/\text{GC} > \text{HNPr}_{2K}/\text{GC} > \text{HNPr}_{3K}/\text{GC}$. The observed values of peak current and peak potential follow a similar trend with the variation of SGBD (nm^{-2}) as we calculated and mentioned earlier. Along with DPV, we have also performed Electrochemical Impedance Spectroscopic (EIS) measurements (**Table 4.2**) which provide various system parameters regarding kinetics and mechanistic information such as charge transfer resistance (R_{CT}), ohmic resistance or solution resistance (R_s), capacitance, the time constant, etc. EIS is mainly consisting of Bode and Nyquist plot. The typical Nyquist diagram provides the variation in real (Z') and imaginary (Z'') part of the impedance at a fixed potential from the higher frequency to lower frequency region. **Figure 4.17C** shows the Nyquist plot for the electro-oxidation of UA at different HNPr/GC electrodes in 0.1M HClO_4 solution in which a semi-circle is observed at the higher frequency region. The diameter of the semi-circle gives the measurement of the R_{CT} (charge transfer resistance) while the intercept in the X-axis provides the R_s (solution resistance) value. The lowest R_{CT} value is obtained for $\text{HNPr}_{250}/\text{GC}$ electrode while $\text{HNPr}_{50}/\text{GC}$ shows the largest R_{CT}

Table 4.2: Different kinetic parameters for cavity shuffled HNPrs obtained from the EIS measurements. Here R_{CT} indicates the charge transfer resistance, W as the Warburg Impedance, CPEas constant phase element, i_0 as the exchange current, and k_0 as the heterogeneous rate constant.

System	$R_{CT}(\text{k}\Omega)$	$W (\Omega \text{ s}^{-1/2})$	n	CPE ($\Omega^{-1}\text{s}$)	$i_0(\text{A})$	$k_0 (\text{cm s}^{-1})$
--------	--------------------------	-------------------------------	---	-------------------------------	-----------------	--------------------------

GC	705.6	6.2×10^{-4}	0.72	6.4×10^{-6}	1.8×10^{-8}	3.3×10^{-6}
HNPr ₅₀	491.8	4.2×10^{-4}	0.84	1.42×10^{-6}	2.6×10^{-8}	4.7×10^{-6}
HNPr ₁₀₀	432.0	1.2×10^{-4}	0.75	1.61×10^{-5}	2.97×10^{-8}	5.4×10^{-6}
HNPr ₂₅₀	71.0	4.0×10^{-3}	0.79	4.27×10^{-5}	18.0×10^{-8}	33.0×10^{-6}
HNPr ₅₀₀	79.5	4.7×10^{-3}	0.65	3.35×10^{-5}	16.1×10^{-8}	29.6×10^{-6}
HNPr _{1K}	115.8	1.2×10^{-4}	0.71	2.87×10^{-5}	11.0×10^{-8}	20.3×10^{-6}
HNPr _{2K}	259.2	1.8×10^{-4}	0.78	1.18×10^{-5}	4.95×10^{-8}	9.0×10^{-6}
HNPr _{3K}	280.0	9.8×10^{-5}	0.66	1.51×10^{-5}	4.58×10^{-8}	8.4×10^{-6}

value as shown in **Figure 4.17D**. These results are consistent with the DPV response of different HNPr/GC electrodes. The exchange current (i_0) and standard heterogeneous rate constant (k_0) has been calculated from the following equations:

$$R_{CT} = \frac{RT}{nFi_0} \dots \dots \dots (1)$$

$$i_0 = nFACk_0 \dots \dots \dots (2)$$

Due to the facile electron transfer between HNPr₂₅₀/GC and UA, the kinetics of the electro-oxidation process is quite faster and results in the lowering of R_{CT} value. The Nyquist plot has been fitted with the modified Randles circuit by incorporating the constant phase element (CPE) and Warburg (W) impedance and the corresponding equivalent circuit is shown in **Figure 4.18**. Elucidation of DPV, EIS, and SWV result clarify that the extent of the catalytic power of different HNPrssupportsour previous arguments.

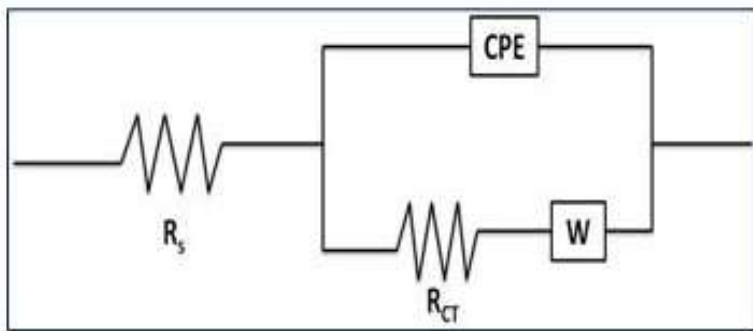


Figure 4.18: Equivalent circuit for the Nyquist plot. Parameters of the Circuit: (i) R_s = Solution resistance, (ii) R_{CT} = Charge transfer resistance, (iii) W = Warburg impedance, a kind of resistance to mass transfer, and (iv) CPE = Constant Phase Element which raises due to the double-layer capacitor.

It is difficult to explain the enhanced catalytic power of $HNPr_{250}/GC$ compared to the other $HNPr/GC$ by the facet dependent kinetics since the crystalline orientation towards $1/3\{422\}$ and $\{220\}$ facets are identical for all $HNPr$ s. Besides, all the structures are flat 2D prisms and the surface area gradually reduces from $HNPr_{50}$ to $HNPr_{3K}$. Hence, if the catalytic activity directly depends on the available nanosurface area then it should simply show a decreasing trend starting from $HNPr_{50}$ and ends up with $HNPr_{3K}$. In reality, the deviation from this monotonous trend of catalytic activity proves that the available surface area is not the prime factor to determine the catalytic activity of different $HNPr$ s. Moreover, since we have used an equal amount of CTAB during synthesis, we may expect a steady reduction in +Ve zeta potential (ξ) as we generate nanostructures with a smaller dimension, i.e., $\xi_{HNPr_{50}} \gg \xi_{HNPr_{3K}}$. Experimentally our measured zeta potentials show a different trend which shows a minimum zeta potential of 55 mV for $HNPr_{50}$ and maximize for $HNPr_{250}$ at 74 mV and then slightly reduce to 68 mV for the other nanostructures till $HNPr_{3K}$. Measured zeta potential for different $HNPr$ s is enlisted in Table 1. The

trend of the variation of zeta potential follows the same trend with the porosity of different HNPrs.

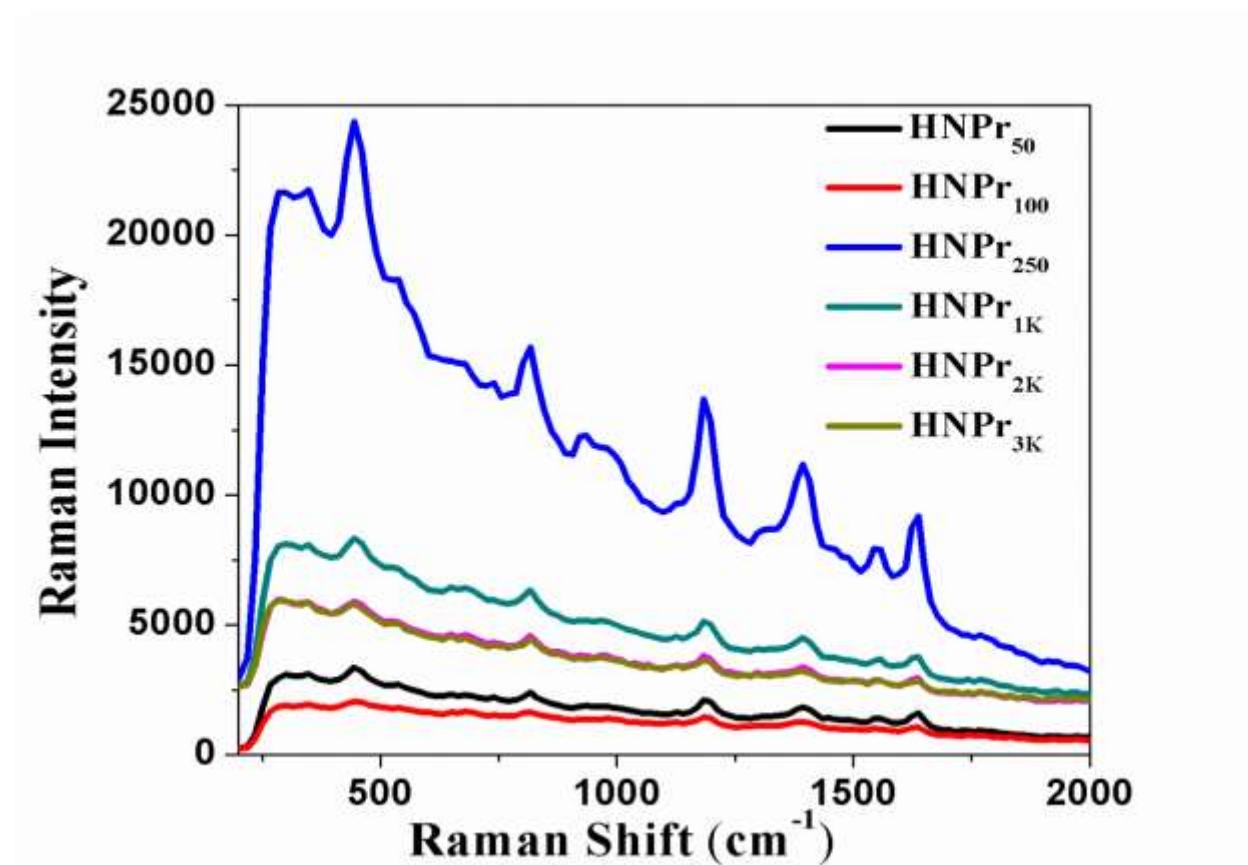


Figure 4.19: SERS spectra of different HNPr with CV (crystal violet) as the Raman reporter in which HNPr₂₅₀ shows maximum Raman intensity. The result is very much well agreed with our previous arguments. The Raman dye binds to the HNPr surface according to the extent of porosity in the central cavity region.

This infers that as the value of Au^0/Ag^0 reaches near 2.42, the porous ligaments in HNPr₂₅₀ allows holding the number of +Vely charged CTAB molecule to increase the overall +Ve zeta potential. Hence the measured values of zeta potential indirectly project the ligamentous nature of their central cavity region to enhance their relative catalytic power concerning the bare GC from 1.17 to 8.39 (from DPV response) when we compare between HNPr₅₀ and HNPr₂₅₀ (**Table**

4.1). In this context, the formation and the extent of various crystal defects like MTB, GB on the crystalline surface of HNPr and compositional characteristics of their porous ligaments can be considered as the most important factor to control their catalytic efficiency.^{186,187} The addition of UA to the active electrochemical (electrode + electrolyte) system leads to the adsorption of UA on the HNPr surface. The extent of analyte adsorption on different nanosurface and the role of porosity induced crystal defects on controlling the efficiency of surface adsorption was cross-verified by recording their SERS spectra in presence of crystal violet (CV) as Raman tagging molecule. In a typical experiment we have taken 180 μL of 10^{-4} M CV and mixed it to 20 μL of concentrated different HNPrs and the result has been depicted in **Figure 4.19**. The assignment of different Raman modes origination from CV on nanosurface has been reported before in the literature.¹⁸⁸ It is clear from **Figure 4.19** that the extent of interaction between HNPr and CV is gradually increasing from HNPr₅₀ to HNPr₂₅₀ and then decreases gradually to HNPr_{3K}. Our high-resolution imaging also shows the same trend of variation both for crystal defect as well as porosity in the central cavity region. The presence of crystal defects and plastic nature in the central cavity region increases the number of unsaturated atoms to enforce the binding with the analyte (here UA) to fulfill their desired coordination for stabilization. On the other hand, the presence of porous ligaments enhances the total surface area for effective adsorption of UA in comparison to nonporous crystalline bimetallic HNPrs. The ability of HNPr surface to interact with UA depends heavily on the possibility of coupling between adsorbate (UA) states and the metal d-states. Interaction energy¹⁸⁹ for an weak coupling may be written as:

$$E_{d-hyb} = -C(f_a, f_d) \frac{V_{ad}^2}{|\epsilon_a - \epsilon_d|} + \alpha V_{ad}^2 \dots\dots\dots (3)$$

Where f_a and f_d is the degree of filling of the adsorbate state and the metal d-state with energy ϵ_a and ϵ_d respectively. The term V_{ad} represents the coupling matrix element between the adsorbate

states and metal d-states. The first term in the above equation denotes the hybridization energy (between adsorbate states and metal d-states) arises due to attraction when the antibonding states are not filled completely. The second term represents repulsion due to the orthogonalization between the adsorbate states and metal d-states. The introduction of the concept of lanthanide contraction¹⁹⁰ can be used to explain the lattice mismatch of bimetallic Au-Ag HNPrs. Recently, the theoretical calculation by considering the relativistic contraction phenomenon and correlation effect predicts that the Au atom should be smaller than that of the Ag atom.^{191,192} According to Vegard's law,¹⁹³ lattice constant changes when a different sized atom has been introduced into the lattice. This change in lattice constant subsequently influences the lattice strain.¹⁹⁴ The introduction of bigger Ag atoms by replacing Au atoms across the heterophase i.e. near the central cavity position in the bimetallic HNPr generates a significant amount of low coordinated crystal irregularities.¹⁹⁵ This reduced coordinated atomic sites leads to a local upshift in d-band (closer to the Fermi level) which can be illustrated by **Equation (3)**. Diminished overlap of the wave function causes narrowing down the d-band with simultaneous increment in the d-band population. As a consequence, the bimetallic Au-Ag alloy nanoparticle (HNPr₂₅₀) is expected to generate greater d-band spacing than their monometallic counterpart in presence of UA resulting in the higher adsorption on the alloy surface. This upshifting of d-band center in HNPr₂₅₀ causes enhancement in reactivity between HNPr₂₅₀ surface and UA (**Equation 3**) as fewer of the antibonding states are occupied now.¹⁸⁹

To corroborate experimental results obtained from our DPV, EIS, and SWV measurements with microscopic analysis of different HNPrs, we have performed *ab initio* calculations to estimate the induced strain generated due to lattice mismatch in bimetallic HNPr with variable Au:Ag composition. We have modeled five systems, HNPr_{pureAu}, HNPr_{pureAg}, HNPr_A, HNPr_B, and

HNPr_C as discussed previously. As strain plays a key role in determining the catalytic property of the prism, we have considered a similar structural geometry for all the modeled HNPrs. First, we have calculated the molecular area along the basal plane for both the pure HNPrs as shown in **Figure 4.20**. The calculated molecular area of the optimized HNPrs for pure Au and Ag are 1007.51 and 1057.30 Å². As both the structures contain a similar number of atoms along the basal plane, we found out that under similar structural restrictions, the Au atoms occupy less surface area compare to Ag atoms. So, with the increase in the concentration of dopant (Ag), we suppose to observe the increase in the lattice strain along with the basal or any exposed surface. Based on the above arguments on pure HNPrs of gold and silver, a theoretical model for lattice strain should follow the order as:

$$\text{HNPr}_{\text{pureAu}} < \text{HNPr}_{50} < \text{HNPr}_{100} < \text{HNPr}_{250} < \text{HNPr}_{500} < \text{HNPr}_{1K} < \text{HNPr}_{2K} < \text{HNPr}_{3K} < \text{HNPr}_{\text{pureAg}}$$

The above model is only valid for similar structural configurations as more Ag character signifies the lattice strain from HNPr₅₀ to HNPr_{3K}. But, with the increase in Ag concentration, the formation of an alloy based HNPr favored over core/shell type geometry which reduces the strain and this is visible from our recorded TEM images. With the increase in Ag concentration from HNPr₅₀ to HNPr₂₅₀ the prism structures retain their shape, however beyond HNPr₂₅₀ due to the enhancement of internal lattice strain the prism shape gradually distorted and finally a hollow disc appears in case of HNPr_{3K}. Due to the lack of structural symmetry, we have modeled only five HNPrs (all are having prismatic shape) for the calculations of strain. Conceptually the strains are defined as the ratio of interatomic displacements divided by reference bond lengths. In general, the strain-induced (ϵ) in a nanoparticle is defined by the following mathematical relation:

$$\epsilon = (d^* - d_0)/d_0 = \delta d/d_0 \dots\dots\dots (4)$$

Where d_0 is the bond length of pure bulk material, and d^* is the average bond length of a particular surface/interface. From the above equation, it is clear that the strain-induced on a surface is strongly affected by surface unsaturation (δd). However, this lattice strain induced within the system is also a function of other parameters such as pressure (P) and temperature (T).

Thus the total lattice strain induced (ϵ_T) can be represented as:

$$\epsilon_T \propto \epsilon(d(P, T)) \dots\dots (5)$$

But, this relation is valid only for a homogeneous system. Due to the presence of mixed covalent radii in heterogeneous systems, the change in the mole-fraction of either component can induce the strain in the lattice for a fixed composition. Hence, we have tried to correlate the lattice strain with dopant concentration with the help of **Equation (6)**

$$\epsilon_{T_j} = \epsilon(d(x_j, P, T)) \dots\dots\dots (6)$$

Here x_j represents the strain-induced over some specific sites (j) due to the variation of dopant concentration. First, we have calculated the effect of compositional variation on lattice strain induced at the basal plane and prismatic face in Au:Ag HNPrs. The calculated average bond-lengths between gold atoms follow the order of HNPr_C (2.808 Å) > HNPr_B (2.800 Å) > HNPr_A (2.800 Å) > HNPr_{Au} (2.773 Å). However, the difference in the bond length is negligible for either any of the compositions and hence we cannot calculate the strain induced by the bond-length parameters. Alternatively, the edge length of HNPrs (along the basal plane) also follows a similar order as we observed for Au-Au bond parameters. The calculated values for edge lengths are 2.773 nm (pure), 2.800 nm (HNPr_A), 2.805 nm (HNPr_B), and 2.808 nm (HNPr_C). Hence, to calculate the strain induced by the Ag doping, we have used the following equation:

$$\epsilon = (l_{Au_{1-x}Ag_x} - l_{Au})/l_{Au} \dots\dots\dots (7)$$

where l_{Au} is the edge length of pure Au HNPr and $l_{Au_{1-x}Ag_x}$ is the edge length of various HNPrs compositions along their basal planes. The calculated percentage strain along the (111) plane obtained from our calculation is 0.974% for HNPr_A, 1.154 % for HNPr_B and 1.190 % for HNPr_C. This gradual increment of strain along (111) plane indicates that the reactivity on {111} facet increases gradually with Ag doping. This results in the transformation from prismatic shape to hollow nanosphere to achieve the

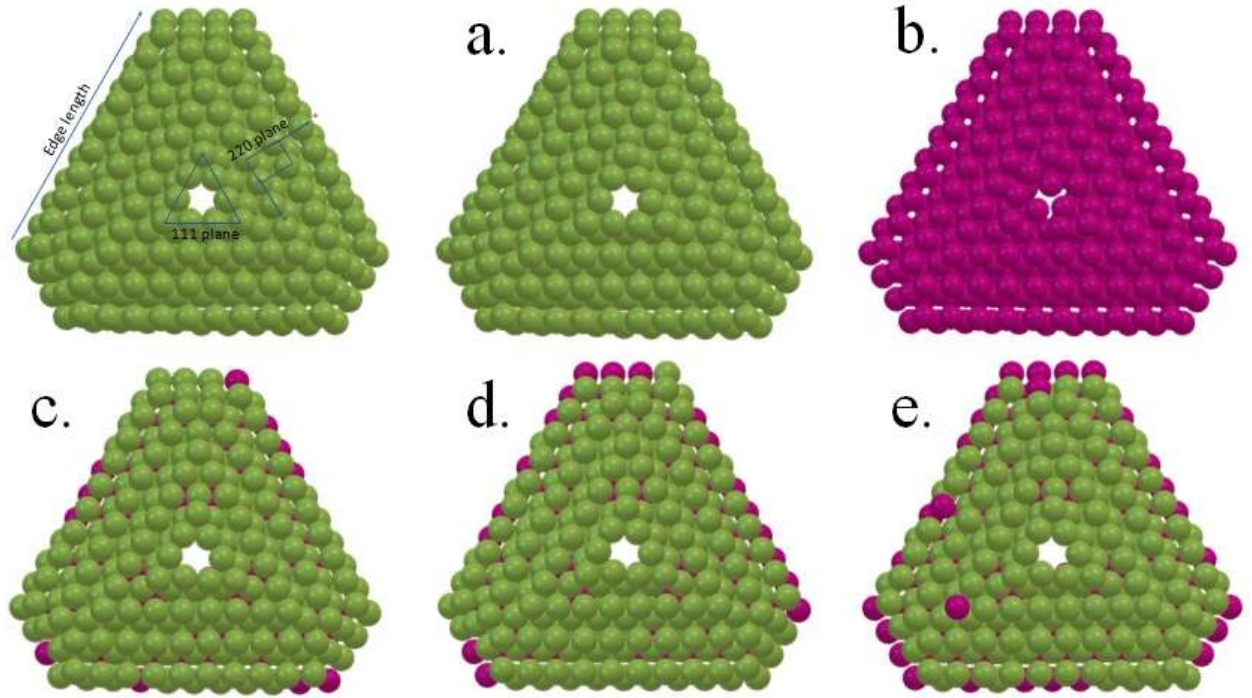


Figure 4.20: Optimized structure for different HNPrs: (a) HNPr_{pureAu}, (b) HNPr_{pureAg}, (c) HNPr_A, (d) HNPr_B, and (e) HNPr_C. The leftmost figure of the top panel shows the model HNPr with different planes (basal and vicinal) along with different structural parameters.

desired stability by reducing their vibrational entropy^{173,174} in the form of developed strain. On the other hand, the more reactive (220) plane which comprises the faces of HNPrs acts as the active facet for effective UA oxidation. If we look carefully the **Table 4.3** then the calculated percentage strain along the {220} facet varies in the following order:

1.143% for $\text{HNPr}_A < 1.718\%$ for $\text{HNPr}_B > 1.451\%$ for HNPr_C .

This indicates that unlike $\{111\}$ facet (top and bottom flat surface of HNPr) the developed strain on reactive $\{220\}$ facet doesn't increase monotonously with Ag-doping, rather maximizer for HNPr_B (modeled) with $\text{Au}^0:\text{Ag}^0$ a fixed composition of 2.45:1 which is close to the experimentally measured composition of HNPr_{250} as mentioned in **Table 4.1**. This maximization of strain on energetically active facet makes HNPr_{250} as the most active HNPr structure for UA oxidation. Hence our calculation is

Table 4.3: Different crystal parameters along with induced strain along (111) basal plane and (220) vicinal plane by optimizing the HNPr structure and calculating % strain by considering **equation 4** and **equation 7**.

Cluster Model	Composition ($\text{Au}^0:\text{Ag}^0$)	Molecular Area ($\times 10^3 \text{\AA}^2$) Along the Basal Plane	Edge Length of Basal Plane (111) nm	Average Strain Vector of Vicinal Plane (220) (Along with Y, \AA)	Strain Induced Along (111) Basal Plane (in %)	Strain Induced Along (220) Vicinal Plane (in %)
$\text{HNPr}_{\text{pureAu}}$	$\infty:0$	1.007	2.772	12.333	NA	NA
HNPr_A	3.03:1	1.026	2.799	12.474	0.974	1.143
HNPr_B	2.45:1	1.028	2.804	12.545	1.154	1.718
HNPr_C	2.02:1	1.040	2.805	12.512	1.190	1.451
$\text{HNPr}_{\text{pureAg}}$	$0:\infty$	1.057	2.827	NA	NA	NA

well-agreed with our predictions that Ag doping in pure Au HNPr increase strain within it and with a suitable value of the indicator, Au^0/Ag^0 (2.45:1), an alloy is formed (in case of HNPr_{250}) to gain the optimum stability in the prismatic structure with maximum strain within it. The present study is not only to explore the role of different physicochemical and intrinsic crystal parameters for enhancing the rate of sluggish oxidation of UA but also to find out whether we can use these nanostructures as efficient catalytic materials for ultra-low sensing of UA in a physiological sample. The efficacy of the $\text{HNPr}_{250}/\text{GC}$ modified electrode encouraged us for

finger printing of UA from normal physiological to deficiency level concentration range. We have applied different electrochemical techniques like SWV, DPV, chronoamperometry for concentration-dependent study (**Figure 4.21**) and found that DPV is the most powerful and reproducible electrochemical methodology for current response in nanomolar (10^{-9} M) range. We are able to get a linear relationship in the concentration range of 40 μ M to 2.5mM from their DPV response as depicted in **Figure 4.21**. We have also performed an interference study for different ions like Cl^- , Br^- , I^- , Ca^{2+} , CO_3^{2-} as well as other interfering agents like ascorbic acid (AA), dopamine (DA), glucose, etc. to show any change during DPV measurements and found that UA redox peak potential does not shift and peak current almost remain constant except for I^- and CO_3^{2-} . This discrepancy in peak potential and peak current for I^- and CO_3^{2-} maybe due to the following reasons: (i) Ag^+ present in the HNPr_{250} may react with I^- to form AgI ¹⁹⁶ as a side product and enhances the peak current slightly at low PH \approx 1 (0.1M HClO_4), and (ii) addition of carbonate will change the pH of the electrolyte (more alkaline) to improve the oxidation process.¹⁹⁷

The formulated assay (HNPrs) is highly stable in nature due to its mixed metal nature and efficient encapsulation by long-chain CTAB molecule, yet energetically active for catalytic activity. Moreover, the devised assay and experimental procedure do not require any surface tagging for selective recognition of analytes which not only reduces the cost of pathology but also offers a rapid detection technique.

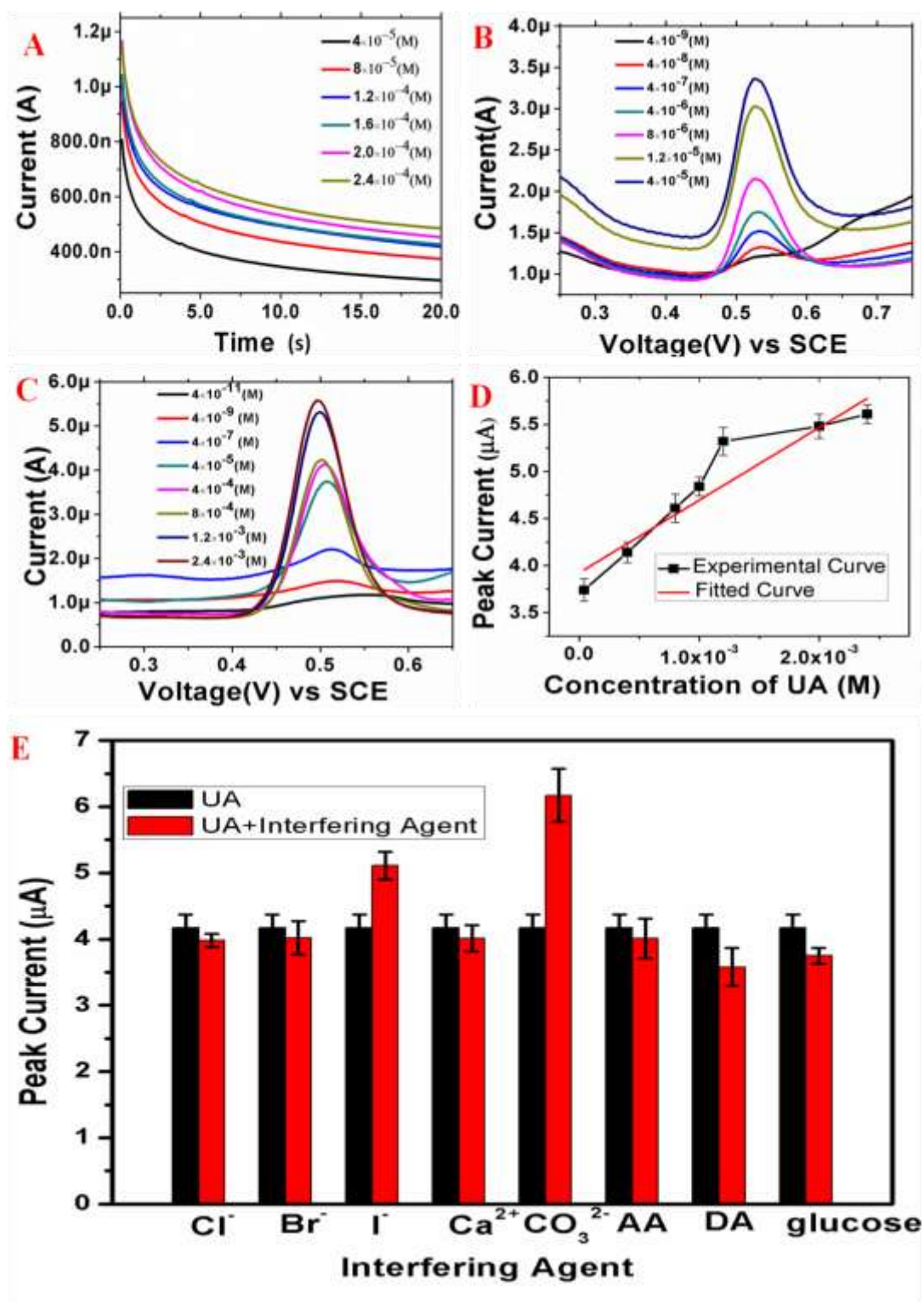


Figure 4.21: (A),(B), and (C) are chronoamperometry, SWV, and DPV responses respectively at variable concentrations of UA on the HNPr₂₅₀/GC electrode.(D) represents the linear fitting of

DPV response with standard deviation. (E) Denotes the peak current shifting for electrooxidation process of 400 μM UA in presence of different interfering agents (the concentration of different interfering agents are taken in millimolar range).

4.6 Conclusion

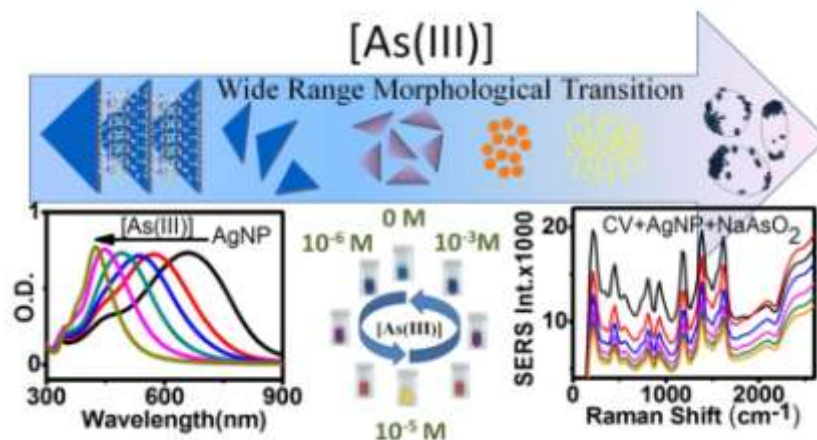
The porosity developed in the central cavity region of HNPr_{250} generates tensile strain due to the atomic replacement (Ag by Au) in our synthesized size (both the hole as well as the edge length) and shape (sharp Vs. truncated 2D prisms or prisms Vs. circular disks) variable HNPrs. The mechanistic investigation for their catalytic activity has been explored in minute details both by experimental methodology and theoretical modeling. We have demonstrated that the HNPr_{250} acts as the most efficient catalytic material compared to other HNPrs with the same chemical composition (except the porous ligament core region) for the oxidation of Uric Acid. The superlative catalytic efficiency of HNPr_{250} has been explored in depth by a morphological and atomic-scale architectural study using HRTEM analysis. Differential pulse voltammetry, square wave voltammetry, and electrochemical impedance spectroscopy provide their qualitative and kinetic information. Due to the inducement of multiple twin boundary, grain boundary, and tensile strain in large excess, the d-band shifting in the HNPr_{250} cause greater adsorption of UA on its surface to support the reduction of deprotonation energy (eV) during electrochemical oxidation through vicinal $\{220\}$ facets of hollow nano prisms. This study allowed us not only to investigate the actual reason behind the unprecedented catalytic activity of HNPr_{250} out of other HNPrs but also help us to design a sustainable nanoscopic assay for accurate measurement of UA concentration (in the nanomolar range) for the evaluation of hyperuricemia or hypouricemia which might find potential application in designing low-cost kit in the pathological industry.

CHAPTER-5

Wide Range Morphological Transition of Silver Nanoprism by Selective Interaction with As(III): Tuning-Detuning of Surface Plasmon Offers to Decode the Mechanism

OUTLINE: Specific Points of Discussion

- Na^+ ion-induced cation- π interaction between face-to-face energetically stable {111} surface-bound pyrrolidone groups arranges PVP-based silver nanoprisms (AgNPrs) in an axial stacking geometry.
- Congested interplanar space between AgNPrs allows As(III) selectively to react differentially with silver atoms from facial {111} and peripheral {110} facets to results smaller stacking and finally to nanoseeds.
- Above a critical concentration of As(III), PVP leached-out from nanoparticles to form nanoseed- engulfed emulsions and inducing a controlled aggregation.
- This entire morphological transition has been decoded by recording their SPR and SERS tuning and confirmed by the transmission electron microscopy study.
- Strong affinity and selectivity of As(III) toward the Ag atom (verified by DFT calculation) offers us a low-cost AgNPr-based colorimetric assay with potential application in environmental protection.



5.1 Introduction:

In this chapter, we have engineered axially stacked silver nanoprisms (AgNPrs) from the constituent PVP capped Ag nanoprism monomers and studied their differential interaction with As^{3+} and As^{5+} microscopically via TEM, spectroscopically via UV-visible and SERS spectroscopy, and theoretically via DFT calculations. Arsenic (As) is one of the most profuse toxic elements on Earth's crust.^{198,199} Major arsenic species found in environmental samples are either inorganic salts [arsenite: As(III) and arsenate: As(V)] or stable organic compounds [e.g., dithioarsenate (DTA), dimethylarsinic acid (DMA), and monomethylarsinic acid (MMA)].^{200–202} Sources of As contamination is many-folds which include sulfide ores;²⁰³ natural phenomena like weathering, biological activity, volcanic eruption; together with anthropogenic inputs and spreads through rain and dry fallout.^{201–204} According to the 2009 European Food Safety Authority (EFSA), Parma, Italy²⁰⁵ and World Health Organization (WHO), inorganic arsenic is acutely toxic compared to organic arsenic compounds²⁰⁶ and causes skin lesions, peripheral neuropathy, diabetes, cardiovascular diseases, and cancer of the lung, liver, urinary bladder in addition to the skin. As a result of this, the detection, quantification, and removal of inorganic arsenic from the drinking water gained a lot more momentum compared to organic arsenic. The EFSA and WHO fixed the maximum tolerable concentration of arsenic as 15 $\mu\text{g/kg}$ of

bodyweight and 10 *ppb* in drinking water (old limit of arsenic contamination: 50 *ppb*²⁰⁷). Global hot spots with high arsenic risk include South of Asia (Bangladesh, Mongolia, and Malaysia), South of South America (Chile and Argentina), and Western North America. A large population of South and Southeast Asia are seriously exposed to potentially dangerous levels of carcinogenic arsenic via their drinking water every day.²⁰⁸ By knowing its high toxicity, arsenic-free drinking water is in high demand for the modern healthier lifestyle.

Sufficient reports are also available which explore the positive side of concentration-dependent arsenic contaminations^{209,210} and doping.²¹¹ Hence, the quantification of arsenic is very important both for blissful effect as well as to tackle translational health hazards and indirectly helping us to grow the subject of heavy metal chemistry.²¹² Literature is rich with reports for the detection of arsenic either by laboratory-based analytical procedures^{207,213–224} or by using noble metal nanomaterials^{225–231} but the mechanistic revelation of selective detection of arsenic^{201,232} not only seldom but also superficial in nature. Based on their wealth of optical properties (absorption, emission, and scattering) the noble-metal nanoparticles find high throughput applications in different advanced fields^{4,233–236} which include sensing, diagnostics, therapeutics, optoelectronics, catalysis, alternate energy, etc. Surface plasmon resonance (SPR)^{237–240} bands of noble-metal nanoparticles are typically located in the vis-NIR region and are strongly dependent on nanoparticle size, shape, composition, crystallinity, interparticle spacing, and local dielectric environment.^{238,241–245} Out of several noble-metal NPs, silver nanoprism (AgNPr) is one of the most promising candidates for multicolor diagnostic labeling purposes because of their easy tunability of the broad-band *in-plane* dipole SPR simply by adjusting the aspect ratios ($AR_s = \frac{L}{T}$ where L = side length of the prism and T = thickness of the prism and by inducing their 2D &

3D assemblies.²⁴⁶ Yu et al.²⁴⁷ and others²⁴⁸ found that silver nanoplates are sensitive to several inorganic anions and results SPR band tuning between 650 and 450 nm by adjusting the added anions concentration. Though Yu et al.²⁴⁷ explained this as the effect of surface electron injection, Xu et al.²⁴⁹ cites the color change of AgNPr as the sculpting effect of chloride ion which transforms the triangular shape into circular disk-like shape by surface etching. Recently, two groups, Xu et al.²⁴⁹ and Tsai et al.,²⁴⁰ independently found the threshold concentrations for Cl^- , Br^- and I^- as $\sim 3 \times 10^{-4}$, $\sim 1 \times 10^{-6}$ and $\sim 1.5 \times 10^{-6}$ M respectively compared to $\sim 4 \times 10^{-4}$ M of SCN^- to initiate the same sculpting process. Like surface Plasmon behaviors, noble metal nanomaterials also show interesting inelastic scattering properties and can be verified easily and cost effectively by recording their surface enhanced Raman scattering (SERS) spectra. Like SPR, SERS also show size and shape dependent (of the nanoparticle) enhancement of Raman spectra for the Raman active molecule when they are adsorbed onto a nanosurface due to the change in active surface area (by increasing their individual size or by generating controlled aggregation) to be available for molecular adsorption or a variation in the extent of field enhancement (localized enhanced field: E_s) at the nanosurface. Although the literature is rich where SERS has been used to measure the size²⁵⁰ of the active nano surface or to find out the surface curvature to estimate their relative capability of field enhancement by lightning rod effect,²⁵¹ a direct SERS method to trace their morphological change during their interaction with specific chemical at different concentration is seldom and attracts our attention to use it for ultrasensitive and highly specific detection. Due to their sharp features (compared to SPR) and strong intensity, SERS can also be used as an efficient sensing tool to understand the morphological transition of nanomaterials during their selective interaction with an analyte but obviously not a direct spectroscopic method and depends heavily on the ability of the dye to adsorb on the specific

nanosurface. Out of several nanomaterials-based technologies^{229, 12,252–254} the colorimetric technique²⁰² for selective and sensitive detection is of most useful for its large scale application associated with its low cost implementation. Most of the nanomaterials-induced colorimetric techniques are based on the formation of controlled aggregation by exploiting their surface bound ligand chemistry in presence of heavy metal ions which tune their SPR to show different colors. They bear a common plasmon feature of shifting to higher wavelength associated with reduction in intensity and broadening. Moreover, in this strategy we don't induce any morphological change of the individual nanomaterials rather simply changes their interparticle relative distance to induce plasmon coupling. Getting inspired from these facts we have tried here to induce morphological change simply by adding increasing concentration of As (III or V) in AgNPr solution which results the tuning of plasmon band as a combined effect of breaking down the AgNPr overlay stacking by arsenic ion intercalation, leaching of disintegrated AgNPrs, removal of PVP surfactant from AgNPr surface to form size variable emulsions and thereby inducing emulsion incorporated controlled aggregations or even complete dissolution of AgNPr to form unpredicted composites to lose plasmonic characteristics. Here the characteristics of the polymeric surfactant (functional group, molecular weight, etc) are crucial to induce both overlay stacking as well as emulsion incorporated aggregation. This concentration dependent morphological transition is only sensitive for arsenite[As(III)], leaving apart all other common alkali, alkaline and toxic transition metal ions including arsenate [As(V)] and has been confirmed by TEM. A plausible explanation of the color coded sensing of As(III) has been presented by analyzing their tunable surface plasmon and surface enhanced Raman spectra. This low cost, easy-to-perform and error-free As(III) detection technique will provide us a versatile tool to find enormous application in the field measurements.²⁰²

5.2 Synthesis of silver nanoprism:

The initial triangular silver nanoprisms were synthesized by following the Mirkin's method²⁴⁶ with slight modification. Briefly, 25 mL of Milli-Q water was taken in a 50 mL beaker and then 250 μL of 10^{-2} M AgNO_3 was added drop by drop in it. To this diluted AgNO_3 solution we then added 1.5 mL of 30 mM TSC, 1.5 mL of 0.24 mM PVP ($M_w \sim 10,000$) and 60 μL of 30 wt % H_2O_2 successively. Between each addition, 30 s time lag was given for the proper mixing of reagents. To this final mixture, 250 μL of 10^{-1} M NaBH_4 was rapidly injected and the solution turns into yellow color initially which becomes colorless after some time. The solution was stirred for an additional 30 min; the color was darkened to a deep yellow which indicates the formation of small Ag nanoparticles. Over the next several seconds, the color of the solution changes from yellow to blue in a stepwise pattern. Synthesized nanoprism was then kept in room temperature for 24 h before we make TEM sample by a known technique described in previous reports^{54, 61} for clean monolayer sample preparation on carbon film 300 mesh copper grid (CF300-CU).

5.3. Results and Discussion:

The exploitation of SPR for selective detection of an analyte is long known in the literature²⁰² where we utilize their surface-bound ligand chemistry for specificity^{255,256} and gigantic cross-section (absorption and scattering) of the metal core for sensitivity.^{257,258} In this scheme we use the surface-bound ligand as a *fishing net* and the metal core as a *yardstick* to identify and quantify an analyte respectively without observing any morphological change of the individual nanoparticles.

In another approach of colorimetric detection where the metal core of the nanoparticle acts both as *fishing net* as well as a *yardstick* and in presence of analyte (ionic or molecular) the

unstable (and hence reactive) exposed surface atoms directly react with the analyte to create a permanent morphological change of the nanomaterial. Since the change of color in this approach is due to the analyte induced morphological change of nanoparticles, it does not encourage forming aggregate, or in other words the formed morphological intermediates are very stable to explore their reaction mechanism. In our present study, we have adopted the second approach of selective color-coded sensing of As(III) by using AgNPr as the nanomaterial and compared the colorimetric result in the same experimental condition for all other common alkali, alkaline and toxic transition metal ions including arsenate As(V). The absorption spectra of the synthesized AgNPrs are shown in **Figure 5.1A** where the plasmon band in the range 650-750 nm corresponds to *in-plane dipole* mode and the plasmon band near 330nm is due to the *out-of-plane quadrupole* mode of the nanoprism²⁴⁰.

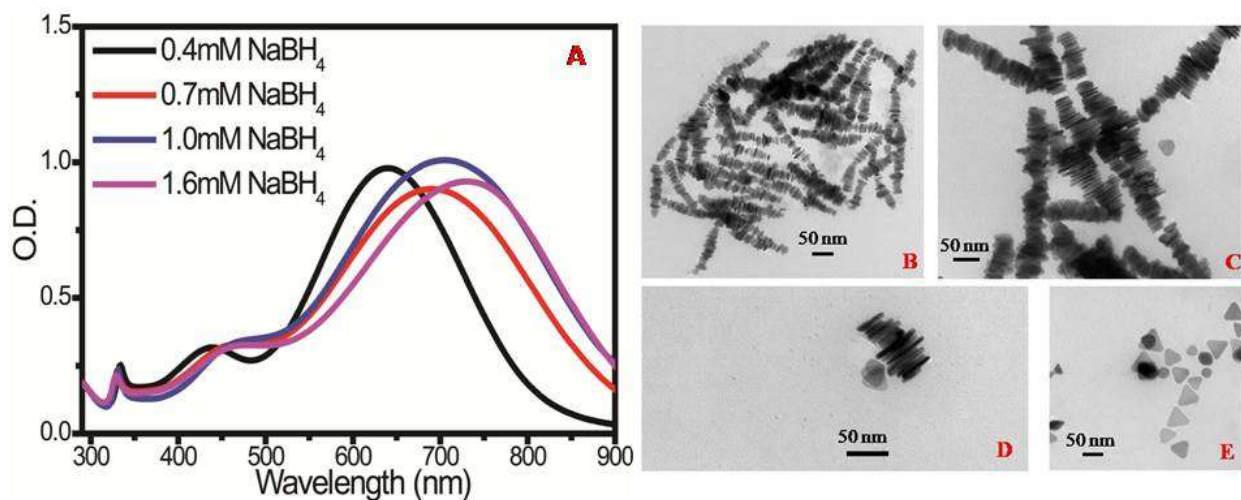


Figure 5.1: (A) Stacking length-dependent plasmon tuning. TEM images to show the effect of Na⁺ ion concentration induced cation- π interaction on average stacking length variation between 198 and 0 nm, where (B) at M (molar ratio between NaBH₄ and AgNO₃) =16, L =198 nm and N =26 the obtained $d(400 \mu L) = 6.4 \text{ \AA}$ with $\zeta(400 \mu L) = -10.5 \text{ mV}$; (C) at M =10, L =136 nm and N =18 the obtained $d(250 \mu L) = 5.9 \text{ \AA}$ with $\zeta(250 \mu L) = -14.6 \text{ mV}$; (D) at M =7, L =93 nm and N =18 the obtained $d(250 \mu L) = 5.9 \text{ \AA}$ with $\zeta(250 \mu L) = -14.6 \text{ mV}$; (E) at M =5, L =71 nm and N =18 the obtained $d(250 \mu L) = 5.9 \text{ \AA}$ with $\zeta(250 \mu L) = -14.6 \text{ mV}$.

and $N=12$ the obtained $d(175\ \mu\text{L}) = 8.2\ \text{\AA}$ with $\xi(175\ \mu\text{L}) = -17.2\ \text{mV}$ and (E) at $M=4$ they don't form stacking structures rather distributed as individual prisms with $\xi(100\ \mu\text{L}) = -25.4\ \text{mV}$.

The broad peak in the range 440-460 nm is attributed to two closely spaced SPR bands, *in-plane quadrupole* and *out-of-plane dipole* modes of AgNPrs. Details of the HRTEM study of these nanoprisms are presented in **Figure 5.2** and in our previous report²⁴¹ which shows both frontal and sideways bright-field TEM images. The selected area electron diffraction (SAED) indicates that the as-prepared nanoprisms are single crystals with a $\{111\}$ lattice plane as the basal plane (inter planar spacing = $2.36\ \text{\AA}$). The flat surface of the silver nanoprisms is parallel to the $\{111\}$ plane as also been suggested in the literature^{259,260}. The SAED pattern also shows another set of faint spots with hexagonal symmetry which has been indexed as $1/3\{422\}$ reflections with a lattice spacing of $2.50\ \text{\AA}$, indicating the presence of a single twinning boundary within the $\{111\}$ planes. For single crystal *fcc* metals, these spots are forbidden, but they can appear when there are two twin planes parallel to one another.^{241,259} The appearance of the forbidden $1/3\{422\}$ reflection is often observed in silver or gold nanostructures in the form of thin plates or films bound by atomically flat top and bottom faces. In previous literature, reports, it's already been reported that for thin AgNPrs the atomically flat top and bottom faces have $[111]$ facets and the edges have $[110]$ facets.

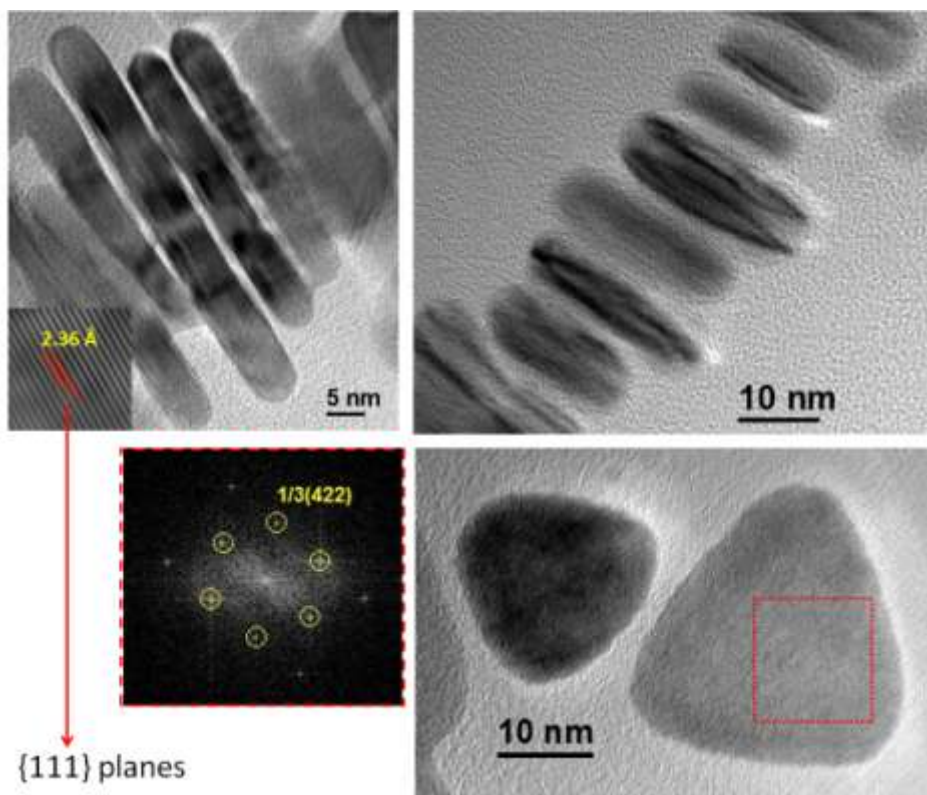


Figure 5.2: Frontal and sideways bright-field and HRTEM of our synthesized nanoprisms with $\{111\}$ lattice plane as the basal plane and $1/3\{422\}$ reflections indicate the presence of a single twinning boundary within the $\{111\}$ planes.

The measured thickness of these nanoprisms has been reported as ~ 7 nm.²⁴¹ Both the relative thickness map and the corresponding line profile indicates their two-dimensional growth.²⁴¹ The AgNPr synthesized by using 250 μL of 0.1 M NaBH_4 has been taken throughout this study which shows bright blue color with absorption maxima at 704 nm. The corresponding TEM images in **Figure 5.3A** and **5.3B** show a highly overlay stacking structure that transforms into an isotropically distributed arrangement by the application of ultrasonic wave at 40% power of 53 kHz frequency at 27 $^\circ\text{C}$ for 10 s. This implies that the binding force between $\{111\}$ faces of AgNPrs in the overlay stacking arrangement is quite a weak and easily breakable by applying weak ultrasonic force.

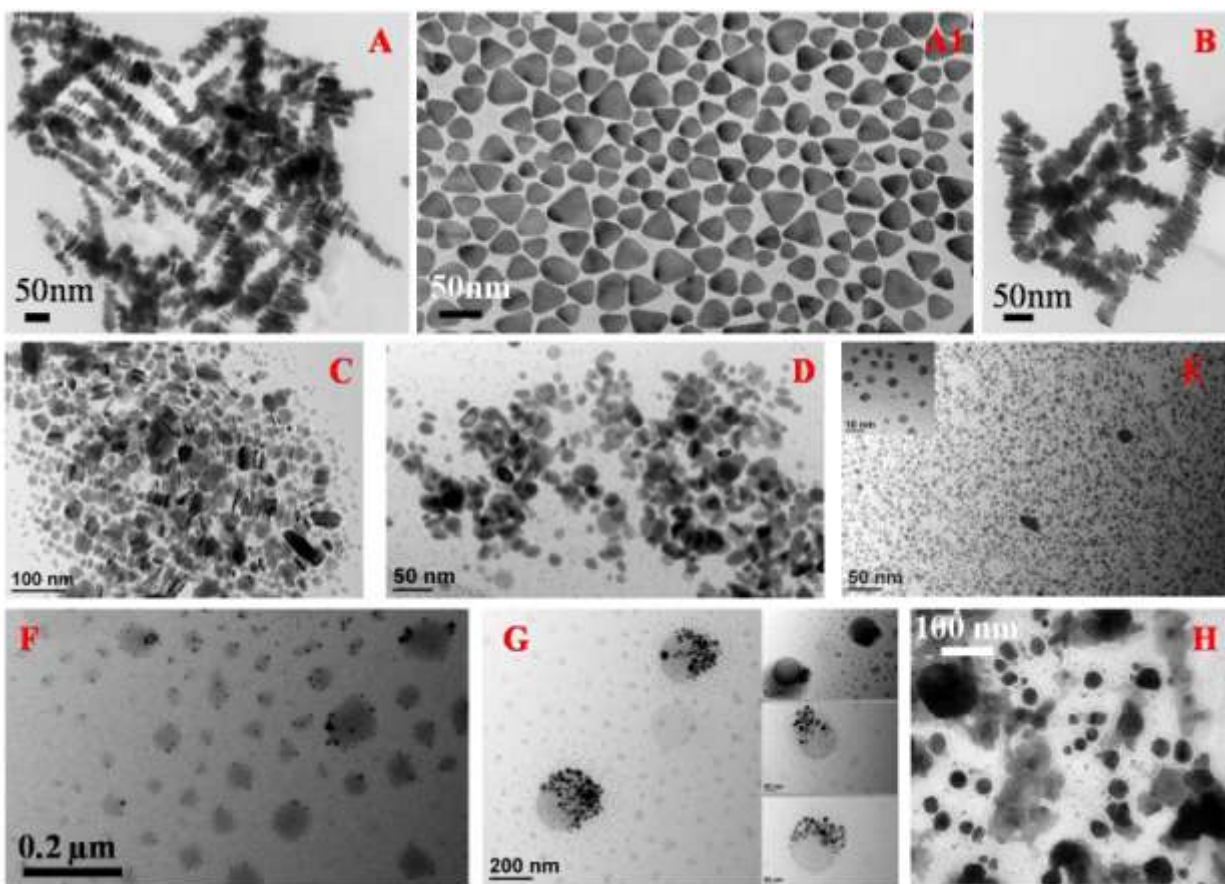
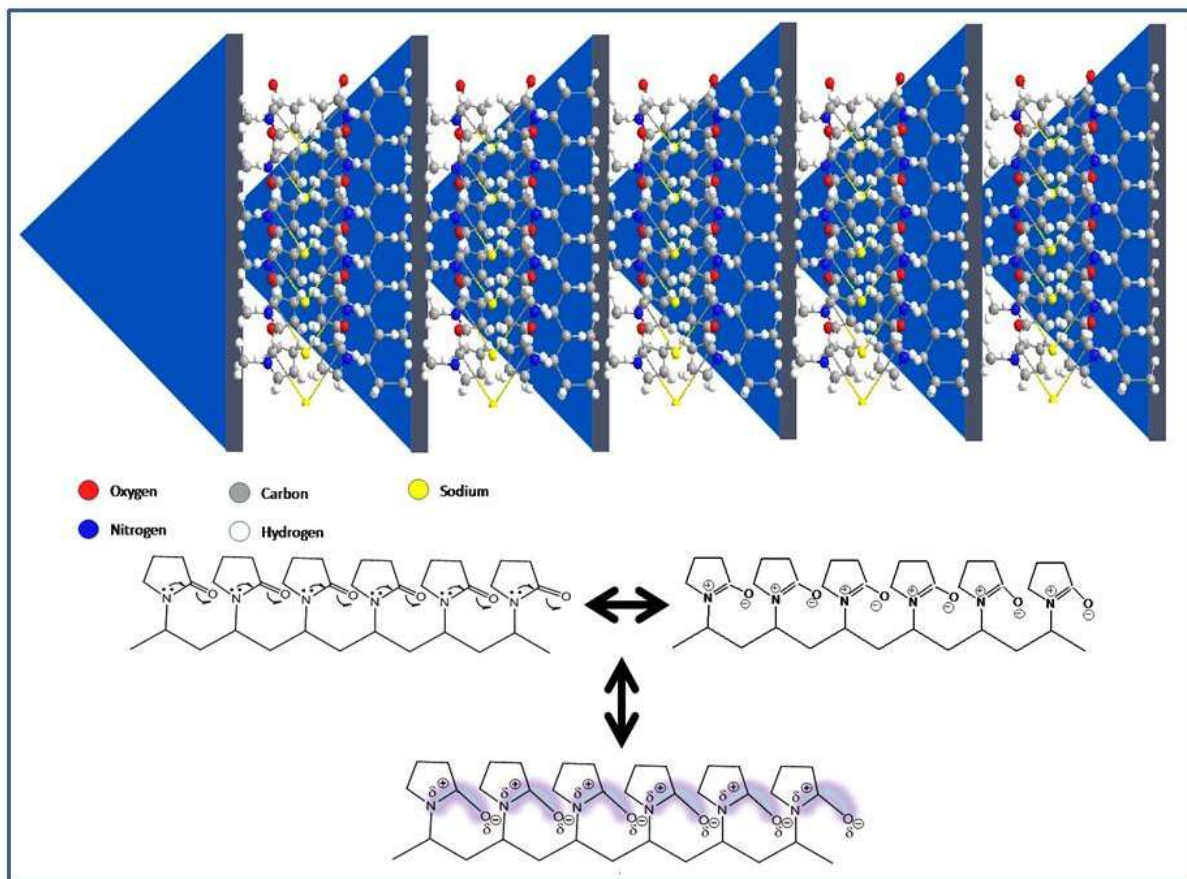


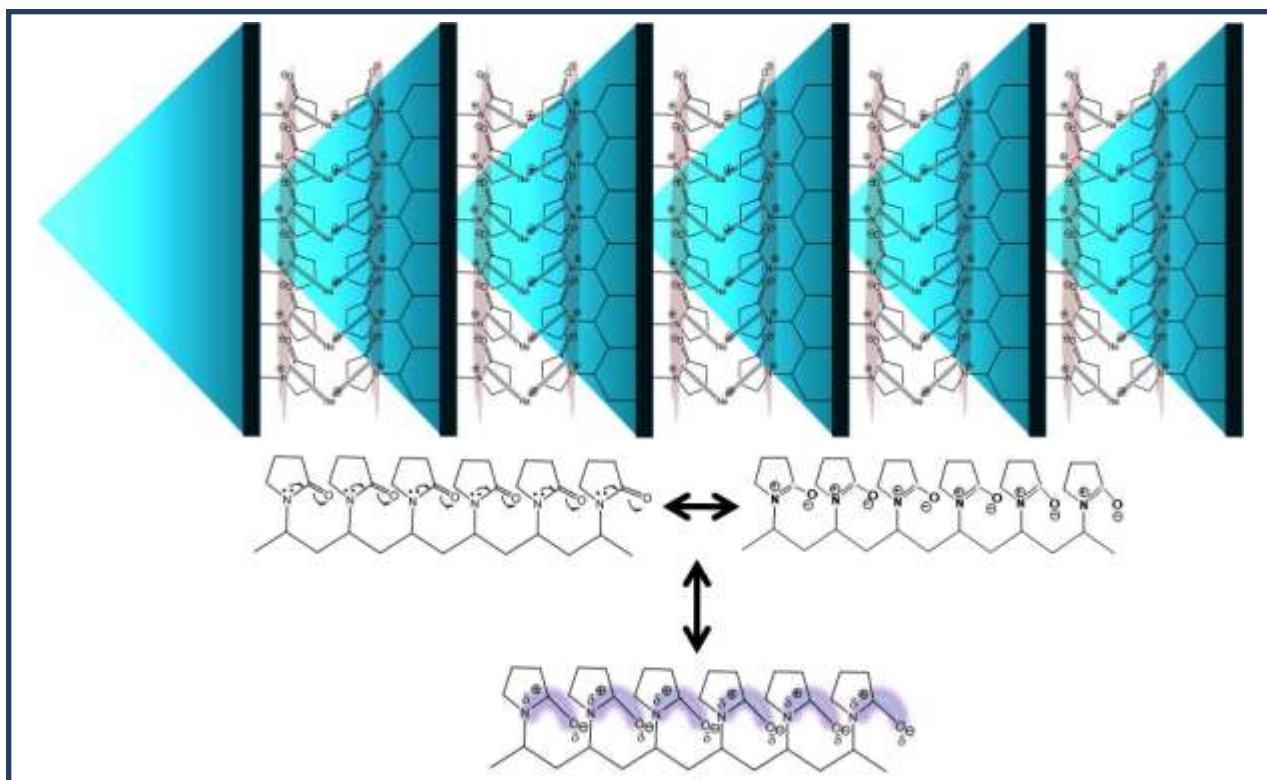
Figure 5.3: (A-H) Morphological change of AgNPr by destacking, followed by leaching of nanoprisms and emulsion induced controlled aggregation of silver seeds at increasing concentration of As(III). (A1) indicates the as-synthesized AgNPrs after the application of ultrasonic wave at 40 % power of 53 kHz frequency at 27 °C for 10 s. Here different TEM images correspond to the effect of concentration-dependent As(III) exposure on AgNPr structure where A, B, C, D, and E correspond to the As(III) concentration of 0, 1-2, 2-4, 5-7, and 8-40 μM , respectively. Similarly, the frames F, G, and H correspond to the effect of As(III) at concentrations of 40-80 μM , 350-750 μM , and $> 1 \text{ mM}$ respectively. A range of concentrations means that the morphology does not change throughout this range. Effect of As(III) at various intermediate concentrations has not been shown to avoid the complicity of the presentation.

Though the literature is affluent^{246,261–264} with reports of AgNPr overlay stacking, the actual reasons are still unknown. In an earlier report of AgNPr synthesis by using Bis(p-sulfonatophenyl)phenylphosphinedihydrate dipotassium salt (BSPP) as a surfactant also shows axial overlay stacking and has been explained by Mirkin^{263,264} and others as a result of π - π stacking offered by the benzene rings in triphenyl phosphine group of BSPP. The same explanation (π - π stacking) of axial overlay stacking also holds for PVP-mediated AgNPr synthesis due to the presence of short-chain π -electron moiety in the N-C=O region originating from each pyrrolidone group of surface-adsorbed PVP. Pyrrolidone molecules from Parallely oriented {111} facets of AgNPrs then can results π - π stacking but in that case, the distance between two flat prisms should not be more than 3.2 Å (the limit of π - π interaction is the sum of the van der Waals (VDW) radius between atoms involved where $r_{VDW}^C = 1.7$ Å, $r_{VDW}^N = 1.55$ Å and $r_{VDW}^O = 1.52$ Å).²⁶⁵ On the other hand if we consider cation- π interaction²⁶⁶ between available cations (Ag^+ and Na^+ ; $r_{VDW}^{Ag} = 1.72$ Å and $r_{VDW}^{Na} = 2.57$ Å) and surface adsorbed N-C=O π -electron moieties then the distance between AgNPrs should fall in the range 6.6-8.3 Å and the obtained TEM results indicate that cation- π as the most probable interaction pathway between AgNPrs to form an axially stacked sandwich geometry similar to ferrocene, $Fe(C_5H_5)_2$, structure. Geometrically the cation- π stacking in case of PVP is much weaker than the corresponding ferrocene type of molecules²⁶⁷ due to less degree of orbital overlap and can easily breakable by the application of weak ultrasonic wave as discussed before. **Scheme 5.1** explains the actual cation- π interaction among axially stacked AgNPrs where the ball-and-stick molecular geometry shows the orientation of surface bound PVP molecules and intercalated Na^+ ions. Atomic model of this cation- π interaction among surface adsorbed PVP molecules through

intercalated Na^+ ions which enforce them to arrange in an axial stacking configuration is shown in **Scheme 5.2** for better understanding the orientation of electrostatic interaction.



Scheme 5.1. Schematic representation of cation- π interaction among surface adsorbed PVP molecules through intercalated Na^+ ions which enforce them to arrange in an axial stacking configuration. Here all the interacting atoms and molecules are shown in the ball-and-stick model and π -electron cloud in violet color.



Scheme 5.2: Schematic representation of cation- π interaction among surface adsorbed PVP molecules through intercalated Na^+ ions which enforce them to arrange in an axial stacking configuration. Here all the interacting atoms and molecules are shown in the atomic model for better understanding the electrostatic interaction and π -electron cloud in violet color for better visualization.

It is worth mentioning that our zeta potential study (**Table 5.1**) confirms that these AgNPs are negatively charged and their zeta potential reduces gradually as we increase the amount of NaBH_4 during the synthesis. This $-Ve$ charge induces repulsion among AgNPs to destabilize their axial stacking and hence the relative contribution between cation- π interaction and the extent of electrostatic repulsion governs the distance between two AgNPs and may vary between idealistic 4 Å to a maximum of 10 Å. According to the literature, the free energies

associated with the crystallographic planes of an *fcc* metal increases in the order²⁶⁰: $\gamma_{\{111\}} < \gamma_{\{100\}} < \gamma_{\{110\}}$ and explains the axial stacking through $\{111\}$ facets.

Table 5.1: Variation of zeta potential (ξ) and stacking length (L) as we vary the molar ratio (M) between NaBH₄ and AgNO₃.

$M(\text{NaBH}_4:\text{AgNO}_3)$	4	7	9	16
ξ in mV	-25.4	-17.2	-14.6	-10.5
L in nm	0	93	136	198

Since the reduction potential for Na⁺, Ag⁺ and NaBH₄ are -2.71, 0.8 and -1.24 V respectively, NaBH₄ can easily reduce Ag⁺ but not Na⁺. Besides that, the concentration of NaBH₄ added during synthesis is more than enough for complete reduction of Ag⁺ which rules out the possibility of any free silver ion after AgNPr synthesis. As a result of this, an increased amount of NaBH₄ raises the concentration of Na⁺ ions not only to enhance the possibility of the cation- π interaction and thereby stacking length but also to reduce the effective negative charge of AgNPr assemblies. Obtained AgNPrs show a gradual approach towards neutral zeta potential with an increase in stacking length, L, as we increase the concentration of Na⁺ originates from NaBH₄. We can define the molar ratio (M) of NaBH₄ to AgNO₃ as:

$$M = V_{\text{NaBH}_4} \times S_{\text{NaBH}_4} : V_{\text{AgNO}_3} \times S_{\text{AgNO}_3}$$

Here ‘V’ and ‘S’ represent the volume and molar strength respectively. By varying the molar ratio (M) between 16 and 4 we have achieved different stacking lengths with an unchanged edge length of 50±20 nm for individual nanoparticles. By knowing the stacking number (N, the average number of AgNPr present in each stack) and thickness of individual AgNPrs (T) we can easily calculate the spacing (d_i , i =amount of NaBH₄) between AgNPrs in different stacks as

$d_i = \{L - (N \times T)\} / (N - 1)$. The effect of increasing concentration of NaBH_4 on stacking length has been clearly presented in **Figure 5.1B-E** where the average stacking length changes between 198 nm to 0 nm. Though the concentration of Na^+ is crucial in making of stacking patterns of AgNPrs, detection, and quantification of sodium ions as stacking intercalators is not easy by recording their Energy Dispersed X-Ray (EDX) spectra.^{268,269}

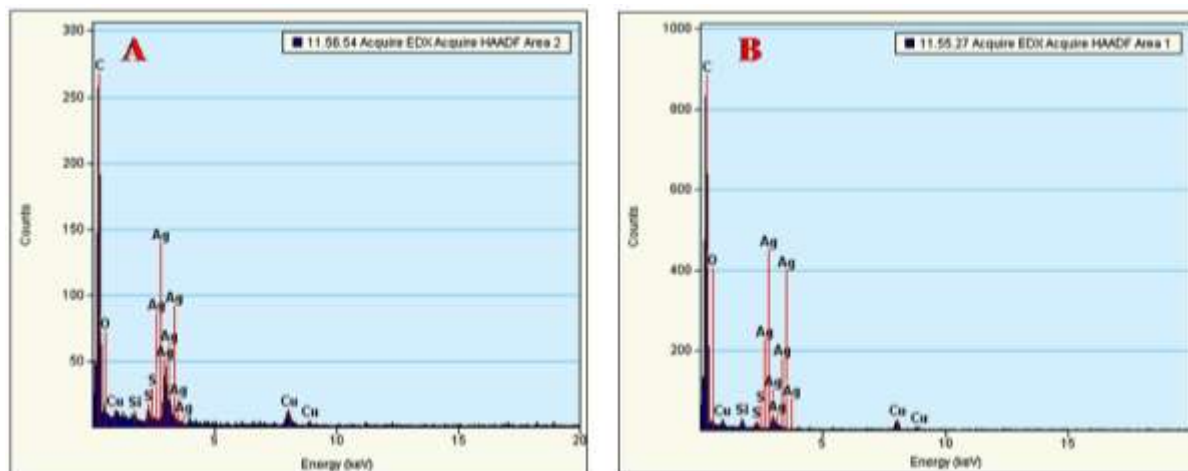


Figure 5.4: EDX spectra obtained from two different areas (Area-1 and Area-2) of AgNPr stacking to analyze the relative abundance of different elements.

Detection and quantification of an element through EDX depends mainly on two factors, (i) efficiency of detection for ejected electrons with energy less than 3 keV and (ii) whether the abundance of the element is less than 1000 ppm or not. Since the abundance of Na^+ -ion in our synthesis is in the range of 15-60 ppm, the efficiency of the detection of Na solely depends on the ejected electron energy. As most of the EDX detectors have virtually constant efficiency (~100%) in the range 3-10 keV, the probability and relative height observed for the families of X-ray lines depends heavily on the energy of the ejected electron from the sample. As a result of this, elements with the atomic number up to 17 (Cl: Chlorine) having K-edge below 3 keV is

difficult to detect. According to this logistic, ^{11}Na with K-edge at 1.08 keV will be difficult to detect from the EDX spectrum and the absence of Na-line is been depicted in **Figure 5.4**.

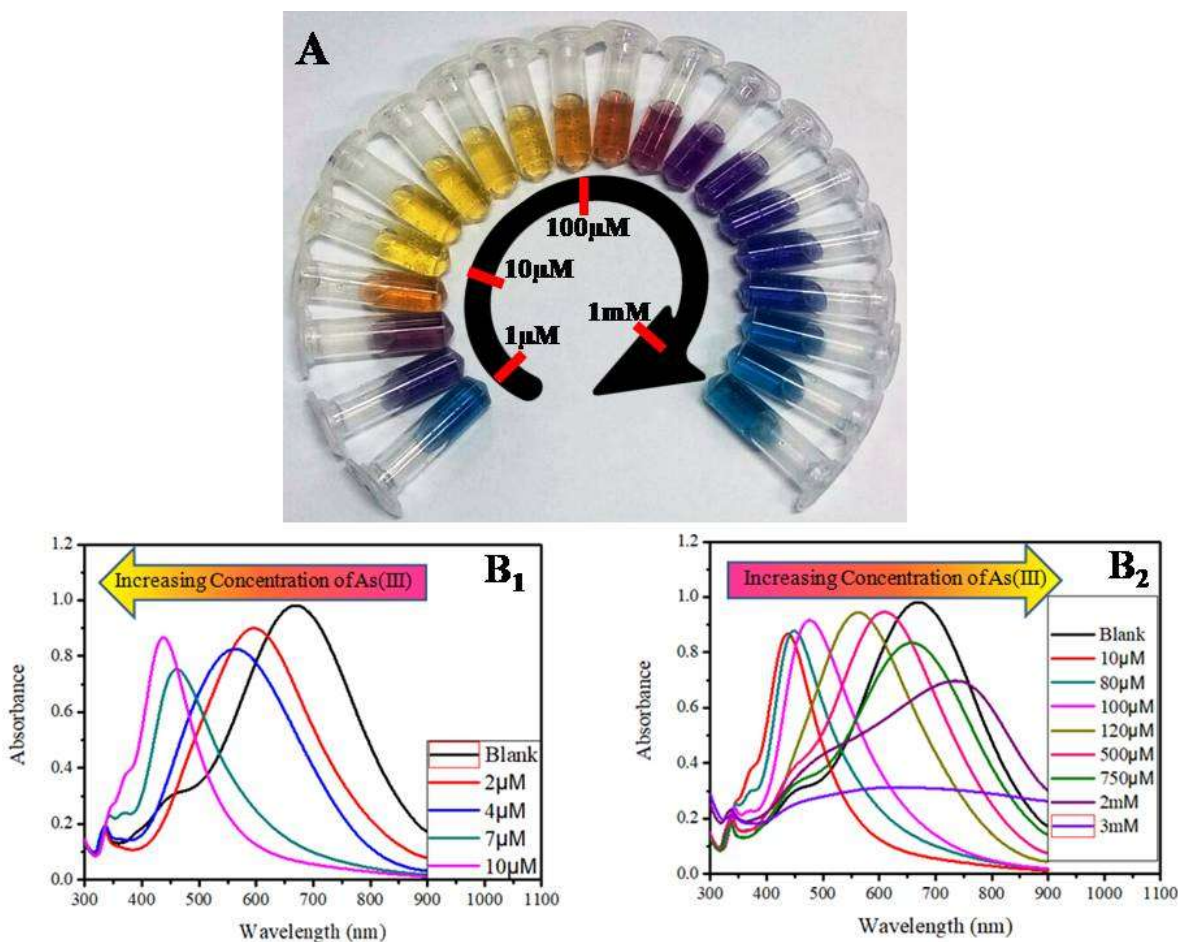


Figure 5.5: (A) Concentration-dependent color-coded sensing of As(III) between the concentration range of 10^{-6} M to 10^{-3} M, (B) Tuning of surface plasmon resonance as a result of morphological change of AgNPr at different concentration of As(III) between 10^{-6} M to 10^{-3} M where (B₁) shows the variation of plasmon band at the different lower concentration of As(III) in the range of 0.0-10.0 μM [0.0 μM (blank): Black trace ($\lambda_{\text{max}}=704$ nm), 1.0-2.0 μM : Blue trace, 2.0-4.0 μM : Orange trace, 5.0-7.0 μM : Red-Violet trace, 8.0-10.0 μM : Blue Violet trace] and (B₂) at different higher concentration of As(III). The Plasmon band and hence the color of the nanomaterials change in a distinct manner where a specific color remains unchanged in a broader

range of growing concentrations as 10.0-80.0 μM : Yellow, 90.0-100.0 μM : Orange, 110.0-200.0 μM : Dark Red, 250.0-500.0 μM : Purple, 750.0 μM -2 mM: Different shades of blue, 3 mM-10 mM: Faded Blue and above 10mM the color becomes faint blue to gray or almost colorless.

As reported in the early literature^{223,270} that As(III) can form a sparingly soluble stable complex with atomic or ionic silver as Ag_3AsO_3 complex, the chemical affinity between As(III) and atomic silver (Ag^0) on AgNPr surface can easily overcome the electrostatic repulsion between AsO_2^- and the negatively charged NPrs to induce the surface leaching. Upon the addition of increasing concentration of arsenite (AsO_2^-) the original blue color gradually changes to purple at 1-2 μM ($\equiv 75\text{-}150$ ppb), burgundy at 2-4 μM , pastel orange at 6-7 μM , golden yellow at 8-9 μM , yellow at 10-40 μM , light yellow at 40-80 μM and repeated these colors as pastel orange at 90-100 μM , brown at 110-150 μM , burgundy at 150-200 μM , blue-violet at 200-350 μM , lavender at 350-500 μM , deep blue at 500-750 μM and finally light blue at 750 μM -2 mM of As(III) (original color of the AgNPr). Corresponding color coding and UV-Vis spectra of each morphologically modified AgNPr is shown in **Figure 5.5A** and **5.5B** respectively. To understand the plasmonic change at lower (in the sub- μM concentration) and higher (above 10 μM concentration) concentration of As(III) we have plotted their UV-Vis spectra in two different figures as **Figure 5.5B₁** and **5.5B₂** respectively. Both **Figure 5.3 (5.3A-5.3E)** and **Figure 5.5B₁** shows the ability of our assay to detect As(III) in the μM level concentration.

With the consequent step-wise morphological change of the nanoprisms which shows a distinct color from the previous morphology²⁴⁸ due to the interaction of As(III) with the metallic core of the nanoprism, we have clearly represented this phenomena by recording the TEM image for each intermediate and has been portrayed details in **Figure 5.3A-H**.

Electronic configuration of As is $[\text{Ar}] 3d^{10}4s^24p^3$ and the corresponding As(III) is $[\text{Ar}] 3d^{10}4s^2$ and As(V) is $[\text{Ar}] 3d^{10}$. Due to the full filled electronic shell structure, As(V) is more stable and inert compared to As(III) having two valance electron to support its reactivity. Moreover due to the bulkier size of arsenate (AsO_3^-) compared to the arsenite (AsO_2^-), accessibility of inter planer space (6-8 Å) in AgNPr stacking by As(V) is less probable than As(III). Along with these two factors, by considering the formation of stable silver arsenite (Ag_3AsO_3) and silver arsenate (Ag_3AsO_4) compounds we have drawn them in Gauss View 5 and performed their geometry optimization by using HF/3-21g* level of theory. Energies for all the components of the following reaction was obtained to calculate the free energy of the reaction: $\text{Ag}_3\text{AsO}_3 + \frac{1}{2}\text{O}_2 \rightarrow \text{Ag}_3\text{AsO}_4$. The absolute energies are shown in **Table 5.2**. Optimized structures of Ag_3AsO_3 and Ag_3AsO_4 are shown in **Figure 5.6** and the information of different atoms of Ag_3AsO_3 followed by Ag_3AsO_4 are given in **Table 5.3**. The free energy of the reaction was found to be -118.5 kcal/mol suggesting Ag_3AsO_4 to be the more stable species.

Table 5.2: Energies obtained at HF/3-21g* level of theory

Compounds	Energy (Hartree/particle)
Ag_3AsO_4	-18043.05142490
Ag_3AsO_3	-17968.59515180
$\frac{1}{2}\text{O}_2$	-74.26744989

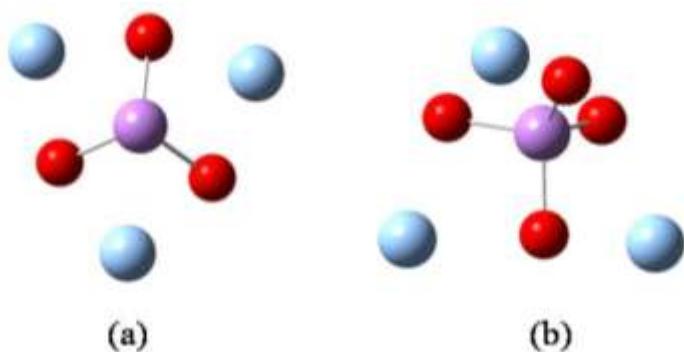


Figure 5.6: Optimized structures of Ag_3AsO_3 and Ag_3AsO_4 . Ag is shown in blue, As in purple and O in red.

Table 5.3: Optimized parameters of Ag_3AsO_3 and Ag_3AsO_4

E (RHF) = -17968.5951518 A.U. after 9 cycles

Standard orientation: Ag_3AsO_3

Center Number	Atomic Number	Atomic Type	Coordinates (Angstroms)		
			X	Y	Z
1	33	0	0.000019	0.000065	1.530613
2	8	0	-1.403607	-0.635236	0.645606
3	8	0	1.251808	-0.897880	0.645174
4	8	0	0.151592	1.533088	0.645129
5	47	0	-1.800588	1.291239	-0.468101
6	47	0	2.018600	0.913665	-0.468039
7	47	0	-0.217990	-2.204944	-0.468063

E (RHF) = -18043.0514249 A.U. after 9 cycles

Standard orientation: Ag_3AsO_4

Center Number	Atomic Number	Atomic Type	Coordinates (Angstroms)		
			X	Y	Z
1	33	0	0.000047	-0.000030	1.016691
2	8	0	-1.491375	0.451258	0.255757
3	8	0	0.354953	-1.517206	0.255592
4	8	0	1.136481	1.066017	0.255688
5	8	0	0.000135	-0.000151	2.651569
6	47	0	-0.569259	2.432903	-0.431888
7	47	0	2.391636	-0.723481	-0.431944
8	47	0	-1.822443	-1.709387	-0.431906

This relative chemical activity and steric hindrance caused by As(III) and As(V) will be discussed in the next section as a factor to explain the selectivity and sensitivity of As(III) for color-coded sensing. Due to the NaBH_4 reduction procedure to synthesize AgNPrs which results from a nanoparticle solution with pH 8.4 and the formation of stable and sparingly soluble silver arsenite (Ag_3AsO_3) and silver arsenate (Ag_3AsO_4) compounds at higher pH, organized assembly of AgNPrs can react instantly with arsenic ions in the intrinsic basic medium. Moreover, due to high pH of the AgNPr solution, it also diminishes the possibility of silver leaching through

oxygen reduction reaction (ORR: $\text{O}_2(\text{g}) + 4\text{H}^+(\text{l}) + 4\text{Ag}(\text{s}) \rightarrow 2\text{H}_2\text{O} + 4\text{Ag}^+$).²⁷¹ As we increase the concentration of As(III), due to the difference in stability between flat surface-bound [111] facets and edge bound [110] facets (free energies increases in the order²⁶⁰: $\gamma_{\{111\}} < \gamma_{\{100\}} < \gamma_{\{110\}}$) the number of pyrrolidone bound silver atoms from edges will be released more compared to flat surfaces. This will result the formation of smaller stackings due to the increase of surface charge originating from pyrrolidone molecules as we observed as an effect of As(III) addition between 1.0-6.0 μM . A gradual reduction in the dimension of AgNPr as a result of increasing the addition of As(III) (by comparing the dimension between B and E of **Figure 5.2**) confirms the removal of pyrrolidone bound silver atoms from [110] facets. The appearance of different surface Plasmon at different lower concentrations (between 1.0-6.0 μM) of As(III) has been depicted in **Figure 5.5B₁** which matches well with the obtained surface plasmons (**Figure 5.1A**) from different stacking lengths synthesized by using different amount of NaBH_4 . Hence at a lower concentration of As(III), the appearance of a different color is due to the transformation of longer AgNPr stacking into smaller piles. At the range of 6.0-7.0 μM of As(III), the stacking of AgNPrs disintegrated completely along with partial leaching of the tips as well as the surface of AgNPrs to produce isotropically distributed silver nanodiscs (average diameter between 15-25 nm) with surface plasmon band appears near 450 nm (green colored spectra in **Figure 5.5B₁**) and the corresponding TEM is shown in **Figure 5.1E**.

If we increase the As(III) concentration further in the range of 8.0-80 μM , silver nanodiscs are leached further to generate smaller nanoparticle (*silver seeds*) with size range 5-7 nm which gives different shades of yellow ($\lambda_{\text{max}}=410\text{-}430$ nm) as we mentioned before and has been represented in **Figure 5.3E**. Similar structural changes have also been observed as an effect of KSCN addition to light blue colored AgNPr solution reported by Tsai et al.²⁴⁰ Further increment

of As(III) concentration (between 90 μM -2 mM), the spontaneous reaction between silver seeds with arsenic removes PVP from nanosurface to initiate the formation of PVP-based controlled emulsions with an average diameter between 50-200 nm which starts incorporating silver seeds and induces controlled aggregation (smaller to larger) with a plasmon shifting between pastel orange to light blue (90-100 μM : λ_{max} = 460-470 nm, 110-200 μM : λ_{max} = 550-560 nm, 250-500 μM : λ_{max} = 600-610 nm and 750 μM - 2mM: λ_{max} =680-720 nm) and the corresponding TEM images are shown in **Figure 5.3F** and **5.3G**. If we increase the concentration of As(III) beyond 2 mM, a reaction between arsenic and silver is so vicious that it ultimately converts all nanomaterials into silver arsenate (Ag_3AsO_3) and forms unpredicted composites to lose plasmonic characteristics of silver nanoparticles which loses its blue color as shown in **Figure 5.3H** to shift the plasmon band much beyond 704 nm and ultimately disappears. Though the generated Ag_3AsO_3 is yellow, black colored aggregated silver material can easily mask the yellow color precipitation originating from Ag_3AsO_3 .

To find out the selectivity of As(III) for the morphological change of AgNPr which results from color-coded sensing of arsenic contamination, we have repeated the same set of experiments (absorbance, TEM and colorimetry) with several other metal salts which includes common alkali, alkaline and toxic transition metal ions including arsenate As(V) and the colorimetric result has been depicted in **Figure 5.7A**. To observe a sharp contrast in colorimetry and to avoid any unwanted interference (from morphological change²⁴⁸) from halogens we have used 30 μM concentration for all non-halide metal salts. Except for some minor contrast change, colorimetry can selectively and sensitively detect As(III).

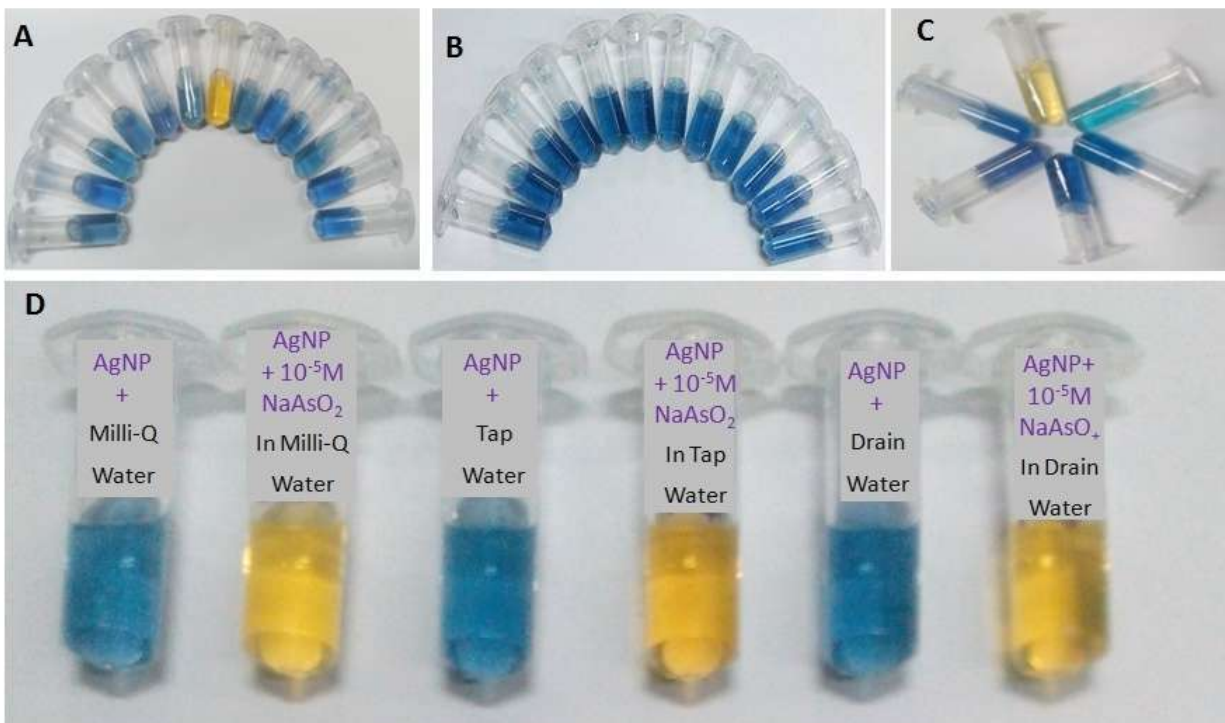


Figure 5.7: Colorimetric change of AgNPr solution upon addition of (A) 30 μM (left to right) Na^+ , K^+ , Ca^{2+} , Mg^{2+} , Sr^{2+} , Cd^{2+} , As^{3+} , Fe^{3+} , Hg^{2+} , Fe^{2+} , Pb^{2+} , Zn^{2+} and As^{5+} metal ions ; (B) NaOH in the concentration range 10 μM -1 mM; (C) Different concentration of arsenic prone water sample into the AgNPr colorimetric assay (D) 0.1 μM NaAsO_2^- dissolved in Milli-Q, tap water and drain water.

To confirm that the color change is not due to the pH change of the solution after the addition of the As(III) salt, we have checked the pH of the blank AgNPr solution and the same solution after the addition of the As(III) salt. We observed that the pH of all the solution was increasing slightly than that of the blank upon the gradual addition of As(III). We have performed a control experiment by adding an equal concentration of NaOH instead of the As(III) salt by considering 1 M NaAsO_2 to generate 1 M NaOH after complete dissolution. The pH in both cases is listed in **Table 5.4**. No color change (**Figure 5.7B**) was observed for pH change due to the addition of NaOH which proves that the role of pH for color tuning is negligible.

Table 5.4: Variation of pH due to gradual the addition of NaAsO₂ and NaOH to 1 mL AgNPr solution

Volume of NaAsO ₂ or NaOH added in 1 mL AgNPr colloidal solution (μL)	pH on addition of NaAsO ₂ (Stock Concentration: 10 ⁻² M)	pH on the addition of NaOH(Stock Concentration 10 ⁻² M)
1	8.39	8.40
5	8.42	8.47
10	8.46	8.54
20	8.48	8.60
40	8.56	8.70
50	8.60	8.82
100	8.80	9.01
Blank	8.34	-

The morphological change of AgNPr upon addition of different concentrations of As(III) which results in the appearance of different colors is also been traced by recording their SERS spectra in presence of crystal violet (CV) as Raman tagging molecule. We have taken 5 μL of 10⁻⁴ M CV and then added to 195 μL of the morphology modified color-tuned AgNPr solutions which we have obtained by adding the same amount of differentially diluted NaAsO₂ into same stock solution of AgNPr to avoid any dilution factor. Obtained SERS spectra from different morphology modified AgNPr are depicted in **Figure 5.8** in a relative intensity scale which includes the SERS signal as a result of As(III) addition in the range of 0-5 mM. It is clear from **Figure 5.8** that there is a gradual increment of the SERS signal intensity as we increase the As(III) concentration from 0 M to 8 μM. It is also clear from the TEM results (**Figure 5.3**) that the gradual increment of As(III) up to 8 μM results the initial destacking of AgNPrs and finally disintegrate each nanoprisms into smaller silver nanoparticles to increase the effective surface

area and results in a gradual increment of SERS signal for the formation of the higher number of hotspots. As we increase the concentration of As(III), the color of the resulted nanoparticle solution changes from golden yellow at 8-9 μM to yellow at 10-40 μM and light yellow at 40-80 μM As(III) due to the formation of smaller sized silver nanoparticles (seeds) and we observed a slight increment of SERS signal. Further addition of As(III) beyond 80 μM , SERS signal gradually reduces till 2 mM concentration and beyond 2 mM concentration of As(III) the resultant materials don't show any detectable Raman signal. Details about the mechanism of SERS and the mathematical formulation of the Raman enhancement factor, G , has been described in detail elsewhere.²⁷² G can be derived by the following equation:

$$G = \frac{I_{SERS}/N_{surf}}{I_{NRS}/N_{vol}}$$

where I_{SERS} is the surface-enhanced Raman intensity, N_{surf} is the number of molecules bound to the nanometallic substrate in the excitation volume, I_{NRS} is the normal Raman intensity and N_{vol} is the number of molecules in the excitation volume. In our estimation of enhancement factor, we have considered the excitation zone as a cube with a dimension of 100 μm or a volume of 10^{-6}cc . By considering the final concentration of CV in SERS experiment and normal Raman experiment as $2.5 \times 10^{-6}\text{ M}$ and 1 M respectively, the number of molecules adsorbed on the nanosurface and in bulk in the excitation volume has been estimated as 15×10^8 and 6×10^{14} molecules respectively. By comparing the Raman peak intensity at 1380 cm^{-1} the obtained enhancement factor (G) in the absence and in presence of $8\mu\text{M}$ (close to maximum SERS signal) of As(III) was calculated as 3×10^6 and 8×10^6 respectively. Depending on the increasing concentration of added As(III), the extent of released PVP also increases and allows the system

to form different diameter polymeric emulsions to incorporate smaller silver nanoparticles formed in the concentration range of 10-80 μM of As(III). Due to the bigger and thicker PVP layer, the accessibility of crystal violet to the core silver nanoparticles decreases gradually as we are forming different morphologically modified AgNPrs at higher concentrations of As(III). This gradual increment of the inaccessibility of CV to nanosurface incorporated inside emulsion results in a gradual reduction in SERS signal as observed in the concentration range between 80 μM -2 mM. Since the emulsion incorporated nanoparticles lose their plasmonic properties beyond 2 mM As(III) concentration, the observed SERS signal at 3 mM disappears as depicted in **Figure 5.8**. Assignments of different Surface Enhanced Raman line originating from CV have been reported and described elsewhere.²⁷³

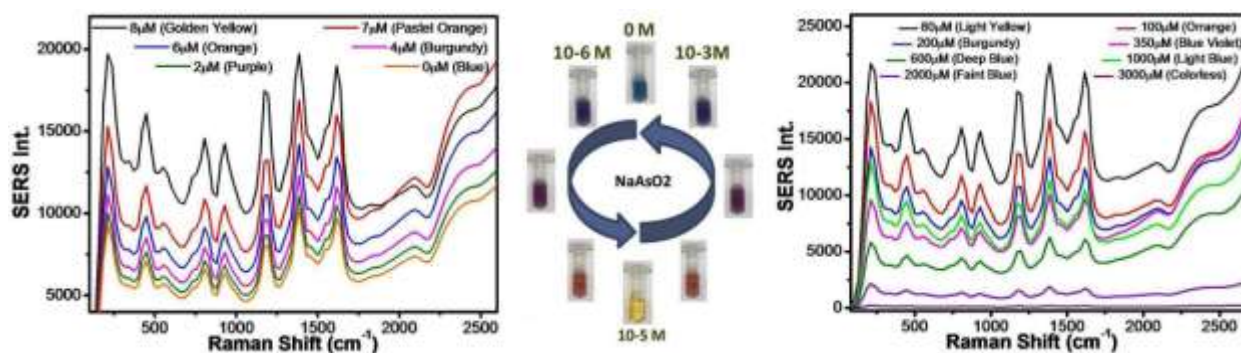


Figure 5.8. (Left) SERS based assay to monitor the morphological modification of AgNPr on the addition of different concentration NaAsO_2 in the concentration range 0-8 μM and the corresponding colorimetric response has been shown by the adjacent anti clockwise arrow;(Right) SERS response in the concentration range 80 μM - 3 mM and the corresponding colorimetric response by the adjacent anticlockwise arrow.

To find the applicability of our proposed AgNPr colorimetric-assay we have performed our investigation on real samples. For high specificity sensing and quantification of As(III) from real

samples, we have collected water from an arsenic prone zone of West Bengal (Duttapukur, North 24 Paraganas), India which has been used years as drinking water by the local people. We have taken 1 mL of our synthesized blue color AgNPr stock solution in each of six different centrifuge tubes (assay tubes) and then added different volumes of arsenic-contaminated water sample (filtrated by 0.2 μm syringe filter) in the range of 0-1 mL. Assay tubes containing arsenic-contaminated water samples less than 50 μL do not show any color change while other assay tubes having contaminated water volume more than 50 μL show usual color change as we have observed in our ideal highly specific colorimetric assay sensing of As(III). Colorimetric transition observed in AgNPr assay upon addition of the different amounts of arsenic prone water sample is shown in **Figure 5.7C**. The detection and quantification of As(III) from the real sample is not very straight forward and may associate with other problems. One such prominent problems come from the considerable presence of additional halides (Cl^- , Br^- and I^-) in the environmental water samples. The morphological effect of halides on AgNPr has been reported earlier²⁴⁸ and discussed in the previous section. So the observed color change may originate both from halide ions and As(III). To confirm the origin of color change, we have titrated the water sample against 10^{-2} M AgNO_3 solution using KCrO_4 as the indicator. From the endpoint, we have calculated the amount of precipitable salt as ~ 2.1 mM. From the literature²⁴⁸ it is known that the color change of AgNPr is observable only when the concentration of halide ion present in the water sample is ≥ 20 mM. Since the precipitable salt concentration is only 2.1 mM in our studied sample which is 10-times less than the threshold halide concentration for color change, rules out the presence of any substantial amount of halide which can independently cause color change. Hence, the observed color change is solely originating from As(III) present in the water sample and the threshold concentration for As(III) detection in the micromolar range (1-2 μM)

shows its hypersensitivity. Along with arsenic-contaminated real water sample, we have applied our assay on different sourced water samples collected from Milli-Q filtration system (Synergy, UV), Tap water and drain water from Kolkata region. After initial filtration by 0.2 μm syringe filter we have infused them separately with NaAsO_2 to reach the desired 100 μM concentration of As(III). Once we add 100 μL of Milli-Q water as control and As(III) infused water as test samples separately in a set of two 900 μL blue color AgNPr solution, all of them show desired golden yellow color for the infused samples and no color change for the blank which proves zero interference from other components of water. Since WHO reports that the average halide (mainly Cl^-) concentration in water is only 4 μM (much lower than the interference level) in drinking water, our AgNPr-based assay can successfully be used for As(III) sensing in drinking water without much interference from halide ions.

5.4 Conclusion:

AgNPr-based assay has been designed and the experimental procedure has been elaborated to achieve the wide range morphologically modified surface Plasmon tuning-detuning for accurately color-coded detection and sensing of As(III) over other alkali, alkaline, and transition metals. Wide range morphological modification of AgNPr is measured and confirmed by TEM measurement and a plausible explanation has been provided to understand the mechanism of selective interaction of As(III) with axially stacked AgNPrs based on their zeta potential, plasmon tuning-detuning and surface enhanced Raman spectroscopy along with DFT calculation. Plasmon tuning-detuning positively not only confirms the presence of As(III) but also can detect the As(III) concentration up to a limit of 75 *ppb* which is close to the old EPA limit for As(III) content in drinking water. This is probably the first report where we have

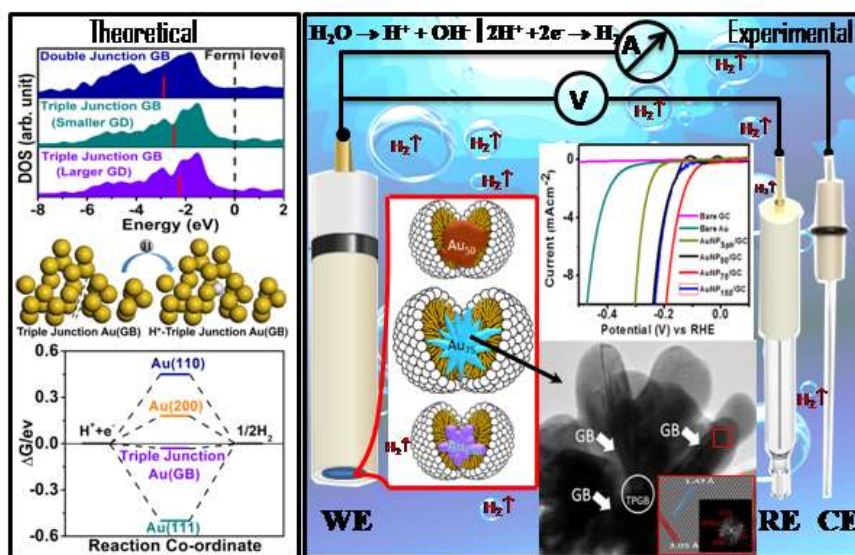
explored the critical role of PVP for wide range morphological modification followed by emulsion induced aggregation to effectively tune the surface plasmon for color-coded sensing of heavy metals. Ours cross-check with As(III) containing real sample from arsenic prone area of West Bengal, India and As(III) infused real water sample from different sources proves the potential applicability of this assay as a colorimetric sensor for field application towards environmental protection drive.

CHAPTER-6

Unveiling the Excellent Electrocatalytic Activity of Grain-Boundary Enriched Anisotropic Pure Gold Nanostructures towards Hydrogen Evolution Reaction: A Combined Approach of Experiment and Theory

OUTLINE: Specific Points of Discussion

- The role of grain-boundary and grain size of our newly synthesized flower-like gold nanostructures for the hydrogen evolution reaction (HER) has been investigated quantitatively.
- All the synthesized anisotropic gold nanoparticles (AⁿGNPs) and especially the AuNP₇₅ exhibit outstanding catalytic activity (in terms of both overpotential and turnover frequency) towards HER compared to spherical shaped gold nanoparticles (S^pGNPs).
- The effective contribution of grain-boundaries towards the free energy of hydrogen adsorption (ΔG_{H^*}) and the position of the d-band center has been explored by DFT-calculation which matches well with our experimental findings.



6.1 Introduction

In the recent few years, considerable attention has been paid to developing the strategies to generate renewable energy as it is an alternative and naturally replenished source to that of the limited resource of fossil fuel.^{274,275} With the increasing demand for fuel as well as for environmental benefits, renewable energy is more preferable to other traditional energy sources.²⁷⁶ Among different renewable energy, Hydrogen is regarded as a green fuel with high energy density and pollution-free fuel (cost-effectiveness and environmentally friendly) which can be an alternate and competitive to that of coal or oil.^{277–280} Electrolysis of water is the most feasible approach^{281,282} to get the molecular hydrogen effectively and enormously as the source is unlimited and replenished inhuman timescale. The electrochemical water splitting involves two half-cell reactions wherein the oxygen evolution reaction (OER) occurs at the anode and the hydrogen evolution reaction (HER) takes place to that of the cathode.²⁸³ However, both of these reactions are extremely sluggish in nature which requires a larger overpotential.^{284,285} Though a large group of scientists throughout the Globe has put their extreme effort to design an array of suitable electrocatalysts, enough effort has not been put forward to explore different characteristics within the traditional materials by tweaking their nanoscale crystallization pattern or bringing folds within single- or multi-twinned nanoparticle for boosting the reaction kinetics. This will not only reduce the effort to design a new class of materials and cost to perform their complete characterization, but also to control environmental pollution. It has been found that the Platinum based materials especially carbon supported Platinum (Pt/C) are the most viable and efficient electrocatalysts for the HER till date,^{286–288} but their high cost and low abundance restrict themselves for commercialization and large scale production of H₂.^{289,290} Several attempts have been taken to accelerate the reaction kinetics by employing various transition metal-based catalysts (e.g. Ru-, Mo-, Ir-based materials),^{291–293} metal alloys,²⁹⁴ chalcogenides,²⁹⁵

metal-organic frameworks,²⁹⁶ etc. In this aspect, the noble metals like gold is rarely been explored due to the poor adsorption or binding efficiency of H-atom on the gold surface which requires higher free energy to step up the reaction.²⁹⁷ HER generally consists of two step process in which the first step is the adsorption of hydrogen atoms on the surface of the catalyst (this step is called Volmer step) and the second step leads to the generation of hydrogen molecule followed by desorption from the catalyst's surface (this step is known as Tafel or Heyrovsky step).²⁹⁸ Sabatier's principle suggests that the adsorption energy should neither be very high nor very low for a preferable catalyst since the higher adsorption energy leads to an endothermic process resulting weaker adsorption while the lower adsorption energy possesses exothermic process which results in the slow desorption.²⁹⁹ It has been predicted from the Volcano plot that the Gibbs free energy (ΔG) for an effective electrocatalyst towards HER process should be close to zero (i.e. $\Delta G \approx 0$). In the Volcano plot, the Pt metal possesses the highest activity in terms of both current density (j_0) as well as favorable ΔG value. However, in case of Au metal, the poor interaction of H-1s orbital with the d-band of metal makes the gold nanoparticles as a poor candidate for HER.²⁹⁸ Most of the literature reports covered the influence of other metals (e.g. alloys of Au)³⁰⁰ or semiconductor or organic molecules³⁰¹ with gold nanoparticles for the HER activity. Therefore, it is really a challenging task to build a feasible electrocatalyst for HER using pure gold nanoparticles.

Further, it is worth to mention that among various noble metals, gold nanoparticle has attracted greater attention over the last few decades due to their distinct physicochemical properties e.g. easier size and shape tenability to achieve both larger surface to volume ratio (S/V) and differential electric field lensing at the surface or vertex, enhanced surface Plasmon resonance (SPR) and hence the extinction coefficient in the VIS-to-NIR region. Higher reduction

potential of Au^{3+}/Au system ($E^0 = 1.50 \text{ V vs SHE}$) allows to use weak reducing agent resulting slow crystallization and hence programmable crystal twinning, easy manipulation of facet energetic as well as ease of surface modification (for selectivity and sensitivity) in comparison with that of bulk gold.³⁰² The fine blending of distinctive optical and electrical properties of gold nanoparticles (AuNPs) rendered themselves as a potential candidate in extensive fields of research such as catalysis,³⁰³ biomedicine,³⁰⁴ biosensors,³⁰⁵ and surface-enhanced Raman spectroscopy.³⁰⁶ Indeed, the performance of the AuNPs in the aforementioned applications, more specifically the catalytic performance strongly rely on their morphology, surface charge, crystal irregularity as well as crystal facet energy.³⁰⁷⁻³⁰⁹ In the recent few years, the anisotropic gold nanomaterials (i.e. flowers, multipod, star-shaped, branched) have extensively been focused since they reveal unique SPR, SERS as well as efficient catalytic power than the corresponding spherical particles.^{59,310} The remarkable catalytic efficiency of the AⁿGNPs is associated with the appearance of high the density low coordination site atoms on edges, terraces, steps, ledges, and kinks which may alter the surface energy.³¹¹ Further, the presence of planner defects such as grain boundary, twin boundary, stacking fault into the nanocrystal can significantly alter the reactivity of nanomaterials.³¹² In recent reports, it has been shown that the electrocatalytic activity of AuNPs is significantly boosted for the reduction of CO_2 due to the occurrence of the high density of grain boundaries.^{21,79} In addition, the grain boundary induced catalytic activities with remarkable efficiency are also observed for copper nanoparticles towards the electroreduction of CO .³¹³ Further, the presence of multiple twin boundaries (MTB) onto the nanoparticle surface enhances the catalytic ability for the oxidation of methanol via facile chemisorption of analytes.³¹⁴ In addition, from our previous study³¹⁵ we know that the anisotropic nanomaterials which result in sharp tips with enhanced ability to focus the surface

electric field and hence modulate the charge density has a distinct influence on their catalytic activity. Hence, the anisotropic nanomaterials are more preferable for both catalytic performances as well as to explore the new aspects related to catalysis than the isotropic counterparts. However, the anisotropic growths of nanoparticles are strongly dependent on the adopted synthetic procedure. Therefore, the synthetic methodologies are also crucial for the inducement of important physico-chemical properties into noble metal nanoparticles.

The standard protocols have already been well documented in the literature for the generation of AⁿGNPs including template-based reaction,³¹⁶ multi-step seeding methodology,^{317,318} utilization of specific capping agents,³¹⁹ fine tuning of physical parameters (i.e. temperature, pH, viscosity) during synthesis. The seeding growth approach is the most familiar method for the anisotropic growth of AuNPs since the degree of anisotropy (i.e. aspect ratio, tunable geometry) can be altered simply by varying the amount of seed solution, introducing specific impurities (e.g., AgNO₃, NaCl)³²⁰ as well as by altering the concentration of capping agent. However, the main drawback of this technique is its time-consuming nature as well as the growth of nanoparticles which depends mostly on the nature of nanoseed. On the other hand, template-based synthesis is more fascinating since they offer an interesting and useful characteristic to the nano materials such as controlled sizes, morphologies, and different physicochemical properties.²⁴⁵ Both soft and hard templates have been successfully employed for the synthesis of different shaped AuNPs viz. nanorods, nanorings, nanotubes, as well as porous structures. The soft templates are mainly large organic compounds (i.e. surfactants or polymers), used for surface stabilization while the porous solid inorganic materials such as an anodic aluminum oxide (AAO), mesoporous oxides, and carbon nanotubes (CNTs) can be used as hard templates.³²¹ Although the hard templates having better control over the structure of

nanomaterials, on account of their difficulty in the removal process after synthesis may destroy or alter the actual physical properties of templated nanoparticles. Besides, the surfactant (soft templates) assisted wet chemical synthesis is more preferable due to its ease of surfactant removal, large scale production, and remarkable ability to generate variable size and shape nanoparticles through the micelle formation.³²¹ Hence, surfactant induced rapid, a single-step methodology is worth enviable for the synthesis of anisotropic metal nanoparticles.

In the present study, we have reported a facile, one-step synthesis of gold nanoparticle using hydroquinone (HQ) as a reducing agent in the presence of sodium dodecyl sulfate (SDS). The proposed synthetic protocol is new in the literature, cost-effective, rapid yet generates high quality monodispersed nanoparticles with excellent stability. The morphology as well as the size of gold nanoparticles can easily be tuned from bud to flower (bloom) to over-bloomed shape by simple variation in the concentration of HQ. The characterizations of the synthesized nanoparticles have been carried out using UV-Vis, SEM, HRTEM, XPS and Zeta Potential analysis. The synthesized nanoparticles with variable grain parameters exhibit an outstanding electrocatalytic activity towards hydrogen evolution reaction (HER) in different pH medium (i.e. acidic, neutral, and basic) with a low onset potential of -76 mV. Besides, it requires mere 190, 285, 325 mV (vs RHE) of overpotentials to achieve 10, 50, 100 mAcm⁻² current density in 0.5 M H₂SO₄ medium. DFT study shows that the presence of high-density grain boundary with the larger dimension of each grain on the surface of nanocrystal can significantly enhance the reaction kinetics for HER and hence improves the HER activity.

6.2 Synthesis of AuNPs using HQ:

In a typical synthesis, 0.058 g of SDS was added to 20 mL of Milli-Q water in a 50 mL conical flask and stirred (500 rpm) for five minutes to make 0.01 M solution. After the complete

dissolution of SDS, 0.5 mL of 10^{-2} M $\text{HAuCl}_4 \cdot 3\text{H}_2\text{O}$ (Final concentration: 2.5×10^{-4} M) was added into the solution. Subsequently, 75 μL of 0.1 M HQ (Final concentration: 3.75×10^{-4} M) was added dropwise to the above solution mixture under the same constant stirring. The color of the solution changes immediately (within 5 s) from light yellow to cyan color and the resultant solution was kept undisturbed for another 6 hours for complete growth of nanoparticles. The synthesized nanoparticles were then washed repeatedly by centrifugation at a speed of 2000 rpm for 45 minutes initially and then 30 minutes in order to ensure the removal of excess surfactant and other unwanted products. The entire reaction was carried out at 25 ± 1 °C. In order to study the effect of concentration of reducing agent, a similar protocol was also adopted for synthesizing AuNPs using the variable concentration of HQ at identical concentrations of metal ion and SDS as mentioned earlier. The addition of the lower amount of HQ (50 μL of 0.1 M) into the reaction mixture leads to change the color of solution from light yellow to pink color while at the higher concentration of HQ (150 μL of 0.1 M), the solution turns into bluish color indicating the formation of different sized and/or shaped nanoparticles. The synthesized nanoparticles were washed using the same procedure as mentioned earlier. The prepared AuNPs using 50, 75, and 150 μL of HQ are designated as AuNP_{50} , AuNP_{75} and AuNP_{150} respectively.

6.3 Computational Details:

All the spin-polarized calculations were performed within the framework of density functional theory (DFT) using the plane-wave technique as implemented in Vienna Ab Initio Simulation Package (VASP).¹¹⁵ The exchange-correlation energy was accounted within the generalized gradient approximation method (GGA) parameterized by the Perdew-Burke-Ernzerhof (PBE).³²² We used the projector augmented wave potential (PAW) to treat the ion-electron interactions. The DFT-D2 empirical correction method proposed by Grimme was

applied for describing the effect of van der Waals interactions.³²³ In all computations, the kinetic energy cut off is set to be 500 eV in the plane-wave expansion. All the structures were fully relaxed (lattice constant and atomic position) using the conjugate gradient method and the convergence threshold was set to be 10^{-4} eV in energy and 0.01 eV/Å in force. For geometry optimization, the Brillouin zone was sampled using a 5×5×1 Monkhorst-Pack k-point mesh while a higher 7×7×1 Monkhorst-Pack grid was used to calculate electronic density of states (DOS). The relative free energy of adsorbed atomic hydrogen (H*) was calculated as^{134,300}

$$\Delta G_{H^*} = \Delta E_{H^*} + 0.24$$

where ΔE_{H^*} for the adsorption of H* on various surfaces were determined using the relation

$$\Delta E_{H^*} = E_{surface+H} - E_{surface} - \frac{1}{2}E_{H_2}$$

In order to model Au (111) and (110) surfaces, we considered a 2-layer periodic 3×3 slabs of cell (8.11×8.11 Å²) and (7.91×7.93 Å²) with 18 atoms respectively, whereas Au (200) surface was constructed with 3-layer periodic 3×3 slab of the cell (7.95×7.95 Å²) with 27 atoms. Grain boundaries (GB) have been constructed with different surfaces where GB_a corresponds to the grain boundary between (110) and (111) planes as well as GB_b, GB_c, GB_d, GB_e corresponding to the grain boundaries among (110) and (200), (200) and (111), (110)(200) and (111) with smaller grain diameter, (111), (110)(200) and (111) with larger grain diameter respectively. GB_a, GB_b, GB_c, GB_d and GB_e have been modelled with periodic supercell consisted with 16, 20, 20, 28, and 28 Au atoms respectively. To avoid the spurious interactions between the neighboring slabs, a vacuum layer of 20 Å was used in the direction perpendicular to the surfaces (along the Z-direction) and the nearest distance between the two adsorbed hydrogen atoms in the adjacent supercell is ~10 Å.

6.4 Results and Discussion

6.4.1 Optical and Structural analysis of AⁿGNPs

The synthesis of AⁿGNPs using HQ as the reducing agent in the presence of SDS as a template is schematically shown in **Figure 6.1A**. In general, the surfactant form micelle through the hydrophilic-hydrophobic interaction with the solvent molecule above a particular concentration termed as critical micelle concentration (CMC). Since in the present study we have employed a larger concentration of SDS (0.01 M) than its CMC (CMC of SDS is 0.0082 M), the formation of micelles takes place obviously (shown in **Figure 6.1A**). The addition of metal salt into the SDS solution may lead to the incorporation of metal ion ($[\text{AuCl}_4]^-$) into the SDS micellar cavity. However, the incorporation of chloroaurate ion into SDS micelles is less favorable in this context due to the hydrophobic nature of the inner core of micelles (where the long tail i.e. hydrophobic part remains inside and hydrophilic part remains outside of the core). The presence of metal ion (chloroaurate ion) at the periphery of the micelles is more complimentary on account of its facile interaction with the hydrophilic part of the surfactant. It is worth mentioning here that $[\text{AuCl}_4]^-$ ion may be repelled at the periphery of the micelle due to the presence of anionic group of the surfactant. Indeed, this possibility is nullified on account of the existence of counter ion of SDS i.e. Na^+ with the anionic part $[\text{CH}_3(\text{CH}_2)_{11}\text{OSO}_3]^-$. It has been reported that, the increase in concentration of counter ion of surfactant (i.e. Na^+) leads to alter the size of micelle which provides the confirmation for the occurrence of Na^+ surrounding the micelle of SDS.^{324,325} The occurrence of Na^+ at the periphery of micelles diminishes the repulsion between hydrophilic head group and $[\text{AuCl}_4]^-$ and hence the later can exist close to the SDS micelle. The addition of HQ in the reaction mixture results in the reduction of Au^{3+} to Au^0 and this Au^0 incorporate into the micelle core as schematically represented in **Figure 6.1A**. In this case, two

possibilities may arise; either the Au atoms begin to associate with each other followed by encapsulation into the micelle core or get incorporated into the micelle core followed by preferable crystallization or assembling.

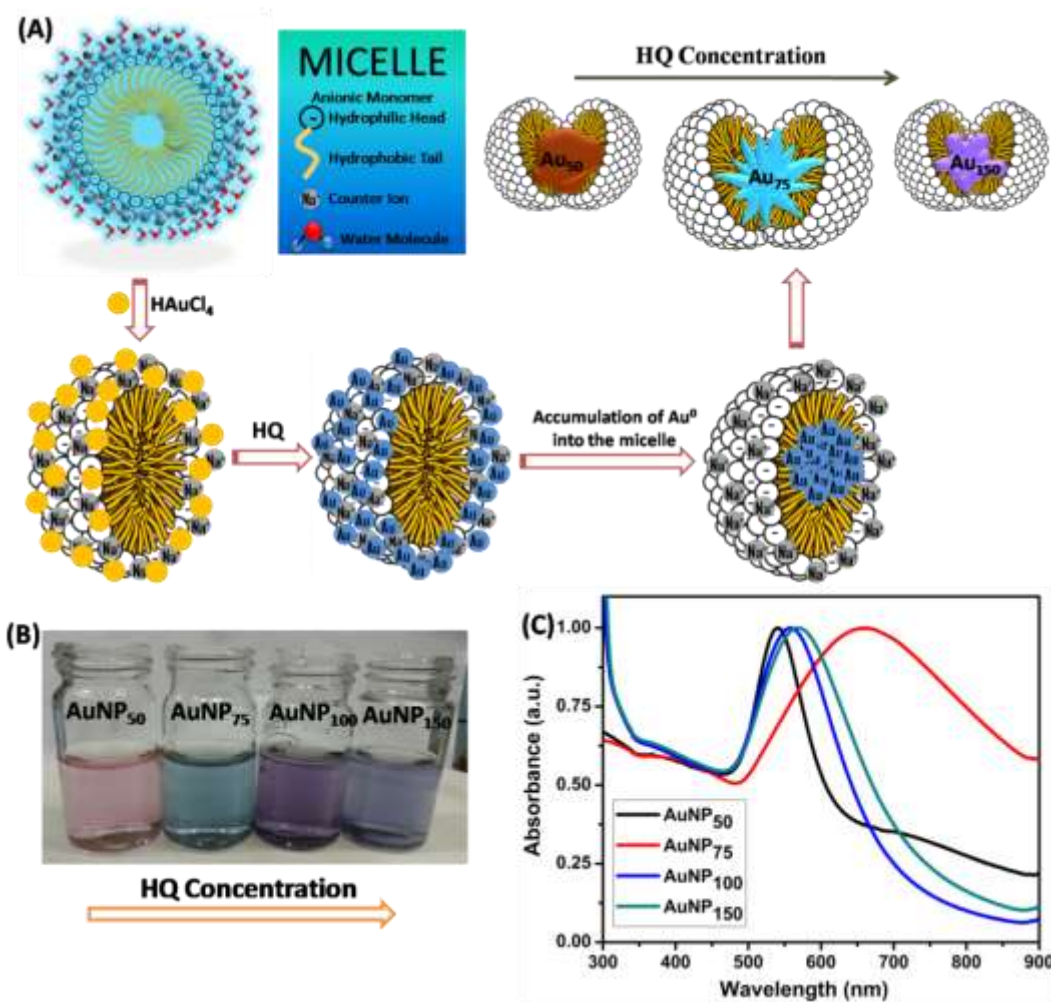


Figure 6.1: (A) Schematic representation for the synthesis and growth of AⁿGNPs inside the SDS micelle's core. Effects of HQ concentration (250-750 μ M) on (B) visual color appearance (pink to blue) and (C) plasmon spectra (540-660 nm) of colloidal AⁿGNPs.

Change in the concentration of HQ leads to alter the color of the resultant colloidal solution (**Figure 6.1B**) which predicts the formation of different nanoparticles with variable physico-chemical properties. The initial assessment of the synthesized AⁿGNPs was carried out

by UV–Vis spectroscopy (**Figure 6.1C**) in the aqueous medium. The AⁿGNPs prepared using 50 μL of HQ (10^{-1} M) in presence of SDS exhibit a sharp surface plasmon resonance (SPR) band in the wavelength range of 500–600 nm with λ_{max} at 540 nm. The color of the colloidal solution (pink) and the nature of the absorption band (i.e. single plasmon band with λ_{max} : 540 nm) suggests the formation of monodispersed spherical shaped-gold nanoparticles (AuNPs).

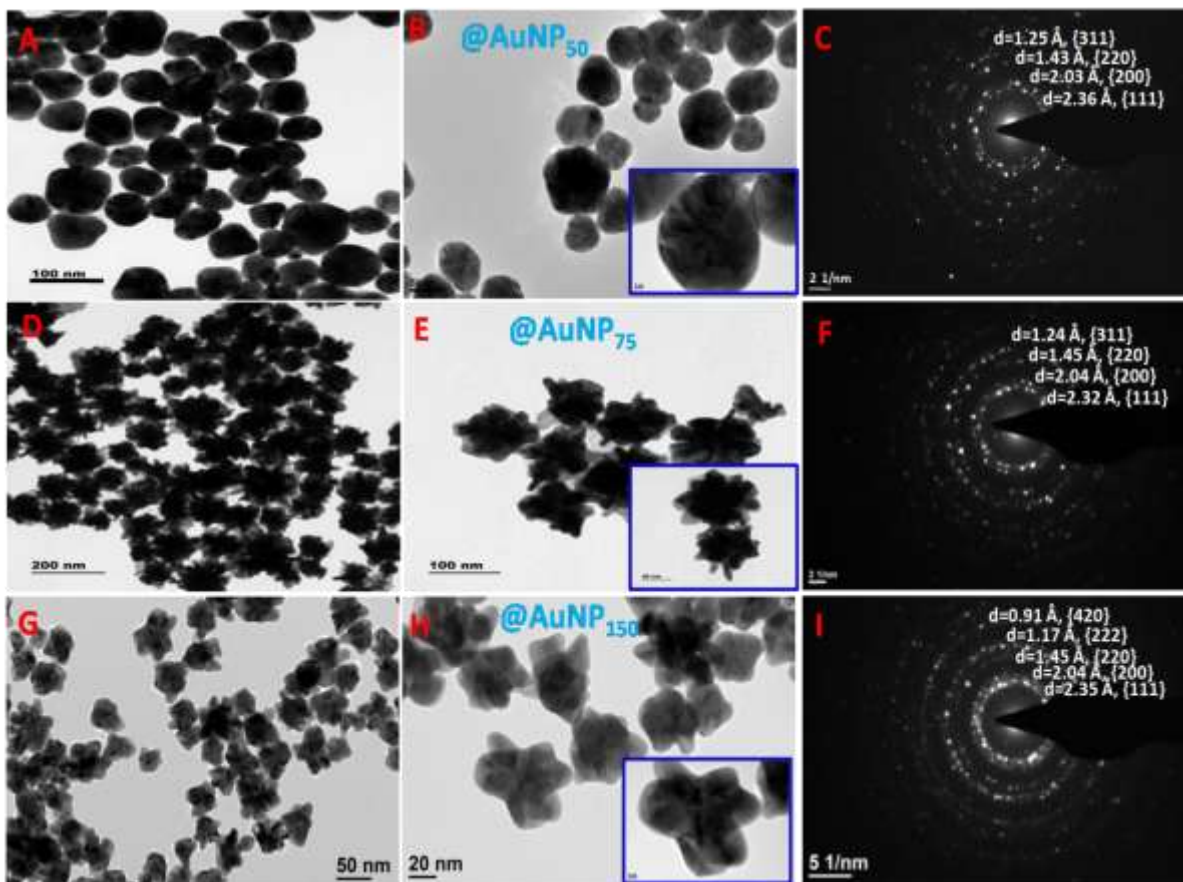


Figure 6.2: The TEM images of bud or spherical (A, B), flower or bloom (D, E) and hexapod or over bloom (G, I) shaped AuNPs synthesized using 50 μL , 75 μL and 150 μL of HQ respectively at different magnification. The SAED patterns of AuNP₅₀ (C) AuNP₇₅ (F) and AuNP₁₅₀ (I) exhibit the polycrystalline nature of different shaped AⁿGNPs and the presence of different crystal planes. The inset in (B), (E) and (H) represent magnified images of the individual nanoparticles.

Increasing the amount of HQ from 50 to 75 μL results in the red shifting of SPR band from ca. 540 nm to ca. 660 nm and also the color of the colloid changes from pink to cyan. The appearance of the absorption band at higher wavelength region in association with broadening nature suggests the formation of large-sized nanoparticles or anisotropic formation of AuNPs as indicated earlier in the literature.³²⁶ Further rise in the amount of HQ from 75 to 100 or 150 μL results in the alteration of color from cyan to bluish along with the blue shifting of the SPR band from 660 nm to ca. 580 nm. The stability and surface charge of these AⁿGNPs are investigated using zeta potential measurements wherein all of these nanoparticles show the zeta potential value of ~ -35 mV indicating the good stability of our designed AuNPs. The negative charge of the nanoparticles can be correlated to the presence of anionic surfactant SDS on their surface.

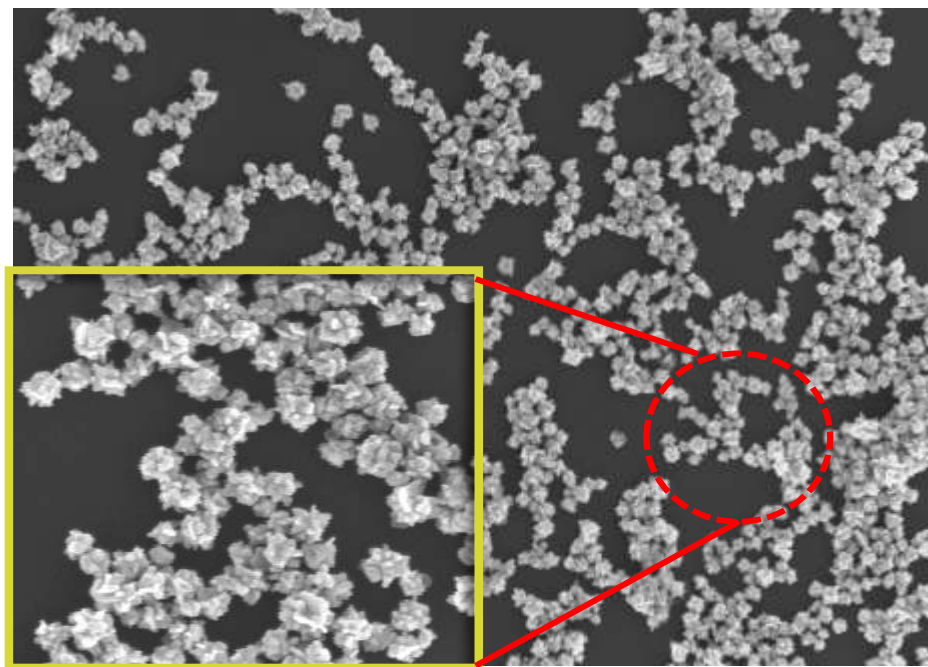


Figure 6.3: SEM image of flower or bloom shaped AuNPs i.e. AuNP₇₅.

The role of HQ on the morphology of AⁿGNPs has been studied wherein the geometry varies with the concentration of reducing agent. At lower concentration of HQ (i.e. 50 μL of 0.1 M) in presence of a fixed concentration of SDS and Au³⁺ leads to the formation of distorted

spherical shaped AuNPs as can be revealed from TEM images (**Figure 6.2 A, B**). The obtained nanosphere can also be considered as bud shaped geometry in which the multiple facets are clearly observable. The average diameter of these nanospheres varies from 55-65 nm. As the concentration or the amount of HQ increases from 50 to 75 μL , the geometry of AuNPs changes from bud to flower or bloom shape which can be observed from the corresponding TEM images (**Figure 6.2D, E**). These gold nanoblooms are monodispersed in nature. In general, these flower-like anisotropic nanostructures can further be considered as a distorted sphere consisting of sharp tips or branches on their surface. The average diameter of these nanostructures is 90 ± 5 nm. These tips or branches of AuNP₇₅ are originating from the core of the nanostructures as can be observed from the HRTEM images. Each of the nanostructures consists of more than ten tips or pods and hence this shape can also be termed as multipodal nanoparticle. The scanning electron microscopy (SEM) image also depicts highly monodisperse bloom or flower-like morphology as shown in **Figure 6.3**.

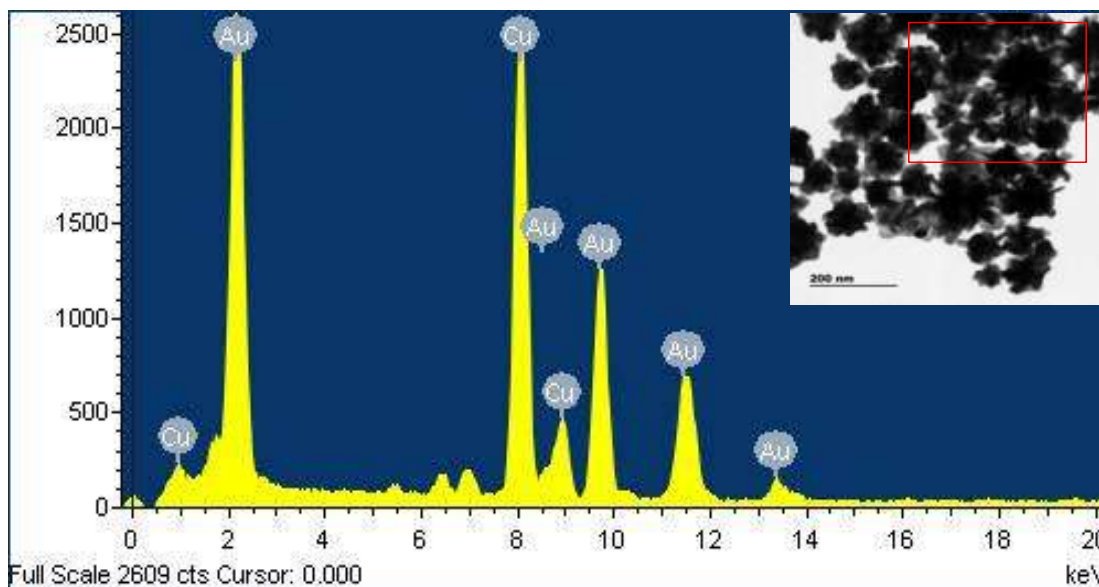


Figure 6.4: EDAX spectra of flower or bloom shaped AuNPs i.e. AuNP₇₅.

The energy dispersive X-ray (EDX) analysis also confirms the presence of Au in the flower-like nanostructures (**Figure 6.4**). Further rise in the concentration of HQ (100-150 μL of 0.1 M) results the formation of over-bloomed morphology. Each of this over-bloomed (popcorn shaped) structure consists of five to six pods or tips (in 2D space) and these tips are blunted in comparison with the flower shaped AuNPs (**Figure 6.2G, H**). The average dimension of these popcorns is 60 ± 5 nm. All these nanostructures synthesized here are poly-crystalline in nature and are randomly oriented along with the face centered cubic (fcc) structural pattern as evidenced from the selected area electron diffraction (SAED, **Figure 6.2C, F and I**) patterns. Increase in concentration of HQ from 50 μL to 75 μL leads to alter the morphology as well as the size of AuNPs from sphere to flower (bloom) shape which can be explained in the following manner: At higher concentration of HQ, the reaction kinetics for the reduction of Au^{3+} to Au^0 is faster which also increases the population of Au^0 . The availability of higher amount of Au^0 in the reaction mixture enhances the growth rate and thereby assists the preferential deposition of Au^0 on the high energy facets leading to the formation of flower or bloom shaped GNPs. Further rise in amount of HQ from 75 μL to 150 μL (of 10^{-1} M) result in the formation of over-bloom shaped AuNPs. In this synthetic protocol, the role of HQ can be envisaged in multiple directions. At higher concentration of HQ, the reduction rate as well as the population density of Au^0 enhances. Besides, HQ undergoes oxidation (as shown before; during the reduction of metal ions) by the removal of hydrogen ion (H^+) which alter the pH of the medium. Increase in concentration of HQ results the enhancement in the liberation of H^+ ions and thereby decreases the pH of the medium. Change in pH result the variation in the shape and size of micelle/micelle core as reported earlier.³²⁷ In this case also the higher concentration of HQ changes the shape and size of

micelles from its original structure due to the alteration in pH and facilitates the formation of hexapod-like AuNPs.

In order to explore the oxidation state of metal as well as the binding phenomena with different functional groups, we have studied the X-ray photoelectron spectroscopy (XPS) for the

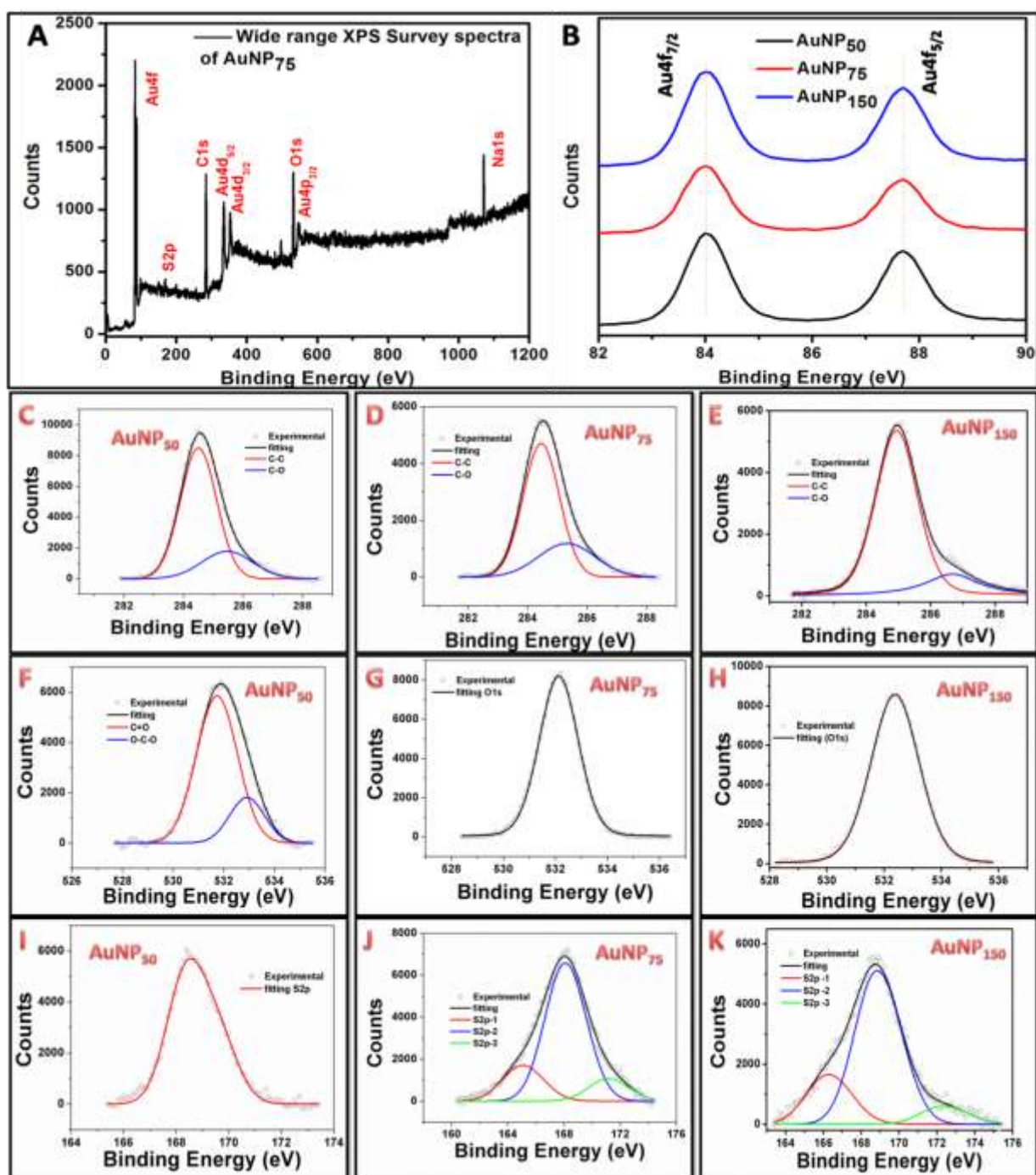


Figure 6.5: XPS spectra of variable shaped AⁿGNPs: (A) Wide range survey spectrum indicating the presence of different elements into AuNP₇₅. (B) Au4f high-resolution spectra. (C, D, E) represent C1s spectra while (F, G, H) show O1s spectra and (I, J, K) depict the S2p spectra (~165 eV (S2p-1) for free R-SH, ~169 eV (S2p-2) and ~172 eV (S2p-3) for Na₂SO₄) for different AuNPs.

synthesized AⁿGNPs. Essentially all the AⁿGNPs shows a similar feature in the wide range survey spectrum (**Figure 6.5A** and **Figure 6.6**) as well as in the Au binding energy spectra (**Figure 6.5B**). The survey spectra show the presence of gold, sulfur, carbon and oxygen element. The Au4f binding energy spectra are split into Au4f_{5/2} and Au4f_{7/2} for all the nanoparticles which appear at 84 eV and 87.5 eV respectively. These values are consistent with the elemental gold (Au⁰), indicating the presence of pure AuNPs.³²⁸ However, the binding energy spectra for different elements (e.g. C, O, and S) that are present into the AⁿGNPs are dissimilar. The source of C, O, and S elements into the nanoparticle are from the surfactant SDS or the reducing agent HQ. The high-resolution scan for C binding energy spectra shows two deconvoluted peaks at 284.5 eV and 285.5 eV due to C-C and C-O bond respectively which are similar for both AuNP₅₀ and AuNP₇₅; however, a shift is observed in C-O bond (286.7 eV) for AuNP₁₅₀.

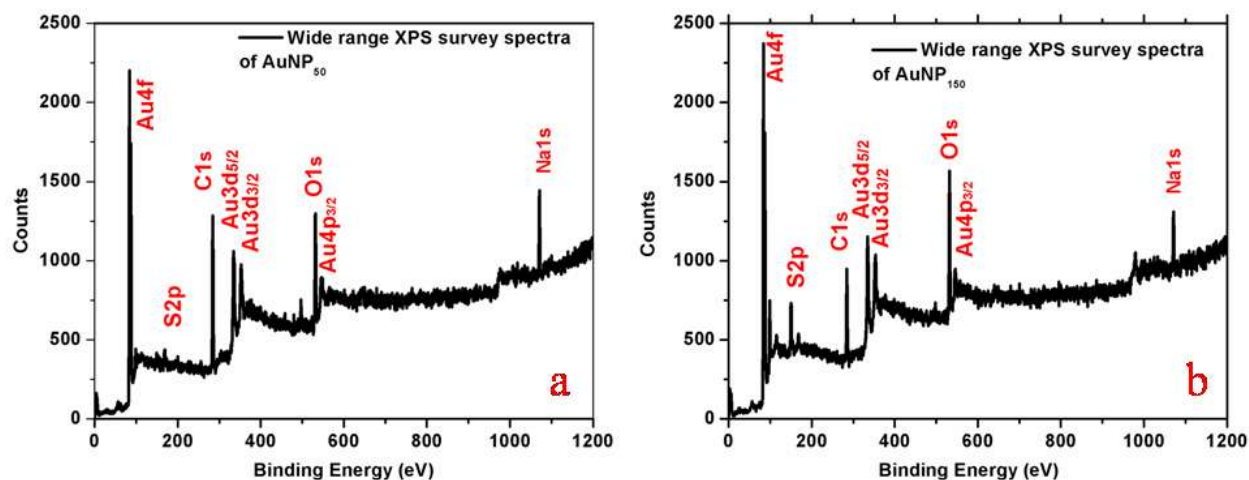


Figure 6.6: Wide range survey spectrum indicating the presence of different elements into (a) AuNP₅₀ and (b) AuNP₁₅₀.

Further, the resolution scan for O binding energy spectra depicts exclusively one deconvoluted peak for both AuNP₇₅ and AuNP₁₅₀ at ~532 eV which is attributed to C=O. While a dissimilar trend is noticed for AuNP₅₀ in which two deconvoluted peaks arise for C=O and O-C-O at ~531.5 and 533 eV respectively. The presence of C=O is due to the formation of quinone (as Au³⁺ reduces, thereby the oxidation of hydroquinone occurs). The resolution scan for S binding energy spectra exhibits three deconvoluted peaks at ~165, ~168 and ~171 eV for AuNP₇₅ as well as AuNP₁₅₀ with slight alter in peak position. However, for AuNP₅₀, only one peak observed at ~168.5 eV. The peak appears at 165 eV is due to free R-SH while the peaks at around 168-172 eV are due to the sulphates. This clearly indicates the presence of surfactants into the nanosurface of the different AⁿGNPs synthesized here. From the variation in the binding energy spectra of the various elements for different geometries, it can be predicted that the change in the concentration of reducing agent leads to alter the micellar properties of the surfactants as discussed above.

6.4.2 Electrocatalytic Performance of AⁿGNPs for Hydrogen Evolution Reaction:

In order to investigate the electrocatalytic activity of the synthesized AⁿGNPs towards hydrogen evolution reaction (HER), we have performed HER in different electrolyte medium (e.g. H₂SO₄, PBS, KOH) with variable pH. The HER activity of the variable shaped AuNPs was studied with the aid of linear sweep voltammetry (LSV) techniques at a scan rate of 10 mV/s with the stirring rate of 500 rpm. **Figure 6.7A** depicts the LSV response of different shaped AuNPs in 0.5 M H₂SO₄ medium (pH=0) wherein the flower-shaped AuNPs i.e. AuNP₇₅ modified GC electrode exhibit much lower onset potential value of -76 mV vs RHE compared to that of other morphologies i.e. AuNP₅₀ (-124 mV vs RHE) and AuNP₁₅₀ (-111 mV vs RHE). The bare GC electrode does not show any significant response towards HER while the bare Au electrode exhibits a large onset potential of ~-300 mV vs RHE. For comparing the catalytic efficiency of synthesized AⁿGNPs in the present study with other AuNPs, we have also recorded the LSV response of spherical shaped AuNPs (S^pGNP) and it displays a higher onset potential value of -179 mV vs RHE in 0.5M H₂SO₄ medium. The overpotential (η) value has been analyzed at a fixed current density of 10 mA cm⁻² for the variable AⁿGNPs modified GC electrodes (**Figure 6.7A** inset) in which the AuNP₇₅ possesses the lower overpotential value (η =194 mV) in comparison with the bud shaped (η =235 mV) and over-bloomed shaped (η =227 mV) AuNPs.

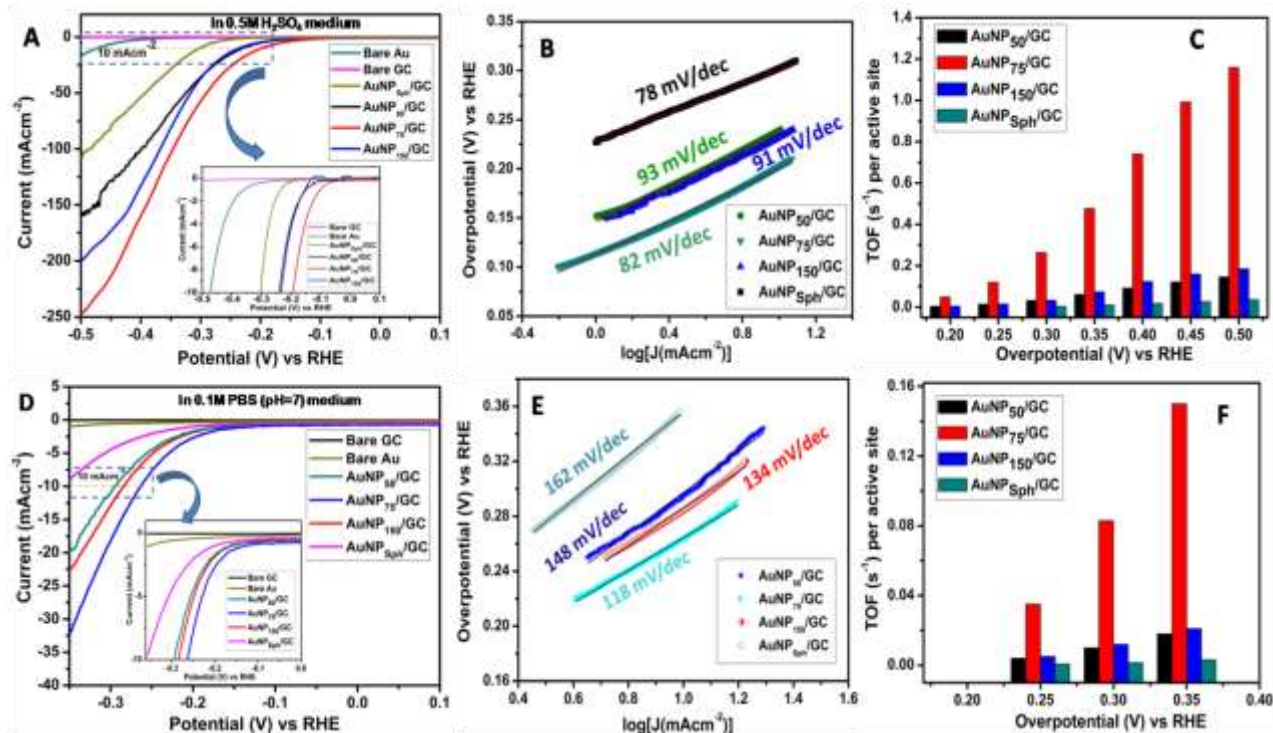


Figure 6.7 : Electrocatalytic performance of different AⁿGNPs modified electrode towards HER. Linear Sweep Voltammetric (LSV) response of bare GC, bare Au, AuNP₅₀/GC, AuNP₇₅/GC, AuNP₁₅₀/GC and S^pGNP/GC at the scan rate of 10 mV/s in (A) 0.5 M H₂SO₄ (pH=0) medium (D) 0.1 M PBS (pH=7) medium. Inset in (A) and (D) represent the magnified LSV curve for estimating the overpotential at the current response value of 10 mAcm⁻² in H₂SO₄ and PBS medium respectively. Tafel Plot and the corresponding Tafel slope for the HER activity of different AⁿGNPs modified GC electrode in (B) H₂SO₄ and (E) PBS medium. Bar diagram for comparing the Turn over frequency (TOF) value for HER as estimated from LSV response at the different potential for variable AuNPs in (C) 0.5 M H₂SO₄ and (F) 0.1 M PBS medium.

In this context, it is noteworthy to mention that the spherical shaped AuNPs possess a larger overpotential value of 302 mV. This signifies that the flower shaped AuNPs reveal their highest electrocatalytic performance towards HER among other synthesized AuNPs. The Tafel slope which is an important parameter for HER activity has also been evaluated from the Tafel

plot (overpotential (η) vs $\log j$ plot) for all the AⁿGNPs modified system as depicted in **Figure 6.7B** and AuNP₇₅/GC shows the Tafel slope of 82 mVdec⁻¹ which is smaller than AuNP₅₀/GC (91 mVdec⁻¹) and AuNP₁₅₀/GC (93 mVdec⁻¹). This study qualitatively indicates that all of the different AⁿGNPs surfaces exhibit similar HER mechanism with AuNP₇₅/GC having faster HER kinetics.³²⁹ However, the S^pGNP shows the lowest Tafel slope value (78 mVdec⁻¹) than our synthesized AⁿGNPs. Though the overpotential value and Tafel slope can qualitatively specify the catalytic efficiency of the AⁿGNPs towards HER, the turnover frequency (TOF) is the most relevant parameter for any catalyst. For estimating the TOF, we have measured the concentration of AⁿGNPs (as used for the electrocatalytic studies) by performing ICP-OES measurements at two different wavelengths, 242.7 and 267.5 nm. Before the measurement, we have initially calibrated the system using different concentration of Au³⁺ metal ions (viz. 1 ppm, 5 ppm, 15 ppm, 25 ppm, 50 ppm and 100 ppm) with the help of the number of counts per each concentration. Once the calibration curve has been constructed, we have used the diluted solution of AuNPs for the measurement. Here we have maintained the same dilution of AuNPs as employed during the HER activity. The measured concentrations of AuNPs are obtained as follows:

Sample	Measured Concentration (ppm) @ 242.7 nm	Measured Concentration (ppm) @ 267.5 nm
AuNP ₅₀	29.321±0.097	27.720±0.089
AuNP ₇₅	9.5228±0.0237	8.8993±0.0354
AuNP ₁₅₀	27.257±0.082	26.470±0.017

Conversion of ppm to Molarity (M):

$$C_{AuNP_{50}} = 29.32 \text{ ppm i.e., } 29.32 \text{ mg/litre}$$

Each Au atom has the molecular weight of 197. Each of the nano particles is consisting of multiple numbers of Au atoms. The number of Au atoms present in a particle can be calculated as follows:

Volume of each AuNP₅₀ nanoparticle = 143720 nm³ (Average Diameter 65±5nm)

Volume of each Au atom = $\frac{4}{3}\pi r^3$; where r is the radius of Au atom (r=166 pm or 0.166 nm)
= 0.0192 nm³

Therefore, the number of Au atom present in each AuNP₅₀ = 143720/0.0192 = 7.49×10⁶

$$\begin{aligned} C_{AuNP_{50}} &= 29.32 \frac{mg}{litre} = 29.32 \times 10^{-3} \frac{g}{litre} \\ &= \frac{29.32 \times 10^{-3}}{7.49 \times 10^6 \times 197} \text{ mol/litre} \\ &= 2.00 \times 10^{-11} \text{ M} \end{aligned}$$

By considering at least 10-15 cone shaped tips (with based diameter: 10nm and length: 10nm) on the spherical core of diameter: 73nm the calculated average volume of each AuNP₇₅ nanoparticle = 211789.33 nm³

Therefore, the number of Au atom present in each AuNP₇₅ = 211789/0.0192 = 1.10×10⁷

$$\begin{aligned} C_{AuNP_{75}} &= 9.52 \text{ ppm} = 9.52 \frac{mg}{litre} = 9.52 \times 10^{-3} \frac{g}{litre} \\ &= \frac{9.52 \times 10^{-3}}{1.10 \times 10^7 \times 197} \text{ mol/litre} \\ &= 4.01 \times 10^{-12} \text{ M} \end{aligned}$$

In the similar way, we have also calculated the concentration of AuNP₁₅₀ as 1.97×10⁻¹¹M by considering the core diameter as 35 nm with 6-7 cone shaped tips (with based diameter: 14nm and length: 12nm) on the spherical core. Once we know the actual concentration of AⁿGNPs ,the TOF has been calculated using the formula as^{284,330}

$$TOF(s^{-1}) = \frac{J \times A}{n \times F \times N}$$

where, J is the current density (Acm^{-2}) at a given overpotential; A is the geometrical area of the electrode (0.0706 cm^2), n is the number of electron transfer ($n=2$), F is the Faraday constant ($F=96500\text{ C mol}^{-1}$) and N is the mole of active site present on the electrode. Assuming all the sites of the nanoparticles are catalytically active, we have estimated the TOF value at a different potential from the LSV response of variable shaped AuNPs in $0.5M\text{ H}_2\text{SO}_4$ medium (**Figure 6.7C**). The flower shaped AuNPs exhibit highest TOF at different potentials in comparison with other morphologies and the order of TOF follow the trend as $TOF_{AuNP_{75}} (1.16\text{ s}^{-1}) \gg TOF_{AuNP_{150}} (0.18\text{ s}^{-1}) > TOF_{AuNP_{50}} (0.14\text{ s}^{-1})$ at the overpotential of $0.5V$ vs RHE. This emphasizes that the flower shaped AuNPs shows superior catalytic performance towards the HER in comparison with other morphology of AⁿGNPs where the TOF is enhanced by eightfold and six-fold than that of bud shaped ($AuNP_{50}$) and over-bloomed shaped ($AuNP_{150}$) AuNPs respectively. Though the change in Tafel slope is not very much considerable between $AuNP_{75}$ and S^pGNP, the TOF is significantly altered between these two. Almost forty-fold enhancements in the TOF value is observed for flower-shaped than that of normal spherical shaped AuNPs $\left(\frac{TOF_{AuNP_{75}}}{TOF_{AuNP_{Sph}}} = 40 \right)$ and this clearly highlights that the gold nanoparticles itself (without composites or alloy) can also be a potential candidate for HER activity with satisfactory TOF and low overpotential. For inspecting the outstanding catalytic behavior of the synthesized AⁿGNPs in different pH medium, we have further carried out the HER study in $0.1M$ PBS (pH=7) buffer solution. In this case, a similar trend is observed in which the flower-shaped AuNPs reveal the superior activity in terms of onset potential, overpotential (η), Tafel slope and TOF as shown in **Figure 6.7D, E and F**. The $AuNP_{75}$ exhibits a slight shift in both the onset

potential (-107 mV) and η_{10} value (262.1 mV) in PBS medium than H_2SO_4 medium. Indeed, for all the nanoparticles, the similar behavior is noticed wherein the onset potential as well as η_{10} value get shifted towards the higher potential region in PBS medium than that of H_2SO_4 medium and this behavior is consistent with other reported HER studies in the literature.⁵⁰ Like in H_2SO_4 medium, the overpotential value gets decrease around 100 mV for AuNP_{75} in PBS medium of pH=7 in comparison with $\text{S}^{\text{p}}\text{GNP}$ (**Figure 6.7D** Inset). Further, the Tafel slope as deduced from the Tafel plot (**Figure 6.7E**) is lowest for $\text{AuNP}_{75}/\text{GC}$ (118 mV/dec) followed by $\text{AuNP}_{150}/\text{GC}$ (134 mV/dec) and $\text{AuNP}_{50}/\text{GC}$ (148 mV/dec) while $\text{S}^{\text{p}}\text{GNP}$ exhibited the higher Tafel slope value (162 mV/dec) than other morphologies of Au surfaces in PBS solution of pH 7. The significant change in TOF value is observed among variable shaped AuNPs in 0.1M PBS (pH=7) wherein fifty-fold enhancement in the TOF is observed for AuNP_{75} than that of $\text{S}^{\text{p}}\text{GNP}$. **Table 6.1** shows the comparative analysis among different parameters related to HER activity of variable shaped AuNPs.

Table 6.1: Comparison among different parameters related to HER activity of the electrocatalytic performance of different AuNPs in various electrolyte solutions.

System	Onset potential (mV) vs RHE		Overpotential (mV) vs RHE @ 10 mAcm^{-2}		Tafel Slope (mV/dec)		TOF (s^{-1}) @ $\eta =$ 0.35 V	
	in 0.5 M H_2SO_4	in 0.1 M PBS	in 0.5 M H_2SO_4	in 0.1 M PBS	in 0.5 M H_2SO_4	in 0.1 M PBS	in 0.5 M H_2SO_4	in 0.1 M PBS
Bare GC	----	----	-----	----	----	----	----	----
Bare Au	-288 mV	-338 mV	472.2 mV	----	----	----	----	----

AuNP₅₀/ GC	-124 mV	-154 mV	235.7 mV	296.2 mV	93 mV/dec	148 mV/dec	0.061s ⁻¹	0.018 s ⁻¹
AuNP₇₅/ GC	-76 mV	-107 mV	194. mV	262.1mV	82mV/ dec	118 mV/dec	0.48 s ⁻¹	0.15 s ⁻¹
AuNP₁₅₀/ GC	-111 mV	-141 mV	227.5 mV	283.7 mV	91 mV/dec	134 mV/dec	0.074s ⁻¹	0.021 s ⁻¹
AuNP_{Sph}/ GC	-179 mV	-201 mV	302.6 mV	360.5mV	78 mV/dec	162 mV/dec	0.01 s ⁻¹	0.003 s ⁻¹

For comprehending the excellent catalytic activity of our synthesized AⁿGNPs towards HER, the electrochemical impedance spectroscopy (EIS) was also studied in different electrolyte medium. The utilization of EIS technique is fruitful for understanding the electrode kinetics along with for evaluating several system parameters i.e. solution resistance, charge transfer resistance, double layer capacitance, the heterogeneous rate constant and Warburg impedance.⁷²

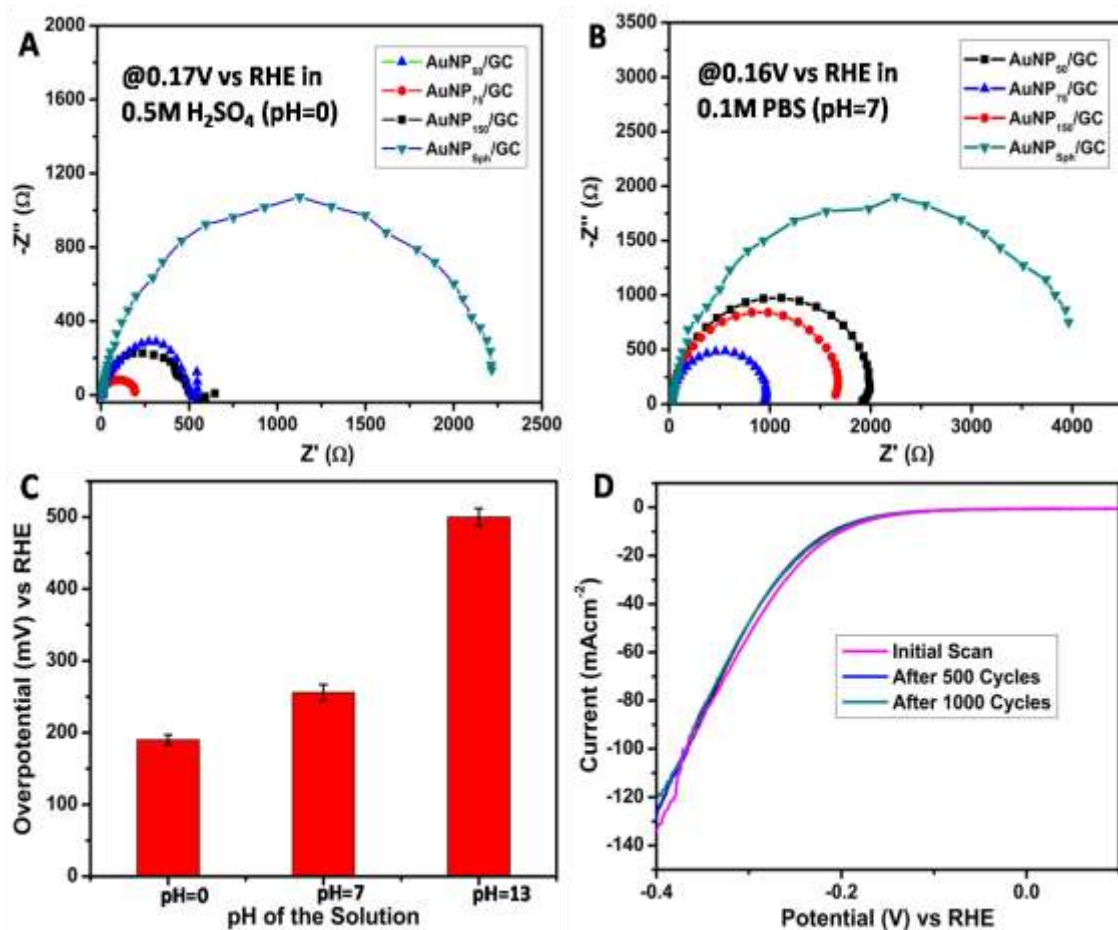


Figure 6.8: Electrochemical Impedance Spectroscopy (EIS) study for HER: Nyquist plot pertaining the comparison among different AⁿGNPs modified GC electrode in the frequency region of 10⁵ to 10⁻¹ HZ with the AC amplitude of 5 mV at (A) 0.17 V vs RHE in 0.5 M H₂SO₄ medium and (B) 0.16 V vs RHE in 0.1M PBS medium. (C) Bar diagram shows the overpotential (η_{10} @ $j=10 \text{ mAcm}^{-2}$) required for AuNP₇₅/GC electrode to reach the current density value of 10 mAcm⁻² at different pH medium. (D) Cycling stability of AuNP₇₅/GC electrode in 0.5 M H₂SO₄ medium during HER before and after 1000 cycles.

Figure 6.8A and **B** depict the typical Nyquist plot of variable shaped AuNPs/GC electrode for HER study in 0.5 M H₂SO₄ and 0.1 M PBS respectively wherein the customary semicircle is observed for all the variable AuNPs modified GC electrode at the higher frequency region. The

diameter under the semicircle provides the charge transfer resistance (R_{CT}) which is varying with the morphology of AuNPs during HER. From this R_{CT} value we can also predict the standard heterogeneous rate constant (k_0) as it is inversely proportional to the former (i.e. $k_0 \propto \frac{1}{R_{CT}}$).⁷² The flower-shaped AuNPs reveals the lowest R_{CT} value in both the electrolyte medium than that of other shaped AuNPs indicating the facile electron transfer between AuNP₇₅/GC and H^+ ion during HER.

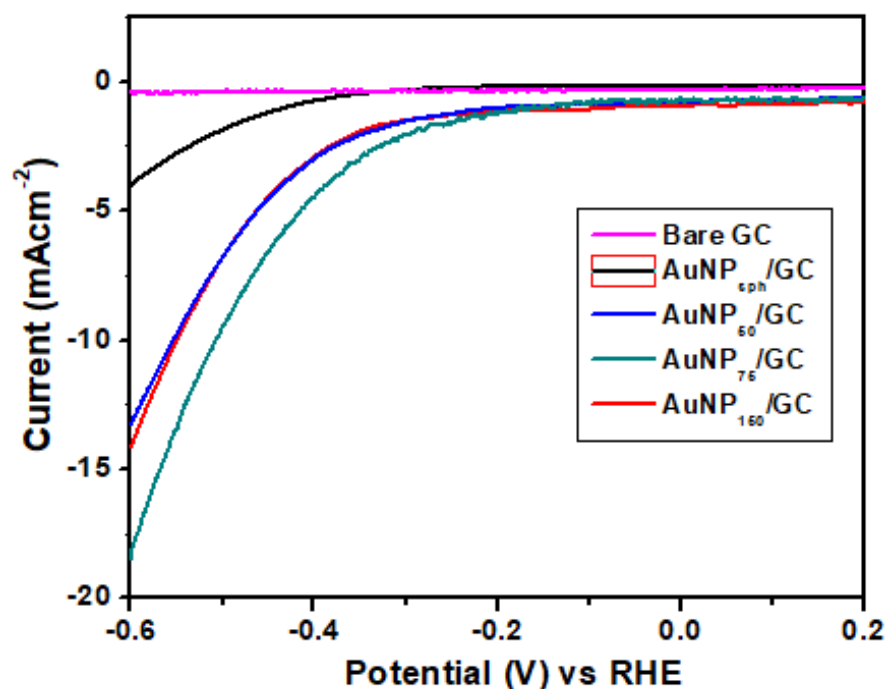


Figure 6.9: Linear sweep Voltammetric response of variable AuNPs modified GC electrode in 0.1 M KOH solution. Scan rate 10 mV/s.

The spherical shaped AuNPs i.e. S^pGNPs shows highest R_{CT} value signifying the poorer electron transfer kinetics during the reduction of H^+ on the nanoparticle surface. The HER activity of the AⁿGNPs was also investigated in 0.1M KOH medium wherein the AuNP₇₅ exhibits the superior catalytic activity among others (**Figure 6.9**). From these studies, we can infer that the flower shaped AuNPs i.e. AuNP₇₅ is the best potential candidate for HER among all other AⁿGNPs as investigated here. The HER activity of AuNP₇₅/GC electrode in variable pH

medium was compared and depicted in **Figure 6.8C** wherein the overpotential value increases with a rise in pH of the solution. This behavior is consistent with other reported HER studies using AuNPs in different pH medium.⁵⁰ Stability is an important factor that governs the suitability of any preferable catalyst towards any reaction. In the present study, the stability of the AuNP₇₅coatedGCElectrode during HER was checked by electrochemical cycling in acidic medium. The polarization curve of AuNP₇₅/GC electrode shows a slight shift in potential along with a negligibly small change in current density even after 1000 cycles as can be noticed from **Figure 6.8D** signifying that the synthesized AⁿGNPsexhibit satisfactory stability along with superior activity than normal spherical AuNPs and the catalytic activity (α) follow the trend as:

$$Z_{AuNP_{Sph}} \ll Z_{AuNP_{75}} > Z_{AuNP_{150}} > Z_{AuNP_{50}}.$$

The difference in the catalytic activity of various-shaped AuNPs towards the HER can be explained by considering various factors such as surface charge, effective surface area, crystal facet energy and crystal defects. Since the present investigation is based on the reduction of hydrogen ion using different shaped AuNPs, the magnitude of surface charge of the individual nanomaterials may alter the catalytic efficiency. The zeta potential measurement (as discussed previously) indicates that surface charges of differently shaped AuNPs are negative and the order of zeta potential follows the trend as: ζ_{AuNP50} (-31 mV) < ζ_{AuNP75} (-39 mV) < $\zeta_{AuNP150}$ (-41 mV). This indicates that the availability of free electron for the reduction of H⁺ is maximum in case of over bloomed particle and minimum for bud shaped one. Hence, according to the variation in ζ value, the higher HER efficiency should be observable for over bloomed AuNPs (AuNP₁₅₀) though in reality the flower-shaped AuNPs (AuNP₇₅) shows the superior performance over other structures. Therefore, simply by considering their change in surface charge, we cannot explain completely the observed considerable difference in electrocatalytic activity among different

shaped nanoparticles. Besides their surface charge, the surface area of nanoparticle is also an important parameter which can tune the catalytic behavior depending upon their size. The sizes of the AⁿGNPs varies as AuNP₅₀ (d=65 nm) \approx AuNP₁₅₀ (d=60 nm) < AuNP₇₅ (d=90 nm). We have calculated their (AuNP₇₅ and AuNP₁₅₀) actual surface area and volume (provided in **Table 6.2**) by considering individual petals and their average numbers.

Along with surface area, different geometrical parameters of variable shaped AuNPs were estimated by considering the bud shaped AuNPs as spherical while the cores of bloom and over-bloomed shaped AuNPs to be spherical and the tips are cone-shaped. The surface area of the core was calculated using the formula $4\pi r^2$, while the surface-to-volume ratio of the core was defined as $[4\pi r^2 / (4\pi r^3 / 3)] = 3/r$, where r is the radius of the spherical core. In general, the effective surface area of a core that is exposed to the environment can be measured as $4\pi r_c^2 - N\pi r_c^2$, where r_c is the average radius of the base of each cone and N is the total number of cones. The term $N\pi r_c^2$ denotes the surface area of the central core which is captured by N number of sharp tips. Similarly, by disregarding the base area of the cones, the effective surface area (A) of the cone-shaped tips can be expressed as $A = N\pi r_c \sqrt{r_c^2 + h_c^2}$, where h_c is the height of the individual tips. Therefore, the total effective surface area can be calculated by summing the effective core area and effective petal areas for an individual AuNPs. By following the methodology stated above, we have also calculated the effective volume of various-shaped AuNPs. Detailed structural parameters obtained from the TEM images by using the above formulas are listed in **Table 6.2**.

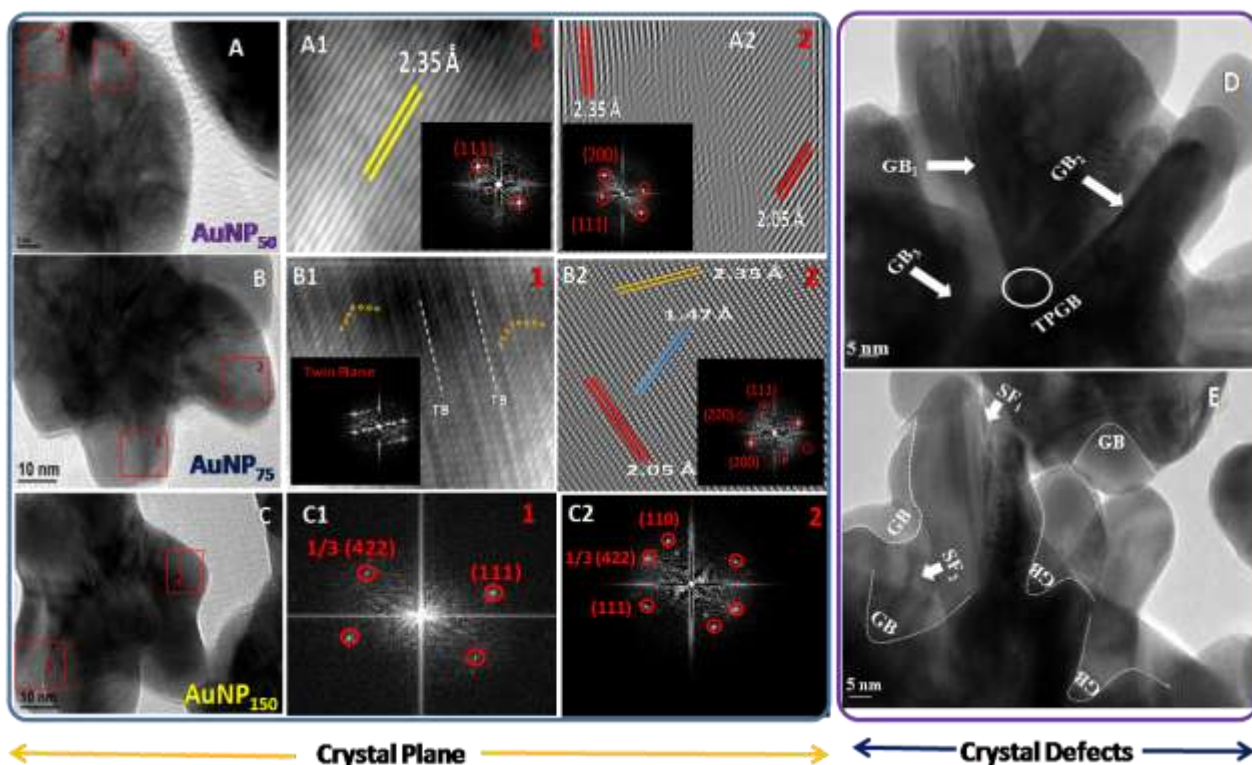


Figure 6.10: The presence of different crystal plane into the synthesized variable shaped AuNPs (A) AuNP₅₀ (B) AuNP₇₅ (C) AuNP₁₅₀. The areas selected in (A), (B) and (C) show the FFT (Fast Fourier transformation) images. (D) and (E) show the HRTEM images of AuNP₇₅ pertaining the appearance of high-density grain boundary.

As can be seen from **Table 6.2** that the availability of surface area per unit volume (mass) for hydrogen adsorption as well as desorption is higher for the smaller sized AuNP₁₅₀ and thereby the rate of catalysis should follow the trend as: $k_0^{AuNP_{150}} > k_0^{AuNP_{75}} > k_0^{AuNP_{50}}$ which is not the case in our study. Hence, both the surface charges and surface areas are not capable enough to estimate their actual catalytic activity in this context. Incapability to explain the catalytic activity by considering the surface charge and active surface area allow us to consider the role of crystal facet energy for the electrocatalytic performance of our synthesized nanomaterials. The crystal facet energy (γ) of different crystallographic plane in *fcc* crystal of

AuNPs follows the trend as: $\gamma_{(111)} < \gamma_{(100)} < \gamma_{(110)}$.⁹⁰ The presence of high energy crystal facets leads to greater reactivity and thereby better catalytic efficiency. The bud shaped AuNP i.e. AuNP₅₀ possesses energetically favorable i.e. lowest energy {111} plane along with only higher energy {200} plane [**Figure 6.10A**]. In comparison, the flower shaped AuNP i.e. AuNP₇₅ contains multiple higher energy {200} and {220} planes in conjunction with the lower energy {111} plane [**Figure 6.10B**] and these high energy crystal facets provide flower shaped AuNPs more reactive than the bud shaped AuNPs. Besides, the over-bloom shaped AuNPs i.e. AuNP₁₅₀ contains the {111} plane along with {110} and $[1/3\{422\}]$ plane [**Figure 6.10C**]. The presence of higher energy crystal facet of {110} plane in conjunction with $[1/3\{422\}]$ plane enriches the reactivity of over-bloom shaped AuNPs. Though, the higher energy crystal facet in AuNP₁₅₀ offers the better catalytic activity than the flower shaped AuNPs (AuNP₇₅), we observed that the former having the lower catalytic ability than the flower shaped AuNPs. Hence, the crystal facet energy is again not the only parameter to govern the excellent catalytic activity of flower shaped AuNPs. The ambiguity in the observed catalytic performance of AuNPs requires further enquiry to explore the factors which are having a crucial role for the observed catalytic activity.

Since the aforementioned three factors (surface charge, surface area and active facet energy) are not able to explain the observed catalytic efficiency alone we have explored the role of crystal defect density in great details. A detailed investigation on the HRTEM images of our synthesized AuNPs reveals the appearance of several different types of crystal defects. The HRTEM images of fully bloomed or flower shaped AuNPs exhibit different crystal defects viz. stepped surfaces, islands, dislocations, grain boundary and twin boundary as depicted in **Figure 6.10**. Out of several defects, the high density of grain boundary has appeared very prominently in AuNP₇₅ as shown in **Figure 6.10D** and **E**. Grain boundary is defined as the boundary or the

interface between two grains or crystallites and is generated during the nucleation step which finally turns into crystals or crystalline structures. In the case of polycrystalline materials, the simultaneous growth of nuclei in multiple regions meets each other and thereby hindering the growth of crystal in that orientation to generate grain boundary (GB) at that point. In polycrystalline materials, multitudes of grains are separated by multiple GBs. GBs are also termed as rotation boundary and depending upon the magnitude of rotation (θ), they are classified into small ($\theta < 10^\circ$) and large angle grain boundaries ($\theta > 15^\circ$). In our present study, all the synthesized AⁿGNPs are polycrystalline in nature as can be seen from SAED pattern (**Figure 6.2C, F, I**). Indeed, the large number of GBs is observed for the flower shaped AuNPs (**Figure 6.10D**) and the appearance of high density GBs possesses greater strain and thereby leading to plastic deformation.^{331,332} The plastic deformation in single phase polycrystalline grain boundary rich nanomaterials can be illustrated by the Hall-Petch relation^{331,333}:

$$\sigma_y = \sigma_0 + k_y d^{-\frac{1}{2}} \dots\dots\dots(4)$$

where, ' σ_y ' denotes yield stress for plastic deformation and ' σ_0 ' is the material constant for starting stress, ' k_y ' and ' d ' represent strengthening coefficient and average size or diameter of grain boundary respectively. The Hall-Petch relation predicts that for lower grain size ($d < 10$ nm) the value of yield stress increases and the nanostructure become stable whereas for higher grain size ($d > 10$ nm), the motion of the dislocation prevented from one grain to adjacent grain and the strain within the nanomaterial increases.^{334,335} For a comparative analysis of yield stress (σ_y) among various shaped AuNPs used in this study, the average grain diameter has been calculated using two different methods namely Jeffries and mean intercept length method.

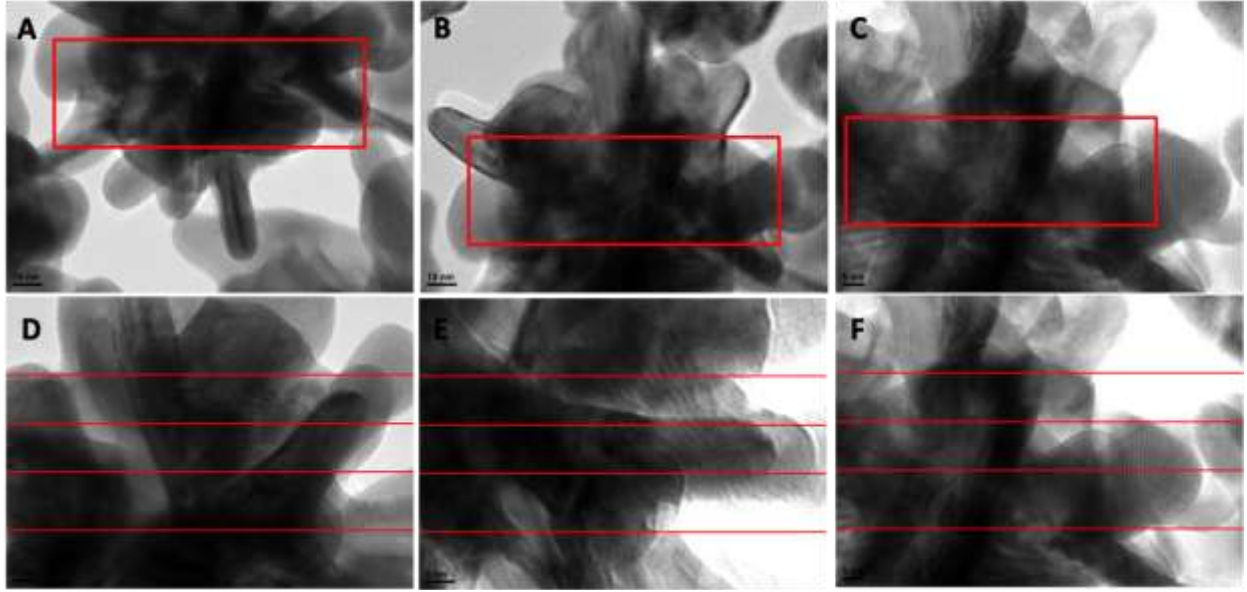


Figure 6.11: Different HRTEM images of AuNP₇₅ in which the rectangular area in (A, B and C) is selected for determining the average grain sizes using the Jeffries method. The parallel line in (D, E and F) is drawn on the TEM images of AuNP₇₅ for determining the average grain sizes using mean intercept length method.

In Jeffries method,³³⁶ we have selected a rectangular area on a particular nanostructure in which a full grain is considered as 1.0 and partial grain as 0.5. The average number of grain boundary per unit area (N_A) is measured from the selected rectangular area (nm^2) and N_A is related with the average grain diameter (d) by $d=1/(N_A)^{1/2}$. We have chosen rectangles of 4000 nm^2 ($100 \text{ nm} \times 40 \text{ nm}$) area for **Figure 6.11A** and **6.11B** whereas 1875 nm^2 ($75 \text{ nm} \times 25 \text{ nm}$) for **Figure 6.11C** in the HRTEM images of AuNP₇₅ where the numbers of GBs are counted using ImageJ software and by this method, 50 different frames (with identical area) of the same nanostructure have also been selected. Thereby, the average diameter of grain boundary is evaluated from the equation, $d_i = \sum_{i=1}^{50} \frac{1}{(N_A)^{1/2}}$. From the Jeffries method, the calculated d_i value

is in the range of 17.5-18.2 nm for fully bloomed shaped AuNPs while for over-bloomed and bud shaped the d_i values are 10.7-12.1 nm and <10 nm respectively.

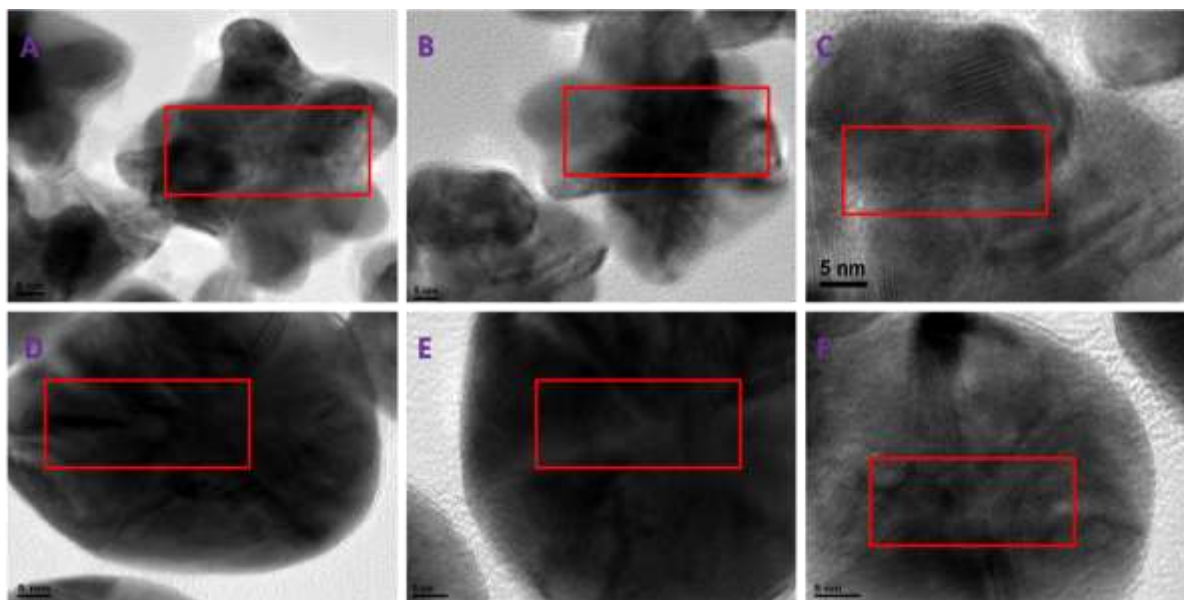


Figure 6.12: Different TEM images of AuNP₁₅₀ (A, B and C) and AuNP₅₀ (D, E and F) in which the rectangular area is selected for determining the average grain sizes using Jeffries method.

Further to verify the accuracy of the Jeffries method, we have also adopted the mean intercept length method³³⁶ for measuring the average grain sizes. In polycrystalline materials, a set of parallel lines are drawn on the nanosurface using ImageJ software and the number of intersection per unit length (P_L) on the GBs are counted. The average diameter of the grain boundary (d_i) is defined as $d_i = 1/P_L$. In this method also, we have selected for 50 other frames of the same nanostructure (**Figure 6.11D, E and F and 6.12D, E, F**) as followed in the previous method. The calculated d_i value using this method for AuNP₇₅ is in the range of 15.7-16.4 nm which has close proximity to the d_i value (17.5-18.2 nm) calculated from the Jeffries method. For other morphologies of AⁿGNPs, the d_i value is in the range of 10.5-11.2 nm and 9.1 nm for AuNP₁₅₀ and AuNP₅₀ respectively. In our present study, the most catalytically active AuNP₇₅

have an average grain size (d_i) around 18.2 ± 1 nm which is higher than the average grain size of AuNP₅₀ ($d_i \approx 9$ nm) and AuNP₁₅₀ ($d_i \approx 11$ nm). In general, the grain boundary dependent plasticity can be interpreted by the average grain size of the nanomaterial. For $d > 10$ nm the plasticity is mainly due to the full dislocation activity whereas for $d < 10$ nm the plasticity mainly because of partial dislocation and grain boundary induced deformation like grain sliding, grain rotation.³³⁷

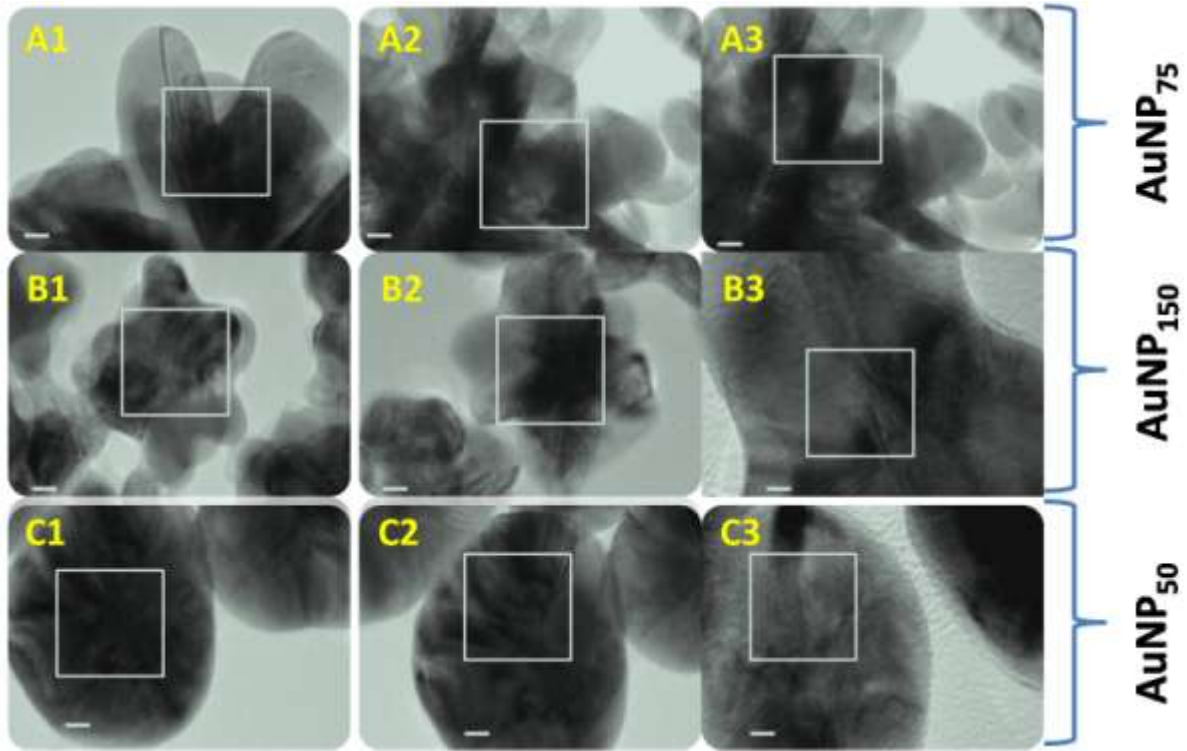


Figure 6.13: Variations in defect density in various shaped AuNPs with 50 frames considered for each of the three different surface zones with surface areas of $400 (20 \times 20) \text{ nm}^2$ for each AuNP. The scale bar in each of the figure represents 5 nm. Here frames labeled with As represent AuNP₇₅, Bs represent AuNP₁₅₀, and Cs represent AuNP₅₀.

The pile up of multiple dislocations near the bigger grain in AuNP₇₅ creates tensile strain within it and becomes catalytically most reactive in this context. Moreover, recent studies reveal the energetic nature of triple junction (TPGB, where three different grains meet in a nanomaterial³⁴)

and their role in catalysis. In general at the triple junction, fracture or crack occurs much easily than the other parts of the nanomaterial. From the HRTEM picture of AuNP₇₅, we can locate multiple triple junctions over the nanosurface than that of AuNP₅₀ and AuNP₁₅₀. All these cumulative effects make polycrystalline grain boundary rich AuNP₇₅ becomes energetically much more reactive than AuNP₅₀ and AuNP₁₅₀. During the electrocatalytic activity towards HER, these grain boundaries act as active sites for preferential accumulation of hydrogen ions onto the flower shaped AuNPs. Further, the presence of higher extent as well as larger diameter of GBs on AuNP₇₅ enhances the diffusion of adsorbates (here, H⁺) from bulk to the nanosurface compared to the other two structures. This results in facile adsorption of hydrogen ion on the polycrystalline nanoflower which results higher TOF for HER. In order to evaluate the crystal defect density into the nanomaterials, a surface area of 400 (20×20) nm² have been considered on the TEM images of each AuNPs. For each surface zone of an individual structure, we have considered 50frames. The details of the defect density are provided in **Table 6.2**, which includes different defects viz. GBs, TB, and SFs. Various types of crystal defect density were calculated using the expression:

$$\text{Crystal defects density (CDD)} = \sum_{i=1}^{50} \frac{n_i}{A_i}$$

Where, n_i is the number of respective defects in selected area of A_i.

The procedure to calculate different crystal defect density from TEM images has been elaborately in **Figure 6.13** and the obtained defect density value from this method is enlisted in **Table 6.2**. The presence of various type of crystal defects, mainly planer defect (GBs, TBs, and SFs), in higher extent (as can be noticed from **Table 6.2**) enriches the host-guest interaction on the surface of the negatively charged AⁿGNPs and thereby enhancing the catalytic efficiency of fully bloomed shaped AuNPs in comparison with other synthesized AⁿGNPs.

Table 6.2: Structural parameters of different AⁿGNPs.

Parameters	AuNP ₅₀	AuNP ₇₅	AuNP ₁₅₀
Surface Charge	-(31.7±0.5)	-(38.9±0.7)	-(41.1±0.9)
Surface Area (nm ²)	11304.0	22387.3	6124.81
Volume (nm ³)	113040	211789.3	26037.4
Surface to volume ratio (nm ⁻¹)	0.1	0.11	0.23
Grain boundary Density (nm ⁻²)	0.08	0.68	0.28
Grain boundary diameter (nm)	9.6±0.5	17.4±0.7	11±0.6
Twin boundary Density (nm ⁻²)	0.01	0.05	0.03
Stacking Fault Density (nm ⁻²)	0.15	0.57	0.21

6.4.3 Computational Studies:

In order to gain better insight about the enhanced HER activity of the AⁿGNPs, we have performed density functional theory study based on first-principle calculations using VASP simulation package.¹¹⁵ As revealed from HRTEM study, the key differences between differently shaped AuNPs namely bud shaped AuNP₅₀, bloom shaped AuNP₇₅ and over bloom shaped AuNP₁₅₀ are a) surface exposed crystallographic planes, b) length and density of the grain boundaries present in different surfaces. The surfaces of AuNP₅₀, AuNP₇₅, AuNP₁₅₀ are modelled with (111), (200) and (110) surface planes and their corresponding grain boundaries according to HRTEM analysis (**Figure 6.14-6.16**).

To evaluate the HER activity of a catalyst, the free energy diagram of H* adsorption on catalyst surface can be considered as a key physical quantity.^{300,338} We have calculated change of Gibbs free energy for hydrogen adsorption (ΔG_{H^*}) on different Au surfaces according to the work of Norskov et al (**Figure 6.17a** and **Figure 6.14-6.16**).^{134,300}

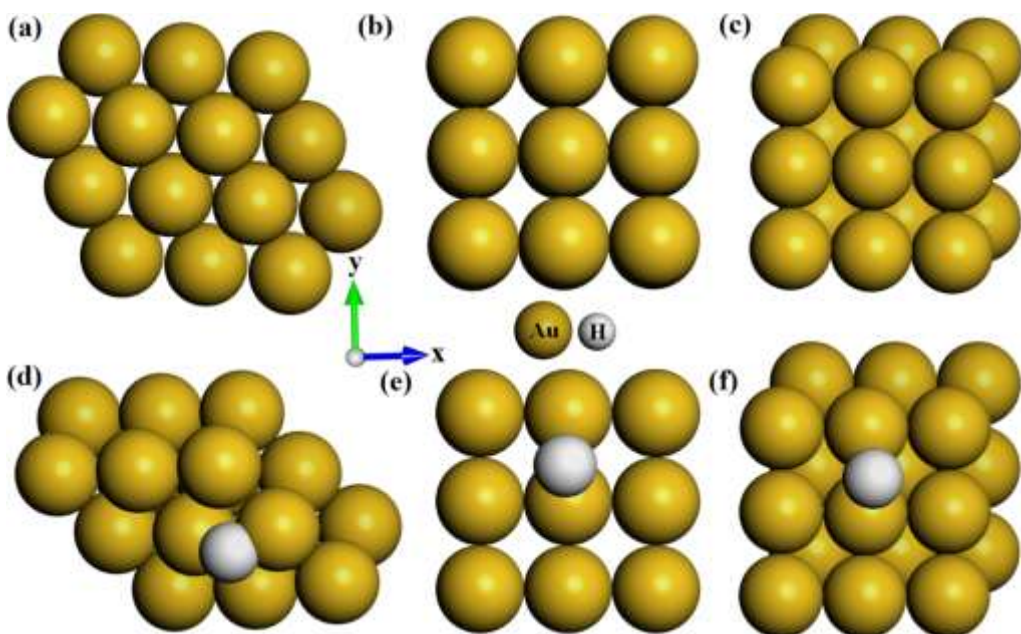


Figure 6.14: Optimized structure of (a) Au (111), (b) Au (200) and (c) Au (110) surfaces.

Structures of H* adsorbed Au surfaces (d) H*-Au (111), (e) H*-Au (200), (f) H*-Au (110).

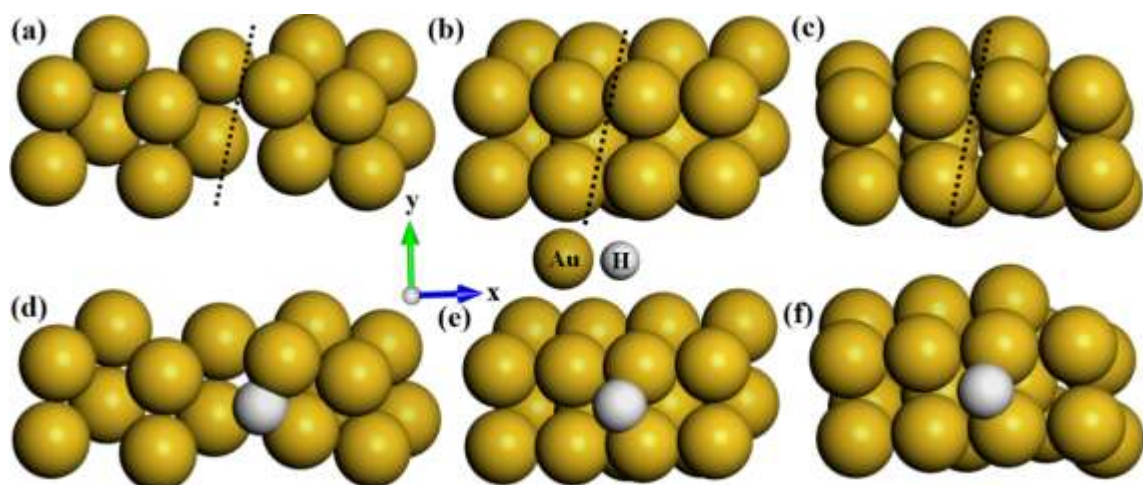


Figure 6.15: Optimized structure of (a) GB_a, (b) GB_b and (c) GB_c Au grain boundary surfaces

(dotted line shows grain boundary region). Structures of H* adsorbed Au grain boundary surfaces

(d) H*-GB_a, (e) H*-GB_b, (f) H*-GB_c.

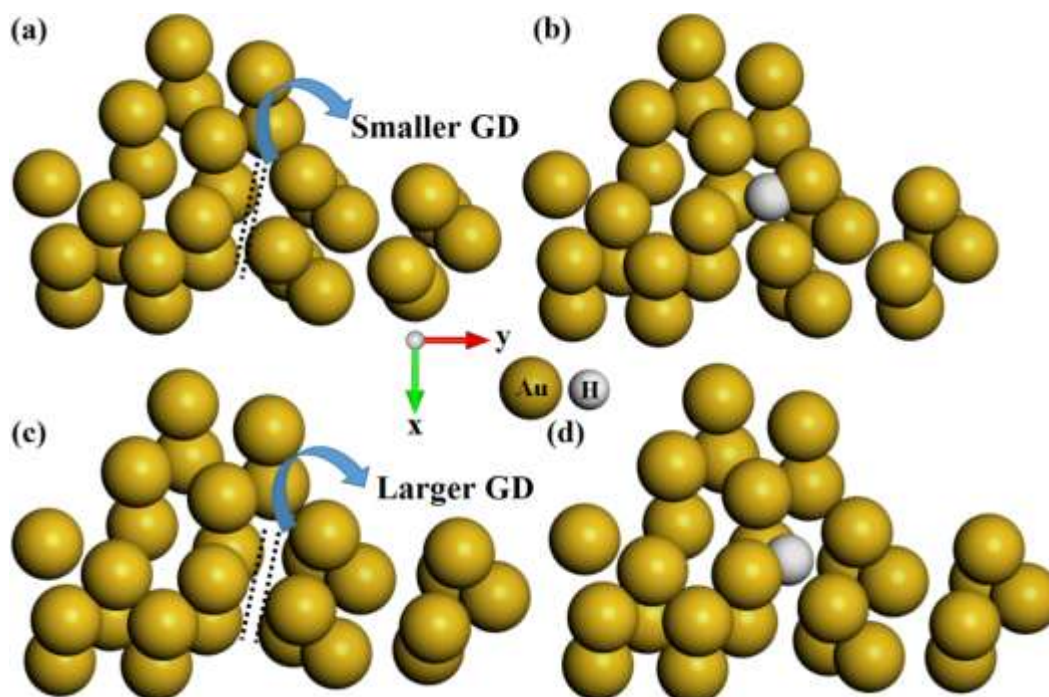


Figure 6.16: Optimized structure of (a) GB_d, (c) GB_e/Augrain boundary surfaces (dotted region shows smaller and larger grain diameter). Structures of H* adsorbed Au grain boundary surfaces (b) H*-GB_d, (d) H*-GB_e.

The ΔG_{H^*} values for the pristine Au (110), (200), (111) surfaces are 0.45, 0.18, -0.50 eV respectively. According to the Sabatier principle, most active catalytic site will have moderate hydrogen adsorption energy with $\Delta G_{H^*} \approx 0$.³³⁹ Therefore, Au (200) surface with moderate H* adsorption energy (0.18 eV) is the best surface among (110), (200) and (111) surfaces. However, mere presence of different surface planes cannot conclude about the difference in HER activities of differently shaped AuNPs as both bud shaped AuNP₅₀ and bloom shaped AuNP₇₅ contains (200) plane. A closer look into the HRTEM analysis clearly reveals that all the differently shaped polycrystalline AuNPs surfaces are having grain boundaries with presence of two and /or three planes. The effect of grain boundary (GB) on electrocatalysis is well explored in literature.^{340,341} Therefore, effect of GB can play an important role in HER.

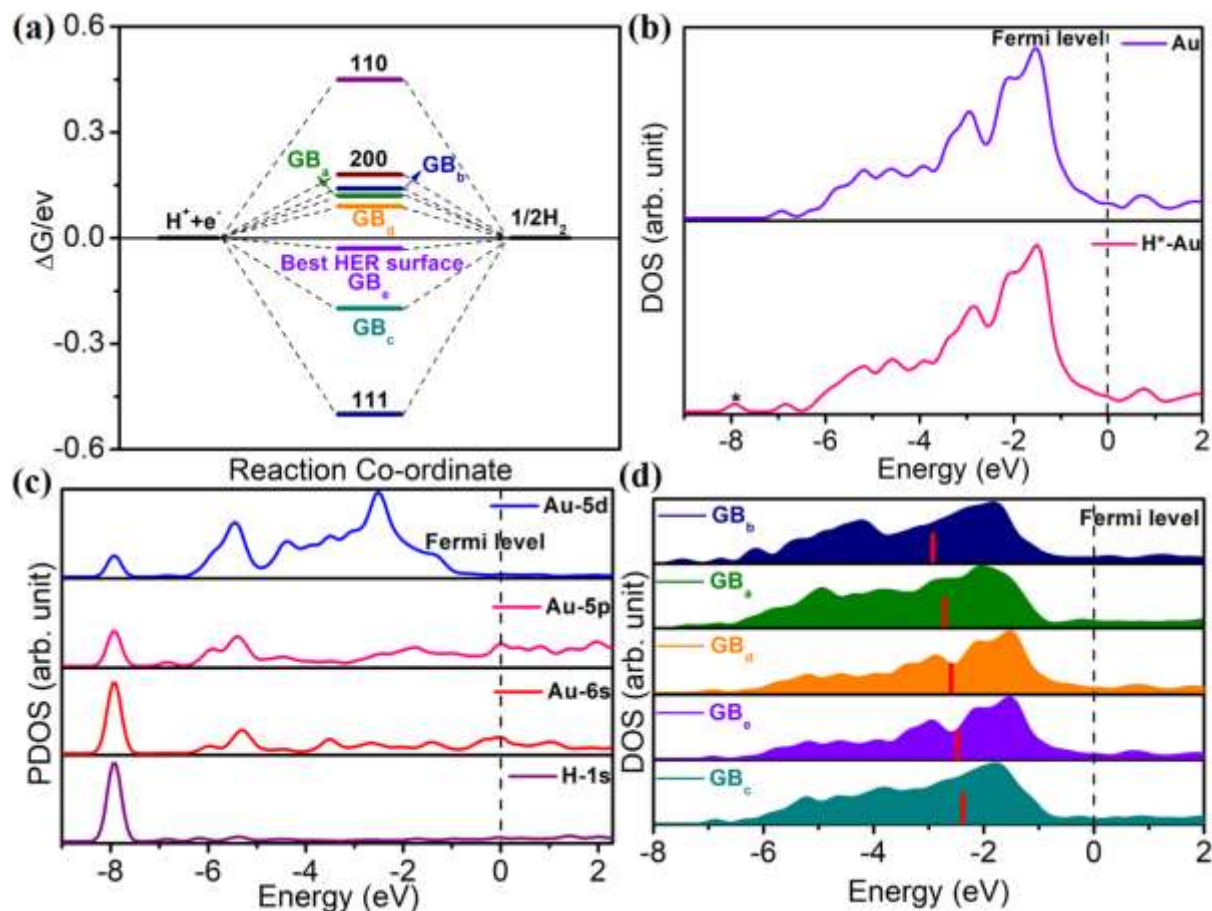


Figure 6.17:(a) Free energy diagram for H* adsorption on various Au surfaces for HER, (b) DOS plots for GB_e and H*-GB_e Au surfaces (asterisk shows contribution from H-1s), (c) PDOSs for Au-5d, Au-5p, Au-6s and H-1s of H*-GB_e Au surface, (d) DOSs on Au atoms for different grain boundary surfaces. The thick red bar indicates the position of d-band centre (E_d) on Au surfaces.

To find out the role of GB, we have constructed various GBs with different surface planes. Among all the GBs, the ones (GB_d, GB_e) consisting of three planes [(110), (200) and (111)] show $\Delta G_{H^*} \approx 0$ (0.09 and -0.03 eV) in comparison with other GBs (GB_a, GB_b, GB_c) consisted with either of two planes among (110), (200) and (111). These findings nicely corroborates with experimental results. As evident from HRTEM analysis, bloom shaped AuNP₇₅ surface, the best HER Au surface, contains GB_{d/e}[GB with (110), (200) and (111)]

planes]. To get better insight about the effect of the size of grain diameter, we have modelled GB surfaces (consisting of (110), (200) and (111) planes) with smaller (GB_d) and larger (GB_e) grain diameters. Interestingly, with the increase of grain diameter and hence grain density there is a substantial change of ΔG_{H^*} from 0.09 to -0.03 eV. This study indicates that nanoparticle surface with larger grain diameter and /or grain density will exhibit improved activity in HER, which is in good agreement with the experiment.

Table 6.3: The position of DBCs for different AuNP grain boundary surfaces.

Au grain boundary Surfaces	Position of DBCs (in eV)
GB_b	-2.88
GB_a	-2.75
GB_d	-2.52
GB_e	-2.38
GB_c	-2.25

The bonding interaction of H with the most active Au surface GB_e is well understood through the density of states (DOS) plot. It can be vividly visualized from the DOS plot of H^* -Au (**Figure 6.17b**) that there is a generation of H-1s state near -8.0 eV (asterisk indicates a contribution from H-1s). Besides, the projected density of states (PDOSs) analysis confirms the bonding between H-1s and Au s, p and d-orbitals. Though Au-6s orbital mainly contributes to Au-H bond, there is also a significant contribution from Au-5p and Au-5d (**Figure 6.17c**).

From the above discussion, it can be concluded that larger diameter GB_e grain boundary surface consisting of (110), (200) and (111) planes is the best HER Au surface among the studied ones. These findings can be further justified by well-known d-band model, correlating the d-band center (DBC) with adsorption energy of intermediates (here H atom).^{342,343} The DBCs for different Au surfaces are tabulated in **Table 6.3**. As shown in **Figure 6.17d**, with the change in surface planes of grain boundaries (from GB_a to GB_e), the d-band centre shifts towards fermi

level resulting the decrease of ΔG_{H^*} which corresponds to stronger adsorption of hydrogen on Au surface. However, the best Au surface (GB_e) exhibits a value of -2.38 eV whereas GB_c that of -2.25 eV. The DBC position of GB_c is more closer to Fermi level than that of GB_e indicating much stronger adsorption of H^* on GB_c surface which results in deterioration of HER activity. This study also reveals that GB_e surface has the optimum DBC position for moderate H^* adsorption and confirms the superiority in HER activity.

6.5 Conclusions:

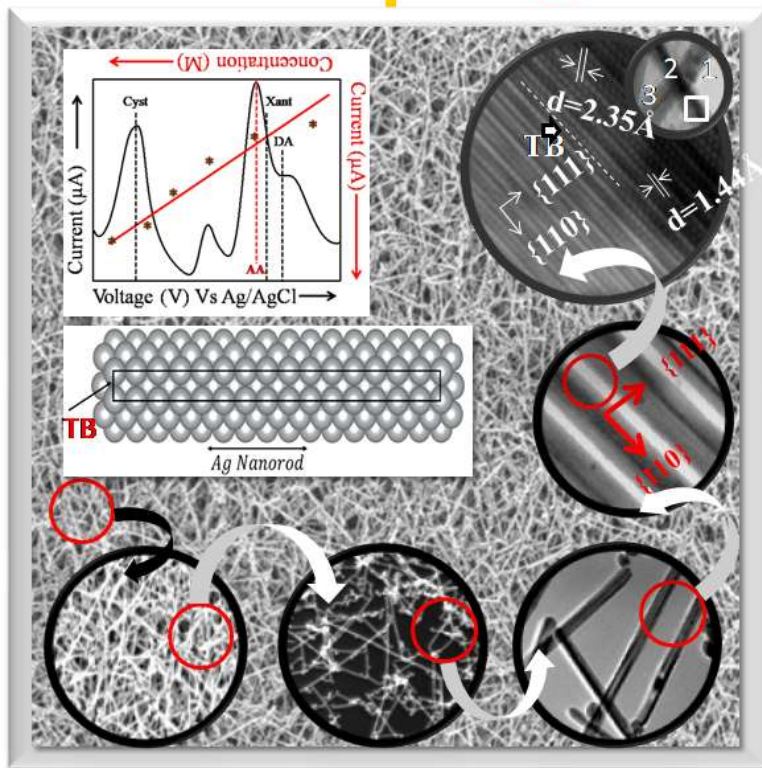
A simple, cost-effective and rapid synthesis of highly monodispersed gold nanoparticle is reported here using hydroquinone (HQ) as the reducing agent in the presence of sodium dodecyl sulfate (SDS). The mere variation in concentration of HQ leads to alter the morphology as well as size of gold nanoparticles from bud to flower (bloom) to over-bloomed shape. Our study first time nullifies the role of size, shape and density of high energy facets on HER activity of multigrain anisotropic nanomaterials and demonstrates how triple junction grain boundary can remarkably enhance catalytic performance towards HER. The detailed HRTEM, analysis reveals the presence of high-density grain boundary into the flower shaped AuNPs which proves to be a suitable and efficient candidate towards hydrogen evolution reaction (HER) in different pH medium (i.e. acidic, neutral and basic). Theoretical investigation also confirms the presence of high density grain boundary with larger size into the nanocrystal can significantly change the free energy and position of d-band center leading to enhanced reaction kinetics towards HER.

CHAPTER-7

Au-Seeded Ag-Nanorod-Based Thiol Mediated Strained 2D Network as Non-Enzymatic Universal Electrocatalytic Sensing Platform: A Mechanistic Exploration

OUTLINE: Specific Points of Discussion

- Spherical gold nanoseed (~5-6 nm)-induced (but not seed-mediated) Hy-Au@AgNRs of variable length have been synthesized by a novel methodology.
- High-resolution characterization and DFT-based theoretical modeling quantify the presence of an enhanced number of multiple coaxial twin boundaries for longer Hy-Au@AgNRs which ultimately results in an increased mechanical strain.
- Greater mechanical strain shifts the density of states (DOS) towards the Fermi level to assist the tremendous catalytic activity of the longest NR (Hy-Au@AgNR₈₄₀)
- Further assembling of these inherently active Hy-Au@AgNR₈₄₀s by thiol click chemistry results in a uniform 2D platform which shows better adsorptivity and easy moldability on electrode surface for increased self-life, uniform porous structure to trap large extent of redox systems, enhanced stability in a broad pH and solvent range along with its enhanced catalytic activity to increase the applicability, and long term stability under the ambient condition for safe storing make this material a unique non-enzymatic scalable universal electrocatalytic platform.
- The ability of this material as a non-enzymatic universal catalytic platform has been verified by applying it for highly specific and ultrasensitive detection of a series of human metabolites.
- This study first time mechanistically explores the combined role of anisometric seeding to create intermetallic twin boundary along with their size to control their strain-induced catalytic activity to offer us a universal 2D electrocatalytic sensing platform.



7.1 Introduction:

In this chapter, we have explored the application of Au-seeded Ag-nanorod-based thiol mediated strained 2D network as a non-enzymatic universal electrocatalytic sensing platform. Application of enzyme as a catalytic biosensor is long known in the literature³⁴⁴ but due to their possible denaturation and digestion in abnormal conditions (higher temperature, variable pH, non-aqueous environment, etc), high costs in preparation and purification, the requirement of expertise to handle enzyme-based assays, and lack of large scale production, the fabrication of enzymatic catalytic sensing platform for daily use in industrial-scale is not become feasible till now.^{30,31} In comparison to catalytic enzyme biosensors,³² non-enzymatic nanomaterials-based catalytic sensors also have the same essential components of an effective catalyst, i.e., a chemical receptor or more universal porous moiety to hold the analyte selectively or non-selectively and a transducer with lower Faradic electron transfer resistance³⁴⁵ to generate a high-throughput electrical signal for ultrasensitive sensing. As mentioned, to avoid drawbacks of enzymatic catalysts, new generation non-enzymatic universal nanoscale catalytic sensing platforms with enhanced catalytic activity governed by the inherent crystal defects and grain boundaries³⁴ within the nanomaterials, catalytic hotspots at the cross junctions,³⁵ durability due to efficient surface passivation,³⁶ excellent stability over a pH and solvent range,^{20,38} and low cost of fabrication, is in demand for high throughput physiological diagnosis. Over the past few decades, scientists are harvesting their constant effort to create synthetic nanostructures or their assemblies to mimic their enzymatic functions^{346–350} and promote their catalytic activities. A variety of Nanoscale materials with enzyme mimicking characteristics have largely been categorized into three classes: carbon-,^{351,352} metal-,^{348,353–356} and metal-oxide-^{30,357–359} based. Due to the limitations originating from low capacitance and improper grafting on electrode surface for carbon-based

nanomaterials³⁶⁰ along with limited electronic conductivity³⁶¹ and insoluble nature of nanoscale metal oxides make them inferior compared to metallic nanostructures as the effective catalyst. The importance of porous nanostructure along with a large accessible 3-dimensional surface area to offer large catalytic activity has been demonstrated before.^{345,362} Hence, fabrication of isotropically distributed super-nanoporous and evenly thick cross-linked metallic nanostructure with better adsorptivity on the electrode surface (for increased self-life) and enhanced catalytic activity in variable physicochemical conditions is in high demand both as a catalytic material as well as the reliable electrochemical sensor. Exploiting the effect of multiple metals within single nanostructure^{363,364} for the construction of a universal electrocatalytic platform, both for sensing and theranostics, have been demonstrated before but the mechanistic exploration for their astonishing catalytic activity or applicability without incorporating the screening-assisted ligand³⁶⁵ has not been studied extensively. Though scientists have designed expensive materials (e.g., Pt, Au, Ru, and mixed metal-based nanomaterials) with very high catalytic activities,^{366,367} equal efforts have not been put forward to explore the combination of different catalytic enhancement factors within the traditional nanomaterials simply by adjoining them in a single nanostructure. Assisted by the differential crystallization at the interface between metals (due to the difference in crystal parameters)³⁶⁸ as well as defective crystal boundaries (to reduce surface free energy, induced by internal tensile strain) at the surface,³⁶⁹ seed induced hybrid plasmonic nanoparticle (HyPNP) stimulates various physicochemical changes compared to their monometallic counterpart which includes (1) longitudinal and transverse modes of localized surface Plasmon resonance (SPR) of HyPNP varies as a direct function of the metal composition and shifting of SPR may occur simply by varying the metal-to-metal ratio,^{370,14} (2) HyPNP shows exceptional catalytic reactivity towards various reactions, e.g., CO oxidation,³⁷¹

hydrogenation of phenylacetylene,³⁷² hydrogen fuel production,³⁷³ etc. (3) broadening of the XRD curve observed for HyPNPs due to the increment of their internal tensile strain as an indirect effect of the raise in crystal defect density,³⁷⁴ etc.

The catalytic activity of monometallic plasmonic nanomaterials depends on various factors like their size & shape,^{375,376} effective charge density on the edges or tips,⁹⁸ differential chemical states of metals within single nanostructure,^{377–380} presence of low coordination sites,³⁸¹ and density as well as the area of crystal defects.³⁸² Compared to monometallic plasmonic nanostructures, bimetallic^{7,383–385} or multimetallic (both as seeded or unseeded) nanostructures³⁷² may add up several additional factors which have a potential role to influence their catalytic activity. Possible additional factors include differential crystal boundaries between metals due to their difference in crystal parameters³⁶⁸, inclusion of highly energetic twin boundaries to terminate the nanostructure growth,³⁸⁶ and the direct influence on the d-band shifting with respect to the Fermi energy surface.³⁸⁷ Since all these factors are directly related to the activation energy of a catalytic reaction, imposing these factors in an optimum content is probably the best trick to make the desired catalyst from the low-cost materials for our high throughput future endeavor.

In a general strategy to develop a good Nanoscale catalytic material, we need to modify the electrode surface by this material having the above-desired characteristics which also demands better adsorptivity on the metal electrode and to make the resultant electrocatalytic sensing platform (metal electrode + multimetallic nanostructure) for universal applicability. To fulfill above criteria, it should hold few essential characteristics which include: uniform structure for proper surface moldability (non-bulging electrode surface), close to two dimensional (2D) cross-linking structure with uniform pore size for quantitative trapping of redox system as well

as to reduce the distance between the electrode surface and analyst for an efficient redox reaction, and extended stability in variable physicochemical conditions. Easy grafting of thiols on glassy carbon electrode is known in the literature³⁸⁸ and the same idea of efficient thiol grafting has been applied for our thiol-mediated cross-linked HyPNP-based electrocatalytic sensing platform.

With these above achievable targets, in the present study, we have engineered Au-seed-induced hybrid silver nanorods (Hy-Au@AgNRs) of variable length from ~120 nm to ~840 nm with a coaxial twin boundary (TB) on the surface by a newly developed synthetic methodology. Depending upon the length of the Hy-Au@AgNRs, we have designated them as Hy-Au@AgNR₁₂₀ (for 120 nm rod), Hy-Au@AgNR₄₅₀ (for 450 nm rod) and Hy-Au@AgNR₈₄₀ (for 840 nm rod). By considering these Hy-Au@AgNRs as potential nanoscale catalytic materials, we have assembled them into a porous hybrid bimetallic network structure by thiol-based chemical cross-linking methodology. Catalytic behavior, as well as the ability of Hy-Au@AgNRs and their assemblies (Hy-Au@AgNR_x-Ass, x: length of the particular nanorod used for the assembly), has been performed by using differential pulse voltammetry (DPV), chronoamperometry, and electrochemical impedance spectroscopy (EIS) techniques. To understand the factors and mechanism responsible for the high catalytic activity of the targeted materials we have performed their atomic-scale resolution spectroscopy (X-Ray Diffraction, X-Ray Photoelectron Spectroscopy, Energy Dispersive X-Ray Analysis), high precision scattering measurements (Surface Enhanced Raman Spectroscopy, Dynamic Light Scattering, and Electrophoretic Light Scattering), and high-resolution imaging (High-Resolution Transmission Electron Microscopy, Scanning Electron Microscopy, and Atomic Force Microscopy) studies. Finally, the obtained result was verified through density functional theory (DFT) calculations by

modeling Hy-Au@AgNRs with the incorporation of necessary crystal information by quantifying the generated mechanical strain within the individual nanostructures. Once we quantify the high catalytic activity of Hy-Au@AgNRs, Hy-Au@AgNRx-Ass (Ass: Assembly) has been used as a universal non-enzymatic electrocatalytic sensing platform for highly specific and ultrasensitive detection of a series of human metabolites which include different important vitamins, potent endogenous antioxidants, essential amino acids for the biosynthesis of proteins, simple monosaccharides, and essential trace metal ions. Our study first time mechanistically explores the combined role of anisometric seeding to create intermetallic twin boundary along with their size to control their strain-induced catalytic activity to offer us a universal 2D electrocatalytic sensing platform by a combined approach of experiment and theory.

7.2 Material synthesis:

7.2.1 Synthesis of Au Nanoseed:

Spherical shape Au-nanoseed (~ 5 - 6 nm in size) was prepared by sodium borohydride reduction of Au(III)-ion in the presence of trisodium citrate (TSC) as capping agent. In a typical synthesis, 500 μL of 10^{-2} M $\text{HAuCl}_4 \cdot 3\text{H}_2\text{O}$ was added to 20 mL of MiliQ water under constant stirring. In the next step, 200 μL of 2.5×10^{-2} M trisodium citrate was added to it followed by a dropwise addition of instantly prepared and ice-cold 60 μL of 10^{-1} M sodium borohydride to the above mixture. The color of the solution changes from yellowish to brown. The solution was then kept at 30°C in dark in open mouth condition to release the excess hydrogen for the next 2hr. The solution turns gradually to wine red color which implies the formation of small nanoseeds. Formation of nanoseed was further confirmed by recording their absorption spectra, performing DLS measurements, and obtaining TEM images as shown in **Figure 7.1**.

7.2.2 Synthesis of Au-seed induced Ag nanorod:

Au-seed-induced Ag rod was prepared in a temperature-controlled synthetic procedure. In the first step 0.01 g CTAC was dissolved in 45 mL of MiliQ water and heated at 55-60 °C under constant stirring. Upon complete dissolution of CTAC, 2 mL of Au nanoseed prepared in the previous step was then added to this homogeneous CTAC solution and stirred for an additional one minute. Then 2 mL of 10^{-2} M AgNO_3 is added drop by drop to the above solution followed by the addition of 500 μL of 10^{-1} M ascorbic acid (AA) and left the mixture at the constant stirring condition for additional 4hr. During the reaction, the temperature was maintained strictly between 55-60 °C to avoid the destruction of the resultant rod-shaped nanostructures.

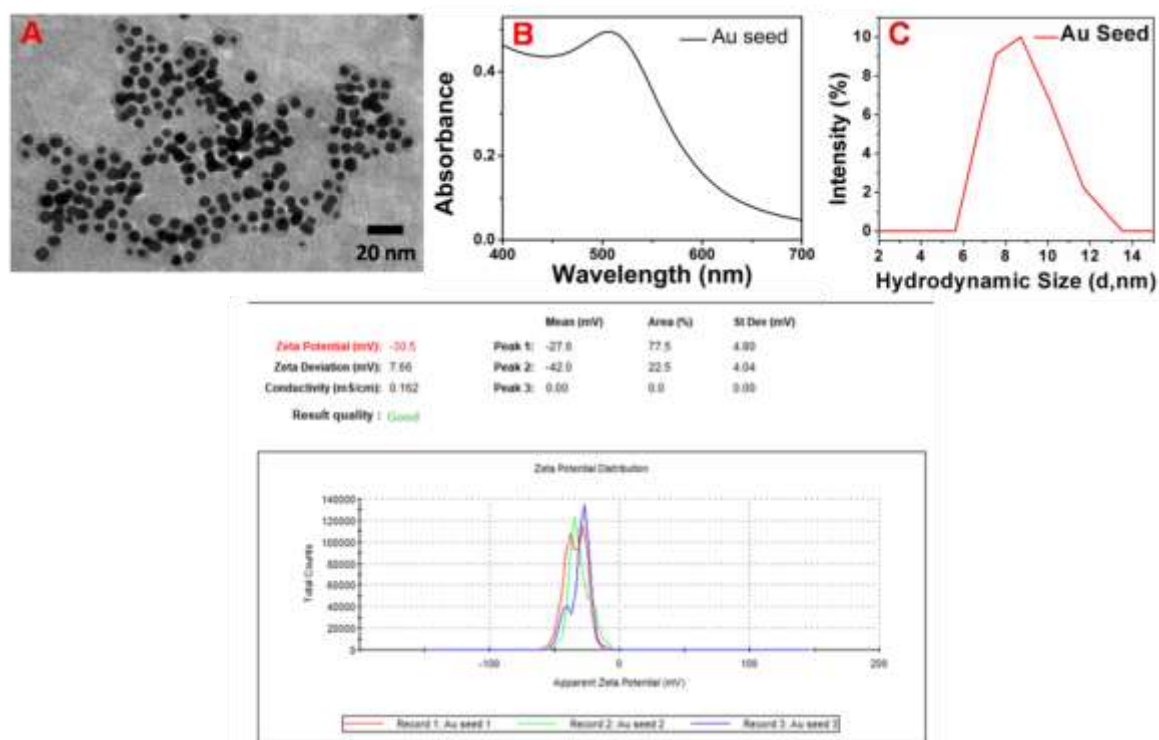


Figure 7.1: (A) True diameter from TEM image, (B) plasmon band from absorption spectra, (C) hydrodynamic size from DLS measurement, and (D) surface charge from the zeta-potential measurement of Au nanoseed.

The temperature dependence of the Au-seed induced silver nanorod (Hy-Au@AgNRs) formation is discussed in detail in the supporting information section. The length of Hy-Au@AgNRs was controlled by varying the amount of CTAC during synthesis. It has been observed that by increasing the amount of CTAC from 0.01 g to 0.05 g during synthesis we could reduce the length of the rod from 840 nm to 120 nm as shown in **Figure 7.2**. Since we are not varying the concentration of metal precursors, we need not vary the amount of AA as the reducing agent. The Hy-Au@AgNR formed by applying .01g CTAC is approximately 840 nm long in length and is designated as Hy-Au@AgNR₈₄₀. The other two rods are designated as Hy-Au@AgNR₄₅₀ (by using 0.025 g of CTAC) and Hy-Au@AgNR₁₂₀ (by using 0.05 g of CTAC). Synthesized Hy-Au@AgNRs were separated by two times fractional centrifugation at 6000 rpm in Mili-Q[®] water. (Catalytic activity of gold seed will be discussed later to explain the efficiency of AA as a reducing agent to convert Ag⁺ to Ag⁰ for effective AgNR formation. As we increase the amount of gold seed, reducing power of AA increases so much that it almost acts as a strong reducing agent and thereby resulting in rapid nucleation to initiate less anisotropy).

7.2.3 Synthesis of Au-Ag Network:

Finally, the Au-seed-induced hybrid silver nanorod-based cross-linked assembly (Hy-Au@AgNRs-Ass) was prepared by a dithiothreitol-based chemical cross-linking methodology. The centrifuged and concentrated (final volume: 500 μ L) colloidal Hy-Au@AgNR₈₄₀ solution is redispersed into 50 mL of water and stirred at 200 rpm. After complete dispersion of Hy-Au@AgNR₈₄₀, 100 μ L of 10⁻² M freshly prepared DTT was added to it and stirred for an additional 2 minutes. The color of the solution changes from yellowish-green to brown indicating the formation of nanorod-network as shown in **Figure 7.3**. The resultant solution was then centrifuged at 2000 rpm for 2 h at 30 ⁰C and washed with Mili-Q[®] water. The reason behind the

selection of Hy-Au@AgNR₈₄₀ for the preparation of Hy-Au@AgNR₈₄₀-Ass is that Hy-Au@AgNR₈₄₀ shows the best electrocatalytic oxidation efficiency among other Hy-Au@AgNRs as discussed earlier.

7.2.4 Collection and preparation of human serum samples:

To perform different electrochemical experiments we have collected blood samples from healthy willing volunteers without any medical complications. The age group of donors is recorded as 25-35 years and they were both male and female. The segregation in terms of age and sex was done that will provide us with a vivid understanding of the blood metabolite level in order to reduce the minimum deviation in our experimentation with respect to control. Human serum was separated from the collected blood samples by centrifuging each sample for 20 min at 2500 rpm. Detail about the experimentation with the obtained serum is described in the Discussion section.

7.2.5 Theoretical modeling:

With the help of TEM as well as SEM images (**Figure 7.2**), we have constructed several Au-seeded Ag nanorods (Hy-Au@AgNRs) by varying the size of nanorods (**Figure 7.14**) from 40 Å – 80 Å with a fixed diameter of 8.2 Å. For the construction of nanorods, the < 111 > facet was considered as the surface of the rod and length of the rod varies along the < 110 > crystal facet as shown clearly in **Figure 7.2C** and **7.2F**. The separation between the two < 111 > facets was achieved by the formation of a twin boundary. In each nanorod, the seeding of Au was carried out for mechanical strain calculation along the twin boundary. We have considered two different types (spherical and rod-shaped) of Au seeding as they can have the same numbers of Au and Ag atoms (**Figure 7.14**). Our calculated total energies indicate that the spherical shaped Au seeding is favorable (by 1.43 eV) over the rod-shaped Au-seeding and therefore, all the Hy-

Au@AgNR calculations have been performed using the spherical Au seed as a nucleation center. The calculated energy values support the experimental findings as the formation of a spherical Au seed-induced Ag nanorod is shown in **Figure 7.14**. For the construction and manipulation of the required modeled structures, the VESTA³⁸⁹ program was used. We have simulated the following Ag nanorods; 40 Å (with 230 atoms), 60 Å (314 atoms), and 80 Å (422 atoms) with and without gold seed as the nucleation center. As it was impossible to simulate nanorods of length from 120 nm to 840 nm by using the *ab initio* methods, we have tried to mimic the electronic and structural properties by keeping the $\frac{diameter}{length}$ ratio fixed based on our experimental findings (**Figure 7.2**). After keeping the ratio of length to diameter fixed, the Au seeding was carried out in the equivalent % mass variations (as shown in the experiments). All the DFT calculations are performed within the Vienna *ab initio* Simulation Package (VASP).^{115,116,322} A gamma-centered k-point is used during the calculations. The force convergence criterion was set to 0.01 eV/Å per atom for a better description of Heyman Forces between the atoms. The energy convergence criterion was set to 10^{-6} eV for minimization of total energies. The GGA-PBE potentials are used with the Methfessel smearing method for the calculation of DFT energies and geometrical parameters. Electronic smearing of 0.2 eV was used throughout the calculations, as Ag-Au systems describe the perfect metallic nature of nanorods.

7.3. Results and Discussion:

Synthesized Hy-Au@AgNRs show rich optoelectronic properties with a tunable Plasmon band in the infrared region. The plasmonic nature of our synthesized individual Hy-Au@AgNRs is directly related to their length as seen from **Figure 7.4**. Hy-Au@AgNR₈₄₀ has a single longitudinal plasmonic band at 1147.5 nm, however for Hy-Au@AgNR₁₂₀ and Hy-Au@AgNR₄₅₀ the corresponding band appears at 818.0 and 957.6 nm respectively. After assembling the Hy-

Au@AgNR₈₄₀ by DTT to prepare Hy-Au@AgNR₈₄₀-Ass, we found that the absorption maximum of the resultant cross-linked assembly moves to higher wavelength beyond 1300 nm and due to the absorption of water we could not record their actual plasmon peak. Moreover, assembling of Hy-Au@AgNR₈₄₀ broadened the plasmon peak and this broadening may originate both from the lower energy density at per-unit higher wavelength and wider size distribution of the resultant Hy-Au@AgNR₈₄₀-Ass. To understand the morphology, composition, and crystallization of our synthesized Hy-Au@AgNRs before and after assembling, we have performed their SEM, TEM, and HRTEM study. Combined analysis of Hy-Au@AgNR₁₂₀, Hy-Au@AgNR₈₄₀, and Hy-Au@AgNR₈₄₀-Ass is given in **Figure 7.2**. SEM images (**Figure 7.2A**, **7.2D**, and **7.2G**) clearly show that our synthesized Hy-Au@AgNRs are highly monodispersed in nature. The porous nature of Hy-Au@AgNR₈₄₀-Ass is clearly visible from their SEM image in which each Hy-Au@AgNR₈₄₀ preserve their morphology while crosslinked each other through DTT thiol linker. If we look carefully at their TEM images (**Figure 7.2B**, **7.2E**, and **7.2H**) then for each Hy-Au@AgNR there is a small Au nanoseed of ~5-6 nm diameter situated anisotropically within the nanorod. Anisotropic placement of Au nanoseed within Hy-Au@AgNRs indicates a nonconventional growth mechanism distinguishable from traditional seeded growth. The high-resolution TEM (HRTEM) of Hy-Au@AgNR₁₂₀ and Hy-Au@AgNR₈₄₀ are shown in **Figure 7.2C** and **7.2F** respectively. HRTEM images not only show the crystal arrangement in each Hy-Au@AgNRs but also differential focusing plane between the surface atoms and seed atoms indirectly proves that the seed is indeed situated within the core of the rod but not on the periphery. Both for Hy-Au@AgNR₁₂₀ and Hy-Au@AgNR₈₄₀ we could clearly see the presence of coaxial twin boundary (**Figure 7.2C** and **7.2F**) and directed towards <110> orientation of *fcc* crystal lattice. Comparison between **Figure 7.2C** and **7.2F** evidently shows the

enriched presence of multiple coaxial twin boundaries in Hy-Au@AgNR₈₄₀ which plays a crucial role in determining their tensile strain-induced catalysis and will be discussed later in more detail.

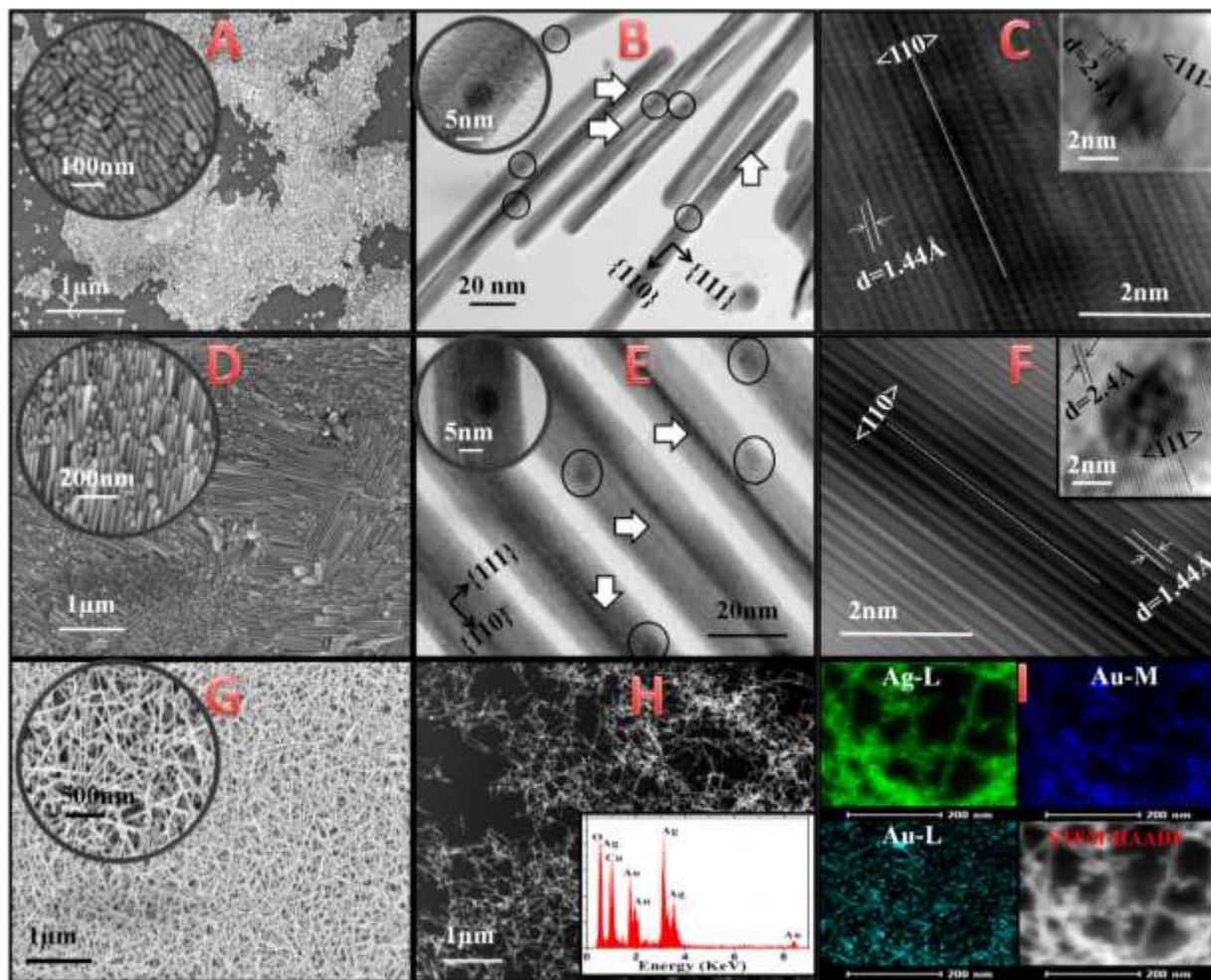


Figure 7.2: (A, B, C) and (D, E, F) are the SEM, TEM, and HRTEM images of Hy-Au@AgNR₁₂₀ and Hy-Au@AgNR₈₄₀ respectively. In (B) and (E), arrows and circles represent the presence of twin boundary on the surface and nanoseed inside Hy-Au@AgNRs. (G) is the SEM image of Hy-Au@AgNR₈₄₀-Ass which shows their clear uniform porous nature by keeping their individual rod-shaped morphology intact. (H) presents the HAADF image and EDX area profile to confirm the existence of Au and Ag. Figure (I) shows the elemental mapping of Hy-

Au@AgNR₈₄₀-Ass and the presence of Ag-L, Au-M, and Au-L lines which represent its multimetallic composition.

It is also clearly visible from **Figure 7.2C** and **7.2F** that the long axis (length) of all Hy-Au@AgNRs is directed towards $\langle 110 \rangle$ whereas the short axis (diameter) is directed along $\langle 111 \rangle$. EDX elemental mapping for Hy-Au@AgNR₈₄₀-Ass is shown in **Figure 7.2I**, where the presence of Ag-L, Au-L, and Au-M lines proves their multimetallic composition. Besides elemental mapping, we have also carried out the EDX area profile and HAADF imaging for Hy-Au@AgNR₈₄₀-Ass as shown in **Figure 7.2H**. Thus the obtained TEM, SEM, HAADF, and EDX images collectively confirm that our synthesized Hy-Au@AgNR₈₄₀-Ass is certainly a porous Au-Ag network. It is also clearly visible from **Figure 7.2H** that the morphology and symmetry of each individual Hy-Au@AgNR₈₄₀s are preserved in Hy-Au@AgNR₈₄₀-Ass.



Figure 7.3: Different colors of nanorods: From left to right Hy-Au@AgNR₈₄₀, Hy-Au@AgNR₄₅₀, Hy-Au@AgNR₁₂₀, Hy-Au@AgNR₈₄₀-Ass.

We have also performed Atomic Force Microscopy (AFM) and Energy Filtered TEM (EFTEM) measurements to achieve the 3D topographic view of Hy-Au@AgNR₈₄₀-Ass as shown in **Figure 7.5** and **7.6** respectively. **Figure 7.5** shows a time-dependent mesh-like porous structure formation for Hy-Au@AgNR₈₄₀-Ass.

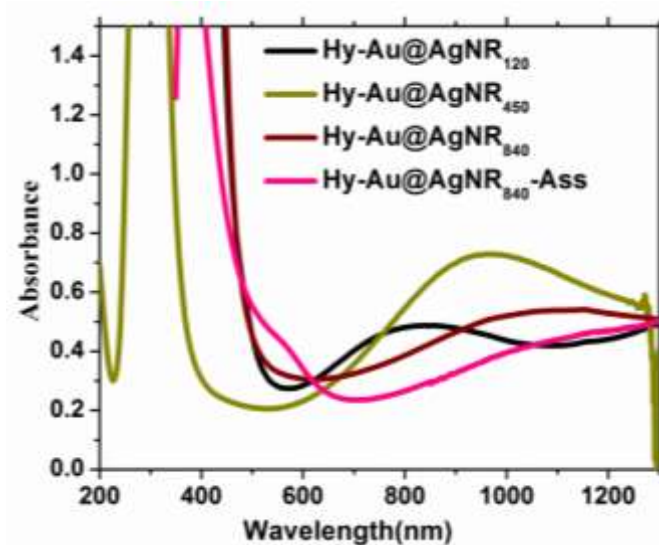


Figure 7.4: UV absorption spectra of different Hy-Au@AgNRs and Hy-Au@AgNR₈₄₀-Ass.

AFM images are taken at a regular time interval of 0 s, 30 s, 60 s, and 120 s after the addition of 1,4-dithiothreitol (DTT) to Hy-Au@AgNR₈₄₀. By aiming to prepare a porous network structure by DTT-based crosslinking, we have added different concentrations of DTT into a fixed concentration of Hy-Au@AgNR₈₄₀ solution and found that 20 μ M final concentration of DTT gives the best quality Hy-Au@AgNRs-Ass structures. Above 20 μ M, we observe a DTT-induced aggregation while below 20 μ M it shows the formation of a less porous structure.

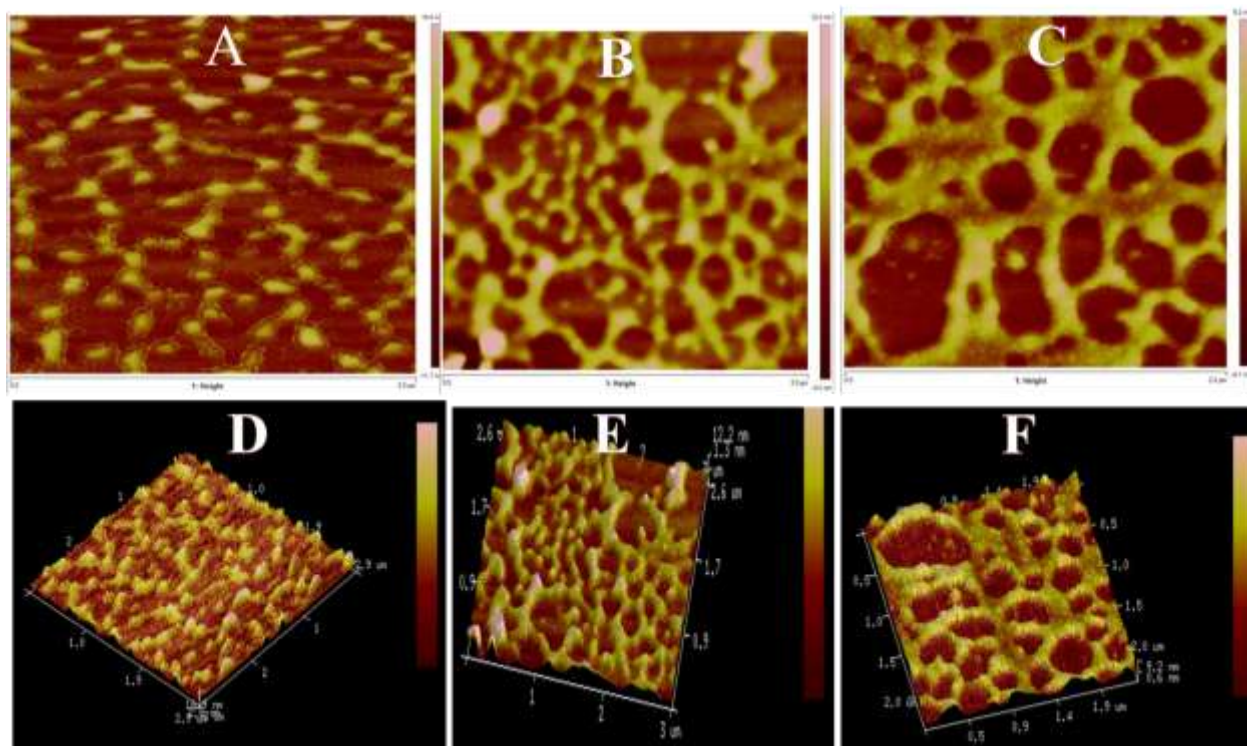


Figure 7.5: A, B, C are the time-dependent 2D images of Hy-Au@AgNR₈₄₀-Ass formation. The images are taken after DTT addition to Hy-Au@AgNR₈₄₀ at 30 s, 60 s, and 120 s interval. The 3D images of A, B, C are D, E, F respectively.

In brief, after the formation of Hy-Au@AgNR₈₄₀-Ass in a reaction vial, aliquots are taken at 0 s, 30 s, 60 s, and 120 s, while the reaction progresses and dried it immediately over the (3-mercaptopropyl)trimethoxysilane (MPTMS) modified mica plate under a controlled ultrapure argon stream as explained in details in the experimental section. It was observed that at the beginning there is an uncontrolled assembly of Hy-Au@AgNR₈₄₀s. However, as time progresses the Hy-Au@AgNR₈₄₀-Ass is formed with an average pore size of around 221 nm (**Figure 7.6a**).

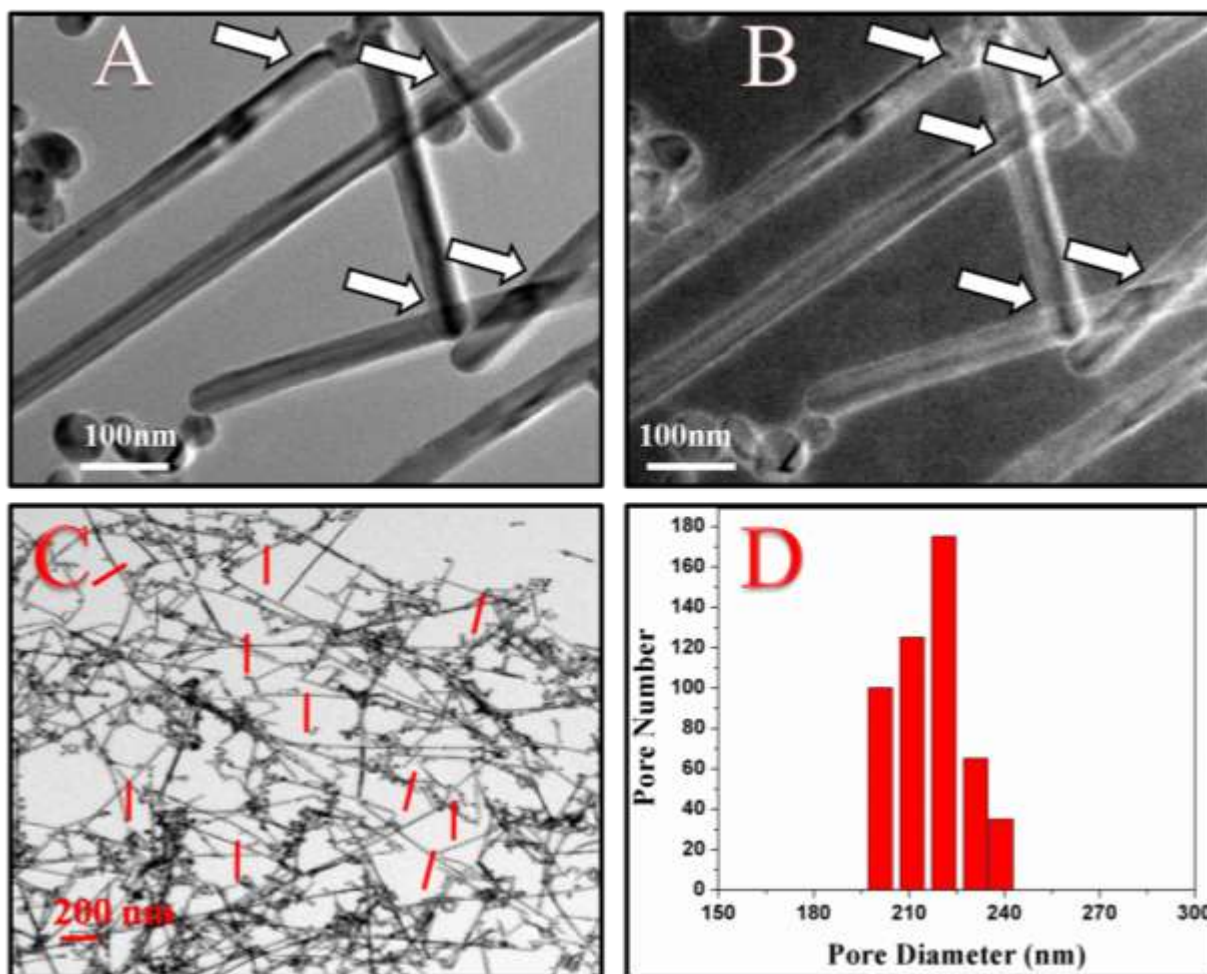


Figure 7.6a: (A) Unfiltered TEM image of Hy-Au@AgNR₈₄₀-Ass which shows that the symmetry and morphology of individual nanorods are not broken during the assembly formation, (B) Elastic TEM image of Hy-Au@AgNR₈₄₀-Ass which shows that the assembly of nanorods is eventually formed through 2D stacking of Hy-Au@AgNR₈₄₀ on XY-plane via thiol linkage where Hy-Au@AgNR₈₄₀s are randomly oriented and fused at their cross junction points, respectively, (C) Distribution of pore diameters is a large area TEM image, and (D) Histogram of the average pore diameter which is ~221 nm.

The average size distribution of different Hy-Au@AgNRs, measured by TEM and SEM, is shown in **Figure 7.6b**. The average height profile in 3D images shows that the height of Hy-Au@AgNR₈₄₀-Ass is ~12-13 nm which is close to the diameter of the individual Hy-

Au@AgNR₈₄₀ (10-12 nm). This implies that the assembly is actually formed through 2D stacking of Hy-Au@AgNR₈₄₀ on XY-plane via thiol linkage where Hy-Au@AgNR₈₄₀s are randomly oriented and fused at their cross junction points. The affinity of MPTMS towards the Hy-Au@AgNR₈₄₀ surface does not allow them to arrange through head-to-tail (J-type aggregate) or one-over-other (H- type aggregate) type of arrangement. Since the orientation of nanorods is both kinetically and chemically controlled, though at the beginning we observe an uncontrolled assembling of Hy-Au@AgNR₈₄₀, as time progresses a stable network structure is formed with high porosity in nature. The EFTEM images of Hy-Au@AgNR₈₄₀-Ass in **Figure 7.6a** show a better view of the 2D assembly of Hy-Au@AgNR₈₄₀.

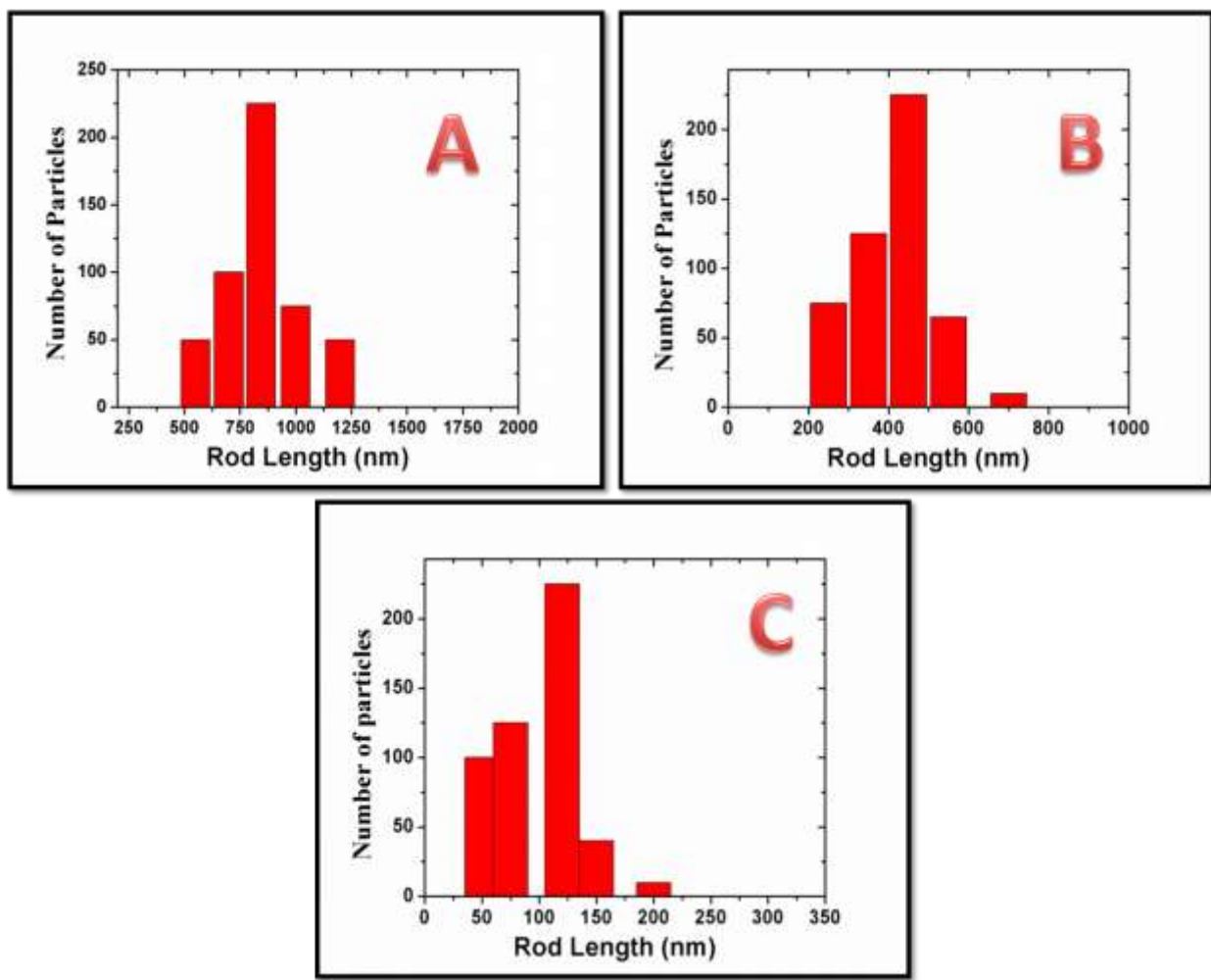


Figure 7.6b: Histogram of the nanorods (A) Hy-Au@AgNR₈₄₀, (B) Hy-Au@AgNR₄₅₀, and (C) Hy-Au@AgNR₁₂₀.

To authenticate the above-stated growth mechanism, we have also performed their detailed *in situ* DLS (**Figure 7.7 to 7.9**) and Raman measurements (**Figure 7.10**). Our *in situ* zeta potential measurements show the overall positive surface charge for all the Au@AgNRs and the corresponding Hy-Au@AgNR₈₄₀-Ass and follow the order: Hy-Au@AgNR₈₄₀ (+37 mV) > Hy-Au@AgNR₄₅₀ (+28.3 mV) > Hy-Au@AgNR₁₂₀ (+21.5 mV) > Hy-Au@AgNR₈₄₀-Ass (+17 mV). Whereas, the *in situ* Raman confirms that Ag-S bond formation (DTT as the source of sulfur) is solely responsible for assembly formation from the constituent Hy-Au@AgNR₈₄₀s. Details about the *in situ* DLS and Raman are elaborated in the following section.

***In situ* DLS measurement for different Hy-Au@AgNRs and their time-dependent assembly formation**

The recorded DLS spectrum (**Figure 7.7bC**) shows closely spaced sharp peaks at 36 nm for Hy-Au@AgNR₁₂₀, 40 nm for Hy-Au@AgNR₄₅₀, and 138 nm for Hy-Au@AgNR₈₄₀, representing their hydrodynamic diameter (d_{hyd}). We have also observed three additional low intense broad peaks for these nanostructures at 615, 947, and 5485 nm respectively. After assembling Hy-Au@AgNR₈₄₀s into Hy-Au@AgNR₈₄₀-Ass, the d_{hyd} increases from 138 nm to 213 nm as shown in **Figure 7.7bC** and this increment in d_{hyd} is due to the formation of bigger assembled mesh structured network of Hy-Au@AgNR₈₄₀, though the DLS peak at 5485 nm disappears. We have also measured the zeta potential of Hy-Au@AgNRs and Hy-Au@AgNR₈₄₀-Ass as shown in **Figure 7.7bB**. Due to the presence of positively charged CTAC molecules as the surfactant, all the Hy-Au@AgNRs and Hy-Au@AgNR₈₄₀-Ass show positive zeta potential (ξ). Measured ξ for the studied nanomaterials follow the order: Hy-Au@AgNR₈₄₀ (+37 mV) >

Hy-Au@AgNR₄₅₀ (+28.3 mV) > Hy-Au@AgNR₁₂₀ (+21.5 mV) > Hy-Au@AgNR₈₄₀-Ass (+17 mV). The trend of ξ variation is contrary to our general conception of the observation of higher ξ for nanostructure made with a higher amount of charged surfactant as discussed in the experimental section. Again, the observed ξ does not follow the order of their relative size as we measured lowest ξ of +17 mV for the biggest Hy-Au@AgNR₈₄₀-Ass nanostructure.

To evaluate this discrepancy in measured ξ and to understand the mechanism of porous network (Hy-Au@AgNR₈₄₀-Ass) formation from the constituent Hy-Au@AgNR₈₄₀s, an *in situ* DLS study has been performed. For rigid noninteracting rods at infinite dilution, the depolarize dynamic light scattering (DDLS)-based autocorrelation function $G(\tau)$ which measures the decay constant (Γ) depends heavily on both rotational and translational motion of the rod hence their respective rotational (D_R) and translational (D_T) diffusion coefficients.^{390,391} Owing to the differential contribution of rotational and translational motion, the d_{hyd} obtained from DLS measurement largely differ from TEM e.g., length and diameter of Hy-Au@AgNR₈₄₀ available from TEM is ~840 nm and ~15 nm, but from DLS we get two maximum in intensity distribution curve for Hy-Au@AgNR₈₄₀ at 138 nm for rotational motion and 5485 nm for combined rotational and translational motion. Beyond spherical geometry, D_R and D_T depend heavily on their aspect ratio (L/d) for anisotropic nanostructures with an aspect ratio greater than 5. Glidden et al. have calculated the aspect ratios of different sized gold nanorods using depolarized dynamic light scattering by differentiating two major components of the autocorrelation function.³⁹² The autocorrelation function is an exponential decaying function and it is related to the correlator time delay τ as $G(\tau) = A\{1 + B \exp(-2\Gamma\tau)\}$, where $G(\tau)$ is the autocorrelation function, A is the baseline, and B is the intercept of $G(\tau)$. The term Γ stands for relaxation rates and has two major components for rotational (Γ_{rot}) and translational (Γ_{tra}) motion of purely

monodispersed Hy-Au@AgNR₈₄₀ in solution. Change in size (d_{hyd}) and correlation coefficient $G(\tau)$, for any change in Γ_{rot} and Γ_{tra} , as a function of time during the addition of DTT in Hy-Au@AgNR₈₄₀ for an *in situ* monitoring of growth rate for Hy-Au@AgNR₈₄₀-Ass is shown in **Figure 7.7aA-C** and **Figure 7.7aD-F** respectively. The peaks at lower d_{hyd} are due to their translational motion while rotational motion contributes heavily to the peaks at higher d_{hyd} . It is observable from **Figure 7.7aA-C** that immediately after the addition of DTT (20 μM), the d_{hyd} of Hy-Au@AgNR₈₄₀ shifted from 138 nm to 939 nm within 30 s and shifts back to 202 nm after 60 s. In both cases, the peak at 5485 nm remains intact. However, after 120s we get a steady value of d_{hyd} at 193 nm and the maximum at 5485 nm has been disappeared. The disappearance of the longer maximum at 5485 nm indicates that all the rods are assembled by DTT and restrict any rotational motion. The d_{hyd} obtained after 120 s of the addition of DTT is bigger than d_{hyd} of Hy-Au@AgNR₈₄₀ (138 nm) but very close to d_{hyd} of the final form of Hy-Au@AgNR₈₄₀-Ass (213 nm). Obtained average nanopore size within Hy-Au@AgNR₈₄₀-Ass from our TEM measurement (221 nm), as shown in **Figure 7.6a** by averaging over 500 pores, is comparable with d_{hyd} values acquired from DLS experiment (213 nm). These nanopores behave like a hollow sphere in solution and the outer shell of the pore scatters the excitation light (He-Ne laser operating at 633nm). In contrast to Hy-Au@AgNR₈₄₀, these nanopores scatter light only due to the translational diffusion and hence in absence of rotational diffusion we observe only one peak (**Figure 7.7bC**) for d_{hyd} at 213 nm. Along with the size distribution, we have also recorded the change in autocorrelation function as a function of time after the addition of DTT (20 μM). In a $G(\tau)$ vs time (μs), the time at which the correlation starts to decay gives an indication of the mean size of the sample. Therefore if the curve is steeper it denotes the sample is monodispersed whereas a wider correlation confirms the presence of a polydispersed sample. From **Figure**

7.7aD it is clearly visible that at 30 s the correlation coefficient is much wider, which indicates a polydispersed sample in the solution i.e. at the beginning of the assembly forming reaction the Hy-Au@AgNR₈₄₀s tend to aggregate by DTT and a network is forming. However at 60 s, the correlation curve becomes much steeper and at 120s, the correlation coefficient attends a steady value which is much steeper than the previous one. The correlation curve obtained at 120s is much similar to the correlation curve of Hy-Au@AgNR₈₄₀-Ass, which signifies the completion of network formation.

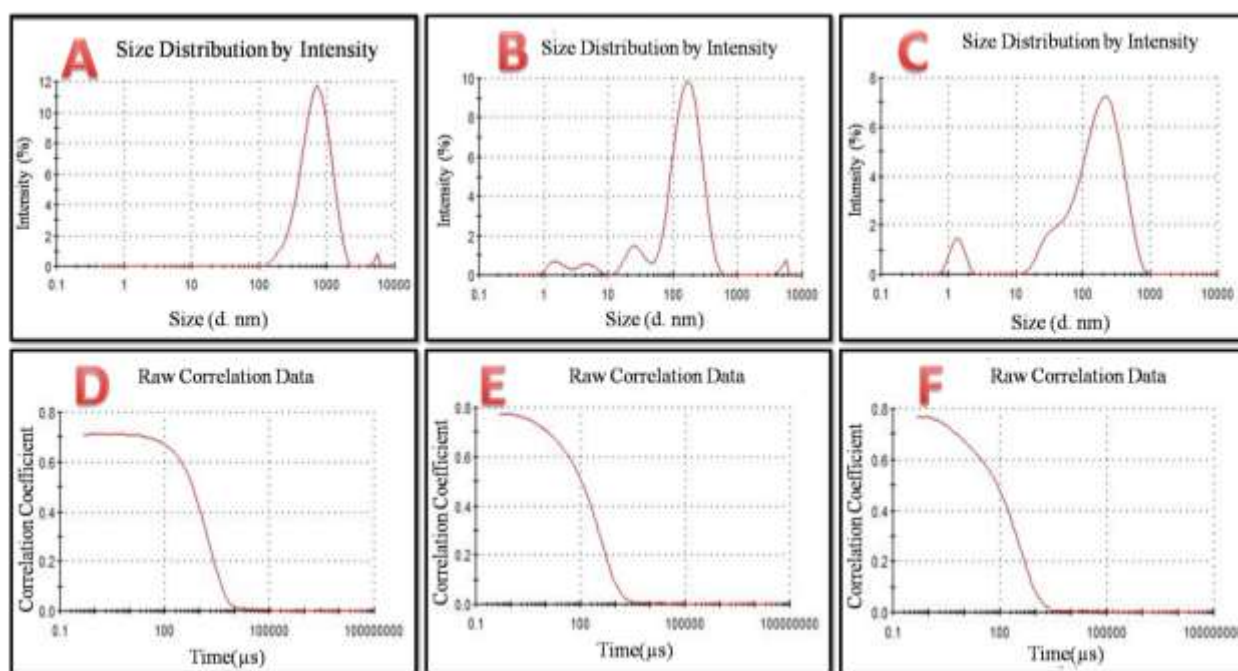


Figure 7.7a: A, B, C are Intensity (percent) vs size (nm) curve of Hy-Au@AgNR₈₄₀-Ass formation at 30 s, 60 s, and 120 s time interval in the reaction medium. D, E, F are the Correlation coefficient vs time (μs) curves for the same time intervals.

A parallel observation was also been carried out besides the DLS measurements to understand the conversion kinetics from Hy-Au@AgNR₈₄₀ to Hy-Au@AgNR₈₄₀-Ass by recording the zeta-potential (ξ) at a regular time interval of 30 s, 60 s, and 120 s. **Figure 7.7bA** describes how the surface charge changes during the formation of Hy-Au@AgNR₈₄₀-Ass. Final ξ

for all the synthesized Hy-Au@AgNRs and Hy-Au@AgNR₈₄₀-Ass are shown in **Figure 7.7bB**.

By comparing **Figure 7.7bB** and **Figure 7.7bA**, it is clearly visible that the ξ changes from +37 mV to -15 mV within 30 s of the addition of DTT to Hy-Au@AgNR₈₄₀s.

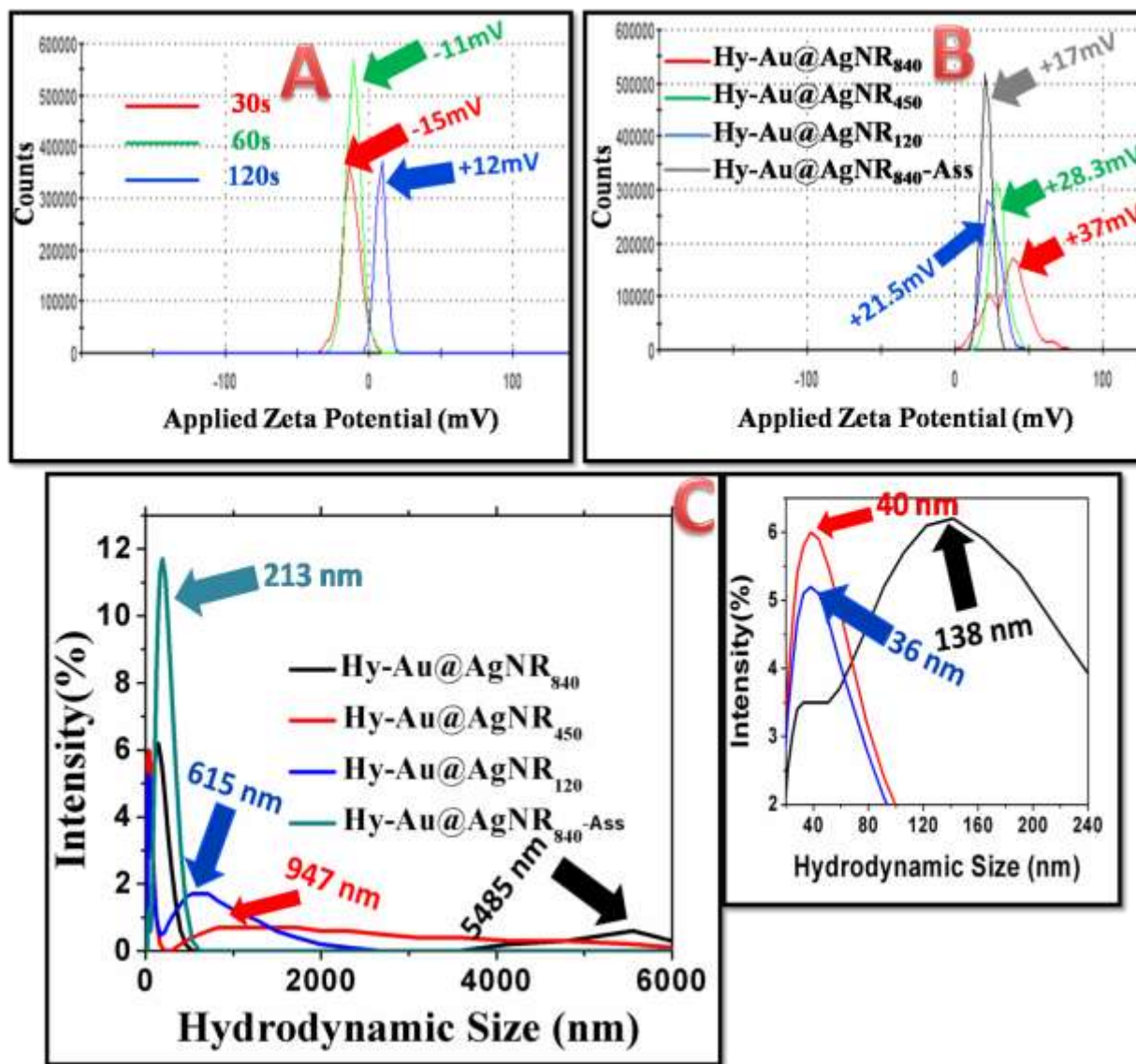


Figure 7.7b: (A) Change in zeta potential during the formation of Hy-Au@AgNR₈₄₀-Ass at different time intervals, (B, C) Final ξ and d_{hyd} of all the Hy-Au@AgNRs and Hy-Au@AgNR₈₄₀-Ass respectively.

This jump in ξ from positive to negative is due to the presence of multiple electron-rich -SH and -OH groups originating from DTT. After 60 s, ξ increases slightly from -15 mV to -11 mV and finally approaches +12 mV after 120 s which is very close to the ξ of Hy-Au@AgNR₈₄₀-Ass (+17 mV) in the equilibrium condition. The negatively charged -SH group binds the positively charged Hy-Au@AgNR₈₄₀ easily and thereby reduces the overall surface charge of Hy-Au@AgNR₈₄₀ from +37 mV to +17 mV for Hy-Au@AgNR₈₄₀-Ass.

The discrepancy of measured ξ for different Hy-Au@AgNRs with the amount of CTAC used in their synthesis can be explained both by considering their relative size and mobility.³⁹³ Due to the bigger dimension of Hy-Au@AgNR₈₄₀, they hold a larger number of positively charged CTAC molecules and hence show higher positive zeta potential and vice versa for Hy-Au@AgNR₁₂₀. Explanation of ξ variation with mobility is not simple and can be understood from their electrophoretic mobility. In brief, during ξ measurement an electric field is applied in the solution and the particles under the influence of this electric field scatter the incident light (633 nm). Depending upon the mobility (μ_e) of the nanoparticle, scattered light shifted from its original frequency. This shift is called Phase (or Doppler) shift and measured by the difference between the frequency of the scattered and incident light ($|v_{sca}-v_{inc}|$). The nanoparticle velocity (V) is measured from the Doppler shift in $\mu\text{m/s}$ by applying the equation $\mu_m = V/E$, where E is the applied electric field. For our synthesized Hy-Au@AgNRs, all the physical parameters like pH, ionic strength, viscosity, etc. remain constant except their size varies. Bigger sized Hy-Au@AgNR₈₄₀ scatters the incident light more than Hy-Au@AgNR₄₅₀ and Hy-Au@AgNR₁₂₀ due to the enhanced contribution of translational and rotational motion under the electric field. This phenomenon is known as electrophoretic light scattering (ELS). We have shown the frequency plot, phase plot, and mobility plot of Hy-Au@AgNRs in **Figure 7.8**. It is clear from **Figure 7.8**

that the mobility (μ_e) for Hy-Au@AgNR₈₄₀ is 2.795 $\mu\text{m.cm/Vs}$ whereas for Hy-Au@AgNR₄₅₀ and Hy-Au@AgNR₁₂₀ are 2.11 and 1.96 $\mu\text{m.cm/Vs}$ respectively. Henry's equation³⁹⁴ concludes that μ_e varies proportionally with ξ . Thus Hy-Au@AgNR₈₄₀, having the bigger in size, shows maximum Doppler shift (**Figure 7.8**) and maximum electrophoretic mobility and hence maximum ξ . Therefore, ξ variation for Hy-Au@AgNRs is not simply due to the amount of CTAC used during their synthesis but also depends upon the size and μ_e of the nanoparticle. A frequency plot, phase plot, and mobility plot to understand the phenomenon of real-time kinetics of Hy-Au@AgNR₈₄₀-Ass formation from the constituent Hy-Au@AgNRs is shown in **Figure 7.9**. At 30 s, μ_e shifts from +2.795 $\mu\text{m.cm/Vs}$ to -1.2 $\mu\text{m.cm/Vs}$ due to the presence of multiple -SH and -OH groups on the nanostructure, originating from DTT, which causes the motion towards positively charged electrodes during electrophoresis. However, at 60 s, μ_e increases to -0.8349 $\mu\text{m.cm/Vs}$ and at 120 s, it's further shifted to 0.787 $\mu\text{m.cm/Vs}$ which is close to the μ_e value of the resultant Hy-Au@AgNR₈₄₀-Ass (1.49 $\mu\text{m.cm/Vs}$).

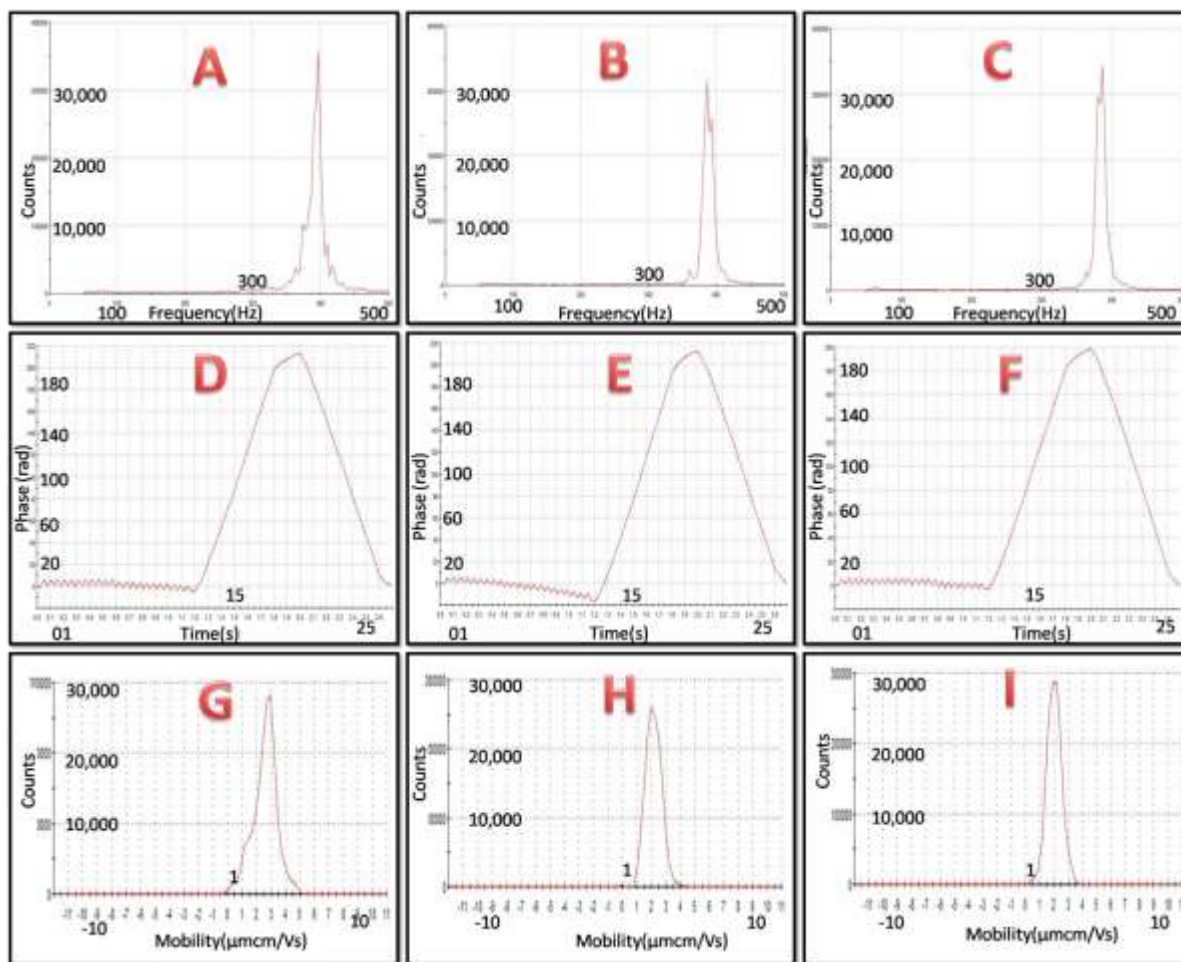


Figure 7.8: A, B, C are the frequency plot whereas D, E, F presents the phase shift and G, H, I are velocity distributions of Hy-Au@AgNR₈₄₀, Hy-Au@AgNR₄₅₀, and Hy-Au@AgNR₁₂₀ respectively.

A similar trend of frequency shift and phase shift are also observable as a function of time as clearly shown in **Figure 7.9**. Thus *in-situ* monitoring of DLS and ELS corroborates the results of a time-dependent study of AFM that after 120 s of the addition of DTT to Hy-Au@AgNR₈₄₀, the assembly forming reaction tends to complete.

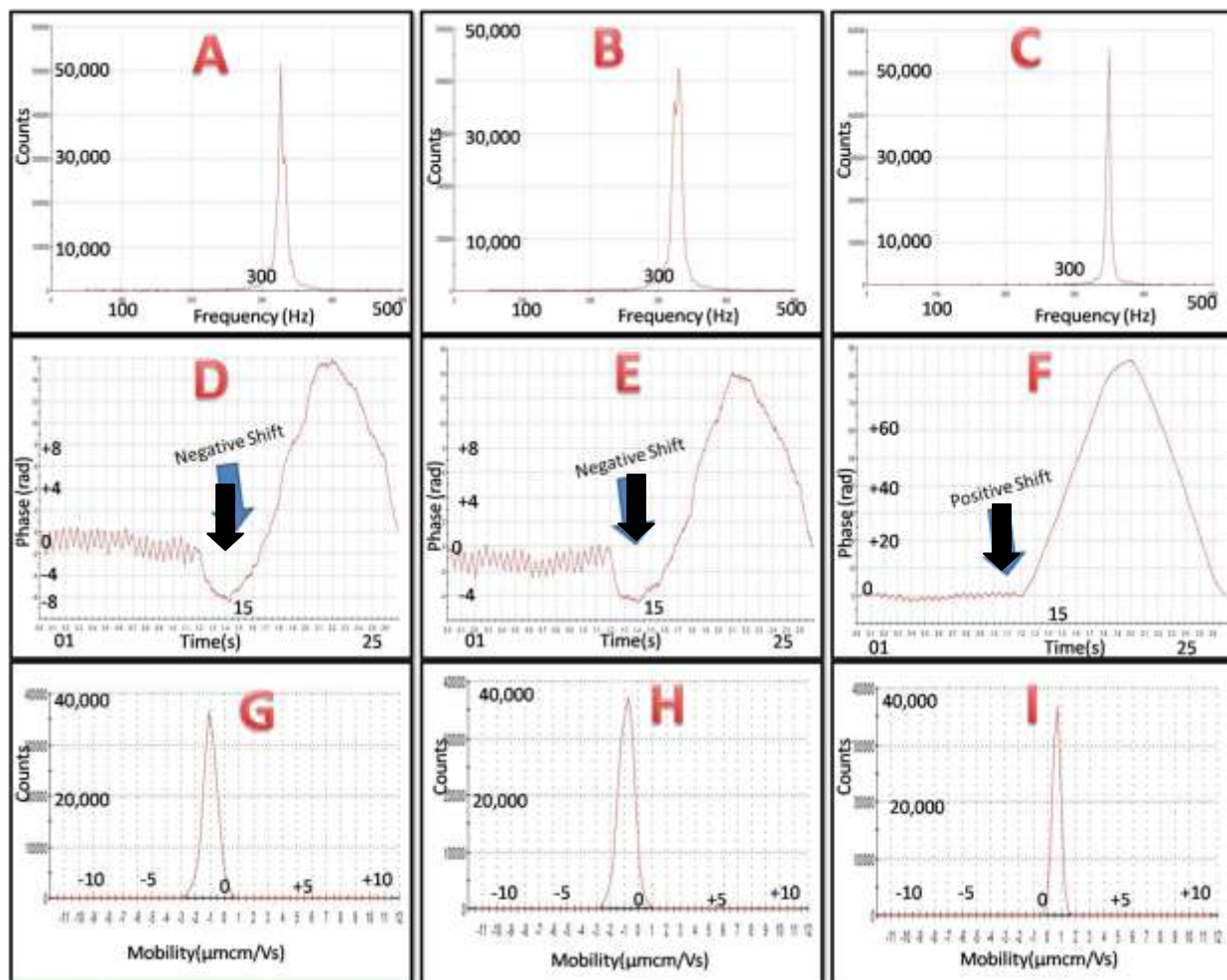


Figure 7.9: A, B, C are frequency plot; D, E, F are phase plot; G, H, I are velocity distribution curve at 30 s, 60 s, and 120 s of reaction time. The negative phase shift in D and E implies zeta potential was negative at 30 s and 60 s but becomes positive at 120 s.

***In situ* SERS measurement for different Hy-Au@AgNR₈₄₀ and their time-dependent assembly formation**

Besides DLS and ELS, we have also performed *in-situ* Raman spectroscopy for monitoring the degree of assembling of Hy-Au@AgNR₈₄₀ by DTT in the reaction medium. The basic difference between Raman scattering and dynamic light scattering is that Raman scattering is inelastic in nature and the intensity of scattering light falls within 1 in 10 million of the

radiation source whereas DLS records Rayleigh scattering which is elastic in nature and has an intensity about 10^{-1} to 10^{-3} of the incident photon. DLS provides us the information for any change in morphological transition during reaction whereas from Raman measurements we can figure out if there is any change in Polarizability owing to the appearance of Ag-S bond during Hy-Au@AgNR₈₄₀-Ass formation.

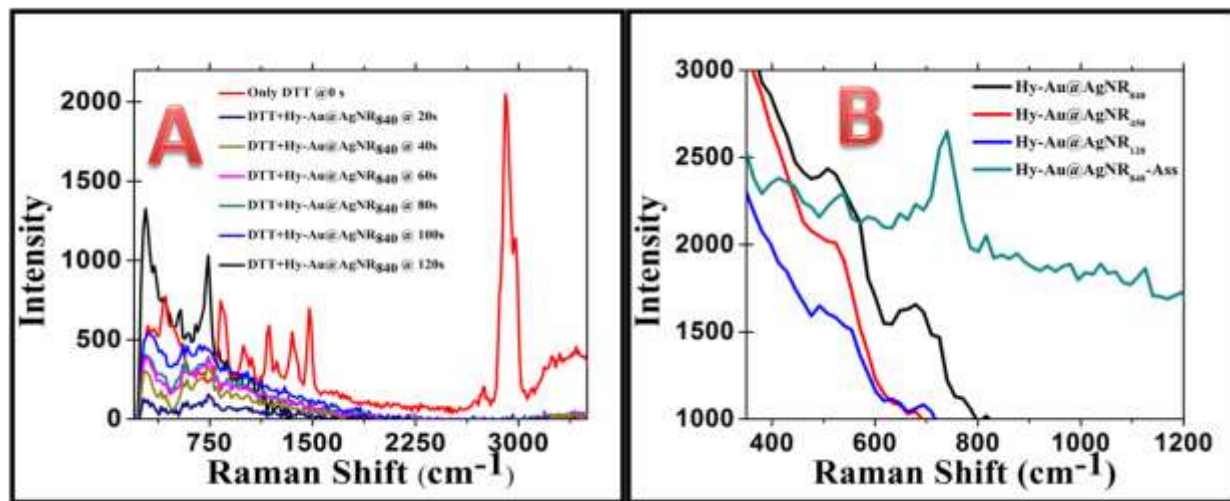


Figure 7.10: (A) SERS measurement of the time-dependent formation of Hy-Au@AgNR₈₄₀-Ass by adding Hy-Au@AgNR₈₄₀S into the DTT solution. (B) SERS spectra of different Hy-Au@AgNRs and Hy-Au@AgNR₈₄₀-Ass.

We have recorded the Raman spectra of pure Hy-Au@AgNR₈₄₀ and pure DTT (10^{-3} M) and we found that Hy-Au@AgNR₈₄₀ is Raman inactive. However, pure DTT produces sharp peaks³⁹⁵ for $\nu_{\text{stretching}}$ (C-H) at 2911 cm^{-1} , ν_{bending} (S-H) at 983 cm^{-1} , along with several other peaks, as clearly observable from **Figure 7.10**. *In situ* Raman measurements were carried out in two different ways, (1) we have added DTT ($20 \mu \text{ M}$) to the Hy-Au@AgNR₈₄₀ solution and found that the peaks at 741 cm^{-1} and 283 cm^{-1} , responsible for Ag-S bond formation³⁹⁶ getting intensified, (2) the reverse process, i.e. Hy-Au@AgNR₈₄₀ was added to pure DTT, where we observed that both the Raman peaks for $\nu_{\text{stretching}}$ (C-H) at 2911 cm^{-1} , ν_{bending} (S-H) at 983 cm^{-1}

originating from pure DTT reduces gradually and disappear finally whereas $\nu_{\text{stretching}}(\text{Ag-S})$ at 741 cm^{-1} increases gradually with time progression. Both the observations indicate the strong chemical interaction between Ag from NPR_{840} and S from DTT. Both Raman and DLS measurements provide well-agreed results for *in-situ* monitoring of Hy-Au@AgNR₈₄₀-Ass formation in the reaction medium.

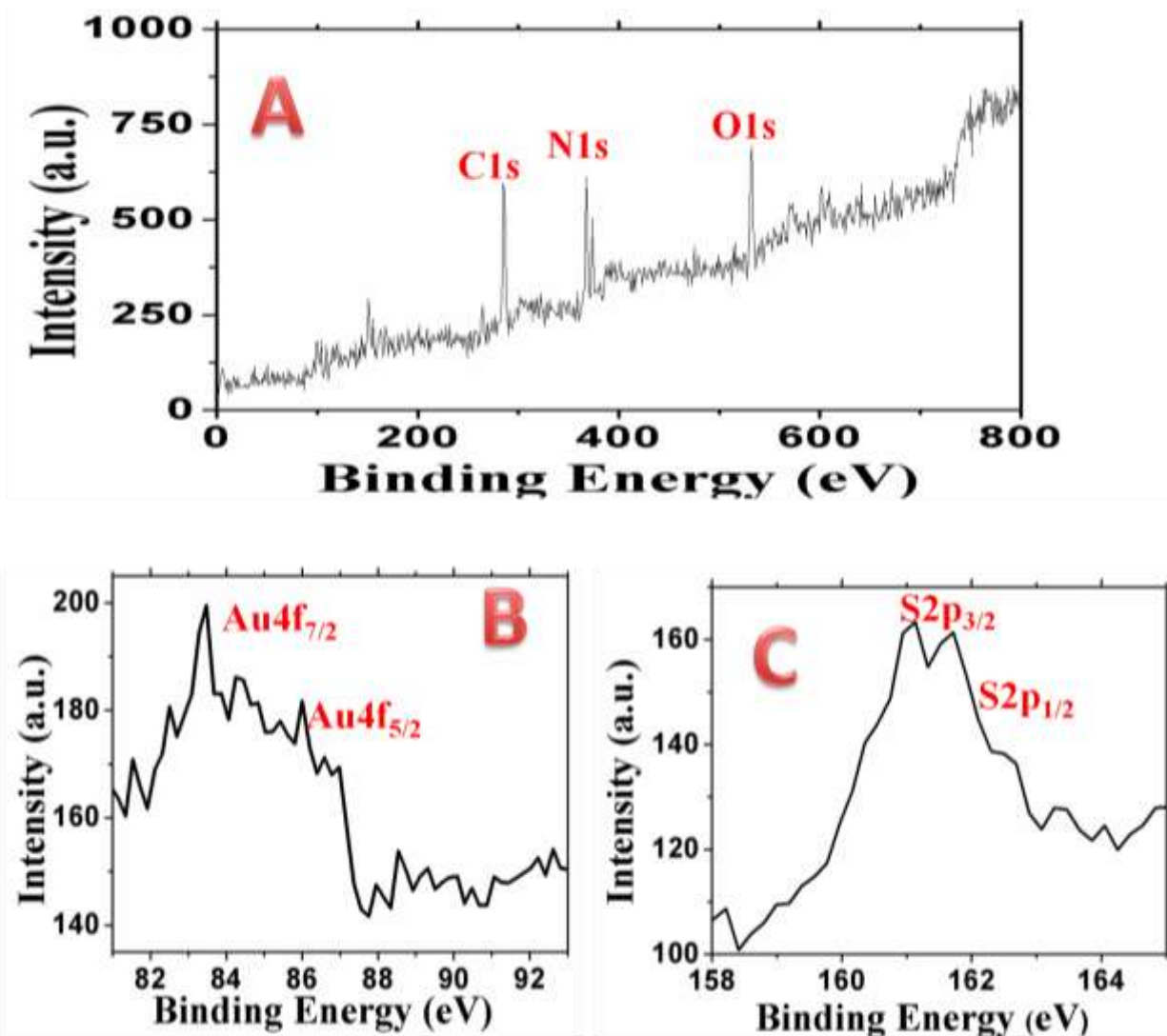


Figure 7.11: (A) XPS survey spectrum of Hy-Au@AgNR₈₄₀-Ass, (B) signature of the presence of trace amount of Au in Hy-Au@AgNR₈₄₀, and (C) S2p lines in Hy-Au@AgNR₈₄₀-Ass. The source of C is from CTAC whereas S and O come from DTT. The intensity of the Au signal is

very poor as we mentioned previously and hard to find appreciable Au in the large distribution of Ag in Hy-Au@AgNR₈₄₀.

To find out the presence of Au as nanoseed in each Hy-Au@AgNRs we have performed their XPS measurements. Despite their trace amount within a large distribution of Ag, we were able to get a very low intensified XPS signature of Au in Hy-Au@AgNR_s as shown in **Figure 7.11B** where Au4f_{7/2} peak appears at 84.0eV. In contrast to Au, the intensity of the Ag spectrum is much higher in XPS for Hy-Au@AgNR₈₄₀. The fitted curve for Ag in Hy-Au@AgNR₈₄₀ shows that Ag present in two oxidation states, in metallic silver Ag(0) and oxidized silver Ag(I).

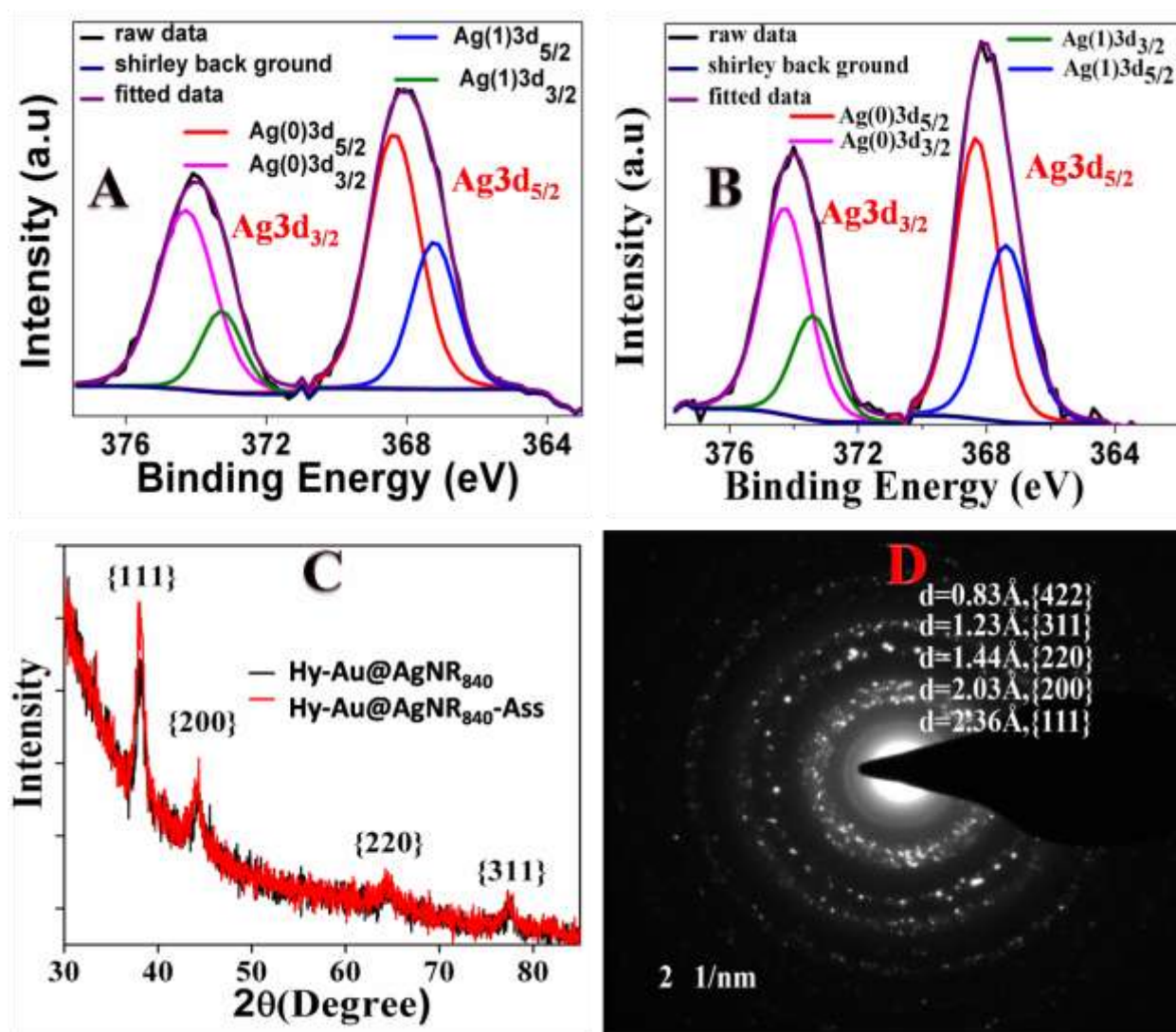


Figure 7.12: A and B are the XPS of Ag3d_{5/2} and Ag3d_{3/2} lines for Hy-Au@AgNR₈₄₀ and Hy-Au@AgNR₈₄₀-Ass. In figure C the XRD of Hy-Au@AgNR₈₄₀ and Hy-Au@AgNR₈₄₀-Ass are shown whereas D shows the SAED pattern of Hy-Au@AgNR₈₄₀-Ass to confirm the {111} is the most intense plane.

The binding energy of Ag3d_{5/2} appears at 368.3 eV for Ag(0) and at 367.2 eV for Ag(I). The presence of Ag(0) is in accordance with our expectation, originating from the reduction of Ag(I) to Ag(0) by AA during Hy-Au@AgNR₈₄₀ synthesis. The presence of Ag(I) is due to the *in situ* formation of AgCl during Hy-Au@AgNR₈₄₀, where Cl comes from the surfactant, cetyltrimethylammonium chloride (CTAC), used in synthesis. The percentage of Ag(0) and Ag(I) is found to be 67.73 % and 32.27 % in Hy-Au@AgNR₈₄₀. In case of Hy-Au@AgNR₈₄₀-Ass, the Ag3d_{5/2} appears at 368.3 eV and 367.39 eV for Ag(0) and Ag(I) respectively. The percentage of Ag(0) and Ag(I) in Hy-Au@AgNR₈₄₀-Ass is 61.11 % and 38.9 %. In general higher binding energy is observed for higher oxidation state for transition metals, however, silver is an exception where lower binding energy is observed for higher oxidation state.¹⁷⁹ Thus Ag(I) appears at lower binding energy than Ag(0) as shown in **Figure 7.12**. The interaction between the –SH and –OH group of DTT and Ag from Hy-Au@AgNR₈₄₀ causes the origination of more oxidized silver i.e. Ag(I) in Hy-Au@AgNR₈₄₀-Ass than Hy-Au@AgNR₈₄₀. The XPS for Ag3d_{5/2} and Ag3d_{3/2} lines in Hy-Au@AgNR₈₄₀ and Hy-Au@AgNR₈₄₀-Ass are shown in **Figure 7.12**. We have also provided the XPS survey spectrum of Hy-Au@AgNR₈₄₀-Ass to confirm the presence of C1s, S2p, etc., in **Figure 7.11**.

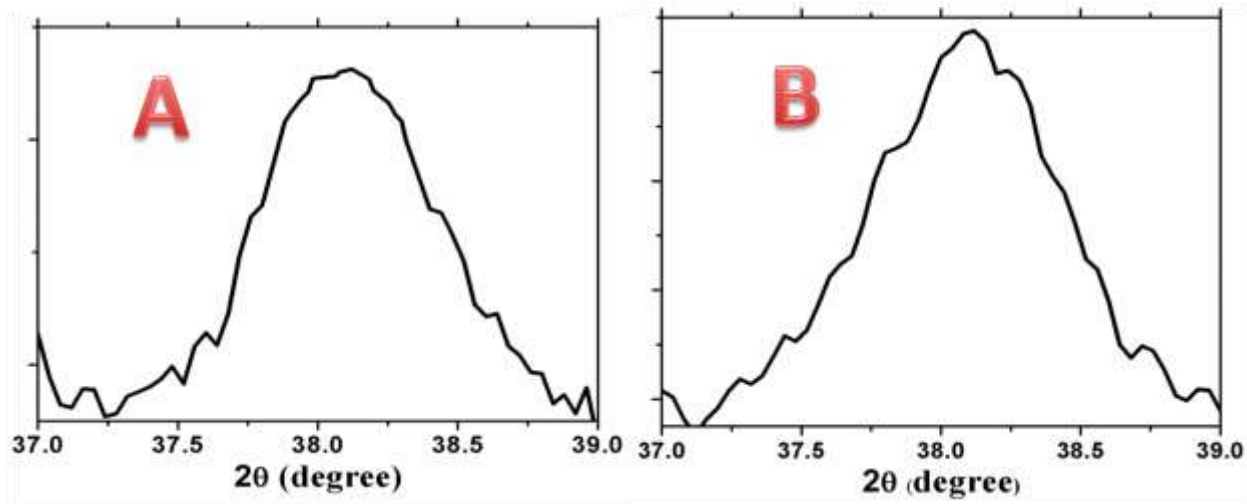


Figure 7.13: The fitted curve of (A) Hy-Au@AgNR₈₄₀-Ass and (B) Hy-Au@AgNR₈₄₀ at $2\theta \approx 38.25^\circ$ for *fcc* {111} facet.

To understand the crystal arrangement, crystal defects, and crystal defect-induced internal tensile strain in more detail for our synthesized Hy-Au@AgNRs or Hy-Au@AgNR₈₄₀-Ass, we have performed their XRD measurements (**Figure 7.12C**) along with their HRTEM. Our XRD measurements show that all the Hy-Au@AgNRs have {111} facet with the most intensified XRD signal than other facets like {200}, {311}, {220}, etc (**Figure 7.12C and 7.12D**). In a perfect nanocrystal, the scattering from the atoms adds constructively which generates a delta function like intensity distribution in the XRD pattern. However, in defect enriched crystals like Hy-Au@AgNRs which contain a coaxial long twin boundary (TB) over their surface (**Figure 7.2**), the symmetry of the crystal lattice destroyed and results in rearrangement of the intensity distribution. Therefore, irregularities in crystals cause the broadening of XRD curves due to the defect induced strain generation. We have calculated the generated strain in different Hy-Au@AgNRs by applying Williamson-Hall isotropic strain model.³⁹⁷ From the fitted curve at $2\theta \approx 38.25^\circ$ ({111} facet appears at 38.25° and gives the most intense peak), as depicted in **Figure 7.13**, we observed that Hy-Au@AgNR₈₄₀ is the most strained one among all the other Hy-

Au@AgNRs which further increases for Hy-Au@AgNR₈₄₀-Ass. The strain within the nanostructure is calculated by Williamson-Hall isotropic model. We have mentioned previously that the extent of broadening is proportional to the crystal defect density. The HRTEM and SEM images confirm that Hy-Au@AgNR₈₄₀-Ass is a crystal defect enriched nanostructure than the Hy-Au@AgNR₈₄₀. To get a comparative study we have calculated the strain from XRD broadening of the curve.

The full width at half maximum (β) for Hy-Au@AgNR₈₄₀-Ass is 0.88° whereas for Hy-Au@AgNR₈₄₀ is 0.79° . Mathematically the generated strain (ϵ) is defined as:

$\epsilon = \beta/4\tan\theta$, where θ is in radian.

Since $\{111\}$ facet appears for both Hy-Au@AgNR₈₄₀-Ass and Hy-Au@AgNR₈₄₀ at $2\theta = 38.25^\circ$, the value of $\theta = 0.33$ in radian unit for the above equation.

By incorporating the respective value of β for different nanostructures and $\theta = 0.33$, obtained values of ϵ for Hy-Au@AgNR₈₄₀-Ass and Hy-Au@AgNR₈₄₀ are 1.11×10^{-2} and 0.95×10^{-2} respectively. **Table 7.1** shows the estimated strain values (ϵ) for different Hy-Au@AgNRs and the targeted Hy-Au@AgNR₈₄₀-Ass, calculated from the measured 2θ value and fitted full width half maximum or FWHM (β) from the recorded XRD spectra. The origin of maximum internal strain for Hy-Au@AgNR₈₄₀ can easily be understood by analyzing their TEM and HRTEM and comparing it with other Hy-Au@AgNRs as shown in **Figure 7.2**. From TEM and HRTEM, it is clearly visible that each Hy-Au@AgNRs has a central TB on their surface. Twinned nanorods (Hy-Au@AgNRs) experience more internal tensile strain than untwined ones because atoms situated on TB are coordinatively unsaturated. Having the largest and enriched TB on its surface, Hy-Au@AgNR₈₄₀ should hold the maximum number of unsaturated atoms and expected to show greater XRD broadening than Hy-Au@AgNR₄₅₀ and Hy-Au@AgNR₁₂₀. However, when Hy-

Au@AgNR₈₄₀-Ass is prepared by assembling multiple Hy-Au@AgNR₈₄₀s, further broadening in the XRD curve occurs (**Figure 7.13**). This broadening in XRD is due to the appearance of multiple low-coordinated crystal defects on Hy-Au@AgNR₈₄₀-Ass due to its porous structure as confirmed from TEM and HRTEM images (**Figure 7.2**). The order of internal tensile strain due to crystal irregularities within the nanostructures is thus Hy-Au@AgNR₈₄₀-Ass > Hy-Au@AgNR₈₄₀ > Hy-Au@AgNR₄₅₀ > Hy-Au@AgNR₁₂₀.

Table 7.1: Estimation of developed strain within different Hy-Au@AgNRs and the targeted Hy-Au@AgNR₈₄₀-Ass from the measured FWHM (β) and θ values (in radian) in XRD spectra.

System	FWHM, β (in Degree)	FWHM, β (in Radian)	internal tensile strain (ϵ)
Hy-Au@AgNR ₈₄₀ -Ass	0.88	0.0154	1.1×10^{-2}
Hy-Au@AgNR ₈₄₀	0.79	0.0138	9.5×10^{-3}
Hy-Au@AgNR ₄₅₀	0.71	0.0123	8.9×10^{-3}
Hy-Au@AgNR ₁₂₀	0.65	0.0113	8.2×10^{-3}

To understand the role of gold seed, length of Hy-Au@AgNRs, and TB on their surface to control their internal tensile strain, we have calculated the strain values for all the modeled systems. In the present work, the diameter can also play an essential role in determining their mechanical strain. Therefore, we have calculated the mechanical properties of the Hy-Au@AgNR_s by changing their lengths and diameters. More specifically, we have focused on calculating the Au-seed induced mechanical strain for the modeled Hy-Au@AgNRs. For this, we have constructed pure Ag-nanorods with lengths of 40 Å, 60 Å and 80 Å and diameters of ~8.3 Å. After the optimization, spherical Au seed has been incorporated inside each of the nanorods for modeling the < 111 > surface along with the < 110 >, and twin boundary planes.

Table 7.2: Optimized parameters (length, diameter, and strain) for pure AgNRs and Hy-Au@AgNRs. Here D is the optimized diameter of pure AgNRs, $D^\#$ is the optimized diameter of Hy-Au@AgNRs, $D - D^\#$ is the difference in diameter between the optimized diameter of pure AgNRs and Hy-Au@AgNRs, and $d^*_{\text{Ag-Ag}}$ is the average Ag-Ag bond length on the surface and twin boundary for Hy-Au@AgNRs. $\Delta d^*_{\text{Ag-Ag}}$ is the difference between the Ag-Ag bond length in bulk Ag metal and different Hy-Au@AgNRs.

Rod name	Optimized Length of Hy-Au@AgNRs	Diameter (D) of pure AgNRs	Diameter ($D^\#$) of Hy-Au@AgNRs	$D - D^\#$	$d^*_{\text{Ag-Ag}}$ in Hy-Au@AgNRs	$\Delta d^*_{\text{Ag-Ag}}$ in Hy-Au@AgNRs	Strain in Hy-Au@AgNRs
40 Å	41.26 Å	8.32 Å	8.32 Å	0.00 Å	2.75 Å	0.14 Å	4.84 %
60 Å	57.57 Å	8.35 Å	8.34 Å	0.01 Å	2.74 Å	0.15 Å	5.19 %
80 Å	79.26 Å	8.43 Å	8.40 Å	0.03 Å	2.73 Å	0.16 Å	5.53 %

We have then measured the geometrical parameters for all the structures as given in **Table 7.2**. It is observable that with increasing the rod length, the average Ag-Ag bond length reduces which results in a contraction in the optimized rod length. The same effect (i.e. contraction) should also be observable for the optimized rod diameter, though the diameter of the rod increases gradually. These two effects of shortening the optimized rod length and lengthening of optimized rod diameter are contrary to each other. Therefore, the stability of rods can be increased by increasing their diameter with a shorter Ag-Ag bond by the coaxial formation of twin boundaries. We indeed observed increments in the optimized diameter of the modeled NRs through Au seeding though we have incorporated only one Au seed for each

modeled NRs. However, this can't influence a homogeneous increment of rod diameter throughout the rod length (40-80 Å). This could be the reason for twin boundary formation as observed experimentally. Hence the presence of TB along the <110> facet of the nanorod may increase the stability of the rod.

For the calculation of strain (ε) in the Hy-Au@AgNRs, we have used the following relation⁷

$$\varepsilon = (d^* - d_0)/d_0 = \delta d/d_0 \dots\dots\dots(1)$$

Here, d^* is the average Ag-Ag bond-length of the system under consideration and d_0 is the Ag-Ag bond-length (2.89 Å) in their pure face-centered cubic bulk structure. The above relation signifies the effect on the mechanical strain when a system (bulk) goes through structural reconstruction/evolution. We find that the calculated strain is maximum for the longer size Hy-Au@AgNRs. Therefore, the resultant mechanical strain increases proportionally with the NR length. These opposing effects of the shortening of Ag-Ag bond length (compared to *fcc* bulk Ag) and lengthening of the diameter may play an important role in the formation of TB on the Hy-Au@AgNRs surface.

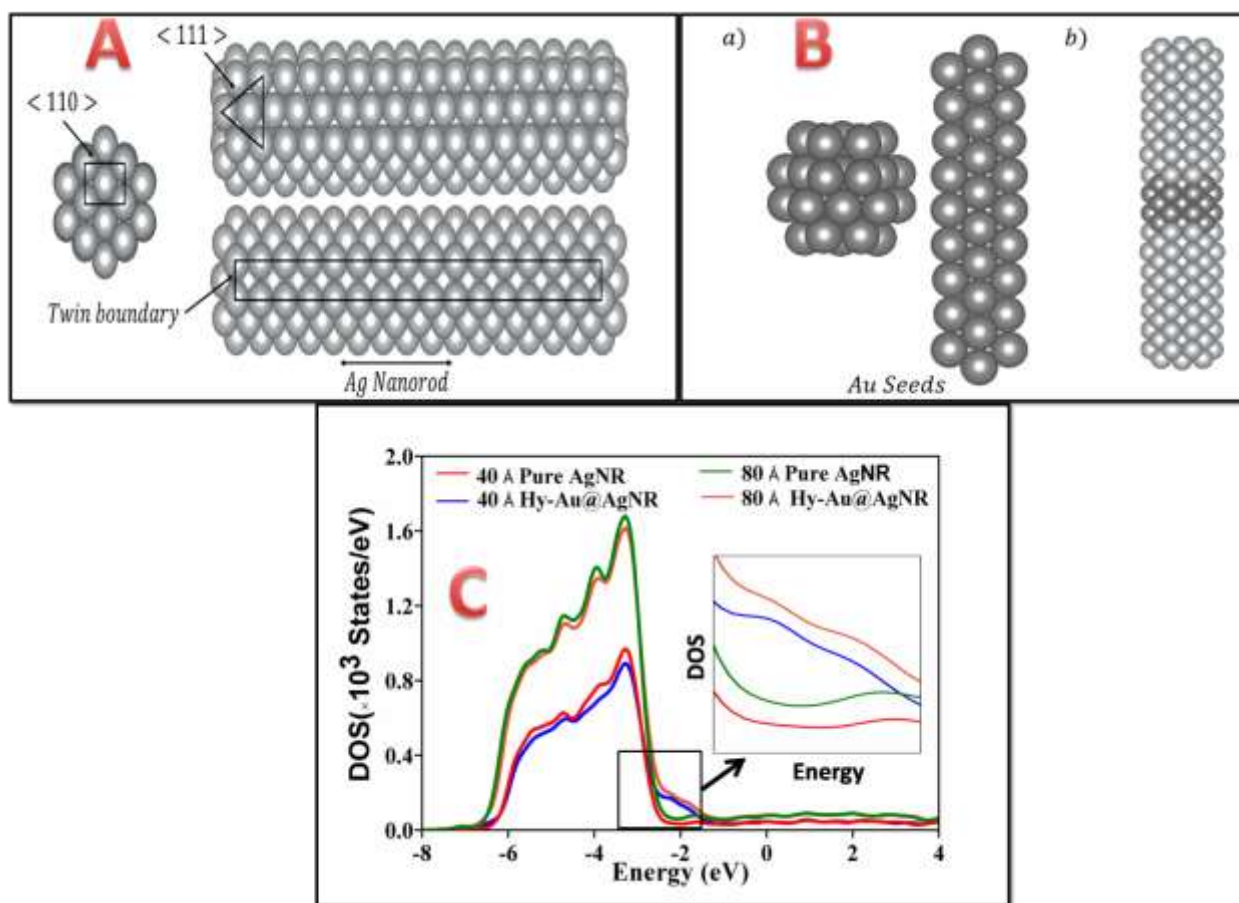


Figure 7.14: (A) Modeled nanorod structure with <111> and <110> facets. (B) Possible Au seeding (spherical and rod-shaped) and spherical Au seeded Hy-Au@AgNRs. (C) The density of states (DOS) of pure Ag and Au-seeded AgNRs with 40 Å and 80 Å lengths.

To find out the effect of Au-seed incorporation on the electronic properties of Hy-Au@AgNRs, we have calculated their density of states (DOS). As shown in **Figure 7.14**, with increasing the length of rods, the electron density shifts towards the Fermi level. Interestingly, the shift is higher for Au seeded Ag NRs. So, this indicates that the Hy-Au@AgNR₈₄₀ should show more upshift of DOS towards the Fermi level than the Hy-Au@AgNR₄₅₀ and Hy-Au@AgNR₁₂₀. When Hy-Au@AgNR₈₄₀ is assembled into Hy-Au@AgNR₈₄₀-Ass, it creates multiple low coordinated crystal sites like stepped surface, terrace, kinks, edges, etc., as shown in **Figure 7.15**, which further increase the internal strain as seen from XRD broadening and

explained in SI section. Hence DOS of Hy-Au@AgNR₈₄₀-Ass will be more upshifted towards the Fermi level than the corresponding Hy-Au@AgNR₈₄₀.

From the above discussion, we can say that Au-seed induced longer Hy-Au@AgNRs may shift the d-band center more towards the Fermi level. Therefore, the question arises whether it is possible to prepare Au-Ag NR more than 840 nm to maximize this effect?

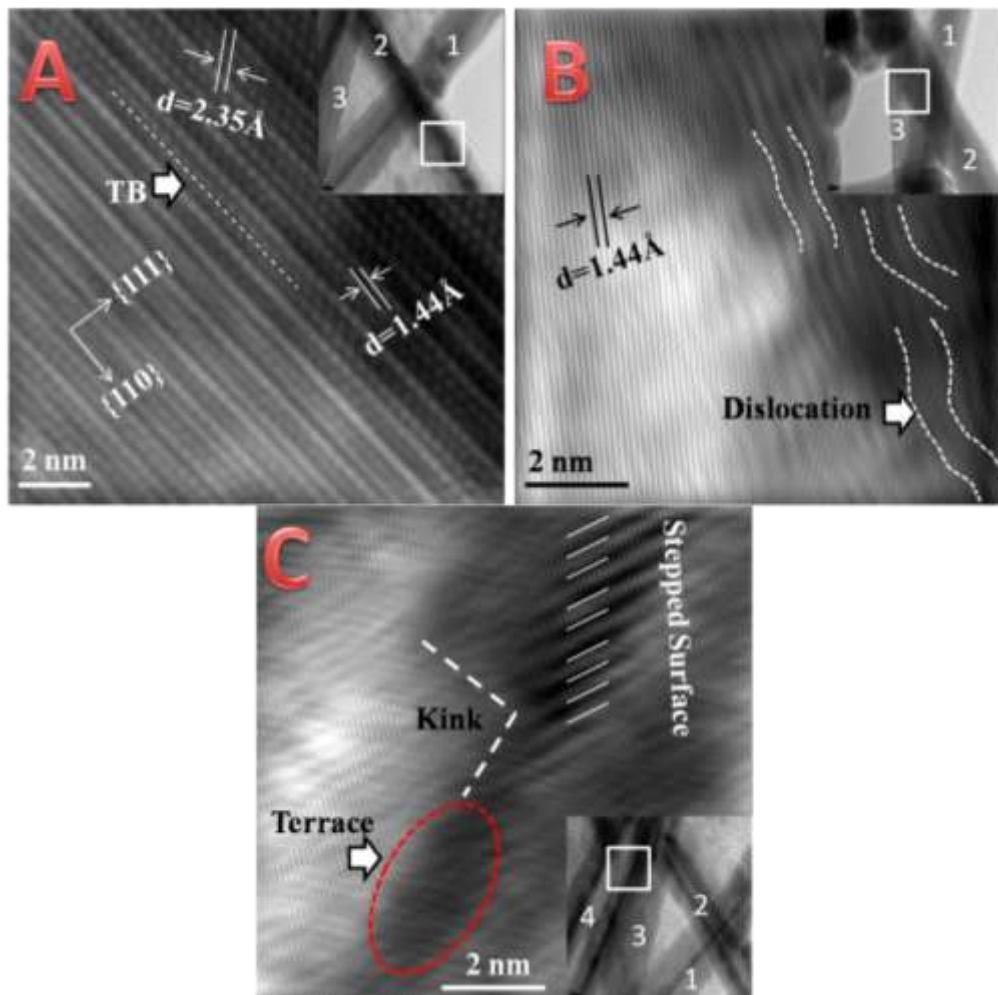


Figure 7.15: Creation of multiple low coordinated crystal sites like stepped surface, terrace, kinks, edges, etc., during the formation of Hy-Au@AgNR₈₄₀-Ass from the constituents Hy-Au@AgNR₈₄₀S.

We have previously reported pure Ag nanorods with lengths of more than 10 μm .³⁹⁸ Bimetallic Au-Ag nanorods of length $\sim 1.2 \mu\text{m}$ have also been reported¹⁴ earlier. Details about the synthesis and control of length, morphology, monodispersity, and efficiency of assembly formation are included in the following section (**Figure 7.16-7.22**). Due to their very low yield and poor stability which converts them into spherical particles with time, Hy-Au@AgNRs with length beyond 840 nm have not been used for further study.

Synthesis and control of Hy-Au@AgNRs and Hy-Au@AgNR₈₄₀-Ass:

We have mentioned previously that different length Au doped Ag rods were prepared by varying the surfactant concentration at constant temperature (55° - 60°C). However, we have also monitored the effect of the variation of other parameters during synthesis like seed concentration, silver nitrate concentration, AA concentration, DTT concentration, etc. and optimized the condition for preparing the longest NR (Hy-Au@AgNR₈₄₀) and its assembly (Hy-Au@AgNR₈₄₀-Ass). Details are discussed below:

Effect of temperature:

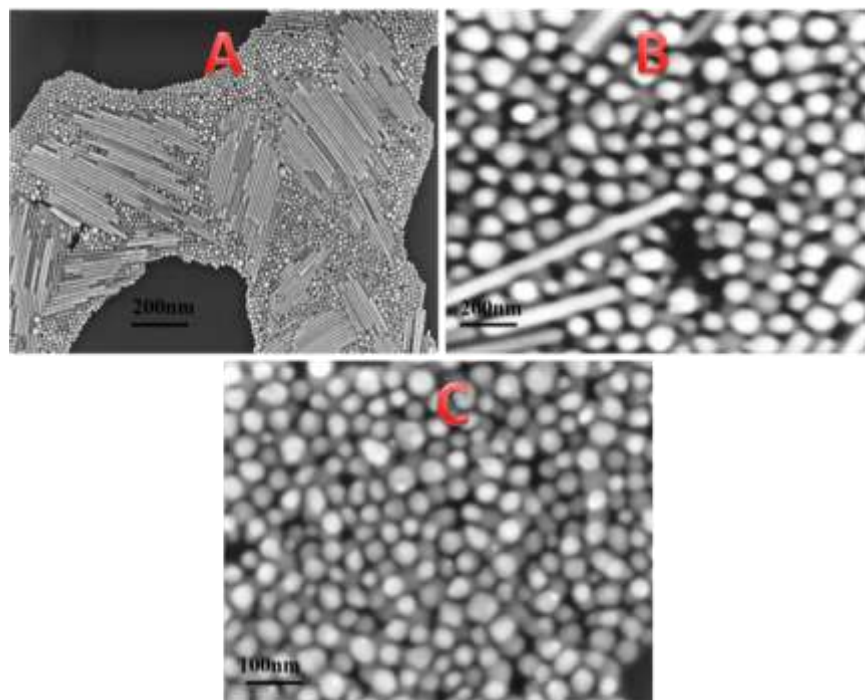


Figure 7.16a: Effect of temperature on Hy-Au@AgNR₄₅₀ morphology, at (A) 60-70 °C, (B) 70-80 °C, and (C) 80-90 °C. In all cases, optimized conditions for other physical and chemical parameters remain unchanged.

During the synthesis of Hy-Au@AgNRs, the temperature was always kept constant within the range of 55-60 °C. As we increase the temperature beyond this range, the aspect ratio of the rod gradually reduces with temperature and finally transform into spherical- and oval-shaped particle as shown in **Figure 7.16a**. When the temperature exceeds 60 °C, it was found that two Au seeds are piled up and Ag deposited onto it as shown in **Figure 7.16b**. Below 60 °C there is no sign of aggregation of Au seeds and at room temperature (30 – 40 °C) AgNO₃ cannot be reduced by ascorbic acid.

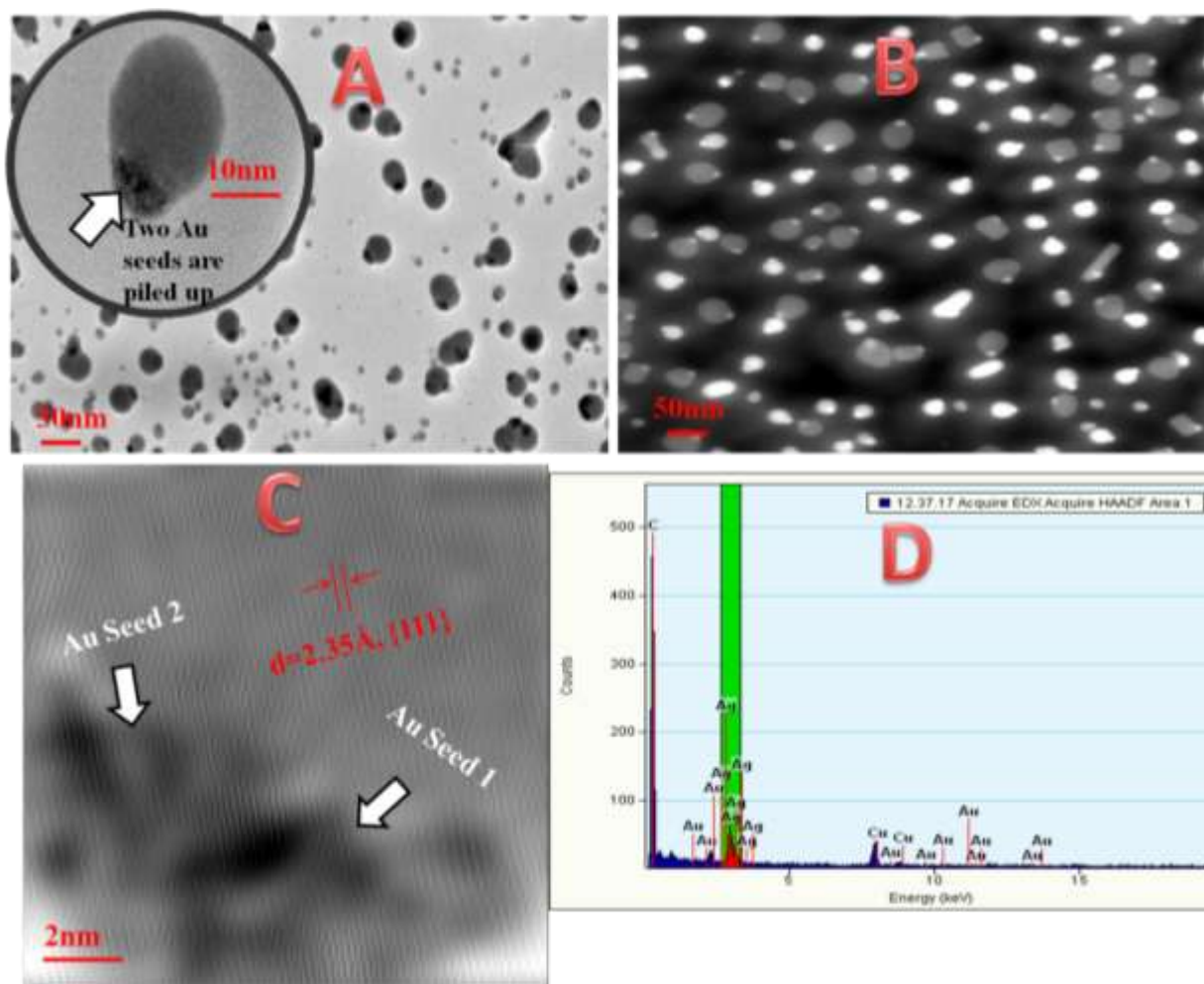


Figure 7.16b: Association of Au seed followed by Ag deposition at a higher temperature. Stacking up of Au seeds is verified by (A) TEM, (B) HAADF, (C) HRTEM, and (D) EDX.

Effect of Au seed:

If we use Ag seed during synthesis we did not get any rod-shaped particle, instead, a colloidal solution of Ag is formed only. On the contrary, the addition of Au seed initiates the seeding process of Hy-Au@AgNR efficiently. As the reduction potential of Au(III)/Au(0) is much higher (+1.5V) is much higher than the reduction potential of Ag(I)/Ag(0) system, leaching of Au seed in the latter case can easily be discarded. By observing the above cases we can suggest that Au seed acts as a catalyst here to enhance the reducing power of AA to assist the reduction of Ag^+ to

Ag^0 . The amount of Au seed was optimized to 2 mL in 50 mL of the reaction mixture. The kinetics of nanoparticles formation by using Ag and Au seed by keeping the synthesis protocol the same is shown in **Figure 7.17a** and the effect of the variation of Au seed amount is shown in **Figure 7.17b**.

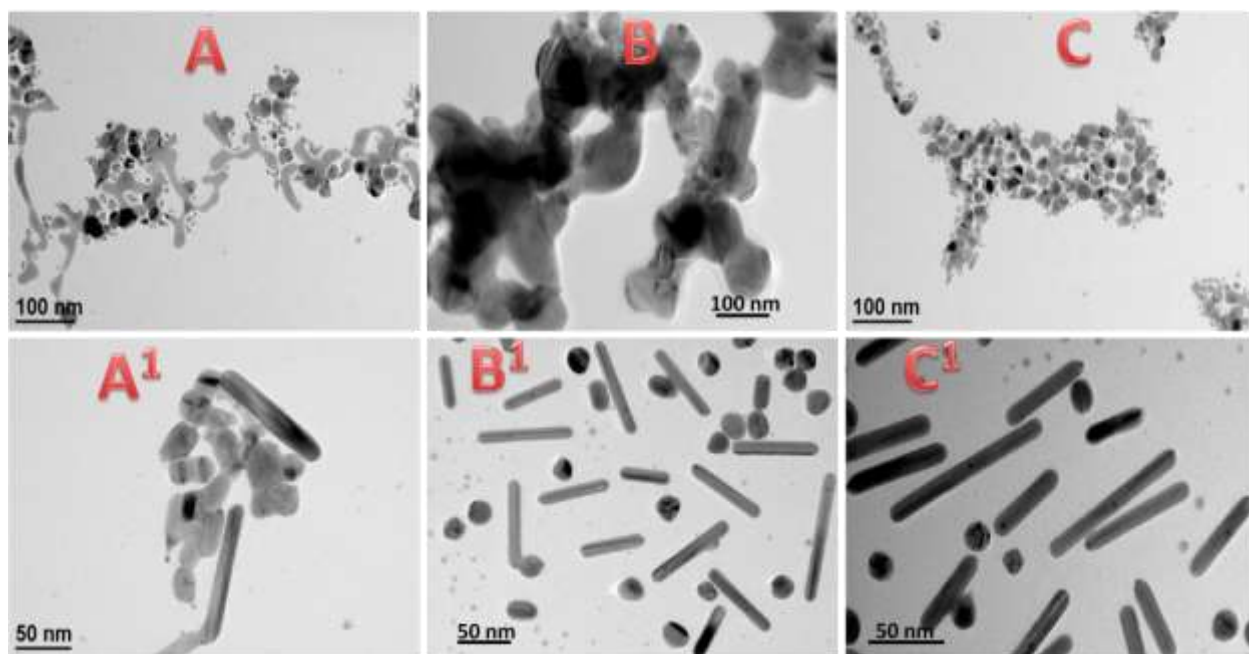


Figure 7.17a: Kinetics of Ag seed-based nanorod formation at (A) 30 min, (B) 60 min, and (C) 90 min and Au seed-based Hy-Au@AgNR₁₂₀ formation at (A') 30 min, (B') 60 min, and (C') 90 min. In all cases, optimized conditions for other physical and chemical parameters remain unchanged.

A greater amount of Au seed than the optimized volume results in the decrease of nanorod length whereas, a lower amount of Au seed results in the decrease of nanorod yield.

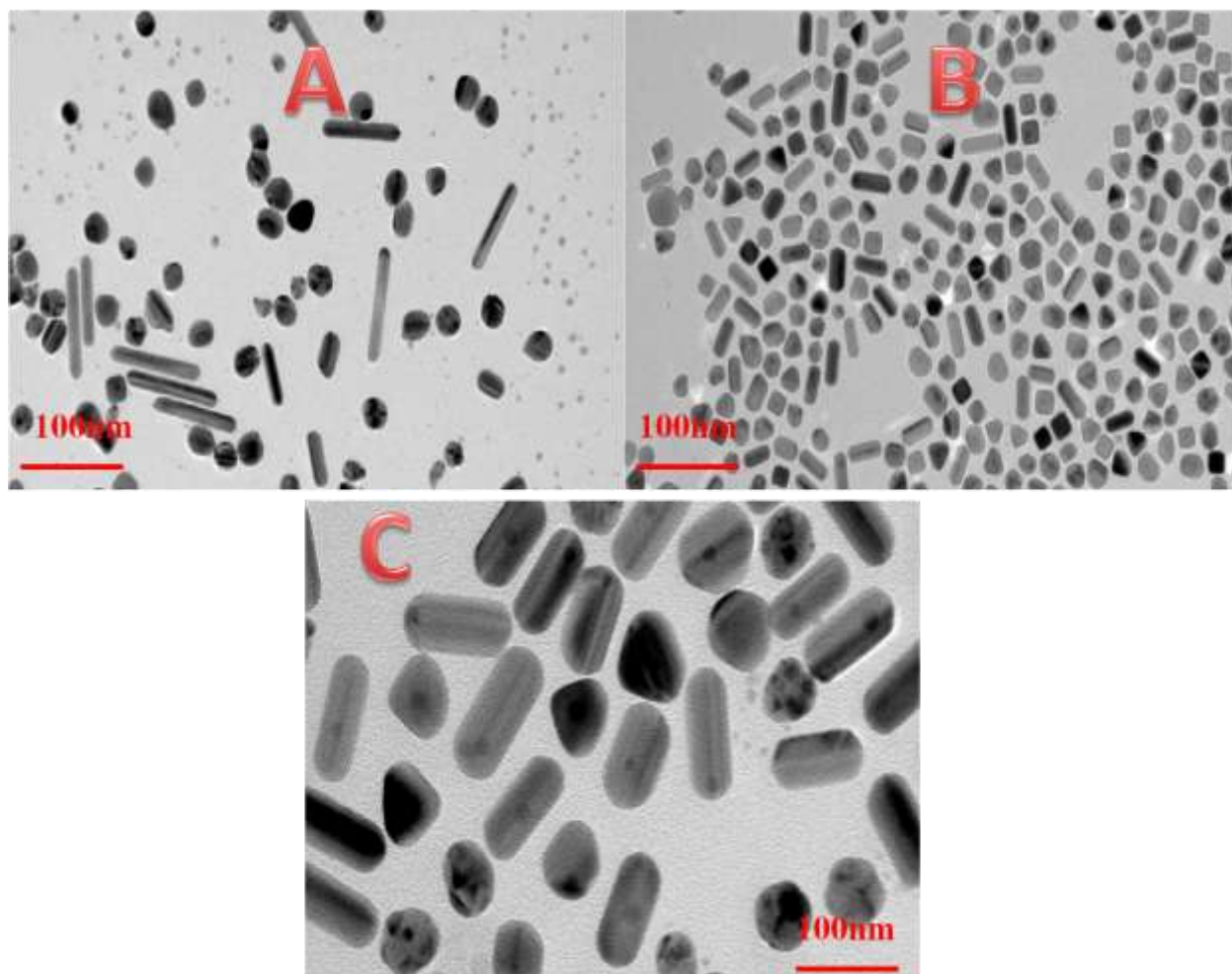


Figure 7.17b: The effect of the variation Au seed amount [(A) 1 mL, (B) 4 mL, and (C) 2 mL] on Hy-Au@AgNR₁₂₀ synthesis. In all cases, optimized conditions for other physical and chemical parameters remain unchanged.

Effect of silver nitrate concentration:

The addition of AgNO₃ to the CTAC solution during synthesis forms insoluble AgCl immediately which turns the solution turbid. However, in presence of Au seed, the amount of AgCl formation is much less as the added Au seeds act as catalysts to assist the reduction of Ag⁺

ions by enhancing the reducing power of AA as discussed before. The concentration was adjusted to 2 mL of 10^{-2} (M) AgNO_3 into 45 mL of CTAC solution. Greater (> 2 mL) amount of AgNO_3 causes the formation of more Ag spheres whereas a lower amount of AgNO_3 reduces the nanorod length. The effect of the variation of the AgNO_3 amount is shown in **Figure 7.18**.

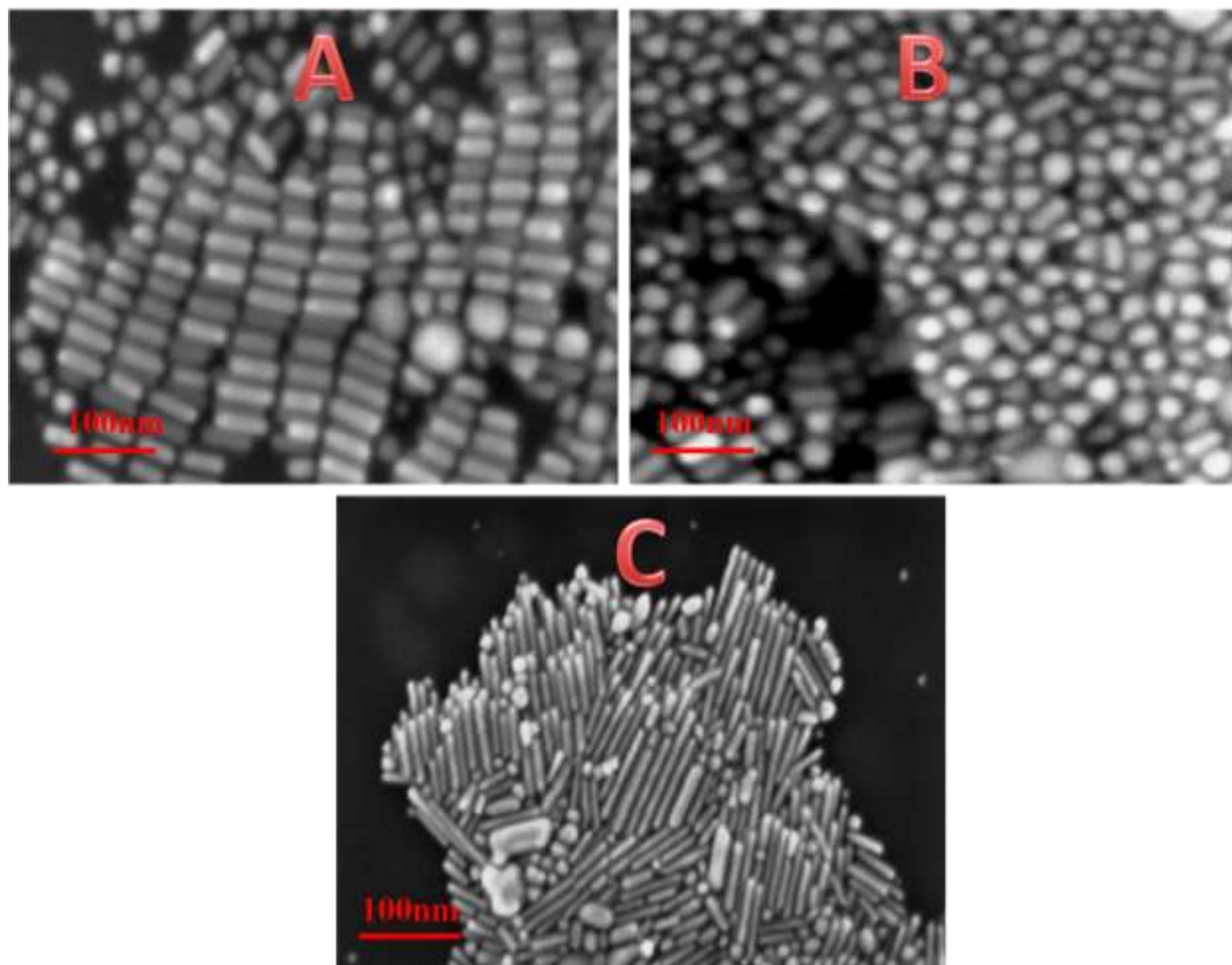


Figure 7.18: Effect of AgNO_3 concentration (in the reaction mixture) on the efficiency of Hy-Au@AgNR₁₂₀ formation. (A) 1 mL of 10^{-2} (M) AgNO_3 generates nanorods of length ~ 50 nm, (B) 4 mL of 10^{-2} (M) AgNO_3 generates nanospheres of diameter ~ 20 -25 nm, and (C) 2 mL of 10^{-2} (M) AgNO_3 generates Hy-Au@AgNR₁₂₀s. In all cases, optimized conditions for other physical and chemical parameters remain unchanged.

Effect of CTAC concentration:

We have mentioned in the main manuscript that a greater amount of CTAC reduces the length of Hy-Au@AgNRs. To prepare the longest Hy-Au@AgNR, the amount of CTAC was optimized to 0.01g CTAC in 45 mL of water. By using less than 0.01 g CTAC in 45 mL water we couldn't generate any Hy-Au@AgNR. The formation of Hy-Au@AgNRs by using 0.01 gm CTAC in 45 mL water has been detailed in the main manuscript. The effect of the variation of CTAC concentration above 0.01 gm/45 mL is shown in **Figure 7.19**.

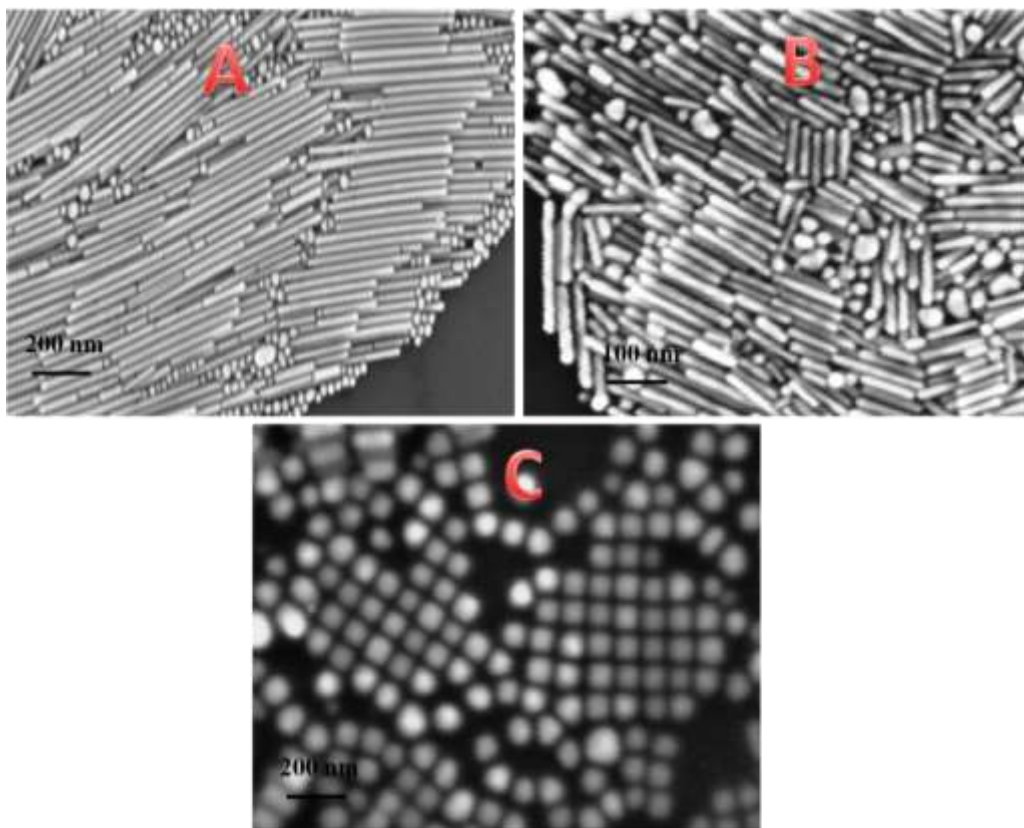


Figure 7.19: Effect of CTAC concentration with (A) 0.025 gm CTAC in 45 mL water for the formation of Hy-Au@AgNR₄₅₀, (B) 0.05 gm CTAC in 45 mL water for the formation of Hy-Au@AgNR₁₂₀, and (C) 0.1 gm CTAC in 45 mL water for the formation of Hy-Au@AgNR₅₀. In all cases, optimized conditions for other physical and chemical parameters remain unchanged.

Effect of ascorbic acid concentration:

A literature survey provides that ascorbic acid (AA) acts as a mild reducing agent.^{174,319} As mentioned earlier that at room temperature ascorbic acid cannot reduce Ag^+ to Ag^0 , though, its reduction power increases at elevated temperature (at 60 °C). Contrary to that, the presence of Au seed enhances the reducing power of AA substantially and efficiently converts all Ag^+ into Ag^0 at 60 °C. We have varied the AA concentration and optimized the amount as 500 μL of 10^{-1} M of AA to generate well structured Hy-Au@AgNRs. The effect of the variation of AA concentration is shown in **Figure 7.20**.

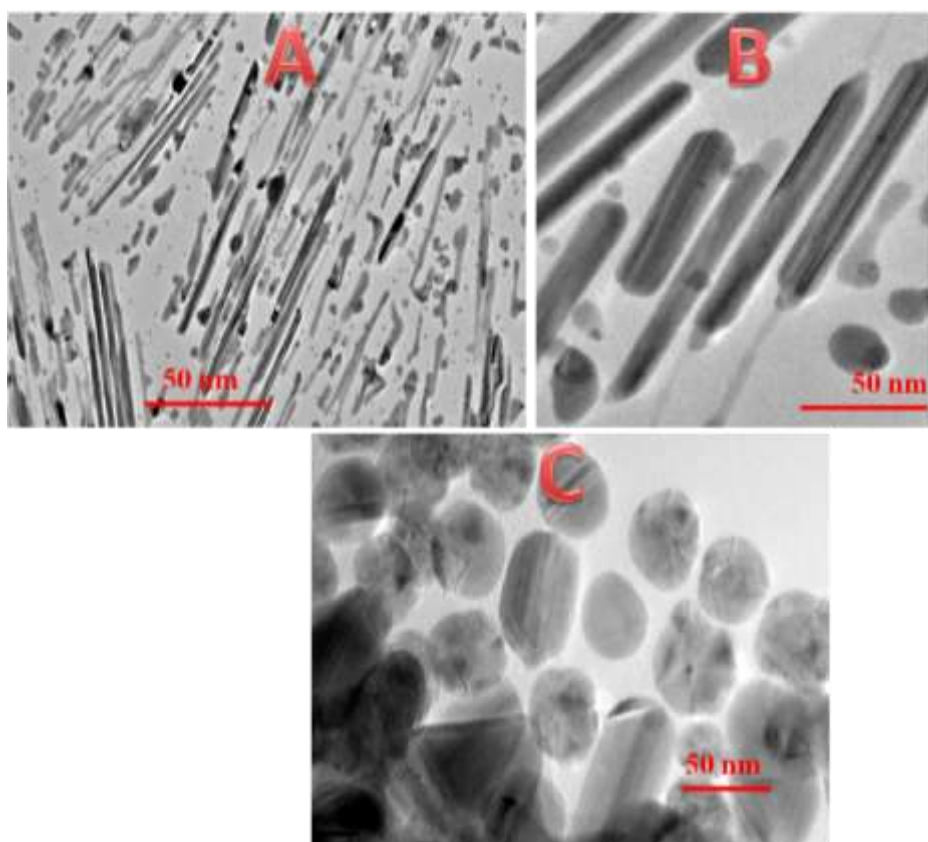


Figure 7.20: The effect of the variation of AA concentration on Hy-Au@AgNR₁₂₀ formation with (A) 250 μL 10^{-1} M of AA, (B) 500 μL 10^{-1} M of AA (optimized condition), and (C) 1 mL 10^{-1} M of AA. In all cases, optimized conditions for other physical and chemical parameters remain unchanged.

Effect of DTT concentration:

During Hy-Au@AgNRs preparation, we have used 20 μM DTT at room temperature. Each DTT molecule has two -SH groups attached to it. Sulfur has a strong binding affinity to noble metals like Au, Cu, and Ag.³⁹⁹ Binding energy calculations by using density functional theory (BP86, B3LYP, and CAM-B3LYP) and ab initio methods³⁹⁹ (MP2 and CCSD(T)) indicate that for pure metal clusters, the tendency of a metal to interact with -SH group varies in the order of $\text{Au} > \text{Cu} > \text{Ag}$. In binary alloy clusters, alloying Au with Cu and Ag decreases the attraction of Au towards -SH, while alloying Ag and Cu by Au increases the attraction of Ag and Cu towards -SH significantly.

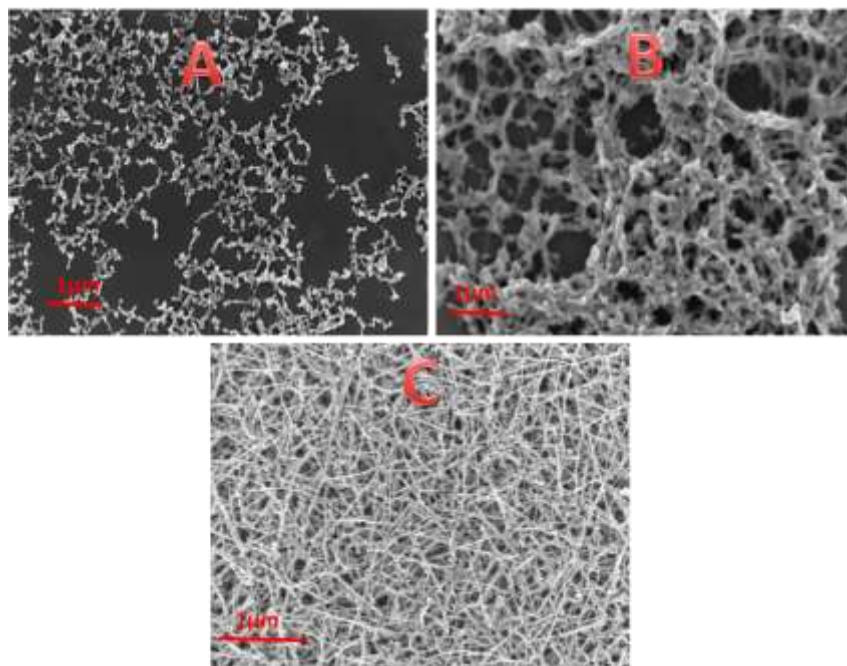


Figure 7.21: The effect of the variation of DTT concentration on the efficiency of Hy-Au@AgNR-Ass formation with the final concentration of DTT in the Hy-Au@AgNR₈₄₀ solution as (A) $< 20 \mu\text{M}$, (B) $> 20 \mu\text{M}$, and (C) $= 20 \mu\text{M}$.

Since in our case the synthesized Hy-Au@AgNRs are a case of alloying Ag by Au, we expect a strong affinity of -SH group from DTT towards the nanorod surface. Moreover, the dissociation energy values in their study⁷⁵ for isolated metal clusters specify the more favorable

formation of binary alloy clusters (Au_nAg_m) over pure ones. Hence the inherent stability of Hy-Au@AgNRs due to gold doping and increased attraction of Ag towards $-\text{SH}$ enhances the stability of the resultant Hy-Au@AgNR-Ass by preserving the individual NR's morphology. Variation of DTT concentration to control the effective assembly formation shows that a DTT concentration less than $20\ \mu\text{M}$ causes less efficient assembly formation and hence a nanostructure with less and uneven porous nature. On the contrary, DTT with a concentration greater than $20\ \mu\text{M}$ causes a more aggregated structure of Hy-Au@AgNR₈₄₀ and precipitates out from the solution. The effect of the variation of DTT concentration on the efficiency of Hy-Au@AgNR-Ass formation is shown in **Figure 7.21**. Hence to achieve catalytically most active Hy-Au@AgNR-Ass formation, optimized conditions are (i) use of 0.01 g CTAC in 45 mL of water with controlled heating at $55\text{--}60\ ^\circ\text{C}$, (ii) followed by addition of 2 mL Au seed, 2 mL of 10^{-2} (M) AgNO_3 , 500 μL of 10^{-1} (M) of AA, and finally (iii) 100 μL of 10^{-2} M freshly prepared DTT into the total volume of centrifuges Hy-Au@AgNR₈₄₀.

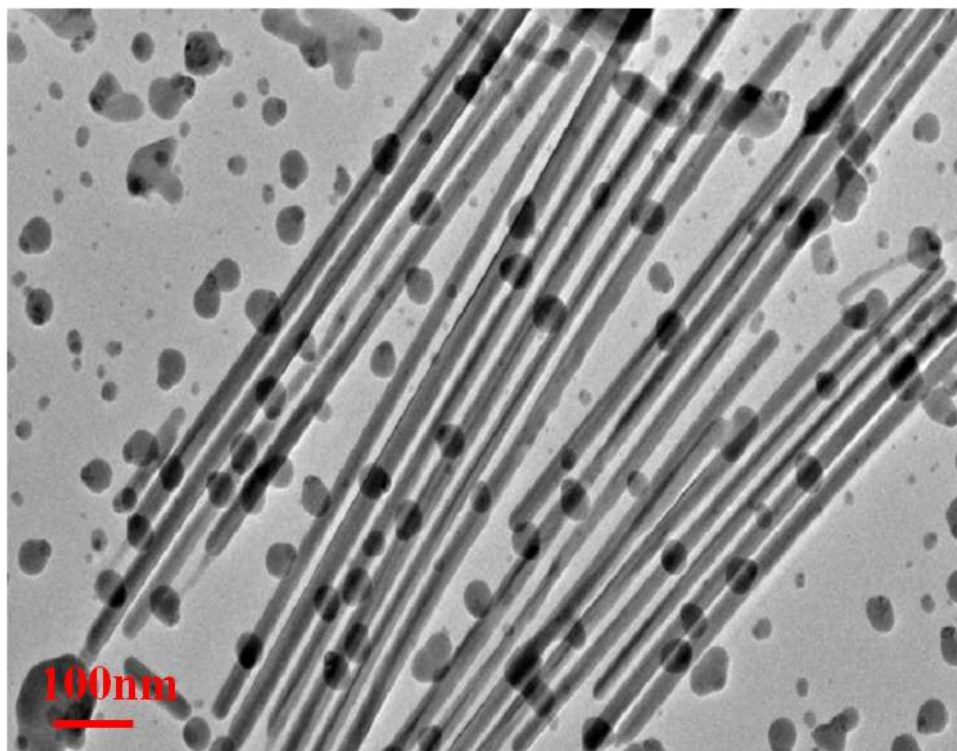


Figure 7.22: Formation of Hy-Au@AgNR with length $\sim 1\text{-}1.2\ \mu\text{m}$ by maintaining the molar ratio between AgNO_3 and AA at 1:20 during synthesis.

At our optimized condition, we conclude that the nanorods of higher length (Hy-Au@AgNR₈₄₀) can be prepared by applying .01 g CTAC, and maintaining the molar ratio between AgNO_3 and AA at 2:5. However, an increase in AA volume (1 mL) to maintain the ratio at 1:5, bigger nanorods of length about $1\text{-}1.2\ \mu\text{m}$ can easily be prepared as shown in **Figure 7.22**. By comparing **Figure 7.22** with **Figure 7.2E**, it is clearly visible from **Figure 7.22** that we could generate longer nanorods but their yield and stability are very poor and with time they convert into spherical particles. Due to their rapid structural deformation (from rod to a sphere) which results in the disappearance of surface coaxial twin boundaries, their tested catalytic activity is not promising. As a result of these limitations, we restrict our synthesis, characterization, and catalytic activity measurements of Hy-Au@AgNRs with length till 840 nm as described before. Beyond the developed strain within the nanostructure and resultant DOS with respect to the Fermi level, there are so many other factors on which their catalytic activity depends substantially. In our previous studies, we have shown that pure gold nanostructure with {110} facet has a strong affinity for ascorbic acid.⁴ In contrast, gold-silver nano-alloy with {220} orientation shows enormous oxidizing capability for uric acid.⁷ Thus, chemical composition (pure Vs alloy) of the nanocatalyst determines the adsorption efficiency and facet selectivity of the substrate and subsequent bond-breaking and bond-forming process during a reaction. However, to construct a universal catalyst, one has to think every aspect of catalytic properties i.e. (a) it should be stable in a broad pH range, (b) the catalytic activity should be in the equal order in both the organic or aqueous solvent, and (c) it should show long term stability under ambient condition. Our synthesized Hy-Au@AgNR₈₄₀-Ass shows its stability in a broad pH

range. The catalytic activity was checked in both the acidic and basic solution for the electrooxidation of L-tryptophan by Hy-Au@AgNR₈₄₀-Ass modified GC (Hy-Au@AgNR₈₄₀-Ass/GC) and it was found that Hy-Au@AgNR₈₄₀-Ass/GC is equally capable to oxidize L-tryptophan in both acidic and basic pH medium. The Hy-Au@AgNR₈₄₀-Ass/GC is also capable to oxidize vitamin K3 in the organic solvent (acetonitrile). Synthesized Hy-Au@AgNR₈₄₀-Ass remain stable (no visible, spectroscopic, and structural change) in the ambient condition (room temperature, in presence of oxygen, and aqueous solution) over 6 months. Hence, our main focus that developing a TB-enriched strain-dependent universal catalyst is efficiently achieved by our engineered Hy-Au@AgNR₈₄₀-Ass material. To correlate the influence of TB-induced tensile strain and electrocatalytic activity of Hy-Au@AgNRs and the resultant Hy-Au@AgNR₈₄₀-Ass/GC, we need to understand the d-band model of transition metals in more details. In a d-band theory, it is assumed that when an adsorbate state (σ) reacts with the metal d orbitals, it forms one bonding orbital ($d-\sigma$) and one antibonding orbital ($d-\sigma$)*. If the d band center of the metal is lower in energy, more antibonding orbital will be occupied.⁴⁰⁰ Therefore, the degree of interaction between adsorbate state and metal d state will be reduced. However, if a d-band center is higher in energy, then an upshift of antibonding orbital ($d-\sigma$)* will happen which will increase the interaction between adsorbate state and metal d state. In the case of pure Ag or pure Au rod, the d-band center is lower in energy. In contrast, Au-nanoseed incorporated Ag rod i.e. in Hy-Au@AgNR₈₄₀ the d-band center is upshifted towards the Fermi level as shown in **Figure 7.14**. Due to this upshifting of d-band, more antibonding orbital will remain vacant, which results in more bonding interactions between the metal and the reactant which may further improve the catalytic activity. In the case of Hy-Au@AgNR₈₄₀-Ass, as explained earlier that the density of crystal defects is much higher than the corresponding Hy-Au@AgNR₈₄₀ which will not only

increase the tensile strain further but also will move the d-band center more towards the Fermi level. Thus the trend of electrons occupying the (d- σ)* state may give the following order: Hy-Au@AgNR₈₄₀-Ass < Hy-Au@AgNR₈₄₀ < Hy-Au@AgNR₄₅₀ < Hy-Au@AgNR₁₂₀ and hence the Hy-Au@AgNR/Hy-Au@AgNR₈₄₀-Ass may show maximum catalytic activity. Our measured ICP-OES data quantifies the actual concentration of different elements as ~10mg/L of Ag, ~1.11mg/L of S, and an infinitesimal amount of Au present in the resultant Hy-Au@AgNR₈₄₀-Ass that has been used as the desired catalytic material.

The expected trend of strain-dependent electrocatalytic activity was verified by recording the electrooxidation of L-tryptophan on different catalytic materials. The I-V response in DPV for L-tryptophan oxidation is shown in **Figure 7.23B** which clearly shows that the peak potentials for both Hy-Au@AgNR₈₄₀ and Hy-Au@AgNR₈₄₀-Ass are equivalent with a slight increment in peak current for Hy-Au@AgNR₈₄₀-Ass. This authenticates our expectation that Hy-Au@AgNR₈₄₀-Ass/GC acts as the best catalyst with the lowest peak potential (**Table 7.3**) and highest peak current compared to other catalysts (viz. Hy-Au@AgNR₈₄₀/GC, Hy-Au@AgNR₄₅₀/GC, and Hy-Au@AgNR₁₂₀/GC). We have also tried our DPV experiment for other systems like the reduction of glucose (**Figure 7.23A**) and oxidation of vitamin K3 (**Figure 7.23C**) and observed similar enhanced catalytic activity for Hy-Au@AgNR₈₄₀-Ass/GC system.

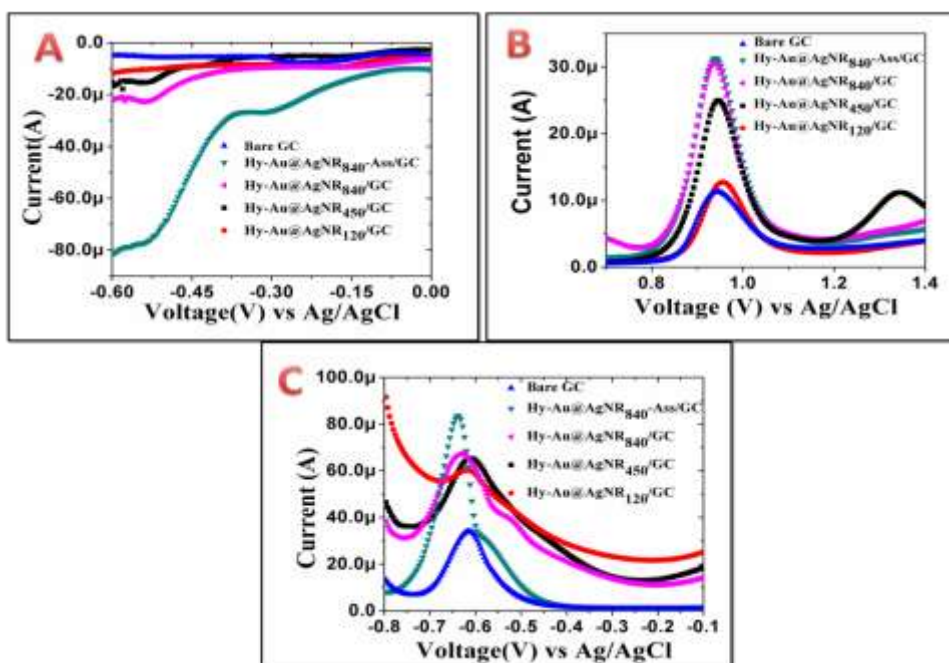


Figure 7.23: A is the DPV response for the reduction glucose (4×10^{-4} M) in 0.1 M HClO₄, B is DPV response for the oxidation of L-tryptophan (4×10^{-4} M) in 0.1 M HClO₄, C is the DPV response for the oxidation of vitamin K3 (4×10^{-4} M) in 0.1 M LiClO₄ + acetonitrile.

Table 7.3: The I-V responses in DPV for different system Hy-Au@AgNR₈₄₀-Ass/GC, Hy-Au@AgNR₈₄₀/GC, Hy-Au@AgNR₄₅₀/GC, Hy-Au@AgNR₁₂₀/GC.

System	Glucose	Vitamin K3	L-tryptophan
Bare GC	-0.8 V, -4.6 μA	-0.61 V, 35.06 μA	0.96 V, 11.3 μA
Hy-Au@AgNR ₈₄₀ -Ass/GC	-0.53 V, -76.53 μA	-0.638 V, 83.64 μA	0.93 V, 31.79 μA
Hy-Au@AgNR ₈₄₀ /GC	-0.535 V, -24.03 μA	-0.631 V, 68.89 μA	0.93 V, 30.80 μA
Hy-Au@AgNR ₄₅₀ /GC	-0.54 V, -15.67 μA	-0.61 V, 66.32 μA	0.95 V, 25.10 μA
Hy-Au@AgNR ₁₂₀ /GC	-0.55 V, -9.38 μA	-0.61 V, 59.33 μA	0.96 V, 13.0 μA

The analogous trend is also observed in chronoamperometric and impedance measurements (Figure 7.24A, B, C & Figure 7.25A, B, C respectively) for all the above three systems.

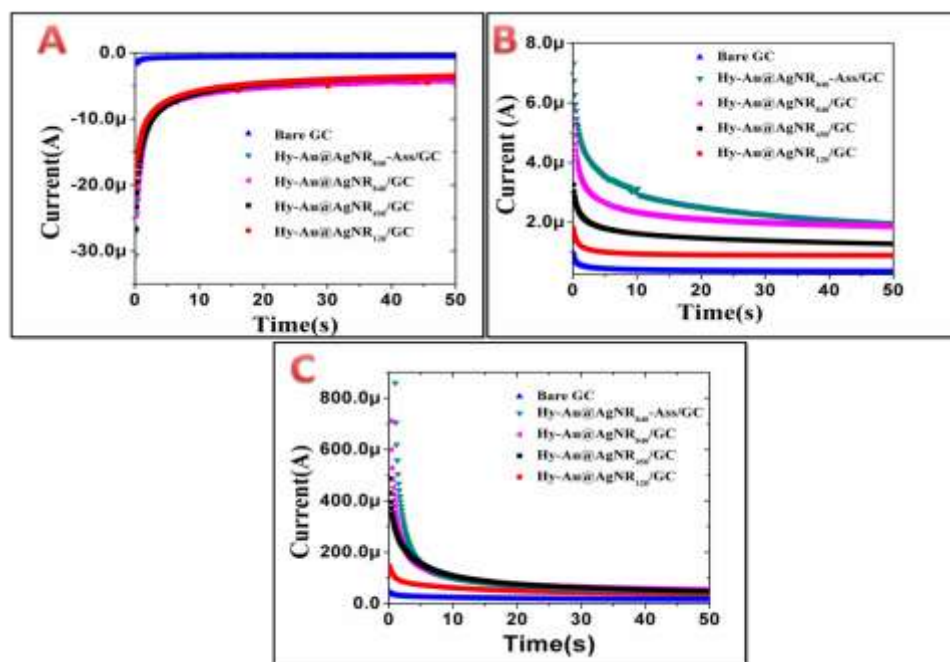


Figure 7.24: A is the chronoamperometric response for the reduction glucose (4×10^{-4} M) in 0.1 M HClO₄, B is the chronoamperometric response for the oxidation of L-tryptophan (4×10^{-4} M) in 0.1 M HClO₄, C is the chronoamperometric response for the oxidation of vitamin K3 (4×10^{-4} M) in 0.1 M LiClO₄ + acetonitrile.

The engineered Hy-Au@AgNR₈₄₀-Ass has used not only an efficient catalytic material for the electrochemical redox-based sensing of L-tryptophan, Glucose, and Vitamin K3 but also find equal application as a pathological kit for a variety of analytes enlisted below. The importance of all those analytes in human physiology and the significance of their accurate estimation from the pathological sample has been elaborated in the following section.

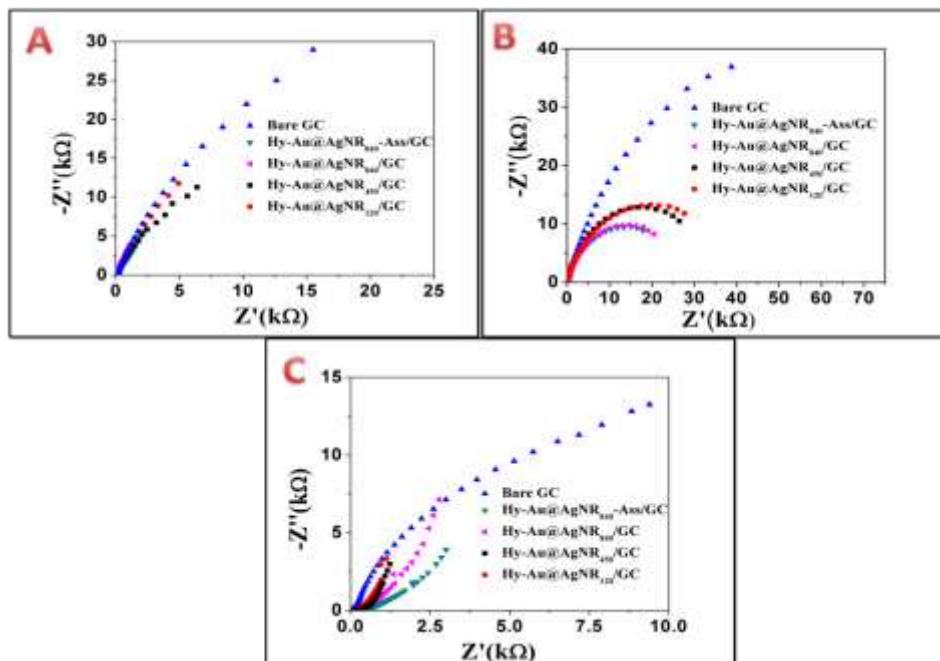


Figure 7.25: A is the impedance response for the reduction glucose (4×10^{-4} M) in 0.1 M HClO_4 , B is impedance response for the oxidation of L-tryptophan (4×10^{-4} M) in 0.1 M HClO_4 , C is the impedance response for oxidation of vitamin K3 (4×10^{-4} M) in 0.1 M LiClO_4 + acetonitrile.

Importance of different analytes considered in the current study:

In the current study, we have considered more than 20 different analytes which include both water-soluble & insoluble organic human metabolites and a variety of metal ions (inorganic metabolites). Water-soluble organic metabolites include Pantothenic acid (PA), Riboflavin (Rb), uric acid (UA), Creatinine (Ct), Xanthine (Xa), Urea (U), Ascorbic acid (AA), Cysteamine (Cyst), Folic acid (FA), Dopamine (DA), L-tryptophan (L-Trp), Glucose (Glc), Inositol (Inos), and Thiamine (Thia). One of the most common water-insoluble organic metabolites is Vitamin K3 (VK3). Though there is a long list of metal ions used as inorganic human metabolites, the most common and important metabolites include Cr^{3+} , Co^{2+} , Fe^{3+} , Cu^{2+} , Pb^{2+} , Hg^{2+} , and Ni^{2+} . Hence, we have considered a total of twenty-two different analytes to justify the universal catalytic ability of our engineered Au-seeded Ag-nanorod-based thiol mediated strained network.

Though the biological importance of most of these metabolites is well known to us but the driving force behind selecting them in the present study is enlisted as below:

(1) Pantothenic acid (PA): Pantothenic acid is popularly known as vitamin B₅ which is a water-soluble human metabolite. Pantothenic acid is an essential human nutrient. Animals require Pantothenic acid for synthesizing coenzyme-A (CoA) which helps in the synthesis and oxidation of fatty acids.⁴⁰¹ It also helps to synthesize and metabolize proteins, carbohydrates, and fats.

(2) Riboflavin (Rb): Riboflavin (vitamin B₂) helps to break down protein, carbohydrates, fats to adenosine triphosphate (ATP) for energy supply to the body.⁴⁰¹

(3) Uric acid (UA): UA (a purine metabolic product and can act as a free radical scavenger) is one of the major antioxidants in human serum and may cause arthritis when remains present at higher concentration in the blood due to the deposition of UA crystals in joints like ankle, feet, knees, and wrists.⁴⁰²

(4) Creatinine (Ct): Creatinine is a waste product produced by muscles from the breakdown of a compound called creatine. Creatinine is removed from the body by the kidneys, which filter out almost all of it from the blood and release it into the urine. By measuring the amount of creatinine in the blood and/or urine we can find out the efficiency of the kidney.⁴⁰³

(5) Xanthine (Xa): Xanthine is a purine base found in human body tissues and fluids. The decomposition of adenosine triphosphate (ATM) can also produce Xa.⁴⁰⁴ Derivatives of Xanthine act as stimulants for the treatment of asthma and influenza. In clinical diagnosis, Xa usually acts as a sensitive indicator for some clinical disorders such as perinatal asphyxia and adult respiratory distress syndrome.^{405,406}

(6) Urea (U): Renal nitrogen metabolism primarily involves urea and ammonia metabolism, and is essential to normal health. Urea produces and excreted through the renal system as a result of the degradation of dietary and endogenous proteins.⁴⁰⁷

(7) Ascorbic acid (AA): AA, a water-soluble antioxidant produces type I interferons, which up-regulates NK cell and cytotoxic T-lymphocyte activity to prevent early viral infection. Besides, AA has the ability to inactivate both RNA and DNA viruses and can detoxify the viral products which cause pain and infections.⁴⁰⁸

(8) Cysteamine (Cyst): Cysteamine is an essential metabolite in the human body.⁴⁰⁹ *Cystamine*, the oxidized form of *cysteamine* which inhibits erythrocyte sickling in sickle cell anemia. Cystamine in the body is reduced into cysteamine and RS-cysteamine mixed disulfide by the thiol-disulfide exchange. This is done by the consumption of intracellular glutathione.

(9) Folic acid (FA): Folic acid is the synthetic form of folate, a water-soluble B vitamin that takes part in several critical functions in the human body.⁴¹⁰ The active form of folate is tetrahydrofolic acid. It serves in one carbon reductions reactions. These reactions are involved in the synthesis of nucleotides and amino acids. Folic acid is required for erythropoiesis, thus folic acid deficiency leads to megaloblastic anemia. Adequate dietary intake of folic acid is critical for DNA repair and normal cell growth.

(10) Dopamine (DA): Dopamine acts both as a hormone and neurotransmitter, and plays several important roles in the brain and body. Dopamine plays a major role in the motivational component of reward-motivated behavior. Individual electrocatalytic sensing of dopamine has been performed previously.⁴¹¹

(11) L-tryptophan (L-Trp): L-tryptophan metabolized product serotonin causes platelet aggregation and considered as a prognostic biomarker for dengue hemorrhagic fever (DHF) such

as that high level of serotonin or low level of L-tryptophan is an indicator for Dengue-2 (DENV-2) infection.⁴¹²

(12) Glucose (Glc): Type 2 diabetes patients are at high risk of hyperglycemia due to excess concentration of glucose and may cause damage to the nervous system, cell organs, vessels whereas hypoglycemia results in loss of consciousness, seizures.⁴¹³

(13) Inositol (Inos): Inositol is a carbocyclic sugar that is abundant in the brain and other mammalian tissues, mediates cell signal transduction in response to a variety of hormones, neurotransmitters, growth factors, and participates in osmoregulation.⁴¹⁴ It is made naturally in humans from glucose.

(14) Thiamine: Thiamine (vitamin B₁) is considered an essential metabolite for glucose metabolism and plays a key role in muscle, heart, and brain functions.^{401,415}

(15) Vitamin K3 (VK3): When vitamin K3 present in higher concentrations in newborns, it produces a bile product bilirubin which causes brain damage, mental retardation, loss of appetite, and deafness.⁴¹⁶

(16) Cr³⁺: Hexavalent Cr(VI) is considered as carcinogenic as it has the capability to penetrate the cell membrane and reacting with proteins and nucleic acids but Cr(III) cannot cross the cell membrane and hence less toxic⁴¹⁷ than Cr(VI).

(17) Co²⁺: Co helps to absorb vitamin B₁₂ in the body and also found it useful to treat anemia and infectious diseases.^{401,418}

(18) Fe³⁺: Fe has a role in DNA synthesis, electron transport, and oxygen transport.⁴¹⁹

(19) Cu²⁺: Cu is essential for maintaining the strength of skin, blood vessel, epithelial and connective tissues.⁴²⁰

(20) Pb^{2+} : Excess Pb exposure bring several unwanted disorders in human metabolism like the disruption of the biosynthesis of hemoglobin, rise in blood pressure, etc.⁴²¹

(21) Hg^{2+} : Mercury is a highly toxic metal present in the body mostly as methyl mercury (MeHg^+) with an average half-life ($t_{1/2}$) varies widely between 30-150 days in the human body. The body burden of MeHg^+ originates mainly from sea-fish consumption or dental amalgam. Though the chief toxic target of Hg^{2+} is the brain, other noted toxicity includes the disordering of peripheral nerve function, renal function, immune function, endocrine, and muscle function.⁴²²

(22) Ni^{2+} : Ni present in RNA and DNA of our body, where it functions in association with a nucleic acid to involve in protein structure formation.⁴²³

Almost 20 odd different pathological analytes have been detected and estimated by using our engineered material ($\text{Au@AgNR}_{840}\text{-Ass}$) as a universal catalyst which has been broadly categorized as:

(1) **Trace metal ions:** Different trace metal ions like Co^{2+} , Cr^{3+} , Cu^{2+} , Hg^{2+} , Ni^{2+} , Fe^{3+} , and Pb^{2+} have been detected and estimated by electrochemical reduction in 0.1 (M) HClO_4 as shown in **Figure 7.26 (A-G)**.

(3) **Water-insoluble human metabolite:** Due to its insoluble nature in polar medium, vitamin K3 has been estimated by oxidizing it in a 0.1 (M) LiClO_4 + acetonitrile medium as shown in **Figure 7.26H**.

(3) **Water-soluble human metabolites:** Different metabolites like ascorbic acid (AA), creatinine, Dopamine (DA), thiamine, riboflavin, Pantothenic acid (PA), urea, uric acid (UA), inositol, Xanthine, Cysteamine (Cyst), glucose, L-tryptophan, and folic acid (FA) have been detected and estimated by oxidizing them in 0.1 (M) NaOH is as shown in **Figure 7.27a** and **7.27b** respectively.

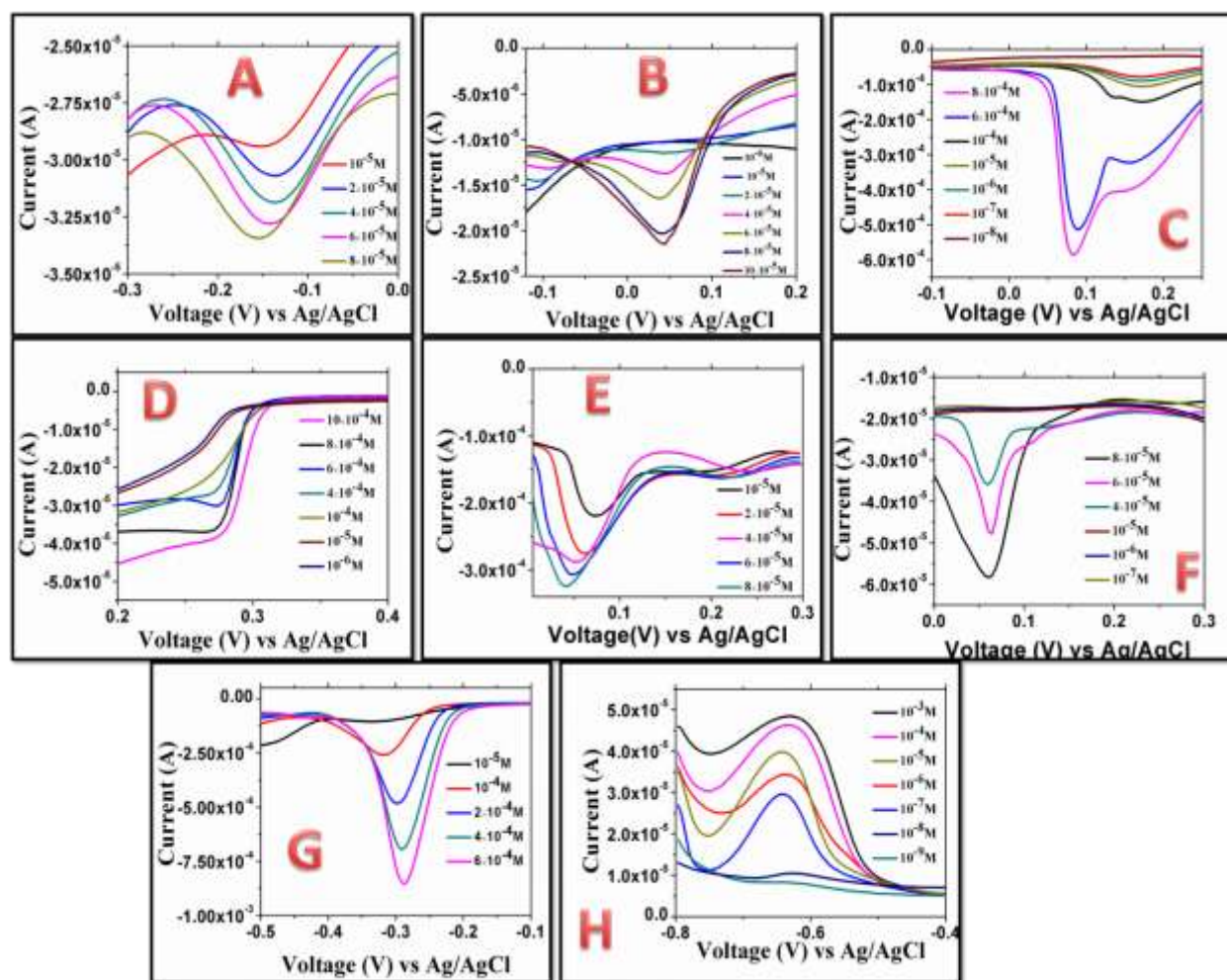


Figure 7.26: Electrochemical reduction of metal ions in 0.1 M HClO₄ (A) Co²⁺, (B) Cr³⁺, (C) Cu²⁺ (D) Hg²⁺, (E) Ni²⁺, (F) Fe³⁺, (G) Pb²⁺, (H) is for vitamin K3 oxidation in 0.1 (M) LiClO₄+ acetonitrile.

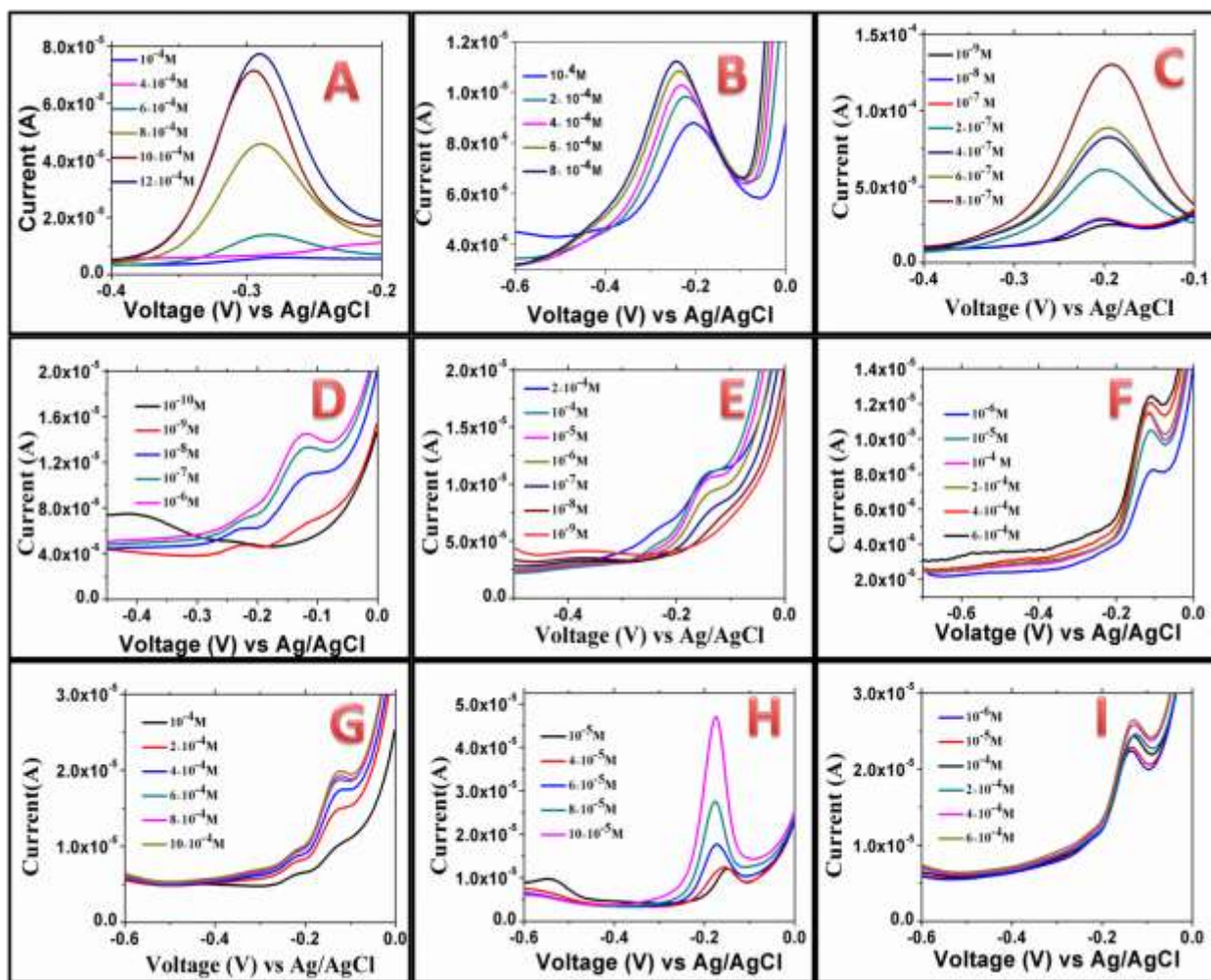


Figure 7.27a: Oxidation of metabolites in 0.1 M NaOH medium: (A) AA , (B) Creatinine (C) Dopamine (DA), (D) thiamine, (E) riboflavin, (F) Pantothenic acid (PA) (G) urea (H) uric acid (UA), (I) inositol.

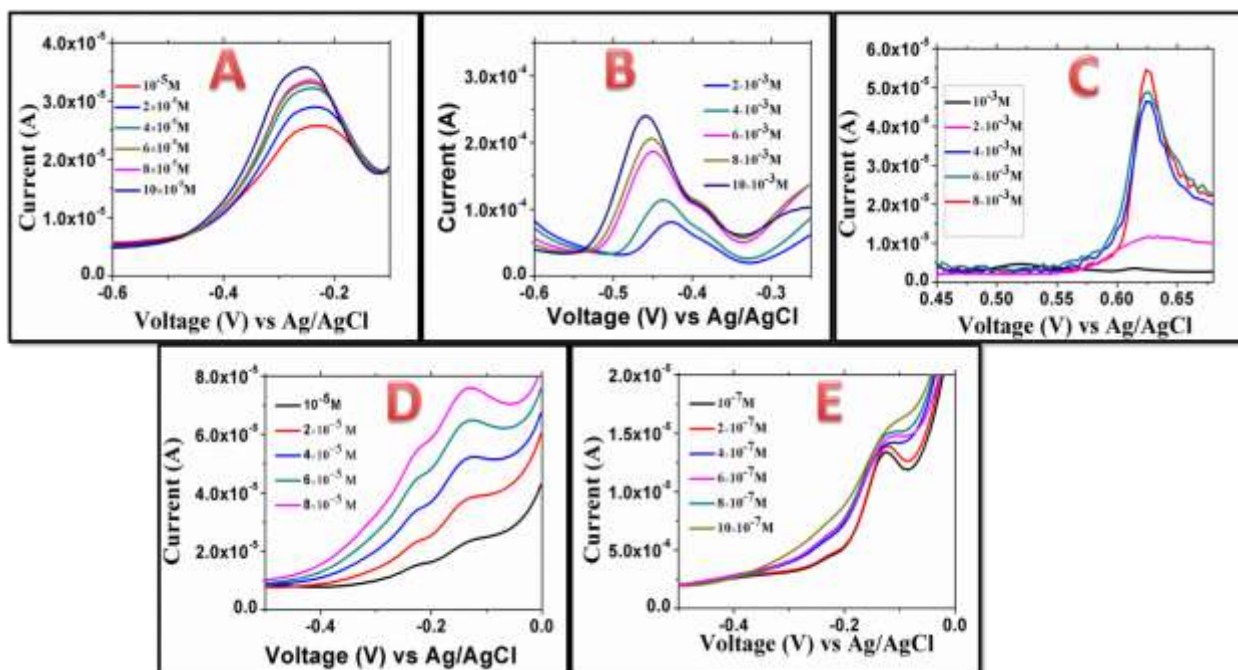


Figure 7.27b: oxidation of metabolites in 0.1 M NaOH; (A) Xanthine, (B) Cysteamine (Cyst) (C) glucose, (D) L-tryptophan, (E) folic acid (FA).

The utility of using the above electrolytes is that they are either acidic or basic in chemical nature. Whenever human serum is added to those electrolytes, the plasma proteins are precipitated out but the other blood ingredients like salts (NaCl, KCl, CaCl₂, etc) and metabolites (vitamins, amino acids, etc) will stay in the solution without any modification. During measurements of the above metal ions or metabolites, we have prepared a stock solution first. Then the stock solution was spiked into the human serum and the plasma proteins from serum are precipitated out. The solution was then centrifuged to remove the coagulated proteins and the supernatant solution with all the essential analytes being diluted for electrochemical measurements e.g., for vitamin K3 we first prepared a stock solution of 10⁻² (M) in acetonitrile medium and spiked it directly to the human serum. The coagulated proteins are then precipitated and the resultant solution was collected by centrifuging. The resultant supernatant is then diluted up to the nanomolar level for electrochemical measurements. The utility of I-V measurements in

human serum is that the oxidation and reduction of metabolites or trace metal ions in presence of other ingredients of blood like Na^+ , K^+ , Ca^{2+} , etc., can be carried while sensing of a particular analyte without being any interference. Most of the water-soluble human metabolites show linear fitting of ion current during their catalytic oxidation in their physiological concentration level as shown in **Figure 7.28A-7.28I**. Soluble metabolites that are not following the I-C (C is the concentration) linear fitting rather showing an exponential rise in current have been fitted by plotting the ion current against the logarithm of concentration to show their linear sensing behavior.

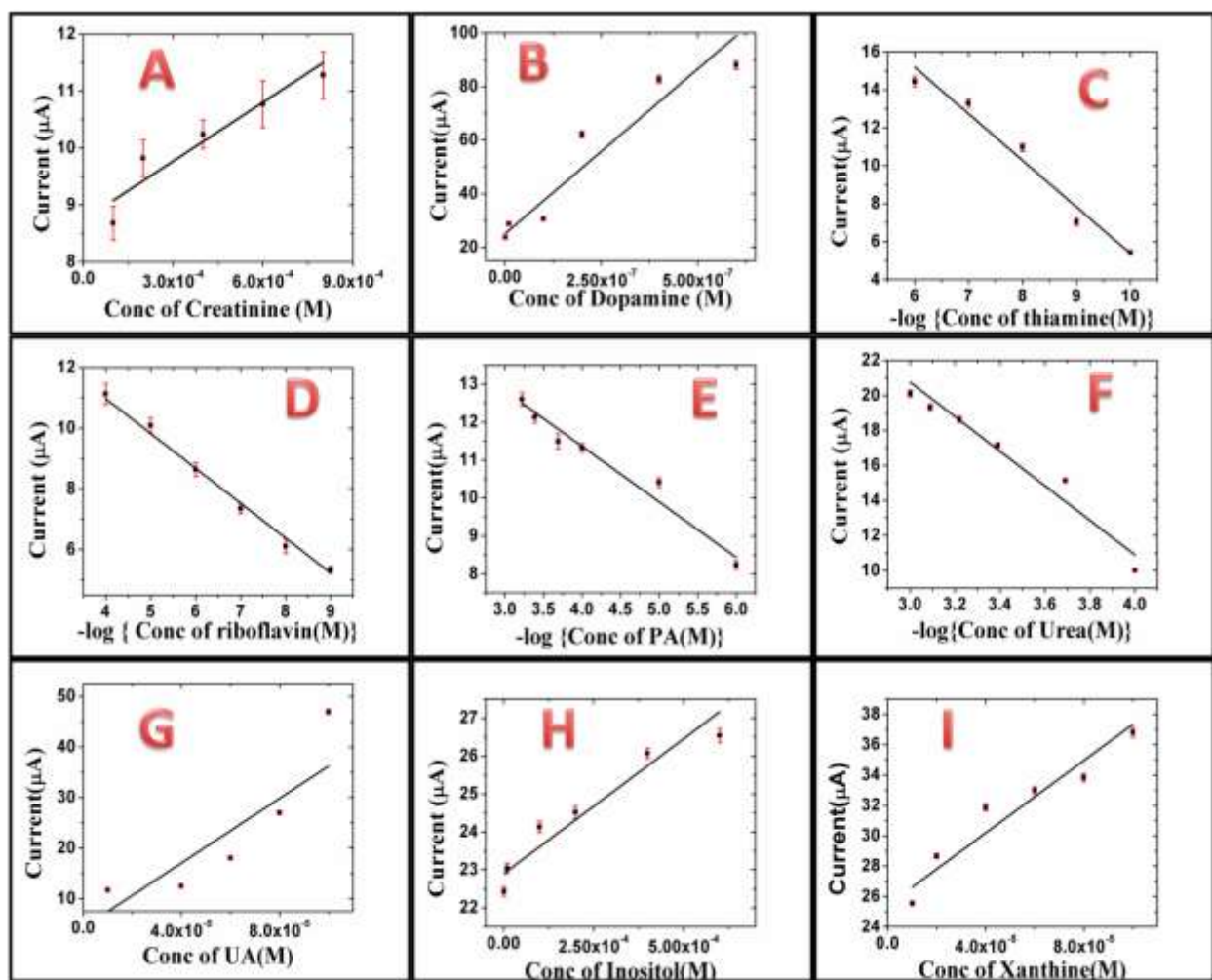


Figure 7.28: I-C linear fitting for different water-soluble human metabolites as mentioned in the figure during their catalytic oxidation at their physiological concentration level.

Not only the soluble human metabolites but also the trace metal ions and organic soluble vitamin K3 show similar I-C linear fittings during their reduction in their physiological concentration level. The I-C linear fitting for trace metal ions are shown in **Figure 7.29 (A-F)** and for vitamin K3 in **Figure 7.29G**.

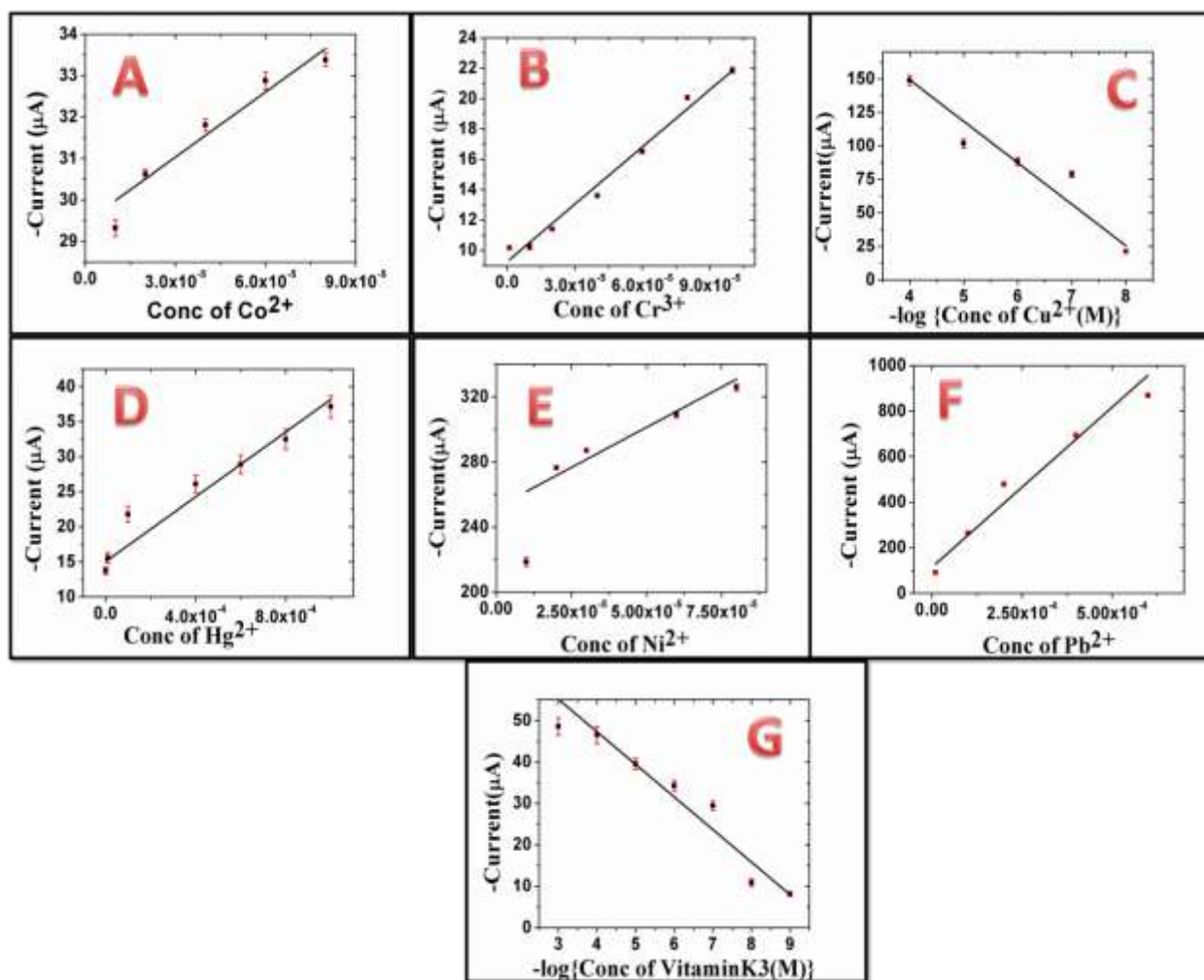


Figure 7.29: Linear Calibration plot of metal ions. Just like human metabolites (**Figure 7**) where we did not find any linear relation with concentration we take logarithm as shown in (C) for Cu^{2+} and in (G) for vitamin K3.

Besides the sensing of individual metal ions or human metabolites, we have also carried out interference tests and simultaneous detection of the above metabolites or trace metal ions in a single shot. **Figure 7.30A-D** shows the I-V sensing at the variable concentration for metabolites Riboflavin, Uric acid (UA), Pantothenic acid (PA), and Creatinine (Ct) respectively in a mixture of all four. Except for the specific metabolite under the investigation, the other three metabolites act as interfering analytes where their concentration has been kept constant at 1 μ M.

Table 7.4: Peak Potential of different metabolites and trace metal ions in I-V responses of DPV.

System	PA	Rb	UA	Creatinine	Xanthine	Urea	AA	Cysteamine
Peak Potential (V)	-0.115	-0.145	-0.17	-0.24	-0.25	-0.128	-0.29	-0.45
System	FA	DA	L-Tryptophan	Glucose	Inositol	Thiamine	Vitamin K3	Cr ³⁺
Peak Potential (V)	-0.121	-0.19	-0.135	+0.62	-0.131	-0.115	-0.63	+0.044
System	Co ²⁺	Fe ³⁺	Cu ²⁺ (<10 ⁻⁴ M)	Cu ²⁺ (>10 ⁻⁴ M)	Pb ²⁺	Hg ²⁺	Ni ²⁺	
Peak Potential (V)	-0.147	+0.059	+0.17	+0.083	-0.28	+0.27	+0.043	

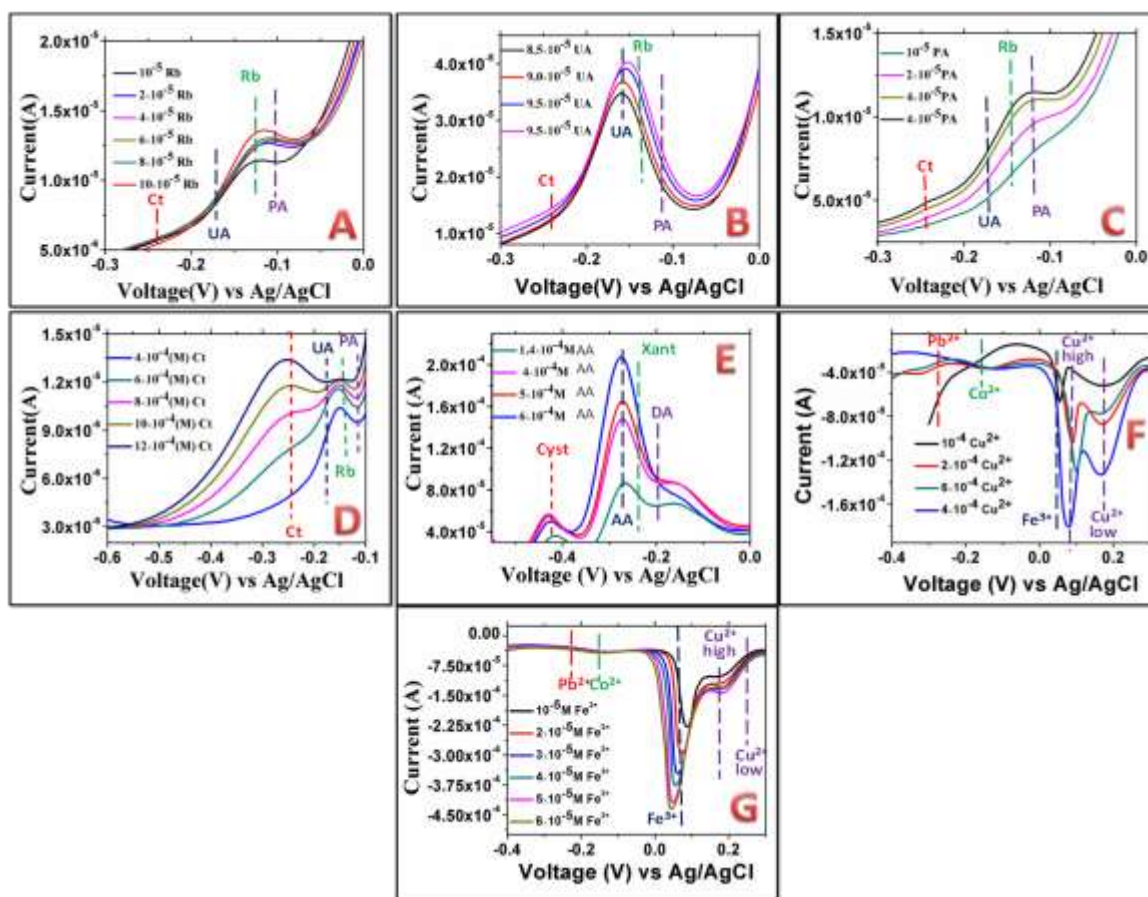


Figure 7.30: Interference test of Riboflavin, Rb (A); Uric acid, UA (B), Pantothenic acid, PA (C), Creatinine, Ct (D), Ascorbic acid, AA (E), Cu^{2+} (F), and Fe^{3+} (G). Cu^{2+} high and Cu^{2+} low indicate respective potentials at high and low concentrations of Cu^{2+} . Colour coded vertical dotted lines in each plot (A-G) show the expected peak potential for different metabolites.

In **Figure 7.30 E** we have shown the I-V sensing of Ascorbic acid (AA) in presence of dopamine (DA), Xanthine, and cysteamine (Cyst) where the concentration of all the analytes except AA is kept constant at 1 μM while the concentration of AA varies between 0.14 – 0.6 mM. Similarly, **Figure 7.30 F** and **7.30 G** show the I-V sensing for Cu^{2+} and Fe^{3+} respectively. For Cu^{2+} we have used Fe^{3+} , Co^{2+} , and Pb^{2+} as interfering salts and for Fe^{3+} we have used Cu^{2+} , Co^{2+} , and Pb^{2+} as interfering salts. In both cases, interfering salt concentration is 1 μM . It is to be noted that Cu^{2+} has two peak potentials in their I-V curves at higher and lower concentration

range. Fingerprinting at different peak potential for individual human metabolites enables the electrocatalytic method to detect them specifically as well as sensitively from a mixture, as appears in plasma samples. Details about the peak potentials for each analyte under the investigation have been enlisted in **Table 7.4**.

7.4. Conclusion:

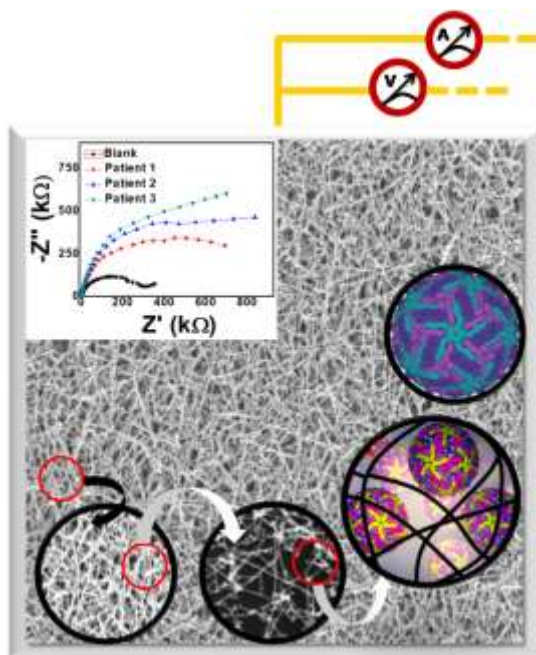
Highly strained Au-seed incorporated Ag nanorods (Hy-Au@AgNRs) of variable length were synthesized by a novel methodology. The strain within the Hy-Au@AgNRs is verified both theoretically through *ab initio* simulation and experimentally from XRD broadening. Among various Hy-Au@AgNRs, Hy-Au@AgNR₈₄₀ with the longest TB over its surface offers noticeably more strain than Hy-Au@AgNR₄₅₀ and Hy-Au@AgNR₁₂₀. The engineered Hy-Au@AgNR₈₄₀ was then assembled by DTT to produce Hy-Au@AgNR₈₄₀-Ass with multiple defects enriched active catalytic sites. It was found that Hy-Au@AgNR₈₄₀-Ass acts as a superior nanostructure for strain-dependent universal catalysis as verified from the electrochemical oxidation/reduction of a series of organic and inorganic human metabolites by performing their DPV, EIS, and chronoamperometry. Hy-Au@AgNR₈₄₀-Ass modified GC was used as a pathological kit that offers a linear calibration plot for all the studied human metabolites in the physiological concentration range. Moreover, the reported electrochemical pathological kit shows long term stability under the ambient condition in wide solvent systems as well as broad-scale pH range. Besides, Hy-Au@AgNR₈₄₀-Ass/GC is also able to detect simultaneously more than one analyte at a time from the I-V responses of DPV. Thus a low cost, rapid, and nanorod-based 2D network for a non-enzymatic user-friendly pathological kit is developed for simultaneous detection and quantification of the multiple human analytes which will surely find potential application in error-free electrochemical sensor technology.

CHAPTER-8

Fabrication of Highly Specific DNA Based Porous Au-Ag Nanobioconjugate as Electrode Coat for Rapid Impedimetric Direct Sensing of DENV-2 from Infected Whole Blood

OUTLINE: Specific Points of Discussion

- An efficient nanobioconjugate has been developed as electrode coating material by hybridizing our newly synthesized porous Au-Ag nano-network (Chapter-7) with a thiol modified DNA aptamer for the early-stage specific detection and quantification of DENV-2.
- The binding affinity between the bioconjugate and different serotypes of dengue was studied here through low cost electrochemical impedimetric spectroscopy (EIS).
- This study for the first time presents highly specific and sensitive detection of the most prevalent DENV-2 by impedimetric technique.
- The key achievement of this study lies in its ability of the direct detection of DENV-2 serotype without the aid of an enzyme or antibody in dengue infected blood up to $\sim 10^{-2}$ PFU/mL.



Dengue virus (DENV) belongs to the virus family of Flaviviridae and is responsible for a seasonal febrile disease in humans with potentially fatal consequences. In addition to humans, DENV can infect mosquitoes in which the infectious virus accumulates in the salivary gland fluid and from where it is transmitted into humans during a blood meal. It is considered to be an endemic disease, causing approximately 22,000 deaths every year in tropical and subtropical regions of the world.^{424,425} Mathematical modeling based on existing known cases projects more than 300 million people to be at risk of developing DENV infection.⁴²⁶ Globally there are four serologically distinct groups or serotypes of Dengue (DENV) designated as DENV-1, DENV-2, DENV-3, DENV-4, however, a recent report suggests the existence of a new serotype DENV-5.⁴²⁷ As in other members of Flaviviridae, the DENV genome consists of a single-stranded plus-sense RNA encoding for a single polyprotein that is cleaved by proteases (encoded by either the host or the viral genome) at precise sites to generate structural and non-structural viral proteins. A comparison of the polyprotein sequence from different serotypes shows a 65-70% identity in

the amino acid sequence between DENV 1-4. Each serotype is further classified into genotypes depending on differences in the viral genome sequence.

Upon entry into human skin through a mosquito bite, DENV is known to infect resident Dendritic cells by attaching to surface receptor molecules of the protein DC-SIGN.⁴²⁸ Subsequent to attachment, the virus-receptor complex is internalized by endocytosis leading to the formation of endosomes, which are then acidified through the activity of proton pumps on their surface.⁴²⁹ Endosome acidification causes drastic structural changes in the viral surface proteins, changing their conformation and leading them to induce a fusion between the membrane of the virus particle and that of the endosome. Subsequently, the viral genomic RNA is released into the host cell to initiate translation of viral protein followed by replication of genomic RNA and the formation of new virus particles.

The plus-sense and single-stranded genomic RNA can directly serve as a template for protein synthesis by host ribosomes. The presence of a type-I cap structure at the 5' end of the RNA performs dual functions through efficient recruitment of ribosomes in addition to protecting the genomic RNA from cleavage by host exonucleases. Translation of the genome produces a single polyprotein that gets cleaved into three structural proteins (Envelope or E, precursor Membrane or prM and Capsid or C) and seven non-structural proteins (NS1, NS2A, NS2B, NS3, NS4A, NS4B, and NS5).⁴³⁰ The structural proteins form part of virion particles that are produced from the infected cell, while the non-structural proteins catalyze replication and assembly of virions in addition to subverting the innate-antiviral response of the host cell. Synthesis of the viral proteins takes place in close association with the endoplasmic reticulum membrane of the host cells and both the E and prM proteins are glycosylated⁴³¹. Replication of the viral genome also takes place in replication complexes (RCs) that are produced on the ER

membrane, in which the NS5 protein catalyzes the replication of the genomic RNA with the aid of other non-structural proteins. Mature viral particles are assembled in close association with the RCs and these are secreted out of the host cells through the host cell trans-Golgi network (TGN) secretory pathway. The replicated and newly formed each viral RNA then enclosed by the C proteins and forms the nucleocapsid. Newly formed nucleocapsids are then surrounded by E and prM proteins within the envelope of ER to form a protective outer layer and construct the immature form of the virus. The virus in the immature form then traveled by the Golgi apparatus towards other parts of the body where they get matured and infect the other cells⁴³² and the cycle continues.

The virion particles of DENV are almost spherical in shape with the diameter varying between approximately 50 (in the mature and infectious form) to 60 nm (in the immature and non-infectious form).⁴³³ The core of each virus is a nucleocapsid consisting of a single copy of the viral genome encapsulated with capsid proteins (C), which is surrounded by a glycoprotein shell made up of a lipid bilayer containing 180 copies each of an Envelope (E) and Membrane (M) proteins.⁴³⁴ The E protein has three distinct domains E-I, E-II, and E-III among which E-III is responsible for binding to the receptor. After endocytosis and endosome acidification, E-I undergoes a structural transition and the E-II helps in the fusion of viral membrane with that of the endosome. In an extracellular virion particle, the 180 molecules of the E protein are arranged as 90 homodimers with the axis of bilateral symmetry being parallel to the viral surface. Upon endosome acidification, these molecules rearrange to form 60 trimeric spikes which pose the E-II domain to mediate membrane fusion. While the E protein is produced in its final mature form during viral protein synthesis, the M protein is produced in an immature precursor form called prM. Immediately after assembly inside the host cell, all virus particles contain only prM on their

surface, which is cleaved by a host protease called Furin during the release of the virus through the secretory trans-Golgi network (TGN). However, the efficiency of this enzymatic cleavage might vary depending on the cell type thereby producing virus particles with a varying number of prM and M protein on their surface. The virus particles that only have prM on their surfaces are incapable of infection.⁴³⁵

Signal sequences within the polyprotein translocate nonstructural NS1 and structural prM and E proteins into the ER lumen while the C, NS3, and NS5 proteins are localized in the cytoplasm. NS2A/B and NS4A/B remain as a transmembrane protein. With the help of ER signalases and NS3-NS2B & NS5 nonstructural protein pairs, viral RNA replication starts through various RNA synthesis and assembling processes.⁴³⁰ The replication of four different serotypes of DENV is similar but they differ only in the specific interaction between the structural protein on virion and the receptors on the host cell. The key factor of binding to the cell receptors by different DENV serotypes lies in the relative arrangement of different domains of E protein monomer. As we discussed before, each E protein monomer has three different domains DI, DII, and DIII.⁴³⁶ The hydrophobic virus fusion loop peptide located at the tip of DII is shielded by DIII which is responsible for binding to the receptor. In the current manuscript, we have designed the aptamer according to the previously reported work,⁴³⁷ by selecting DIII as a specific binding site. The aptamer has a specific DNA sequence and derived from DNA aptamer libraries and the selection is based on best ELISA affinity ranking for DIII of a specific serotype of DENV.

Usually, during a seasonal epidemic, a predominant number of infections have been observed to be caused by one particular serotype. However, after a certain number of seasons, this serotype is replaced by another. Therefore, diagnostic methods have to incorporate features

to distinguish the serotype of the virus detected. There is still no clarity about the association of any given serotype with greater pathology^{438–440}. Among the four different dengue serotypes, DENV-2 shows a strong correlation with greater disease severity. It is found that DENV-2 is most likely to cause Dengue Hemorrhagic Fever (DHF) whereas for DENV-4 infected patients DHF is less likely to occur.⁴⁴¹ Clinical manifestation of dengue patients signifies that DHF occurs about 92% for secondary infections of DENV-2, which is associated with ascites and pleural effusions.⁴⁴¹ Due to this greater pathogenic behavior of DENV-2, we have selected it as a specific one for electrochemical aptamer-based detection. We have prepared a nanobioconjugate by covalently adsorbing the DENV-2 specific thiol modified aptamer on a porous Au-Ag network. The resultant nanobioconjugate was then used as an electrode coating material in impedimetric measurement for different concentrations of DENV-2. Since at the initial stage it is difficult to predict the resilience of virus particles to differentiate the experimental conditions, we have used inactivated Dengue virions generated by Psoralen mediated photo-inactivation method.⁴⁴² Details of Psoralen-mediated Dengue virions inactivation is described below.

Inactivation of DENV-2:

Preparation of Psoralen:

Psoralen was dissolved to prepare a concentration ~0.3mg/mL as a stock solution. It is photoreactive so the solution was covered by aluminum foil and stored in dark condition. It was vortexed before every use.

Viral Propagation:

Dengue viruses were propagated in C6/36 cell lines, and grown in a maintenance media (L15, medium, 10% FBS, 1% Penicillin-Streptomycin) at 37°C and 5% CO₂. The culture was collected 5 days post-infection and concentrated in a centricon at 10,000rpm for 5-10mins.⁴⁴³

Viral Inactivation:

Firstly, we took about 10-12mL of viral supernatant and AMT, 4'-aminomethyltrioxsalen, (10 µg/mL) was added to it. After gentle mixing, we distributed the supernatant by 2mL in each well in a 6 well polystyrene plates of diameter approx. 3.5cm (**Corning™ Costar™**). Then we prepared a set up for UV-A photoirradiation. we have used a UV torch (UVP UVLMS-38EL series 3UV lamp Upland CA, USA, 8-Watt 230V-50Hz, 0.16 Amps) of wavelength 365nm(UV-A) with an exposure time of about 20mins. After complete inactivation, 1 mL aliquot was taken out and kept it at -80°C for future use.

Validation of Inactivation with Immunofluorescence Assay:

We have infected the Vero cells with inoculum using a standard protocol^{443,444} and incubated for 48h. Aliquots of the virus from each inactivation test time points were placed in cell culture flasks containing Vero cell monolayers grown at 95% confluency. Flasks were incubated at 37°C at 5% CO₂ for 10days and periodically observed for cytopathic effect (CPE). Cultures were allowed to incubate for the maximum possible time to allow any viable virus to have a chance to replicate to detectable levels. After 10days a portion of each culture supernatant was placed into cell culture flasks and incubated under the same conditions for 10 days and observed for the cytopathic effect. The resulting cell monolayers were scraped and applied to the slides. Briefly, droplets of cell suspension were applied to slides and allowed to dry at room temperature in the biosafety cabinet (BSC). The images were viewed under a fluorescence microscope at 10X magnifications. The primary antibody used MAB8705 (1:400) and secondary antibody Antimouse Alexa 488 (1:500).

Maintenance of Vero Cell Line:

Vero cells are derived from normal kidney cells; because the cells are not transformed, they have not lost their contact inhibition. The Vero cells are maintained in Dulbecco's modified Eagle medium (DMEM) supplemented with 2% Fetal Bovine Serum (FBS) and incubated at 37 °C in a 5% CO₂ atmosphere.⁴⁴⁵ When these cells reach confluency, they stop growing and start to die; therefore, it is extremely important to monitor Vero cells and to subculture them as they form confluent monolayers. Actively growing Vero cell cultures become double approximately every 24 hours⁴⁴⁶. Depending on the number of cells seeded and the flask size, the cells usually need to be passaged for 2-3 times per week. This protocol describes the subculturing of Vero cells in 75cm² tissue culture flasks.

The antigenic property of the DENV-2 doesn't alter after this method of inactivation and therefore the affinity of nanobioconjugate towards the inactivated virions should reflect that against ones.⁴⁴³ The preference of early-stage detection of DENV-2 by electrochemical Impedimetric methods over the present ongoing methods is due to its user-friendly, cost-effective, and highly specific nature.

In the absence of either a universally accepted vaccine to give support to prophylactic measures or a therapeutic drug to suppress viral multiplication in infected patients, early detection of DENV is key for measures that will reduce the economic and social burden of this disease. Diagnostic methods in the acute phase for blood-borne viruses like DENV involve either a direct detection of infectious virus or any of biomolecule derived from the virus e.g. viral nucleic acid, viral protein secreted from infected cells into the blood, etc. Detection of infectious virus can be done through either plaque-forming unit assay or a fluorescent-foci forming assay, both of which are laborious, time-consuming and require skilled personnel working in dedicated, furnished facilities. Specific detection of viral genomic RNA can be performed by extraction of

the viral RNA from plasma samples, followed by reverse-transcription and Quantitative real-time PCR (qPCR)⁴⁴⁷. Although this method is fast compared to the former, it still requires skilled personnel and dedicated facilities that maintain high standards of cleanliness. Human cells infected with DENV secrete the NS1 protein into the blood which can be detected within 1-2 days after onset of symptoms. In view of this diagnostic kits presently available in the market that detect the NS1 antigen in addition to anti-DENV Immunoglobulin-M (IgM) produced by the host adaptive immune cells. Although a sensitive test, these kits however cannot differentiate between the different DENV serotypes and therefore need to be complemented by qPCR methods for that purpose.

In addition to these established methods, various techniques have been demonstrated to have the potential for the development of diagnostic kits. These include the use of DNAzymes⁴⁴⁸, Ribozymes⁴⁴⁹, Fluorescent *in-situ* hybridization or FISH⁴⁴⁷, Reverse-transcription Loop-mediated isothermal amplification or RT-LAMP^{450,451}, Carbon nanotube-based affinity biosensor⁴⁵², and dot-blot assay for NS1 antigen⁴⁵³. AuNPs have been employed in detection methods too^{448,454-456}.

Compared to several approaches stated above, the impedimetric technique is not only cost-effective but also sensitive enough for early detection of DENV-2 up to 10^{-2} PFU/mL with high specificity. The cross-reactivity of DENV-2 was also checked in the presence of other flaviviruses of the same genus like DENV-3, DENV-1, and other bacteria like *E.coli*, *Staphylococcus aureus*, and *H. influenza*. Details about the materials and synthesis have been included in the supporting information section. To utilize the strong affinity of thiol group for efficient binding with noble metals like Au or Ag (constituents of nanomaterials used here), we have procured the -S-H modified aptamer and stored it at -80°C before we use it.¹⁷ The aptamer

has the specific sequence ($MW=22680.0$) for DIII domain of DENV-2 and modified at 5' and 3' position by -SH group denoted as:

5'HS_ATACGGGAGCCAACACCATGGGGACCAACTGTCCGGAGAGAGTCCTGTCTGAG
GGAGAGCAGGTGTGACGGAT_SH3'

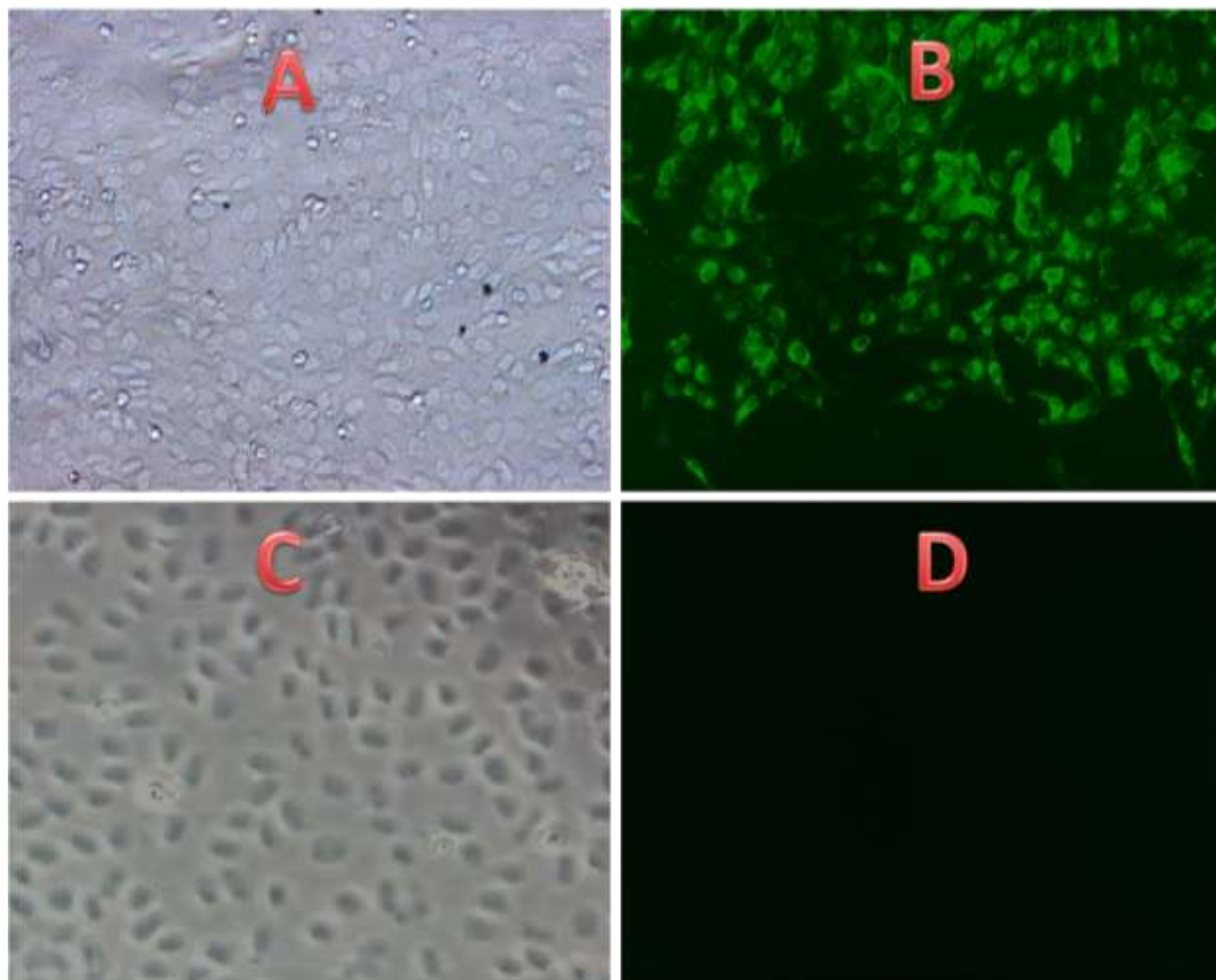


Figure 8.1: A and B are the bright field and fluorescence image of the control, respectively. C and D are the bright field and fluorescence images of the inactivated virus, respectively.

The porosity in the Au-Ag network helps to constitute an efficient covalent binding coverage by the thiol modified aptamer. The entire (100 nmol) lyophilized form of the procured aptamer was then dissolved in 500 μ L of Milli-Q® water. Though different nanobioconjugates

were prepared by mixing in several volumetric ratios of Au-Ag network and thiolated aptamer like 1:2, 1:3, 1:4, 4:1, 2:1, etc, we found that the impedimetric response was best for the 1:4 nanobioconjugate. In brief, we have taken 10 μ L of the Au-Ag network and 40 μ L of the dilute aptamer solution, as mentioned before, was added to it and mixed properly.

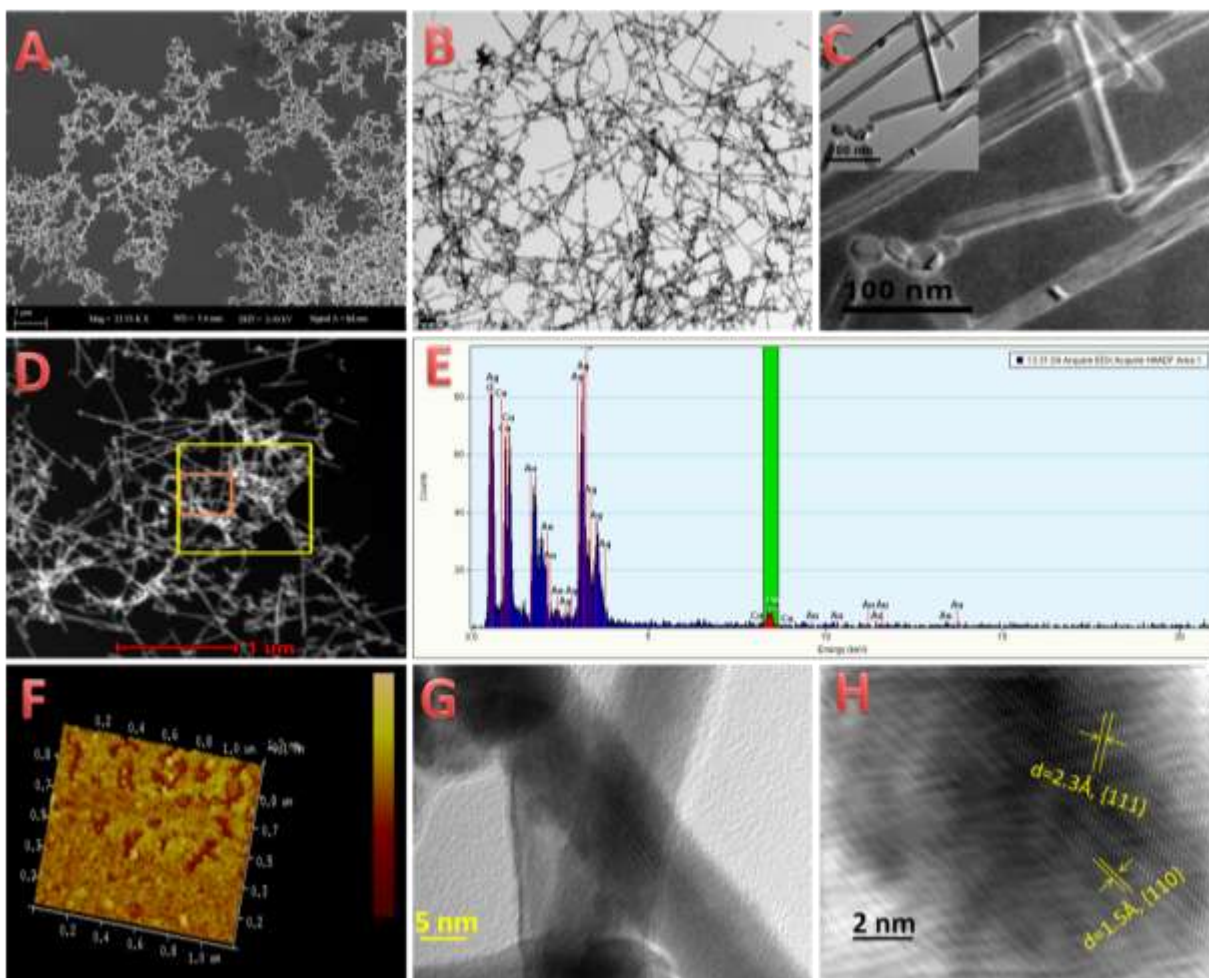


Figure 8.2: A and B is the SEM and TEM image of the Au-Ag network. C is the EFTEM image of the network. D is the HAADF image and E is EDX of Au-Ag network. F is the 3D topographic view of the network. G is the HRTEM image and H is the IFFT image of the porous network which shows two different orientations {111} and {110}.

The resultant nanobioconjugate (i.e. 50 μ L) then further diluted to 1 mL to achieve our stock solution for the rest of the experiments. The resultant nanobioconjugate is stored at 4 $^{\circ}$ C and

remains stable for months. In our study, we use Vero cells, derived from normal kidney cells, for studying the rate of viral infectivity. Details of the maintenance of the Vero cell line is described in the previous section. As we discussed before, throughout our study we have used psoralen-mediated inactivated virion particles to avoid any accidental infection. Psoralen is a photoreactive compound that freely permeates the phospholipid membranes and intercalates between nucleic acids by forming a cross-link.⁴⁴⁵ Following exposure to UV-A photoirradiation, the intercalated psoralen covalently cross-links pyrimidine residue and leading to viral inactivation through the inhibition of genome replication. Psoralen is chosen because the interaction of psoralen with viral nucleic acids leaves immunogenic surface epitopes intact.⁴⁵⁷ Psoralen-based viral genome inactivation is shown in **Figure 8.1**.

Synthesis and structural analysis of the cross-linked porous Au-Ag network has been described in the previous chapter in detail. To confirm the reproducibility of our previous report, the same porous Au-Ag network has been synthesized once again and their structural analysis by TEM is performed in an FEI, Tecnai G2 F30 S-Twin microscope and SEM in a Zeiss Supra 40, Field Emission instrument. The obtained morphology of our engineered Au-Ag cross-linked network shows a well-agreed structure with our previous study as shown in **Figures 8.2A** and **8.2B**. We have also performed their AFM imaging in a Bruker made BioScope Catalyst instrument over a mica plate to record the 3D topographic image of nanobioconjugate and activated/inactivated DENV-2 virus. The activated virus was measured as ~50-60nm and inactivated ones are larger than that in diameter which matches well with the previously reported measurements in the literature.⁴³⁰ All the electrochemical experiments were performed in 0.1M phosphate buffer where a screen-printed electrode (reference screen-printed electrode is shown in **Figure 8.3**.) is used as the working electrode to detect DENV-2. In each experiment, we have

drop cast 40 μ L of the nanobioconjugate over the electrode and dried it for 6h (since the nanobioconjugate is in an aqueous medium, drying is quite fast in dry RT). The same modified electrode was then used to perform several electrochemical measurements. During impedimetric measurements of different DENV-2 concentrations, we have applied a fixed potential of 0.8V within the frequency range of 10^5 to 10^{-1} Hz and an amplitude value of 0.01. In each measurement of different DENV-2 concentrations the overall volume was maintained at ~10mL in an electrochemical cell (we can use a custom-made cell with lesser volume too). The modified screen-printed electrode was then immersed in the diluted virion solutions. The stock concentration of the inactivated DENV-2 was $\sim 10^5$ PFU/mL which was serially diluted by 0.1M phosphate buffer to get different concentrations of virus solution for our electrochemical experiments. We have cross-checked the response of the unmodified and modified electrode in different DENV-2 concentrations and found that the unmodified electrode is non-responsive to the DENV-2 concentrations but the modified one shows well resolute DENV-2 concentration-dependent variation of impedance.



Figure 8.3: A panel of screen-printed electrode use for impedimetric assay.

The Au-Ag network appears to be highly porous in nature both from our TEM and SEM studies as shown in **Figures 8.2A** and **8.2B**. The EDX spectrum, given in **Figure 8.2E**, confirms the existence of Au in trace amount and Ag in a larger proportion. The 3D topographic view of the network is shown in **Figure 8.2F**. The energy-filtered TEM (EFTEM) image of the Au-Ag porous network structure is given in **Figure 8.2C** and it shows an excellent view of the sidewise assembly of the nanorod. The HRTEM and IFFT image of the network is given in **Figure 8.2G** and **8.2H** respectively, which confirms the existence of two prominent facets $\{111\}$ and $\{110\}$.

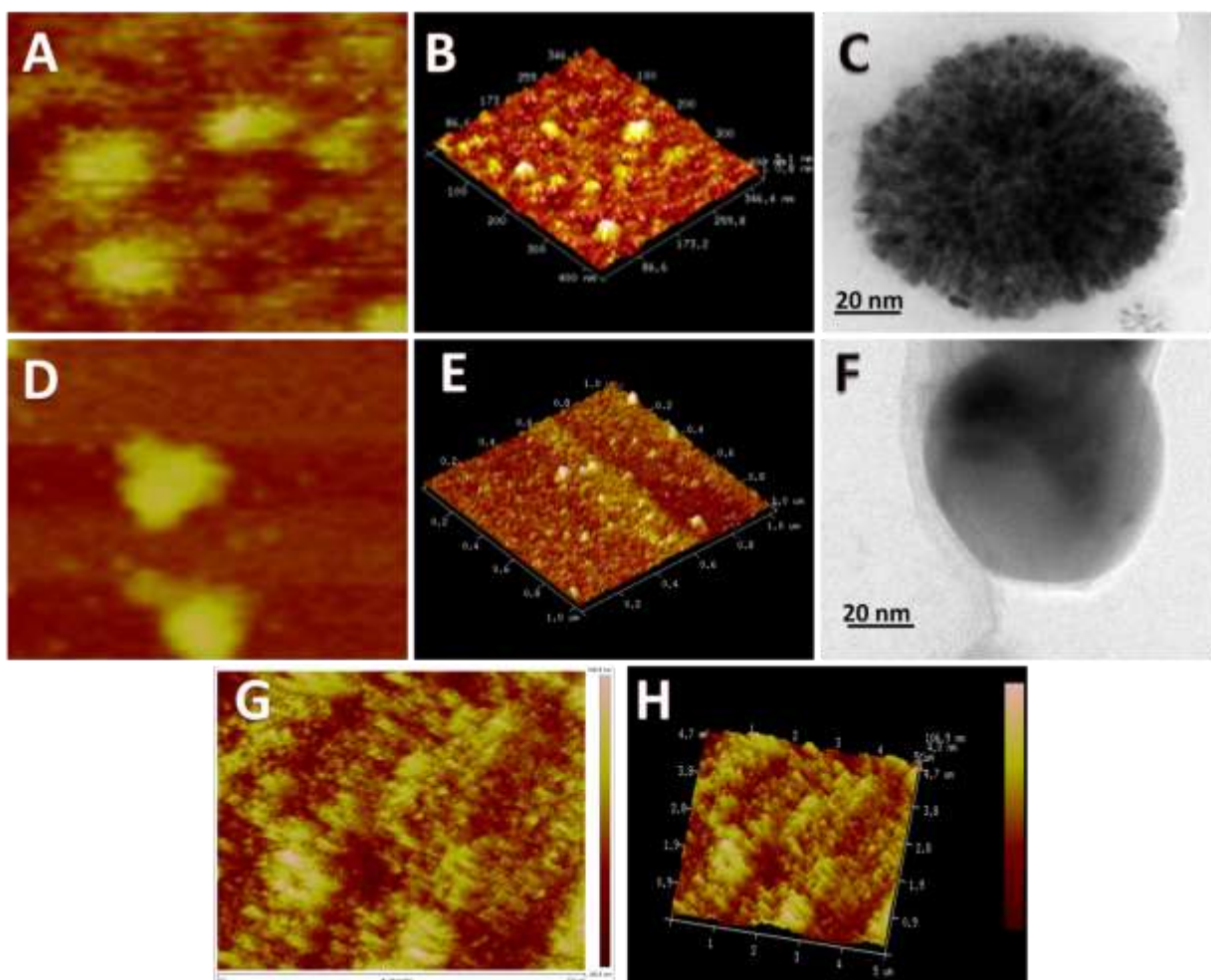


Figure 8.4: A and B are the two-dimensional and three-dimensional AFM image of the inactivated virus, whereas C is the TEM image of single inactivated DENV-2. D and E are the two-dimensional and three-dimensional AFM images of the infectious DENV-2 virus and F is the TEM image of single activated DENV-2. G and H represent the two-dimensional and three-dimensional AFM images of the nanobioconjugate respectively.

As discussed in the earlier section that after the psoralen treatment, the smooth wall of the DENV-2 virus converts into a spiky surface which is confirmed by our TEM study (**Figure 8.4C** and **8.4F**). The same morphological transition for DENV-2 from its inactivated to activated form is also provided by recording AFM images in two dimensions in **Figure 8.4A** and **8.4D** respectively whereas the corresponding 3D images are given in **Figure 8.4B** and **8.4E**. This

proves the ability of psoralen for the transition from activated to the inactivated form of DENV-2. It is already reported in the literature⁴⁵⁷ that the psoralen treatment however does not change the immunogenetic surface epitope of DENV-2.

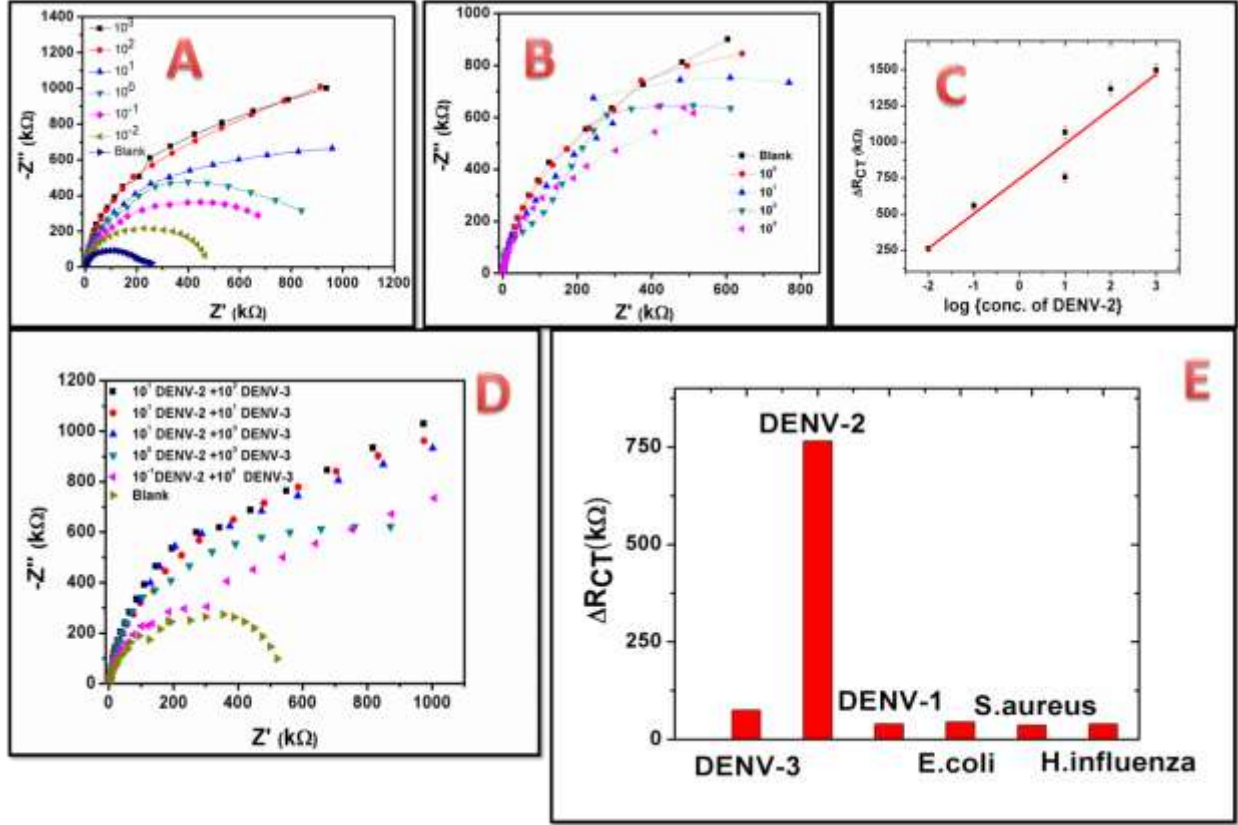


Figure 8.5: A and B are the Nyquist plot for DENV-2 and DENV-3 where all the virus concentrations are in PFU/mL unit. C is the calibration plot for DENV-2. D is the cross-reactivity check by impedance response in a mixture of DENV-2+ DENV-3. E is the ΔR_{CT} of DENV-2 in the presence of other DENV serotypes and bacteria. For all the samples we used the concentration at 10^1 PFU/mL.

Hence, our aim to target the DIII of glycoprotein-E of DENV-2 will not be obstructed by the psoralen inactivation process. In this work, we are targeting the direct detection of the dengue virus by designing a high specificity aptamer with respect to the DIII domain of DENV-2 glycoprotein-E and adsorbed it on to the nanobioconjugate. Reasons behind selecting the

engineered porous Au-Ag network as the electrode coating material for our highly sensitive impedimetric detection are (i) excellent covalent surface binding coverage of thiolated aptamers on Au-Ag network offers enhanced E-protein recognition on virion particles, (ii) the broad environmental stability (broader solvent polarity range and wider pH range of the medium) of the Au-Ag-DDT composite nanonetwork allows us to perform our sensing and detection in any environment, and (iii) better adsorptivity of the coating material on the electrode surface (a basic property of the Ag/Au-thiol composite materials) enhances the durability of the assay. We have also recorded the AFM images of the nanobioconjugate as shown in **Figure 8.4G** and **8.4H** represents its 2D and 3D views respectively.

Impedance measurements are performed by recording the Nyquist plot for different concentrations of DENV-II as shown in **Figure 8.5A**. In a Nyquist plot, the Y-axis and X-axis represent the imaginary and real part of the impedance. Obtained curves from the Nyquist plot are then fitted to the Randles cell through simulation (**Figure 8.6**). We found that the increase in DENV-2 concentration leads to an enhancement in R_{CT} as a result of a larger extent of binding of the DENV-2 with the nanobioconjugate modified electrode surface.

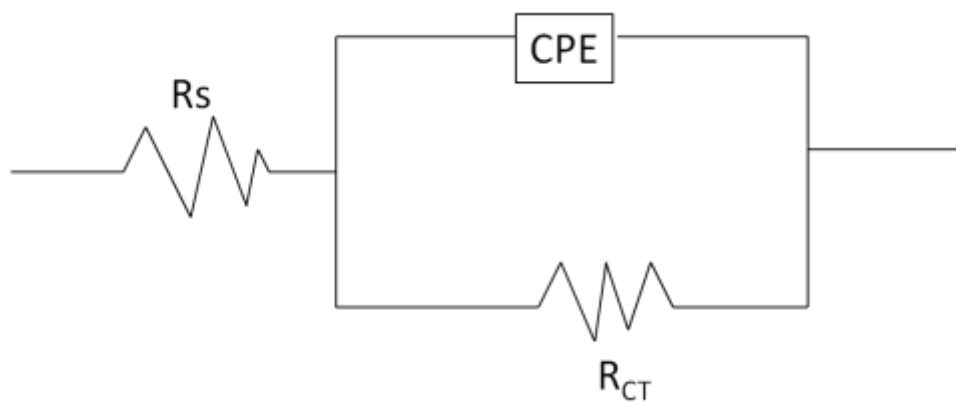


Figure 8.6: Randles cell used for fitting Nyquist plot. Where R_s appears due to solution resistance, CPE is the constant phase element and R_{CT} is the charge transfer resistance for any kind of process happening at the electrode surface.

Due to this more binding of DENV-2 on the electrode surface which makes an insulating layer on the electrode coating, less current flows and subsequently R_{ct} increase. To prove the specificity of our engineered nanobioconjugate assay, the same impedance measurement is carried out for inactivated DENV-3, as shown in **Figure 8.5B**, which is a closely related serotype (based on DIII domain of glycoprotein-E) of DENV-2. The change in impedance is negligible in comparison to the blank phosphate buffer which clearly signifies that there is no specific binding (antigen-aptamer interaction) between DENV-3 and the nanobioconjugate and agrees well with our prediction.

Fitted parameters from Randles cell (**Figure 8.6**) like charge transfer resistance (R_{CT}), constant phase element (CPE), solution resistance (R_s), etc are discussed detailed in SI section and listed in **Table 8.1**. During each measurement, we have recorded the blank response i.e. response of the modified electrode in phosphate buffer. We introduced a new physical parameter, ΔR_{CT} , for calibration curves of DENV-2, which is obtained by subtracting R_{CT} of blank solution from the R_{CT} of a particular concentration of DENV-2 solution under investigation. Hereafter we plot ΔR_{CT} vs $\log[\text{DENV-2}]$ ($[\text{DENV-2}]$ is the concentration of DENV-2) to get a linear calibration plot for different virion samples with a concentration between 10^3 to 10^{-2} PFU/mL as plotted in **Figure 8.5C**. The cross-reactivity is checked through impedance measurement in a mixed solution of two closely related serotypes i.e. DENV-2 and DENV-3.

Table 8.1: Parameters obtained from the Nyquist plot for DENV-2 as shown in Figure 3A by fitting into the Randles cell.

Conc (PFU/mL)	R_s (Ω)	$R_{CT}(k \Omega)$	n	Y_0
Blank	200	229	.88	2.1×10^{-6}
10^{-2}	200	488	.92	1×10^{-6}

10^{-1}	200	785	.94	9.5×10^{-7}
10^0	200	985	.96	9×10^{-7}
10^1	200	1290	.94	9×10^{-7}
10^2	200	1600	.98	9×10^{-7}
10^3	200	1730	.98	9×10^{-7}

It is observable from the impedance plot (**Figure 8.5D**) that with increasing DENV-2 concentration the impedance is increasing linearly and closely following **Figure 8.5C** though the impedance is independent to [DENV-3] while we kept [DENV-3] constant. This signifies that even if a host is infected by DENV-2 and DENV-3, the nanobioconjugate will respond only to DENV-2.

We have also provided a histogram in **Figure 8.5E** to record the ΔR_{CT} in presence of different types of bacteria which remain present in the human body, like *E. coli*, *Staphylococcus aureus*, and *H. influenza* along with different dengue serotypes like DENV-3, DENV-1, etc. (at the same concentration) to estimate the broader cross-reactivity of our reported assay. This demonstrates the specificity of our nanobioconjugate towards DENV-2 only and we found that DENV-2 shows exclusively high impedance towards the engineered nanobioconjugate. The obtained positive result from cross-reactivity experiments allows us to go for real sample analysis collected from infected patients. The infected DENV-2 blood serum was collected from Belegkata ID & BG Hospital, Kolkata, INDIA.

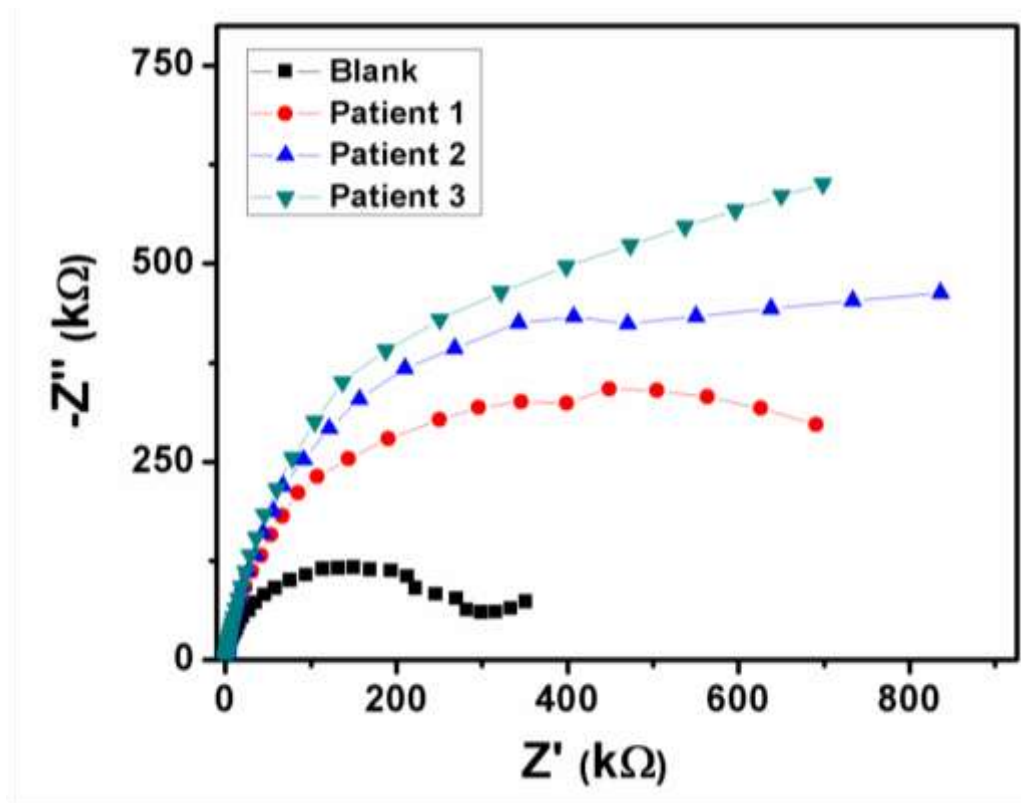


Figure 8.7: Nyquist plot for real sample designated as Patient1, Patient 2, and Patient 3.

The blood samples with DENV-2 infection are initially assessed through qRT-PCR which shows a good amount of viral load. We have estimated the impedance response for 3 such DENV-2 samples collected from 3 different DENV-2 positive patients as shown in **Figure 8.7**. Recorded high impedance values, R_{CT} , and the corresponding virus concentration from the calibration plot for three different DENV-2 positive samples are listed in **Table 8.2**.

Table 8.2: parameters obtained from the Nyquist plot for DENV-II infected real blood samples drawn from 3 different patients.

Sample	R_s (Ω)	R_{CT} (kΩ)	n	Y_0	Virus concentration from calibration plot (PFU/mL)
Blank	250	300	.86	1×10^{-6}	NA
Patient 1	250	725	.94	1×10^{-6}	.879

Patient 2	250	940	.96	9×10^{-7}	7.53
Patient 3	250	1140	.96	1×10^{-6}	45.70

Obtained results clearly show our ability to develop a user-friendly, cost-effective, rapid, sensitive, and highly specific biosensor for DENV-2 detection in all possible physicochemical environments. Specific and noted advantage of our developed nanobiosensor include: (i) direct detection method nullifies the necessity of NS1 antigen test as done in ELISA method, (ii) need not to separate viral RNA as done in qRT-PCR, (iii) quashes the requirement of expansive enzymes as done in the enzymatic assay, and (iv) sample requirement is only 40 μ L for each test. Hence, a thiol modified DNA aptamer-based porous Au-Ag nanobioconjugated network can easily, efficiently, and sensitively detect the DENV-2 serotype from any real sample.

In conclusion, a highly stable (in the broad physicochemical environment), non-expansive, aptamer-based Au-Ag nanobioconjugate with porous network structure has been developed with good adsorptivity on electrode surface for highly specific and ultrasensitive (up to 10^{-2} PFU/mL) detection of DENV-2 through a non-enzymatic assay. The developed impedimetric assay is a simple electrochemical assay which does not seek any laborious processes like RNA isolation, gel electrophoresis, fluorescence measurement, and optical density measurement or requires any expansive accessories like tunable electron or light sources. This is a direct detection technique (i.e. we need not any preprocessing of the blood/swab sample) where we recognize the specific dengue serotype through aptamer-based E-protein binding which results a recordable change in impedance. The developed nanobioconjugate allows us to detect DENV-2 highly specifically from the infected blood sample up to concentration as low as $\sim 10^{-2}$ PFU/mL. In our current investigation, we used a low-cost screen-printed electrode (Cost: Rs.

100/p) as the working electrode of our electrochemical assay which reduces the cost of the detection to a bare minimum. Undoubtedly this is the first report of user-friendly impedimetric sensing of lethal DENV-2 which has all the potentials to replace the ELISA-based technique for real sample analysis.

CHAPTER-9A

Future Direction

Synthesis of $\text{Ag}_{\text{core}}\text{Au}_{\text{shell}}$ nanostructures and the corresponding $\text{NP}_{\text{matrix}}$ as a bifunctional catalyst for the fabrication of high throughput alcohol fuel cells.

OUTLINE: Specific Points of Discussion

- Despite being unfavorable redox reactions, we were successfully able to produce desired $\text{Ag}_{\text{core}}\text{Au}_{\text{shell}}$ nanostructures by controlling the $\text{Au}^{3+}/\text{Au}^0$ kinetics and using CTAB as a surfactant.
- The final $\text{NP}_{\text{matrix}}$ is synthesized from $\text{Ag}_{\text{core}}\text{Au}_{\text{shell}}$ nanostructures by a galvanic replacement reaction.
- As a bifunctional catalyst, the developed $\text{NP}_{\text{matrix}}$ will help us to produce high current density from alcohol fuel cells.
- $\text{NP}_{\text{matrix}}$ finds itself as a substitute to the Pt/C as an efficient catalyst for the future generation of clean fuel with long term durability.
- We need a substantial amount of additional study to draw the final conclusion.

9A.1 Introduction:

Due to their unique properties, porous bimetallic gold-silver (Au-Ag) nanoparticles have received weighty attention in present days for determining the responsible factors behind the atomic origin of their promising catalytic activity towards various redox reactions e.g. oxidation of mono-, di-, and tri-ols⁴⁵⁸⁻⁴⁶⁰ (e.g., methanol, ethylene glycol, and glycerol) for fuel cell applications, oxidation of water⁴⁶¹ for oxygen evolution reaction (OER), reduction of water for hydrogen evolution reaction⁵⁰ (HER), oxidation of CO to CO₂⁴⁶², reduction of nitrogen to ammonia and CO₂ to methanol^{463,464}, etc. In this context, a critical question arises: which one is the decision-making factor behind the enhanced catalytic efficacy for porous Au-Ag nano-alloy compared to other conventional materials? Several arguments have been brought up in search of the above query which includes (i) critical surface composition (Au/Ag) of the nano-alloy,⁴⁶⁵ (ii) structural rearrangement of the nanoporous gold during the catalytic reaction,⁴⁶⁶ (iii) presence of a large extent of crystal defects (stepped surface, terrace, kink, dislocation, grain boundary, twin boundary, etc on the exposed nano-alloy surface⁴, enhanced active surface area, suitable surface charge and curvature-induced charge density³¹⁵, efficiency in narrowing of d-band centre, large extent of tensile strain generated for lattice mismatch due to the introduction of bigger Ag atom in the nano-crystal made by smaller size Au atoms,⁷ etc. To investigate the prime factors responsible for determining their catalytic efficacy, we have engineered several Au-Ag alloy nanocrystals. The synthesized Au-Ag alloy nanocrystals were then used as electro-catalysts for the oxidation of n-ols (methanol, ethylene glycol, and glycerol) and reduction of oxygen (ORR) for fuel cell applications. In both cases, i.e., oxidation of alcohol (withdrawing electrons from the reactant) and reduction of oxygen (ORR) (donating electrons to the reactant), the bimetallic Au-

Ag matrix ($\text{NP}_{\text{matrix}}$) is found to be catalytically most active. The enhanced catalytic activity of $\text{NP}_{\text{matrix}}$ can be explained by measuring the extent of voids or defects (both act as active catalytic sites) formation through the Kirkendall effect (differential diffusion rate of Ag^0 and Au^0) during the galvanic replacement of Ag^0 by Au^{3+} over the nano-alloy surface. The surface chemical micro-environment of a nano-alloy can be described as $\text{M}_\text{R} + \text{N}_\text{R} + \text{ligands} \rightarrow \text{Mp@ligands} + \text{N}_\text{P}$ where M_R is the starting material, N_R is the assisted reactant (In this case M_R is Au^{3+} or Ag^+ and N_R is ascorbic acid and the ligand is CTAB moiety). In general, the ligands give stabilization to the nanoparticles by binding (coordinate bonds) to the ‘unsaturated metal-dangling bonds’⁴⁶⁷. The catalytic activity of a nano-alloy is thus proportional to the density of these ‘dangling bonds’ on the nano-surface. In nanoparticles there are mainly two types of bonds, one is saturated internal bonds and the other is the unsaturated or dangling bonds situated over the edges or terraces. The CTAB ligands in $\text{NP}_{\text{matrix}}$ constitutes coordinate bonds to the unsaturated atoms ($\text{R}_4\text{N}^+ \dots \text{Br}^-$ is a bound ion pair and considered to be $2e^-$ donor) and thereby give some stability to deny aggregation in the dispersion medium. However, some of the dangling bonds still remain ‘naked’ and creates multiple crystal defects which are considered to be chemically active sites for oxidation (that means withdrawing electron clouds from the reactants). In our present study, we have performed n-ols oxidation reactions e.g., the oxidation of methanol, ethylene glycol, and glycerol which are considered as clean and silent liquid fuels with high energy conversion efficiency. Pt is considered to be the most efficient catalyst for oxidizing such organic molecules however the affinity of CO adsorption over the Pt surface during electro-oxidation of alcohols retard the reaction kinetics.⁴⁶⁸ Our synthesized $\text{NP}_{\text{matrix}}$ with high defect enriched catalytically active sites is found to be highly chemically reactive for the oxidation of methanol both in acidic and basic medium. To apply our $\text{NP}_{\text{matrix}}$ as electrocatalytic material in a

broader aspect, we have utilized it in electro-oxidation of a di-ol (ethylene glycol) and a tri-ol (glycerol) along with mono-ol (methanol) to show that the above-mentioned material is catalytically active for the oxidation of long-chain and higher molecular weight alcohols too. Besides alcohol oxidation, oxygen reduction reaction (ORR) is a crucial cathodic process in alcohol fuel cells. The sluggish electron transfer kinetics in ORR needs efficient electro-catalysts to accelerate the process. Pt-based nano-alloys have been widely used as a catalyst to assist the four-electron reduction of oxygen to water. However, due to their high-cost, less tolerance, and low durability, Pt-based nano-alloy are substituted nowadays by transition metal nitrides, chalcogenides, oxides,⁴⁶⁹ etc. We have engineered the Au-Ag matrix ($\text{NP}_{\text{matrix}}$) with low-cost and having the ability of long term catalytic performance, whose stability has been checked through several cycling during ORR.

9A.2 Material Synthesis:

9A.2.1 Synthesis of Au Nanoseed:

In a typical synthesis, 500 μL of 10^{-2}M $\text{HAuCl}_4 \cdot 3\text{H}_2\text{O}$ was added in 20 mL of MiliQ (18 $\text{M}\Omega\text{ cm}$) water under constant stirring (150 rpm) followed by the addition of 200 μL of $2.5 \times 10^{-2}\text{M}$ of TSC. The solution was kept under stirring at room temperature for an additional 30 s. To this solution, 60 μL of 10^{-1}M NaBH_4 (ice cold) was added dropwise. The solution turns brownish immediately which we kept in dark for an additional 2 hr in an open mouth condition to facilitate the release of evolved hydrogen until the color turns to wine red.

9A.2.2 Synthesis of Au-Ag Nano-alloy:

Au-Ag nano-alloy with different morphology was synthesized by varying the CTAC concentration and temperature. In a typical synthetic procedure, 45mL of MiliQ water was taken

in a 100 mL 3-neck round-bottomed flask fitted with condenser under a continuous flow of tap water where the flask is kept in a water bath at 85⁰C. To this solution, 0.01g CTAC was added and kept for further 5 minutes under constant stirring (400 rpm) to make it dissolved completely. Once the CTAC becomes soluble, 2mL of as-prepared Au nanoseed was added to it followed by the addition of 2 mL of 10⁻² M AgNO₃ and 500 μ L of 10⁻¹ M of AA. The solution was kept at 85⁰C and 400 rpm for an additional 4 h. The whole solution turns into a yellowish-green color; which we cooled to room temperature before centrifuged it at 6000 rpm for 1 h at 30⁰C. After centrifugation, the precipitated oval-shaped Au-Ag nano-alloy (~50 nm in length) was collected from the centrifuge tube and the final volume was adjusted to 500 μ L by adding an appropriate amount of MiliQ water. The concentrated Au-Ag nano-alloy was then stored at 4⁰-8⁰C 4⁰C which remains stable for months as we checked it's stability by verifying its plasmonic nature (UV-vis-NIR), TEM, HRTEM, and XPS spectra. The morphology of different Au-Ag nano-alloy was controlled by varying the surfactant concentration and the temperature during synthesis. We have checked the catalytic activity of each Au-Ag nano-alloy towards electrochemical oxidation of methanol and found that the oval-shaped Au-Ag nano-alloy synthesized at 85⁰C (by applying .01g CTAC), as stated above, is the most effective one. Further, we have modified its morphology to the Ag_{core}Au_{shell} structure for increasing its catalytic efficiency towards the electrochemical oxidation of methanol. The modification is discussed below.

9A.2.3 Synthesis of Ag_{core}Au_{shell} structure by Template Method:

The oval-shaped Au-Ag nanoalloy (~50 nm in length) prepared in the previous step was dispersed in 15 mL of MiliQ water and the resultant solution is then used as a template for the next step. In this step, 0.05 g of CTAB was dissolved in 45 mL of MiliQ water at 30⁰C. The diluted CTAB solution was then kept under constant stirring at 200 rpm. To this solution, 2mL of

10^{-2} M $\text{HAuCl}_4 \cdot 3\text{H}_2\text{O}$ was added followed by the addition of 300 μL of 10^{-2} M of AgNO_3 . The above mixture was kept under the same constant stirring for an additional 45 s. The solution turns reddish-yellow. To this solution, 320 μL of AA was added drop-by-drop and once the reddish-yellow color turns to colorless. We have added different volumes of the template solution (100 μL , 1 mL, and 3 mL) to this colorless solution. The whole solution was stirred for another 1 minute before we kept it for overnight (12 h) in dark (closed mouth condition) at 30 $^{\circ}\text{C}$. After 12 h, the solution was centrifuged at 2000 rpm at 30 $^{\circ}\text{C}$ for 2 h. Precipitated core-shell structures were then collected and stored at room temperature. Our catalytic study shows that the core-shell structure engineered by using 3 mL of the template solution ($\text{Ag}_{\text{core}}\text{Au}_{\text{shell}}$) is catalytically the most active one among all and used further to synthesize the void enriched Au-Ag ($\text{NP}_{\text{matrix}}$) matrix.

9A.2.4 Synthesis of void Enriched Au-Ag Matrix ($\text{NP}_{\text{matrix}}$) by Galvanic Replacement

Method:

The centrifuged $\text{Ag}_{\text{core}}\text{Au}_{\text{shell}}$ structures obtained in the previous step was redispersed into 50 mL of water and stirred for 5 minutes at 200 rpm by keeping the temperature constant at 30 $^{\circ}\text{C}$. To this solution, 2 mL of 10^{-2} M $\text{HAuCl}_4 \cdot 3\text{H}_2\text{O}$ was added at a time and stirred for an additional 10 minutes and after which the reaction mixture was kept undisturbed for 12 h in dark. The as-synthesized Au-Ag $\text{NP}_{\text{matrix}}$ was then concentrated by centrifuging the solution at 2000 rpm at 30 $^{\circ}\text{C}$. The final precipitate is then diluted to 500 μL by MilliQ water and used for all the catalytic experiments.

9A.3 Results & Discussion:

As the reduction potential of Ag^+/Ag^0 (0.79 V) is much lower than that of $\text{Au}^{3+}/\text{Au}^0$ (1.51 V),⁷ the formation of $\text{Ag}_{\text{core}}\text{Au}_{\text{shell}}$ structure is quite difficult as the galvanic reaction may leach

out the Ag-core by transforming insoluble Ag^0 into Ag^+ . Despite that, we were successfully able to produce the desired $\text{Ag}_{\text{core}}\text{Au}_{\text{shell}}$ structure, by controlling the $\text{Au}^{3+}/\text{Au}^0$ kinetics and using CTAB as a surfactant. The synthesized $\text{Ag}_{\text{core}}\text{Au}_{\text{shell}}$ nanostructures as a function of the template (oval-shaped particles as synthesized in the 2nd step of the synthesis) volume (100 μL to 2 mL) are depicted below in **Figure 9A.1**.

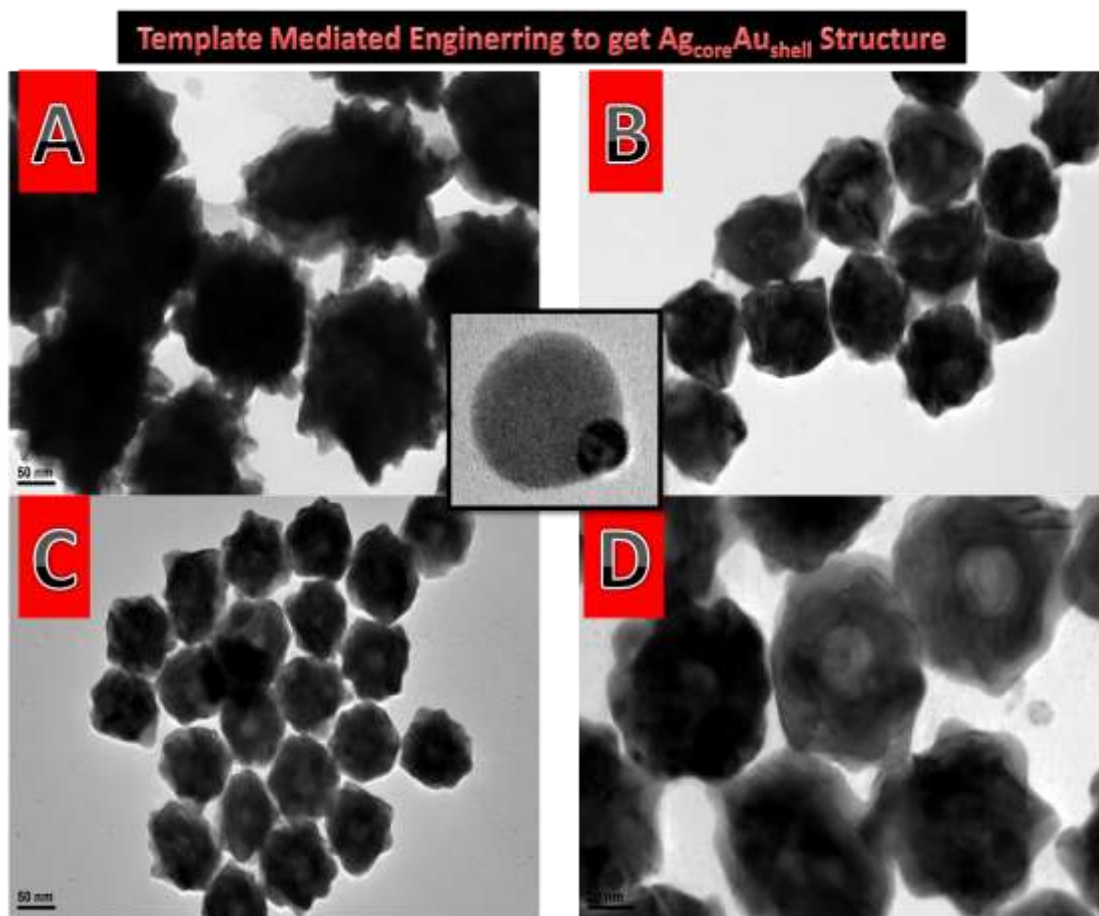


Figure 9A.1: The synthesized $\text{Ag}_{\text{core}}\text{Au}_{\text{shell}}$ nanostructures as a function of the template volume.

(A) 100 μL , (B) , (C) , and (D) 2 mL.

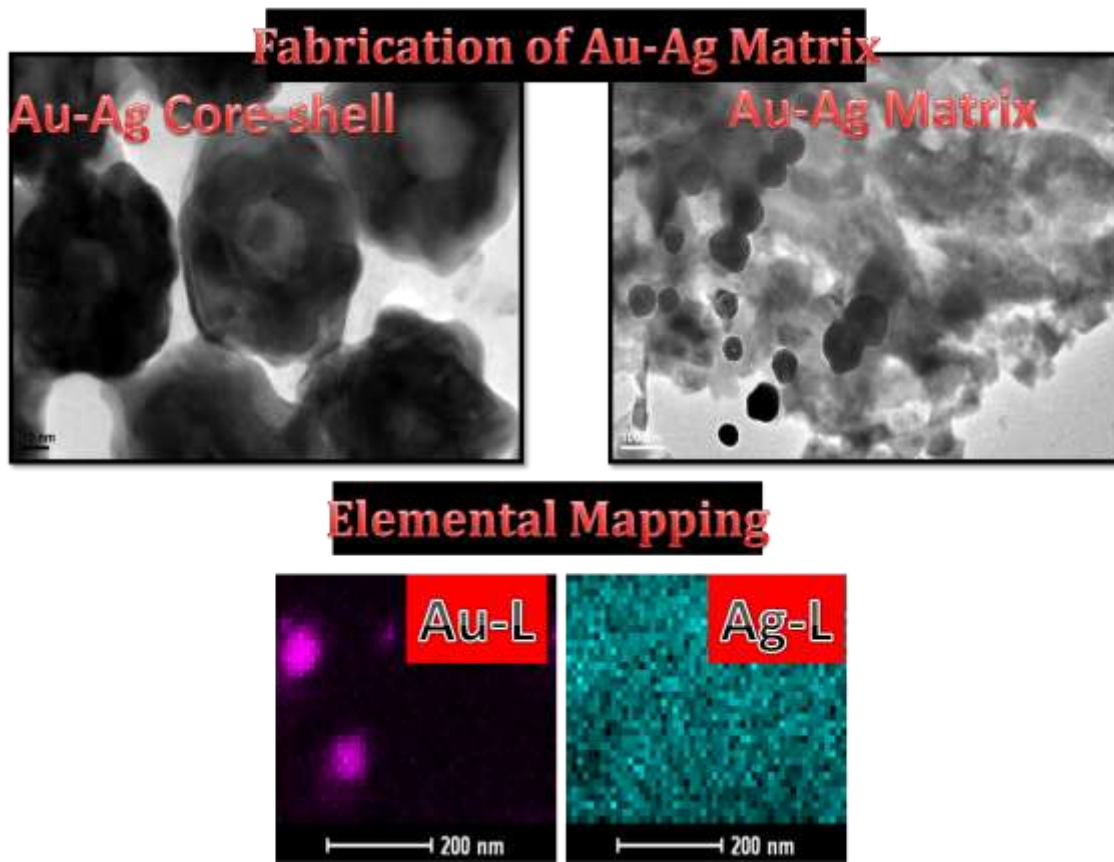


Figure 9A.2: Fabrication of $\text{NP}_{\text{matrix}}$ from $\text{Ag}_{\text{core}}\text{Au}_{\text{shell}}$, and their elemental mapping.

As we increase the volume of the template while keeping the surfactant concentration constant (0.05gm in 45mL of water), the size of the engineered $\text{Ag}_{\text{core}}\text{Au}_{\text{shell}}$ reduced gradually while the Addition of Au^{3+} which induces the galvanic replacement from $\text{Ag}_{\text{core}}\text{Au}_{\text{shell}}$ nanostructures to generate the desired highly void enriched Au-Ag Matrix ($\text{NP}_{\text{matrix}}$) is shown in **Figure 9A.2**. Generated $\text{NP}_{\text{matrix}}$ is found to be extremely effective for alcohol oxidation and ORR.

Electrocatalytic Activity of Au-Ag Matrix

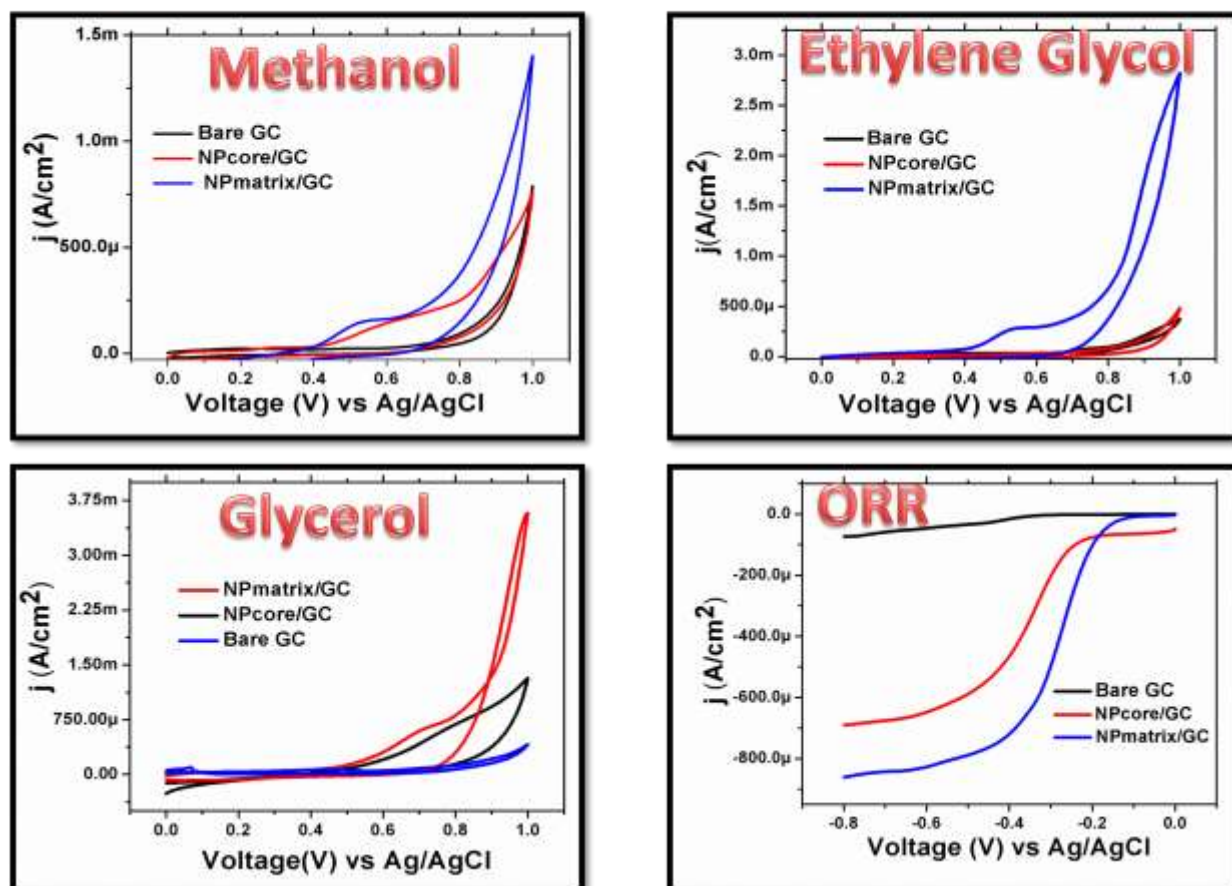


Figure 9A.3: Comparison of electrocatalytic activity of NP_{matrix} structure with Ag_{core}Au_{shell} and bare GC for the oxidation of methanol, ethylene glycol, and glycerol and reduction of oxygen. The concentration of methanol is fixed at 2M whereas for both ethylene glycol and glycerol is fixed at 3M.

We have tested the catalytic activity of the desired NP_{matrix} as mentioned earlier through cyclic voltammetry and linear sweep voltammetry for the oxidation of methanol, ethylene glycol, and glycerol and reduction of oxygen and compared their catalytic activity with bare GC and Ag_{core}Au_{shell} as shown in **Figure 9A.3**.

9A.3 Conclusion:

From the preliminary electrocatalysis results, we want to explore the alcohol fuel cell in more detail both from the experimental and theoretical points of view. As a bifunctional catalyst, the developed NP_{matrix} will help us to produce high current density from alcohol fuel cells. Thus a substitute of Pt/C can be developed for the future generation of clean fuel with long term durability.

CHAPTER-9B

Future Direction

Fabrication of Ag_{core}Au_{shell} nanostructure-based nanobioconjugate as an anti-dengue assay.

OUTLINE: Specific Points of Discussion

- Fabrication of PVP-coated Ag_{core}Au_{shell} nanostructures
- Fabrication of DENV-2 tagged PVP-coated Ag_{core}Au_{shell} nanostructure as the desired nanobioconjugate for sensitive detection of DENV-2 and therapeutic study.
- Currently, we are performing an antiviral assay of DENV-2 in the Vero cell line and planning to apply in an animal model in due course by using this nanobioconjugate.
- We need an extensive further study for more information and to reach into a conclusion about their applicability as a successful anti-dengue assay.

Besides applying our newly synthesized $\text{Ag}_{\text{core}}\text{Au}_{\text{shell}}$ nanostructures in alcohol fuel cells, we are planning to use the same core-shell nanomaterials (as described in Chapter-9A) to design a selective and sensitive antiviral assay within zero toxic levels for highly pandemic Dengue virus. The antiviral activity of Ag nanoparticle is well known in the literature, e.g. Ag nanoparticle/Chitosan composite is found to be highly active against H_1N_1 influenza A virus infection,⁴⁷⁰ commercially available PVP capped Ag nanoparticle is found to be effective for anti-HIV activity by binding to gp120 which prevents CD_4 dependent virion binding, fusion, and infectivity,⁴⁷¹ electrochemically synthesized Ag nanoparticle is found to be effective against poliovirus,⁴⁷² etc. Despite their high antiviral activity, Ag nanoparticles have limitations in nanovaccine industry due to their remarkable cyto- and geno-toxicity and difficulty in cellular uptake.⁴⁷³ Besides, nanoparticle size is a dominant factor for successful exo- and endocytosis processes in a cellular mechanism, e.g. a 50 nm diameter of nanoparticle is optimized for cellular uptake in nonphagocytic cells.⁴⁷⁴ In this regard, we have synthesized a bimetallic Au-Ag nanoalloy with a diameter of < 50 nm and found to be zero toxic at viral doses. The use of Au coating over the Ag_{core} (in an $\text{Ag}_{\text{core}}\text{Au}_{\text{shell}}$ nanostructure) reduces the toxicity of the synthesized nanoalloy by preventing the release of Ag^+ into the cellular media. $\text{Ag}_{\text{core}}\text{Au}_{\text{shell}}$ nanostructures are further modified by treating them with 0.1% polyvinyl alcohol (PVA) to make them more favorable for medical purposes. The toxicity was checked in HCT-116, RAW, HeLa, and HePG2 cell lines by MTT assay. The concentration of Ag in our synthesized PVP-capped $\text{Ag}_{\text{core}}\text{Au}_{\text{shell}}$ nanostructure was measured by ICP-OES technique. Variation of cell viability as a function of $\text{Ag}_{\text{core}}\text{Au}_{\text{shell}}$ nanoparticle and hence Ag concentration is shown in **Figure 9B.1** for HCT-116 cell line.

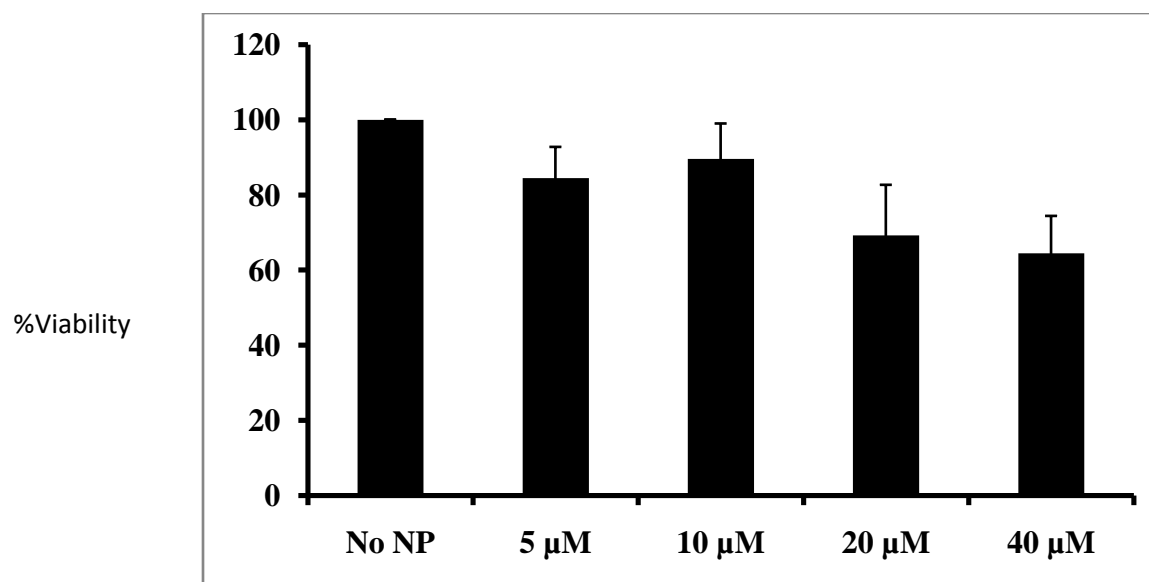
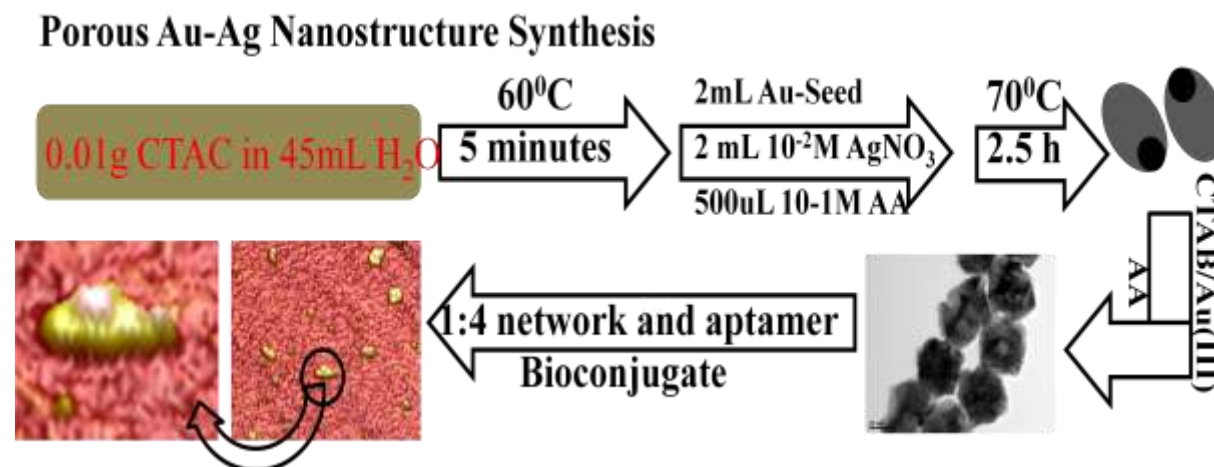


Figure 9B.1: Variation of cell viability as a function of available Ag concentration from the synthesized $\text{Ag}_{\text{core}}\text{Au}_{\text{shell}}$ nanostructure.

Further, the synthesized $\text{Ag}_{\text{core}}\text{Au}_{\text{shell}}$ nanostructure was treated with DENV-2 specific thiol modified aptamer (as mentioned in Chapter in 8) for highly sensitive DENV-2 detection as well as therapeutic application. A stepwise schematic presentation from the synthesis of $\text{Ag}_{\text{core}}\text{Au}_{\text{shell}}$ nanostructure to bioconjugate preparation is depicted in **Scheme 9B.1**.



Scheme 9B.1: A stepwise schematic presentation from the synthesis of Ag_{core}Au_{shell} nanostructure to bioconjugate preparation. The inserted AFM image shows how the aptamer is wrapped around the nanoparticle.

With this specific bioconjugate, we are now performing an antiviral assay of DENV-2 in the Vero cell line and planning to apply in an animal model in due course.

Thesis Abstract

The present thesis is an in-depth study of crystal growth and design of plasmonic Au, Ag, and Au-Ag alloy nanoparticles along with the observation and role of crystal irregularities like grain boundary, twin boundary, stacking faults, dislocation, etc, within the nanocrystal. The low coordinated crystal defects have been thoroughly studied through high-resolution Transmission Electron Microscopy (HRTEM) to find out the active centers of catalysis. The defect enriched nanostructures were then used for electrocatalytic sensing for different human metabolites and trace metal ions through the implication of Differential Pulse Voltammetry (DPV) and Electrochemical Impedance Spectroscopy (EIS). In **Chapter 1** we have discussed the origin of different crystal defects in various nanoparticles and their application in technology, pathology, theranostics, whereas **Chapter 2** comprises the detailed instrumentation techniques. In **Chapter 3**, we have highlighted the synthesis of different sized and shaped bud to blossom gold nanoflowers and their application in the sensing of Vitamin C. Experimental studies have been supported by theoretical *ab initio* simulation. In **Chapter 4**, we have provided the synthetic protocol of bimetallic Au-Ag nano prisms with the various extent of porosity at the center of gravity, and their tensile strain-dependent catalytic activity for uric acid oxidation. **Chapter 5** highlights the As^{3+} sensing through colorimetric and spectrometric approaches by studying the morphological transition of Ag nano prisms upon interaction with As^{3+} . **Chapter 6** provides grain boundary dependent hydrogen evolution reaction (HER) study through electrochemical linear sweep voltammetry (LSV) of different Au nanostructures. In **Chapter 7**, we describe the synthesis of porous 2D bimetallic Au-Ag nanoalloy and their application for electrocatalytic sensing of a series of human metabolites and trace metal ions. **Chapter 8** implements the idea of DNA-aptamer-based direct sensing of the DENV-2 virus in real samples through EIS approaches. In **Chapter 9**, we have given our future directions to use Au-Ag nano-alloy for alcohol fuel cell and antiviral assay.

**Crystal Engineering to Fabricate Au, Ag, and Au-Ag Alloy
Nanoparticles: Application in Technology, Pathology, and
Theranostics**

By

Sandip Kumar De

CHEM05201504003

Saha Institute of Nuclear Physics, Kolkata

A thesis submitted to the Board of Studies in Chemical Sciences

In partial fulfillment of requirements for the degree of

DOCTOR OF PHILOSOPHY

Of

HOMI BHABHA NATIONAL INSTITUTE



July, 2020

Homi Bhabha National Institute

Recommendations of the Viva Voce Committee

As members of the Viva Voce Committee, we certify that we have read the dissertation prepared by **Shri Sandip Kumar De** entitled “**Crystal Engineering to Fabricate Au, Ag, and Au-Ag Alloy Nanoparticles: Application in Technology, Pathology and Theranostics**” and recommend that it may be accepted as fulfilling the thesis requirement for the award of Degree of Doctor of Philosophy.

Chairman - Prof. Susanta Lahiri

Susanta Lahiri
22/9/2020

Guide / Convener - Prof. Dulal Senapati

Dulal Senapati
22.9.2020

Examiner - Prof. Nikhil R. Jana, IACS-Kolkata

Nikhil R. Jana
22/9/2020

Member 1- Prof. Padmaja Prasad Mishra

Padmaja Prasad Mishra
22/09/2020

Member 2- Prof. Montu K. Hazra

Montu K. Hazra
22/09/2020

Member 3- Prof. Pintu Sen, VECC-Kolkata

Final approval and acceptance of this thesis is contingent upon the candidate's submission of the final copies of the thesis to HBNI.

I hereby certify that I have read this thesis prepared under my direction and recommend that it may be accepted as fulfilling the thesis requirement.

Date:

Place:

Signature

Guide

STATEMENT BY AUTHOR

This dissertation has been submitted in partial fulfillment of requirements for an advanced degree at Homi Bhabha National Institute (HBNI) and is deposited in the Library to be made available to borrowers under rules of HBNI.

Brief quotations from this dissertation are allowable without special permission, provided that accurate acknowledgement of the source is made. Requests for permission for extended quotations from or reproduction of this manuscript in whole or in part may be granted by the Competent Authority of HBNI when in his or her judgment the proposed use of the material is in the interests of scholarship. In all other instances, however, permission must be obtained from the author.

Sandip Kumar De

DECLARATION

I, hereby declare that the investigation presented in the thesis has been carried out by me. The work is original and has not been submitted earlier as a whole or in part for a degree/diploma at this or any other Institution/University.

Sandip Kumar De

List of Publications arising from the thesis

Journal

- (1) Crystal-Defect-Induced Facet-Dependent Electrocatalytic Activity of 3D Gold Nanoflowers for the Selective Nanomolar Detection of Ascorbic Acid, De, S. K.; Mondal, S.; Sen, P.; Pal, U.; Pathak, B.; Rawat, K. S.; Bardhan, M.; Bhattacharya, M.; Satpati, B.; De, A.; Senapati, D. *Nanoscale* **2018**, *10* (23), 11091-11102.
<https://doi.org/10.1039/c8nr03087a>.
- (2) Zone-Specific Crystallization and a Porosity-Directed Scaling Marker for the Catalytic Efficacy of Au-Ag Alloy Nanoparticles, De, S. K.; Mondal, S.; Roy, A.; Kumar, S.; Mukherjee, M.; Das Chakraborty, S.; Sen, P.; Pathak, B.; Satpati, B.; Mukhopadhyay, M.; Senapati, D. *ACS Appl. Nano Mater.* **2019**, *2* (12), 7669-7685.
<https://doi.org/10.1021/acsanm.9b01748>.
- (3) Wide Range Morphological Transition of Silver Nanoprisms by Selective Interaction with As(III): Tuning-Detuning of Surface Plasmon Offers to Decode the Mechanism, Das Chakraborty, S.; Mondal, S.; Satpati, B.; Pal, U.; De, S. K.; Bhattacharya, M.; Ray, S.; Senapati, D. *J. Phys. Chem. C* **2019**, *123* (17), 11044-11054.
<https://doi.org/10.1021/acs.jpcc.8b10799>.
- (4) Au-Seeded Ag-Nanorod Networks for Electrocatalytic Sensing, De, S. K.; Kumar, S.; Ray, S.; Mondal, S.; Ray, A.; Bhattacharjee, G.; Nandy, A.; Roy, A.; Pathak, B.; Senapati, D. <https://doi.org/10.1021/acsanm.0c01976>

(5) Unveiling the Excellent Electrocatalytic Activity of Grain-Boundary Enriched Anisotropic Gold Nanostructures towards Hydrogen Evolution Reaction: A Combined Approach of Experiment and Theory, Mondal, S.; De, S. K.; Jana, R.; Roy, A.; Mukherjee, M.; Datta, A.; Satpati, B.; Senapati, D. **(Under Revision)**

(6) Fabrication of Highly Specific DNA Based Porous Au-Ag Nanobioconjugate as Electrode Coat for Impedimetric DENV-2 Infected Direct Blood Sensing, De, S. K.; Roy, S.; Bhattacharyya, S.; Mondal, S.; Nandy, A.; Roy, A.; Sadhukhan, P.; Senapati, D. **(Communicated Work)**

Chapters in books and lectures notes: None

Conferences:

- (1) Poster Presentation in ICANN 2017, IIT Guwahati, Assam, India
- (2) Attended a One Day Workshop on “Biomedical Device Technology” in ICANN 2017, Assam, India
- (3) Poster Presentation in SAFETY AND OCCUPATIONAL HEALTH AWARENESS PROGRAMME 2018, December 2018, SINP, Kolkata
- (4) Poster Presentation in Nano India 2019, Mahatma Gandhi University, DST, Kottayam , Kerala
- (5) Oral Presentation (**BEST ORAL PRESENTATION & GIVEN ACS TRAVEL AWARD**) in SMST 2020, Goa, India
- (6) Poster Presentation (**BEST POSTER PRESENTATION & GIVEN BEST POSTER AWARD by ACS APPLIED NANOMATERIALS**) in ICONSAT 2020, SNBNCBS, Kolkata, India

(7) Oral Presentation in KYE-2019, SINP, India

(8) Oral Presentation in SciMeeting, ACS National Meeting, Spring, 2020- Cancelled due to COVID Pandemic.

Sandip Kumar De

Dedicated to my Parents.....

ACKNOWLEDGEMENT

First of all, I would like to acknowledge my thesis supervisor Dr. Dulal Senapati for giving me academic freedom throughout my doctoral tenure. He has given me support with scientific discussion and proper guidance. I was a student from Organic Chemistry, and was introduced to a new field, Nanoscience and Nanotechnology in my PhD. My supervisor stands by me all the time by encouraging my motivation and by planning a perfect project with appropriate experimental and theoretical approaches. I would like to acknowledge my past and present HODs of our Chemical Sciences Division (CSD), Professor Samita Basu & Professor Susanta Lahiri, for sharing their scientific ideas with me and providing all academic help throughout my PhD tenure. A special thanks to Prof. Pintu Sen from Variable Energy Cyclotron Centre (VECC) for allowing me to use his instrumental facilities. I would like to express my sincere gratitude to Dr. Padmaja P. Mishra, Dr. Montu K. Hazra, Prof. Maitreyee Nandi, Prof. Munna Sarkar and all other CSD members along with Prof. Tapas Chini, Prof. Manabendra Mukherjee, Dr. Biswarup Satpati, Dr. Mrinmay Mukherjee, Prof. Sangam Banerjee, Mr. Goutam Sarkar, and Mr. Debraj Dey from Surface Physics and Material Science Division for all their help. I convey my sincere acknowledgement to Prof. Biswarup Pathak from IIT Indore for sharing his vast knowledge in theoretical simulation with our group. Throughout my PhD tenure, my lab members were part of my life. I express my thanks to my senior colleagues Dr. Subrata Mondal, Dr. Sarmistha Ray, Dr. Munmun Bardhan, Dr. Uttam Pal, Dr. Maitreyee Bhattacharya, Dr. Sudeshna Das Chakraborty and my junior colleagues Arpita, Anuradha, Sourav, and Manorama along with my Post-MSc friends. I feel lucky to get such parents who acted as supportive friends to assist me in all aspects of my life. I express my sincere thanks to our Guruji Sri Anukulchandra Chakravarty to appear as a philosopher in my life. My brother Subhadeep and sister Bunty are more than family member to me.

Contents:

Chapter-1: Introduction

1. Introduction.....	1
1.1 Zero-dimensional point defects.....	3
1.1a Vacancies.....	3
1.1b Interstitials.....	3
1.1c Impurities.....	5
1.1d Schottky defect and Frenkel defect.....	5
1.2 One dimensional line defects.....	6
1.2a Edge dislocation.....	6
1.2b Screw dislocation.....	6
1.3 Two-dimensional planer defects.....	8
1.3a Grain Boundary.....	8
1.3b Twin Boundary.....	9
1.3c Stacking Fault.....	10
1.4 3D Defects.....	11
1.5 Application of noble metal nanocatalyst in Pathological Industry.....	12
1.5a Sensing of Metabolites.....	12
1.5b Sensing of Trace Metal Ions.....	16
1.5c Sensing of Virus.....	18
1.6. Application in Fuel Cell Technology.....	21
1.6a Alcohol Fuel Cell.....	21
1.6b ORR activity.....	23
1.6c Reduction of CO ₂	24
1.6d HER and OER.....	26

1.7Theranostics Application of Plasmonic Noble Metal Nanoalloy.....	27
---	----

Chapter-2: Methodology and Experimental Set Up

2.1 Chemical Materials.....	30
2.2 Biochemical Materials.....	31
2.3 Biological materials.....	31
2.4 Methods.....	32
2.4.1 Ultraviolet-Visible-NearInfrared (UV-Vis-NIR) Absorption Spectroscopy.....	32
2.4.2 Dynamic Light Scattering and Zeta Potential Measurement.....	34
2.4.3 X-ray Photoelectron Spectroscopy.....	37
2.4.4 X-ray Diffraction Spectroscopy.....	39
2.4.5 Inductively Coupled Plasma Optical Emission Spectrometry.....	41
2.4.6 Surface-Enhanced Raman Spectroscopy.....	42
2.4.7 Atomic Force Microscopy.....	43
2.4.8 Scanning Electron Microscopy.....	45
2.4.9 Transmission Electron Microscopy.....	47
2.4.10 Electrochemical Measurements.....	49
2.4.10.1 Linear sweep voltammetry.....	50
2.4.10.2 Cyclic Voltammetry.....	51
2.4.10.3 Differential Pulse Voltammetry.....	53
2.4.10.4 Square Wave Voltammetry.....	54
2.4.10.5 Chronoamperometry.....	56
2.4.10.6 Electrochemical Impedance Spectroscopy.....	57

Chapter-3: Crystal Defect Induced Facet Dependent Electrocatalytic Activity of 3D Gold Nanoflower towards the Selective Nanomolar (*nM*) Detection of Ascorbic Acid

Outline.....	58
3.1 Introduction.....	59
3.2 Synthesis of AuNPs.....	62
3.3 Theoretical ab initio simulation.....	63
3.4 Density Functional Theory.....	64
3.5 Results & Discussion.....	64
3.6 Conclusion.....	89

Chapter-4: Zone-Specific Crystallization and a Porosity-Directed Scaling Marker for the Catalytic Efficacy of Au-Ag Alloy Nanoparticles

Outline.....	90
4.1 Introduction.....	91
4.2 Material Synthesis.....	95
4.3 Materials Purification.....	97
4.4 Theoretical Modeling of HNPr.....	97
4.5 Results and Discussion.....	98
4.6 Conclusion.....	136

Chapter-5: Wide Range Morphological Transition of Silver Nanoprism by Selective Interaction with As(III): Tuning-Detuning of Surface Plasmon Offers to Decode the Mechanism

Outline.....	137
5.1 Introduction.....	138
5.2 Synthesis of silver nanoprism.....	141
5.3 Results and Discussion.....	142
5.4 Conclusion.....	163

Chapter-6: Unveiling the Excellent Electrocatalytic Activity of Grain Boundary Enriched Anisotropic Pure Gold Nanostructures towards Hydrogen Evolution Reaction: A Combined Approach of Experiment and Theory

Outline.....	165
6.1 Introduction.....	166
6.2 Synthesis of AuNPs using HQ.....	170
6.3 Computational Details.....	171
6.4 Results and Discussion.....	173
6.4.1 Optical and Structural analysis of A ⁿ GNPs.....	173
6.4.2 Electrocatalytic Performance of A ⁿ GNPs for Hydrogen Evolution Reaction.....	182
6.4.3 Computational Studies.....	200
6.5 Conclusions.....	205

Chapter-7: Au-Seeded Ag-Nanorod-Based Thiol Mediated Strained 2D Network as Non-Enzymatic Universal Electrocatalytic Sensing Platform: A Mechanistic Exploration

Outline.....	206
7.1 Introduction.....	208
7.2 Material synthesis.....	212
7.2.1 Synthesis of Au Nanoseed.....	212
7.2.2 Synthesis of Au-seed induced Ag nanorod.....	213
7.2.3 Synthesis of Au-Ag Network.....	214
7.2.4 Collection and preparation of human serum samples.....	215
7.2.5 Theoretical modeling.....	215
7.3. Results and Discussion.....	216
7.4. Conclusion.....	271

Chapter-8: Fabrication of Highly Specific DNA Based Porous Au-Ag Nanobioconjugate as Electrode Coat for Rapid Impedimetric Direct Sensing of DENV-2 from Infected Whole Blood

Outline.....	272
Discussion.....	273

Chapter- 9A: Synthesis of Ag_{core}Au_{shell} nanostructures and the corresponding NP_{matrix} as a bifunctional catalyst for the fabrication of high throughput alcohol fuel cells

Outline.....	293
9A.1 Introduction.....	294
9A.2 Material Synthesis.....	296
9A.2.1 Synthesis of Au Nanoseed.....	296
9A.2.2 Synthesis of Au-Ag Nano-alloy.....	297
9A.2.3 Synthesis of Ag _{core} Au _{shell} structure by Template Method.....	298
9A.2.4 Synthesis of void Enriched Au-Ag Matrix (NP _{matrix}) by Galvanic Replacement Method.....	298
9A.3 Results and discussion.....	298
9A.4 Conclusion.....	302

Chapter- 9B Fabrication of Ag_{core}Au_{shell} nanostructure-based nanobioconjugate as an anti-dengue assay

Outline.....	303
Discussion.....	304
References.....	307

Thesis Highlight

Name of the Student: Sandip Kumar De

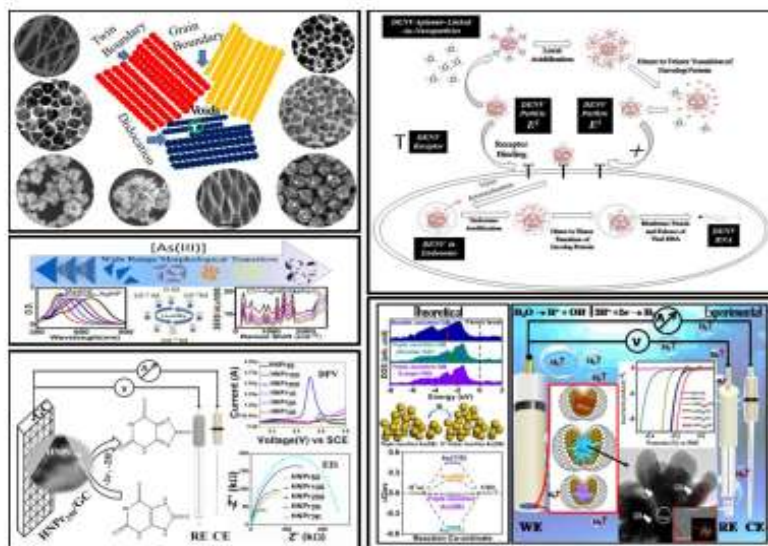
Name of the CI/OCC: Saha Institute of Nuclear Physics **Enrolment No.:** CHEM05201504003

Thesis Title: Crystal Engineering to Fabricate Au, Ag, & Au-Ag Alloy Nanoparticles: Application in Technology, Pathology & Theranostics

Discipline: Chemical Sciences

Sub-Area of Discipline: Nanomaterials

Crystal designing of noble metal nanoparticles (Au, Ag, Au-Ag nanoalloy) is a striking field of research in present days due to their tremendous applications in technology, pathology, and theranostics. In this thesis, I have discussed in-depth about the fabrication of Au, Ag, and Au-Ag alloy nanoparticles with multiple reduced coordinated defects enriched active crystal sites like grain boundary, twin boundary, stacking fault, cracks, and voids which are responsible for internal tensile strain within the nanocrystal. We have performed different electrocatalytic redox reactions by using those strain-induced nanocrystals for sensing of metabolites like ascorbic acid, uric acid, L-tryptophan; etc via recording their characteristic I-V curves obtained from differential pulse voltammetry experiments. Besides various electrochemical techniques, we



have also performed surface-enhanced Raman spectroscopy and ultraviolet-visible (UV-vis) spectroscopy for selective detection of metal ion like As^{3+} from real samples. Including their tremendous applications in the pathological field, we also found the parallel applications of Au-Ag alloy nanoparticles in fuel cell technology which include a methanol fuel cell, water oxidation, etc. We found that our developed nanomaterials are equally capable as a bifunctional catalyst for oxidation of methanol, ethylene

glycol, glycerol, and reduction of oxygen. Experimental observations have been verified by theoretical *ab initio* simulation by calculating the shift in the d-band center due to the appearance of crystal irregularities along with free energy calculation over different facets (like $\langle 111 \rangle$, $\langle 110 \rangle$, $\langle 200 \rangle$, etc) of Au nanocrystal, to find the energetically most favorable pathway. We have also performed theranostics applications of our synthesized highly porous nanomaterials and their assemblies for selective detection of dengue-II from clinical samples and its inhibition in the Vero cell line. Selective detection of dengue strain through highly sensitive impedimetric technique in the animal model along with inhibition of viral replication is an encouraging process to carry forward in the near future.

List of Figures:

Figure 1.1a: Point defect originating from vacancies	3
Figure 1.1b(i): Interstitial point defect created by foreign atom.....	4
Figure 1.1b(ii): Interstitial point defect created by moving an atom from a lattice point to an off-lattice site.....	4
Figure 1.1c: Point defect originating from impurity.....	5
Figure 1.2a: Schematic presentation of edge dislocation.....	6
Figure 1.2b: Schematic representation of edge dislocation and screw dislocation.....	7
Figure:1.2c Presentation of burger vector.....	8
Figure1.3a: Schematic Presentation of GB over a crystal lattice.....	9
Figure 1.3b: Schematic presentation of a twin boundary over a fcc lattice.....	10
Figure 1.3c: Schematic Presentation of intrinsic and extrinsic SF in fcc lattice.....	11
Figure1.4: A fcc lattice with regular arrangement and void enriched arrangement.....	12
Figure 1.5a(i): A. DPV response for AuNP@MoS ₂ modified GCE for AA (1mM to 70mM), DA (0.01μM to 7μM), UA (.01mM to 12mM).	14
Figure 1.5a(ii): DPV responses of individual analytes in physiological concentration limit in presence of other analytes (Ref41).....	15
Figure 1.5b(i): (A) DPV response for AuNP/GC electrode for simultaneous detection of Cd ²⁺ , Pb ²⁺ , Cu ²⁺ , Hg ²⁺ at a time (Ref-43).....	17
Figure 1.5b(ii): Statistical distribution of AuNP used for the detection of different viruses in which HBV is the most reported one for using AuNP as a sensing probe.(Ref-44).....	18
Figure 1.5c: EIS response from the sensor with different concentrations of viral load by using an external pulse. (Ref-45).....	20
Figure 1.6a: Electrooxidation of methanol for different Au-Ag system(Ref-20).....	22

Figure 1.6b. Comparative ORR activity of Different AuNP system.(Ref-48).....	24
Figure 1.6c. Schematic Presentation of the Au-Cu system for selective conversion of CO ₂ to Formate (Ref-49).....	25
Figure 1.6d: OER Polarization curve (Ref-51).....	27
Figure 1.7: Antibacterial activity of Au-Ag NP(ref-55).....	29
Figure 2.1: (A) JASCO V-770 UV-Vis-NIR spectrophotometer with spectral range 190-3200 nm, (B) JASCO V-650 UV-Vis spectrometer fitted with Peltier for temperature dependent study with spectral range 190-900 nm.....	32
Figure 2.2: Optical configurations of the Malvern Zetasizer Nano series for dynamic light scattering measurements	36
Figure 2.3: Malvern Zetasizer ZS90 instrument.....	37
Figure 2.4: Experimental set up and lay out for XPS.....	39
Figure 2.5: Experimental set up and lay out for XRD.....	40
Figure 2.6: Experimental set up and lay out for ICP-OES.....	41
Figure 2.7: (A) Details of the SERS set up, (B) Layout of the instrument.....	42
Figure 2.8: Schematic presentation and picture of AFM.....	45
Figure 2.9: Schematic presentation and picture of SEM.....	47
Figure 2.10: Schematic presentation and picture of TEM.....	49
Figure 2.11: i-t-E curve for LSV (Ref-72).....	51
Figure 2.12: Representative curve for CV(Ref-72).....	52
Figure 2.13: (A) Representative DPV curve, (B) Working principle of DPV (Ref-72)....	54
Figure 2.14: Representative curve for SWV (Ref-72).....	56
Figure 3.1: TEM image of AuNFs.....	65

Figure 3.2: DPV for the oxidation of AA on AuNF modified GC electrode.....	70
Figure 3.3: Randomly selected crystal defects on bud structured AuNF.....	76
Figure 3.4: Different crystal defects on AuNF surfaces.....	77
Figure 3.5: HRTEM image of the bud shaped AuNF.....	78
Figure 3.6: Variation of defect density with different flourishing stages	81
Figure 3.7: Top and Side views of the optimized AA.	83
Figure 3.8: DPV response of AA at lower & higher concentration.....	85
Figure 3.9: optimized geometries of ascorbic acid in presence of gold clusters.....	87
Figure 3.10: Interference test of ascorbic acids.....	88
Figure 4.1: (A), (B) and (C) SEM images of HNPr ₂₅₀ with HAuCl ₄ .3H ₂ O addition rate (second step of seeded growth) of 1mL/min, 2mL/min and 3mL/min respectively. (D) Absorption spectra of different HNPrs.....	96
Figure 4.2: TEM image of individual HNPr synthesized by using a different amount of Ag seed.	99
Figure 4.3: Histogram of size distribution for each HNPr. 100 TEM frames have been considered for each HNPr to calculate their average edge length.....	100
Figure 4.4: TEM images of time-dependent (A: 10 min, B: 1 h and C: 6h) porosity generation at the center of gravity of HNPr ₂₅₀	102
Figure 4.5: SAED pattern and EDX profile of different HNPr.....	104
Figure 4.6: XRD pattern of HNPr ₅₀ , HNPr ₂₅₀ , and HNPr _{2K}	105
Figure 4.7: Fitted curve of XRD at {111} facet to calculate the strain.....	106
Figure 4.8a: EDX spectra and HAADF–STEM image of HNPr ₁₀₀ for the confirmation of bimetallic (Au–Ag) nature.....	107
Figure 4.8b: EDX spectra and HAADF–STEM image of HNPr ₅₀₀ for the confirmation of bimetallic (Au–Ag) nature.....	108
Figure 4.8c: EDX spectra and HAADF–STEM image of HNPr _{3K} for the confirmation of bimetallic (Au–Ag) nature.....	108

Figure 4.9: XPS study of HNPr ₁₀₀ , HNPr ₂₅₀ , and HNPr _{2K} nanostructures are shown in the top, middle and bottom panel respectively	110
Figure 4.10: XPS survey spectrum of Cl ⁻ (2p), C(1s) and N(1s) in HNPr ₁₀₀ which confirms their presence in the sample.....	111
Figure 4.11: Porosity and Crystalline zone for different HNPr.....	113
Figure 4.12: Thickness Profile of HNPr ₂₅₀	114
Figure 4.13: Representative twin boundaries on the HNPr ₂₅₀ surface, spotted in three different zones outside the central cavity zone. The twin angle (with reference to the twin boundary) varies in the range of 55–57°	115
Figure 4.14: Appearance of different crystal defects on HNPr surfaces.	118
Figure 4.15: TEM images of the distribution of different grains over individual HNPr surface.....	119
Figure 4.16(a): Presentation of different HNPr ₂₅₀ frames for the calculation of Surface Grain Boundary Density (SGBD).....	120
Figure 4.16(b): Edge length and cavity radius determination in HNPr ₂₅₀ by using digital micrograph software.....	121
Figure 4.17: (A) and (B) represent DPV and SWV of 4×10 ⁻⁵ M UA at different HNPr/GC electrode. Inset in (A) represents the DPV of bare GC. (C) Nyquist plot for the electrooxidation of UA at an applied potential of 0.4V within a frequency range of 10 ⁵ to 10 ⁻² Hz, (D) Comparison of R _{CT} and k ₀ value of different HNPr/GC towards the oxidation of UA.....	123
Figure 4.18: Equivalent circuit for the Nyquist plot.....	126
Figure 4.19: SERS spectra of different HNPr with CV (crystal violet) as the Raman reporter in which HNPr ₂₅₀ shows maximum Raman intensity.....	127
Figure 4.20: Optimized structure for different HNPrs: (a) HNPr _{pureAu} , (b) HNPr _{pureAg} , (c) HNPr _A , (d) HNPr _B , and (e) HNPr _C . The leftmost figure of the top panel shows the model HNPr with different planes (basal and vicinal) along with different structural parameters.....	132
Figure 4.21: (A), (B) and (C) are chronoamperometry, SWV, and DPV responses respectively at variable concentrations of UA on the HNPr ₂₅₀ /GC electrode. (D) represents the linear fitting of DPV response with standard deviation. (E) Denotes the peak current shifting for electrooxidation	

process of 400 μ M UA in presence of different interfering agents	135
Figure 5.1: (A) Stacking length-dependent plasmon tuning through TEM study.....	143
Figure 5.2: Frontal and sideways bright-field and HRTEM of our synthesized nanoprisms with {111} lattice plane as the basal plane and 1/3{422} reflections indicate the presence of a single twinning boundary within the {111} planes.....	145
Figure 5.3: (A-H) Morphological change of AgNPr by destacking, followed by leaching of nanoprisms and emulsion induced controlled aggregation of silver seeds at increasing concentration of As(III).	146
Figure 5.4: EDX spectra obtained from two different areas (Area-1 and Area-2) of AgNPr stacking to analyze the relative abundance of different elements.....	150
Figure 5.5: Concentration dependent color codes sensing of As(III).....	152
Figure 5.6: Optimized structures of Ag ₃ AsO ₃ and Ag ₃ AsO ₄ . Ag is shown in blue, As in purple and O in red.....	154
Figure 5.7: Colorimetric change of AgNPr solution upon addition.....	156
Figure 5.8: SERS based assay to monitor the morphological modification of AgNPr on addition of different concentration NaAsO ₂	161
Figure 6.1: (A) Schematic representation for the synthesis and growth of A ⁿ GNPs inside the SDS micelle's core. Effects of HQ concentration (250-750 μ M) on (B) visual color appearance (pink to blue) and (C) plasmon spectra (540-660 nm) of colloidal A ⁿ GNPs.....	172
Figure 6.2: TEM, SAED of different AuNP.....	175
Figure 6.3: SEM image of flower or bloom shaped AuNPs i.e. AuNP ₇₅	176
Figure 6.4: EDAX spectra of flower or bloom shaped AuNPs i.e. AuNP ₇₅	177
Figure 6.5: XPS spectra of variable shaped A ⁿ GNPs.....	180
Figure 6.6: Wide range survey spectrum indicating the presence of different elements into (a) AuNP ₅₀ and (b) AuNP ₁₅₀	181
Figure 6.7 : Electrocatalytic performance of different A ⁿ GNPs modified electrode towards HER.....	183
Figure 6.8: Electrochemical Impedance Spectroscopy (EIS) study for HER.....	189

Figure 6.9: Linear sweep Voltammetric response of variable AuNPs modified GC electrode in 0.1M KOH solution. Scan rate 10 mV/s..... 190

Figure 6.10:The presence of different crystal plane into the synthesized variable shaped AuNPs (A) AuNP₅₀ (B) AuNP₇₅ (C) AuNP₁₅₀. The areas selected in (A), (B) and (C) show the FFT (Fast Fourier transformation) images. (D) and (E) show the HRTEM images of AuNP₇₅ pertaining the appearance of high-density grain boundary.....193

Figure 6.11:Different HRTEM images of AuNP₇₅in which the rectangular area in (A, B and C) is selected for determining the average grain sizes using Jeffries method.196

Figure 6.12: Different TEM images of AuNP₁₅₀ (A, B and C) and AuNP₅₀ (D, E and F) in which the rectangular area is selected for determining the average grain sizes using Jeffries method.197

Figure 6.13:Variations in defect density in various shaped AuNPs with 50 frames considered for each of the three different surface zones with surface areas of 400 (20×20) nm² for each AuN.....198

Figure 6.14: Optimized structure of (a) Au (111), (b) Au (200)and (c) Au (110) surfaces. Structures of H* adsorbed Au surfaces (d) H*-Au (111), (e) H*-Au (200), (f) H*-Au (110)...201

Figure 6.15: Optimized structure of (a) GB_a, (b) GB_b and (c) GB_cAugrain boundary surfaces (dotted line shows grain boundary region). Structures of H* adsorbed Augrain boundary surfaces (d) H*-GB_a, (e) H*-GB_b, (f) H*-GB_c.201

Figure 6.16: Optimized structure of (a) GB_d, (c) GB_eAugrain boundary surfaces (dotted region shows smaller and larger grain diameter). Structures of H* adsorbed Au grain boundary surfaces (b) H*-GB_d, (d) H*-GB_e.....202

Figure 6.17:(a) Free energy diagram for H* adsorption on various Au surfaces for HER, (b) DOS plots for GB_e and H*-GB_e Au surfaces, (c) PDOSs for Au-5d, Au-5p, Au-6s and H-1s of H*-GB_e Au surface, (d) DOSs on Au atoms for different grain boundary surfaces. 203

Figure 7.1: (A) True diameter from TEM image, (B) plasmon band from absorption spectra, (C) hydrodynamic size from DLS measurement, and (D) surface charge from the zeta-potential measurement of Au nanoseed.....213

Figure 7.2: (A, B, C) and (D, E, F) are the SEM, TEM, and HRTEM images of Hy-Au@AgNR₁₂₀ and Hy-Au@AgNR₈₄₀ respectively.218

Figure 7.3: Different colors of nanorods: From left to right Hy-Au@AgNR₈₄₀, Hy-Au@AgNR₄₅₀, Hy-Au@AgNR₁₂₀, Hy-Au@AgNR₈₄₀-Ass.....219

Figure 7.4: UV absorption spectra of different Hy-Au@AgNRs

and Hy-Au@AgNR₈₄₀-Ass.....220

Figure 7.5: A, B, C are the time-dependent 2D images of Hy-Au@AgNR₈₄₀-Ass formation. The images are taken after DTT addition to Hy-Au@AgNR₈₄₀ at 30 s, 60 s, and 120 s interval. The 3D images of A, B, C are D, E, F respectively.....221

Figure 7.6a: Unfiltered and Elastic TEM images of different Nanorod.....222

Figure 7.6b: Histogram of the nanorods (A) Hy-Au@AgNR₈₄₀, (B) Hy-Au@AgNR₄₅₀, and (C) Hy-Au@AgNR₁₂₀.....222

Figure 7.7a: A, B, C are Intensity (percent) vs size (nm) curve of Hy-Au@AgNR₈₄₀-Ass formation at 30 s, 60 s, and 120 s time interval in the reaction medium. D, E, F are the Correlation coefficient vs time (μ s) curves for the same time intervals.....227

Figure 7.7b: (A) Change in zeta potential during the formation of Hy-Au@AgNR₈₄₀-Ass at different time intervals, (B, C) Final ξ and d_{hyd} of all the Hy-Au@AgNRs and Hy-Au@AgNR₈₄₀-Ass respectively.....228

Figure 7.8: A, B, C are the frequency plot whereas D, E, F presents the phase shift and G, H, I are velocity distributions of Hy-Au@AgNR₈₄₀, Hy-Au@AgNR₄₅₀, and Hy-Au@AgNR₁₂₀ respectively.....231

Figure 7.9: A, B, C are frequency plot; D, E, F are phase plot; G, H, I are velocity distribution curve at 30 s, 60 s, and 120 s of reaction time. The negative phase shift in D and E implies zeta potential was negative at 30 s and 60 s but becomes positive at 120 s.....232

Figure 7.10: (A) SERS measurement of the time-dependent formation of Hy-Au@AgNR₈₄₀-Ass by adding Hy-Au@AgNR₈₄₀s into the DTT solution. (B) SERS spectra of different Hy-Au@AgNRs and Hy-Au@AgNR₈₄₀-Ass.....233

Figure 7.11: XPS spectra of nanorod and assembly structure.....234

Figure 7.12: A and B are the XPS of Ag3d5/2 and Ag3d3/2 lines for Hy-Au@AgNR₈₄₀ and Hy-Au@AgNR₈₄₀-Ass. In figure C the XRD of Hy-Au@AgNR₈₄₀ and Hy-Au@AgNR₈₄₀-Ass are shown whereas D shows the SAED pattern of Hy-Au@AgNR₈₄₀-Ass to confirm the {111} is the most intense plane.....235

Figure 7.13: The fitted curve of (A) Hy-Au@AgNR ₈₄₀ -Ass and (B) Hy-Au@AgNR ₈₄₀ at $2\theta \approx 38.25^\circ$ for $fcc\{111\}$ facet.....	237
Figure 7.14: (A) Modeled nanorod structure with $\langle 111 \rangle$ and $\langle 110 \rangle$ facets. (B) Possible Au seeding (spherical and rod-shaped) and spherical Au seeded Hy-Au@AgNRs. (C) The density of states (DOS) of pure Ag and Au-seeded AgNRs with 40 Å and 80 Å lengths.....	242
Figure 7.15: Creation of multiple low coordinated crystal sites like stepped surface, terrace, kinks, edges, etc., during the formation of Hy-Au@AgNR ₈₄₀ -Ass from the constituents Hy-Au@AgNR ₈₄₀ S.....	243
Figure 7.16a: Effect of temperature on Hy-Au@AgNR ₄₅₀ morphology, at (A) 60-70 °C, (B) 70-80 °C, and (C) 80-90 °C.	244
Figure 7.16b: Association of Au seed followed by Ag deposition at a higher temperature. Stacking up of Au seeds is verified by (A) TEM, (B) HAADF, (C) HRTEM, and (D) EDX.....	245
Figure 7.17a: Kinetics of Ag seed-based nanorod formation at (A) 30 min, (B) 60 min, and (C) 90 min and Au seed-based Hy-Au@AgNR ₁₂₀ formation at (A') 30 min, (B') 60 min, and (C') 90 min.	246
Figure 7.17b: The effect of the variation Au seed amount [(A) 1 mL, (B) 4 mL, and (C) 2 mL] on Hy-Au@AgNR ₁₂₀ synthesis.	247
Figure 7.18: Effect of AgNO ₃ concentration (in the reaction mixture) on the efficiency of Hy-Au@AgNR ₁₂₀ formation.....	248
Figure 7.19: Effect of CTAC concentration with (A) 0.025 gm CTAC in 45 mL water for the formation of Hy-Au@AgNR ₄₅₀ , (B) 0.05 gm CTAC in 45 mL water for the formation of Hy-Au@AgNR ₁₂₀ , and (C) 0.1 gm CTAC in 45 mL water for the formation of Hy-Au@AgNR ₅₀ ..	249
Figure 7.20: The effect of the variation of AA concentration on Hy-Au@AgNR ₁₂₀ formation	250
Figure 7.21: The effect of the variation of DTT concentration on the efficiency of Hy-Au@AgNR-Ass formation	251
Figure 7.22: Formation of Hy-Au@AgNR with length ~1-1.2 µm by maintaining the molar ratio between AgNO ₃ and AA at 1:20 during synthesis.....	253
Figure 7.23: A is the DPV response for the reduction glucose (4×10^{-4} M) in 0.1 M HClO ₄ , B is DPV response for the oxidation of L-tryptophan (4×10^{-4} M) in 0.1 M HClO ₄ , C is the DPV response for the reduction of vitamin K3 (4×10^{-4} M) in 0.1 M LiClO ₄ + acetonitrile.....	256

Figure 7.24: A is the chronoamperometric response for the reduction glucose (4×10^{-4} M) in 0.1 M HClO ₄ , B is the chronoamperometric response for the oxidation of L-tryptophan (4×10^{-4} M) in 0.1 M HClO ₄ , C is the chronoamperometric response for the reduction of vitamin K3 (4×10^{-4} M) in 0.1 M LiClO ₄ + acetonitrile.....	258
Figure 7.25: A is the impedance response for the reduction glucose (4×10^{-4} M) in 0.1 M HClO ₄ , B is impedance response for the oxidation of L-tryptophan (4×10^{-4} M) in 0.1 M HClO ₄ , C is the impedance response for reduction of vitamin K3 (4×10^{-4} M) in 0.1M LiClO ₄ + acetonitrile.....	259
Figure 7.26: Electrochemical reduction of metal ions in 0.1 M HClO ₄ (A) Co ²⁺ , (B) Cr ³⁺ , (C) Cu ²⁺ (D) Hg ²⁺ , (E) Ni ²⁺ , (F) Fe ³⁺ , (G) Pb ²⁺ , (H) is for vitamin K3 oxidation in 0.1 (M) LiClO ₄ + acetonitrile.....	264
Figure 7.27a: Oxidation of metabolites in 0.1M NaOH medium: (A) AA , (B) Creatinine (C) Dopamine (DA), (D) thiamine, (E) riboflavin, (F) Pantothenic acid (PA) (G) urea (H) uric acid (UA), (I) inositol.....	265
Figure 7.27b: oxidation of metabolites in 0.1M NaOH; (A) Xanthine, (B) Cysteamine (Cyst) (C) glucose, (D) L-tryptophan, (E) folic acid (FA).....	266
Figure 7.28: I-C linear fitting for different water-soluble human metabolites as mentioned in the figure during their catalytic oxidation at their physiological concentration level.....	267.
Figure 7.29: Linear Calibration plot of metal ions. Just like human metabolites (Figure 7) where we did not find any linear relation with concentration we take logarithm as shown in (C) for Cu ²⁺ and in (G) for vitamin K3.....	268
Figure 7.30: Interference test through DPV assay for different metabolites.....	270
Figure 8.1: A and B are the bright field and fluorescence image of the control, respectively. C and D are the bright field and fluorescence image of the inactivated virus, respectively.....	281
Figure 8.2: SEM, TEM, HAADF, AFM of Au-Ag network.....	282
Figure 8.3: A panel of screen-printed electrode use for impedimetric assay.....	284
Figure 8.4: AFM and TEM images of activated and inactivated viruses.....	285
Figure 8.5: Nyquist plot and Impedance measurent for different DENV samples.....	286
Figure 8.6: Randles cell used for fitting Nyquist plot.....	288

Figure 8.7: Nyquist plot for real sample designated as Patient1, Patient 2, and Patient 3.....	290
Figure 9A.1: The synthesized $\text{Ag}_{\text{core}}\text{Au}_{\text{shell}}$ nanostructures as a function of the template volume. (A) 100 μL , (B) , (C) , and (D) 2 mL.....	299
Figure 9A.2: Fabrication of $\text{NP}_{\text{matrix}}$ from $\text{Ag}_{\text{core}}\text{Au}_{\text{shell}}$, and their elemental mapping.....	300
Figure 9A.3: Comparison of electrocatalytic activity of $\text{NP}_{\text{matrix}}$ structure with $\text{Ag}_{\text{core}}\text{Au}_{\text{shell}}$ and bare GC for the oxidation of methanol, ethylene glycol, and glycerol and reduction of oxygen.....	301
Figure 9B.1: Variation of cell viability as a function of available Ag concentration from the synthesized $\text{Ag}_{\text{core}}\text{Au}_{\text{shell}}$ nanostructure.....	306

List of Tables:

Table 3.1 Physical and electrostatic parameters of synthesized different flourishing stages of AuNFs.....	66
Table 3.2: Different structural parameters along with their total effective surface area calculated for our synthesized differently flourishing stages of AuNFs.....	68
Table 3.3: Experimental observations and system parameters deduced from DPV and EIS measurement towards the oxidation of AA on different flourishing AuNF coated GC electrode	72
Table 3.4: Density (nm^{-2}) of Different Crystal Defects (dislocation, steps, kinks, islands, and differently packed crystal boundaries) for Various Shaped AuNFs Synthesized at Tunable Concentration (M) of CTAB.....	74
Table 3.5: Calculated reaction free energy for the oxidation of AA on different crystal facets of gold	84
Table 4.1: Compositional Analysis and current responses of different HNPr and HNPr-modified GC electrode based on EDX, XPS, ICP-OES, DPV, SWV measurements.....	117
Table 4.2: Different kinetic parameters for cavity shuffled HNPrs obtained from the EIS measurements. Here R_{CT} indicates the charge transfer resistance, W as the Warburg Impedance, CPE as constant phase element, i_0 as the exchange current, and k_0 as the heterogeneous rate constant.....	124

Table 4.3: Different crystal parameters along with induced strain along (111) basal plane and (220) vicinal plane	133
Table 5.1: Variation of zeta potential (ξ) and stacking length (L) as we vary the molar ratio (M) between NaBH_4 and AgNO_3	149
Table 5.2: Energies obtained at HF/3-21g* level of theory.....	154
Table 5.3: Optimized parameters of Ag_3AsO_3 and Ag_3AsO_4	155
Table 5.4: Variation of pH due to gradual the addition of NaAsO_2 and NaOH to 1mL AgNPr solution.....	159
Table 6.1: Comparison among different parameters related to HER activity of the electrocatalytic performance of different AuNPs in various electrolyte solutions.....	187
Table 6.2: Structural parameters of different A^nGNPs	200
Table 6.3: The position of DBCs for different AuNP grain boundary surfaces.....	203
Table 7.1: Estimation of developed strain within different Hy-Au@AgNRsand the targeted Hy-Au@AgNR ₈₄₀ -Ass from the measured FWHM (β) and θ values (in radian) in XRD spectra...	239
Table7.2: Theoretical strain calculation on different length rod.....	240
Table7.3: The I-V responses in DPV for different system Au@AgNR ₈₄₀ -Ass/GC, Au@AgNR ₈₄₀ /GC, Au@AgNR ₄₅₀ /GC,	257
Table 7.4: Peak Potential of different metabolites and trace metal ions in I-V responses of DPV	269
Table 8.1: Parameters obtained from the Nyquist plot for DENV-2 as shown in Figure 3A by fitting into the Randles cell.....	289
Table 8.2: parameters obtained from the Nyquist plot for DENV-2 infected real blood samples drawn from 3 different patients.....	291

CHAPTER-1

Introduction

Nanoparticles are a collection of atoms or molecules (by considering a gold atom of radius 0.15 nm, at least 300, 3×10^5 , and 3×10^8 Au atoms are there in a spherical gold nanoparticle of radius 1, 10, and 100 nm respectively¹) within a regime of 1-100 nm if they are dispersed in gaseous, liquid or solid media. Nanoparticles having intermediate sizes between bulk and single atom shows different behavior in optical, electronic, magnetic, and catalytic properties from their counterparts.¹ This discrepancy in physiochemical properties is due to the (i) high surface to volume ratio (S/V),² (ii) ordered arrangement of electric and magnetic dipoles or multipoles,³ (iii) appearance of low coordinated crystal defects like grain boundary, twin boundary, stacking fault, dislocation,⁴ etc, to rearrange the bandgap, (iv) quantum size effect,⁵ and (iv) electrodynamic interactions.⁶ Out of several nanomaterials, noble metal nanoparticles have got catchy attention in the recent times and find enormous applications in various fields which include photo- and electro-catalysis, pathological sensing, and theranostics^{4,7} This increased attention towards plasmonic noble metal nanoparticles and noble metal nano-alloy like gold-silver (Au-Ag) is due to their greater resistance to corrosion and oxidation in air, enhanced catalytic activity, larger stability, and our ability to make them tailored porous and layered structure.⁸ The plasmonic nanomaterials and nanoalloys can be prepared by various methodologies like electrochemical methods,⁹ hydrothermal methods,¹⁰ sonochemical methods,¹¹ etc. Out of the various methodologies, hydrothermal synthetic methodology has got the key attention in past decades due to its ease friendly approach e.g. (i) during a surfactant controlled

synthesis by CTAB, CTAC, and SDS, the size and shape of the nanomaterials can be altered simply by varying the surfactant concentration¹² whereas in a seed mediated synthesis the size and shape¹³ can be changed by varying the amount of seed, (ii) The standard reduction potential of Au^{3+} and Ag^+ are +1.5 V and +0.8 V, so they can easily be reduced to Au^0 or Ag^0 by using common mild reducing agents like AA, hydroquinone, hydrogen peroxide,⁷ etc, (iii) The plasmonic gold (Au), silver (Ag) or gold-silver (Au-Ag) nanomaterials prepared by chemical synthesis can easily be separated by fractional centrifugation,¹⁴ (iv) Due to the close lattice parameters of Au and Ag, the Au-Ag nano-alloy of different morphology can be prepared by co-precipitation method without applying any external mechanical force like pressure, temperature, magnetic field, etc⁷ and (v) The nanomaterials or nanoalloys with programmable defect enrichment can be prepared by wet chemical synthesis by monitoring their growth mechanism through direct imaging techniques like *in-situ* TEM.¹⁵ Without elaborating on all aspects, the present discussion will be highlighting mainly the origin of outstanding catalytic properties of homogeneous (Au or Ag) or heterogeneous (Au-Ag) nanoparticles. Based on their enhanced catalytic property, I will discuss their multidirectional applications as (a) biosensor for metabolites, virus, bacteria, etc, (b) electrocatalyst for fuel cell application in oxidation of methanol, ethanol, reduction of CO_2 , O_2 , etc, and (c) as an antiviral or antibacterial agent to prevent the infectious diseases caused by virus and bacteria in mammalian kingdom. In search of their outstanding catalytic activity, we have studied their crystal growth and resultant crystal patterns by high-resolution microscopy (TEM, SEM, and AFM) and atomic-scale spectroscopy (XRD, XPS, and ICP-OES) to correlate different crystal irregularities in nanocrystals with their catalytic activity for several redox reactions and are discussed in details in the following sections. Based on the dimensionality, crystal defects can be categorized into four different

groups and these are: (i) Zero-dimensional point defects (e.g. vacancy, doping, interstitial, substitutional, etc), (ii) One dimensional line defects (e.g. edge dislocation, screw dislocation, etc), (iii) two-dimensional planar defects (e.g. grain boundary, tilt boundary, twin boundary, microcracks, etc), and (iv) three-dimensional volume defects (e.g. void, pore, crack, inclusion, precipitation, etc). Throughout this thesis, these different crystals defects and their contributions will be elaborated.

1.1 Zero-dimensional point defects: Point defects are a type of defects where an atom is missing or extra plane (crystal) constituting atoms or impurity atoms are added to the normal crystal array. There are three major types of point defects: Vacancies, Interstitials, and Impurities¹⁶. They may be built-in with the original crystal growth or activated by heat. They may also be the result of radiation, electric current, etc.

1.1.a Vacancies: A Vacancy is the absence of an atom from a site normally occupied in the lattice.

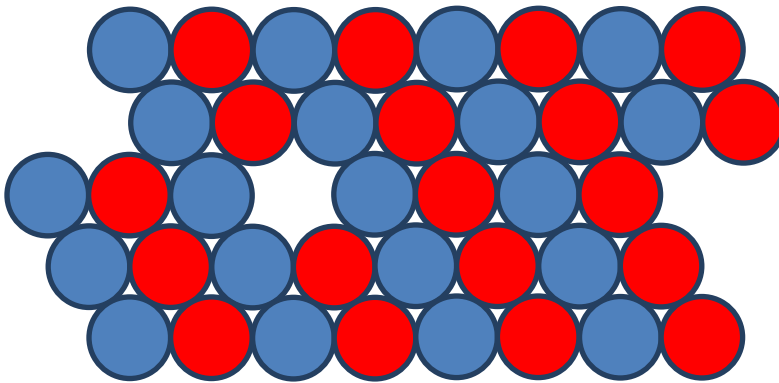


Figure 1.1a: Point defect originating from vacancies. Here the red and blue color circles show the normal lattice points and the empty space shows the position of the vacancy point defect.

1.1.b Interstitials: An Interstitial defect occurs when an atom takes the interstitial position (non-lattice site) of the lattice structure. There needs to be enough room to keep an atom in a non-

lattice site to create this type of defect. Hence, this type of defect occurs in open covalent structures or metallic structures with large atoms.

An interstitial may be a foreign atom or an off-lattice regular atom as shown below:

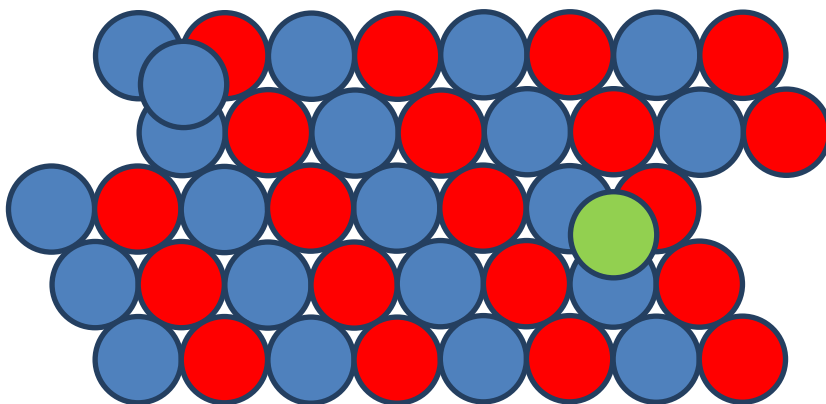


Figure 1.1b(i): Interstitial point defect created by foreign atom(s). Here the red and blue color (contain one off-lattice regular atom as an interstitial point) circles show the normal lattice points whereas the green circle indicates the foreign atom.

An interstitial defect may form by moving an atom from a lattice point to an off-lattice site and thereby creating a vacancy at the lattice point.

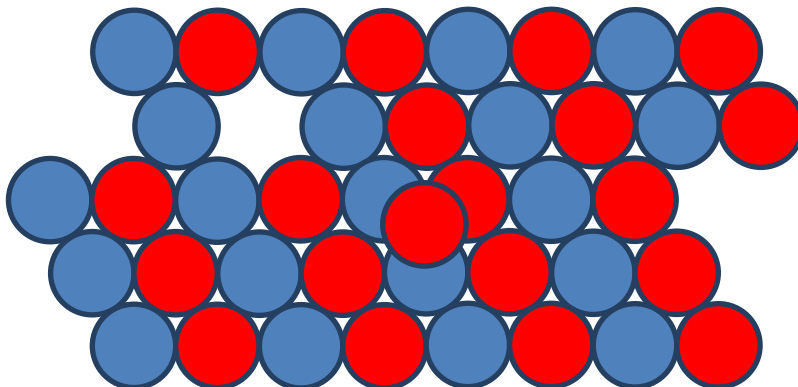


Figure 1.1b(ii): Interstitial point defect created by moving an atom from a lattice point to an off-lattice site. Here the red and blue color circles show the normal lattice points.

1.1.c Impurities: An Impurity is the substitution of a regular lattice atom with an atom that does not normally occupy that site. The atom may come from within the crystal (e.g. a Chlorine atom on a Sodium site in a NaCl crystal) or from the addition of impurities. This is also known as the **Substitutional Defect**. A foreign atom, or a regular atom out of place, is also defined as an **impurity**.

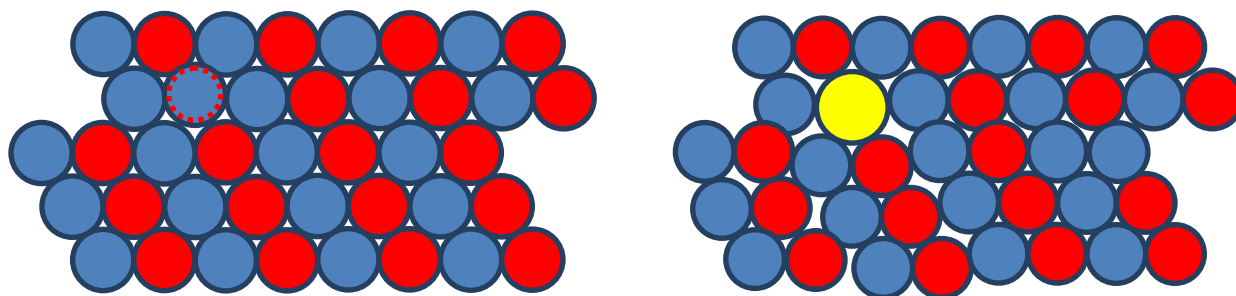


Figure 1.1c: (Left) Impurity atom comes from within the crystal (in a NaCl crystal, the impurity Cl atom is shown by the red dotted circle), and (Right) Impurity comes from an additional atom (shown by the yellow circle with a different radius) out of the crystal.

1.1d Schottky defect and Frenkel defect: Another two prominent defects are Schottky defect and Frenkel defect. The **Schottky defect** is a type of Point Defect that occurs in ionic crystals. The Schottky defect occurs when oppositely charged atoms (cation and anion) leave their corresponding lattice sites and create a pair of Vacancy Defects. **Frenkel defect** also occurs in ionic solids. It occurs when an ion jumps from a normal lattice point to an interstitial site, leaving behind a vacancy (vacancy + interstitial)¹⁷. Usually, this type of defect is observed in ionic solids, where the size of the anion is substantially larger than the size of the cation. Some of the examples of **Frenkel defect** are AgBr, ZnS, AgCl, and AgI.

The concentration of point defects in a crystal is typically between 0.1% and 1% of the atomic sites, however, extremely pure materials can now be grown. The concentrations and movement of point defects in a solid are very important in controlling their color and deformation.

1.2 One dimensional line defects: One-dimensional defects are also called as dislocations. They are abrupt changes in the regular ordering of atoms along a line, known as dislocation line, in a solid. They occur in high densities and strongly influence the mechanical properties of materials. There are two basic types of dislocation and they are:

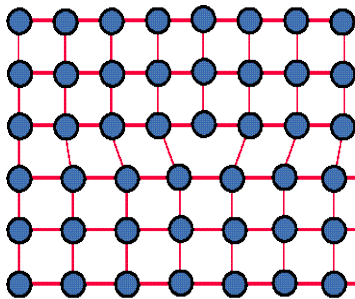


Figure 1.2a: Schematic representation of the edge dislocation

1.2.a Edge dislocation: An *Edge dislocation* in a Metal may be regarded as the insertion (or removal) of an extra half-plane of atoms in the crystal structure¹⁸.

The regions surrounding the dislocation line are made of essentially perfect crystal as shown in the above figure. The only severe disruption to the crystal structure occurs along the dislocation line (perpendicular to the crystal plane, here the page). Note that, perpendicular to the crystal plane, the line may step up or down. These steps are known as *jogs*.¹⁹

1.2.b Screw dislocation: Screw dislocation in the lattice structure of a crystal is a type of line dislocations in which the atoms are arranged in a helical pattern that is normal to the direction of the stress²⁰. Any type of dislocations either screw or edge is assigned by the burger vector (\vec{b}). In short, the burger vector is a measure of the lattice distortion due to dislocation line.

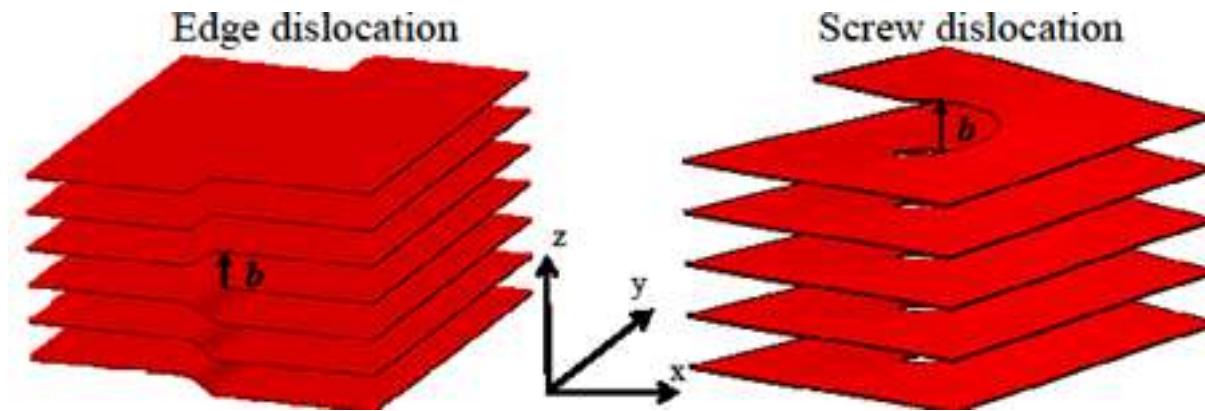


Figure 1.2b: Schematic representation of edge dislocation and screw dislocation

To quantify the burger vector one has to draw a circuit by connecting the lattice sites in a crystal e.g. A circuit is made around a dislocation line by clockwise direction such that each site of the lattice is connected to be fully coordinated, as shown in figure 1.2c, then it is transferred to a perfect lattice (figure 1.2c) where dislocation line is absent. The circuit will fail to close with its starting point in dislocation free lattice and the connecting line between endpoint & starting point of the circuit is called burger vector. The type of dislocations is assigned by burger vector i.e. in edge dislocation the burger vector lies in perpendicular to the dislocation line whereas in screw dislocation the burger vector lies parallel to the dislocation line. In fcc (Au, Ag, Au-Ag, Pt, Pd, etc) or bcc (Fe, Mo, W etc) crystal the burger vector is denoted by $b = a/2\langle hkl \rangle$ whereas in a cubic crystal it is denoted by $b = a\langle hkl \rangle$.

Besides, mentioning the direction of the dislocation line, the burger vector also signifies the direction of deformation or the slip plane in a lattice. In any type of crystal, there exist mainly two types of deformation named as, elastic deformation (in which a lattice get can back to its previous stage after feeling stress) and plastic deformation (where a lattice gets permanently distorted that is either tensed or compressed and can't get back to its previous stage). The plastic deformation in a lattice occurs through the slip plane, where the dislocation line can move very

easily e.g. in an fcc type of crystal 12 slip system exists whereas in bcc crystal 48 slip system can occur. Thereby, the elasticity and plasticity of a dislocation enriched crystal lattice are determined by the burger vectors which can be monitored through HRTEM, field ion microscopy, atom probe techniques, and chemical etching.

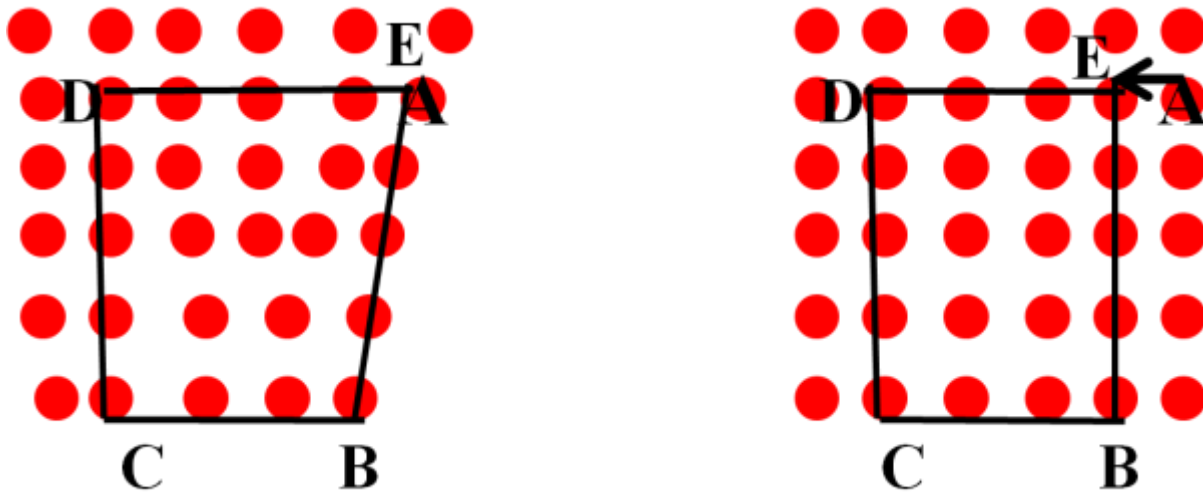


Figure: 1.2c: (Left) A dislocation enriched lattice where the starting point A and the endpoint E meets at a point to completes the circuit, (Right) A perfect lattice where A and E do not meet and the vector AE is defined as the burger vector.

1.3 Two-dimensional planer defects: A Planar Defect is a discontinuity of the perfect crystal structure across a plane. Planer defect can be of several different types which include (i) grain boundary, (ii) twin boundary, and (iii) stacking fault.

1.3a Grain Boundary:

A grain boundary (GB) is the interface between the two differently oriented crystals in a polycrystalline material.^{21,22} Depending upon the angle between the interfaces of two different crystals they are designated either low ($<5^\circ$) or high angle GB ($>5^\circ$). The smaller angle GB is

accounted for lower in energy than higher angle GB. Besides, angle-dependent difference GB can also be divided by the axis of rotation as a tilt boundary (where rotation axis is parallel to the boundary plane) and twist boundary (where the rotation axis is perpendicular to the boundary plane). Irrespective of the type, a GB on the lattice surface contains multiple reduced coordinated active sites and it retards the motion of a dislocation line, which accumulates near the GB. Thereby, a GB enriched crystal is considered to be highly strained than GB free crystal.

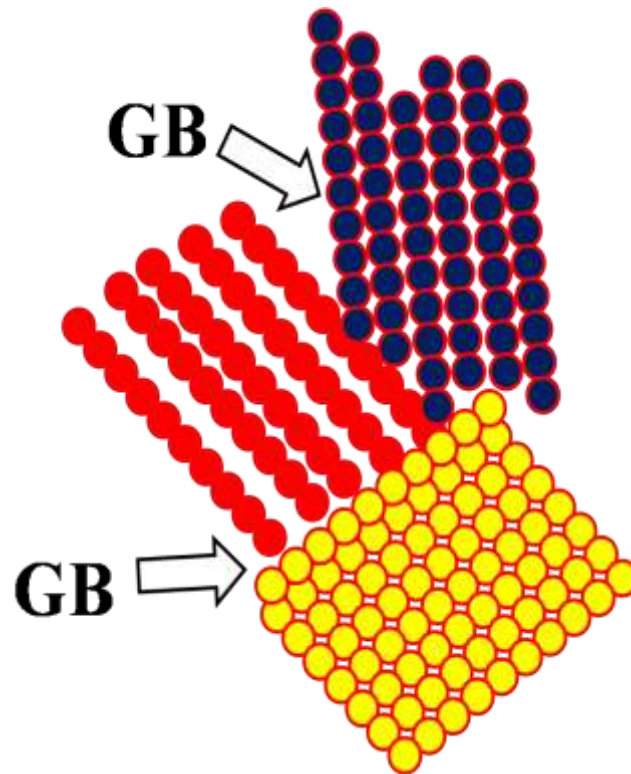


Figure1.3a: Schematic Presentation of GB over a crystal lattice.

1.3b Twin Boundary:

When two separate crystals share their plane in a symmetrical way i.e. one half of the plane becomes the mirror image of the other, they called a twin boundary (TB).^{23,24} There are mainly two types of twinning crystal named as transformation twins and deformation twins. Transformation twins sometimes designated as annealing twins and appear in fcc crystal during the cooling process. In short, when a metal is heated and leave for cooling suddenly, it can't get

back to its previous stage and twins are formed over the crystal to get a stable structure. Deformation twin is another type of twin that appears due to shear stress on it and is most prevalent in bcc and hcp type of crystal. A schematic presentation of the twin boundary that appears in an fcc lattice is shown below in **Figure 1.3b**. In an fcc lattice, the atomic rearrangement can be presented as ABCABCABC....twin boundary appears when one plane is shared symmetrically which can be represented as ABCABCBA. The plane C is the TB. Due to the non-planar nature, the atoms situated on the TB are unsaturated in coordination number and considered to be highly active than nontwinned atomic sites.

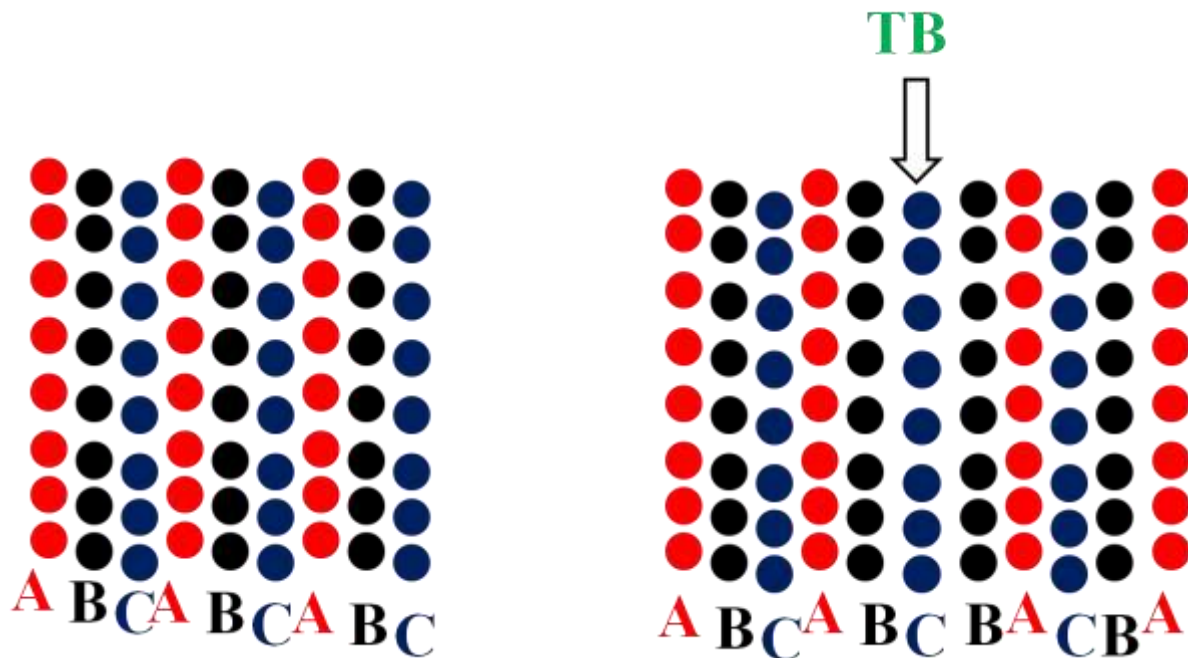


Figure 1.3b: Schematic presentation of a twin boundary over an fcc lattice.

1.3c Stacking Fault:

Stacking fault (SF) is a 2D effect that appears in fcc or hcp mainly.²⁵ SF can be of two types designated as intrinsic SF when a regular row of atoms is absent in a lattice or extrinsic SF when an extra row of atoms appear in a lattice e.g. in an fcc lattice, as we stated previously, the

stacking sequence is presented by ABCABCABC.... if one of the stacking is absent as shown in figure 1.3c, it will be an intrinsic stacking or if an extra stacking is present it will be termed as extrinsic stacking.

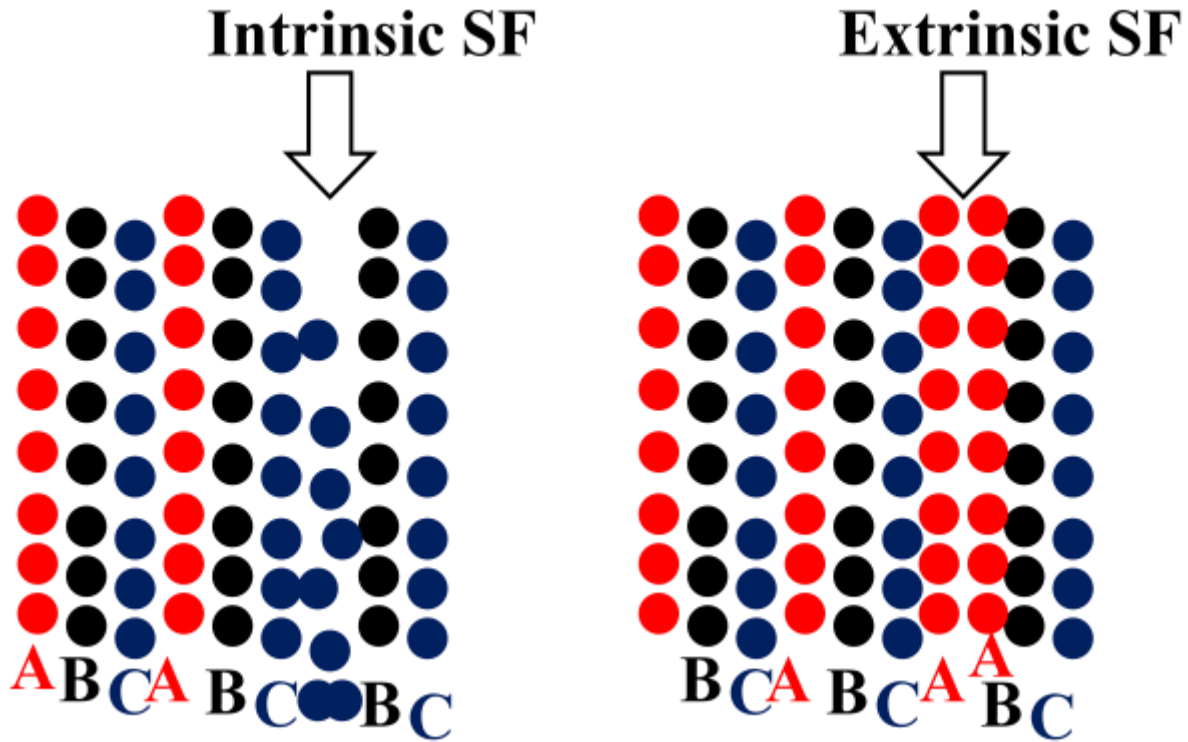


Figure 1.3c: Schematic Presentation of intrinsic and extrinsic SF in fcc lattice.

1.4 3D Defects:

3D defects are sometimes termed as volume defects²⁶ and cause overall changing in volume by creating voids (a small region within the crystal where a set of atoms are missing e.g. during the reaction of Ag nanoparticle with Au^{3+} , galvanic replacement occur and the Kirkendall voids¹⁵ are formed), inclusion²⁷ (a 3D defect when other phases trapped within the base material e.g. carbides in steels), cracks²⁸ (that appears due to the bond breaking or bond-forming within the crystal) etc.

A schematic presentation of the void defect is shown below in **Figure 1.4**.

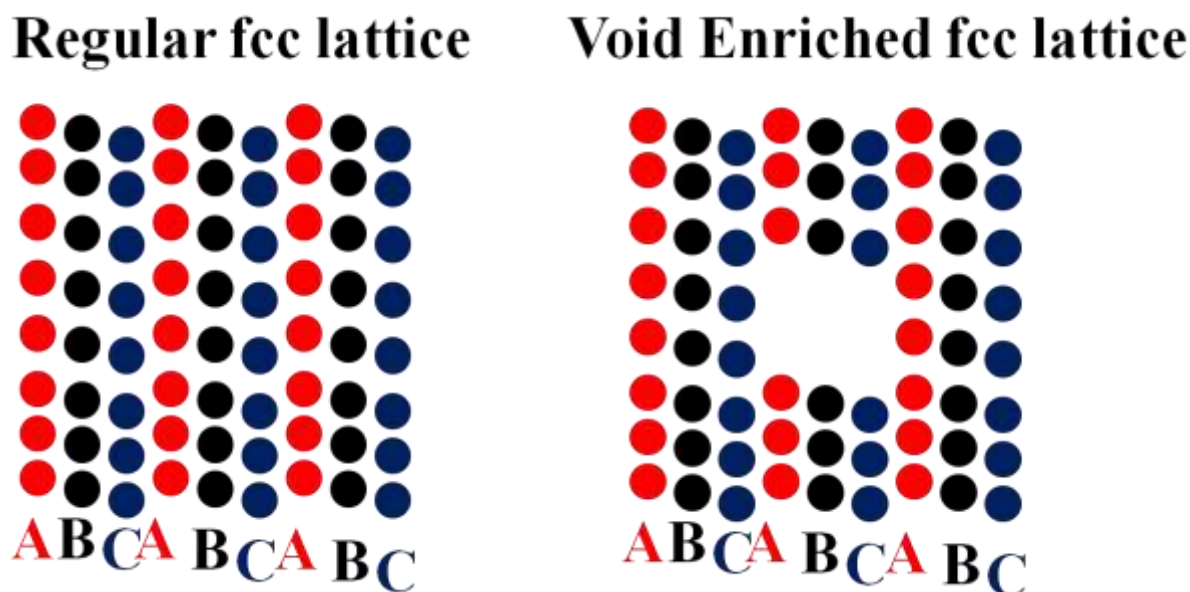


Figure1.4: An fcc lattice with the regular arrangement and void enriched arrangement.

1.5 Application of noble metal nanocatalyst in Pathological Industry

1.5a. Sensing of Metabolites

In the modern age of the clinical industry, we need rapid and accurate biochemical techniques to detect human metabolites like vitamin C, uric acid, vitamin K, Vitamin B, amino acids, glucose, etc. Most of the present methods to detect metabolites are based on the enzymatic assay. Application of enzyme as a catalytic biosensor is long known in the literature²⁹ but due to their possible denaturation and digestion in abnormal conditions (higher temperature, variable pH, non-aqueous environment, etc), high costs in preparation and purification, the requirement of expertise to handle enzyme-based assays, and lack of large scale production, the fabrication of enzymatic catalytic platform for daily use in industrial-scale is not become feasible till now.^{30,31} In comparison to catalytic enzyme biosensors³², electrochemical methods like DPV, EIS, Chronoamperometry can produce accurate results within the physiological concentration level

with an appropriate non-enzymatic electrode material. In this regard, noble metal nanoalloy is accounted for its well known catalytic property to oxidize or reduce metabolites by producing their characteristic I-V curve in physiological concentration limit. Hence for nonenzymatic, cost-effective, and time-saving techniques, electrochemical methods find promising applications in the pathological industry by using Au-Ag nanoalloy as an active electrode material. An additional benefit of electrochemical methods is its ability to detect more than one metabolite at a time. In a study by Su et al. the simultaneous detection of AA, DA, UA, and NO_2^- was done through DPV by modifying the working electrode with graphene nanoribbons.³³ In one of our studies, we have used our synthesized bud to blossom shaped gold nanoflowers with multifaceted orientations like {111}, {110}, etc as the electrode material for the oxidation of AA. We could not only easily achieve the detection limit of AA up to the nanomolar (nM) range but also were able to detect DA, UA, and glucose simultaneously.⁴ In our next study, we planned to explore the role of zone-specific crystallization and porosity directed crystal strain to control the catalytic oxidation of Uric Acid (UA) on Au-Ag nanoalloy material. In our last study in the direction of human metabolites sensing, we target to develop a universal nanoscale catalytic platform with enhanced catalytic activity governed by the inherent crystal defects and grain boundaries³⁴ within the nanomaterials, catalytic hotspots at the cross junctions,³⁵ durability due to efficient surface passivation,³⁶ excellent stability over a pH and solvent range,^{37,38} and low cost of fabrication. The catalytic activity of the designed material has been tested for a series of water-soluble metabolites, like AA, UA, DA, Pantothenic acid (PA), urea, uric acid (UA), etc in 0.1 (M) NaOH and water-insoluble metabolites, like vitamin E, vitamin K3, serotonin, etc. in 0.1 (M) LiClO_4 + acetonitrile medium. The utility of using the above electrolytes is that they are either acidic or basic in chemical nature. Whenever human serum is added to those electrolytes,

the plasma proteins are precipitated out but the other blood ingredients like salts (NaCl, KCl, CaCl₂, etc) and metabolites (vitamins, amino acids, etc) will stay in the solution without any modification. Besides the protein precipitation, the other benefit of using a wide range of P_H is to record maximum current during the electrochemical study at an appropriate pH.

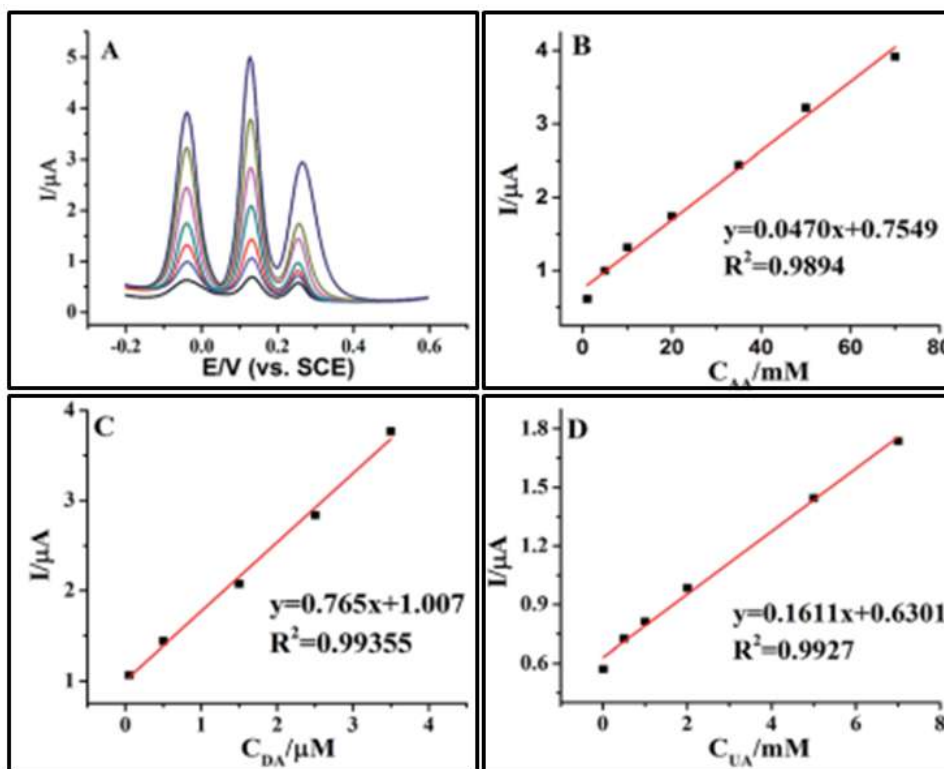


Figure 1.5a(i): (A) DPV response for AuNP@MoS₂ modified GCE for AA (1mM to 70mM), DA (0.01μM to 7μM), UA (.01mM to 12mM). (B-D) Corresponding linear calibration plots for AA, DA, UA with Peak current vs concentration in DPV response.³⁹

In a study by Farida et al.⁴⁰, it was found that the peak potential is shifted towards a more negative side with increasing pH for electrochemical oxidation of AA along with enhancement of peak current which signifies faster oxidation in a basic medium for AA than in acidic medium. Thereby Au-Ag nanocatalyst having the capacity to work in a wide range of pH and different solvents can be considered as an appropriate biosensor for human metabolites. Out of the several

electrochemical methods stated earlier like CV, DPV, EIS, Chronoamperometry, etc, the DPV method is used the most for simultaneous detection of more than one metabolite at a time because of producing sharp and characteristic peak potential and peak current for individual metabolites.

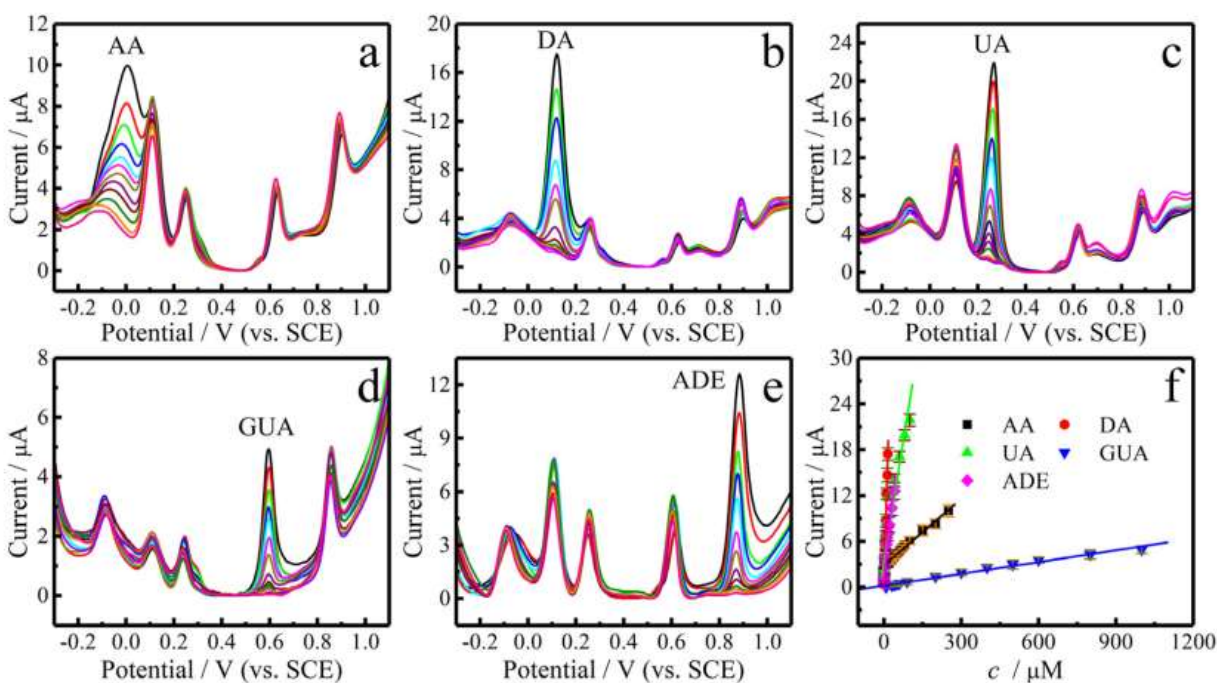


Figure 1.5a(ii): DPV responses of individual analytes in physiological concentration limit in presence of other analytes. (a) AA (5-250 μM), (b) DA (0.3-15 μM), (c) UA (0.5-100 μM), (d) GUA (7-1000 μM), (e) ADE (0.1-40 μM). In figure (f) linear calibration plot of each analyte has been shown.⁴¹

In a study by Sun et al.³⁹ has performed simultaneous detection of AA, UA, and DA by using AuNP@MoS₂ as the electrode material in DPV response with a significant peak potential separation between AA and DA as 151 mV, AA and UA as 288 mV, and UA and DA as 137 mV. They were able to perform the simultaneous detection of the above metabolites in physiological concentration limit and have got a linear calibration plot which was subsequently used for real sample analysis. In another study, Gao et al. have detected AA, DA, UA, guanine

(GUA), and adenine (ADE) simultaneously by electrochemical deposition of Au nanoparticle on horizontally graphene-modified tantalum wire.⁴¹ Thus Au and Ag nanoparticle or Au-Ag alloy nanoparticle modified electrodes can potentially be used as biosensors for human metabolite detection with high accuracy and cost-effectively.

1.5b. Sensing of Trace Metal Ions:

Besides molecular metabolites sensing, the detection of trace metal ion metabolites via electrochemical approaches can also be performed. Xu et al. has synthesized Au nanoparticle by a laser ablation method and deposited onto a glassy carbon (GC) electrode to make a AuNP/GC composite. The AuNP/GC is then used to detect Cd^{2+} , Pb^{2+} , Cu^{2+} , and Hg^{2+} simultaneously by using differential pulse anodic stripping voltammetric (DPASV) technique.⁴²

With the open-end ongoing pollution from industrial wastages, heavy metal contamination is growing up in daily foods (including vegetables, grains, fish, and meat) and drinking water at an alarming rate. Excess of metal ion concentration, compared to a normal physiological condition, in the human body may cause danger e.g. excess Cu^{2+} concentration in blood may damage the liver, high level of Pb^{2+} may cause neurological damage. etc. Thereby a rapid detection of these heavy metal ions is necessary from a pathological point of view. The ongoing noted methods of accurate metal ion detections include AAS, AFS, ICP-OES, ICP-MS, etc. But all the methods are time-consuming and complex due to their lengthy instrumentation analysis procedure and also expensive to find difficulty in common use.

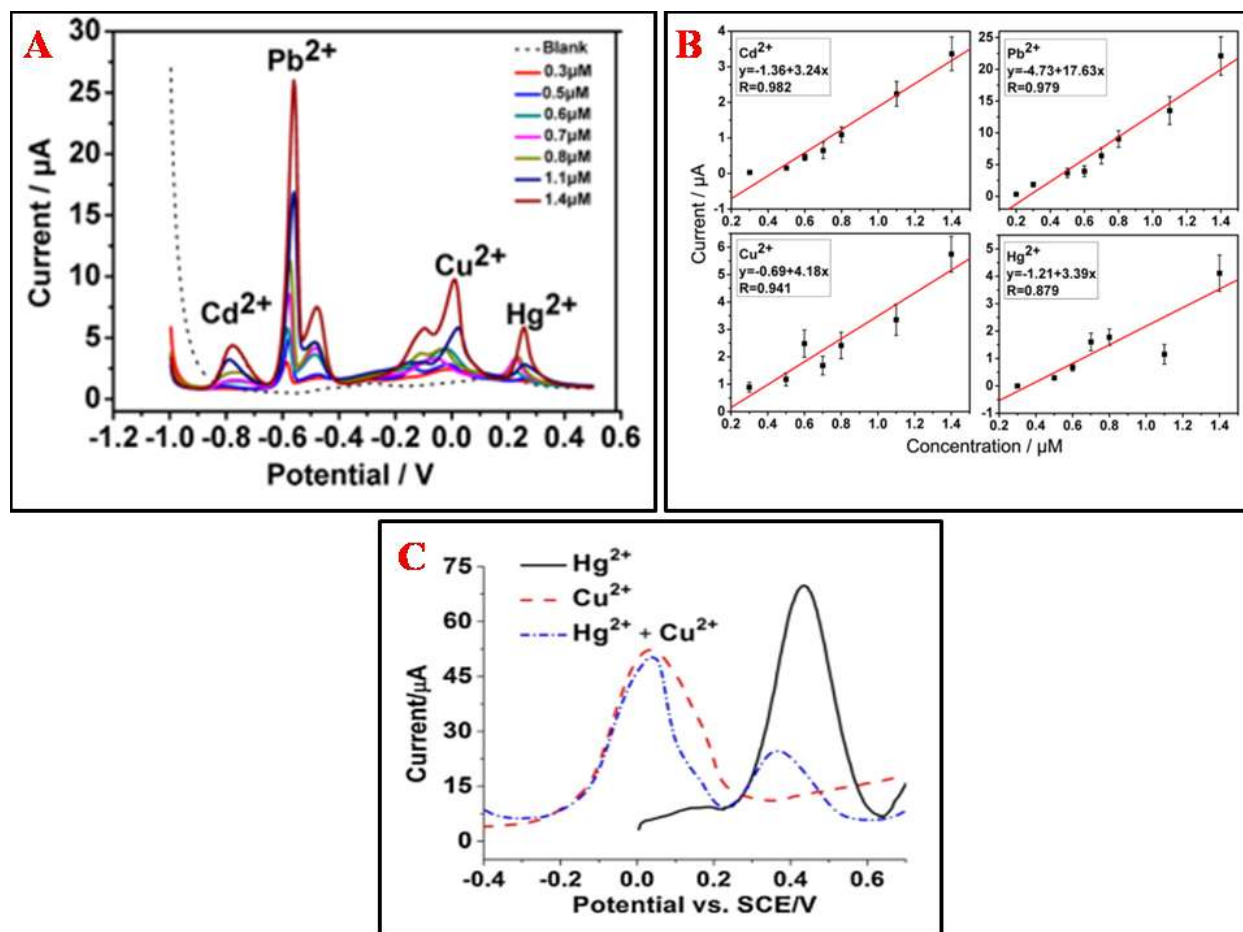


Figure 1.5b(i): (A) DPASV response for AuNP/GC electrode for simultaneous detection of Cd^{2+} , Pb^{2+} , Cu^{2+} , Hg^{2+} at a time over a concentration range of 0.1-1.4 μ M, (B) Linear calibration plot for Cd^{2+} , Pb^{2+} , Cu^{2+} , Hg^{2+} from figure 1.5bi (A)⁴², (C) A comparison of anodic stripping voltammetry of 0.5 μ M Hg^{2+} and 0.5 μ M Cu^{2+} and a mixture of both.⁴³

In contrast, electrochemical techniques are less expensive and easy-to-handle but have advanced adequately to a level by which we can use them for rapid quantitative measurements too. In a recent report, Ting et al. have shown that graphene quantum dot (GQD) functionalized Au nanoparticle was used for low-level detection of Hg^{2+} (0.02 nM) and Cu^{2+} (0.05 nM).⁴³ They were also able to perform simultaneous detection of Hg^{2+} and Cu^{2+} by anodic stripping voltammetry as shown in **Figure 1.5(i)C**.

Therefore, noble metal nanocatalyst and nanocomposites are equally capable in both sensing and quantification of trace metal ion metabolites by producing characteristic peak potential and peak current in DPV response respectively. In our study, we have synthesized a highly porous Au-Ag network (Described in Chapter-7 in detail) and used it as an electrode material for reducing heavy metal ion metabolites like $\text{Hg}^{2+} \rightarrow \text{Hg}^0$, $\text{Cu}^{2+} \rightarrow \text{Cu}^0$, etc and were able to record sharp peaks for individual metal ions. We were also able to perform simultaneous electrochemical detection of multiple heavy metal ion metabolites by using our synthesized porous Au-Ag network as electrode material.

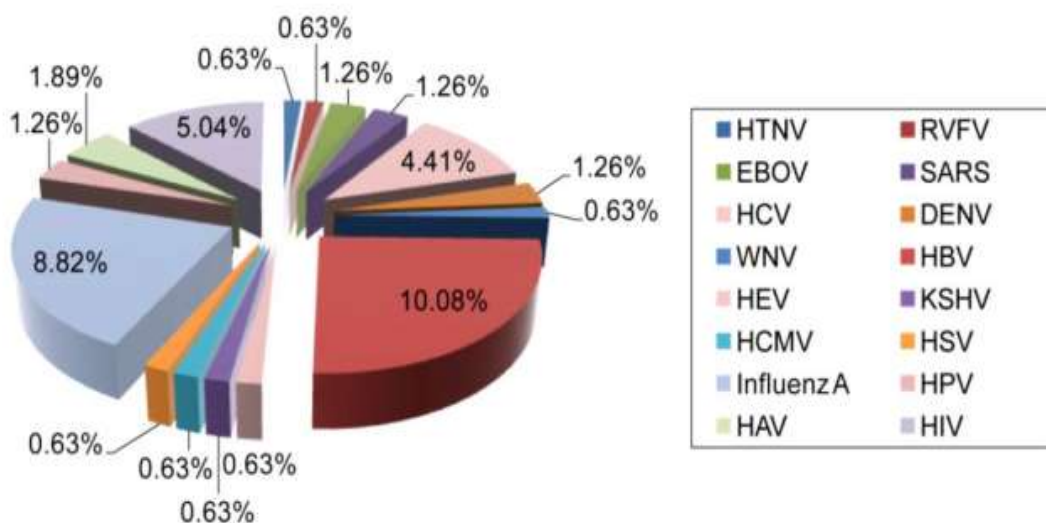


Figure 1.5b(ii): Statistical distribution of AuNP used for the detection of different viruses in which HBV is the most reported one for using AuNP as a sensing probe.⁴⁴

1.5c. Sensing of Virus:

AuNPs have widely been used before for the ultrasensitive detection of viruses. In a study by Draz et al.⁴⁴ have shown that AuNP-hybrid system composed of AuNP and a receptor (like DNA/RNA aptamer or antibody) has been widely used for the detection of different groups

of viruses like Bunyaviridae, Rift Valley Fever Virus, Coronaviridae, Filoviridae, Flaviviridae, etc.

Out of the several methodologies to detect viruses like zika, dengue, chikungunya, influenza, etc in the infected human serum, the most trusted one is the RT-qPCR for the specification of the serotype of a virus along with its quantification. But due to their cost-ineffectiveness, time-consuming nature, and complicated performance procedure, we do need to develop an ease-handling and low-cost approach to carry out sensing for viruses, bacteria, etc. Electrochemical techniques are much more accepted in this regard. In most of the reported electrochemical approaches, the EIS technique has been used for the detection of viral RNA both quantitatively and qualitatively. In a study by Dutta Chowdhury et al.⁴⁵, as shown in **Figure 1.5c**, the Hepatitis E virus has been detected by using gold nanoparticle embedded polyaniline nanowires and graphene quantum dot via EIS technique. The polyaniline chain was conjugated with the HEV-specific antibody and it was found that the sensor was very effective for each serotype of HEV and the result gives close agreement with the recorded RT-qPCR. It was shown that with the application of an external pulse between 0-1.2 V during viral loading, the sensitivity (in terms of impedance) was increasing accordingly. The Nyquist plot was then fitted to the equivalent Randles cell to obtain the charge transfer resistance (R_{ct}). The reason behind increasing the impedance with increasing viral load is that specific binding to the electrode surface with increasing virus concentration which results in less current passed across the electrode surface.

In recent times, DNA/RNA aptamers have been used instead of antibody and the applied aptamers can easily be modified by thiol group for specific binding to the Au-Ag nanoalloy due to the strong chemical affinity of the thiol group (-S-H) toward noble metals like Au, Ag, and

Cu. In our study also we have used a thiol modified aptamer for making a bioconjugate with the synthesized porous Au-Ag nanoalloy. The bioconjugate was then used as an electrode material for specific binding and the resultant detection of DENV-2 in presence of other related serotypes of DENV by impedimetric assay.

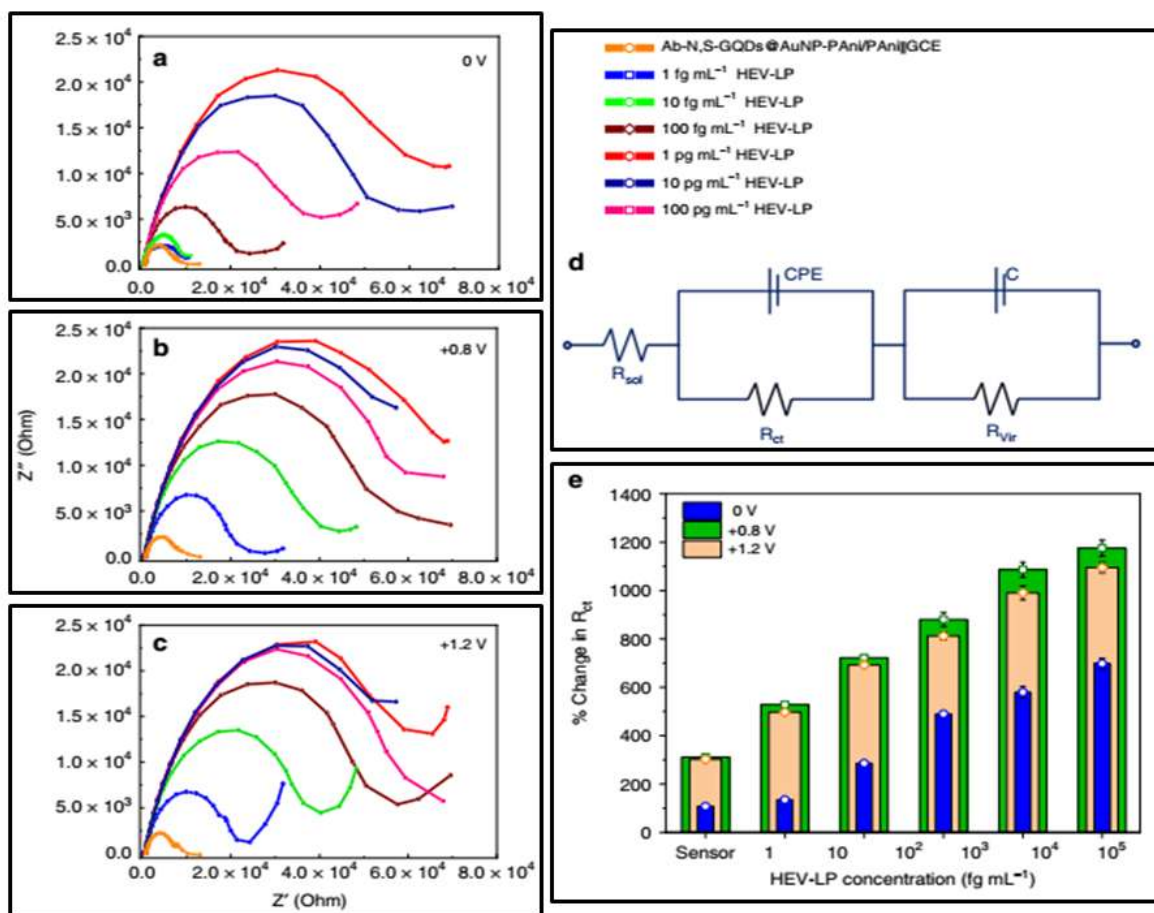


Figure 1.5c: EIS response from the sensor with different concentrations of viral load by using an external pulse of (a) 0 V, (b) + 0.8 V, and (c) + 1.2 V. In (d) an equivalent Randles cell has been shown to obtain the R_{ct} value. (e) A typical histogram is provided for sensitivity with a variable external pulse. It is clear at + 1.2V external pulse, maximum response with selectivity has been achieved.⁴⁵

The greater stability of AuNP or Au-Ag nanoalloy under an applied potential in electrochemical measurements allows us to detect the viruses accurately. Since a DNA- or RNA- aptamer cannot stabilize themselves on the electrode surface, here we have used the thiol-linked nanoalloy as a support material. Au-Ag nanoalloy being very easy to synthesize with high porosity and can bind the thiol modified aptamer by preparing a bioconjugate or nanohybrid system which is stable over the electrode surface.

1.6. Application in Fuel Cell Technology:

1.6a Alcohol Fuel Cell:

Direct-methanol fuel cells (DMFCs) are considered to be one of the most promising sustainable and cleaner energy alternatives compared to traditional fuels like petrol and diesel. Since in a direct methanol fuel cell we perform the oxidation of methanol, we pay more attention towards the anodic reaction to improve its faradic efficiency by applying suitable catalytic material on the anode surface. Out of the several electrocatalysts reported so far, Pt or Pt-based materials are considered to be the best. The presence of CO as a dissociative product of methanol plays a big role to reduce the catalytic efficiency (poisoning of catalyst) of Pt by blocking its active sites for the hydrogen oxidation reaction (HOR). In this regard Au-Ag electrocatalyst can be considered as an alternative for the electrooxidation of MeOH. In the past, Au is not considered to be suitable for any catalytic applications due to its high overpotential and low redox kinetics. Au is the only metal that has endothermic O₂ absorption energy and hence illustrating its inert behavior in an oxygen atmosphere ⁴⁶. On the contrary, tailored Au, Ag, or Au-Ag nanoparticles defect enriched active sites, acts as efficient as the Pt/C catalyst in alcohol oxidation. Xiong et al. ²⁰ in their study have observed that Au₃Ag nano-frame with multiple edges and screw dislocation defects act as active sites for efficient MeOH oxidation in 0.5M KOH

solution with greater faradic efficiency than the commercial Pt/C. Catalytic ability of Au₃Ag nano-frame by comparing with standard Pt/C and other nanoalloy has been detailed in **Figure 1.6a**. The onset potential for the Au₃Ag nano-frame appears at 0.3 V wherein for Pt/C the onset is 0.4 V. The peak current density is also lower for Pt/C than the corresponding Au₃Ag nano-frames. The CO stripping experiment indicates less CO poisoning for the Au₃Ag nano-frame than Pt/C. Besides MeOH, electrooxidation of other alcohols like EtOH (C₂H₅OH), ethylene glycol (C₂H₆O₂), and glycerol (C₃H₈O₃) has also been studied by using our synthesized Au-Ag nanoalloy and a detailed discussion has been included as a separate chapter in this thesis.

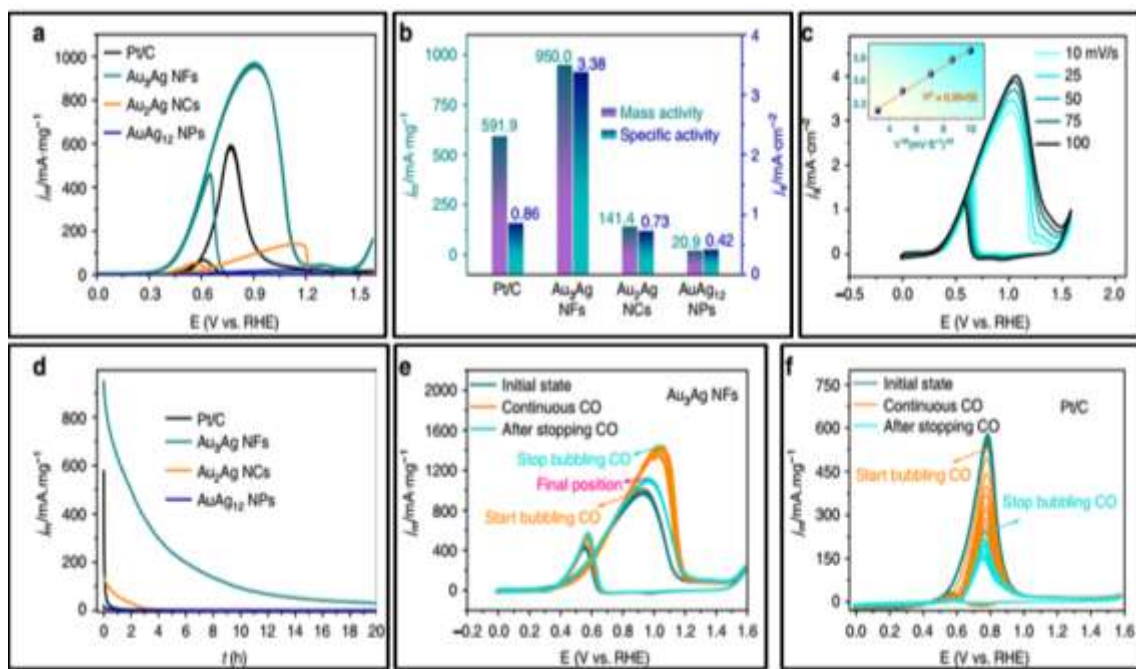


Figure 1.6a: (a) Comparison of CV for the electrooxidation of 2 M methanol in 0.5 M KOH at a scan rate of 20 mV/S with other related catalysts, (b) histogram for (a) with specific activity and mass activity, (c) CV of Au₃Ag nano-frame at different scan rate, (d) comparative chronoamperometric I-t curve for 20 h for different electrocatalysts, (e) CV curve for Au₃Ag nano-frame under CO supply with turn on and turn off mechanism, (f) CV curve for Pt/C under CO supply with turn on and turn off mechanism. ²⁰

1.6b ORR activity:

In an alcohol fuel cell, the overall reaction is represented as: $\text{ROH} + \text{O}_2 \rightarrow \text{CO}_2 + \text{H}_2\text{O}$, where ROH is the alcohol under study. This means that the efficiency of alcohol oxidation depends heavily on the effective simultaneous reduction of O_2 . In any kind of fuel cell, the reduction of O_2 is a key step to get an overall high faradic efficiency. In this regard, it is essential to develop a suitable catalyst that can support the faster reaction kinetics for both alcohol oxidation and O_2 reduction. Pt is always regarded as the best catalyst in this respect. But due to its high cost and scarcity in abundance, a substitute to Pt catalyst is absolutely necessary in the present scenario to find their profitable industrial applications. Literature is rich to find the potential application of noble metal electrocatalysts in oxygen reduction reaction (ORR). In a study by Shim et al.,⁴⁷ high faradic efficiencies were observed for AuNPs during ORR by electrochemical performances. In another study by Wang et al.⁴⁸ has shown that smaller gold nanoclusters supported on carbon (C) demonstrate high reactivity in comparison to that of commercial Pt/C. The smallest nanocluster Au_{25} shows the highest catalytic property with an onset potential of 0.92V to the reference hydrogen electrode (RHE) and a higher number of electron transfers within the potential range of + 0.5 to + 0.8 V as shown in **Figure 1.6b**.⁴⁸ Also, the number of electron transfer within the potential range + 0.5 to + 0.8 V was higher for Au_{25} and porous C composite (3.6-3.92) compared to other Au nanocluster (Au_{38} and Au_{144}) and porous carbon composites.

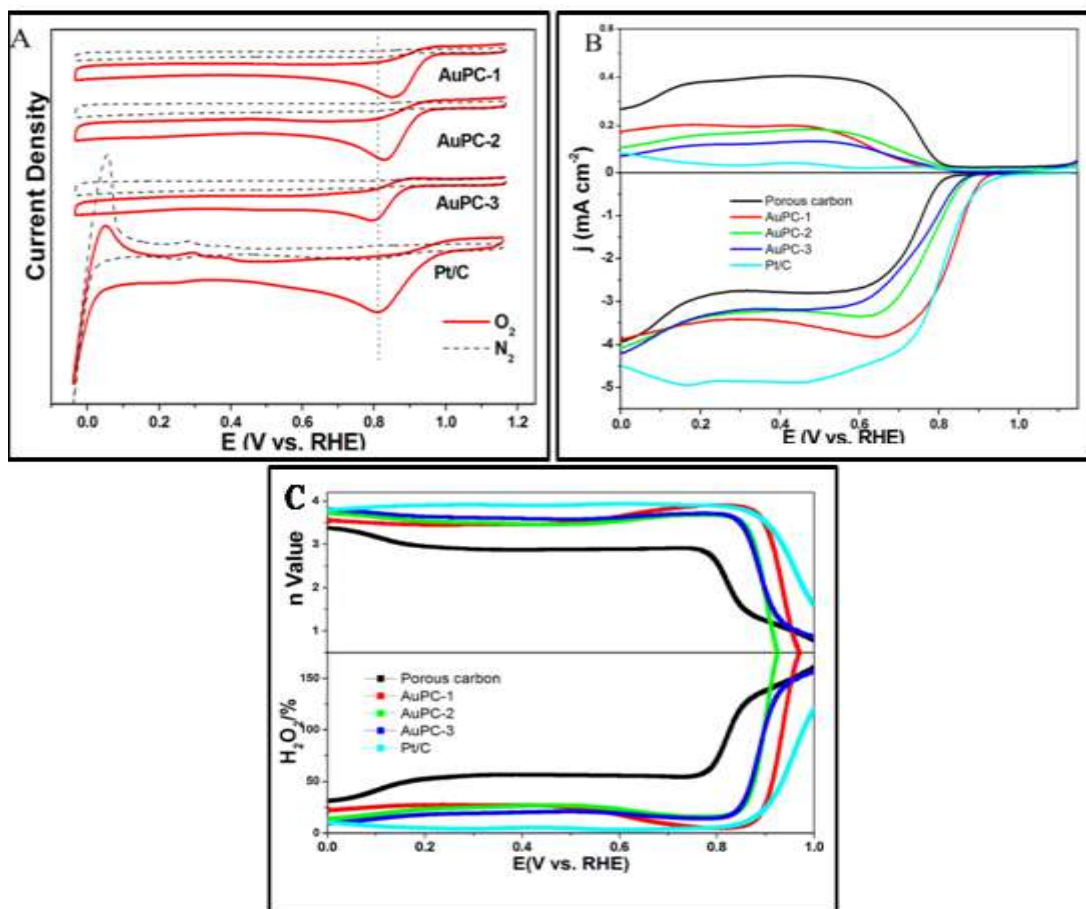


Figure 1.6b. (A) CV curves of AuPC-1, AuPC-2, AuPC-3 nanocomposites, and commercial Pt/C catalysts recorded in nitrogen-saturated and oxygen-saturated 0.1 M KOH. Here AuPC means Au nanocluster and porous C composite. (B) The ORR polarization curves of porous carbon, AuPC-1, AuPC-2, AuPC-3 nanocomposites, and commercial Pt/C catalysts in O₂-saturated 0.1 M KOH with a rotation speed of 2500 rpm. (C) Variation of H₂O₂ yield and electron transfer number at various potentials.⁴⁸

1.6c Reduction of CO₂:

During the combustion of fuel whether it is petrol, diesel, or alcohol, the resultant emitter is CO₂ which is one of the major greenhouse gases. To reduce this greenhouse burden from our

environment, conversion of CO_2 to fuel like methanol for close-end CO_2 recycling is very important and opens up a hot research topic in the present days. Recently it has been observed that Au-Cu bimetallic catalyst is very effective for CO_2 conversion to formate⁴⁹ though individually Au and Cu monometallic nanoparticles are not so attractive for the mentioned job. A schematic representation of the Au-Cu bimetallic system and its catalytic pathways is shown in **Figure 1.6c**. It was observed that Cu mesh when used as electrocatalyst converts CO_2 to CH_4 , CO , and C_2H_4 with a faradic efficiency $< 70\%$ at -0.96 V. Similarly, Au nanocatalyst tends to convert CO_2 to CO . Thus a high selectivity is always in demand for catalytic conversion of CO_2 to methanol. In a study by Tao et al. has shown that when Au nanoparticles are embedded in CuO , the resultant Au-Cu bimetallic system is highly efficient for CO_2 to formate conversion than CuO .

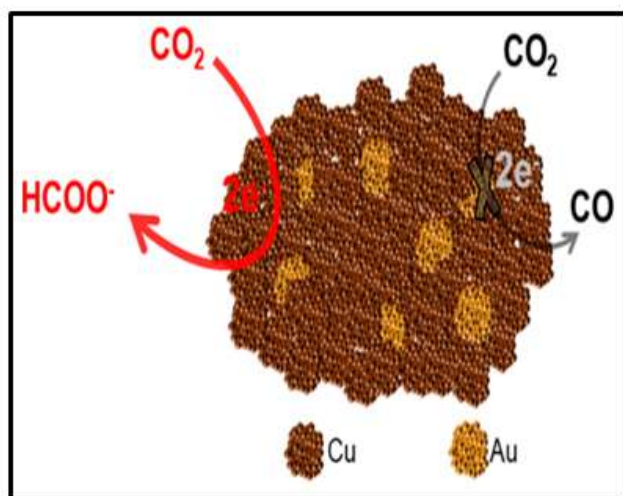


Figure 1.6c: A schematic presentation of the Au-Cu system where selectivity achieved for the conversion of CO_2 to formate and the reaction of CO_2 to CO has been hidden.⁴⁹

In the Au-Cu bimetallic system, Au acts as a promoter. Quasi in-situ XPS was performed to observe the oxidation state of Au and Cu and it was observed that Cu^+ exists in the Au-Cu system along with the existence of Au^0 and Cu^0 . Even after long term catalytic performances, the oxidation states of metals retained. The existence of Cu^+ is accounted for the selectivity for CO_2 to formate conversion which can be easily reduced to methanol.

1.6d HER and OER:

Photochemical or electrochemical water splitting to produce H_2 is a high-demanding research field to overcome the shortage of fuel. Hydrogen is regarded as a green fuel with high energy density and pollution-free (cost-effectiveness and environmentally friendly) which can be alternative and competitive to that of coal or oil. Thereby low-cost production and safe storage of H_2 are precious steps in the H_2 economy. Pt/C is regarded as the most efficient catalyst in this aspect. However, as discussed before, we need an alternative one for reducing the production price. In this regard tailored shaped Au nanoparticle with multiple active sites can be considered as an alternative. In a study by Tran et al.⁵⁰ have shown that Au nanoparticle with an average diameter of 13 nm acts as a good electrocatalyst for hydrogen evolution reaction (HER) with an overpotential around 200 mV and turnover frequency around 0.3 s^{-1} . In our study, we have designed sodium dodecyl sulfate (SDS) capped anisotropic gold nanoparticles (A^nGNPs) which exhibit outstanding catalytic activity (in terms of both overpotential and turnover frequency) towards hydrogen HER in different pH medium compared to that of normal spherical shaped gold nanoparticles (e.g. TSC-capped 25 nm S^pGNPs) in similar physical conditions (**Ref. ACS App. Ener. Mater., Communicated, chapter 6 in this thesis**). Besides, the designed nanomaterials require a mere 190 mV (vs RHE) of overpotential to achieve 10 mA cm^{-2} current density in 0.5 M H_2SO_4 medium.

Besides HER, plasmonic nanomaterials can also be used in oxygen evolution reaction (OER). In a study by Zhao et al. has shown that gold nanocluster Au₂₅, when embedded into CoSe₂, the resultant Au₂₅/CoSe₂ composite exhibits high OER activity in alkaline medium with an overpotential of 0.43 V at 10 mA/cm² current density as shown in **Figure 1.6d**.⁵¹

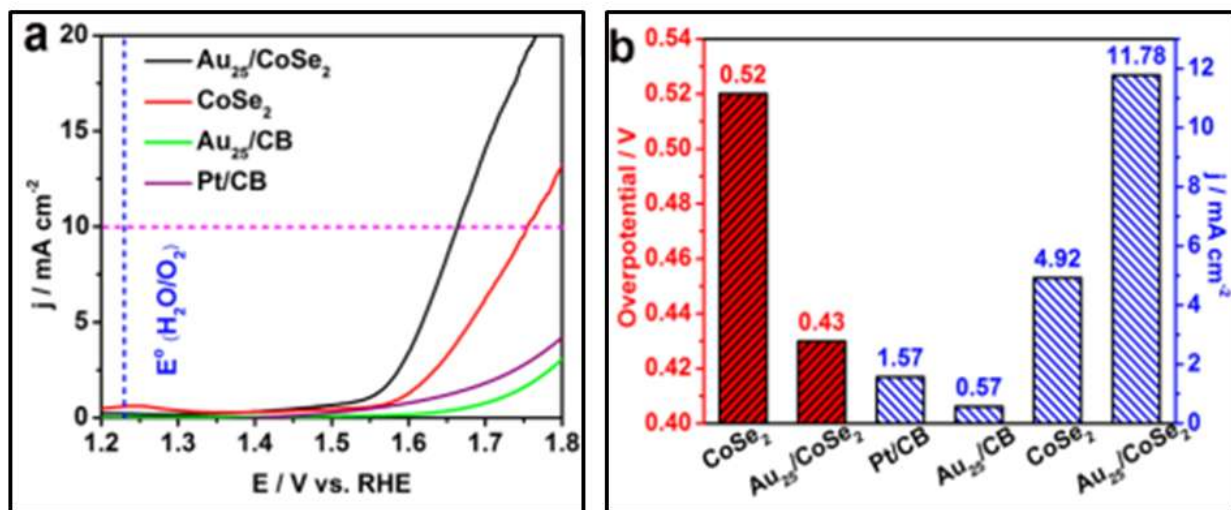


Figure 1.6d: (a) OER polarization curve for different systems in which Au₂₅/CoSe₂ shows the higher current, (b) a histogram for comparison of current density and overpotential for different systems.⁵¹

1.7. Theranostics Application of Plasmonic Noble Metal Nanoalloy:

Theranostics is a new field into which targeted therapy is carried out based on the specific diagnostic test rather than the traditional medicinal approach⁵². In modern days, DNA aptamer-based targeted therapy caught attention for reducing infections, pain, and wounds caused by viral or bacterial infections⁵³. There are enormous reports in the literature in which Au and Ag nanoparticles are used as antibacterial or antiviral agents in mammals. However, there is always a question that arises regarding their cyto- or geno-toxicity towards mammalian cells. In this regard, the synthesis of biocompatible tailored shaped plasmonic nano-alloy gets significant attention in the present days. Biocompatible Au, Ag, and Au-Ag nanoalloy can be prepared by

using several capping agents like chitosan, oligonucleotides, amino acids, etc.⁵⁴ However, the stability of those biocompatible nanomaterials is always under question. In physiological pH (in the blood) level, in presence of high-level salt concentration, nanomaterials get aggregated. To avoid these drawbacks and to improve their retention in physiological conditions for long term circulation in body fluid, surfactant capped Au, Ag, or Au-Ag nanoalloy can be used as a strategy. The use of surfactants should be at a minimal level, only to stabilize the nanoparticle and to get a monodisperse solution, without disturbing their inherent theranostics properties. The CTAB or CTAC (known to cytotoxic surfactants) capped plasmonic nanoalloys can be made biocompatible by coating with PVA. In our study, during targeted treatment against Dengue serotype-2 (DENV-2), we have used PVA capped tailored Au-Ag nanoalloy with diameter < 40nm. The toxicity was checked in HCT-116, RAW, and HEPG2 cell lines by MTT assay and it was observed that it was non-toxic in the concentration level which was used to inactivate the DENV-2.

Thus biocompatible Au, Ag or Au-Ag nanoalloy can be used as good substitutes for traditional antibacterial agents. In a study, by Jena et al.⁵⁵ have shown that Au-Ag nanoaggregates are effective for bacterial inhibitions compared to their non-aggregated monometallic or bimetallic counterparts, as shown in **Figure 1.7**. The result concludes that with multiple defects enrich surface sites, Au-Ag alloy nanoparticles are highly strained and efficient to prohibit bacterial growth at a low dose level where it is zero-toxic to mammals.

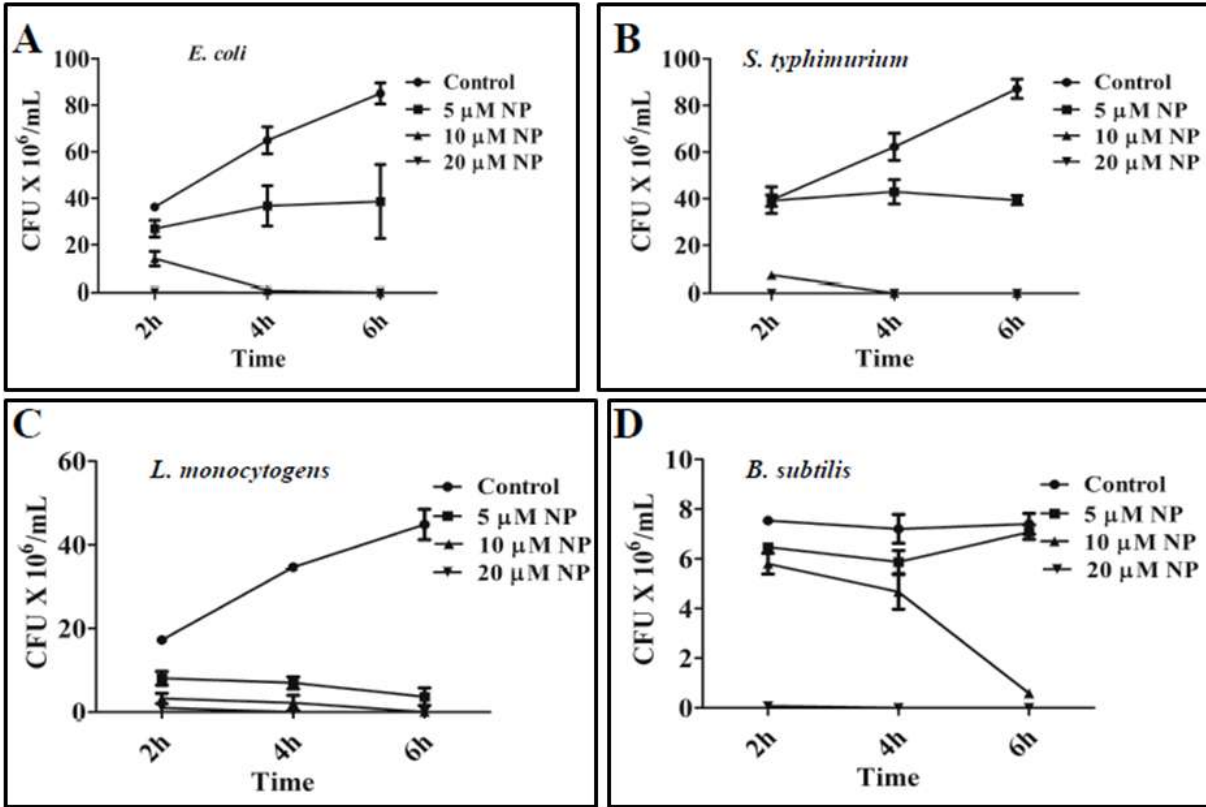


Figure 1.7: Antibacterial activity of Au-Ag NP. Viability determination of **A. *E. coli***, **B. *S. typhimurium***, **C. *L. monocytogenes***, **D. *B. subtilis*** in presence of different concentrations of Au-Ag NP for 2, 4 & 6 hours. Approximately $2-3 \times 10^7$ /mL number of bacteria were used at 0 hour time for *E. coli* and *S. typhimurium*, $1-2 \times 10^7$ /mL for *L. monocytogenes*, and 3×10^6 /mL for *B. subtilis*. The NP treated cultures were serially diluted after indicated time points and plated in LB agar to count the viable colonies. Results are shown with mean and SD. **E. Live-dead staining.** *E. coli* cells expressing MreB^{SW}-mVenus were incubated with Au-Ag NP, A22, and CCCP for 4 hours, stained with PI for 10 mins, washed and observed under the microscope to distinguish dead and live cells. Images shown for MreB are deconvolved.⁵⁵

CHAPTER-2

Methodology and Experimental Set-Up

2.1 Chemical Materials

Almost all the essential chemicals were purchased from Sigma Aldrich and used without any further purification. Milli-Q water with a resistivity of 18.2 MΩ.cm was used for all the preparation steps.

Reagent Name	Specification	Company
Ethylene glycol	EG, Anhydrous 99.8%	Sigma Aldrich
Gold(III) chloride trihydrate	HAuCl ₄ .3H ₂ O; ≥ 99.9%, trace metals basis	Sigma Aldrich
Silver Nitrate	Bioextra ≥ 99%, titration	Sigma Aldrich
Sodium borohydride	NaBH ₄ , 10-40mesh, 98%	Sigma Aldrich
L-ascorbic acid	C ₈ H ₈ O ₆ , ACS reagent, 99%	Sigma Aldrich
Hexadecyltrimethylammonium bromide, CTAB	C ₁₉ H ₄₂ BrN, assay, ≥ 99%, AT	Sigma Aldrich
Hexadecyltrimethylammonium Chloride, CTAC	C ₁₉ H ₄₂ BrN, ≥ 98%, NT	Sigma Aldrich
Sodium citrate tribasic dihydrate	C ₆ H ₅ Na ₃ O ₇ .2H ₂ O; Bioultra, for molecular biology, ≥ 99.5% (NT)	Sigma Aldrich
Spectrasol (EtOH)	Spectroscopic grade	Spectrochem
Water	Ultrapure, Milli-Q, resistivity 18.2 MΩ.cm at 25 °C	Merck Millipore
Polyvinyl alcohol, (PVA)	Powder, MW-30,000-70,000	Sigma Aldrich
Acetonitrile	Spectroscopic grade	Spectrochem
Sodium chloride	NaCl, AR, ≥ 99.9%	Sigma Aldrich

Phenol	BioUltra, for molecular biology, \geq 99.5% (GC)	Sigma Aldrich
Chloroform	EMPARTA ACS 99.4%	Merck
Phenol – chloroform – isoamyl alcohol mixture	BioUltra, for molecular biology, 25:24:1	Sigma Aldrich
Isopropanol	BioReagent, for molecular biology, \geq 99.5%	Sigma Aldrich
Sodium acetate	Anhydrous, for molecular biology, \geq 99%	Sigma Aldrich
Hydrochloric acid	HCl, ACS reagent, 37%	Sigma Aldrich
Trizma® base	T1503 Primary Standard and Buffer, \geq 99.9%	Sigma Aldrich
NH ₄ OH	ACS reagent 28-30% NH ₃ Basis	Sigma Aldrich
FeCl ₂	Reagent grade, 98%	Sigma Aldrich
FeCl ₃	Reagent grade, 97%	Sigma Aldrich

2.2 Biochemical Materials

The Dengue-2 specific aptamer was ordered from Ascension life science, India. The aptamer has a specific sequence ($MW=22680.0$) for DIII of DENV-2 and modified at 5' and 3' position by –SH group denoted as:

5'HS_ATACGGGAGCCAACACCATGGGGACCAACTGTCCGGAGAGAGTCCTGTCTGAG
GGAGAGCAGGTGTGACGGAT_SH3'

2.3 Biological materials

Different Dengue serotypes ((including Dengue-1, Dengue-2, Dengue-3, Dengue-4) infected serum was collected from Belegghata ID & BG Hospital with proper cautions and maintain ethical issues. The HCT-116 and Vero cell lines obtained from the National Centre of Cell Sciences (NCCS), Pune, India.

2.4 Methods

2.4.1 Ultraviolet-Visible-NearInfrared (UV-Vis-NIR) Absorption Spectroscopy

The UV-vis-NIR experiments are based on the principles of Beer-Lambert law: when a beam of monochromatic light falls on a solution and absorbed by the substances present within the solution, the rate at which the intensity of the beam decreases, is proportional to the concentration of the substance⁵⁶. Not like molecules, we need to know the exact extinction coefficient which varies with size and shape, to measure the exact concentration of nanoparticles in the solution by absorption spectroscopy. In most cases, we adopt a combination of TEM/SEM and Atomic Absorption Spectroscopy (AAS)/Inductively Coupled Plasma Mass Spectroscopy (ICPMS) to measure the concentration of a monodispersed geometric shaped nanoparticle. As a result, the absorption spectrum is always considered as an indirect technique to make an idea about the variation of concentration of a specific type of nanoparticle solution. In general, for plasmonic nanomaterials we measure their surface plasmon resonance (SPR) which is defined by the quantized oscillation of the surface charge produced by an external electromagnetic field and is characterized by a specific frequency associated with its absorbance.⁵⁷ Due to the different frequency of SPR, a similar size Au and Ag nanoparticles have different colors (red and yellow) in solution. The characteristics of Plasmon band depends on the following factors: (1) **Effect of Size:** Considering the surface free electrons in a one-dimensional potential box, red shifting of the Plasmon band is proportional to their size which means a nanoparticle with the same shape but with a bigger dimension shows a red-shifted Plasmon band and vice versa⁵⁷. (2) **Effect of shape:** Depending on the shape of the nanoparticle and hence the availability of different modes of free electron oscillations we may observe more than one Plasmon bands.⁵⁸ In general, for isotropic (uniformity in all orientations) nanoparticles we observe a single Plasmon band whereas

for anisotropic (property of being directionally dependent) nanoparticles we observe more than one Plasmon band and the number of observed bands increases with increasing the anisotropy.⁵⁹ For example, a spherical or isotropically surface-tip projected star-shaped nanoparticle shows a single Plasmon band⁶⁰ whereas a rod-shaped nanoparticle shows two Plasmon bands due to the presence of longitudinal and transverse surface electron oscillation modes. (3) ***Effect of refractive index***: The refractive index (n) near the nanoparticle surface also influences the optical properties of the Au/Ag nanomaterials.⁶¹ As the refractive index near the nanoparticle surface increases, the extinction spectra of nanoparticles shift to longer wavelengths. Thus if we move from water ($n=1.33$) to air ($n=1$) media, Plasmon band of the nanoparticle will shift towards the shorter wavelength (blue-shifting) whereas if we move to oil ($n=1.5$) surface Plasmon will shift towards the higher wavelength (red-shifting) ; (4) ***Effect of particle association***: Followed by the same principle of Molecular Orbital Theory (MOT), nanoparticle association induces the delocalization and hence sharing of conduction electron cloud among nearby nanoparticles to increase the path length of surface free electrons (in a one-dimensional potential box) which causes a lowering in Plasmon excitation energy and hence red shifting of Surface Plasmon Resonance band detectable primarily by UV-Vis-NIR absorption spectroscopy,⁶² and (5) ***Effect of mole fraction in an alloy***: Due to the modified electronic level structure, the absorption property of a plasmonic nanoalloy differs significantly from its monometallic counterpart. In a bimetallic Au-Ag nanoalloy, an increased mole fraction of Ag causes a blue-shifting whereas an increased mole fraction of Au causes a red-shifting of their Plasmon spectra.⁶³

All the UV-Vis-NIR spectral measurements are performed in JASCO V770 and JASCO V650 spectrophotometers, as shown in **Figure 2.1**. In general, before each measurement, we have

diluted the centrifuged solution to keep the overall absorbance below 1.0 following Beers law. For all absorbance measurements, we have used a quartz cuvette of 10 mm path length.



Figure 2.1: (A) JASCO V-770 UV-Vis-NIR spectrophotometer with spectral range 190-3200 nm, (B) JASCO V-650 UV-Vis spectrometer fitted with Peltier for temperature-dependent study with spectral range 190-900 nm.

2.4.2 Dynamic Light Scattering and Zeta Potential Measurement

The principle of dynamic light scattering (DLS) is based on the Brownian motion of particles in a liquid medium. Nanoparticles in a solution move randomly and collide with the fast-moving solvent molecules and thereby transfer their energy. This causes the prohibition of motion for smaller nanoparticles heavily than larger particles. If the other parameters (temperature, pressure, ionic strength, etc.) kept constant, one can determine the hydrodynamic size of the nanoparticle using Stokes-Einstein relation⁶⁴, $D = k_B T / 6\pi\eta R_H$, where D is the translational diffusion coefficient, k_B is the Boltzman constant, T is the temperature, η is the viscosity, and R_H is the hydrodynamic radius. A single-frequency laser (632.8 nm: He-Ne laser) is used as the light source in DLS measurements in our Malvern Zetasizer ZS90 instrument. The scattered light is detected at a certain angle (in our case 90°) and the signal is used to determine the diffusion coefficient using correlation function as programmed in the instrument. In our DLS

measurements, only the translational motion of the nanoparticles is considered during the execution of their Brownian motion and hence the obtained hydrodynamic diameter gets the contribution from the translational motion only. During all DLS measurements, we need to follow an important parameter called polydispersity index (PDI) which signifies the monodispersity of the nanomaterials. A value of <10% of PDI indicates a monodispersed sample. The optical set up for a DLS instrument is shown below (**Figure 2.2**) for the Malvern series where the detector is placed at different angles to identify the scattered light. An attenuator is used in the instrument for controlling the light intensity to the detector e.g. if the particles are very small then the intensity of scattered light will be less, hence the attenuator will allow more light to pass through whereas if the particles are large enough then the intensity of scattered light will be more and the attenuator will allow less light to pass through. In DLS measurements the concentration of the sample should be optimized during each measurement so that the scattering signal should not be oversaturated or too little to detect.

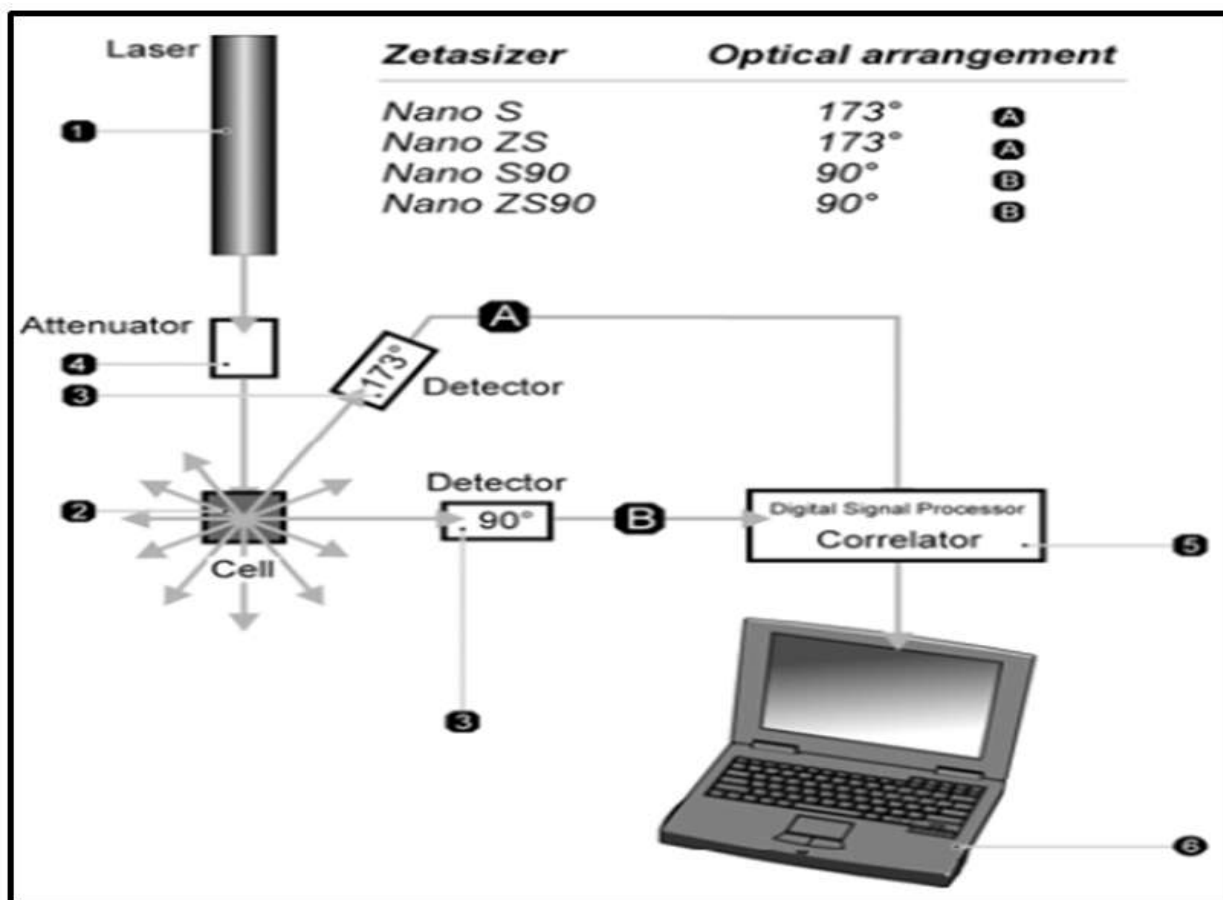


Figure 2.2: Optical configurations of the Malvern Zetasizer Nano series for dynamic light scattering measurements where ① is the laser source, ② is the sample cell, ③ is the detector, ④ is an attenuator, ⑤ is the digital processing board called a correlator, and ⑥ is the data processing computer. Here (A) represents the detector position at 173° and (B) at 90° with respect to the exciting light source. In all cases, the excitation wavelength is 632.8 nm.

The technique used in our Malvern Zetasizer ZS90 instrument (**Figure 2.3**) to measure the zeta potential is Electrophoretic Light Scattering (ELS) where a specific potential is applied between two electrodes (in our case Au electrode) and the ionic mobility is measured from the Doppler shift i.e. shift in the scattered and incident light. Depending upon the mobility (μ_e) of the

nanoparticle, scattered light shifted from its original frequency. This shift is called Phase (or Doppler) shift⁶⁵ and measured by the difference between the frequency of the scattered (ν_{sca}) and incident (ν_{inc}) light ($|\nu_{\text{sca}} - \nu_{\text{inc}}|$). The nanoparticle velocity (V) is measured from the Doppler shift in $\mu\text{m/s}$ by applying the equation $\mu\text{m} = V/E$, where E is the applied electric field. If nanoparticles are made up of any negative surfactants like SDS, trisodium citrate (TSC), etc, the particles possess an overall negative charge and hence move towards the positive electrode and show a negative zeta potential. The reverse case happens if we use any positive surfactants like CTAB, CTAC, etc where particles show positive ionic mobility and attracted towards the negative electrode to show a positive zeta potential.



Figure 2.3: Malvern Zetasizer ZS90 instrument

2.4.3 X-ray Photoelectron Spectroscopy:

X-ray photoelectron spectroscopy (XPS) is a surface-sensitive quantitative spectroscopic technique based on the principle of the photoelectric effect that can provide information about the elemental composition of the material. Besides, XPS provides information regarding the oxidation states, overall electronic structure, and density of the electronic states of the material.⁶⁶ The oxidation states of constituent elements of the material can be determined from the shifting

and splitting of the XPS peak for a particular element. In general, except hydrogen and helium, other elements can be detected from XPS survey spectra by scanning at a particular position where the element shows its ionization energy. From XPS spectra one can also predict the bonding nature of the element, e.g. if elements like N and S are detected in the survey spectra, then by analyzing their peak shifting one can identify whether there is any bonding between N and S and also the nature of the bond. All the XPS measurements are carried out in a vacuum ($\sim 10^{-6}$ Pa) or an ultra-high vacuum ($< 10^{-7}$ Pa). In a laboratory-based XPS instrument, we use either a 10-30 mm beam diameter non-monochromatic Al K α or Mg K α anode radiation or a focused 20-500 μm beam diameter monochromatic Al K α radiation. Most of our XPS measurements have been carried out on the Omicron Multiprobe spectrometer (Omicron Nanotechnology GmbH, Germany) fitted with an EA125 hemispherical analyzer as shown in **Figure 2.4**. Monochromatic Al K α X-ray source operated at 150W was used for all of our XPS measurements. During our XPS measurements, we drop cast samples on a tilted (45° angle) Si wafers to prepare a monolayer of the sample on the wafer surface and dried it overnight in vacuum to remove any excess water present in samples.

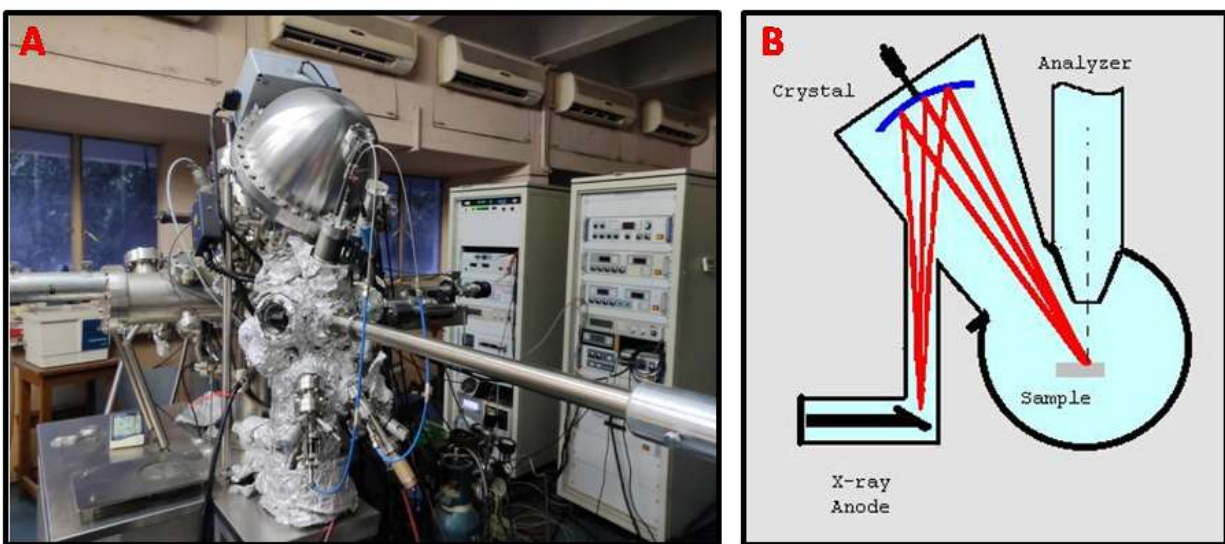


Figure 2.4: (A) Experimental set up for XPS measurement, (B) Layout of an XPS instrument.

2.4.4 X-ray Diffraction Spectroscopy:

X-rays are electromagnetic radiation of shorter wavelength produced by the electronic transition of inner orbital electrons of atoms. X-ray diffraction on nanostructures follows the Braggs law, ($n\lambda = 2d\sin\theta$) where λ is the wavelength of X-ray, θ is the angle of incident of X-ray on the nano surfaces and d is the interplanar distance.⁶⁷ From the XRD measurement, we can predict the number of facets present in a nanostructure like $\{111\}$, $\{110\}$, etc, along with their directions (towards the major axis, minor axis, etc) and relative densities of appearance. XRD gives us the information of a nanostructure on a macroscopic scale and hence the result might vary from TEM measurements which provide similar information on a microscopic scale. In this thesis, we have effectively used the obtained XRD results not only to know the crystal information but also to calculate the generated strain along a crystal plane within the nanocrystal by analyzing the broadening of XRD peaks for individual facets. An ideal crystal will show an appropriate sharp peak for a particular orientation like $\{111\}$ and if any irregularities or defects in crystal arise the XRD curve will be broadened due to the internal strain generated within it. By fitting the curve and using the Williamson-Hall isotropic model we have calculated the strain generated within the nanocrystal and we observed that nanocrystals with more defect enriched sites show more broadening. The strain is defined as $\varepsilon = \beta/4\tan\theta_{hkl}$, where ε is the strain generated in the nanocrystal, β is the full-width at half maximum of the XRD curve (individual peak) at angle θ (2θ is the central peak position of the fitted XRD curve) in radian. Here, h , k , l denotes the miller indices. In general, to calculate the strain we select the most intense peak, i.e. if any XRD curve of nanocrystals shows multiple facets like $\{111\}$, $\{110\}$, $\{200\}$, etc, and $\{111\}$ is the most intense one among them, we select the $\{111\}$ plane as the reference for strain calculation.

All our XRD measurements have been performed in a Rigaku Smartlab X-ray Diffractometer as shown in **Figure 2.5**. We have used a drop cast method for sample preparation. In short, we drop cast the sample on a tilted (45° angle) glass slide to prepare a monolayer over it and dried overnight under the vacuum. The strong adhesion property of our synthesized nanomaterials with glass slide doesn't require any binder to use.

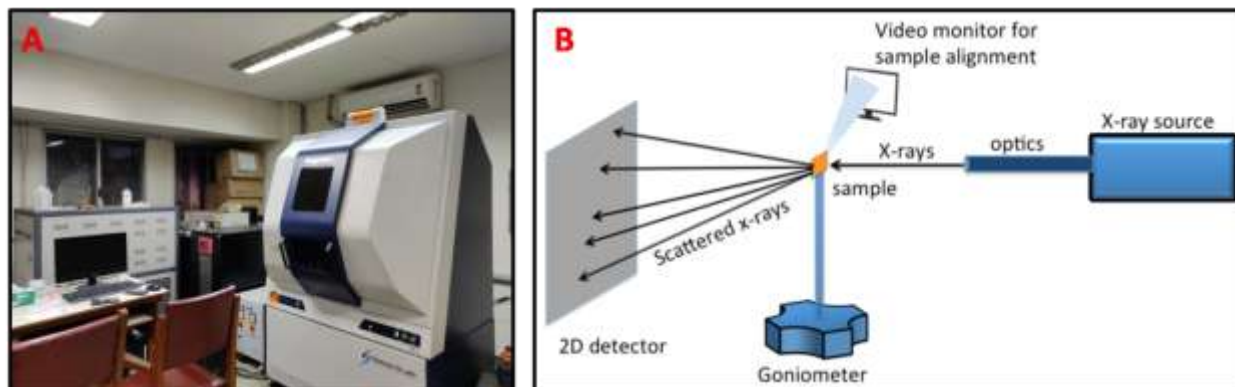


Figure 2.5: (A) Rigaku Smartlab X-ray Diffractometer, (B) Layout of an XRD instrument.

2.4.5 Inductively Coupled Plasma Optical Emission Spectrometry:

Inductively coupled Plasma Optical Emission Spectrometry (ICP-OES) is a technique where the plasma form of substances is used for the measurement of the qualitative and quantitative presence of elements. An energy source is used to atomize the test samples and high-resolution optics to analyze the optical emission spectra from different samples are used along with a detector to measure the intensity of the emitted light.⁶⁸ All our ICP-OES measurements have been carried out in a Thermo Scientific iCAP6000 spectrometer (Freemont CA, USA), as shown in **Figure 2.6**, with NIST standards of 50 ppb, 0.5 ppm, 1 ppm, 15 ppm, 25 ppm, 50 ppm,

and 100 ppm. The wavelengths selected for Au are 242.7 nm, 267.5 nm, 283.5 nm and for Ag are 224.6 nm, 328.0 nm, 338.2 nm, and for S are 182.0 nm, 182.6 nm. Before each measurement the centrifuged samples are diluted (50 μ L to 5mL) in Milli-Q[®] ultrapure water and sonicated for 10 minutes.

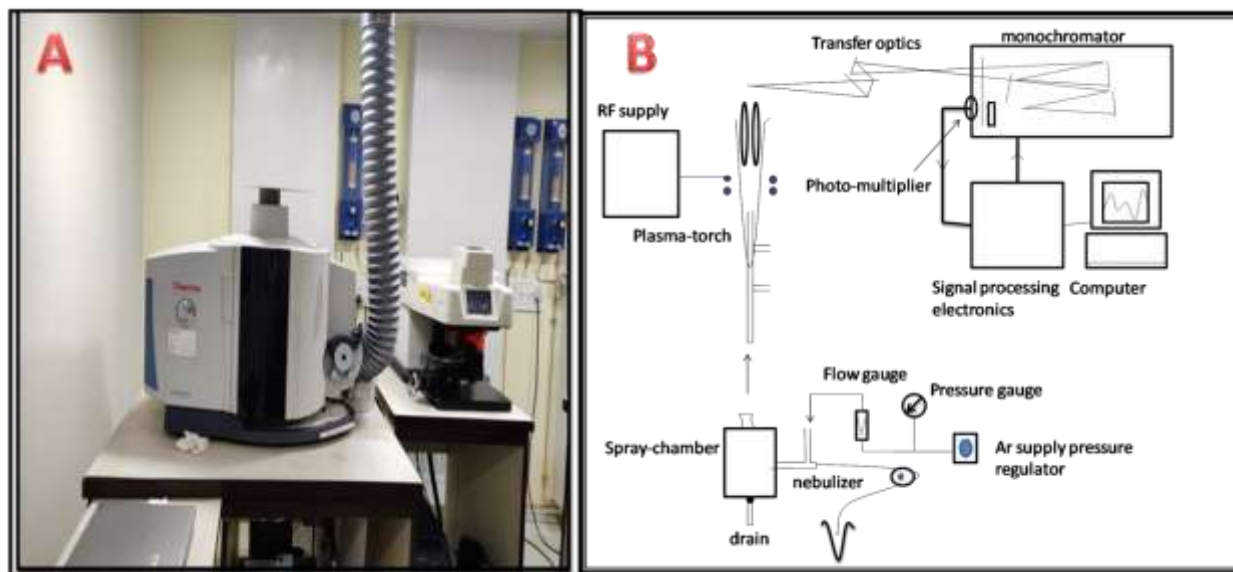


Figure 2.6: (A) Thermo Scientific iCAP6000 ICP-OES spectrometer (Freemont CA, USA), (B) Layout of an ICP-OES instrument.

2.4.6 Surface-Enhanced Raman Spectroscopy:

Surface-Enhanced Raman Spectroscopy (SERS) experiments were performed using a homemade Raman setup. We used a continuous-wavelength diode-pumped solid-state laser from Laserglow Technologies, Canada, operating at 671 (LRS0671-PFM-00300-03) or 532 nm (LRS0532-PFM-00300-03) as excitation light sources (at a fixed excitation energy of 3 mW, using neutral density filters throughout the experiment). For efficient focusing and filtering, we used In Photonicsmade 670 nm and 532 nm fiber optics Raman probe with a spectral range of 200–3900 cm^{-1} (Stokes) for sample excitation and data collection. The Raman probe consists of

two single fibers (105 μm excitation fiber and 200 μm collection fiber) with filtering and steering micro-optics (numerical aperture 0.22). The excitation fiber was connected to a THORLABS made fiber port to align the laser, whereas the collection fiber was connected to a spectrometer. A miniaturized QE65000 scientific-grade spectrometer from Ocean Optics was used as the Raman detector with a spectral response range of 220–3600 cm^{-1} . The Raman spectrometer was equipped with a TE-cooled 2048 pixel charge-coupled device and was interfaced to a computer through a USB port. In the end, the Raman spectrum was collected using the Ocean Optics data acquisition Spectra Suite spectroscopy software. Details of the SERS set up and the layout of the instrument is shown in **Figure 2.7**.

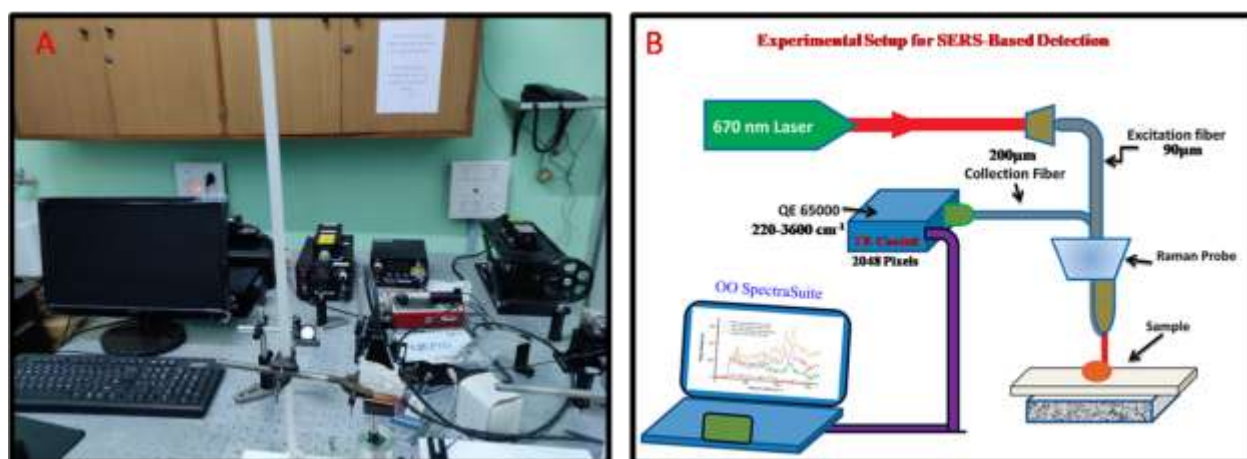


Figure 2.7: (A) Details of the SERS set up, (B) Layout of the instrument.

2.4.7 Atomic Force Microscopy:

Atomic Force Microscopy (AFM) or Scanning Force Microscopy (SFM) is a type of Scanning Probe Microscopy (SPM) with a very high resolution in the order of a fraction of nanometer which is 1000 times better than the optical diffraction limit. The principle of atomic force microscopy is based on the scanning of a specimen surface by a cantilever with a sharp tip, the probe, to construct the topography of that surface.⁶⁹ The cantilever is typically made of silicon or silicon nitride with a tip radius of curvature (κ) on the order of nanometers. When the

tip is brought into the proximity of a sample surface, forces (mechanical force, chemical force, electrostatic force, thermal force, magnetic force, van der Waals force, capillary force, etc) between the tip and the sample lead to a deflection of the cantilever according to Hooke's law. The basic difference of AFM with other microscopies like SEM and TEM is that AFM directly measures the height of a surface by scanning it with a mechanical probe. Depending on the nature and extent of bending of the cantilever and thereby changing the amount of reflected laser light from the tip to the photodiode we can image the sample surface that corresponds to a constant probe-sample interaction. This mode of scanning thus allows us to achieve more accurate resolution and information on surface topography. Besides, for SEM and TEM techniques we need to create a vacuum environment for measurements, however, AFM need not, it can be done openly or in other words, AFM is an ambient imaging technique and the sample preparation is very easy and can be performed with very low concentrations too. The major components of an AFM instrument are (1) Microscope Stage: which combined a moving AFM tip, sample holder, and a force sensor; (2) Control Electronics: which have an optical microscope and a vibration controller; (3) Computer & Detector: Used for analysis of the force signal and detecting it to construct the 3D topographic view. During the measurement in AFM, a piezoelectric transducer moves the tip over the surface and either the force transducer senses the force between the tip and the surface or the deflection of the laser light as it scans the surface depending on the surface topology. A schematic presentation of AFM measurement and the obtained force curve is shown in **Figure 2.8**. In general, for stiffness measurements, we record data during tip approaches and for adhesion experiments, we record data during tip retract. Depending on the nature of tip motion, AFM operation is mainly divided into three different modes as contact mode (or static mode), tapping mode (or intermittent contact mode, AC mode,

amplitude modulation mode), and non-contact mode (or frequency modulation mode). Most of our imaging of solid nanostructures is performed in tapping mode wherein to take any image in the liquid medium we have selected contact mode. All the AFM imaging was performed on mica plates by modifying their surfaces with 500 μM of 3-mercaptopropyltrimethoxysilane (MPTMS) solution which makes a monolayer of MPTMS (around ~ 2 nm in height from the blank mica plate). Diluted nanomaterial was then drop cast on the modified mica plate and kept undisturbed for 20 minutes for complete binding of nanomaterials sample with the mica surface through MPTMS. After complete binding, we wash the sample coated mica plate repetitively by Mili-Q[®] water to remove any excess unbounded nanostructures and finally dried it in a controlled ultrapure argon stream. All the AFM experiments were performed on a Bruker BioScope Catalyst AFM instrument using Nanoscope software as shown in **Figure 2.8C**.

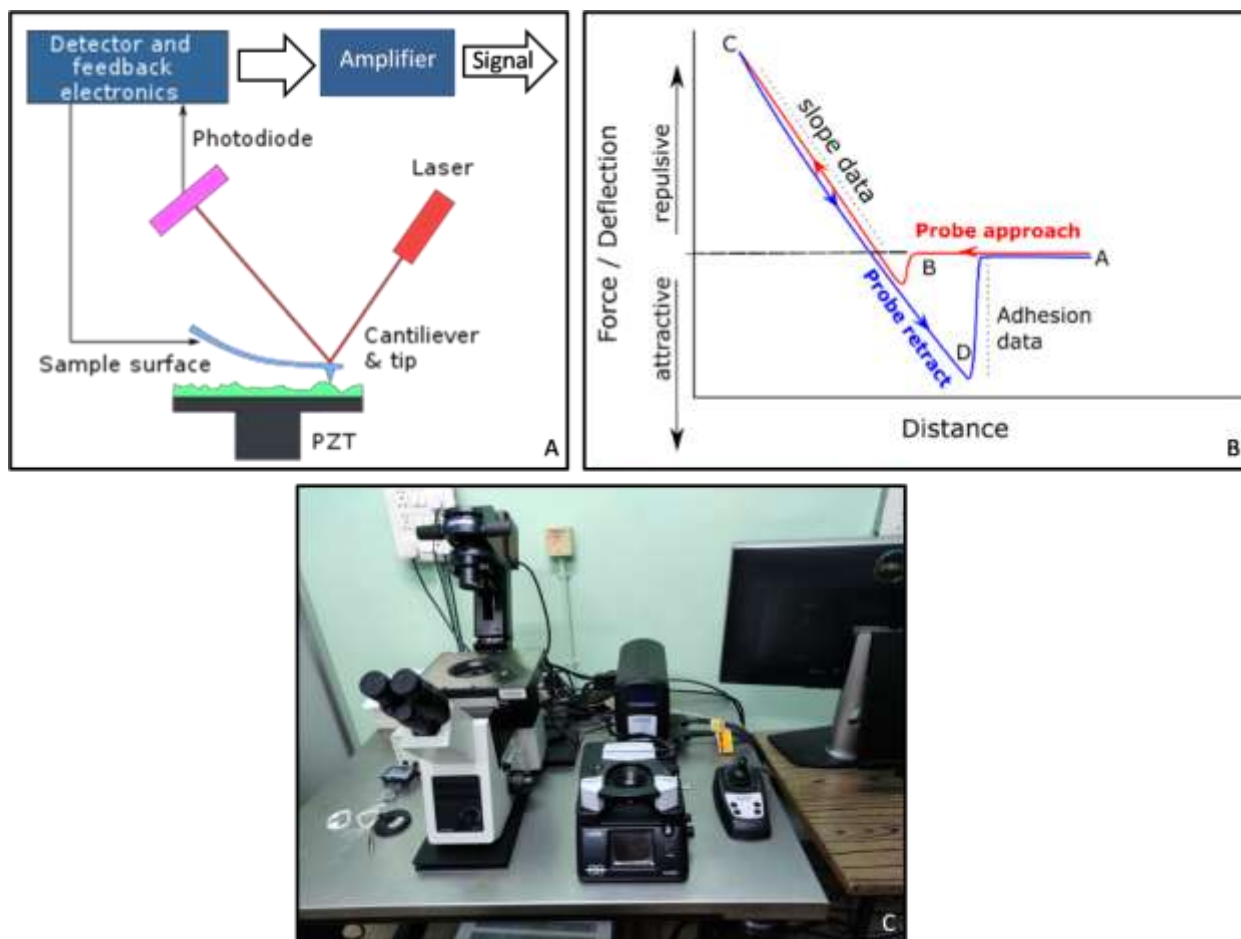


Figure 2.8: (A) schematic presentation of AFM measurement with essential components of the instrument, (B) Representative force curve as a function of distance, and (C) Bruker made BioScope Catalyst AFM instrument.

2.4.8 Scanning Electron Microscopy:

Scanning Electron Microscopy (SEM) is based on the principle of imaging of surface by scanning over it with a focused beam of electrons. Interactions of the electrons with surface atoms produce various signals that give preliminary information about the surface topography. In general, the nanostructures we have developed are observed under a high vacuum, whereas in environmental SEM, a low vacuum is used to study the biological sample.⁷⁰ Different reflected electrons by elastic scattering of the sample are emitted from different parts of the interaction

volume as a result of the interaction between the electron beam and the sample. Different signals include the Auger Electrons (AE) comes from the top layer of the sample which gives the information about the surface atomic composition, Secondary Electrons (SE) comes from the next layer of interaction volume which gives the information about the topographical information of the sample, and Backscattered Electrons (BSE) comes from a further dip of the sample layer which gives the information of atomic numbers. Followed by, photons of characteristic X-rays (EDX) and Cathodoluminescence (CL) from next dipper layers give information regarding thickness atomic composition and electronic state information respectively. Contrary to the reflected electrons, the transmitted electrons give the morphological information as we record from TEM measurements. Details about the zone-specific interaction of the focused electron beam and the thin sample are shown in **Figure 2.9A**. The resolution of SEM images obtained by secondary electrons is much higher than that of backscattered electrons. From SEM, we do not get any information about the atomic distribution of elements present in the sample. Throughout this thesis, we have used a Zeiss Supra 40 field emission electron microscope (**Figure 2.9B**) to record the SEM images of our synthesized nanomaterials. Before each measurement, we have thoroughly washed our sample to remove any excess surfactant over it because the interaction of the electrons beam with unused surfactant within the sample produces local heating that melts the sample under study which may also cause the damage to the detector. The surfactant-free samples then drop cast over a silicon wafer and dried overnight to remove any adsorbed water in the sample. During drop-casting, we have maintained a single layer of the nanostructures by injecting the sample on a tilted silicon wafer. The picture of the Zeiss Supra instrument is given below.

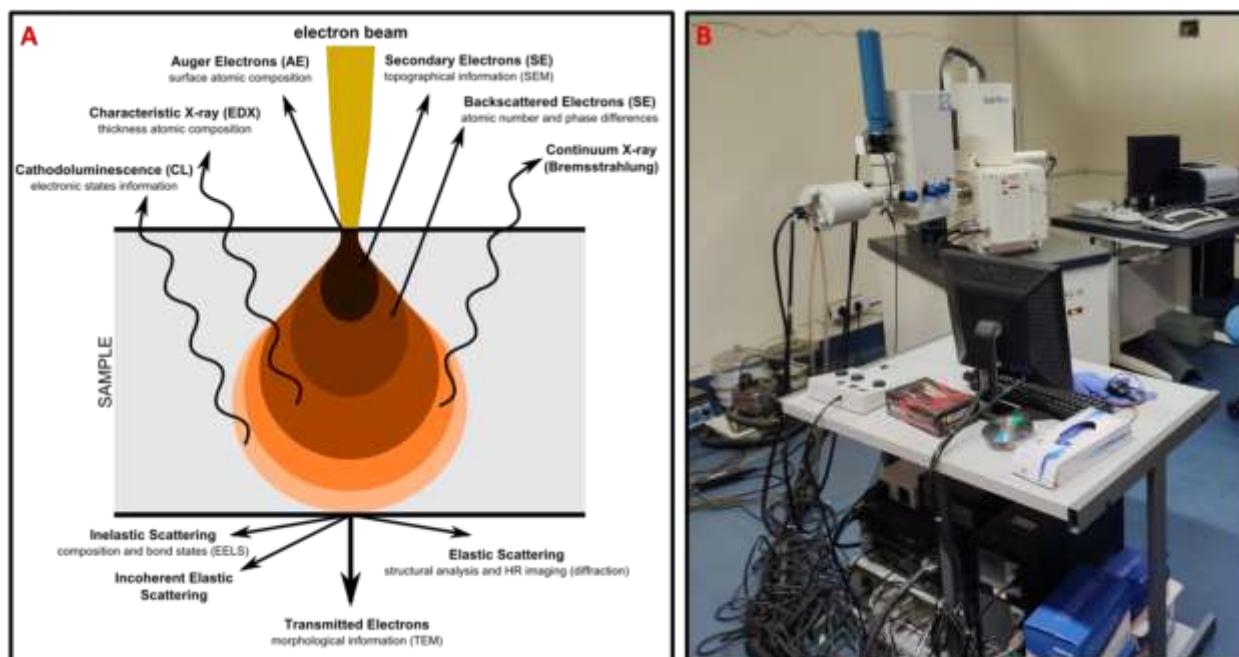


Figure 2.9: (A) Zone-specific interaction of focused electron beam and the thin sample, (B) Zeiss Supra 40 field emission electron microscope.

2.4.9 Transmission Electron Microscopy:

Transmission electron microscopy (TEM) is a technique where a beam of electrons is transmitted through a thin specimen with thickness $< 100\text{nm}$. In general, we use a carbon-coated Cu grid for preparing samples and in some special cases (especially for negatively charged particles) we use a formvar-coated Cu grid to avoid any grid induced aggregation. TEM generally provides more in-depth information including a column of atoms can be imaged from which we can determine the orientation of different crystal plane like $\{111\}$, $\{110\}$, $\{100\}$, etc. The technique called high-resolution TEM (HRTEM) to get atomic information of the imaged nanostructures. Besides the orientation of different crystal planes, we can determine crystal irregularities within the nanostructures from their respective HRTEM measurements.⁷¹ In general, the TEM instrument is coupled with other facilities that enable us to record the scanning TEM imaging (STEM) of samples, perform their energy-dispersive X-ray spectroscopy (EDX),

and obtain their diffraction spectra. The diffraction spectra help to analyze the crystal parameters like the presence of different facets, interplanar distances, etc. From EDX spectra we obtain an elemental mapping of the nanostructures from which atomic distribution of the nanostructures can be observed. In TEM, an electron gun (tungsten filament or lanthanum hexaboride) is used as the electron source. The electron gun is connected to a high voltage source (in our instrument the voltage source is 300 kV) and, given sufficient current, the gun begins to emit electrons either by thermionic or field electron emission into the vacuum. Often the combination of the cathode and a set of electrostatic lenses for effective electron beam shaping is called the “electron gun”. Upon the application of required voltage (here 300 kV), a beam of electrons ejected from the electron gun and transmitted through the sample, and finally, the obtained image is focused onto an imaging device, such a phosphor screen made by fine ZnS, a photographic film, or a dopped YAG screen attached to a Charge-coupled device (CCD). We use digital micrograph software for analysis of the TEM data. During sample preparation, a dip and dry method was followed in which we dipped a carbon-coated Cu grid in the surfactant-free concentrated colloidal solution; the hydrophobic carbon coating allowed us to make a monolayer of the sample to stick on the copper mesh which we dried in vacuum for overnight. The instrument used for the analysis is FEI Tecnai G2 F30 S-Twin microscope operating at 300 kV as shown in **Figure 2.10**.

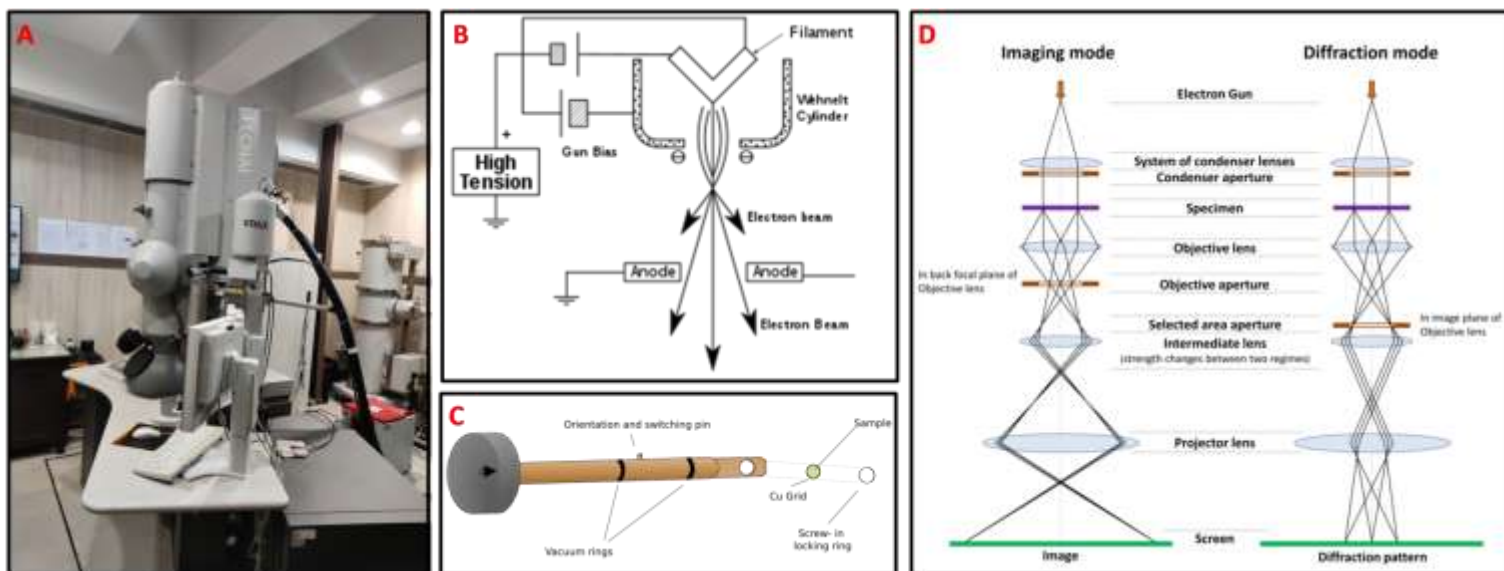


Figure 2.10: (A) FEI Tecnai G2 F30 S-Twin Transmission Electron Microscope (TEM) operating at 300 kV, (B) Electron gun assembly, (C) Single-axis tilt sample holder for insertion into a TEM goniometer, (D) Imaging and diffraction assembly.

2.4.10 Electrochemical Measurements:

All the electrochemical measurements have been performed in a CH6092E electrochemical work station (CH Instruments, USA) where we have used a Pt wire or graphite rod as a counter electrode and a Glassy Carbon (GC) electrode of 3 mm diameter as the working electrode. Saturated calomel electrode or Ag/AgCl was used as a reference. In most of the electrochemical measurements, we have used Cyclic Voltammetry (CV) for finding any redox peak in the system; Differential Pulse Voltammetry (DPV) for finding the most intense peak from I-V curve; Linear Sweep Voltammetry (LSV) for measuring the overpotential during HER; Electrochemical Impedance Spectroscopy (EIS) for measuring the resistance, the heterogeneous rate constant, exchange current density; etc. Besides, we have also used chronoamperometry to observe the long term catalytic stability of our developed nanomaterials. Prior to use, the Glassy carbon (GC) electrode was initially cleaned by polishing with alumina powder of different

grades (0.3 and 0.05 μm) followed by washing and sonication in Milli-Q water for five minutes. We performed traditional drop-casting methods for modifying the bare GC electrode, in which approximately 10 to 20 μL of concentrated nanomaterials (colloidal nanomaterials obtained after centrifugation) was dropped on the bare GC and dried for overnight. The strong adhesion property of our developed Au, Ag, Au-Ag alloy nanomaterials with GC electrodes allows us not to use any binder like nafion. Moreover, we did not use any other substances like Carbon powder or conducting polymers, e.g. polypyrrole, polyaniline, etc, to prepare a composite with our developed nanomaterials for enhancing current responses, due to the reason that the nanomaterials itself can produce sharp peaks in their I-V curves from DPV measurements. Thus it is encouraging to use our synthesized nanomaterials as an electrode material for sensing of biomolecules from their characteristic I-V curves obtained from DPV measurements or catalysis in alcohol/ H_2 fuel cells by checking their long term catalytic performances acquired from the corresponding Chronoamperometry measurements. The details of the electrochemical techniques are discussed below with an instrumental description.

2.4.10.1 Linear sweep voltammetry:

The electrochemical behavior of any redox system can be described by a three-dimensional i-t-E surface. To describe a stationary electrode with multisystem species, the i-t-E curve is complex to illustrate because in a multisystem species one could not identify each system systematically. Thus we can split the three-dimensional i-t-E curve into i-E and i-t curves for recognizing a particular redox system. In linear sweep voltammetry (LSV), the potential is swept with times and i-E curve is recorded directly from the instrument. In general, the potential is varied linearly with time and with sweep rates ranging from 10 mV/s to 1000 V/s in our

conventional electrodes like GC, Au, and Pt electrodes. Thus, the recording of ‘current (i)’ with ‘Potential (E)’ is equivalent to the record of ‘I’ with ‘time (t)’.

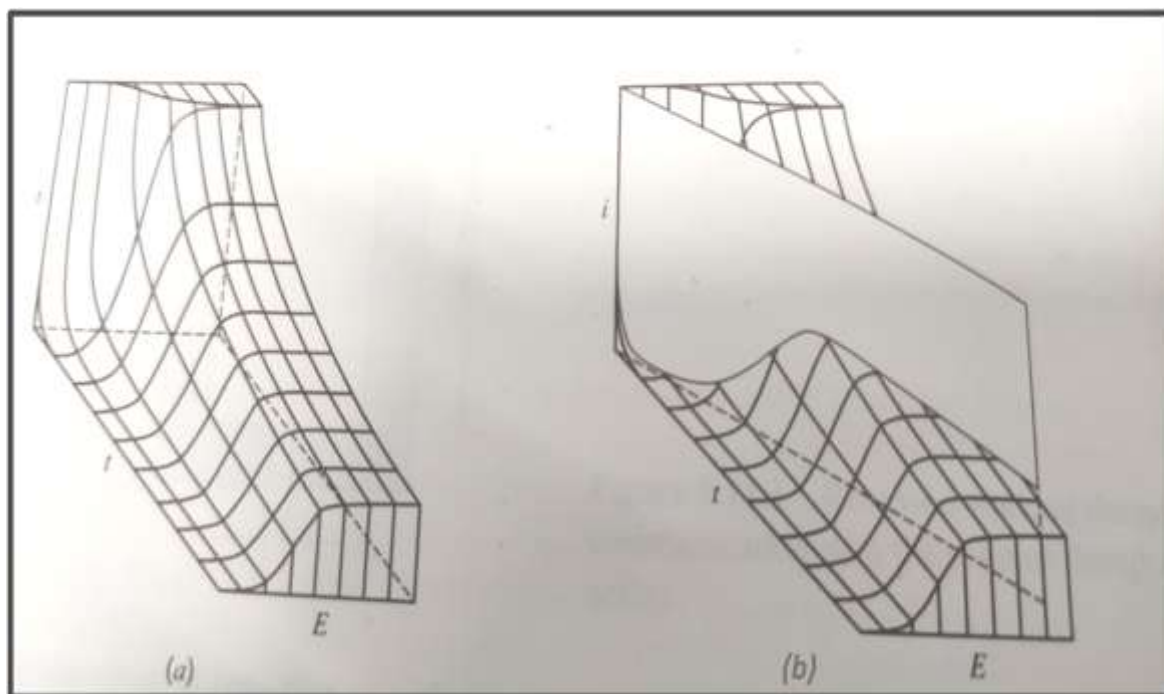


Figure 2.11: (a) A i-t-E surface in 3D for a Nernstian system, (b) linear potential sweep across the surface.⁷²

In an LSV experiment, the current responses are increased with increasing scan rate and different behaviors have been observed for reversible, quasi-reversible, and irreversible systems.

2.4.10.2 Cyclic Voltammetry:

Cyclic voltammetry (CV) is a technique where current is measured under a potential range. CV is performed by cycling the potential of a working electrode. In general, the reversal of LSV is performed by switching the potential at a certain time by the opposite scan. The potential at any time is given by

$$(0 < t < \lambda) E = E_i - vt$$

$$(t > \lambda) E = E_i - 2v\lambda + vt. \text{ Here 'v' is the scan rate.}$$

For a reversible Nernstian system, the two important parameters in i - E curve of cyclic voltammetry are i_{pc} (cathodic peak current) and i_{pa} (anodic peak current) and the separation in peak potential, i.e. $\Delta E_p = E_{pa} - E_{pc}$. For a reversible system, $i_{pa}/i_{pc} = 1$, regardless of scan rate and diffusion coefficients. ΔE_p is a function of switching potential E_λ , but should be very close to $2.3RT/nF$. If the cathodic sweep is stopped and the current is allowed to set zero then anodic sweep will be identical to cathodic sweep. CV for a reversible system at different E_λ values as a function of time is shown below in **Figure 2.12A**. A similar curve can also be plotted as a function of potential as shown below in **Figure 2.12B**.

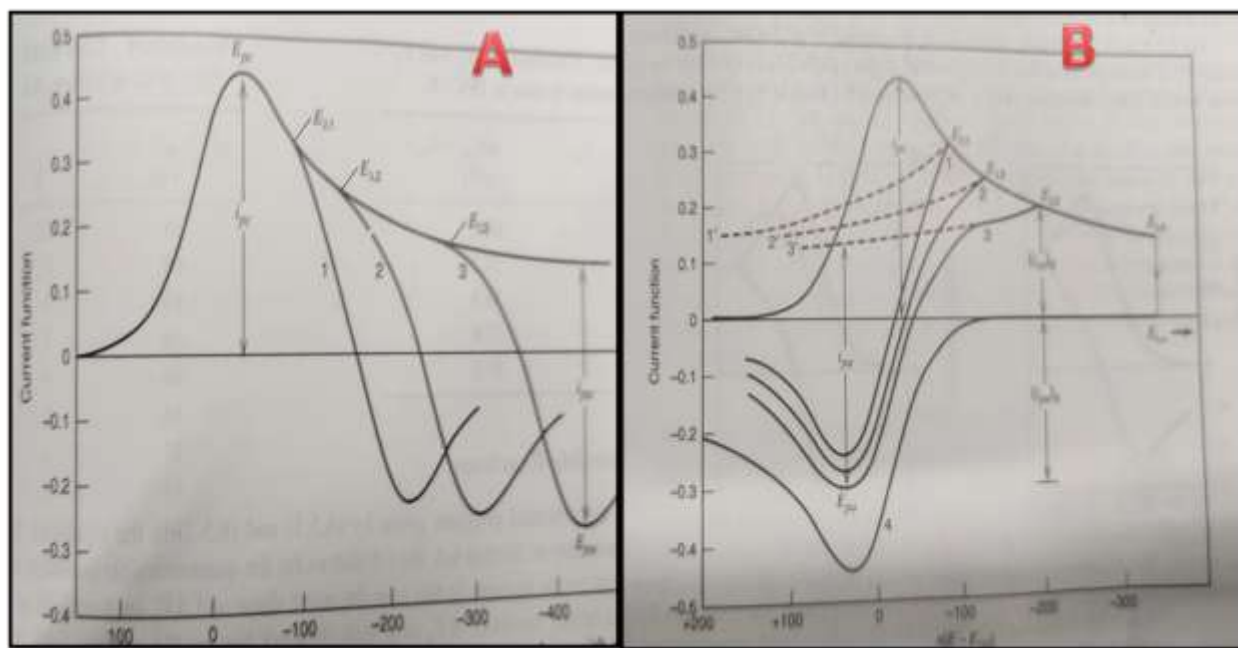


Figure 2.12: (A) CV for a reversible system at different E_λ values as a function of time, (B) CV for a reversible system at different E_λ values as a function of potential (E_λ).⁷²

The measurement of peak currents in CV is imprecise, as uncertainty arises during the correction of charging current. In the case of reversal processes uncertainty is more because the folded faradic response cannot be defined properly for the forward process as seen in 1', 2', and 3' in **Figure 2.12B**. Thus CV is not an ideal method for quantitative analysis, however, for qualitative

estimation, it can be used. The nature of a CV curve changes with moving from reversible to an irreversible or a quasi-reversible system where $i_{pa}/i_{pc} \neq 1$ and $\Delta E_p \neq 2.3RT/F$.

2.4.10.3 Differential Pulse Voltammetry:

In electrochemistry, Differential Pulse Voltammetry (DPV) is considered to be the most sensitive technique. The sensitivity can be achieved by applying a series of small amplitude regular voltage pulses, superimposed on the potential linear sweep or stairsteps as shown in **Figure 2.13**, and the current is measured immediately before each potential change. In DPV the measured current difference as a result of potential change is plotted as a function of potential. In the case of normal pulse voltammetry, the current from a series of ever large pulses is compared with the current at a constant 'baseline' voltage. Important characteristics of DPV are: (i) The base potential applied in DPV during drop fall is not constant rather it increases with time; (2) the pulse height lies between 10 to 100 mV and maintains a constant level with the base potential of the corresponding pulse; (3) two current samples are taken into consideration for the DPV measurement, one before the drop fall time, τ , and another after the drop fall time, τ' , (4) the experimental DPV curve is a result of plotting the current difference $\delta i = i(\tau) - i(\tau')$ versus the base potential.

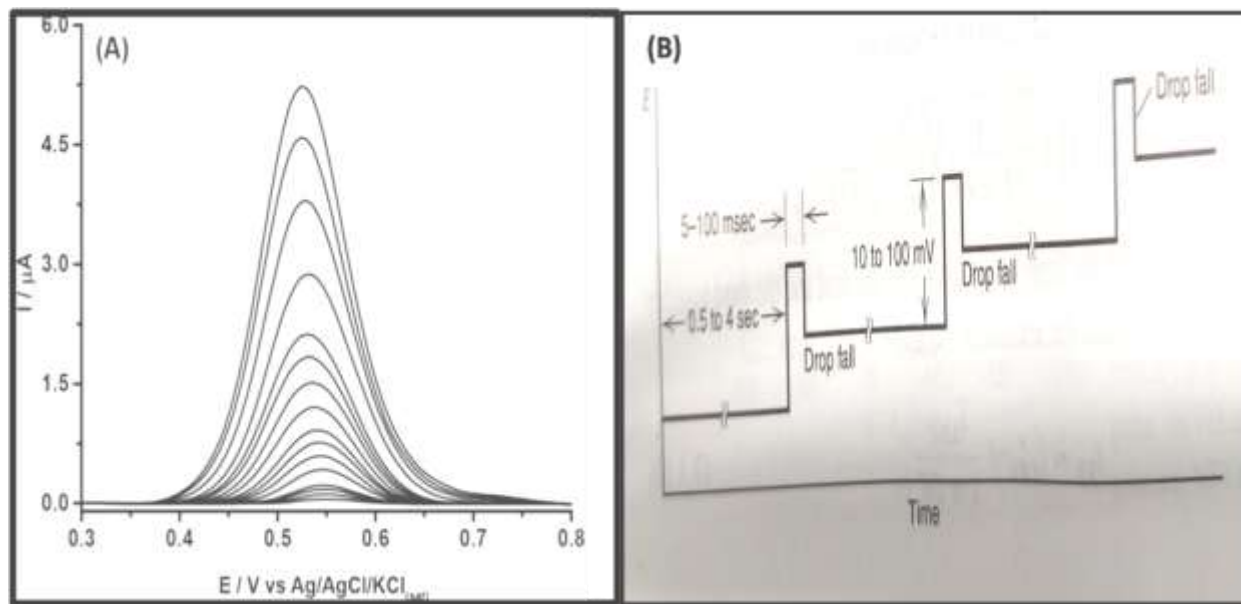


Figure 2.13: (A) Representative DPV curve, (B) Working principle of DPV.⁷²

Throughout the thesis, we have used DPV as a sensitive electrochemical detection tool for the selective determination of various analytes from their corresponding I-V curves. DPV is capable to produce specific peak potential with higher current densities than the corresponding CV measurements. As a result of this, DPV is considered to be a more appropriate electrochemical technique for the quantitative estimation of analytes than the CV.

2.4.10.4 Square Wave Voltammetry:

Square wave voltammetry (SWV) is a special technique that has been developed by combining the best aspects of several pulse voltammetric methods, including the background suppression and sensitivity of differential pulse voltammetry, the diagnostic value of normal pulse voltammetry, and the ability to interrogate products directly in much the manner of reverse pulse voltammetry. SWV also offers a wider time range compared to other pulse polarographic techniques.⁷² SWV is normally carried out at a stationary electrode. The basic difference between SWV and DPV is that SWV has no polarographic mode. The waveform used in SWV

can be viewed as a special case of that used for DPV (as shown in **Figure 2.13B**) where the preelectrolysis and pulse periods are of equal duration, and the pulse is in opposite from the scan direction as shown in **Figure 2.14**. The square waveform is characterized by various parameters as clearly shown in **Figure 2.14** and these are (i) Pulse height, ΔE_p : measured with respect to the corresponding tread of the staircase (shown as a thin horizontal line), (ii) Pulse width, t_p : time gap between the forward sample and reverse sample, (iii) Square wave frequency, f : pulse width and frequency in a square waveform is related by $f = 1/2 t_p$, (iv) Staircase shift, ΔE_s : the potential gap between two staircases at the beginning of each cycle, and it relates with the (v) Scan rate, v as: $v = \Delta E_s / 2t_p = f \Delta E_s$.

In SWV, current samples are taken twice per, at the end of each pulse. The difference current, ΔI , is formulated as $\Delta i = i_f - i_r$, where i_f is the forward current sample arises from the first pulse in the direction of staircase and i_r is the reverse current sample is taken at the end of the second pulse. Thus the result of a single square wave run is the combination of three voltammograms showing forward, reverse, and difference currents vs. the potential on the corresponding staircase tread.

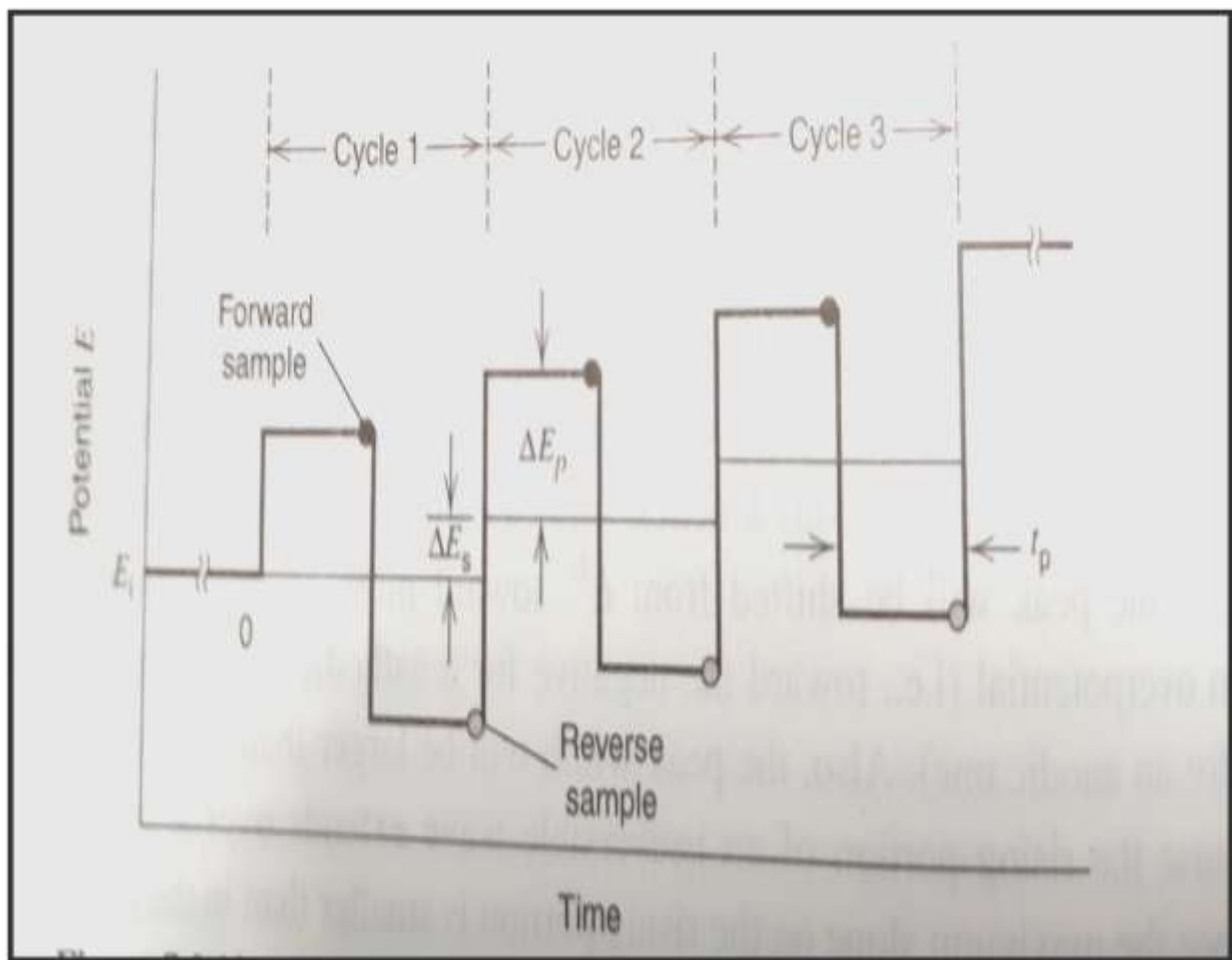


Figure 2.14: Waveform and measurement scheme along with different important parameters for SWV.⁷²

2.4.10.5 Chronoamperometry:

Chronoamperometry is a Current (i) vs time (t) plot for a faradic process where the potential of the working electrode is stepped and the resulting current is monitored as a function of time. In contrast to other stepped processes in electrochemistry, chronoamperometry generates a large current in any redox reaction and decays exponentially. Limited information can be achieved from the chronoamperometric i - t curve which includes (i) it gives the idea about the long term ability of a catalyst and its stability in the electrocatalytic environment, and (ii) the specific potential at which a redox reaction occurs.

2.4.10.6 Electrochemical Impedance Spectroscopy:

The term impedance refers to frequency-dependent resistance to current flow in a circuit.

Impedance Z_w is defined as $Z_w = E_w / I_w$.

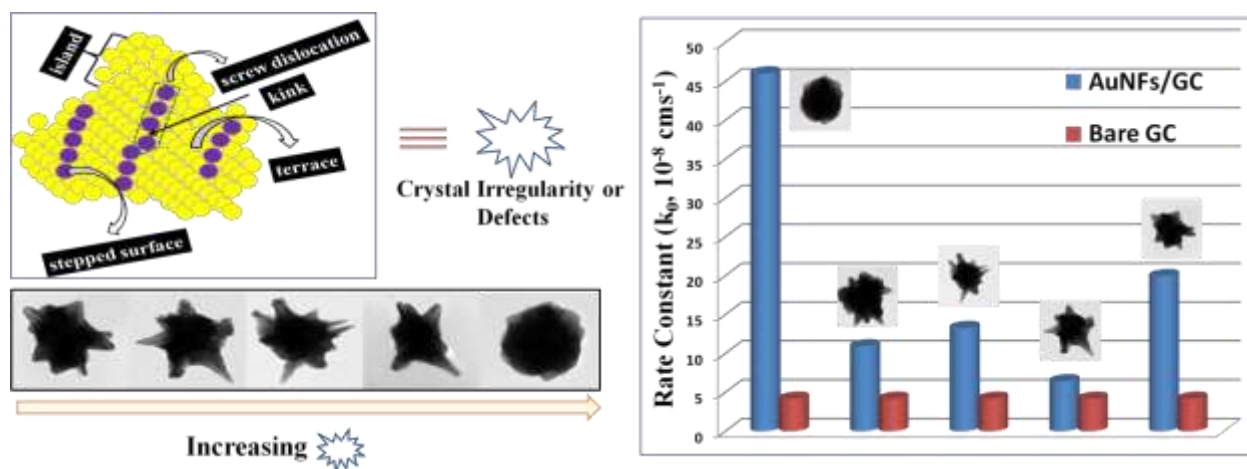
Though it is very complex to study frequency-dependent resistance, EIS is very helpful to carry out various electrochemical analyses as (i) EIS is an information-rich technique compared to any simple DC techniques. For example, by fitting the EIS (Nyquist plot) into Randles cell, one can gather information for various parameters like the heterogeneous rate constant, porosity, exchange current density, etc, (ii) EIS can identify diffusion-limited reactions, and (iii) EIS also gives information about the capacitive behavior of the system. The total impedance consists of two parts, one is the imaginary part and the other is the real part. The data extracted from EIS is fitted into the software with an equivalent circuit from which the parameters mentioned above can be determined. The most important parameter derived from EIS is the charge transfer resistance, R_{ct} . In Chapter 8, we have efficiently detected dengue serotype-2 (DENV-2) virus via impedimetric techniques where we have plotted R_{ct} as a function of known concentration of DENV-2 for calibration and unknown concentration of infected samples have been measured from the measured R_{ct} values. EIS is equally applicable in the sensing of other biological samples like cancer cells, bacteria, metabolites, etc.

CHAPTER-3

Crystal Defect Induced Facet Dependent Electrocatalytic Activity of 3D Gold Nanoflower towards the Selective Nanomolar (nM) Detection of Ascorbic Acid

OUTLINE: Specific Points of Discussion

- Role of crystal defects on the electrocatalytic activity of nanocrystals
- Role of surface energy (γ) of different facets in controlling the electrocatalytic activity of nanomaterials
- Bud shaped gold nanoflower (AuNF) shows the remarkable electrocatalytic efficiency towards the oxidation of ascorbic acid (AA) in the nanomolar (nM) concentration range.
- The ability of nano-bud in multi-component sensing [$i_p^{AuNF} (Bud)/i_p^{GC} \cong 100$] in a single potential sweep
- The role of different crystal facets and inter- & intra-molecular hydrogen bonding within AA molecules to control the resultant fingerprinted peak potentials at variable concentrations has been explored by ab initio and DFT calculation respectively



3.1 Introduction:

In this chapter, we have discussed the synthesis of bud to blossom gold nanoflower and their catalytic applications towards the electrochemical oxidation of Vitamin C. The specific peak potential for Vitamin C (Ascorbic acid, AA) helps us to find its signature in a pathological sample and thereby we can develop a potential biosensor for the pathological detection of AA. We have thoroughly analyzed the crystal structures of individual gold nanoflower to find out the presence of different active crystal sites within them and explored their role in controlling the unusually enhanced electrocatalytic oxidation of AA which is originally known to be a sluggish reaction. Instigation of unique catalytic activity of anisotropic gold nanoparticles (AuNP) encouraged modern science to shade lights on the concept of location and nature of active-site dependent catalysis.⁷³⁻⁷⁷ The unusual high catalytic activity of nanometer-sized gold particles (AuNPs) is primarily understood due to the generation of highly dense low coordination site atoms on edges, terraces, steps, ledges, kinks, etc.⁷⁸⁻⁸¹ Any crystal plane which remain at an angle $\theta \neq 0^\circ$ with a closely packed crystal plane, holds more number of broken bonds compared to the close-packed plane. In any general orientation of that additional crystal plane in a stereographic orientation with the close-packed crystal plane, generates ledges and kinks of certain density in an appropriate terrace orientation. These low coordinated site atoms then react more strongly because of their modified localized electronic structure.^{82,83} Most of the noble metal nanoparticles crystallizes according to the *fcc* pattern^{84,85} (However iron nanoparticles crystallize in *bcc* pattern,⁸⁶ gold and silver nanoparticles crystallizes as a superlattice in hexagonal close-packed structures⁸⁷ or simple cubic super crystals containing PbTe nanocubes⁸⁸) and the coordination number (C.N) of different facets in a unit cell of *fcc* are 7 for {110}, 8 for {100} and 9 for {111} planes whereas the C.N of an atom in *fcc* unit cell is 12. Thus the highest

number of bond breaking, i.e., $12-7 = 5$, takes place during the creation of $\{110\}$ facets.⁸⁹ According to the broken bond model, the number of bond breaking is proportional to surface energy.⁸⁹ Hence the surface energy (γ) of different facets in an *fcc* crystal will follow the order as $\gamma(111) < \gamma(100) < \gamma(110)$,⁹⁰ reflecting that the $\{110\}$ facet as the most reactive one among the lowest order crystal facets. Besides the broken bond model, microscopically the surface energy also directly depends on the atomic density of facets and geometry of the terraces, ledges, and kinks formed during anisotropic facet formation. The high reactivity of $\{110\}$ facets can also be explained in terms of planar density (the number of atoms in a plane). Greater the number of atoms in a plane, greater will be the planar density and hence it will be described as the most closely packed facet. The planar density of different crystalline facets of an unit cell of *fcc* are $0.177/R^2$ for $\{110\}$, $0.25/R^2$ for $\{100\}$ and $0.29/R^2$ for $\{111\}$ where R is the radius of a gold atom.⁹¹ In other words, relative planar density of $\{110\}$, $\{100\}$ and $\{111\}$ crystalline planes follow the ratio of 1: 1.4: 1.6. Thus $\{111\}$ plane is the most densely packed plane^{92,93} making it least reactive than the other two crystal planes, i.e., $\{100\}$ and $\{110\}$. Besides broken bond generation and planar density modulation, a detailed microscopic study of gold nanostructure demonstrates that the catalytic activity increased effectively with the increment of surface energy as a result of increasing the density of dislocation planes.^{94,95,96} Generation of more number of dislocation planes increases the catalytic activity due to the crystal lattice irregularity.⁹⁷ The other dominant factors that control the catalytic activity are combined effective surface charge,⁹⁸ zeta potential,⁹⁹ charge density at the curvature,⁹⁸ and effective surface area.¹⁰⁰

In the present study, we have investigated the electrocatalytic behavior of different size and shaped [three dimensional (3D) bud to blossom¹², confirmed by electron tomography study] gold nanoflowers (AuNFs) having a similar composition with variable curvature of the tips with

different degree of crystal defects and crystalline orientations towards the electrochemical oxidation of ‘Vitamin C’ by considering the aforementioned possible catalytic factors. The anisotropic AuNFs with the increasing number of concave petals oriented towards energetically unfavorable crystal plane possesses efficient catalytic activity due to the increased number of crystal defects such as steps, kinks, and dislocation sites.^{78,82} The high over-potential and poor reproducibility (fouling effects) of bare electrodes usually limit the usage of them¹⁰¹ as efficient electrode materials. Driven by the needs, the cutting edge modification of bare electrodes is done in this study by drop-casting of AuNFs (on bare glassy carbon electrode) via covalent binding or electrostatic interaction¹⁰² to study the catalytic function on the oxidation of biologically active molecules like Vitamin C, uric acid, glucose, dopamine, etc. Dynamics of crystal facet dependent reaction for different size and shaped AuNP modified electrode has recently been reported where {100} and {110} facets of AuNPs show higher catalytic activity for oxygen reduction reaction (ORR).^{103–105} However, the modification of AuNPs with Cu and Ag layers leads to {111} facet the most reactive one for ORR.¹⁰⁶ Our experimental work reports here the study of the electrochemical activity of different tailored shaped bud to blossom AuNFs with single {110} to twin plane orientation of their tips (one-half of the tips oriented along the {111} and the other half along {100}). The residual Ag used during the synthesis plays the key factor by suppressing the dynamics of {111} facet and preserving the high density of crystal defects on {110} facet for greater chemical reactivity.⁷⁵ The experimental result of facet and crystal defect dependent catalytic activity is further supported by using a projected augmented wave (PAW)¹⁰⁷ method. We have also used Density Functional Theory based computational calculation to understand the molecular basis of the dynamics of peak potential as a function of AA concentration. **Scheme-3.1** shows the schematic presentation of facile electrostatic interaction between bare glassy

carbon (GC) electrode and different AuNFs followed by crystal irregularity dependent AA oxidation.

The key driving force behind this electrochemical study of AA is due to its crucial role as a powerful antioxidant as well as an efficient scavenger for free radicals.¹⁰⁸ The ratio of Ascorbic Acid (AA) to dehydroascorbic acid (DHAA) acts as a biomarker of oxidative stress.

Various methods have been proposed for the quantitative estimation of AA like fluorimetric methods,¹⁰⁹ titration methods,¹⁰⁹ electrochemical detections,^{110,111} etc. However, most of these techniques suffer from interference due to the common basic molecular backbone of closely related pathological components like dopamine (DA), uric acid (UA), etc.^{112–114} which hinders their highly specific sensing applicability. Out of several other electrochemical methods, Differential Pulse Voltammetry (DPV) and Electrochemical Impedance Spectroscopy (EIS) are the two most powerful and error-free techniques used in the literature to measure the concentration of specific electro-active species in a fingerprinting voltammetric way and to get the insight on the kinetics of multiple electrochemical processes respectively. Thus the combination of DPV and EIS as active electrochemical techniques and facet originated crystal defect modulated nanomaterials as dynamic electrode coating offers the designing of most suitable transducer both to understand a surface-enhanced redox reaction as well as to use as a signal amplifier for ultrasensitive error-free fingerprinting detection in a multi-component physiological environment.

3.2 Synthesis of AuNPs:

The synthesis of different flourishing stages of AuNFs was carried out by using a nano-templated seeded growth technique (three-step synthesis protocol) as reported earlier by Bardhan et al.¹² In brief, trisodium citrate capped ~5nm gold nanoparticles (GNPs) were synthesized in

the first step by NaBH₄ reduction method which we used as the seed to prepare CTAB based gold nanopopcorn (GNPop) in the second step. In the third and final step, we used GNPop as nanotemplates to prepare different flourishing stages of AuNF simply by employing different concentrations of CTAB as the surfactant. The different nano-templated growth solution was then kept overnight for completing the growth process. The generation of AuNFs was confirmed by recording their UV-vis-NIR absorption spectra or examining their SEM and TEM images.

3.3 Theoretical *ab initio* simulation:

Theoretical modeling to calculate the reaction free energy (ΔG) and the corresponding activation energy (ΔE) have been carried out by using a projected augmented wave (PAW)¹⁰⁷ method, as implemented in the Vienna *ab initio* Simulation Package (VASP).^{115–117} The exchange-correlation functional Perdew–Burke–Ernzerhof (PBE) described within the generalized gradient approximation¹¹⁸ implemented with the projector augmented wave function (PAW). The bulk Au{100}, Au{110}, Au{111}, and Au{211} surfaces are modeled with (4×4), (4×4), (5×5) and (2×5) supercell respectively to minimize the lateral interactions between the repeating images with four layers of gold atoms. A vacuum of more than 12Å is used along the z-direction to avoid periodic interactions. The Monkhorst–Pack generates a set of (5×5×1) K-points which is used to optimize the supercell of Au{100} and Au{211} facets, while (4×3×1) is used for the Au{110} facet. The Brillouin zone is sampled with a gamma point (5×5×1) for the Au{111} facet. All four layers are fully relaxed for the bulk surfaces, while two atomic layers from the bottom of the slab are fixed. Other layers are relaxed while performing the thermodynamic study. Plane-wave with a kinetic energy cut-off of 470 eV is used to expand the electronic wave functions. The convergence criteria for total energy and forces are set at 10⁻⁴ eV and 0.02 eVÅ⁻¹ respectively while optimizing the geometry. The van der Waals interactions have

been included using the Grimme's D3-type of semiempirical method while optimizing the structures for the thermodynamic calculations.¹¹⁹ Zero-point energy (ZPE) and entropy corrections have included for the reaction free energy calculations. Zero-point energy (ZPE) is calculated using the following equation:

$$ZPE = \sum_i \frac{1}{2} h \nu_i \quad (1)$$

Where 'h' is the Planck constant and ' ν_i ' is the frequency of the i^{th} vibrational mode.

3.4 Density Functional Theory:

Finer details of the interactions of vitamin C with different Au-clusters have been probed by density functional theory. The structure of L-ascorbic acid was obtained from PubChem (CID: 54670067). The structure of its dimer and the gold complexes with the monomer and dimer were modeled in GaussView 5.0. Two to four gold atom clusters were used in these models. Both the two possible orientations for the interaction of gold clusters with the monomer were explored. All the possible binding modes were geometry optimized with density functional theory at B3LYP level¹²⁰⁻¹²² using 6-31G (d) basis set for all H, C, and O atoms, whereas, Stuttgart/Dresden basis set, SDD/6-31G(d), for all the Au atoms.^{123,124} A scalar relativistic effective core potential was applied to all the Au atoms.¹²⁵ Frequency calculations were performed on the optimized structures using the same level of theory. Gaussian 09W Rev. C¹²⁶ was used for geometry optimization and frequency calculations. Molecular orbitals were generated in GaussView 5.

3.5 Results & Discussion:

This research work presents a comprehensive study on the role of different form of crystal defects along with other factors (crystal facet free energy, the curvature at sharp tips, total surface area, surface charge, etc.) on an anisotropic gold nanoflower to control the

electrocatalytic affinity of Vitamin C in a multi-component physiological/pathological sample. Obtained results will lead us to create a new field of research namely “potentiometric fingerprinting” for error-free Pathological sensing in the nanomolar (nM) concentration range which not only has academic importance to understand the mechanism of electro-catalysis on defective crystal lattice but also supports potential market value for the fabrication of prototype electrochemical sensors for rapid clinical assessment. The synthesized gold nanoparticles, as shown in **Figure 3.1**, were characterized by using SEM, TEM, and zeta potential measurements.

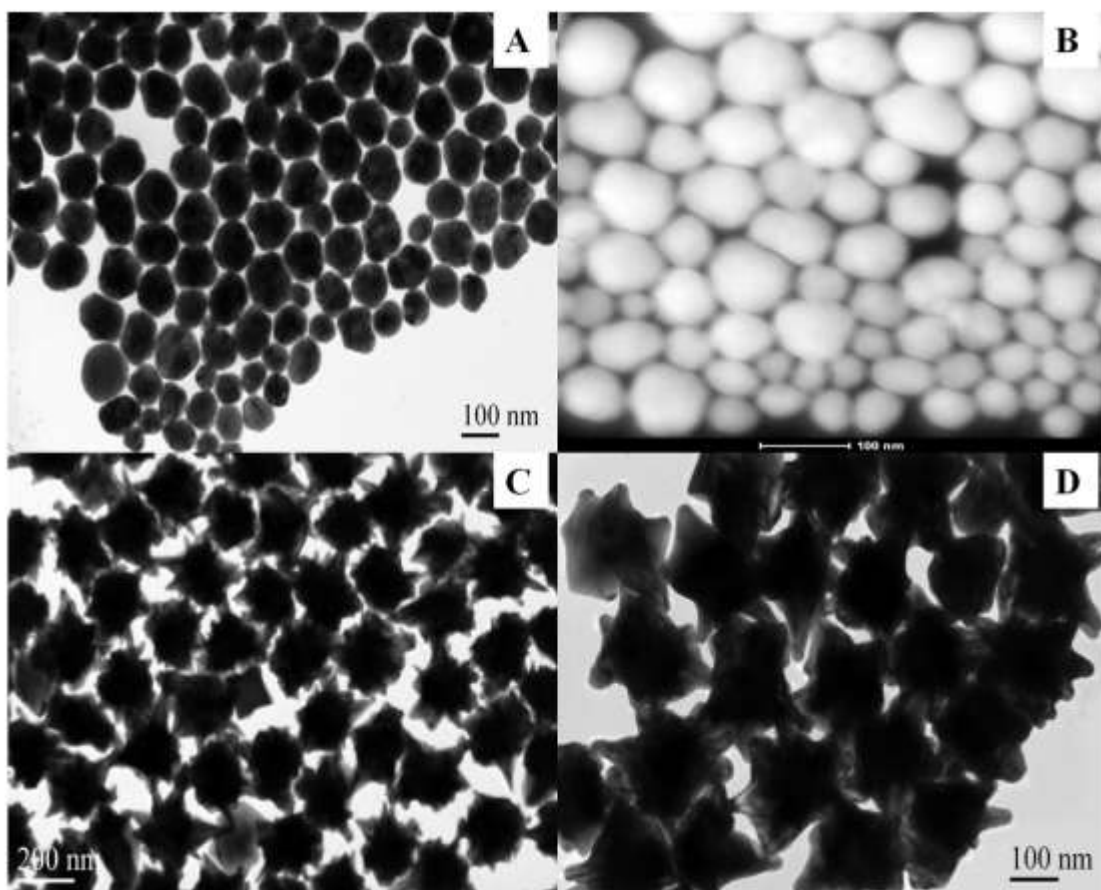


Figure 3.1: TEM image of AuNFs synthesized by using (A) 2.8×10^{-4} M CTAB, bud shape (B) HAADF of (A), (C) Fully blossomed AuNF at 2.8×10^{-2} M CTAB concentration and (D) overblossomed at 8.4×10^{-2} M CTAB.

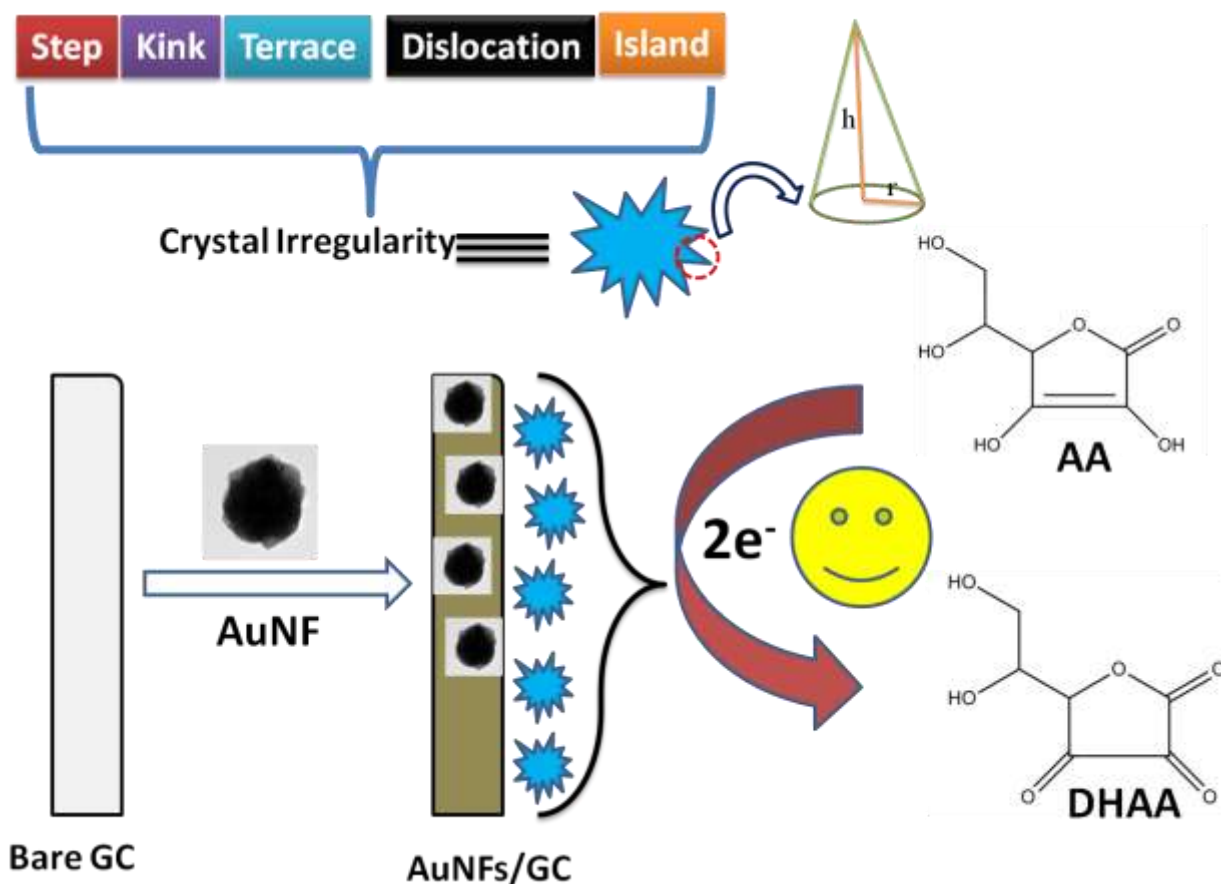
From our previously reported HRTEM measurements on AuNFs¹² it is clear that the lowest concentration of CTAB (2.8×10^{-4} M) generates bud structure with the crystal facets oriented in the $\{110\}$ plane. According to the literature survey, the surface free energy follows the order $\gamma(111) < \gamma(100) < \gamma(110)$.⁹⁰ Hence the bud structured AuNFs are energetically most unstable to provide maximum expected catalytic activity simply by receiving electrons (\equiv electrocatalytic oxidation) from the active molecular system (AA) to gain back the C.N. of an atom in *fcc* unit cell. As the CTAB concentration was increased to 2.8×10^{-2} M, crystal facet changes its direction towards energetically more stable planes to result in the formation of a half blossomed nanostructure where half of each petal directed along $\{111\}$ direction and another half towards the $\{100\}$ orientation. So, a mixed orientation of tipped petals has been obtained due to the synergistic effect of viscosity of the medium and crystal facet free energy as discussed in our previous report in details. The crystallographic direction of tips remain same in case of AuNFs synthesized at higher CTAB concentration (5.6×10^{-2} M) whereas they transform into blunted tipped structures along with energetically unfavorable $\{100\}$ crystalline packing at the CTAB concentration of 8.4×10^{-2} M. The TEM images of bud to blossom AuNFs as synthesized using variable concentration of CTAB exhibit highly homogeneity in shape and size as clearly visible from **Figure 3.1**. Obtained petal statistics from our TEM analysis along with the zeta potentials recorded for different nanoflower structures has been listed in **Table 3.1**.

Table 3.1 Physical and electrostatic parameters of synthesized different flourishing stages of AuNFs.

AuNFs at CTAB concentrations (M)	AuNF Core dia. (nm)	Individual average petal length (nm)	Average Number of petals	Zeta Potential (+ mV)
----------------------------------	---------------------	--------------------------------------	--------------------------	-----------------------

2.8×10^{-4}	110	0	0	11.9
2.8×10^{-3}	140	15	15	18.1
2.8×10^{-2}	155	85	54	27.3
5.6×10^{-2}	140	105	68	31.9
8.4×10^{-2}	135	70	45	34.8

By considering the above petal statistics, geometrical parameters of different AuNFs with different morphology were estimated by considering the core of different AuNFs as spherical and the tips as cone-shaped (**Scheme 3.1**). The surface area of the core is calculated by the formula $4\pi r^2$ and the surface to volume ratio (of the core) is defined as $\frac{4\pi r^2}{\frac{4}{3}\pi r^3} = \frac{3}{r}$ where r is the radius of the spherical core. On the other hand, the effective surface area of the core which is exposed to the environment is defined by $4\pi r_c^2 - N\pi r_c^2$ where r_c is the average radius of the base of each cone and N is the total number of cones. The mathematical term $N\pi r_c^2$ measures the extent of the surface area of the central core which is captured by N number of sharp tips. Similarly, the effective surface area (A) of the cone-shaped tips by disregarding the base area of cones can be expressed as $A = N\pi r_1 \left\{ \sqrt{r_c^2 + h_c^2} \right\}$ where h_c is the height of individual tips. The total effective surface area thus can be calculated by summing up the effective core area and effective petal areas for an individual AuNF. From the TEM images and by considering the above formulas, the detailed structural parameters are listed in **Table 3.2**.



Scheme 3.1: Schematic representation of the modification of the GC electrode (GCE) surface with positively charged AuNFs through electrostatic interaction followed by crystal defects dependent oxidation of ascorbic acid.

Table 3.2: Different structural parameters along with their total effective surface area calculated for our synthesized differently flourishing stages of AuNFs.

AuNF at CTAB Conc. (M)	Core radius (nm)	Effective surface area of core (mm ²)	S/V ratio of core (nm ⁻¹)	Cone-shaped tip base radius (nm)	Effective surface area of tips (nm ²)	Total effective surface area (nm ²)	Tip Diameter (nm)	Charge Density@ tip (cm ⁻¹)
------------------------	------------------	---	---------------------------------------	----------------------------------	---	---	-------------------	---

2.8×10^{-4}	55.0	38013.27	0.055	0	0	38013.3	No observed tip	-----
2.8×10^{-3}	70.0	61151.08	0.043	3	2162.57	63313.7	20	2.0×10^6
2.8×10^{-2}	77.5	26449.07	0.038	17	249993.17	276442.2	12	3.3×10^6
5.6×10^{-2}	70.0	~0	0.043	27	11486.38	611404.2	14	2.9×10^6
8.4×10^{-2}	67.5	25446.91	0.044	15	151810.42	177257.3	27	1.4×10^6

From the viewpoint of free energy, the catalytic activity of AuNFs should reduce with increase in the concentration of CTAB as at higher CTAB concentration the produced nanostructures are made up with petals having lower surface free energy by transforming from solely {110} to either a mixture of {111} and {100} or exclusively {100}. On the contrary, the extent of anisotropy (more number of petals) as well as the magnitude of surface charge (positive) increases with CTAB concentration should in turn enhance the catalytic oxidative power. Similarly, the effective surface area per AuNF increases monotonously and hence we can expect a gradual increment of catalytic power due to their ability to hold an increasing number of molecules on their surface. On the other hand, if we consider the charge (+Ve) density at the tip is the leading factor to control their catalytic oxidative power as we have shown in our previous result⁹⁸ then the reported AuNFs should show a fluctuating catalytic activity according to **Table 3.3**. To verify these expectations and assessments of the catalytic activity of different flourishing stages of AuNFs towards AA, we have measured their peak potential [E_p (V)] and peak current [i_p (μ A)] by using differential pulse voltammetry technique. **Figure 3.2A** depicts the differential pulse voltammogram of bare GC electrode in 0.4 mM AA wherein the anodic peak appears at 0.72 V due to the oxidation of AA. The modification of the GC electrode with different

geometries of AuNFs leads to a significant decrease in peak potential as well as enhancement in peak current for the electrooxidation of AA. This indicates that AuNFs exhibits electrocatalytic behavior for the oxidation of AA. However, the shift in peak potential and the magnitude of peak current alter with the different geometries of AuNFs for the electrooxidation of AA as can be inferred from **Figure 3.2A**. Among various AuNFs, the bud structure which was synthesized by using 2.8×10^{-4} M CTAB exhibits the highest catalytic activity in terms of $\Delta E_p(\text{V})$ and i_p^{AuNF} / i_p^{GC} where ΔE_p is the shift in peak potential for the electrooxidation of AA at AuNFs/GC compared to the bare GC electrode and i_p^{AuNF} & i_p^{GC} represent the corresponding peak current for the oxidation of AA at AuNFs/GC and bare GC electrode respectively. A comparison analysis has provided in **Table 3.3** for the electrocatalytic activity of various-shaped AuNFs/GC electrodes towards the oxidation of AA.

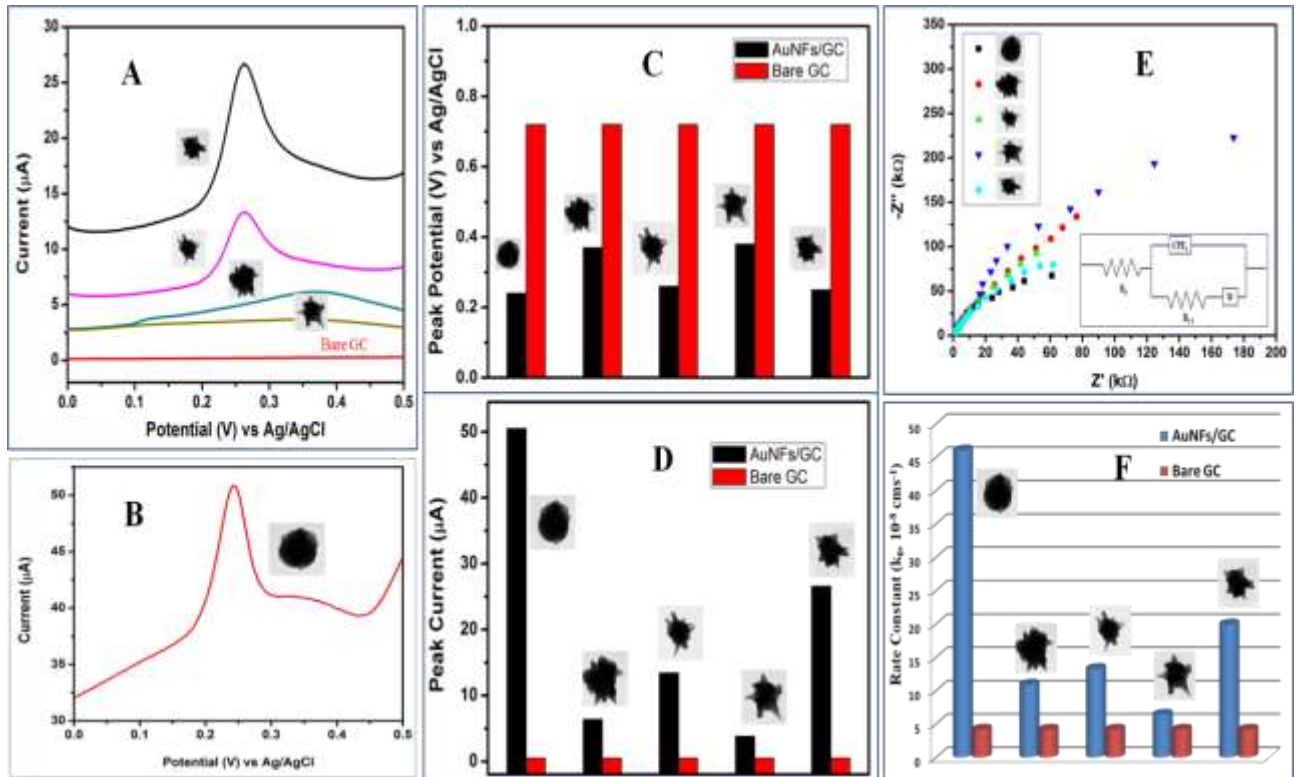


Figure 3.2: DPV for the oxidation of AA (4×10^{-4} M) on AuNF modified GC electrode synthesized using CTAB concentration as (A) 2.8×10^{-3} to 8.4×10^{-2} M, (B) 2.8×10^{-4} M, (C) and (D) show the comparison of modified GC and bare GC electrode in terms of peak potential and peak current respectively for the oxidation of AA, (E) Nyquist plot for different AuNFs modified electrode and the corresponding equivalent circuit for the Nyquist plot, (F) measured rate constant for the electro-catalytic oxidation of AA to DHAA on the surface of different AuNFs.

Interpretation of the DPV results confirms that the bud structure with crystal facet orientation towards $\{110\}$ is the most efficient one for the electrochemical catalytic conversion of AA to DHAA. The lowest peak potential (0.24 V) associated with the highest peak current (50.5 μ A) of the bud structure modified GC electrode is well supported by our previous argument of the dependence of electrocatalytic activity on facet energetic. Characteristic DPV for the oxidation of AA on bud shaped AuNF modified GC electrode is shown in **Figure 3.2B**, separately. Though the argument on facet energetic to explain the highest catalytic activity of bud structured AuNF shows the expected result, charge density at the tip does not support it due to the absence of any tip on the bud structure. Moreover, the trend of catalytic activity for different flowering stages of AuNFs does not follow a linear relation with the CTAB concentration as it is expected both from facet energetic and charge density consideration. In the same line of argument, other factors which include the extent of anisotropy (more number of petals), total surface charge, and effective surface charge, all increases monotonously with CTAB concentration and suppose to show a gradual increment of catalytic activity towards AA oxidation. Obtained catalytic activity (in terms of a shift in peak potential and relative peak current) shows a zig-zag pattern and cannot be explained by those above factors. These

observations forced us to consider other unexplored factors as major players to control their observed electrocatalytic activity.

Table 3.3: Experimental observations and system parameters deduced from DPV and EIS measurement towards the oxidation of AA on different flourishing AuNF coated GC electrode

AuNFs at CTAB concentrations (M)	Peak potentials, E_p (V)	Peak current (μA)	Relative peak current $\left[\frac{i_p^{\text{AuNF}}}{i_p^{\text{GC}}} \right]$	R_{CT} ($k\Omega$)	i_0 (10^{-8} A)	k_0 (10^{-6} cm s^{-1})
Bare GC	0.72	0.5	NA	2978.5	0.43	0.79
2.8×10^{-4}	0.24	50.5	101.0	51.4	25.08	46.03
2.8×10^{-3}	0.37	6.39	12.78	215.0	5.97	10.95
2.8×10^{-2}	0.26	13.44	26.88	177.4	7.25	13.30
5.6×10^{-2}	0.38	3.82	7.64	364.2	3.52	6.45
8.4×10^{-2}	0.25	26.58	53.16	117.1	10.9	19.97

Out of several other factors, the extent of crystal defect¹²⁷ could be a major aspect to control the observed catalytic activity. The HRTEM study clearly shows the presence of several different types of defects originating from crystal plane dislocations, stepped surface, kinks, islands, or from differently packed crystal boundaries. A pictorial representation of different types of crystal defects originates from bud structured and fully blossomed AuNFs are shown in **Figure 3.3** and **Figure 3.4**. In an *fcc* crystal, the normal stacking sequence of the planes generally represented as ABCABCABC..... pattern. Characteristic twin boundary (TB) generates when one plane acts as a mirror of the other two. In **Figure 3.3D** a twin defect appears via the unusual sequence

ABCBA patterning where the C presents a mirror plane to that of AB planes. The atoms situated on the twin boundary, C plane, have reduced coordination numbers and catalytically more active than the other closely packed planes. By comparing all five different flourishing stages of AuNF synthesized at different concentrations of CTAB, it has been observed that a greater defect density has been observed for the bud shaped structure compared to the other flourishing stages of AuNF.

A crystal plane at an angle θ to a close-packed plane can generate terraces (inclined surface with respect to the low indexed [low energy] atomically flat surface), ledges (structural defect which accommodate the terrace inclination) and kinks (defect in the ledge) to result in additional broken bonds in these inclined planes compared to the reference close-packed planes. Any general orientation within the stereographic triangle (Euler Triangle) can be constructed with ledges and kinks of a certain density in an appropriate terrace orientation.¹²⁸ These ledges and kinks are the sites where atoms of growing crystal or foreign atoms/molecules can preferentially attach compared to the flat terraces. By considering the angle between terraces and ledges as θ and between ledges (ledges are constructed as a combination of several kinks) and kinks as ϕ , mathematically we can define the surface energy offered by ledges and kinks are $\gamma(\theta) = (\gamma_T \cos\theta + \gamma_L \sin\theta)$ and $\gamma(\phi) = (\gamma_L \cos\phi + \gamma_K \sin\phi)$ respectively where ‘T’ stands for terrace, ‘L’ for ledges and ‘K’ for kinks.¹²⁸ Besides steps, kinks, and edges; dislocation planes^{94,96} (which is also a source of the active catalytic site) has also been observed in the growing tips of different AuNFs. In general, dislocation defects are formed when atoms in a regular crystal are out of position to form a distorted region. For a polycrystalline material, this disorientation of crystallites is known as boundary (grain or twin) defects. In general, these small misfits (angular: boundary defect and linear: same lattice defect) between crystals or crystal

planes can be accommodated by structural dislocations. Broadly this structural dislocation can be subdivided into three categories as tilt (rotation axis lies on the boundary plane), misfit (stretching of one particular plane), and twist (rotation axis lies perpendicular to the boundary plane) dislocation. Misfit and twist can also be defined as edge dislocation and screw dislocation as has been clearly shown in **Figure 3.3E & 3.3F** respectively on a bud structured AuNF. For a better understanding of crystal defects, we have also provided the HRTEM images for bud shaped AuNF in **Figure 3.5**, which shows the direction of the growing tip towards energetically unfavorable {110} facet.

A Crystal defect originated from the formation of islands is also a dominant feature to control their overall catalytic activity. In general, an island grows or shrinks to maintain equilibrium vacancy concentration via atom migration from the crystal to the surface.¹²⁹ A recent work by Ganesh et al.¹³⁰ has studied the intriguing catalytic activity of surface-active islands on nanostructures for efficient direct formic acid oxidation. The modulation of different crystal defects during their shapes evaluation to control the catalytic power^{80,81} of a nanoparticle is the main theme of this study to achieve the most suitable nanostructure with desired crystal orientation for the highest catalytic activity. A detail of this shape-dependent defect study is summarized in **Table 3.4** which includes different types of defects originated from structural dislocation, steps, kinks, islands, and differently packed crystal boundaries.

Table 3.4: Density (nm^{-2}) of Different Crystal Defects (dislocation, steps, kinks, islands, and differently packed crystal boundaries) for Various Shaped AuNFs Synthesized at Tunable Concentration (M) of CTAB.

Different Types of Crystal Defects	Density (nm^{-2}) of Different Crystal Defects for Different Shaped AuNFs Synthesized at Different Concentration (M) of CTAB
---------------------------------------	--

	2.8×10^{-4}	2.8×10^{-3}	2.8×10^{-2}	5.6×10^{-2}	8.4×10^{-2}
Edge dislocation	0.35	0.05	0.17	0.01	0.22
Screw dislocation	0.57	0.11	0.14	0.07	0.35
Stepped surface	0.18	0.06	0.08	0.02	0.13
kink	0.58	0.23	0.31	0.17	0.43
island	0.43	0.07	0.19	0.03	0.37
Twin boundary (TB)	1.11	0.05	0.85	0.01	0.93
Grain boundary (GB)	1.77	0.13	0.89	0.11	0.95

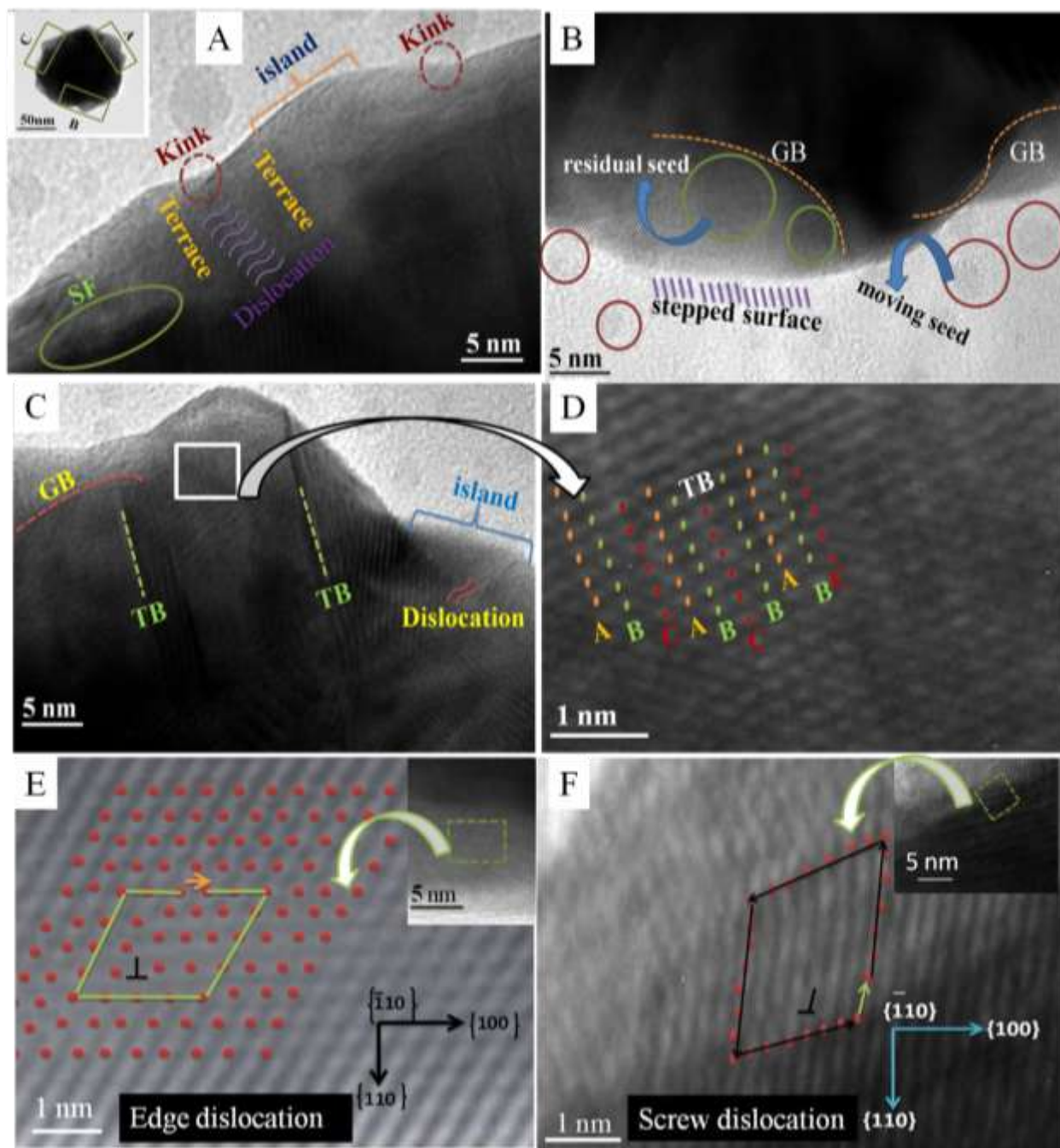


Figure 3.3: Randomly selected three different surface regions (A, B and C) of a bud structured AuNF to find out the existence of different crystal defects, (D) zoomed region on frame C to understand the crystal plane arrangement in twine boundary, detailed vectorial representation of (E) edge dislocation and (F) screw dislocation.

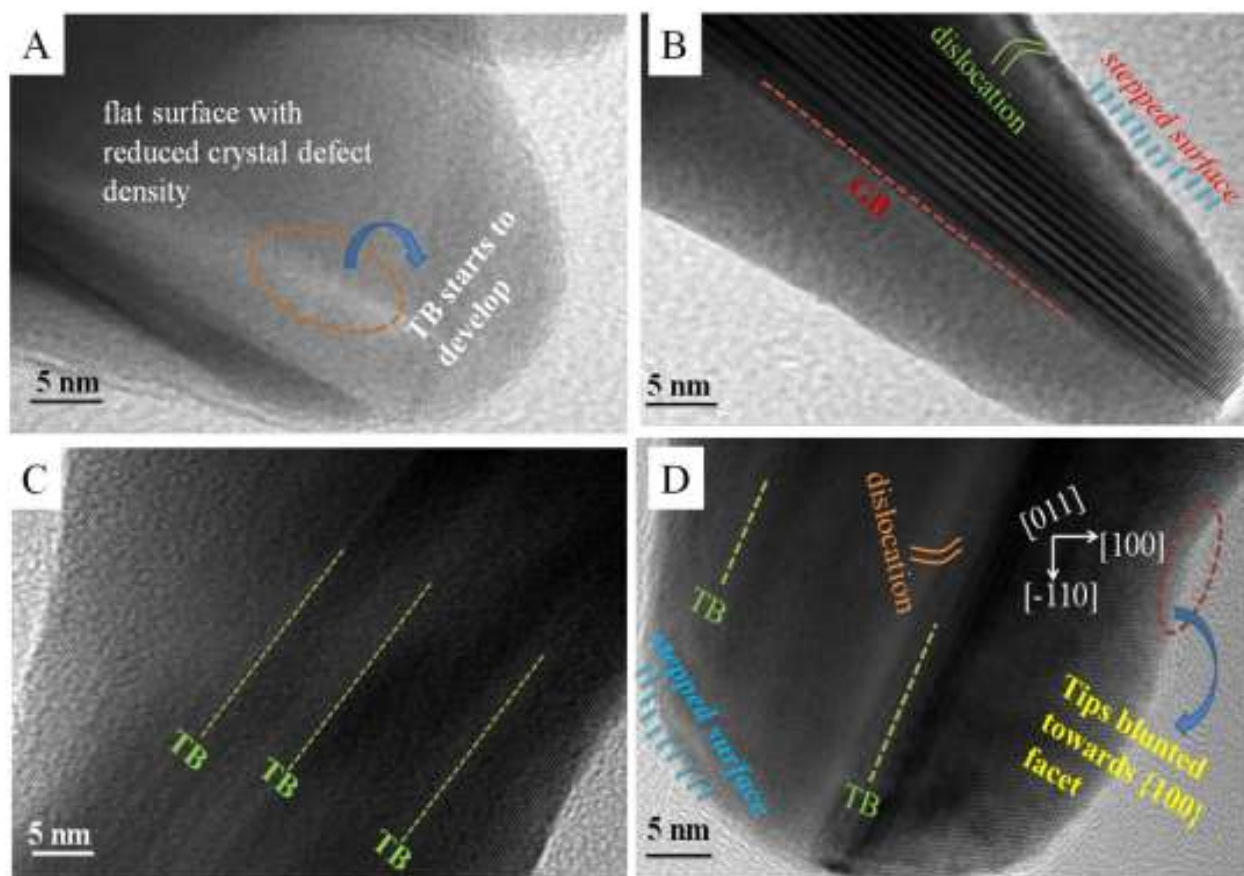


Figure 3.4: (A) AuNF synthesized at 2.8×10^{-3} M CTAB with reduced crystal defect density, (B) With increasing CTAB concentration at 2.8×10^{-3} M CTAB, the AuNF produced show enhanced crystal defect density, (C) Fully blossomed AuNF produced at 5.6×10^{-2} M CTAB Shows only twin boundary defect, (D) Overgrown AuNF synthesized at 8.4×10^{-2} M CTAB exhibit blunted tips towards energetically unfavorable $\{110\}$ facet.

HRTEM based density of different crystal defects (nm^{-2}) for different shaped AuNFs has been detailed in **Figure 3.6**. Our HRTEM study clearly shows that irrespective of the type of defects, the defect density is maximum for bud structure which reduces in a zigzag pattern as different flourishing stages of AuNF evolves at an increased concentration of CTAB. Incremental contribution of dislocation planes along with steps, kinks, islands, and differently

packed crystal boundaries supports the presence of a maximum number of catalytic active sites on leading highly energetic {110} facets of bud shaped structure to offer highest AA oxidizing power.

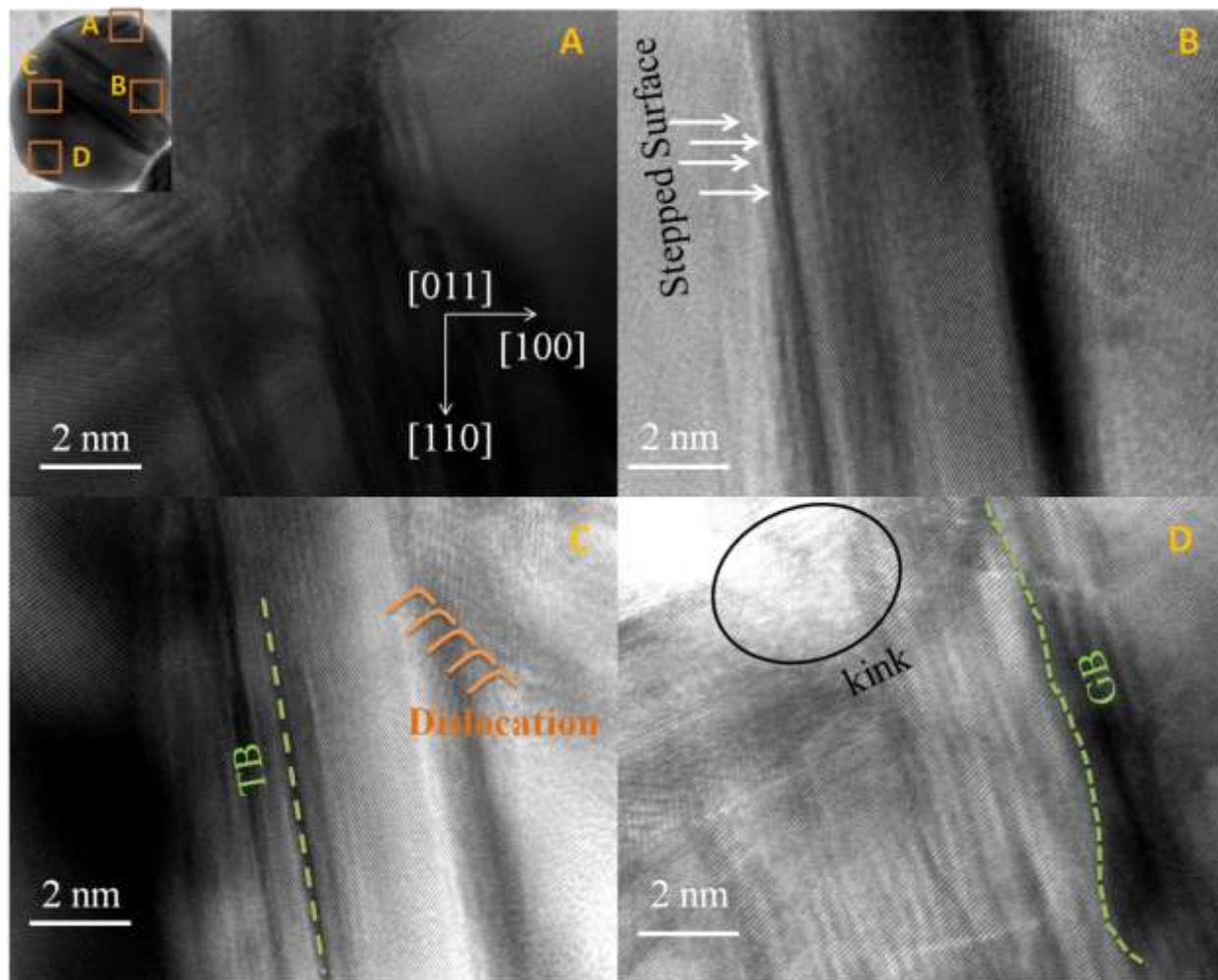


Figure 3.5: HRTEM image of the bud shaped AuNF. Different parts of the bud structure is focused where (A) indicates the direction of the growing tips towards {110}, and (B), (C), (D) indicates the presence of multiple crystal defects like stepped surface, GB, TB, Dislocation, etc.

Here CTAB concentration regulates the shape of the AuNFs and described in detail in our previous publication.¹² The oxidizing ability of AuNF at CTAB concentrations between $2.8 \times 10^{-3} \text{ M}$ and $8.4 \times 10^{-2} \text{ M}$ shows a zig-zag pattern. This observation can easily be described in terms of

the variation of defect density with different flourishing stages where for each shaped AuNFs we have considered three different surface zones with different surface areas (25, 100, and 225 nm²). For each surface zone of an individual structure, we have considered 100 frames and hence **Table 3.4** is bearing the statistics of $5 \times 3 \times 100 = 1500$ frames. A detail of defect study is summarized in **Table 3.4** which includes different types of defects originated from structural dislocation, steps, kinks, islands, and differently packed crystal boundaries. Various type of crystal defects density was calculated by employing the expression as: Crystal defects density (CDD) = $\sum_{i=1}^{i=100} \frac{n_i}{A_i}$, where, n_i denotes the number of respective defects in the selected area A_i . Considering similar statistical analysis we have also presented the charge density at the apex in **Table 3.2** which gets maximum for the highest curvature tips.⁹⁸

Charge density is mathematically calculated as 2κ , where κ is the radius of curvature ($\kappa = 1/R$) and R is the tip radius. Though the charge density at the tip is a formidable factor to achieve higher catalytic activity as we have reported previously.⁹⁸ The obtained result in this report does not explain their growing role over crystal defect density. Hence out of several factors which include (i) generation of crystal defects due to the presence of low coordination atoms on steps, kinks, islands, and edges, (ii) increment of internal surface area due to the dislocation, (iii) orientation of crystal facets on the projected tips of AuNFs, and (iv) charge density at the tip; the statistics of defect density leads the rally.

Though we used the DPV technique for fingerprinting the characteristic redox peak-current and peak-potentials of the electrocatalytic oxidation of AA; we have adopted here alternate EIS technique also to acquire the kinetics information as well as to measure the ability of a circuit to flow electrical current. Electrochemical impedance spectroscopy (EIS) is one of the most powerful and reliable techniques for getting various electrochemical parameters such as double-

layer capacitance (C_{dl}), charge transfer resistance (R_{CT}),¹³¹ solution resistance (R_s), the standard heterogeneous rate constant (k_0),¹³² etc. The typical Nyquist plot obtained from the EIS experiment indicates the variation of real and imaginary parts (of impedance) over a higher to lower frequency range (e.g. 10^5 to 10^{-2} Hz) at a fixed potential.⁷² The distorted semicircles are observed from the Nyquist plot (**Figure 3.2E**) for various shaped AuNFs modified GC electrode towards the electrooxidation of AA wherein diameter of the semicircle in the X-axis gives an estimation of R_{CT} value between the modified electrode and analyte (AA). However, a variation in the R_{CT} value is noticed for different morphology of AuNFs in which the fully flourished AuNF-modified GC electrodes exhibit the highest R_{CT} value while the bud shaped AuNF shows lowest R_{CT} values. R_{CT} values for other AuNFs lie in between the limits and their magnitude follows the trend as $R_{CT}^{2.8 \times 10^{-4}} < R_{CT}^{8.4 \times 10^{-2}} < R_{CT}^{2.8 \times 10^{-2}} < R_{CT}^{2.8 \times 10^{-3}} < R_{CT}^{5.6 \times 10^{-2}}$. From this R_{CT} value, we have estimated the exchange current densities (i_0) as well as the standard heterogeneous electron transfer rate constant (k_0) by adopting the following equations⁷²:

$$R_{CT} = \frac{RT}{nFi_0} \text{ and } i_0 = nFAC_{OX}^{(1-\alpha)}C_{Red}^{\alpha}k_0 \quad (2)$$

$$\text{by assuming } C_{OX}^{(1-\alpha)} = C_{Red}^{\alpha} = C, i_0 = nFACk_0$$

where ‘n’ denotes the number of electrons (here, $n = 2$), ‘A’ denotes the active surface area, C_{OX} and C_{Red} denote the bulk concentrations of ascorbic acid (AA) and dehydroascorbic acid

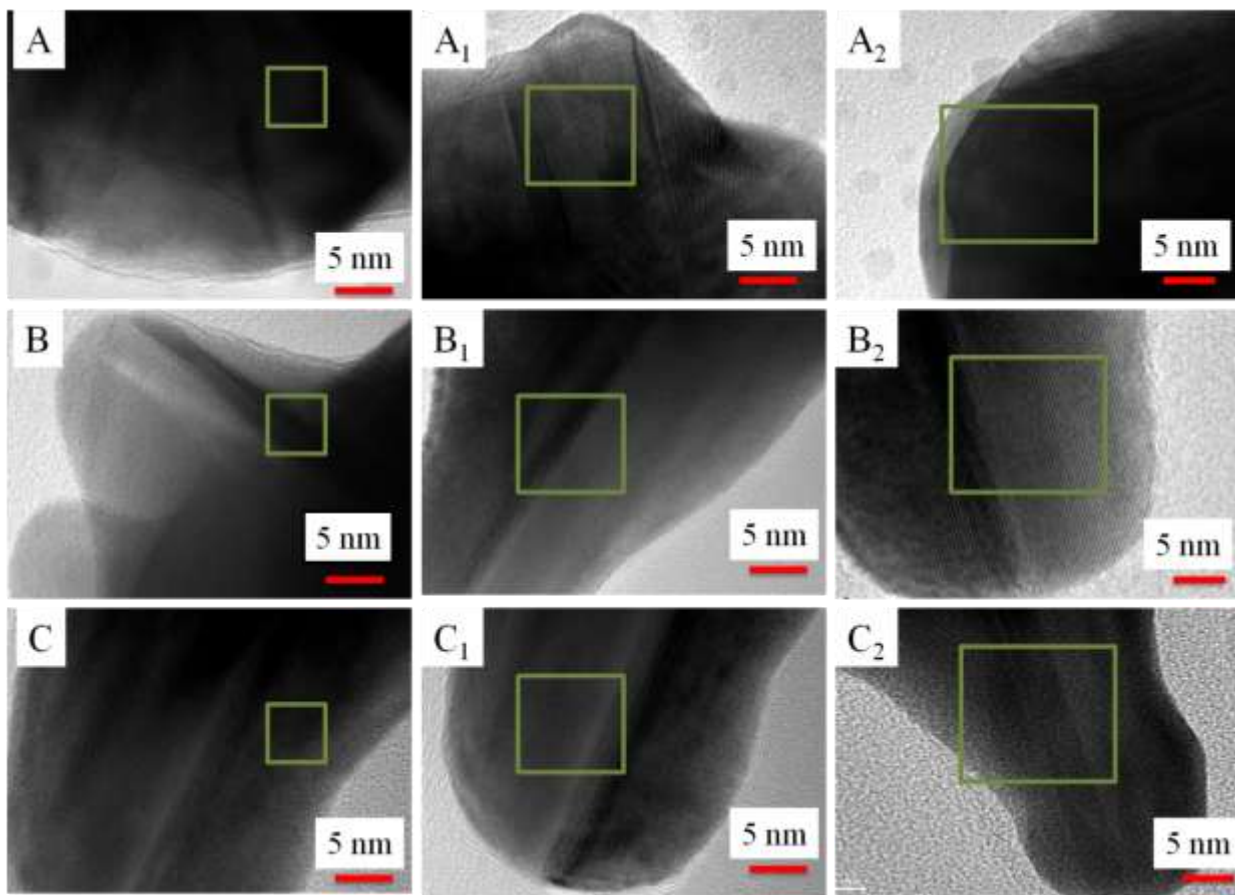


Figure 3.6: Variation of defect density with different flourishing stages (Top panel for bud structure with 2.8×10^{-4} M CTAB, Central panel for half blossomed AuNF with 2.8×10^{-2} M CTAB and bottom panel for the overgrown AuNF with 8.4×10^{-2} M CTAB) where for each shaped AuNFs we have considered 100 frames each for three different surface zones with different surface areas (25, 100 and 225 nm^2).

(DHAA), respectively and α being the symmetry factor. For the quantitative evaluation of various system parameters, a modified Randles equivalent circuit (by blending the parameter constant phase element; CPE)¹³³ is constructed (**Figure 3.2E** inset) to fit the experimental Nyquist plot and the fitting parameters are tabulated in **Table 3.3**. As can be seen from **Table**

3.3, the bud shaped AuNFs (prepared using 2.8×10^{-4} M CTAB) shows the highest exchange current, as well as the utmost standard heterogeneous rate constant in comparison to other AuNF, modified electrodes. The heterogeneous rate constant follows the trend as: $k_0^{2.8 \times 10^{-4}} > k_0^{8.4 \times 10^{-2}} > k_0^{2.8 \times 10^{-2}} > k_0^{2.8 \times 10^{-3}} > k_0^{5.6 \times 10^{-2}}$. Indeed, this behavior is consistent with the DPV response of AuNFs/GC towards the electro-oxidation of AA. Thus, it can be concluded that the morphology which having higher crystal defects (steps, kinks, edges, dislocation) exhibits superior catalytic activity than that of others.

To get the idea about the feasibility of AA oxidation reaction on different crystal facets we have used here Vienna *Ab initio* Simulation Package (VASP) where the reaction free energy (ΔG) have been calculated by using the computational hydrogen electrode (CHE) model as proposed by Nørskov and co-workers.^{131,134}

For example, the reaction free energy for a general reaction is calculated at zero voltage as follow:



Reaction free energy: $\Delta G = G(A^*) + \left[\frac{1}{2} G(H_{2(g)}) \right] - G(AH^*)$ (4)

We have calculated the reaction free energy change for the reaction presented in **Scheme 3.1**. The optimized structures of AA on different crystalline gold facets have shown in **Figure 3.7**. Our calculated reaction free energy (**Table 3.5**) suggests that the oxidation of ascorbic acid shows different reactivity with different crystal facets of the gold surface. The Au{110} surface is more reactive with minimum activation energy (1.04 eV) and lowest reaction free energy (0.64 eV) compared to the {111} and {100} surfaces. On the other hand, the reaction is more favorable with the free energy change of 0.59 eV in the presence of stepped surface {211} which inclined towards {111} and {100} surfaces. Simulated results match exactly what we observed for

experimental electrocatalytic activity on different flourishing stages of AuNFs. Both experimental observation and simulated prediction show the highest catalytic activity for bud shaped AuNF with active crystal faces oriented towards $\{110\}$ direction.

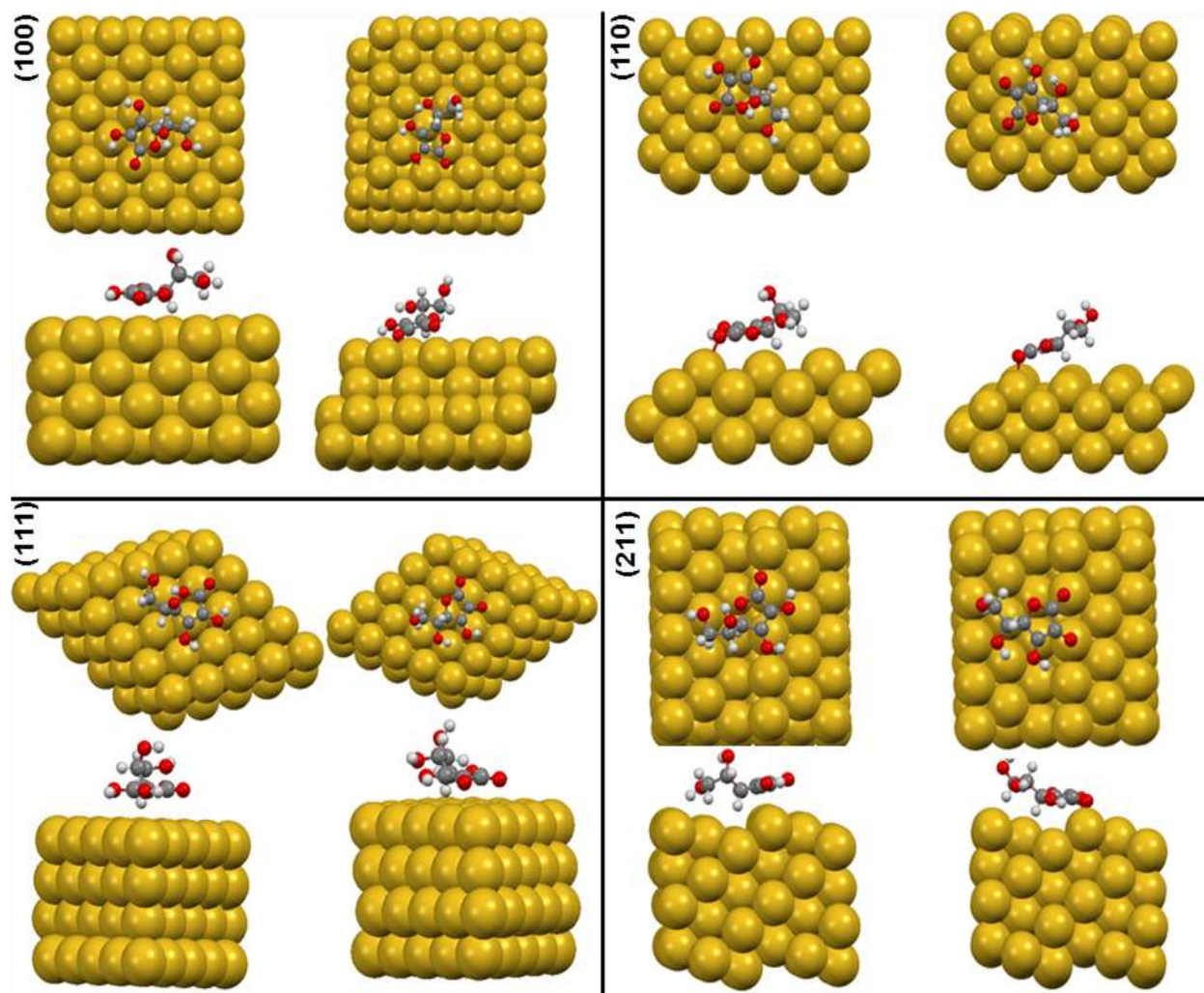


Figure 3.7: Top and Side views of the optimized AA on different crystalline lowest order $\{111\}$, $\{100\}$ and $\{110\}$ and stepped $\{211\}$ Au facets. Optimized molecules are shown in the ball-and-stick model where red balls indicate oxygen atoms, gray balls as carbon atoms and white balls as hydrogen atoms.

Table 3.5: Calculated reaction free energy for the oxidation of AA on different crystal facets of gold

Surface	$\Delta E(\text{eV})$	$\Delta G(\text{eV})$
100	1.14	0.70
110	1.04	0.64
111	1.51	1.05
211	0.97	0.59

The highest oxidizing power of the bud structured AuNF encouraged us to utilize this nanomaterial for AA sensing by utilizing electrochemical measurement techniques. The appearance of variable peak potentials at different concentrations and interpretation of the obtained result through the structural contribution of AA is quite interesting in terms of the intra- and inter-molecular hydrogen bonding¹³⁵ among themselves. At lower AA concentrations (**Figure 3.8A**) the peak potential appears at 0.345 V and the DPV curve at variable concentration is broad in nature. The current vs. concentration curve shows an exponential and linear growth type in the lower (4×10^{-5} to 4×10^{-8} M) and higher (10^{-3} to 10^{-4} M) range of AA concentrations respectively as shown in **Figure 3.8C** and **3.8D**. Single peak potential for AA oxidation can easily be explained by considering an intramolecular hydrogen bond to facilitate the oxidation of AA to DHAA. At intermediate concentration range (10^{-4} to 10^{-5} M), a dual humped curve has been observed indicating a two-electron oxidation of AA. As the concentration of AA increases and reaches above mM concentration, the distance between AA molecules reduces to allow both intramolecular and intermolecular hydrogen bonding to show an additional peak at 0.24 V origination from AA-dimers along with the original peak potential at 0.345 V due to the AA oxidation through intramolecular hydrogen bonding trajectory. The two-electron oxidation of AA is clearly shown in **Figure 3.8B** where one peak potential arises at 0.24 V and another one

at 0.345 V. At a very high concentration of AA ($>10^{-3}$ M), the peak potential shifts further to lower potential at 0.20 V indicates much faster oxidation. Thus, quantitative and qualitative fingerprinting of AA can easily be done from the prescribed electrochemical measurements.

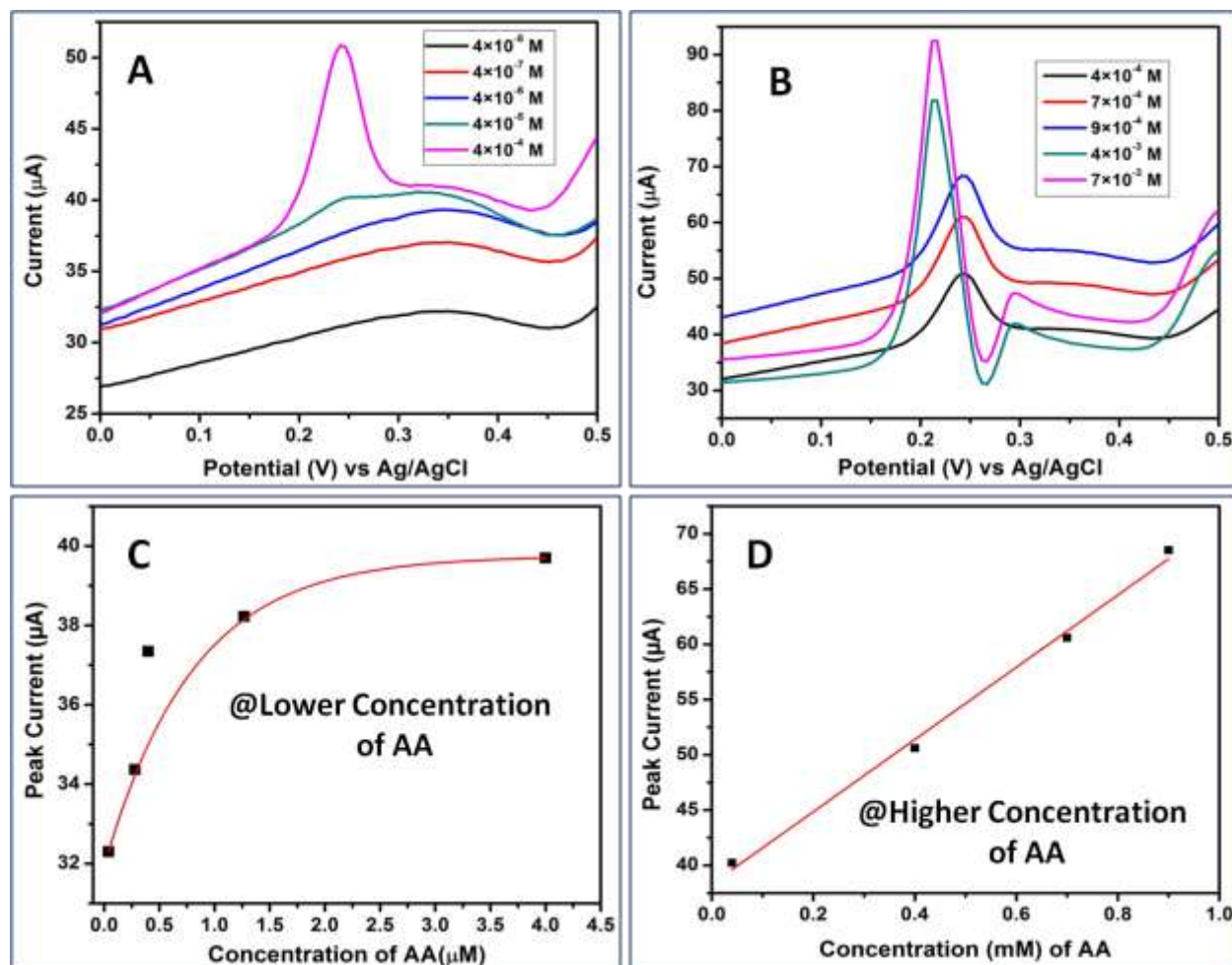


Figure 3.8: (A) DPV of AA at lower concentration level (4×10^{-5} to 4×10^{-8} M), (B) DPV of AA at higher concentration level (10^{-3} to 10^{-4} M), (C) The exponential growth of peak current at a lower concentration of AA, and (D) The linear variation of peak current at higher concentration of AA.

To understand the mechanism of AA oxidation in the molecular level, we have studied their redox reaction on a few atom gold clusters by using Density Functional Theory.^{120–122}

Using this quantum mechanical analysis we have obtained the optimized geometries of the

monomer, dimer, and the gold complexes of L-ascorbic acid (AA) as shown in **Figure 3.9a** and **3.9b**. Whereas the electron densities in the highest occupied molecular orbital (HOMO) and lowest unoccupied molecular orbital (LUMO) of the gold cluster complex with monomer and dimer of AA are shown in panel A and B of **Figure 3.9a** and **3.9b** respectively. The vibrational frequencies of the first O-H bond stretching in monomer as well as in the intermolecular hydrogen-bonded dimer were monitored in presence of increasing number of gold atoms and the changes are plotted in **Figure 3.9c** whereas the changes in the O-H bond lengths are shown in **Figure 3.9d**. O-H bond weakening was observed in monomer (bonded to Au through either H or O atom of AA) as well as in the dimer of ascorbic acid in presence of Au. In monomer, O-H stretching frequency was decreased by around 300 cm^{-1} , thus, facilitating the deprotonation process. Intermolecular hydrogen bonding also weakens this OH bond^{136,137} and the decrease in the stretching frequency was about 400 cm^{-1} . Au cluster was found to further decrease the stretching frequency by 300 cm^{-1} . Therefore at higher concentration AA, the presence of gold cluster reduces the OH stretching frequency up to 700 cm^{-1} effectively. Alternatively, at higher concentrations where ascorbic acid molecules remain hydrogen-bonded, oxidation occurs more easily in the presence of gold as we have observed experimentally. Experimentally we have observed that the peak potential for AA oxidation shifted from 0.345 V at very low concentration (4×10^{-5} to 4×10^{-8} M) to 0.24 V at an intermediate concentration (10^{-4} to 10^{-5} M) and finally shifted to 0.205 V at very high concentration ($>10^{-3}$ M) of AA. This directly provides the true mechanistic explanation behind the electrocatalytic oxidation of AA.

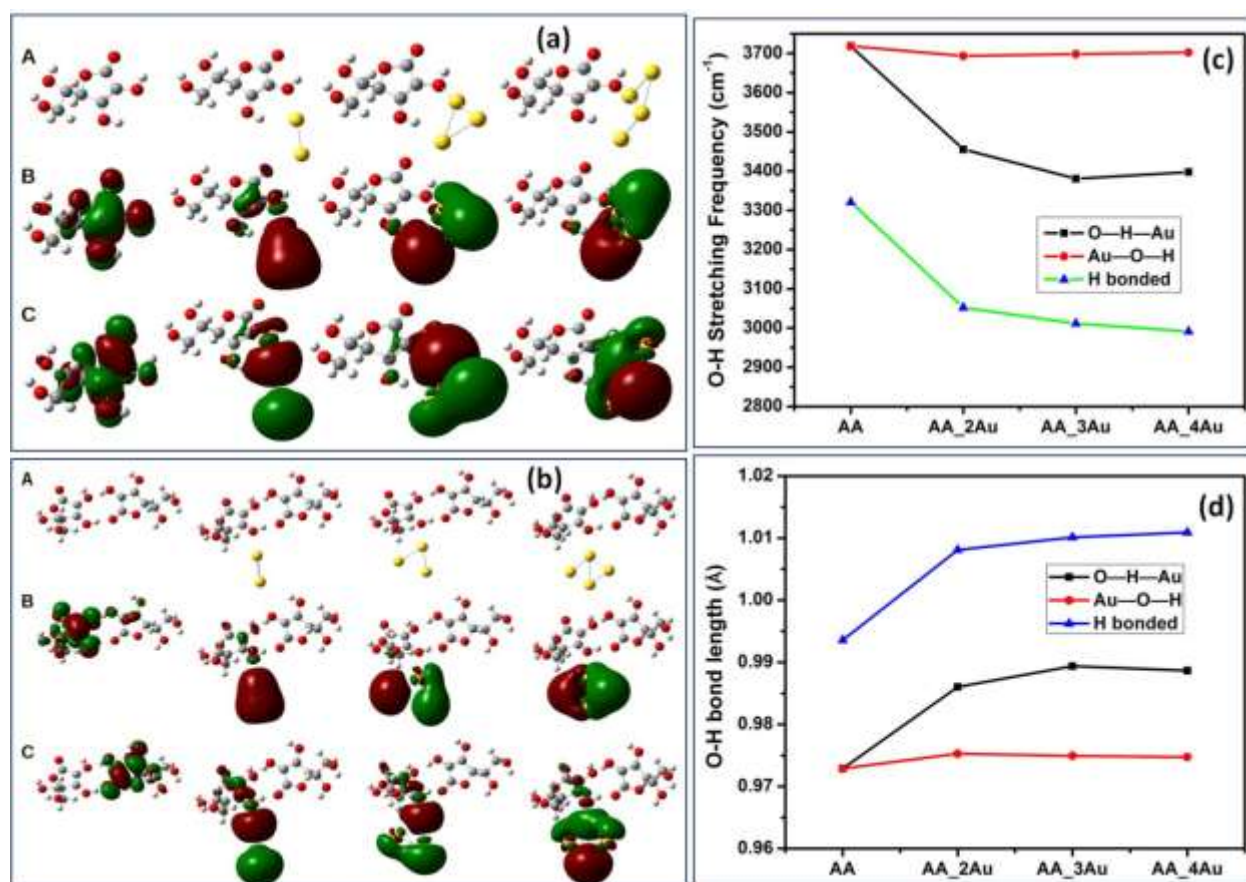


Figure 3.9: Optimized geometries and the electronic distributions of ascorbic acid monomer (a) and dimer (b) in the presence of gold. (A) Optimized geometries of ascorbic acid (monomer or dimer) and its gold complexes. (B) HOMO/SOMO of the respective complexes. (C) LUMO of the respective complexes. (c) Changes in the stretching frequency and (d) the bond length of the first OH group in L-ascorbic acid (AA) in presence of increasing number of Au atoms (two to four).

Based on the high catalytic activity of the bud structured AuNF and from the complete understanding about their mechanism of action along with molecular and crystal level driving forces for its enhanced activity, we encouraged to use this bud shaped AuNF structure for ultra-low sensing of AA in presence of other closely related biological components^{138,139} like DA, UA, and Glucose. The DPV response (**Figure 3.10A**) of bud shaped AuNF modified GC electrode at

the equimolar mixture of biological components show clear individual peaks for the respective components with unchanged peak position (0.245 V for AA, 0.41 V for DA, 0.535 V for UA and 0.63 V for glucose) for each element. As the peak potential for individual components is well separated from each other, in a single potential sweep we can identify all the available components in a multicomponent pathological sample. From the DPV response, we have constructed the calibration plot (**Figure 3.10B**) for all four components during the simultaneous detection of these species. This detection methodology holds true for those components which do not interact with each other to produce another component in the mixture of analytes.

The main criteria of a successful sensor is to show a linear variation of the identifiable and measurable quantity (here peak current) with concentration. It is clear from **Figure 3.10** that the peak current for individual components in a test sample shows a linear variation in a physiologically viable concentration range. Moreover, all the components can easily be identified in a single potential sweep from a multicomponent pathological sample. Hence, the bud structured AuNF has the unique potential to use it as an efficient electrocatalytic sensor for pathological sensing.

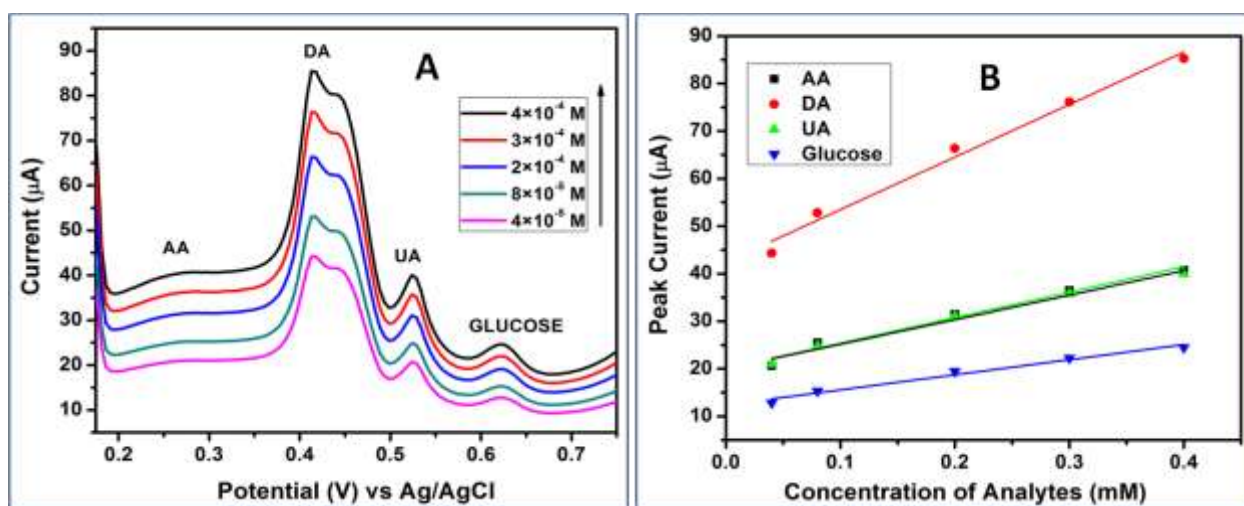


Figure 3.10: (A) DPV at a variable concentration of an equimolar mixture of AA, DA, UA, and Glucose. (B) A linear fit of peak current for individual components at a variable physiological concentration range.

3.6 Conclusion:

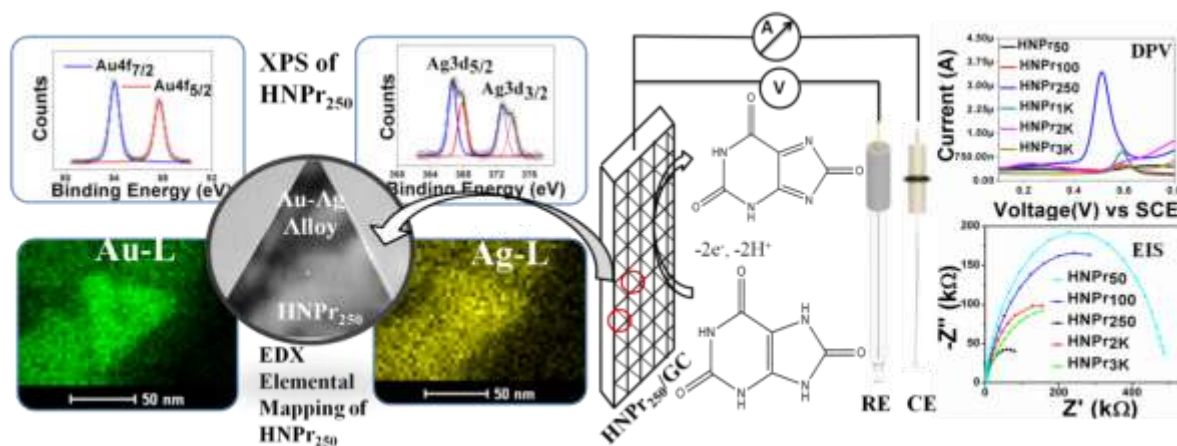
The DPV response and EIS data for the oxidation of AA clarify that there is a strong correlation between the electro-catalytic activity and the extent of crystal defect density (nm^{-2}) of different AuNFs. The defect density on nanocrystals has been calculated from the recorded HRTEM measurements by considering all possible defects originated during their growth. Among various controlling factors, the crystal defect density plays a crucial role in determining the superior catalytic ability. The bud shaped AuNF shows superior catalytic activity in comparison with other AuNFs due to the presence of the highest crystal irregularity on its surface. Moreover, bud shaped AuNF shows the effective fingerprinting ability of AA in the presence of other closely related compounds in a multi-component pathological sample. Besides, the role of different crystal facets [$\{111\}$, $\{100\}$, $\{110\}$, and $\{221\}$] on the catalytic performance of AuNFs has been explored by calculating the reaction free energy (ΔG) using computational hydrogen electrode (CHE) model on VASP platform which is consistent with our proposed mechanism. Variation of peak potential for AA oxidation at different concentration range has been demonstrated using DFT by considering their intramolecular (monomer) and intermolecular (dimer) interaction in the presence of different sized Au clusters. The fingerprinted peak potential and linear fit of peak current for individual components (AA, UA, DA, and glucose) at variable physiological concentration prove the ability of the bud shaped AuNF as an efficient electrocatalytic sensor for multicomponent pathological sensing.

CHAPTER-4

Zone-Specific Crystallization and a Porosity-Directed Scaling Marker for the Catalytic Efficacy of Au-Ag Alloy Nanoparticles

OUTLINE: Specific Points of Discussion

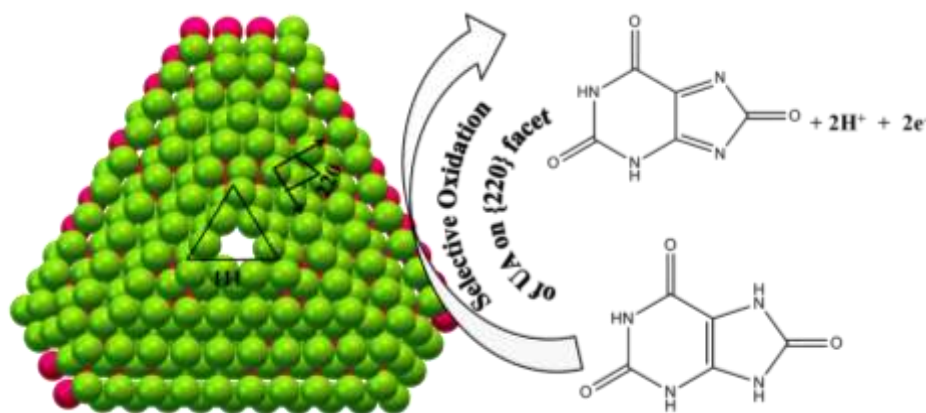
- Modified seed-mediated growth followed by the sacrificial galvanic replacement method has been adopted to synthesize Bimetallic Au-Ag hollow nano prisms (HNPr) with variable effective surface area, dynamic atomic composition (Au: Ag), and distinct stepped surface between the central porous region and crystalline periphery.
- The role of numerous low coordinated crystal defects along with extended d-orbital spacing in the central cavity region of HNPrs to control their adsorption efficiency for different redox reactions has been explored in detail.
- The presence of high-density grain boundary with preferable Au^0 : Ag^0 ratio in HNPr₂₅₀ helps to form an extensive porous ligamentous central cavity and accelerate the kinetics of the Uric Acid (UA) oxidation for their nM detection.
- Experimental observations have been supported by DFT calculation to approximate the effective Au-Au displacement in explaining their catalytic activity.



4.1 Introduction:

In this chapter, we have synthesized different bimetallic Au-Ag hollow nanoprisms and checked their catalytic activity through electrochemical oxidation of uric acid. Irregularities or defects of nano-crystalline materials differentiate them in novel properties from their bulk counterparts.¹⁴⁰ Alloying of noble metal induces a plethora of unknown and unexplored properties of nanomaterials which include superconductivity¹⁴¹, superparamagnetism¹⁴², highly stressed nanoscale materials to generate reactive oxygen,¹⁴³ etc. Besides these properties, the alloying of noble metal nanoparticles is believed to be one of the most crucial factors to generate defects like grain boundary, dislocations, etc. which drastically alters the catalytic property along with various Physico-chemical properties viz., mechanical strength (which include tensile strain, compressive strain, etc.) and toughness of the material.¹⁴⁴ It has been reported that nano-crystalline materials having grain boundary (GB) rich surface is effective for CO reduction¹⁴⁵ with high turnover frequency. Additionally, another controlling factor that enhances the catalytic property is the presence of multiple twin boundary (MTB) defects which are exposed to high energy facets.¹⁴⁶ The active site of a heterogeneous catalyst can be considered as a direct collection of atoms which can be introduced into the lattice by a high density of stacking faults and twin boundaries.¹⁴⁷ The multiple twinned gold nanoparticles supported on TiO₂ surface exhibit superior catalytic performance for CO oxidation than twin-free gold nanocrystals.¹⁴⁸ Similarly, polycrystalline gold nanoparticles (most probably with an enormous number of grain boundaries but not analyzed extensively) show the enhanced catalytic activity of UA oxidation¹⁴⁹. In addition, the planner defects e.g., stacking fault, dislocations, etc. originate during the crystal growth of gold nanostructures that are found to be effective for electrocatalytic oxidation of methanol¹⁵⁰. Out of a large pool of available mixed metal nanomaterials, Au-Ag

alloy nanomaterials draw special attention due to their similarity in lattice parameters (Au: 4.08 Å and Ag: 4.09 Å) to create most stable periodically folded atomic nanocrystals.¹⁵¹ Different strategies are reported and have been adopted to generate mixed metal nanomaterials either by adopting leaching methodology¹⁵² or selectively depositing on active sites.¹⁵³ Out of several different types of mixed metal nanostructures, designing specially engineered pseudo porous bimetallic nanomaterials is our target to generate novel materials that are expected to show the extraordinary catalytic property (along with several other exciting physical and chemical properties) contrary to their monometallic counterparts.¹⁵⁴ Schematic representation of two-electron oxidation of UA on Au-Ag alloy nanoprisms with the central porous cavity is shown in **Scheme 4.1**.



Scheme 4.1: Two electron electrochemical oxidation of uric acid on {220} facet of HNPr.

Origination of porosity during the growth of bimetallic Au-Ag nano-crystals constitutes various crystal imperfections¹⁵⁵ which are suitable for their enhanced catalytic activity. The low coordinated perimeter appears near the central cavity (or central porous moiety) of hollow nano prisms (HNPr) has been considered as the prime factor for generating active catalytic sites.^{156,157} It is believed that during the synthesis of nano-alloy (Au-Ag) Au-Ag alloy nanoparticles the residual Ag does not leach out (oxidation of Ag^0 seed by Au^{3+}) completely rather it segregate

defect sites (steps, kinks, etc.) and void spaces near the two metal interfaces (i.e., the central porous region of HNPr) due to the differential diffusion rates between two inter-diffusing atomic species (here inward flux of Au^0 from surrounding and outward flux of Ag^0 from the core) which creates a net vacancy flux through Kirkendall Effect.¹⁵ The appearance of Kirkendall voids in Au-Ag alloy nanoparticle is linearly dependent on tensile strain or stress. Tensile stress again tends to exaggerate the grain boundaries and creates more vacancies whereas compressive stress cements the grain boundaries by reducing the extent of void formation. Therefore it is necessary to find the chemical marker of void formation in Au-Ag alloy nanoparticles.¹⁵⁸ The presence of different oxidation states of Au (Au^0 , Au^+ (aurous) and Au^{3+} (auric)) and Ag (Ag^+ and Ag^0) and their extent in the interfacial central porous region of HNPr plays a key role in alloy nanoparticle formation.¹⁵⁹ The percentage of metallic (Ag^0 and Au^0) and oxidized (Ag^+ , Au^+ , and Au^{3+}) form of silver and gold in the individual nanoporous HNPr can be monitored through XPS and EDX spectrum and the ratio Au^0/Ag^0 can be considered as a chemical marker for the atomic origin of high catalytic activity of different HNPrs. The building of atomic segregation in the bimetallic heterophase junction (Au-Ag) through Kirkendall Effect may generate dislocation and d-band shifting which in turn enhances the activity towards various electrochemical redox reactions.¹⁶⁰ In our previous study, we have estimated the concentration of ascorbic acid (AA) by performing their electrochemical oxidation reaction on gold nanoflower (AuNF) surface and efficiently we could quantify different biologically active components like UA, dopamine (DA), AA and Glucose from a single pathological sample.⁴ Out of several components, UA shows the most prominent ion current peak in DPV response which encouraged us to consider it as the reference analyte to study the role of porosity induced tensile strain on a nanomaterial with minimal variation of crystal facets to influence their catalytic activity. Moreover, uric acid is a

biologically important compound that plays a crucial role in metabolism. The purine metabolic product uric acid (UA), when present at higher concentrations (hyperuricemia) in the blood may cause several ailments like cardiovascular disease, gout (a form of arthritis), kidney disease, heart disease,^{161–163}, etc. Though not very common it is also possible to have too little UA in our body which points out the initiation of liver and kidney disease. In general, we define this symptom as Fanconi syndrome,¹⁶⁴ a disorder of the kidney tubules that prevent the absorption of uric acid and rapid removal by urine to reduce the UA level in the blood to create hypouricemia. Hence the quantification (high or low level) of UA is crucial from the pathological screening point of view too. The normal uric acid level for a healthy female is 142–356 μM (2.4–6.0 mg/dL) and for a healthy male is 202–416 μM (3.4–7.0 mg/dL).^{165,166} Various analytical approaches like chemiluminescence,¹⁶⁷ spectrofluorometric,¹⁶⁷ enzymatic processes,¹⁶⁸, etc. have been reported for the quantitative detection of UA to micromolar (μM) level. However, electrochemical techniques are more preferable in this context on account of their ease of handling, cost-effectiveness, and higher accuracy level to avoid any false positive signaling. Electrochemical techniques like differential pulse voltammetry (DPV), Chronoamperometry (CA), square wave voltammetry (SWV) are powerful tools among others to carry out sensing of UA at physiological concentration level by modifying the bare electrode with polymers¹⁶⁹ (ethylene glycol, methacrylate, dimethylaminoethyl methacrylate, etc.) and biomaterials^{170,171} (norepinephrine, propionylcholine, etc). In the present study, we have examined the detailed structural analysis of seven different bimetallic Au-Ag HNPs and their catalytic activity towards the electrochemical oxidation of UA (**Scheme 4.1**) to figure out their structure-catalytic activity relationship. The modification of the bare glassy carbon (GC) electrode by adsorbing different bimetallic Au-Ag HNPs on their surface leads to efficient adsorption of UA and enhances the

electron transfer kinetics. Further, HNPr modified GC electrodes encouraged us for fingerprinting of UA upto nano-molar (nM) level within a limited time interval. The prominent role of the chemical marker (Au^0/Ag^0) in the mixed metal HNPrs for the increment of tensile strain was explained through DFT calculations as implemented in Vienna *Ab initio* Simulation Package (VASP).

4.2 Material Synthesis:

The synthesis of different HNPrs was carried out in the two-step seeding method. In the first step, 500 μL of 10^{-2} M ice-cooled freshly prepared $AgNO_3$ was added at a constant rate of 1 mL/min into 19 mL of Milli-Q (18 $M\Omega$ cm) water kept under constant rate (150 rpm) of stirring. After that, we have added 500 μL of 10^{-2} M ice-cooled freshly prepared trisodiumcitrate (TSC) at the same rate of 1 mL/min to the diluted $AgNO_3$ solution. Immediately after the completion of TSC addition, we have added 60 μL of 10^{-1} M freshly prepared ice-cooled $NaBH_4$ at a time and left the mixture undisturbed for 30 s before we turn off the stirring. The solution turns immediately into a bright and transparent bumblebee yellow color. The solution was then kept undisturbed in the dark for 2 h under open mouth condition to release out evolved H_2 gas from the reaction mixture.

In the second step, 0.5 g of CTAB was dissolved in 45 mL of water by 10 min sonication at 30 $^{\circ}C$. To this CTAB solution, maintained at 30 $^{\circ}C$, 2 mL of 10^{-2} M $AgNO_3$ was added at a constant rate of 1 mL/min under steady stirring condition. Next, 300 μL of 10^{-2} M ice-cooled $HAuCl_4$ was added to the above mixture at a constant rate of 1 mL/min. The color of the solution turns transparent yellow-brown. This was followed by a dropwise addition (1 mL/min) of 320 μL of 10^{-1} M ice-cooled ascorbic acid (AA) that changes the color of the solution from yellow-

brown to colorless due to Au(III) reduction. The stepwise addition of Au(III) and AA of the same respective volume are repeated for one more time with an additional rate of 2 mL/min. Quick or delayed addition of Au(III) than that of 2 mL/min in the second step may cause the loss of crystalline nature of our synthesized HNPrs and results in distorted structures with irregular shapes and sizes as shown in **Figure 4.1**. The porous ligaments in the central cavity region for different HNPrs were achieved through carefully maintaining the addition rate of gold solution (2 mL/min) and the time gap (~3 to 4 s) between Au(III) and AA into the reaction mixture.

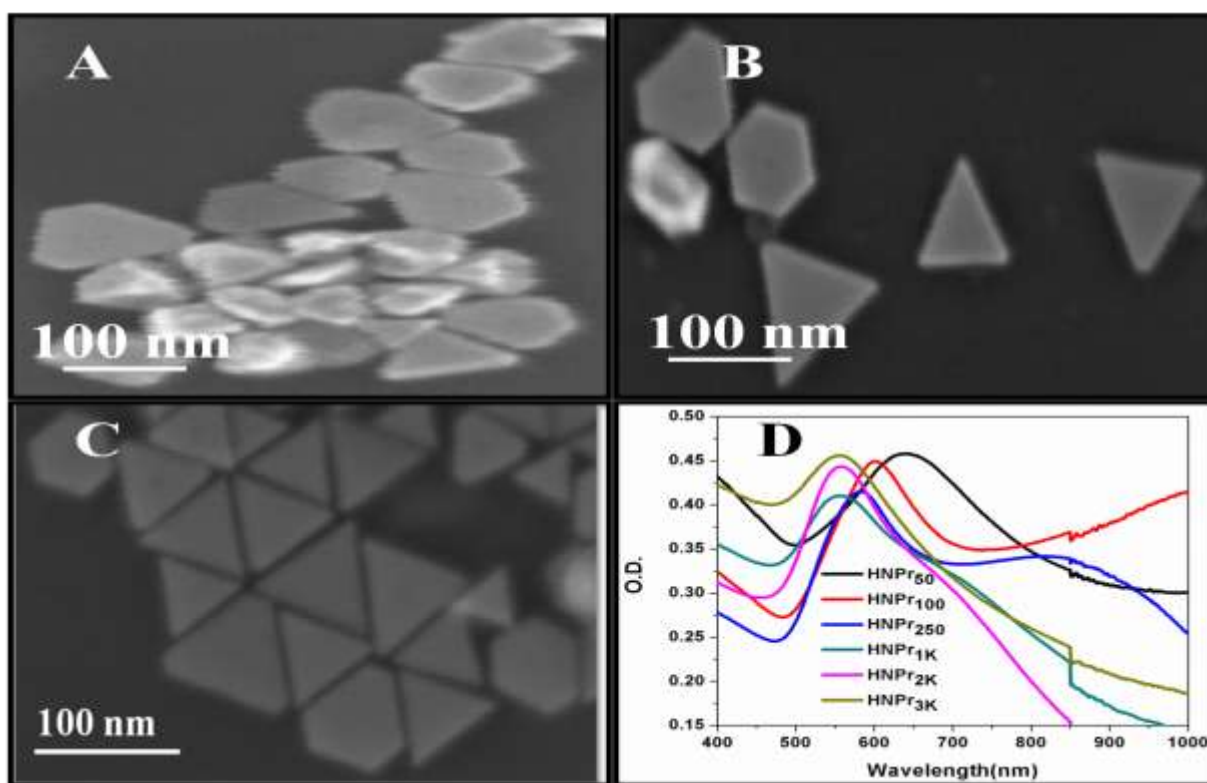


Figure 4.1: (A), (B) and (C) SEM images of HNPr₂₅₀ with HAuCl₄·3H₂O addition rate (second step of seeded growth) of 1 mL/min, 2 mL/min and 3 mL/min respectively. (D) Absorption spectra of different HNPrs.

Subsequently, a different amount (varying the amount between 50 μL and 3 mL) of pre-synthesized seed solution was added into the reaction mixture. Variation in the amount of seed solution led to the formation of various HNPrs with different edge lengths and porous cavity diameters. Synthesized HNPrs by using 50, 100, 250, 500, 1000, 2000, and 3000 μL of Ag seed are designated as HNPr₅₀, HNPr₁₀₀, HNPr₂₅₀, HNPr₅₀₀, HNPr_{1K}, HNPr_{2K}, and HNPr_{3K}, respectively. The plasmonic nature of individual HNPrs was confirmed from their UV-Vis-NIR spectra as shown in **Figure 4.1**. Throughout the synthesis, we have maintained the reaction temperature at 30 °C. We have observed that in absence of seed by using the same protocol does not produce any nanoprisms (rather produces arbitrary shaped colloidal particles with no regular size) which directly proves the necessity of the seed to form the nano prisms structure or in other words, indeed this is a seed-mediated synthesis.

4.3 Materials Purification:

After synthesizing; the cavity diameter, shape, and size variable HNPrs; we kept them overnight to complete their growth and stabilization. Size of HNPr₅₀ and HNPr₁₀₀ are so big that they become settled down by leaving unreacted ligands and precursors in the top solution which we have decanted to separate the nanoparticles. Separated nanoparticles (~1 mL) then diluted by 5mL Milli-Q water and centrifuge at 1000 rpm for 1.5 h whereas for other HNPrs which didn't settle down with time have been centrifuged for two times at different rates. Firstly, they are centrifuged at 2000 rpm for 1.5 h and then at 3000 rpm for 30 minutes. Finally, we have collected the centrifuged nanoparticles each with a total volume of 500 μL .

4.4 Theoretical Modeling of HNPr:

It is very difficult to construct a theoretical model for different HNPrs with variable Au:Ag composition because the introduction of Ag atom in the Au cluster will generate an infinite

number of possible structures. Here, initially, we have constructed some structure based on TEM images and XPS data (**Table 4.1**). We have constructed flat surfaces of HNPrs parallel to $\{111\}$ plane and faces having $\{220\}$ planes according to the previously reported work.¹⁷² We have simulated a series of different HNPrs (each one made by a total of 363 atoms) with different Au:Ag composition. We have varied the $\text{Au}^0\text{:Ag}^0$ compositions among different HNPrs as: HNPr_A (3.03:1), HNPr_B (2.45:1), HNPr_C (2.02:1), HNPr_{pureAg} (0: ∞) and HNPr_{pureAu} (∞ :0). These compositions cover the entire HNPr series as reported in **Table 4.1**. The primary motive behind the consideration of the above-mentioned compositions is to observe the effect of Ag impurity/doping on the pure Au clusters. For the geometrical optimization, we have used Generalized Gradient Approximation (GGA) and Perdew-Burke-Ernzerhof (PBE) functional as implemented in VASP for each Au:Ag composition. A gamma centered k-point was applied for the calculation and a force convergence criterion of -0.05 eV/\AA per atom was set to obtain the accurate bond-length between Au and Ag atoms. The PBE potential with the Methfessel-Paxton smearing method has been used to calculate the total energies.

4.5 Results and Discussion:

TEM analysis in **Figure 4.2** noticeably clarifies the formation of nano prism along with the appearance of hollowness at the center of the mass coordinate for each HNPr. It has been observed that the enrichment of Ag seed from 50 μL to 3 mL during synthesis leads to the linear increment of both the edge length between 150-25 nm and central porous cavity diameter between 1.5 - 11.5 nm. The TEM image of each HNPr (HNPr₅₀ to HNPr_{3K}) in **Figure 4.2** and the corresponding histogram in **Figure 4.3** proves that the synthesized HNPrs are highly monodispersed in nature. The HNPr₅₀ and HNPr₁₀₀ appear almost as two-dimensional triangles

(thickness <10 nm) with sharp edges (edge lengths are 150 and 102 nm respectively) and a tiny cavity at the center. Compared to HNPr₅₀ and HNPr₁₀₀, edges of the HNPr₂₅₀ (edge length: 105 nm) are much more truncated in nature (**Figure 4.2**).

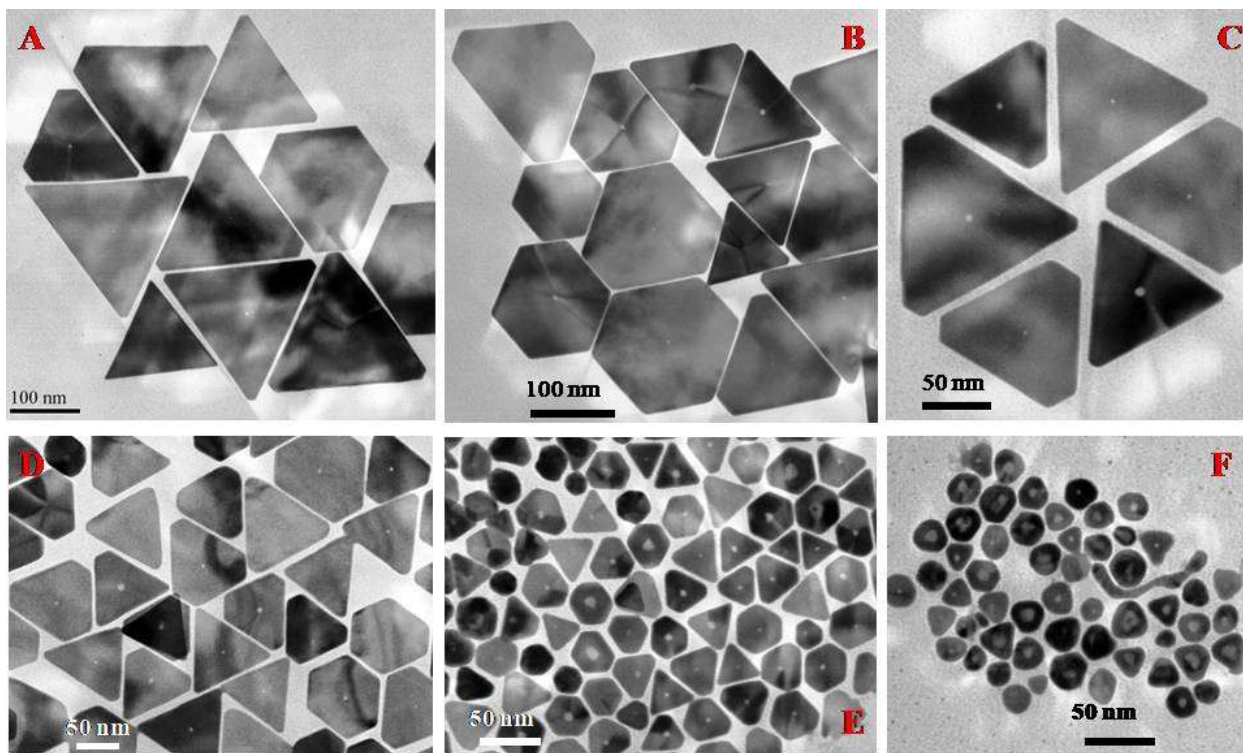


Figure 4.2: TEM image of individual HNPr synthesized by using a different amount of Ag seed. Here A-F represents the synthesized HNPrs by using 50 μ L, 100 μ L, 250 μ L, 1 mL, 2 mL and 3 mL of Ag seed and abbreviated as HNPr₅₀, HNPr₁₀₀, HNPr₂₅₀, HNPr_{1K}, HNPr_{2K}, and HNPr_{3K} respectively. Due to the structural similarity with HNPr₂₅₀, we have not included the TEM image of HNPr₅₀₀ in this figure.

Further distortion from the prism structure was observed for HNPr₅₀₀, HNPr_{1K}, HNPr_{2K} (edge lengths are 102, 62 and 43 nm respectively) and a hollow sphere (diameter: 25 nm) appearance with a large cavity diameter around 11.5 nm for HNPr_{3K}. The role of Au(III) and the amount of

seed in controlling the size and crystallinity of the central cavity can be explained by considering the reduction potentials of the component redox systems ($\text{Au}^{3+}/\text{Au}^0$, Ag^+/Ag^0 , AA^{2+}/AA) present in the reaction mixture.

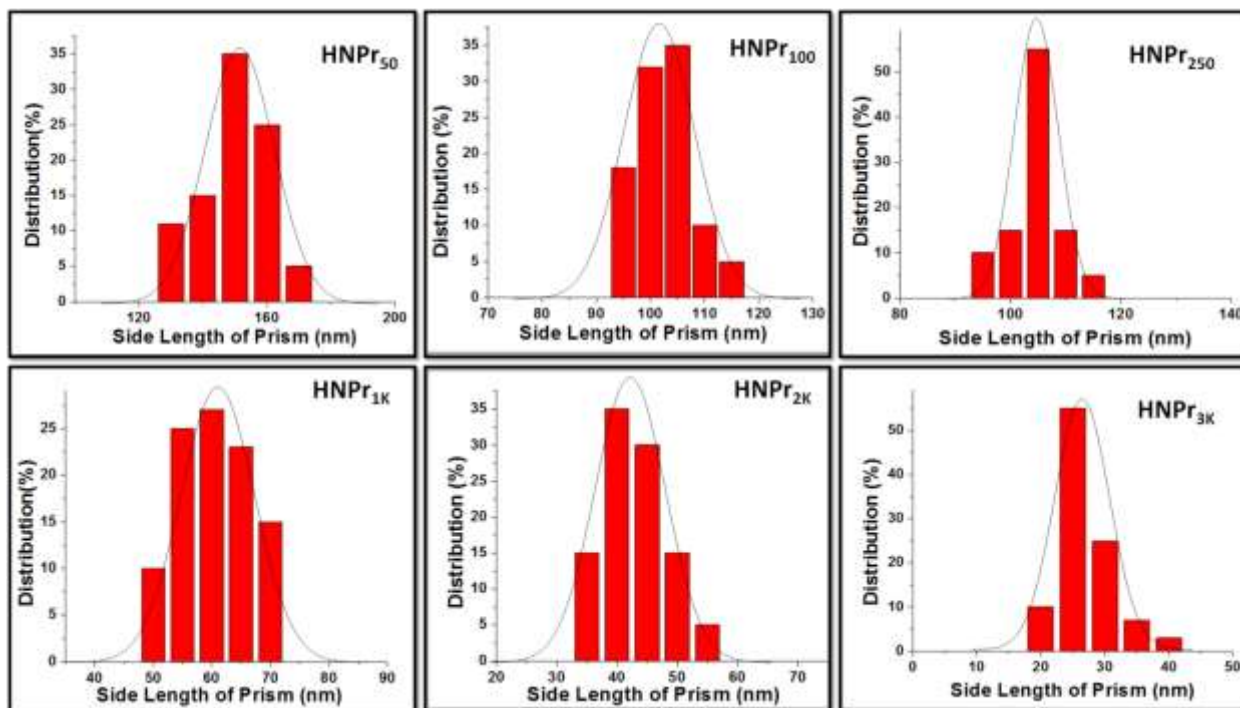


Figure 4.3: Histogram of size distribution for each HNPr. 100 TEM frames have been considered for each HNPr to calculate their average edge length.

Reported reduction potentials for $\text{Au}^{3+}/\text{Au}^0$, Ag^+/Ag^0 , AA^{2+}/AA are 1.5, 0.81, and -0.066 V (at pH:7) respectively.^{173,152} As explained before in our previous report¹⁷⁴ that the presence of Au(III) enhances the differential reduction potential of AA from 0.8 V (between Ag^+/Ag^0 and AA^{2+}/AA) to 1.5 V (between $\text{Au}^{3+}/\text{Au}^0$ and AA^{2+}/AA) which forces AA to acts as an efficient reducing agent and results in all the available AA being used in the reduction of Au(III) and Ag(I) to form seed-mediated alloy structure. When we add a little amount of seed then the volume to surface ratio i.e., $(\pi R^2 h)/(2\pi R^2)$ of the nucleation zone to accommodate all the Au^0 and Ag^0 into prismatic geometry should be very small compared to the total surface of the

HNPr and vice versa for a large amount of seed. Here we considered ‘R’ as the radius of the central cavity and ‘h’ is the approximate thickness (may vary due to stepped geometry) of the prism. Hence we should expect a gradual increment of cavity area with the amount of added seed and matches well with our observed result. Moreover, when the nucleation zone is made by one or fewer nanoseeds the active crystal facets of seed can contribute more accurately in the crystallization to generate sharp edged HNPrs compared to a large collection of nanoseed as the nucleation centre. During seeded crystallization if there is any residual Au(III) leftover in the system then only it will try to contribute in the galvanic replacement reaction from the seed surface to result the amorphous nature of the central cavity. Depending on the relative ratios of Au^{3+} , Ag^+ and Ag^0 the extent of the resultant porous nature varies for different HNPrs. It is clear from our study that the crystalline central core (as nucleation centre) for individual HNPr gradually changes to amorphous porous cavity and the extent of porosity has been measured by recording their time dependent TEM image. TEM based growth kinetics and the associated porosity development in the central core for HNPr₂₅₀ is shown in **Figure 4.4**. Analysis of the HRTEM images through digital micrograph software along with XRD measurements and SAED pattern confirms the presence of high energy facets $1/3\{422\}$ and $\{220\}$ on each HNPr surface (**Figure 4.4, 4.5, and 4.6**). The thermal vibration of reduced coordination sites (steps, kinks, etc.) strengthens the average vibrational amplitude of vicinal surfaces ($1/3\{422\}$ and $\{220\}$). As a result, excess vibrational entropy of vicinal surfaces is much higher than that of low index $\{111\}$ surface.^{175,176} Thus, low coordinated atomic sites are considered to be chemically more active than that of close-packed Au-Ag surfaces (1st order *fcc* surfaces) and these defects stimulate the emergence of internal lattice strain.^{146,177}

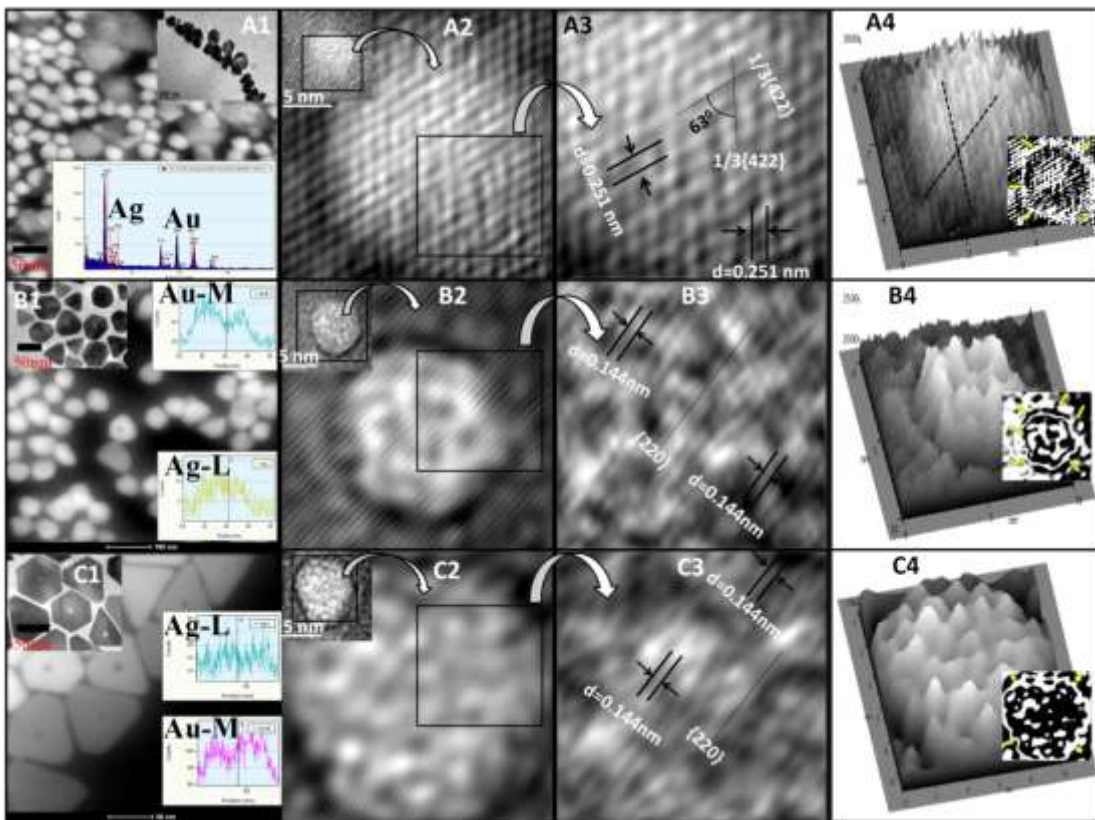


Figure 4.4: TEM images of time-dependent (A: 10 min, B: 1 h and C: 6 h) porosity generation at the center of gravity of HNPr₂₅₀. Porosity has started to develop after 1 hr and reaches a maximum after 6 hr. (A1), (B1) and (C1) are time variable HAADF-STEM images with their respective EDX line profiles; (A2), (B2), (C2) are IFFT images of HNPr₂₅₀ after 10 min, 1h and 6 h of synthesis; (A3), (B3) and (C3) are the zoomed version of the selected area on respective porous cavities; and (A4), (B4) and (C4) is the surface plot of (A2), (B2) and (C2) respectively to clarify the degree of porosity change with time whereas the contour plot is given as inset to identify the boundary between porous and crystalline surface of HNPr as marked by the yellow-colored arrow. Though at the beginning (10 min) of the HNPr growth there is only one active crystal plane i.e., $1/3\{422\}$ which has two different orientations with an internal angle of 63° , after 1 hr a new $\{220\}$ plane appears in the central cavity and the $1/3\{422\}$ plane disappears completely after 6 hr.

The lattice strain (compressive or tensile) in the nanocrystal leads to fluctuating different mechanical properties by modifying their energy band structures.¹⁷⁸ Although the $1/3\{422\}$ plane is forbidden, the appearance of this plane in the bimetallic Au-Ag plate-like structure has been reported earlier and this creates stacking faults laying parallel to the $\{111\}$ facets.¹⁷² In our synthesized HNPrs, we found that each HNPr contains the $1/3\{422\}$ plane both on the crystalline surface area as well as the central cavity area except for HNPr₂₅₀ where the $1/3\{422\}$ plane is missing in the central porous region. We have crosschecked the presence of $1/3\{422\}$ and $\{220\}$ planes along with $\{111\}$ plane in different HNPrs by performing their XRD measurements and verified it from JCPDS data as mentioned in **Figure 4.6**. Unfortunately, the S/N ratio for the recorder XRD plot is quite low and that could be due to high SAXS (small-angle X-ray scattering) background from the CTAB molecules and also the glass substrates at the low angle regime. To keep the nanostructures intact we could not wash the nanoparticles beyond two times as further washing could destroy the particles and results in very weak diffraction peaks. Here the important point is the peak position corresponding to $1/3\{422\}$ and this is also a supportive data to the strong evidence observed from HRTEM and SAED patterns. Collecting data over a quite long time may improve the SNR a little but this will not significantly improve the data quality. Moreover, as we know the errors in counts in scattering experiments follow the Poisson distribution and that results in little improvement in noise even if we collect data for a long time unless the peak is quite strong or data has been taken in much stronger x-ray source like x-ray synchrotron sources. The origin of the $1/3\{422\}$ peak is the stacking fault lying parallel to the $\{111\}$ surface and hence supposed to be very weak compared to the $\{111\}$ peak as observed in **Figure 4.6**.

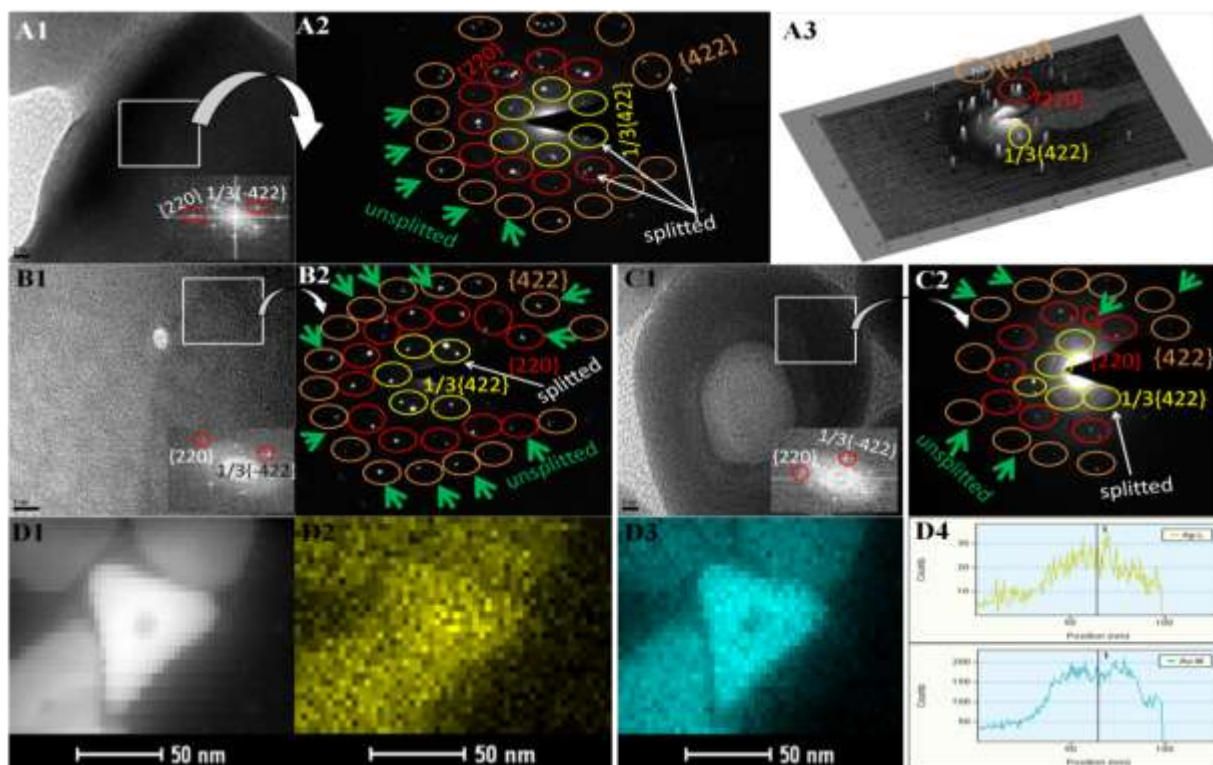


Figure 4.5: (A2) is the SAED pattern of HNPr_{250} as marked by the white-colored square box in (A1) whereas corresponding FFT is given as inset to show the existence of $1/3\{422\}$ and $\{220\}$ and $\{422\}$ facets. All the diffraction spots in (A2) either along $1/3\{422\}$ or $\{220\}$ facets are completely splitted and some are unsplitted along $\{422\}$ as marked by the green color arrow. (A3) is the surface plot of (A2) which shows a better representation of splitted diffraction spots. (B2) and (C2) represents the SAED pattern from HNPr_{100} and HNPr_{3K} whereas (B1) and (C1) is the corresponding TEM images of HNPr_{100} and HNPr_{3K} respectively. Here diffraction spots are not completely splitted as we marked them unsplitted along $\{220\}$ and $\{422\}$ facets and indicates that these structures contain less number of twin boundaries compared to HNPr_{250} along $\{220\}$ and $\{422\}$ planes. (D1) represents drift corrected STEM image for line profile; (D2) and (D3) is the EDX elemental mapping of Ag-L and Au-M respectively to clarify the distribution of Ag and Au over HNPr_{250} surface; and (D4) confirms the Ag-L and Au-M line along the EDX line profile.

Though the spectra are bit noisy, still there is a clear sign of the peak for the $1/3\{422\}$ in the XRD pattern as the other two stronger peaks are clearly visible for all the three different HNPrs in **Figure 4.6**.

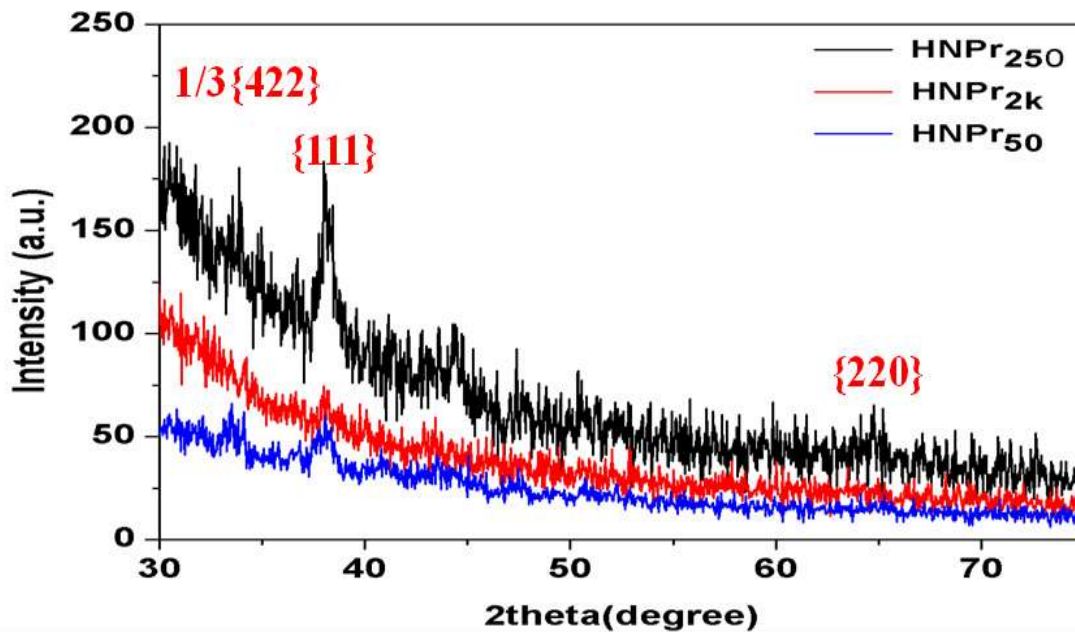


Figure 4.6: XRD pattern of HNPr₅₀, HNPr₂₅₀, and HNPr_{2K}.

So strong evidence in HRTEM and SAED pattern along with XRD (supportive) we think the existence of $1/3\{422\}$ is quite clear. Besides the signature of different planes from XRD data, we have calculated the generated strain along different planes from their respective line shapes (obtained 2θ) as shown in **Figure 4.7** specifically for $\{111\}$ facet. Recorded XRD pattern in **Figure 4.6** confirms the presence of $\{111\}$ at $2\theta \approx 38.25^\circ$, $1/3\{422\}$ at $2\theta \approx 34.00^\circ$, and $\{220\}$ at $2\theta \approx 65.00^\circ$ facets in HNPr₂₅₀, HNPr₅₀ and HNPr_{2K}. The broadening of the XRD curve in HNPr₂₅₀ at $\{111\}$ crystal facet ($2\theta \approx 38.25^\circ$) compared to that of HNPr₅₀ and HNPr_{3K} is owing to the lattice strain, which arises due to the (i) prevention of motion of dislocation from central porous region to the crystalline periphery by grain boundary (ii) appearance of Kirkendall voids during replacement of

Ag⁰ by Au³⁺ and (iii) various crystal irregularities. The strain (ϵ) within HNPr can be calculated through the Williamson–Hall isotropic strain model and represented by:

$$\epsilon = \beta_{\epsilon} / 4 \tan \theta_{hkl} \dots \dots \dots (1)$$

where $\{hkl\} = \{111\}$ in this case and β_{ϵ} is full-width half maxima⁴ for the diffraction peak. We have calculated the strain from XRD data by applying the above equation and it follows the same order as observed for catalytic activity: HNPr₂₅₀ \approx HNPr₅₀₀ > HNPr_{1K} > HNPr_{2K} > HNPr_{3K} > HNPr₁₀₀ > HNPr₅₀.

In the case of HNPr₂₅₀, the strain (dimensionless, as it is a ratio of two length unit) calculation is given here. We have fitted the curve at $2\theta \approx 38.25^\circ$ for HNPr₂₅₀ which is shown below:

where $\beta_{\epsilon} = 0.8^\circ$ (at $2\theta \approx 38.25^\circ$)

By converting β_{ϵ} in radian we can write $\beta_{\epsilon} = 0.0139$ radian

Hence, the calculated strain for HNPr₂₅₀ by equation (1) can be expressed as:

$\epsilon = 0.0139 / (4 \times \tan 0.33) = .01 = 1 \times 10^{-2}$. For this equation, we have converted the θ into radian too.

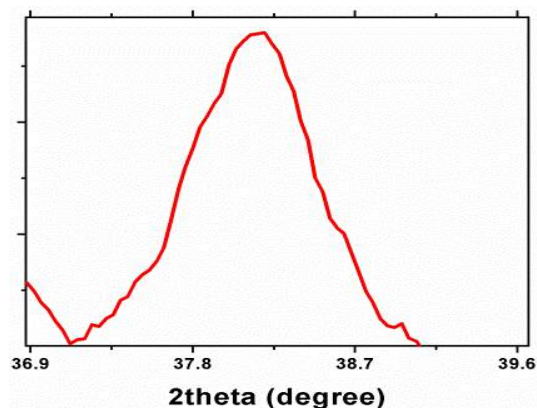


Figure 4.7: Fitted curve of XRD at $\{111\}$ facet to calculate the strain.

A similar curve fitting was carried out for other facets in the XRD curve like $1/3\{422\}$ and $\{220\}$. We then calculate the strain of each HNPr by taking the average of three fitted curves.

The EDX line profile of various HNPrs authenticates the bimetallic nature by confirming the existence of Ag-K, Ag-L, Au-L, and Au-M (**Figure 4.8a–4.8c**) lines. Besides that, we have

performed EDX elemental mapping (**Figure 4.5**) to show the presence of less amount of gold in the central porous region (a sudden dip of line profile in the central porous region) compared to the crystalline periphery in HNPr₂₅₀.

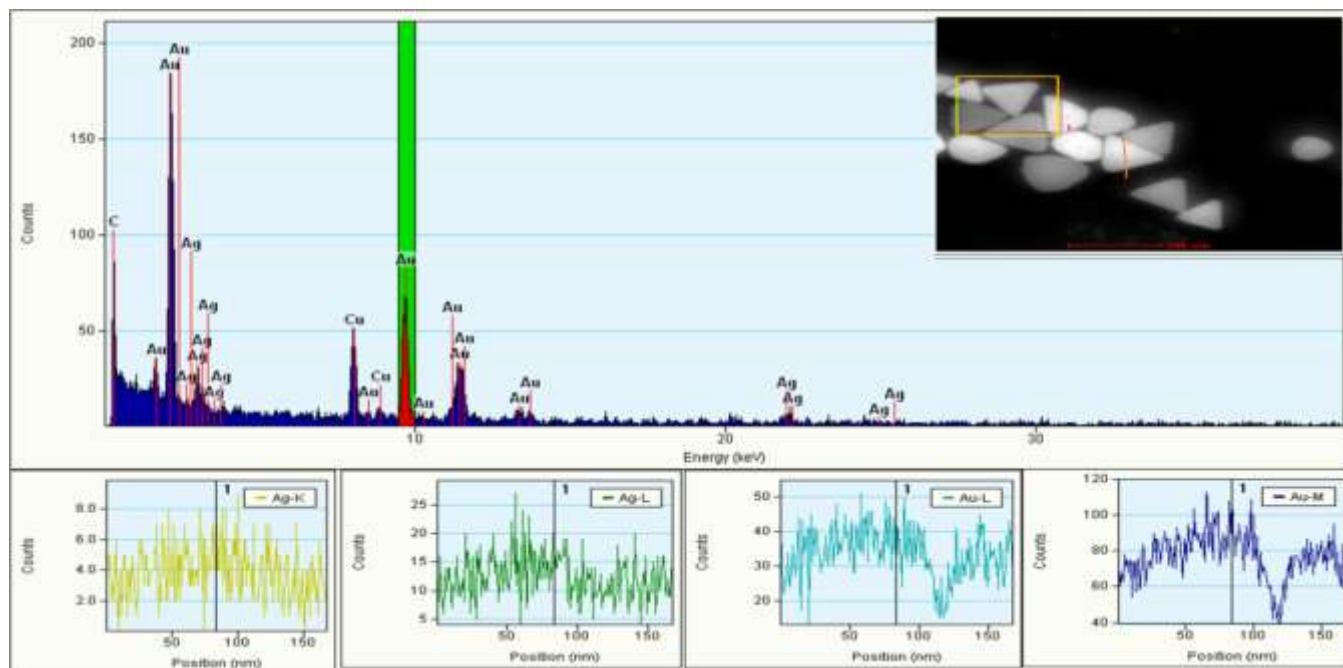


Figure 4.8a: EDX spectra and HAADF–STEM image of HNPr₁₀₀ for the confirmation of bimetallic (Au–Ag) nature.

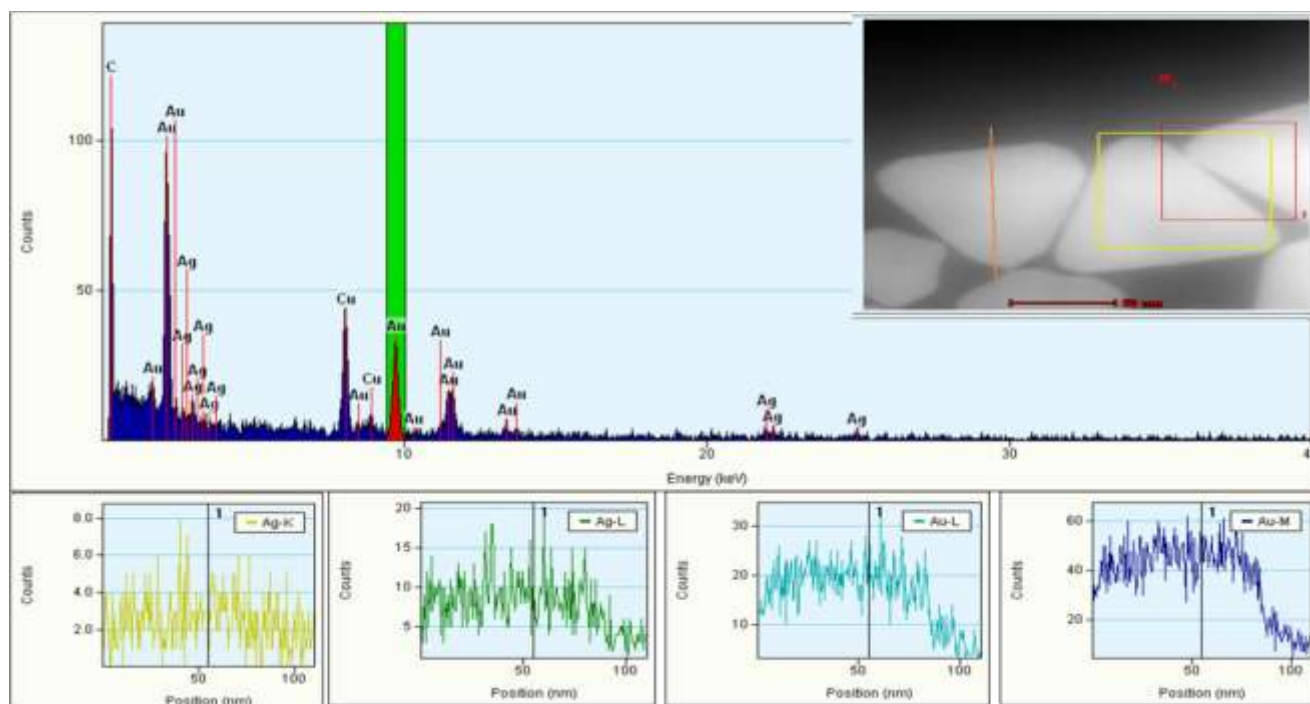


Figure 4.8b: EDX spectra and HAADF-STEM image of HNPr₅₀₀ for the confirmation of bimetallic (Au-Ag) nature.

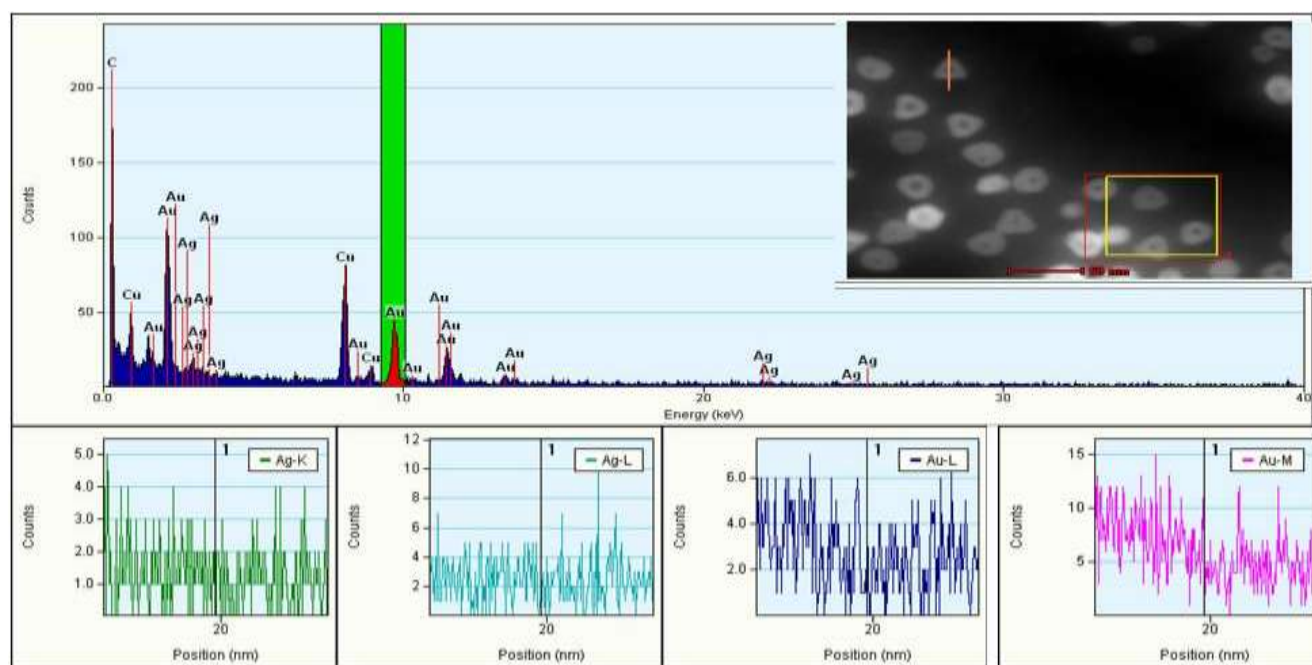


Figure 4.8c: EDX spectra and HAADF–STEM image of HNP_{r3K} for the confirmation of bimetallic (Au–Ag) nature.

Elemental composition in different HNPrs was also verified through ICP-OES and XPS analysis. ICP-OES measures Au and Ag concentration in *ppm* (mg/L) level which is well-agreed with our predictions (**Table 4.1**). As the amount of Ag seed increases from 50 μ L to 3 mL for synthesizing HNP_{r50} to HNP_{r3K}, the ICP-OES results show a gradual increment in Ag concentration while Au concentration remains almost the same. Since the ICP-OES measurements give the idea of total Ag ($\text{Ag}^0 + \text{Ag}^+$) concentration only, we have performed their XPS measurements to get precise knowledge about the ratio of oxidized silver (Ag^+) and metallic silver (Ag^0) in individual nanostructures. The fitted XPS curves of different HNPrs are given in **Figure 4.9** which clearly shows the presence of Au^0 , Ag^+ , and Ag^0 in HNP_{r50}, HNP_{r250}, HNP_{2k} with maximum splitting both for $\text{Ag}3d_{5/2}$ and $\text{Ag}3d_{3/2}$ peaks in HNP_{r250}. The absence of any splitting for $\text{Au}4f_{7/2}$ and $\text{Au}4f_{5/2}$ peaks indicates that the constituent gold atoms remain only in the metallic form (i.e., Au^0). Besides that, we have also noticed the presence of $\text{Br}^-(3d)$, $\text{Cl}^-(2p)$, $\text{N}(1s)$ and $\text{C}(1s)$ peaks in the XPS survey spectrum (**Figure 4.10**). The source of Br^- , N , and C is CTAB (during synthesis we use CTAB as a surfactant) whereas Cl^- comes from HAuCl_4 .

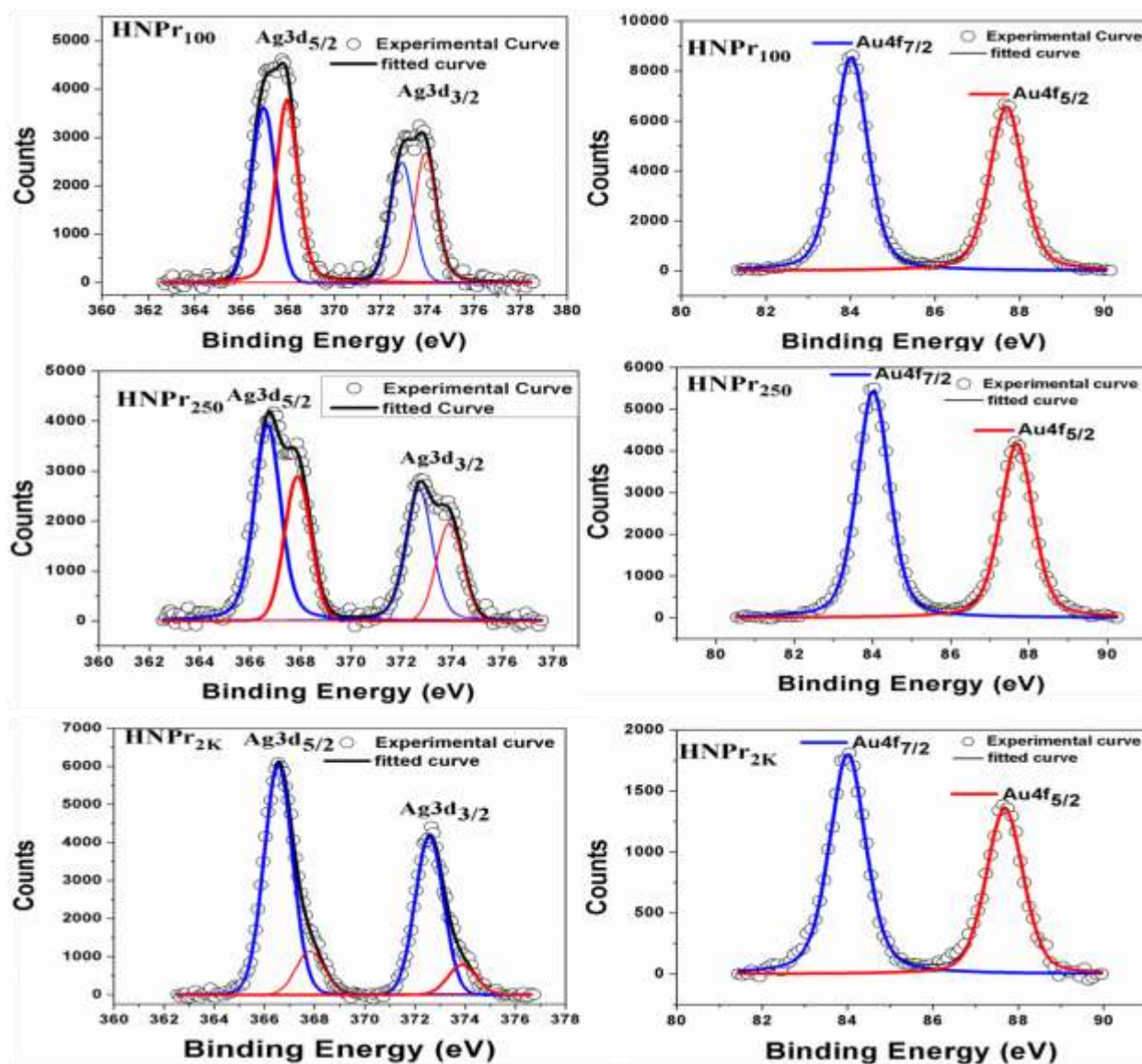


Figure 4.9: XPS study of HNPr₁₀₀, HNPr₂₅₀, and HNPr_{2K} nanostructures are shown in the top, middle and bottom panel respectively where the left and right figure in each panel corresponds to the XPS for Ag and Au separately. The Ag3d_{5/2} and Ag3d_{3/2} splitted in each HNPr and confirms the presence of ionic (Ag⁺) and metallic (Ag⁰) form, however Au present only in the metallic form i.e., Au⁰. The fitted blue curve in XPS for silver indicates the extent of Ag⁺ whereas the red curve indicates the % of Ag⁰. In the case of gold XPS, both the blue and red curves indicate the relative abundance of different spin-orbit states (Au 4f_{7/2} and Au 4f_{5/2}) of Au⁰ only.

Quantitative analysis of XPS (**Figure 4.9**) results for $\text{Ag}3d_{5/2}$ and $\text{Ag}3d_{3/2}$ peaks indicate that Ag^+ concentration is highest (80% Ag^+ and 20% Ag^0) for HNPr_{2K} which gradually falls to 61% and 48% for HNPr_{250} and HNPr_{100} respectively (**Table 4.1**). The observed core-level binding energies for most transition metals shift towards higher binding energies whereas silver is one such exception that shows lower binding energy in the oxidized state.¹⁷⁹ Though the Ag^+ in the central core region of HNPr is counterbalanced by Br^- from CTAB and stabilizes the low coordinated atomic sites, the relative abundance of Ag^0 over Ag^+ plays a crucial role to govern their differential porosity. According to Pauling's table, electronegativity for Au^0 is higher than that of Ag^0 .

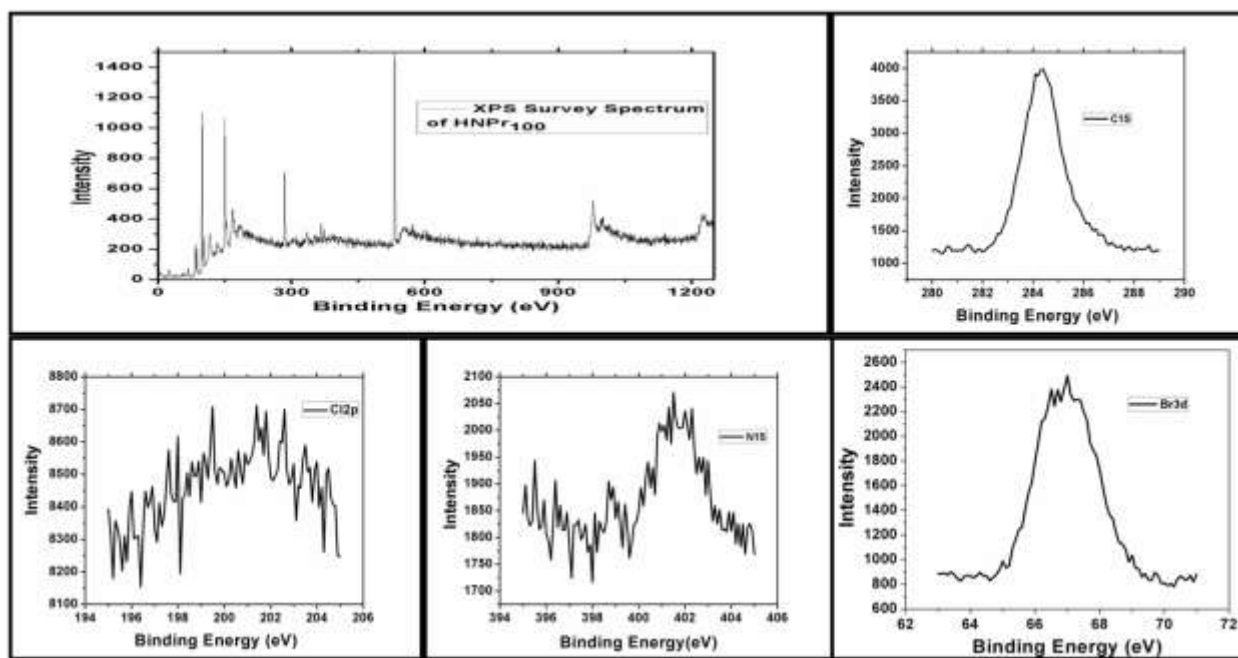


Figure 4.10: XPS survey spectrum of $\text{Cl}(2p)$, $\text{C}(1s)$, and $\text{N}(1s)$ in HNPr_{100} which confirms their presence in the sample.

By considering their minimal difference in lattice parameters, an intermediate ratio between Au^0 and Ag^0 (Au^0/Ag^0) can be defined as an ‘indicator’ to quantify their relative alloy

nature. The value of the ‘**indicator**’ ranges between ∞ and 0. A higher and lower value of the ‘**indicator**’ implies that HNPr contains more Au and Ag character respectively. Therefore the value of 2.42 for Au^0/Ag^0 in HNPr_{250} (**Table 4.1**) which appears as an intermediate value between 2.75 for HNPr_{50} and 1.83 for HNPr_{3K} can be considered as the suitable ‘**indicator**’ for alloy formation by transferring part of electron cloud from silver to the adjacent gold atom.¹⁸⁰ A shift towards the lower energy binding site for Au $4f_{5/2}$ in HNPr_{250} (Au $4f_{5/2}$ peak appears at 87.65 eV for HNPr_{250} whereas in case of pure gold it is 87.70 eV, however, due to the large distribution of Au^0 over Ag^0 on the crystalline HNPr surface, we are unable to get any signature of peak shifting in Au $4f_{7/2}$) proves the above fact of electron cloud transfer. Besides, the shifting of Ag $3d_{5/2}$ peak for Ag^0 in HNPr_{250} (367.85 eV) can be considered as a signature of alloy formation as Ag $3d_{5/2}$ appears at 368.3 eV for pure metallic silver (Ag^0). We have depicted earlier that silver is one such exception where lower binding energy is observed at higher oxidation state and hence we can get a crystal clear picture from the above fact that some electron cloud has been transferred from Ag^0 to Au^0 by forming a heterogeneous metallic network of the type $\text{Ag}^{\delta+}-\text{Au}^{\delta-}$. The $\text{Ag}^{\delta+}-\text{Au}^{\delta-}$ network creates zigzag porous ligaments in the central cavity of HNPr_{250} . In the case of HNPr_{100} and HNPr_{2K} the Ag $3d_{5/2}$ peak appears at 367.98 eV and 368.0 eV, which indicates less electron cloud transfer from metallic silver to metallic gold and thereby less probable for alloy formation.

It is evident from **Figure 4.11** that the porous ligaments are appearing gradually from HNPr_{50} and become prominent in HNPr_{100} which finally reaches a maximum for HNPr_{250} . The interconnected ligaments in the central cavity of HNPr_{250} developed in a zig-zag pattern which creates nanosized hollow space in between them. To understand the change in porous nature of the central cavity region of our synthesized HNPrs, we have performed the surface plot, HRTEM

and FFT (**Figure 4.11**) of the central porous region for four different cases (HNPr₅₀, HNPr₂₅₀, HNPr_{2K}, and HNPr_{3K}) which shows the transition in crystallinity in their corresponding HRTEM.

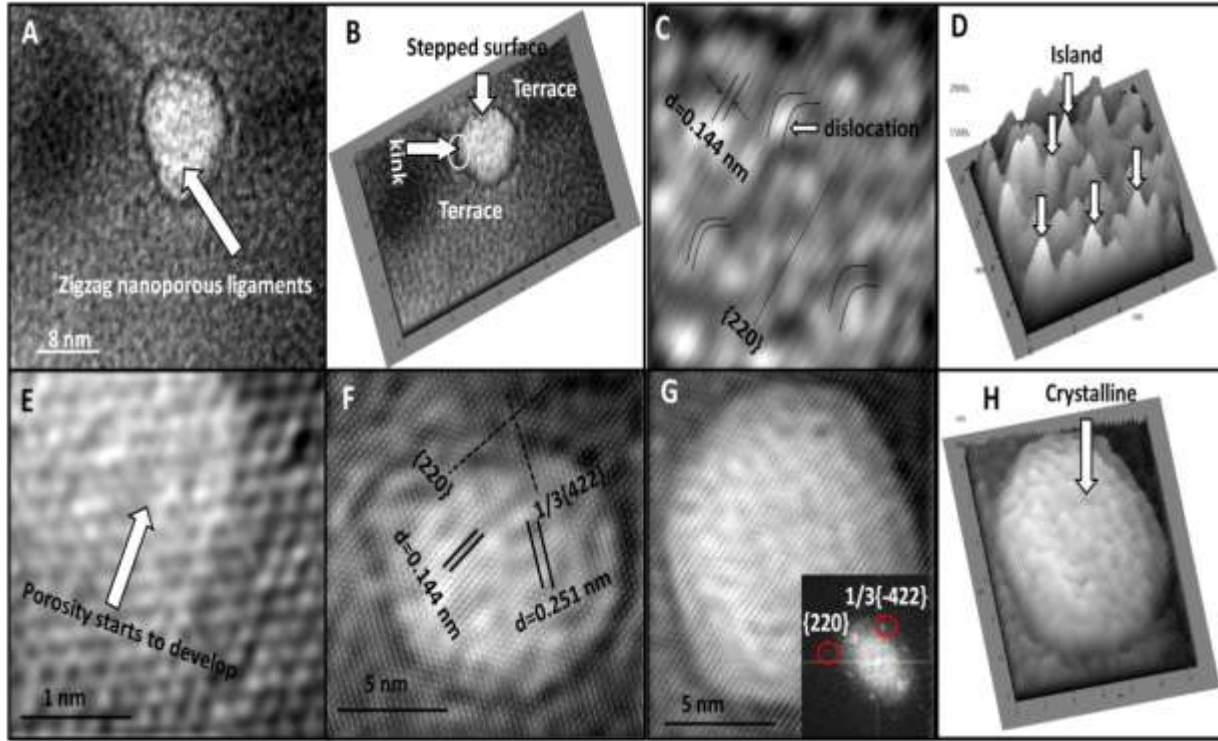


Figure 4.11: (A) is the TEM image of the central porous cavity of HNPr₂₅₀ where nanoporous ligaments have been observed. (B) is the surface plot to show the stepped surface along the cavity region whereas (C) is the corresponding HRTEM image to show the presence of {220} plane only (absence of 1/3{422} plane) in the central porous zone of HNPr₂₅₀ and (D) is the corresponding surface plot to highlight the existence of multiple islands in porous cavity region. (E) and (F) is the HRTEM images of the central cavity area of HNPr₅₀ and HNPr_{2K} respectively where we have shown how the porosity starts to develop in HNPr₅₀ and the coexistence of 1/3{422} and {220} planes in HNPr_{2K}. In (G) we have shown the FFT of HNPr_{3K} whereas (H) is the corresponding surface plot. Comparison of (D) and (H) show how the multiple low

coordinated islands are disappearing and crystalline structure appearing in the central cavity zone of HNPr_{3K}.

It is also clear from **Figure 4.11** that the atomic density in the porous cavity region is minimum for HNPr₂₅₀ which gives its plastic nature. The porous ligaments have a significant number of low coordinated atomic sites (kink, terrace, stepped surface, atomic islands, etc.). Interestingly, the porous nature is found to be reduced gradually from HNPr₂₅₀ to HNPr_{2K} and completely disappears for HNPr_{3K}.

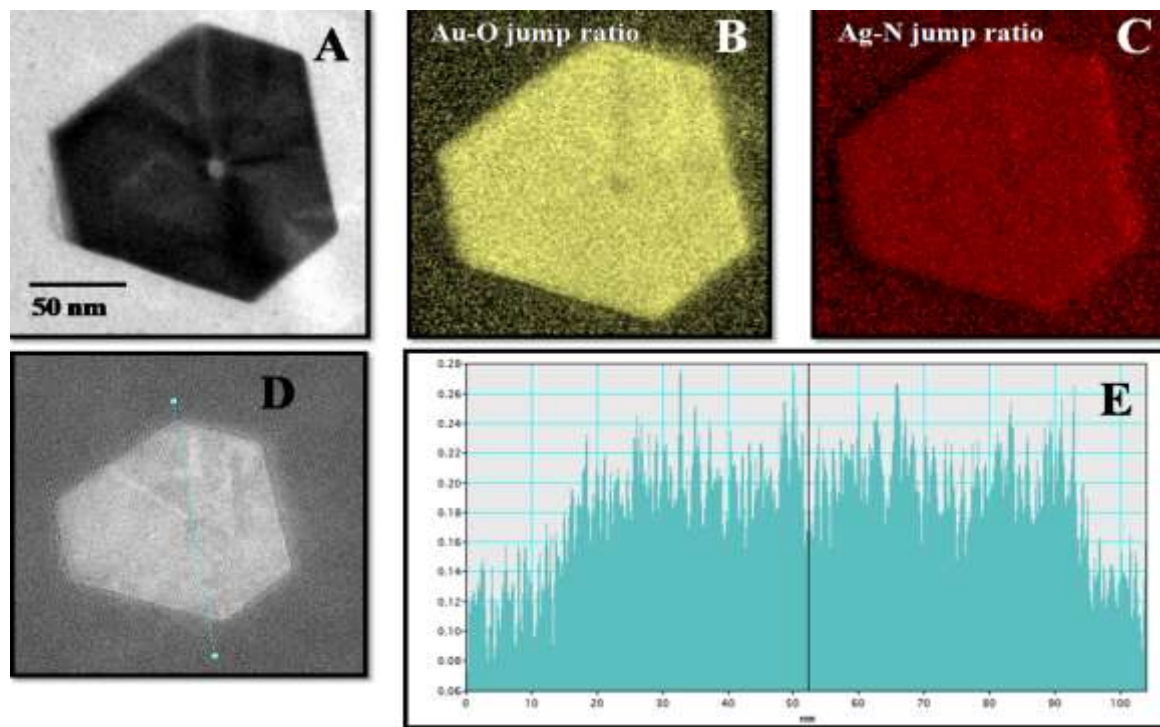


Figure 4.12: Thickness, as well as elemental mapping of HNPr₂₅₀ where (A) shows the TEM image of a single HNPr₂₅₀, (B) & (C), are the elemental mapping for Au and Ag respectively and the dark region in the central cavity region of Au mapping proves the presence of Ag in large extent compared to Au, (D) high annular dark field image of the single HNPr₂₅₀ with a scanning line through the central cavity in the green line, and (E) the corresponding thickness profile for opposite edge-to-edge 100 nm scanning.

Figure 4.11 clearly shows a pure crystalline nature of the central cavity region for HNPr_{3K}. The extent of porosity in different HNPrs can be explained through Kirkendall voids formation during galvanic replacement of Ag⁰ (nano seed) by Au³⁺. It is clear from **Figure 4.4** with time progression, a collection of voids has started to appear at the central cavity zone of HNPr₂₅₀. These voids accelerate the outward diffusion rate of Ag⁺ and grow spontaneously until a cage-like structure achieved¹⁸¹. As mentioned before, along with their porous nature, the thickness of the central cavity is different from their crystalline periphery to generate a stepped geometry. To show the stepped geometry at the central cavity we have performed the thickness profile for different HNPrs and specifically for HNPr₂₅₀ is shown in **Figure 4.12**.

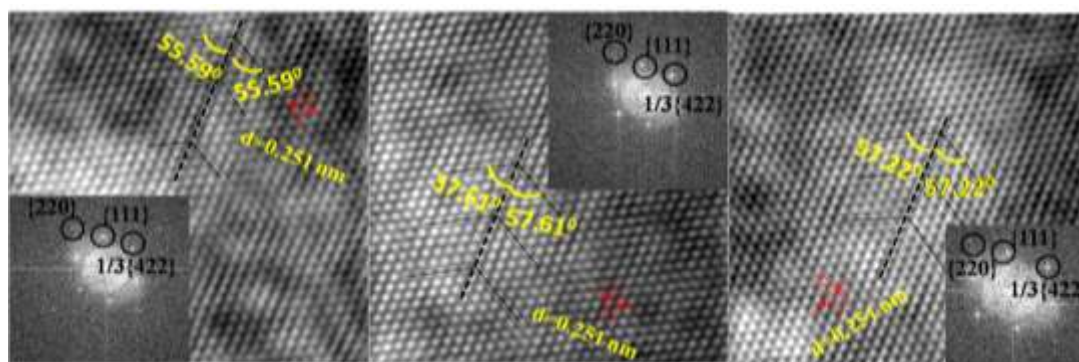


Figure 4.13: Representative twin boundaries on the HNPr₂₅₀ surface, spotted in three different zones outside the central cavity zone. The twin angle (concerning the twin boundary) varies in the range of 55–57°.

Our synthetic method is novel enough so that we can reach an optimized value of Au⁰/Ag⁰ to achieve maximum porosity at the center. During our synthesis, we have used a variable amount of Ag seed ranging from 50 µL to 3000 µL by keeping all other parameters constant and thereby we get different Au⁰/Ag⁰ for individual HNPr with different a rate of mass diffusion between Au and Ag for controlled voids formation. In HNPr₂₅₀, we can get a standard value of Au⁰/Ag⁰ to generate maximum voids which constitute porous ligaments and increases the lattice

mismatch.¹⁸² Besides, the lattice mismatch creates multiple reduced coordinated crystal irregularities on the crystalline HNPr surface (away from the central cavity regions). The splitted diffraction spots indicate the presence of multiple twin boundaries on different HNPr surfaces (**Figure 4.5**). Representative twin boundaries on the HNPr₂₅₀ surface are shown in **Figure 4.13**. Due to the nonplanar nature, the atoms situated on the twin boundary (TB) have less coordination number than the perfect crystal lattices and can be accounted for an active site for catalysis. According to the Fridel's theory¹⁸³ of four different twin types, the *fcc* crystal bears the signature with $\Sigma > 1$ and $\phi = 0$ where Σ is the inverse of the fraction of lattice sites common to the two components of the twin and ϕ (twin obliquity) is defined as disorientation of one crystal concerning the other. In the absence of axial chromatic aberration (Cc) or axial spherical aberration (Cs)-corrected HRTEM, the best characterization technique for identifying the presence of twin planes is the appearance of splitted diffraction spots. In the direct TEM images, the twin boundaries appear from translational interfaces because of the background intensity difference on the two sides of TB.¹⁸⁴ When the twin interface coincides with the mirror plane it is called coherent boundary. The mirror plane can be determined from the diffraction patterns and creates unsplit spots wherein the other reflections are splitted depending upon the distance from the common row. The HRTEM images and corresponding diffraction patterns in **Figure 4.5**, indicate that the diffraction spots are splitted for HNPr₂₅₀ however for HNPr₁₀₀ and HNPr_{3K} the diffraction, as well as XRD curve (**Figure 4.6**), does not show the desired splitting of diffraction spots to prove that HNPr₂₅₀ contains much more MTB compared to HNPr₁₀₀ and HNPr_{3K}. Besides TB, the low coordinated GB on HNPr₂₅₀ (**Figure 4.14** and **Figure 4.15**) surface plays a crucial role to create tensile stress within the alloy nanoparticle by retarding the motion of dislocation from central porous region to the crystalline periphery. HNPr₂₅₀ contains multiple

dislocations and is considered as one of the most active sites for heterogeneous catalyst. Recently it has been shown that twisted bismuth nanocrystals¹⁸⁵ containing lattice misfit and larger dislocation density is found to be much more active for CO₂ reduction than the corresponding dislocation deficit crystals.

Table 4.1: Compositional Analysis and current responses of different HNPr and HNPr modified GC electrode-based on EDX, XPS, ICP-OES, DPV, SWV measurements

System		HNPr ₅₀	HNPr ₁₀₀	HNPr ₂₅₀	HNPr ₅₀₀	HNPr _{1K}	HNPr _{2K}	HNPr _{3K}	Bare GC
Atomic composition	EDX	2.86	2.73	2.35	2.25	1.98	1.88	1.77	NA
	XPS	2.75	2.72	2.42	2.31	2.11	1.57	1.67	NA
Ag ⁺ /Ag ⁰	XPS	0.43	0.92	1.56	1.66	1.85	4	4.33	NA
Elemental composition	XPS	1.6	1.4	0.95	0.88	0.63	0.26	0.20	NA
	ICP-OES	1.49	1.29	1.01	0.93	0.58	0.33	0.25	NA
ξ (+mV)		55	61	74	71	69	69	68	NA
SGBD(nm ⁻²)		0.00035	0.0006	0.00287	0.0021	0.0018	0.0013	0.001	NA
Peak Current (μ A)	DPV	.48	0.51	3.44	1.21	0.92	0.64	0.53	0.41
	SWV	0.42	0.46	3.8	1.55	0.95	0.77	0.49	0.41
Peak Potential(V)	DPV	0.69	0.61	0.51	0.55	0.59	0.60	0.60	0.72
	SWV	0.64	0.64	0.53	0.55	0.59	0.62	0.62	0.71
i_p^{HNPr}/i_p^{GC}	DPV	1.17	1.24	8.39	2.95	2.24	1.56	1.29	NA
	SWV	1.02	1.12	9.26	3.78	2.31	1.87	1.19	NA

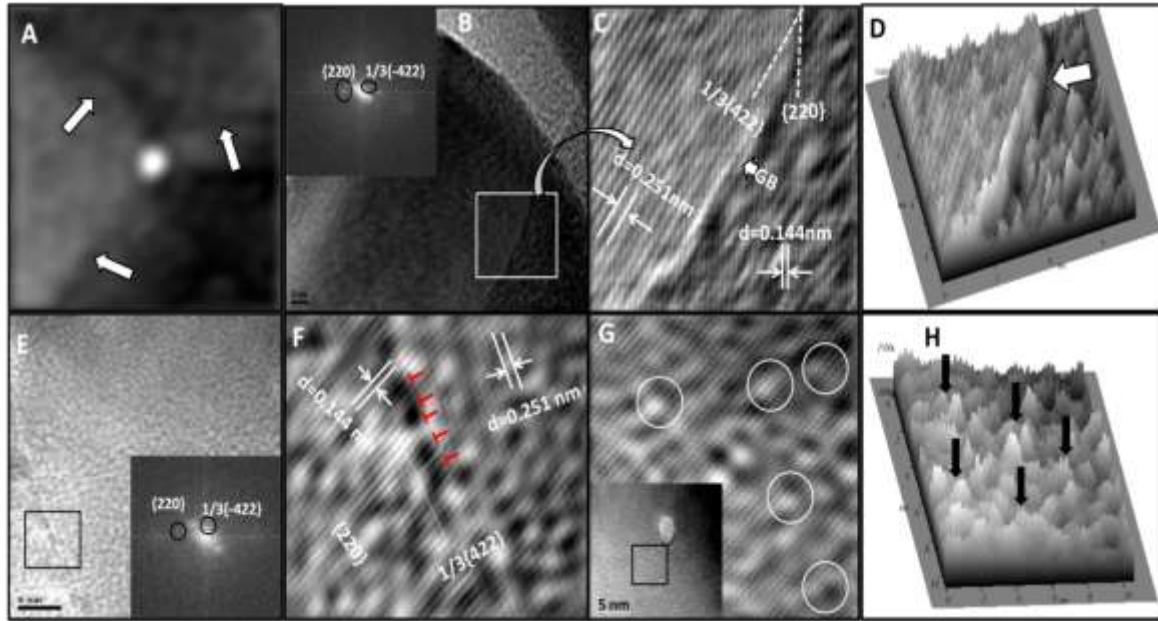


Figure 4.14: (A) IFFT of HNPr₂₅₀ to show the position of grain boundaries around the central cavity region of HNPr₂₅₀. (B) shows a specific GB over the HNPr₂₅₀ surface whereas (C) is the HRTEM of the marked square zone in (A). In (C) we have shown how a grain appears between two crystalline facets $1/3\{422\}$ and $\{220\}$ whereas the corresponding surface plot in (D) indicates the position of grain boundary as marked by the white-colored arrow. (E) is a dislocation enriched area over the HNPr₂₅₀ surface. The HRTEM of the marked square zone in (E) is shown in (F) where we have shown the position of dislocation(marked by reversed T) across the junction of $1/3\{422\}$ and $\{220\}$ planes. (G) is the HRTEM of HNPr₂₅₀ immediately outside the central cavity region in which we have detected multiple islands as marked by the white circles. (H) is the corresponding surface plot of (G) which signifies the islands are starting to create before entering into the porous regions. By comparing **Figure** (D) and (H), one can detect how the extent and pattern of crystallinity changing when we come across from the HNPr₂₅₀ crystalline surface to the central porous cavity.

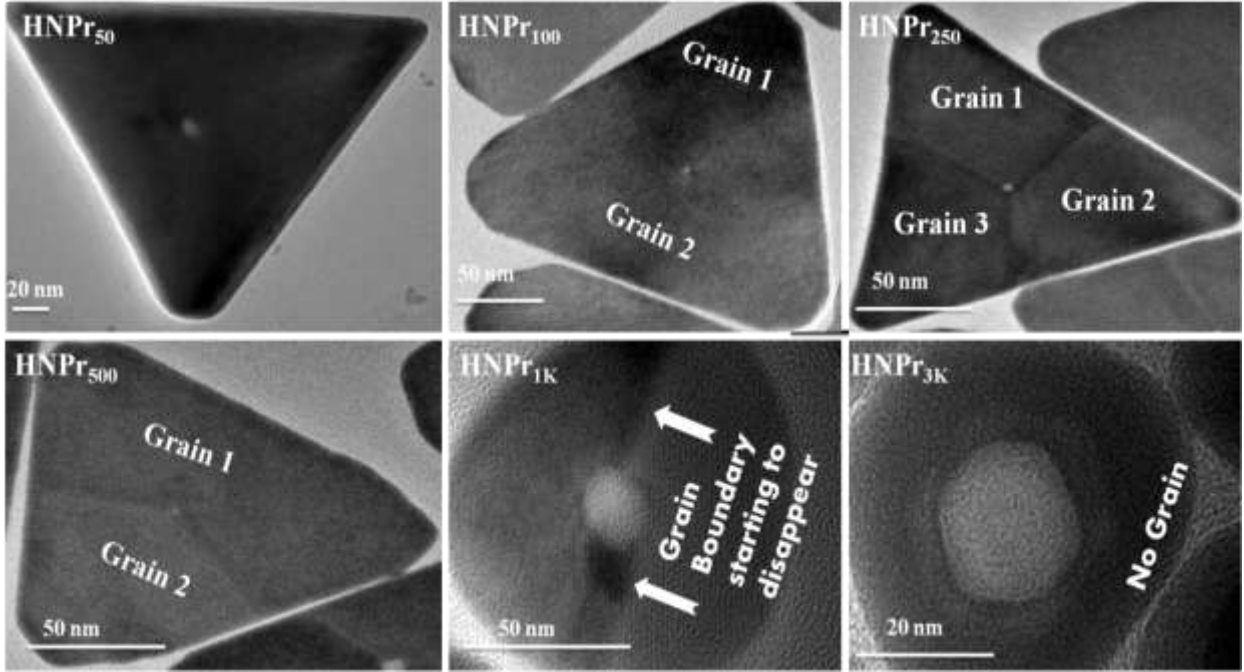


Figure 4.15. TEM images of the distribution of different grains over individual HNPr surface.

To accumulate a comprehensive study on surface GB density (SGBD) for the region surrounding the porous periphery, we have measured the SGBD for individual HNPrs (**Figure 4.16(a)**). For the statistical calculation of SGBD, we have selected different HNPr structures (**Table 4.1**) with at least 100 frames for each category as described details in **Figure 4.16(a)**. Characteristic SGBD (C_i) was measured by counting the number of GB (n_i) per unit area (nm^{-2}) in which the total area (A_i) is the surface area of the HNPr surface (calculated from the dimension off the HNPr as depicted in **Figure 4.16(b)**). SGBD of i 'th HNPr is formulated as

$$C_i = \sum_{i=1}^{i=100} n_i / A_i.$$

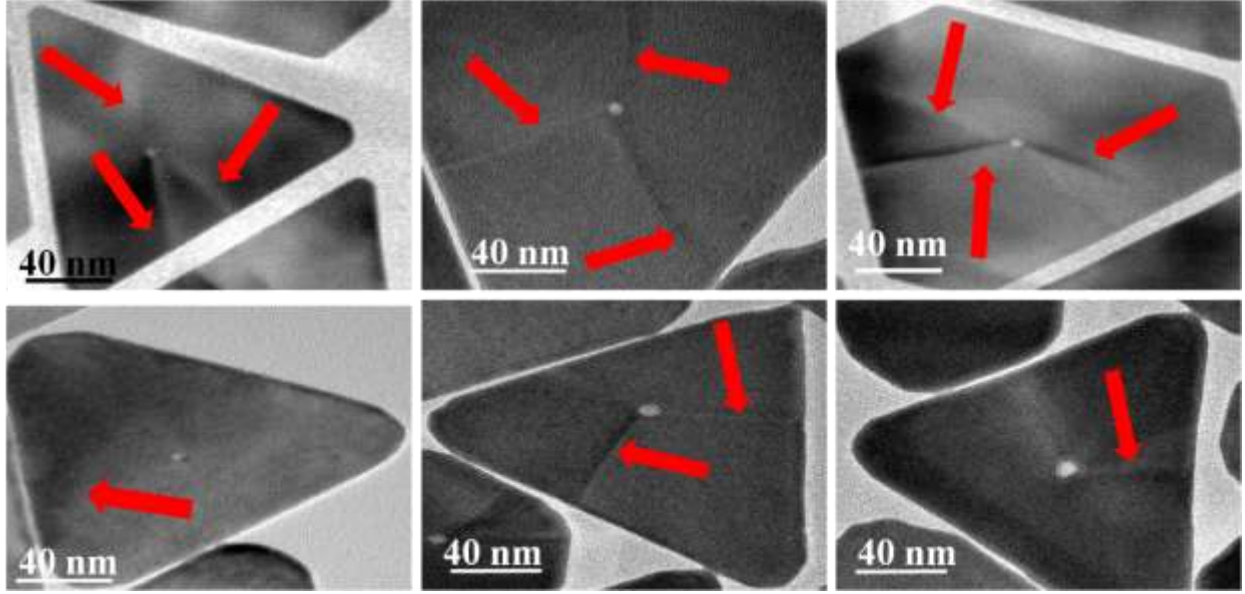


Figure 4.16(a): Presentation of different HNPr₂₅₀ frames for the calculation of Surface Grain Boundary Density (SGBD).

We have considered each HNPr as an equilateral triangle and central core as a sphere. Since there is no GB on the central cavity as we have discussed previously, the effective surface area is calculated by subtracting to the central spherical cavity area from the total HNPr area.

$$Ai = \frac{\sqrt{3}}{4} a^2 - \pi r^2$$

Where a is the side length of HNPr and r is the radius of the central cavity.

As an example,

For HNPr₂₅₀ (**Figure 4.16b**)

$$a \approx 105 \text{ nm and } r \approx 4.25 \text{ nm}$$

$$\begin{aligned} \text{So } Ai &= \left\{ \frac{\sqrt{3}}{4} (105)^2 - \pi * (4.25)^2 \right\} \text{ nm}^2 \\ &= 9491.18 \text{ nm}^2 \end{aligned}$$

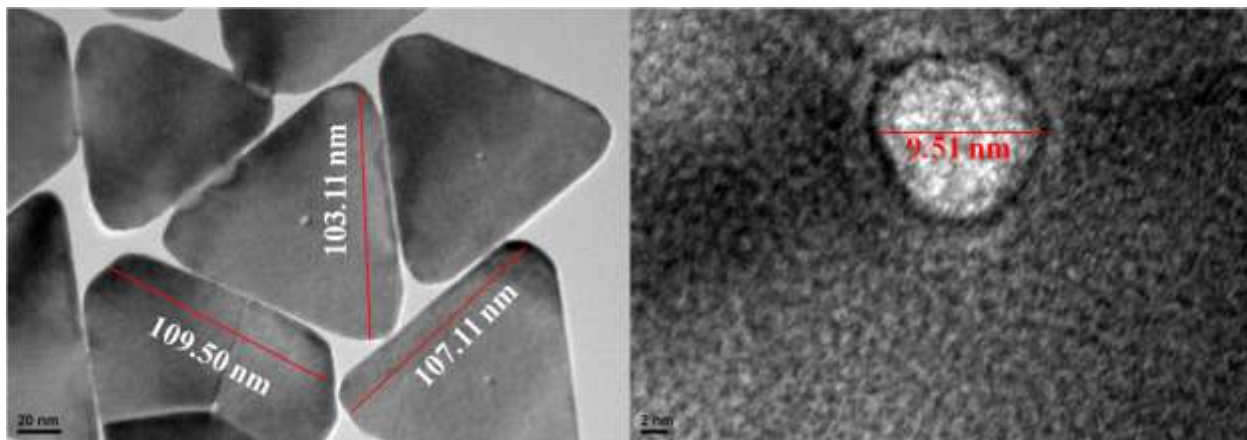


Figure 4.16(b): Edge length and cavity radius determination in HNPr₂₅₀ by using digital micrograph software.

So if we carry out the approximate calculation of SGBD according to **Figure 4.16a** by counting the number of GBs/ frame and carry out the calculation up to 100th frame,

It appears as:

$$C_i =$$

$$\frac{3}{9491.18} + \frac{3}{9491.18} + \frac{3}{9491.18} + \frac{1}{9491.18} + \frac{2}{9491.18} + \frac{1}{9491.18} + \dots \dots \dots +$$

$$\frac{3}{9491.18} \text{ (upto 100th term)}$$

$$= 0.00287 \text{ nm}^{-2}$$

Calculated C_i for individual HNPr perceptibly recognizes that the HNPr₂₅₀ has the maximum surface GB density with an estimated value of 0.00287 nm^{-2} as listed in **Table 4.1**.

The calculated C_i values (**Table 4.1**) have the following decreasing trend:

$$C_{\text{HNPr}_{250}} > C_{\text{HNPr}_{500}} > C_{\text{HNPr}_{1K}} > C_{\text{HNPr}_{2K}} > C_{\text{HNPr}_{3K}} > C_{\text{HNPr}_{100}} > C_{\text{HNPr}_{50}}$$

which is well-agreed with our observed catalytic power.

To investigate the catalytic activity of these HNPrs, the electrochemical oxidation of UA has been studied on the HNPr modified GC electrode (HNPr/GC). The DPV for the electro-oxidation of UA at bare GC electrode shows a poor voltammetric response in which the anodic peak potential appears at 0.72 V along with a lower peak current value of 0.41 μA (zoomed in the insets) as shown in **Figure 4.17A**. DPV and SWV response of the HNPr/GC electrode in $4 \times 10^{-5}\text{M}$ UA is depicted in **Figures 4.17A** and **4.17B** respectively where the peak potential (for the oxidation of UA) gets shifted towards the more negative region in comparison with bare GC electrode along with the enhancement in peak current. The decrease in peak potential and increase in peak current for various HNPr/GC demonstrates that different bimetallic HNPrs can act as efficient electrocatalysts for the oxidation

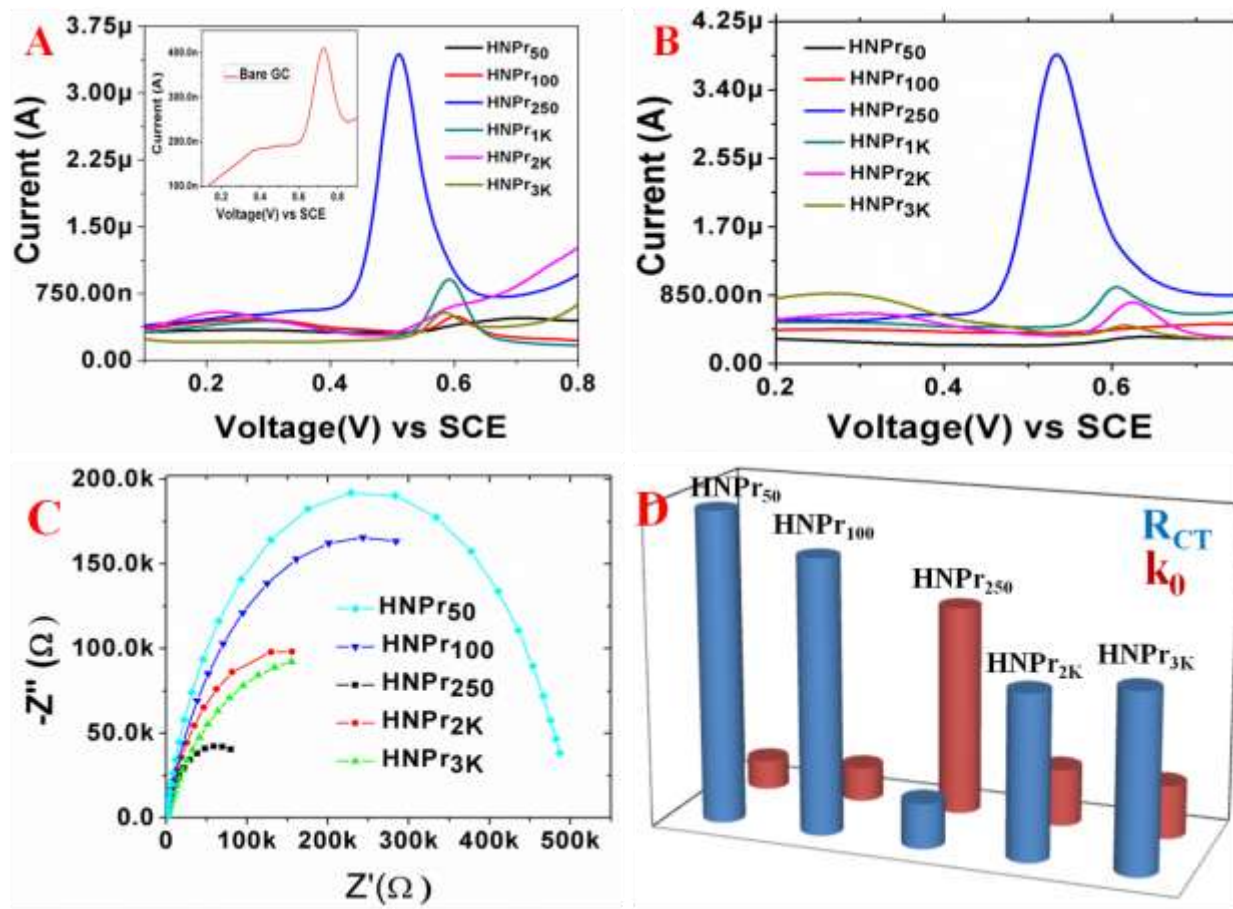


Figure 4.17: (A) and (B) represent DPV and SWV of 4×10^{-5} M UA at different HNPr/GC electrode. Inset in (A) represents the DPV of bare GC. (C) Nyquist plot for the electrooxidation of UA at an applied potential of 0.4V within a frequency range of 10^5 to 10^{-2} Hz (To avoid overcrowding we have not included impedance spectra of HNPr₅₀₀ and HNPr_{1K} in figure (C)), (D) Comparison of R_{CT} and k_0 value of different HNPr/GC towards the oxidation of UA.

However, the extent of catalytic activity differs from each other is worth to mention. The HNPr₂₅₀/GC composite exhibits superior catalytic activity in which the peak potential (0.51 V) gets shifted by ~ 210 mV towards the more negative region and the peak current also get boosted by ~ 8.39 times $\left(\frac{i_P^{HNPr_{250}}}{i_P^{GC}} = 8.39 \right)$ compared to that of the bare GC in DPV response.

Characteristic parameters obtained from DPV measurements for various HNPr/GC are tabulated in **Table 4.1**. The enhancement in peak current and decrease in peak potential in comparison with bare GC follows the trend as $\text{HNPr}_{50}/\text{GC} < \text{HNPr}_{100}/\text{GC} < \text{HNPr}_{250}/\text{GC} > \text{HNPr}_{500}/\text{GC} > \text{HNPr}_{1K}/\text{GC} > \text{HNPr}_{2K}/\text{GC} > \text{HNPr}_{3K}/\text{GC}$. The observed values of peak current and peak potential follow a similar trend with the variation of SGBD (nm^{-2}) as we calculated and mentioned earlier. Along with DPV, we have also performed Electrochemical Impedance Spectroscopic (EIS) measurements (**Table 4.2**) which provide various system parameters regarding kinetics and mechanistic information such as charge transfer resistance (R_{CT}), ohmic resistance or solution resistance (R_s), capacitance, the time constant, etc. EIS is mainly consisting of Bode and Nyquist plot. The typical Nyquist diagram provides the variation in real (Z') and imaginary (Z'') part of the impedance at a fixed potential from the higher frequency to lower frequency region. **Figure 4.17C** shows the Nyquist plot for the electro-oxidation of UA at different HNPr/GC electrodes in 0.1M HClO_4 solution in which a semi-circle is observed at the higher frequency region. The diameter of the semi-circle gives the measurement of the R_{CT} (charge transfer resistance) while the intercept in the X-axis provides the R_s (solution resistance) value. The lowest R_{CT} value is obtained for $\text{HNPr}_{250}/\text{GC}$ electrode while $\text{HNPr}_{50}/\text{GC}$ shows the largest R_{CT}

Table 4.2: Different kinetic parameters for cavity shuffled HNPrs obtained from the EIS measurements. Here R_{CT} indicates the charge transfer resistance, W as the Warburg Impedance, CPEas constant phase element, i_0 as the exchange current, and k_0 as the heterogeneous rate constant.

System	$R_{CT}(\text{k}\Omega)$	$W (\Omega \text{ s}^{-1/2})$	n	CPE ($\Omega^{-1}\text{s}$)	$i_0(\text{A})$	$k_0 (\text{cm s}^{-1})$
--------	--------------------------	-------------------------------	---	-------------------------------	-----------------	--------------------------

GC	705.6	6.2×10^{-4}	0.72	6.4×10^{-6}	1.8×10^{-8}	3.3×10^{-6}
HNPr ₅₀	491.8	4.2×10^{-4}	0.84	1.42×10^{-6}	2.6×10^{-8}	4.7×10^{-6}
HNPr ₁₀₀	432.0	1.2×10^{-4}	0.75	1.61×10^{-5}	2.97×10^{-8}	5.4×10^{-6}
HNPr ₂₅₀	71.0	4.0×10^{-3}	0.79	4.27×10^{-5}	18.0×10^{-8}	33.0×10^{-6}
HNPr ₅₀₀	79.5	4.7×10^{-3}	0.65	3.35×10^{-5}	16.1×10^{-8}	29.6×10^{-6}
HNPr _{1K}	115.8	1.2×10^{-4}	0.71	2.87×10^{-5}	11.0×10^{-8}	20.3×10^{-6}
HNPr _{2K}	259.2	1.8×10^{-4}	0.78	1.18×10^{-5}	4.95×10^{-8}	9.0×10^{-6}
HNPr _{3K}	280.0	9.8×10^{-5}	0.66	1.51×10^{-5}	4.58×10^{-8}	8.4×10^{-6}

value as shown in **Figure 4.17D**. These results are consistent with the DPV response of different HNPr/GC electrodes. The exchange current (i_0) and standard heterogeneous rate constant (k_0) has been calculated from the following equations:

$$R_{CT} = \frac{RT}{nFi_0} \dots \dots \dots (1)$$

$$i_0 = nFACk_0 \dots \dots \dots (2)$$

Due to the facile electron transfer between HNPr₂₅₀/GC and UA, the kinetics of the electro-oxidation process is quite faster and results in the lowering of R_{CT} value. The Nyquist plot has been fitted with the modified Randles circuit by incorporating the constant phase element (CPE) and Warburg (W) impedance and the corresponding equivalent circuit is shown in **Figure 4.18**. Elucidation of DPV, EIS, and SWV result clarify that the extent of the catalytic power of different HNPrssupportsour previous arguments.

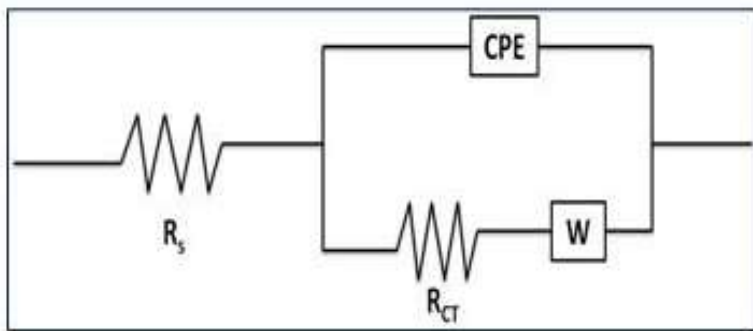


Figure 4.18: Equivalent circuit for the Nyquist plot. Parameters of the Circuit: (i) R_s = Solution resistance, (ii) R_{CT} = Charge transfer resistance, (iii) W = Warburg impedance, a kind of resistance to mass transfer, and (iv) CPE = Constant Phase Element which raises due to the double-layer capacitor.

It is difficult to explain the enhanced catalytic power of $\text{HNPr}_{250}/\text{GC}$ compared to the other HNPr/GC by the facet dependent kinetics since the crystalline orientation towards $1/3\{422\}$ and $\{220\}$ facets are identical for all HNPrs . Besides, all the structures are flat 2D prisms and the surface area gradually reduces from HNPr_{50} to HNPr_{3K} . Hence, if the catalytic activity directly depends on the available nanosurface area then it should simply show a decreasing trend starting from HNPr_{50} and ends up with HNPr_{3K} . In reality, the deviation from this monotonous trend of catalytic activity proves that the available surface area is not the prime factor to determine the catalytic activity of different HNPrs . Moreover, since we have used an equal amount of CTAB during synthesis, we may expect a steady reduction in +Ve zeta potential (ξ) as we generate nanostructures with a smaller dimension, i.e., $\xi_{\text{HNPr}_{50}} \gg \xi_{\text{HNPr}_{3K}}$. Experimentally our measured zeta potentials show a different trend which shows a minimum zeta potential of 55 mV for HNPr_{50} and maximize for HNPr_{250} at 74mV and then slightly reduce to 68 mV for the other nanostructures till HNPr_{3K} . Measured zeta potential for different HNPrs is enlisted in Table 1. The

trend of the variation of zeta potential follows the same trend with the porosity of different HNPrs.

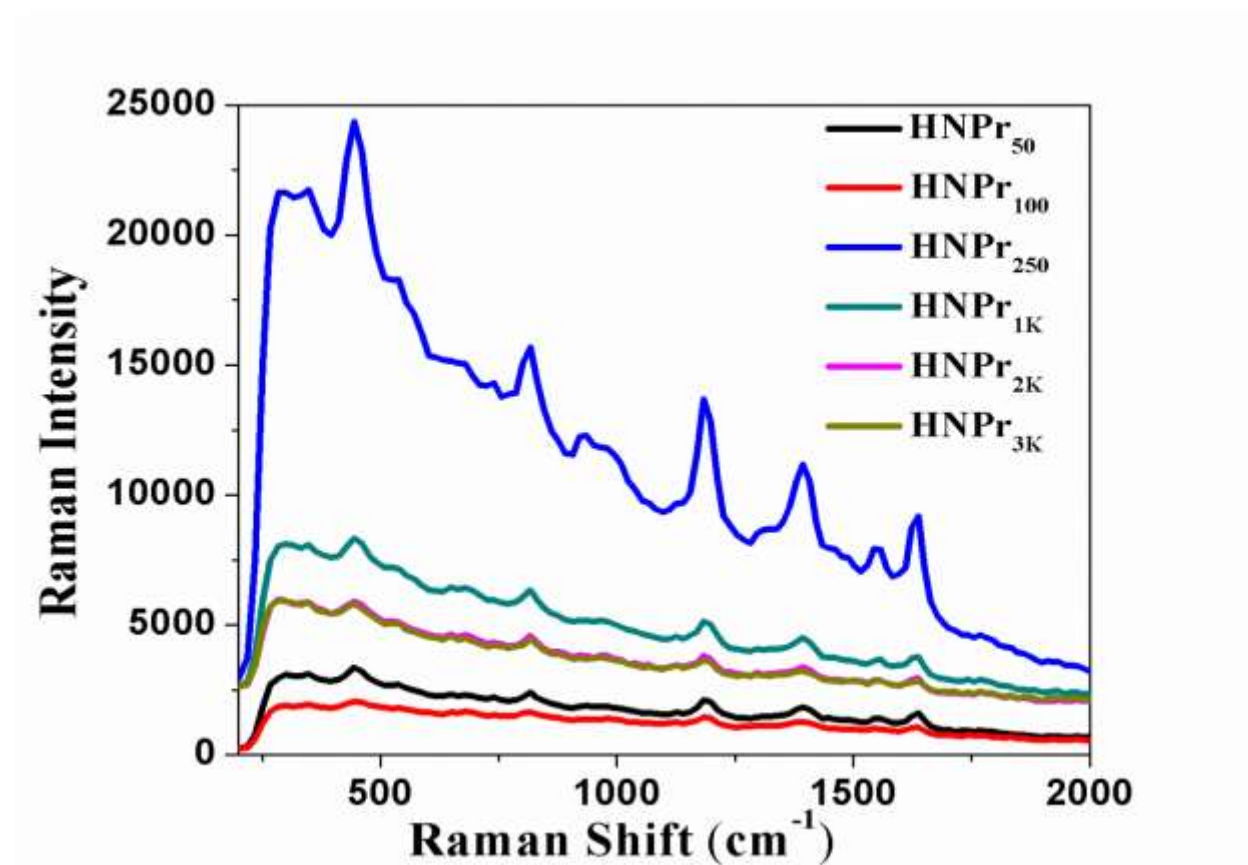


Figure 4.19: SERS spectra of different HNPr with CV (crystal violet) as the Raman reporter in which HNPr₂₅₀ shows maximum Raman intensity. The result is very much well agreed with our previous arguments. The Raman dye binds to the HNPr surface according to the extent of porosity in the central cavity region.

This infers that as the value of Au^0/Ag^0 reaches near 2.42, the porous ligaments in HNPr₂₅₀ allows holding the number of +Vely charged CTAB molecule to increase the overall +Ve zeta potential. Hence the measured values of zeta potential indirectly project the ligamentous nature of their central cavity region to enhance their relative catalytic power concerning the bare GC from 1.17 to 8.39 (from DPV response) when we compare between HNPr₅₀ and HNPr₂₅₀ (**Table**

4.1). In this context, the formation and the extent of various crystal defects like MTB, GB on the crystalline surface of HNPr and compositional characteristics of their porous ligaments can be considered as the most important factor to control their catalytic efficiency.^{186,187} The addition of UA to the active electrochemical (electrode + electrolyte) system leads to the adsorption of UA on the HNPr surface. The extent of analyte adsorption on different nanosurface and the role of porosity induced crystal defects on controlling the efficiency of surface adsorption was cross-verified by recording their SERS spectra in presence of crystal violet (CV) as Raman tagging molecule. In a typical experiment we have taken 180 μL of 10^{-4} M CV and mixed it to 20 μL of concentrated different HNPrs and the result has been depicted in **Figure 4.19**. The assignment of different Raman modes origination from CV on nanosurface has been reported before in the literature.¹⁸⁸ It is clear from **Figure 4.19** that the extent of interaction between HNPr and CV is gradually increasing from HNPr₅₀ to HNPr₂₅₀ and then decreases gradually to HNPr_{3K}. Our high-resolution imaging also shows the same trend of variation both for crystal defect as well as porosity in the central cavity region. The presence of crystal defects and plastic nature in the central cavity region increases the number of unsaturated atoms to enforce the binding with the analyte (here UA) to fulfill their desired coordination for stabilization. On the other hand, the presence of porous ligaments enhances the total surface area for effective adsorption of UA in comparison to nonporous crystalline bimetallic HNPrs. The ability of HNPr surface to interact with UA depends heavily on the possibility of coupling between adsorbate (UA) states and the metal d-states. Interaction energy¹⁸⁹ for an weak coupling may be written as:

$$E_{d-hyb} = -C(f_a, f_d) \frac{V_{ad}^2}{|\epsilon_a - \epsilon_d|} + \alpha V_{ad}^2 \dots \dots \dots (3)$$

Where f_a and f_d is the degree of filling of the adsorbate state and the metal d-state with energy ϵ_a and ϵ_d respectively. The term V_{ad} represents the coupling matrix element between the adsorbate

states and metal d-states. The first term in the above equation denotes the hybridization energy (between adsorbate states and metal d-states) arises due to attraction when the antibonding states are not filled completely. The second term represents repulsion due to the orthogonalization between the adsorbate states and metal d-states. The introduction of the concept of lanthanide contraction¹⁹⁰ can be used to explain the lattice mismatch of bimetallic Au-Ag HNPrs. Recently, the theoretical calculation by considering the relativistic contraction phenomenon and correlation effect predicts that the Au atom should be smaller than that of the Ag atom.^{191,192} According to Vegard's law,¹⁹³ lattice constant changes when a different sized atom has been introduced into the lattice. This change in lattice constant subsequently influences the lattice strain.¹⁹⁴ The introduction of bigger Ag atoms by replacing Au atoms across the heterophase i.e. near the central cavity position in the bimetallic HNPr generates a significant amount of low coordinated crystal irregularities.¹⁹⁵ This reduced coordinated atomic sites leads to a local upshift in d-band (closer to the Fermi level) which can be illustrated by **Equation (3)**. Diminished overlap of the wave function causes narrowing down the d-band with simultaneous increment in the d-band population. As a consequence, the bimetallic Au-Ag alloy nanoparticle (HNPr₂₅₀) is expected to generate greater d-band spacing than their monometallic counterpart in presence of UA resulting in the higher adsorption on the alloy surface. This upshifting of d-band center in HNPr₂₅₀ causes enhancement in reactivity between HNPr₂₅₀ surface and UA (**Equation 3**) as fewer of the antibonding states are occupied now.¹⁸⁹

To corroborate experimental results obtained from our DPV, EIS, and SWV measurements with microscopic analysis of different HNPrs, we have performed *ab initio* calculations to estimate the induced strain generated due to lattice mismatch in bimetallic HNPr with variable Au:Ag composition. We have modeled five systems, HNPr_{pureAu}, HNPr_{pureAg}, HNPr_A, HNPr_B, and

HNPr_C as discussed previously. As strain plays a key role in determining the catalytic property of the prism, we have considered a similar structural geometry for all the modeled HNPrs. First, we have calculated the molecular area along the basal plane for both the pure HNPrs as shown in **Figure 4.20**. The calculated molecular area of the optimized HNPrs for pure Au and Ag are 1007.51 and 1057.30 Å². As both the structures contain a similar number of atoms along the basal plane, we found out that under similar structural restrictions, the Au atoms occupy less surface area compare to Ag atoms. So, with the increase in the concentration of dopant (Ag), we suppose to observe the increase in the lattice strain along with the basal or any exposed surface. Based on the above arguments on pure HNPrs of gold and silver, a theoretical model for lattice strain should follow the order as:

$$\text{HNPr}_{\text{pureAu}} < \text{HNPr}_{50} < \text{HNPr}_{100} < \text{HNPr}_{250} < \text{HNPr}_{500} < \text{HNPr}_{1K} < \text{HNPr}_{2K} < \text{HNPr}_{3K} < \text{HNPr}_{\text{pureAg}}$$

The above model is only valid for similar structural configurations as more Ag character signifies the lattice strain from HNPr₅₀ to HNPr_{3K}. But, with the increase in Ag concentration, the formation of an alloy based HNPr favored over core/shell type geometry which reduces the strain and this is visible from our recorded TEM images. With the increase in Ag concentration from HNPr₅₀ to HNPr₂₅₀ the prism structures retain their shape, however beyond HNPr₂₅₀ due to the enhancement of internal lattice strain the prism shape gradually distorted and finally a hollow disc appears in case of HNPr_{3K}. Due to the lack of structural symmetry, we have modeled only five HNPrs (all are having prismatic shape) for the calculations of strain. Conceptually the strains are defined as the ratio of interatomic displacements divided by reference bond lengths. In general, the strain-induced (ϵ) in a nanoparticle is defined by the following mathematical relation:

$$\epsilon = (d^* - d_0)/d_0 = \delta d/d_0 \dots\dots\dots (4)$$

Where d_0 is the bond length of pure bulk material, and d^* is the average bond length of a particular surface/interface. From the above equation, it is clear that the strain-induced on a surface is strongly affected by surface unsaturation (δd). However, this lattice strain induced within the system is also a function of other parameters such as pressure (P) and temperature (T).

Thus the total lattice strain induced (ϵ_T) can be represented as:

$$\epsilon_T \propto \epsilon(d(P, T)) \dots\dots (5)$$

But, this relation is valid only for a homogeneous system. Due to the presence of mixed covalent radii in heterogeneous systems, the change in the mole-fraction of either component can induce the strain in the lattice for a fixed composition. Hence, we have tried to correlate the lattice strain with dopant concentration with the help of **Equation (6)**

$$\epsilon_{T_j} = \epsilon(d(x_j, P, T)) \dots\dots\dots (6)$$

Here x_j represents the strain-induced over some specific sites (j) due to the variation of dopant concentration. First, we have calculated the effect of compositional variation on lattice strain induced at the basal plane and prismatic face in Au:Ag HNPrs. The calculated average bond-lengths between gold atoms follow the order of HNPr_C (2.808 Å) > HNPr_B (2.800 Å) > HNPr_A (2.800 Å) > HNPr_{Au} (2.773 Å). However, the difference in the bond length is negligible for either any of the compositions and hence we cannot calculate the strain induced by the bond-length parameters. Alternatively, the edge length of HNPrs (along the basal plane) also follows a similar order as we observed for Au-Au bond parameters. The calculated values for edge lengths are 2.773 nm (pure), 2.800 nm (HNPr_A), 2.805 nm (HNPr_B), and 2.808 nm (HNPr_C). Hence, to calculate the strain induced by the Ag doping, we have used the following equation:

$$\epsilon = (l_{Au_{1-x}Ag_x} - l_{Au})/l_{Au} \dots\dots\dots (7)$$

where l_{Au} is the edge length of pure Au HNPr and $l_{Au_{1-x}Ag_x}$ is the edge length of various HNPrs compositions along their basal planes. The calculated percentage strain along the (111) plane obtained from our calculation is 0.974% for HNPr_A, 1.154 % for HNPr_B and 1.190 % for HNPr_C. This gradual increment of strain along (111) plane indicates that the reactivity on {111} facet increases gradually with Ag doping. This results in the transformation from prismatic shape to hollow nanosphere to achieve the

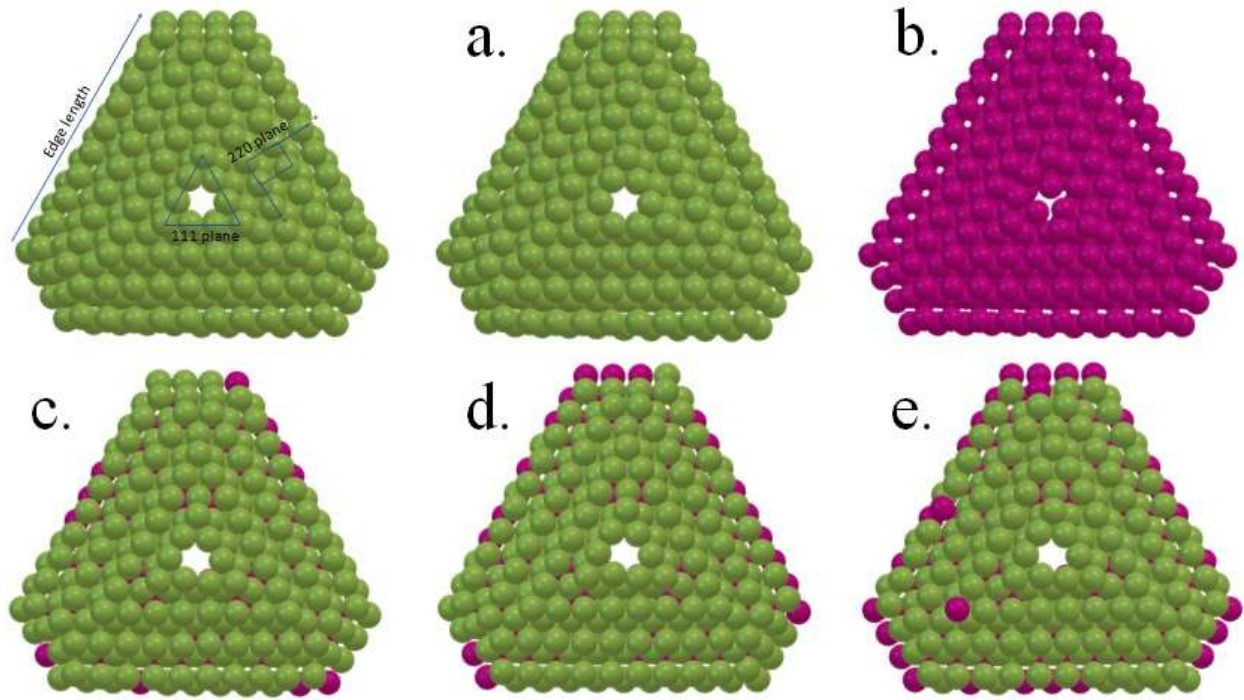


Figure 4.20: Optimized structure for different HNPrs: (a) HNPr_{pureAu}, (b) HNPr_{pureAg}, (c) HNPr_A, (d) HNPr_B, and (e) HNPr_C. The leftmost figure of the top panel shows the model HNPr with different planes (basal and vicinal) along with different structural parameters.

desired stability by reducing their vibrational entropy^{173,174} in the form of developed strain. On the other hand, the more reactive (220) plane which comprises the faces of HNPrs acts as the active facet for effective UA oxidation. If we look carefully the **Table 4.3** then the calculated percentage strain along the {220} facet varies in the following order:

1.143% for $\text{HNPr}_A < 1.718\%$ for $\text{HNPr}_B > 1.451\%$ for HNPr_C .

This indicates that unlike $\{111\}$ facet (top and bottom flat surface of HNPr) the developed strain on reactive $\{220\}$ facet doesn't increase monotonously with Ag-doping, rather maximizer for HNPr_B (modeled) with $\text{Au}^0:\text{Ag}^0$ a fixed composition of 2.45:1 which is close to the experimentally measured composition of HNPr_{250} as mentioned in **Table 4.1**. This maximization of strain on energetically active facet makes HNPr_{250} as the most active HNPr structure for UA oxidation. Hence our calculation is

Table 4.3: Different crystal parameters along with induced strain along (111) basal plane and (220) vicinal plane by optimizing the HNPr structure and calculating % strain by considering **equation 4** and **equation 7**.

Cluster Model	Composition ($\text{Au}^0:\text{Ag}^0$)	Molecular Area ($\times 10^3 \text{\AA}^2$) Along the Basal Plane	Edge Length of Basal Plane (111) nm	Average Strain Vector of Vicinal Plane (220) (Along with Y, \AA)	Strain Induced Along (111) Basal Plane (in %)	Strain Induced Along (220) Vicinal Plane (in %)
$\text{HNPr}_{\text{pureAu}}$	$\infty:0$	1.007	2.772	12.333	NA	NA
HNPr_A	3.03:1	1.026	2.799	12.474	0.974	1.143
HNPr_B	2.45:1	1.028	2.804	12.545	1.154	1.718
HNPr_C	2.02:1	1.040	2.805	12.512	1.190	1.451
$\text{HNPr}_{\text{pureAg}}$	$0:\infty$	1.057	2.827	NA	NA	NA

well-agreed with our predictions that Ag doping in pure Au HNPr increase strain within it and with a suitable value of the indicator, Au^0/Ag^0 (2.45:1), an alloy is formed (in case of HNPr_{250}) to gain the optimum stability in the prismatic structure with maximum strain within it. The present study is not only to explore the role of different physicochemical and intrinsic crystal parameters for enhancing the rate of sluggish oxidation of UA but also to find out whether we can use these nanostructures as efficient catalytic materials for ultra-low sensing of UA in a physiological sample. The efficacy of the $\text{HNPr}_{250}/\text{GC}$ modified electrode encouraged us for

finger printing of UA from normal physiological to deficiency level concentration range. We have applied different electrochemical techniques like SWV, DPV, chronoamperometry for concentration-dependent study (**Figure 4.21**) and found that DPV is the most powerful and reproducible electrochemical methodology for current response in nanomolar (10^{-9} M) range. We are able to get a linear relationship in the concentration range of 40 μ M to 2.5mM from their DPV response as depicted in **Figure 4.21**. We have also performed an interference study for different ions like Cl^- , Br^- , I^- , Ca^{2+} , CO_3^{2-} as well as other interfering agents like ascorbic acid (AA), dopamine (DA), glucose, etc. to show any change during DPV measurements and found that UA redox peak potential does not shift and peak current almost remain constant except for I^- and CO_3^{2-} . This discrepancy in peak potential and peak current for I^- and CO_3^{2-} maybe due to the following reasons: (i) Ag^+ present in the HNPr_{250} may react with I^- to form AgI ¹⁹⁶ as a side product and enhances the peak current slightly at low PH \approx 1 (0.1M HClO_4), and (ii) addition of carbonate will change the pH of the electrolyte (more alkaline) to improve the oxidation process.¹⁹⁷

The formulated assay (HNPrs) is highly stable in nature due to its mixed metal nature and efficient encapsulation by long-chain CTAB molecule, yet energetically active for catalytic activity. Moreover, the devised assay and experimental procedure do not require any surface tagging for selective recognition of analytes which not only reduces the cost of pathology but also offers a rapid detection technique.

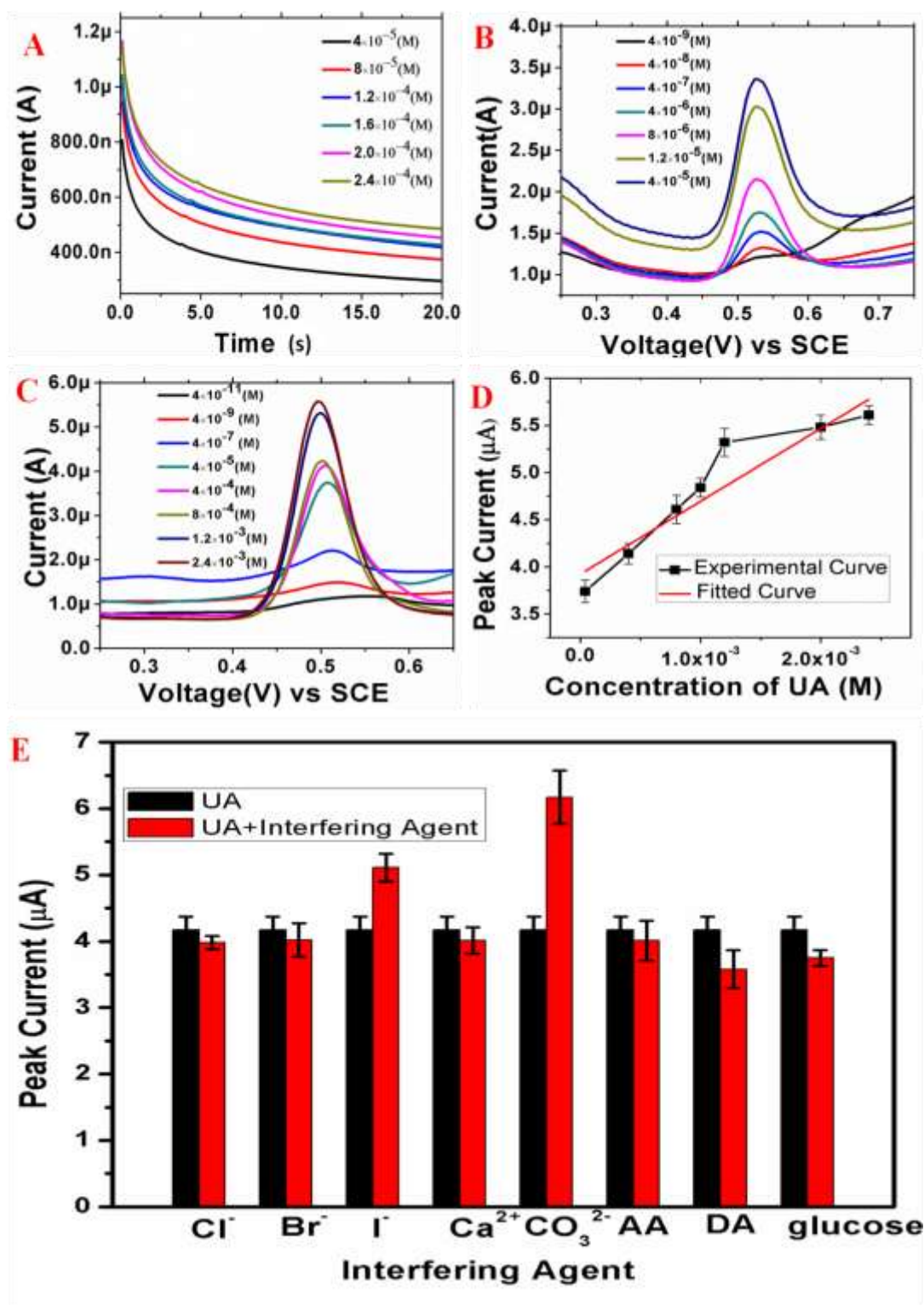


Figure 4.21: (A),(B), and (C) are chronoamperometry, SWV, and DPV responses respectively at variable concentrations of UA on the HNPr₂₅₀/GC electrode.(D) represents the linear fitting of

DPV response with standard deviation. (E) Denotes the peak current shifting for electrooxidation process of 400 μM UA in presence of different interfering agents (the concentration of different interfering agents are taken in millimolar range).

4.6 Conclusion

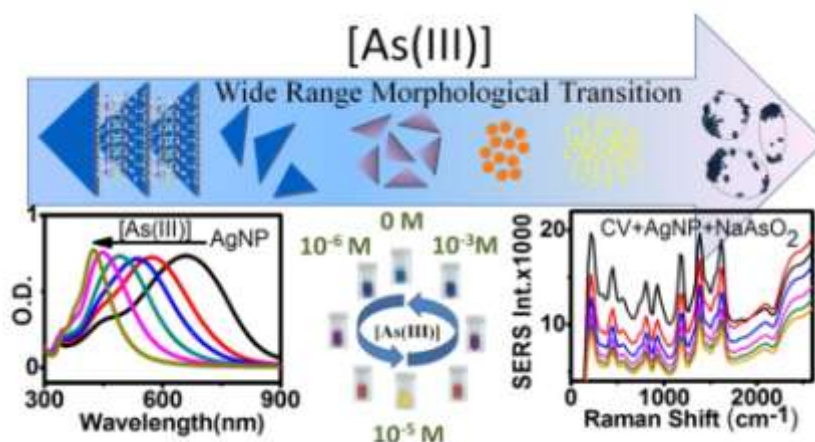
The porosity developed in the central cavity region of HNPr_{250} generates tensile strain due to the atomic replacement (Ag by Au) in our synthesized size (both the hole as well as the edge length) and shape (sharp Vs. truncated 2D prisms or prisms Vs. circular disks) variable HNPrs. The mechanistic investigation for their catalytic activity has been explored in minute details both by experimental methodology and theoretical modeling. We have demonstrated that the HNPr_{250} acts as the most efficient catalytic material compared to other HNPrs with the same chemical composition (except the porous ligament core region) for the oxidation of Uric Acid. The superlative catalytic efficiency of HNPr_{250} has been explored in depth by a morphological and atomic-scale architectural study using HRTEM analysis. Differential pulse voltammetry, square wave voltammetry, and electrochemical impedance spectroscopy provide their qualitative and kinetic information. Due to the inducement of multiple twin boundary, grain boundary, and tensile strain in large excess, the d-band shifting in the HNPr_{250} cause greater adsorption of UA on its surface to support the reduction of deprotonation energy (eV) during electrochemical oxidation through vicinal $\{220\}$ facets of hollow nano prisms. This study allowed us not only to investigate the actual reason behind the unprecedented catalytic activity of HNPr_{250} out of other HNPrs but also help us to design a sustainable nanoscopic assay for accurate measurement of UA concentration (in the nanomolar range) for the evaluation of hyperuricemia or hypouricemia which might find potential application in designing low-cost kit in the pathological industry.

CHAPTER-5

Wide Range Morphological Transition of Silver Nanoprism by Selective Interaction with As(III): Tuning-Detuning of Surface Plasmon Offers to Decode the Mechanism

OUTLINE: Specific Points of Discussion

- Na^+ ion-induced cation- π interaction between face-to-face energetically stable {111} surface-bound pyrrolidone groups arranges PVP-based silver nanoprisms (AgNPrs) in an axial stacking geometry.
- Congested interplanar space between AgNPrs allows As(III) selectively to react differentially with silver atoms from facial {111} and peripheral {110} facets to results smaller stacking and finally to nanoseeds.
- Above a critical concentration of As(III), PVP leached-out from nanoparticles to form nanoseed- engulfed emulsions and inducing a controlled aggregation.
- This entire morphological transition has been decoded by recording their SPR and SERS tuning and confirmed by the transmission electron microscopy study.
- Strong affinity and selectivity of As(III) toward the Ag atom (verified by DFT calculation) offers us a low-cost AgNPr-based colorimetric assay with potential application in environmental protection.



5.1 Introduction:

In this chapter, we have engineered axially stacked silver nanoprisms (AgNPrs) from the constituent PVP capped Ag nanoprism monomers and studied their differential interaction with As^{3+} and As^{5+} microscopically via TEM, spectroscopically via UV-visible and SERS spectroscopy, and theoretically via DFT calculations. Arsenic (As) is one of the most profuse toxic elements on Earth's crust.^{198,199} Major arsenic species found in environmental samples are either inorganic salts [arsenite: As(III) and arsenate: As(V)] or stable organic compounds [e.g., dithioarsenate (DTA), dimethylarsinic acid (DMA), and monomethylarsinic acid (MMA)].^{200–202} Sources of As contamination is many-folds which include sulfide ores;²⁰³ natural phenomena like weathering, biological activity, volcanic eruption; together with anthropogenic inputs and spreads through rain and dry fallout.^{201–204} According to the 2009 European Food Safety Authority (EFSA), Parma, Italy²⁰⁵ and World Health Organization (WHO), inorganic arsenic is acutely toxic compared to organic arsenic compounds²⁰⁶ and causes skin lesions, peripheral neuropathy, diabetes, cardiovascular diseases, and cancer of the lung, liver, urinary bladder in addition to the skin. As a result of this, the detection, quantification, and removal of inorganic arsenic from the drinking water gained a lot more momentum compared to organic arsenic. The EFSA and WHO fixed the maximum tolerable concentration of arsenic as 15 $\mu\text{g/kg}$ of bodyweight and 10 *ppb* in drinking water (old limit of arsenic contamination: 50 *ppb*²⁰⁷). Global hot spots with high arsenic risk include South of Asia (Bangladesh, Mongolia, and Malaysia), South of South America (Chili and Argentina), and Western North America. A large population of South and Southeast Asia are seriously exposed to potentially dangerous levels of carcinogenic arsenic via their drinking water every day.²⁰⁸ By knowing its high toxicity, arsenic-free drinking water is in high demand for the modern healthier lifestyle.

Sufficient reports are also available which explore the positive side of concentration-dependent arsenic contaminations^{209,210} and doping.²¹¹ Hence, the quantification of arsenic is very important both for blissful effect as well as to tackle translational health hazards and indirectly helping us to grow the subject of heavy metal chemistry.²¹² Literature is rich with reports for the detection of arsenic either by laboratory-based analytical procedures^{207,213–224} or by using noble metal nanomaterials^{225–231} but the mechanistic revelation of selective detection of arsenic^{201,232} not only seldom but also superficial in nature. Based on their wealth of optical properties (absorption, emission, and scattering) the noble-metal nanoparticles find high throughput applications in different advanced fields^{4,233–236} which include sensing, diagnostics, therapeutics, optoelectronics, catalysis, alternate energy, etc. Surface plasmon resonance (SPR)^{237–240} bands of noble-metal nanoparticles are typically located in the vis-NIR region and are strongly dependent on nanoparticle size, shape, composition, crystallinity, interparticle spacing, and local dielectric environment.^{238,241–245} Out of several noble-metal NPs, silver nanoprism (AgNPr) is one of the most promising candidates for multicolor diagnostic labeling purposes because of their easy tunability of the broad-band *in-plane* dipole SPR simply by adjusting the aspect ratios (AR_s) = $\frac{L}{T}$ where L = side length of the prism and T = thickness of the prism and by inducing their 2D & 3D assemblies.²⁴⁶ Yu et al.²⁴⁷ and others²⁴⁸ found that silver nanoplates are sensitive to several inorganic anions and results SPR band tuning between 650 and 450 nm by adjusting the added anions concentration. Though Yu et al.²⁴⁷ explained this as the effect of surface electron injection, Xu et al.²⁴⁹ cites the color change of AgNPr as the sculpting effect of chloride ion which transforms the triangular shape into circular disk-like shape by surface etching. Recently, two groups, Xu et al.²⁴⁹ and Tsai et al.,²⁴⁰ independently found the threshold concentrations for

Cl^- , Br^- and I^- as $\sim 3 \times 10^{-4}$, $\sim 1 \times 10^{-6}$ and $\sim 1.5 \times 10^{-6}$ M respectively compared to $\sim 4 \times 10^{-4}$ M of SCN^- to initiate the same sculpting process. Like surface Plasmon behaviors, noble metal nanomaterials also show interesting inelastic scattering properties and can be verified easily and cost effectively by recording their surface enhanced Raman scattering (SERS) spectra. Like SPR, SERS also show size and shape dependent (of the nanoparticle) enhancement of Raman spectra for the Raman active molecule when they are adsorbed onto a nanosurface due to the change in active surface area (by increasing their individual size or by generating controlled aggregation) to be available for molecular adsorption or a variation in the extent of field enhancement (localized enhanced field: E_s) at the nanosurface. Although the literature is rich where SERS has been used to measure the size²⁵⁰ of the active nano surface or to find out the surface curvature to estimate their relative capability of field enhancement by lightning rod effect,²⁵¹ a direct SERS method to trace their morphological change during their interaction with specific chemical at different concentration is seldom and attracts our attention to use it for ultrasensitive and highly specific detection. Due to their sharp features (compared to SPR) and strong intensity, SERS can also be used as an efficient sensing tool to understand the morphological transition of nanomaterials during their selective interaction with an analyte but obviously not a direct spectroscopic method and depends heavily on the ability of the dye to adsorb on the specific nanosurface. Out of several nanomaterials-based technologies^{229, 12,252–254} the colorimetric technique²⁰² for selective and sensitive detection is of most useful for its large scale application associated with its low cost implementation. Most of the nanomaterials-induced colorimetric techniques are based on the formation of controlled aggregation by exploiting their surface bound ligand chemistry in presence of heavy metal ions which tune their SPR to show different colors. They bear a common plasmon feature of shifting to higher wavelength associated with

reduction in intensity and broadening. Moreover, in this strategy we don't induce any morphological change of the individual nanomaterials rather simply changes their interparticle relative distance to induce plasmon coupling. Getting inspired from these facts we have tried here to induce morphological change simply by adding increasing concentration of As (III or V) in AgNPr solution which results the tuning of plasmon band as a combined effect of breaking down the AgNPr overlay stacking by arsenic ion intercalation, leaching of disintegrated AgNPrs, removal of PVP surfactant from AgNPr surface to form size variable emulsions and thereby inducing emulsion incorporated controlled aggregations or even complete dissolution of AgNPr to form unpredicted composites to lose plasmonic characteristics. Here the characteristics of the polymeric surfactant (functional group, molecular weight, etc) are crucial to induce both overlay stacking as well as emulsion incorporated aggregation. This concentration dependent morphological transition is only sensitive for arsenite[As(III)], leaving apart all other common alkali, alkaline and toxic transition metal ions including arsenate [As(V)] and has been confirmed by TEM. A plausible explanation of the color coded sensing of As(III) has been presented by analyzing their tunable surface plasmon and surface enhanced Raman spectra. This low cost, easy-to-perform and error-free As(III) detection technique will provide us a versatile tool to find enormous application in the field measurements.²⁰²

5.2 Synthesis of silver nanoprism:

The initial triangular silver nanoprisms were synthesized by following the Mirkin's method²⁴⁶ with slight modification. Briefly, 25 mL of Milli-Q water was taken in a 50 mL beaker and then 250 μ L of 10^{-2} M AgNO₃ was added drop by drop in it. To this diluted AgNO₃ solution we then added 1.5 mL of 30 mM TSC, 1.5 mL of 0.24 mM PVP ($M_w \sim 10,000$) and 60 μ L of 30 wt % H₂O₂ successively. Between each addition, 30 s time lag was given for the proper mixing of reagents. To this final mixture, 250 μ L of 10^{-1} M NaBH₄ was rapidly injected and the solution

turns into yellow color initially which becomes colorless after some time. The solution was stirred for an additional 30 min; the color was darkened to a deep yellow which indicates the formation of small Ag nanoparticles. Over the next several seconds, the color of the solution changes from yellow to blue in a stepwise pattern. Synthesized nanoprism was then kept in room temperature for 24 h before we make TEM sample by a known technique described in previous reports^{54, 61} for clean monolayer sample preparation on carbon film 300 mesh copper grid (CF300-CU).

5.3. Results and Discussion:

The exploitation of SPR for selective detection of an analyte is long known in the literature²⁰² where we utilize their surface-bound ligand chemistry for specificity^{255,256} and gigantic cross-section (absorption and scattering) of the metal core for sensitivity.^{257,258} In this scheme we use the surface-bound ligand as a *fishing net* and the metal core as a *yardstick* to identify and quantify an analyte respectively without observing any morphological change of the individual nanoparticles.

In another approach of colorimetric detection where the metal core of the nanoparticle acts both as *fishing net* as well as a *yardstick* and in presence of analyte (ionic or molecular) the unstable (and hence reactive) exposed surface atoms directly react with the analyte to create a permanent morphological change of the nanomaterial. Since the change of color in this approach is due to the analyte induced morphological change of nanoparticles, it does not encourage forming aggregate, or in other words the formed morphological intermediates are very stable to explore their reaction mechanism. In our present study, we have adopted the second approach of selective color-coded sensing of As(III) by using AgNPr as the nanomaterial and compared the

colorimetric result in the same experimental condition for all other common alkali, alkaline and toxic transition metal ions including arsenate As(V). The absorption spectra of the synthesized AgNPrs are shown in **Figure 5.1A** where the plasmon band in the range 650-750 nm corresponds to *in-plane dipole* mode and the plasmon band near 330nm is due to the *out-of-plane quadrupole* mode of the nanoprism²⁴⁰.

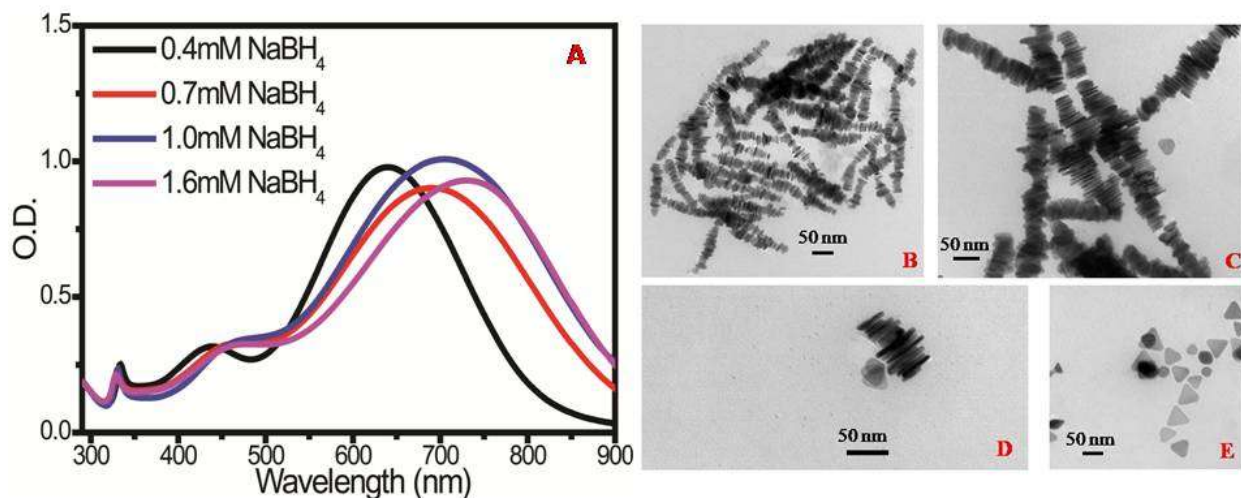


Figure 5.1: (A) Stacking length-dependent plasmon tuning. TEM images to show the effect of Na⁺ ion concentration induced cation- π interaction on average stacking length variation between 198 and 0 nm, where (B) at M (molar ratio between NaBH₄ and AgNO₃) =16, L =198 nm and N =26 the obtained $d(400 \mu\text{L}) = 6.4 \text{ \AA}$ with $\zeta(400 \mu\text{L}) = -10.5 \text{ mV}$; (C) at M =10, L =136 nm and N =18 the obtained $d(250 \mu\text{L}) = 5.9 \text{ \AA}$ with $\zeta(250 \mu\text{L}) = -14.6 \text{ mV}$; (D) at M =7, L =93 nm and N =12 the obtained $d(175 \mu\text{L}) = 8.2 \text{ \AA}$ with $\zeta(175 \mu\text{L}) = -17.2 \text{ mV}$ and (E) at M =4 they don't form stacking structures rather distributed as individual prisms with $\zeta(100 \mu\text{L}) = -25.4 \text{ mV}$.

The broad peak in the range 440-460 nm is attributed to two closely spaced SPR bands, *in-plane quadrupole* and *out-of-plane dipole* modes of AgNPrs. Details of the HRTEM study of

these nanoprisms are presented in **Figure 5.2** and in our previous report²⁴¹ which shows both frontal and sideways bright-field TEM images. The selected area electron diffraction (SAED) indicates that the as-prepared nanoprisms are single crystals with a $\{111\}$ lattice plane as the basal plane (interplanar spacing = 2.36 Å). The flat surface of the silver nanoprisms is parallel to the $\{111\}$ plane as also been suggested in the literature^{259,260}. The SAED pattern also shows another set of faint spots with hexagonal symmetry which has been indexed as $1/3\{422\}$ reflections with a lattice spacing of 2.50 Å, indicating the presence of a single twinning boundary within the $\{111\}$ planes. For single crystal *fcc* metals, these spots are forbidden, but they can appear when there are two twin planes parallel to one another.^{241,259} The appearance of the forbidden $1/3\{422\}$ reflection is often observed in silver or gold nanostructures in the form of thin plates or films bound by atomically flat top and bottom faces. In previous literature, reports, it's already been reported that for thin AgNPs the atomically flat top and bottom faces have $[111]$ facets and the edges have $[110]$ facets.

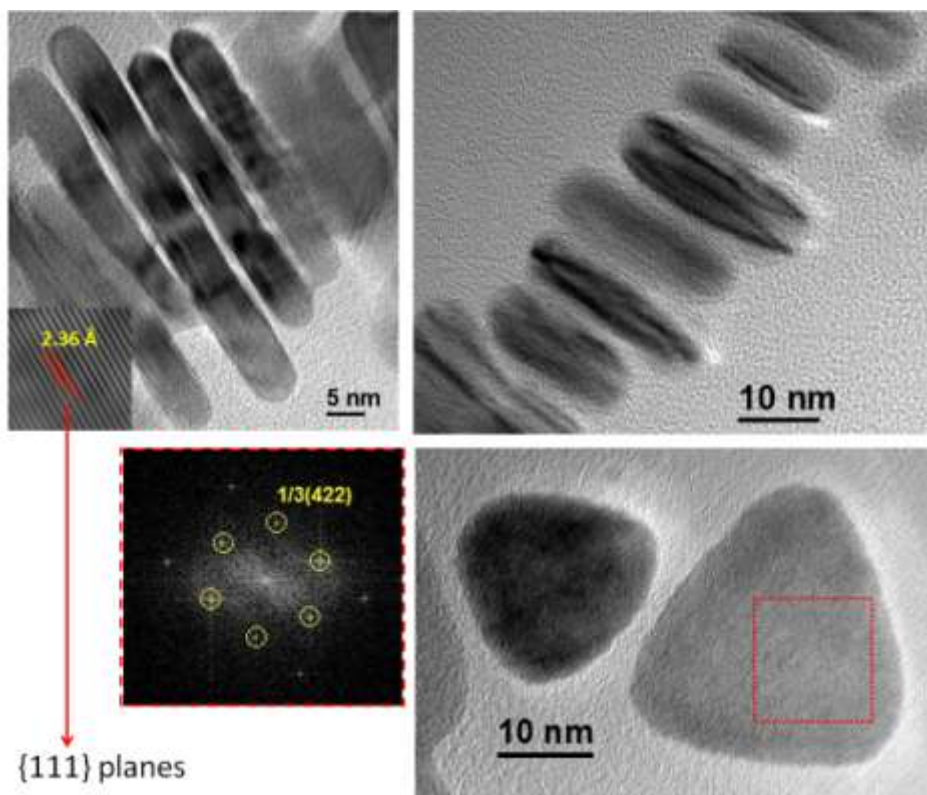


Figure 5.2: Frontal and sideways bright-field and HRTEM of our synthesized nanoprisms with $\{111\}$ lattice plane as the basal plane and $1/3\{422\}$ reflections indicate the presence of a single twinning boundary within the $\{111\}$ planes.

The measured thickness of these nanoprisms has been reported as ~ 7 nm.²⁴¹ Both the relative thickness map and the corresponding line profile indicates their two-dimensional growth.²⁴¹ The AgNPr synthesized by using 250 μL of 0.1 M NaBH_4 has been taken throughout this study which shows bright blue color with absorption maxima at 704 nm. The corresponding TEM images in **Figure 5.3A** and **5.3B** show a highly overlay stacking structure that transforms into an isotropically distributed arrangement by the application of ultrasonic wave at 40% power of 53 kHz frequency at 27 $^\circ\text{C}$ for 10 s. This implies that the binding force between $\{111\}$ faces of AgNPrs in the overlay stacking arrangement is quite a weak and easily breakable by applying weak ultrasonic force.

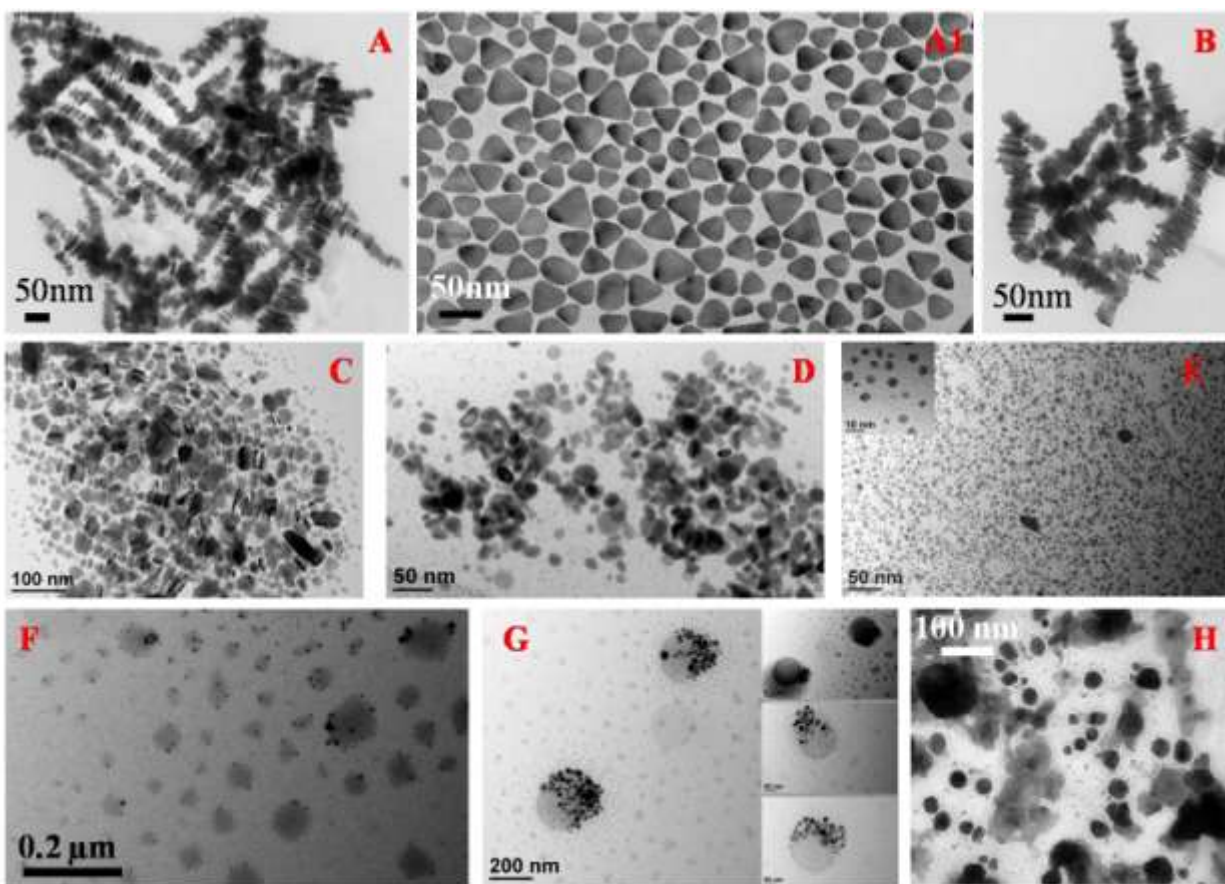
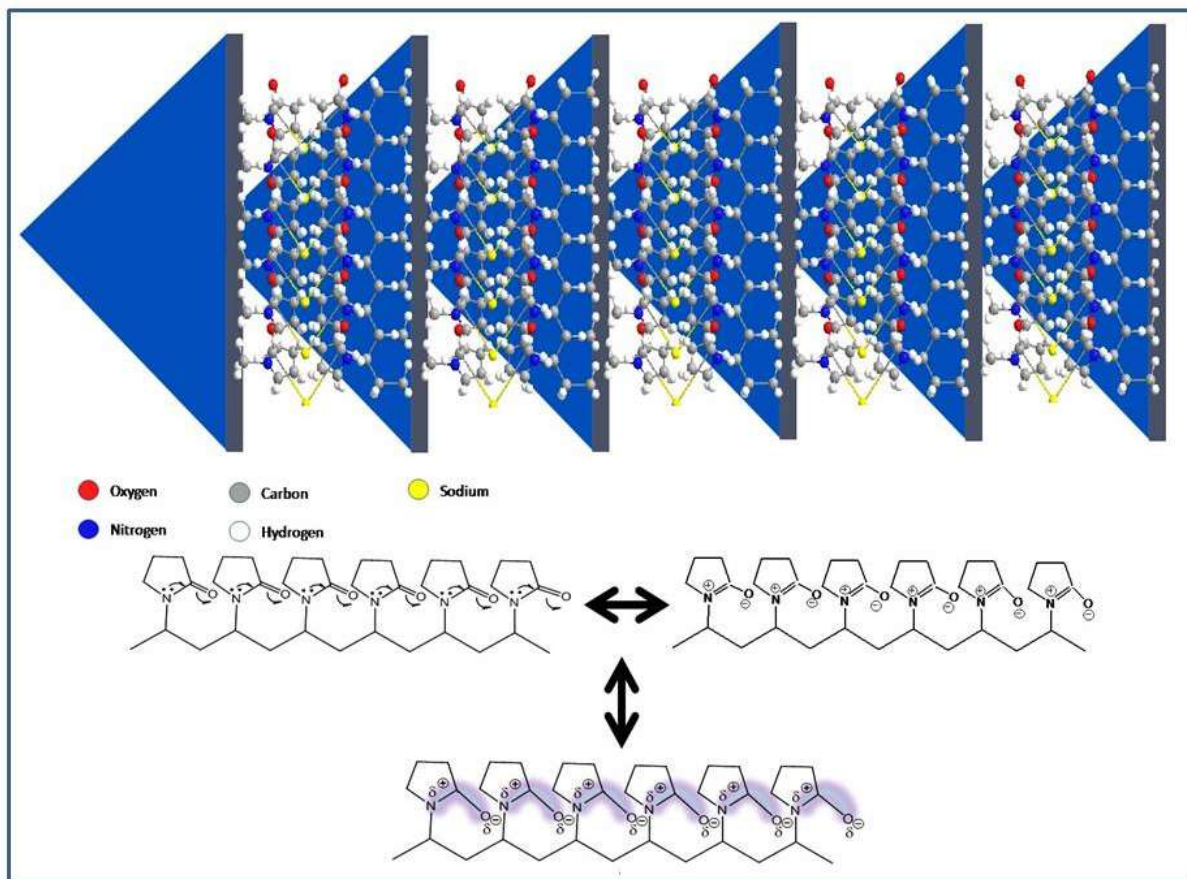


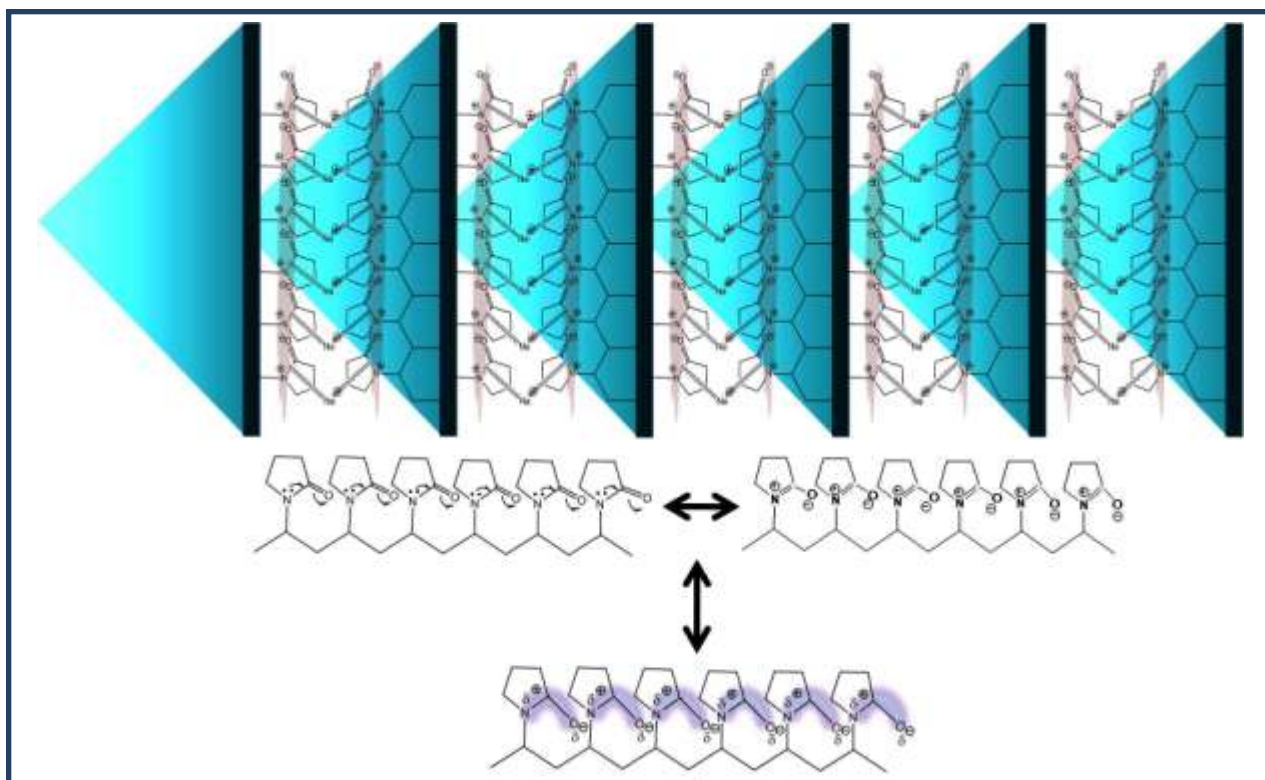
Figure 5.3: (A-H) Morphological change of AgNPr by destacking, followed by leaching of nanoprisms and emulsion induced controlled aggregation of silver seeds at increasing concentration of As(III). (A1) indicates the as-synthesized AgNPrs after the application of ultrasonic wave at 40 % power of 53 kHz frequency at 27 °C for 10 s. Here different TEM images correspond to the effect of concentration-dependent As(III) exposure on AgNPr structure where A, B, C, D, and E correspond to the As(III) concentration of 0, 1-2, 2-4, 5-7, and 8-40 μM , respectively. Similarly, the frames F, G, and H correspond to the effect of As(III) at concentrations of 40-80 μM , 350-750 μM , and $> 1 \text{ mM}$ respectively. A range of concentrations means that the morphology does not change throughout this range. Effect of As(III) at various intermediate concentrations has not been shown to avoid the complicity of the presentation.

Though the literature is affluent^{246,261–264} with reports of AgNPr overlay stacking, the actual reasons are still unknown. In an earlier report of AgNPr synthesis by using Bis(p-sulfonatophenyl)phenylphosphinedihydrate dipotassium salt (BSPP) as a surfactant also shows axial overlay stacking and has been explained by Mirkin^{263,264} and others as a result of π - π stacking offered by the benzene rings in triphenyl phosphine group of BSPP. The same explanation (π - π stacking) of axial overlay stacking also holds for PVP-mediated AgNPr synthesis due to the presence of short-chain π -electron moiety in the N-C=O region originating from each pyrrolidone group of surface-adsorbed PVP. Pyrrolidone molecules from Parallely oriented {111} facets of AgNPrs then can results π - π stacking but in that case, the distance between two flat prisms should not be more than 3.2 Å (the limit of π - π interaction is the sum of the van der Waals (VDW) radius between atoms involved where $r_{VDW}^C = 1.7$ Å, $r_{VDW}^N = 1.55$ Å and $r_{VDW}^O = 1.52$ Å).²⁶⁵ On the other hand if we consider cation- π interaction²⁶⁶ between available cations (Ag^+ and Na^+ ; $r_{VDW}^{\text{Ag}} = 1.72$ Å and $r_{VDW}^{\text{Na}} = 2.57$ Å) and surface adsorbed N-C=O π -electron moieties then the distance between AgNPrs should fall in the range 6.6-8.3 Å and the obtained TEM results indicate that cation- π as the most probable interaction pathway between AgNPrs to form an axially stacked sandwich geometry similar to ferrocene, $\text{Fe}(\text{C}_5\text{H}_5)_2$, structure. Geometrically the cation- π stacking in case of PVP is much weaker than the corresponding ferrocene type of molecules²⁶⁷ due to less degree of orbital overlap and can easily breakable by the application of weak ultrasonic wave as discussed before. **Scheme 5.1** explains the actual cation- π interaction among axially stacked AgNPrs where the ball-and-stick molecular geometry shows the orientation of surface bound PVP molecules and intercalated Na^+ ions. Atomic model of this cation- π interaction among surface adsorbed PVP molecules through

intercalated Na^+ ions which enforce them to arrange in an axial stacking configuration is shown in **Scheme 5.2** for better understanding the orientation of electrostatic interaction.



Scheme 5.1. Schematic representation of cation- π interaction among surface adsorbed PVP molecules through intercalated Na^+ ions which enforce them to arrange in an axial stacking configuration. Here all the interacting atoms and molecules are shown in the ball-and-stick model and π -electron cloud in violet color.



Scheme 5.2: Schematic representation of cation- π interaction among surface adsorbed PVP molecules through intercalated Na^+ ions which enforce them to arrange in an axial stacking configuration. Here all the interacting atoms and molecules are shown in the atomic model for better understanding the electrostatic interaction and π -electron cloud in violet color for better visualization.

It is worth mentioning that our zeta potential study (**Table 5.1**) confirms that these AgNPs are negatively charged and their zeta potential reduces gradually as we increase the amount of NaBH_4 during the synthesis. This $-Ve$ charge induces repulsion among AgNPs to destabilize their axial stacking and hence the relative contribution between cation- π interaction and the extent of electrostatic repulsion governs the distance between two AgNPs and may vary between idealistic 4 Å to a maximum of 10 Å. According to the literature, the free energies

associated with the crystallographic planes of an *fcc* metal increases in the order²⁶⁰: $\gamma_{\{111\}} < \gamma_{\{100\}} < \gamma_{\{110\}}$ and explains the axial stacking through $\{111\}$ facets.

Table 5.1: Variation of zeta potential (ξ) and stacking length (L) as we vary the molar ratio (M) between NaBH₄ and AgNO₃.

$M(\text{NaBH}_4:\text{AgNO}_3)$	4	7	9	16
ξ in mV	-25.4	-17.2	-14.6	-10.5
L in nm	0	93	136	198

Since the reduction potential for Na⁺, Ag⁺ and NaBH₄ are -2.71, 0.8 and -1.24 V respectively, NaBH₄ can easily reduce Ag⁺ but not Na⁺. Besides that, the concentration of NaBH₄ added during synthesis is more than enough for complete reduction of Ag⁺ which rules out the possibility of any free silver ion after AgNPr synthesis. As a result of this, an increased amount of NaBH₄ raises the concentration of Na⁺ ions not only to enhance the possibility of the cation- π interaction and thereby stacking length but also to reduce the effective negative charge of AgNPr assemblies. Obtained AgNPrs show a gradual approach towards neutral zeta potential with an increase in stacking length, L, as we increase the concentration of Na⁺ originates from NaBH₄. We can define the molar ratio (M) of NaBH₄ to AgNO₃ as:

$$M = V_{\text{NaBH}_4} \times S_{\text{NaBH}_4} : V_{\text{AgNO}_3} \times S_{\text{AgNO}_3}$$

Here ‘V’ and ‘S’ represent the volume and molar strength respectively. By varying the molar ratio (M) between 16 and 4 we have achieved different stacking lengths with an unchanged edge length of 50±20 nm for individual nanoparticles. By knowing the stacking number (N, the average number of AgNPr present in each stack) and thickness of individual AgNPrs (T) we can easily calculate the spacing (d_i , i=amount of NaBH₄) between AgNPrs in different stakes as

$d_i = \{L - (N \times T)\} / (N - 1)$. The effect of increasing concentration of NaBH_4 on stacking length has been clearly presented in **Figure 5.1B-E** where the average stacking length changes between 198 nm to 0 nm. Though the concentration of Na^+ is crucial in making of stacking patterns of AgNPrs, detection, and quantification of sodium ions as stacking intercalators is not easy by recording their Energy Dispersed X-Ray (EDX) spectra.^{268,269}

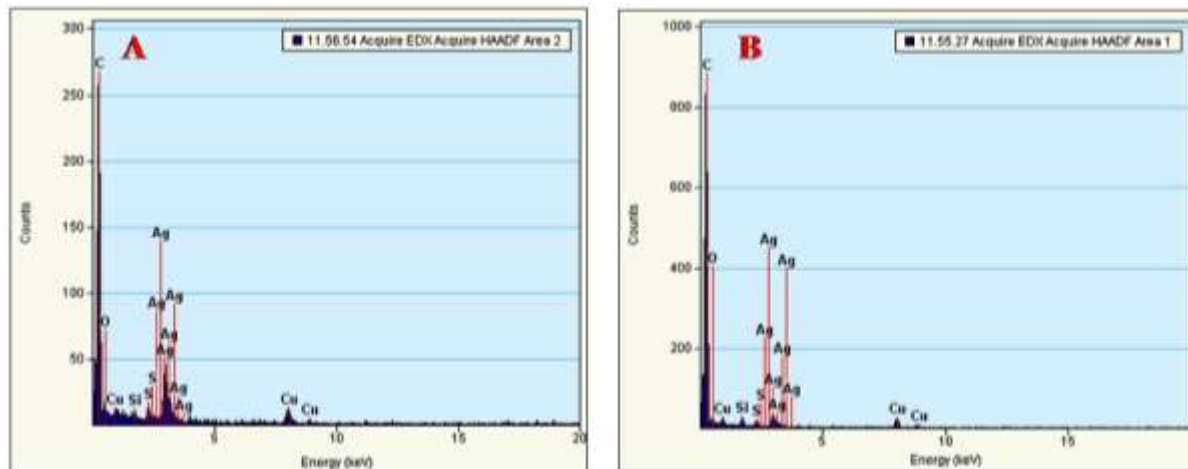


Figure 5.4: EDX spectra obtained from two different areas (Area-1 and Area-2) of AgNPr stacking to analyze the relative abundance of different elements.

Detection and quantification of an element through EDX depends mainly on two factors, (i) efficiency of detection for ejected electrons with energy less than 3 keV and (ii) whether the abundance of the element is less than 1000 ppm or not. Since the abundance of Na^+ -ion in our synthesis is in the range of 15-60 ppm, the efficiency of the detection of Na solely depends on the ejected electron energy. As most of the EDX detectors have virtually constant efficiency (~100%) in the range 3-10 keV, the probability and relative height observed for the families of X-ray lines depends heavily on the energy of the ejected electron from the sample. As a result of this, elements with the atomic number up to 17 (Cl: Chlorine) having K-edge below 3 keV is

difficult to detect. According to this logistic, ^{11}Na with K-edge at 1.08 keV will be difficult to detect from the EDX spectrum and the absence of Na-line is been depicted in **Figure 5.4**.

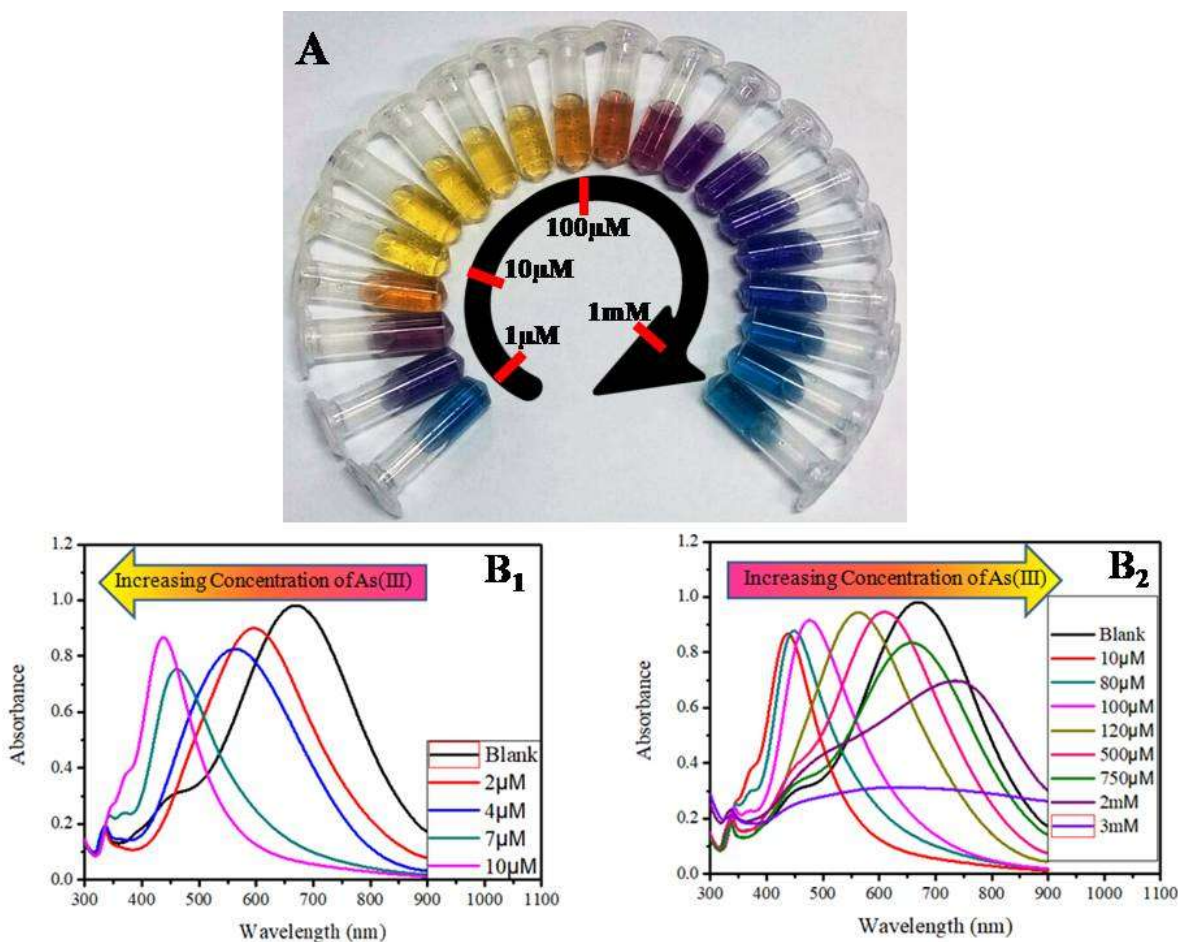


Figure 5.5: (A) Concentration-dependent color-coded sensing of As(III) between the concentration range of 10^{-6} M to 10^{-3} M, (B) Tuning of surface plasmon resonance as a result of morphological change of AgNPr at different concentration of As(III) between 10^{-6} M to 10^{-3} M where (B₁) shows the variation of plasmon band at the different lower concentration of As(III) in the range of 0.0-10.0 μM [0.0 μM (blank): Black trace (λ_{max} =704 nm), 1.0-2.0 μM: Blue trace, 2.0-4.0 μM: Orange trace, 5.0-7.0 μM: Red-Violet trace, 8.0-10.0 μM: Blue Violet trace] and (B₂) at different higher concentration of As(III). The Plasmon band and hence the color of the nanomaterials change in a distinct manner where a specific color remains unchanged in a broader

range of growing concentrations as 10.0-80.0 μM : Yellow, 90.0-100.0 μM : Orange, 110.0-200.0 μM : Dark Red, 250.0-500.0 μM : Purple, 750.0 μM -2 mM: Different shades of blue, 3 mM-10 mM: Faded Blue and above 10mM the color becomes faint blue to gray or almost colorless.

As reported in the early literature^{223,270} that As(III) can form a sparingly soluble stable complex with atomic or ionic silver as Ag_3AsO_3 complex, the chemical affinity between As(III) and atomic silver (Ag^0) on AgNPr surface can easily overcome the electrostatic repulsion between AsO_2^- and the negatively charged NPrs to induce the surface leaching. Upon the addition of increasing concentration of arsenite (AsO_2^-) the original blue color gradually changes to purple at 1-2 μM ($\equiv 75\text{-}150\text{ ppb}$), burgundy at 2-4 μM , pastel orange at 6-7 μM , golden yellow at 8-9 μM , yellow at 10-40 μM , light yellow at 40-80 μM and repeated these colors as pastel orange at 90-100 μM , brown at 110-150 μM , burgundy at 150-200 μM , blue-violet at 200-350 μM , lavender at 350-500 μM , deep blue at 500-750 μM and finally light blue at 750 μM -2 mM of As(III) (original color of the AgNPr). Corresponding color coding and UV-Vis spectra of each morphologically modified AgNPr is shown in **Figure 5.5A** and **5.5B** respectively. To understand the plasmonic change at lower (in the sub- μM concentration) and higher (above 10 μM concentration) concentration of As(III) we have plotted their UV-Vis spectra in two different figures as **Figure 5.5B₁** and **5.5B₂** respectively. Both **Figure 5.3 (5.3A-5.3E)** and **Figure 5.5B₁** shows the ability of our assay to detect As(III) in the μM level concentration.

With the consequent step-wise morphological change of the nanoprisms which shows a distinct color from the previous morphology²⁴⁸ due to the interaction of As(III) with the metallic core of the nanoprism, we have clearly represented this phenomena by recording the TEM image for each intermediate and has been portrayed details in **Figure 5.3A-H**.

Electronic configuration of As is $[\text{Ar}] 3d^{10}4s^24p^3$ and the corresponding As(III) is $[\text{Ar}] 3d^{10}4s^2$ and As(V) is $[\text{Ar}] 3d^{10}$. Due to the full filled electronic shell structure, As(V) is more stable and inert compared to As(III) having two valance electron to support its reactivity. Moreover due to the bulkier size of arsenate (AsO_3^-) compared to the arsenite (AsO_2^-), accessibility of inter planer space (6-8 Å) in AgNPr stacking by As(V) is less probable than As(III). Along with these two factors, by considering the formation of stable silver arsenite (Ag_3AsO_3) and silver arsenate (Ag_3AsO_4) compounds we have drawn them in Gauss View 5 and performed their geometry optimization by using HF/3-21g* level of theory. Energies for all the components of the following reaction was obtained to calculate the free energy of the reaction: $\text{Ag}_3\text{AsO}_3 + \frac{1}{2}\text{O}_2 \rightarrow \text{Ag}_3\text{AsO}_4$. The absolute energies are shown in **Table 5.2**. Optimized structures of Ag_3AsO_3 and Ag_3AsO_4 are shown in **Figure 5.6** and the information of different atoms of Ag_3AsO_3 followed by Ag_3AsO_4 are given in **Table 5.3**. The free energy of the reaction was found to be -118.5 kcal/mol suggesting Ag_3AsO_4 to be the more stable species.

Table 5.2: Energies obtained at HF/3-21g* level of theory

Compounds	Energy (Hartree/particle)
Ag_3AsO_4	-18043.05142490
Ag_3AsO_3	-17968.59515180
$\frac{1}{2}\text{O}_2$	-74.26744989

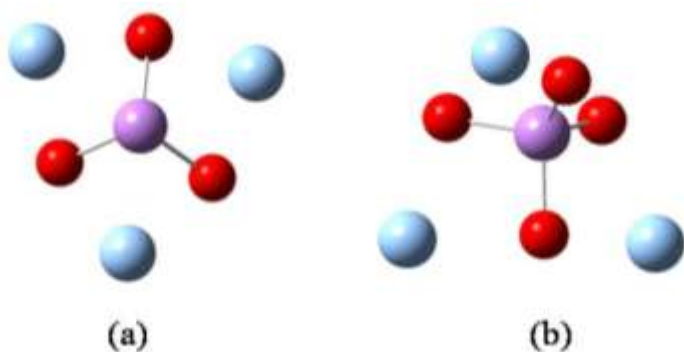


Figure 5.6: Optimized structures of Ag_3AsO_3 and Ag_3AsO_4 . Ag is shown in blue, As in purple and O in red.

Table 5.3: Optimized parameters of Ag_3AsO_3 and Ag_3AsO_4

E (RHF) = -17968.5951518 A.U. after 9 cycles

Standard orientation: Ag_3AsO_3

Center Number	Atomic Number	Atomic Type	Coordinates (Angstroms)		
			X	Y	Z
1	33	0	0.000019	0.000065	1.530613
2	8	0	-1.403607	-0.635236	0.645606
3	8	0	1.251808	-0.897880	0.645174
4	8	0	0.151592	1.533088	0.645129
5	47	0	-1.800588	1.291239	-0.468101
6	47	0	2.018600	0.913665	-0.468039
7	47	0	-0.217990	-2.204944	-0.468063

E (RHF) = -18043.0514249 A.U. after 9 cycles

Standard orientation: Ag_3AsO_4

Center Number	Atomic Number	Atomic Type	Coordinates (Angstroms)		
			X	Y	Z
1	33	0	0.000047	-0.000030	1.016691
2	8	0	-1.491375	0.451258	0.255757
3	8	0	0.354953	-1.517206	0.255592
4	8	0	1.136481	1.066017	0.255688
5	8	0	0.000135	-0.000151	2.651569
6	47	0	-0.569259	2.432903	-0.431888
7	47	0	2.391636	-0.723481	-0.431944
8	47	0	-1.822443	-1.709387	-0.431906

This relative chemical activity and steric hindrance caused by As(III) and As(V) will be discussed in the next section as a factor to explain the selectivity and sensitivity of As(III) for color-coded sensing. Due to the NaBH_4 reduction procedure to synthesize AgNPrs which results from a nanoparticle solution with pH 8.4 and the formation of stable and sparingly soluble silver arsenite (Ag_3AsO_3) and silver arsenate (Ag_3AsO_4) compounds at higher pH, organized assembly of AgNPrs can react instantly with arsenic ions in the intrinsic basic medium. Moreover, due to high pH of the AgNPr solution, it also diminishes the possibility of silver leaching through

oxygen reduction reaction (ORR: $\text{O}_2(\text{g}) + 4\text{H}^+(\text{l}) + 4\text{Ag}(\text{s}) \rightarrow 2\text{H}_2\text{O} + 4\text{Ag}^+$).²⁷¹ As we increase the concentration of As(III), due to the difference in stability between flat surface-bound [111] facets and edge bound [110] facets (free energies increases in the order²⁶⁰: $\gamma_{\{111\}} < \gamma_{\{100\}} < \gamma_{\{110\}}$) the number of pyrrolidone bound silver atoms from edges will be released more compared to flat surfaces. This will result the formation of smaller stackings due to the increase of surface charge originating from pyrrolidone molecules as we observed as an effect of As(III) addition between 1.0-6.0 μM . A gradual reduction in the dimension of AgNPr as a result of increasing the addition of As(III) (by comparing the dimension between B and E of **Figure 5.2**) confirms the removal of pyrrolidone bound silver atoms from [110] facets. The appearance of different surface Plasmon at different lower concentrations (between 1.0-6.0 μM) of As(III) has been depicted in **Figure 5.5B₁** which matches well with the obtained surface plasmons (**Figure 5.1A**) from different stacking lengths synthesized by using different amount of NaBH_4 . Hence at a lower concentration of As(III), the appearance of a different color is due to the transformation of longer AgNPr stacking into smaller piles. At the range of 6.0-7.0 μM of As(III), the stacking of AgNPrs disintegrated completely along with partial leaching of the tips as well as the surface of AgNPrs to produce isotropically distributed silver nanodiscs (average diameter between 15-25 nm) with surface plasmon band appears near 450 nm (green colored spectra in **Figure 5.5B₁**) and the corresponding TEM is shown in **Figure 5.1E**.

If we increase the As(III) concentration further in the range of 8.0-80 μM , silver nanodiscs are leached further to generate smaller nanoparticle (*silver seeds*) with size range 5-7 nm which gives different shades of yellow ($\lambda_{\text{max}}=410\text{-}430$ nm) as we mentioned before and has been represented in **Figure 5.3E**. Similar structural changes have also been observed as an effect of KSCN addition to light blue colored AgNPr solution reported by Tsai et al.²⁴⁰ Further increment

of As(III) concentration (between 90 μM -2 mM), the spontaneous reaction between silver seeds with arsenic removes PVP from nanosurface to initiate the formation of PVP-based controlled emulsions with an average diameter between 50-200 nm which starts incorporating silver seeds and induces controlled aggregation (smaller to larger) with a plasmon shifting between pastel orange to light blue (90-100 μM : λ_{max} = 460-470 nm, 110-200 μM : λ_{max} = 550-560 nm, 250-500 μM : λ_{max} = 600-610 nm and 750 μM - 2mM: λ_{max} =680-720 nm) and the corresponding TEM images are shown in **Figure 5.3F** and **5.3G**. If we increase the concentration of As(III) beyond 2 mM, a reaction between arsenic and silver is so vicious that it ultimately converts all nanomaterials into silver arsenate (Ag_3AsO_3) and forms unpredicted composites to lose plasmonic characteristics of silver nanoparticles which loses its blue color as shown in **Figure 5.3H** to shift the plasmon band much beyond 704 nm and ultimately disappears. Though the generated Ag_3AsO_3 is yellow, black colored aggregated silver material can easily mask the yellow color precipitation originating from Ag_3AsO_3 .

To find out the selectivity of As(III) for the morphological change of AgNPr which results from color-coded sensing of arsenic contamination, we have repeated the same set of experiments (absorbance, TEM and colorimetry) with several other metal salts which includes common alkali, alkaline and toxic transition metal ions including arsenate As(V) and the colorimetric result has been depicted in **Figure 5.7A**. To observe a sharp contrast in colorimetry and to avoid any unwanted interference (from morphological change²⁴⁸) from halogens we have used 30 μM concentration for all non-halide metal salts. Except for some minor contrast change, colorimetry can selectively and sensitively detect As(III).

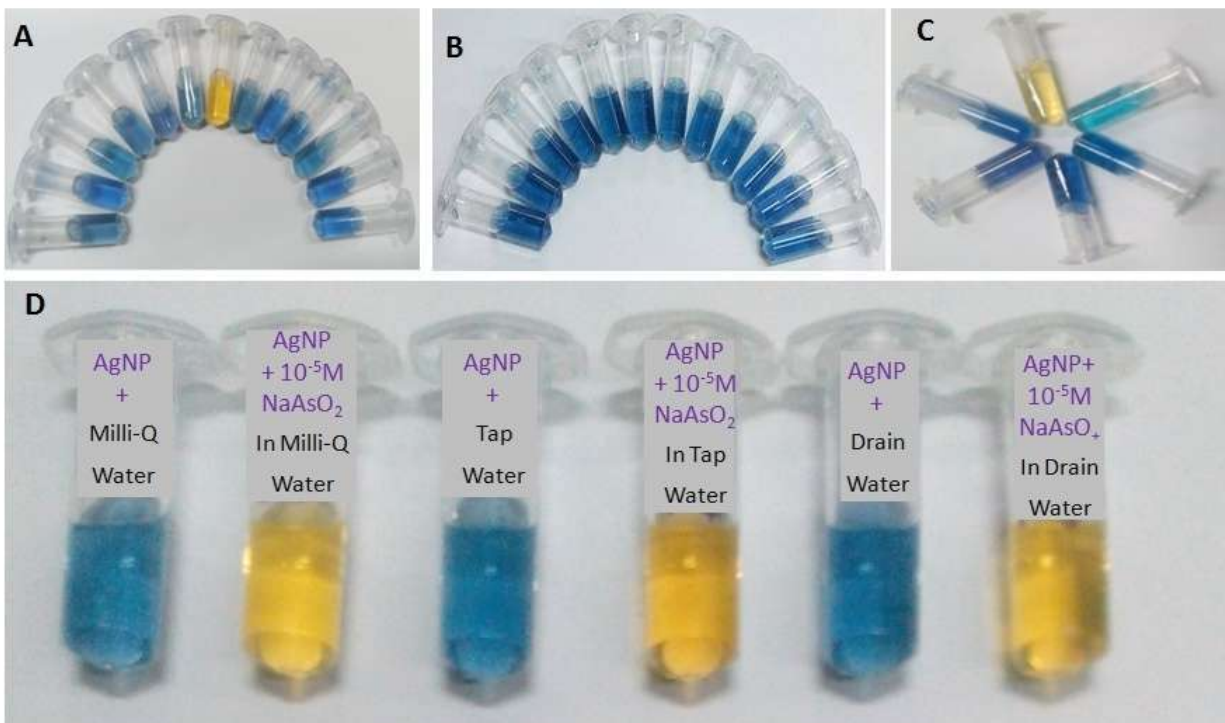


Figure 5.7: Colorimetric change of AgNPr solution upon addition of (A) 30 μM (left to right) Na^+ , K^+ , Ca^{2+} , Mg^{2+} , Sr^{2+} , Cd^{2+} , As^{3+} , Fe^{3+} , Hg^{2+} , Fe^{2+} , Pb^{2+} , Zn^{2+} and As^{5+} metal ions ; (B) NaOH in the concentration range 10 μM -1 mM; (C) Different concentration of arsenic prone water sample into the AgNPr colorimetric assay (D) 0.1 μM NaAsO_2^- dissolved in Milli-Q, tap water and drain water.

To confirm that the color change is not due to the pH change of the solution after the addition of the As(III) salt, we have checked the pH of the blank AgNPr solution and the same solution after the addition of the As(III) salt. We observed that the pH of all the solution was increasing slightly than that of the blank upon the gradual addition of As(III). We have performed a control experiment by adding an equal concentration of NaOH instead of the As(III) salt by considering 1 M NaAsO_2 to generate 1 M NaOH after complete dissolution. The pH in both cases is listed in **Table 5.4**. No color change (**Figure 5.7B**) was observed for pH change due to the addition of NaOH which proves that the role of pH for color tuning is negligible.

Table 5.4: Variation of pH due to gradual the addition of NaAsO₂ and NaOH to 1 mL AgNPr solution

Volume of NaAsO ₂ or NaOH added in 1 mL AgNPr colloidal solution (μL)	pH on addition of NaAsO ₂ (Stock Concentration: 10 ⁻² M)	pH on the addition of NaOH (Stock Concentration 10 ⁻² M)
1	8.39	8.40
5	8.42	8.47
10	8.46	8.54
20	8.48	8.60
40	8.56	8.70
50	8.60	8.82
100	8.80	9.01
Blank	8.34	-

The morphological change of AgNPr upon addition of different concentrations of As(III) which results in the appearance of different colors is also been traced by recording their SERS spectra in presence of crystal violet (CV) as Raman tagging molecule. We have taken 5 μL of 10⁻⁴ M CV and then added to 195 μL of the morphology modified color-tuned AgNPr solutions which we have obtained by adding the same amount of differentially diluted NaAsO₂ into same stock solution of AgNPr to avoid any dilution factor. Obtained SERS spectra from different morphology modified AgNPr are depicted in **Figure 5.8** in a relative intensity scale which includes the SERS signal as a result of As(III) addition in the range of 0-5 mM. It is clear from **Figure 5.8** that there is a gradual increment of the SERS signal intensity as we increase the As(III) concentration from 0 M to 8 μM. It is also clear from the TEM results (**Figure 5.3**) that the gradual increment of As(III) up to 8 μM results the initial destacking of AgNPrs and finally disintegrate each nanoprisms into smaller silver nanoparticles to increase the effective surface

area and results in a gradual increment of SERS signal for the formation of the higher number of hotspots. As we increase the concentration of As(III), the color of the resulted nanoparticle solution changes from golden yellow at 8-9 μM to yellow at 10-40 μM and light yellow at 40-80 μM As(III) due to the formation of smaller sized silver nanoparticles (seeds) and we observed a slight increment of SERS signal. Further addition of As(III) beyond 80 μM , SERS signal gradually reduces till 2 mM concentration and beyond 2 mM concentration of As(III) the resultant materials don't show any detectable Raman signal. Details about the mechanism of SERS and the mathematical formulation of the Raman enhancement factor, G , has been described in detail elsewhere.²⁷² G can be derived by the following equation:

$$G = \frac{I_{SERS}/N_{surf}}{I_{NRS}/N_{vol}}$$

where I_{SERS} is the surface-enhanced Raman intensity, N_{surf} is the number of molecules bound to the nanometallic substrate in the excitation volume, I_{NRS} is the normal Raman intensity and N_{vol} is the number of molecules in the excitation volume. In our estimation of enhancement factor, we have considered the excitation zone as a cube with a dimension of 100 μm or a volume of 10^{-6}cc . By considering the final concentration of CV in SERS experiment and normal Raman experiment as $2.5 \times 10^{-6}\text{ M}$ and 1 M respectively, the number of molecules adsorbed on the nanosurface and in bulk in the excitation volume has been estimated as 15×10^8 and 6×10^{14} molecules respectively. By comparing the Raman peak intensity at 1380 cm^{-1} the obtained enhancement factor (G) in the absence and in presence of $8\mu\text{M}$ (close to maximum SERS signal) of As(III) was calculated as 3×10^6 and 8×10^6 respectively. Depending on the increasing concentration of added As(III), the extent of released PVP also increases and allows the system

to form different diameter polymeric emulsions to incorporate smaller silver nanoparticles formed in the concentration range of 10-80 μM of As(III). Due to the bigger and thicker PVP layer, the accessibility of crystal violet to the core silver nanoparticles decreases gradually as we are forming different morphologically modified AgNPrs at higher concentrations of As(III). This gradual increment of the inaccessibility of CV to nanosurface incorporated inside emulsion results in a gradual reduction in SERS signal as observed in the concentration range between 80 μM -2 mM. Since the emulsion incorporated nanoparticles lose their plasmonic properties beyond 2 mM As(III) concentration, the observed SERS signal at 3 mM disappears as depicted in **Figure 5.8**. Assignments of different Surface Enhanced Raman line originating from CV have been reported and described elsewhere.²⁷³

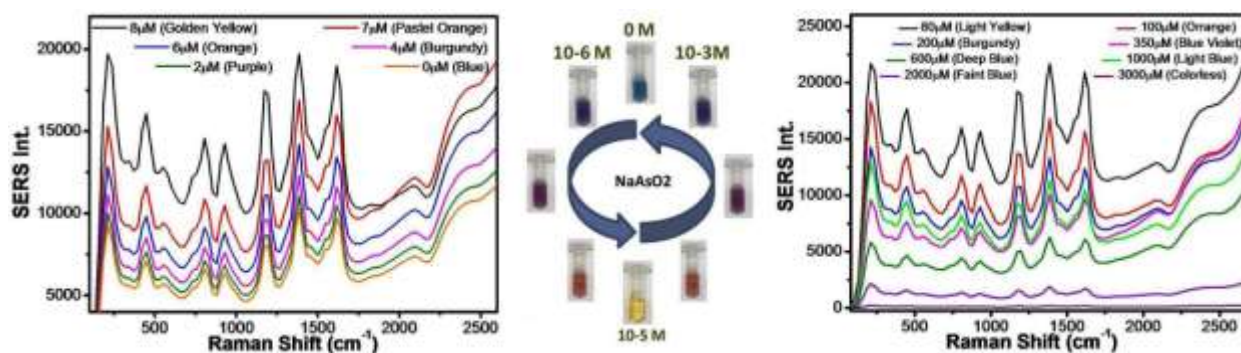


Figure 5.8. (Left) SERS based assay to monitor the morphological modification of AgNPr on the addition of different concentration NaAsO_2 in the concentration range 0-8 μM and the corresponding colorimetric response has been shown by the adjacent anti clockwise arrow;(Right) SERS response in the concentration range 80 μM - 3 mM and the corresponding colorimetric response by the adjacent anticlockwise arrow.

To find the applicability of our proposed AgNPr colorimetric-assay we have performed our investigation on real samples. For high specificity sensing and quantification of As(III) from real

samples, we have collected water from an arsenic prone zone of West Bengal (Duttapukur, North 24 Paraganas), India which has been used years as drinking water by the local people. We have taken 1 mL of our synthesized blue color AgNPr stock solution in each of six different centrifuge tubes (assay tubes) and then added different volumes of arsenic-contaminated water sample (filtrated by 0.2 μm syringe filter) in the range of 0-1 mL. Assay tubes containing arsenic-contaminated water samples less than 50 μL do not show any color change while other assay tubes having contaminated water volume more than 50 μL show usual color change as we have observed in our ideal highly specific colorimetric assay sensing of As(III). Colorimetric transition observed in AgNPr assay upon addition of the different amounts of arsenic prone water sample is shown in **Figure 5.7C**. The detection and quantification of As(III) from the real sample is not very straight forward and may associate with other problems. One such prominent problems come from the considerable presence of additional halides (Cl^- , Br^- and I^-) in the environmental water samples. The morphological effect of halides on AgNPr has been reported earlier²⁴⁸ and discussed in the previous section. So the observed color change may originate both from halide ions and As(III). To confirm the origin of color change, we have titrated the water sample against 10^{-2} M AgNO_3 solution using KCrO_4 as the indicator. From the endpoint, we have calculated the amount of precipitable salt as ~ 2.1 mM. From the literature²⁴⁸ it is known that the color change of AgNPr is observable only when the concentration of halide ion present in the water sample is ≥ 20 mM. Since the precipitable salt concentration is only 2.1 mM in our studied sample which is 10-times less than the threshold halide concentration for color change, rules out the presence of any substantial amount of halide which can independently cause color change. Hence, the observed color change is solely originating from As(III) present in the water sample and the threshold concentration for As(III) detection in the micromolar range (1-2 μM)

shows its hypersensitivity. Along with arsenic-contaminated real water sample, we have applied our assay on different sourced water samples collected from Milli-Q filtration system (Synergy, UV), Tap water and drain water from Kolkata region. After initial filtration by 0.2 μm syringe filter we have infused them separately with NaAsO_2 to reach the desired 100 μM concentration of As(III). Once we add 100 μL of Milli-Q water as control and As(III) infused water as test samples separately in a set of two 900 μL blue color AgNPr solution, all of them show desired golden yellow color for the infused samples and no color change for the blank which proves zero interference from other components of water. Since WHO reports that the average halide (mainly Cl^-) concentration in water is only 4 μM (much lower than the interference level) in drinking water, our AgNPr-based assay can successfully be used for As(III) sensing in drinking water without much interference from halide ions.

5.4 Conclusion:

AgNPr-based assay has been designed and the experimental procedure has been elaborated to achieve the wide range morphologically modified surface Plasmon tuning-detuning for accurately color-coded detection and sensing of As(III) over other alkali, alkaline, and transition metals. Wide range morphological modification of AgNPr is measured and confirmed by TEM measurement and a plausible explanation has been provided to understand the mechanism of selective interaction of As(III) with axially stacked AgNPrs based on their zeta potential, plasmon tuning-detuning and surface enhanced Raman spectroscopy along with DFT calculation. Plasmon tuning-detuning positively not only confirms the presence of As(III) but also can detect the As(III) concentration up to a limit of 75 *ppb* which is close to the old EPA limit for As(III) content in drinking water. This is probably the first report where we have

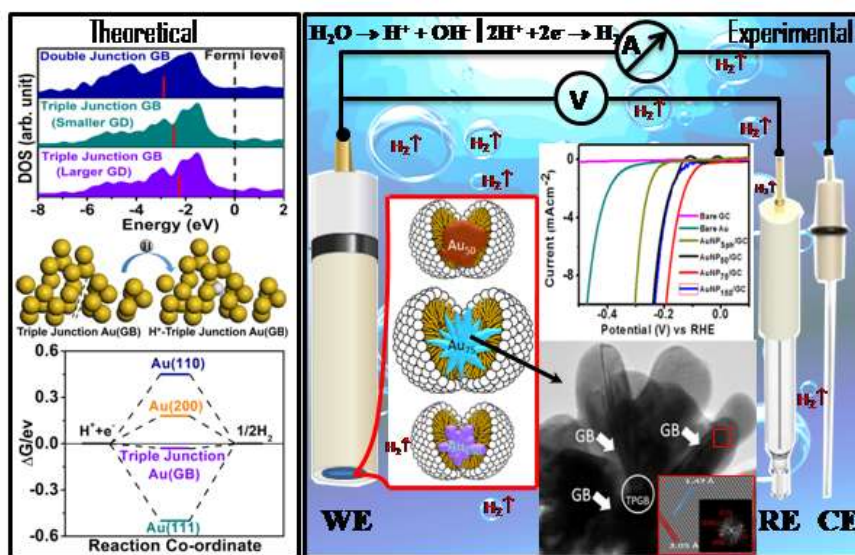
explored the critical role of PVP for wide range morphological modification followed by emulsion induced aggregation to effectively tune the surface plasmon for color-coded sensing of heavy metals. Ours cross-check with As(III) containing real sample from arsenic prone area of West Bengal, India and As(III) infused real water sample from different sources proves the potential applicability of this assay as a colorimetric sensor for field application towards environmental protection drive.

CHAPTER-6

Unveiling the Excellent Electrocatalytic Activity of Grain-Boundary Enriched Anisotropic Pure Gold Nanostructures towards Hydrogen Evolution Reaction: A Combined Approach of Experiment and Theory

OUTLINE: Specific Points of Discussion

- The role of grain-boundary and grain size of our newly synthesized flower-like gold nanostructures for the hydrogen evolution reaction (HER) has been investigated quantitatively.
- All the synthesized anisotropic gold nanoparticles (A^n GNPs) and especially the $AuNP_{75}$ exhibit outstanding catalytic activity (in terms of both overpotential and turnover frequency) towards HER compared to spherical shaped gold nanoparticles (S^p GNPs).
- The effective contribution of grain-boundaries towards the free energy of hydrogen adsorption (ΔG_{H^*}) and the position of the d-band center has been explored by DFT-calculation which matches well with our experimental findings.



6.1 Introduction

In the recent few years, considerable attention has been paid to developing the strategies to generate renewable energy as it is an alternative and naturally replenished source to that of the limited resource of fossil fuel.^{274,275} With the increasing demand for fuel as well as for environmental benefits, renewable energy is more preferable to other traditional energy sources.²⁷⁶ Among different renewable energy, Hydrogen is regarded as a green fuel with high energy density and pollution-free fuel (cost-effectiveness and environmentally friendly) which can be an alternate and competitive to that of coal or oil.^{277–280} Electrolysis of water is the most feasible approach^{281,282} to get the molecular hydrogen effectively and enormously as the source is unlimited and replenished inhuman timescale. The electrochemical water splitting involves two half-cell reactions wherein the oxygen evolution reaction (OER) occurs at the anode and the hydrogen evolution reaction (HER) takes place to that of the cathode.²⁸³ However, both of these reactions are extremely sluggish in nature which requires a larger overpotential.^{284,285} Though a large group of scientists throughout the Globe has put their extreme effort to design an array of suitable electrocatalysts, enough effort has not been put forward to explore different characteristics within the traditional materials by tweaking their nanoscale crystallization pattern or bringing folds within single- or multi-twinned nanoparticle for boosting the reaction kinetics. This will not only reduce the effort to design a new class of materials and cost to perform their complete characterization, but also to control environmental pollution. It has been found that the Platinum based materials especially carbon supported Platinum (Pt/C) are the most viable and efficient electrocatalysts for the HER till date,^{286–288} but their high cost and low abundance restrict themselves for commercialization and large scale production of H₂.^{289,290} Several attempts have been taken to accelerate the reaction kinetics by employing various transition metal-based catalysts (e.g. Ru-, Mo-, Ir-based materials),^{291–293} metal alloys,²⁹⁴ chalcogenides,²⁹⁵

metal-organic frameworks,²⁹⁶ etc. In this aspect, the noble metals like gold is rarely been explored due to the poor adsorption or binding efficiency of H-atom on the gold surface which requires higher free energy to step up the reaction.²⁹⁷ HER generally consists of two step process in which the first step is the adsorption of hydrogen atoms on the surface of the catalyst (this step is called Volmer step) and the second step leads to the generation of hydrogen molecule followed by desorption from the catalyst's surface (this step is known as Tafel or Heyrovsky step).²⁹⁸ Sabatier's principle suggests that the adsorption energy should neither be very high nor very low for a preferable catalyst since the higher adsorption energy leads to an endothermic process resulting weaker adsorption while the lower adsorption energy possesses exothermic process which results in the slow desorption.²⁹⁹ It has been predicted from the Volcano plot that the Gibbs free energy (ΔG) for an effective electrocatalyst towards HER process should be close to zero (i.e. $\Delta G \approx 0$). In the Volcano plot, the Pt metal possesses the highest activity in terms of both current density (j_0) as well as favorable ΔG value. However, in case of Au metal, the poor interaction of H-1s orbital with the d-band of metal makes the gold nanoparticles as a poor candidate for HER.²⁹⁸ Most of the literature reports covered the influence of other metals (e.g. alloys of Au)³⁰⁰ or semiconductor or organic molecules³⁰¹ with gold nanoparticles for the HER activity. Therefore, it is really a challenging task to build a feasible electrocatalyst for HER using pure gold nanoparticles.

Further, it is worth to mention that among various noble metals, gold nanoparticle has attracted greater attention over the last few decades due to their distinct physicochemical properties e.g. easier size and shape tenability to achieve both larger surface to volume ratio (S/V) and differential electric field lensing at the surface or vertex, enhanced surface Plasmon resonance (SPR) and hence the extinction coefficient in the VIS-to-NIR region. Higher reduction

potential of Au^{3+}/Au system ($E^0 = 1.50 \text{ V vs SHE}$) allows to use weak reducing agent resulting slow crystallization and hence programmable crystal twinning, easy manipulation of facet energetic as well as ease of surface modification (for selectivity and sensitivity) in comparison with that of bulk gold.³⁰² The fine blending of distinctive optical and electrical properties of gold nanoparticles (AuNPs) rendered themselves as a potential candidate in extensive fields of research such as catalysis,³⁰³ biomedicine,³⁰⁴ biosensors,³⁰⁵ and surface-enhanced Raman spectroscopy.³⁰⁶ Indeed, the performance of the AuNPs in the aforementioned applications, more specifically the catalytic performance strongly rely on their morphology, surface charge, crystal irregularity as well as crystal facet energy.^{307–309} In the recent few years, the anisotropic gold nanomaterials (i.e. flowers, multipod, star-shaped, branched) have extensively been focused since they reveal unique SPR, SERS as well as efficient catalytic power than the corresponding spherical particles.^{59,310} The remarkable catalytic efficiency of the AⁿGNPs is associated with the appearance of high the density low coordination site atoms on edges, terraces, steps, ledges, and kinks which may alter the surface energy.³¹¹ Further, the presence of planner defects such as grain boundary, twin boundary, stacking fault into the nanocrystal can significantly alter the reactivity of nanomaterials.³¹² In recent reports, it has been shown that the electrocatalytic activity of AuNPs is significantly boosted for the reduction of CO_2 due to the occurrence of the high density of grain boundaries.^{21,79} In addition, the grain boundary induced catalytic activities with remarkable efficiency are also observed for copper nanoparticles towards the electroreduction of CO .³¹³ Further, the presence of multiple twin boundaries (MTB) onto the nanoparticle surface enhances the catalytic ability for the oxidation of methanol via facile chemisorption of analytes.³¹⁴ In addition, from our previous study³¹⁵ we know that the anisotropic nanomaterials which result in sharp tips with enhanced ability to focus the surface

electric field and hence modulate the charge density has a distinct influence on their catalytic activity. Hence, the anisotropic nanomaterials are more preferable for both catalytic performances as well as to explore the new aspects related to catalysis than the isotropic counterparts. However, the anisotropic growths of nanoparticles are strongly dependent on the adopted synthetic procedure. Therefore, the synthetic methodologies are also crucial for the inducement of important physico-chemical properties into noble metal nanoparticles.

The standard protocols have already been well documented in the literature for the generation of AⁿGNPs including template-based reaction,³¹⁶ multi-step seeding methodology,^{317,318} utilization of specific capping agents,³¹⁹ fine tuning of physical parameters (i.e. temperature, pH, viscosity) during synthesis. The seeding growth approach is the most familiar method for the anisotropic growth of AuNPs since the degree of anisotropy (i.e. aspect ratio, tunable geometry) can be altered simply by varying the amount of seed solution, introducing specific impurities (e.g., AgNO₃, NaCl)³²⁰ as well as by altering the concentration of capping agent. However, the main drawback of this technique is its time-consuming nature as well as the growth of nanoparticles which depends mostly on the nature of nanoseed. On the other hand, template-based synthesis is more fascinating since they offer an interesting and useful characteristic to the nano materials such as controlled sizes, morphologies, and different physicochemical properties.²⁴⁵ Both soft and hard templates have been successfully employed for the synthesis of different shaped AuNPs viz. nanorods, nanorings, nanotubes, as well as porous structures. The soft templates are mainly large organic compounds (i.e. surfactants or polymers), used for surface stabilization while the porous solid inorganic materials such as an anodic aluminum oxide (AAO), mesoporous oxides, and carbon nanotubes (CNTs) can be used as hard templates.³²¹ Although the hard templates having better control over the structure of

nanomaterials, on account of their difficulty in the removal process after synthesis may destroy or alter the actual physical properties of templated nanoparticles. Besides, the surfactant (soft templates) assisted wet chemical synthesis is more preferable due to its ease of surfactant removal, large scale production, and remarkable ability to generate variable size and shape nanoparticles through the micelle formation.³²¹ Hence, surfactant induced rapid, a single-step methodology is worth enviable for the synthesis of anisotropic metal nanoparticles.

In the present study, we have reported a facile, one-step synthesis of gold nanoparticle using hydroquinone (HQ) as a reducing agent in the presence of sodium dodecyl sulfate (SDS). The proposed synthetic protocol is new in the literature, cost-effective, rapid yet generates high quality monodispersed nanoparticles with excellent stability. The morphology as well as the size of gold nanoparticles can easily be tuned from bud to flower (bloom) to over-bloomed shape by simple variation in the concentration of HQ. The characterizations of the synthesized nanoparticles have been carried out using UV-Vis, SEM, HRTEM, XPS and Zeta Potential analysis. The synthesized nanoparticles with variable grain parameters exhibit an outstanding electrocatalytic activity towards hydrogen evolution reaction (HER) in different pH medium (i.e. acidic, neutral, and basic) with a low onset potential of -76 mV. Besides, it requires mere 190, 285, 325 mV (vs RHE) of overpotentials to achieve 10, 50, 100 mAcm⁻² current density in 0.5 M H₂SO₄ medium. DFT study shows that the presence of high-density grain boundary with the larger dimension of each grain on the surface of nanocrystal can significantly enhance the reaction kinetics for HER and hence improves the HER activity.

6.2 Synthesis of AuNPs using HQ:

In a typical synthesis, 0.058 g of SDS was added to 20 mL of Milli-Q water in a 50 mL conical flask and stirred (500 rpm) for five minutes to make 0.01 M solution. After the complete

dissolution of SDS, 0.5 mL of 10^{-2} M $\text{HAuCl}_4 \cdot 3\text{H}_2\text{O}$ (Final concentration: 2.5×10^{-4} M) was added into the solution. Subsequently, 75 μL of 0.1 M HQ (Final concentration: 3.75×10^{-4} M) was added dropwise to the above solution mixture under the same constant stirring. The color of the solution changes immediately (within 5 s) from light yellow to cyan color and the resultant solution was kept undisturbed for another 6 hours for complete growth of nanoparticles. The synthesized nanoparticles were then washed repeatedly by centrifugation at a speed of 2000 rpm for 45 minutes initially and then 30 minutes in order to ensure the removal of excess surfactant and other unwanted products. The entire reaction was carried out at 25 ± 1 °C. In order to study the effect of concentration of reducing agent, a similar protocol was also adopted for synthesizing AuNPs using the variable concentration of HQ at identical concentrations of metal ion and SDS as mentioned earlier. The addition of the lower amount of HQ (50 μL of 0.1 M) into the reaction mixture leads to change the color of solution from light yellow to pink color while at the higher concentration of HQ (150 μL of 0.1 M), the solution turns into bluish color indicating the formation of different sized and/or shaped nanoparticles. The synthesized nanoparticles were washed using the same procedure as mentioned earlier. The prepared AuNPs using 50, 75, and 150 μL of HQ are designated as AuNP_{50} , AuNP_{75} and AuNP_{150} respectively.

6.3 Computational Details:

All the spin-polarized calculations were performed within the framework of density functional theory (DFT) using the plane-wave technique as implemented in Vienna Ab Initio Simulation Package (VASP).¹¹⁵ The exchange-correlation energy was accounted within the generalized gradient approximation method (GGA) parameterized by the Perdew-Burke-Ernzerhof (PBE).³²² We used the projector augmented wave potential (PAW) to treat the ion-electron interactions. The DFT-D2 empirical correction method proposed by Grimme was

applied for describing the effect of van der Waals interactions.³²³ In all computations, the kinetic energy cut off is set to be 500 eV in the plane-wave expansion. All the structures were fully relaxed (lattice constant and atomic position) using the conjugate gradient method and the convergence threshold was set to be 10^{-4} eV in energy and 0.01 eV/Å in force. For geometry optimization, the Brillouin zone was sampled using a 5×5×1 Monkhorst-Pack k-point mesh while a higher 7×7×1 Monkhorst-Pack grid was used to calculate electronic density of states (DOS). The relative free energy of adsorbed atomic hydrogen (H*) was calculated as^{134,300}

$$\Delta G_{H^*} = \Delta E_{H^*} + 0.24$$

where ΔE_{H^*} for the adsorption of H* on various surfaces were determined using the relation

$$\Delta E_{H^*} = E_{surface+H} - E_{surface} - \frac{1}{2}E_{H_2}$$

In order to model Au (111) and (110) surfaces, we considered a 2-layer periodic 3×3 slabs of cell (8.11×8.11 Å²) and (7.91×7.93 Å²) with 18 atoms respectively, whereas Au (200) surface was constructed with 3-layer periodic 3×3 slab of the cell (7.95×7.95 Å²) with 27 atoms. Grain boundaries (GB) have been constructed with different surfaces where GB_a corresponds to the grain boundary between (110) and (111) planes as well as GB_b, GB_c, GB_d, GB_e corresponding to the grain boundaries among (110) and (200), (200) and (111), (110)(200) and (111) with smaller grain diameter, (111), (110)(200) and (111) with larger grain diameter respectively. GB_a, GB_b, GB_c, GB_d and GB_e have been modelled with periodic supercell consisted with 16, 20, 20, 28, and 28 Au atoms respectively. To avoid the spurious interactions between the neighboring slabs, a vacuum layer of 20 Å was used in the direction perpendicular to the surfaces (along the Z-direction) and the nearest distance between the two adsorbed hydrogen atoms in the adjacent supercell is ~10 Å.

6.4 Results and Discussion

6.4.1 Optical and Structural analysis of AⁿGNPs

The synthesis of AⁿGNPs using HQ as the reducing agent in the presence of SDS as a template is schematically shown in **Figure 6.1A**. In general, the surfactant form micelle through the hydrophilic-hydrophobic interaction with the solvent molecule above a particular concentration termed as critical micelle concentration (CMC). Since in the present study we have employed a larger concentration of SDS (0.01 M) than its CMC (CMC of SDS is 0.0082 M), the formation of micelles takes place obviously (shown in **Figure 6.1A**). The addition of metal salt into the SDS solution may lead to the incorporation of metal ion ($[\text{AuCl}_4]^-$) into the SDS micellar cavity. However, the incorporation of chloroaurate ion into SDS micelles is less favorable in this context due to the hydrophobic nature of the inner core of micelles (where the long tail i.e. hydrophobic part remains inside and hydrophilic part remains outside of the core). The presence of metal ion (chloroaurate ion) at the periphery of the micelles is more complimentary on account of its facile interaction with the hydrophilic part of the surfactant. It is worth mentioning here that $[\text{AuCl}_4]^-$ ion may be repelled at the periphery of the micelle due to the presence of anionic group of the surfactant. Indeed, this possibility is nullified on account of the existence of counter ion of SDS i.e. Na^+ with the anionic part $[\text{CH}_3(\text{CH}_2)_{11}\text{OSO}_3]^-$. It has been reported that, the increase in concentration of counter ion of surfactant (i.e. Na^+) leads to alter the size of micelle which provides the confirmation for the occurrence of Na^+ surrounding the micelle of SDS.^{324,325} The occurrence of Na^+ at the periphery of micelles diminishes the repulsion between hydrophilic head group and $[\text{AuCl}_4]^-$ and hence the later can exist close to the SDS micelle. The addition of HQ in the reaction mixture results in the reduction of Au^{3+} to Au^0 and this Au^0 incorporate into the micelle core as schematically represented in **Figure 6.1A**. In this case, two

possibilities may arise; either the Au atoms begin to associate with each other followed by encapsulation into the micelle core or get incorporated into the micelle core followed by preferable crystallization or assembling.

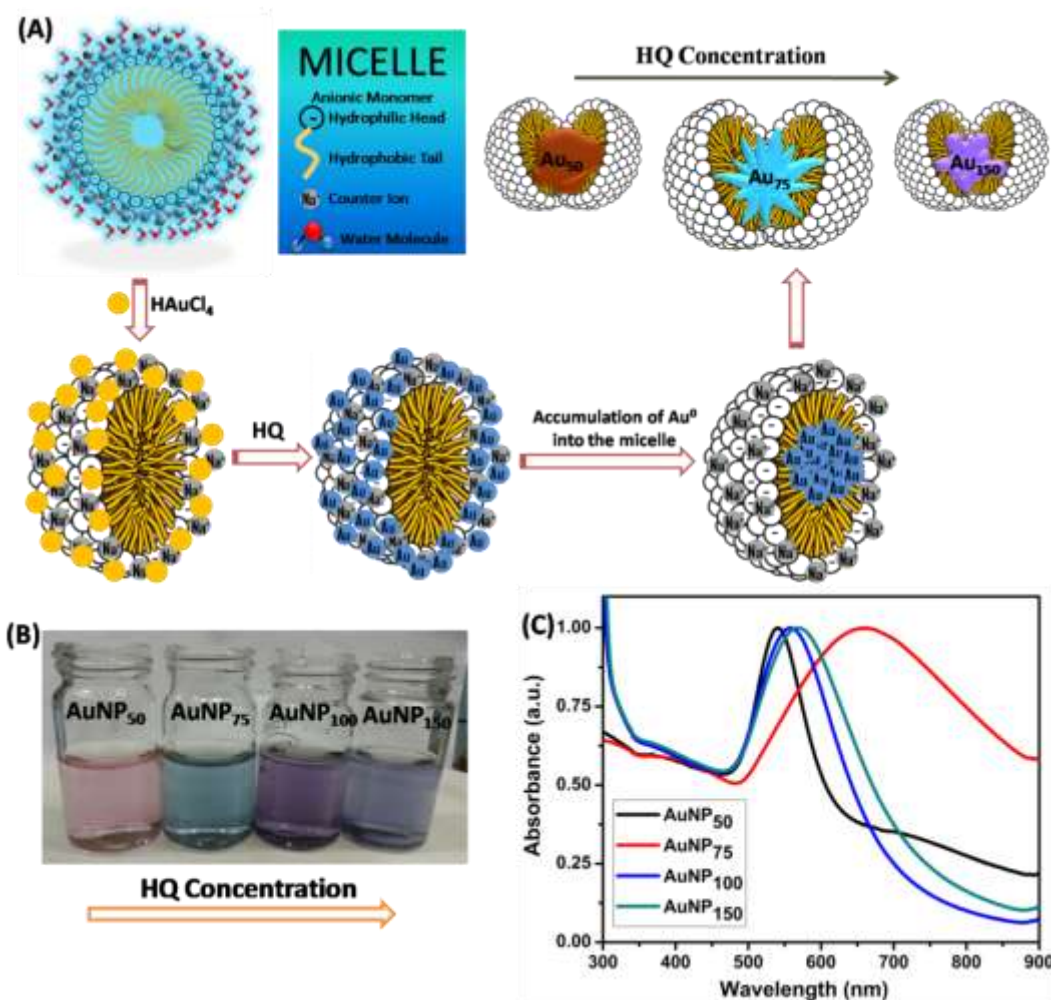


Figure 6.1: (A) Schematic representation for the synthesis and growth of AⁿGNPs inside the SDS micelle's core. Effects of HQ concentration (250-750 μ M) on (B) visual color appearance (pink to blue) and (C) plasmon spectra (540-660 nm) of colloidal AⁿGNPs.

Change in the concentration of HQ leads to alter the color of the resultant colloidal solution (**Figure 6.1B**) which predicts the formation of different nanoparticles with variable physico-chemical properties. The initial assessment of the synthesized AⁿGNPs was carried out

by UV–Vis spectroscopy (**Figure 6.1C**) in the aqueous medium. The AⁿGNPs prepared using 50 μL of HQ (10^{-1} M) in presence of SDS exhibit a sharp surface plasmon resonance (SPR) band in the wavelength range of 500–600 nm with λ_{max} at 540 nm. The color of the colloidal solution (pink) and the nature of the absorption band (i.e. single plasmon band with λ_{max} : 540 nm) suggests the formation of monodispersed spherical shaped-gold nanoparticles (AuNPs).

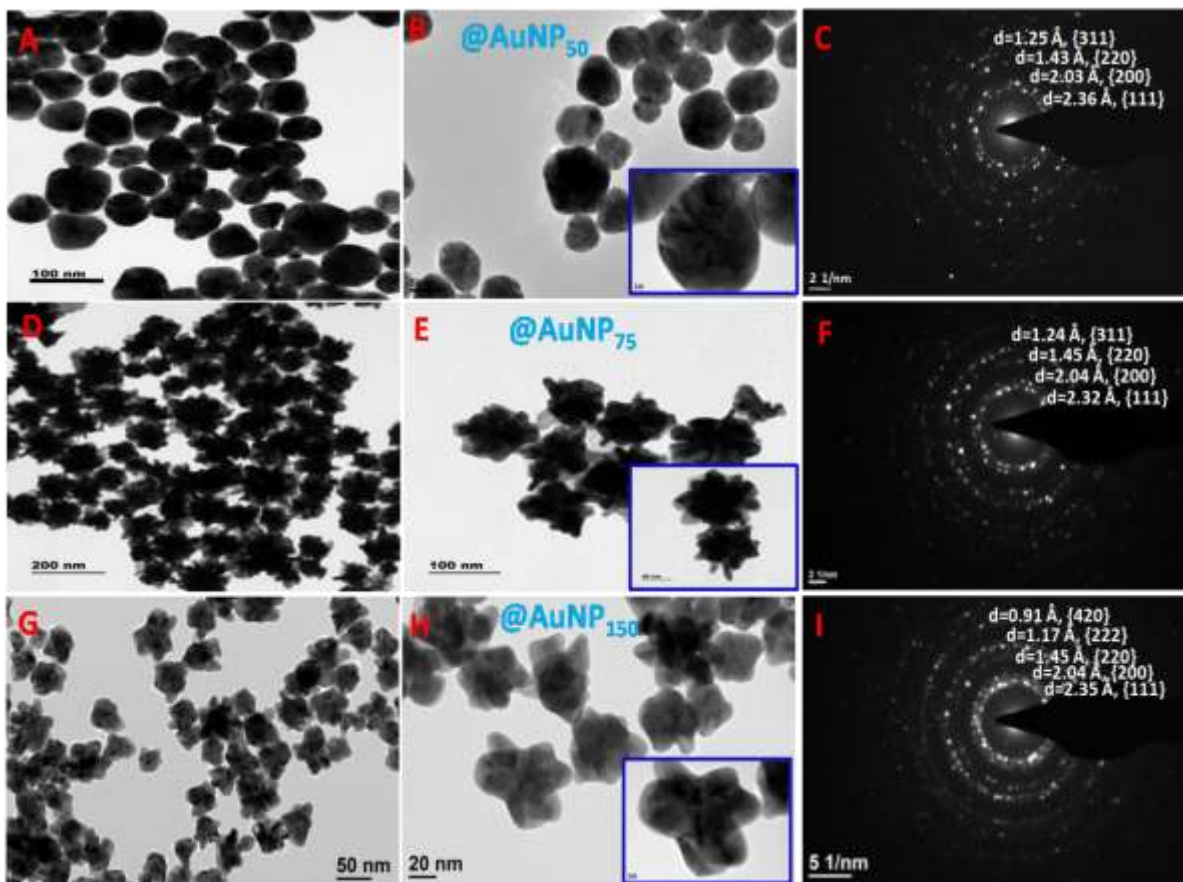


Figure 6.2: The TEM images of bud or spherical (A, B), flower or bloom (D, E) and hexapod or over bloom (G, I) shaped AuNPs synthesized using 50 μL , 75 μL and 150 μL of HQ respectively at different magnification. The SAED patterns of AuNP₅₀ (C) AuNP₇₅ (F) and AuNP₁₅₀ (I) exhibit the polycrystalline nature of different shaped AⁿGNPs and the presence of different crystal planes. The inset in (B), (E) and (H) represent magnified images of the individual nanoparticles.

Increasing the amount of HQ from 50 to 75 μL results in the red shifting of SPR band from ca. 540 nm to ca. 660 nm and also the color of the colloid changes from pink to cyan. The appearance of the absorption band at higher wavelength region in association with broadening nature suggests the formation of large-sized nanoparticles or anisotropic formation of AuNPs as indicated earlier in the literature.³²⁶ Further rise in the amount of HQ from 75 to 100 or 150 μL results in the alteration of color from cyan to bluish along with the blue shifting of the SPR band from 660 nm to ca. 580 nm. The stability and surface charge of these AⁿGNPs are investigated using zeta potential measurements wherein all of these nanoparticles show the zeta potential value of ~ -35 mV indicating the good stability of our designed AuNPs. The negative charge of the nanoparticles can be correlated to the presence of anionic surfactant SDS on their surface.

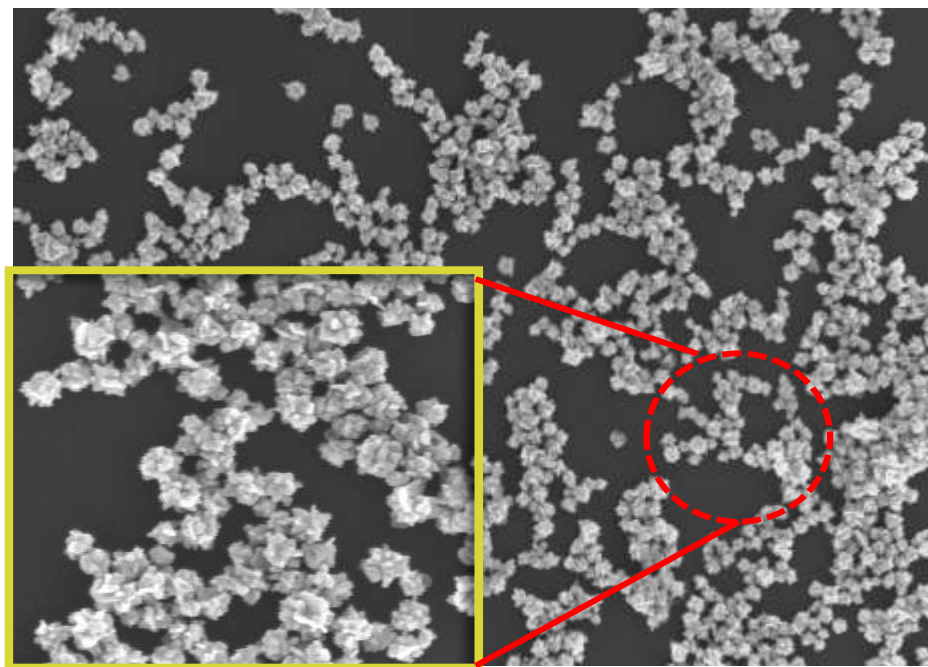


Figure 6.3: SEM image of flower or bloom shaped AuNPs i.e. AuNP₇₅.

The role of HQ on the morphology of AⁿGNPs has been studied wherein the geometry varies with the concentration of reducing agent. At lower concentration of HQ (i.e. 50 μL of 0.1 M) in presence of a fixed concentration of SDS and Au³⁺ leads to the formation of distorted

spherical shaped AuNPs as can be revealed from TEM images (**Figure 6.2 A, B**). The obtained nanosphere can also be considered as bud shaped geometry in which the multiple facets are clearly observable. The average diameter of these nanospheres varies from 55-65 nm. As the concentration or the amount of HQ increases from 50 to 75 μL , the geometry of AuNPs changes from bud to flower or bloom shape which can be observed from the corresponding TEM images (**Figure 6.2D, E**). These gold nanoblooms are monodispersed in nature. In general, these flower-like anisotropic nanostructures can further be considered as a distorted sphere consisting of sharp tips or branches on their surface. The average diameter of these nanostructures is 90 ± 5 nm. These tips or branches of AuNP₇₅ are originating from the core of the nanostructures as can be observed from the HRTEM images. Each of the nanostructures consists of more than ten tips or pods and hence this shape can also be termed as multipodal nanoparticle. The scanning electron microscopy (SEM) image also depicts highly monodisperse bloom or flower-like morphology as shown in **Figure 6.3**.

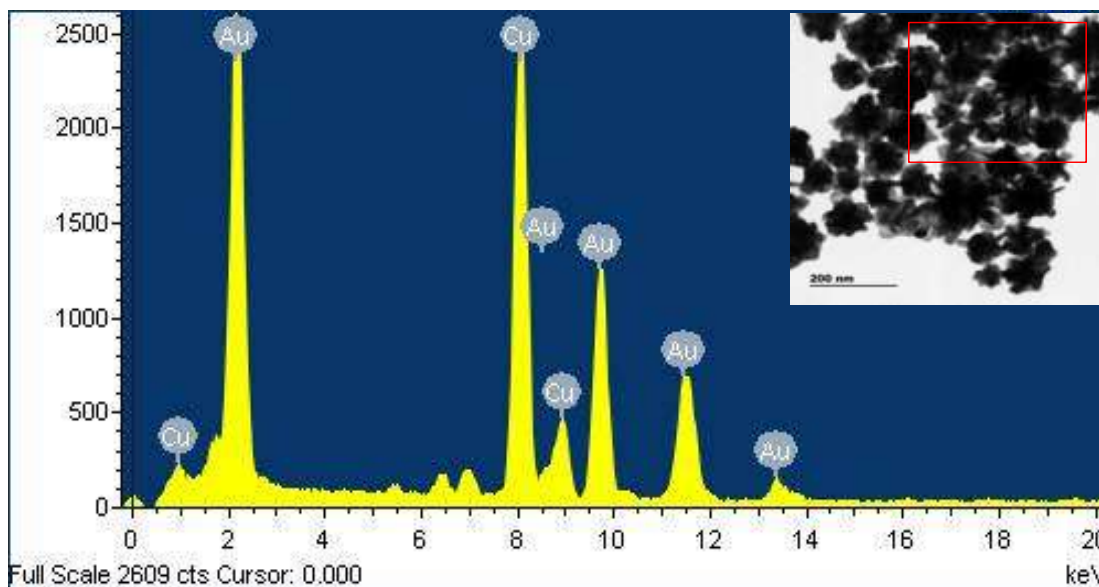


Figure 6.4: EDAX spectra of flower or bloom shaped AuNPs i.e. AuNP₇₅.

The energy dispersive X-ray (EDX) analysis also confirms the presence of Au in the flower-like nanostructures (**Figure 6.4**). Further rise in the concentration of HQ (100-150 μL of 0.1 M) results the formation of over-bloomed morphology. Each of this over-bloomed (popcorn shaped) structure consists of five to six pods or tips (in 2D space) and these tips are blunted in comparison with the flower shaped AuNPs (**Figure 6.2G, H**). The average dimension of these popcorns is 60 ± 5 nm. All these nanostructures synthesized here are poly-crystalline in nature and are randomly oriented along with the face centered cubic (fcc) structural pattern as evidenced from the selected area electron diffraction (SAED, **Figure 6.2C, F and I**) patterns. Increase in concentration of HQ from 50 μL to 75 μL leads to alter the morphology as well as the size of AuNPs from sphere to flower (bloom) shape which can be explained in the following manner: At higher concentration of HQ, the reaction kinetics for the reduction of Au^{3+} to Au^0 is faster which also increases the population of Au^0 . The availability of higher amount of Au^0 in the reaction mixture enhances the growth rate and thereby assists the preferential deposition of Au^0 on the high energy facets leading to the formation of flower or bloom shaped GNPs. Further rise in amount of HQ from 75 μL to 150 μL (of 10^{-1} M) result in the formation of over-bloom shaped AuNPs. In this synthetic protocol, the role of HQ can be envisaged in multiple directions. At higher concentration of HQ, the reduction rate as well as the population density of Au^0 enhances. Besides, HQ undergoes oxidation (as shown before; during the reduction of metal ions) by the removal of hydrogen ion (H^+) which alter the pH of the medium. Increase in concentration of HQ results the enhancement in the liberation of H^+ ions and thereby decreases the pH of the medium. Change in pH result the variation in the shape and size of micelle/micelle core as reported earlier.³²⁷ In this case also the higher concentration of HQ changes the shape and size of

micelles from its original structure due to the alteration in pH and facilitates the formation of hexapod-like AuNPs.

In order to explore the oxidation state of metal as well as the binding phenomena with different functional groups, we have studied the X-ray photoelectron spectroscopy (XPS) for the

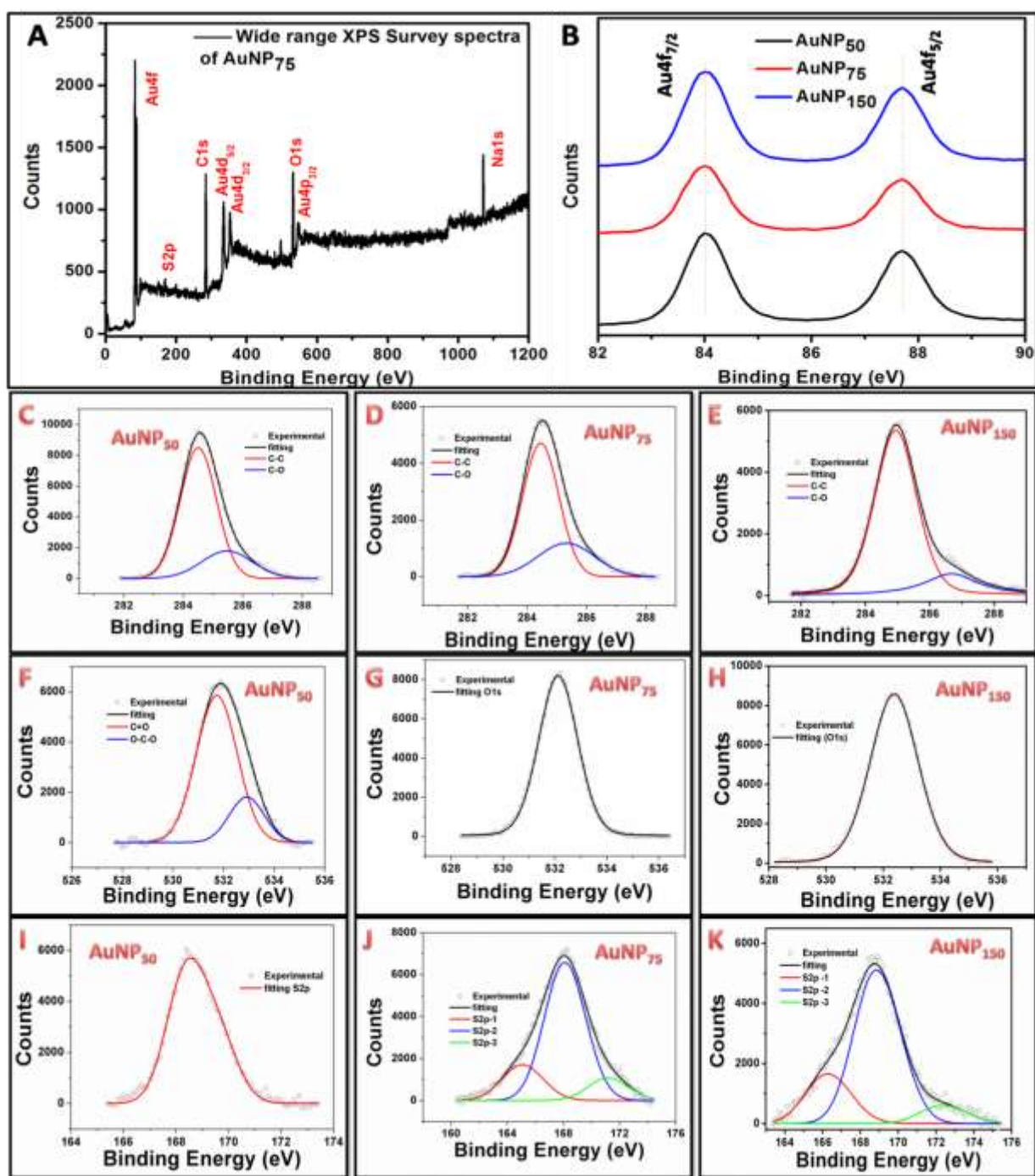


Figure 6.5: XPS spectra of variable shaped AⁿGNPs: (A) Wide range survey spectrum indicating the presence of different elements into AuNP₇₅. (B) Au4f high-resolution spectra. (C, D, E) represent C1s spectra while (F, G, H) show O1s spectra and (I, J, K) depict the S2p spectra (~165 eV (S2p-1) for free R-SH, ~169 eV (S2p-2) and ~172 eV (S2p-3) for Na₂SO₄) for different AuNPs.

synthesized AⁿGNPs. Essentially all the AⁿGNPs shows a similar feature in the wide range survey spectrum (**Figure 6.5A** and **Figure 6.6**) as well as in the Au binding energy spectra (**Figure 6.5B**). The survey spectra show the presence of gold, sulfur, carbon and oxygen element. The Au4f binding energy spectra are split into Au4f_{5/2} and Au4f_{7/2} for all the nanoparticles which appear at 84 eV and 87.5 eV respectively. These values are consistent with the elemental gold (Au⁰), indicating the presence of pure AuNPs.³²⁸ However, the binding energy spectra for different elements (e.g. C, O, and S) that are present into the AⁿGNPs are dissimilar. The source of C, O, and S elements into the nanoparticle are from the surfactant SDS or the reducing agent HQ. The high-resolution scan for C binding energy spectra shows two deconvoluted peaks at 284.5 eV and 285.5 eV due to C-C and C-O bond respectively which are similar for both AuNP₅₀ and AuNP₇₅; however, a shift is observed in C-O bond (286.7 eV) for AuNP₁₅₀.

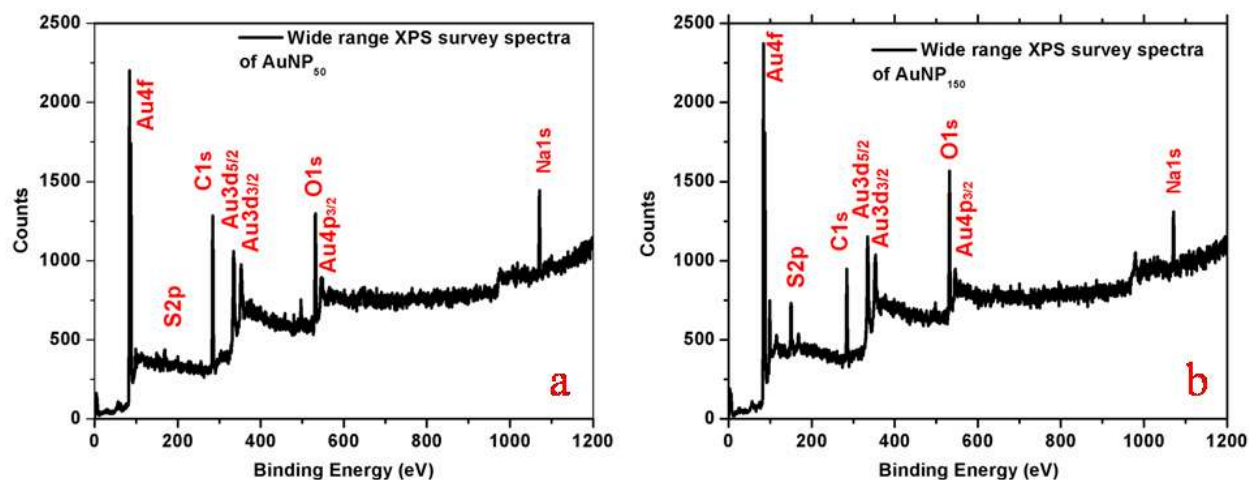


Figure 6.6: Wide range survey spectrum indicating the presence of different elements into (a) AuNP₅₀ and (b) AuNP₁₅₀.

Further, the resolution scan for O binding energy spectra depicts exclusively one deconvoluted peak for both AuNP₇₅ and AuNP₁₅₀ at ~532 eV which is attributed to C=O. While a dissimilar trend is noticed for AuNP₅₀ in which two deconvoluted peaks arise for C=O and O-C-O at ~531.5 and 533 eV respectively. The presence of C=O is due to the formation of quinone (as Au³⁺ reduces, thereby the oxidation of hydroquinone occurs). The resolution scan for S binding energy spectra exhibits three deconvoluted peaks at ~165, ~168 and ~171 eV for AuNP₇₅ as well as AuNP₁₅₀ with slight alter in peak position. However, for AuNP₅₀, only one peak observed at ~168.5 eV. The peak appears at 165 eV is due to free R-SH while the peaks at around 168-172 eV are due to the sulphates. This clearly indicates the presence of surfactants into the nanosurface of the different AⁿGNPs synthesized here. From the variation in the binding energy spectra of the various elements for different geometries, it can be predicted that the change in the concentration of reducing agent leads to alter the micellar properties of the surfactants as discussed above.

6.4.2 Electrocatalytic Performance of AⁿGNPs for Hydrogen Evolution Reaction:

In order to investigate the electrocatalytic activity of the synthesized AⁿGNPs towards hydrogen evolution reaction (HER), we have performed HER in different electrolyte medium (e.g. H₂SO₄, PBS, KOH) with variable pH. The HER activity of the variable shaped AuNPs was studied with the aid of linear sweep voltammetry (LSV) techniques at a scan rate of 10 mV/s with the stirring rate of 500 rpm. **Figure 6.7A** depicts the LSV response of different shaped AuNPs in 0.5 M H₂SO₄ medium (pH=0) wherein the flower-shaped AuNPs i.e. AuNP₇₅ modified GC electrode exhibit much lower onset potential value of -76 mV vs RHE compared to that of other morphologies i.e. AuNP₅₀ (-124 mV vs RHE) and AuNP₁₅₀ (-111 mV vs RHE). The bare GC electrode does not show any significant response towards HER while the bare Au electrode exhibits a large onset potential of ~-300 mV vs RHE. For comparing the catalytic efficiency of synthesized AⁿGNPs in the present study with other AuNPs, we have also recorded the LSV response of spherical shaped AuNPs (S^pGNP) and it displays a higher onset potential value of -179 mV vs RHE in 0.5M H₂SO₄ medium. The overpotential (η) value has been analyzed at a fixed current density of 10 mA cm⁻² for the variable AⁿGNPs modified GC electrodes (**Figure 6.7A** inset) in which the AuNP₇₅ possesses the lower overpotential value (η =194 mV) in comparison with the bud shaped (η =235 mV) and over-bloomed shaped (η =227 mV) AuNPs.

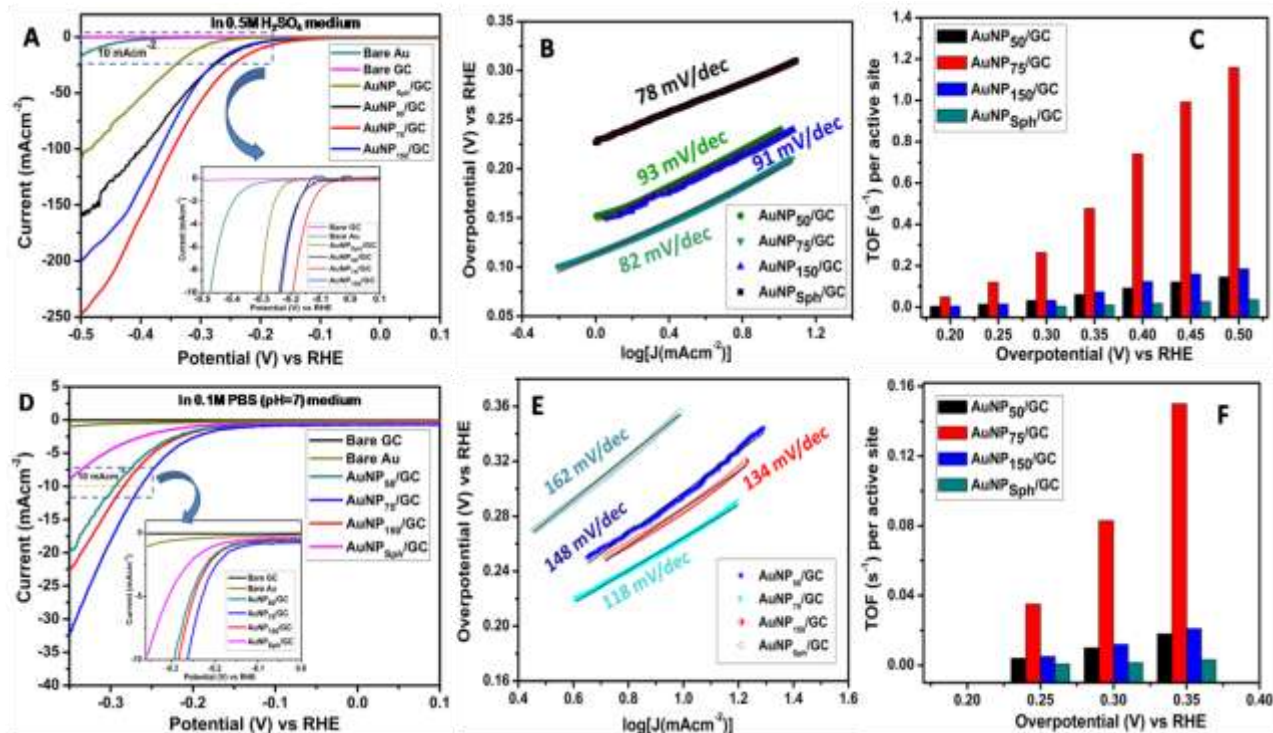


Figure 6.7 : Electrocatalytic performance of different AⁿGNPs modified electrode towards HER. Linear Sweep Voltammetric (LSV) response of bare GC, bare Au, AuNP₅₀/GC, AuNP₇₅/GC, AuNP₁₅₀/GC and S^pGNP/GC at the scan rate of 10 mV/s in (A) 0.5 M H₂SO₄ (pH=0) medium (D) 0.1 M PBS (pH=7) medium. Inset in (A) and (D) represent the magnified LSV curve for estimating the overpotential at the current response value of 10 mAcm⁻² in H₂SO₄ and PBS medium respectively. Tafel Plot and the corresponding Tafel slope for the HER activity of different AⁿGNPs modified GC electrode in (B) H₂SO₄ and (E) PBS medium. Bar diagram for comparing the Turn over frequency (TOF) value for HER as estimated from LSV response at the different potential for variable AuNPs in (C) 0.5 M H₂SO₄ and (F) 0.1 M PBS medium.

In this context, it is noteworthy to mention that the spherical shaped AuNPs possess a larger overpotential value of 302 mV. This signifies that the flower shaped AuNPs reveal their highest electrocatalytic performance towards HER among other synthesized AuNPs. The Tafel slope which is an important parameter for HER activity has also been evaluated from the Tafel

plot (overpotential (η) vs $\log j$ plot) for all the AⁿGNPs modified system as depicted in **Figure 6.7B** and AuNP₇₅/GC shows the Tafel slope of 82 mVdec⁻¹ which is smaller than AuNP₅₀/GC (91 mVdec⁻¹) and AuNP₁₅₀/GC (93 mVdec⁻¹). This study qualitatively indicates that all of the different AⁿGNPs surfaces exhibit similar HER mechanism with AuNP₇₅/GC having faster HER kinetics.³²⁹ However, the S^pGNP shows the lowest Tafel slope value (78 mVdec⁻¹) than our synthesized AⁿGNPs. Though the overpotential value and Tafel slope can qualitatively specify the catalytic efficiency of the AⁿGNPs towards HER, the turnover frequency (TOF) is the most relevant parameter for any catalyst. For estimating the TOF, we have measured the concentration of AⁿGNPs (as used for the electrocatalytic studies) by performing ICP-OES measurements at two different wavelengths, 242.7 and 267.5 nm. Before the measurement, we have initially calibrated the system using different concentration of Au³⁺ metal ions (viz. 1 ppm, 5 ppm, 15 ppm, 25 ppm, 50 ppm and 100 ppm) with the help of the number of counts per each concentration. Once the calibration curve has been constructed, we have used the diluted solution of AuNPs for the measurement. Here we have maintained the same dilution of AuNPs as employed during the HER activity. The measured concentrations of AuNPs are obtained as follows:

Sample	Measured Concentration (ppm) @ 242.7 nm	Measured Concentration (ppm) @ 267.5 nm
AuNP ₅₀	29.321±0.097	27.720±0.089
AuNP ₇₅	9.5228±0.0237	8.8993±0.0354
AuNP ₁₅₀	27.257±0.082	26.470±0.017

Conversion of ppm to Molarity (M):

$$C_{AuNP_{50}} = 29.32 \text{ ppm i.e., } 29.32 \text{ mg/litre}$$

Each Au atom has the molecular weight of 197. Each of the nano particles is consisting of multiple numbers of Au atoms. The number of Au atoms present in a particle can be calculated as follows:

Volume of each AuNP₅₀ nanoparticle = 143720 nm³ (Average Diameter 65±5nm)

Volume of each Au atom = $\frac{4}{3}\pi r^3$; where r is the radius of Au atom (r=166 pm or 0.166 nm)

= 0.0192 nm³

Therefore, the number of Au atom present in each AuNP₅₀ = 143720/0.0192 = 7.49×10⁶

$$\begin{aligned} C_{AuNP_{50}} &= 29.32 \frac{mg}{litre} = 29.32 \times 10^{-3} \frac{g}{litre} \\ &= \frac{29.32 \times 10^{-3}}{7.49 \times 10^6 \times 197} \text{ mol/litre} \\ &= 2.00 \times 10^{-11} \text{ M} \end{aligned}$$

By considering at least 10-15 cone shaped tips (with based diameter: 10nm and length: 10nm) on the spherical core of diameter: 73nm the calculated average volume of each AuNP₇₅ nanoparticle = 211789.33 nm³

Therefore, the number of Au atom present in each AuNP₇₅ = 211789/0.0192 = 1.10×10⁷

$$\begin{aligned} C_{AuNP_{75}} &= 9.52 \text{ ppm} = 9.52 \frac{mg}{litre} = 9.52 \times 10^{-3} \frac{g}{litre} \\ &= \frac{9.52 \times 10^{-3}}{1.10 \times 10^7 \times 197} \text{ mol/litre} \\ &= 4.01 \times 10^{-12} \text{ M} \end{aligned}$$

In the similar way, we have also calculated the concentration of AuNP₁₅₀ as 1.97×10⁻¹¹M by considering the core diameter as 35 nm with 6-7 cone shaped tips (with based diameter: 14nm and length: 12nm) on the spherical core. Once we know the actual concentration of AⁿGNPs ,the TOF has been calculated using the formula as^{284,330}

$$TOF(s^{-1}) = \frac{J \times A}{n \times F \times N}$$

where, J is the current density (Acm^{-2}) at a given overpotential; A is the geometrical area of the electrode (0.0706 cm^2), n is the number of electron transfer ($n=2$), F is the Faraday constant ($F=96500\text{ C mol}^{-1}$) and N is the mole of active site present on the electrode. Assuming all the sites of the nanoparticles are catalytically active, we have estimated the TOF value at a different potential from the LSV response of variable shaped AuNPs in $0.5M\text{ H}_2\text{SO}_4$ medium (**Figure 6.7C**). The flower shaped AuNPs exhibit highest TOF at different potentials in comparison with other morphologies and the order of TOF follow the trend as $TOF_{AuNP\ 75}$ (1.16 s^{-1}) \gg $TOF_{AuNP\ 150}$ (0.18 s^{-1}) $>$ $TOF_{AuNP\ 50}$ (0.14 s^{-1}) at the overpotential of $0.5V$ vs RHE. This emphasizes that the flower shaped AuNPs shows superior catalytic performance towards the HER in comparison with other morphology of AⁿGNPs where the TOF is enhanced by eightfold and six-fold than that of bud shaped ($AuNP_{50}$) and over-bloomed shaped ($AuNP_{150}$) AuNPs respectively. Though the change in Tafel slope is not very much considerable between $AuNP_{75}$ and S^pGNP , the TOF is significantly altered between these two. Almost forty-fold enhancements in the TOF value is observed for flower-shaped than that of normal spherical shaped AuNPs $\left(\frac{TOF_{AuNP\ 75}}{TOF_{AuNP\ Sph}} = 40 \right)$ and this clearly highlights that the gold nanoparticles itself (without composites or alloy) can also be a potential candidate for HER activity with satisfactory TOF and low overpotential. For inspecting the outstanding catalytic behavior of the synthesized AⁿGNPs in different pH medium, we have further carried out the HER study in $0.1M$ PBS (pH=7) buffer solution. In this case, a similar trend is observed in which the flower-shaped AuNPs reveal the superior activity in terms of onset potential, overpotential (η), Tafel slope and TOF as shown in **Figure 6.7D, E and F**. The $AuNP_{75}$ exhibits a slight shift in both the onset

potential (-107 mV) and η_{10} value (262.1 mV) in PBS medium than H_2SO_4 medium. Indeed, for all the nanoparticles, the similar behavior is noticed wherein the onset potential as well as η_{10} value get shifted towards the higher potential region in PBS medium than that of H_2SO_4 medium and this behavior is consistent with other reported HER studies in the literature.⁵⁰ Like in H_2SO_4 medium, the overpotential value gets decrease around 100 mV for AuNP_{75} in PBS medium of pH=7 in comparison with $\text{S}^{\text{p}}\text{GNP}$ (**Figure 6.7D** Inset). Further, the Tafel slope as deduced from the Tafel plot (**Figure 6.7E**) is lowest for $\text{AuNP}_{75}/\text{GC}$ (118 mV/dec) followed by $\text{AuNP}_{150}/\text{GC}$ (134 mV/dec) and $\text{AuNP}_{50}/\text{GC}$ (148 mV/dec) while $\text{S}^{\text{p}}\text{GNP}$ exhibited the higher Tafel slope value (162 mV/dec) than other morphologies of Au surfaces in PBS solution of pH 7. The significant change in TOF value is observed among variable shaped AuNPs in 0.1M PBS (pH=7) wherein fifty-fold enhancement in the TOF is observed for AuNP_{75} than that of $\text{S}^{\text{p}}\text{GNP}$. **Table 6.1** shows the comparative analysis among different parameters related to HER activity of variable shaped AuNPs.

Table 6.1: Comparison among different parameters related to HER activity of the electrocatalytic performance of different AuNPs in various electrolyte solutions.

System	Onset potential (mV) vs RHE		Overpotential (mV) vs RHE @ 10 mAcm^{-2}		Tafel Slope (mV/dec)		TOF (s^{-1}) @ $\eta =$ 0.35 V	
	in 0.5 M H_2SO_4	in 0.1 M PBS	in 0.5 M H_2SO_4	in 0.1 M PBS	in 0.5 M H_2SO_4	in 0.1 M PBS	in 0.5 M H_2SO_4	in 0.1 M PBS
Bare GC	----	----	-----	----	----	----	----	----
Bare Au	-288 mV	-338 mV	472.2 mV	----	----	----	----	----

AuNP₅₀/ GC	-124 mV	-154 mV	235.7 mV	296.2 mV	93 mV/dec	148 mV/dec	0.061s ⁻¹	0.018 s ⁻¹
AuNP₇₅/ GC	-76 mV	-107 mV	194. mV	262.1mV	82mV/ dec	118 mV/dec	0.48 s ⁻¹	0.15 s ⁻¹
AuNP₁₅₀/ GC	-111 mV	-141 mV	227.5 mV	283.7 mV	91 mV/dec	134 mV/dec	0.074s ⁻¹	0.021 s ⁻¹
AuNP_{Sph}/ GC	-179 mV	-201 mV	302.6 mV	360.5mV	78 mV/dec	162 mV/dec	0.01 s ⁻¹	0.003 s ⁻¹

For comprehending the excellent catalytic activity of our synthesized AⁿGNPs towards HER, the electrochemical impedance spectroscopy (EIS) was also studied in different electrolyte medium. The utilization of EIS technique is fruitful for understanding the electrode kinetics along with for evaluating several system parameters i.e. solution resistance, charge transfer resistance, double layer capacitance, the heterogeneous rate constant and Warburg impedance.⁷²

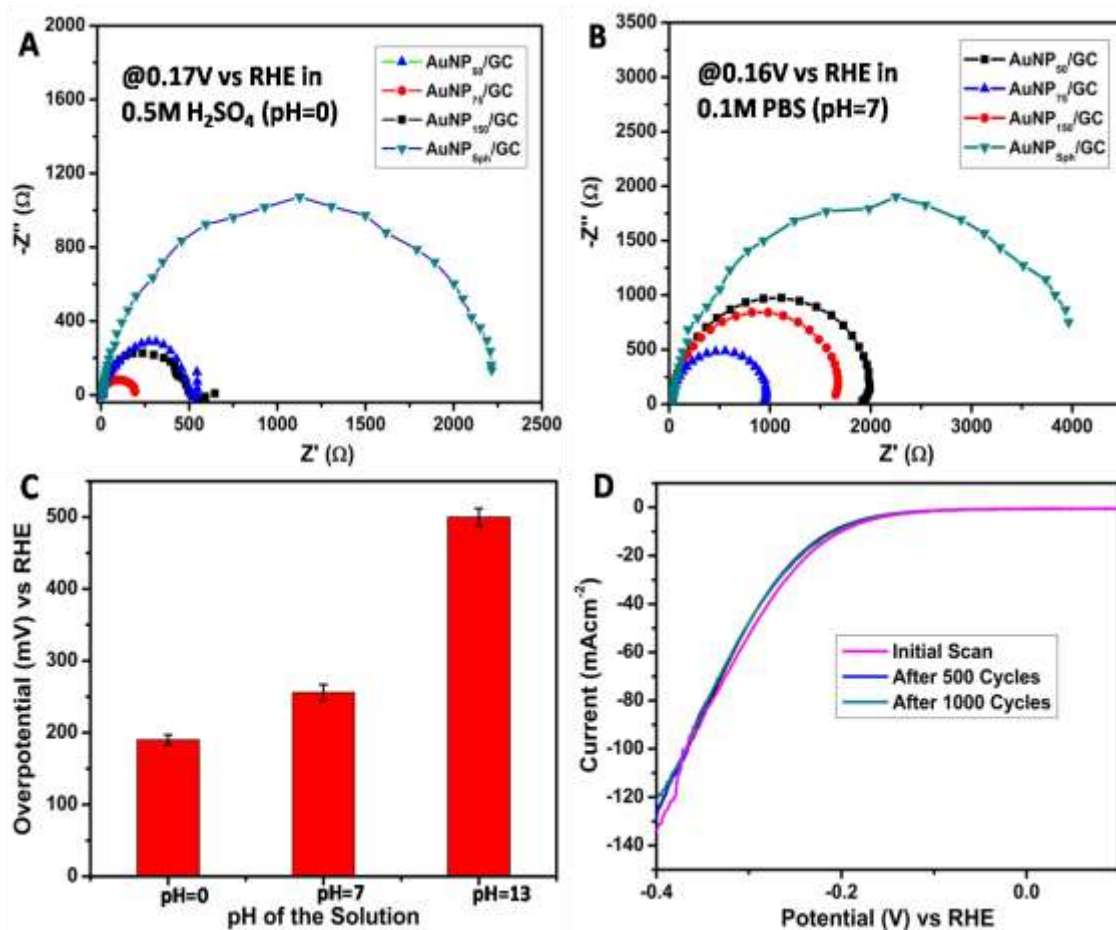


Figure 6.8: Electrochemical Impedance Spectroscopy (EIS) study for HER: Nyquist plot pertaining the comparison among different AⁿGNPs modified GC electrode in the frequency region of 10⁵ to 10⁻¹ HZ with the AC amplitude of 5 mV at (A) 0.17 V vs RHE in 0.5 M H₂SO₄ medium and (B) 0.16 V vs RHE in 0.1M PBS medium. (C) Bar diagram shows the overpotential (η_{10} @ $j=10$ mAcm⁻²) required for AuNP₇₅/GC electrode to reach the current density value of 10 mAcm⁻² at different pH medium. (D) Cycling stability of AuNP₇₅/GC electrode in 0.5 M H₂SO₄ medium during HER before and after 1000 cycles.

Figure 6.8A and **B** depict the typical Nyquist plot of variable shaped AuNPs/GC electrode for HER study in 0.5 M H₂SO₄ and 0.1 M PBS respectively wherein the customary semicircle is observed for all the variable AuNPs modified GC electrode at the higher frequency region. The

diameter under the semicircle provides the charge transfer resistance (R_{CT}) which is varying with the morphology of AuNPs during HER. From this R_{CT} value we can also predict the standard heterogeneous rate constant (k_0) as it is inversely proportional to the former (i.e. $k_0 \propto \frac{1}{R_{CT}}$).⁷² The flower-shaped AuNPs reveals the lowest R_{CT} value in both the electrolyte medium than that of other shaped AuNPs indicating the facile electron transfer between AuNP₇₅/GC and H^+ ion during HER.

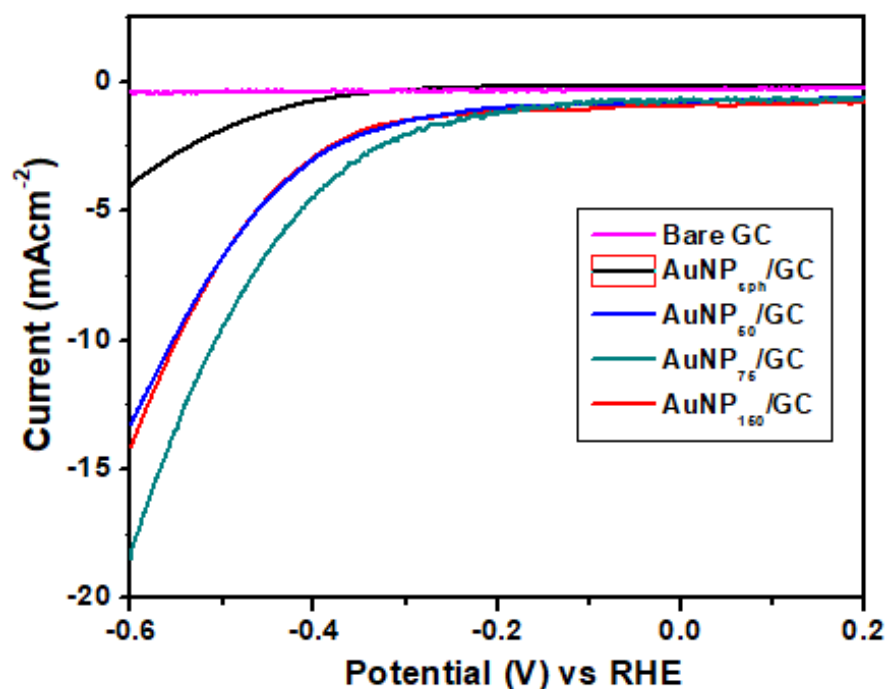


Figure 6.9: Linear sweep Voltammetric response of variable AuNPs modified GC electrode in 0.1 M KOH solution. Scan rate 10 mV/s.

The spherical shaped AuNPs i.e. S^pGNPs shows highest R_{CT} value signifying the poorer electron transfer kinetics during the reduction of H^+ on the nanoparticle surface. The HER activity of the AⁿGNPs was also investigated in 0.1M KOH medium wherein the AuNP₇₅ exhibits the superior catalytic activity among others (**Figure 6.9**). From these studies, we can infer that the flower shaped AuNPs i.e. AuNP₇₅ is the best potential candidate for HER among all other AⁿGNPs as investigated here. The HER activity of AuNP₇₅/GC electrode in variable pH

medium was compared and depicted in **Figure 6.8C** wherein the overpotential value increases with a rise in pH of the solution. This behavior is consistent with other reported HER studies using AuNPs in different pH medium.⁵⁰ Stability is an important factor that governs the suitability of any preferable catalyst towards any reaction. In the present study, the stability of the AuNP₇₅coatedGCElectrode during HER was checked by electrochemical cycling in acidic medium. The polarization curve of AuNP₇₅/GC electrode shows a slight shift in potential along with a negligibly small change in current density even after 1000 cycles as can be noticed from **Figure 6.8D** signifying that the synthesized AⁿGNPsexhibit satisfactory stability along with superior activity than normal spherical AuNPs and the catalytic activity (α) follow the trend as:

$$Z_{AuNP_{sph}} \ll Z_{AuNP_{75}} > Z_{AuNP_{150}} > Z_{AuNP_{50}}.$$

The difference in the catalytic activity of various-shaped AuNPs towards the HER can be explained by considering various factors such as surface charge, effective surface area, crystal facet energy and crystal defects. Since the present investigation is based on the reduction of hydrogen ion using different shaped AuNPs, the magnitude of surface charge of the individual nanomaterials may alter the catalytic efficiency. The zeta potential measurement (as discussed previously) indicates that surface charges of differently shaped AuNPs are negative and the order of zeta potential follows the trend as: ζ_{AuNP50} (-31 mV) < ζ_{AuNP75} (-39 mV) < $\zeta_{AuNP150}$ (-41 mV). This indicates that the availability of free electron for the reduction of H⁺ is maximum in case of over bloomed particle and minimum for bud shaped one. Hence, according to the variation in ζ value, the higher HER efficiency should be observable for over bloomed AuNPs (AuNP₁₅₀) though in reality the flower-shaped AuNPs (AuNP₇₅) shows the superior performance over other structures. Therefore, simply by considering their change in surface charge, we cannot explain completely the observed considerable difference in electrocatalytic activity among different

shaped nanoparticles. Besides their surface charge, the surface area of nanoparticle is also an important parameter which can tune the catalytic behavior depending upon their size. The sizes of the AⁿGNPs varies as AuNP₅₀ (d=65 nm) \approx AuNP₁₅₀ (d=60 nm) < AuNP₇₅ (d=90 nm). We have calculated their (AuNP₇₅ and AuNP₁₅₀) actual surface area and volume (provided in **Table 6.2**) by considering individual petals and their average numbers.

Along with surface area, different geometrical parameters of variable shaped AuNPs were estimated by considering the bud shaped AuNPs as spherical while the cores of bloom and over-bloomed shaped AuNPs to be spherical and the tips are cone-shaped. The surface area of the core was calculated using the formula $4\pi r^2$, while the surface-to-volume ratio of the core was defined as $[4\pi r^2 / (4\pi r^3 / 3)] = 3/r$, where r is the radius of the spherical core. In general, the effective surface area of a core that is exposed to the environment can be measured as $4\pi r_c^2 - N\pi r_c^2$, where r_c is the average radius of the base of each cone and N is the total number of cones. The term $N\pi r_c^2$ denotes the surface area of the central core which is captured by N number of sharp tips. Similarly, by disregarding the base area of the cones, the effective surface area (A) of the cone-shaped tips can be expressed as $A = N\pi r_c \sqrt{r_c^2 + h_c^2}$, where h_c is the height of the individual tips. Therefore, the total effective surface area can be calculated by summing the effective core area and effective petal areas for an individual AuNPs. By following the methodology stated above, we have also calculated the effective volume of various-shaped AuNPs. Detailed structural parameters obtained from the TEM images by using the above formulas are listed in **Table 6.2**.

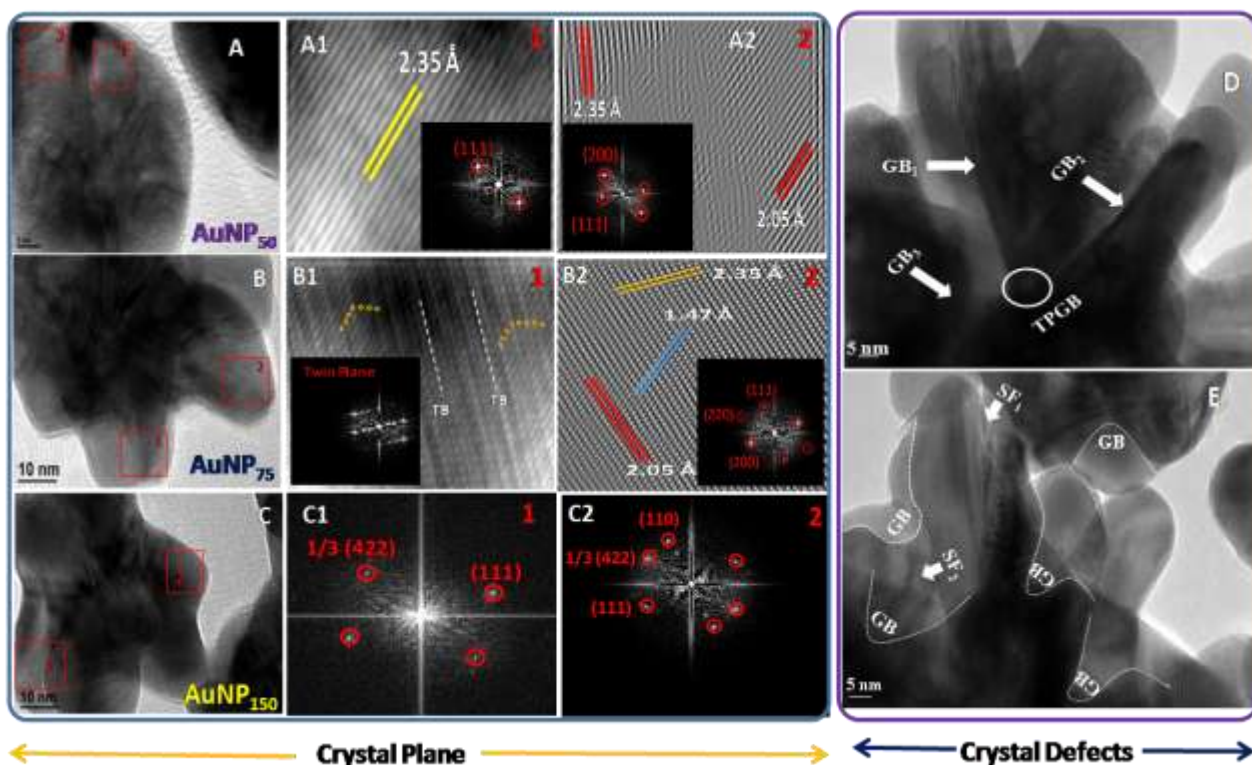


Figure 6.10: The presence of different crystal plane into the synthesized variable shaped AuNPs (A) AuNP₅₀ (B) AuNP₇₅ (C) AuNP₁₅₀. The areas selected in (A), (B) and (C) show the FFT (Fast Fourier transformation) images. (D) and (E) show the HRTEM images of AuNP₇₅ pertaining the appearance of high-density grain boundary.

As can be seen from **Table 6.2** that the availability of surface area per unit volume (mass) for hydrogen adsorption as well as desorption is higher for the smaller sized AuNP₁₅₀ and thereby the rate of catalysis should follow the trend as: $k_0^{AuNP_{150}} > k_0^{AuNP_{75}} > k_0^{AuNP_{50}}$ which is not the case in our study. Hence, both the surface charges and surface areas are not capable enough to estimate their actual catalytic activity in this context. Incapability to explain the catalytic activity by considering the surface charge and active surface area allow us to consider the role of crystal facet energy for the electrocatalytic performance of our synthesized nanomaterials. The crystal facet energy (γ) of different crystallographic plane in *fcc* crystal of

AuNPs follows the trend as: $\gamma_{(111)} < \gamma_{(100)} < \gamma_{(110)}$.⁹⁰ The presence of high energy crystal facets leads to greater reactivity and thereby better catalytic efficiency. The bud shaped AuNP i.e. AuNP₅₀ possesses energetically favorable i.e. lowest energy {111} plane along with only higher energy {200} plane [**Figure 6.10A**]. In comparison, the flower shaped AuNPs i.e. AuNP₇₅ contains multiple higher energy {200} and {220} planes in conjunction with the lower energy {111} plane [**Figure 6.10B**] and these high energy crystal facets provide flower shaped AuNPs more reactive than the bud shaped AuNPs. Besides, the over-bloom shaped AuNPs i.e. AuNP₁₅₀ contains the {111} plane along with {110} and $[1/3\{422\}]$ plane [**Figure 6.10C**]. The presence of higher energy crystal facet of {110} plane in conjunction with $[1/3\{422\}]$ plane enriches the reactivity of over-bloom shaped AuNPs. Though, the higher energy crystal facet in AuNP₁₅₀ offers the better catalytic activity than the flower shaped AuNPs (AuNP₇₅), we observed that the former having the lower catalytic ability than the flower shaped AuNPs. Hence, the crystal facet energy is again not the only parameter to govern the excellent catalytic activity of flower shaped AuNPs. The ambiguity in the observed catalytic performance of AuNPs requires further enquiry to explore the factors which are having a crucial role for the observed catalytic activity.

Since the aforementioned three factors (surface charge, surface area and active facet energy) are not able to explain the observed catalytic efficiency alone we have explored the role of crystal defect density in great details. A detailed investigation on the HRTEM images of our synthesized AuNPs reveals the appearance of several different types of crystal defects. The HRTEM images of fully bloomed or flower shaped AuNPs exhibit different crystal defects viz. stepped surfaces, islands, dislocations, grain boundary and twin boundary as depicted in **Figure 6.10**. Out of several defects, the high density of grain boundary has appeared very prominently in AuNP₇₅ as shown in **Figure 6.10D** and **E**. Grain boundary is defined as the boundary or the

interface between two grains or crystallites and is generated during the nucleation step which finally turns into crystals or crystalline structures. In the case of polycrystalline materials, the simultaneous growth of nuclei in multiple regions meets each other and thereby hindering the growth of crystal in that orientation to generate grain boundary (GB) at that point. In polycrystalline materials, multitudes of grains are separated by multiple GBs. GBs are also termed as rotation boundary and depending upon the magnitude of rotation (θ), they are classified into small ($\theta < 10^\circ$) and large angle grain boundaries ($\theta > 15^\circ$). In our present study, all the synthesized AⁿGNPs are polycrystalline in nature as can be seen from SAED pattern (**Figure 6.2C, F, I**). Indeed, the large number of GBs is observed for the flower shaped AuNPs (**Figure 6.10D**) and the appearance of high density GBs possesses greater strain and thereby leading to plastic deformation.^{331,332} The plastic deformation in single phase polycrystalline grain boundary rich nanomaterials can be illustrated by the Hall-Petch relation^{331,333}:

$$\sigma_y = \sigma_0 + k_y d^{-\frac{1}{2}} \dots\dots\dots(4)$$

where, ' σ_y ' denotes yield stress for plastic deformation and ' σ_0 ' is the material constant for starting stress, ' k_y ' and ' d ' represent strengthening coefficient and average size or diameter of grain boundary respectively. The Hall-Petch relation predicts that for lower grain size ($d < 10$ nm) the value of yield stress increases and the nanostructure become stable whereas for higher grain size ($d > 10$ nm), the motion of the dislocation prevented from one grain to adjacent grain and the strain within the nanomaterial increases.^{334,335} For a comparative analysis of yield stress (σ_y) among various shaped AuNPs used in this study, the average grain diameter has been calculated using two different methods namely Jeffries and mean intercept length method.

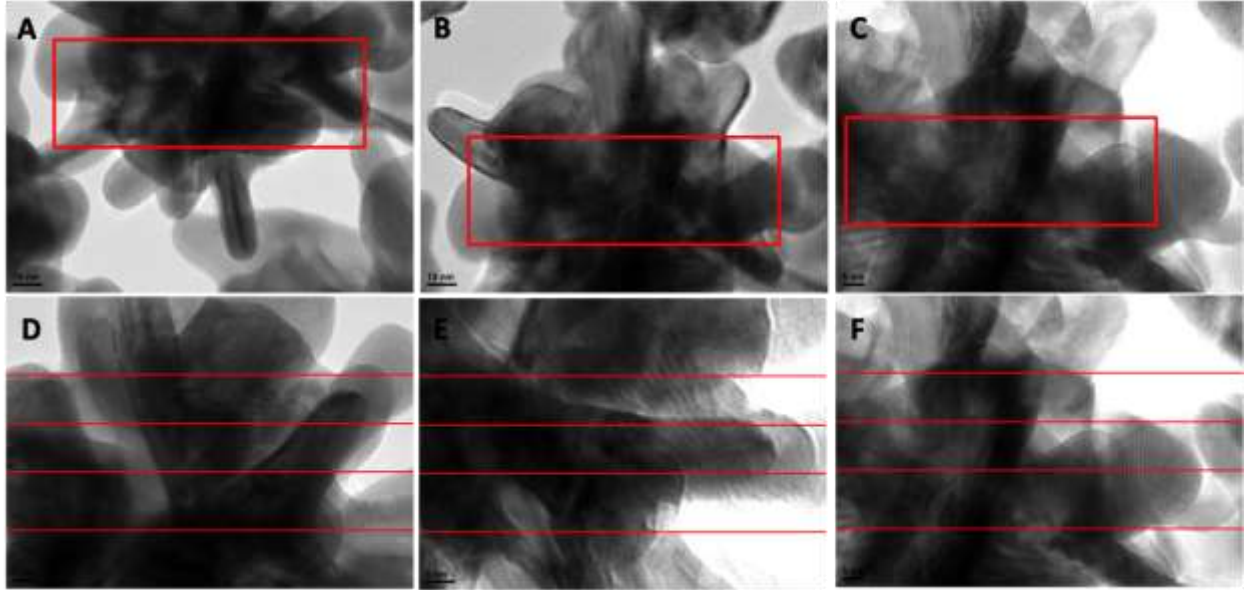


Figure 6.11: Different HRTEM images of AuNP₇₅ in which the rectangular area in (A, B and C) is selected for determining the average grain sizes using the Jeffries method. The parallel line in (D, E and F) is drawn on the TEM images of AuNP₇₅ for determining the average grain sizes using mean intercept length method.

In Jeffries method,³³⁶ we have selected a rectangular area on a particular nanostructure in which a full grain is considered as 1.0 and partial grain as 0.5. The average number of grain boundary per unit area (N_A) is measured from the selected rectangular area (nm^2) and N_A is related with the average grain diameter (d) by $d=1/(N_A)^{1/2}$. We have chosen rectangles of 4000 nm^2 ($100 \text{ nm} \times 40 \text{ nm}$) area for **Figure 6.11A** and **6.11B** whereas 1875 nm^2 ($75 \text{ nm} \times 25 \text{ nm}$) for **Figure 6.11C** in the HRTEM images of AuNP₇₅ where the numbers of GBs are counted using ImageJ software and by this method, 50 different frames (with identical area) of the same nanostructure have also been selected. Thereby, the average diameter of grain boundary is evaluated from the equation, $d_i = \sum_{i=1}^{50} \frac{1}{(N_A)^{1/2}}$. From the Jeffries method, the calculated d_i value

is in the range of 17.5-18.2 nm for fully bloomed shaped AuNPs while for over-bloomed and bud shaped the d_i values are 10.7-12.1 nm and <10 nm respectively.

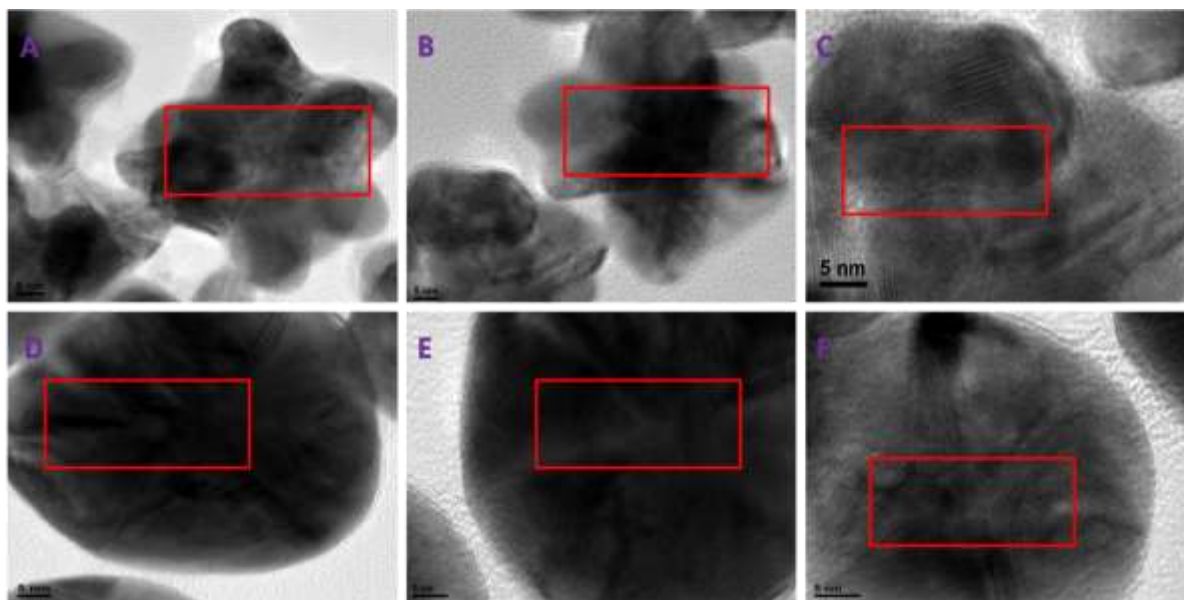


Figure 6.12: Different TEM images of AuNP₁₅₀ (A, B and C) and AuNP₅₀ (D, E and F) in which the rectangular area is selected for determining the average grain sizes using Jeffries method.

Further to verify the accuracy of the Jeffries method, we have also adopted the mean intercept length method³³⁶ for measuring the average grain sizes. In polycrystalline materials, a set of parallel lines are drawn on the nanosurface using ImageJ software and the number of intersection per unit length (P_L) on the GBs are counted. The average diameter of the grain boundary (d_i) is defined as $d_i = 1/P_L$. In this method also, we have selected for 50 other frames of the same nanostructure (**Figure 6.11D, E and F and 6.12D, E, F**) as followed in the previous method. The calculated d_i value using this method for AuNP₇₅ is in the range of 15.7-16.4 nm which has close proximity to the d_i value (17.5-18.2 nm) calculated from the Jeffries method. For other morphologies of AⁿGNPs, the d_i value is in the range of 10.5-11.2 nm and 9.1 nm for AuNP₁₅₀ and AuNP₅₀ respectively. In our present study, the most catalytically active AuNP₇₅

have an average grain size (d_i) around 18.2 ± 1 nm which is higher than the average grain size of AuNP₅₀ ($d_i \approx 9$ nm) and AuNP₁₅₀ ($d_i \approx 11$ nm). In general, the grain boundary dependent plasticity can be interpreted by the average grain size of the nanomaterial. For $d > 10$ nm the plasticity is mainly due to the full dislocation activity whereas for $d < 10$ nm the plasticity mainly because of partial dislocation and grain boundary induced deformation like grain sliding, grain rotation.³³⁷

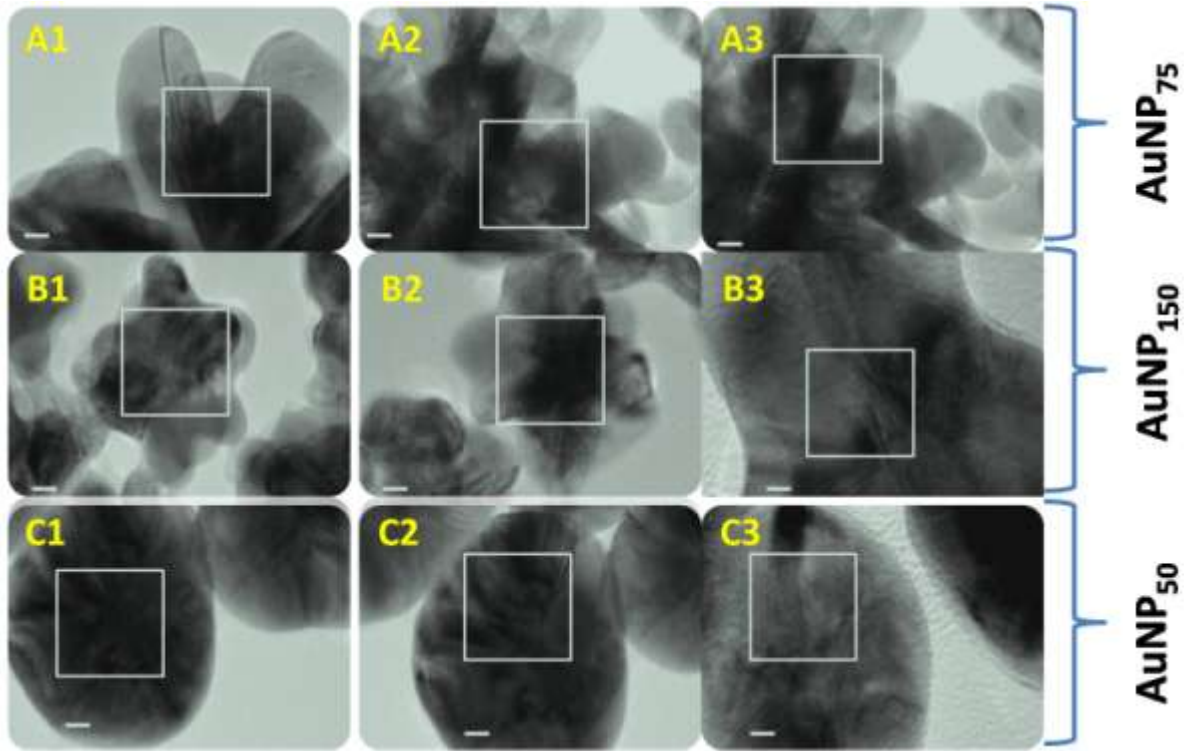


Figure 6.13: Variations in defect density in various shaped AuNPs with 50 frames considered for each of the three different surface zones with surface areas of $400 (20 \times 20) \text{ nm}^2$ for each AuNP. The scale bar in each of the figure represents 5 nm. Here frames labeled with As represent AuNP₇₅, Bs represent AuNP₁₅₀, and Cs represent AuNP₅₀.

The pile up of multiple dislocations near the bigger grain in AuNP₇₅ creates tensile strain within it and becomes catalytically most reactive in this context. Moreover, recent studies reveal the energetic nature of triple junction (TPGB, where three different grains meet in a nanomaterial³⁴)

and their role in catalysis. In general at the triple junction, fracture or crack occurs much easily than the other parts of the nanomaterial. From the HRTEM picture of AuNP₇₅, we can locate multiple triple junctions over the nanosurface than that of AuNP₅₀ and AuNP₁₅₀. All these cumulative effects make polycrystalline grain boundary rich AuNP₇₅ becomes energetically much more reactive than AuNP₅₀ and AuNP₁₅₀. During the electrocatalytic activity towards HER, these grain boundaries act as active sites for preferential accumulation of hydrogen ions onto the flower shaped AuNPs. Further, the presence of higher extent as well as larger diameter of GBs on AuNP₇₅ enhances the diffusion of adsorbates (here, H⁺) from bulk to the nanosurface compared to the other two structures. This results in facile adsorption of hydrogen ion on the polycrystalline nanoflower which results higher TOF for HER. In order to evaluate the crystal defect density into the nanomaterials, a surface area of 400 (20×20) nm² have been considered on the TEM images of each AuNPs. For each surface zone of an individual structure, we have considered 50frames. The details of the defect density are provided in **Table 6.2**, which includes different defects viz. GBs, TB, and SFs. Various types of crystal defect density were calculated using the expression:

$$\text{Crystal defects density (CDD)} = \sum_{i=1}^{50} \frac{n_i}{A_i}$$

Where, n_i is the number of respective defects in selected area of A_i.

The procedure to calculate different crystal defect density from TEM images has been elaborately in **Figure 6.13** and the obtained defect density value from this method is enlisted in **Table 6.2**. The presence of various type of crystal defects, mainly planer defect (GBs, TBs, and SFs), in higher extent (as can be noticed from **Table 6.2**) enriches the host-guest interaction on the surface of the negatively charged AⁿGNPs and thereby enhancing the catalytic efficiency of fully bloomed shaped AuNPs in comparison with other synthesized AⁿGNPs.

Table 6.2: Structural parameters of different AⁿGNPs.

Parameters	AuNP ₅₀	AuNP ₇₅	AuNP ₁₅₀
Surface Charge	-(31.7±0.5)	-(38.9±0.7)	-(41.1±0.9)
Surface Area (nm ²)	11304.0	22387.3	6124.81
Volume (nm ³)	113040	211789.3	26037.4
Surface to volume ratio (nm ⁻¹)	0.1	0.11	0.23
Grain boundary Density (nm ⁻²)	0.08	0.68	0.28
Grain boundary diameter (nm)	9.6±0.5	17.4±0.7	11±0.6
Twin boundary Density (nm ⁻²)	0.01	0.05	0.03
Stacking Fault Density (nm ⁻²)	0.15	0.57	0.21

6.4.3 Computational Studies:

In order to gain better insight about the enhanced HER activity of the AⁿGNPs, we have performed density functional theory study based on first-principle calculations using VASP simulation package.¹¹⁵ As revealed from HRTEM study, the key differences between differently shaped AuNPs namely bud shaped AuNP₅₀, bloom shaped AuNP₇₅ and over bloom shaped AuNP₁₅₀ are a) surface exposed crystallographic planes, b) length and density of the grain boundaries present in different surfaces. The surfaces of AuNP₅₀, AuNP₇₅, AuNP₁₅₀ are modelled with (111), (200) and (110) surface planes and their corresponding grain boundaries according to HRTEM analysis (**Figure 6.14-6.16**).

To evaluate the HER activity of a catalyst, the free energy diagram of H* adsorption on catalyst surface can be considered as a key physical quantity.^{300,338} We have calculated change of Gibbs free energy for hydrogen adsorption (ΔG_{H^*}) on different Au surfaces according to the work of Norskov et al (**Figure 6.17a** and **Figure 6.14-6.16**).^{134,300}

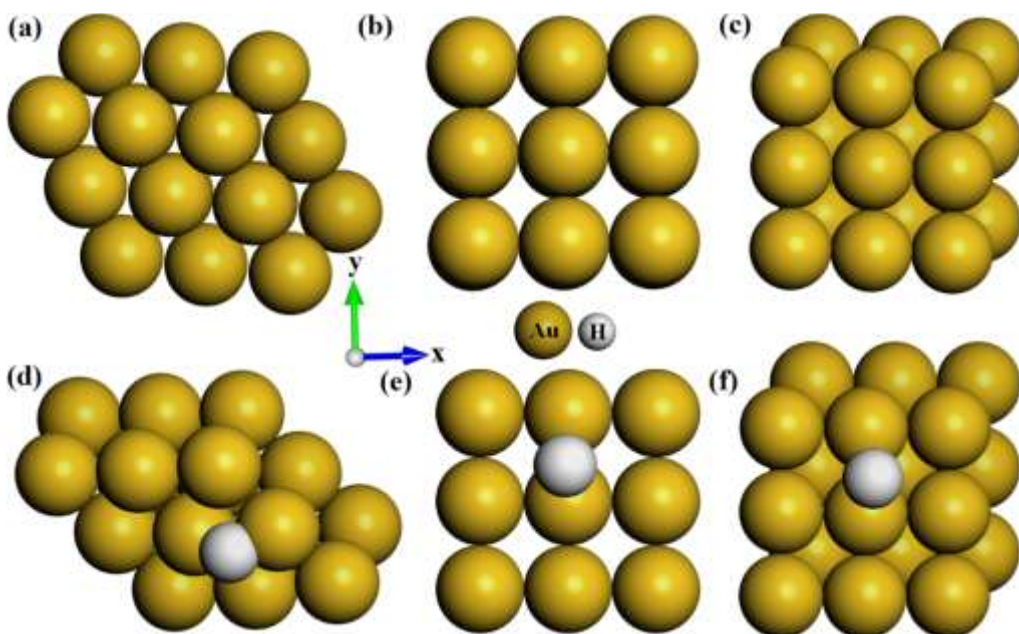


Figure 6.14: Optimized structure of (a) Au (111), (b) Au (200) and (c) Au (110) surfaces.

Structures of H* adsorbed Au surfaces (d) H*-Au (111), (e) H*-Au (200), (f) H*-Au (110).

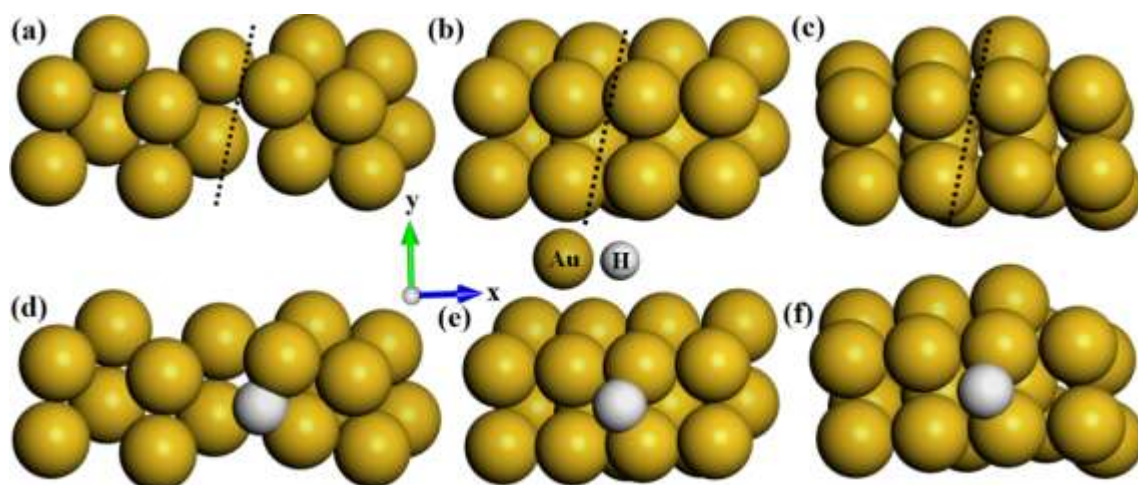


Figure 6.15: Optimized structure of (a) GB_a, (b) GB_b and (c) GB_c Au grain boundary surfaces

(dotted line shows grain boundary region). Structures of H* adsorbed Au grain boundary surfaces

(d) H*-GB_a, (e) H*-GB_b, (f) H*-GB_c.

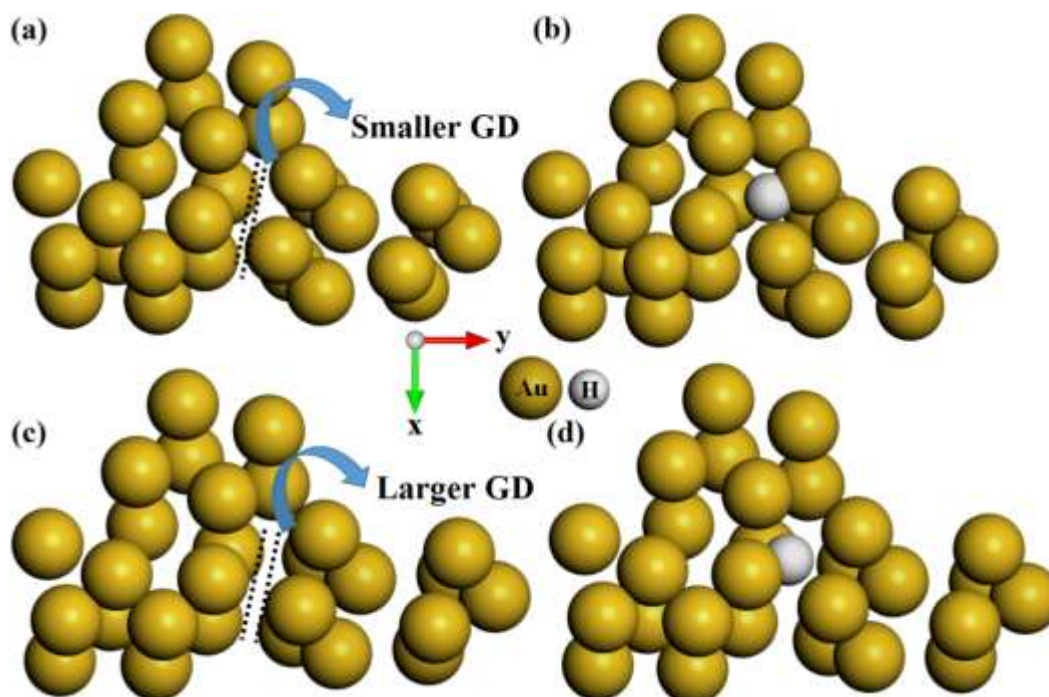


Figure 6.16: Optimized structure of (a) GB_d, (c) GB_e/Au grain boundary surfaces (dotted region shows smaller and larger grain diameter). Structures of H* adsorbed Au grain boundary surfaces (b) H*-GB_d, (d) H*-GB_e.

The ΔG_{H^*} values for the pristine Au (110), (200), (111) surfaces are 0.45, 0.18, -0.50 eV respectively. According to the Sabatier principle, most active catalytic site will have moderate hydrogen adsorption energy with $\Delta G_{H^*} \approx 0$.³³⁹ Therefore, Au (200) surface with moderate H* adsorption energy (0.18 eV) is the best surface among (110), (200) and (111) surfaces. However, mere presence of different surface planes cannot conclude about the difference in HER activities of differently shaped AuNPs as both bud shaped AuNP₅₀ and bloom shaped AuNP₇₅ contains (200) plane. A closer look into the HRTEM analysis clearly reveals that all the differently shaped polycrystalline AuNPs surfaces are having grain boundaries with presence of two and /or three planes. The effect of grain boundary (GB) on electrocatalysis is well explored in literature.^{340,341} Therefore, effect of GB can play an important role in HER.

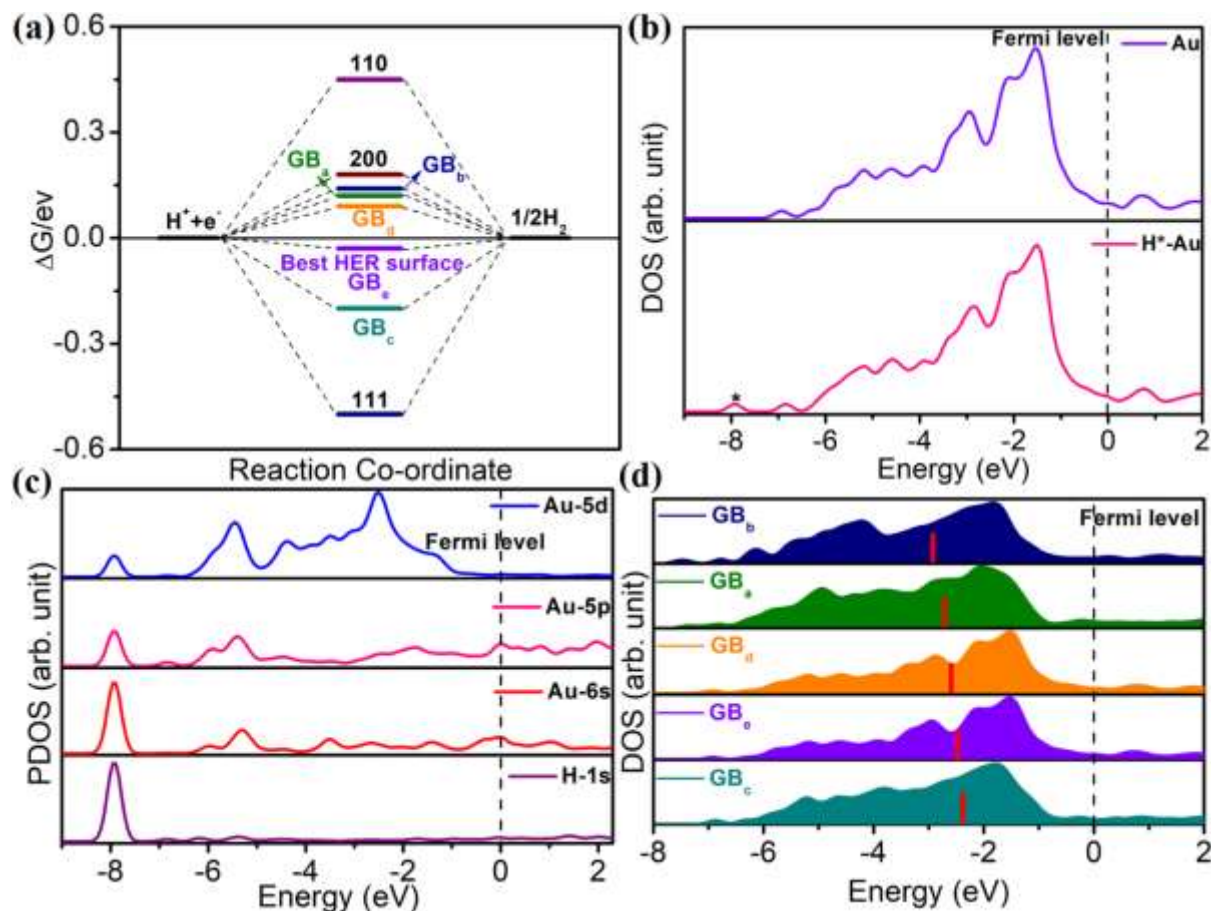


Figure 6.17:(a) Free energy diagram for H* adsorption on various Au surfaces for HER, (b) DOS plots for GB_e and H*-GB_e Au surfaces (asterisk shows contribution from H-1s), (c) PDOSs for Au-5d, Au-5p, Au-6s and H-1s of H*-GB_e Au surface, (d) DOSs on Au atoms for different grain boundary surfaces. The thick red bar indicates the position of d-band centre (E_d) on Au surfaces.

To find out the role of GB, we have constructed various GBs with different surface planes. Among all the GBs, the ones (GB_d, GB_e) consisting of three planes [(110), (200) and (111)] show $\Delta G_{H^*} \approx 0$ (0.09 and -0.03 eV) in comparison with other GBs (GB_a, GB_b, GB_c) consisted with either of two planes among (110), (200) and (111). These findings nicely corroborates with experimental results. As evident from HRTEM analysis, bloom shaped AuNP₇₅ surface, the best HER Au surface, contains GB_{d/e}[GB with (110), (200) and (111)]

planes]. To get better insight about the effect of the size of grain diameter, we have modelled GB surfaces (consisting of (110), (200) and (111) planes) with smaller (GB_d) and larger (GB_e) grain diameters. Interestingly, with the increase of grain diameter and hence grain density there is a substantial change of ΔG_{H^*} from 0.09 to -0.03 eV. This study indicates that nanoparticle surface with larger grain diameter and /or grain density will exhibit improved activity in HER, which is in good agreement with the experiment.

Table 6.3: The position of DBCs for different AuNP grain boundary surfaces.

Au grain boundary Surfaces	Position of DBCs (in eV)
GB_b	-2.88
GB_a	-2.75
GB_d	-2.52
GB_e	-2.38
GB_c	-2.25

The bonding interaction of H with the most active Au surface GB_e is well understood through the density of states (DOS) plot. It can be vividly visualized from the DOS plot of H^* -Au (**Figure 6.17b**) that there is a generation of H-1s state near -8.0 eV (asterisk indicates a contribution from H-1s). Besides, the projected density of states (PDOSs) analysis confirms the bonding between H-1s and Au s, p and d-orbitals. Though Au-6s orbital mainly contributes to Au-H bond, there is also a significant contribution from Au-5p and Au-5d (**Figure 6.17c**).

From the above discussion, it can be concluded that larger diameter GB_e grain boundary surface consisting of (110), (200) and (111) planes is the best HER Au surface among the studied ones. These findings can be further justified by well-known d-band model, correlating the d-band center (DBC) with adsorption energy of intermediates (here H atom).^{342,343} The DBCs for different Au surfaces are tabulated in **Table 6.3**. As shown in **Figure 6.17d**, with the change in surface planes of grain boundaries (from GB_a to GB_e), the d-band centre shifts towards fermi

level resulting the decrease of ΔG_{H^*} which corresponds to stronger adsorption of hydrogen on Au surface. However, the best Au surface (GB_e) exhibits a value of -2.38 eV whereas GB_c that of -2.25 eV. The DBC position of GB_c is more closer to Fermi level than that of GB_e indicating much stronger adsorption of H^* on GB_c surface which results in deterioration of HER activity. This study also reveals that GB_e surface has the optimum DBC position for moderate H^* adsorption and confirms the superiority in HER activity.

6.5 Conclusions:

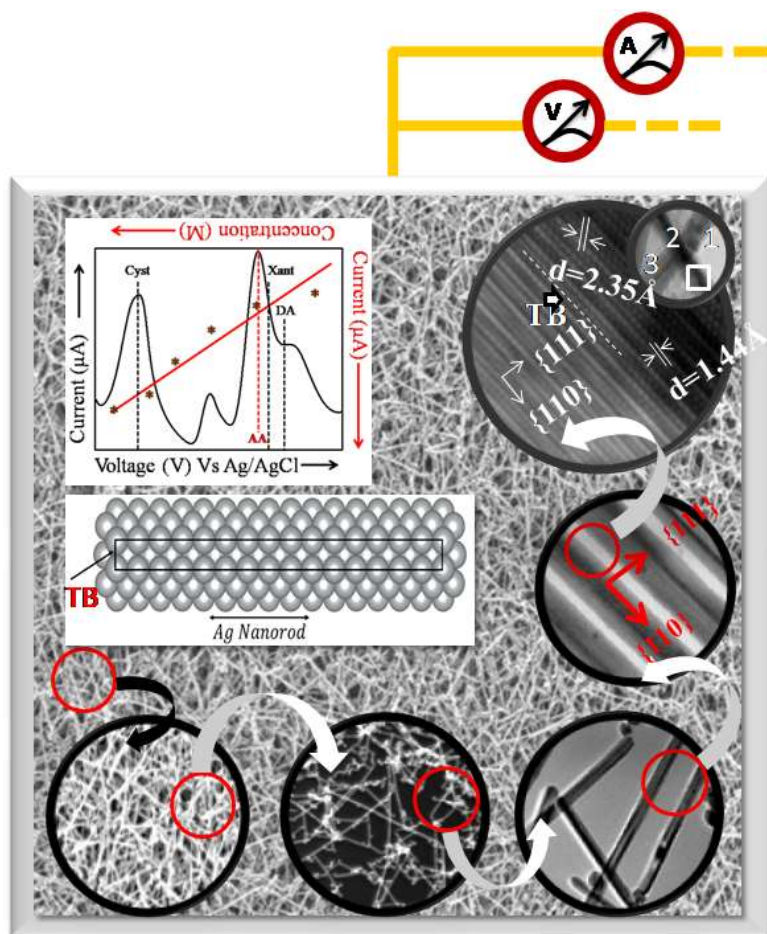
A simple, cost-effective and rapid synthesis of highly monodispersed gold nanoparticle is reported here using hydroquinone (HQ) as the reducing agent in the presence of sodium dodecyl sulfate (SDS). The mere variation in concentration of HQ leads to alter the morphology as well as size of gold nanoparticles from bud to flower (bloom) to over-bloomed shape. Our study first time nullifies the role of size, shape and density of high energy facets on HER activity of multigrain anisotropic nanomaterials and demonstrates how triple junction grain boundary can remarkably enhance catalytic performance towards HER. The detailed HRTEM, analysis reveals the presence of high-density grain boundary into the flower shaped AuNPs which proves to be a suitable and efficient candidate towards hydrogen evolution reaction (HER) in different pH medium (i.e. acidic, neutral and basic). Theoretical investigation also confirms the presence of high density grain boundary with larger size into the nanocrystal can significantly change the free energy and position of d-band center leading to enhanced reaction kinetics towards HER.

CHAPTER-7

Au-Seeded Ag-Nanorod-Based Thiol Mediated Strained 2D Network as Non-Enzymatic Universal Electrocatalytic Sensing Platform: A Mechanistic Exploration

OUTLINE: Specific Points of Discussion

- Spherical gold nanoseed (~5-6 nm)-induced (but not seed-mediated) Hy-Au@AgNRs of variable length have been synthesized by a novel methodology.
- High-resolution characterization and DFT-based theoretical modeling quantify the presence of an enhanced number of multiple coaxial twin boundaries for longer Hy-Au@AgNRs which ultimately results in an increased mechanical strain.
- Greater mechanical strain shifts the density of states (DOS) towards the Fermi level to assist the tremendous catalytic activity of the longest NR (Hy-Au@AgNR₈₄₀)
- Further assembling of these inherently active Hy-Au@AgNR₈₄₀s by thiol click chemistry results in a uniform 2D platform which shows better adsorptivity and easy moldability on electrode surface for increased self-life, uniform porous structure to trap large extent of redox systems, enhanced stability in a broad pH and solvent range along with its enhanced catalytic activity to increase the applicability, and long term stability under the ambient condition for safe storing make this material a unique non-enzymatic scalable universal electrocatalytic platform.
- The ability of this material as a non-enzymatic universal catalytic platform has been verified by applying it for highly specific and ultrasensitive detection of a series of human metabolites.
- This study first time mechanistically explores the combined role of anisometric seeding to create intermetallic twin boundary along with their size to control their strain-induced catalytic activity to offer us a universal 2D electrocatalytic sensing platform.



7.1 Introduction:

In this chapter, we have explored the application of Au-seeded Ag-nanorod-based thiol mediated strained 2D network as a non-enzymatic universal electrocatalytic sensing platform. Application of enzyme as a catalytic biosensor is long known in the literature³⁴⁴ but due to their possible denaturation and digestion in abnormal conditions (higher temperature, variable pH, non-aqueous environment, etc), high costs in preparation and purification, the requirement of expertise to handle enzyme-based assays, and lack of large scale production, the fabrication of enzymatic catalytic sensing platform for daily use in industrial-scale is not become feasible till now.^{30,31} In comparison to catalytic enzyme biosensors,³² non-enzymatic nanomaterials-based catalytic sensors also have the same essential components of an effective catalyst, i.e., a chemical receptor or more universal porous moiety to hold the analyte selectively or non-selectively and a transducer with lower Faradic electron transfer resistance³⁴⁵ to generate a high-throughput electrical signal for ultrasensitive sensing. As mentioned, to avoid drawbacks of enzymatic catalysts, new generation non-enzymatic universal nanoscale catalytic sensing platforms with enhanced catalytic activity governed by the inherent crystal defects and grain boundaries³⁴ within the nanomaterials, catalytic hotspots at the cross junctions,³⁵ durability due to efficient surface passivation,³⁶ excellent stability over a pH and solvent range,^{20,38} and low cost of fabrication, is in demand for high throughput physiological diagnosis. Over the past few decades, scientists are harvesting their constant effort to create synthetic nanostructures or their assemblies to mimic their enzymatic functions^{346–350} and promote their catalytic activities. A variety of Nanoscale materials with enzyme mimicking characteristics have largely been categorized into three classes: carbon-,^{351,352} metal-,^{348,353–356} and metal-oxide-^{30,357–359} based. Due to the limitations originating from low capacitance and improper grafting on electrode surface for carbon-based

nanomaterials³⁶⁰ along with limited electronic conductivity³⁶¹ and insoluble nature of nanoscale metal oxides make them inferior compared to metallic nanostructures as the effective catalyst. The importance of porous nanostructure along with a large accessible 3-dimensional surface area to offer large catalytic activity has been demonstrated before.^{345,362} Hence, fabrication of isotropically distributed super-nanoporous and evenly thick cross-linked metallic nanostructure with better adsorptivity on the electrode surface (for increased self-life) and enhanced catalytic activity in variable physicochemical conditions is in high demand both as a catalytic material as well as the reliable electrochemical sensor. Exploiting the effect of multiple metals within single nanostructure^{363,364} for the construction of a universal electrocatalytic platform, both for sensing and theranostics, have been demonstrated before but the mechanistic exploration for their astonishing catalytic activity or applicability without incorporating the screening-assisted ligand³⁶⁵ has not been studied extensively. Though scientists have designed expensive materials (e.g., Pt, Au, Ru, and mixed metal-based nanomaterials) with very high catalytic activities,^{366,367} equal efforts have not been put forward to explore the combination of different catalytic enhancement factors within the traditional nanomaterials simply by adjoining them in a single nanostructure. Assisted by the differential crystallization at the interface between metals (due to the difference in crystal parameters)³⁶⁸ as well as defective crystal boundaries (to reduce surface free energy, induced by internal tensile strain) at the surface,³⁶⁹ seed induced hybrid plasmonic nanoparticle (HyPNP) stimulates various physicochemical changes compared to their monometallic counterpart which includes (1) longitudinal and transverse modes of localized surface Plasmon resonance (SPR) of HyPNP varies as a direct function of the metal composition and shifting of SPR may occur simply by varying the metal-to-metal ratio,^{370,14} (2) HyPNP shows exceptional catalytic reactivity towards various reactions, e.g., CO oxidation,³⁷¹

hydrogenation of phenylacetylene,³⁷² hydrogen fuel production,³⁷³ etc. (3) broadening of the XRD curve observed for HyPNPs due to the increment of their internal tensile strain as an indirect effect of the raise in crystal defect density,³⁷⁴ etc.

The catalytic activity of monometallic plasmonic nanomaterials depends on various factors like their size & shape,^{375,376} effective charge density on the edges or tips,⁹⁸ differential chemical states of metals within single nanostructure,^{377–380} presence of low coordination sites,³⁸¹ and density as well as the area of crystal defects.³⁸² Compared to monometallic plasmonic nanostructures, bimetallic^{7,383–385} or multimetallic (both as seeded or unseeded) nanostructures³⁷² may add up several additional factors which have a potential role to influence their catalytic activity. Possible additional factors include differential crystal boundaries between metals due to their difference in crystal parameters³⁶⁸, inclusion of highly energetic twin boundaries to terminate the nanostructure growth,³⁸⁶ and the direct influence on the d-band shifting with respect to the Fermi energy surface.³⁸⁷ Since all these factors are directly related to the activation energy of a catalytic reaction, imposing these factors in an optimum content is probably the best trick to make the desired catalyst from the low-cost materials for our high throughput future endeavor.

In a general strategy to develop a good Nanoscale catalytic material, we need to modify the electrode surface by this material having the above-desired characteristics which also demands better adsorptivity on the metal electrode and to make the resultant electrocatalytic sensing platform (metal electrode + multimetallic nanostructure) for universal applicability. To fulfill above criteria, it should hold few essential characteristics which include: uniform structure for proper surface moldability (non-bulging electrode surface), close to two dimensional (2D) cross-linking structure with uniform pore size for quantitative trapping of redox system as well

as to reduce the distance between the electrode surface and analyte for an efficient redox reaction, and extended stability in variable physicochemical conditions. Easy grafting of thiols on glassy carbon electrode is known in the literature³⁸⁸ and the same idea of efficient thiol grafting has been applied for our thiol-mediated cross-linked HyPNP-based electrocatalytic sensing platform.

With these above achievable targets, in the present study, we have engineered Au-seed-induced hybrid silver nanorods (Hy-Au@AgNRs) of variable length from ~120 nm to ~840 nm with a coaxial twin boundary (TB) on the surface by a newly developed synthetic methodology. Depending upon the length of the Hy-Au@AgNRs, we have designated them as Hy-Au@AgNR₁₂₀ (for 120 nm rod), Hy-Au@AgNR₄₅₀ (for 450 nm rod) and Hy-Au@AgNR₈₄₀ (for 840 nm rod). By considering these Hy-Au@AgNRs as potential nanoscale catalytic materials, we have assembled them into a porous hybrid bimetallic network structure by thiol-based chemical cross-linking methodology. Catalytic behavior, as well as the ability of Hy-Au@AgNRs and their assemblies (Hy-Au@AgNR_x-Ass, x: length of the particular nanorod used for the assembly), has been performed by using differential pulse voltammetry (DPV), chronoamperometry, and electrochemical impedance spectroscopy (EIS) techniques. To understand the factors and mechanism responsible for the high catalytic activity of the targeted materials we have performed their atomic-scale resolution spectroscopy (X-Ray Diffraction, X-Ray Photoelectron Spectroscopy, Energy Dispersive X-Ray Analysis), high precision scattering measurements (Surface Enhanced Raman Spectroscopy, Dynamic Light Scattering, and Electrophoretic Light Scattering), and high-resolution imaging (High-Resolution Transmission Electron Microscopy, Scanning Electron Microscopy, and Atomic Force Microscopy) studies. Finally, the obtained result was verified through density functional theory (DFT) calculations by

modeling Hy-Au@AgNRs with the incorporation of necessary crystal information by quantifying the generated mechanical strain within the individual nanostructures. Once we quantify the high catalytic activity of Hy-Au@AgNRs, Hy-Au@AgNRx-Ass (Ass: Assembly) has been used as a universal non-enzymatic electrocatalytic sensing platform for highly specific and ultrasensitive detection of a series of human metabolites which include different important vitamins, potent endogenous antioxidants, essential amino acids for the biosynthesis of proteins, simple monosaccharides, and essential trace metal ions. Our study first time mechanistically explores the combined role of anisometric seeding to create intermetallic twin boundary along with their size to control their strain-induced catalytic activity to offer us a universal 2D electrocatalytic sensing platform by a combined approach of experiment and theory.

7.2 Material synthesis:

7.2.1 Synthesis of Au Nanoseed:

Spherical shape Au-nanoseed (~ 5 - 6 nm in size) was prepared by sodium borohydride reduction of Au(III)-ion in the presence of trisodium citrate (TSC) as capping agent. In a typical synthesis, 500 μL of 10^{-2} M $\text{HAuCl}_4 \cdot 3\text{H}_2\text{O}$ was added to 20 mL of MiliQ water under constant stirring. In the next step, 200 μL of 2.5×10^{-2} M trisodium citrate was added to it followed by a dropwise addition of instantly prepared and ice-cold 60 μL of 10^{-1} M sodium borohydride to the above mixture. The color of the solution changes from yellowish to brown. The solution was then kept at 30°C in dark in open mouth condition to release the excess hydrogen for the next 2hr. The solution turns gradually to wine red color which implies the formation of small nanoseeds. Formation of nanoseed was further confirmed by recording their absorption spectra, performing DLS measurements, and obtaining TEM images as shown in **Figure 7.1**.

7.2.2 Synthesis of Au-seed induced Ag nanorod:

Au-seed-induced Ag rod was prepared in a temperature-controlled synthetic procedure. In the first step 0.01 g CTAC was dissolved in 45 mL of MiliQ water and heated at 55-60 °C under constant stirring. Upon complete dissolution of CTAC, 2 mL of Au nanoseed prepared in the previous step was then added to this homogeneous CTAC solution and stirred for an additional one minute. Then 2 mL of 10^{-2} M AgNO_3 is added drop by drop to the above solution followed by the addition of 500 μL of 10^{-1} M ascorbic acid (AA) and left the mixture at the constant stirring condition for additional 4hr. During the reaction, the temperature was maintained strictly between 55-60 °C to avoid the destruction of the resultant rod-shaped nanostructures.

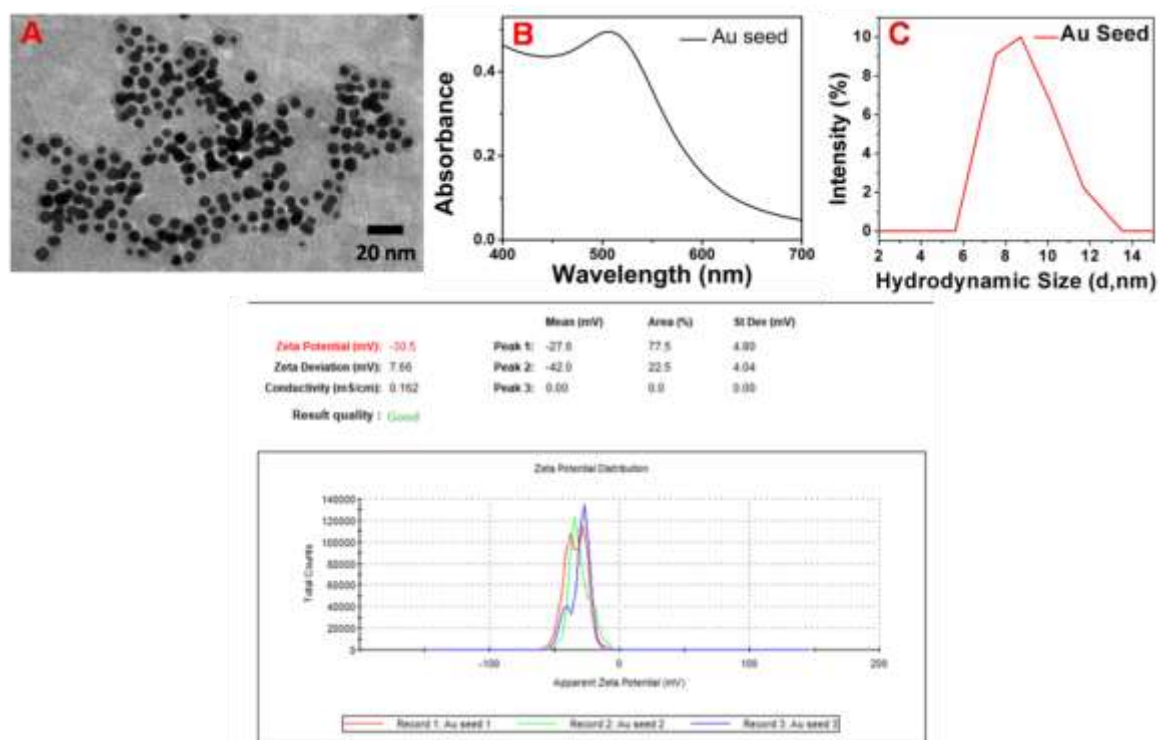


Figure 7.1: (A) True diameter from TEM image, (B) plasmon band from absorption spectra, (C) hydrodynamic size from DLS measurement, and (D) surface charge from the zeta-potential measurement of Au nanoseed.

The temperature dependence of the Au-seed induced silver nanorod (Hy-Au@AgNRs) formation is discussed in detail in the supporting information section. The length of Hy-Au@AgNRs was controlled by varying the amount of CTAC during synthesis. It has been observed that by increasing the amount of CTAC from 0.01 g to 0.05 g during synthesis we could reduce the length of the rod from 840 nm to 120 nm as shown in **Figure 7.2**. Since we are not varying the concentration of metal precursors, we need not vary the amount of AA as the reducing agent. The Hy-Au@AgNR formed by applying .01g CTAC is approximately 840 nm long in length and is designated as Hy-Au@AgNR₈₄₀. The other two rods are designated as Hy-Au@AgNR₄₅₀ (by using 0.025 g of CTAC) and Hy-Au@AgNR₁₂₀ (by using 0.05 g of CTAC). Synthesized Hy-Au@AgNRs were separated by two times fractional centrifugation at 6000 rpm in Mili-Q[®] water. (Catalytic activity of gold seed will be discussed later to explain the efficiency of AA as a reducing agent to convert Ag⁺ to Ag⁰ for effective AgNR formation. As we increase the amount of gold seed, reducing power of AA increases so much that it almost acts as a strong reducing agent and thereby resulting in rapid nucleation to initiate less anisotropy).

7.2.3 Synthesis of Au-Ag Network:

Finally, the Au-seed-induced hybrid silver nanorod-based cross-linked assembly (Hy-Au@AgNRs-Ass) was prepared by a dithiothreitol-based chemical cross-linking methodology. The centrifuged and concentrated (final volume: 500 μ L) colloidal Hy-Au@AgNR₈₄₀ solution is redispersed into 50 mL of water and stirred at 200 rpm. After complete dispersion of Hy-Au@AgNR₈₄₀, 100 μ L of 10⁻² M freshly prepared DTT was added to it and stirred for an additional 2 minutes. The color of the solution changes from yellowish-green to brown indicating the formation of nanorod-network as shown in **Figure 7.3**. The resultant solution was then centrifuged at 2000 rpm for 2 h at 30 ⁰C and washed with Mili-Q[®] water. The reason behind the

selection of Hy-Au@AgNR₈₄₀ for the preparation of Hy-Au@AgNR₈₄₀-Ass is that Hy-Au@AgNR₈₄₀ shows the best electrocatalytic oxidation efficiency among other Hy-Au@AgNRs as discussed earlier.

7.2.4 Collection and preparation of human serum samples:

To perform different electrochemical experiments we have collected blood samples from healthy willing volunteers without any medical complications. The age group of donors is recorded as 25-35 years and they were both male and female. The segregation in terms of age and sex was done that will provide us with a vivid understanding of the blood metabolite level in order to reduce the minimum deviation in our experimentation with respect to control. Human serum was separated from the collected blood samples by centrifuging each sample for 20 min at 2500 rpm. Detail about the experimentation with the obtained serum is described in the Discussion section.

7.2.5 Theoretical modeling:

With the help of TEM as well as SEM images (**Figure 7.2**), we have constructed several Au-seeded Ag nanorods (Hy-Au@AgNRs) by varying the size of nanorods (**Figure 7.14**) from 40 Å – 80 Å with a fixed diameter of 8.2 Å. For the construction of nanorods, the < 111 > facet was considered as the surface of the rod and length of the rod varies along the < 110 > crystal facet as shown clearly in **Figure 7.2C** and **7.2F**. The separation between the two < 111 > facets was achieved by the formation of a twin boundary. In each nanorod, the seeding of Au was carried out for mechanical strain calculation along the twin boundary. We have considered two different types (spherical and rod-shaped) of Au seeding as they can have the same numbers of Au and Ag atoms (**Figure 7.14**). Our calculated total energies indicate that the spherical shaped Au seeding is favorable (by 1.43 eV) over the rod-shaped Au-seeding and therefore, all the Hy-

Au@AgNR calculations have been performed using the spherical Au seed as a nucleation center. The calculated energy values support the experimental findings as the formation of a spherical Au seed-induced Ag nanorod is shown in **Figure 7.14**. For the construction and manipulation of the required modeled structures, the VESTA³⁸⁹ program was used. We have simulated the following Ag nanorods; 40 Å (with 230 atoms), 60 Å (314 atoms), and 80 Å (422 atoms) with and without gold seed as the nucleation center. As it was impossible to simulate nanorods of length from 120 nm to 840 nm by using the *ab initio* methods, we have tried to mimic the electronic and structural properties by keeping the $\frac{diameter}{length}$ ratio fixed based on our experimental findings (**Figure 7.2**). After keeping the ratio of length to diameter fixed, the Au seeding was carried out in the equivalent % mass variations (as shown in the experiments). All the DFT calculations are performed within the Vienna *ab initio* Simulation Package (VASP).^{115,116,322} A gamma-centered k-point is used during the calculations. The force convergence criterion was set to 0.01 eV/Å per atom for a better description of Heyman Forces between the atoms. The energy convergence criterion was set to 10^{-6} eV for minimization of total energies. The GGA-PBE potentials are used with the Methfessel smearing method for the calculation of DFT energies and geometrical parameters. Electronic smearing of 0.2 eV was used throughout the calculations, as Ag-Au systems describe the perfect metallic nature of nanorods.

7.3. Results and Discussion:

Synthesized Hy-Au@AgNRs show rich optoelectronic properties with a tunable Plasmon band in the infrared region. The plasmonic nature of our synthesized individual Hy-Au@AgNRs is directly related to their length as seen from **Figure 7.4**. Hy-Au@AgNR₈₄₀ has a single longitudinal plasmonic band at 1147.5 nm, however for Hy-Au@AgNR₁₂₀ and Hy-Au@AgNR₄₅₀ the corresponding band appears at 818.0 and 957.6 nm respectively. After assembling the Hy-

Au@AgNR₈₄₀ by DTT to prepare Hy-Au@AgNR₈₄₀-Ass, we found that the absorption maximum of the resultant cross-linked assembly moves to higher wavelength beyond 1300 nm and due to the absorption of water we could not record their actual plasmon peak. Moreover, assembling of Hy-Au@AgNR₈₄₀ broadened the plasmon peak and this broadening may originate both from the lower energy density at per-unit higher wavelength and wider size distribution of the resultant Hy-Au@AgNR₈₄₀-Ass. To understand the morphology, composition, and crystallization of our synthesized Hy-Au@AgNRs before and after assembling, we have performed their SEM, TEM, and HRTEM study. Combined analysis of Hy-Au@AgNR₁₂₀, Hy-Au@AgNR₈₄₀, and Hy-Au@AgNR₈₄₀-Ass is given in **Figure 7.2**. SEM images (**Figure 7.2A**, **7.2D**, and **7.2G**) clearly show that our synthesized Hy-Au@AgNRs are highly monodispersed in nature. The porous nature of Hy-Au@AgNR₈₄₀-Ass is clearly visible from their SEM image in which each Hy-Au@AgNR₈₄₀ preserve their morphology while crosslinked each other through DTT thiol linker. If we look carefully at their TEM images (**Figure 7.2B**, **7.2E**, and **7.2H**) then for each Hy-Au@AgNR there is a small Au nanoseed of ~5-6 nm diameter situated anisotropically within the nanorod. Anisotropic placement of Au nanoseed within Hy-Au@AgNRs indicates a nonconventional growth mechanism distinguishable from traditional seeded growth. The high-resolution TEM (HRTEM) of Hy-Au@AgNR₁₂₀ and Hy-Au@AgNR₈₄₀ are shown in **Figure 7.2C** and **7.2F** respectively. HRTEM images not only show the crystal arrangement in each Hy-Au@AgNRs but also differential focusing plane between the surface atoms and seed atoms indirectly proves that the seed is indeed situated within the core of the rod but not on the periphery. Both for Hy-Au@AgNR₁₂₀ and Hy-Au@AgNR₈₄₀ we could clearly see the presence of coaxial twin boundary (**Figure 7.2C** and **7.2F**) and directed towards <110> orientation of *fcc* crystal lattice. Comparison between **Figure 7.2C** and **7.2F** evidently shows the

enriched presence of multiple coaxial twin boundaries in Hy-Au@AgNR₈₄₀ which plays a crucial role in determining their tensile strain-induced catalysis and will be discussed later in more detail.

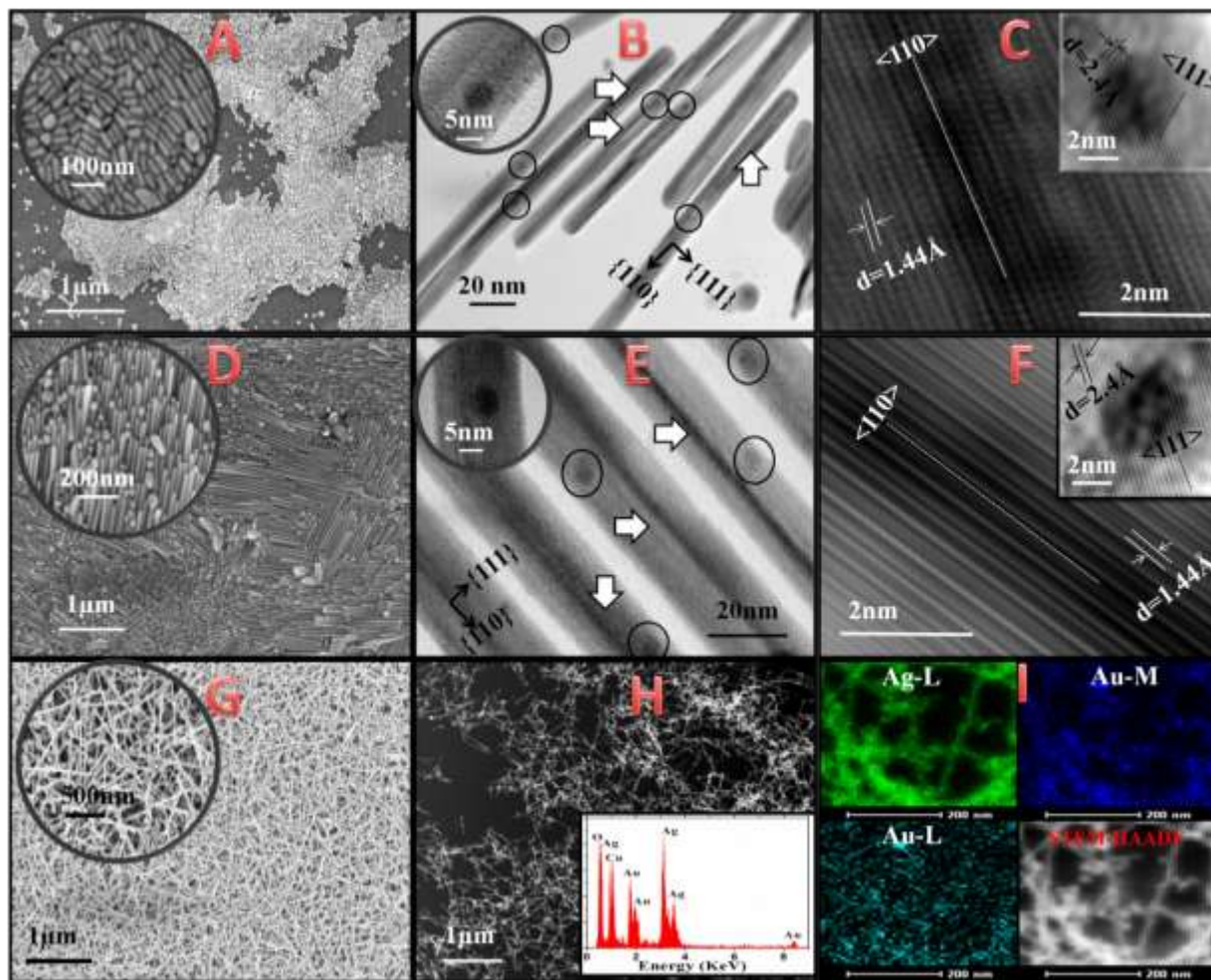


Figure 7.2: (A, B, C) and (D, E, F) are the SEM, TEM, and HRTEM images of Hy-Au@AgNR₁₂₀ and Hy-Au@AgNR₈₄₀ respectively. In (B) and (E), arrows and circles represent the presence of twin boundary on the surface and nanoseed inside Hy-Au@AgNRs. (G) is the SEM image of Hy-Au@AgNR₈₄₀-Ass which shows their clear uniform porous nature by keeping their individual rod-shaped morphology intact. (H) presents the HAADF image and EDX area profile to confirm the existence of Au and Ag. Figure (I) shows the elemental mapping of Hy-

Au@AgNR₈₄₀-Ass and the presence of Ag-L, Au-M, and Au-L lines which represent its multimetallic composition.

It is also clearly visible from **Figure 7.2C** and **7.2F** that the long axis (length) of all Hy-Au@AgNRs is directed towards $\langle 110 \rangle$ whereas the short axis (diameter) is directed along $\langle 111 \rangle$. EDX elemental mapping for Hy-Au@AgNR₈₄₀-Ass is shown in **Figure 7.2I**, where the presence of Ag-L, Au-L, and Au-M lines proves their multimetallic composition. Besides elemental mapping, we have also carried out the EDX area profile and HAADF imaging for Hy-Au@AgNR₈₄₀-Ass as shown in **Figure 7.2H**. Thus the obtained TEM, SEM, HAADF, and EDX images collectively confirm that our synthesized Hy-Au@AgNR₈₄₀-Ass is certainly a porous Au-Ag network. It is also clearly visible from **Figure 7.2H** that the morphology and symmetry of each individual Hy-Au@AgNR₈₄₀s are preserved in Hy-Au@AgNR₈₄₀-Ass.



Figure 7.3: Different colors of nanorods: From left to right Hy-Au@AgNR₈₄₀, Hy-Au@AgNR₄₅₀, Hy-Au@AgNR₁₂₀, Hy-Au@AgNR₈₄₀-Ass.

We have also performed Atomic Force Microscopy (AFM) and Energy Filtered TEM (EFTEM) measurements to achieve the 3D topographic view of Hy-Au@AgNR₈₄₀-Ass as shown in **Figure 7.5** and **7.6** respectively. **Figure 7.5** shows a time-dependent mesh-like porous structure formation for Hy-Au@AgNR₈₄₀-Ass.

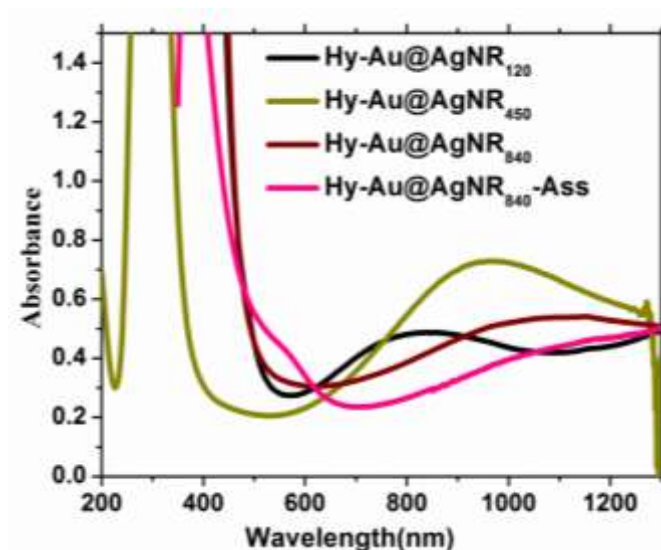


Figure 7.4: UV absorption spectra of different Hy-Au@AgNRs and Hy-Au@AgNR₈₄₀-Ass.

AFM images are taken at a regular time interval of 0 s, 30 s, 60 s, and 120 s after the addition of 1,4-dithiothreitol (DTT) to Hy-Au@AgNR₈₄₀. By aiming to prepare a porous network structure by DTT-based crosslinking, we have added different concentrations of DTT into a fixed concentration of Hy-Au@AgNR₈₄₀ solution and found that 20 μ M final concentration of DTT gives the best quality Hy-Au@AgNRs-Ass structures. Above 20 μ M, we observe a DTT-induced aggregation while below 20 μ M it shows the formation of a less porous structure.

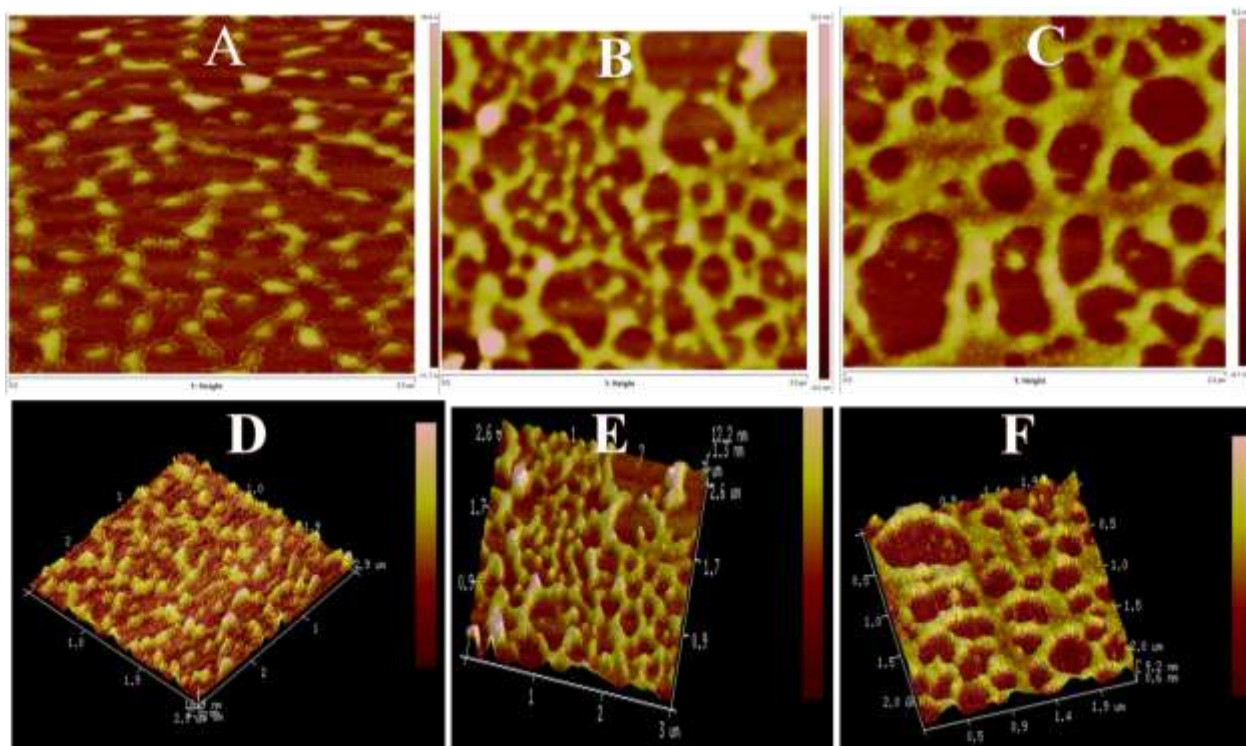


Figure 7.5: A, B, C are the time-dependent 2D images of Hy-Au@AgNR₈₄₀-Ass formation. The images are taken after DTT addition to Hy-Au@AgNR₈₄₀ at 30 s, 60 s, and 120 s interval. The 3D images of A, B, C are D, E, F respectively.

In brief, after the formation of Hy-Au@AgNR₈₄₀-Ass in a reaction vial, aliquots are taken at 0 s, 30 s, 60 s, and 120 s, while the reaction progresses and dried it immediately over the (3-mercaptopropyl)trimethoxysilane (MPTMS) modified mica plate under a controlled ultrapure argon stream as explained in details in the experimental section. It was observed that at the beginning there is an uncontrolled assembly of Hy-Au@AgNR₈₄₀s. However, as time progresses the Hy-Au@AgNR₈₄₀-Ass is formed with an average pore size of around 221 nm (**Figure 7.6a**).

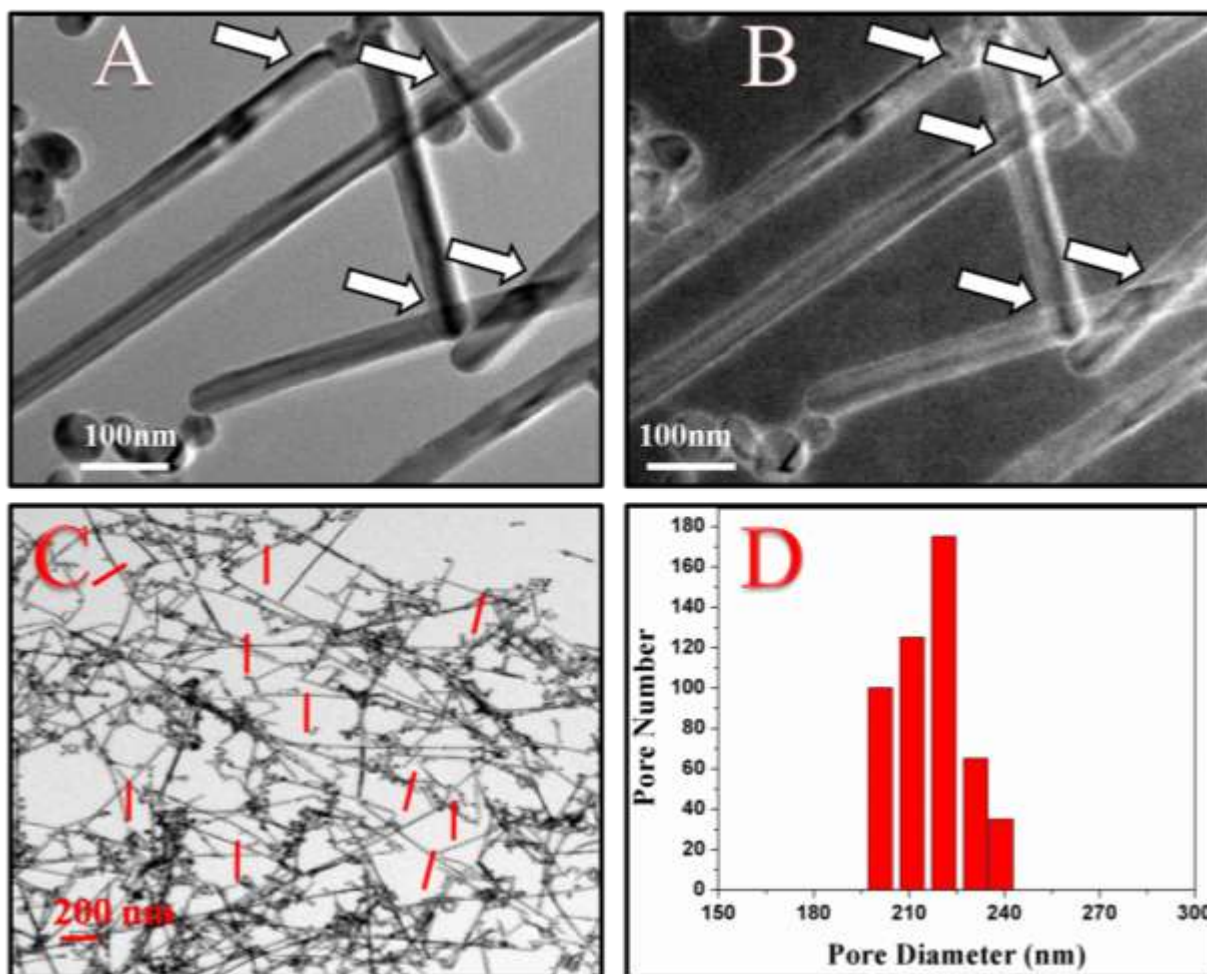


Figure 7.6a: (A) Unfiltered TEM image of Hy-Au@AgNR₈₄₀-Ass which shows that the symmetry and morphology of individual nanorods are not broken during the assembly formation, (B) Elastic TEM image of Hy-Au@AgNR₈₄₀-Ass which shows that the assembly of nanorods is eventually formed through 2D stacking of Hy-Au@AgNR₈₄₀ on XY-plane via thiol linkage where Hy-Au@AgNR₈₄₀s are randomly oriented and fused at their cross junction points, respectively, (C) Distribution of pore diameters is a large area TEM image, and (D) Histogram of the average pore diameter which is ~221 nm.

The average size distribution of different Hy-Au@AgNRs, measured by TEM and SEM, is shown in **Figure 7.6b**. The average height profile in 3D images shows that the height of Hy-Au@AgNR₈₄₀-Ass is ~12-13 nm which is close to the diameter of the individual Hy-

Au@AgNR₈₄₀ (10-12 nm). This implies that the assembly is actually formed through 2D stacking of Hy-Au@AgNR₈₄₀ on XY-plane via thiol linkage where Hy-Au@AgNR₈₄₀s are randomly oriented and fused at their cross junction points. The affinity of MPTMS towards the Hy-Au@AgNR₈₄₀ surface does not allow them to arrange through head-to-tail (J-type aggregate) or one-over-other (H- type aggregate) type of arrangement. Since the orientation of nanorods is both kinetically and chemically controlled, though at the beginning we observe an uncontrolled assembling of Hy-Au@AgNR₈₄₀, as time progresses a stable network structure is formed with high porosity in nature. The EFTEM images of Hy-Au@AgNR₈₄₀-Ass in **Figure 7.6a** show a better view of the 2D assembly of Hy-Au@AgNR₈₄₀.

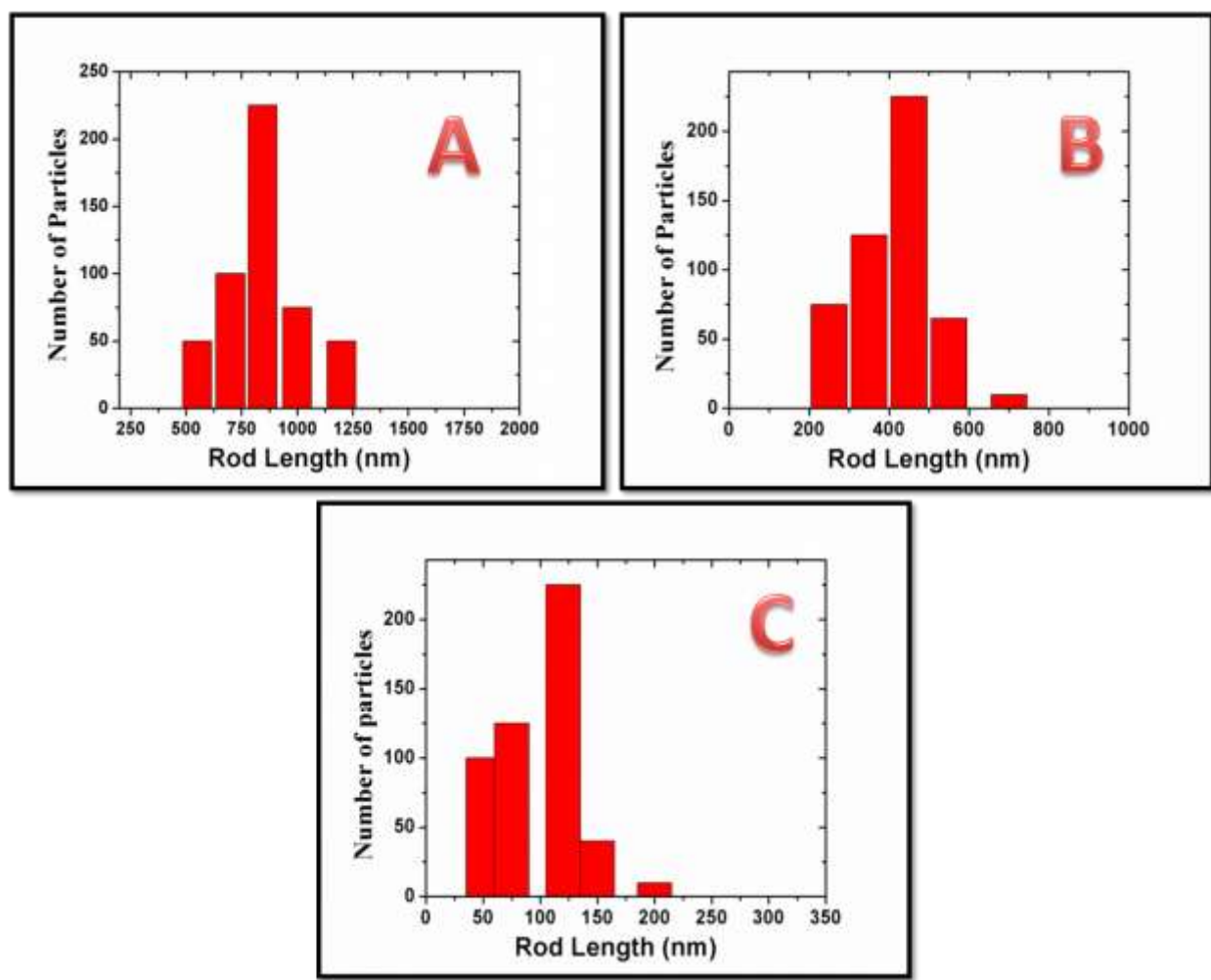


Figure 7.6b: Histogram of the nanorods (A) Hy-Au@AgNR₈₄₀, (B) Hy-Au@AgNR₄₅₀, and (C) Hy-Au@AgNR₁₂₀.

To authenticate the above-stated growth mechanism, we have also performed their detailed *in situ* DLS (**Figure 7.7** to **7.9**) and Raman measurements (**Figure 7.10**). Our *in situ* zeta potential measurements show the overall positive surface charge for all the Au@AgNRs and the corresponding Hy-Au@AgNR₈₄₀-Ass and follow the order: Hy-Au@AgNR₈₄₀ (+37 mV) > Hy-Au@AgNR₄₅₀ (+28.3 mV) > Hy-Au@AgNR₁₂₀ (+21.5 mV) > Hy-Au@AgNR₈₄₀-Ass (+17 mV). Whereas, the *in situ* Raman confirms that Ag-S bond formation (DTT as the source of sulfur) is solely responsible for assembly formation from the constituent Hy-Au@AgNR₈₄₀s. Details about the *in situ* DLS and Raman are elaborated in the following section.

***In situ* DLS measurement for different Hy-Au@AgNRs and their time-dependent assembly formation**

The recorded DLS spectrum (**Figure 7.7bC**) shows closely spaced sharp peaks at 36 nm for Hy-Au@AgNR₁₂₀, 40 nm for Hy-Au@AgNR₄₅₀, and 138 nm for Hy-Au@AgNR₈₄₀, representing their hydrodynamic diameter (d_{hyd}). We have also observed three additional low intense broad peaks for these nanostructures at 615, 947, and 5485 nm respectively. After assembling Hy-Au@AgNR₈₄₀s into Hy-Au@AgNR₈₄₀-Ass, the d_{hyd} increases from 138 nm to 213 nm as shown in **Figure 7.7bC** and this increment in d_{hyd} is due to the formation of bigger assembled mesh structured network of Hy-Au@AgNR₈₄₀, though the DLS peak at 5485 nm disappears. We have also measured the zeta potential of Hy-Au@AgNRs and Hy-Au@AgNR₈₄₀-Ass as shown in **Figure 7.7bB**. Due to the presence of positively charged CTAC molecules as the surfactant, all the Hy-Au@AgNRs and Hy-Au@AgNR₈₄₀-Ass show positive zeta potential (ξ). Measured ξ for the studied nanomaterials follow the order: Hy-Au@AgNR₈₄₀ (+37 mV) >

Hy-Au@AgNR₄₅₀ (+28.3 mV) > Hy-Au@AgNR₁₂₀ (+21.5 mV) > Hy-Au@AgNR₈₄₀-Ass (+17 mV). The trend of ξ variation is contrary to our general conception of the observation of higher ξ for nanostructure made with a higher amount of charged surfactant as discussed in the experimental section. Again, the observed ξ does not follow the order of their relative size as we measured lowest ξ of +17 mV for the biggest Hy-Au@AgNR₈₄₀-Ass nanostructure.

To evaluate this discrepancy in measured ξ and to understand the mechanism of porous network (Hy-Au@AgNR₈₄₀-Ass) formation from the constituent Hy-Au@AgNR₈₄₀s, an *in situ* DLS study has been performed. For rigid noninteracting rods at infinite dilution, the depolarize dynamic light scattering (DDLS)-based autocorrelation function $G(\tau)$ which measures the decay constant (Γ) depends heavily on both rotational and translational motion of the rod hence their respective rotational (D_R) and translational (D_T) diffusion coefficients.^{390,391} Owing to the differential contribution of rotational and translational motion, the d_{hyd} obtained from DLS measurement largely differ from TEM e.g., length and diameter of Hy-Au@AgNR₈₄₀ available from TEM is ~840 nm and ~15 nm, but from DLS we get two maximum in intensity distribution curve for Hy-Au@AgNR₈₄₀ at 138 nm for rotational motion and 5485 nm for combined rotational and translational motion. Beyond spherical geometry, D_R and D_T depend heavily on their aspect ratio (L/d) for anisotropic nanostructures with an aspect ratio greater than 5. Glidden et al. have calculated the aspect ratios of different sized gold nanorods using depolarized dynamic light scattering by differentiating two major components of the autocorrelation function.³⁹² The autocorrelation function is an exponential decaying function and it is related to the correlator time delay τ as $G(\tau) = A\{1 + B \exp(-2\Gamma\tau)\}$, where $G(\tau)$ is the autocorrelation function, A is the baseline, and B is the intercept of $G(\tau)$. The term Γ stands for relaxation rates and has two major components for rotational (Γ_{rot}) and translational (Γ_{tra}) motion of purely

monodispersed Hy-Au@AgNR₈₄₀ in solution. Change in size (d_{hyd}) and correlation coefficient $G(\tau)$, for any change in Γ_{rot} and Γ_{tra} , as a function of time during the addition of DTT in Hy-Au@AgNR₈₄₀ for an *in situ* monitoring of growth rate for Hy-Au@AgNR₈₄₀-Ass is shown in **Figure 7.7aA-C** and **Figure 7.7aD-F** respectively. The peaks at lower d_{hyd} are due to their translational motion while rotational motion contributes heavily to the peaks at higher d_{hyd} . It is observable from **Figure 7.7aA-C** that immediately after the addition of DTT (20 μM), the d_{hyd} of Hy-Au@AgNR₈₄₀ shifted from 138 nm to 939 nm within 30 s and shifts back to 202 nm after 60 s. In both cases, the peak at 5485 nm remains intact. However, after 120s we get a steady value of d_{hyd} at 193 nm and the maximum at 5485 nm has been disappeared. The disappearance of the longer maximum at 5485 nm indicates that all the rods are assembled by DTT and restrict any rotational motion. The d_{hyd} obtained after 120 s of the addition of DTT is bigger than d_{hyd} of Hy-Au@AgNR₈₄₀ (138 nm) but very close to d_{hyd} of the final form of Hy-Au@AgNR₈₄₀-Ass (213 nm). Obtained average nanopore size within Hy-Au@AgNR₈₄₀-Ass from our TEM measurement (221 nm), as shown in **Figure 7.6a** by averaging over 500 pores, is comparable with d_{hyd} values acquired from DLS experiment (213 nm). These nanopores behave like a hollow sphere in solution and the outer shell of the pore scatters the excitation light (He-Ne laser operating at 633nm). In contrast to Hy-Au@AgNR₈₄₀, these nanopores scatter light only due to the translational diffusion and hence in absence of rotational diffusion we observe only one peak (**Figure 7.7bC**) for d_{hyd} at 213 nm. Along with the size distribution, we have also recorded the change in autocorrelation function as a function of time after the addition of DTT (20 μM). In a $G(\tau)$ vs time (μs), the time at which the correlation starts to decay gives an indication of the mean size of the sample. Therefore if the curve is steeper it denotes the sample is monodispersed whereas a wider correlation confirms the presence of a polydispersed sample. From **Figure**

7.7aD it is clearly visible that at 30 s the correlation coefficient is much wider, which indicates a polydispersed sample in the solution i.e. at the beginning of the assembly forming reaction the Hy-Au@AgNR₈₄₀s tend to aggregate by DTT and a network is forming. However at 60 s, the correlation curve becomes much steeper and at 120s, the correlation coefficient attends a steady value which is much steeper than the previous one. The correlation curve obtained at 120s is much similar to the correlation curve of Hy-Au@AgNR₈₄₀-Ass, which signifies the completion of network formation.

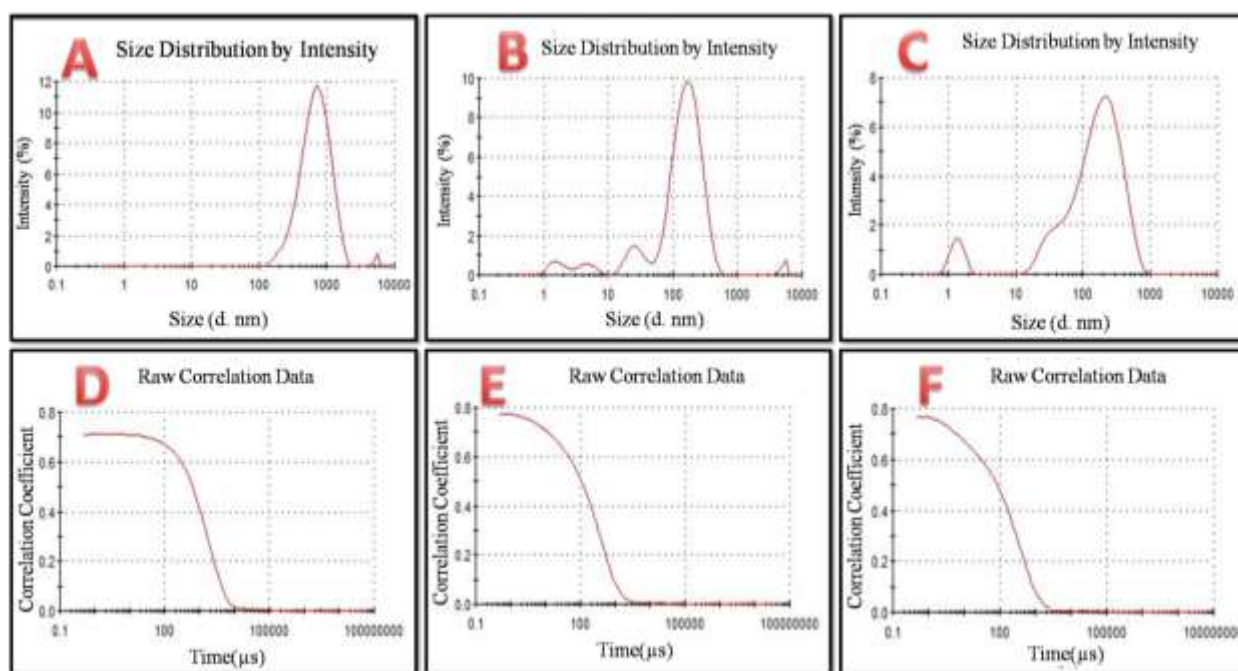


Figure 7.7a: A, B, C are Intensity (percent) vs size (nm) curve of Hy-Au@AgNR₈₄₀-Ass formation at 30 s, 60 s, and 120 s time interval in the reaction medium. D, E, F are the Correlation coefficient vs time (μs) curves for the same time intervals.

A parallel observation was also been carried out besides the DLS measurements to understand the conversion kinetics from Hy-Au@AgNR₈₄₀ to Hy-Au@AgNR₈₄₀-Ass by recording the zeta-potential (ξ) at a regular time interval of 30 s, 60 s, and 120 s. **Figure 7.7bA** describes how the surface charge changes during the formation of Hy-Au@AgNR₈₄₀-Ass. Final ξ

for all the synthesized Hy-Au@AgNRs and Hy-Au@AgNR₈₄₀-Ass are shown in **Figure 7.7bB**.

By comparing **Figure 7.7bB** and **Figure 7.7bA**, it is clearly visible that the ξ changes from +37 mV to -15 mV within 30 s of the addition of DTT to Hy-Au@AgNR₈₄₀s.

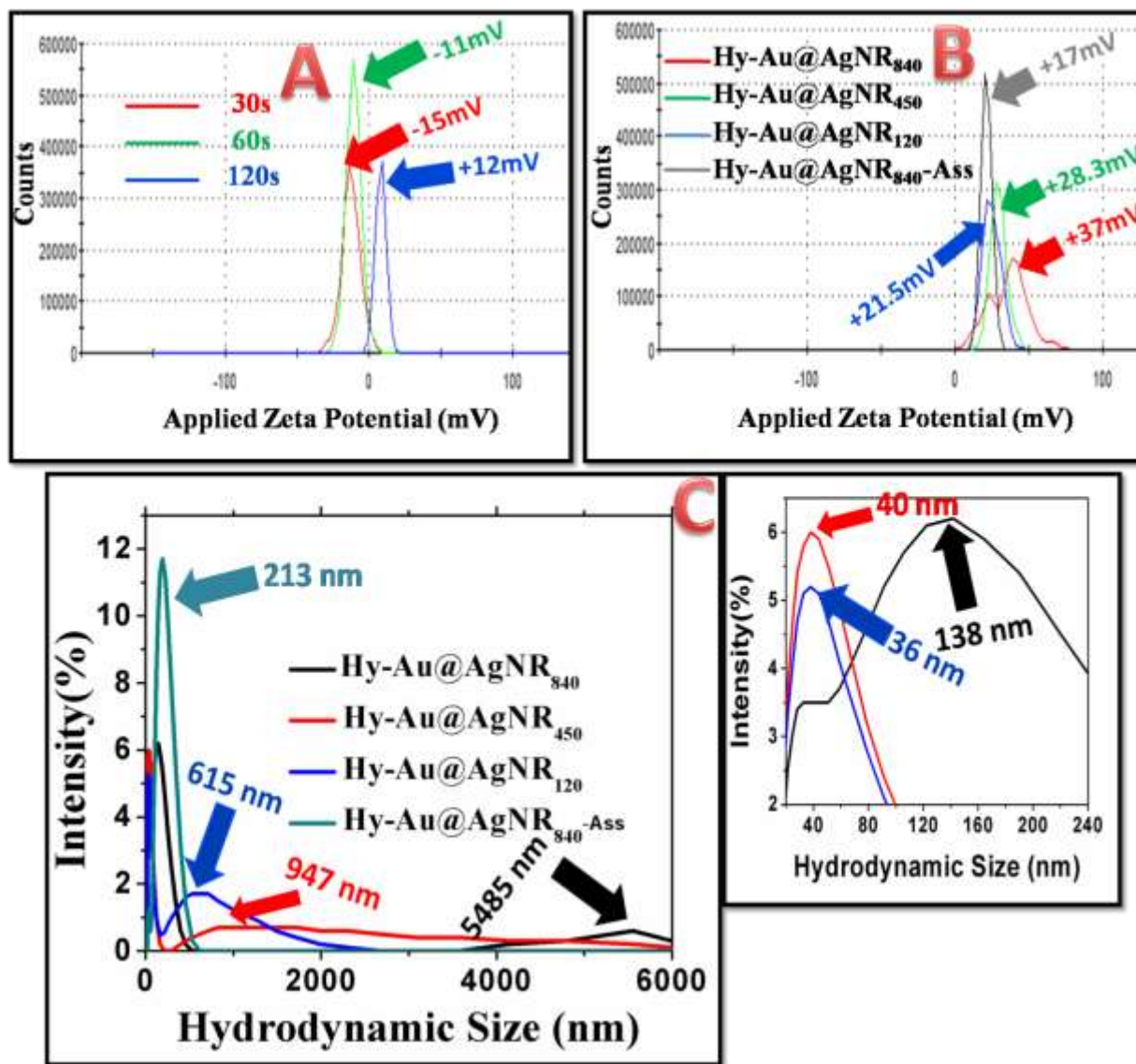


Figure 7.7b: (A) Change in zeta potential during the formation of Hy-Au@AgNR₈₄₀-Ass at different time intervals, (B, C) Final ξ and d_{hyd} of all the Hy-Au@AgNRs and Hy-Au@AgNR₈₄₀-Ass respectively.

This jump in ξ from positive to negative is due to the presence of multiple electron-rich -SH and -OH groups originating from DTT. After 60 s, ξ increases slightly from -15 mV to -11 mV and finally approaches +12 mV after 120 s which is very close to the ξ of Hy-Au@AgNR₈₄₀-Ass (+17 mV) in the equilibrium condition. The negatively charged -SH group binds the positively charged Hy-Au@AgNR₈₄₀ easily and thereby reduces the overall surface charge of Hy-Au@AgNR₈₄₀ from +37 mV to +17 mV for Hy-Au@AgNR₈₄₀-Ass.

The discrepancy of measured ξ for different Hy-Au@AgNRs with the amount of CTAC used in their synthesis can be explained both by considering their relative size and mobility.³⁹³ Due to the bigger dimension of Hy-Au@AgNR₈₄₀, they hold a larger number of positively charged CTAC molecules and hence show higher positive zeta potential and vice versa for Hy-Au@AgNR₁₂₀. Explanation of ξ variation with mobility is not simple and can be understood from their electrophoretic mobility. In brief, during ξ measurement an electric field is applied in the solution and the particles under the influence of this electric field scatter the incident light (633 nm). Depending upon the mobility (μ_e) of the nanoparticle, scattered light shifted from its original frequency. This shift is called Phase (or Doppler) shift and measured by the difference between the frequency of the scattered and incident light ($|v_{sca}-v_{inc}|$). The nanoparticle velocity (V) is measured from the Doppler shift in $\mu\text{m/s}$ by applying the equation $\mu\text{m} = V/E$, where E is the applied electric field. For our synthesized Hy-Au@AgNRs, all the physical parameters like pH, ionic strength, viscosity, etc. remain constant except their size varies. Bigger sized Hy-Au@AgNR₈₄₀ scatters the incident light more than Hy-Au@AgNR₄₅₀ and Hy-Au@AgNR₁₂₀ due to the enhanced contribution of translational and rotational motion under the electric field. This phenomenon is known as electrophoretic light scattering (ELS). We have shown the frequency plot, phase plot, and mobility plot of Hy-Au@AgNRs in **Figure 7.8**. It is clear from **Figure 7.8**

that the mobility (μ_e) for Hy-Au@AgNR₈₄₀ is 2.795 $\mu\text{m.cm/Vs}$ whereas for Hy-Au@AgNR₄₅₀ and Hy-Au@AgNR₁₂₀ are 2.11 and 1.96 $\mu\text{m.cm/Vs}$ respectively. Henry's equation³⁹⁴ concludes that μ_e varies proportionally with ξ . Thus Hy-Au@AgNR₈₄₀, having the bigger in size, shows maximum Doppler shift (**Figure 7.8**) and maximum electrophoretic mobility and hence maximum ξ . Therefore, ξ variation for Hy-Au@AgNRs is not simply due to the amount of CTAC used during their synthesis but also depends upon the size and μ_e of the nanoparticle. A frequency plot, phase plot, and mobility plot to understand the phenomenon of real-time kinetics of Hy-Au@AgNR₈₄₀-Ass formation from the constituent Hy-Au@AgNRs is shown in **Figure 7.9**. At 30 s, μ_e shifts from +2.795 $\mu\text{m.cm/Vs}$ to -1.2 $\mu\text{m.cm/Vs}$ due to the presence of multiple -SH and -OH groups on the nanostructure, originating from DTT, which causes the motion towards positively charged electrodes during electrophoresis. However, at 60 s, μ_e increases to -0.8349 $\mu\text{m.cm/Vs}$ and at 120 s, it's further shifted to 0.787 $\mu\text{m.cm/Vs}$ which is close to the μ_e value of the resultant Hy-Au@AgNR₈₄₀-Ass (1.49 $\mu\text{m.cm/Vs}$).

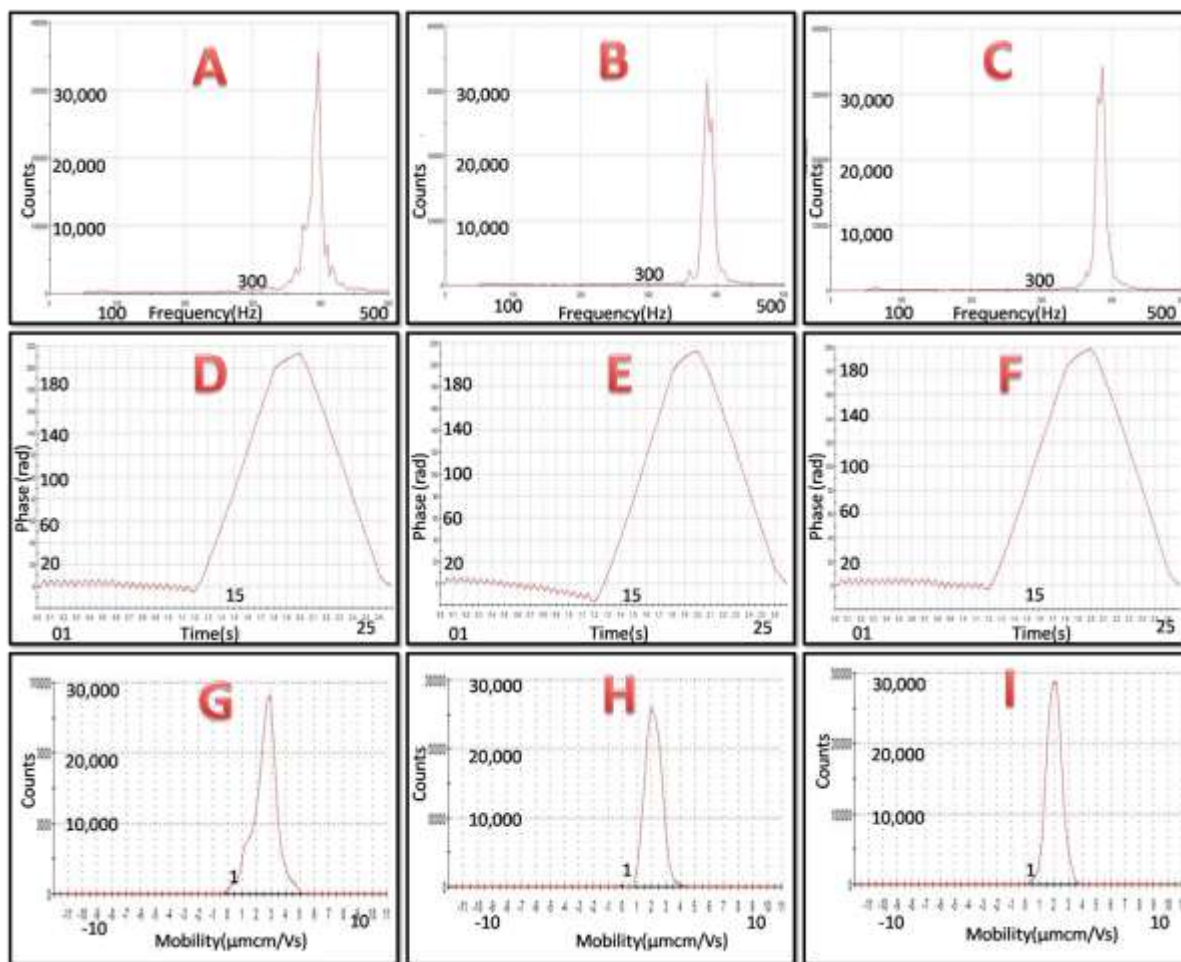


Figure 7.8: A, B, C are the frequency plot whereas D, E, F presents the phase shift and G, H, I are velocity distributions of Hy-Au@AgNR₈₄₀, Hy-Au@AgNR₄₅₀, and Hy-Au@AgNR₁₂₀ respectively.

A similar trend of frequency shift and phase shift are also observable as a function of time as clearly shown in **Figure 7.9**. Thus *in-situ* monitoring of DLS and ELS corroborates the results of a time-dependent study of AFM that after 120 s of the addition of DTT to Hy-Au@AgNR₈₄₀, the assembly forming reaction tends to complete.

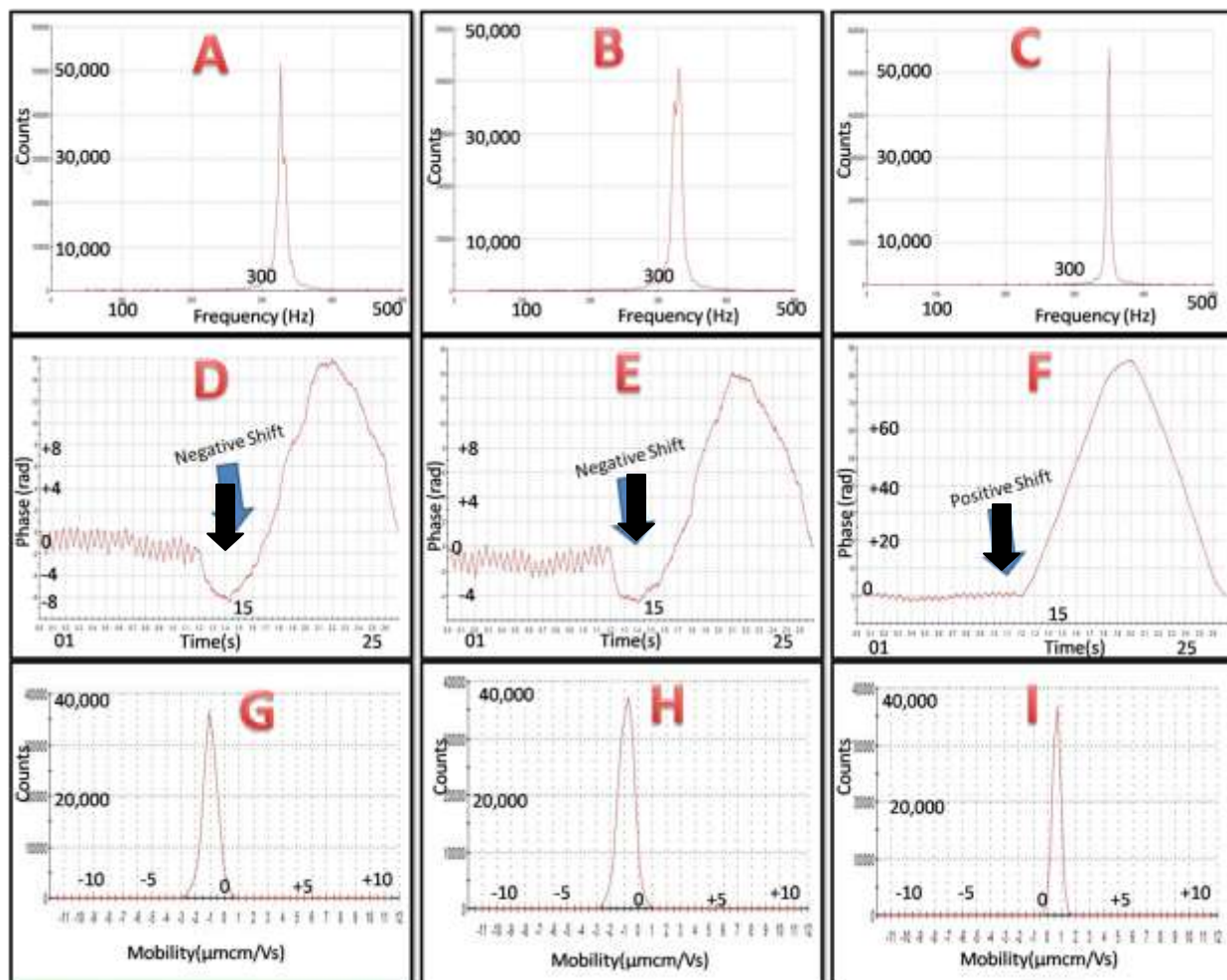


Figure 7.9: A, B, C are frequency plot; D, E, F are phase plot; G, H, I are velocity distribution curve at 30 s, 60 s, and 120 s of reaction time. The negative phase shift in D and E implies zeta potential was negative at 30 s and 60 s but becomes positive at 120 s.

***In situ* SERS measurement for different Hy-Au@AgNR₈₄₀ and their time-dependent assembly formation**

Besides DLS and ELS, we have also performed *in-situ* Raman spectroscopy for monitoring the degree of assembling of Hy-Au@AgNR₈₄₀ by DTT in the reaction medium. The basic difference between Raman scattering and dynamic light scattering is that Raman scattering is inelastic in nature and the intensity of scattering light falls within 1 in 10 million of the

radiation source whereas DLS records Rayleigh scattering which is elastic in nature and has an intensity about 10^{-1} to 10^{-3} of the incident photon. DLS provides us the information for any change in morphological transition during reaction whereas from Raman measurements we can figure out if there is any change in Polarizability owing to the appearance of Ag-S bond during Hy-Au@AgNR₈₄₀-Ass formation.

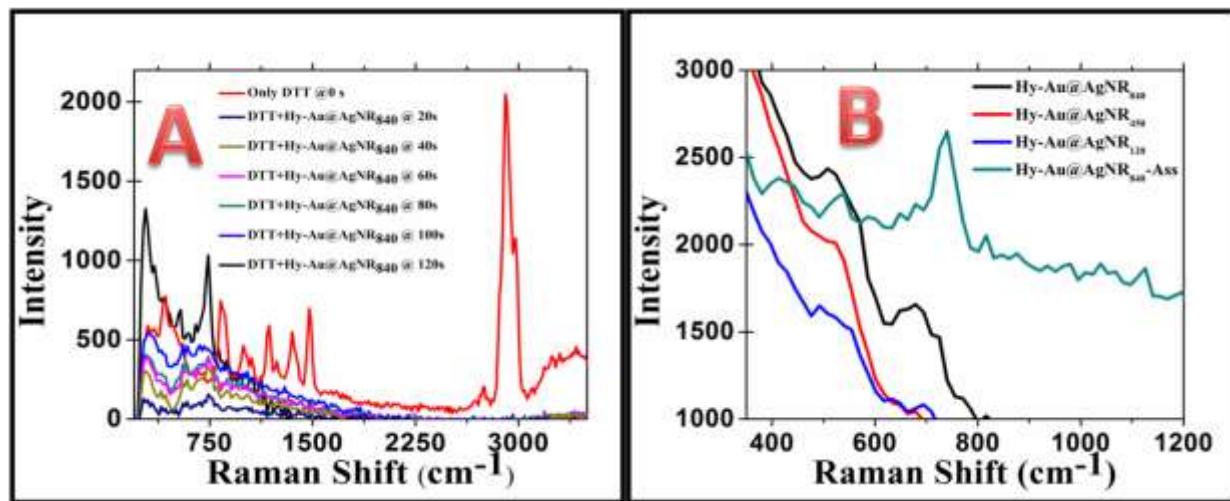


Figure 7.10: (A) SERS measurement of the time-dependent formation of Hy-Au@AgNR₈₄₀-Ass by adding Hy-Au@AgNR₈₄₀s into the DTT solution. (B) SERS spectra of different Hy-Au@AgNRs and Hy-Au@AgNR₈₄₀-Ass.

We have recorded the Raman spectra of pure Hy-Au@AgNR₈₄₀ and pure DTT (10^{-3} M) and we found that Hy-Au@AgNR₈₄₀ is Raman inactive. However, pure DTT produces sharp peaks³⁹⁵ for $\nu_{\text{stretching}}$ (C-H) at 2911 cm^{-1} , ν_{bending} (S-H) at 983 cm^{-1} , along with several other peaks, as clearly observable from **Figure 7.10**. *In situ* Raman measurements were carried out in two different ways, (1) we have added DTT ($20 \mu \text{ M}$) to the Hy-Au@AgNR₈₄₀ solution and found that the peaks at 741 cm^{-1} and 283 cm^{-1} , responsible for Ag-S bond formation³⁹⁶ getting intensified, (2) the reverse process, i.e. Hy-Au@AgNR₈₄₀ was added to pure DTT, where we observed that both the Raman peaks for $\nu_{\text{stretching}}$ (C-H) at 2911 cm^{-1} , ν_{bending} (S-H) at 983 cm^{-1}

originating from pure DTT reduces gradually and disappear finally whereas $\nu_{\text{stretching}}(\text{Ag-S})$ at 741 cm^{-1} increases gradually with time progression. Both the observations indicate the strong chemical interaction between Ag from NPR_{840} and S from DTT. Both Raman and DLS measurements provide well-agreed results for *in-situ* monitoring of Hy-Au@AgNR₈₄₀-Ass formation in the reaction medium.

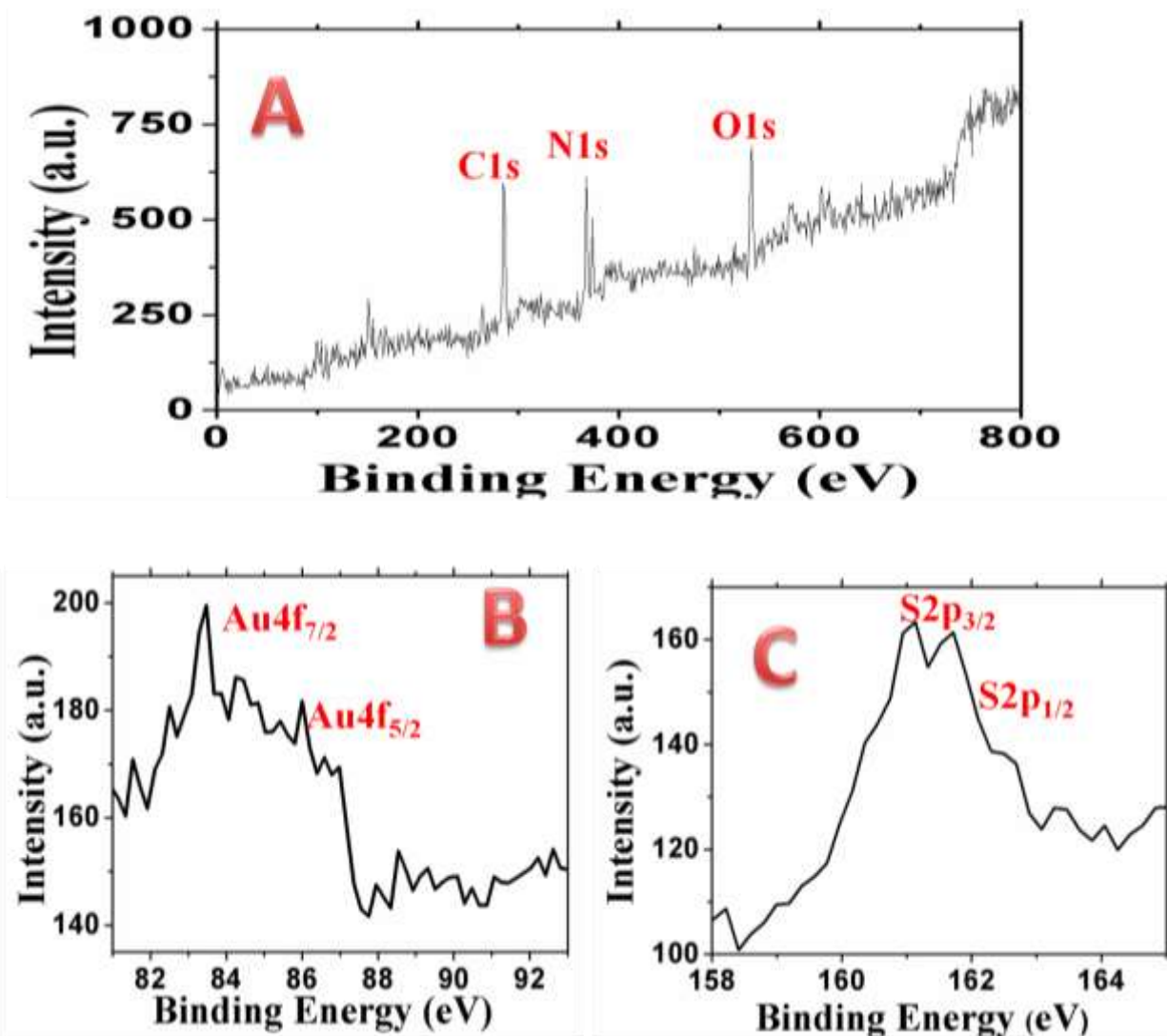


Figure 7.11: (A) XPS survey spectrum of Hy-Au@AgNR₈₄₀-Ass, (B) signature of the presence of trace amount of Au in Hy-Au@AgNR₈₄₀, and (C) S2p lines in Hy-Au@AgNR₈₄₀-Ass. The source of C is from CTAC whereas S and O come from DTT. The intensity of the Au signal is

very poor as we mentioned previously and hard to find appreciable Au in the large distribution of Ag in Hy-Au@AgNR₈₄₀.

To find out the presence of Au as nanoseed in each Hy-Au@AgNRs we have performed their XPS measurements. Despite their trace amount within a large distribution of Ag, we were able to get a very low intensified XPS signature of Au in Hy-Au@AgNR_s as shown in **Figure 7.11B** where Au4f_{7/2} peak appears at 84.0eV. In contrast to Au, the intensity of the Ag spectrum is much higher in XPS for Hy-Au@AgNR₈₄₀. The fitted curve for Ag in Hy-Au@AgNR₈₄₀ shows that Ag present in two oxidation states, in metallic silver Ag(0) and oxidized silver Ag(I).

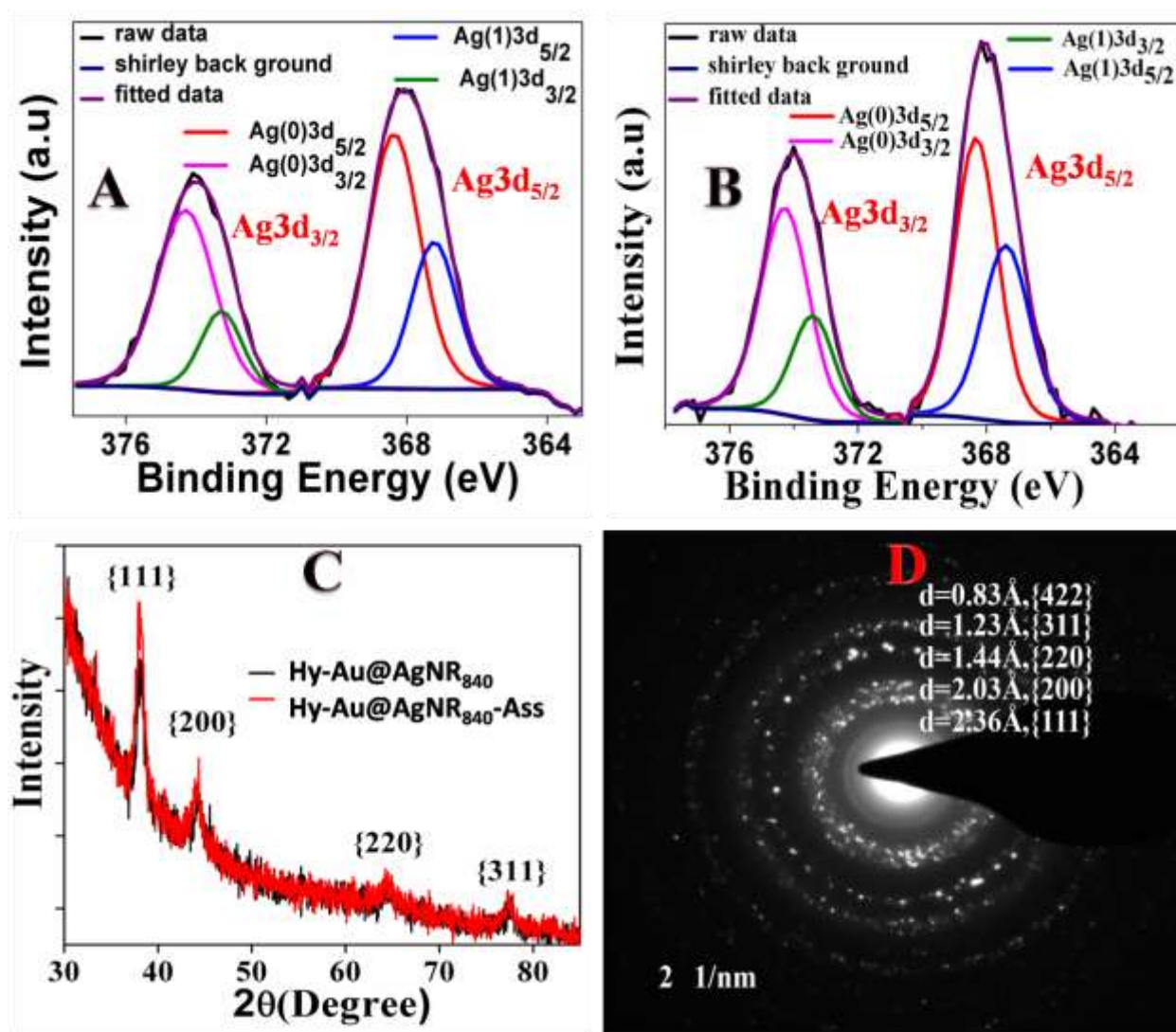


Figure 7.12: A and B are the XPS of Ag3d_{5/2} and Ag3d_{3/2} lines for Hy-Au@AgNR₈₄₀ and Hy-Au@AgNR₈₄₀-Ass. In figure C the XRD of Hy-Au@AgNR₈₄₀ and Hy-Au@AgNR₈₄₀-Ass are shown whereas D shows the SAED pattern of Hy-Au@AgNR₈₄₀-Ass to confirm the {111} is the most intense plane.

The binding energy of Ag3d_{5/2} appears at 368.3 eV for Ag(0) and at 367.2 eV for Ag(I). The presence of Ag(0) is in accordance with our expectation, originating from the reduction of Ag(I) to Ag(0) by AA during Hy-Au@AgNR₈₄₀ synthesis. The presence of Ag(I) is due to the *in situ* formation of AgCl during Hy-Au@AgNR₈₄₀, where Cl comes from the surfactant, cetyltrimethylammonium chloride (CTAC), used in synthesis. The percentage of Ag(0) and Ag(I) is found to be 67.73 % and 32.27 % in Hy-Au@AgNR₈₄₀. In case of Hy-Au@AgNR₈₄₀-Ass, the Ag3d_{5/2} appears at 368.3 eV and 367.39 eV for Ag(0) and Ag(I) respectively. The percentage of Ag(0) and Ag(I) in Hy-Au@AgNR₈₄₀-Ass is 61.11 % and 38.9 %. In general higher binding energy is observed for higher oxidation state for transition metals, however, silver is an exception where lower binding energy is observed for higher oxidation state.¹⁷⁹ Thus Ag(I) appears at lower binding energy than Ag(0) as shown in **Figure 7.12**. The interaction between the –SH and –OH group of DTT and Ag from Hy-Au@AgNR₈₄₀ causes the origination of more oxidized silver i.e. Ag(I) in Hy-Au@AgNR₈₄₀-Ass than Hy-Au@AgNR₈₄₀. The XPS for Ag3d_{5/2} and Ag3d_{3/2} lines in Hy-Au@AgNR₈₄₀ and Hy-Au@AgNR₈₄₀-Ass are shown in **Figure 7.12**. We have also provided the XPS survey spectrum of Hy-Au@AgNR₈₄₀-Ass to confirm the presence of C1s, S2p, etc., in **Figure 7.11**.

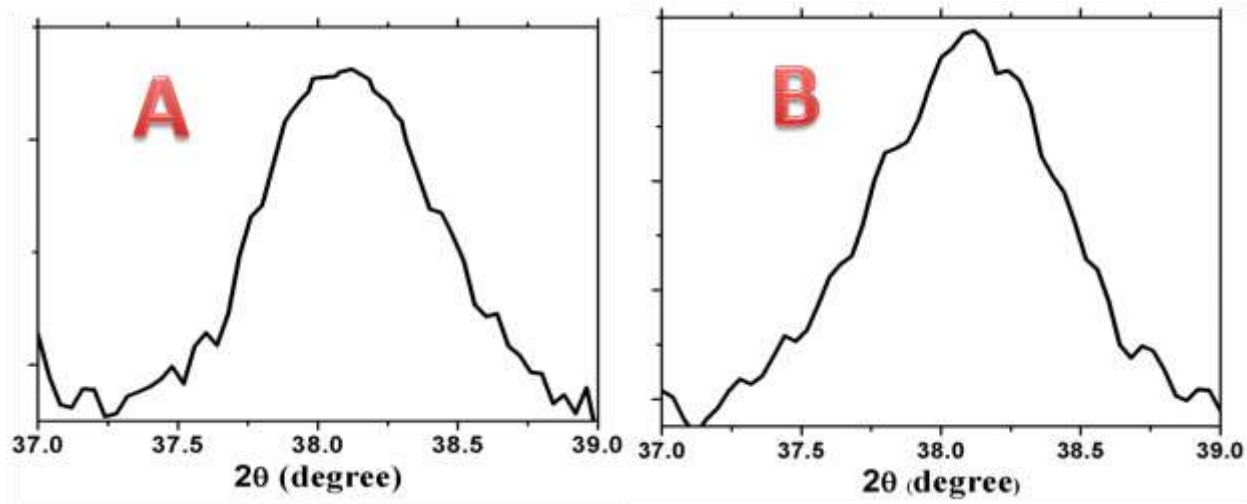


Figure 7.13: The fitted curve of (A) Hy-Au@AgNR₈₄₀-Ass and (B) Hy-Au@AgNR₈₄₀ at $2\theta \approx 38.25^\circ$ for *fcc* {111} facet.

To understand the crystal arrangement, crystal defects, and crystal defect-induced internal tensile strain in more detail for our synthesized Hy-Au@AgNRs or Hy-Au@AgNR₈₄₀-Ass, we have performed their XRD measurements (**Figure 7.12C**) along with their HRTEM. Our XRD measurements show that all the Hy-Au@AgNRs have {111} facet with the most intensified XRD signal than other facets like {200}, {311}, {220}, etc (**Figure 7.12C and 7.12D**). In a perfect nanocrystal, the scattering from the atoms adds constructively which generates a delta function like intensity distribution in the XRD pattern. However, in defect enriched crystals like Hy-Au@AgNRs which contain a coaxial long twin boundary (TB) over their surface (**Figure 7.2**), the symmetry of the crystal lattice destroyed and results in rearrangement of the intensity distribution. Therefore, irregularities in crystals cause the broadening of XRD curves due to the defect induced strain generation. We have calculated the generated strain in different Hy-Au@AgNRs by applying Williamson-Hall isotropic strain model.³⁹⁷ From the fitted curve at $2\theta \approx 38.25^\circ$ ({111} facet appears at 38.25° and gives the most intense peak), as depicted in **Figure 7.13**, we observed that Hy-Au@AgNR₈₄₀ is the most strained one among all the other Hy-

Au@AgNRs which further increases for Hy-Au@AgNR₈₄₀-Ass. The strain within the nanostructure is calculated by Williamson-Hall isotropic model. We have mentioned previously that the extent of broadening is proportional to the crystal defect density. The HRTEM and SEM images confirm that Hy-Au@AgNR₈₄₀-Ass is a crystal defect enriched nanostructure than the Hy-Au@AgNR₈₄₀. To get a comparative study we have calculated the strain from XRD broadening of the curve.

The full width at half maximum (β) for Hy-Au@AgNR₈₄₀-Ass is 0.88° whereas for Hy-Au@AgNR₈₄₀ is 0.79° . Mathematically the generated strain (ϵ) is defined as:

$\epsilon = \beta/4\tan\theta$, where θ is in radian.

Since $\{111\}$ facet appears for both Hy-Au@AgNR₈₄₀-Ass and Hy-Au@AgNR₈₄₀ at $2\theta = 38.25^\circ$, the value of $\theta = 0.33$ in radian unit for the above equation.

By incorporating the respective value of β for different nanostructures and $\theta = 0.33$, obtained values of ϵ for Hy-Au@AgNR₈₄₀-Ass and Hy-Au@AgNR₈₄₀ are 1.11×10^{-2} and 0.95×10^{-2} respectively. **Table 7.1** shows the estimated strain values (ϵ) for different Hy-Au@AgNRs and the targeted Hy-Au@AgNR₈₄₀-Ass, calculated from the measured 2θ value and fitted full width half maximum or FWHM (β) from the recorded XRD spectra. The origin of maximum internal strain for Hy-Au@AgNR₈₄₀ can easily be understood by analyzing their TEM and HRTEM and comparing it with other Hy-Au@AgNRs as shown in **Figure 7.2**. From TEM and HRTEM, it is clearly visible that each Hy-Au@AgNRs has a central TB on their surface. Twinned nanorods (Hy-Au@AgNRs) experience more internal tensile strain than untwined ones because atoms situated on TB are coordinatively unsaturated. Having the largest and enriched TB on its surface, Hy-Au@AgNR₈₄₀ should hold the maximum number of unsaturated atoms and expected to show greater XRD broadening than Hy-Au@AgNR₄₅₀ and Hy-Au@AgNR₁₂₀. However, when Hy-

Au@AgNR₈₄₀-Ass is prepared by assembling multiple Hy-Au@AgNR₈₄₀s, further broadening in the XRD curve occurs (**Figure 7.13**). This broadening in XRD is due to the appearance of multiple low-coordinated crystal defects on Hy-Au@AgNR₈₄₀-Ass due to its porous structure as confirmed from TEM and HRTEM images (**Figure 7.2**). The order of internal tensile strain due to crystal irregularities within the nanostructures is thus Hy-Au@AgNR₈₄₀-Ass > Hy-Au@AgNR₈₄₀ > Hy-Au@AgNR₄₅₀ > Hy-Au@AgNR₁₂₀.

Table 7.1: Estimation of developed strain within different Hy-Au@AgNRs and the targeted Hy-Au@AgNR₈₄₀-Ass from the measured FWHM (β) and θ values (in radian) in XRD spectra.

System	FWHM, β (in Degree)	FWHM, β (in Radian)	internal tensile strain (ϵ)
Hy-Au@AgNR ₈₄₀ -Ass	0.88	0.0154	1.1×10^{-2}
Hy-Au@AgNR ₈₄₀	0.79	0.0138	9.5×10^{-3}
Hy-Au@AgNR ₄₅₀	0.71	0.0123	8.9×10^{-3}
Hy-Au@AgNR ₁₂₀	0.65	0.0113	8.2×10^{-3}

To understand the role of gold seed, length of Hy-Au@AgNRs, and TB on their surface to control their internal tensile strain, we have calculated the strain values for all the modeled systems. In the present work, the diameter can also play an essential role in determining their mechanical strain. Therefore, we have calculated the mechanical properties of the Hy-Au@AgNR_s by changing their lengths and diameters. More specifically, we have focused on calculating the Au-seed induced mechanical strain for the modeled Hy-Au@AgNRs. For this, we have constructed pure Ag-nanorods with lengths of 40 Å, 60 Å and 80 Å and diameters of ~8.3 Å. After the optimization, spherical Au seed has been incorporated inside each of the nanorods for modeling the < 111 > surface along with the < 110 >, and twin boundary planes.

Table 7.2: Optimized parameters (length, diameter, and strain) for pure AgNRs and Hy-Au@AgNRs. Here D is the optimized diameter of pure AgNRs, $D^\#$ is the optimized diameter of Hy-Au@AgNRs, $D-D^\#$ is the difference in diameter between the optimized diameter of pure AgNRs and Hy-Au@AgNRs, and $d_{\text{Ag-Ag}}^*$ is the average Ag-Ag bond length on the surface and twin boundary for Hy-Au@AgNRs. $\Delta d_{\text{Ag-Ag}}^*$ is the difference between the Ag-Ag bond length in bulk Ag metal and different Hy-Au@AgNRs.

Rod name	Optimized Length of Hy-Au@AgNRs	Diameter (D) of pure AgNRs	Diameter ($D^\#$) of Hy-Au@AgNRs	$D - D^\#$	$d_{\text{Ag-Ag}}^*$ in Hy-Au@AgNRs	$\Delta d_{\text{Ag-Ag}}^*$ in Hy-Au@AgNRs	Strain in Hy-Au@AgNRs
40 Å	41.26 Å	8.32 Å	8.32 Å	0.00 Å	2.75 Å	0.14 Å	4.84 %
60 Å	57.57 Å	8.35 Å	8.34 Å	0.01 Å	2.74 Å	0.15 Å	5.19 %
80 Å	79.26 Å	8.43 Å	8.40 Å	0.03 Å	2.73 Å	0.16 Å	5.53 %

We have then measured the geometrical parameters for all the structures as given in **Table 7.2**. It is observable that with increasing the rod length, the average Ag-Ag bond length reduces which results in a contraction in the optimized rod length. The same effect (i.e. contraction) should also be observable for the optimized rod diameter, though the diameter of the rod increases gradually. These two effects of shortening the optimized rod length and lengthening of optimized rod diameter are contrary to each other. Therefore, the stability of rods can be increased by increasing their diameter with a shorter Ag-Ag bond by the coaxial formation of twin boundaries. We indeed observed increments in the optimized diameter of the modeled NRs through Au seeding though we have incorporated only one Au seed for each

modeled NRs. However, this can't influence a homogeneous increment of rod diameter throughout the rod length (40-80 Å). This could be the reason for twin boundary formation as observed experimentally. Hence the presence of TB along the <110> facet of the nanorod may increase the stability of the rod.

For the calculation of strain (ε) in the Hy-Au@AgNRs, we have used the following relation⁷

$$\varepsilon = (d^* - d_0)/d_0 = \delta d/d_0 \dots\dots\dots(1)$$

Here, d^* is the average Ag-Ag bond-length of the system under consideration and d_0 is the Ag-Ag bond-length (2.89 Å) in their pure face-centered cubic bulk structure. The above relation signifies the effect on the mechanical strain when a system (bulk) goes through structural reconstruction/evolution. We find that the calculated strain is maximum for the longer size Hy-Au@AgNRs. Therefore, the resultant mechanical strain increases proportionally with the NR length. These opposing effects of the shortening of Ag-Ag bond length (compared to *fcc* bulk Ag) and lengthening of the diameter may play an important role in the formation of TB on the Hy-Au@AgNRs surface.

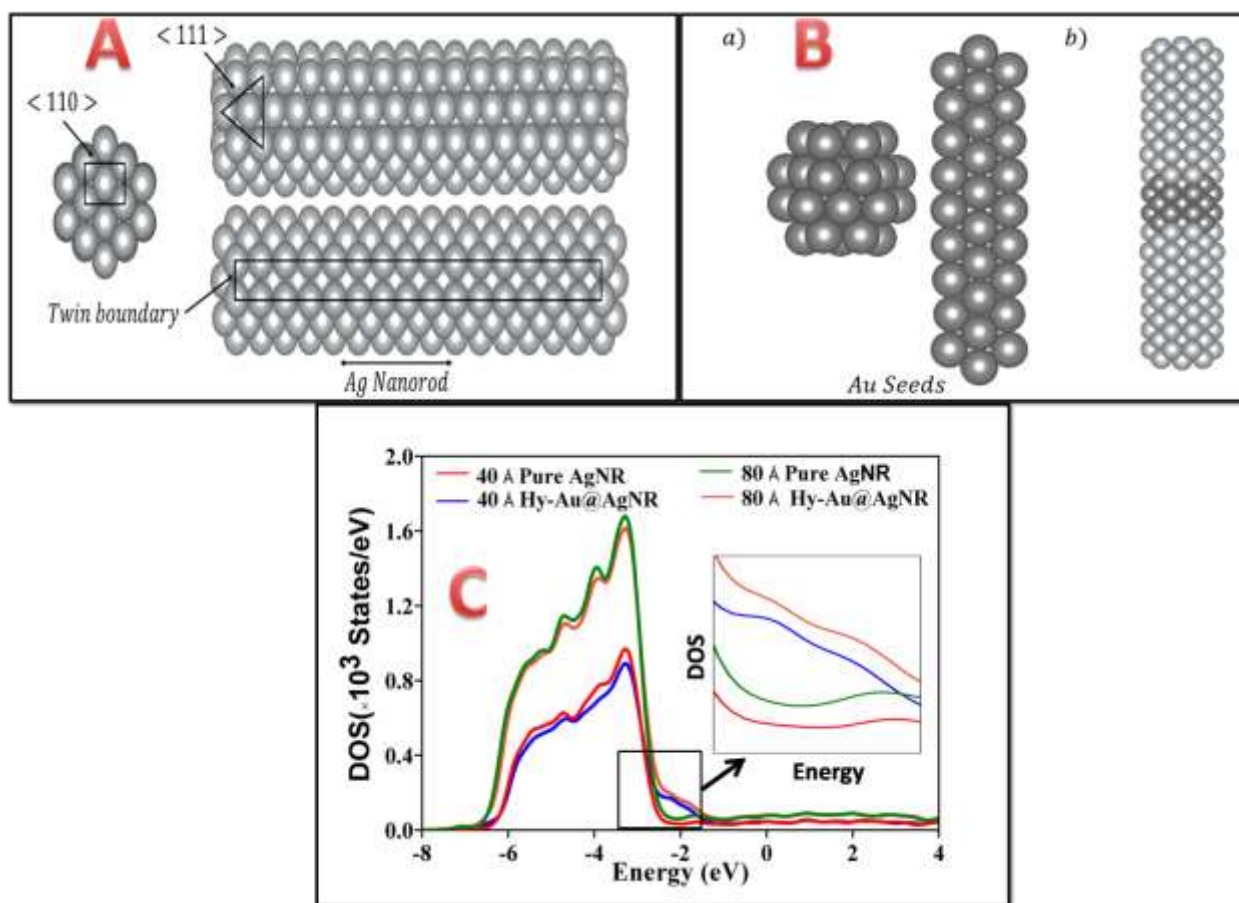


Figure 7.14: (A) Modeled nanorod structure with <111> and <110> facets. (B) Possible Au seeding (spherical and rod-shaped) and spherical Au seeded Hy-Au@AgNRs. (C) The density of states (DOS) of pure Ag and Au-seeded AgNRs with 40 Å and 80 Å lengths.

To find out the effect of Au-seed incorporation on the electronic properties of Hy-Au@AgNRs, we have calculated their density of states (DOS). As shown in **Figure 7.14**, with increasing the length of rods, the electron density shifts towards the Fermi level. Interestingly, the shift is higher for Au seeded Ag NRs. So, this indicates that the Hy-Au@AgNR₈₄₀ should show more upshift of DOS towards the Fermi level than the Hy-Au@AgNR₄₅₀ and Hy-Au@AgNR₁₂₀. When Hy-Au@AgNR₈₄₀ is assembled into Hy-Au@AgNR₈₄₀-Ass, it creates multiple low coordinated crystal sites like stepped surface, terrace, kinks, edges, etc., as shown in **Figure 7.15**, which further increase the internal strain as seen from XRD broadening and

explained in SI section. Hence DOS of Hy-Au@AgNR₈₄₀-Ass will be more upshifted towards the Fermi level than the corresponding Hy-Au@AgNR₈₄₀.

From the above discussion, we can say that Au-seed induced longer Hy-Au@AgNRs may shift the d-band center more towards the Fermi level. Therefore, the question arises whether it is possible to prepare Au-Ag NR more than 840 nm to maximize this effect?

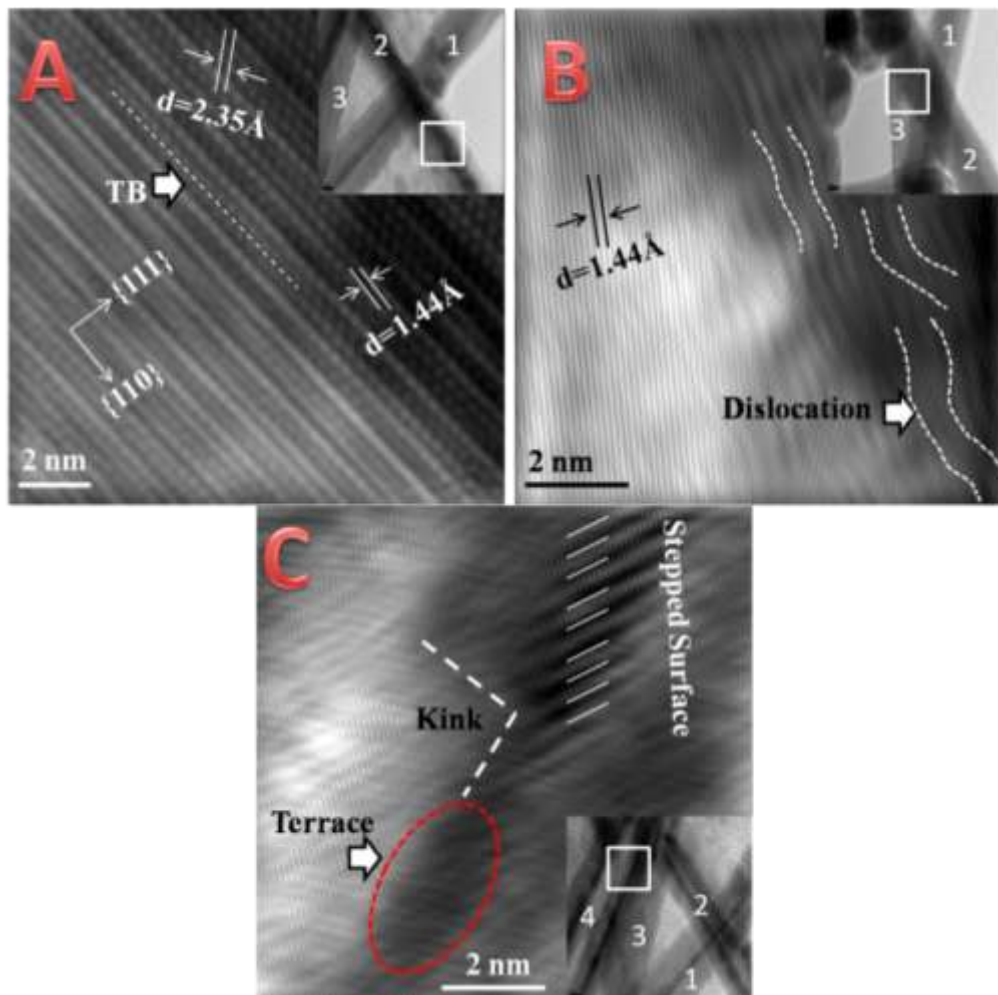


Figure 7.15: Creation of multiple low coordinated crystal sites like stepped surface, terrace, kinks, edges, etc., during the formation of Hy-Au@AgNR₈₄₀-Ass from the constituents Hy-Au@AgNR₈₄₀S.

We have previously reported pure Ag nanorods with lengths of more than 10 μm .³⁹⁸ Bimetallic Au-Ag nanorods of length $\sim 1.2 \mu\text{m}$ have also been reported¹⁴ earlier. Details about the synthesis and control of length, morphology, monodispersity, and efficiency of assembly formation are included in the following section (**Figure 7.16-7.22**). Due to their very low yield and poor stability which converts them into spherical particles with time, Hy-Au@AgNRs with length beyond 840 nm have not been used for further study.

Synthesis and control of Hy-Au@AgNRs and Hy-Au@AgNR₈₄₀-Ass:

We have mentioned previously that different length Au doped Ag rods were prepared by varying the surfactant concentration at constant temperature (55° - 60°C). However, we have also monitored the effect of the variation of other parameters during synthesis like seed concentration, silver nitrate concentration, AA concentration, DTT concentration, etc. and optimized the condition for preparing the longest NR (Hy-Au@AgNR₈₄₀) and its assembly (Hy-Au@AgNR₈₄₀-Ass). Details are discussed below:

Effect of temperature:

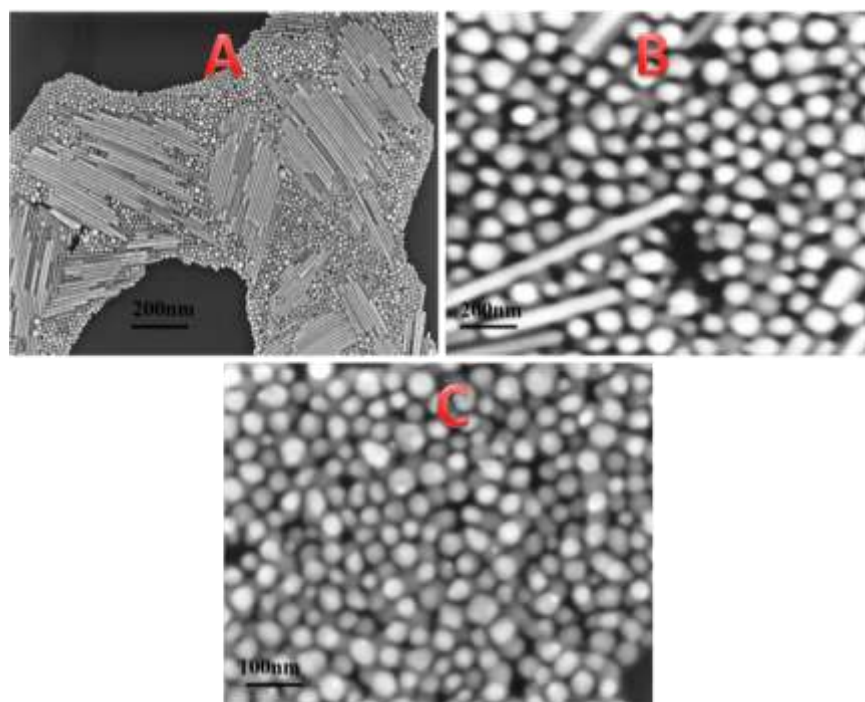


Figure 7.16a: Effect of temperature on Hy-Au@AgNR₄₅₀ morphology, at (A) 60-70 °C, (B) 70-80 °C, and (C) 80-90 °C. In all cases, optimized conditions for other physical and chemical parameters remain unchanged.

During the synthesis of Hy-Au@AgNRs, the temperature was always kept constant within the range of 55-60 °C. As we increase the temperature beyond this range, the aspect ratio of the rod gradually reduces with temperature and finally transform into spherical- and oval-shaped particle as shown in **Figure 7.16a**. When the temperature exceeds 60 °C, it was found that two Au seeds are piled up and Ag deposited onto it as shown in **Figure 7.16b**. Below 60 °C there is no sign of aggregation of Au seeds and at room temperature (30 – 40 °C) AgNO₃ cannot be reduced by ascorbic acid.

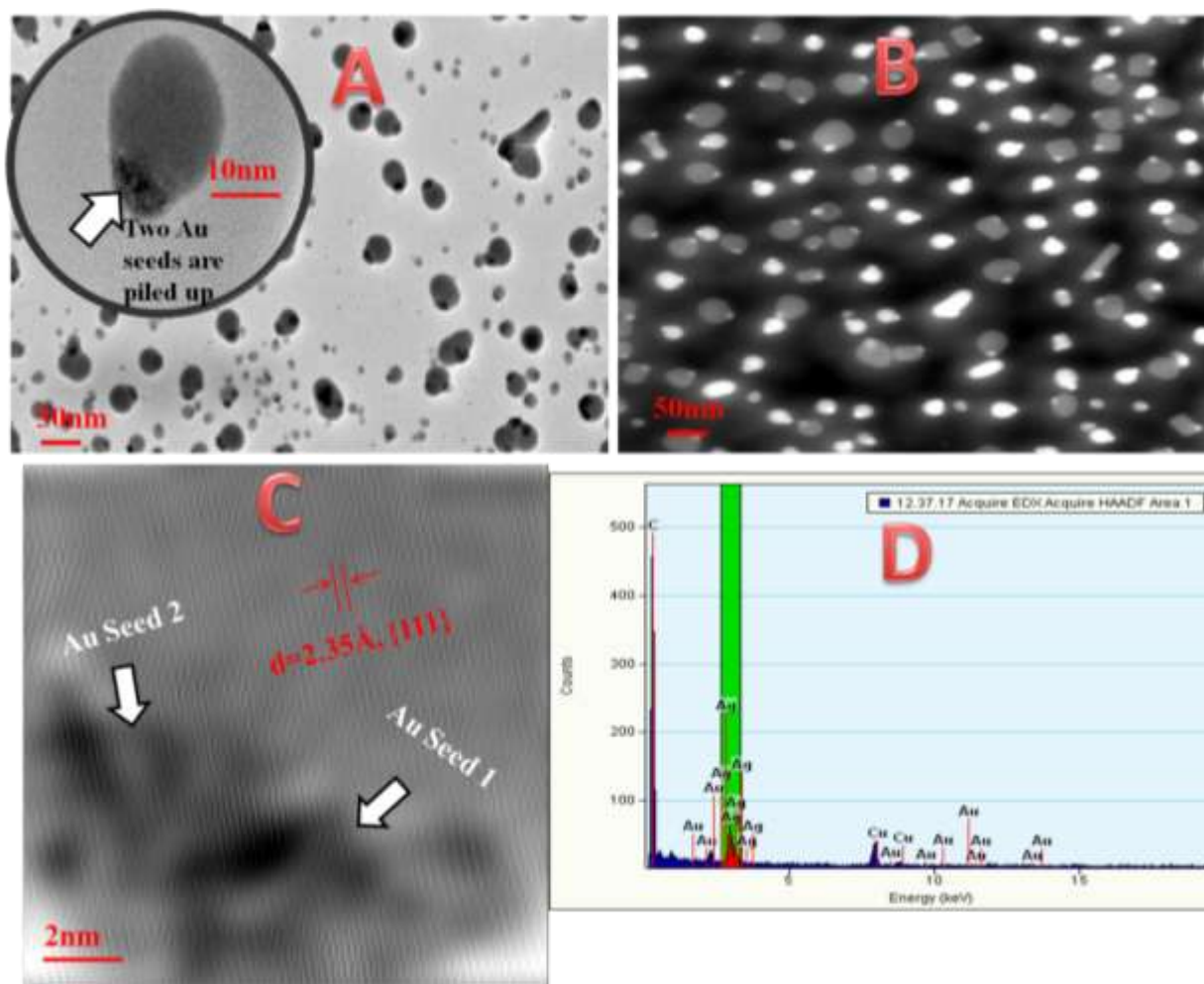


Figure 7.16b: Association of Au seed followed by Ag deposition at a higher temperature. Stacking up of Au seeds is verified by (A) TEM, (B) HAADF, (C) HRTEM, and (D) EDX.

Effect of Au seed:

If we use Ag seed during synthesis we did not get any rod-shaped particle, instead, a colloidal solution of Ag is formed only. On the contrary, the addition of Au seed initiates the seeding process of Hy-Au@AgNR efficiently. As the reduction potential of Au(III)/Au(0) is much higher (+1.5V) is much higher than the reduction potential of Ag(I)/Ag(0) system, leaching of Au seed in the latter case can easily be discarded. By observing the above cases we can suggest that Au seed acts as a catalyst here to enhance the reducing power of AA to assist the reduction of Ag^+ to

Ag^0 . The amount of Au seed was optimized to 2 mL in 50 mL of the reaction mixture. The kinetics of nanoparticles formation by using Ag and Au seed by keeping the synthesis protocol the same is shown in **Figure 7.17a** and the effect of the variation of Au seed amount is shown in **Figure 7.17b**.

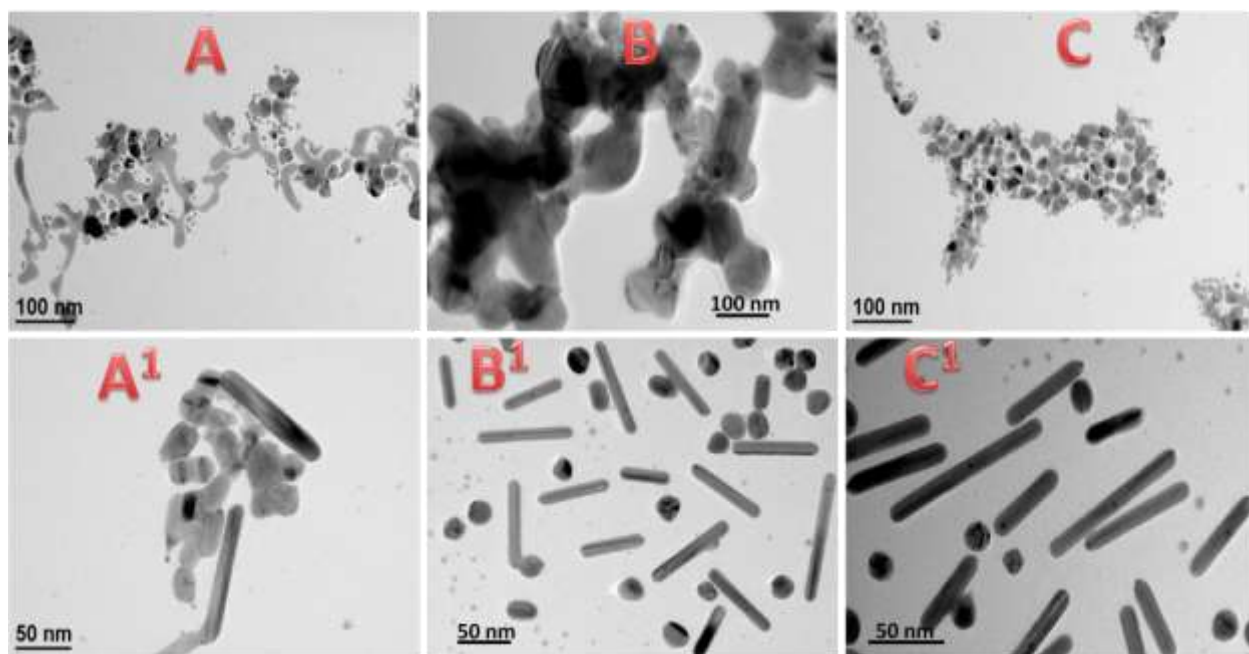


Figure 7.17a: Kinetics of Ag seed-based nanorod formation at (A) 30 min, (B) 60 min, and (C) 90 min and Au seed-based Hy-Au@AgNR₁₂₀ formation at (A') 30 min, (B') 60 min, and (C') 90 min. In all cases, optimized conditions for other physical and chemical parameters remain unchanged.

A greater amount of Au seed than the optimized volume results in the decrease of nanorod length whereas, a lower amount of Au seed results in the decrease of nanorod yield.

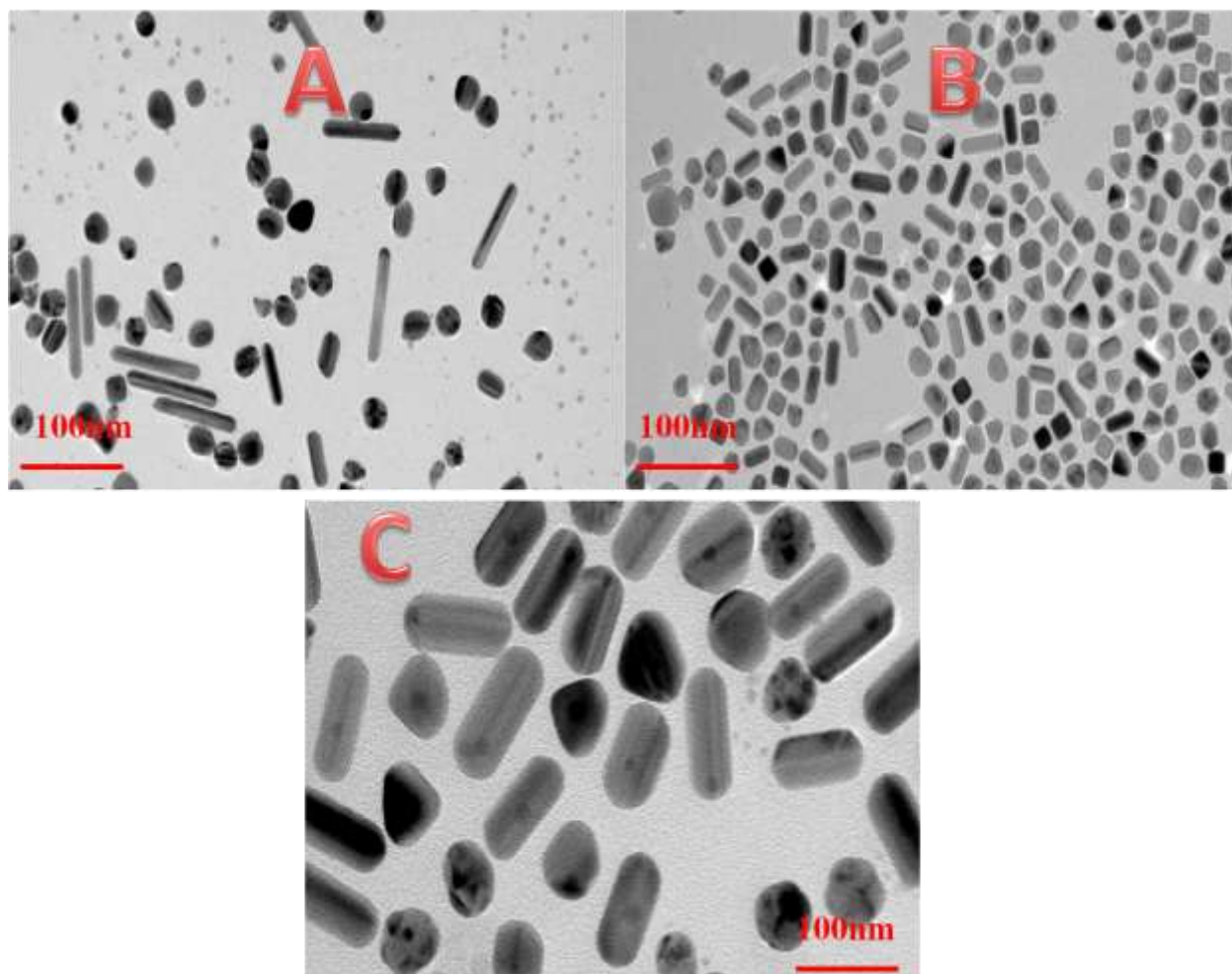


Figure 7.17b: The effect of the variation Au seed amount [(A) 1 mL, (B) 4 mL, and (C) 2 mL] on Hy-Au@AgNR₁₂₀ synthesis. In all cases, optimized conditions for other physical and chemical parameters remain unchanged.

Effect of silver nitrate concentration:

The addition of AgNO₃ to the CTAC solution during synthesis forms insoluble AgCl immediately which turns the solution turbid. However, in presence of Au seed, the amount of AgCl formation is much less as the added Au seeds act as catalysts to assist the reduction of Ag⁺

ions by enhancing the reducing power of AA as discussed before. The concentration was adjusted to 2 mL of 10^{-2} (M) AgNO_3 into 45 mL of CTAC solution. Greater (> 2 mL) amount of AgNO_3 causes the formation of more Ag spheres whereas a lower amount of AgNO_3 reduces the nanorod length. The effect of the variation of the AgNO_3 amount is shown in **Figure 7.18**.

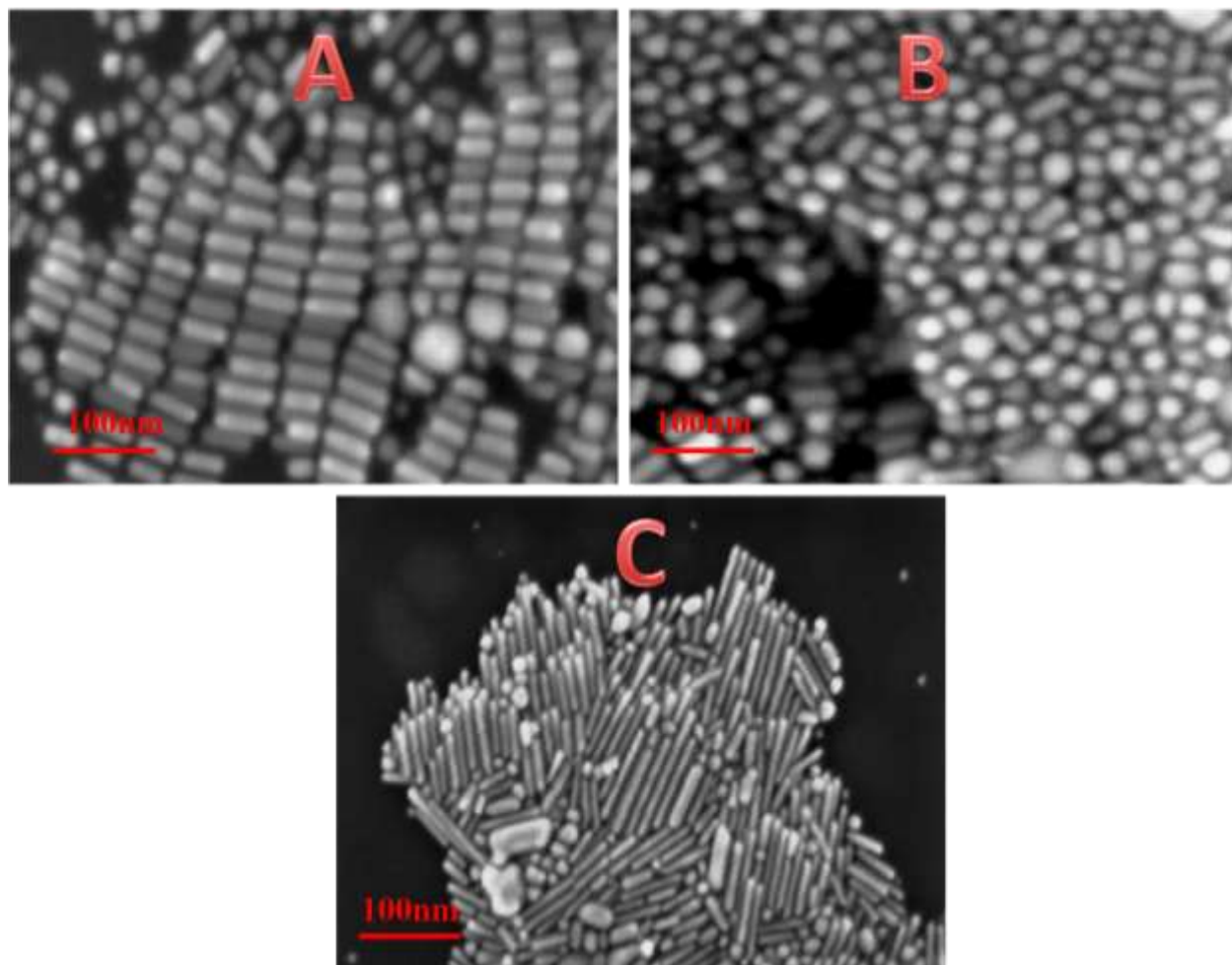


Figure 7.18: Effect of AgNO_3 concentration (in the reaction mixture) on the efficiency of Hy-Au@AgNR₁₂₀ formation. (A) 1 mL of 10^{-2} (M) AgNO_3 generates nanorods of length ~ 50 nm, (B) 4 mL of 10^{-2} (M) AgNO_3 generates nanospheres of diameter ~ 20 -25 nm, and (C) 2 mL of 10^{-2} (M) AgNO_3 generates Hy-Au@AgNR₁₂₀s. In all cases, optimized conditions for other physical and chemical parameters remain unchanged.

Effect of CTAC concentration:

We have mentioned in the main manuscript that a greater amount of CTAC reduces the length of Hy-Au@AgNRs. To prepare the longest Hy-Au@AgNR, the amount of CTAC was optimized to 0.01g CTAC in 45 mL of water. By using less than 0.01 g CTAC in 45 mL water we couldn't generate any Hy-Au@AgNR. The formation of Hy-Au@AgNRs by using 0.01 gm CTAC in 45 mL water has been detailed in the main manuscript. The effect of the variation of CTAC concentration above 0.01 gm/45 mL is shown in **Figure 7.19**.

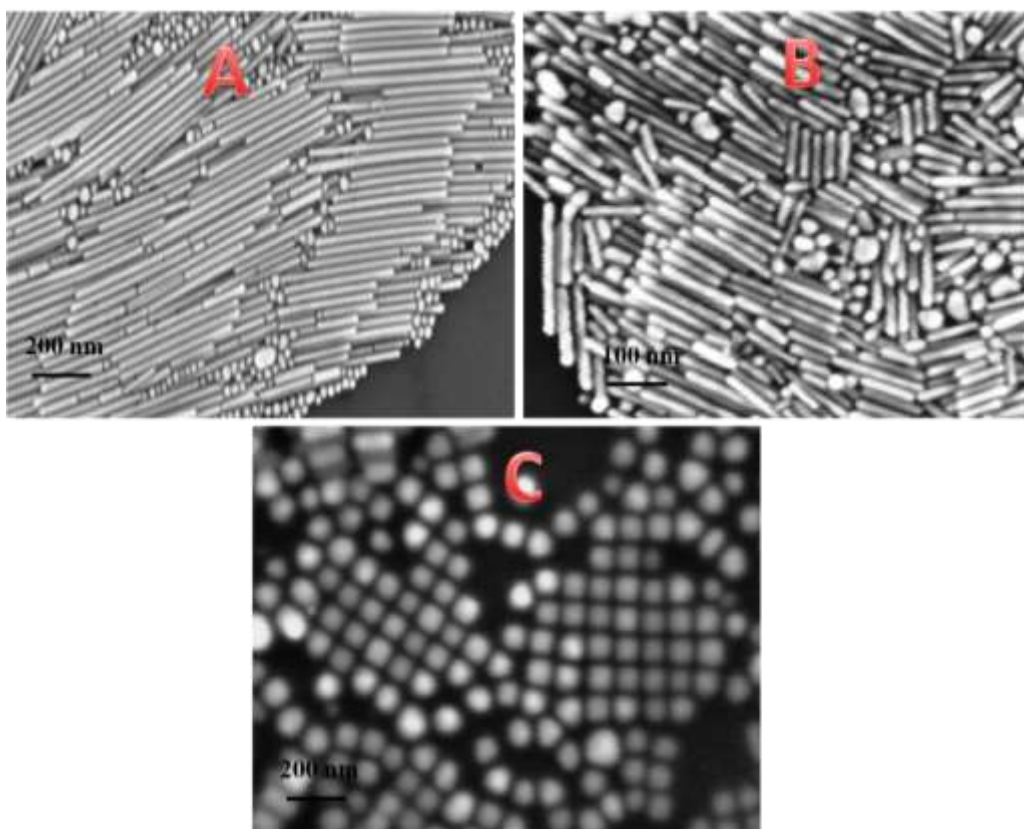


Figure 7.19: Effect of CTAC concentration with (A) 0.025 gm CTAC in 45 mL water for the formation of Hy-Au@AgNR₄₅₀, (B) 0.05 gm CTAC in 45 mL water for the formation of Hy-Au@AgNR₁₂₀, and (C) 0.1 gm CTAC in 45 mL water for the formation of Hy-Au@AgNR₅₀. In all cases, optimized conditions for other physical and chemical parameters remain unchanged.

Effect of ascorbic acid concentration:

A literature survey provides that ascorbic acid (AA) acts as a mild reducing agent.^{174,319} As mentioned earlier that at room temperature ascorbic acid cannot reduce Ag^+ to Ag^0 , though, its reduction power increases at elevated temperature (at 60 °C). Contrary to that, the presence of Au seed enhances the reducing power of AA substantially and efficiently converts all Ag^+ into Ag^0 at 60 °C. We have varied the AA concentration and optimized the amount as 500 μL of 10^{-1} M of AA to generate well structured Hy-Au@AgNRs. The effect of the variation of AA concentration is shown in **Figure 7.20**.

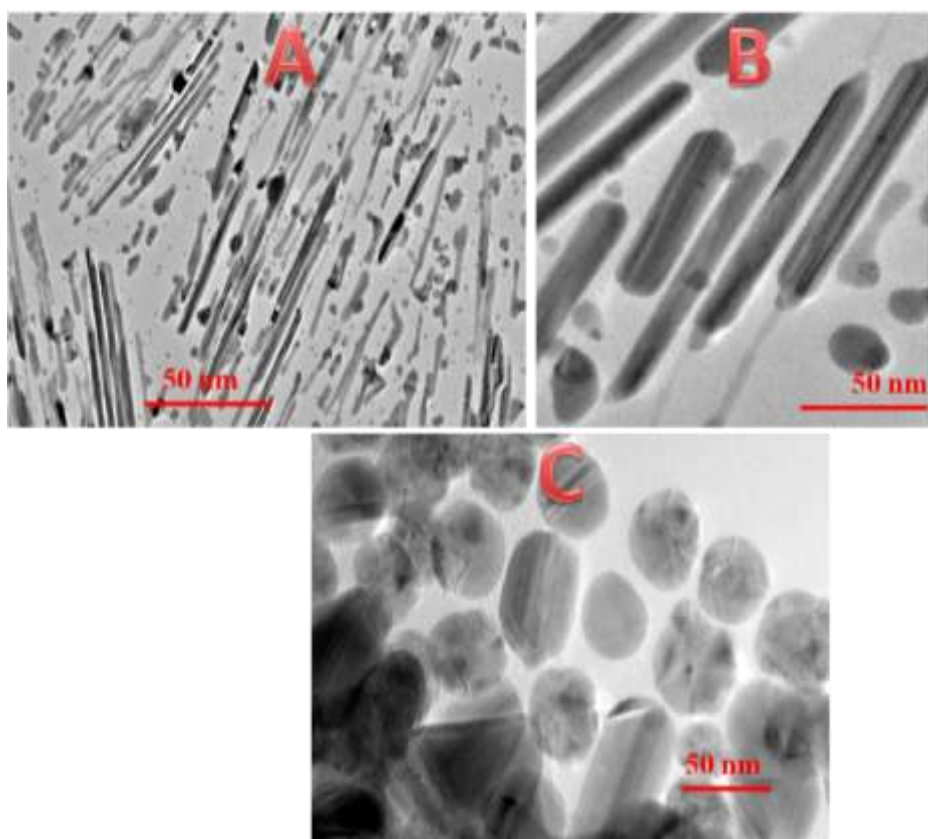


Figure 7.20: The effect of the variation of AA concentration on Hy-Au@AgNR₁₂₀ formation with (A) 250 μL 10^{-1} M of AA, (B) 500 μL 10^{-1} M of AA (optimized condition), and (C) 1 mL 10^{-1} M of AA. In all cases, optimized conditions for other physical and chemical parameters remain unchanged.

Effect of DTT concentration:

During Hy-Au@AgNRs preparation, we have used 20 μM DTT at room temperature. Each DTT molecule has two -SH groups attached to it. Sulfur has a strong binding affinity to noble metals like Au, Cu, and Ag.³⁹⁹ Binding energy calculations by using density functional theory (BP86, B3LYP, and CAM-B3LYP) and ab initio methods³⁹⁹ (MP2 and CCSD(T)) indicate that for pure metal clusters, the tendency of a metal to interact with -SH group varies in the order of $\text{Au} > \text{Cu} > \text{Ag}$. In binary alloy clusters, alloying Au with Cu and Ag decreases the attraction of Au towards -SH, while alloying Ag and Cu by Au increases the attraction of Ag and Cu towards -SH significantly.

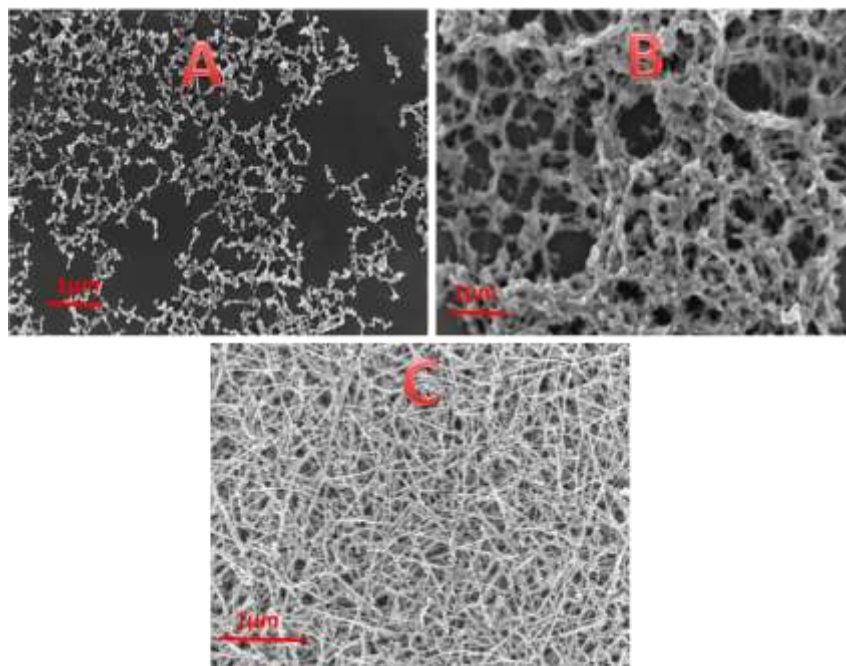


Figure 7.21: The effect of the variation of DTT concentration on the efficiency of Hy-Au@AgNR-Ass formation with the final concentration of DTT in the Hy-Au@AgNR₈₄₀ solution as (A) $< 20 \mu\text{M}$, (B) $> 20 \mu\text{M}$, and (C) $= 20 \mu\text{M}$.

Since in our case the synthesized Hy-Au@AgNRs are a case of alloying Ag by Au, we expect a strong affinity of -SH group from DTT towards the nanorod surface. Moreover, the dissociation energy values in their study⁷⁵ for isolated metal clusters specify the more favorable

formation of binary alloy clusters (Au_nAg_m) over pure ones. Hence the inherent stability of Hy-Au@AgNRs due to gold doping and increased attraction of Ag towards $-\text{SH}$ enhances the stability of the resultant Hy-Au@AgNR-Ass by preserving the individual NR's morphology. Variation of DTT concentration to control the effective assembly formation shows that a DTT concentration less than $20\ \mu\text{M}$ causes less efficient assembly formation and hence a nanostructure with less and uneven porous nature. On the contrary, DTT with a concentration greater than $20\ \mu\text{M}$ causes a more aggregated structure of Hy-Au@AgNR₈₄₀ and precipitates out from the solution. The effect of the variation of DTT concentration on the efficiency of Hy-Au@AgNR-Ass formation is shown in **Figure 7.21**. Hence to achieve catalytically most active Hy-Au@AgNR-Ass formation, optimized conditions are (i) use of 0.01 g CTAC in 45 mL of water with controlled heating at $55\text{--}60\ ^\circ\text{C}$, (ii) followed by addition of 2 mL Au seed, 2 mL of 10^{-2} (M) AgNO_3 , 500 μL of 10^{-1} (M) of AA, and finally (iii) 100 μL of 10^{-2} M freshly prepared DTT into the total volume of centrifuges Hy-Au@AgNR₈₄₀.

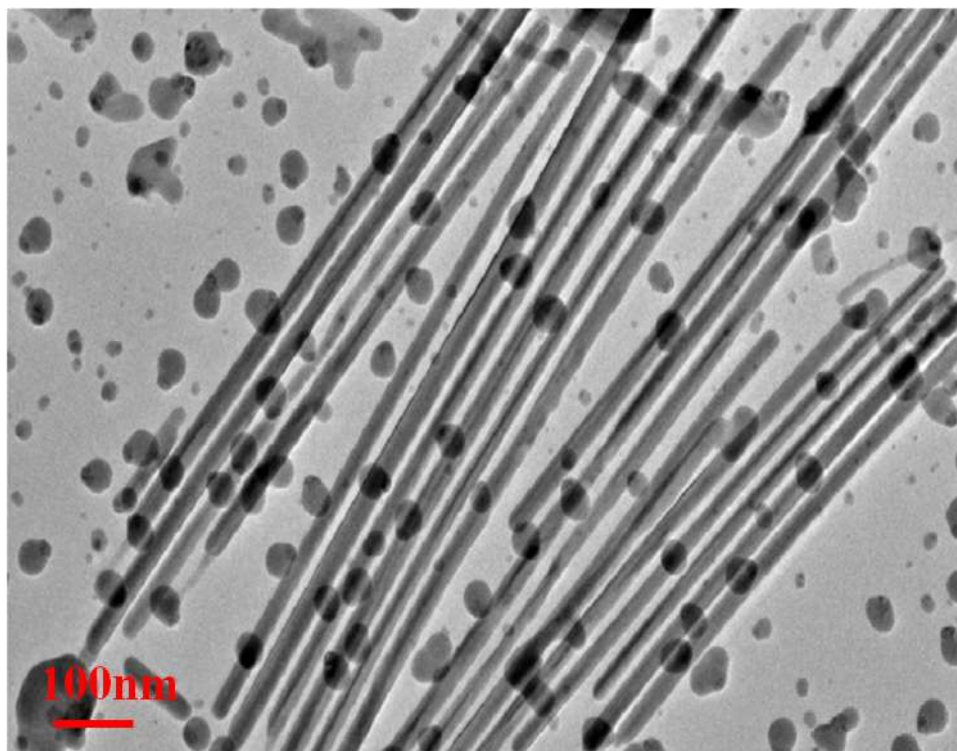


Figure 7.22: Formation of Hy-Au@AgNR with length $\sim 1\text{-}1.2\ \mu\text{m}$ by maintaining the molar ratio between AgNO_3 and AA at 1:20 during synthesis.

At our optimized condition, we conclude that the nanorods of higher length (Hy-Au@AgNR₈₄₀) can be prepared by applying .01 g CTAC, and maintaining the molar ratio between AgNO_3 and AA at 2:5. However, an increase in AA volume (1 mL) to maintain the ratio at 1:5, bigger nanorods of length about $1\text{-}1.2\ \mu\text{m}$ can easily be prepared as shown in **Figure 7.22**. By comparing **Figure 7.22** with **Figure 7.2E**, it is clearly visible from **Figure 7.22** that we could generate longer nanorods but their yield and stability are very poor and with time they convert into spherical particles. Due to their rapid structural deformation (from rod to a sphere) which results in the disappearance of surface coaxial twin boundaries, their tested catalytic activity is not promising. As a result of these limitations, we restrict our synthesis, characterization, and catalytic activity measurements of Hy-Au@AgNRs with length till 840 nm as described before. Beyond the developed strain within the nanostructure and resultant DOS with respect to the Fermi level, there are so many other factors on which their catalytic activity depends substantially. In our previous studies, we have shown that pure gold nanostructure with {110} facet has a strong affinity for ascorbic acid.⁴ In contrast, gold-silver nano-alloy with {220} orientation shows enormous oxidizing capability for uric acid.⁷ Thus, chemical composition (pure Vs alloy) of the nanocatalyst determines the adsorption efficiency and facet selectivity of the substrate and subsequent bond-breaking and bond-forming process during a reaction. However, to construct a universal catalyst, one has to think every aspect of catalytic properties i.e. (a) it should be stable in a broad pH range, (b) the catalytic activity should be in the equal order in both the organic or aqueous solvent, and (c) it should show long term stability under ambient condition. Our synthesized Hy-Au@AgNR₈₄₀-Ass shows its stability in a broad pH

range. The catalytic activity was checked in both the acidic and basic solution for the electrooxidation of L-tryptophan by Hy-Au@AgNR₈₄₀-Ass modified GC (Hy-Au@AgNR₈₄₀-Ass/GC) and it was found that Hy-Au@AgNR₈₄₀-Ass/GC is equally capable to oxidize L-tryptophan in both acidic and basic pH medium. The Hy-Au@AgNR₈₄₀-Ass/GC is also capable to oxidize vitamin K3 in the organic solvent (acetonitrile). Synthesized Hy-Au@AgNR₈₄₀-Ass remain stable (no visible, spectroscopic, and structural change) in the ambient condition (room temperature, in presence of oxygen, and aqueous solution) over 6 months. Hence, our main focus that developing a TB-enriched strain-dependent universal catalyst is efficiently achieved by our engineered Hy-Au@AgNR₈₄₀-Ass material. To correlate the influence of TB-induced tensile strain and electrocatalytic activity of Hy-Au@AgNRs and the resultant Hy-Au@AgNR₈₄₀-Ass/GC, we need to understand the d-band model of transition metals in more details. In a d-band theory, it is assumed that when an adsorbate state (σ) reacts with the metal d orbitals, it forms one bonding orbital ($d-\sigma$) and one antibonding orbital ($d-\sigma$)*. If the d band center of the metal is lower in energy, more antibonding orbital will be occupied.⁴⁰⁰ Therefore, the degree of interaction between adsorbate state and metal d state will be reduced. However, if a d-band center is higher in energy, then an upshift of antibonding orbital ($d-\sigma$)* will happen which will increase the interaction between adsorbate state and metal d state. In the case of pure Ag or pure Au rod, the d-band center is lower in energy. In contrast, Au-nanoseed incorporated Ag rod i.e. in Hy-Au@AgNR₈₄₀ the d-band center is upshifted towards the Fermi level as shown in **Figure 7.14**. Due to this upshifting of d-band, more antibonding orbital will remain vacant, which results in more bonding interactions between the metal and the reactant which may further improve the catalytic activity. In the case of Hy-Au@AgNR₈₄₀-Ass, as explained earlier that the density of crystal defects is much higher than the corresponding Hy-Au@AgNR₈₄₀ which will not only

increase the tensile strain further but also will move the d-band center more towards the Fermi level. Thus the trend of electrons occupying the (d- σ)* state may give the following order: Hy-Au@AgNR₈₄₀-Ass < Hy-Au@AgNR₈₄₀ < Hy-Au@AgNR₄₅₀ < Hy-Au@AgNR₁₂₀ and hence the Hy-Au@AgNR/Hy-Au@AgNR₈₄₀-Ass may show maximum catalytic activity. Our measured ICP-OES data quantifies the actual concentration of different elements as ~10mg/L of Ag, ~1.11mg/L of S, and an infinitesimal amount of Au present in the resultant Hy-Au@AgNR₈₄₀-Ass that has been used as the desired catalytic material.

The expected trend of strain-dependent electrocatalytic activity was verified by recording the electrooxidation of L-tryptophan on different catalytic materials. The I-V response in DPV for L-tryptophan oxidation is shown in **Figure 7.23B** which clearly shows that the peak potentials for both Hy-Au@AgNR₈₄₀ and Hy-Au@AgNR₈₄₀-Ass are equivalent with a slight increment in peak current for Hy-Au@AgNR₈₄₀-Ass. This authenticates our expectation that Hy-Au@AgNR₈₄₀-Ass/GC acts as the best catalyst with the lowest peak potential (**Table 7.3**) and highest peak current compared to other catalysts (viz. Hy-Au@AgNR₈₄₀/GC, Hy-Au@AgNR₄₅₀/GC, and Hy-Au@AgNR₁₂₀/GC). We have also tried our DPV experiment for other systems like the reduction of glucose (**Figure 7.23A**) and oxidation of vitamin K3 (**Figure 7.23C**) and observed similar enhanced catalytic activity for Hy-Au@AgNR₈₄₀-Ass/GC system.

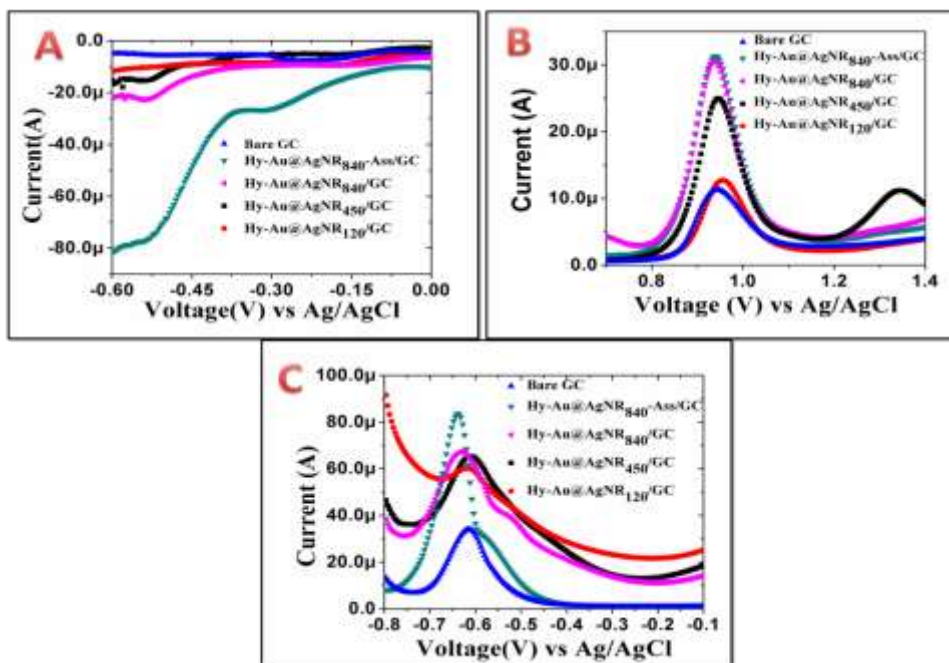


Figure 7.23: A is the DPV response for the reduction glucose (4×10^{-4} M) in 0.1 M HClO_4 , B is DPV response for the oxidation of L-tryptophan (4×10^{-4} M) in 0.1 M HClO_4 , C is the DPV response for the oxidation of vitamin K3 (4×10^{-4} M) in 0.1 M LiClO_4 + acetonitrile.

Table 7.3: The I-V responses in DPV for different system Hy-Au@AgNR₈₄₀-Ass/GC, Hy-Au@AgNR₈₄₀/GC, Hy-Au@AgNR₄₅₀/GC, Hy-Au@AgNR₁₂₀/GC.

System	Glucose	Vitamin K3	L-tryptophan
Bare GC	-0.8 V, -4.6 μA	-0.61 V, 35.06 μA	0.96 V, 11.3 μA
Hy-Au@AgNR ₈₄₀ -Ass/GC	-0.53 V, -76.53 μA	-0.638 V, 83.64 μA	0.93 V, 31.79 μA
Hy-Au@AgNR ₈₄₀ /GC	-0.535 V, -24.03 μA	-0.631 V, 68.89 μA	0.93 V, 30.80 μA
Hy-Au@AgNR ₄₅₀ /GC	-0.54 V, -15.67 μA	-0.61 V, 66.32 μA	0.95 V, 25.10 μA
Hy-Au@AgNR ₁₂₀ /GC	-0.55 V, -9.38 μA	-0.61 V, 59.33 μA	0.96 V, 13.0 μA

The analogous trend is also observed in chronoamperometric and impedance measurements (Figure 7.24A, B, C & Figure 7.25A, B, C respectively) for all the above three systems.

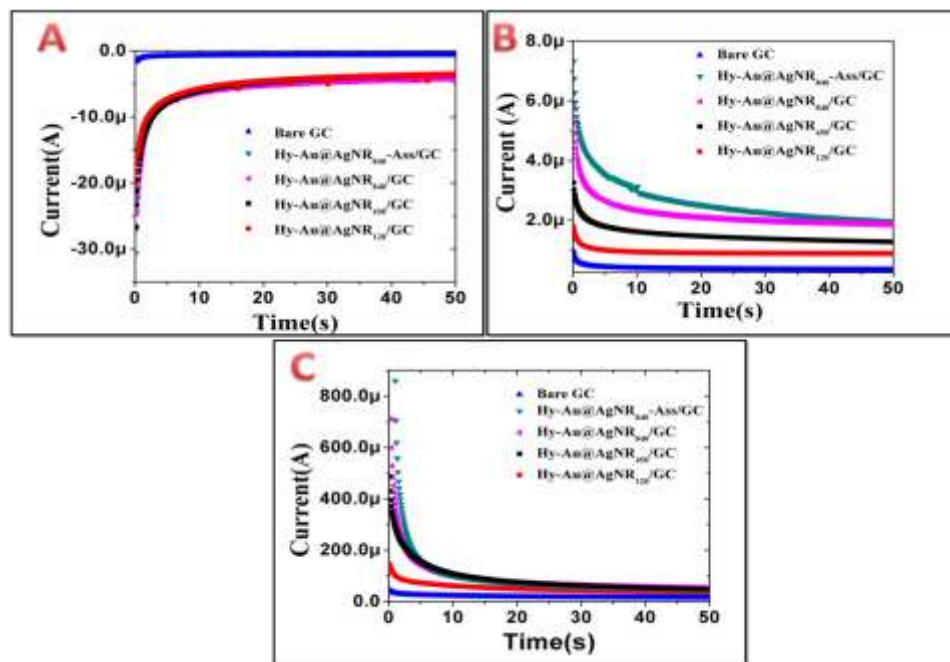


Figure 7.24: A is the chronoamperometric response for the reduction glucose (4×10^{-4} M) in 0.1 M HClO₄, B is the chronoamperometric response for the oxidation of L-tryptophan (4×10^{-4} M) in 0.1 M HClO₄, C is the chronoamperometric response for the oxidation of vitamin K3 (4×10^{-4} M) in 0.1 M LiClO₄ + acetonitrile.

The engineered Hy-Au@AgNR₈₄₀-Ass has used not only an efficient catalytic material for the electrochemical redox-based sensing of L-tryptophan, Glucose, and Vitamin K3 but also find equal application as a pathological kit for a variety of analytes enlisted below. The importance of all those analytes in human physiology and the significance of their accurate estimation from the pathological sample has been elaborated in the following section.

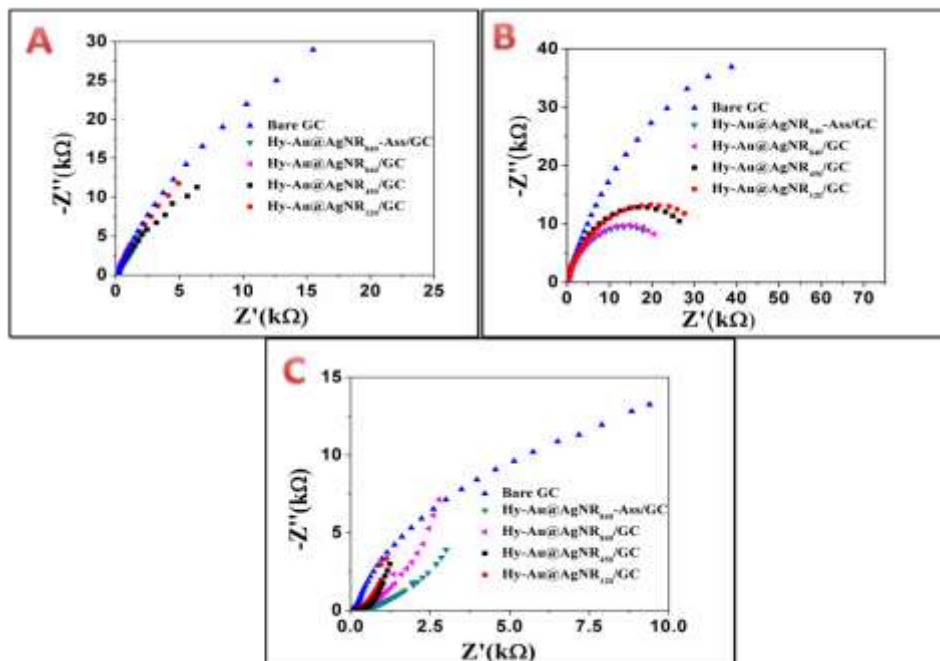


Figure 7.25: A is the impedance response for the reduction glucose (4×10^{-4} M) in 0.1 M HClO_4 , B is impedance response for the oxidation of L-tryptophan (4×10^{-4} M) in 0.1 M HClO_4 , C is the impedance response for oxidation of vitamin K3 (4×10^{-4} M) in 0.1 M LiClO_4 + acetonitrile.

Importance of different analytes considered in the current study:

In the current study, we have considered more than 20 different analytes which include both water-soluble & insoluble organic human metabolites and a variety of metal ions (inorganic metabolites). Water-soluble organic metabolites include Pantothenic acid (PA), Riboflavin (Rb), uric acid (UA), Creatinine (Ct), Xanthine (Xa), Urea (U), Ascorbic acid (AA), Cysteamine (Cyst), Folic acid (FA), Dopamine (DA), L-tryptophan (L-Trp), Glucose (Glc), Inositol (Inos), and Thiamine (Thia). One of the most common water-insoluble organic metabolites is Vitamin K3 (VK3). Though there is a long list of metal ions used as inorganic human metabolites, the most common and important metabolites include Cr^{3+} , Co^{2+} , Fe^{3+} , Cu^{2+} , Pb^{2+} , Hg^{2+} , and Ni^{2+} . Hence, we have considered a total of twenty-two different analytes to justify the universal catalytic ability of our engineered Au-seeded Ag-nanorod-based thiol mediated strained network.

Though the biological importance of most of these metabolites is well known to us but the driving force behind selecting them in the present study is enlisted as below:

(1) Pantothenic acid (PA): Pantothenic acid is popularly known as vitamin B₅ which is a water-soluble human metabolite. Pantothenic acid is an essential human nutrient. Animals require Pantothenic acid for synthesizing coenzyme-A (CoA) which helps in the synthesis and oxidation of fatty acids.⁴⁰¹ It also helps to synthesize and metabolize proteins, carbohydrates, and fats.

(2) Riboflavin (Rb): Riboflavin (vitamin B₂) helps to break down protein, carbohydrates, fats to adenosine triphosphate (ATP) for energy supply to the body.⁴⁰¹

(3) Uric acid (UA): UA (a purine metabolic product and can act as a free radical scavenger) is one of the major antioxidants in human serum and may cause arthritis when remains present at higher concentration in the blood due to the deposition of UA crystals in joints like ankle, feet, knees, and wrists.⁴⁰²

(4) Creatinine (Ct): Creatinine is a waste product produced by muscles from the breakdown of a compound called creatine. Creatinine is removed from the body by the kidneys, which filter out almost all of it from the blood and release it into the urine. By measuring the amount of creatinine in the blood and/or urine we can find out the efficiency of the kidney.⁴⁰³

(5) Xanthine (Xa): Xanthine is a purine base found in human body tissues and fluids. The decomposition of adenosine triphosphate (ATM) can also produce Xa.⁴⁰⁴ Derivatives of Xanthine act as stimulants for the treatment of asthma and influenza. In clinical diagnosis, Xa usually acts as a sensitive indicator for some clinical disorders such as perinatal asphyxia and adult respiratory distress syndrome.^{405,406}

(6) Urea (U): Renal nitrogen metabolism primarily involves urea and ammonia metabolism, and is essential to normal health. Urea produces and excreted through the renal system as a result of the degradation of dietary and endogenous proteins.⁴⁰⁷

(7) Ascorbic acid (AA): AA, a water-soluble antioxidant produces type I interferons, which up-regulates NK cell and cytotoxic T-lymphocyte activity to prevent early viral infection. Besides, AA has the ability to inactivate both RNA and DNA viruses and can detoxify the viral products which cause pain and infections.⁴⁰⁸

(8) Cysteamine (Cyst): Cysteamine is an essential metabolite in the human body.⁴⁰⁹ *Cystamine*, the oxidized form of *cysteamine* which inhibits erythrocyte sickling in sickle cell anemia. Cystamine in the body is reduced into cysteamine and RS-cysteamine mixed disulfide by the thiol-disulfide exchange. This is done by the consumption of intracellular glutathione.

(9) Folic acid (FA): Folic acid is the synthetic form of folate, a water-soluble B vitamin that takes part in several critical functions in the human body.⁴¹⁰ The active form of folate is tetrahydrofolic acid. It serves in one carbon reductions reactions. These reactions are involved in the synthesis of nucleotides and amino acids. Folic acid is required for erythropoiesis, thus folic acid deficiency leads to megaloblastic anemia. Adequate dietary intake of folic acid is critical for DNA repair and normal cell growth.

(10) Dopamine (DA): Dopamine acts both as a hormone and neurotransmitter, and plays several important roles in the brain and body. Dopamine plays a major role in the motivational component of reward-motivated behavior. Individual electrocatalytic sensing of dopamine has been performed previously.⁴¹¹

(11) L-tryptophan (L-Trp): L-tryptophan metabolized product serotonin causes platelet aggregation and considered as a prognostic biomarker for dengue hemorrhagic fever (DHF) such

as that high level of serotonin or low level of L-tryptophan is an indicator for Dengue-2 (DENV-2) infection.⁴¹²

(12) Glucose (Glc): Type 2 diabetes patients are at high risk of hyperglycemia due to excess concentration of glucose and may cause damage to the nervous system, cell organs, vessels whereas hypoglycemia results in loss of consciousness, seizures.⁴¹³

(13) Inositol (Inos): Inositol is a carbocyclic sugar that is abundant in the brain and other mammalian tissues, mediates cell signal transduction in response to a variety of hormones, neurotransmitters, growth factors, and participates in osmoregulation.⁴¹⁴ It is made naturally in humans from glucose.

(14) Thiamine: Thiamine (vitamin B₁) is considered an essential metabolite for glucose metabolism and plays a key role in muscle, heart, and brain functions.^{401,415}

(15) Vitamin K3 (VK3): When vitamin K3 present in higher concentrations in newborns, it produces a bile product bilirubin which causes brain damage, mental retardation, loss of appetite, and deafness.⁴¹⁶

(16) Cr³⁺: Hexavalent Cr(VI) is considered as carcinogenic as it has the capability to penetrate the cell membrane and reacting with proteins and nucleic acids but Cr(III) cannot cross the cell membrane and hence less toxic⁴¹⁷ than Cr(VI).

(17) Co²⁺: Co helps to absorb vitamin B₁₂ in the body and also found it useful to treat anemia and infectious diseases.^{401,418}

(18) Fe³⁺: Fe has a role in DNA synthesis, electron transport, and oxygen transport.⁴¹⁹

(19) Cu²⁺: Cu is essential for maintaining the strength of skin, blood vessel, epithelial and connective tissues.⁴²⁰

(20) Pb^{2+} : Excess Pb exposure bring several unwanted disorders in human metabolism like the disruption of the biosynthesis of hemoglobin, rise in blood pressure, etc.⁴²¹

(21) Hg^{2+} : Mercury is a highly toxic metal present in the body mostly as methyl mercury (MeHg^+) with an average half-life ($t_{1/2}$) varies widely between 30-150 days in the human body. The body burden of MeHg^+ originates mainly from sea-fish consumption or dental amalgam. Though the chief toxic target of Hg^{2+} is the brain, other noted toxicity includes the disordering of peripheral nerve function, renal function, immune function, endocrine, and muscle function.⁴²²

(22) Ni^{2+} : Ni present in RNA and DNA of our body, where it functions in association with a nucleic acid to involve in protein structure formation.⁴²³

Almost 20 odd different pathological analytes have been detected and estimated by using our engineered material ($\text{Au@AgNR}_{840}\text{-Ass}$) as a universal catalyst which has been broadly categorized as:

(1) **Trace metal ions:** Different trace metal ions like Co^{2+} , Cr^{3+} , Cu^{2+} , Hg^{2+} , Ni^{2+} , Fe^{3+} , and Pb^{2+} have been detected and estimated by electrochemical reduction in 0.1 (M) HClO_4 as shown in **Figure 7.26 (A-G)**.

(3) **Water-insoluble human metabolite:** Due to its insoluble nature in polar medium, vitamin K3 has been estimated by oxidizing it in a 0.1 (M) LiClO_4 + acetonitrile medium as shown in **Figure 7.26H**.

(3) **Water-soluble human metabolites:** Different metabolites like ascorbic acid (AA), creatinine, Dopamine (DA), thiamine, riboflavin, Pantothenic acid (PA), urea, uric acid (UA), inositol, Xanthine, Cysteamine (Cyst), glucose, L-tryptophan, and folic acid (FA) have been detected and estimated by oxidizing them in 0.1 (M) NaOH is as shown in **Figure 7.27a** and **7.27b** respectively.

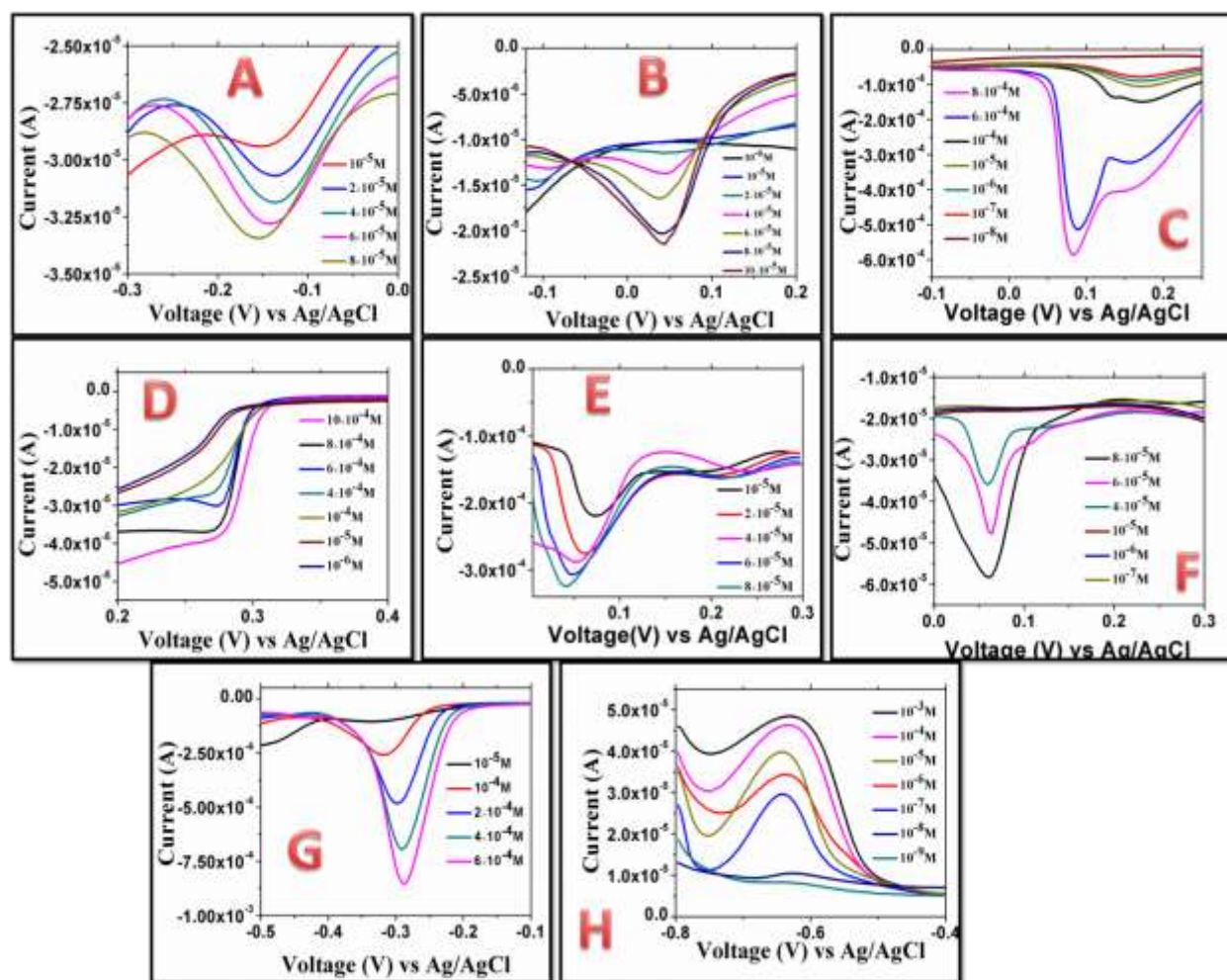


Figure 7.26: Electrochemical reduction of metal ions in 0.1 M HClO₄ (A) Co²⁺, (B) Cr³⁺, (C) Cu²⁺ (D) Hg²⁺, (E) Ni²⁺, (F) Fe³⁺, (G) Pb²⁺, (H) is for vitamin K3 oxidation in 0.1 (M) LiClO₄+ acetonitrile.

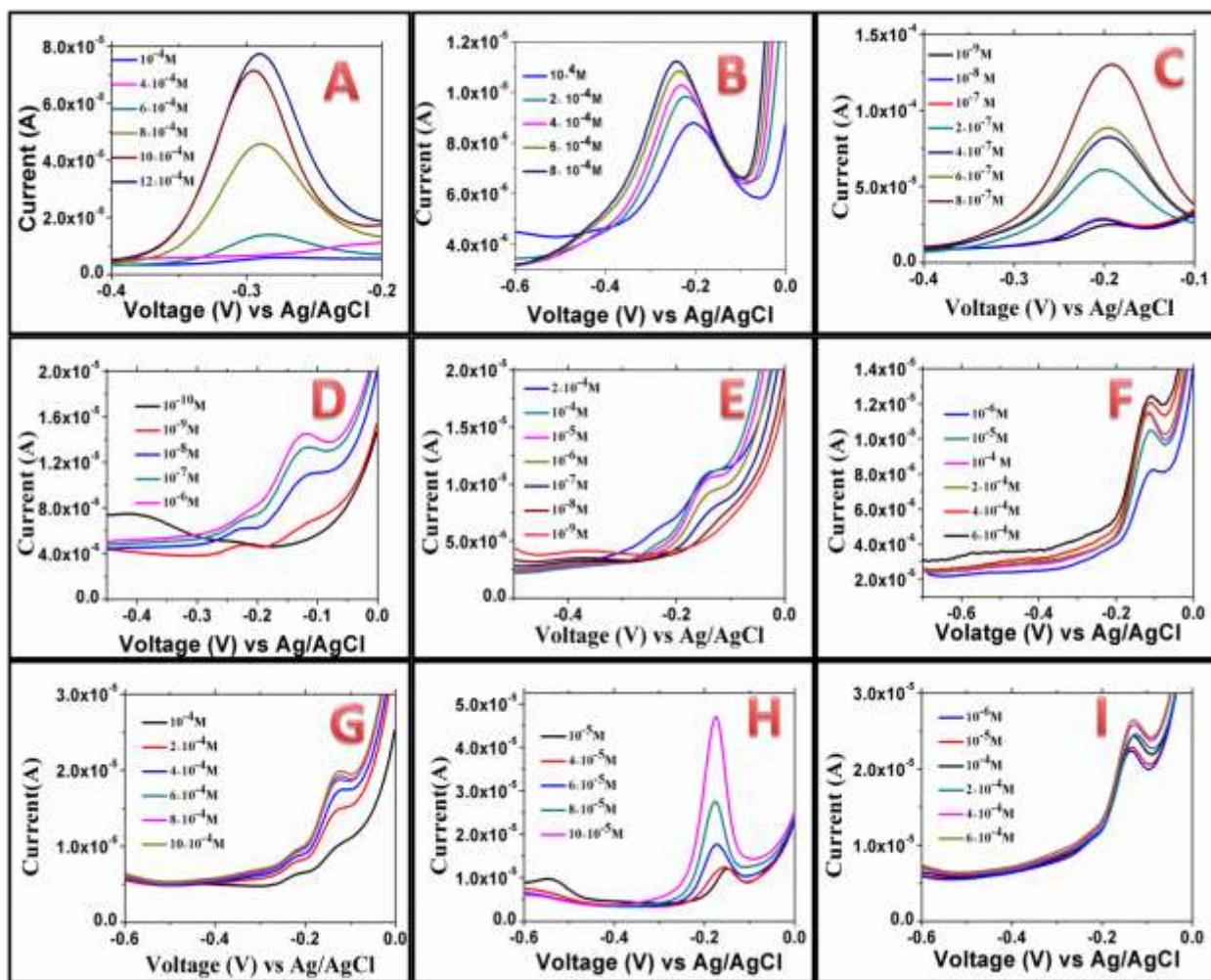


Figure 7.27a: Oxidation of metabolites in 0.1 M NaOH medium: (A) AA , (B) Creatinine (C) Dopamine (DA), (D) thiamine, (E) riboflavin, (F) Pantothenic acid (PA) (G) urea (H) uric acid (UA), (I) inositol.

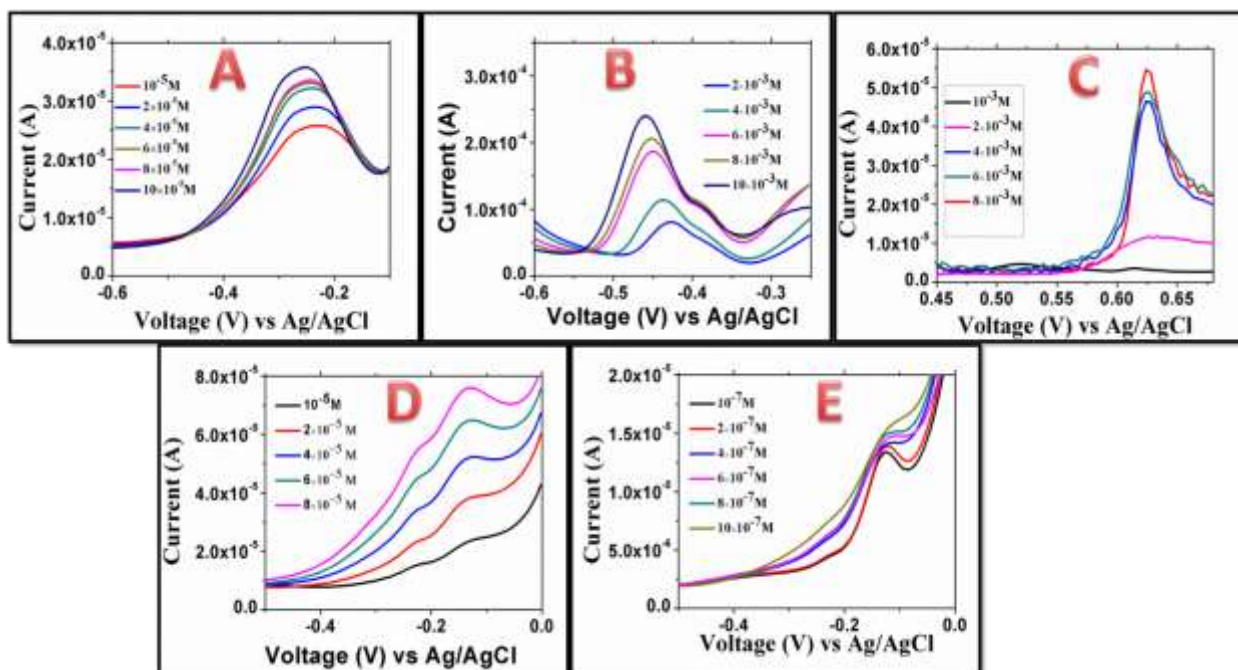


Figure 7.27b: oxidation of metabolites in 0.1 M NaOH; (A) Xanthine, (B) Cysteamine (Cyst) (C) glucose, (D) L-tryptophan, (E) folic acid (FA).

The utility of using the above electrolytes is that they are either acidic or basic in chemical nature. Whenever human serum is added to those electrolytes, the plasma proteins are precipitated out but the other blood ingredients like salts (NaCl, KCl, CaCl₂, etc) and metabolites (vitamins, amino acids, etc) will stay in the solution without any modification. During measurements of the above metal ions or metabolites, we have prepared a stock solution first. Then the stock solution was spiked into the human serum and the plasma proteins from serum are precipitated out. The solution was then centrifuged to remove the coagulated proteins and the supernatant solution with all the essential analytes being diluted for electrochemical measurements e.g., for vitamin K3 we first prepared a stock solution of 10⁻² (M) in acetonitrile medium and spiked it directly to the human serum. The coagulated proteins are then precipitated and the resultant solution was collected by centrifuging. The resultant supernatant is then diluted up to the nanomolar level for electrochemical measurements. The utility of I-V measurements in

human serum is that the oxidation and reduction of metabolites or trace metal ions in presence of other ingredients of blood like Na^+ , K^+ , Ca^{2+} , etc., can be carried while sensing of a particular analyte without being any interference. Most of the water-soluble human metabolites show linear fitting of ion current during their catalytic oxidation in their physiological concentration level as shown in **Figure 7.28A-7.28I**. Soluble metabolites that are not following the I-C (C is the concentration) linear fitting rather showing an exponential rise in current have been fitted by plotting the ion current against the logarithm of concentration to show their linear sensing behavior.

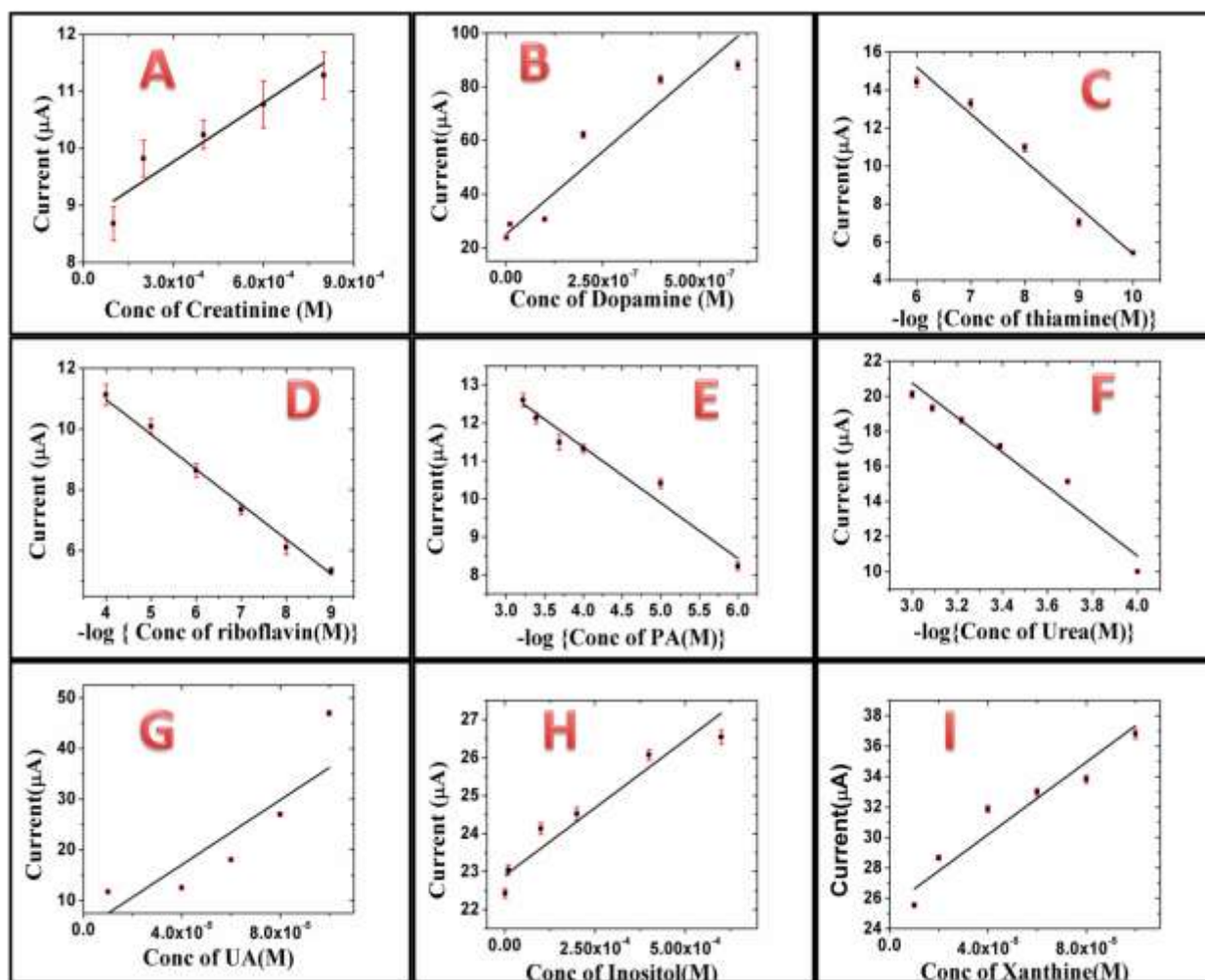


Figure 7.28: I-C linear fitting for different water-soluble human metabolites as mentioned in the figure during their catalytic oxidation at their physiological concentration level.

Not only the soluble human metabolites but also the trace metal ions and organic soluble vitamin K3 show similar I-C linear fittings during their reduction in their physiological concentration level. The I-C linear fitting for trace metal ions are shown in **Figure 7.29 (A-F)** and for vitamin K3 in **Figure 7.29G**.

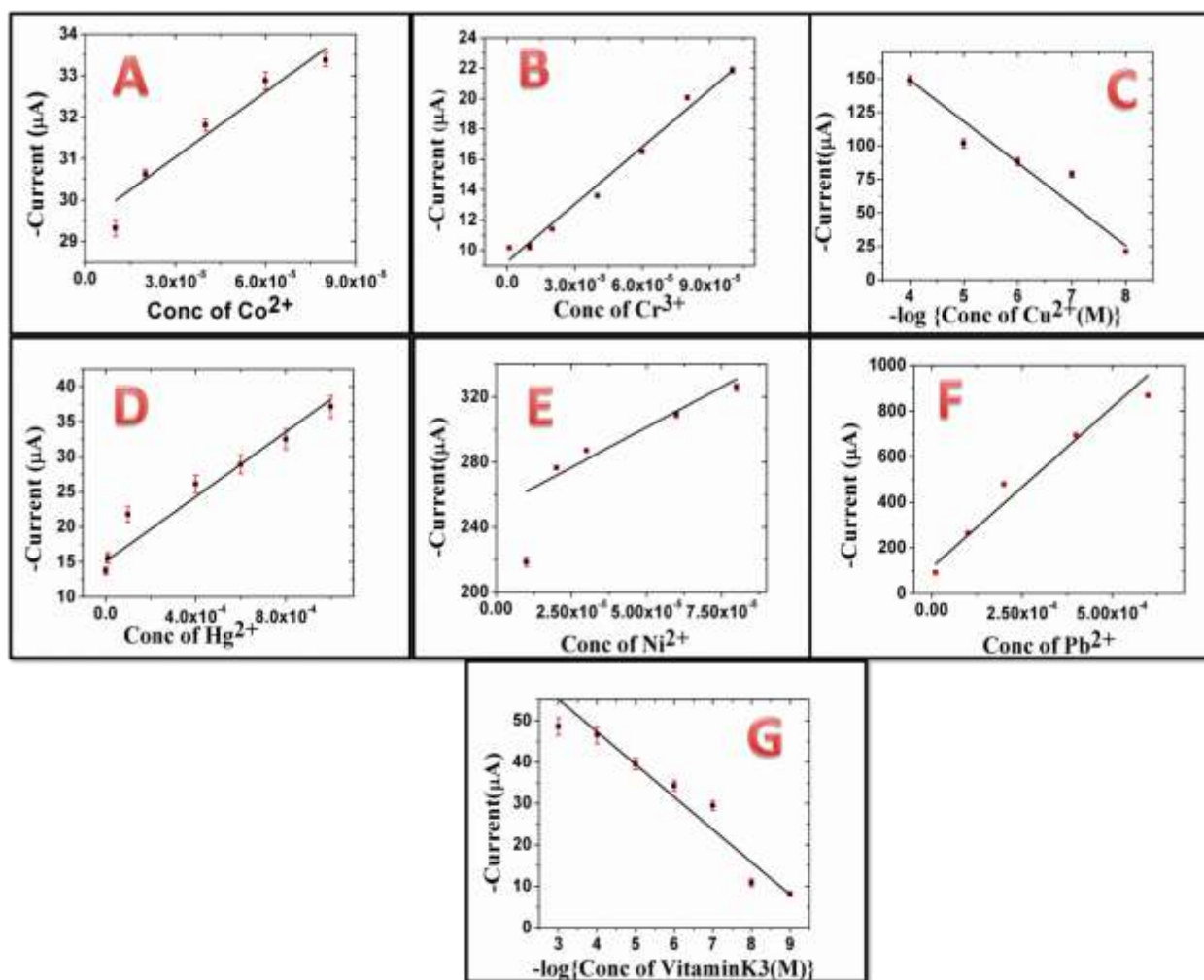


Figure 7.29: Linear Calibration plot of metal ions. Just like human metabolites (**Figure 7**) where we did not find any linear relation with concentration we take logarithm as shown in (C) for Cu^{2+} and in (G) for vitamin K3.

Besides the sensing of individual metal ions or human metabolites, we have also carried out interference tests and simultaneous detection of the above metabolites or trace metal ions in a single shot. **Figure 7.30A-D** shows the I-V sensing at the variable concentration for metabolites Riboflavin, Uric acid (UA), Pantothenic acid (PA), and Creatinine (Ct) respectively in a mixture of all four. Except for the specific metabolite under the investigation, the other three metabolites act as interfering analytes where their concentration has been kept constant at 1 μ M.

Table 7.4: Peak Potential of different metabolites and trace metal ions in I-V responses of DPV.

System	PA	Rb	UA	Creatinine	Xanthine	Urea	AA	Cysteamine
Peak Potential (V)	-0.115	-0.145	-0.17	-0.24	-0.25	-0.128	-0.29	-0.45
System	FA	DA	L-Tryptophan	Glucose	Inositol	Thiamine	Vitamin K3	Cr ³⁺
Peak Potential (V)	-0.121	-0.19	-0.135	+0.62	-0.131	-0.115	-0.63	+0.044
System	Co ²⁺	Fe ³⁺	Cu ²⁺ (<10 ⁻⁴ M)	Cu ²⁺ (>10 ⁻⁴ M)	Pb ²⁺	Hg ²⁺	Ni ²⁺	
Peak Potential (V)	-0.147	+0.059	+0.17	+0.083	-0.28	+0.27	+0.043	

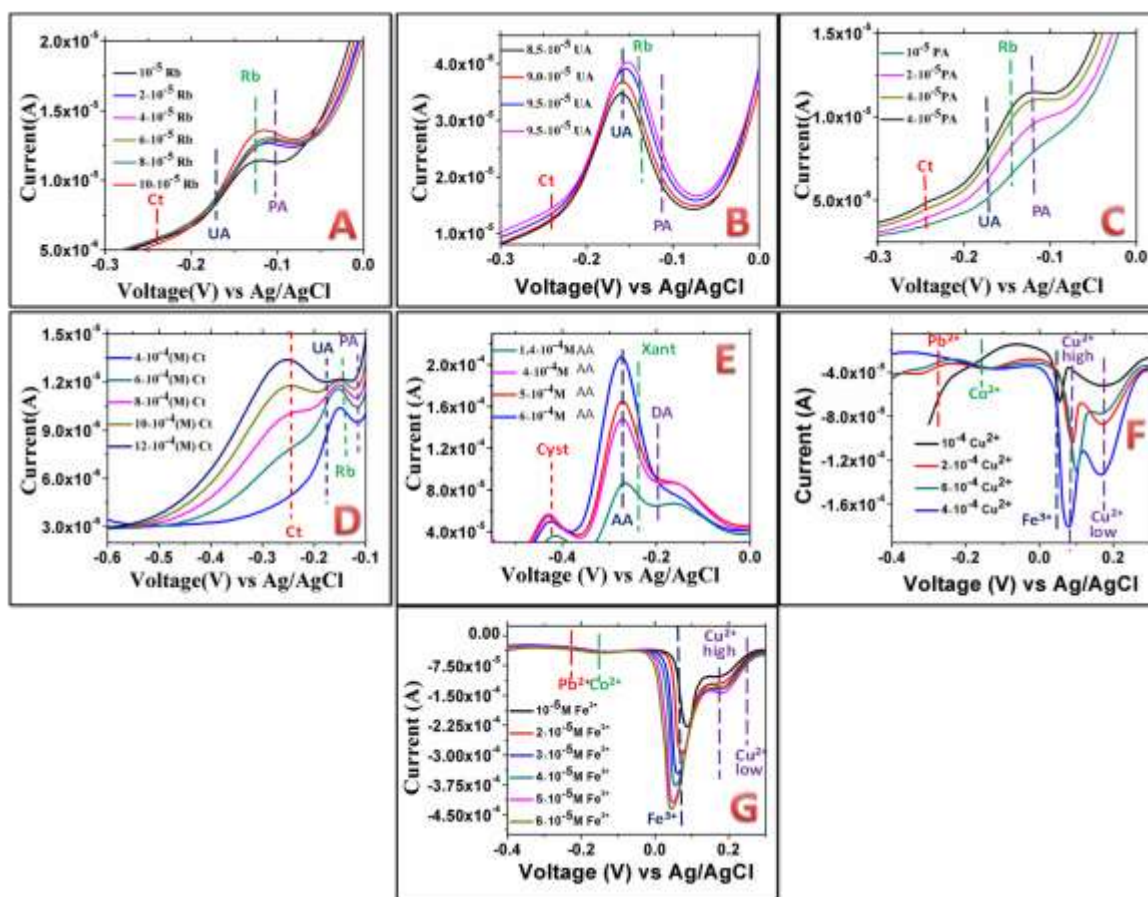


Figure 7.30: Interference test of Riboflavin, Rb (A); Uric acid, UA (B), Pantothenic acid, PA (C), Creatinine, Ct (D), Ascorbic acid, AA (E), Cu^{2+} (F), and Fe^{3+} (G). Cu^{2+} high and Cu^{2+} low indicate respective potentials at high and low concentrations of Cu^{2+} . Colour coded vertical dotted lines in each plot (A-G) show the expected peak potential for different metabolites.

In **Figure 7.30 E** we have shown the I-V sensing of Ascorbic acid (AA) in presence of dopamine (DA), Xanthine, and cysteamine (Cyst) where the concentration of all the analytes except AA is kept constant at 1 μM while the concentration of AA varies between 0.14 – 0.6 mM. Similarly, **Figure 7.30 F** and **7.30 G** show the I-V sensing for Cu^{2+} and Fe^{3+} respectively. For Cu^{2+} we have used Fe^{3+} , Co^{2+} , and Pb^{2+} as interfering salts and for Fe^{3+} we have used Cu^{2+} , Co^{2+} , and Pb^{2+} as interfering salts. In both cases, interfering salt concentration is 1 μM . It is to be noted that Cu^{2+} has two peak potentials in their I-V curves at higher and lower concentration

range. Fingerprinting at different peak potential for individual human metabolites enables the electrocatalytic method to detect them specifically as well as sensitively from a mixture, as appears in plasma samples. Details about the peak potentials for each analyte under the investigation have been enlisted in **Table 7.4**.

7.4. Conclusion:

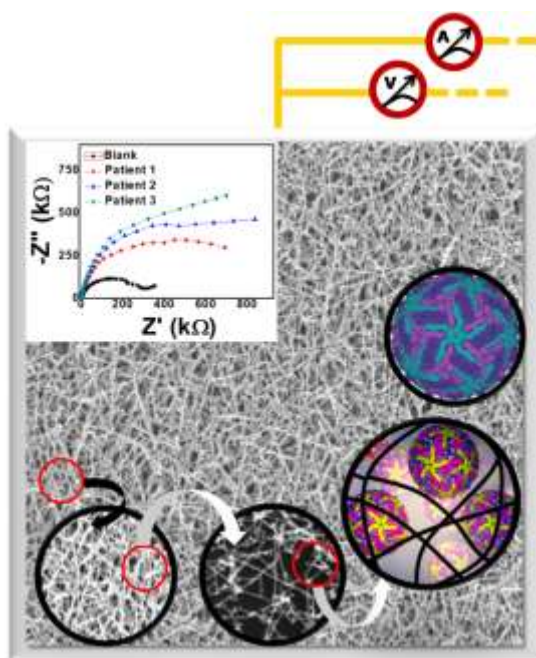
Highly strained Au-seed incorporated Ag nanorods (Hy-Au@AgNRs) of variable length were synthesized by a novel methodology. The strain within the Hy-Au@AgNRs is verified both theoretically through *ab initio* simulation and experimentally from XRD broadening. Among various Hy-Au@AgNRs, Hy-Au@AgNR₈₄₀ with the longest TB over its surface offers noticeably more strain than Hy-Au@AgNR₄₅₀ and Hy-Au@AgNR₁₂₀. The engineered Hy-Au@AgNR₈₄₀ was then assembled by DTT to produce Hy-Au@AgNR₈₄₀-Ass with multiple defects enriched active catalytic sites. It was found that Hy-Au@AgNR₈₄₀-Ass acts as a superior nanostructure for strain-dependent universal catalysis as verified from the electrochemical oxidation/reduction of a series of organic and inorganic human metabolites by performing their DPV, EIS, and chronoamperometry. Hy-Au@AgNR₈₄₀-Ass modified GC was used as a pathological kit that offers a linear calibration plot for all the studied human metabolites in the physiological concentration range. Moreover, the reported electrochemical pathological kit shows long term stability under the ambient condition in wide solvent systems as well as broad-scale pH range. Besides, Hy-Au@AgNR₈₄₀-Ass/GC is also able to detect simultaneously more than one analyte at a time from the I-V responses of DPV. Thus a low cost, rapid, and nanorod-based 2D network for a non-enzymatic user-friendly pathological kit is developed for simultaneous detection and quantification of the multiple human analytes which will surely find potential application in error-free electrochemical sensor technology.

CHAPTER-8

Fabrication of Highly Specific DNA Based Porous Au-Ag Nanobioconjugate as Electrode Coat for Rapid Impedimetric Direct Sensing of DENV-2 from Infected Whole Blood

OUTLINE: Specific Points of Discussion

- An efficient nanobioconjugate has been developed as electrode coating material by hybridizing our newly synthesized porous Au-Ag nano-network (Chapter-7) with a thiol modified DNA aptamer for the early-stage specific detection and quantification of DENV-2.
- The binding affinity between the bioconjugate and different serotypes of dengue was studied here through low cost electrochemical impedimetric spectroscopy (EIS).
- This study for the first time presents highly specific and sensitive detection of the most prevalent DENV-2 by impedimetric technique.
- The key achievement of this study lies in its ability of the direct detection of DENV-2 serotype without the aid of an enzyme or antibody in dengue infected blood up to $\sim 10^{-2}$ PFU/mL.



Dengue virus (DENV) belongs to the virus family of Flaviviridae and is responsible for a seasonal febrile disease in humans with potentially fatal consequences. In addition to humans, DENV can infect mosquitoes in which the infectious virus accumulates in the salivary gland fluid and from where it is transmitted into humans during a blood meal. It is considered to be an endemic disease, causing approximately 22,000 deaths every year in tropical and subtropical regions of the world.^{424,425} Mathematical modeling based on existing known cases projects more than 300 million people to be at risk of developing DENV infection.⁴²⁶ Globally there are four serologically distinct groups or serotypes of Dengue (DENV) designated as DENV-1, DENV-2, DENV-3, DENV-4, however, a recent report suggests the existence of a new serotype DENV-5.⁴²⁷ As in other members of Flaviviridae, the DENV genome consists of a single-stranded plus-sense RNA encoding for a single polyprotein that is cleaved by proteases (encoded by either the host or the viral genome) at precise sites to generate structural and non-structural viral proteins. A comparison of the polyprotein sequence from different serotypes shows a 65-70% identity in the amino acid sequence between DENV 1-4. Each serotype is further classified into genotypes depending on differences in the viral genome sequence.

Upon entry into human skin through a mosquito bite, DENV is known to infect resident Dendritic cells by attaching to surface receptor molecules of the protein DC-SIGN.⁴²⁸ Subsequent to attachment, the virus-receptor complex is internalized by endocytosis leading to the formation of endosomes, which are then acidified through the activity of proton pumps on their surface.⁴²⁹ Endosome acidification causes drastic structural changes in the viral surface proteins, changing their conformation and leading them to induce a fusion between the membrane of the virus particle and that of the endosome. Subsequently, the viral genomic RNA

is released into the host cell to initiate translation of viral protein followed by replication of genomic RNA and the formation of new virus particles.

The plus-sense and single-stranded genomic RNA can directly serve as a template for protein synthesis by host ribosomes. The presence of a type-I cap structure at the 5' end of the RNA performs dual functions through efficient recruitment of ribosomes in addition to protecting the genomic RNA from cleavage by host exonucleases. Translation of the genome produces a single polyprotein that gets cleaved into three structural proteins (Envelope or E, precursor Membrane or prM and Capsid or C) and seven non-structural proteins (NS1, NS2A, NS2B, NS3, NS4A, NS4B, and NS5).⁴³⁰ The structural proteins form part of virion particles that are produced from the infected cell, while the non-structural proteins catalyze replication and assembly of virions in addition to subverting the innate-antiviral response of the host cell. Synthesis of the viral proteins takes place in close association with the endoplasmic reticulum membrane of the host cells and both the E and prM proteins are glycosylated⁴³¹. Replication of the viral genome also takes place in replication complexes (RCs) that are produced on the ER membrane, in which the NS5 protein catalyzes the replication of the genomic RNA with the aid of other non-structural proteins. Mature viral particles are assembled in close association with the RCs and these are secreted out of the host cells through the host cell trans-Golgi network (TGN) secretory pathway. The replicated and newly formed each viral RNA then enclosed by the C proteins and forms the nucleocapsid. Newly formed nucleocapsids are then surrounded by E and prM proteins within the envelope of ER to form a protective outer layer and construct the immature form of the virus. The virus in the immature form then traveled by the Golgi apparatus towards other parts of the body where they get matured and infect the other cells⁴³² and the cycle continues.

The virion particles of DENV are almost spherical in shape with the diameter varying between approximately 50 (in the mature and infectious form) to 60 nm (in the immature and non-infectious form).⁴³³ The core of each virus is a nucleocapsid consisting of a single copy of the viral genome encapsulated with capsid proteins (C), which is surrounded by a glycoprotein shell made up of a lipid bilayer containing 180 copies each of an Envelope (E) and Membrane (M) proteins.⁴³⁴ The E protein has three distinct domains E-I, E-II, and E-III among which E-III is responsible for binding to the receptor. After endocytosis and endosome acidification, E-I undergoes a structural transition and the E-II helps in the fusion of viral membrane with that of the endosome. In an extracellular virion particle, the 180 molecules of the E protein are arranged as 90 homodimers with the axis of bilateral symmetry being parallel to the viral surface. Upon endosome acidification, these molecules rearrange to form 60 trimeric spikes which pose the E-II domain to mediate membrane fusion. While the E protein is produced in its final mature form during viral protein synthesis, the M protein is produced in an immature precursor form called prM. Immediately after assembly inside the host cell, all virus particles contain only prM on their surface, which is cleaved by a host protease called Furin during the release of the virus through the secretory trans-Golgi network (TGN). However, the efficiency of this enzymatic cleavage might vary depending on the cell type thereby producing virus particles with a varying number of prM and M protein on their surface. The virus particles that only have prM on their surfaces are incapable of infection.⁴³⁵

Signal sequences within the polyprotein translocate nonstructural NS1 and structural prM and E proteins into the ER lumen while the C, NS3, and NS5 proteins are localized in the cytoplasm. NS2A/B and NS4A/B remain as a transmembrane protein. With the help of ER signalases and NS3-NS2B & NS5 nonstructural protein pairs, viral RNA replication starts

through various RNA synthesis and assembling processes.⁴³⁰ The replication of four different serotypes of DENV is similar but they differ only in the specific interaction between the structural protein on virion and the receptors on the host cell. The key factor of binding to the cell receptors by different DENV serotypes lies in the relative arrangement of different domains of E protein monomer. As we discussed before, each E protein monomer has three different domains DI, DII, and DIII.⁴³⁶ The hydrophobic virus fusion loop peptide located at the tip of DII is shielded by DIII which is responsible for binding to the receptor. In the current manuscript, we have designed the aptamer according to the previously reported work,⁴³⁷ by selecting DIII as a specific binding site. The aptamer has a specific DNA sequence and derived from DNA aptamer libraries and the selection is based on best ELISA affinity ranking for DIII of a specific serotype of DENV.

Usually, during a seasonal epidemic, a predominant number of infections have been observed to be caused by one particular serotype. However, after a certain number of seasons, this serotype is replaced by another. Therefore, diagnostic methods have to incorporate features to distinguish the serotype of the virus detected. There is still no clarity about the association of any given serotype with greater pathology^{438–440}. Among the four different dengue serotypes, DENV-2 shows a strong correlation with greater disease severity. It is found that DENV-2 is most likely to cause Dengue Hemorrhagic Fever (DHF) whereas for DENV-4 infected patients DHF is less likely to occur.⁴⁴¹ Clinical manifestation of dengue patients signifies that DHF occurs about 92% for secondary infections of DENV-2, which is associated with ascites and pleural effusions.⁴⁴¹ Due to this greater pathogenic behavior of DENV-2, we have selected it as a specific one for electrochemical aptamer-based detection. We have prepared a nanobioconjugate by covalently adsorbing the DENV-2 specific thiol modified aptamer on a porous Au-Ag

network. The resultant nanobioconjugate was then used as an electrode coating material in impedimetric measurement for different concentrations of DENV-2. Since at the initial stage it is difficult to predict the resilience of virus particles to differentiate the experimental conditions, we have used inactivated Dengue virions generated by Psoralen mediated photo-inactivation method.⁴⁴² Details of Psoralen-mediated Dengue virions inactivation is described below.

Inactivation of DENV-2:

Preparation of Psoralen:

Psoralen was dissolved to prepare a concentration ~0.3mg/mL as a stock solution. It is photoreactive so the solution was covered by aluminum foil and stored in dark condition. It was vortexed before every use.

Viral Propagation:

Dengue viruses were propagated in C6/36 cell lines, and grown in a maintenance media (L15, medium, 10% FBS, 1% Penicillin-Streptomycin) at 37°C and 5% CO₂. The culture was collected 5 days post-infection and concentrated in a centricon at 10,000rpm for 5-10mins.⁴⁴³

Viral Inactivation:

Firstly, we took about 10-12mL of viral supernatant and AMT, 4'-aminomethyltrioxsalen, (10 µg/mL) was added to it. After gentle mixing, we distributed the supernatant by 2mL in each well in a 6 well polystyrene plates of diameter approx. 3.5cm (Corning™ Costar™). Then we prepared a set up for UV-A photoirradiation. we have used a UV torch (UVP UVLMS-38EL series 3UV lamp Upland CA, USA, 8-Watt 230V-50Hz, 0.16 Amps) of wavelength 365nm(UV-A) with an exposure time of about 20mins. After complete inactivation, 1 mL aliquot was taken out and kept it at -80°C for future use.

Validation of Inactivation with Immunofluorescence Assay:

We have infected the Vero cells with inoculum using a standard protocol^{443,444} and incubated for 48h. Aliquots of the virus from each inactivation test time points were placed in cell culture flasks containing Vero cell monolayers grown at 95% confluency. Flasks were incubated at 37°C at 5% CO₂ for 10days and periodically observed for cytopathic effect (CPE). Cultures were allowed to incubate for the maximum possible time to allow any viable virus to have a chance to replicate to detectable levels. After 10days a portion of each culture supernatant was placed into cell culture flasks and incubated under the same conditions for 10 days and observed for the cytopathic effect. The resulting cell monolayers were scraped and applied to the slides. Briefly, droplets of cell suspension were applied to slides and allowed to dry at room temperature in the biosafety cabinet (BSC). The images were viewed under a fluorescence microscope at 10X magnifications. The primary antibody used MAB8705 (1:400) and secondary antibody Antimouse Alexa 488 (1:500).

Maintenance of Vero Cell Line:

Vero cells are derived from normal kidney cells; because the cells are not transformed, they have not lost their contact inhibition. The Vero cells are maintained in Dulbecco's modified Eagle medium (DMEM) supplemented with 2% Fetal Bovine Serum (FBS) and incubated at 37 °C in a 5% CO₂ atmosphere.⁴⁴⁵ When these cells reach confluency, they stop growing and start to die; therefore, it is extremely important to monitor Vero cells and to subculture them as they form confluent monolayers. Actively growing Vero cell cultures become double approximately every 24 hours⁴⁴⁶. Depending on the number of cells seeded and the flask size, the cells usually need to be passaged for 2-3 times per week. This protocol describes the subculturing of Vero cells in 75cm² tissue culture flasks.

The antigenic property of the DENV-2 doesn't alter after this method of inactivation and therefore the affinity of nanobioconjugate towards the inactivated virions should reflect that against ones.⁴⁴³ The preference of early-stage detection of DENV-2 by electrochemical Impedimetric methods over the present ongoing methods is due to its user-friendly, cost-effective, and highly specific nature.

In the absence of either a universally accepted vaccine to give support to prophylactic measures or a therapeutic drug to suppress viral multiplication in infected patients, early detection of DENV is key for measures that will reduce the economic and social burden of this disease. Diagnostic methods in the acute phase for blood-borne viruses like DENV involve either a direct detection of infectious virus or any of biomolecule derived from the virus e.g. viral nucleic acid, viral protein secreted from infected cells into the blood, etc. Detection of infectious virus can be done through either plaque-forming unit assay or a fluorescent-foci forming assay, both of which are laborious, time-consuming and require skilled personnel working in dedicated, furnished facilities. Specific detection of viral genomic RNA can be performed by extraction of the viral RNA from plasma samples, followed by reverse-transcription and Quantitative real-time PCR (qPCR)⁴⁴⁷. Although this method is fast compared to the former, it still requires skilled personnel and dedicated facilities that maintain high standards of cleanliness. Human cells infected with DENV secrete the NS1 protein into the blood which can be detected within 1-2 days after onset of symptoms. In view of this diagnostic kits presently available in the market that detect the NS1 antigen in addition to anti-DENV Immunoglobulin-M (IgM) produced by the host adaptive immune cells. Although a sensitive test, these kits however cannot differentiate between the different DENV serotypes and therefore need to be complemented by qPCR methods for that purpose.

In addition to these established methods, various techniques have been demonstrated to have the potential for the development of diagnostic kits. These include the use of DNAzymes⁴⁴⁸, Ribozymes⁴⁴⁹, Fluorescent *in-situ* hybridization or FISH⁴⁴⁷, Reverse-transcription Loop-mediated isothermal amplification or RT-LAMP^{450,451}, Carbon nanotube-based affinity biosensor⁴⁵², and dot-blot assay for NS1 antigen⁴⁵³. AuNPs have been employed in detection methods too^{448,454–456}.

Compared to several approaches stated above, the impedimetric technique is not only cost-effective but also sensitive enough for early detection of DENV-2 up to 10^{-2} PFU/mL with high specificity. The cross-reactivity of DENV-2 was also checked in the presence of other flaviviruses of the same genus like DENV-3, DENV-1, and other bacteria like *E.coli*, *Staphylococcus aureus*, and *H. influenza*. Details about the materials and synthesis have been included in the supporting information section. To utilize the strong affinity of thiol group for efficient binding with noble metals like Au or Ag (constituents of nanomaterials used here), we have procured the -S-H modified aptamer and stored it at -80°C before we use it.¹⁷ The aptamer has the specific sequence ($MW=22680.0$) for DIII domain of DENV-2 and modified at 5' and 3' position by -SH group denoted as:

5'HS_ATACGGGAGCCAACACCATGGGGACCAACTGTCCGGAGAGAGTCCTGTCTGAG
GGAGAGCAGGTGTGACGGAT_SH3'

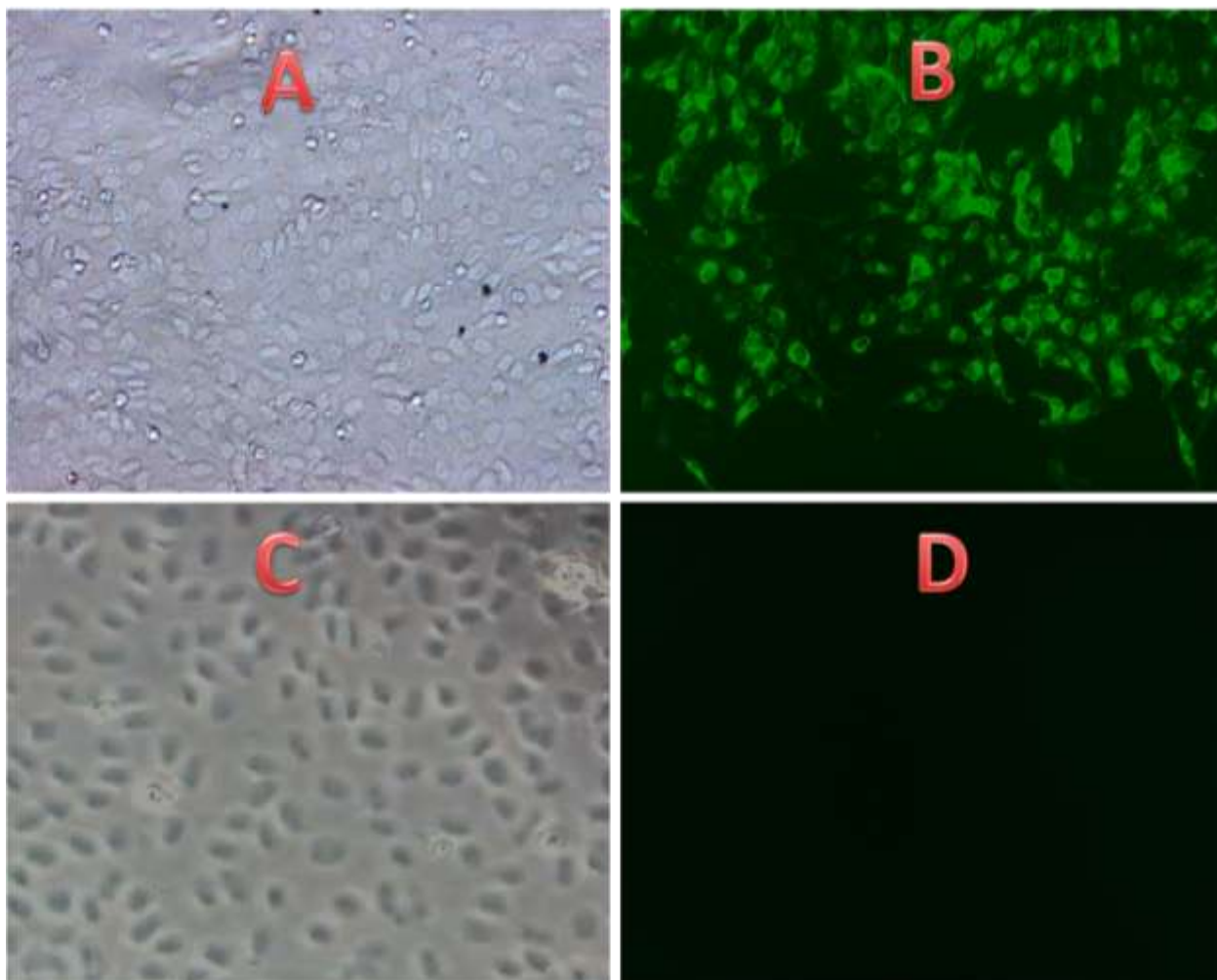


Figure 8.1: A and B are the bright field and fluorescence image of the control, respectively. C and D are the bright field and fluorescence images of the inactivated virus, respectively.

The porosity in the Au-Ag network helps to constitute an efficient covalent binding coverage by the thiol modified aptamer. The entire (100 nmol) lyophilized form of the procured aptamer was then dissolved in 500 μ L of Milli-Q® water. Though different nanobioconjugates were prepared by mixing in several volumetric ratios of Au-Ag network and thiolated aptamer like 1:2, 1:3, 1:4, 4:1, 2:1, etc, we found that the impedimetric response was best for the 1:4 nanobioconjugate. In brief, we have taken 10 μ L of the Au-Ag network and 40 μ L of the dilute aptamer solution, as mentioned before, was added to it and mixed properly.

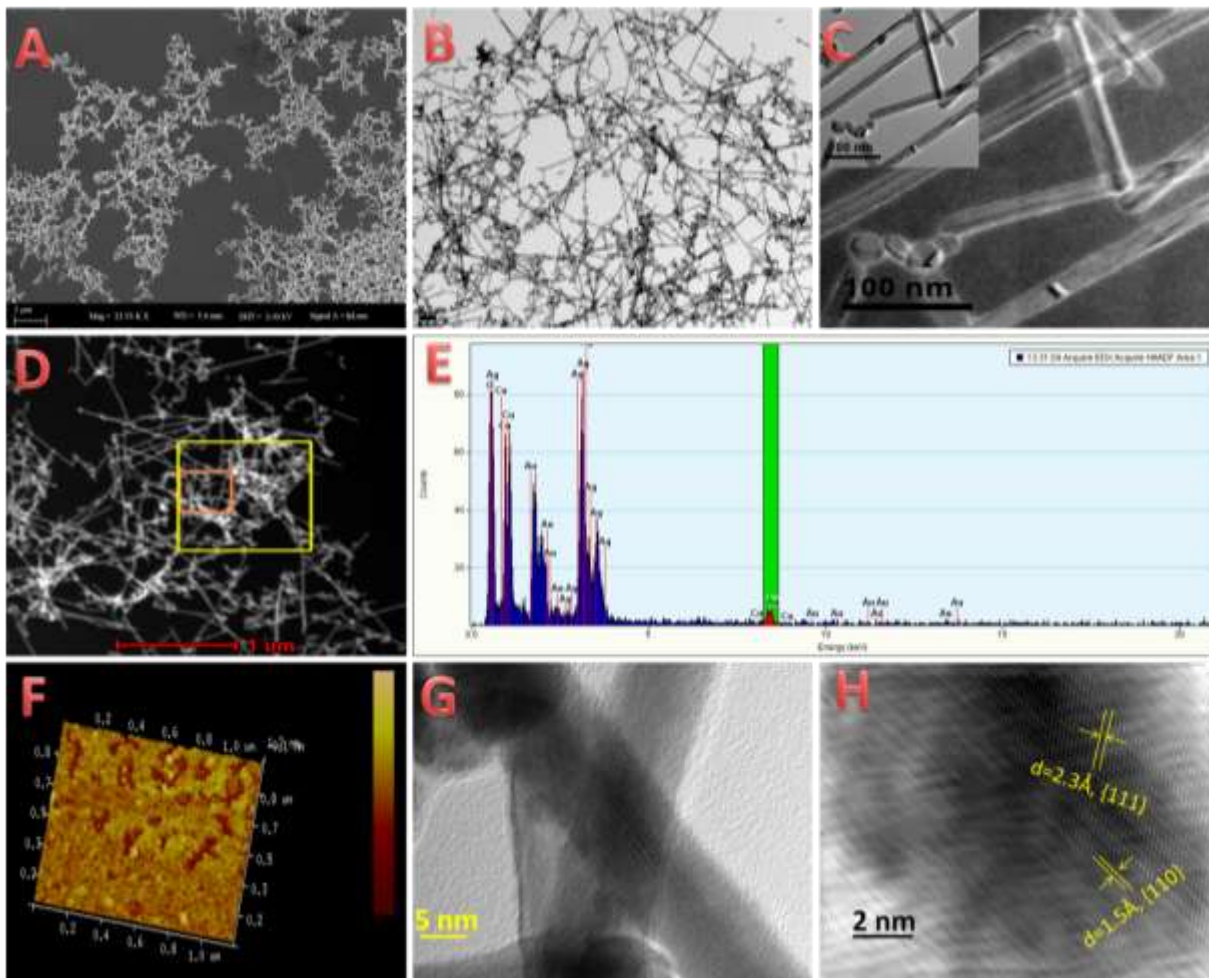


Figure 8.2: A and B is the SEM and TEM image of the Au-Ag network. C is the EFTEM image of the network. D is the HAADF image and E is EDX of Au-Ag network. F is the 3D topographic view of the network. G is the HRTEM image and H is the IFFT image of the porous network which shows two different orientations {111} and {110}.

The resultant nanobioconjugate (i.e. 50 μ L) then further diluted to 1 mL to achieve our stock solution for the rest of the experiments. The resultant nanobioconjugate is stored at 4⁰C and remains stable for months. In our study, we use Vero cells, derived from normal kidney cells, for studying the rate of viral infectivity. Details of the maintenance of the Vero cell line is described in the previous section. As we discussed before, throughout our study we have used psoralen-mediated inactivated virion particles to avoid any accidental infection. Psoralen is a

photoreactive compound that freely permeates the phospholipid membranes and intercalates between nucleic acids by forming a cross-link.⁴⁴⁵ Following exposure to UV-A photoirradiation, the intercalated psoralen covalently cross-links pyrimidine residue and leading to viral inactivation through the inhibition of genome replication. Psoralen is chosen because the interaction of psoralen with viral nucleic acids leaves immunogenic surface epitopes intact.⁴⁵⁷ Psoralen-based viral genome inactivation is shown in **Figure 8.1**.

Synthesis and structural analysis of the cross-linked porous Au-Ag network has been described in the previous chapter in detail. To confirm the reproducibility of our previous report, the same porous Au-Ag network has been synthesized once again and their structural analysis by TEM is performed in an FEI, Tecnai G2 F30 S-Twin microscope and SEM in a Zeiss Supra 40, Field Emission instrument. The obtained morphology of our engineered Au-Ag cross-linked network shows a well-agreed structure with our previous study as shown in **Figures 8.2A** and **8.2B**. We have also performed their AFM imaging in a Bruker made BioScope Catalyst instrument over a mica plate to record the 3D topographic image of nanobioconjugate and activated/inactivated DENV-2 virus. The activated virus was measured as ~50-60nm and inactivated ones are larger than that in diameter which matches well with the previously reported measurements in the literature.⁴³⁰ All the electrochemical experiments were performed in 0.1M phosphate buffer where a screen-printed electrode (reference screen-printed electrode is shown in **Figure 8.3**.) is used as the working electrode to detect DENV-2. In each experiment, we have drop cast 40μL of the nanobioconjugate over the electrode and dried it for 6h (since the nanobioconjugate is in an aqueous medium, drying is quite fast in dry RT). The same modified electrode was then used to perform several electrochemical measurements. During impedimetric measurements of different DENV-2 concentrations, we have applied a fixed potential of 0.8V

within the frequency range of 10^5 to 10^{-1} Hz and an amplitude value of 0.01. In each measurement of different DENV-2 concentrations the overall volume was maintained at ~10 mL in an electrochemical cell (we can use a custom-made cell with lesser volume too). The modified screen-printed electrode was then immersed in the diluted virion solutions. The stock concentration of the inactivated DENV-2 was $\sim 10^5$ PFU/mL which was serially diluted by 0.1 M phosphate buffer to get different concentrations of virus solution for our electrochemical experiments. We have cross-checked the response of the unmodified and modified electrode in different DENV-2 concentrations and found that the unmodified electrode is non-responsive to the DENV-2 concentrations but the modified one shows well resolute DENV-2 concentration-dependent variation of impedance.



Figure 8.3: A panel of screen-printed electrode use for impedimetric assay.

The Au-Ag network appears to be highly porous in nature both from our TEM and SEM studies as shown in **Figures 8.2A** and **8.2B**. The EDX spectrum, given in **Figure 8.2E**, confirms the existence of Au in trace amount and Ag in a larger proportion. The 3D topographic view of the network is shown in **Figure 8.2F**. The energy-filtered TEM (EFTEM) image of the Au-Ag porous network structure is given in **Figure 8.2C** and it shows an excellent view of the sidewise assembly of the nanorod. The HRTEM and IFFT image of the network is given in **Figure 8.2G** and **8.2H** respectively, which confirms the existence of two prominent facets $\{111\}$ and $\{110\}$.

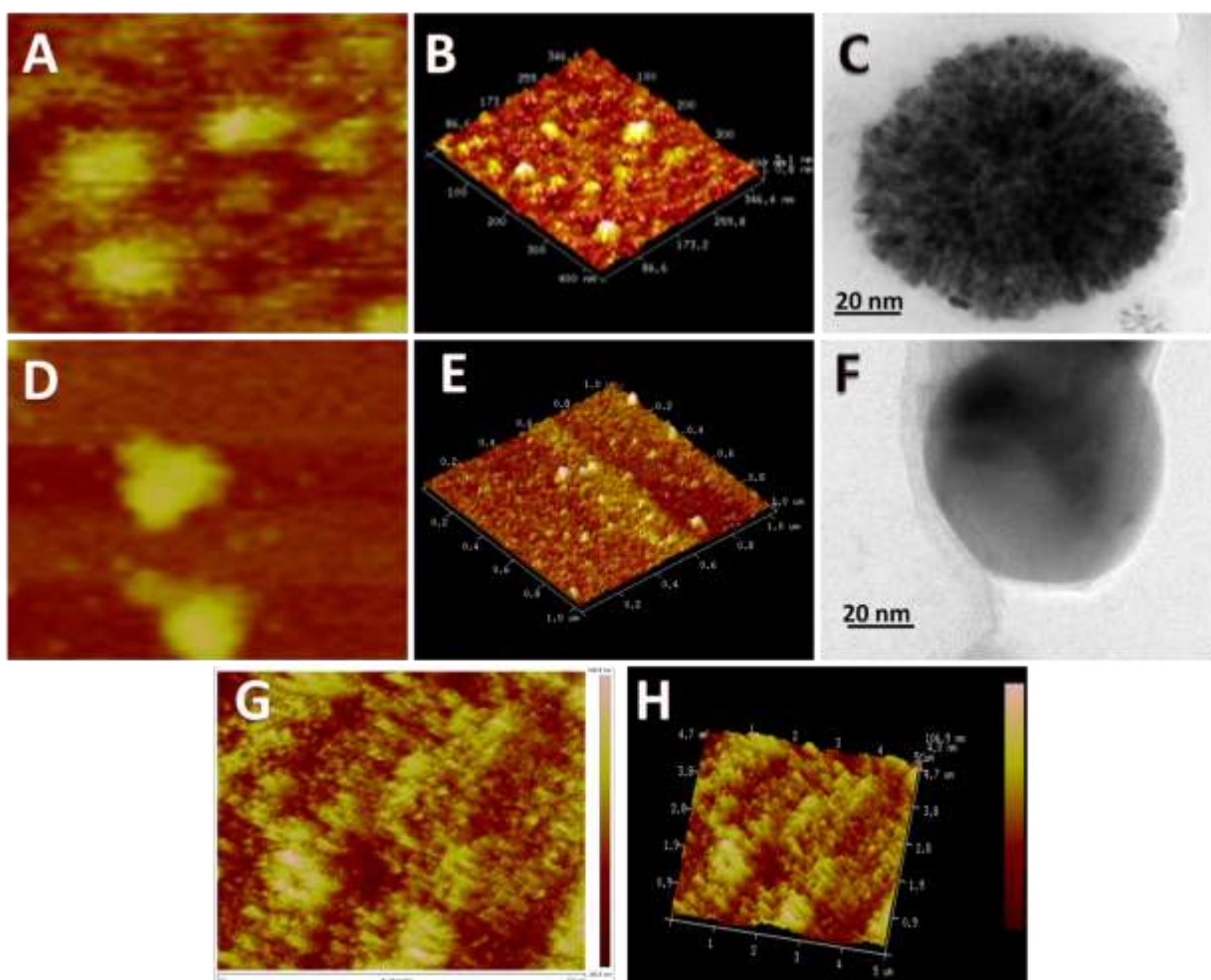


Figure 8.4: A and B are the two-dimensional and three-dimensional AFM image of the inactivated virus, whereas C is the TEM image of single inactivated DENV-2. D and E are the two-dimensional and three-dimensional AFM images of the infectious DENV-2 virus and F is

the TEM image of single activated DENV-2. G and H represent the two-dimensional and three-dimensional AFM images of the nanobioconjugate respectively.

As discussed in the earlier section that after the psoralen treatment, the smooth wall of the DENV-2 virus converts into a spiky surface which is confirmed by our TEM study (**Figure 8.4C** and **8.4F**). The same morphological transition for DENV-2 from its inactivated to activated form is also provided by recording AFM images in two dimensions in **Figure 8.4A** and **8.4D** respectively whereas the corresponding 3D images are given in **Figure 8.4B** and **8.4E**. This proves the ability of psoralen for the transition from activated to the inactivated form of DENV-2. It is already reported in the literature⁴⁵⁷ that the psoralen treatment however does not change the immunogenetic surface epitope of DENV-2.

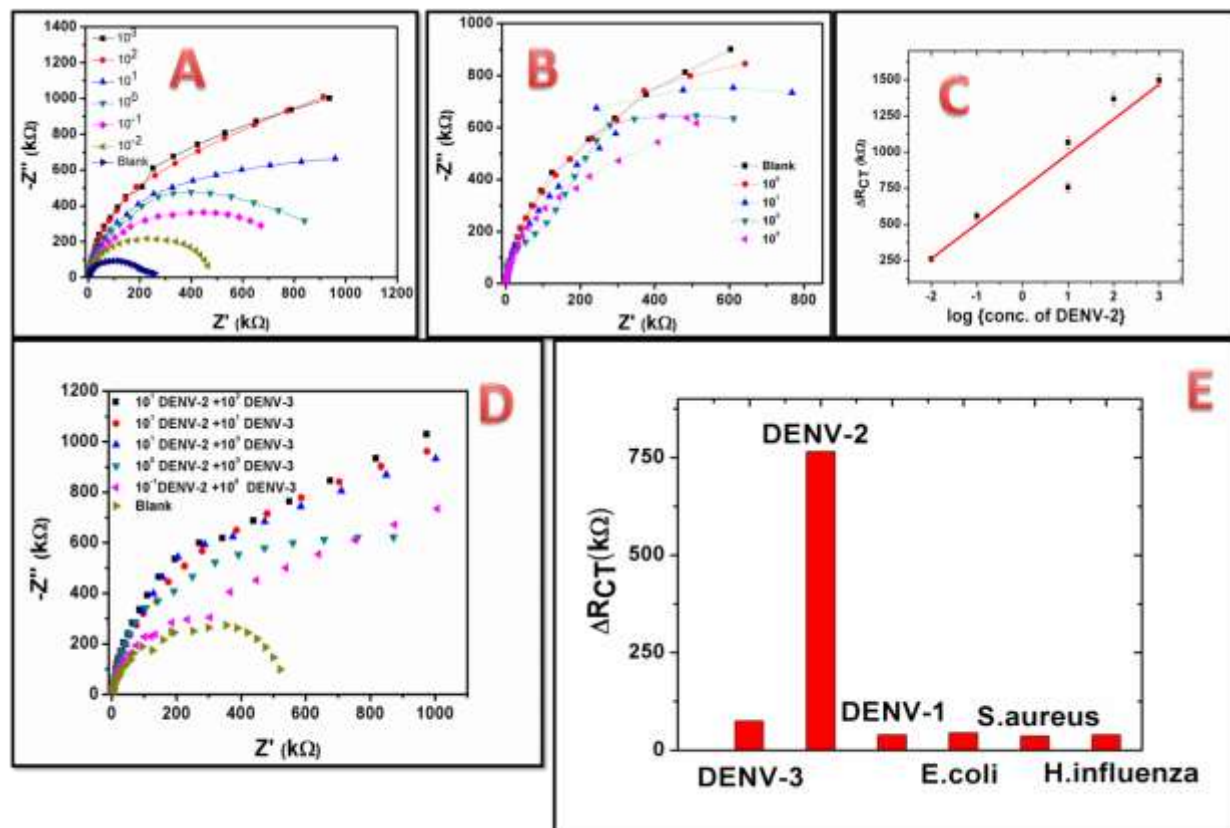


Figure 8.5: A and B are the Nyquist plot for DENV-2 and DENV-3 where all the virus concentrations are in PFU/mL unit. C is the calibration plot for DENV-2. D is the cross-

reactivity check by impedance response in a mixture of DENV-2+ DENV-3. E is the ΔR_{CT} of DENV-2 in the presence of other DENV serotypes and bacteria. For all the samples we used the concentration at 10^1 PFU/mL.

Hence, our aim to target the DIII of glycoprotein-E of DENV-2 will not be obstructed by the psoralen inactivation process. In this work, we are targeting the direct detection of the dengue virus by designing a high specificity aptamer with respect to the DIII domain of DENV-2 glycoprotein-E and adsorbed it on to the nanobioconjugate. Reasons behind selecting the engineered porous Au-Ag network as the electrode coating material for our highly sensitive impedimetric detection are (i) excellent covalent surface binding coverage of thiolated aptamers on Au-Ag network offers enhanced E-protein recognition on virion particles, (ii) the broad environmental stability (broader solvent polarity range and wider pH range of the medium) of the Au-Ag-DTT composite nanonetwork allows us to perform our sensing and detection in any environment, and (iii) better adsorptivity of the coating material on the electrode surface (a basic property of the Ag/Au-thiol composite materials) enhances the durability of the assay. We have also recorded the AFM images of the nanobioconjugate as shown in **Figure 8.4G** and **8.4H** represents its 2D and 3D views respectively.

Impedance measurements are performed by recording the Nyquist plot for different concentrations of DENV-II as shown in **Figure 8.5A**. In a Nyquist plot, the Y-axis and X-axis represent the imaginary and real part of the impedance. Obtained curves from the Nyquist plot are then fitted to the Randles cell through simulation (**Figure 8.6**). We found that the increase in DENV-2 concentration leads to an enhancement in R_{CT} as a result of a larger extent of binding of the DENV-2 with the nanobioconjugate modified electrode surface.

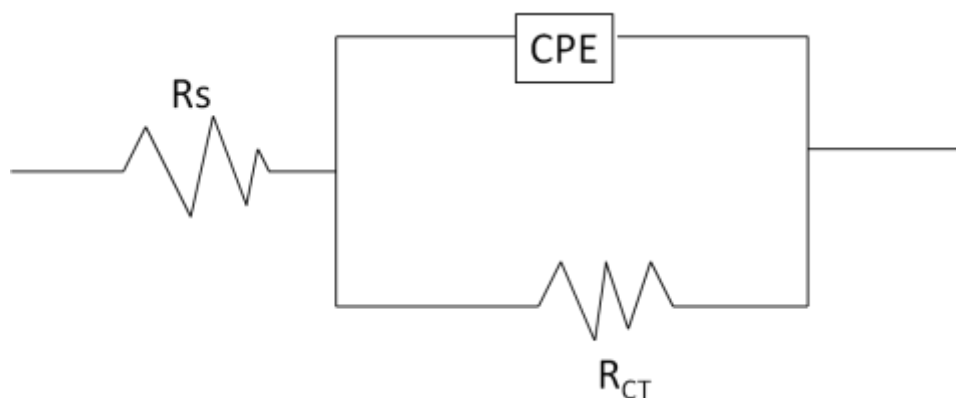


Figure 8.6: Randles cell used for fitting Nyquist plot. Where R_s appears due to solution resistance, CPE is the constant phase element and R_{CT} is the charge transfer resistance for any kind of process happening at the electrode surface.

Due to this more binding of DENV-2 on the electrode surface which makes an insulating layer on the electrode coating, less current flows and subsequently R_{ct} increase. To prove the specificity of our engineered nanobioconjugate assay, the same impedance measurement is carried out for inactivated DENV-3, as shown in **Figure 8.5B**, which is a closely related serotype (based on DIII domain of glycoprotein-E) of DENV-2. The change in impedance is negligible in comparison to the blank phosphate buffer which clearly signifies that there is no specific binding (antigen-aptamer interaction) between DENV-3 and the nanobioconjugate and agrees well with our prediction.

Fitted parameters from Randles cell (**Figure 8.6**) like charge transfer resistance (R_{CT}), constant phase element (CPE), solution resistance (R_s), etc are discussed detailed in SI section and listed in **Table 8.1**. During each measurement, we have recorded the blank response i.e. response of the modified electrode in phosphate buffer. We introduced a new physical parameter, ΔR_{CT} , for calibration curves of DENV-2, which is obtained by subtracting R_{CT} of blank solution from the R_{CT} of a particular concentration of DENV-2 solution under investigation. Hereafter we plot ΔR_{CT} vs $\log[\text{DENV-2}]$ ($[\text{DENV-2}]$ is the concentration of DENV-2) to get a linear

calibration plot for different virion samples with a concentration between 10^3 to 10^{-2} PFU/mL as plotted in **Figure 8.5C**. The cross-reactivity is checked through impedance measurement in a mixed solution of two closely related serotypes i.e. DENV-2 and DENV-3.

Table 8.1: Parameters obtained from the Nyquist plot for DENV-2 as shown in Figure 3A by fitting into the Randles cell.

Conc (PFU/mL)	R_s (Ω)	R_{CT} (k Ω)	n	Y_0
Blank	200	229	.88	2.1×10^{-6}
10^{-2}	200	488	.92	1×10^{-6}
10^{-1}	200	785	.94	9.5×10^{-7}
10^0	200	985	.96	9×10^{-7}
10^1	200	1290	.94	9×10^{-7}
10^2	200	1600	.98	9×10^{-7}
10^3	200	1730	.98	9×10^{-7}

It is observable from the impedance plot (**Figure 8.5D**) that with increasing DENV-2 concentration the impedance is increasing linearly and closely following **Figure 8.5C** though the impedance is independent to [DENV-3] while we kept [DENV-3] constant. This signifies that even if a host is infected by DENV-2 and DENV-3, the nanobioconjugate will respond only to DENV-2.

We have also provided a histogram in **Figure 8.5E** to record the ΔR_{CT} in presence of different types of bacteria which remain present in the human body, like *E. coli*, *Staphylococcus aureus*, and *H. influenza* along with different dengue serotypes like DENV-3, DENV-1, etc. (at the same concentration) to estimate the broader cross-reactivity of our reported assay. This

demonstrates the specificity of our nanobioconjugate towards DENV-2 only and we found that DENV-2 shows exclusively high impedance towards the engineered nanobioconjugate. The obtained positive result from cross-reactivity experiments allows us to go for real sample analysis collected from infected patients. The infected DENV-2 blood serum was collected from Belegghata ID & BG Hospital, Kolkata, INDIA.

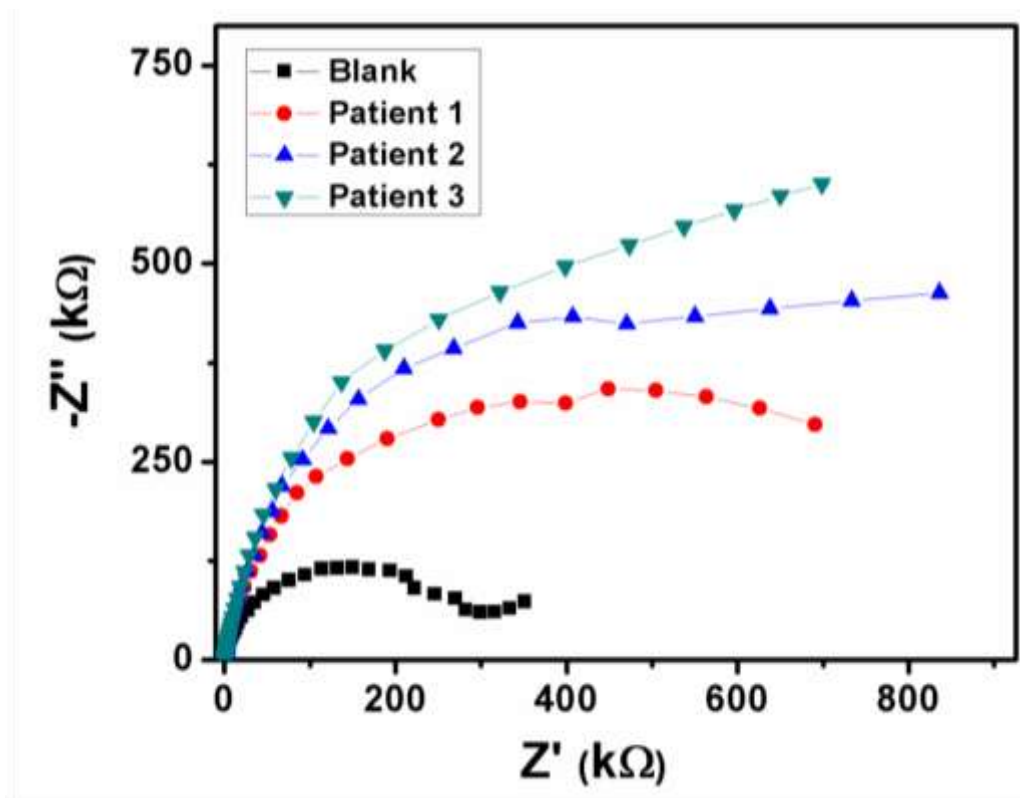


Figure 8.7: Nyquist plot for real sample designated as Patient1, Patient 2, and Patient 3.

The blood samples with DENV-2 infection are initially assessed through qRT-PCR which shows a good amount of viral load. We have estimated the impedance response for 3 such DENV-2 samples collected from 3 different DENV-2 positive patients as shown in **Figure 8.7**. Recorded high impedance values, R_{CT} , and the corresponding virus concentration from the calibration plot for three different DENV-2 positive samples are listed in **Table 8.2**.

Table 8.2: parameters obtained from the Nyquist plot for DENV-II infected real blood samples drawn from 3 different patients.

Sample	$R_s (\Omega)$	$R_{CT} (k\Omega)$	n	Y_0	Virus concentration from calibration plot (PFU/mL)
Blank	250	300	.86	1×10^{-6}	NA
Patient 1	250	725	.94	1×10^{-6}	.879
Patient 2	250	940	.96	9×10^{-7}	7.53
Patient 3	250	1140	.96	1×10^{-6}	45.70

Obtained results clearly show our ability to develop a user-friendly, cost-effective, rapid, sensitive, and highly specific biosensor for DENV-2 detection in all possible physicochemical environments. Specific and noted advantage of our developed nanobiosensor include: (i) direct detection method nullifies the necessity of NS1 antigen test as done in ELISA method, (ii) need not to separate viral RNA as done in qRT-PCR, (iii) quashes the requirement of expansive enzymes as done in the enzymatic assay, and (iv) sample requirement is only 40 μ L for each test. Hence, a thiol modified DNA aptamer-based porous Au-Ag nanobioconjugated network can easily, efficiently, and sensitively detect the DENV-2 serotype from any real sample.

In conclusion, a highly stable (in the broad physicochemical environment), non-expansive, aptamer-based Au-Ag nanobioconjugate with porous network structure has been developed with good adsorptivity on electrode surface for highly specific and ultrasensitive (up to 10^{-2} PFU/mL) detection of DENV-2 through a non-enzymatic assay. The developed impedimetric assay is a simple electrochemical assay which does not seek any laborious processes like RNA isolation, gel electrophoresis, fluorescence measurement, and optical density

measurement or requires any expansive accessories like tunable electron or light sources. This is a direct detection technique (i.e. we need not any preprocessing of the blood/swab sample) where we recognize the specific dengue serotype through aptamer-based E-protein binding which results a recordable change in impedance. The developed nanobioconjugate allows us to detect DENV-2 highly specifically from the infected blood sample up to concentration as low as $\sim 10^{-2}$ PFU/mL. In our current investigation, we used a low-cost screen-printed electrode (Cost: Rs. 100/p) as the working electrode of our electrochemical assay which reduces the cost of the detection to a bare minimum. Undoubtedly this is the first report of user-friendly impedimetric sensing of lethal DENV-2 which has all the potentials to replace the ELISA-based technique for real sample analysis.

CHAPTER-9A

Future Direction

Synthesis of $\text{Ag}_{\text{core}}\text{Au}_{\text{shell}}$ nanostructures and the corresponding $\text{NP}_{\text{matrix}}$ as a bifunctional catalyst for the fabrication of high throughput alcohol fuel cells.

OUTLINE: Specific Points of Discussion

- Despite being unfavorable redox reactions, we were successfully able to produce desired $\text{Ag}_{\text{core}}\text{Au}_{\text{shell}}$ nanostructures by controlling the $\text{Au}^{3+}/\text{Au}^0$ kinetics and using CTAB as a surfactant.
- The final $\text{NP}_{\text{matrix}}$ is synthesized from $\text{Ag}_{\text{core}}\text{Au}_{\text{shell}}$ nanostructures by a galvanic replacement reaction.
- As a bifunctional catalyst, the developed $\text{NP}_{\text{matrix}}$ will help us to produce high current density from alcohol fuel cells.
- $\text{NP}_{\text{matrix}}$ finds itself as a substitute to the Pt/C as an efficient catalyst for the future generation of clean fuel with long term durability.
- We need a substantial amount of additional study to draw the final conclusion.

9A.1 Introduction:

Due to their unique properties, porous bimetallic gold-silver (Au-Ag) nanoparticles have received weighty attention in present days for determining the responsible factors behind the atomic origin of their promising catalytic activity towards various redox reactions e.g. oxidation of mono-, di-, and tri-ols⁴⁵⁸⁻⁴⁶⁰ (e.g., methanol, ethylene glycol, and glycerol) for fuel cell applications, oxidation of water⁴⁶¹ for oxygen evolution reaction (OER), reduction of water for hydrogen evolution reaction⁵⁰ (HER), oxidation of CO to CO₂⁴⁶², reduction of nitrogen to ammonia and CO₂ to methanol^{463,464}, etc. In this context, a critical question arises: which one is the decision-making factor behind the enhanced catalytic efficacy for porous Au-Ag nano-alloy compared to other conventional materials? Several arguments have been brought up in search of the above query which includes (i) critical surface composition (Au/Ag) of the nano-alloy,⁴⁶⁵ (ii) structural rearrangement of the nanoporous gold during the catalytic reaction,⁴⁶⁶ (iii) presence of a large extent of crystal defects (stepped surface, terrace, kink, dislocation, grain boundary, twin boundary, etc on the exposed nano-alloy surface⁴, enhanced active surface area, suitable surface charge and curvature-induced charge density³¹⁵, efficiency in narrowing of d-band centre, large extent of tensile strain generated for lattice mismatch due to the introduction of bigger Ag atom in the nano-crystal made by smaller size Au atoms,⁷ etc. To investigate the prime factors responsible for determining their catalytic efficacy, we have engineered several Au-Ag alloy nanocrystals. The synthesized Au-Ag alloy nanocrystals were then used as electro-catalysts for the oxidation of n-ols (methanol, ethylene glycol, and glycerol) and reduction of oxygen (ORR) for fuel cell applications. In both cases, i.e., oxidation of alcohol (withdrawing electrons from the reactant) and reduction of oxygen (ORR) (donating electrons to the reactant), the bimetallic Au-Ag matrix (NP_{matrix}) is found to be catalytically most active. The enhanced catalytic activity of

NP_{matrix} can be explained by measuring the extent of voids or defects (both act as active catalytic sites) formation through the Kirkendall effect (differential diffusion rate of Ag⁰ and Au⁰) during the galvanic replacement of Ag⁰ by Au³⁺ over the nano-alloy surface. The surface chemical micro-environment of a nano-alloy can be described as $M_R + N_R + \text{ligands} \rightarrow \text{Mp@ligands} + N_P$ where M_R is the starting material, N_R is the assisted reactant (In this case M_R is Au³⁺ or Ag⁺ and N_R is ascorbic acid and the ligand is CTAB moiety). In general, the ligands give stabilization to the nanoparticles by binding (coordinate bonds) to the ‘unsaturated metal-dangling bonds’⁴⁶⁷. The catalytic activity of a nano-alloy is thus proportional to the density of these ‘dangling bonds’ on the nano-surface. In nanoparticles there are mainly two types of bonds, one is saturated internal bonds and the other is the unsaturated or dangling bonds situated over the edges or terraces. The CTAB ligands in NP_{matrix} constitutes coordinate bonds to the unsaturated atoms (R₄N⁺.....Br⁻ is a bound ion pair and considered to be 2e⁻ donor) and thereby give some stability to deny aggregation in the dispersion medium. However, some of the dangling bonds still remain ‘naked’ and creates multiple crystal defects which are considered to be chemically active sites for oxidation (that means withdrawing electron clouds from the reactants). In our present study, we have performed n-ols oxidation reactions e.g., the oxidation of methanol, ethylene glycol, and glycerol which are considered as clean and silent liquid fuels with high energy conversion efficiency. Pt is considered to be the most efficient catalyst for oxidizing such organic molecules however the affinity of CO adsorption over the Pt surface during electro-oxidation of alcohols retard the reaction kinetics.⁴⁶⁸ Our synthesized NP_{matrix} with high defect enriched catalytically active sites is found to be highly chemically reactive for the oxidation of methanol both in acidic and basic medium. To apply our NP_{matrix} as electrocatalytic material in a broader aspect, we have utilized it in electro-oxidation of a di-ol (ethylene glycol) and a tri-ol

(glycerol) along with mono-ol (methanol) to show that the above-mentioned material is catalytically active for the oxidation of long-chain and higher molecular weight alcohols too. Besides alcohol oxidation, oxygen reduction reaction (ORR) is a crucial cathodic process in alcohol fuel cells. The sluggish electron transfer kinetics in ORR needs efficient electro-catalysts to accelerate the process. Pt-based nano-alloys have been widely used as a catalyst to assist the four-electron reduction of oxygen to water. However, due to their high-cost, less tolerance, and low durability, Pt-based nano-alloy are substituted nowadays by transition metal nitrides, chalcogenides, oxides,⁴⁶⁹ etc. We have engineered the Au-Ag matrix ($\text{NP}_{\text{matrix}}$) with low-cost and having the ability of long term catalytic performance, whose stability has been checked through several cycling during ORR.

9A.2 Material Synthesis:

9A.2.1 Synthesis of Au Nanoseed:

In a typical synthesis, 500 μL of 10^{-2}M $\text{HAuCl}_4 \cdot 3\text{H}_2\text{O}$ was added in 20 mL of MiliQ (18 $\text{M}\Omega\text{ cm}$) water under constant stirring (150 rpm) followed by the addition of 200 μL of $2.5 \times 10^{-2}\text{M}$ of TSC. The solution was kept under stirring at room temperature for an additional 30 s. To this solution, 60 μL of 10^{-1}M NaBH_4 (ice cold) was added dropwise. The solution turns brownish immediately which we kept in dark for an additional 2 hr in an open mouth condition to facilitate the release of evolved hydrogen until the color turns to wine red.

9A.2.2 Synthesis of Au-Ag Nano-alloy:

Au-Ag nano-alloy with different morphology was synthesized by varying the CTAC concentration and temperature. In a typical synthetic procedure, 45mL of MiliQ water was taken in a 100 mL 3-neck round-bottomed flask fitted with condenser under a continuous flow of tap

water where the flask is kept in a water bath at 85⁰C. To this solution, 0.01g CTAC was added and kept for further 5 minutes under constant stirring (400 rpm) to make it dissolved completely. Once the CTAC becomes soluble, 2mL of as-prepared Au nanoseed was added to it followed by the addition of 2 mL of 10⁻² M AgNO₃ and 500 μL of 10⁻¹ M of AA. The solution was kept at 85⁰C and 400 rpm for an additional 4 h. The whole solution turns into a yellowish-green color, which we cooled to room temperature before centrifuged it at 6000 rpm for 1 h at 30⁰C. After centrifugation, the precipitated oval-shaped Au-Ag nano-alloy (~50 nm in length) was collected from the centrifuge tube and the final volume was adjusted to 500 μL by adding an appropriate amount of MiliQ water. The concentrated Au-Ag nano-alloy was then stored at 4⁰-8⁰C which remains stable for months as we checked it's stability by verifying its plasmonic nature (UV-vis-NIR), TEM, HRTEM, and XPS spectra. The morphology of different Au-Ag nano-alloy was controlled by varying the surfactant concentration and the temperature during synthesis. We have checked the catalytic activity of each Au-Ag nano-alloy towards electrochemical oxidation of methanol and found that the oval-shaped Au-Ag nano-alloy synthesized at 85⁰C (by applying .01g CTAC), as stated above, is the most effective one. Further, we have modified its morphology to the Ag_{core}Au_{shell} structure for increasing its catalytic efficiency towards the electrochemical oxidation of methanol. The modification is discussed below.

9A.2.3 Synthesis of Ag_{core}Au_{shell} structure by Template Method:

The oval-shaped Au-Ag nanoalloy (~50 nm in length) prepared in the previous step was dispersed in 15 mL of MiliQ water and the resultant solution is then used as a template for the next step. In this step, 0.05 g of CTAB was dissolved in 45 mL of MiliQ water at 30⁰C. The diluted CTAB solution was then kept under constant stirring at 200 rpm. To this solution, 2mL of 10⁻² M HAuCl₄·3H₂O was added followed by the addition of 300 μL of 10⁻² M of AgNO₃. The

above mixture was kept under the same constant stirring for an additional 45 s. The solution turns reddish-yellow. To this solution, 320 μL of AA was added drop-by-drop and once the reddish-yellow color turns to colorless. We have added different volumes of the template solution (100 μL , 1 mL, and 3mL) to this colorless solution. The whole solution was stirred for another 1 minute before we kept it for overnight (12 h) in dark (closed mouth condition) at 30 $^{\circ}\text{C}$. After 12 h, the solution was centrifuged at 2000 rpm at 30 $^{\circ}\text{C}$ for 2 h. Precipitated core-shell structures were then collected and stored at room temperature. Our catalytic study shows that the core-shell structure engineered by using 3 mL of the template solution ($\text{Ag}_{\text{core}}\text{Au}_{\text{shell}}$) is catalytically the most active one among all and used further to synthesize the void enriched Au-Ag ($\text{NP}_{\text{matrix}}$) matrix.

9A.2.4 Synthesis of void Enriched Au-Ag Matrix ($\text{NP}_{\text{matrix}}$) by Galvanic Replacement

Method:

The centrifuged $\text{Ag}_{\text{core}}\text{Au}_{\text{shell}}$ structures obtained in the previous step was redispersed into 50 mL of water and stirred for 5 minutes at 200 rpm by keeping the temperature constant at 30 $^{\circ}\text{C}$. To this solution, 2 mL of 10^{-2} M $\text{HAuCl}_4 \cdot 3\text{H}_2\text{O}$ was added at a time and stirred for an additional 10 minutes and after which the reaction mixture was kept undisturbed for 12 h in dark. The as-synthesized Au-Ag $\text{NP}_{\text{matrix}}$ was then concentrated by centrifuging the solution at 2000 rpm at 30 $^{\circ}\text{C}$. The final precipitate is then diluted to 500 μL by MiliQ water and used for all the catalytic experiments.

9A.3 Results & Discussion:

As the reduction potential of Ag^+/Ag^0 (0.79 V) is much lower than that of $\text{Au}^{3+}/\text{Au}^0$ (1.51 V),⁷ the formation of $\text{Ag}_{\text{core}}\text{Au}_{\text{shell}}$ structure is quite difficult as the galvanic reaction may leach out the Ag-core by transforming insoluble Ag^0 into Ag^+ . Despite that, we were successfully able

to produce the desired $\text{Ag}_{\text{core}}\text{Au}_{\text{shell}}$ structure, by controlling the $\text{Au}^{3+}/\text{Au}^0$ kinetics and using CTAB as a surfactant. The synthesized $\text{Ag}_{\text{core}}\text{Au}_{\text{shell}}$ nanostructures as a function of the template (oval-shaped particles as synthesized in the 2nd step of the synthesis) volume (100 μL to 2 mL) are depicted below in **Figure 9A.1**.

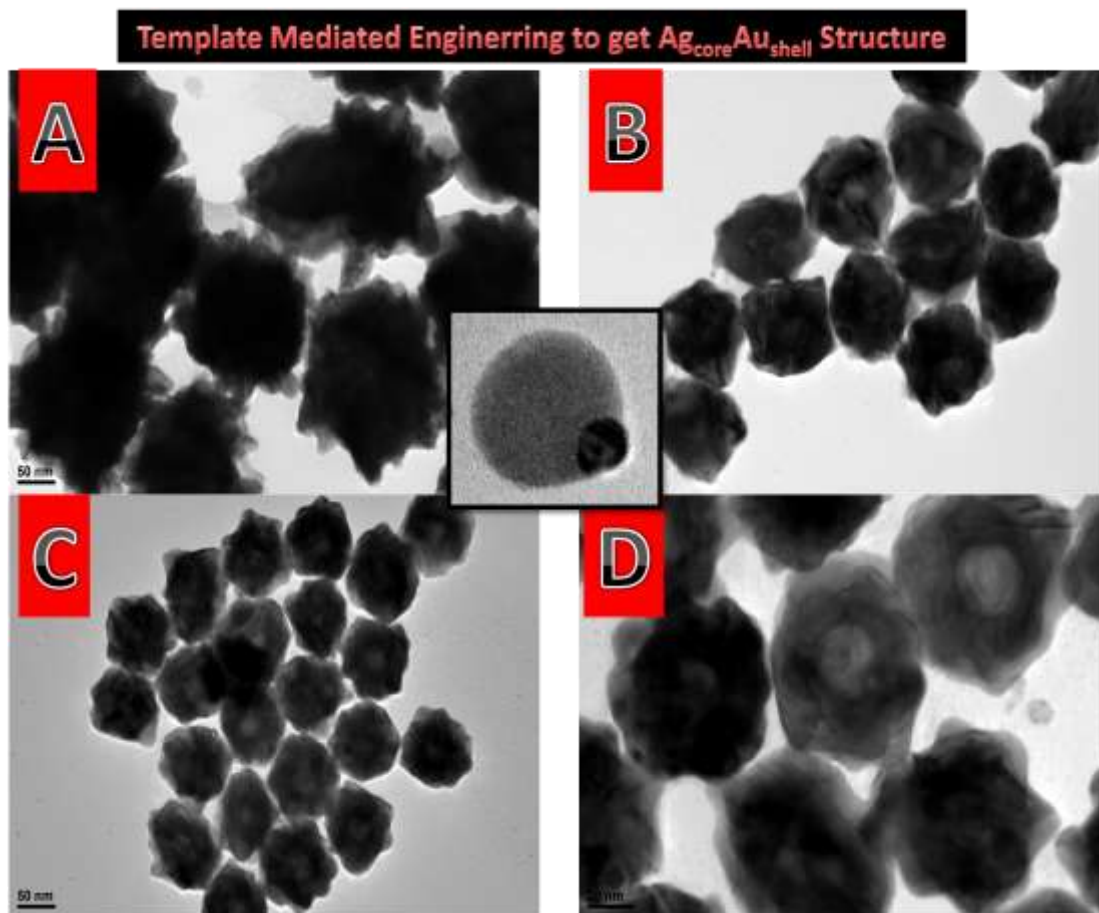


Figure 9A.1: The synthesized $\text{Ag}_{\text{core}}\text{Au}_{\text{shell}}$ nanostructures as a function of the template volume.

(A) 100 μL , (B) , (C) , and (D) 2 mL.

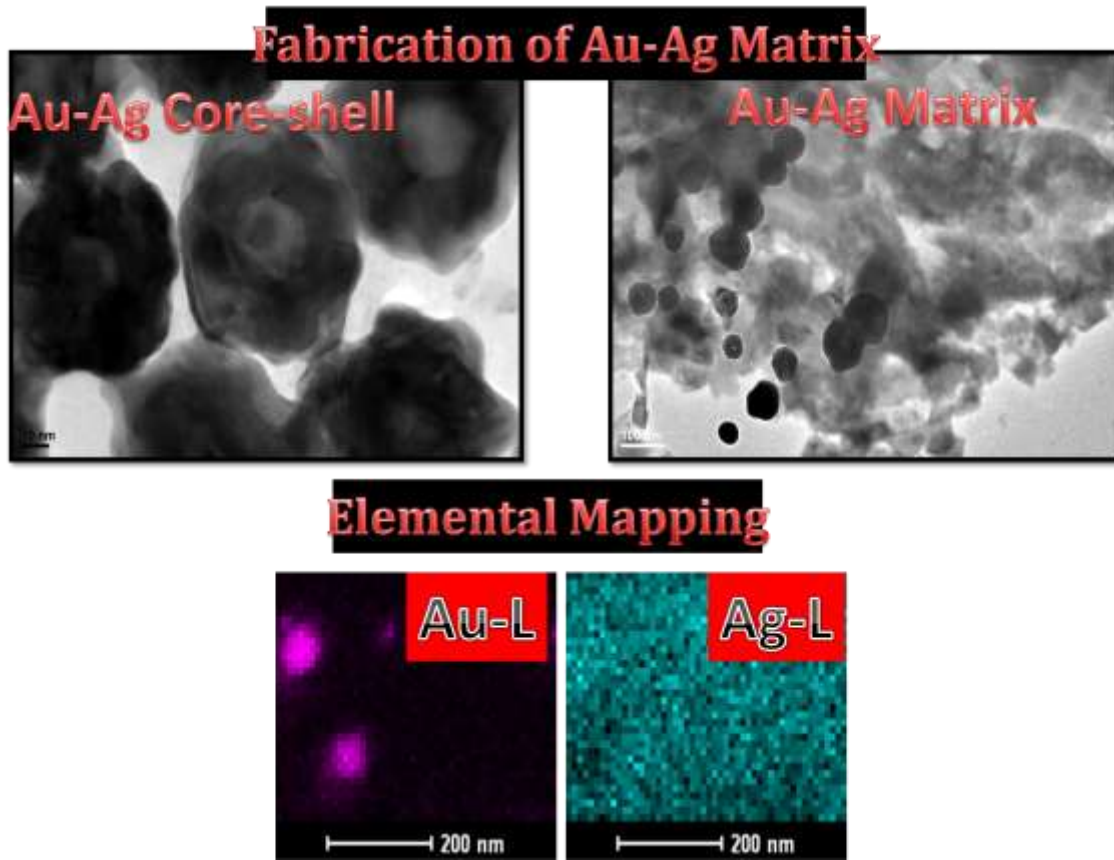


Figure 9A.2: Fabrication of $\text{NP}_{\text{matrix}}$ from $\text{Ag}_{\text{core}}\text{Au}_{\text{shell}}$, and their elemental mapping.

As we increase the volume of the template while keeping the surfactant concentration constant (0.05gm in 45mL of water), the size of the engineered $\text{Ag}_{\text{core}}\text{Au}_{\text{shell}}$ reduced gradually while the Addition of Au^{3+} which induces the galvanic replacement from $\text{Ag}_{\text{core}}\text{Au}_{\text{shell}}$ nanostructures to generate the desired highly void enriched Au-Ag Matrix ($\text{NP}_{\text{matrix}}$) is shown in **Figure 9A.2**. Generated $\text{NP}_{\text{matrix}}$ is found to be extremely effective for alcohol oxidation and ORR.

Electrocatalytic Activity of Au-Ag Matrix

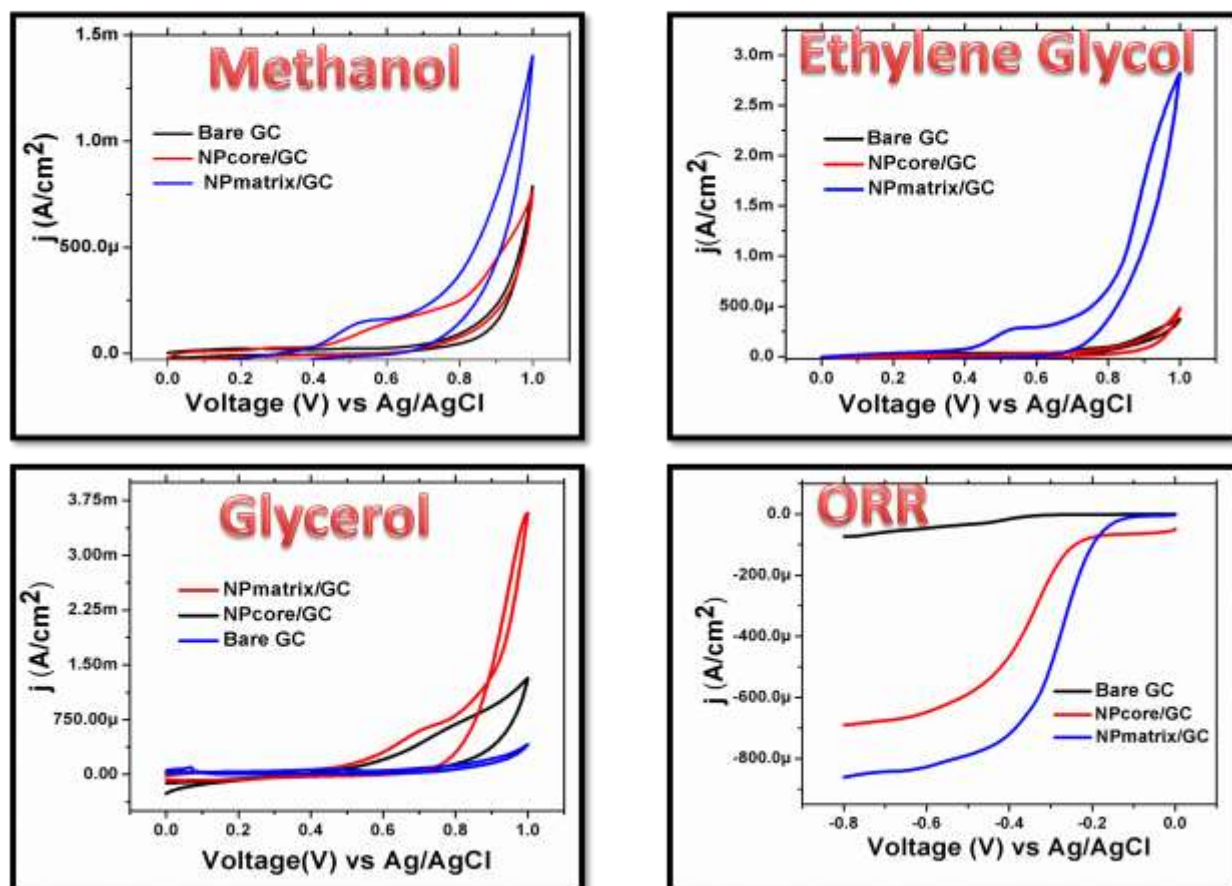


Figure 9A.3: Comparison of electrocatalytic activity of NP_{matrix} structure with Ag_{core}Au_{shell} and bare GC for the oxidation of methanol, ethylene glycol, and glycerol and reduction of oxygen. The concentration of methanol is fixed at 2M whereas for both ethylene glycol and glycerol is fixed at 3M.

We have tested the catalytic activity of the desired NP_{matrix} as mentioned earlier through cyclic voltammetry and linear sweep voltammetry for the oxidation of methanol, ethylene glycol, and glycerol and reduction of oxygen and compared their catalytic activity with bare GC and Ag_{core}Au_{shell} as shown in **Figure 9A.3**.

9A.3 Conclusion:

From the preliminary electrocatalysis results, we want to explore the alcohol fuel cell in more detail both from the experimental and theoretical points of view. As a bifunctional catalyst, the developed NP_{matrix} will help us to produce high current density from alcohol fuel cells. Thus a substitute of Pt/C can be developed for the future generation of clean fuel with long term durability.

CHAPTER-9B

Future Direction

Fabrication of Ag_{core}Au_{shell} nanostructure-based nanobioconjugate as an anti-dengue assay.

OUTLINE: Specific Points of Discussion

- Fabrication of PVP-coated Ag_{core}Au_{shell} nanostructures
- Fabrication of DENV-2 tagged PVP-coated Ag_{core}Au_{shell} nanostructure as the desired nanobioconjugate for sensitive detection of DENV-2 and therapeutic study.
- Currently, we are performing an antiviral assay of DENV-2 in the Vero cell line and planning to apply in an animal model in due course by using this nanobioconjugate.
- We need an extensive further study for more information and to reach into a conclusion about their applicability as a successful anti-dengue assay.

Besides applying our newly synthesized $\text{Ag}_{\text{core}}\text{Au}_{\text{shell}}$ nanostructures in alcohol fuel cells, we are planning to use the same core-shell nanomaterials (as described in Chapter-9A) to design a selective and sensitive antiviral assay within zero toxic levels for highly pandemic Dengue virus. The antiviral activity of Ag nanoparticle is well known in the literature, e.g. Ag nanoparticle/Chitosan composite is found to be highly active against H_1N_1 influenza A virus infection,⁴⁷⁰ commercially available PVP capped Ag nanoparticle is found to be effective for anti-HIV activity by binding to gp120 which prevents CD_4 dependent virion binding, fusion, and infectivity,⁴⁷¹ electrochemically synthesized Ag nanoparticle is found to be effective against poliovirus,⁴⁷² etc. Despite their high antiviral activity, Ag nanoparticles have limitations in nanovaccine industry due to their remarkable cyto- and geno-toxicity and difficulty in cellular uptake.⁴⁷³ Besides, nanoparticle size is a dominant factor for successful exo- and endocytosis processes in a cellular mechanism, e.g. a 50 nm diameter of nanoparticle is optimized for cellular uptake in nonphagocytic cells.⁴⁷⁴ In this regard, we have synthesized a bimetallic Au-Ag nanoalloy with a diameter of < 50 nm and found to be zero toxic at viral doses. The use of Au coating over the Ag_{core} (in an $\text{Ag}_{\text{core}}\text{Au}_{\text{shell}}$ nanostructure) reduces the toxicity of the synthesized nanoalloy by preventing the release of Ag^+ into the cellular media. $\text{Ag}_{\text{core}}\text{Au}_{\text{shell}}$ nanostructures are further modified by treating them with 0.1% polyvinyl alcohol (PVA) to make them more favorable for medical purposes. The toxicity was checked in HCT-116, RAW, HeLa, and HePG2 cell lines by MTT assay. The concentration of Ag in our synthesized PVP-capped $\text{Ag}_{\text{core}}\text{Au}_{\text{shell}}$ nanostructure was measured by ICP-OES technique. Variation of cell viability as a function of $\text{Ag}_{\text{core}}\text{Au}_{\text{shell}}$ nanoparticle and hence Ag concentration is shown in **Figure 9B.1** for HCT-116 cell line.

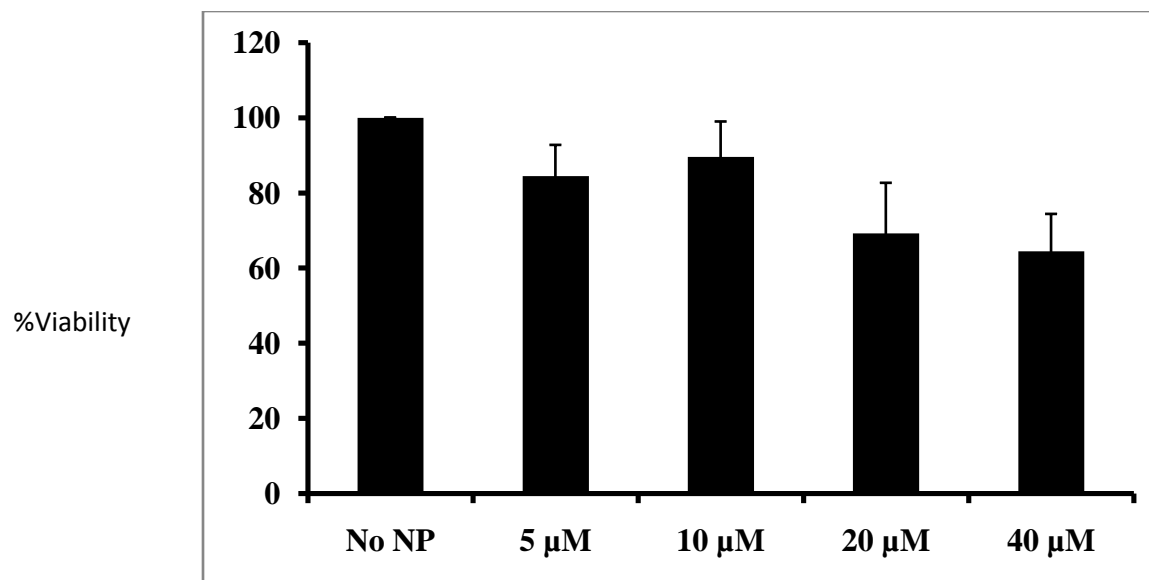
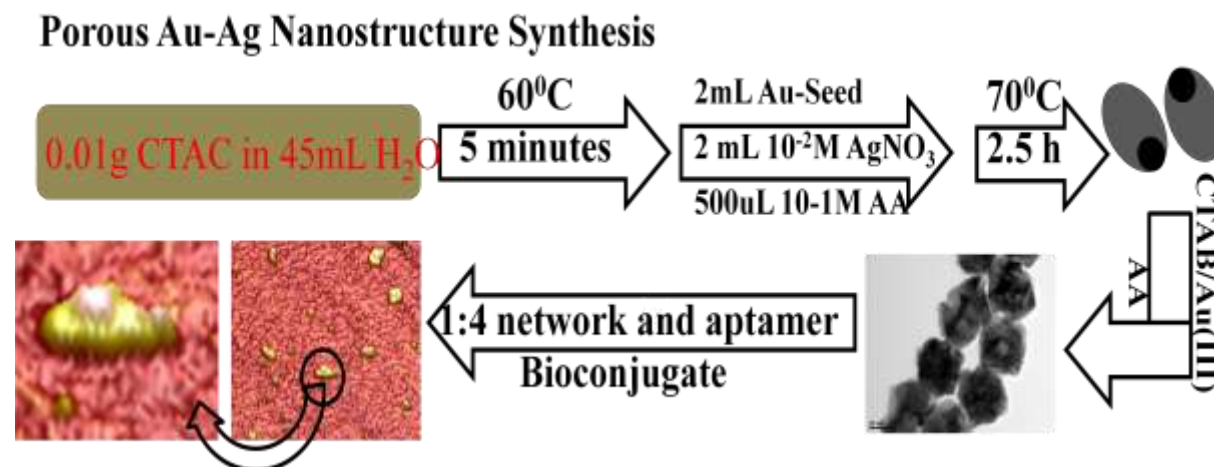


Figure 9B.1: Variation of cell viability as a function of available Ag concentration from the synthesized $\text{Ag}_{\text{core}}\text{Au}_{\text{shell}}$ nanostructure.

Further, the synthesized $\text{Ag}_{\text{core}}\text{Au}_{\text{shell}}$ nanostructure was treated with DENV-2 specific thiol modified aptamer (as mentioned in Chapter in 8) for highly sensitive DENV-2 detection as well as therapeutic application. A stepwise schematic presentation from the synthesis of $\text{Ag}_{\text{core}}\text{Au}_{\text{shell}}$ nanostructure to bioconjugate preparation is depicted in **Scheme 9B.1**.



Scheme 9B.1: A stepwise schematic presentation from the synthesis of Ag_{core}Au_{shell} nanostructure to bioconjugate preparation. The inserted AFM image shows how the aptamer is wrapped around the nanoparticle.

With this specific bioconjugate, we are now performing an antiviral assay of DENV-2 in the Vero cell line and planning to apply in an animal model in due course.

References:

- (1) Ghosh, S. K.; Pal, T. Interparticle Coupling Effect on the Surface Plasmon Resonance of Gold Nanoparticles: From Theory to Applications. *Chemical Reviews*. November 2007, pp 4797–4862. <https://doi.org/10.1021/cr0680282>.
- (2) Navya, P. N.; Daima, H. K. Rational Engineering of Physicochemical Properties of Nanomaterials for Biomedical Applications with Nanotoxicological Perspectives. *Nano Conver.* **2016**, 3 (1), 1–14. <https://doi.org/10.1186/s40580-016-0064-z>.
- (3) Neugebauer, N.; Fabian, A.; Elm, M. T.; Hofmann, D. M.; Czerner, M.; Heiliger, C.; Klar, P. J. Investigation of the Dipole Interaction in and between Ordered Arrangements of Magnetic Nanoparticles. *Phys. Rev. B* **2020**, 101 (10), 1–12. <https://doi.org/10.1103/PhysRevB.101.104409>.
- (4) De, S. K.; Mondal, S.; Sen, P.; Pal, U.; Pathak, B.; Rawat, K. S.; Bardhan, M.; Bhattacharya, M.; Satpati, B.; De, A.; et al. Crystal-Defect-Induced Facet-Dependent Electrocatalytic Activity of 3D Gold Nanoflowers for the Selective Nanomolar Detection of Ascorbic Acid. *Nanoscale* **2018**, 10 (23), 11091–11102. <https://doi.org/10.1039/c8nr03087a>.
- (5) Volokitin, Y.; Sinzig, J.; De Jongh, L. J.; Schmidt, G.; Vargaftik, M. N.; Moiseev, I. I. Quantum-Size Effects in the Thermodynamic Properties of Metallic Nanoparticles. *Nature* **1996**, 384 (6610), 621–623. <https://doi.org/10.1038/384621a0>.
- (6) Kyslychyn, D.; Piatnytsia, V.; Lozovski, V. Electrodynamical Interaction between a Nanoparticle and the Surface of a Solid. *Phys. Rev. E - Stat. Nonlinear, Soft Matter Phys.* **2013**, 88 (5), 1–12. <https://doi.org/10.1103/PhysRevE.88.052403>.
- (7) Kumar De, S.; Mondal, S.; Roy, A.; Kumar, S.; Mukherjee, M.; Das Chakraborty, S.; Sen,

- P.; Pathak, B.; Satpati, B.; Mukhopadhyay, M.; et al. Zone-Specific Crystallization and a Porosity-Directed Scaling Marker for the Catalytic Efficacy of Au–Ag Alloy Nanoparticles. *ACS Appl. Nano Mater.* **2019**, *2* (12), 7669–7685. <https://doi.org/10.1021/acsanm.9b01748>.
- (8) Cano, I.; Huertos, M. A.; Chapman, A. M.; Buntkowsky, G.; Gutmann, T.; Groszewicz, P. B.; Van Leeuwen, P. W. N. M. Air-Stable Gold Nanoparticles Ligated by Secondary Phosphine Oxides as Catalyst for the Chemoselective Hydrogenation of Substituted Aldehydes: A Remarkable Ligand Effect. *J. Am. Chem. Soc.* **2015**, *137* (24), 7718–7727. <https://doi.org/10.1021/jacs.5b02802>.
- (9) German, N.; Ramanavicius, A.; Ramanaviciene, A. Electrochemical Deposition of Gold Nanoparticles on Graphite Rod for Glucose Biosensing. *Sensors Actuators, B Chem.* **2014**, *203*, 25–34. <https://doi.org/10.1016/j.snb.2014.06.021>.
- (10) Chang, C. C.; Wu, H. L.; Kuo, C. H.; Huang, M. H. Hydrothermal Synthesis of Monodispersed Octahedral Gold Nanocrystals with Five Different Size Ranges and Their Self-Assembled Structures. *Chem. Mater.* **2008**, *20* (24), 7570–7574. <https://doi.org/10.1021/cm8021984>.
- (11) Okitsu, K.; Ashokkumar, M.; Grieser, F. Sonochemical Synthesis of Gold Nanoparticles: Effects of Ultrasound Frequency. *J. Phys. Chem. B* **2005**, *109* (44), 20673–20675. <https://doi.org/10.1021/jp0549374>.
- (12) Bardhan, M.; Satpati, B.; Ghosh, T.; Senapati, D. Synergistically Controlled Nano-Templated Growth of Tunable Gold Bud-to-Blossom Nanostructures: A Pragmatic Growth Mechanism. *J. Mater. Chem. C* **2014**, *2* (19), 3795–3804. <https://doi.org/10.1039/c4tc00160e>.

- (13) Senapati, D.; Senapati, T.; Wate, P. S.; Kanchanapally, R.; Fan, Z.; Kumar Singh, A.; Chandra Ray, P. Length Dependent NLO Properties of 2D Hollow Gold Nanoprisms Formed by Guided Assembly. *Chem. Commun.* **2012**, 48 (48), 6034. <https://doi.org/10.1039/c2cc32007j>.
- (14) Bhattacharjee, G.; Bhattacharya, M.; Roy, A.; Senapati, D.; Satpati, B. Core–Shell Gold@Silver Nanorods of Varying Length for High Surface-Enhanced Raman Scattering Enhancement. *ACS Appl. Nano Mater.* **2018**, 1 (10), 5589–5600. <https://doi.org/10.1021/acsanm.8b01175>.
- (15) Chee, S. W.; Tan, S. F.; Baraissov, Z.; Bosman, M.; Mirsaidov, U. Direct Observation of the Nanoscale Kirkendall Effect during Galvanic Replacement Reactions. *Nat. Commun.* **2017**, 8 (1), 1224. <https://doi.org/10.1038/s41467-017-01175-2>.
- (16) Bollmann, W.; Bollmann, W. Point Defects. *Cryst. Defects Cryst. Interfaces* **1970**, 37–40. https://doi.org/10.1007/978-3-642-49173-3_4.
- (17) Van Gog, H.; Van Huis, M. A. Structural and Electronic Properties of Frenkel and Schottky Defects at the MgO{100} Surface: Spin Polarization, Mid-Band Gap States, and Charge Trapping at Vacancy Sites. *J. Phys. Chem. C* **2019**, 123 (23), 14408–14420. <https://doi.org/10.1021/acs.jpcc.9b01908>.
- (18) Li, X.; Su, X.; Pei, Y.; Liu, J.; Zheng, X.; Tang, K.; Guan, G.; Hao, X. Generation of Edge Dislocation Defects in Co₃O₄ Catalysts: An Efficient Tactic to Improve Catalytic Activity for Oxygen Evolution. *J. Mater. Chem. A* **2019**, 7 (17), 10745–10750. <https://doi.org/10.1039/c9ta01697j>.
- (19) Brækhus, J.; Lothe, J. Dislocation Jog and Kink Interactions in Ionic Crystals. *Phys. Status Solidi* **1972**, 51 (1), 149–153. <https://doi.org/10.1002/pssb.2220510115>.

- (20) Xiong, L.; Sun, Z.; Zhang, X.; Zhao, L.; Huang, P.; Chen, X.; Jin, H.; Sun, H.; Lian, Y.; Deng, Z.; et al. Octahedral Gold-Silver Nanoframes with Rich Crystalline Defects for Efficient Methanol Oxidation Manifesting a CO-Promoting Effect. *Nat. Commun.* **2019**, *10* (1), 1–11. <https://doi.org/10.1038/s41467-019-11766-w>.
- (21) Feng, X.; Jiang, K.; Fan, S.; Kanan, M. W. Grain-Boundary-Dependent CO₂ Electroreduction Activity. *J. Am. Chem. Soc.* **2015**, *137* (14), 4606–4609. <https://doi.org/10.1021/ja5130513>.
- (22) Ishida, T.; Murayama, T.; Taketoshi, A.; Haruta, M. Importance of Size and Contact Structure of Gold Nanoparticles for the Genesis of Unique Catalytic Processes. *Chem. Rev.* **2020**, *120* (2), 464–525. <https://doi.org/10.1021/acs.chemrev.9b00551>.
- (23) Tang, C.; Shi, J.; Bai, X.; Hu, A.; Xuan, N.; Yue, Y.; Ye, T.; Liu, B.; Li, P.; Zhuang, P.; et al. CO₂ Reduction on Copper's Twin Boundary. *ACS Catal.* **2020**, *10* (3), 2026–2032. <https://doi.org/10.1021/acscatal.9b03814>.
- (24) Yin, B.; Huang, X.; Mishra, R.; Sadtler, B. Compositionally Induced Twin Defects Control the Shape of Ternary Silver Halide Nanocrystals. *Chem. Mater.* **2017**, *29* (3), 1014–1021. <https://doi.org/10.1021/acs.chemmater.6b03660>.
- (25) Li, Z.; Fu, J. Y.; Feng, Y.; Dong, C. K.; Liu, H.; Du, X. W. A Silver Catalyst Activated by Stacking Faults for the Hydrogen Evolution Reaction. *Nat. Catal.* **2019**, *2* (12), 1107–1114. <https://doi.org/10.1038/s41929-019-0365-9>.
- (26) Sudarshan, K.; Sharma, S. K.; Gupta, R.; Gupta, S. K.; Sayed, F. N.; Pujari, P. K. Role of Surface Defects in Catalytic Properties of CeO₂ Nanoparticles towards Oxygen Reduction Reaction. *Mater. Chem. Phys.* **2017**, *200*, 99–106. <https://doi.org/10.1016/j.matchemphys.2017.07.064>.

- (27) Curd, M. E.; Burnett, T. L.; Fellowes, J.; Yan, P.; Withers, P. J. Redistribution of Carbon Caused by Butterfly Defects in Bearing Steels. *Acta Mater.* **2020**, *183*, 390–397. <https://doi.org/10.1016/j.actamat.2019.10.057>.
- (28) Buffiere, J. Y. Fatigue Crack Initiation and Propagation from Defects in Metals: Is 3D Characterization Important? *Procedia Struct. Integr.* **2017**, *7*, 27–32. <https://doi.org/10.1016/j.prostr.2017.11.056>.
- (29) Economou, S.K. Karapetis, G.-P. Nikoleli, D .P. Nikolelis, S. B. and T. H. V. Enzyme-Based Sensors Enzyme-Based Sensors Introduction to Enzymatic Biosensors. **2017**, No. February 2018, 231–250. <https://doi.org/10.1002/9781119105916.ch9>.
- (30) Gao, L.; Zhuang, J.; Nie, L.; Zhang, J.; Zhang, Y.; Gu, N.; Wang, T.; Feng, J.; Yang, D.; Perrett, S.; et al. Intrinsic Peroxidase-like Activity of Ferromagnetic Nanoparticles. *Nat. Nanotechnol.* **2007**, *2* (9), 577–583. <https://doi.org/10.1038/nnano.2007.260>.
- (31) Xie, J.; Zhang, X.; Wang, H.; Zheng, H.; Huang, Y.; Xie, J. Analytical and Environmental Applications of Nanoparticles as Enzyme Mimetics. *TrAC - Trends Anal. Chem.* **2012**, *39*, 114–129. <https://doi.org/10.1016/j.trac.2012.03.021>.
- (32) Murakami, Y.; Kikuchi, J. I.; Hisaeda, Y.; Hayashida, O. Artificial Enzymes. *Chem. Rev.* **1996**, *96* (2), 721–758. <https://doi.org/10.1021/cr9403704>.
- (33) Su, C. H.; Sun, C. L.; Liao, Y. C. Printed Combinatorial Sensors for Simultaneous Detection of Ascorbic Acid, Uric Acid, Dopamine, and Nitrite. *ACS Omega* **2017**, *2* (8), 4245–4252. <https://doi.org/10.1021/acsomega.7b00681>.
- (34) Adlakha, I.; Solanki, K. N. Structural Stability and Energetics of Grain Boundary Triple Junctions in Face Centered Cubic Materials. *Sci. Rep.* **2015**, *5* (1), 8692. <https://doi.org/10.1038/srep08692>.

- (35) Hartman, T.; Wondergem, C. S.; Kumar, N.; Van Den Berg, A.; Weckhuysen, B. M. Surface- and Tip-Enhanced Raman Spectroscopy in Catalysis. *J. Phys. Chem. Lett.* **2016**, 7 (8), 1570–1584. <https://doi.org/10.1021/acs.jpcllett.6b00147>.
- (36) Singh, S. K.; Kashyap, V.; Manna, N.; Bhange, S. N.; Soni, R.; Boukherroub, R.; Szunerits, S.; Kurungot, S. Efficient and Durable Oxygen Reduction Electrocatalyst Based on CoMn Alloy Oxide Nanoparticles Supported over N-Doped Porous Graphene. *ACS Catal.* **2017**, 7 (10), 6700–6710. <https://doi.org/10.1021/acscatal.7b01983>.
- (37) Luo, Y.; Tang, L.; Khan, U.; Yu, Q.; Cheng, H. M.; Zou, X.; Liu, B. Morphology and Surface Chemistry Engineering toward PH-Universal Catalysts for Hydrogen Evolution at High Current Density. *Nat. Commun.* **2019**, 10 (1), 1–9. <https://doi.org/10.1038/s41467-018-07792-9>.
- (38) Sievers, C.; Scott, S. L.; Noda, Y.; Qi, L.; Albuquerque, E. M.; Rioux, R. M. Phenomena Affecting Catalytic Reactions at Solid–Liquid Interfaces. *ACS Catal.* **2016**, 6 (12). <https://doi.org/10.1021/acscatal.6b02532>.
- (39) Sun, H.; Chao, J.; Zuo, X.; Su, S.; Liu, X.; Yuwen, L.; Fan, C.; Wang, L. Gold Nanoparticle-Decorated MoS₂ Nanosheets for Simultaneous Detection of Ascorbic Acid, Dopamine and Uric Acid. *RSC Adv.* **2014**, 4 (52), 27625–27629. <https://doi.org/10.1039/c4ra04046e>.
- (40) Farida, A. N.; Fitriany, E.; Baktir, A.; Kurniawan, F.; Harsini, M. Voltammetric Study of Ascorbic Acid Using Polymelamine/Gold Nanoparticle Modified Carbon Paste Electrode. *IOP Conf. Ser. Earth Environ. Sci.* **2019**, 217 (1). <https://doi.org/10.1088/1755-1315/217/1/012004>.
- (41) Gao, S.; Li, H.; Li, M.; Li, C.; Qian, L.; Yang, B. A Gold-Nanoparticle/Horizontal-

- Graphene Electrode for the Simultaneous Detection of Ascorbic Acid, Dopamine, Uric Acid, Guanine, and Adenine. *J. Solid State Electrochem.* **2018**, 22 (10), 3245–3254. <https://doi.org/10.1007/s10008-018-4019-7>.
- (42) Xu, X.; Duan, G.; Li, Y.; Liu, G.; Wang, J.; Zhang, H.; Dai, Z.; Cai, W. Fabrication of Gold Nanoparticles by Laser Ablation in Liquid and Their Application for Simultaneous Electrochemical Detection of Cd²⁺, Pb²⁺, Cu²⁺, Hg²⁺. *ACS Appl. Mater. Interfaces* **2014**, 6 (1), 65–71. <https://doi.org/10.1021/am404816e>.
- (43) Ting, S. L.; Ee, S. J.; Ananthanarayanan, A.; Leong, K. C.; Chen, P. Graphene Quantum Dots Functionalized Gold Nanoparticles for Sensitive Electrochemical Detection of Heavy Metal Ions. *Electrochim. Acta* **2015**, 172, 7–11. <https://doi.org/10.1016/j.electacta.2015.01.026>.
- (44) Draz, M. S.; Shafiee, H. Applications of Gold Nanoparticles in Virus Detection. *Theranostics* **2018**, 8 (7), 1985–2017. <https://doi.org/10.7150/thno.23856>.
- (45) Chowdhury, A. D.; Takemura, K.; Li, T. C.; Suzuki, T.; Park, E. Y. Electrical Pulse-Induced Electrochemical Biosensor for Hepatitis E Virus Detection. *Nat. Commun.* **2019**, 10 (1), 4–7. <https://doi.org/10.1038/s41467-019-11644-5>.
- (46) Schaefer, H.-E.; Schaefer, H.-E. IntroductionIntroduction and Some Physical Principlesphysical Principles. In *Nanoscience*; Springer Berlin Heidelberg, 2010; pp 1–47. https://doi.org/10.1007/978-3-642-10559-3_1.
- (47) Shim, J. H.; Kim, J.; Lee, C.; Lee, Y. Electrocatalytic Activity of Gold and Gold Nanoparticles Improved by Electrochemical Pretreatment. *J. Phys. Chem. C* **2011**, 115 (1), 305–309. <https://doi.org/10.1021/jp1067507>.
- (48) Wang, L.; Tang, Z.; Yan, W.; Yang, H.; Wang, Q.; Chen, S. Porous Carbon-Supported

- Gold Nanoparticles for Oxygen Reduction Reaction: Effects of Nanoparticle Size. *ACS Appl. Mater. Interfaces* **2016**, *8* (32), 20635–20641. <https://doi.org/10.1021/acsami.6b02223>.
- (49) Tao, Z.; Wu, Z.; Yuan, X.; Wu, Y.; Wang, H. Copper-Gold Interactions Enhancing Formate Production from Electrochemical CO₂ Reduction. *ACS Catal.* **2019**, *9* (12), 10894–10898. <https://doi.org/10.1021/acscatal.9b03158>.
- (50) Tran, T. D.; Nguyen, M. T. T.; Le, H. V.; Nguyen, D. N.; Truong, Q. D.; Tran, P. D. Gold Nanoparticles as an Outstanding Catalyst for the Hydrogen Evolution Reaction. *Chem. Commun.* **2018**, *54* (27), 3363–3366. <https://doi.org/10.1039/c8cc00038g>.
- (51) Zhao, S.; Jin, R.; Abroshan, H.; Zeng, C.; Zhang, H.; House, S. D.; Gottlieb, E.; Kim, H. J.; Yang, J. C.; Jin, R. Gold Nanoclusters Promote Electrocatalytic Water Oxidation at the Nanocluster/CoSe₂ Interface. *J. Am. Chem. Soc.* **2017**, *139* (3), 1077–1080. <https://doi.org/10.1021/jacs.6b12529>.
- (52) Jeelani, S.; Jagat Reddy, R. C.; Maheswaran, T.; Asokan, G. S.; Dany, A.; Anand, B. Theranostics: A Treasured Tailor for Tomorrow. *J. Pharm. Bioallied Sci.* **2014**, *6* (SUPPL. 1), 6–9. <https://doi.org/10.4103/0975-7406.137249>.
- (53) Zhu, G.; Chen, X. Aptamer-Based Targeted Therapy. *Adv. Drug Deliv. Rev.* **2018**, *134*, 65–78. <https://doi.org/10.1016/j.addr.2018.08.005>.
- (54) Gautam, A.; Van Veggel, F. C. J. M. Synthesis of Nanoparticles, Their Biocompatibility, and Toxicity Behavior for Biomedical Applications. *J. Mater. Chem. B* **2013**, *1* (39), 5186–5200. <https://doi.org/10.1039/c3tb20738b>.
- (55) Jena, P.; Bhattacharya, M.; Bhattacharjee, G.; Satpati, B.; Mukherjee, P.; Senapati, D.; Srinivasan, R. Bimetallic Gold-Silver Nanoparticles Mediate Bacterial Killing by

- Disrupting the Actin Cytoskeleton MreB. *Nanoscale* **2020**, *12* (6), 3731–3749.
<https://doi.org/10.1039/c9nr10700b>.
- (56) Holleran, E. M. The Beer-Lambert Law and the Combination of Proportional Dependences. *J. Chem. Educ.* **1955**, *32* (12), 636–637. <https://doi.org/10.1021/ed032p636>.
- (57) Haiss, W.; Thanh, N. T. K.; Aveyard, J.; Fernig, D. G. Determination of Size and Concentration of Gold Nanoparticles from UV-Vis Spectra. *Anal. Chem.* **2007**, *79* (11), 4215–4221. <https://doi.org/10.1021/ac0702084>.
- (58) Agrawal, A.; Kriegel, I.; Milliron, D. J. Shape-Dependent Field Enhancement and Plasmon Resonance of Oxide Nanocrystals. *J. Phys. Chem. C* **2015**, *119* (11), 6227–6238. <https://doi.org/10.1021/acs.jpcc.5b01648>.
- (59) Li, N.; Zhao, P.; Astruc, D. Anisotropic Gold Nanoparticles: Synthesis, Properties, Applications, and Toxicity. *Angew. Chemie Int. Ed.* **2014**, *53* (7), 1756–1789. <https://doi.org/10.1002/anie.201300441>.
- (60) Shi, W.; Casas, J.; Venkataramasubramani, M.; Tang, L. Synthesis and Characterization of Gold Nanoparticles with Plasmon Absorbance Wavelength Tunable from Visible to Near Infrared Region. *ISRN Nanomater.* **2012**, *2012*, 1–9. <https://doi.org/10.5402/2012/659043>.
- (61) Chen, H.; Kou, X.; Yang, Z.; Ni, W.; Wang, J. Shape- and Size-Dependent Refractive Index Sensitivity of Gold Nanoparticles. *Langmuir* **2008**, *24* (10), 5233–5237. <https://doi.org/10.1021/la800305j>.
- (62) Amendola, V.; Meneghetti, M. Size Evaluation of Gold Nanoparticles by UV-Vis Spectroscopy. *J. Phys. Chem. C* **2009**, *113* (11), 4277–4285. <https://doi.org/10.1021/jp8082425>.

- (63) Godfrey, I. J.; Dent, A. J.; Parkin, I. P.; Maenosono, S.; Sankar, G. Structure of Gold--Silver Nanoparticles. *J. Phys. Chem. C* **2017**, *121* (3), 1957–1963.
- (64) Stetefeld, J.; McKenna, S. A.; Patel, T. R. Dynamic Light Scattering: A Practical Guide and Applications in Biomedical Sciences. *Biophys. Rev.* **2016**, *8* (4), 409–427. <https://doi.org/10.1007/s12551-016-0218-6>.
- (65) Tucker, I. M.; Corbett, J. C. W.; Fatkin, J.; Jack, R. O.; Kaszuba, M.; MacCreath, B.; McNeil-Watson, F. Laser Doppler Electrophoresis Applied to Colloids and Surfaces. *Curr. Opin. Colloid Interface Sci.* **2015**, *20* (4), 215–226. <https://doi.org/10.1016/j.cocis.2015.07.001>.
- (66) Oswald, S. *X-Ray Photoelectron Spectroscopy in Analysis of Surfaces*; 2013. <https://doi.org/10.1002/9780470027318.a2517.pub2>.
- (67) Bunaciu, A. A.; Udriștioiu, E. gabriela; Aboul-Enein, H. Y. X-Ray Diffraction: Instrumentation and Applications. *Crit. Rev. Anal. Chem.* **2015**, *45* (4), 289–299. <https://doi.org/10.1080/10408347.2014.949616>.
- (68) Trevizan, L. C.; Nóbrega, J. A. Inductively Coupled Plasma Optical Emission Spectrometry with Axially Viewed Configuration: An Overview of Applications. *J. Braz. Chem. Soc.* **2007**, *18* (4), 678–690. <https://doi.org/10.1590/S0103-50532007000400003>.
- (69) Vahabi, S.; Nazemi Salman, B.; Javanmard, A. Atomic Force Microscopy Application in Biological Research: A Review Study. *Iran. J. Med. Sci.* **2013**, *38* (2), 76–83.
- (70) Hayes, T. L.; Pease, R. F. *The Scanning Electron Microscope: Principles and Applications in Biology and Medicine.*; ACADEMIC PRESS, INC., 1968; Vol. 12. <https://doi.org/10.1016/b978-1-4831-9928-3.50006-0>.
- (71) Winey, M.; Meehl, J. B.; O'Toole, E. T.; Giddings, T. H. Conventional Transmission

- Electron Microscopy. *Mol. Biol. Cell* **2014**, 25 (3), 319–323.
<https://doi.org/10.1091/mbc.E12-12-0863>.
- (72) Bard, A. J.; Faulkner, L. R. *Electrochemical Methods: Fundamentals and Applications*, 2nd Editio.; Wiley; New York, 2001.
- (73) Wang, J.; McEntee, M.; Tang, W.; Neurock, M.; Baddorf, A. P.; Maksymovych, P.; Yates, J. T. Formation, Migration, and Reactivity of Au–CO Complexes on Gold Surfaces. *J. Am. Chem. Soc.* **2016**, 138 (5), 1518–1526.
<https://doi.org/10.1021/jacs.5b09052>.
- (74) McEntee, M.; Tang, W.; Neurock, M.; Yates, J. T. Selective Catalytic Oxidative-Dehydrogenation of Carboxylic Acids—Acrylate and Crotonate Formation at the Au/TiO₂ Interface. *J. Am. Chem. Soc.* **2014**, 136 (13), 5116–5120.
<https://doi.org/10.1021/ja500928h>.
- (75) Green, I. X.; Tang, W.; Neurock, M.; Yates, J. T. Insights into Catalytic Oxidation at the Au/TiO₂ Dual Perimeter Sites. *Acc. Chem. Res.* **2014**, 47 (3), 805–815.
<https://doi.org/10.1021/ar400196f>.
- (76) Xu, Y.; Chen, L.; Wang, X.; Yao, W.; Zhang, Q. Recent Advances in Noble Metal Based Composite Nanocatalysts: Colloidal Synthesis, Properties, and Catalytic Applications. *Nanoscale* **2015**, 7 (24), 10559–10583. <https://doi.org/10.1039/C5NR02216A>.
- (77) Jiang, J.; Du, X. Sensitive Electrochemical Sensors for Simultaneous Determination of Ascorbic Acid, Dopamine, and Uric Acid Based on Au@Pd-Reduced Graphene Oxide Nanocomposites. *Nanoscale* **2014**, 6 (19), 11303–11309.
<https://doi.org/10.1039/C4NR01774A>.
- (78) Pedireddy, S.; Lee, H. K.; Tjiu, W. W.; Phang, I. Y.; Tan, H. R.; Chua, S. Q.; Troadec, C.;

- Ling, X. Y. One-Step Synthesis of Zero-Dimensional Hollow Nanoporous Gold Nanoparticles with Enhanced Methanol Electrooxidation Performance. *Nat. Commun.* **2014**, *5*, 4947. <https://doi.org/10.1038/ncomms5947>.
- (79) Lang, X.-Y.; Fu, H.-Y.; Hou, C.; Han, G.-F.; Yang, P.; Liu, Y.-B.; Jiang, Q. Nanoporous Gold Supported Cobalt Oxide Microelectrodes as High-Performance Electrochemical Biosensors. *Nat. Commun.* **2013**, *4*, 2169. <https://doi.org/10.1038/ncomms3169>.
- (80) Chin, Y.-H.; Buda, C.; Neurock, M.; Iglesia, E. Reactivity of Chemisorbed Oxygen Atoms and Their Catalytic Consequences during CH_4 – O_2 Catalysis on Supported Pt Clusters. *J. Am. Chem. Soc.* **2011**, *133* (40), 15958–15978. <https://doi.org/10.1021/ja202411v>.
- (81) Falicov, L. M.; Somorjai, G. A. Correlation between Catalytic Activity and Bonding and Coordination Number of Atoms and Molecules on Transition Metal Surfaces: Theory and Experimental Evidence. *Proc. Natl. Acad. Sci.* **1985**, *82* (8), 2207–2211.
- (82) Fujita, T.; Guan, P.; McKenna, K.; Lang, X.; Hirata, A.; Zhang, L.; Tokunaga, T.; Arai, S.; Yamamoto, Y.; Tanaka, N.; et al. Atomic Origins of the High Catalytic Activity of Nanoporous Gold. *Nat. Mater.* **2012**, *11* (9), 775–780. <https://doi.org/10.1038/nmat3391>.
- (83) Lopez-Acevedo, O.; Kacprzak, K. A.; Akola, J.; Häkkinen, H. Quantum Size Effects in Ambient CO Oxidation Catalysed by Ligand-Protected Gold Clusters. *Nat. Chem.* **2010**, *2* (4), 329–334. <https://doi.org/10.1038/nchem.589>.
- (84) Stoeva, S. I.; Prasad, B. L. V.; Uma, S.; Stoimenov, P. K.; Zaikovski, V.; Christopher M. Sorensen, A.; Klabunde, K. J. Face-Centered Cubic and Hexagonal Closed-Packed Nanocrystal Superlattices of Gold Nanoparticles Prepared by Different Methods†. *J Phys Chem B* **2003**, *107* (30), 7441–7448. <https://doi.org/10.1021/JP030013+>.
- (85) Hill, H. D.; Macfarlane, R. J.; Senesi, A. J.; Lee, B.; Park, S. Y.; Mirkin, C. A. Controlling

- the Lattice Parameters of Gold Nanoparticle FCC Crystals with Duplex DNA Linkers. *Nano Lett.* **2008**, 8 (8), 2341–2344. <https://doi.org/10.1021/nl8011787>.
- (86) Lacroix, L.-M.; Frey Huls, N.; Ho, D.; Sun, X.; Cheng, K.; Sun, S. Stable Single-Crystalline Body Centered Cubic Fe Nanoparticles. *Nano Lett.* **2011**, 11 (4), 1641–1645. <https://doi.org/10.1021/nl200110t>.
- (87) Harfenist, S. A.; Wang, Z. L.; Whetten, R. L.; Vezmar, I.; Alvarez, M. M. Three-Dimensional Hexagonal Close-Packed Superlattice of Passivated Ag Nanocrystals. *Adv. Mater.* **1997**, 9 (10), 817–822. <https://doi.org/10.1002/adma.19970091012>.
- (88) Zhang, J.; Kumbhar, A.; He, J.; Das, N. C.; Yang, K.; Wang, J.-Q.; Wang, H.; Stokes, K. L.; Fang, J. Simple Cubic Super Crystals Containing PbTe Nanocubes and Their Core–Shell Building Blocks. *J. Am. Chem. Soc.* **2008**, 130 (45), 15203–15209. <https://doi.org/10.1021/ja806120w>.
- (89) Eberhart, J. G.; Horner, S. Bond-Energy and Surface-Energy Calculations in Metals. *J. Chem. Educ.* **2010**, 87 (6), 608–612. <https://doi.org/10.1021/ed100189v>.
- (90) Wang, Z. L. Transmission Electron Microscopy of Shape-Controlled Nanocrystals and Their Assemblies. *J Phys Chem B* **2000**, 104 (6), 1153–1175. <https://doi.org/10.1021/JP993593C>.
- (91) Callister, W. D. *Materials Science and Engineering : An Introduction*, 6th ed.; John Wiley & Sons: New York, 2003.
- (92) Huang, Y.-Y.; Hsu, J.-Y.; Hsin-Lung Chen, A.; Hashimoto, T. Existence of Fcc-Packed Spherical Micelles in Diblock Copolymer Melt. *Macromolecules* **2007**, 40 (3), 406–409. <https://doi.org/10.1021/MA062149M>.
- (93) And, J. B.; Lodge, T. P. Mechanisms and Epitaxial Relationships between Close-Packed

- and BCC Lattices in Block Copolymer Solutions. *J Phys Chem B* **2003**, *107* (44), 12071–12081. <https://doi.org/10.1021/JP035065D>.
- (94) Pandey, A. D.; Güttel, R.; Leoni, M.; Schüth, F.; Weidenthaler, C. Influence of the Microstructure of Gold–Zirconia Yolk–Shell Catalysts on the CO Oxidation Activity. *J. Phys. Chem. C* **2010**, *114* (45), 19386–19394. <https://doi.org/10.1021/jp106436h>.
- (95) Hall, J. W.; Rase, H. F. Relation between Dislocation Density and Catalytic Activity and Effects of Physical Treatment. *Ind. Eng. Chem. Fundam.* **1964**, *3* (2), 158–167. <https://doi.org/10.1021/i160010a013>.
- (96) THOMAS, J. M.; EVANS, E. L. Enhanced Reactivity at Dislocations in Layer Structures. *Nature* **1967**, *214* (5084), 167–168. <https://doi.org/10.1038/214167a0>.
- (97) Liu, H. *Ammonia Synthesis Catalysts*; Ltd., W. S. P. C. P., Ed.; WORLD SCIENTIFIC / CHEMICAL INDUSTRY PRESS, CHINA, 2013. <https://doi.org/10.1142/8199>.
- (98) Mandal, D.; Mondal, S.; Senapati, D.; Satpati, B.; Sangaranarayanan, M. V. Charge Density Modulated Shape-Dependent Electrocatalytic Activity of Gold Nanoparticles for the Oxidation of Ascorbic Acid. *J. Phys. Chem. C* **2015**, *119* (40), 23103–23112. <https://doi.org/10.1021/acs.jpcc.5b07710>.
- (99) Zhu, X.; Chunwei Yuan, A.; Chen, H. Photocatalytic Degradation of Pesticide Pyridaben. 3. In Surfactant/TiO₂ Aqueous Dispersions. *Environ. Sci. Technol.* **2007**, *41* (1), 263–269. <https://doi.org/10.1021/ES061178+>.
- (100) Murugadoss, A.; Chattopadhyay, A. Surface Area Controlled Differential Catalytic Activities of One-Dimensional Chain-like Arrays of Gold Nanoparticles. *J. Phys. Chem. C* **2008**, *112* (30), 11265–11271. <https://doi.org/10.1021/jp802605n>.
- (101) Gao, Z.; Siow, K. S.; Ng, A.; Zhang, Y. ANALYTICA CHIMICA ACTA

- Determination of Ascorbic Acid in a Mixture of Ascorbic Acid and Uric Acid at a Chemically Modified Electrode. *Anal. Chim. Acta* **1997**, *343*, 49–57.
- (102) Sagara, T.; Naoyuki Kato, A.; Nakashima, N. Electreflectance Study of Gold Nanoparticles Immobilized on an Aminoalkanethiol Monolayer Coated on a Polycrystalline Gold Electrode Surface. *J Phys Chem B* **2002**, *106* (6), 1205–1212. <https://doi.org/10.1021/JP011807W>.
- (103) Štrbac, S.; Adžić, R. R. The Influence of OH[–] Chemisorption on the Catalytic Properties of Gold Single Crystal Surfaces for Oxygen Reduction in Alkaline Solutions. *J. Electroanal. Chem.* **1996**, *403* (1–2), 169–181. [https://doi.org/10.1016/0022-0728\(95\)04389-6](https://doi.org/10.1016/0022-0728(95)04389-6).
- (104) Štrbac, S.; Adžić, R. R. The Influence of PH on Reaction Pathways for O₂ Reduction on the Au(100) Face. *Electrochim. Acta* **1996**, *41* (18), 2903–2908. [https://doi.org/10.1016/0013-4686\(96\)00120-X](https://doi.org/10.1016/0013-4686(96)00120-X).
- (105) El-Deab, M. S.; Sotomura, T.; Ohsaka, T. Oxygen Reduction at Electrochemically Deposited Crystallographically Oriented Au(1 0 0)-like Gold Nanoparticles. *Electrochem. commun.* **2005**, *7* (1), 29–34. <https://doi.org/10.1016/J.ELECOM.2004.10.010>.
- (106) Ben Aoun, S.; Dursun, Z.; Sotomura, T.; Taniguchi, I. Effect of Metal Ad-Layers on Au(1 1 1) Electrodes on Electrocatalytic Reduction of Oxygen in an Alkaline Solution. *Electrochem. commun.* **2004**, *6* (8), 747–752. <https://doi.org/10.1016/J.ELECOM.2004.05.026>.
- (107) Zreik, T. G.; Kodaman, P. H.; Jones, E. E.; Olive, D. L.; Behrman, H. Identification and Characterization of an Ascorbic Acid Transporter in Human Granulosa-lutein Cells. *Mol. Hum. Reprod.* **1999**, *5* (4), 299–302. <https://doi.org/10.1093/molehr/5.4.299>.

- (108) Kim, Y.; Kim, M.-G. HPLC-UV Method for the Simultaneous Determinations of Ascorbic Acid and Dehydroascorbic Acid in Human Plasma. *Transl. Clin. Pharmacol.* **2016**, *24* (1), 37. <https://doi.org/10.12793/tcp.2016.24.1.37>.
- (109) Finley, J. W.; Duang, E. Resolution of Ascorbic, Dehydroascorbic and Diketogulonic Acids by Paire-Ion Reversed-Phase Chromatography. *J. Chromatogr. A* **1981**, *207* (3), 449–453. [https://doi.org/10.1016/S0021-9673\(00\)88753-1](https://doi.org/10.1016/S0021-9673(00)88753-1).
- (110) Leubolt, R.; Klein, H. Determination of Sulphite and Ascorbic Acid by High-Performance Liquid Chromatography with Electrochemical Detection. *J. Chromatogr. A* **1993**, *640* (1–2), 271–277. [https://doi.org/10.1016/0021-9673\(93\)80190-J](https://doi.org/10.1016/0021-9673(93)80190-J).
- (111) Khan, A. F.; Brownson, D. A. C.; Randviir, E. P.; Smith, G. C.; Banks, C. E. 2D Hexagonal Boron Nitride (2D-HBN) Explored for the Electrochemical Sensing of Dopamine. *Anal. Chem.* **2016**, *88* (19), 9729–9737. <https://doi.org/10.1021/acs.analchem.6b02638>.
- (112) Muguruma, H.; Inoue, Y.; Inoue, H.; Ohsawa, T. Electrochemical Study of Dopamine at Electrode Fabricated by Cellulose-Assisted Aqueous Dispersion of Long-Length Carbon Nanotube. *J. Phys. Chem. C* **2016**, *120* (22), 12284–12292. <https://doi.org/10.1021/acs.jpcc.6b03715>.
- (113) Jiang, L.; Nelson, G. W.; Abda, J.; Foord, J. S. Novel Modifications to Carbon-Based Electrodes to Improve the Electrochemical Detection of Dopamine. *ACS Appl. Mater. Interfaces* **2016**, *8* (42), 28338–28348. <https://doi.org/10.1021/acsami.6b03879>.
- (114) Greivenkamp, J. E. *Field Guide to Geometrical Optics*; SPIE Press, 2004.
- (115) Kresse, G.; Hafner, J. *Ab Initio* Molecular Dynamics for Liquid Metals. *Phys. Rev. B* **1993**, *47* (1), 558–561. <https://doi.org/10.1103/PhysRevB.47.558>.

- (116) Kresse, G.; Hafner, J. *Ab Initio* Molecular-Dynamics Simulation of the Liquid-Metal–Amorphous-Semiconductor Transition in Germanium. *Phys. Rev. B* **1994**, *49* (20), 14251–14269. <https://doi.org/10.1103/PhysRevB.49.14251>.
- (117) Kresse, G.; Joubert, D. From Ultrasoft Pseudopotentials to the Projector Augmented-Wave Method. *Phys. Rev. B* **1999**, *59* (3), 1758–1775. <https://doi.org/10.1103/PhysRevB.59.1758>.
- (118) Perdew, J. P.; Chevary, J. A.; Vosko, S. H.; Jackson, K. A.; Pederson, M. R.; Singh, D. J.; Fiolhais, C. Atoms, Molecules, Solids, and Surfaces: Applications of the Generalized Gradient Approximation for Exchange and Correlation. *Phys. Rev. B* **1992**, *46* (11), 6671–6687. <https://doi.org/10.1103/PhysRevB.46.6671>.
- (119) Grimme, S.; Antony, J.; Ehrlich, S.; Krieg, H. A Consistent and Accurate *Ab Initio* Parametrization of Density Functional Dispersion Correction (DFT-D) for the 94 Elements H–Pu. *J. Chem. Phys.* **2010**, *132* (15), 154104. <https://doi.org/10.1063/1.3382344>.
- (120) Lee, C.; Yang, W.; Parr, R. G. Development of the Colle-Salvetti Correlation-Energy Formula into a Functional of the Electron Density. *Phys. Rev. B* **1988**, *37* (2), 785–789. <https://doi.org/10.1103/PhysRevB.37.785>.
- (121) Miehlich, B.; Savin, A.; Stoll, H.; Preuss, H. Results Obtained with the Correlation Energy Density Functionals of Becke and Lee, Yang and Parr. *Chem. Phys. Lett.* **1989**, *157* (3), 200–206. [https://doi.org/10.1016/0009-2614\(89\)87234-3](https://doi.org/10.1016/0009-2614(89)87234-3).
- (122) Becke, A. D. Density-functional Thermochemistry. III. The Role of Exact Exchange. *J. Chem. Phys.* **1993**, *98* (7), 5648–5652. <https://doi.org/10.1063/1.464913>.
- (123) Fang, R.; Yang, L. Mechanism of the Gold(I)-Catalyzed Rearrangement of Alkynyl

- Sulfoxides: A DFT Study. *Organometallics* **2012**, *31* (8), 3043–3055.
<https://doi.org/10.1021/om201159t>.
- (124) Preuß, D. A. H. D. S. Energy-Adjustedab Initio Pseudopotentials for the Second and Third Row Transition Elements. *Theor. Chim. Acta* **1990**, *77* (2), 123–141.
<https://doi.org/10.1007/BF01114537>.
- (125) Weigend, F.; Furche, F.; Ahlrichs, R. Gaussian Basis Sets of Quadruple Zeta Valence Quality for Atoms H–Kr. *J. Chem. Phys.* **2003**, *119* (24), 12753–12762.
<https://doi.org/10.1063/1.1627293>.
- (126) Frisch, M. J.; Trucks, G.W.; Schlegel, H. B.; Scuseria, G. E.; Robb, M. A.; Cheeseman, J. R.; Scalmani, G.; Barone, V.; Mennucci, B.; Petersson, G. A.; Nakatsuji, H.; Caricato, M.; Li, X.; Hratchian, H. P.; Izmaylov, A. F.; Bloino, J.; Zheng, G.; Sonnenbe, D. J. Gaussian 09. *Gaussian, Inc. Wallingford CT*. 2009. <https://doi.org/111>.
- (127) Pal, P.; Singha, R. K.; Saha, A.; Bal, R.; Panda, A. B. Defect-Induced Efficient Partial Oxidation of Methane over Nonstoichiometric Ni/CeO₂ Nanocrystals. *J. Phys. Chem. C* **2015**, *119* (24), 13610–13618. <https://doi.org/10.1021/acs.jpcc.5b01724>.
- (128) Kelly, A. (Anthony); Groves, G. W.; Kidd, P. *Crystallography and Crystal Defects*; John Wiley & Sons, 2000.
- (129) McCarty, K. F.; Nobel, J. A.; Bartelt, N. C. Vacancies in Solids and the Stability of Surface Morphology. *Nature* **2001**, *412* (6847), 622–625.
<https://doi.org/10.1038/35088026>.
- (130) Ganesh, P. A.; Jeyakumar, D. Intriguing Catalytic Activity of Surface Active Gold-Platinum Islands on Nano-Porous Au in Determining Efficient Direct Formic Acid Oxidation Pathway. *ChemistrySelect* **2017**, *2* (12), 3562–3571.

<https://doi.org/10.1002/slct.201700670>.

- (131) Peterson, A. A.; Abild-Pedersen, F.; Studt, F.; Rossmeisl, J.; Nørskov, J. K. How Copper Catalyzes the Electroreduction of Carbon Dioxide into Hydrocarbon Fuels. *Energy Environ. Sci.* **2010**, 3 (9), 1311. <https://doi.org/10.1039/c0ee00071j>.
- (132) Huang, B.; Jia, N.; Chen, L.; Tan, L.; Yao, S. Electrochemical Impedance Spectroscopy Study on Polymerization of L-Lysine on Electrode Surface and Its Application for Immobilization and Detection of Suspension Cells. *Anal. Chem.* **2014**, 86 (14), 6940–6947. <https://doi.org/10.1021/ac500753f>.
- (133) Retter, U.; Widmann, A.; Siegler, K.; Kahlert, H. On the Impedance of Potassium Nickel(II) Hexacyanoferrate(II) Composite Electrodes—the Generalization of the Randles Model Referring to Inhomogeneous Electrode Materials. *J. Electroanal. Chem.* **2003**, 546, 87–96. [https://doi.org/10.1016/S0022-0728\(03\)00150-5](https://doi.org/10.1016/S0022-0728(03)00150-5).
- (134) J. K. Nørskov; J. Rossmeisl; A. Logadottir, A.; Lindqvist, L.; Kitchin, J. R.; Bligaard, T.; Jónsson, H. Origin of the Overpotential for Oxygen Reduction at a Fuel-Cell Cathode. *J Phys Chem B* **2004**, 108, 17886–17892. <https://doi.org/10.1021/JP047349J>.
- (135) Liu, H.; Xiang, B.; Qu, L. Structure Analysis of Ascorbic Acid Using Near-Infrared Spectroscopy and Generalized Two-Dimensional Correlation Spectroscopy. *J. Mol. Struct.* **2006**, 794 (1–3), 12–17. <https://doi.org/10.1016/J.MOLSTRUC.2006.01.028>.
- (136) Pal, U.; Sen, S.; Maiti, N. C. C_α–H Carries Information of a Hydrogen Bond Involving the Geminal Hydroxyl Group: A Case Study with a Hydrogen-Bonded Complex of 1,1,1,3,3,3-Hexafluoro-2-Propanol and Tertiary Amines. *J. Phys. Chem. A* **2014**, 118 (6), 1024–1030. <https://doi.org/10.1021/jp411488a>.
- (137) Banerji, B.; Chatterjee, M.; Pal, U.; Maiti, N. C. Molecular Details of Acetate Binding to a

- New Diamine Receptor by NMR and FT-IR Analyses. *J. Phys. Chem. A* **2016**, *120* (15), 2330–2341. <https://doi.org/10.1021/acs.jpca.6b01078>.
- (138) Xu, T.-Q.; Zhang, Q.-L.; Zheng, J.-N.; Lv, Z.-Y.; Wei, J.; Wang, A.-J.; Feng, J.-J. Simultaneous Determination of Dopamine and Uric Acid in the Presence of Ascorbic Acid Using Pt Nanoparticles Supported on Reduced Graphene Oxide. *Electrochim. Acta* **2014**, *115*, 109–115. <https://doi.org/10.1016/J.ELECTACTA.2013.10.147>.
- (139) Chen, L.-X.; Zheng, J.-N.; Wang, A.-J.; Wu, L.-J.; Chen, J.-R.; Feng, J.-J. Facile Synthesis of Porous Bimetallic Alloyed PdAg Nanoflowers Supported on Reduced Graphene Oxide for Simultaneous Detection of Ascorbic Acid, Dopamine, and Uric Acid. *Analyst* **2015**, *140* (9), 3183–3192. <https://doi.org/10.1039/C4AN02200A>.
- (140) Ulvestad, A.; Clark, J. N.; Harder, R.; Robinson, I. K.; Shpyrko, O. G. 3D Imaging of Twin Domain Defects in Gold Nanoparticles. *Nano Lett.* **2015**, *15* (6), 4066–4070. <https://doi.org/10.1021/acs.nanolett.5b01104>.
- (141) Rapp, Ö. Superconductivity in Noble Metal Alloys: Correlations and Predictions. *Phys. Lett. A* **1977**, *64* (1), 75–77. [https://doi.org/10.1016/0375-9601\(77\)90532-1](https://doi.org/10.1016/0375-9601(77)90532-1).
- (142) Bagga, K.; Brougham, D. F.; Keyes De, T. E.; Brabazon, D. Cite This. *Phys. Chem. Chem. Phys* **2796**, *17*, 27968. <https://doi.org/10.1039/c5cp01219h>.
- (143) He, W.; Jia, H.; Yang, D.; Xiao, P.; Fan, X.; Zheng, Z.; Kim, H.-K.; Wamer, W. G.; Yin, J.-J. Composition Directed Generation of Reactive Oxygen Species in Irradiated Mixed Metal Sulfides Correlated with Their Photocatalytic Activities. *ACS Appl. Mater. Interfaces* **2015**, *7* (30), 16440–16449. <https://doi.org/10.1021/acsami.5b03626>.
- (144) Zou, L.; Yang, C.; Lei, Y.; Zakharov, D.; Wiezorek, J. M. K.; Su, D.; Yin, Q.; Li, J.; Liu, Z.; Stach, E. A.; et al. Dislocation Nucleation Facilitated by Atomic Segregation. *Nat.*

- Mater.* **2017**, *17* (1), 56–63. <https://doi.org/10.1038/nmat5034>.
- (145) Verdaguer-Casadevall, A.; Li, C. W.; Johansson, T. P.; Scott, S. B.; McKeown, J. T.; Kumar, M.; Stephens, I. E. L.; Kanan, M. W.; Chorkendorff, I. Probing the Active Surface Sites for CO Reduction on Oxide-Derived Copper Electrocatalysts. *J. Am. Chem. Soc.* **2015**, *137* (31), 9808–9811. <https://doi.org/10.1021/jacs.5b06227>.
- (146) Choi, S.-I.; Herron, J. A.; Scaranto, J.; Huang, H.; Wang, Y.; Xia, X.; Lv, T.; Park, J.; Peng, H.-C.; Mavrikakis, M.; et al. A Comprehensive Study of Formic Acid Oxidation on Palladium Nanocrystals with Different Types of Facets and Twin Defects. *ChemCatChem* **2015**, *7* (14), 2077–2084. <https://doi.org/10.1002/cctc.201500094>.
- (147) Greeley, J. P. Chemistry. Active Site of an Industrial Catalyst. *Science* **2012**, *336* (6083), 810–811. <https://doi.org/10.1126/science.1222974>.
- (148) Ohyama, J.; Koketsu, T.; Yamamoto, Y.; Arai, S.; Satsuma, A. Preparation of TiO₂-Supported Twinned Gold Nanoparticles by CO Treatment and Their CO Oxidation Activity † ChemComm. *Chem. Commun* **2015**, *51*, 15823–15826. <https://doi.org/10.1039/c5cc05484b>.
- (149) Kannan, P.; John, S. A. Determination of Nanomolar Uric and Ascorbic Acids Using Enlarged Gold Nanoparticles Modified Electrode. *Anal. Biochem.* **2009**, *386* (1), 65–72. <https://doi.org/10.1016/j.ab.2008.11.043>.
- (150) Sun, J.; Wang, F.; Liu, Y.; Ni, Y.; Zhou, H.; Guo, C. F.; Chen, S. Gold Micromeshes as Highly Active Electrocatalysts for Methanol Oxidation Reaction. *RSC Adv.* **2017**, *7* (36), 22479–22484. <https://doi.org/10.1039/C7RA02505J>.
- (151) Ristig, S.; Prymak, O.; Loza, K.; Gocyla, M.; Meyer-Zaika, W.; Heggen, M.; Raabe, D.; Epple, M. Cite This. *J. Mater. Chem. B* **2015**, *3*, 4654.

<https://doi.org/10.1039/c5tb00644a>.

- (152) Gabriella S. Métraux; Yunwei Charles Cao; Rongchao Jin, and; Mirkin*, C. A. Triangular Nanoframes Made of Gold and Silver. **2003**. <https://doi.org/10.1021/NL034097+>.
- (153) Xia, B.; He, F.; Li, L. Preparation of Bimetallic Nanoparticles Using a Facile Green Synthesis Method and Their Application. *Langmuir* **2013**, 29 (15), 4901–4907. <https://doi.org/10.1021/la400355u>.
- (154) Ai-Qin Wang, †; Chun-Ming Chang, ‡ and; Chung-Yuan Mou*, †. Evolution of Catalytic Activity of Au–Ag Bimetallic Nanoparticles on Mesoporous Support for CO Oxidation. **2005**. <https://doi.org/10.1021/JP051530Q>.
- (155) Wittstock, A.; Zielasek, V.; Biener, J.; Friend, C. M.; Bäumer, M. Nanoporous Gold Catalysts for Selective Gas-Phase Oxidative Coupling of Methanol at Low Temperature. *Science* **2010**, 327 (5963), 319–322. <https://doi.org/10.1126/science.1183591>.
- (156) Cheng, M.-J.; Clark, E. L.; Pham, H. H.; Bell, A. T.; Head-Gordon, M. Quantum Mechanical Screening of Single-Atom Bimetallic Alloys for the Selective Reduction of CO₂ to C₁ Hydrocarbons. *ACS Catal.* **2016**, 6 (11), 7769–7777. <https://doi.org/10.1021/acscatal.6b01393>.
- (157) Zhou, Y.; Zhu, Y.; Wang, Z.-Q.; Zou, S.; Ma, G.; Xia, M.; Kong, X.; Xiao, L.; Gong, X.-Q.; Fan, J. Catalytic Activity Control via Crossover between Two Different Microstructures. *J. Am. Chem. Soc.* **2017**, 139 (39), 13740–13748. <https://doi.org/10.1021/jacs.7b05476>.
- (158) Li, S.; Sellers, M. S.; Basaran, C.; Schultz, A. J.; Kofke, D. A. Lattice Strain Due to an Atomic Vacancy. *Int. J. Mol. Sci.* **2009**, 10 (6), 2798–2808.

- <https://doi.org/10.3390/ijms10062798>.
- (159) Zielasek, V.; Jürgens, B.; Schulz, C.; Biener, J.; Biener, M. M.; Hamza, A. V.; Bäumer, M. Gold Catalysts: Nanoporous Gold Foams. *Angew. Chemie Int. Ed.* **2006**, *45* (48), 8241–8244. <https://doi.org/10.1002/anie.200602484>.
- (160) Dowben, P. A.; Miller, A. *Surface Segregation Phenomena*; CRC Press, 1990.
- (161) Huang, S.-H.; Shih, Y.-C.; Wu, C.-Y.; Yuan, C.-J.; Yang, Y.-S.; Li, Y.-K.; Wu, T.-K. Detection of Serum Uric Acid Using the Optical Polymeric Enzyme Biochip System. *Biosens. Bioelectron.* **2004**, *19* (12), 1627–1633. <https://doi.org/10.1016/j.bios.2003.12.026>.
- (162) Nishida, Y.; Takahashi, Y.; Susa, N.; Kanou, N.; Nakayama, T.; Asai, S. Comparative Effect of Angiotensin II Type I Receptor Blockers on Serum Uric Acid in Hypertensive Patients with Type 2 Diabetes Mellitus: A Retrospective Observational Study. *Cardiovasc. Diabetol.* **2013**, *12* (1), 159. <https://doi.org/10.1186/1475-2840-12-159>.
- (163) Alderman, M.; Aiyyer, K. J. V. Uric Acid: Role in Cardiovascular Disease and Effects of Losartan. *Curr. Med. Res. Opin.* **2004**, *20* (3), 369–379. <https://doi.org/10.1185/030079904125002982>.
- (164) Karatzas, A.; Paridis, D.; Kozyrakis, D.; Tzortzis, V.; Samarinas, M.; Dailiana, Z.; Karachalios, T. Fanconi Syndrome in the Adulthood. The Role of Early Diagnosis and Treatment. *J. Musculoskelet. Neuronal Interact.* **2017**, *17* (4), 303–306.
- (165) Barbieri, L.; Verdoia, M.; Schaffer, A.; Marino, P.; Suryapranata, H.; De Luca, G.; Novara Atherosclerosis Study Group (NAS). Impact of Sex on Uric Acid Levels and Its Relationship with the Extent of Coronary Artery Disease: A Single-Centre Study. *Atherosclerosis* **2015**, *241* (1), 241–248.

<https://doi.org/10.1016/j.atherosclerosis.2015.03.030>.

- (166) Desideri, G.; Castaldo, G.; Lombardi, A.; Mussap, M.; Testa, A.; Pontremoli, R.; Punzi, L.; Borghi, C. Is It Time to Revise the Normal Range of Serum Uric Acid Levels? *Eur. Rev. Med. Pharmacol. Sci.* **2014**, *18* (9), 1295–1306.
- (167) He, D.; Zhang, Z.; Huang, Y.; Hu, Y.; Zhou, H.; Chen, D. Chemiluminescence Microflow Injection Analysis System on a Chip for the Determination of Uric Acid without Enzyme. *Luminescence* **2005**, *20* (20), 271–275. <https://doi.org/10.1002/bio.847>.
- (168) Martinez-Pérez, D.; Ferrer, M. L.; Mateo, C. R. A Reagent Less Fluorescent Sol-Gel Biosensor for Uric Acid Detection in Biological Fluids. *Anal. Biochem.* **2003**, *322* (2), 238–242. <https://doi.org/10.1016/J.AB.2003.08.018>.
- (169) Leshchinskaya, A. P.; Polyakova, I. V.; Groshikova, A. R.; Pisarev, O. A.; Panarin, E. F. Selective Sorption of Uric Acid by Novel Molecularly Imprinted Polymers. *Mol. Imprinting* **2013**, *1*, 17–26. <https://doi.org/10.2478/molim-2012-0003>.
- (170) Zare, H. R.; Memarzadeh, F.; Ardakani, M. M.; Namazian, M.; Golabi, S. M. Norepinephrine-Modified Glassy Carbon Electrode for the Simultaneous Determination of Ascorbic Acid and Uric Acid. *Electrochim. Acta* **2005**, *50* (16–17), 3495–3502. <https://doi.org/10.1016/J.ELECTACTA.2004.12.026>.
- (171) Lin, X.-Q.; Jin, G.-P. Monolayer Modification of Glassy Carbon Electrode by Using Propionylcholine for Selective Detection of Uric Acid. *Electrochim. Acta* **2005**, *50* (16–17), 3210–3216. <https://doi.org/10.1016/J.ELECTACTA.2004.11.057>.
- (172) Germain, V.; Li, J.; Ingert, D.; Z. L. Wang, A.; Pileni, M. P. Stacking Faults in Formation of Silver Nanodisks. *J. Phys. Chem. B* **2003**, *107* (34), 8717–8720. <https://doi.org/10.1021/JP0303826>.

- (173) Yugang Sun; Brian T. Mayers, and; Xia*, Y. Template-Engaged Replacement Reaction: A One-Step Approach to the Large-Scale Synthesis of Metal Nanostructures with Hollow Interiors. **2002**. <https://doi.org/10.1021/NL025531V>.
- (174) Mandal, A.; Bhattacharya, M.; Kuznetsov, D. V.; Ghosh, T.; Das Chakraborty, S.; Satpati, B.; Mazov, V.; Senapati, D. Decoupled In-Plane Dipole Resonance Modulated Colorimetric Assay-Based Optical Ruler for Ultra-Trace Gold (Au) Detection. *Sci. Rep.* **2018**, 8 (1), 868. <https://doi.org/10.1038/s41598-018-19148-w>.
- (175) Durukanog-tildelu, S.; Kara, A.; Rahman, T. S. Local Structural and Vibrational Properties of Stepped Surfaces: Cu(211), Cu(511), and Cu(331). *Phys. Rev. B* **1997**, 55 (20), 13894–13903. <https://doi.org/10.1103/PhysRevB.55.13894>.
- (176) Kara, A.; Durukanoglu, S.; Rahman, T. S. Vibrational Dynamics and Thermodynamics of Ni(977). *J. Chem. Phys.* **1998**, 106 (5), 2031. <https://doi.org/10.1063/1.473309>.
- (177) Walsh, M. J.; Yoshida, K.; Kuwabara, A.; Pay, M. L.; Gai, P. L.; Boyes, E. D. On the Structural Origin of the Catalytic Properties of Inherently Strained Ultrasmall Decahedral Gold Nanoparticles. *Nano Lett.* **2012**, 12 (4), 2027–2031. <https://doi.org/10.1021/nl300067q>.
- (178) Dingreville, R.; Qu, J.; Cherkaoui, M. Surface Free Energy and Its Effect on the Elastic Behavior of Nano-Sized Particles, Wires and Films ARTICLE IN PRESS. *J. Mech. Phys. Solids* **2005**, 53, 1827–1854. <https://doi.org/10.1016/j.jmps.2005.02.012>.
- (179) Tjeng, L. H.; Meinders, M. B. J.; van Elp, J.; Ghijsen, J.; Sawatzky, G. A.; Johnson, R. L. Electronic Structure of Ag_2O . *Phys. Rev. B* **1990**, 41 (5), 3190–3199. <https://doi.org/10.1103/PhysRevB.41.3190>.
- (180) Chimentão, R. J.; Cota, I.; Dafinov, A.; Medina, F.; Sueiras, J. E.; Gómez De La Fuente, J.

- L.; Fierro, J. L. G.; Cesteros, Y.; Salagre, P. Synthesis of Silver-Gold Alloy Nanoparticles by a Phase-Transfer System. **2019**. <https://doi.org/10.1557/JMR.2006.0014>.
- (181) Chee, S. W.; Tan, S. F.; Baraissov, Z.; Bosman, M.; Mirsaidov, U. Direct Observation of the Nanoscale Kirkendall Effect during Galvanic Replacement Reactions. *Nat. Commun.* **2017**, 8 (1), 1224. <https://doi.org/10.1038/s41467-017-01175-2>.
- (182) Ding, Y.; Chen, M. Nanoporous Metals for Catalytic and Optical Applications. *MRS Bull.* **2009**, 34 (08), 569–576. <https://doi.org/10.1557/mrs2009.156>.
- (183) Beatty, M. F.; Hayes, M. A. *Mechanics and Mathematics of Crystals*; WORLD SCIENTIFIC, 2005. <https://doi.org/10.1142/5795>.
- (184) Stocks, G. M.; Gonis, A. *Alloy Phase Stability*; Springer Netherlands, 1989.
- (185) Zhang, X.; Sun, X.; Guo, S.-X.; Bond, A. M.; Zhang, J. Formation of Lattice-Dislocated Bismuth Nanowires on Copper Foam for Enhanced Electrocatalytic CO₂ Reduction at Low Overpotential. *Energy Environ. Sci.* **2019**. <https://doi.org/10.1039/C9EE00018F>.
- (186) Xu, C.; Su, J.; Xu, X.; Liu, P.; Zhao, H.; Fang Tian, A.; Yi Ding. Low Temperature CO Oxidation over Unsupported Nanoporous Gold. *J. Am. Chem. Soc.* **2007**, 129 (1), 42–43. <https://doi.org/10.1021/JA0675503>.
- (187) Molina, L. M.; Hammer, B. Theoretical Study of CO Oxidation on Au Nanoparticles Supported by MgO(100). *Phys. Rev. B* **2004**, 69 (15), 155424. <https://doi.org/10.1103/PhysRevB.69.155424>.
- (188) Jiang, J.; Ou-Yang, L.; Zhu, L.; Zou, J.; Tang, H. Novel One-Pot Fabrication of Lab-on-a-Bubble@Ag Substrate without Coupling-Agent for Surface Enhanced Raman Scattering. *Sci. Rep.* **2014**, 4, 3942. <https://doi.org/10.1038/srep03942>.
- (189) Ruban, A.; Hammer, B.; Stoltze, P.; Skriver, H. .; Nørskov, J. Surface Electronic Structure

- and Reactivity of Transition and Noble Metals. *J. Mol. Catal. A Chem.* **1997**, *115* (3), 421–429. [https://doi.org/10.1016/S1381-1169\(96\)00348-2](https://doi.org/10.1016/S1381-1169(96)00348-2).
- (190) Bayler, A.; Schier, A.; Graham A. Bowmaker, A.; Hubert Schmidbaur. Gold Is Smaller than Silver. Crystal Structures of [Bis(Trimesitylphosphine)Gold(I)] and [Bis(Trimesitylphosphine)Silver(I)] Tetrafluoroborate. *J. Am. Chem. Soc.*, *1996*, *118* **1996**, *118* (29), 7006–7007. <https://doi.org/10.1021/JA961363V>.
- (191) Schwerdtfeger, P.; Dolg, M.; Schwarz, W. H. E.; Bowmaker, G. A.; Boyd, P. D. W. Relativistic Effects in Gold Chemistry. I. Diatomic Gold Compounds. *J. Chem. Phys.* **1989**, *91* (3), 1762–1774. <https://doi.org/10.1063/1.457082>.
- (192) Schwerdtfeger, P.; Boyd, P. D. W.; Burrell, A. K.; Robinson, W. T.; Taylor, M. J. Relativistic Effects in Gold Chemistry. 3. Gold(I) Complexes. *Inorg. Chem.* **1990**, *29* (18), 3593–3607. <https://doi.org/10.1021/ic00343a057>.
- (193) Denton, A. R.; Ashcroft, N. W. Vegard's Law. *Phys. Rev. A* **1991**, *43* (6), 3161–3164. <https://doi.org/10.1103/PhysRevA.43.3161>.
- (194) Groß, A. Reactivity of Bimetallic Systems Studied from First Principles. *Top. Catal.* **2006**, *37* (1), 29–39. <https://doi.org/10.1007/s11244-006-0005-x>.
- (195) Kitchin, J. R.; Nørskov, J. K.; Barteau, M. A.; Chen, J. G. Role of Strain and Ligand Effects in the Modification of the Electronic and Chemical Properties of Bimetallic Surfaces. *Phys. Rev. Lett.* **2004**, *93* (15), 156801. <https://doi.org/10.1103/PhysRevLett.93.156801>.
- (196) and, J. S. H.; Karanfil*, T.; Serkiz, S. M. Removal and Sequestration of Iodide Using Silver-Impregnated Activated Carbon. **2002**. <https://doi.org/10.1021/ES010972M>.
- (197) Simic, M. G.; Jovanovic8, S. V. *Antioxidation Mechanisms of Uric Acid'I'*; 1989; Vol.

111.

- (198) Solutions - The Rare Earth Crisis - The Supply/Demand Situation for 2010–2015 | Sigma-Aldrich <https://www.sigmaaldrich.com/technical-documents/articles/material-matters/the-rare-earth-crisis.html> (accessed Jul 25, 2020).
- (199) Council, N. R. *Arsenic*; National Academies Press: Washington, D.C., 1977. <https://doi.org/10.17226/9003>.
- (200) Thomas, D. J. Is Arsenic an Aphrodisiac? The Sociochemistry of an Element. By William R. Cullen. *Angew. Chemie Int. Ed.* **2009**, 48 (7), 1188–1188. <https://doi.org/10.1002/anie.200885628>.
- (201) Cullen, W. R.; Reimer, K. J. Arsenic Speciation in the Environment. *Chem. Rev.* **1989**, 89 (4), 713–764. <https://doi.org/10.1021/cr00094a002>.
- (202) Kalluri, J. R.; Arbnesi, T.; Khan, S. A.; Neely, A.; Candice, P.; Varisli, B.; Washington, M.; McAfee, S.; Robinson, B.; Banerjee, S.; et al. Use of Gold Nanoparticles in a Simple Colorimetric and Ultrasensitive Dynamic Light Scattering Assay: Selective Detection of Arsenic in Groundwater. *Angew. Chemie - Int. Ed.* **2009**, 48 (51), 9668–9671. <https://doi.org/10.1002/anie.200903958>.
- (203) Boyle, R. W.; Jonasson, I. R. The Geochemistry of Arsenic and Its Use as an Indicator Element in Geochemical Prospecting. *J. Geochemical Explor.* **1973**, 2 (3), 251–296. [https://doi.org/10.1016/0375-6742\(73\)90003-4](https://doi.org/10.1016/0375-6742(73)90003-4).
- (204) Fendorf, S.; Michael, H. A.; Van Geen, A. Spatial and Temporal Variations of Groundwater Arsenic in South and Southeast Asia. *Science*. Science May 28, 2010, pp 1123–1127. <https://doi.org/10.1126/science.1172974>.
- (205) Scientific Opinion on Arsenic in Food. *EFSA J.* **2009**, 7 (10), 1351.

- <https://doi.org/10.2903/j.efsa.2009.1351>.
- (206) WHO | Arsenic. *WHO* **2019**.
- (207) Luong, J. H. T.; Majid, E.; Male, K. B. Analytical Tools for Monitoring Arsenic in the Environment. *Open Anal. Chem. J.* **2007**, *1* (1), 7–14. <https://doi.org/10.2174/1874065000701010007>.
- (208) Association for the Advancement of Science, A. Arsenic in Asia. *Science* (80-.). **2010**, *328* (5982), 1071–1071. <https://doi.org/10.1126/science.328.5982.1071-c>.
- (209) Fasci, D.; Anania, V. G.; Lill, J. R.; Salvesen, G. S. SUMO Deconjugation Is Required for Arsenic-Triggered Ubiquitylation of PML. *Sci. Signal.* **2015**, *8* (380). <https://doi.org/10.1126/scisignal.aaa3929>.
- (210) Service, R. F. Nanotechnology Takes Aim at Cancer. *Science* (80-.). **2005**, *310* (5751), 1132–1134. <https://doi.org/10.1126/science.310.5751.1132>.
- (211) Cho, A. A New Take on Doping in Iron-Based Superconductors. *Science* (80-.). **2009**, *324* (5926), 452–453. https://doi.org/10.1126/science.324_452a.
- (212) Bachtold, D. Toxicology: Arsenic Victims to Take British Science Body to Court. *Science*. American Association for the Advancement of Science May 16, 2003, p 1066. <https://doi.org/10.1126/science.300.5622.1066a>.
- (213) Majid, E.; Hrapovic, S.; Liu, Y.; Male, K. B.; Luong, J. H. T. Electrochemical Determination of Arsenite Using a Gold Nanoparticle Modified Glassy Carbon Electrode and Flow Analysis. *Anal. Chem.* **2006**, *78* (3), 762–769. <https://doi.org/10.1021/ac0513562>.
- (214) Johanna Buschmann; Alexandra Kappeler; Ursula Lindauer; David Kistler; Michael Berg, and; Sigg, L. Arsenite and Arsenate Binding to Dissolved Humic Acids: Influence

- of PH, Type of Humic Acid, and Aluminum. **2006**. <https://doi.org/10.1021/es061057>.
- (215) Fischer, D. C. *Colorimetric Determination and Speciation of Arsenic with Silver Diethyldithiocarbamate*. *Colorimetric Determination and Speciation of Arsenic with Silver Diethyldithiocarbamate*.
- (216) Tahir, M. A.; Rasheed, H.; Malana, A. Earth System Science Data Method Development for Arsenic Analysis by Modification in Spectrophotometric Technique. *Drink. Water Eng. Sci* **2012**, 5, 1–8. <https://doi.org/10.5194/dwes-5-1-2012>.
- (217) Melamed, D. Monitoring Arsenic in the Environment: A Review of Science and Technologies with the Potential for Field Measurements. *Analytica Chimica Acta*. Elsevier March 7, 2005, pp 1–13. <https://doi.org/10.1016/j.aca.2004.10.047>.
- (218) Richardson, S. D.; Ternes, T. A. Water Analysis: Emerging Contaminants and Current Issues. *Analytical Chemistry*. American Chemical Society January 2, 2018, pp 398–428. <https://doi.org/10.1021/acs.analchem.7b04577>.
- (219) Muñoz, E.; Palmero, S. Analysis and Speciation of Arsenic by Stripping Potentiometry: A Review. *Talanta*. Elsevier B.V. February 15, 2005, pp 613–620. <https://doi.org/10.1016/j.talanta.2004.07.034>.
- (220) BAGHEL, A.; SINGH, B.; PANDEY, P.; SEKHAR, K. A Rapid Field Detection Method for Arsenic in Drinking Water. *Anal. Sci.* **2007**, 23 (2), 135–137. <https://doi.org/10.2116/analsci.23.135>.
- (221) Danforth, N.; Mia, E.; Danielson, R. *I I-APHA Annual Meeting Continuing Education Program Course Descriptions CE INSTITUTE 1: INCLUDING MEN IN REPRODUCTIVE*.
- (222) Protection Agency, E. *EPA1600f4-79f020 & EPA Methods for Chemical Analysis of Water*

and Wastes; 1983.

- (223) Annual Book of ASTM Standards - Volume 11.01: Water (I) | NHBS Academic & Professional Books <https://www.nhbs.com/annual-book-of-astm-standards-volume-1101-water-i-book> (accessed Jul 25, 2020).
- (224) Fishman, M. J.; Friedman, L. C. *Techniques of Water-Resources Investigations of the United States Geological Survey METHODS FOR DETERMINATION OF INORGANIC SUBSTANCES IN WATER AND FLUVIAL SEDIMENTS*.
- (225) Mulvihill, M.; Tao, A.; Benjauthrit, K.; Arnold, J.; Yang, P. Surface-Enhanced Raman Spectroscopy for Trace Arsenic Detection in Contaminated Water. *Angew. Chemie - Int. Ed.* **2008**, 47 (34), 6456–6460. <https://doi.org/10.1002/anie.200800776>.
- (226) Domínguez-González, R.; González Varela, L.; Bermejo-Barrera, P. Functionalized Gold Nanoparticles for the Detection of Arsenic in Water. *Talanta* **2014**, 118, 262–269. <https://doi.org/10.1016/j.talanta.2013.10.029>.
- (227) Ma, J.; Sengupta, M. K.; Yuan, D.; Dasgupta, P. K. Speciation and Detection of Arsenic in Aqueous Samples: A Review of Recent Progress in Non-Atomic Spectrometric Methods. *Analytica Chimica Acta*. Elsevier June 11, 2014, pp 1–23. <https://doi.org/10.1016/j.aca.2014.04.029>.
- (228) Xiao, L.; Wildgoose, G. G.; Compton, R. G. Sensitive Electrochemical Detection of Arsenic (III) Using Gold Nanoparticle Modified Carbon Nanotubes via Anodic Stripping Voltammetry. *Anal. Chim. Acta* **2008**, 620 (1–2), 44–49. <https://doi.org/10.1016/j.aca.2008.05.015>.
- (229) Moghimi, N.; Mohapatra, M.; Leung, K. T. Bimetallic Nanoparticles for Arsenic Detection. *Anal. Chem.* **2015**, 87 (11), 5546–5552. <https://doi.org/10.1021/ac504116d>.

- (230) Weng, C. I.; Cang, J. S.; Chang, J. Y.; Hsiung, T. M.; Unnikrishnan, B.; Hung, Y. L.; Tseng, Y. T.; Li, Y. J.; Shen, Y. W.; Huang, C. C. Detection of Arsenic(III) through Pulsed Laser-Induced Desorption/ Ionization of Gold Nanoparticles on Cellulose Membranes. *Anal. Chem.* **2014**, *86* (6), 3167–3173. <https://doi.org/10.1021/ac500053e>.
- (231) VanDorn, D.; Ravalli, M. T.; Small, M. M.; Hillery, B.; Andreescu, S. Adsorption of Arsenic by Iron Oxide Nanoparticles: A Versatile, Inquiry-Based Laboratory for a High School or College Science Course. *J. Chem. Educ.* **2011**, *88* (8), 1119–1122. <https://doi.org/10.1021/ed100010c>.
- (232) Ezeh, V. C.; Harrop, T. C. A Sensitive and Selective Fluorescence Sensor for the Detection of Arsenic(III) in Organic Media. *Inorg. Chem.* **2012**, *51* (3), 1213–1215. <https://doi.org/10.1021/ic2023715>.
- (233) Zhang, B.; Wang, H.; Lu, L.; Ai, K.; Zhang, G.; Cheng, X. Large-Area Silver-Coated Silicon Nanowire Arrays for Molecular Sensing Using Surface-Enhanced Raman Spectroscopy. *Adv. Funct. Mater.* **2008**, *18* (16), 2348–2355. <https://doi.org/10.1002/adfm.200800153>.
- (234) Lu, W.; Singh, A. K.; Khan, S. A.; Senapati, D.; Yu, H.; Ray, P. C. Gold Nano-Popcorn-Based Targeted Diagnosis, Nanotherapy Treatment, and in Situ Monitoring of Photothermal Therapy Response of Prostate Cancer Cells Using Surface-Enhanced Raman Spectroscopy. *J. Am. Chem. Soc.* **2010**, *132* (51), 18103–18114. <https://doi.org/10.1021/ja104924b>.
- (235) Beck, F. J.; Stavrinadis, A.; Diedenhofen, S. L.; Lasanta, T.; Konstantatos, G. Surface Plasmon Polariton Couplers for Light Trapping in Thin-Film Absorbers and Their Application to Colloidal Quantum Dot Optoelectronics. *ACS Photonics* **2014**, *1* (11),

- 1197–1205. <https://doi.org/10.1021/ph5002704>.
- (236) Sau, T. K.; Rogach, A. L.; Jäckel, F.; Klar, T. A.; Feldmann, J. Properties and Applications of Colloidal Nonspherical Noble Metal Nanoparticles. *Advanced Materials*. John Wiley & Sons, Ltd April 22, 2010, pp 1805–1825. <https://doi.org/10.1002/adma.200902557>.
- (237) Ross, M. B.; Mirkin, C. A.; Schatz, G. C. Optical Properties of One-, Two-, and Three-Dimensional Arrays of Plasmonic Nanostructures. *J. Phys. Chem. C* **2016**, *120* (2), 816–830. <https://doi.org/10.1021/acs.jpcc.5b10800>.
- (238) Kelly, K. L.; Coronado, E.; Zhao, L. L.; Schatz, G. C. The Optical Properties of Metal Nanoparticles: The Influence of Size, Shape, and Dielectric Environment. *J. Phys. Chem. B* **2003**, *107* (3), 668–677. <https://doi.org/10.1021/jp026731y>.
- (239) Sherry, L. J.; Jin, R.; Mirkin, C. A.; Schatz, G. C.; Van Duyne, R. P. Localized Surface Plasmon Resonance Spectroscopy of Single Silver Triangular Nanoprisms. *Nano Lett.* **2006**, *6* (9), 2060–2065. <https://doi.org/10.1021/nl061286u>.
- (240) Tsai, C. M.; Hsu, M. S.; Chen, J. C.; Huang, C. L. Mechanistic Study of Shape Evolution of Silver Nanoprisms in the Presence of KSCN. *J. Phys. Chem. C* **2012**, *116* (1), 461–467. <https://doi.org/10.1021/jp209840n>.
- (241) Ghosh, T.; Satpati, B.; Senapati, D. Characterization of Bimetallic Core-Shell Nanorings Synthesized via Ascorbic Acid-Controlled Galvanic Displacement Followed by Epitaxial Growth. *J. Mater. Chem. C* **2014**, *2* (13), 2439–2447. <https://doi.org/10.1039/c3tc32340d>.
- (242) Senapati, D.; Singh, A. K.; Ray, P. C. Real Time Monitoring of the Shape Evolution of Branched Gold Nanostructure. *Chem. Phys. Lett.* **2010**, *487* (1–3), 88–91. <https://doi.org/10.1016/j.cplett.2010.01.015>.

- (243) Amendola, V.; Scaramuzza, S.; Agnoli, S.; Polizzi, S.; Meneghetti, M. Strong Dependence of Surface Plasmon Resonance and Surface Enhanced Raman Scattering on the Composition of Au-Fe Nanoalloys. *Nanoscale* **2014**, *6* (3), 1423–1433. <https://doi.org/10.1039/c3nr04995g>.
- (244) Zhu, J.; Li, J. J.; Zhao, J. W. Local Dielectric Environment Dependent Local Electric Field Enhancement in Double Concentric Silver Nanotubes. *J. Phys. Chem. C* **2013**, *117* (1), 584–592. <https://doi.org/10.1021/jp310676s>.
- (245) Bhattacharya, M.; Mazov, V.; Satpati, B.; Jena, P.; Chakraborty, S. Das; Kumar, S.; Pathak, B.; Kuznetsov, D. V.; Senapati, D. Exploiting Le Chatelier's Principle for a One-Pot Synthesis of Nontoxic HHogGNPs with the Sharpest Nanoscopic Features Suitable for Tunable Plasmon Spectroscopy and High Throughput SERS Sensing. *Chem. Commun.* **2017**, *53* (75), 10402–10405.
- (246) Métraux, G. S.; Mirkin, C. A. Rapid Thermal Synthesis of Silver Nanoprisms with Chemically Tailorable Thickness. *Adv. Mater.* **2005**, *17* (4), 412–415. <https://doi.org/10.1002/adma.200401086>.
- (247) Jiang, X. C.; Yu, A. B. Silver Nanoplates: A Highly Sensitive Material toward Inorganic Anions. *Langmuir* **2008**, *24* (8), 4300–4309. <https://doi.org/10.1021/la7032252>.
- (248) Tang, B.; Xu, S.; An, J.; Zhao, B.; Xu, W.; Lombardi, J. R. Kinetic Effects of Halide Ions on the Morphological Evolution of Silver Nanoplates. *Phys. Chem. Chem. Phys.* **2009**, *11* (44), 10286–10292. <https://doi.org/10.1039/b912985e>.
- (249) An, J.; Tang, B.; Zheng, X.; Zhou, J.; Dong, F.; Xu, S.; Wang, Y.; Zhao, B.; Xu, W. Sculpturing Effect of Chloride Ions in Shape Transformation from Triangular to Discal Silver Nanoplates. *J. Phys. Chem. C* **2008**, *112* (39), 15176–15182.

<https://doi.org/10.1021/jp802694p>.

- (250) Li, J.; Chen, L.; Lou, T.; Wang, Y. Highly Sensitive SERS Detection of As³⁺ Ions in Aqueous Media Using Glutathione Functionalized Silver Nanoparticles. *ACS Appl. Mater. Interfaces* **2011**, 3 (10), 3936–3941. <https://doi.org/10.1021/am200810x>.
- (251) Roy, S.; Palui, G.; Banerjee, A. The As-Prepared Gold Cluster-Based Fluorescent Sensor for the Selective Detection of As III Ions in Aqueous Solution. *Nanoscale* **2012**, 4 (8), 2734–2740. <https://doi.org/10.1039/c2nr11786j>.
- (252) Wu, Y.; Zhan, S.; Wang, F.; He, L.; Zhi, W.; Zhou, P. Cationic Polymers and Aptamers Mediated Aggregation of Gold Nanoparticles for the Colorimetric Detection of Arsenic(III) in Aqueous Solution. *Chem. Commun.* **2012**, 48 (37), 4459–4461. <https://doi.org/10.1039/c2cc30384a>.
- (253) Wu, Y.; Zhan, S.; Xing, H.; He, L.; Xu, L.; Zhou, P. Nanoparticles Assembled by Aptamers and Crystal Violet for Arsenic(III) Detection in Aqueous Solution Based on a Resonance Rayleigh Scattering Spectral Assay. *Nanoscale* **2012**, 4 (21), 6841–6849. <https://doi.org/10.1039/c2nr31418e>.
- (254) Chakraborty, S. Das; Sau, A.; Kuznetsov, D. V.; Banerjee, A.; Bardhan, M.; Bhattacharya, M.; Dasgupta, D.; Basu, S.; Senapati, D. Development of a Triplet-Triplet Absorption Ruler: DNA- and Chromatin-Mediated Drug Molecule Release from a Nanosurface. *J. Phys. Chem. B* **2016**, 120 (27), 6872–6881. <https://doi.org/10.1021/acs.jpcc.6b05278>.
- (255) Chen, L.; Chan, L.; Fu, X.; Lu, W. Highly Sensitive and Selective Colorimetric Sensing of Hg²⁺ Based on the Morphology Transition of Silver Nanoprisms. *ACS Appl. Mater. Interfaces* **2013**, 5 (2), 284–290. <https://doi.org/10.1021/am3020857>.
- (256) Chen, N.; Zhang, Y.; Liu, H.; Wu, X.; Li, Y.; Miao, L.; Shen, Z.; Wu, A. High-

- Performance Colorimetric Detection of Hg²⁺ Based on Triangular Silver Nanoprisms. *ACS Sensors* **2016**, *1* (5), 521–527. <https://doi.org/10.1021/acssensors.6b00001>.
- (257) Yakoh, A.; Rattanarat, P.; Siangproh, W.; Chailapakul, O. Simple and Selective Paper-Based Colorimetric Sensor for Determination of Chloride Ion in Environmental Samples Using Label-Free Silver Nanoprisms. *Talanta* **2018**, *178*, 134–140. <https://doi.org/10.1016/j.talanta.2017.09.013>.
- (258) Lofton, C.; Sigmund, W. Mechanisms Controlling Crystal Habits of Gold and Silver Colloids. *Adv. Funct. Mater.* **2005**, *15* (7), 1197–1208. <https://doi.org/10.1002/adfm.200400091>.
- (259) Wang, Z. L. Transmission Electron Microscopy of Shape-Controlled Nanocrystals and Their Assemblies. *J. Phys. Chem. B* **2000**, *104* (6), 1153–1175. <https://doi.org/10.1021/jp993593c>.
- (260) Panzarasa, G. Just What Is It That Makes Silver Nanoprisms so Different, so Appealing? *J. Chem. Educ.* **2015**, *92* (11), 1918–1923. <https://doi.org/10.1021/acs.jchemed.5b00320>.
- (261) Tang, B.; Xu, S.; Hou, X.; Li, J.; Sun, L.; Xu, W.; Wang, X. Shape Evolution of Silver Nanoplates through Heating and Photoinduction. *ACS Appl. Mater. Interfaces* **2013**, *5* (3), 646–653. <https://doi.org/10.1021/am302072u>.
- (262) Jin, R.; Cao, Y. C.; Hao, E.; Métraux, G. S.; Schatz, G. C.; Mirkin, C. A. Controlling Anisotropic Nanoparticle Growth through Plasmon Excitation. *Nature* **2003**, *425* (6957), 487–490. <https://doi.org/10.1038/nature02020>.
- (263) Jin, R.; Cao, Y.; Mirkin, C. A.; Kelly, K. L.; Schatz, G. C.; Zheng, J. G. Photoinduced Conversion of Silver Nanospheres to Nanoprisms. *Science* (80-.). **2001**, *294* (5548), 1901–1903. <https://doi.org/10.1126/science.1066541>.

- (264) Batsanov, S. S. Van Der Waals Radii of Elements. *Inorg. Mater.* **2001**, 37 (9), 871–885.
<https://doi.org/10.1023/A:1011625728803>.
- (265) Alireza Haghiril Ilkhechi, Jose M. Mercero, In aki Silanes, Michael Bolte, Matthias Scheibitz, Hans-Wolfram Lerner, Jesus M. Ugalde, and M. W.; Contribution. Ref-11b-A Joint Experimental and Theoretical Study of Cation- π . Pdf. *J. Am. Chem. Soc.* **2005**, 127, 10656–10666. <https://doi.org/10.1021/ja051544>.
- (266) Blanchard, M. D.; Hughes, R. P.; Concolino, T. E.; Rheingold, A. L. π -Stacking between Pentafluorophenyl and Phenyl Groups as a Controlling Feature of Intra- and Intermolecular Crystal Structure Motifs in Substituted Ferrocenes. Observation of Unexpected Face-to-Face Stacking between Pentafluorophenyl Rings. *Chem. Mater.* **2000**, 12 (6), 1604–1610. <https://doi.org/10.1021/cm000093j>.
- (267) Bearden, J. A. X-Ray Wavelengths. *Rev. Mod. Phys.* **1967**, 39 (1), 78–124.
<https://doi.org/10.1103/RevModPhys.39.78>.
- (268) Krause, M. O. Atomic Radiative and Radiationless Yields for K and L Shells. *J. Phys. Chem. Ref. Data* **1979**, 8 (2), 307–327. <https://doi.org/10.1063/1.555594>.
- (269) Analysis of arsenic in dental cements according to the silverdiethyldithiocarbamate photometric method - ISO 2590 - PubMed <https://pubmed.ncbi.nlm.nih.gov/6254189/> (accessed Jul 26, 2020).
- (270) Senarathna, K. G. C.; Randiligama, H. M. S. P.; Rajapakse, R. M. G. Preparation, Characterization and Oxygen Reduction Catalytic Activities of Nanocomposites of Co(II)/Montmorillonite Containing Polypyrrole, Polyaniline or Poly(Ethylenedioxythiophene). *RSC Adv.* **2016**, 6 (114), 112853–112863.
<https://doi.org/10.1039/c6ra23100d>.

- (271) Moskovits, M. Surface-Enhanced Spectroscopy. *Rev. Mod. Phys.* **1985**, 57 (3), 783–826. <https://doi.org/10.1103/RevModPhys.57.783>.
- (272) Kleinman, S. L.; Ringe, E.; Valley, N.; Wustholz, K. L.; Phillips, E.; Scheidt, K. A.; Schatz, G. C.; Van Duyne, R. P. Single-Molecule Surface-Enhanced Raman Spectroscopy of Crystal Violet Isotopologues: Theory and Experiment. *J. Am. Chem. Soc.* **2011**, 133 (11), 4115–4122. <https://doi.org/10.1021/ja110964d>.
- (273) Rahman, M. M.; Mandal, B. K.; Roy Chowdhury, T.; Sengupta, M. K.; Chowdhury, U. K.; Lodh, D.; Chanda, C. R.; Basu, G. K.; Mukherjee, S. C.; Saha, K. C.; et al. Arsenic Groundwater Contamination and Sufferings of People in North 24-Parganas, One of the Nine Arsenic Affected Districts of West Bengal, India. *J. Environ. Sci. Heal. - Part A Toxic/Hazardous Subst. Environ. Eng.* **2003**, 38 (1), 25–59. <https://doi.org/10.1081/ESE-120016658>.
- (274) Walter, M. G.; Warren, E. L.; McKone, J. R.; Boettcher, S. W.; Mi, Q.; Santori, E. A.; Lewis, N. S. Solar Water Splitting Cells. *Chem. Rev.* **2010**, 110 (11), 6446–6473. <https://doi.org/10.1021/cr1002326>.
- (275) Dresselhaus, M. S.; Thomas, I. L. Alternative Energy Technologies. *Nature*. Nature Publishing Group November 15, 2001, pp 332–337. <https://doi.org/10.1038/35104599>.
- (276) Jahan, M.; Liu, Z.; Loh, K. P. A Graphene Oxide and Copper-Centered Metal Organic Framework Composite as a Tri-Functional Catalyst for HER, OER, and ORR. *Adv. Funct. Mater.* **2013**, 23 (43), 5363–5372. <https://doi.org/10.1002/adfm.201300510>.
- (277) Gasteiger, H. A.; Markovic, N. M. Just a Dream or Future Reality? *Science*. April 2009, pp 48–49. <https://doi.org/10.1126/science.1172083>.
- (278) Turner, J. A. Sustainable Hydrogen Production. *Science*. August 2004, pp 972–974.

<https://doi.org/10.1126/science.1103197>.

- (279) Fang, Z.; Peng, L.; Qian, Y.; Zhang, X.; Xie, Y.; Cha, J. J.; Yu, G. Dual Tuning of Ni–Co–A (A = P, Se, O) Nanosheets by Anion Substitution and Holey Engineering for Efficient Hydrogen Evolution. *J. Am. Chem. Soc.* **2018**, *140* (15), 5241–5247. <https://doi.org/10.1021/jacs.8b01548>.
- (280) Schlapbach, L.; Züttel, A. Hydrogen-Storage Materials for Mobile Applications. *Nature*. November 2001, pp 353–358. <https://doi.org/10.1038/35104634>.
- (281) Jiao, Y.; Zheng, Y.; Jaroniec, M.; Qiao, S. Z. Design of Electrocatalysts for Oxygen- and Hydrogen-Involving Energy Conversion Reactions. *Chemical Society Reviews*. Royal Society of Chemistry April 2015, pp 2060–2086. <https://doi.org/10.1039/c4cs00470a>.
- (282) Zheng, Y.; Jiao, Y.; Jaroniec, M.; Qiao, S. Z. Advancing the Electrochemistry of the Hydrogen-Evolution Reaction through Combining Experiment and Theory. *Angew. Chemie Int. Ed.* **2015**, *54* (1), 52–65. <https://doi.org/10.1002/anie.201407031>.
- (283) McCrory, C. C. L.; Jung, S.; Ferrer, I. M.; Chatman, S. M.; Peters, J. C.; Jaramillo, T. F. Benchmarking Hydrogen Evolving Reaction and Oxygen Evolving Reaction Electrocatalysts for Solar Water Splitting Devices. *J. Am. Chem. Soc.* **2015**, *137* (13), 4347–4357. <https://doi.org/10.1021/ja510442p>.
- (284) Bhowmik, T.; Kundu, M. K.; Barman, S. CoFe Layered Double Hydroxide Supported on Graphitic Carbon Nitrides: An Efficient and Durable Bifunctional Electrocatalyst for Oxygen Evolution and Hydrogen Evolution Reactions. *ACS Appl. Energy Mater.* **2018**, *1* (3), 1200–1209. <https://doi.org/10.1021/acsaem.7b00305>.
- (285) Li, Y.; Zhang, L. A.; Qin, Y.; Chu, F.; Kong, Y.; Tao, Y.; Li, Y.; Bu, Y.; Ding, D.; Liu, M. Crystallinity Dependence of Ruthenium Nanocatalyst toward Hydrogen Evolution

- Reaction. *ACS Catal.* **2018**, 8 (7), 5714–5720. <https://doi.org/10.1021/acscatal.8b01609>.
- (286) Conway, B. E.; Tilak, B. V. Interfacial Processes Involving Electrocatalytic Evolution and Oxidation of H₂, and the Role of Chemisorbed H. *Electrochim. Acta* **2002**, 47 (22–23), 3571–3594. [https://doi.org/10.1016/S0013-4686\(02\)00329-8](https://doi.org/10.1016/S0013-4686(02)00329-8).
- (287) Lukowski, M. A.; Daniel, A. S.; Meng, F.; Forticaux, A.; Li, L.; Jin, S. Enhanced Hydrogen Evolution Catalysis from Chemically Exfoliated Metallic MoS₂ Nanosheets. *J. Am. Chem. Soc.* **2013**, 135 (28), 10274–10277. <https://doi.org/10.1021/ja404523s>.
- (288) Koper, M. T. M. Hydrogen Electrocatalysis: A Basic Solution. *Nat. Chem.* **2013**, 5 (4), 255–256. <https://doi.org/10.1038/nchem.1600>.
- (289) Yang, D.-S.; Bhattacharjya, D.; Inamdar, S.; Park, J.; Yu, J.-S. Phosphorus-Doped Ordered Mesoporous Carbons with Different Lengths as Efficient Metal-Free Electrocatalysts for Oxygen Reduction Reaction in Alkaline Media. *J. Am. Chem. Soc.* **2012**, 134 (39), 16127–16130. <https://doi.org/10.1021/ja306376s>.
- (290) Grigoriev, S. A.; Millet, P.; Fateev, V. N. Evaluation of Carbon-Supported Pt and Pd Nanoparticles for the Hydrogen Evolution Reaction in PEM Water Electrolysers. *J. Power Sources* **2008**, 177 (2), 281–285. <https://doi.org/10.1016/j.jpowsour.2007.11.072>.
- (291) Zhang, Z.; Li, P.; Feng, Q.; Wei, B.; Deng, C.; Fan, J.; Li, H.; Wang, H. Scalable Synthesis of a Ruthenium-Based Electrocatalyst as a Promising Alternative to Pt for Hydrogen Evolution Reaction. *ACS Appl. Mater. Interfaces* **2018**, 10 (38), 32171–32179. <https://doi.org/10.1021/acsami.8b10502>.
- (292) Guo, J.; Wang, J.; Wu, Z.; Lei, W.; Zhu, J.; Xia, K.; Wang, D. Controllable Synthesis of Molybdenum-Based Electrocatalysts for a Hydrogen Evolution Reaction. *J. Mater. Chem. A* **2017**, 5 (10), 4879–4885. <https://doi.org/10.1039/c6ta10758c>.

- (293) Lv, F.; Zhang, W.; Yang, W.; Feng, J.; Wang, K.; Zhou, J.; Zhou, P.; Guo, S. Ir-Based Alloy Nanoflowers with Optimized Hydrogen Binding Energy as Bifunctional Electrocatalysts for Overall Water Splitting. *Small Methods* **2019**, 1900129. <https://doi.org/10.1002/smtd.201900129>.
- (294) Chen, J.; Ge, Y.; Feng, Q.; Zhuang, P.; Chu, H.; Cao, Y.; Smith, W. R.; Dong, P.; Ye, M.; Shen, J. Nesting Co₃Mo Binary Alloy Nanoparticles onto Molybdenum Oxide Nanosheet Arrays for Superior Hydrogen Evolution Reaction. *ACS Appl. Mater. Interfaces* **2019**, 11 (9), 9002–9010. <https://doi.org/10.1021/acsami.8b19148>.
- (295) McAllister, J.; Bandeira, N. A. G.; McGlynn, J. C.; Ganin, A. Y.; Song, Y. F.; Bo, C.; Miras, H. N. Tuning and Mechanistic Insights of Metal Chalcogenide Molecular Catalysts for the Hydrogen-Evolution Reaction. *Nat. Commun.* **2019**, 10 (1). <https://doi.org/10.1038/s41467-018-08208-4>.
- (296) Qin, J.-S.; Du, D.-Y.; Guan, W.; Bo, X.-J.; Li, Y.-F.; Guo, L.-P.; Su, Z.-M.; Wang, Y.-Y.; Lan, Y.-Q.; Zhou, H.-C. Ultrastable Polymolybdate-Based Metal–Organic Frameworks as Highly Active Electrocatalysts for Hydrogen Generation from Water. *J. Am. Chem. Soc.* **2015**, 137 (22), 7169–7177. <https://doi.org/10.1021/jacs.5b02688>.
- (297) Hinnemann, B.; Moses, P. G.; Bonde, J.; Jørgensen, K. P.; Nielsen, J. H.; Horch, S.; Chorkendorff, I.; Nørskov, J. K. Biomimetic Hydrogen Evolution: MoS₂ Nanoparticles as Catalyst for Hydrogen Evolution. *J. Am. Chem. Soc.* **2005**, 127 (15), 5308–5309. <https://doi.org/10.1021/ja0504690>.
- (298) Quaino, P.; Juarez, F.; Santos, E.; Schmickler, W. Volcano Plots in Hydrogen Electrocatalysis – Uses and Abuses. *Beilstein J. Nanotechnol.* **2014**, 5, 846–854. <https://doi.org/10.3762/bjnano.5.96>.

- (299) Sheng, M.; Jiang, B.; Wu, B.; Liao, F.; Fan, X.; Lin, H.; Li, Y.; Lifshitz, Y.; Lee, S.-T.; Shao, M. Approaching the Volcano Top: Iridium/Silicon Nanocomposites as Efficient Electrocatalysts for the Hydrogen Evolution Reaction. *ACS Nano* **2019**, *13* (3), 2786–2794. <https://doi.org/10.1021/acsnano.8b07572>.
- (300) Lv, H.; Xi, Z.; Chen, Z.; Guo, S.; Yu, Y.; Zhu, W.; Li, Q.; Zhang, X.; Pan, M.; Lu, G.; et al. A New Core/Shell NiAu/Au Nanoparticle Catalyst with Pt-like Activity for Hydrogen Evolution Reaction. *J. Am. Chem. Soc.* **2015**, *137* (18), 5859–5862. <https://doi.org/10.1021/jacs.5b01100>.
- (301) Lu, J.; Zhou, W.; Wang, L.; Jia, J.; Ke, Y.; Yang, L.; Zhou, K.; Liu, X.; Tang, Z.; Li, L.; et al. Core–Shell Nanocomposites Based on Gold Nanoparticle@Zinc–Iron-Embedded Porous Carbons Derived from Metal–Organic Frameworks as Efficient Dual Catalysts for Oxygen Reduction and Hydrogen Evolution Reactions. *ACS Catal.* **2016**, *6* (2), 1045–1053. <https://doi.org/10.1021/acscatal.5b02302>.
- (302) And, D. M. C.; Astruc*, D. Gold Nanoparticles: Assembly, Supramolecular Chemistry, Quantum-Size-Related Properties, and Applications toward Biology, Catalysis, and Nanotechnology. *Chem. Rev.* **2003**, *104* (1), 293–346. <https://doi.org/10.1021/CR030698+>.
- (303) Huang, Y.; Gao, L.; Cui, H. Assembly of Multifunctionalized Gold Nanoparticles with Chemiluminescent, Catalytic, and Immune Activity for Label-Free Immunoassays. *ACS Appl. Mater. Interfaces* **2018**, *10* (20), 17040–17046. <https://doi.org/10.1021/acsami.8b02521>.
- (304) Goswami, S.; Noh, H.; Redfern, L. R.; Otake, K.; Kung, C.-W.; Cui, Y.; Chapman, K. W.; Farha, O. K.; Hupp, J. T. Pore-Templated Growth of Catalytically Active Gold

- Nanoparticles within a Metal–Organic Framework. *Chem. Mater.* **2019**, *31* (5), 1485–1490. <https://doi.org/10.1021/acs.chemmater.8b04983>.
- (305) Mangadlao, J. D.; Wang, X.; McCleese, C.; Escamilla, M.; Ramamurthy, G.; Wang, Z.; Govande, M.; Babilion, J. P.; Burda, C. Prostate-Specific Membrane Antigen Targeted Gold Nanoparticles for Theranostics of Prostate Cancer. *ACS Nano* **2018**, *12* (4), 3714–3725. <https://doi.org/10.1021/acsnano.8b00940>.
- (306) Bi, L.; Wang, Y.; Yang, Y.; Li, Y.; Mo, S.; Zheng, Q.; Chen, L. Highly Sensitive and Reproducible SERS Sensor for Biological PH Detection Based on a Uniform Gold Nanorod Array Platform. *ACS Appl. Mater. Interfaces* **2018**, *10* (18), 15381–15387. <https://doi.org/10.1021/acsami.7b19347>.
- (307) Kim, W.; Lee, S. H.; Kim, J. H.; Ahn, Y. J.; Kim, Y.-H.; Yu, J. S.; Choi, S. Paper-Based Surface-Enhanced Raman Spectroscopy for Diagnosing Prenatal Diseases in Women. *ACS Nano* **2018**, *12* (7), 7100–7108. <https://doi.org/10.1021/acsnano.8b02917>.
- (308) Coe, S.; Woo, W.-K.; Bawendi, M.; Bulović, V. Electroluminescence from Single Monolayers of Nanocrystals in Molecular Organic Devices. *Nature* **2002**, *420* (6917), 800–803. <https://doi.org/10.1038/nature01217>.
- (309) Alivisatos, A. P. Semiconductor Clusters, Nanocrystals, and Quantum Dots. *Science* (80-.). **1996**, *271* (5251), 933–937. <https://doi.org/10.1126/science.271.5251.933>.
- (310) Wang, J.; Gong, J.; Xiong, Y.; Yang, J.; Gao, Y.; Liu, Y.; Lu, X.; Tang, Z. Shape-Dependent Electrocatalytic Activity of Monodispersed Gold Nanocrystals toward Glucose Oxidation. *Chem. Commun.* **2011**, *47* (24), 6894. <https://doi.org/10.1039/c1cc11784j>.
- (311) Li, J.; Wu, J.; Zhang, X.; Liu, Y.; Zhou, D.; Sun, H.; Zhang, H.; Yang, B. Controllable Synthesis of Stable Urchin-like Gold Nanoparticles Using Hydroquinone to Tune the

- Reactivity of Gold Chloride. *J. Phys. Chem. C* **2011**, *115* (9), 3630–3637.
<https://doi.org/10.1021/jp1119074>.
- (312) Sun, L.; He, X.; Lu, J. Nanotwinned and Hierarchical Nanotwinned Metals: A Review of Experimental, Computational and Theoretical Efforts. *npj Computational Materials*. Nature Publishing Group December 2018. <https://doi.org/10.1038/s41524-018-0062-2>.
- (313) Mariano, R. G.; McKelvey, K.; White, H. S.; Kanan, M. W. Selective Increase in CO₂ Electroreduction Activity at Grain-Boundary Surface Terminations. *Science* **2017**, *358* (6367), 1187–1192. <https://doi.org/10.1126/science.aao3691>.
- (314) Feng, X.; Jiang, K.; Fan, S.; Kanan, M. W. A Direct Grain-Boundary-Activity Correlation for CO Electroreduction on Cu Nanoparticles. *ACS Cent. Sci.* **2016**, *2* (3), 169–174. <https://doi.org/10.1021/acscentsci.6b00022>.
- (315) Mandal, D.; Mondal, S.; Senapati, D.; Satpati, B.; Sangaranarayanan, M. V. Charge Density Modulated Shape-Dependent Electrocatalytic Activity of Gold Nanoparticles for the Oxidation of Ascorbic Acid. *J. Phys. Chem. C* **2015**, *119* (40), 23103–23112. <https://doi.org/10.1021/acs.jpcc.5b07710>.
- (316) Zhang, X.; Guan, P.; Malic, L.; Trudeau, M.; Rosei, F.; Veres, T. Nanoporous Twinned PtPd with Highly Catalytic Activity and Stability. *J. Mater. Chem. A* **2015**, *3* (5), 2050–2056. <https://doi.org/10.1039/C4TA06250G>.
- (317) McCaffrey, R.; Long, H.; Jin, Y.; Sanders, A.; Park, W.; Zhang, W. Template Synthesis of Gold Nanoparticles with an Organic Molecular Cage. *J. Am. Chem. Soc.* **2014**, *136* (5), 1782–1785. <https://doi.org/10.1021/ja412606t>.
- (318) And, T. K. S.; Murphy, C. J. Room Temperature, High-Yield Synthesis of Multiple Shapes of Gold Nanoparticles in Aqueous Solution. *J. Am. Chem. Soc.* **2004**, *126* (28),

- 8648–8649. <https://doi.org/10.1021/JA047846D>.
- (319) Senapati, D.; Singh, A. K.; Ray, P. C. Real Time Monitoring of the Shape Evolution of Branched Gold Nanostructure. *Chem. Phys. Lett.* **2010**, *487* (1–3), 88–91. <https://doi.org/10.1016/J.CPLETT.2010.01.015>.
- (320) Phan, C. M.; Nguyen, H. M. Role of Capping Agent in Wet Synthesis of Nanoparticles. *J. Phys. Chem. A* **2017**, *121* (17), 3213–3219. <https://doi.org/10.1021/acs.jpca.7b02186>.
- (321) Liu, Y.; Goebel, J.; Yin, Y. Templated Synthesis of Nanostructured Materials. *Chem. Soc. Rev.* **2013**, *42* (7), 2610–2653. <https://doi.org/10.1039/C2CS35369E>.
- (322) Perdew, J. P.; Burke, K.; Ernzerhof, M. Generalized Gradient Approximation Made Simple. *Phys. Rev. Lett.* **1996**, *77* (18), 3865–3868. <https://doi.org/10.1103/PhysRevLett.77.3865>.
- (323) Grimme, S. Semiempirical GGA-Type Density Functional Constructed with a Long-Range Dispersion Correction. *J. Comput. Chem.* **2006**, *27* (15), 1787–1799. <https://doi.org/10.1002/jcc.20495>.
- (324) Berr, S.; Jones, R. R. M.; Johnson, J. S. Effect of Counterion on the Size and Charge of Alkyltrimethylammonium Halide Micelles as a Function of Chain Length and Concentration as Determined by Small-Angle Neutron Scattering. *J. Phys. Chem.* **1992**, *96* (13), 5611–5614. <https://doi.org/10.1021/j100192a075>.
- (325) Naskar, B.; Dey, A.; Moulik, S. P. Counter-Ion Effect on Micellization of Ionic Surfactants: A Comprehensive Understanding with Two Representatives, Sodium Dodecyl Sulfate (SDS) and Dodecyltrimethylammonium Bromide (DTAB). *J. Surfactants Deterg.* **2013**, *16* (5), 785–794. <https://doi.org/10.1007/s11743-013-1449-1>.
- (326) Hong Yuan, ; Wanhong Ma, ; Chuncheng Chen, ; Jincal Zhao, ; Jiangwen Liu, ‡;

- Huaiyong Zhu, and; Gao, X. Shape and SPR Evolution of Thorny Gold Nanoparticles Promoted by Silver Ions. *Chem. Mater.* **2007**, *19* (7), 1592–1600. <https://doi.org/10.1021/CM062046I>.
- (327) Rahman, A.; Brown, C. W. Effect of PH on the Critical Micelle Concentration of Sodium Dodecyl Sulphate. *J. Appl. Polym. Sci.* **1983**, *28* (4), 1331–1334. <https://doi.org/10.1002/app.1983.070280407>.
- (328) Tawil, N.; Sacher, E.; Boulais, E.; Mandeville, R.; Meunier, M. X-Ray Photoelectron Spectroscopic and Transmission Electron Microscopic Characterizations of Bacteriophage-Nanoparticle Complexes for Pathogen Detection. *J. Phys. Chem. C* **2013**, *117* (40), 20656–20665. <https://doi.org/10.1021/jp406148h>.
- (329) Jana, R.; Bhim, A.; Bothra, P.; Pati, S. K.; Peter, S. C. Electrochemical Dealloying of PdCu₃ Nanoparticles to Achieve Pt-like Activity for the Hydrogen Evolution Reaction. *ChemSusChem* **2016**, *9* (20), 2922–2927. <https://doi.org/10.1002/cssc.201601081>.
- (330) Zheng, Y.; Jiao, Y.; Zhu, Y.; Li, L. H.; Han, Y.; Chen, Y.; Jaroniec, M.; Qiao, S. Z. High Electrocatalytic Hydrogen Evolution Activity of an Anomalous Ruthenium Catalyst. *J. Am. Chem. Soc.* **2016**, *138* (49), 16174–16181. <https://doi.org/10.1021/jacs.6b11291>.
- (331) E. O. HALL. The Deformation and Ageing of Mild Steel: III Discussion of Results. *Proc. Phys. Soc. B* **1951**, *64*, 747.
- (332) Schiøtz, J.; Di Tolla, F. D.; Jacobsen, K. W. Softening of Nanocrystalline Metals at Very Small Grain Sizes. *Nature* **1998**, *391* (6667), 561–563. <https://doi.org/10.1038/35328>.
- (333) Hansen, N. Hall–Petch Relation and Boundary Strengthening. *Scr. Mater.* **2004**, *51* (8), 801–806. <https://doi.org/10.1016/J.SCRIPMAT.2004.06.002>.
- (334) Armstrong, R.; Codd, I.; Douthwaite, R. M.; Petch, N. J. The Plastic Deformation of

- Polycrystalline Aggregates. *Philos. Mag. A J. Theor. Exp. Appl. Phys.* **1962**, 7 (73), 45–58. <https://doi.org/10.1080/14786436208201857>.
- (335) Sutton, A.P. and Balluffi, R. W. *Grain Boundaries in Crystalline Materials*; Oxford Science Publications, Oxford, 1996.
- (336) Voort, G. F. Vander. *Metallography, Principles and Practice*; McGraw-Hill: New York, 1999.
- (337) Wang, L.; Teng, J.; Liu, P.; Hirata, A.; Ma, E.; Zhang, Z.; Chen, M.; Han, X. Grain Rotation Mediated by Grain Boundary Dislocations in Nanocrystalline Platinum. *Nat. Commun.* **2014**, 5 (1), 4402. <https://doi.org/10.1038/ncomms5402>.
- (338) Jana, R.; Chowdhury, C.; Malik, S.; Datta, A. Pt/Co₃O₄ Surpasses Benchmark Pt/C: An Approach Toward Next Generation Hydrogen Evolution Electrocatalyst. *ACS Appl. Energy Mater.* **2019**, 2 (8), 5613–5621. <https://doi.org/10.1021/acsaem.9b00787>.
- (339) Bligaard, T.; Nørskov, J. K.; Dahl, S.; Matthiesen, J.; Christensen, C. H.; Sehested, J. The Brønsted-Evans-Polanyi Relation and the Volcano Curve in Heterogeneous Catalysis. *J. Catal.* **2004**, 224 (1), 206–217. <https://doi.org/10.1016/j.jcat.2004.02.034>.
- (340) Kim, K.-S.; Kim, W. J.; Lim, H.-K.; Lee, E. K.; Kim, H. Tuned Chemical Bonding Ability of Au at Grain Boundaries for Enhanced Electrochemical CO₂ Reduction. *ACS Catal.* **2016**, 6 (7), 4443–4448. <https://doi.org/10.1021/acscatal.6b00412>.
- (341) Dong, S.; Wang, Z. Grain Boundaries Trigger Basal Plane Catalytic Activity for the Hydrogen Evolution Reaction in Monolayer MoS₂. *Electrocatalysis* **2018**, 9 (6), 744–751. <https://doi.org/10.1007/s12678-018-0485-z>.
- (342) Mavrikakis, M.; Hammer, B.; Nørskov, J. K. Effect of Strain on the Reactivity of Metal Surfaces. *Phys. Rev. Lett.* **1998**, 81 (13), 2819–2822.

- <https://doi.org/10.1103/PhysRevLett.81.2819>.
- (343) Hammer, B.; Norskov, J. K. Why Gold Is the Noblest of All the Metals. *Nature* **1995**, 376 (6537), 238–240. <https://doi.org/10.1038/376238a0>.
- (344) Economou, A.; Karapetis, S. K.; Nikoleli, G.-P.; Nikolelis, D. P.; Bratakou, S.; Varzakas, T. H. Enzyme-Based Sensors. In *Advances in Food Diagnostics*; John Wiley & Sons, Ltd: Chichester, UK, 2017; pp 231–250. <https://doi.org/10.1002/9781119105916.ch9>.
- (345) Luo, J.; Wu, J.; Liu, Z.; Li, Z.; Deng, L. Controlled Synthesis of Porous Co₃O₄ Nanostructures for Efficient Electrochemical Sensing of Glucose. **2019**. <https://doi.org/10.1155/2019/8346251>.
- (346) Kotov, N. A. Inorganic Nanoparticles as Protein Mimics. *Science*. American Association for the Advancement of Science October 8, 2010, pp 188–189. <https://doi.org/10.1126/science.1190094>.
- (347) Park, K. S.; Kim, M. Il; Cho, D. Y.; Park, H. G. Label-Free Colorimetric Detection of Nucleic Acids Based on Target-Induced Shielding against the Peroxidase-Mimicking Activity of Magnetic Nanoparticles. *Small* **2011**, 7 (11), 1521–1525. <https://doi.org/10.1002/smll.201001886>.
- (348) Luo, W.; Zhu, C.; Su, S.; Li, D.; He, Y.; Huang, Q.; Fan, C. Self-Catalyzed, Self-Limiting Growth of Glucose Oxidase-Mimicking Gold Nanoparticles. *ACS Nano* **2010**, 4 (12), 7451–7458. <https://doi.org/10.1021/nn102592h>.
- (349) Natalio, F.; André, R.; Hartog, A. F.; Stoll, B.; Jochum, K. P.; Wever, R.; Tremel, W. Vanadium Pentoxide Nanoparticles Mimic Vanadium Haloperoxidases and Thwart Biofilm Formation. *Nat. Nanotechnol.* **2012**, 7 (8), 530–535. <https://doi.org/10.1038/nnano.2012.91>.

- (350) Jv, Y.; Li, B.; Cao, R. Positively-Charged Gold Nanoparticles as Peroxidase Mimic and Their Application in Hydrogen Peroxide and Glucose Detection. *Chem. Commun.* **2010**, 46 (42), 8017–8019. <https://doi.org/10.1039/c0cc02698k>.
- (351) Song, Y.; Qu, K.; Zhao, C.; Ren, J.; Qu, X. Graphene Oxide: Intrinsic Peroxidase Catalytic Activity and Its Application to Glucose Detection. *Adv. Mater.* **2010**, 22 (19), 2206–2210. <https://doi.org/10.1002/adma.200903783>.
- (352) Song, Y.; Wang, X.; Zhao, C.; Qu, K.; Ren, J.; Qu, X. Label-Free Colorimetric Detection of Single Nucleotide Polymorphism by Using Single-Walled Carbon Nanotube Intrinsic Peroxidase-like Activity. *Chem. - A Eur. J.* **2010**, 16 (12), 3617–3621. <https://doi.org/10.1002/chem.200902643>.
- (353) Pengo, P.; Polizzi, S.; Pasquato, L.; Scrimin, P. Carboxylate-Imidazole Cooperativity in Dipeptide-Functionalized Gold Nanoparticles with Esterase-like Activity. *J. Am. Chem. Soc.* **2005**, 127 (6), 1616–1617. <https://doi.org/10.1021/ja043547c>.
- (354) Comotti, M.; Della Pina, C.; Matarrese, R.; Rossi, M. The Catalytic Activity of “Naked” Gold Particles. *Angew. Chemie - Int. Ed.* **2004**, 43 (43), 5812–5815. <https://doi.org/10.1002/anie.200460446>.
- (355) Zheng, X.; Liu, Q.; Jing, C.; Li, Y.; Li, D.; Luo, W.; Wen, Y.; He, Y.; Huang, Q.; Long, Y. T.; et al. Catalytic Gold Nanoparticles for Nanoplasmonic Detection of DNA Hybridization. *Angew. Chemie - Int. Ed.* **2011**, 50 (50), 11994–11998. <https://doi.org/10.1002/anie.201105121>.
- (356) Bonomi, R.; Selvestrel, F.; Lombardo, V.; Sissi, C.; Polizzi, S.; Mancin, F.; Tonellato, U.; Scrimin, P. Phosphate Diester and DNA Hydrolysis by a Multivalent, Nanoparticle-Based Catalyst. *J. Am. Chem. Soc.* **2008**, 130 (47), 15744–15745.

<https://doi.org/10.1021/ja801794t>.

- (357) Asati, A.; Santra, S.; Kaittanis, C.; Nath, S.; Perez, J. M. Oxidase-like Activity of Polymer-Coated Cerium Oxide Nanoparticles. *Angew. Chemie - Int. Ed.* **2009**, *48* (13), 2308–2312. <https://doi.org/10.1002/anie.200805279>.
- (358) Sun, X.; Guo, S.; Chung, C. S.; Zhu, W.; Sun, S. A Sensitive H₂O₂ Assay Based on Dumbbell-like PtPd-Fe₃O₄ Nanoparticles. *Adv. Mater.* **2013**, *25* (1), 132–136. <https://doi.org/10.1002/adma.201203218>.
- (359) Sun, X.; Guo, S.; Liu, Y.; Sun, S. Dumbbell-like PtPd-Fe₃O₄ Nanoparticles for Enhanced Electrochemical Detection of H₂O₂. *Nano Lett.* **2012**, *12* (9), 4859–4863. <https://doi.org/10.1021/nl302358e>.
- (360) Batteries, Rechargeable. **2001**, 463–483. <https://doi.org/10.1016/B0-08-043152-6/00092-9>.
- (361) Chauhan, M.; Reddy, K. P.; Gopinath, C. S.; Deka, S. Copper Cobalt Sulfide Nanosheets Realizing a Promising Electrocatalytic Oxygen Evolution Reaction. *ACS Catal.* **2017**, *7* (9), 5871–5879. <https://doi.org/10.1021/acscatal.7b01831>.
- (362) Nasiri, N.; Clarke, C. Nanostructured Gas Sensors for Medical and Health Applications: Low to High Dimensional Materials. *Biosensors* **2019**, *9* (1), 43. <https://doi.org/10.3390/bios9010043>.
- (363) Ye, X.; He, X.; Lei, Y.; Tang, J.; Yu, Y.; Shi, H.; Wang, K. One-Pot Synthesized Cu/Au/Pt Trimetallic Nanoparticles with Enhanced Catalytic and Plasmonic Properties as a Universal Platform for Biosensing and Cancer Theranostics. *Chem. Commun.* **2019**, *55* (16), 2321–2324. <https://doi.org/10.1039/c8cc10127b>.
- (364) Yang, H.; Bradley, S. J.; Wu, X.; Chan, A.; Waterhouse, G. I. N.; Nann, T.; Zhang, J.;

- Kruger, P. E.; Ma, S.; Telfer, S. G. General Synthetic Strategy for Libraries of Supported Multicomponent Metal Nanoparticles. *ACS Nano* **2018**, *12* (5), 4594–4604. <https://doi.org/10.1021/acsnano.8b01022>.
- (365) Pang, S. H.; Schoenbaum, C. A.; Schwartz, D. K.; Medlin, J. W. Directing Reaction Pathways by Catalyst Active-Site Selection Using Self-Assembled Monolayers. *Nat. Commun.* **2013**, *4* (1), 1–6. <https://doi.org/10.1038/ncomms3448>.
- (366) Chen, A.; Holt-Hindle, P. Platinum-Based Nanostructured Materials: Synthesis, Properties, and Applications. *Chem. Rev.* **2010**, *110* (6), 3767–3804. <https://doi.org/10.1021/cr9003902>.
- (367) Xu, Y.; Zhang, B. Recent Advances in Porous Pt-Based Nanostructures: Synthesis and Electrochemical Applications. *Chemical Society Reviews*. Royal Society of Chemistry April 21, 2014, pp 2439–2450. <https://doi.org/10.1039/c3cs60351b>.
- (368) Science crystallization microscopic interfacial phenomena | Materials science | Cambridge University Press <https://www.cambridge.org/gb/academic/subjects/engineering/materials-science/science-crystallization-microscopic-interfacial-phenomena?format=PB&isbn=9780521388276> (accessed Jul 26, 2020).
- (369) (No Title)
http://home.iitk.ac.in/~anandh/MSE694/Defect_structure_and_Mechanical_Behaviour_of_nanomaterials.pdf (accessed Jul 26, 2020).
- (370) Chen, C. D.; Cheng, S. F.; Chau, L. K.; Wang, C. R. C. Sensing Capability of the Localized Surface Plasmon Resonance of Gold Nanorods. *Biosens. Bioelectron.* **2007**, *22* (6), 926–932. <https://doi.org/10.1016/j.bios.2006.03.021>.
- (371) Liu, J. H.; Wang, A. Q.; Chi, Y. S.; Lin, H. P.; Mou, C. Y. Synergistic Effect in an Au-Ag

- Alloy Nanocatalyst: CO Oxidation. *J. Phys. Chem. B* **2005**, *109* (1), 40–43.
<https://doi.org/10.1021/jp044938g>.
- (372) Quiroz, J.; Barbosa, E. C. M.; Araujo, T. P.; Fiorio, J. L.; Wang, Y. C.; Zou, Y. C.; Mou, T.; Alves, T. V.; De Oliveira, D. C.; Wang, B.; et al. Controlling Reaction Selectivity over Hybrid Plasmonic Nanocatalysts. *Nano Lett.* **2018**, *18* (11), 7289–7297.
<https://doi.org/10.1021/acs.nanolett.8b03499>.
- (373) Pavliuk, M. V.; Fernandes, A. B.; Abdellah, M.; Fernandes, D. L. A.; Machado, C. O.; Rocha, I.; Hattori, Y.; Paun, C.; Bastos, E. L.; Sá, J. Nano-Hybrid Plasmonic Photocatalyst for Hydrogen Production at 20% Efficiency. *Sci. Rep.* **2017**, *7* (1), 1–9.
<https://doi.org/10.1038/s41598-017-09261-7>.
- (374) Ristig, S.; Prymak, O.; Loza, K.; Gocyla, M.; Meyer-Zaika, W.; Heggen, M.; Raabe, D.; Epple, M. Nanostructure of Wet-Chemically Prepared, Polymer-Stabilized Silver-Gold Nanoalloys (6 Nm) over the Entire Composition Range. *J. Mater. Chem. B* **2015**, *3* (23), 4654–4662. <https://doi.org/10.1039/c5tb00644a>.
- (375) Haruta, M.; Yamada, N.; Kobayashi, T.; Iijima, S. Gold Catalysts Prepared by Coprecipitation for Low-Temperature Oxidation of Hydrogen and of Carbon Monoxide. *J. Catal.* **1989**, *115* (2), 301–309. [https://doi.org/10.1016/0021-9517\(89\)90034-1](https://doi.org/10.1016/0021-9517(89)90034-1).
- (376) Takei, T.; Akita, T.; Nakamura, I.; Fujitani, T.; Okumura, M.; Okazaki, K.; Huang, J.; Ishida, T.; Haruta, M. Heterogeneous Catalysis by Gold. In *Advances in Catalysis*; Academic Press Inc., 2012; Vol. 55, pp 1–126. <https://doi.org/10.1016/B978-0-12-385516-9.00001-6>.
- (377) Bond, G. C.; Thompson, D. T. Gold-Catalysed Oxidation of Carbon Monoxide. *Gold Bull.* **2000**, *33* (2), 41–50. <https://doi.org/10.1007/BF03216579>.

- (378) Guzman, J.; Carrettin, S.; Corma, A. Spectroscopic Evidence for the Supply of Reactive Oxygen during CO Oxidation Catalyzed by Gold Supported on Nanocrystalline CeO₂. *J. Am. Chem. Soc.* **2005**, *127* (10), 3286–3287. <https://doi.org/10.1021/ja043752s>.
- (379) Boyd, D.; Golunski, S.; Hearne, G. R.; Magadzu, T.; Mallick, K.; Raphulu, M. C.; Venugopal, A.; Scurrall, M. S. Reductive Routes to Stabilized Nanogold and Relation to Catalysis by Supported Gold. *Appl. Catal. A Gen.* **2005**, *292* (1–2), 76–81. <https://doi.org/10.1016/j.apcata.2005.05.038>.
- (380) Lopez, N.; Janssens, T. V. W.; Clausen, B. S.; Xu, Y.; Mavrikakis, M.; Bligaard, T.; Nørskov, J. K. On the Origin of the Catalytic Activity of Gold Nanoparticles for Low-Temperature CO Oxidation. *J. Catal.* **2004**, *223* (1), 232–235. <https://doi.org/10.1016/j.jcat.2004.01.001>.
- (381) Mavrikakis, M.; Stoltze, P.; Nørskov, J. K. Making Gold Less Noble. *Catal. Letters* **2000**, *64* (2–4), 101–106. <https://doi.org/10.1023/A:1019028229377>.
- (382) Verdager-Casadevall, A.; Li, C. W.; Johansson, T. P.; Scott, S. B.; McKeown, J. T.; Kumar, M.; Stephens, I. E. L.; Kanan, M. W.; Chorkendorff, I. Probing the Active Surface Sites for CO Reduction on Oxide-Derived Copper Electrocatalysts. *J. Am. Chem. Soc.* **2015**, *137* (31), 9808–9811. <https://doi.org/10.1021/jacs.5b06227>.
- (383) An, K.; Somorjai, G. A. Nanocatalysis I: Synthesis of Metal and Bimetallic Nanoparticles and Porous Oxides and Their Catalytic Reaction Studies. *Catal. Letters* **2015**, *145* (1), 233–248. <https://doi.org/10.1007/s10562-014-1399-x>.
- (384) Gu, J.; Zhang, Y. W.; Tao, F. Shape Control of Bimetallic Nanocatalysts through Well-Designed Colloidal Chemistry Approaches. *Chem. Soc. Rev.* **2012**, *41* (24), 8050–8065. <https://doi.org/10.1039/c2cs35184f>.

- (385) Yu, W.; Porosoff, M. D.; Chen, J. G. Review of Pt-Based Bimetallic Catalysis: From Model Surfaces to Supported Catalysts. *Chemical Reviews*. American Chemical Society November 14, 2012, pp 5780–5817. <https://doi.org/10.1021/cr300096b>.
- (386) Lu, K. Stabilizing Nanostructures in Metals Using Grain and Twin Boundary Architectures. *Nature Reviews Materials*. Nature Publishing Group March 31, 2016, pp 1–13. <https://doi.org/10.1038/natrevmats.2016.19>.
- (387) Nørskov, J. K.; Abild-Pedersen, F.; Studt, F.; Bligaard, T. Density Functional Theory in Surface Chemistry and Catalysis. *Proceedings of the National Academy of Sciences of the United States of America*. National Academy of Sciences January 18, 2011, pp 937–943. <https://doi.org/10.1073/pnas.1006652108>.
- (388) Pchelintsev, N. A.; Vakurov, A.; Hays, H. H.; Millner, P. A. Thiols Deposition onto the Surface of Glassy Carbon Electrodes Mediated by Electrical Potential. *Electrochim. Acta* **2011**, 56 (6), 2696–2702. <https://doi.org/10.1016/j.electacta.2010.12.043>.
- (389) Momma, K.; Izumi, F. VESTA 3 for Three-Dimensional Visualization of Crystal, Volumetric and Morphology Data. *J. Appl. Crystallogr.* **2011**, 44 (6), 1272–1276. <https://doi.org/10.1107/S0021889811038970>.
- (390) Lehner, D.; Lindner, H.; Glatter, O. Determination of the Translational and Rotational Diffusion Coefficients of Rodlike Particles Using Depolarized Dynamic Light Scattering. *Langmuir* **2000**, 16 (4), 1689–1695. <https://doi.org/10.1021/la9910273>.
- (391) Zheng, T.; Bott, S.; Huo, Q. Techniques for Accurate Sizing of Gold Nanoparticles Using Dynamic Light Scattering with Particular Application to Chemical and Biological Sensing Based on Aggregate Formation. *ACS Appl. Mater. Interfaces* **2016**, 8 (33), 21585–21594. <https://doi.org/10.1021/acsami.6b06903>.

- (392) Glidden, M.; Muschol, M. Characterizing Gold Nanorods in Solution Using Depolarized Dynamic Light Scattering. *J. Phys. Chem. C* **2012**, *116* (14), 8128–8137. <https://doi.org/10.1021/jp211533d>.
- (393) Bhattacharjee, S. DLS and Zeta Potential - What They Are and What They Are Not? *Journal of Controlled Release*. Elsevier B.V. August 10, 2016, pp 337–351. <https://doi.org/10.1016/j.jconrel.2016.06.017>.
- (394) Delgado, A. V.; González-Caballero, F.; Hunter, R. J.; Koopal, L. K.; Lyklema, J. Measurement and Interpretation of Electrokinetic Phenomena: (IUPAC Technical Report). *Pure and Applied Chemistry*. De Gruyter October 1, 2005, pp 1753–1805. <https://doi.org/10.1351/pac200577101753>.
- (395) Bazylewski, P.; Divigalpitiya, R.; Fanchini, G. In Situ Raman Spectroscopy Distinguishes between Reversible and Irreversible Thiol Modifications in L-Cysteine. *RSC Adv.* **2017**, *7* (5), 2964–2970. <https://doi.org/10.1039/c6ra25879d>.
- (396) Lee, J. I.; Howard, S. M.; Kellar, J. J.; Cross, W.; Han, K. N. Electrochemical Interaction between Silver and Sulfur in Sodium Sulfide Solutions. *Metall. Mater. Trans. B Process Metall. Mater. Process. Sci.* **2001**, *32* (5), 895–901. <https://doi.org/10.1007/s11663-001-0075-x>.
- (397) Muhammed Shafi, P.; Chandra Bose, A. Impact of Crystalline Defects and Size on X-Ray Line Broadening: A Phenomenological Approach for Tetragonal SnO₂ Nanocrystals. *AIP Adv.* **2015**, *5* (5), 057137. <https://doi.org/10.1063/1.4921452>.
- (398) Bhattacharya, M.; Mandal, A. R.; Chakraborty, S. Das; Maiti, A.; Maity, A.; Kuznetsov, D. V.; Mondal, P.; Senapati, D. Direct Experimental Observation of Salt Induced Aspect Ratio Tunable PFPT Silver-Nanowire Formation: SERS-Based Ppt Level Hg₂⁺ Sensing

- from Ground Water. *RSC Adv.* **2016**, *6* (51), 45279–45289.
<https://doi.org/10.1039/c6ra02900k>.
- (399) Pakiari, A. H.; Jamshidi, Z. Nature and Strength of MS Bonds (M = Au, Ag, and Cu) in Binary Alloy Gold Clusters. *J. Phys. Chem. A* **2010**, *114* (34), 9212–9221.
<https://doi.org/10.1021/jp100423b>.
- (400) Yu, L.; Yan, Q.; Ruzsinszky, A. The Key Role of Antibonding Electron Transfer in Surface Chemisorption and Heterogeneous Catalysis. **2018**.
<https://doi.org/10.1103/PhysRevMaterials.3.092801>.
- (401) Institute of Medicine (US) Standing Committee on the Scientific Evaluation of Dietary Reference Intakes and its Panel on Folate, O. B. V. and C. *Dietary Reference Intakes for Thiamin, Riboflavin, Niacin, Vitamin B6, Folate, Vitamin B12, Pantothenic Acid, Biotin, and Choline*; National Academies Press, 1998. <https://doi.org/10.17226/6015>.
- (402) Sautin, Y. Y.; Johnson, R. J. Uric Acid: The Oxidant-Antioxidant Paradox. In *Nucleosides, Nucleotides and Nucleic Acids*; NIH Public Access, 2008; Vol. 27, pp 608–619. <https://doi.org/10.1080/15257770802138558>.
- (403) Randviir, E. P.; Banks, C. E. Analytical Methods for Quantifying Creatinine within Biological Media. *Sensors and Actuators, B: Chemical*. Elsevier July 5, 2013, pp 239–252. <https://doi.org/10.1016/j.snb.2013.03.103>.
- (404) Tang, X.; Liu, Y.; Hou, H.; You, T. A Nonenzymatic Sensor for Xanthine Based on Electrospun Carbon Nanofibers Modified Electrode. *Talanta* **2011**, *83* (5), 1410–1414.
<https://doi.org/10.1016/j.talanta.2010.11.019>.
- (405) Amiri-Aref, M.; Raoof, J. B.; Ojani, R. A Highly Sensitive Electrochemical Sensor for Simultaneous Voltammetric Determination of Noradrenaline, Acetaminophen, Xanthine

- and Caffeine Based on a Flavonoid Nanostructured Modified Glassy Carbon Electrode. *Sensors Actuators, B Chem.* **2014**, *192*, 634–641. <https://doi.org/10.1016/j.snb.2013.11.006>.
- (406) Liu, G.; Ma, W.; Luo, Y.; Sun, D.-M.; Shao, S. Simultaneous Determination of Uric Acid and Xanthine Using a Poly(Methylene Blue) and Electrochemically Reduced Graphene Oxide Composite Film Modified Electrode. **2014**. <https://doi.org/10.1155/2014/984314>.
- (407) Liu, L.; Mo, H.; Wei, S.; Raftery, D. Quantitative Analysis of Urea in Human Urine and Serum by ¹H Nuclear Magnetic Resonance. *Analyst* **2012**, *137* (3), 595–600. <https://doi.org/10.1039/c2an15780b>.
- (408) Carr, A.; Maggini, S. Vitamin C and Immune Function. *Nutrients* **2017**, *9* (11), 1211. <https://doi.org/10.3390/nu9111211>.
- (409) Kim, Y.; Na, D. H. Simultaneous Determination of Cysteamine and Cystamine in Cosmetics by Ion-Pairing Reversed-Phase High-Performance Liquid Chromatography. *Toxicol. Res.* **2019**, *35* (2), 161–165. <https://doi.org/10.5487/TR.2019.35.2.161>.
- (410) Kalmbach, R.; Paul, L.; Selhub, J. Determination of Unmetabolized Folic Acid in Human Plasma Using Affinity HPLC. In *American Journal of Clinical Nutrition*; Am J Clin Nutr, 2011; Vol. 94. <https://doi.org/10.3945/ajcn.111.013433>.
- (411) Kim, D. S.; Kang, E. S.; Baek, S.; Choo, S. S.; Chung, Y. H.; Lee, D.; Min, J.; Kim, T. H. Electrochemical Detection of Dopamine Using Periodic Cylindrical Gold Nanoelectrode Arrays. *Sci. Rep.* **2018**, *8* (1), 14049. <https://doi.org/10.1038/s41598-018-32477-0>.
- (412) Masri, M. F. Bin; Mantri, C. K.; Rathore, A. P. S.; St. John, A. L. Peripheral Serotonin Causes Dengue Virus-Induced Thrombocytopenia through 5HT₂ Receptors. *Blood* **2019**, *133* (21), 2325–2337. <https://doi.org/10.1182/blood-2018-08-869156>.

- (413) Shi, J.; Dong, B.; Mao, Y.; Guan, W.; Cao, J.; Zhu, R.; Wang, S. Review: Traumatic Brain Injury and Hyperglycemia, a Potentially Modifiable Risk Factor. *Oncotarget*. Impact Journals LLC 2016, pp 71052–71061. <https://doi.org/10.18632/oncotarget.11958>.
- (414) Leung, K. Y.; Mills, K.; Burren, K. A.; Copp, A. J.; Greene, N. D. E. Quantitative Analysis of Myo-Inositol in Urine, Blood and Nutritional Supplements by High-Performance Liquid Chromatography Tandem Mass Spectrometry. *J. Chromatogr. B Anal. Technol. Biomed. Life Sci.* **2011**, 879 (26), 2759–2763. <https://doi.org/10.1016/j.jchromb.2011.07.043>.
- (415) Kennedy, D. O. B Vitamins and the Brain: Mechanisms, Dose and Efficacy—A Review. *Nutrients*. MDPI AG January 27, 2016, p 68. <https://doi.org/10.3390/nu8020068>.
- (416) Per, H.; Arslan, D.; Gümüş, H.; Çoskun, A.; Kumandaş, S. Intracranial Hemorrhages and Late Hemorrhagic Disease Associated Cholestatic Liver Disease. *Neurol. Sci.* **2013**, 34 (1), 51–56. <https://doi.org/10.1007/s10072-012-0965-5>.
- (417) Wang, Y.; Su, H.; Gu, Y.; Song, X.; Zhao, J. Carcinogenicity of Chromium and Chemoprevention: A Brief Update. *OncoTargets and Therapy*. Dove Medical Press Ltd. August 16, 2017, pp 4065–4079. <https://doi.org/10.2147/OTT.S139262>.
- (418) Huwait, E. A.; Kumosani, T. A.; Moselhy, S. S.; Mosaoa, R. M.; Yaghmoor, S. S. Relationship between Soil Cobalt and Vitamin B¹² Levels in the Liver of Livestock in Saudi Arabia: Role of Competing Elements in Soils. *Afr. Health Sci.* **2015**, 15 (3), 993–1008. <https://doi.org/10.4314/ahs.v15i3.38>.
- (419) Abbaspour, N.; Hurrell, R.; Kelishadi, R. Review on Iron and Its Importance for Human Health. *Journal of Research in Medical Sciences*. Isfahan University of Medical Sciences(IUMS) 2014, pp 164–174.

- (420) Osredkar, J.; Sustar, N. Copper and Zinc, Biological Role and Significance of Copper/Zinc Imbalance. *J Clin. Toxicol Heavy Met. Toxic. Osredkar Sustar* **2011**, 3. <https://doi.org/10.4172/2161-0495.S3-001>.
- (421) Wani, A. L.; Ara, A.; Usmani, J. A. Lead Toxicity: A Review. *Interdisciplinary Toxicology. Slovak Toxicology Society* June 1, 2015, pp 55–64. <https://doi.org/10.1515/intox-2015-0009>.
- (422) Rice, K. M.; Walker, E. M.; Wu, M.; Gillette, C.; Blough, E. R. Environmental Mercury and Its Toxic Effects. *Journal of Preventive Medicine and Public Health. Korean Society for Preventive Medicine* 2014, pp 74–83. <https://doi.org/10.3961/jpmp.2014.47.2.74>.
- (423) Phillips, C. M.; Schreiter, E. R.; Guo, Y.; Wang, S. C.; Zamble, D. B.; Drennan, C. L. Structural Basis of the Metal Specificity for Nickel Regulatory Protein NikR. *Biochemistry* **2008**, 47 (7), 1938–1946. <https://doi.org/10.1021/bi702006h>.
- (424) Tuiskunen Bäck, A.; Lundkvist, Å. Dengue Viruses – an Overview. *Infect. Ecol. Epidemiol.* **2013**, 3 (1), 19839. <https://doi.org/10.3402/iee.v3i0.19839>.
- (425) *DENGUE GUIDELINES FOR DIAGNOSIS, TREATMENT, PREVENTION AND CONTROL TREATMENT, PREVENTION AND CONTROL TREATMENT, PREVENTION AND CONTROL.*
- (426) Bhatt, S.; Gething, P. W.; Brady, O. J.; Messina, J. P.; Farlow, A. W.; Moyes, C. L.; Drake, J. M.; Brownstein, J. S.; Hoen, A. G.; Sankoh, O.; et al. The Global Distribution and Burden of Dengue. *Nature* **2013**, 496 (7446), 504–507. <https://doi.org/10.1038/nature12060>.
- (427) Mustafa, M. S.; Rasotgi, V.; Jain, S.; Gupta, V. Discovery of Fifth Serotype of Dengue Virus (Denv-5): A New Public Health Dilemma in Dengue Control. *Medical Journal*

- Armed Forces India. Medical Journal Armed Forces India* 2015, pp 67–70.
<https://doi.org/10.1016/j.mjafi.2014.09.011>.
- (428) Rathore, A. P. S.; St John, A. L. Immune Responses to Dengue Virus in the Skin. *Open Biology*. Royal Society Publishing August 1, 2018. <https://doi.org/10.1098/rsob.180087>.
- (429) Hidari, K. I. P. J.; Suzuki, T. Dengue Virus Receptor. *Tropical Medicine and Health*. BioMed Central 2011, pp 37–43. <https://doi.org/10.2149/tmh.2011-S03>.
- (430) Perera, R.; Kuhn, R. J. Structural Proteomics of Dengue Virus. *Current Opinion in Microbiology*. NIH Public Access August 2008, pp 369–377.
<https://doi.org/10.1016/j.mib.2008.06.004>.
- (431) Idris, F.; Muharram, S. H.; Diah, S. Glycosylation of Dengue Virus Glycoproteins and Their Interactions with Carbohydrate Receptors: Possible Targets for Antiviral Therapy. *Archives of Virology*. Springer-Verlag Wien July 1, 2016, pp 1751–1760.
<https://doi.org/10.1007/s00705-016-2855-2>.
- (432) Novoa, R. R.; Calderita, G.; Arranz, R.; Fontana, J.; Granzow, H.; Risco, C. Virus Factories: Associations of Cell Organelles for Viral Replication and Morphogenesis. *Biol. Cell* **2005**, 97 (2), 147–172. <https://doi.org/10.1042/bc20040058>.
- (433) Normile, D. Surprising New Dengue Virus Throws a Spanner in Disease Control Efforts. *Science* (80-.). **2013**, 342 (6157).
- (434) Byk, L. A.; Gamarnik, A. V. Properties and Functions of the Dengue Virus Capsid Protein. *Annu. Rev. Virol.* **2016**, 3 (1), 263–281. <https://doi.org/10.1146/annurev-virology-110615-042334>.
- (435) Brooke, C. B. Biological Activities of “noninfectious” Influenza A Virus Particles. *Future Virology*. NIH Public Access January 2014, pp 41–51. <https://doi.org/10.2217/fvl.13.118>.

- (436) Halstead, S. B. Licensed Dengue Vaccine: Public Health Conundrum and Scientific Challenge. *American Journal of Tropical Medicine and Hygiene*. American Society of Tropical Medicine and Hygiene October 1, 2016, pp 741–745. <https://doi.org/10.4269/ajtmh.16-0222>.
- (437) Bruno, J. G.; Carrillo, M. P.; Richarte, A. M.; Phillips, T.; Andrews, C.; Lee, J. S. Development, Screening, and Analysis of DNA Aptamer Libraries Potentially Useful for Diagnosis and Passive Immunity of Arboviruses. *BMC Res. Notes* **2012**, 5 (1), 633. <https://doi.org/10.1186/1756-0500-5-633>.
- (438) Balmaseda, A.; Hammond, S. N.; Pérez, L.; Tellez, Y.; Saborío, S. I.; Mercado, J. C.; Cuadra, R.; Rocha, J.; Pérez, M. A.; Silva, S.; et al. Serotype-Specific Differences in Clinical Manifestations of Dengue. *Am. J. Trop. Med. Hyg.* **2006**, 74 (3), 449–456. <https://doi.org/10.4269/ajtmh.2006.74.449>.
- (439) Chan, K. S.; Chang, J. S.; Chang, K.; Lin, C. C.; Huang, J. H.; Lin, W. R.; Chen, T. C.; Hsieh, H. C.; Lin, S. H.; Lin, J. C.; et al. Effect of Serotypes on Clinical Manifestations of Dengue Fever in Adults. *J. Microbiol. Immunol. Infect.* **2009**, 42 (6), 471–478.
- (440) Gardella-Garcia, C. E.; Perez-Ramirez, G.; Navarrete-Espinosa, J.; Cisneros, A.; Jimenez-Rojas, F.; Ramírez-Palacios, L. R.; Rosado-Leon, R.; Camacho-Nuez, M.; Munoz, M. D. L. Specific Genetic Markers for Detecting Subtypes of Dengue Virus Serotype-2 in Isolates from the States of Oaxaca and Veracruz, Mexico. *BMC Microbiol.* **2008**, 8. <https://doi.org/10.1186/1471-2180-8-117>.
- (441) Fried, J. R.; Gibbons, R. V.; Kalayanarooj, S.; Thomas, S. J.; Srikiatkachorn, A.; Yoon, I. K.; Jarman, R. G.; Green, S.; Rothman, A. L.; Cummings, D. A. T. Serotype-Specific Differences in the Risk of Dengue Hemorrhagic Fever: An Analysis of Data Collected in

- Bangkok, Thailand from 1994 to 2006. *PLoS Negl. Trop. Dis.* **2010**, 4 (3). <https://doi.org/10.1371/journal.pntd.0000617>.
- (442) Raviprakash, K.; Sun, P.; Raviv, Y.; Luke, T.; Martin, N.; Kochel, T. Dengue Virus Photo-Inactivated in Presence of 1,5-Iodonaphthylazide (INA) or AMT, a Psoralen Compound (4'-Aminomethyl-Trioxsalen) Is Highly Immunogenic in Mice. *Hum. Vaccin. Immunother.* **2013**, 9 (11), 2336–2341. <https://doi.org/10.4161/hv.25602>.
- (443) Schneider, K.; Wronka-Edwards, L.; Leggett-Embrey, M.; Walker, E.; Sun, P.; Ondov, B.; Wyman, T. H.; Rosovitz, M. J.; Bohn, S. S.; Burans, J.; et al. Psoralen Inactivation of Viruses: A Process for the Safe Manipulation of Viral Antigen and Nucleic Acid. *Viruses* **2015**, 7 (11), 5875–5888. <https://doi.org/10.3390/v7112912>.
- (444) Ozaki, H.; Govorkova, E. A.; Li, C.; Xiong, X.; Webster, R. G.; Webby, R. J. Generation of High-Yielding Influenza A Viruses in African Green Monkey Kidney (Vero) Cells by Reverse Genetics. *J. Virol.* **2004**, 78 (4), 1851–1857. <https://doi.org/10.1128/jvi.78.4.1851-1857.2004>.
- (445) Maves, R. C.; Castillo Oré, R. M.; Porter, K. R.; Kochel, T. J. Immunogenicity of a Psoralen-Inactivated Dengue Virus Type 1 Vaccine Candidate in Mice. *Clin. Vaccine Immunol.* **2010**, 17 (2), 304–306. <https://doi.org/10.1128/CVI.00353-09>.
- (446) Ammerman, N. C.; Beier-Sexton, M.; Azad, A. F. Growth and Maintenance of Vero Cell Lines. *Current Protocols in Microbiology*. NIH Public Access 2008, p Appendix. <https://doi.org/10.1002/9780471729259.mca04es11>.
- (447) Raquin, V.; Wannagat, M.; Zouache, K.; Legras-Lachuer, C.; Moro, C. V.; Mavingui, P. Detection of Dengue Group Viruses by Fluorescence in Situ Hybridization. *Parasites and Vectors* **2012**, 5 (1). <https://doi.org/10.1186/1756-3305-5-243>.

- (448) Carter, J. R.; Balaraman, V.; Kucharski, C. A.; Fraser, T. S.; Fraser, M. J. A Novel Dengue Virus Detection Method That Couples DNzyme and Gold Nanoparticle Approaches. *Viol. J.* **2013**, *10*, 201–201. <https://doi.org/10.1186/1743-422X-10-201>.
- (449) Campbell, T. B.; Cech, T. R. Mutations in the Tetrahymena Ribozyme Internal Guide Sequence: Effects on Docking of the P1 Helix into the Catalytic Core and Correlation with Catalytic Activity. *Biochemistry* **1996**, *35* (35), 11493–11502. <https://doi.org/10.1021/bi960510z>.
- (450) Teoh, B. T.; Sam, S. S.; Tan, K. K.; Johari, J.; Danlami, M. B.; Hooi, P. S.; Md-Esa, R.; AbuBakar, S. Detection of Dengue Viruses Using Reverse Transcription-Loop-Mediated Isothermal Amplification. *BMC Infect. Dis.* **2013**, *13* (1). <https://doi.org/10.1186/1471-2334-13-387>.
- (451) Kim, J. G.; Baek, S. H.; Kim, S.; Kim, H. I.; Lee, S. W.; Phan, L. M. T.; Kailasa, S. K.; Park, T. J. Rapid Discriminative Detection of Dengue Viruses via Loop Mediated Isothermal Amplification. *Talanta* **2018**, *190*, 391–396. <https://doi.org/10.1016/j.talanta.2018.08.019>.
- (452) Wasik, D.; Mulchandani, A.; Yates, M. V. A Heparin-Functionalized Carbon Nanotube-Based Affinity Biosensor for Dengue Virus. *Biosens. Bioelectron.* **2017**, *91*, 811–816. <https://doi.org/10.1016/j.bios.2017.01.017>.
- (453) Falconar, A. K. I.; Romero-Vivas, C. M. E. A Simple, Inexpensive, Robust and Sensitive Dot-Blot Assay for Equal Detection of the Nonstructural-1 Glycoprotein of All Dengue Virus Serotypes. *Viol. J.* **2013**, *10*. <https://doi.org/10.1186/1743-422X-10-126>.
- (454) A method of layer-by-layer gold nanoparticle hybridization in a quartz crystal microbalance DNA sensing system used to detect dengue virus - IOPscience

- <https://iopscience.iop.org/article/10.1088/0957-4484/20/21/215501> (accessed Jul 27, 2020).
- (455) Hsu, I. H.; Chen, W. H.; Wu, T. K.; Sun, Y. C. Gold Nanoparticle-Based Inductively Coupled Plasma Mass Spectrometry Amplification and Magnetic Separation for the Sensitive Detection of a Virus-Specific RNA Sequence. *J. Chromatogr. A* **2011**, *1218* (14), 1795–1801. <https://doi.org/10.1016/j.chroma.2011.02.005>.
- (456) Basso, C. R.; Tozato, C. C.; Crulhas, B. P.; Castro, G. R.; Junior, J. P. A.; Pedrosa, V. A. An Easy Way to Detect Dengue Virus Using Nanoparticle-Antibody Conjugates. *Virology* **2018**, *513*, 85–90. <https://doi.org/10.1016/j.virol.2017.10.001>.
- (457) Brown, F. Review of Accidents Caused by Incomplete Inactivation of Viruses. *Dev. Biol. Stand.* **1993**, *81*, 103–107.
- (458) Zhang, J.; Liu, P.; Ma, H.; Ding, Y. Nanostructured Porous Gold for Methanol Electro-Oxidation. *J. Phys. Chem. C* **2007**, *111* (28), 10382–10388. <https://doi.org/10.1021/jp072333p>.
- (459) Etesami, M.; Mohamed, N. Electrooxidation of Ethylene Glycol Using Gold Nanoparticles Electrodeposited on Pencil Graphite in Alkaline Medium. *Sci. China Chem.* **2012**, *55* (2), 247–255. <https://doi.org/10.1007/s11426-011-4402-z>.
- (460) Gomes, J. F.; Gasparotto, L. H. S.; Tremiliosi-Filho, G. Glycerol Electro-Oxidation over Glassy-Carbon-Supported Au Nanoparticles: Direct Influence of the Carbon Support on the Electrode Catalytic Activity. *Phys. Chem. Chem. Phys.* **2013**, *15* (25), 10339–10349. <https://doi.org/10.1039/c3cp50280e>.
- (461) Al-Akraa, I. M.; Mohammad, A. M.; El-Deab, M. S.; El-Anadouli, B. E. Flower-Shaped Gold Nanoparticles: Preparation, Characterization, and Electrocatalytic Application. *Arab.*

- J. Chem.* **2017**, *10* (6), 877–884. <https://doi.org/10.1016/j.arabjc.2015.05.004>.
- (462) Lopez, N.; Nørskov, J. K. Catalytic CO Oxidation by a Gold Nanoparticle: A Density Functional Study. *J. Am. Chem. Soc.* **2002**, *124* (38), 11262–11263. <https://doi.org/10.1021/ja026998a>.
- (463) Tan, L.; Yang, N.; Huang, X.; Peng, L.; Tong, C.; Deng, M.; Tang, X.; Li, L.; Liao, Q.; Wei, Z. Synthesis of Ammonia: Via Electrochemical Nitrogen Reduction on High-Index Faceted Au Nanoparticles with a High Faradaic Efficiency. *Chem. Commun.* **2019**, *55* (96), 14482–14485. <https://doi.org/10.1039/c9cc06132k>.
- (464) Yang, X.; Kattel, S.; Senanayake, S. D.; Boscoboinik, J. A.; Nie, X.; Graciani, J.; Rodriguez, J. A.; Liu, P.; Stacchiola, D. J.; Chen, J. G. Low Pressure CO₂ Hydrogenation to Methanol over Gold Nanoparticles Activated on a CeO_x/TiO₂ Interface. *J. Am. Chem. Soc.* **2015**, *137* (32), 10104–10107. <https://doi.org/10.1021/jacs.5b06150>.
- (465) Njoki, P. N.; Roots, M. E. D.; Maye, M. M. The Surface Composition of Au/Ag Core/Alloy Nanoparticles Influences the Methanol Oxidation Reaction. *ACS Appl. Nano Mater.* **2018**, *1* (10), 5640–5645. <https://doi.org/10.1021/acsanm.8b01255>.
- (466) Kim, S. H. Nanoporous Gold Films as Catalyst. In *Catalytic Application of Nano-Gold Catalysts*; InTech, 2016. <https://doi.org/10.5772/64081>.
- (467) Yuan, Y.; Wang, Y.; Wang, M.; Liu, J.; Pei, C.; Liu, B.; Zhao, H.; Liu, S.; Yang, H. Effect of Unsaturated Sn Atoms on Gas-Sensing Property in Hydrogenated SnO₂ Nanocrystals and Sensing Mechanism. *Sci. Rep.* **2017**, *7* (1), 1–9. <https://doi.org/10.1038/s41598-017-00891-5>.
- (468) Iwasita, T.; Hoster, H.; John-Anacker, A.; Lin, W. F.; Vielstich, W. Methanol Oxidation on PtRu Electrodes. Influence of Surface Structure and Pt-Ru Atom Distribution.

- Langmuir* **2000**, *16* (2), 522–529. <https://doi.org/10.1021/la990594n>.
- (469) Bhatt, M. D.; Lee, G.; Lee, J. S. Screening of Oxygen-Reduction-Reaction-Efficient Electrocatalysts Based on Ag-M (M = 3d, 4d, and 5d Transition Metals) Nanoalloys: A Density Functional Theory Study. *Energy and Fuels* **2017**, *31* (2), 1874–1881. <https://doi.org/10.1021/acs.energyfuels.6b02991>.
- (470) Mori, Y.; Ono, T.; Miyahira, Y.; Nguyen, V. Q.; Matsui, T.; Ishihara, M. Antiviral Activity of Silver Nanoparticle/Chitosan Composites against H1N1 Influenza A Virus. *Nanoscale Res. Lett.* **2013**, *8* (1), 93. <https://doi.org/10.1186/1556-276x-8-93>.
- (471) Lara, H. H.; Ayala-Núñez, N. V.; Ixtapan-Turrent, L.; Rodríguez-Padilla, C. Mode of Antiviral Action of Silver Nanoparticles against HIV-1. *J. Nanobiotechnology* **2010**, *8* (1), 1. <https://doi.org/10.1186/1477-3155-8-1>.
- (472) Huy, T. Q.; Hien Thanh, N. T.; Thuy, N. T.; Chung, P. Van; Hung, P. N.; Le, A. T.; Hong Hanh, N. T. Cytotoxicity and Antiviral Activity of Electrochemical – Synthesized Silver Nanoparticles against Poliovirus. *J. Virol. Methods* **2017**, *241*, 52–57. <https://doi.org/10.1016/j.jviromet.2016.12.015>.
- (473) Singh, L.; Kruger, H. G.; Maguire, G. E. M.; Govender, T.; Parboosing, R. The Role of Nanotechnology in the Treatment of Viral Infections. *Ther. Adv. Infect. Dis.* **2017**, *4* (4), 105–131. <https://doi.org/10.1177/2049936117713593>.
- (474) Kettler, K.; Veltman, K.; van de Meent, D.; van Wezel, A.; Hendriks, A. J. Cellular Uptake of Nanoparticles as Determined by Particle Properties, Experimental Conditions, and Cell Type. *Environ. Toxicol. Chem.* **2014**, *33* (3), 481–492. <https://doi.org/10.1002/etc.2470.y>